4966

CONTENTS—*Continued from preceding page*

(Continued)

CONTENTS—*Continued from preceding page*

CONTENTS—*Continued from preceding page*

DANIEL W. MARTIN
1918−1999

As this issue goes to press, we must report with sadness the death on Thursday, 7 January, of Dr. Daniel W. Martin, our Editor-in-Chief since 1985. His funeral in Cincinnati, Ohio was attended by our President and Vice President. He will be truly missed by the Society both for the excellence of his many contributions, and for his friendship and thoughtfulness. He will be most remembered for, and was most passionate about, his job as Editor-in-Chief of the Acoustical Society of America. We extend our sympathy to Mrs. Martha Martin and the family.

An obituary will appear in a future issue of JASA and a memorial session is planned for the Fall 1999 meeting in Columbus.

SOUNDINGS

Section Editor: Richard Stern

This front section of the *Journal* includes acoustical news, views, reviews, and general tutorial or selected research articles chosen for wide acoustical interest and written for broad acoustical readership.

ACOUSTICAL NEWS—USA

Elaine Moran
Acoustical Society of America, 500 Sunnyside Boulevard, Woodbury, New York 11797

Editor's Note: Readers of this Journal are asked to submit news items on awards, appointments, and other activities about themselves or their colleagues. Deadline dates for news items and notices are 2 months prior to publication.

New Fellows of the Acoustical Society of America

Alastair Cowley—For contributions to self-noise reduction, bubble acoustics, and ambient noise discrimination.

Gary Weismer—For contributions to understanding disorders of speech motor control.

Mei Q. Wu—For contributions to the measurement and control of noise.

Rosalind Nissim retires

Rosalind Nissim, Chief Production Editor of the *Journal*, retired on 31 December 1998 after a 38-year career at the American Institute of Physics. At the Editorial Board meeting held in October 1998, ASA Editor-in-Chief Dan Martin presented a crystal clock engraved with the ASA logo to Roz in appreciation for her service to the *Journal* (see Fig. 1).

Mrs. Nissim has held the positions of Editorial Supervisor and Chief Production Editor in her 20 years of service to the *Journal*. She has frequently attended ASA meetings to participate in Editorial Board and Publication Policy Committee meetings. Rosalind has also worked on other ASA publications including the JASA 5-year Cumulative indexes, meeting programs, membership directories, and standards.

At a reception in honor of Rosalind's retirement, held at the AIP Woodbury Publishing Center, Rosalind was presented with a certificate from the Acoustical Society of America which read: ''The Executive Council presents this certificate to Rosalind Nissim, in grateful recognition of her dedicated service to The Journal of the Acoustical Society of America.''

The Society extends its best wishes to Rosalind Nissim on the occasion of her retirement.

FIG. 1. ASA Editor-in-Chief Dan Martin (l) presents crystal clock to Rosalind Nissim.

IEEE Honors Guillermo Gaunaurd

Guillermo C. Gaunaurd was elevated to the rank of Fellow of the Institute of Electrical and Electronic Engineers (IEEE) in November 1998.

The citation chosen for this distinction was: ''For contributions to the direct and inverse scattering interaction of acoustic, electromagnetic and elastic waves with matter.''

Dr. Gaunaurd, a Research Physicist at the Naval Surface Warfare Center, Carderock Division in W. Bethesda, MD is also a Fellow of the Acoustical Society of America, American Society of Mechanical Engineers and the Washington Academy of Sciences.

Position Open

Assistant Professor of Physics (Audio Technology): The Department of Physics invites applications for a tenure track faculty position beginning Fall 1999 at the Assistant Professor level. The Audio Technology program, located at the Physics Department, emphasizes the technology, systems, and components of the recording industry as well as the needs of the communication industry and performing arts. Responsibilities include teaching (Bachelor's level), research, student advising, and collaboration with the School of Communication and the Department of Performing Arts. The M.S. in Physics/Audio Technology is required and a Ph.D. is preferred. Candidates with research interests in applicable, modern high-tech areas are encouraged to apply. The Search Committee will begin reviewing applications on 1/15/99 and continue until the position is filled. Send letter of application, resume, and letters from three references to: Prof. Romeo Segnan, Chair, Faculty Search Committee, Department of Physics, American University, 4400 Massachusetts Avenue, NW, Washington, DC 20016-8058.

USA Meetings Calendar

Listed below is a summary of meetings related to acoustics to be held in the U.S. in the near future. The month/year notation refers to the issue in which a complete meeting announcement appeared.

1999

15–19 March   Joint meeting: 137th meeting of the Acoustical Society of America/2nd Convention of the European Acoustics Association: Forum Acusticum, integrating the 25th Anniversary DAGA conference, Berlin, Germany [Acoustical Society of America, 500 Sunnyside Blvd., Woodbury, NY 11797, Tel.: 516-576-2360; Fax: 516-576-2377; E-mail: asa@aip.org; WWW: asa.aip.org].

10–12 May   AIAA/CEAS Aeroacoustics Conference, Bellevue, WA [Belur Shivashankara, The Boeing Company, P.O. Box 3707, MS 67-ML, Seattle, WA 98124-2207; Tel.: 425-234-9551; Fax: 425-237-5247; E-mail: belun.n.shivashankara@boeing.com].

6–7 June   1999 SEM Spring Conference, Cincinnati, OH [Katherine M. Ramsay, Conference Manager, Society for Experimental Mechanics, Inc., 7 School St., Bethel, CT 06801; Tel.: 203-790-6373; Fax: 203-790-4472; E-mail: meetings@sem1.com].

27–30 June   ASME Mechanics and Materials Conference, Blacksburg, VA [Mrs. Norma Guynn, Dept. of Engineering Science and Mechanics, Virginia Tech, Blacksburg, VA 24061-0219; Fax: 540-231-4574; E-mail: nguynn@vt.edu; WWW: http://www.esm.vt.edu/mmconf/].

6–11 July   1999 Clarinetfest, Ostend, Belgium [International Clarinet Association, Keith Koons, Music Dept., Univ. of Central Florida, P.O. Box 161354, Orlando, FL 32816-1354].

7–10 Oct.   Symposium on Occupational Hearing Loss, Philadelphia, PA [American Institute for Voice and Ear Research, Attn: Barbara-Ruth Roberts, 1721 Pine St., Philadelphia, PA 19103, Tel.: 215-545-2068; Fax: 215-735-2725. Deadline for submission of abstracts: 1 May].

1–5 Nov.   138th meeting of the Acoustical Society of America, Columbus, OH [Acoustical Society of America, 500 Sunnyside Blvd., Woodbury, NY 11797, Tel.: 516-576-2360; Fax: 516-576-2377; E-mail: asa@aip.org; WWW: asa.aip.org].

2–4 Dec.   ACTIVE 99, Fort Lauderdale, FL [Institute of Noise Control Engineering, P.O. Box 3206 Arlington Branch, Poughkeepsie, NY 12603, Tel.: 914-462-4006; Fax: 914-463-0201; E-mail: INCEUSA@aol.com; /users.aol.com/inceusa/ince.html].

6–8 Dec.   INTER-NOISE 99, Fort Lauderdale, FL [Institute of Noise Control Engineering, P.O. Box 3206, Arlington Branch, Poughkeepsie, NY 12603, Tel.: 914-462-4006; Fax: 914-463-0201; E-mail: INCEUSA@aol.com; /users.aol.com/inceusa/ince.html].

OBITUARIES

This section of the Journal publishes obituaries concerning the death of Fellows of the Society and other acousticians eminent in the world of acoustics. When notified, the Editor-in-Chief solicits a summary of the person's life and contributions from an ASA member thoroughly familiar with the details, if possible. If a promised obituary is never received, a brief obituary notice may be published later.

Jon R. Sank • 1934–1998
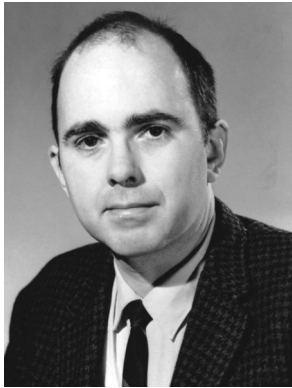
We regret to announce the passing of Jon R. Sank on 25 August 1998. Jon was well known to the audio community for his many articles on microphone evaluations and history. He wrote for and served with the editorial boards of numerous periodicals, including *Audio, Sound & Communications, Sound & Vibration, Aviation Consumer*, and the *Journal of the Audio Engineering Society*. As permanent Secretary/Treasurer, Jon was the motivating force behind the Delaware Valley chapter of the Acoustical Society of America for the last two decades. His professional affiliations included national memberships in ASA, AES, NCAC and Eta Kappa Nu. In 1997, at the 50th Anniversary meeting of the Audio Engineering Society, Jon was honored alongside such notables as Bob Moog and Guy Woodward, as a ''living legend'' for his pioneering work.

Jon received his BSEE from Drexel Institute in 1957 and took graduate studies at the University of Pennsylvania in Mathematics and Physics. He was hired by RCA where he worked in the acoustical laboratories in Camden, New Jersey from 1957 through 1970. His focus there was on network television-oriented microphones, such as the BK-12 lavaliere, for which he was the primary inventor. That transformerless microphone, which used a Swiss-style four-layer winding, was unique to the time because of its small size, and also because of its built-in predistortion to compensate for human throat characteristics. Jon was also the primary designer of the BK-11 bi-directional microphone, and the BK-15 miniature unidirectional ribbon microphone (which never actually went into production but was demonstrated successfully at an NAB show). The BK-14 and BK-16 were essentially also his, since they incorporated the BK-12 elements into a stick (hand-held) housing.

One of Jon's responsibilities at RCA was the factory follow for the manufacturing of earlier microphone products. He assured the quality of the BK-5's, 44's, and 77's that were still being produced. In later years, Jon used to fondly recall having performed repair work on Perry Como's road microphones. Those BK-10 mikes were actually based on Harry Olson's design that used two BK-5's together in a hypercartioid fashion to accommodate Como's soft voice. Sank made this concept work by painstakingly hand-tuning the two ribbons to the same frequency. Other famous clients included President Eisenhower, who required a special customized lectern, and President Johnson, who did not like multiple mikes showing although they were necessary for redundancy, so Jon placed two BK-613's inside of a BK-I body at the suggestion of RCA's marketing department. At RCA, Jon also helped maintain the anechoic, reverberant, and audiometric acoustical test facilities, and he developed phono pickups and amplifiers for broadcast and professional audio applications.

Following his departure from RCA, Jon worked for Control Data Corporation on noise control for tape and card equipment, and on the design of magnetic heads. He then moved on to establish his own business, Cross Country Consultants of Haddonfield, New Jersey. There, he primarily worked in noise abatement, employed as an expert by a wide variety of clients, including Goodrich, DuPont, M&M Mars, Sun Oil, OSHA, and various schools and municipalities. Of special interest to Jon was the sound work he did for radio and television stations, particularly WWDB-FM and WHYY-TV and FM, as he maintained a fondness for radio throughout his life. He was also recognized for his work in church sound reinforcement, with permanent installations at the Bryn Athyn Cathedral and the Haddonfield United Methodist Church, among others.

Jon's many hobbies included astronomy and aviation, where (as a private pilot) he tinkered with direction finding, altitude, and communications devices. He was also the proud owner of a vintage Plymouth Valiant, which he enjoyed maintaining. He designed and built the Greenmount Theater in the basement of his home, and would entertain friends with a monthly selection of classic movie presentations. There, during intermissions, many of the attendees would peruse his collection of RCA and other audio and early TV paraphernalia.

Through the years, many individuals and organizations relied on Jon's advice and knowledge. He was always happy to hear about an audio or acoustics-related question and no one was ever left empty-handed, he either had the answer, could point you to a reference on the subject, or would generously loan you a piece of equipment to use. John Wiggins, of Community Light & Sound, recalled how their early outdoor loudspeaker propagation measurement system had been calibrated by Jon using his own National Bureau of Standards Western Electric 640AA microphone and spherical sound source. In Jon's usual meticulous fashion, he thus assured the accuracy of Community's results. Jim Kogen remembered meeting Jon around 1964 when Shure & RCA worked together on a tone arm and some cartridges. He notes: ''Jon was an excellent engineer. I consulted with him many times. I always received an honest answer, even if it was one I didn't want to hear. He evaluated many of our company's products. If he said there was a problem, I knew we had a problem. If he said it was OK, I knew we had a winner. He never modified his view because we were ''old friends.'' As a friend, colleague, and resource to the audio and acoustics community, Jon Sank will be greatly missed.

Jon is survived by his wife, Sandra, his children, Sharon, Jon Paul, Stephen, and Jeffrey, and five grandchildren. Contributions can be made in his memory to the United Methodist Church of Haddonfield, NJ, for the Jon Sank Sound and Light Memorial Fund.

REBECCA MERCURI

Robin M. Towne • 1919–1998

Robin Max Towne, better known as ''Buzz'' to his many friends and colleagues, died of a stroke on 1 August 1998. Born in Seattle, Washington, Buzz attended public schools in Seattle and graduated from the University of Washington in 1941 with a Bachelor of Science degree in Chemistry. After a tour of duty in the Army during World War II as a commissioned officer, he returned to the University and earned a degree in Mechanical Engineering. He was a registered professional engineer in several states in the western U.S.

From 1947 to 1959 Buzz was a partner in the Mechanical Engineering firm of Stern & Towne. During this period Buzz became interested in solving noise and vibration problems in mechanical systems, an interest that evolved into the areas of architectural acoustics, sound reinforcement systems and environmental noise. These interests culminated in the formation of Robin M. Towne & Associates (later changed to Towne, Richards & Chaudiere), the first firm devoted exclusively to acoustical consulting in the Pacific Northwest. He served as president of the firm until his retirement in 1995.

During his consulting years, Buzz was involved in thousands of projects, covering all categories of building types and environmental noise sources. Notable projects demonstrating the diversity of his consulting efforts included research on the effects of freeway noise on hospitals, design of a permanent noise monitoring system for Seattle-Tacoma International Airport, a study of noise generation from large jet-powered electrical generator stations, and research on infrasound generation during the volcanic activity in the Mt. St. Helens area.

For many years Buzz taught acoustics in the College of Architecture at the University of Washington. He was the second President of the National Council of Acoustical Consultants during its critical formative years, 1963–64. Following his retirement, he organized a national effort to improve the acoustics of primary and secondary school classrooms, with particular emphasis on the special needs of students with hearing impairments and other learning disabilities.

Buzz's strong work ethic and commitment to engineering excellence made him a highly respected member of both the architectural design community, and the fraternity of his colleagues in the acoustical consulting profession. All who knew Buzz will remember him as a dedicated engineer and teacher, whose enthusiasm for acoustics affected all those fortunate enough to have been associated with him. The profession of acoustical consulting in the Pacific Northwest would never have achieved the stature that exists today without Buzz's efforts. We will miss him.

ROY RICHARDS

REVIEWS OF ACOUSTICAL PATENTS

Daniel W. Martin
7349 Clough Pike, Cincinnati, Ohio 45244

The purpose of these acoustical patent reviews is to provide enough information for a Journal reader to decide whether to seek more information from the patent itself. Any opinions expressed here are those of reviewers as individuals and are not legal opinions. Printed copies of United States Patents may be ordered at $3.00 each from the Commissioner of Patents and Trademarks, Washington, DC 20231.

Reviewers for this issue:

DAVID A. PREVES, *Micro-Tech, 3500 Holly Lane N., Plymouth, Minnesota 55447*
D. LLOYD RICE, *11222 Flatiron Drive, Lafayette, Colorado 80026*
KEVIN P. SHEPHERD, *M.S. 463, NASA Langley Research Center, Hampton, Virginia 23681*
ROBERT C. WAAG, *University of Rochester Medical Center, 601 Elmwood Avenue, Rochester, New York 14642*

5,758,486

43.28.Dm METHOD AND APPARATUS FOR KEEPING CLEAN AND/OR CLEANING A GAS TURBINE USING EXTERNALLY GENERATED SOUND

Mircea Fetescu, assignor to Asea Brown Bovari AG
2 June 1988 (Class 60/39.02); filed in Germany 9 December 1993

In a method for keeping clean and/or cleaning, during operation, the inner surfaces affected by deposits of a gas turbine including a turbine part **2** and an upstream compressor part **3**, the ''fouling'' is effectively prevented
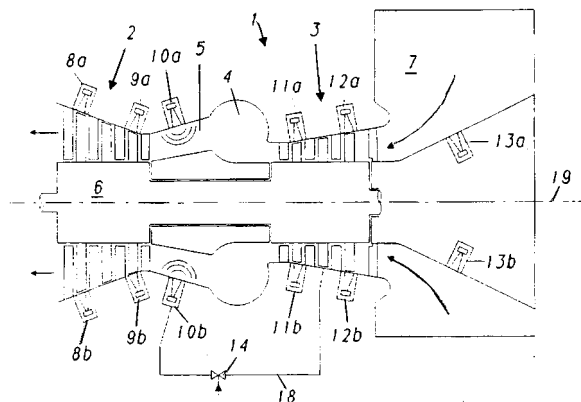
without disturbing the operating procedure by subjecting the inside of the gas turbine **1** to sound waves, at least at times, in particular from sound transmitters (**8a**,…,**13b**) arranged on the gas turbine **1**.—DWM

5,785,012

43.28.Py ACOUSTICALLY ENHANCED COMBUSTION METHOD AND APPARATUS

Jim Parsons *et al.*, assignors to BHA Group Holdings, Incorporated
28 July 1998 (Class 122/235.11); filed 15 December 1992

Combustion chamber **12** has an acoustic energy generator **34** posi-

tioned to transmit acoustic energy to excite particulate and gases flowing therein to increase the combustion efficiency.—DWM
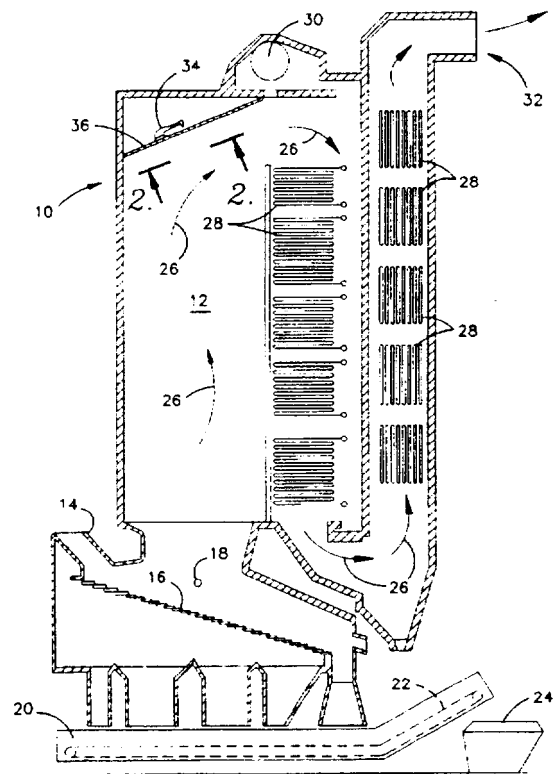
5,794,163

43.38.Si HEADSET FOR HANDS-FREE WIRELESS TELEPHONE

Graeme S. Paterson *et al.*, assignors to SpectraLink Corporation
11 August 1998 (Class 455/568); filed 27 July 1993

The patent addresses a number of problems relating to the use of a detachable, wireless headset which may be used in place of the normal cradle-type handset with a wireless telephone. A major concern is the use in such telephones of time-division rf switching, which causes an audible distortion in a wireless headset. A special noise reduction processor addresses this concern. Another such issue is solved by the ability of the base phone to detect when the headset is attached, allowing it to automatically adjust operating parameters such as ring volume.—DLR

5,765,322

43.40.Ph SEISMIC ISOLATION APPARATUS

Takaharu Kubo *et al.*, assignors to Bridgestone Corporation
16 June 1998 (Class 52/167.7); filed in Japan 29 September 1995

This seismic isolation device is multilayered, ''comprising a plurality of hard plates having rigidity and a plurality of soft plates having viscoelastic property which are arranged to form alternating layers between an upper flange and a lower flange.'' A massive structure such as a single family house is mounted on several of these devices, and is intended to have a seismic resonance frequency in the horizontal direction in the range of 0.8–2 Hz. It is intended to prevent seismic disturbance to the structure and to isolate the building from traffic vibration and shaking by the wind.—DWM
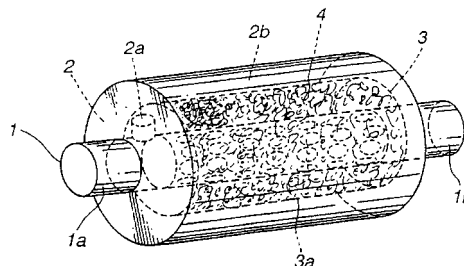
5,781,373

43.50.Gf ACOUSTIC NOISE REDUCTION SYSTEM FOR A DISK DRIVE

Nils Eric Larson and Ajit Fathailal Sancheti, assignors to Western Digital Corporation
14 July 1998 (Class 360/97.02); filed 14 March 1997

A computer disk drive usually includes a housing formed by fitting a cover to a base, thus creating a sealed chamber. This patent describes an arrangement in which a layer of viscoelastic material and a soft metal layer (aluminum foil) in the cover are used to damp vibration and hence reduce acoustic radiation.—KPS

5,782,082

43.50.Gf AIRCRAFT ENGINE ACOUSTIC LINER

William H. Hogeboom and Gerald W. Bielak, assignors to The Boeing Company
21 July 1998 (Class 60/226.1); filed 13 June 1996

An arrangement for acoustical liners within a turbofan aircraft engine is described. The lining consists of two types, both made of honeycomb core material sandwiched between a perforated face sheet and a solid backing surface. Alternating rings or annuluses of absorptive liner **51** and low resistance liner **53** are distributed in the engine exhaust duct. The low resistance
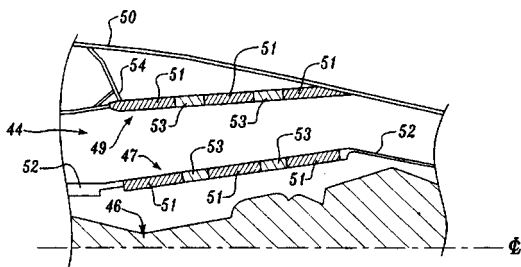
liner, having a low absorption coefficient (less than 0.5) and high ''percent open area'' face sheet, serves to scatter low-mode order noise into high-mode order noise which is subsequently absorbed by the absorptive liner. Geometrical arrangements and fabrication methods are described which enable the depth of the liner to be varied using a buried septum layer.—KPS

5,783,780

43.50.Gf SOUND ABSORPTION STRUCTURE

Kyoichi Watanabe and Kouichi Nemoto, assignors to Nissan Motor Company
21 July 1998 (Class 181/229); filed in Japan 27 November 1995

A muffler for the air intake of an internal combustion engine is described which attenuates sound over a wide frequency range. Duct **3** is of larger diameter than inlet **1** and serves as a cavity-type silencer to attenuate low-frequency sound. Sound absorption material **4** absorbs the medium and

high-frequency noise. The Helmholtz resonator **2** is tuned to absorb the sound that is amplified by the cavity silencer **3**. More than 40 geometrical variations are described, including acoustical performance of each for low, medium, and high frequencies.—KPS

5,783,782

43.50.Gf MULTI-CHAMBER MUFFLER WITH SELECTIVE SOUND ABSORBENT MATERIAL PLACEMENT

Dale E. Sterrett *et al.*, assignors to Tenneco Automotive Incorporated
21 July 1998 (Class 181/272); filed 29 October 1996

A muffler for the exhaust of an internal combustion engine is described which consists of an inlet **32** connected to an expansion chamber **20**. A pipe **40** and chamber **24** form a Helmholtz resonator. A second Helmholtz resonator is formed by the cavity **18** and the passageway **38**. These resona-

tors serve to attenuate the low-frequency sound. Exhaust gases flow though the perforated pipe **46** surrounded by sound absorbing material **64**, which serves to attenuate high-frequency sound. Guidance is provided on effective sizes for the various chambers and construction techniques.—KPS
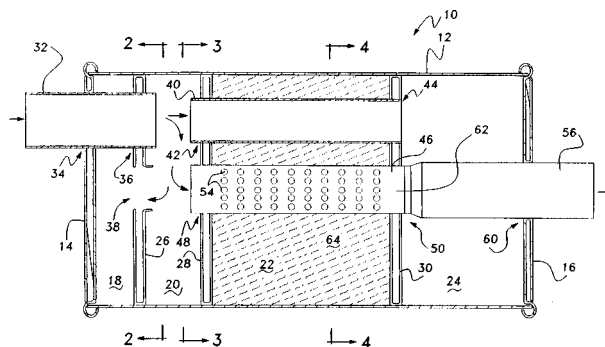
5,788,594

43.50.Gf LOW NOISE BELT FOR CONTINUOUSLY VARIABLE TRANSMISSION

Chung Seob Lee, assignor to Hyundai Motor Company
4 August 1998 (Class 474/244); filed in Korea 26 December 1996

This patent relates to continuously variable automatic transmissions which consist of two pulleys, one attached to an input shaft and the other attached to an output shaft, and connected by steel belts. A belt design is described which increases surface area for frictional contact, thus increasing the transmission of torque and reducing generated noise.—KPS

1446   J. Acoust. Soc. Am., Vol. 105, No. 3, March 1999

Reviews of Acoustical Patents   1446

5,791,141

43.50.Gf METHOD AND APPARATUS FOR REDUCTION OF FLUID BORNE NOISE IN HYDRAULIC SYSTEMS

Edward H. Phillips, assignor to Techno Corporation
11 August 1998 (Class 60/327); filed 18 June 1996

This patent addresses fluid borne noise found in automobile power steering systems. The hose assembly **10** consists of three volumetrically compliant components **12**, **14**, and **16**, and two inductive flow components
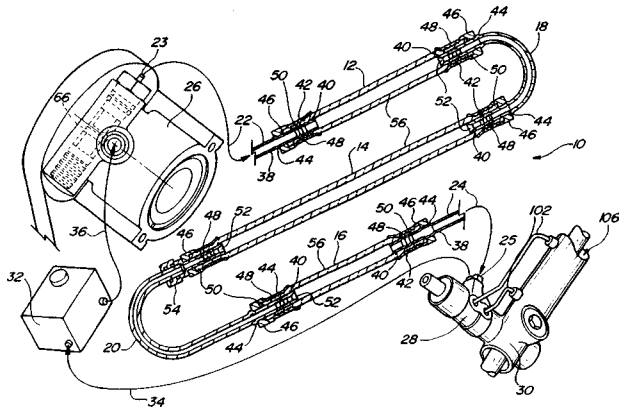
18 and **20**, thus forming a low-pass filter for the pressure fluctuations emanating from the hydraulic pump. Equivalent electrical circuit theory is used to illustrate the performance of the arrangement.—KPS

5,804,777

43.50.Gf SUCTION NOISE MUFFLER FOR HERMETIC COMPRESSOR

Tae Min Kim and Sang Min Lee, assignors to LG Electronics, Incorporated
8 September 1998 (Class 181/229); filed in Korea 2 November 1995

A suction noise muffler for a hermetic compressor is described which consists of an inlet **76** connected to multiple passageways **90**, **91**, **92**, and **93**.
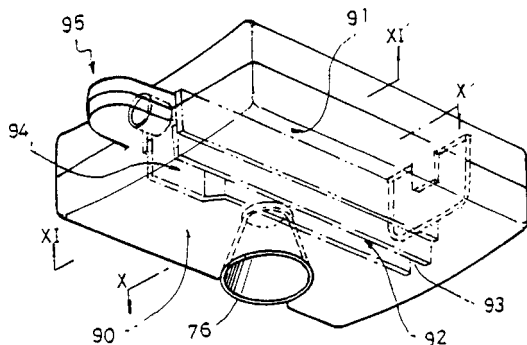
Refrigerant gas exits through **94**. Methods for design and construction of the upper and lower casings are given, as are several geometrical variations.—KPS

5,779,150

43.50.Lj AIRCRAFT ENGINE EJECTOR NOZZLE

Gary L. Lidstone et al., assignors to The Boeing Company
14 July 1998 (Class 239/265.13); filed 1 October 1996

An exhaust nozzle for a turbofan or turbojet aircraft engine is described in which the exhaust duct shape may be altered through geometrical changes. When noise suppression is required, such as at take-off, the con-

figuration consists of a plug assembly forming an ejector for entraining ambient air into the nozzle for reduced noise. During cruise conditions the plug is cleverly reconfigured to form a convergent/divergent nozzle for engine propulsion efficiency.—KPS

5,791,138

43.50.Lj TURBOFAN ENGINE WITH REDUCED NOISE

Robert W. Lillibridge et al., assignors to Burbank Aeronautical Corporation
11 August 1998 (Class 60/262); filed 11 January 1996

This hush kit for the Pratt and Whitney family of JT3D engines commonly found on Boeing 707 and Douglas DC8 aircraft is aimed at reducing noise while maintaining engine thrust levels. A common exit nozzle combines the fan by-pass air with the engine exhaust, and also includes a multi-lobed mixer. Various modifications to the engine inlet region are described which include an acoustically treated inlet center body, reduced clearance between the fan blades and the inlet duct, separation of the fan blade rows and the inlet guide vanes, and the application of acoustical treatment to the duct wall.—KPS

5,800,336

43.66.Ts ADVANCED DESIGNS OF FLOATING MASS TRANSDUCERS

Geoffrey Ball et al., assignors to Symphonix Devices, Incorporated
1 September 1998 (Class 600/25); filed 3 January 1996

The patent describes magnetic and piezoelectric transducers whose vibrations are ultimately conducted to the inner ear. In response to a signal representing sound waves, the vibrations produced by the floating mass relative to a counterblock inside the transducer are transmitted via a me-

chanical connection to the transducer housing. The transducers may be attached to an ossicle in the middle ear or mounted externally on the wearer's skull or teeth.—DAP
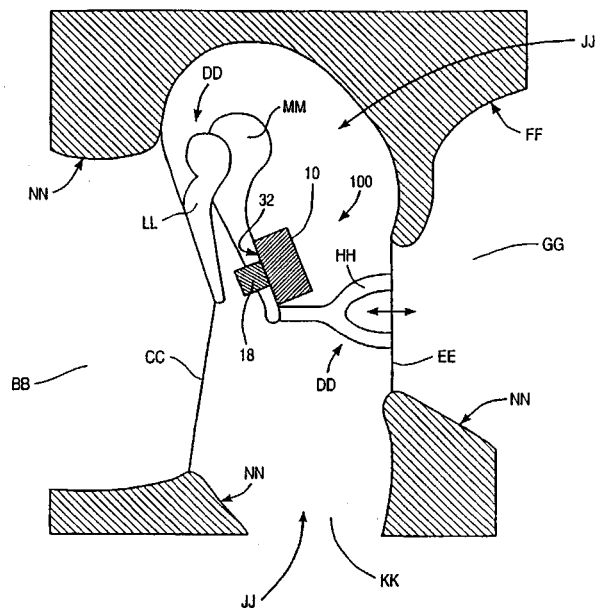
5,800,475

43.66.Ts HEARING AID INCLUDING COCHLEAR IMPLANT

Fardeau Michel Gustave Jules, assignor to Bertin & Cie
1 September 1998 (Class 607/57); filed 29 May 1996

A microphone transduces the acoustical energy in incoming sounds into an electrical output that is split up into several frequency bands. The time distribution of the instantaneous energy in each band is determined with wavelet analysis. After further customized processing, the resulting output is sent via inductive coupling in cyclical order to an implanted multi-electrode array.—DAP

5,802,183

43.66.Ts BTE ASSISTIVE LISTENING RECEIVER WITH INTERCHANGEABLE CRYSTALS

Tom Scheller *et al.*, assignors to Telex Communications, Incorporated
1 September 1998 (Class 381/69); filed 6 December 1995

An rf-based assistive listening device is housed in a behind-the-ear hearing aid case with transducers, amplification stages and controls typically utilized in hearing aids. The rf signal is mixed with the acoustic signal
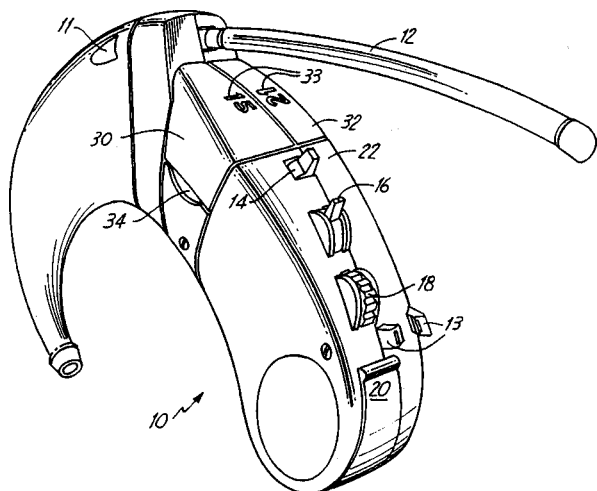
sensed by the hearing aid microphone in a ratio determined by the amount of noise in the listening environment. Crystals may be easily removed by the wearer and others inserted to alter the carrier frequency of the receiver.—DAP

5,812,680

43.66.Ts HEARING AID APPARATUS

Douglas Glendon, North Reading, MA
22 September 1998 (Class 381/69); filed 8 July 1996

Details are given for an earring-style air conduction hearing aid in which the ear canal remains substantially unoccluded. The microphone, amplifier and receiver are packaged in a housing that is attached to the earlobe, and amplified sound is conducted to the ear canal via a detachable tubing that terminates in a partial earmold. Acoustic feedback problems are said to be avoided by the relatively large distance between microphone and sound outlet in the ear canal.—DAP

5,811,681

43.66.Yw MULTIMEDIA FEATURE FOR DIAGNOSTIC INSTRUMENTATION

Leroy Brown and Jack Foreman, assignors to Finnigan Corporation
22 September 1998 (Class 73/585); filed 29 April 1996

This patent describes a digitally based automatic audiometer in which the device automatically switches the output between test tones and sounds signaling the beginning or end of a test or a test error. The device is distinguished from a conventional audiometer by inclusion of a multi-media computer for generating audio messages and visual images.—DAP

5,794,203

43.70.Dn BIOFEEDBACK SYSTEM FOR SPEECH DISORDERS

Thomas David Kehoe, Monte Sereno, CA
11 August 1998 (Class 704/271); filed 22 March 1994

Several forms of feedback of altered speech have been shown to help a disfluent speaker to overcome the disability. This is particularly true in the case of stuttering, where delayed feedback, pitch alteration, and other modifications have been shown to help. This patented therapeutic biometric system monitors and detects the onset of a speech disorder such as stuttering. The patient's speech is then altered (for example) by pitch lowering and played back on earphones. Lasting effects are predicted even though the introduction indicates that this is unlikely in most cases.—DLR

5,757,939

43.72.Ew METHOD FOR DEMONSTRATING SOUND QUALITY DIFFERENCES BETWEEN AUDIO SAMPLES

Lee Begeja *et al.*, assignors to Lucent Technologies, Incorporated
26 May 1998 (Class 381/98); filed 22 December 1994

This method arises from the need to show a distinct difference between a ''good'' sound and a degraded sound in a broadcast such as a television sound track. An obvious way to degrade a sound was by reducing the loudness, but the broadcast system dynamic range compression nullified
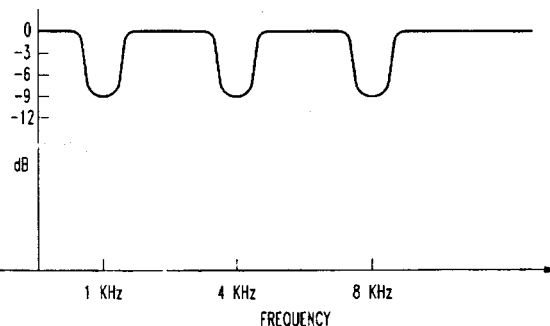
the difference. The problem was solved by notch filtering at selected mid-range frequencies to make a ''bad'' signal which remained bad as broadcast.—DLR

5,787,389

43.72.Gy SPEECH ENCODER WITH FEATURES EXTRACTED FROM CURRENT AND PREVIOUS FRAMES

Shin-Ichi Taumi and Kazunori Ozawa, assignors to NEC Corporation

28 July 1998 (Class 704/219); filed in Japan 17 January 1995

It is desirable to reduce the signal delay imposed by a speech coding system. However, as the analysis frame duration is shortened, short-term variations in speech characteristics interfere with the coding accuracy. This vocoder uses a relatively short frame time of 5 ms. Each frame is perceptually weighted and a set of features is extracted. Past frames are then used to smooth the feature patterns before coding parameters such as frame voicing are extracted.—DLR

5,787,392

43.72.Gy SPEECH SIGNAL PROCESSING CIRCUIT AND METHOD FOR DECODING A CODED SPEECH SIGNAL BY CONTROLLING OPERATION OF A BAND SYNTHESIS FILTER

Hideto Takano and Yoshitaka Shibuya, assignors to NEC Corporation

28 July 1998 (Class 704/230); filed in Japan 30 March 1995

Digital television and its related audio signals are compressed by the relatively complex MPEG system. This MPEG speech decoder achieves a reduction in the processing delay time affecting the speech output, allowing a processed audio track to be synchronized to a video track in real time. The method of speed-up involves a change in the handling of samples being buffered between the inverse quantization and quadrature conversion stages.—DLR

5,797,119

43.72.Gy COMB FILTER SPEECH CODING WITH PRESELECTED EXCITATION CODE VECTORS

Kazunori Ozawa, assignor to NEC Corporation

18 August 1998 (Class 704/223); filed in Japan 29 July 1993

The patent describes a method for improving the quality of a code-excited (CELP) vocoder by using a comb filter to ''precondition'' the excitation waveforms based on the pitch interval. The improvement is most noticeable for female speech, for which the shorter period begins to interfere with the spectral shape. A first order comb filter uses a short codebook excitation pattern and repeats that pattern with reduced gain at the pitch interval, producing good quality excitation with a considerably smaller codebook.—DLR

5,797,121

43.72.Gy METHOD AND APPARATUS FOR IMPLEMENTING VECTOR QUANTIZATION OF SPEECH PARAMETERS

Bruce Alan Fette and Shirley Hsiao-Mei Lee, assignors to Motorola, Incorporated

18 August 1998 (Class 704/230); filed 26 December 1995

The vocoder described here uses vector quantization of the spectral vector rather than the more commonly applied VQ of the excitation. The coefficients of the initially extracted spectral vector are scalar quantized according to the statistics of the codebook contents. This scalar quantization thus provides a set of index values used by specialized hardware to search the spectral codebook.—DLR

5,787,398

43.72.Ja APPARATUS FOR SYNTHESIZING SPEECH BY VARYING PITCH

Andrew Lowry, assignor to British Telecommunications PLC

28 July 1998 (Class 704/268); filed in European Patent Office 18 March 1994

The patent describes a method of varying the pitch in a text-to-speech synthesizer. An excitation component extracted from spoken voiced sounds is modified using an arrangement of multiple, narrow windows. The result-

ing windowed excitation fragments are moved forward or backward in time, then again added to produce a new synthetic excitation with a modified pitch.—DLR
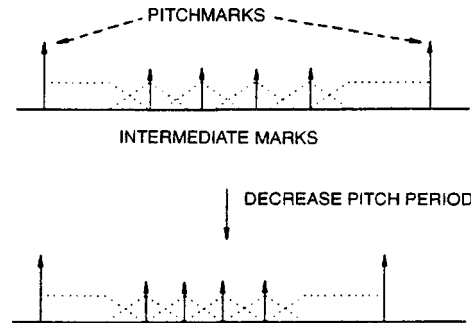
5,787,394

43.72.Ne STATE-DEPENDENT SPEAKER CLUSTERING FOR SPEAKER ADAPTATION

Lalit Rai Bahl *et al.*, assignors to International Business Machines Corporation

28 July 1998 (Class 704/238); filed 13 December 1995

The patent describes a method by which a speaker-independent speech recognizer adapts during usage to a particular speaker's voice characteristics. During training by multiple speakers, separate records are maintained of each speaker's patterns in the acoustic–phonetic classification space. When a new person uses the system, that speaker's patterns are ranked by scores with the training patterns in each subspace, forming a new acoustic model for that speaker.—DLR

5,787,395

43.72.Ne WORD AND PATTERN RECOGNITION THROUGH OVERLAPPING HIERARCHICAL TREE DEFINED BY RELATIONAL FEATURES

Katsuki Minamino, assignor to Sony Corporation

28 July 1998 (Class 704/255); filed in Japan 19 July 1995

A strategy is described for speeding up the computation of word matching in a speech recognizer. Said to be applicable to a phonetic segmentation type of recognizer, the method is more easily understood with respect to an isolated word recognizer. Preliminary scores are computed by
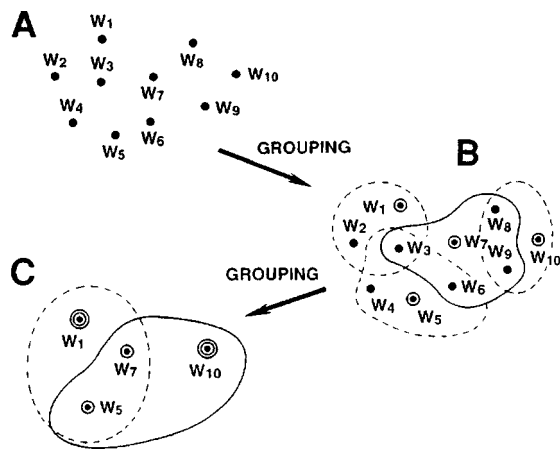
matching a new input item against each of a small set of standard reference items. The resulting scores are used to bound the space searched during a full word match.—DLR

5,787,396

43.72.Ne SPEECH RECOGNITION METHOD

Yasuhiro Komori *et al.*, assignors to Canon Kabushiki Kaisha
28 July 1998 (Class 704/256); filed in Japan 7 October 1994

Improved speech recognition decoding with hidden Markov models (HMMs) is possible by using mixtures of multiple probability density functions. However, this results in large increases in decoding time. This pat-

ented method begins with single-density HMMs, then uses the resulting recognition scores to limit the search using HMMs with multiple density functions.—DLR
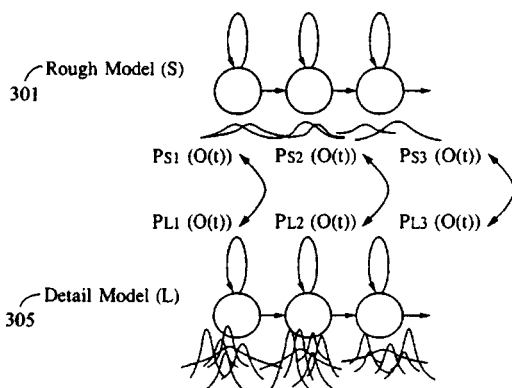
5,794,190

43.72.Ne SPEECH PATTERN RECOGNITION USING PATTERN RECOGNIZERS AND CLASSIFIERS

Robert Linggard *et al.*, assignors to British Telecommunications Public Limited Company
11 August 1998 (Class 704/232); filed in the United Kingdom 26 April 1990

This speech recognition system uses a type of neural network consisting of three layers of weighted summing nodes for word or utterance decoding. The input layer is presented with matching scores obtained from a
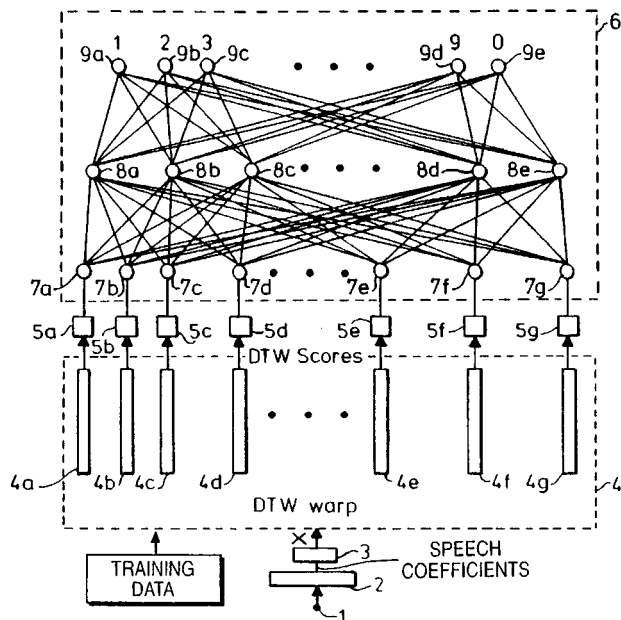
dynamic time warp acoustic alignment. An advantage is cited in that there is no step of preselecting only the highest scores, but rather all scores are considered as valid net inputs.—DLR

5,794,192

43.72.Ne SELF-LEARNING SPEAKER ADAPTATION BASED ON SPECTRAL BIAS SOURCE DECOMPOSITION, USING VERY SHORT CALIBRATION SPEECH

Yunxin Zhao, assignor to Panasonic Technologies, Incorporated
11 August 1998 (Class 704/244); filed 29 April 1993

A method is presented for adapting a speech recognizer to the voice and speech characteristics of a given speaker. A two-stage strategy involves adjusting the acoustic features to normalize the spectral bias patterns and adaptation of the HMM mixture density structures according to observed phonological conditions in the speech signal.—DLR

5,794,197

43.72.Ne SENONE TREE REPRESENTATION AND EVALUATION

Finelo A. Alleva *et al.*, assignors to Microsoft Corporation
11 August 1998 (Class 704/255); filed 21 January 1994

This speech recognizer is said to offer improved performance by the use of a tree representing triphone combinations of phonetic segments classified from the input feature vectors. The tree is built up using information on neighboring segments such that, if a particular triphone is not present in the training data, a close approximation is nevertheless available by traversing the tree. The tree outputs are recognized by a typical HMM decoder.—DLR

5,794,198

43.72.Ne PATTERN RECOGNITION METHOD

Satoshi Takahashi and Shigeki Sagayama, assignors to Nippon Telegraph and Telephone Corporation
11 August 1998 (Class 704/256); filed in Japan 28 October 1994

This novel method of representing the state probability distributions in a hidden Markov model speech recognizer reduces the number of distributions needed without degrading recognition performance. The method con-

sists of tying the distributions on many levels, including individual feature values, feature vector sets, and mixture density models. The tying saves memory space by not storing all of the distributions and saves computation because a tied state, once computed for a given input, need not be recomputed whenever its tied pair occurs.—DLR

5,797,116

43.72.Ne METHOD AND APPARATUS FOR RECOGNIZING PREVIOUSLY UNRECOGNIZED SPEECH BY REQUESTING A PREDICTED-CATEGORY-RELATED DOMAIN-DICTIONARY-LINKING WORD

Masayuki Yamada *et al.*, assignors to Canon Kabushiki Kaisha
18 August 1998 (Class 704/10); filed in Japan 16 June 1993

Perhaps representing an interesting step toward general free-form speech recognition, this system gleans information from any recognized words or phrases surrounding an unrecognized item. Additional information
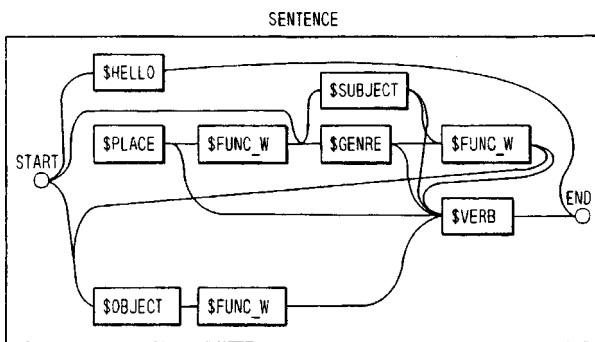
gathered from the context is used to select one or more additional dictionaries. The previously unknown fragment is then re-evaluated using another dictionary until a satisfactory match is obtained.—DLR

5,797,123

43.72.Ne METHOD OF KEY-PHASE DETECTION AND VERIFICATION FOR FLEXIBLE SPEECH UNDERSTANDING

Wu Chou *et al.*, assignors to Lucent Technologies, Incorporated
18 August 1998 (Class 704/256); filed 1 October 1996

The hyphenated word in the title of this patent should read ''key-phrase.'' Akin to a key-word recognizer, the patented system finds specific target phrases embedded within unrecognized speech. In a first pass, phrases are detected by matching against a set of active subgrammars. Initially
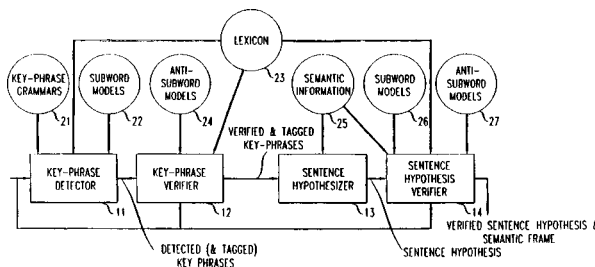
promising phrases are comfirmed by a second decoding pass. The various recognized phrases are then combined using task-specific semantic constraints into complete, meaningful utterances.—DLR

5,780,759

43.75.Bc METHOD FOR PITCH RECOGNITION, IN PARTICULAR FOR MUSICAL INSTRUMENTS WHICH ARE EXCITED BY PLUCKING OR STRIKING

Andreas Szalay, assignor to Blue Chip Music GmbH and to Yamaha Corporation
14 July 1998 (Class 84/454); filed in Germany 12 January 1995

The frequency of a tone produced by a musical instrument has often been obtained by measuring its counterpart, the period of one complex vibration. When the waveform is highly complex with numerous zero crossings within a single waveform, reliable measurement is difficult because a choice must be made among the zero crossings for the measurement. In this patent ''to this end, the magnitude of the gradient of the signal waveform is in each case determined in the region of its zero crossings, and the magnitude of the gradient is used as an assessment criterion for the selection of the zero crossings to be evaluated.''—DWM

5,800,356

43.80.Vj ULTRASONIC DIAGNOSTIC IMAGING SYSTEM WITH DOPPLER ASSISTED TRACKING OF TISSUE MOTION

Alline Laure Criton and Thanasis Loupas, assignors to Advanced Technology Laboratories, Incorporated
1 September 1998 (Class 600/441); filed 29 May 1997

A user identified tissue boundary such as a heart wall is traced and tracked using velocity information derived from the tissue boundary.—RCW

5,800,357

43.80.Vj ULTRASOUND DOPPLER POWER IMAGING SYSTEM FOR DISTINGUISHING TISSUE BLOOD FLOW FROM CHAMBER BLOOD FLOW

Jerome F. Witt and Patrick G. Rafter, assignors to Hewlett-Packard Company
1 September 1998 (Class 600/455); filed 24 December 1996

Ultrasonic echos are processed by two filters. One filter passes echo signals that represent a velocity higher than those in the cardiac wall while
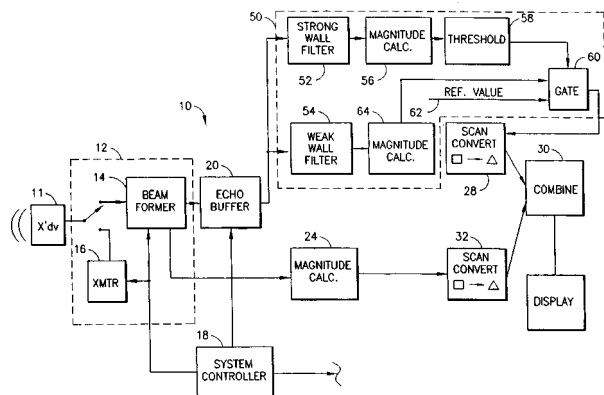
another filter partially inhibits echo signals from low-velocity structures. The filter outputs are used to show echo signals that exceed a threshold.—RCW

43.80.Vj ULTRASONIC DIVERSION OF MICROAIR IN BLOOD

Michael R. Van Driel _et al._, assignors to Medtronic, Incorporated
22 September 1998 (Class 73/19.02); filed 29 April 1997

Microbubbles of air in a blood stream are diverted into a chamber by ultrasonic energy. The diverted bubbles are then collected in a blood filled,
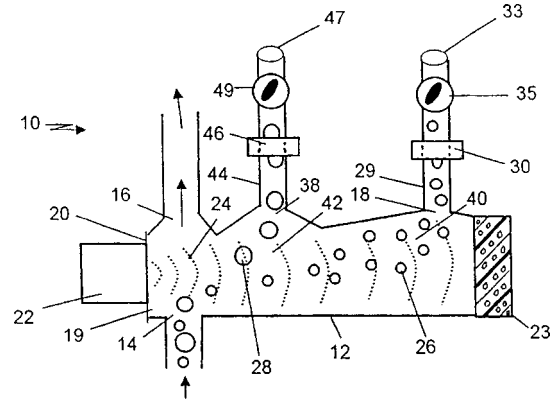
stasis column in which they can be counted. Bubbles of different sizes can be separated by use of multiple stasis columns.—RCW

43.80.Vj UNDERSAMPLED OMNIDIRECTIONAL ULTRASONIC FLOW DETECTOR

Peter G. Webb and Hewlett E. Melton, Jr., assignors Hewlett-Packard Company
1 September 1998 (Class 600/454); filed 31 March 1997

The time between any two pulses in this system is greater than the largest dimension of the range cell divided by the slowest velocity of motion in that range cell. A temporal variation between the envelopes of the pulses is then determined to detect motion in the range cell. Application of this process throughout a field of view can produce images that depict regions of motion.—RCW

FORUM

Report of the 1995/96 F. V. Hunt Fellowship
[43.05.Pc, 43.35.Wa]

Robin Cleveland

Boston University, College of Engineering, Department of Aerospace and Mechanical Engineering, 110 Cummington Street, Boston, Massachusetts 02215

In August of 1995 I left the sunshine of Austin, Texas and was enveloped by the gray of Seattle. As the eighteenth F. V. Hunt Postdoctoral Fellow I went to work with Professor Lawrence Crum at Applied Physics Laboratory (APL) at The University of Washington. My task was to carry out research in extracorporeal shock wave lithotripsy (ESWL)— the medical procedure whereby shock waves are used to break up kidney stones. This is a fascinating topic because, despite the fact that lithotripsy has been successfully used in the hospitals for more than 15 years, the mechanisms which lead to stone destruction and collateral tissue damage are not understood. Crum's group at APL are involved in a collaborative lithotripsy project with Indiana University Medical School and CalTech and in addition have research ties with the Nonlinear Acoustics Group at Moscow State University (MSU) headed by Oleg Rudenko.

The original goal of my fellowship was to model the propagation of lithotripsy shock waves through tissue. In the process of modeling a clinical lithotripter we discovered some interesting nonlinear effects in the propagation in water that had not been discussed before. I also collaborated with researchers from MSU on the propagation of shock waves in relaxing fluids. The numerical work resulted in a manuscript and two presentations.[1–3]

As my tenure progressed I became more involved in experiments. The biologists in Indianapolis investigate the effects of shock waves on *in vitro* cells. The cells are typically placed in a plastic vial before treatment and the effect of the vial on shock waves was not known. We carried out experiments in vials and found that the round ends associated with certain vials led to refraction of the shock waves. The results led to a publication and two presentations.[4–6]

At this point my focus turned once again to the pressure wave inside the body. Some miniature PVDF membrane hydrophones (about the size of a quarter) were constructed to measure shock waves. In collaboration with the group at In-dianapolis, the hydrophones were surgically implanted inside a pig and shock waves were measured around the kidney. The results showed that the shape of the *in vivo* shock wave was similar in nature to that measured in water; however the amplitude was reduced by about 30% and the rise time of the shock wave increased to 100 ns. The results were in fair agreement with the calculations that had been performed. The work was reported in a publication and at two conferences.[7–9]

Meanwhile back in Seattle I installed a research lithotripter in APL with characteristics similar to that of the clinical machine in Indianapolis. Larry Crum's enthusiasm for cavitation is infectious and towards the end of my Hunt year the research progressed in that direction. Visits by Oleg Sapozhnikov from MSU led to the development of a cavitation detection new tool for lithotripsy.[10]

During my tenure as Hunt Fellow I was appointed to the Technical committees of Biomedical Ultrasound/Bioresponse to Vibration (formerly Bioresponse to Vibration) and Physical Acoustics. Following my Hunt year I was appointed as a full-time researcher at APL and continued work in lithotripsy with a growing emphasis on cavitation. Eventually, two fruitful years of research, and many splendid weekends spent in the mountains, were brought to an end in the autumn of 1997 when I became a member of the faculty of the Department of Aerospace and Mechanical Engineering at Boston University.

[1] M. A. Averkiou and R. O. Cleveland, ''Time domain numerical modeling of an electrohydraulic lithotripter,'' submitted to J. Acoust. Soc. Am.

[2] M. A. Averkiou, R. O. Cleveland, and R. A. Roy, ''The small-amplitude, continuous wave reflected field produced by a spherical source placed at the focus of an ellipsoidal reflector,'' J. Acoust. Soc. Am. **100**, 2748(A) (1996).

[3] O. A. Sapozhnikov, V. G. Andreev, V. A. Khokhlova, Y. A. Pischal'nikov, and R. O. Cleveland, ''Propagation of intense acoustic pulses with shocks in relaxing fluids,'' J. Acoust. Soc. Am. **100**, 2591(A) (1996).

[4] R. O. Cleveland, J. A. McAteer, S. P. Andreoli, and L. A. Crum, ''Effect of polypropylene vials on shock waves,'' Ultrasound Med. Biol. **23**, 939–952 (1997).

[5] R. O. Cleveland, M. A. Averkiou, L. A. Crum, and J. A. McAteer, ''Measurements of the effect of polypropylene vials on ultrasound propagation,'' J. Acoust. Soc. Am. **99**, 2478(A) (1996).

[6] J. A. McAteer, S. P. Andreoli, A. P. Evan, D. D. Denman, C. Mallett, R. O. Cleveland, M. A. Averkiou, L. A. Crum, J. E. Lingeman, and D. Lifshitz, ''Shock wave lithotripsy: A demonstration of experimental methods for *in vitro* shock wave exposure and analysis of cell injury,'' J. Acoust. Soc. Am. **99**, 2527(A) (1996).

[7] R. O. Cleveland, D. A. Lifshitz, B. A. Connors, A. P. Evan, L. R. Willis,

and L. A. Crum, ''*In vivo* pressure measurement of lithotripsy shock waves,'' Ultrasound Med. Biol. **24**, 293–306 (1998).

[8] R. O. Cleveland, L. A. Crum, D. A. Lifshitz, B. A. Connors, and A. P. Evan, ''*In vivo* measurements of lithotripsy shock waves in pigs,'' J. Acoust. Soc. Am. **100**, 2617(A) (1996).

[9] A. P. Evan, D. A. Lifshitz, B. A. Connors, L. R. Willis, J. E. Lingeman, R. O. Cleveland, and L. A. Crum, ''*In vivo* measurements of lithotripsy shock waves in pigs,'' in 14th World Congress of Endourology and SWL, Melbourne, Victoria, Australia (1996).

[10] R. O. Cleveland and O. A. Sapozhnikov, ''Localized detection of cavitation generated by lithotripsy shock waves,'' J. Acoust. Soc. Am. **101**, 3139(A) (1997).

Acoustics of children's speech: Developmental changes of temporal and spectral parameters[a]

Sungbok Lee,[b] Alexandros Potamianos, and Shrikanth Narayanan
AT&T Labs–Research, 180 Park Avenue, Florham Park, New Jersey 07932-0971

Changes in magnitude and variability of duration, fundamental frequency, formant frequencies, and spectral envelope of children's speech are investigated as a function of age and gender using data obtained from 436 children, ages 5 to 17 years, and 56 adults. The results confirm that the reduction in magnitude and within-subject variability of both temporal and spectral acoustic parameters with age is a major trend associated with speech development in normal children. Between ages 9 and 12, both magnitude and variability of segmental durations decrease significantly and rapidly, converging to adult levels around age 12. Within-subject fundamental frequency and formant-frequency variability, however, may reach adult range about 2 or 3 years later. Differentiation of male and female fundamental frequency and formant frequency patterns begins at around age 11, becoming fully established around age 15. During that time period, changes in vowel formant frequencies of male speakers is approximately linear with age, while such a linear trend is less obvious for female speakers. These results support the hypothesis of uniform axial growth of the vocal tract for male speakers. The study also shows evidence for an apparent *overshoot* in acoustic parameter values, somewhere between ages 13 and 15, before converging to the canonical levels for adults. For instance, teenagers around age 14 differ from adults in that, on average, they show shorter segmental durations and exhibit less within-subject variability in durations, fundamental frequency, and spectral envelope measures. © *1999 Acoustical Society of America.* [S0001-4966(99)03202-6]

PACS numbers: 43.10.Ln, 43.70.Ep [AL]

INTRODUCTION

In speech-development research, it is important to know how acoustic parameters of speech such as fundamental frequency, formant frequencies, and segmental durations vary as a function of age and gender, and at what age the magnitude and variability of acoustic parameters begin to exhibit adult-like patterns. When properly interpreted, such chronological knowledge of speech acoustics could provide insights into the underlying development of speech organs and speech-motor control in children, and help in creating an accurate developmental model of the vocal tract (cf. Goldstein, 1980). Previous studies have shown that children's speech, compared to adults' speech, exhibits higher pitch and formant frequencies, longer segmental durations, and greater temporal and spectral variability (Eguchi and Hirsh, 1969; Kent, 1976; Kent and Forner, 1980; Smith, 1978, 1992; Smith *et al.*, 1995; Hillenbrand *et al.*, 1995). However, due to inadequate data in terms of either the total number of subjects or the age range of the subjects, these studies provide only limited information on the acoustic patterns of speech from early childhood through adulthood. A more chronologically detailed acoustic database obtained from a larger number of subjects with a wider age range is needed in order to better understand developmental acoustic patterns in

children's speech and their relation to the underlying anatomical and neuromuscular development. This study represents an effort in that direction.

The study is also motivated by speech applications such as automatic speech/speaker recognition and speech synthesis. In recent years, the problem of automatic recognition of children's speech has gained attention (Palethorpe *et al.*, 1996; Potamianos *et al.*, 1997). Potamianos *et al.* (1997) have shown that the performance of a hidden Markov model (HMM) speech-recognition system trained on adults' speech degrades substantially when tested on the speech of children age 12 and younger. In addition to the acoustic differences between children's and adults' speech, the acoustic variability inherent in children's speech contributes to the degradation in recognition performance as demonstrated by the results of Palethorpe *et al.* (1996): Performance in classification of vowels produced by children of 5 years of age is much worse than for that of adults (60%–65% vowel-classification accuracy for children versus over 90% for adults). Chronologically detailed acoustic data obtained from a large number of speakers can be helpful in devising strategies for dealing with the acoustic mismatch between different age groups.

This paper reports on a set of temporal and acoustic parameters measured from a speech database recently collected from 436 subjects ages 5 through 18 and from 56 adults (Miller *et al.*, 1996). For vowels, magnitude and variability of durations, fundamental frequency ($F0$), and the first three formant frequencies ($F1-F3$) as well as spectral-envelope variability are measured and analyzed as a function of age and gender. Duration magnitude and variability are

---

TABLE I. Distribution of subjects by age (in years) and gender.

Age	5	6	7	8	9	10	11	12	13	14	15	16	17	18	5–18	25–50
Male	19	11	11	25	23	25	24	22	16	11	11	11	10	10	229	29
Female	13	16	24	11	25	14	19	21	13	10	11	11	9	10	207	27
Total	32	27	35	36	48	39	43	43	29	21	22	22	19	20	436	56

also measured for the fricative /s/ as well as for the recitation of sentence-length utterances. Results and findings are presented with a focus on age- and gender-dependent acoustic changes occurring during the course of speech development. The paper is organized as follows: In Sec. I, the database used in the current study is described. In Sec. II, procedures used for acoustic measurements and statistical analyses are described. Results are presented in Sec. III, followed by a discussion in Sec. IV.

I. SPEECH DATABASE

The database analyzed in this study was collected from 436 children, ages 5 through 18 with a resolution of 1 year of age, and from 56 adult speakers (ages 25–50). The data collection was a joint effort of Southwestern Bell Technology Resources and the Central Institute for the Deaf (CID), and was carried out over a period of approximately 6 months. The recording site was located in the St. Louis Science Center (Missouri), a popular attraction among children, which enabled easy recruitment of subjects. The distribution of subjects by age and gender is shown in Table I. Among the 492 subjects, 316 were born and raised in the two Midwestern states of Missouri and Illinois.

The speech material consisted of ten monophthongal and five diphthongal vowels in American English and five phonetically rich meaningful sentences (the diphthongs are not analyzed in this paper). Target words for the ten monophthongs analyzed in this study were *bead* (/IY/), *bit* (/IH/), *bet* (/EH/), *bat* (/AE/), *pot* (/AA/), *ball* (/AO/), *but* (/AH/), *put* (/UH/), *boot* (/UW/), and *bird* (/ER/). The target words were produced in the carrier sentence ''I say uh --- again'' except for children of ages 5 and 6, who produced target words in isolation. A schwa-like sound [uh] was used as an attempt to make subjects maintain a neutral vocal tract before producing target words. The five sentences were: (1) ''He has a blue pen.'' (2) ''I am tall.'' (3) ''She needs strawberry jam on her toast.'' (4) ''Chuck seems thirsty after the race.'' (5) ''Did you like the zoo this spring?''

Recordings were made in a sound-treated booth located inside a glass-panel enclosure, using a high-fidelity microphone (Bruel & Kjaer model #4179) connected to a real-time waveform digitizer with 20-kHz sampling rate and 16-bit resolution. The target utterances were presented on a computer monitor *twice* in random order. No specific instructions were given to the subjects regarding the manner of production. Prior to the recording session, any target utterances that the speakers (mostly 5- and 6-year-olds) had difficulty reading were identified and elicited through imitation of a sample prerecorded by a female speech pathologist.

After the data collection, each waveform file was manually examined by listening to the recorded speech. Waveform files that were truncated or of very low recording quality were marked as ''chopped'' or ''bad'' and are excluded from this study. From the initial 24 630 waveform files, 24 152 files were judged to be good and were included in the database.

II. SPEECH ANALYSIS

A. Preprocessing of the database

In order to process the large number of speech samples, an automatic procedure was utilized for the necessary phoneme-level segmentation of each utterance. The AT&T hidden Markov model recognition engine (Ljolje and Riley, 1991) was used for the purpose. Specifically, a set of hidden Markov models (HMMs) of phonemes trained from adult speakers was used to obtain initial phonemic segmentation of the present children's database. Next, in order to minimize the initial phonemic-alignment error due to acoustic differences between adults' and children's speech, the initially segmented children's speech was used to retrain the HMMs. Finally, the database was resegmented using the retrained HMMs.

For each utterance, the automatic segmentation procedure produced a label file in which the beginning and the end of each phoneme and pause period were time-marked, according to the entry time to the first state and the exit time from the last state, respectively, of the corresponding HMM phoneme unit. Time marks have a 10-ms resolution, or uncertainty, which is half the length of the analysis window.

In order to examine the accuracy of the automatic segmentation procedure, durations of 160 vowel utterances from 16 randomly selected subjects of ages 5, 8, 11, and adults were manually measured. Mean segmentation difference between the automatically computed and the manually measured values was -17.5 ms with a standard deviation of 37.0 ms. As indicated by the negative mean difference, vowel durations were somewhat underestimated by the automatic segmentation procedure. However, no appreciable age-dependent trend was found in the mean segmentation difference across the four age groups investigated. Hence, age-dependent duration *trends* in the postsegmentation data are preserved even though duration *values* may be somewhat smaller. It should however be noted that second-order statistics of duration measurements will be noisy (as indicated by the high variance in the manual versus automatic segmentation differences) and should be interpreted with caution. Erroneous segmentation will have minimal effect on the statistics of $F0$ and formant frequency values since comparative

analyses used global median values for each token, as discussed in the next section.

B. Duration

Durations of the ten monophthongal vowels, the fricative portion of /s/ in the carrier sentence ("I [s]ay–"), and the five sentences were measured from the corresponding label files produced by the automatic segmentation procedure. Since each of the sentences was of different length, the sentence durations were normalized with respect to the corresponding mean sentence duration of adult male speakers.

Since the automatic segmentation procedure sometimes erroneously yielded excessively short or long vowel and /s/ durations, a crude effort was made to minimize the inclusion of such outliers using duration histograms. First, vowels with duration less than 80 ms were discarded along with their pair (i.e., repetitions of the same vowel by the same subject). Among the initial 9424 tokens on which durations were successfully measured, 4404 vowel pairs (8808 tokens) were included in the data set. It was noted that correlation of durations between the first and second productions was somewhat weak ($r=0.69$). Next, when difference in duration between two repetitions of the same vowel by the same speaker was greater than 160 ms, that vowel pair was also discarded. This yielded 3793 vowel pairs (7586 tokens) with substantially enhanced correlation ($r=0.83$). These 3793 vowels pairs are analyzed in the current study.[1] In the case of /s/, tokens with duration smaller than 90 ms or larger than 250 ms were discarded. Further, only /s/ tokens collected from subjects with at least 30 repetitions were included in the analysis. Out of the initial 16 897 /s/ tokens from 431 subjects, 15 592 tokens from 396 subjects were included in the final data set.

Duration data were organized by vowel, age, and gender group and analyzed using the SPSS statistical software package. Between- and within-subject variability and group means were estimated and group mean comparisons were performed.

C. Fundamental and formant frequencies

The fundamental frequency ($F0$) and the first three formant frequencies ($F1-F3$) of the ten monophthongs were estimated using the automatic $F0$ and formant-tracking program in the ESPS signal-processing package by Entropic Research Laboratory. The software utilizes a dynamic programming technique to select the best pitch and formant tracks from raw pitch and formant estimates (Secrest and Doddington, 1983). Each speech waveform was downsampled to 12 kHz and processed using a 12-ms Hamming window with 5-ms window update, a first-difference pre-emphasis factor of 0.94, and a 12th-order linear-prediction analysis. The resulting raw $F0$ and formant tracks were smoothed using a 3-point median filter. Global median values of the entire tracks were computed and used as the representative $F0$ and formant frequencies for the tracks.

The performance of the automatic program was evaluated using hand-measured pitch and formant values of 96 randomly selected vocalic segments from 16 subjects ages 5, 8, 11, and adults. The manual estimation was done as follows: (1) three 20-ms segments were selected around the steady-state portion of each vocalic segment, (2) the pitch and formants of each segment were measured by visual inspection of the corresponding discrete Fourier transform (DFT) spectrum, spectrogram, and the locations of formant peaks in the linear predictive (LP) spectral envelope, and (3) the hand-measured values of pitch and formants were averaged over the three subsegments. The manually estimated $F0$ and formant frequencies were compared to the automatically computed ones. Mean differences (standard deviation) between the automatically and manually estimated values in Hz were 7.6 (23.8) for $F0$, 43.6 (87.2) for $F1$, 92.4 (183.8) for $F2$, and 193.1 (400.7) for $F3$.

The automatic formant-tracking program yielded reasonable estimates of the first formant frequency in most cases. $F2$ and $F3$, however, were often inaccurate for vowels produced by young children due to poor spectral resolution at high frequencies (partially caused by wider harmonic spacing and breathy voicing), spurious spectral peaks, and formant-track merging. In such cases, manual estimation of formants from the speech spectrogram was also difficult. Therefore, in order to minimize statistical biases due to erroneously estimated formant frequencies, the raw formant data were refined using the following procedure: the initial formant data of all subjects were grouped according to vowel, age, and gender (10 vowels×15 age groups×2 genders). Next, two two-sigma ellipses were computed from ($F1,F2$) and ($F2,F3$) data sets, respectively, and data points that fell outside the region of either ellipse were removed. After the removal of the outliers, the mean and standard deviation were computed and each data file was visually examined: Whenever one of the $F1-F3$ values was subjectively judged to be too low or too high, the corresponding formant set was discarded. From the initial set of 9424 vowel tokens, 7631 tokens of the first three formant frequencies were included in the final data set analyzed in this study.[2] Despite our efforts to remove erroneous formant values, it is possible that the refined formant-data set still includes some underestimated $F2$ and $F3$ values, especially for children ages 7 and lower.

Pitch tracking by the automatic program was fairly reliable across age and gender except for occasional pitch-halving. The large s.d. (23.8 Hz) of the mean difference between the automatically and manually measured $F0$ data is mostly due to such occurrences. Inclusion of such erroneous $F0$ data was minimized using the two-sigma ellipse method described above applied to individual $F0$ data.

The $F0$ and formant data sets were organized by vowel, age, and gender and analyzed using the SPSS software package. Group means, between- and within-subject variations were estimated. For the computation of within-subject variation of formant frequencies, formant data of only matched vowel pairs (3265 pairs) were considered. In addition, between- and within-subject coefficients of variation (COV) were computed by taking the ratio of s.d. to the corresponding mean. The COV has been used by Eguchi and Hirsh (1969) to minimize a possible positive correlation between magnitude and variability.

D. Spectral-envelope variability

Spectral distance measures using a set of cepstrum coefficients derived from a log-spectral envelope representation are widely used in automatic speech recognition (Rabiner and Juang, 1993). In this paper, two spectral-envelope variability measures are computed from the cepstrum coefficients: (1) spectral distance between two repetitions of the same target vowel, and (2) spectral distance between the first- and second-half portions of vocalic segments including transitional regions from (to) the preceding (following) consonants. The former is compared with the within-subject formant variability in order to test whether the age-dependent reduction of the formant variability is a general phenomenon associated with speech development (Eguchi and Hirsh, 1969). The latter is interpreted as a measure of spectral movement, or transition, inside a vowel. An implicit assumption is that a greater difference in the underlying articulatory configuration between two vocalic segments induces a greater distance between the corresponding spectral envelopes.

The spectral envelope of a given vocalic segment was computed using a mel-frequency filterbank of 29 frequency bands spanning 100 to 6000 Hz (Davis and Mermelstein, 1980). The 12 cepstrum coefficients were computed from the log-spectral envelope using the inverse cosine transform. The distance between two speech segments was computed by first computing the average short-time cepstrum vector for each of the segments using a 20-ms window, and then taking the Euclidean distance between the two average cepstrum vectors. The zeroth-order cepstral coefficient (energy term) was not considered in the spectral distance computation since it does not affect the shape of the spectral envelope.

III. RESULTS

A. Phoneme and sentence durations

1. Vowel durations

Since it was found that the effect of gender on vowel duration is not significant, durations averaged across all vowels and subjects in each age group are shown in Fig. 1(a). Error bars denote between-subject variations. Effect of age is significant [$F(14,3778) = 36.2$, $p < 0.005$].

Multiple *a priori* comparisons (Bonferroni test with significance level 0.05) show that the groups of age 5 (279 ms) and age 6 (264 ms) exhibit significantly longer averaged vowel durations than older age groups. This may be partially due to the difference in the mode of speech elicitation, since the two age groups produced target words in isolation. The multiple comparisons also show that the reduction of vowel duration from age 10 (199 ms) to age 12 (178 ms) and from age 11 (191 ms) to age 15 (168 ms) are significant, while no significant difference in vowel duration exists among age groups older than 12. On average, vowel durations reach minima around age 15. Furthermore, difference in mean duration between age 15 and adults is significant ($t = 2.42$, $df = 644$, $p < 0.02$). Therefore, it is possible that vowel durations increase again in the process of converging toward
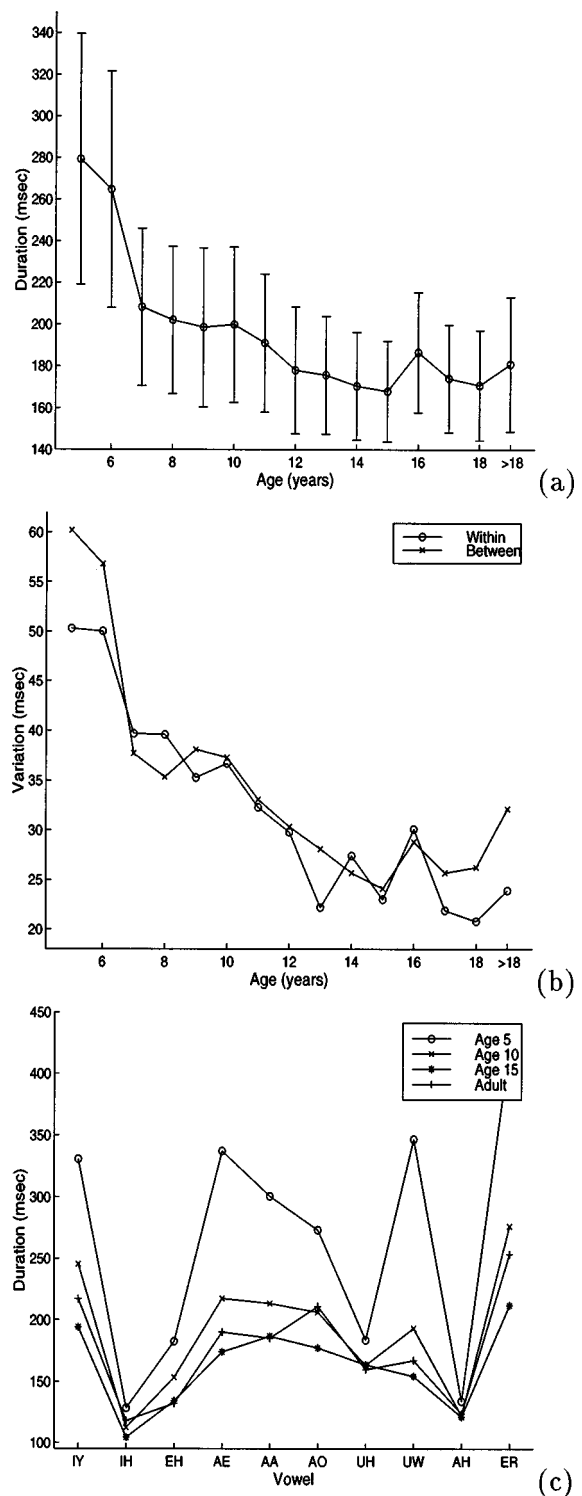
FIG. 1. (a) Averaged-vowel duration across all vowels and subjects in each age group. (b) Within- and between-subject variations. The between-subject variation is reduced by a factor of 2.0. (c) Mean duration of individual vowel averaged across all subjects in each age group is shown for several age groups.

adult range. As will be shown later, similar trends are also observable for both /s/ and sentence durations as well as for some spectral parameters.

In Fig. 1(b), within- and between-subject variations are shown as a function of age. The between-subject variation shown is reduced by a factor of 2.0 in order to facilitate the
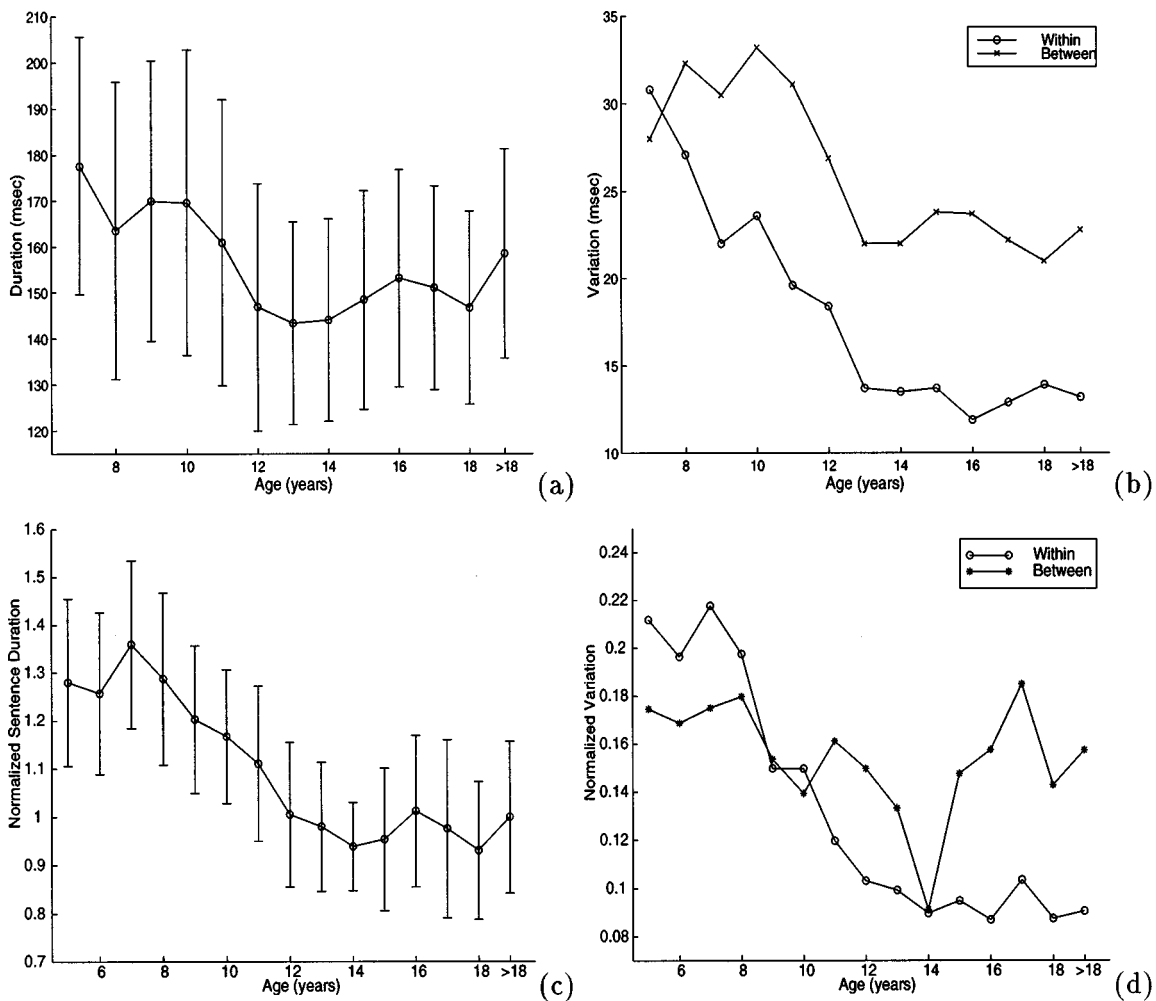
FIG. 2. (a) Duration of /s/. (b) Within- and between-subject variability of /s/ duration (unfilled circle: within-subject, filled circle: between-subject). (c) Normalized duration of sentence. (d) Variability of sentence duration (unfilled circle: within-subject, filled circle: between-subject).

comparison of within- and between-subject variability. It is clear that both within- and between-subject variations decrease with age. For the within-subject variation, the effect of age is significant $[F(14,3778)=18.5, p<0.001]$. The multiple comparisons indicate that the reduction of within-subject variation from age 11 to age 13 is significant ($p<0.05$), while no significant difference exists among the age groups of 13 and older. Therefore, both duration and within-subject variability may reach adult level almost simultaneously around age 12. Also note the remarkably similar behavior of between-subject variability and duration.

Individual vowel durations averaged across subjects in each age group are shown in Fig. 1(c) for several age groups. The similar vowel duration patterns between 5-year-olds and adults suggest that children as young as 5 years old have the ability to control intrinsic vowel duration. However, 5-year-olds show a tendency to exaggerate the duration of "long" vowels, e.g., /IY/, /AE/, /AA/, /ER/, when compared to the other age groups. The fact that children of ages 5 and 6 produced vowels in isolation may be at least partially responsible for this trend.

2. /s/ and sentence production durations

Results of duration and variability measurements are shown in Fig. 2(a) and (b) for /s/ and in Fig. 2(c) and (d) for

sentence productions as a function of age. Since the effect of gender is not significant, values averaged across gender are shown in the figure. However, the effect of age is significant $[F(12,383)=4.178, p<0.001$ for /s/; $F(14,469)=23.1, p<0.001$ for sentences]. Note that in Fig. 2(a) and (b) no data points are shown for ages 5 and 6 since target words were produced in isolation (no /s/ tokens).

The multiple comparisons indicate that the duration of /s/ significantly decreases from age 10 (170 ms) to age 12 (147 ms). On average, the duration of /s/ reaches minima around age 13 and increases again toward adult levels. Adults' mean duration (159 ms) is significantly different from that of age 13 (143 ms) ($t=3.02, df=83, p<0.005$).

The within- and between-subject variability of /s/ [Fig. 2(b)] decrease gradually up to age 13 and then remain more or less constant. The effect of age on the within-subject variation is significant $[F(12,383)=19.3, p<0.001]$. Multiple comparisons indicate that significant reduction of within-subject variation occurs from age 10 (23.6 ms) to age 12 (18.4 ms) and from age 11 (19.6 ms) to age 13 (13.7 ms). After age 13, no significant change of the within-subject variation is observed. Therefore, the within-subject variability reaches adult level around age 13. Note that the significant increase of /s/ duration from age 13 (143 ms) to adult

(159 ms) ($t = 3.01$, $df = 82$, $p < 0.03$) is not accompanied by a similar increase in within-subject variability. In addition, the sudden and substantial reduction in between-subject variability from age 11 to age 13 is worth noticing.

It is likely that sentence duration shown in Fig. 2(c) is mainly determined by the speaking rate, reading ability, and pause duration. The effect of age on sentence duration is significant [$F(14,481) = 23.1$, $p < 0.001$]. It is observed that sentence duration decreases almost linearly from age 7 to age 14, where it attains its minimum value. About a 45% reduction in duration occurs in that time period. The multiple comparisons indicate that the reduction of duration from age 10 to age 12 and from age 11 to age 14 are significant. Mean durations at age 14 and for adults are also significantly different ($t = 2.17$, $df = 75$, $p < 0.05$). Therefore, just as in the case of vowels and /s/, sentence durations also reach a minimum before converging toward adult levels.

Note that the relatively short average-sentence duration for 5- and 6-year-old children [Fig. 2(c)] was not due to measurement errors or the different elicitation method used for some young children with reading problems (sentence durations were very similar for both ''repeat after me'' and ''read'' elicitation methods). From listening to the sentence productions of young children, it was found that disfluencies (phoneme deletions, mumbling of groups of sounds, mispronunciations) were quite common, and are suspected to be the main cause for shorter sentence durations, particularly in 5- and 6-year-olds.

The effect of age on the within-subject variability is significant [$F(14,477) = 14.5$, $p < 0.001$]. Multiple comparisons indicate that the reduction of within-subject variations from age 8 to age 12 is significant, while there is no significant change after age 12. An unexpected and interesting observation is the large between-subject variation for subjects older than age 14.

B. Fundamental frequency

The mean $F0$ of male and female speakers averaged across all vowels and subjects in each age group is shown in Fig. 3(a) as a function of age. Vertical bars denote between-subject variations. The mean $F0$ values for male and female speakers, averaged across all subjects for each vowel and age group, are provided in Tables II and III. A simple factorial analysis of variance (ANOVA) indicates that $F0$ differences between male and female speakers become significant beginning from age 12. For male speakers, multiple comparisons indicate that the drops in $F0$ from age 11 to age 13 and from age 13 to age 15 are significant ($p < 0.05$). About a 78% drop in $F0$ occurs between age 12 ($F0 = 226$ Hz) and age 15 ($F0 = 127$ Hz) in male speakers, and there is no significant pitch change after age 15. This suggests that, on average, pubertal pitch change in male speakers starts between age 12 and 13, and ends around age 15. The relatively large between-subject variation at ages 13 and 14 also suggests that the onset time of puberty is different among speakers in these age groups (cf. Hollien et al., 1994). For female speakers, multiple comparisons indicate that the pitch drop from age 7 ($F0 = 275$ Hz) to age 12 ($F0 = 231$ Hz) is significant,
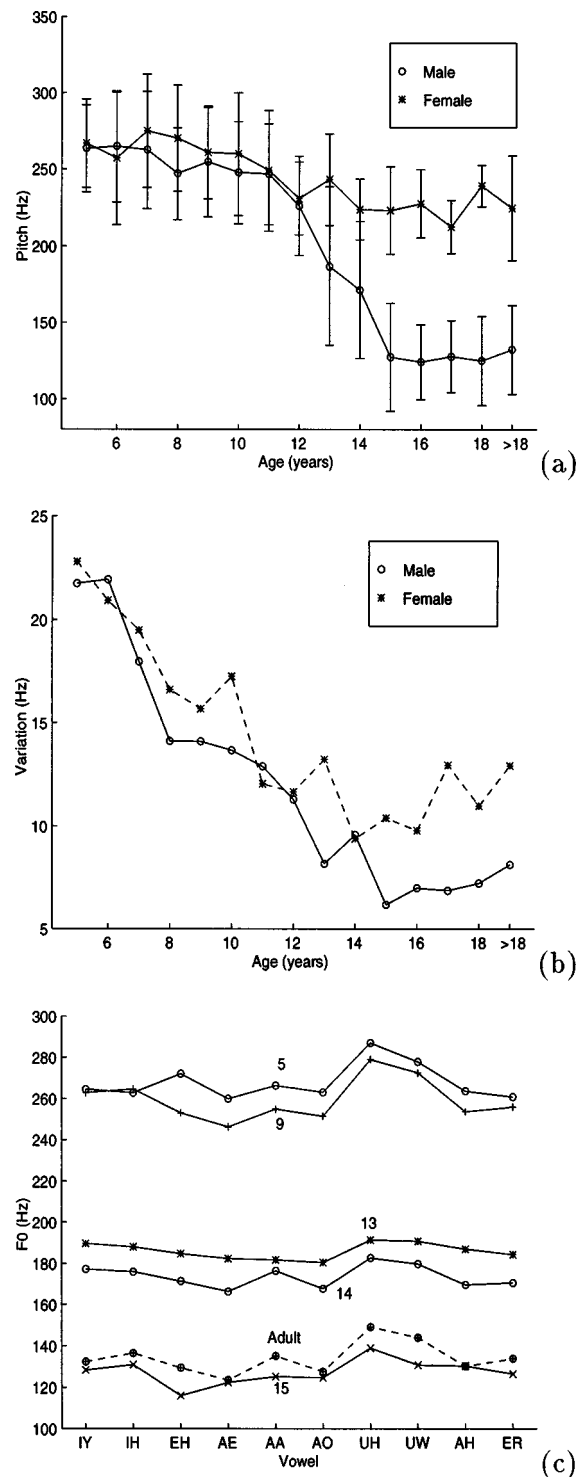
FIG. 3. (a) Averaged fundamental frequency for male and female speakers. Vertical bars denote between-subject variations (i.e., group standard deviations). (b) Within-subject pitch variation as a function of age and gender. (c) Mean pitch of individual vowels for male speaker as a function of age.

and there is no significant pitch change after that age. The $F0$ change for female subjects is more gradual compared to male speakers.

The within-subject variation of pitch is shown in Fig. 3(b) as a function of age and gender. The effect of age is significant for both genders [$F(14,242) = 11.9$, $p < 0.001$ for male speakers; $F(14,217) = 6.0$, $p < 0.001$ for female speakers]. For male speakers, the multiple comparisons indicate

TABLE II. Mean and standard deviation (in parentheses) of fundamental frequency and formant-frequency values for male speakers (# is the number of tokens).

Age		aa	ae	ah	ao	eh	er	ih	iy	uh	uw
	#	26	20	25	28	22	26	23	18	26	22
	F0	266 (33)	260 (37)	263 (31)	263 (35)	272 (34)	260 (35)	262 (35)	264 (32)	287 (42)	277 (35)
5	F1	1166 (98)	1010 (117)	824 (129)	837 (78)	835 (101)	620 (70)	636 (74)	467 (67)	656 (59)	477 (45)
	F2	1750 (165)	2534 (163)	1669 (195)	1226 (99)	2475 (216)	1705 (154)	2608 (171)	3071 (145)	1434 (98)	1508 (285)
	F3	3412 (370)	3452 (252)	3596 (300)	3533 (268)	3469 (321)	2502 (353)	3465 (307)	3653 (215)	3588 (353)	3136 (294)
	#	21	18	18	19	17	15	14	14	18	18
	F0	273 (49)	256 (40)	263 (35)	264 (39)	259 (34)	257 (39)	261 (34)	267 (30)	290 (40)	279 (42)
6	F1	1048 (88)	962 (84)	844 (75)	813 (84)	888 (45)	661 (41)	652 (48)	411 (83)	663 (33)	457 (60)
	F2	1554 (117)	2544 (136)	1534 (107)	1147 (117)	2506 (107)	1565 (180)	2728 (141)	3124 (161)	1363 (120)	1659 (270)
	F3	3292 (322)	3316 (131)	3635 (176)	3410 (273)	3417 (262)	2132 (194)	3510 (287)	3728 (216)	3587 (277)	3241 (216)
	#	19	18	20	17	19	19	16	17	19	14
	F0	265 (44)	253 (38)	264 (40)	260 (39)	258 (37)	260 (43)	268 (42)	266 (42)	281 (61)	281 (40)
7	F1	984 (70)	882 (78)	815 (94)	812 (76)	794 (79)	634 (59)	579 (47)	425 (46)	624 (66)	449 (82)
	F2	1536 (90)	2441 (67)	1642 (148)	1223 (145)	2412 (90)	1637 (130)	2602 (111)	3002 (191)	1542 (136)	1700 (236)
	F3	3137 (378)	3344 (147)	3515 (128)	3354 (235)	3440 (214)	2253 (195)	3533 (192)	3618 (219)	3499 (224)	3205 (151)
	#	41	39	39	40	36	38	40	40	38	39
	F0	247 (32)	242 (35)	248 (38)	241 (30)	249 (30)	245 (31)	251 (29)	257 (32)	270 (40)	265 (39)
8	F1	969 (112)	873 (73)	740 (72)	766 (72)	782 (99)	600 (51)	560 (57)	414 (60)	607 (44)	458 (52)
	F2	1522 (186)	2370 (133)	1553 (162)	1181 (92)	2328 (118)	1695 (147)	2568 (130)	3031 (187)	1432 (128)	1577 (271)
	F3	3188 (312)	3254 (199)	3421 (209)	3392 (307)	3409 (282)	2212 (187)	3420 (321)	3626 (285)	3331 (216)	3165 (261)
	#	37	42	39	36	36	33	33	37	34	34
	F0	255 (37)	246 (32)	253 (40)	251 (31)	253 (33)	256 (41)	264 (39)	262 (45)	279 (46)	272 (45)
9	F1	1011 (77)	872 (75)	793 (75)	756 (76)	797 (77)	618 (55)	583 (58)	382 (62)	626 (54)	471 (73)
	F2	1601 (126)	2319 (143)	1529 (137)	1170 (98)	2287 (93)	1577 (142)	2522 (133)	2979 (147)	1472 (124)	1603 (225)
	F3	3245 (234)	3196 (177)	3391 (222)	3375 (233)	3390 (201)	2104 (205)	3466 (210)	3536 (252)	3340 (189)	3198 (224)
	#	42	41	38	39	37	40	39	43	41	37
	F0	257 (38)	243 (34)	251 (33)	241 (34)	250 (40)	242 (33)	253 (39)	254 (33)	273 (42)	268 (37)
10	F1	970 (89)	904 (78)	751 (66)	748 (51)	758 (69)	621 (43)	590 (53)	424 (69)	631 (59)	482 (63)
	F2	1558 (189)	2269 (103)	1628 (147)	1162 (101)	2254 (139)	1644 (149)	2401 (132)	2959 (167)	1501 (174)	1656 (268)
	F3	3148 (202)	3214 (203)	3318 (205)	3198 (318)	3407 (190)	2170 (211)	3434 (195)	3475 (151)	3267 (173)	3049 (314)
	#	38	38	39	41	39	40	37	42	37	37
	F0	250 (32)	244 (32)	243 (34)	241 (36)	244 (35)	239 (33)	254 (37)	250 (33)	267 (41)	265 (38)
11	F1	900 (76)	875 (67)	741 (55)	742 (54)	725 (58)	574 (54)	540 (37)	400 (60)	589 (37)	475 (53)
	F2	1436 (146)	2170 (88)	1525 (129)	1086 (76)	2136 (98)	1539 (121)	2406 (93)	2894 (133)	1479 (179)	1704 (232)
	F3	3075 (257)	3108 (255)	3166 (250)	3182 (275)	3176 (242)	2013 (186)	3290 (219)	3437 (236)	3072 (168)	2939 (180)
	#	40	37	41	39	37	38	32	36	38	34
	F0	233 (32)	221 (34)	225 (33)	220 (32)	225 (32)	225 (34)	228 (34)	232 (35)	243 (31)	239 (37)
12	F1	891 (76)	818 (70)	718 (63)	716 (55)	714 (66)	574 (66)	517 (36)	358 (47)	581 (54)	424 (51)
	F2	1432 (146)	2090 (137)	1484 (149)	1083 (88)	2026 (188)	1530 (124)	2207 (152)	2755 (155)	1450 (157)	1576 (223)
	F3	2930 (207)	3089 (191)	3081 (161)	3039 (233)	3161 (237)	2007 (170)	3191 (181)	3349 (238)	3006 (200)	2805 (208)
	#	26	25	25	28	29	23	22	25	26	23
	F0	181 (52)	182 (49)	187 (51)	180 (50)	184 (48)	184 (50)	188 (50)	189 (53)	191 (54)	190 (52)
13	F1	793 (58)	734 (46)	660 (39)	662 (43)	657 (46)	545 (29)	512 (27)	360 (57)	542 (24)	420 (41)
	F2	1324 (120)	1959 (116)	1388 (164)	1032 (72)	1923 (135)	1392 (122)	2067 (100)	2523 (159)	1396 (120)	1418 (238)
	F3	2664 (202)	2825 (189)	2807 (240)	2831 (261)	2916 (269)	1925 (167)	2860 (174)	3212 (412)	2834 (267)	2672 (285)
	#	20	20	19	19	18	15	20	21	17	16
	F0	176 (45)	166 (43)	169 (48)	167 (47)	171 (46)	170 (46)	176 (45)	177 (42)	182 (50)	179 (45)
14	F1	844 (88)	767 (83)	665 (61)	679 (61)	673 (56)	508 (45)	513 (34)	350 (32)	559 (35)	401 (23)
	F2	1379 (122)	1982 (177)	1376 (71)	1052 (75)	1955 (157)	1484 (118)	2188 (190)	2671 (220)	1379 (86)	1537 (255)
	F3	2679 (163)	2792 (154)	2882 (199)	2829 (184)	2970 (228)	1874 (133)	3040 (222)	3340 (342)	2794 (187)	2645 (154)
	#	19	18	18	18	15	16	16	20	15	17
	F0	125 (36)	122 (30)	130 (36)	124 (34)	116 (11)	126 (35)	131 (46)	128 (32)	139 (37)	130 (37)
15	F1	731 (57)	676 (56)	600 (51)	617 (40)	609 (38)	499 (18)	478 (37)	310 (33)	519 (34)	343 (44)
	F2	1316 (68)	1728 (91)	1385 (134)	976 (47)	1720 (53)	1337 (65)	1992 (152)	2350 (123)	1335 (67)	1316 (209)
	F3	2507 (139)	2573 (111)	2657 (132)	2634 (246)	2648 (105)	1755 (133)	2757 (142)	2964 (268)	2556 (160)	2433 (134)

TABLE II. (*Continued.*)

Age		aa	ae	ah	ao	eh	er	ih	iy	uh	uw
	#	17	19	18	17	19	14	16	18	16	17
	F0	126 (30)	120 (24)	122 (26)	118 (20)	122 (24)	123 (21)	131 (26)	126 (25)	134 (29)	131 (25)
16	F1	741 (58)	684 (60)	596 (25)	600 (35)	599 (26)	472 (52)	451 (29)	296 (20)	497 (31)	348 (40)
	F2	1261 (78)	1762 (65)	1254 (108)	935 (56)	1766 (105)	1354 (80)	1944 (152)	2334 (177)	1296 (81)	1368 (231)
	F3	2627 (209)	2620 (98)	2682 (185)	2737 (240)	2701 (90)	1754 (88)	2735 (140)	3030 (245)	2611 (114)	2397 (237)
	#	17	16	16	16	16	10	15	17	15	12
	F0	129 (26)	122 (21)	126 (23)	126 (22)	128 (25)	125 (21)	133 (28)	131 (23)	143 (31)	132 (23)
17	F1	713 (43)	685 (63)	585 (20)	612 (32)	581 (25)	491 (38)	457 (28)	289 (26)	514 (28)	322 (17)
	F2	1221 (126)	1759 (83)	1341 (136)	940 (27)	1745 (112)	1284 (42)	1910 (125)	2268 (110)	1348 (100)	1216 (281)
	F3	2637 (127)	2541 (77)	2600 (89)	2689 (187)	2651 (122)	1704 (89)	2724 (154)	3092 (212)	2573 (140)	2468 (242)
	#	15	17	16	17	16	13	16	17	14	8
	F0	124 (27)	123 (29)	122 (28)	125 (26)	120 (27)	123 (27)	136 (29)	123 (23)	142 (42)	134 (32)
18	F1	737 (48)	686 (49)	602 (26)	599 (40)	604 (40)	490 (25)	449 (35)	283 (20)	533 (32)	337 (19)
	F2	1269 (61)	1759 (93)	1252 (70)	881 (52)	1776 (69)	1282 (61)	1955 (117)	2289 (118)	1297 (75)	1144 (169)
	F3	2560 (160)	2560 (96)	2673 (182)	2622 (222)	2633 (89)	1625 (139)	2670 (108)	3050 (238)	2535 (63)	2328 (124)
	#	47	47	44	43	46	30	39	49	43	32
	F0	135 (31)	123 (27)	130 (30)	127 (30)	129 (27)	134 (30)	136 (32)	132 (28)	149 (31)	144 (33)
19+	F1	723 (48)	669 (43)	610 (32)	601 (33)	590 (32)	471 (29)	458 (26)	292 (26)	501 (35)	342 (34)
	F2	1204 (68)	1725 (100)	1288 (119)	929 (62)	1707 (114)	1265 (74)	1851 (110)	2266 (139)	1269 (121)	1185 (117)
	F3	2496 (176)	2532 (151)	2557 (156)	2599 (165)	2549 (134)	1612 (108)	2588 (105)	2930 (184)	2466 (156)	2411 (160)

that the within-subject pitch variation significantly decreases during two periods: from age 6 to age 8 and from age 12 to age 15 (i.e., during puberty). For female speakers, a significant difference in within-subject variability exists between age 10 and age 14 ($t = 2.95$, $df = 22$, $p < 0.01$).

After puberty, the average within-subject $F0$ variation tends to increase again with age for both male and female speakers. Therefore, overshoot of acoustic parameters before reaching adult target levels may occur not only in duration but also in $F0$ variability. An interesting finding is that for subjects older than age 14, the within-subject $F0$ variability is significantly higher in female speakers than in male speakers [$F(1,138) = 37.3$, $p < 0.001$].

The mean $F0$ of individual vowels is shown in Fig. 3(d) for male speakers. It can be seen that male children as young as 5 years exhibit adult-like vowel-dependent $F0$ patterns. Similar observations can be made for female children (not shown here). This suggests that the capability of intrinsic $F0$ control in a given context is acquired earlier than age 5.[3]

C. Formant frequencies

Mean formant frequency values for the first three formants, averaged across all subjects for each vowel and age group, are provided in Tables II and III for male and female speakers, respectively. Two-sigma ellipses for five vowels are shown in Fig. 4(a) and (b) in the $F1–F2$ space for male and female speakers ages 10 to 12, and compared with results from similar studies in the literature. It is observed that the vowel positions produced by children of ages 10 through 12 in the current database are slightly compressed or centralized, compared to children's formant data in Peterson and Barney[4] (1952). This centralization of vowel space is most possibly due to the context difference (i.e., /hVd/ vs /bVt/) as well as dialect differences between the speaker population of the two studies (i.e., midwestern vs Pacific eastern). The most noticeable difference in formant distributions between the current study and the study by Hillenbrand *et al.*[5] (1995) is the proximity of front vowels /IY/ and /AE/ in the latter. It is also observed that despite the differences in vowel-class centroid values in the $F1–F2$ space, within-vowel variances (i.e., orientation of ellipses) are consistent between these studies and, clearly, the vowel $F1–F2$ space is larger for children than for adults.

Scatter plots of mean $F1$ and $F2$ of several vowels are shown in Fig. 4(c) for male speakers and in Fig. 4(d) for female speakers. Each point represents $F1$ and $F2$ values averaged across all subjects in the 5–6, 7–8,..., 17–18 age groups and adults. For instance, the rightmost circle in /IY/ represents mean $F1$ and $F2$ for children of ages 5 and 6, and the leftmost circle represents adults. A linear-scaling trend of male formant frequencies as a function of age is clearly observable from Fig. 4(c), especially between age 11 and age 16. Therefore, the current formant data of male speakers seem to support the notion of "uniform axial growth of the vocal tract," as discussed in Kent (1976). Such a linear trend is, however, not clear for female speakers [Fig. 4(d)]. These trends can be more clearly observed in terms of the formant-scaling factors shown in Fig. 6.

Formant variability in terms of the within-subject COV is shown in Fig. 5(a) for male speakers and Fig. 5(b) for female speakers. The age-dependent reduction of the normalized formant frequency variability agrees with the trend shown in Eguchi and Hirsh (1969). Formant frequency variability may reach adult level around age 14 simultaneously for all formants. It is also observed that the COV is different for $F1$, $F2$, and $F3$ for subjects younger than age 12; specifically, the variability in $F1$ is greater than the variability in $F2$ and $F3$. For male speakers, the COV of $F1$, $F2$, and $F3$ take similar values after age 12, while such a trend is not observed for female speakers.

TABLE III. Mean and standard deviation (in parentheses) of fundamental frequency and formant-frequency values for female speakers (# is the number of tokens).

Age		aa	ae	ah	ao	eh	er	ih	iy	uh	uw
	#	14	16	15	19	16	20	11	13	12	17
	F0	272 (37)	263 (32)	277 (29)	273 (36)	268 (31)	258 (34)	279 (38)	265 (44)	300 (32)	286 (40)
5	F1	1224 (64)	1055 (105)	956 (105)	921 (90)	894 (83)	687 (62)	685 (66)	466 (30)	698 (31)	501 (54)
	F2	1842 (141)	2613 (138)	1772 (108)	1337 (88)	2555 (130)	1707 (137)	2816 (170)	3019 (180)	1376 (65)	1709 (263)
	F3	3435 (387)	3348 (230)	3274 (395)	3675 (250)	3227 (342)	2350 (215)	3526 (289)	3644 (98)	3496 (324)	3332 (161)
	#	25	24	22	25	19	25	23	20	22	20
	F0	265 (53)	248 (43)	258 (38)	259 (41)	259 (44)	252 (40)	264 (39)	271 (45)	282 (41)	280 (58)
6	F1	1163 (53)	972 (121)	839 (52)	844 (76)	828 (58)	654 (52)	643 (66)	433 (71)	670 (61)	512 (67)
	F2	1771 (189)	2671 (183)	1754 (165)	1258 (100)	2661 (115)	1815 (124)	2791 (123)	2986 (151)	1590 (183)	1793 (370)
	F3	3447 (292)	3438 (317)	3759 (233)	3729 (322)	3421 (349)	2458 (381)	3441 (347)	3596 (128)	3665 (381)	3380 (176)
	#	36	28	35	38	21	32	28	35	34	30
	F0	281 (43)	273 (41)	278 (31)	265 (37)	275 (41)	269 (40)	278 (31)	276 (36)	298 (40)	281 (42)
7	F1	1067 (102)	1023 (87)	846 (70)	853 (88)	856 (46)	686 (55)	608 (44)	467 (70)	661 (44)	506 (70)
	F2	1647 (216)	2433 (143)	1723 (162)	1279 (131)	2428 (113)	1740 (184)	2642 (178)	3026 (181)	1566 (110)	1840 (255)
	F3	3493 (361)	3410 (278)	3425 (502)	3569 (336)	3458 (234)	2490 (301)	3482 (283)	3573 (175)	3327 (468)	3316 (255)
	#	14	13	14	16	16	19	11	10	12	14
	F0	273 (31)	268 (40)	268 (37)	261 (33)	264 (31)	260 (39)	280 (35)	274 (42)	303 (50)	294 (49)
8	F1	1108 (64)	1021 (84)	848 (60)	870 (84)	851 (76)	612 (69)	568 (50)	428 (46)	664 (77)	426 (80)
	F2	1660 (57)	2419 (154)	1693 (109)	1274 (73)	2363 (199)	1713 (235)	2674 (192)	2997 (201)	1450 (90)	1539 (165)
	F3	3144 (342)	3271 (282)	3534 (193)	3384 (226)	3263 (352)	2381 (378)	3552 (166)	3604 (164)	3560 (108)	3298 (217)
	#	38	41	38	38	37	37	28	35	38	37
	F0	267 (35)	248 (25)	267 (33)	252 (30)	260 (31)	253 (29)	265 (34)	264 (29)	292 (35)	278 (36)
9	F1	1063 (86)	948 (89)	801 (48)	810 (64)	818 (68)	643 (60)	587 (54)	455 (61)	652 (51)	505 (44)
	F2	1676 (199)	2415 (131)	1658 (144)	1250 (93)	2363 (133)	1757 (163)	2559 (112)	3061 (140)	1506 (107)	1764 (220)
	F3	3284 (275)	3330 (180)	3505 (189)	3387 (248)	3431 (230)	2298 (182)	3516 (205)	3626 (217)	3412 (262)	3247 (195)
	#	25	21	24	24	17	24	22	23	23	22
	F0	263 (41)	255 (48)	257 (38)	258 (44)	259 (45)	258 (42)	267 (45)	261 (35)	275 (50)	273 (44)
10	F1	1037 (95)	970 (68)	791 (79)	822 (92)	860 (62)	612 (72)	609 (51)	472 (45)	636 (51)	496 (54)
	F2	1663 (251)	2318 (140)	1748 (118)	1264 (112)	2306 (92)	1733 (135)	2491 (178)	2969 (134)	1689 (240)	1747 (280)
	F3	3204 (272)	3286 (285)	3431 (227)	3378 (258)	3372 (312)	2264 (258)	3469 (334)	3506 (165)	3307 (270)	3166 (259)
	#	33	34	33	33	31	31	30	28	32	33
	F0	247 (37)	242 (40)	246 (38)	243 (37)	242 (37)	247 (41)	254 (39)	255 (37)	279 (47)	254 (34)
11	F1	980 (83)	878 (84)	765 (58)	791 (59)	775 (50)	638 (50)	590 (49)	467 (57)	637 (39)	475 (38)
	F2	1547 (163)	2219 (138)	1676 (124)	1219 (66)	2245 (109)	1645 (116)	2468 (113)	2971 (96)	1540 (152)	1774 (200)
	F3	3130 (208)	3190 (149)	3282 (165)	3305 (240)	3365 (175)	2167 (148)	3377 (195)	3462 (156)	3207 (139)	3033 (128)
	#	39	35	38	36	35	34	36	37	35	36
	F0	234 (27)	226 (26)	230 (24)	229 (22)	228 (25)	228 (25)	237 (29)	234 (28)	253 (38)	242 (25)
12	F1	939 (108)	836 (128)	742 (100)	761 (56)	712 (87)	620 (47)	537 (73)	439 (52)	591 (58)	452 (42)
	F2	1612 (164)	2215 (188)	1679 (142)	1212 (120)	2189 (170)	1662 (167)	2398 (222)	2884 (182)	1593 (147)	1661 (309)
	F3	3077 (267)	3163 (261)	3287 (221)	3148 (235)	3287 (168)	2247 (398)	3273 (270)	3376 (256)	3148 (233)	2963 (193)
	#	22	23	21	23	21	20	21	22	21	20
	F0	251 (43)	238 (32)	245 (31)	238 (27)	244 (28)	237 (28)	252 (37)	247 (29)	264 (45)	255 (32)
13	F1	959 (71)	824 (60)	779 (62)	753 (49)	770 (49)	627 (37)	592 (42)	426 (62)	654 (32)	490 (51)
	F2	1552 (150)	2187 (134)	1715 (150)	1212 (106)	2199 (96)	1668 (141)	2382 (94)	2861 (77)	1557 (162)	1858 (198)
	F3	3072 (198)	3110 (163)	3245 (148)	3132 (215)	3238 (109)	2161 (187)	3296 (117)	3391 (136)	3146 (179)	2968 (117)
	#	19	19	17	18	18	17	16	18	17	17
	F0	225 (27)	217 (21)	221 (19)	219 (21)	221 (26)	224 (19)	231 (16)	226 (19)	248 (33)	232 (24)
14	F1	893 (88)	824 (77)	756 (55)	746 (58)	736 (50)	627 (57)	573 (59)	415 (28)	630 (44)	433 (35)
	F2	1556 (72)	2010 (100)	1619 (101)	1192 (116)	2032 (114)	1639 (91)	2189 (92)	2693 (130)	1595 (112)	1693 (186)
	F3	2904 (232)	2935 (175)	3019 (173)	2972 (292)	3103 (190)	2115 (181)	3075 (181)	3222 (190)	2966 (194)	2724 (152)
	#	18	19	18	19	18	18	16	19	18	17
	F0	220 (27)	218 (27)	225 (31)	220 (29)	219 (28)	222 (27)	226 (25)	229 (29)	246 (35)	238 (33)
15	F1	900 (48)	851 (86)	738 (42)	767 (39)	744 (36)	594 (38)	564 (51)	378 (27)	620 (53)	434 (22)
	F2	1541 (91)	1942 (99)	1646 (131)	1177 (74)	1971 (118)	1586 (112)	2171 (75)	2653 (153)	1533 (116)	1727 (254)
	F3	2753 (197)	2907 (150)	2931 (157)	2991 (236)	2998 (165)	1949 (109)	3024 (105)	3237 (183)	2827 (149)	2674 (107)
	#	18	20	20	20	21	19	18	19	20	18
	F0	225 (20)	222 (20)	231 (24)	217 (22)	226 (20)	227 (23)	234 (21)	233 (28)	255 (32)	240 (25)
16	F1	851 (55)	835 (68)	737 (44)	749 (43)	735 (47)	602 (43)	541 (46)	423 (52)	613 (48)	447 (35)
	F2	1412 (98)	2050 (100)	1620 (199)	1159 (88)	2003 (143)	1628 (120)	2207 (89)	2776 (147)	1617 (162)	1691 (232)
	F3	2896 (375)	3004 (144)	2991 (146)	2966 (195)	3042 (142)	2056 (126)	3072 (111)	3241 (135)	2927 (155)	2866 (275)

TABLE III. (*Continued.*)

Age		aa	ae	ah	ao	eh	er	ih	iy	uh	uw
	#	17	17	16	15	13	14	16	15	15	13
	F0	219 (20)	205 (20)	212 (24)	204 (21)	206 (15)	207 (17)	217 (21)	217 (17)	236 (26)	225 (22)
17	F1	922 (82)	845 (72)	735 (37)	751 (41)	728 (42)	552 (45)	558 (58)	390 (63)	623 (28)	424 (22)
	F2	1467 (160)	2007 (106)	1514 (171)	1166 (93)	2010 (73)	1581 (135)	2168 (84)	2717 (84)	1575 (198)	1715 (392)
	F3	2803 (135)	2867 (256)	2890 (160)	2921 (161)	2961 (144)	1995 (123)	3024 (165)	3290 (130)	2801 (146)	2685 (138)
	#	18	17	18	17	19	18	16	16	17	17
	F0	242 (15)	233 (16)	238 (14)	230 (16)	232 (18)	237 (13)	250 (17)	246 (16)	262 (24)	256 (19)
18	F1	932 (47)	914 (45)	741 (33)	777 (45)	754 (58)	619 (53)	587 (52)	418 (37)	605 (35)	480 (34)
	F2	1473 (144)	1955 (110)	1631 (123)	1165 (92)	2014 (117)	1569 (142)	2222 (33)	2801 (46)	1579 (140)	1771 (324)
	F3	2914 (153)	2946 (127)	3027 (104)	3042 (207)	3047 (112)	2058 (134)	3080 (117)	3305 (59)	2924 (138)	2860 (89)
	#	48	46	47	44	45	39	41	46	45	45
	F0	231 (40)	215 (36)	218 (35)	213 (29)	219 (35)	222 (34)	235 (40)	228 (30)	246 (40)	243 (36)
19+	F1	894 (76)	787 (66)	740 (56)	726 (47)	694 (52)	543 (43)	532 (59)	360 (45)	595 (62)	412 (48)
	F2	1459 (124)	2078 (102)	1609 (135)	1079 (89)	2057 (123)	1481 (132)	2183 (111)	2757 (145)	1522 (140)	1388 (248)
	F3	2950 (252)	2916 (145)	2957 (161)	2986 (220)	3005 (139)	1884 (144)	3064 (136)	3291 (200)	2887 (155)	2804 (235)

In Fig. 6, formant-scaling factors, as defined in Fant (1975), computed from formant frequencies averaged across vowels are plotted as a function of age for male and female speakers. It is observed that differentiation of male and female $F2$ and $F3$ patterns begins at around age 11 and the formants become fully distinguishable around age 15, i.e., after puberty in male speakers. Between ages 10 and 15, formant frequencies of male speakers decrease faster with age and reach much lower absolute values than those of female speakers. This suggests that the total growth and rate of growth of the vocal tract is greater in male speakers. On average, it is clear that formant values reach adult range
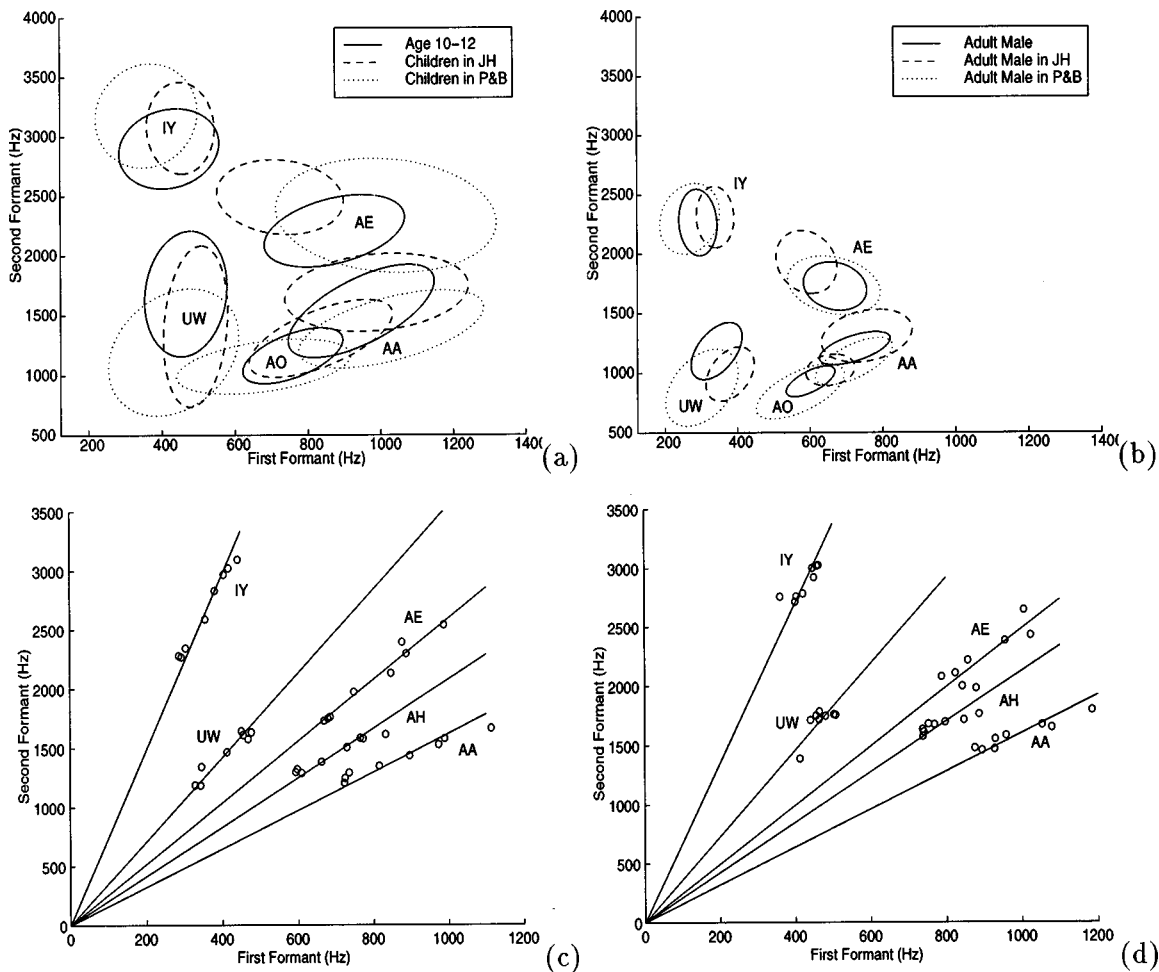
FIG. 4. Current formant data are compared with those in Hillenbrand *et al.* (1995) and Peterson and Barney (1959) for children (ages 10 through 12) and adults in (a) and (b), respectively. Plot of mean $F1$ and $F2$ of vowels /IY/, /AE/, /AA/, /AO/, and /UW/ are shown for males in (c) and for females in (d).
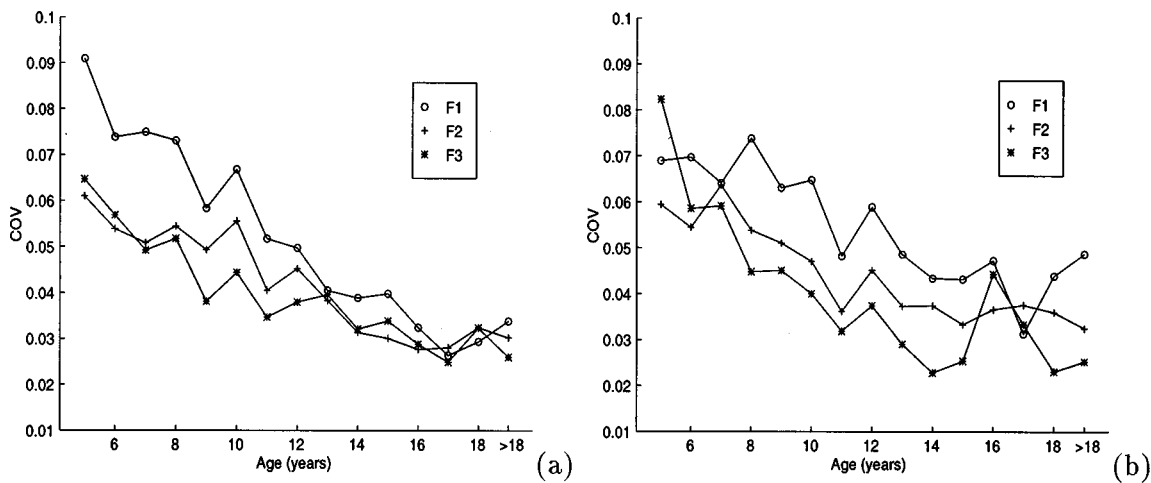
FIG. 5. Plot of within-subject COV of $F1$, $F2$, and $F3$ for (a) Male speakers and (b) Female speakers. It is clear that the within-subject formant variability decreases with age.

around age 15 for males and around age 14 for females. The formant scaling factors also suggest that the growth of vocal tract in male speakers may cease around age 15.

Formant scaling factors of male speakers are approximately the same for all formants and decrease almost linearly between ages 10 and 15. For female speakers, however, each formant evolves differently as a function of age. Differences in the rate of growth of the front and back cavities between female and male speakers could be a reason for this trend (Fant, 1975). Investigation of vowel-specific formant-scaling factors should help to verify this hypothesis.

D. Spectral-envelope variability

In Fig. 7(a), averaged cepstrum distances between two repetitions of the same vowel are shown as a function of age and gender. Vertical bars denote standard errors. The effect of age is significant [$F(14,476)=21.0$, $p<0.001$]. It is observed that spectral variability between vowel productions progressively decreases with age and converges to adult values around age 14 for both genders. Multiple comparisons indicate that variability is significantly reduced from age 5 to age 9 and from age 10 to age 14. There is no significant difference in variability after age 11. These results suggest that children younger that 10 years have not fully established their optimal or stable articulatory targets for vowels. The trend is similar to that of the formant variability shown in the previous section.

In Fig. 7(b), cepstrum distances between the initial and the final half of each vocalic segment are shown as a function of age for both male and female speakers. The effect of age is significant [$F(14,476)=9.8$, $p<0.001$]. Clearly, the within-vowel spectral variability progressively decreases with age. Multiple comparisons indicate that variability decreases significantly from age 10 to age 15. On average, children younger than age 10 display greater within-vowel spectral variability than adults.

As can be seen from Fig. 7(b), speakers display the least within-vowel spectral variation around age 15. Differences in spectral variations between age 15 and adults is significant ($t=2.39$, $df=38$, $p<0.03$). This suggests that in terms of

the dynamics of /CVC/ articulations, an extremum in the production patterns may be achieved around age 15. It is also interesting to observe that female adults show significantly larger within-vowel spectral variation than male adults ($t=2.28$, $df=54$, $p<0.03$).

IV. DISCUSSION

The results of this cross-sectional acoustic study of children's speech, collected from subjects with no known speech pathologies, confirm that the reduction of magnitude and within-subject variability of temporal and spectral parameters with age is a general acoustic phenomenon associated with speech development in children. Furthermore, due to the wider age range of subjects (ages 5–18 years) examined in the current study, it was possible to obtain detailed acoustic information regarding how acoustic properties of chil-
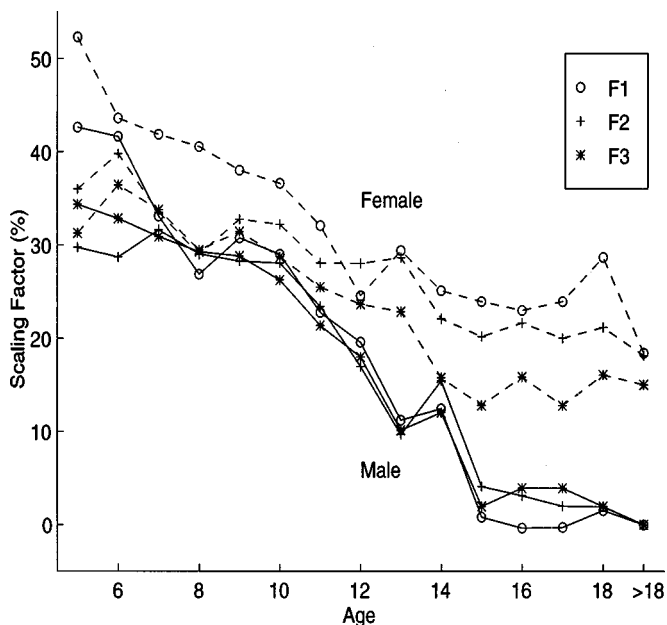
FIG. 6. Formant-scaling factor for $F1$ ($\bigcirc$), $F2$ ($+$), and $F3$ ($*$) scaled by adult male formants. They are computed based on mean formants averaged across all vowels and subjects in each age group.
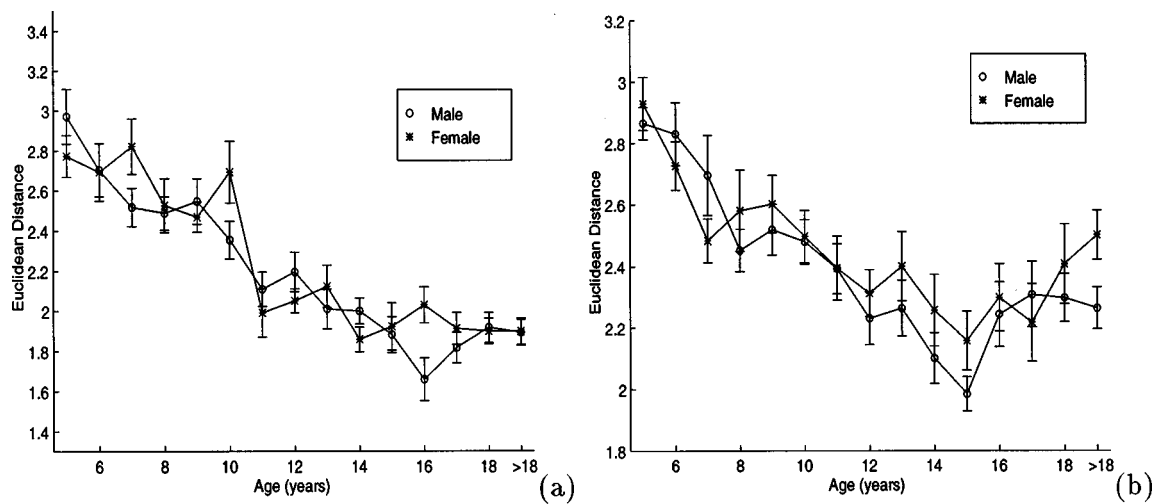
FIG. 7. (a) Mean cepstrum distance between the two repetitions of the same vowels is shown for each age group. (b) Mean cepstrum distance between the first- and second-half segments within vowel is shown for each age group.

dren's speech vary with age and when children begin to exhibit adult-like patterns. The acoustic data obtained in the current study are compared with similar acoustic data published in the literature, and the significance of the age- and gender-dependent acoustic trends observed in our data is discussed.

The main goal of this section is to explore the significance of the acoustic findings of this study based on (1) the physical development of the vocal tract and the voice source, and (2) the neuromuscular factors believed to govern the underlying articulatory dynamics, and hence the acoustic characteristics of speech. It should be noted that some of these interpretations remain to be validated and hence may be deemed speculative.

A. Comparison with previous studies

The acoustic data and age-dependent trends observed in this study are consistent with previously published acoustic data on children, in spite of differences in subject population and data-analysis procedures. For instance, trends in vowel durations measured in the current study and those in Hillenbrand *et al.* (1995) are similar, with an averaged correlation of 0.82 between the two studies for matched age groups. Hillenbrand *et al.* report durations for vowels embedded in /hVd/ target words produced in isolation for children of ages 10 through 12 and adults. Hillenbrand *et al.* also found that adult female speakers show significantly greater vowel durations than male adults. Although not statistically significant, the current data also show a similar trend. Finally, note that the within-subject variability of /s/ duration for male adults is comparable to that measured in Klatt (1972).

As illustrated in Fig. 4(a) and (b), the current formant data is in general agreement with those in Peterson and Barney (1952) as well as in Hillenbrand *et al.* (1995), except for the deviation of the centroids attributed to contextual and dialect differences. Regarding $F0$ measurements, it can be shown that the magnitude of $F0$ as well as the intrinsic $F0$ patterns are also quite similar to those in the two previous studies for matched age groups. Finally, the cross-sectional trend for the onset of pubertal $F0$ change is in agreement

with the longitudinal study of 65 male speakers by Hollien *et al.* (1994), which reported that for the majority of subjects the pubertal-pitch change started between the ages of 12.5 and 14.5 years (mean 13.4) and was completed within 0.5 to 4.0 years (mean 1.5).

B. On *F0* patterns

Average $F0$ and within-subject variability are highly correlated for speakers older than 8 [compare Fig. 3(a) and (c)]. It is thus possible that $F0$ variability can be fully predicted from $F0$ magnitude beyond a certain stage in the development process (e.g., age 8). Using the COV instead of the un-normalized variability measure does not change the essence of the observations made above. It is interesting to note, however, that from age 5 to 8 there is a 50% decrease in variability with essentially no change in average $F0$, suggesting a developmental stabilization of pitch control. Furthermore, female speakers over age 14 show significantly larger within-subject $F0$ variability than male speakers [Fig. 3(b)]. Although the exact reason for this is unclear, this trend may be due to inherent differences in the vocal-fold physiology (e.g., mass and length) of a high-$F0$ voice compared to a low-$F0$ voice.

C. On formant-scaling behavior

Growth curves for the larynx, pharynx, oral cavity, and total vocal-tract length are correlated with the average vowel fundamental frequency, average $F1$, $F2$, and $F3$ values, respectively (see Figs. 3 and 6). For example, $F3$ values agree with those predicted from Goldstein's (1980) model for vocal-tract-length growth in children (at least up to age 15). Good agreement has also been found between average age-dependent $F1$ values and growth of the back vocal-tract cavity (Fant, 1975). However, the limitations imposed by the physical dimensions of the vocal tract on the dynamic range of formants are much more stringent on $F2$ and $F3$ than $F1$. As a consequence, there is greater room for variation in average $F1$ values (averaged over all vowels) of the (child) speaker. In such cases, average $F1$ values may not always be

closely correlated with the physical size of the back oral cavity. For example, the difference in average $F1$ values between young male and female children, and the sudden drop of $F1$ from teenagers to adult females seen in Fig. 6 are not supported by physical growth data. We speculate that social and psychological factors contribute to these deviations in $F1$ values.

Overall, it can be deduced from Figs. 3 and 6 that physical growth of the speech apparatus occurs gradually up to approximately age 14 for females and age 15 for males. For male speakers, a growth spurt occurs somewhere between ages 12 and 15 (puberty) lasts about 1.5 years, and affects not only the larynx but the entire vocal-cavity size. In the developmental model of Goldstein (1980), however, in male speakers the vocal tract is assumed to continue growth beyond age 15 (14.6 cm) until age 20 (16.6 cm), a fact which is not supported by the current formant scaling factors. It does not seem plausible that the vocal-tract length could grow further beyond age 15 without inducing any decrease in the formant frequencies. Further investigation is needed to find the source of this discrepancy.

D. Significance of acoustic findings on underlying articulatory dynamics

First, consider the nearly universal trend of significant reduction in segmental durations, and their convergence to adult values, during the period from around age 9 or 10 to age 12 or 13. This is true irrespective of the segmental levels considered in this study, i.e., vocalic segment [Fig. 1(a)], fricative /s/ [Fig. 2(a)], and sentences [Fig. 2(c)]. Since systematic reduction of duration with age can be concomitant with improvements in speed of articulatory movement, the observation suggests that the underlying neuromuscular control of articulators also rapidly improves and converges to adult levels during that period. Accumulated experience in speech production could also play a role toward contributing to decreased segmental durations.

Second, consider the substantial reduction in within-subject duration variability between ages 8 to 14 years for vowels, the fricative /s/, and sentences [Figs. 1(b), 2(b), and (d)]. Along the lines of the discussion above, this finding may be interpreted as suggesting an *improved* articulatory-timing control being achieved between ages 8 and 14. It is thus thought that the progressive reduction in both duration magnitude and variability prior to age 12 is actually due to improvements in speech motor-timing control with age, and not merely an artifact of longer durations as argued in Kent and Forner (1980), and Crystal and House (1988). The poor correlation between the within-subject variability of /s/ and the mean sentence duration in the current data offers supporting evidence in this direction. For instance, the Pearson's correlation coefficient is 0.11 for adult speakers and 0.09 for children of ages 7 and 8, indicating almost no correlation between an individual's speaking rate and within-subject variability of /s/.

Third, consider the significant reduction in within-subject formant and spectral-envelope variability between about ages 7 and 11 as seen in Figs. 5 and 7(a), respectively. Since both formant structure and spectral-envelope shape are

directly related to an underlying articulatory configuration, the reduced variability in these parameters may be attributed to reduced variability when reaching the individual's canonical articulatory configurations (targets) for a given sound. According to this interpretation of the formant and spectral-envelope data, articulatory ''robustness'' may be almost fully achieved by age 11 or 12. But, as discussed above, variability in reaching articulatory targets may also be correlated with speaking rate. Since the exact relation is not known, it is difficult to speculate further on the development of articulatory target-attainment reliability.

Finally, consider the trend wherein duration magnitude and variability (Figs. 1 and 2) reach minima somewhere between ages 13 and 15 before increasing and converging toward adult range. A similar trend is observed in within-subject formant and spectral-envelope variability (Figs. 5 and 7), which attain minima around 14 or 15 years of age. The smaller pitch variation for teenagers than for adults in Fig. 3(c) offers an additional attestation to this trend. If we assume the final (target) acoustic-parameter values at the completion of human speech development to be those of adults, these findings may be interpreted as demonstrating an apparent *overshoot* phenomenon of acoustic parameters before converging to their final values. Further, these findings may be interpreted as suggesting that teenagers of ages 14 and 15 exhibit an *extremum* in the production patterns among all age groups examined in this study, in terms of both speed of articulatory movements and (to a lesser extent) consistency in achieving desired articulatory configurations. Why that should be the case is not clear, however. This phenomenon may be associated with the learning process. Or it just may be that these patterns reflect the developmental nature of human physiological functions which underlie articulation and peak during the teenage years. Clearly, these overshoot phenomena have to be taken into account when interpreting age-dependent trends in acoustic data.

V. CONCLUDING REMARKS

Not all findings in our acoustic data could be accounted for or readily explained. Some of those cases follow: (1) One unexpected observation was the increase in between-subject variability in the sentence productions of speakers over 14 years old. This result may imply that the decrease in between-subject variability that occurs during speech development ceases after the acquisition of adult-like speech-production patterns simply due to the dominating effects of individual differences (or habit) in speaking rate (causing larger individual deviations from the group mean). (2) There is a significant decrease in $F1$ between the 18-year-old and adult female speakers. This trend was verified by manual estimation and comparison of formant frequencies from a subset of vowel tokens produced by the two age groups. This could be a sociolinguistic phenomenon. (3) There is a rebound and a drop in formant scaling factors between ages 12 and 14 for females, and between ages 13 and 15 for male speakers. This may be retrospective behavior on the part of speakers during puberty. The same trend has also been observed in the within-subject $F0$ variability, which could be the result of a similar retrospective behavior manifested in

*F*0. (4) *F*1 values for young female and male children are significantly different, far larger than any that could be explained by the physiological differences at this age.

Finally, it is noted that the uneven distribution of subjects by age and gender may cause a problem when comparing means of different age groups. This and the fact that subjects of ages 5 and 6 produced the target words for vowels in isolation are flaws of this study, attributed to the design of the speech database-collection procedure.

As demonstrated by the overshoot of acoustic parameters discussed earlier, the maturation process may confound the age-dependent values of other acoustic parameters as well. Furthermore, certain acoustic parameters are associated with more than one aspect of speech development and growth. As a result, additional measurements and different speech-elicitation scenarios are required to map in detail all aspects of speech development. For example, in order to understand if greater temporal variability is due to less precision or simply due to increased exploration (as a result of learning), speech can be elicited in a scenario where children are explicitly asked to minimize temporal variability, as in Smith and Kenney (1994). Direct articulatory and aerodynamic measurements could give clearer answers regarding development of motor control (Sharkey and Folkins, 1985; Smith and McLeane-Muse, 1986; Stathopoulos, 1995; Yang and Kasuya, 1994, 1995). Although many questions in speech development are yet to be answered, the current study nevertheless provides a better insight into the acoustic modeling of children's speech than was available before. From the acoustic modeling point of view, especially for developing speech applications such as automatic speech and speaker recognition, the increased variability in children's speech is a fact that one has to cope with independent of its underlying source.

ACKNOWLEDGMENTS

[1]The age distribution of the tokens discarded from the duration analysis was computed to investigate possible age- or gender-specific bias. Despite the fact that a higher percentage of tokens was discarded for children age 10 and below than for adults (25% versus 21%), no particular age group had more than 25% of the tokens discarded.

[2]Distribution of tokens discarded from formant analysis showed that a relatively small age-dependent trend exists: About 20% more tokens were discarded for children younger than 10 years than for adults.

[3]Because the tongue body and jaw positions affect the position of the larynx and the tension of the vocal folds (and thus *F*0 values), it is possible that the ability of intrinsic *F*0 control does not require any special explicit control mechanism, but is the result of the acquisition of proper articulatory positions for the vowels (cf. Whalen and Levitt, 1995).

[4]Peterson and Barney (1952) used a total of 15 child subjects in their analysis. Although the age range of the children is not provided in their paper, informal comparison with the formant ellipses of Peterson and Barney indicated the best match was with the 8-year-old children in our data.

[5]The study of Hillenbrand *et al.* (1995) was based on a total of 46 subjects ages 10 to 12 years.

Crystal, T. H., and House, A. S. (**1988**). ''A note on the variability of timing control,'' J. Speech Hear. Res. **31**, 497–502.

Davis, S., and Mermelstein, P. (**1980**). ''Comparison of parametric representations for monosyllabic word recognition in continuously spoken sentences,'' IEEE Trans. Acoust., Speech, Signal Process. **28(4)**, 357–366.

Eguchi, S., and Hirsh, I. J. (**1969**). ''Development of speech sounds in children,'' Acta Oto-Laryngol. Suppl. **257**, 1–51.

Fant, G. (**1975**). ''Non-uniform vowel normalization,'' STL-QPSR 2-3/ 1975, 1–19.

Goldstein, U. G. (**1980**). ''An articulatory model for the vocal tracts of growing children,'' Ph.D. thesis (MIT, Cambridge, MA).

Hillenbrand, J., Getty, L. A., Clark, M. J., and Wheeler, K. (**1995**). ''Acoustic characteristics of American English vowels,'' J. Acoust. Soc. Am. **97**, 3099–3111.

Hollien, H., Green, R., and Massey, K. (**1994**). ''Longitudinal research on adolescent voice change in males,'' J. Acoust. Soc. Am. **96**, 2646–2654.

Kent, R. D. (**1976**). ''Anatomical and neuromuscular maturation of the speech mechanism: Evidence from acoustic study,'' J. Speech Hear. Res. **19**, 421–445.

Kent, R. D., and Forner, L. L. (**1980**). ''Speech segment durations in sentence recitations by children and adults,'' Journal of Phonetics **8**, 157–168.

Klatt, D. H. (**1974**). ''The duration of /s/ in English words,'' J. Speech Hear. Res. **17**, 51–63.

Ljolje, A., and Riley, M. D. (**1991**). ''Automatic segmentation and labeling of speech,'' *Proceedings of the International Conference on Acoustics, Speech, and Signal Processing* (Toronto, Canada), pp. 473–476.

Miller, J. D., Lee, S., Uchanski, R. M., Heidbreder, A. H., Richman, B. B., and Tadlock, J. (**1996**). ''Creation of two children's speech databases,'' Proceedings of the ICASSP (Atlanta, GA), pp. 849–852.

Palethorpe, S., Wales, R., Clark, J. E., and Senserrick, T. (**1996**). ''Vowel classification in children,'' J. Acoust. Soc. Am. **100**, 3843–3851.

Peterson, G. E., and Barney, H. L. (**1952**). ''Control methods used in a study of the vowels,'' J. Acoust. Soc. Am. **24**, 175–184.

Potamianos, A., Narayanan, S., and Lee, S. (**1997**). ''Automatic speech recognition for children,'' *Proceedings of European Conference on Speech, Communication and Technology* (Rhodes, Greece), pp. 2371–2734.

Rabiner, L. R., and Juang, B-H. (**1993**). *Fundamentals of Speech Recognition* (Prentice-Hall, Englewood Cliffs, NJ).

Secrest, B. G., and Doddington, G. R. (**1983**). ''An integrated pitch tracking algorithm for speech systems,'' Proceedings of the ICASSP (Boston, MA), pp. 1352–1355.

Sharkey, S. G., and Folkins, J. H. (**1985**). ''Variability of lip and jaw movements in children and adult: Implications for the development of speech motor control,'' J. Speech Hear. Res. **28**, 8–15.

Smith, B. (**1978**). ''Temporal aspects of English speech production: A developmental perspective,'' Journal of Phonetics **6**, 37–67.

Smith, B. L. (**1992**). ''Relationships between duration and temporal variability in children's speech,'' J. Acoust. Soc. Am. **91**, 2165–2174.

Smith, B. L., and Kenney, M. K. (**1994**). ''Variability control in speech production tasks performed by adults and children,'' J. Acoust. Soc. Am. **96**, 699–705.

Smith, B., Kenney, M. K., and Hussain, S. (**1995**). ''A longitudinal investigation of duration and temporal variability in children's speech production,'' J. Acoust. Soc. Am. **99**, 2344–2349.

Smith, B. L., and McLeane-Muse, A. (**1986**). ''Articulatory movement characteristics of labial consonant productions by children and adults,'' J. Acoust. Soc. Am. **80**, 1321–1328.

Stathopoulos, E. T. (**1995**). ''Variability revisited: an acoustic, aerodynamic and respiratory kinematic comparison of children and adults during speech,'' Journal of Phonetics **23**, 67–80.

Whalen, D., and Levitt, A. (**1995**). ''The universality of intrinsic *F*0 of vowels,'' Journal of Phonetics **23**, 349–366.

Yang, C. S., and Kasuya, H. (**1994**). ''Accurate measurement of vocal tract shapes from magnetic resonance images of child, female, and male subjects,'' *Proceedings of the International Conference on Speech Language Processing* (Yokohama, Japan), pp. 623–626.

Yang, C.-S., and Kasuya, H. (**1995**). ''Uniform and non-uniform normalization of vocal tracts measured by MRI across male, female and child subjects,'' IEICE Trans. Inf. and Syst. **E78-D**, No 6, 732–737.

Does music performance allude to locomotion? A model of final *ritardandi* derived from measurements of stopping runners[a]

Anders Friberg[b] and Johan Sundberg[b]

Royal Institute of Technology, Speech, Music, and Hearing, SE-100 44 Stockholm, Sweden

This investigation explores the common assumption that music and motion are closely related by comparing the stopping of running and the termination of a piece of music. Video recordings were made of professional dancers' stopping from running under different deceleration conditions, and instant values of body velocity, step frequency, and step length were estimated. In decelerations that were highly rated for aesthetic quality by a panel of choreographers, the mean body velocity could be approximated by a square-root function of time, which is equivalent to a cubic-root function of position. This implies a linear relationship between kinetic energy and time, i.e., a constant braking power. The mean body velocity showed a striking similarity with the mean tempo pattern of final *ritardandi* in music performances. The constant braking power was used as the basis for a model describing both the changes of tempo in final *ritardandi* and the changes of velocity in runners' decelerations. The translation of physical motion to musical tempo was realized by assuming that velocity and musical tempo are equivalent. Two parameters were added to the model to account for the variation observed in individual *ritardandi* and in individual decelerations: (1) the parameter q controlling the curvature, $q=3$ corresponding to the runners' deceleration, and (2) the parameter v_{end} for the final velocity and tempo value, respectively. A listening experiment was carried out presenting music examples with final *ritardandi* according to the model with different q values or to an alternative function. Highest ratings were obtained for the model with $q=2$ and $q=3$. Out of three functions, the model produced the best fit to individual measured *ritardandi* as well as to individual decelerations. A function previously used for modeling phrase-related tempo variations (interonset duration as a quadratic function of score position) produced the lowest ratings and the poorest fits to individual *ritardandi*. The results thus seem to substantiate the commonly assumed analogies between motion and music. © *1999 Acoustical Society of America.* [S0001-4966(99)01402-2]

PACS numbers: 43.10.Ln, 43.75.St [WJS]

INTRODUCTION

Music performance is often regarded as an area of almost unlimited variability; different artists play the same piece of music in very different ways. On the other hand, our attempts to synthesize music performance (e.g., Friberg, 1995a; Sundberg, 1988) often demonstrated that if a given performance parameter was varied beyond a narrow range, musically unacceptable performances were obtained. Most musicians agree on the importance of, e.g., finding the right tempo for a piece. Also, in many cases, a consensus about various performance parameters can be reached within an ensemble. What is the basis for such agreement? Why is the exact value or change of tempo so important to what is musically acceptable? Is it possible that we use a common reference taken from our extramusical experiences? Two candidates for such a reference have been suggested: speech and motion. By comparing the stopping of running with the final *ritardando*, this article tests the hypothesis that tempo changes allude to locomotional patterns.

Music is commonly associated with motion. This is manifested by the common use of motion words in descriptions of music, such as *lento, andante, corrente* (slow, walking, running). Truslit (1938) even suggested that the performer must imagine an inner motion in order to produce a good performance and that the listener must ''hear'' this inner motion in order to appreciate the music: ''Every *crescendo* and *decrescendo*, every *accelerando* and *decelerando*, is nothing but the manifestation of changing motion energies, regardless of whether they are intended as pure movement or as expression of emotion.'' [Cited from the English synopsis by Repp (1993).] The connection between music and motion has been discussed in a relatively intuitive way in numerous articles and essays partially reviewed by Shove and Repp (1995).

An experimental attempt to test the possibility of a direct connection between music and motion was done by Sundberg *et al.* (1992). The vertical-force patterns exerted by the foot on the ground were measured for different gaits and were then translated to sound-level envelopes of tones. These tones were repeated in sequences with different tempos and evaluated in three listening experiments. In one experiment, the listeners were asked to describe the examples in any terms. Responses relating to motion occurred in up to 50% of the total number of responses in some cases, and was more common (1) when the tone interonset time was the same as

the original step interonset time and (2) at tempos corresponding to about 600-ms interonset time. In another experiment, the listeners rated the sequences along visual analogue scales for each of 24 motion adjectives. The result showed that the tone sequences were classified in qualitative accordance with the original gaits. Thus, information on locomotion characteristics could be transferred to listeners by using the force patterns of the foot as sound-level envelopes.

This investigation represents another attempt to directly link locomotion to music performance. The overall strategy was to find out if the tempo changes in final *ritardandi* can be described by the same mathematical model as the velocity changes during runners' stopping. The article first reviews mathematical representations of tempo and different models that have been used for describing tempo variations in music performance. Then, measurements and visual assessments of runners' decelerations are presented and compared with previous measurements of final *ritardandi*. After this, a mathematical model of the final *ritardando*, derived from the runners' data, is presented and evaluated. Finally, this model is applied to individual cases of runners' decelerations and of final *ritardandi*.

I. BACKGROUND

A. Representation of tempo

Different strategies for representing tempo data have been used in the past. Most researchers have used *score position* as the independent variable. In other words, each note value is represented by a corresponding distance along an axis representing score position. For example, a whole note is represented by the distance 1, a half note by the distance 1/2, etc. Alternatively, the shortest note value occurring in the piece is used as the unit for the score position axis. Thus, if the shortest unit is a 16th note, the distance of 16 will represent a whole note. The commonly used terms *nominal duration* and *deadpan duration* are both used for durations that exactly correspond to note values and are thus equivalent to score position.

Another possibility is to use *time* for the independent variable. This was recommended by Todd (1992, 1995), who argued that ongoing time is more easily perceived than the more abstract score position. There is, however, a computational problem when a given tempo curve, expressed as a function of time, is applied to a music example that by definition is expressed in terms of score position. Therefore, it is necessary to transform the tempo curve into a function of score position. Unfortunately, such transformations have an analytic solution only for some simple mathematical expressions.

A dependent variable *tempo*, defined as the inverse of tone interonset interval (IOI), seems a natural choice. However, *beat* or *tone* IOI have also been used.

Figure 1 shows some simple *ritardando* curves and how they appear in three different representations. The left column of panels in Fig. 1 shows tone IOI as a function of score position x, the middle column of panels shows the same curves transformed into tempo as a function of score position, and the right column of panels shows the same curves
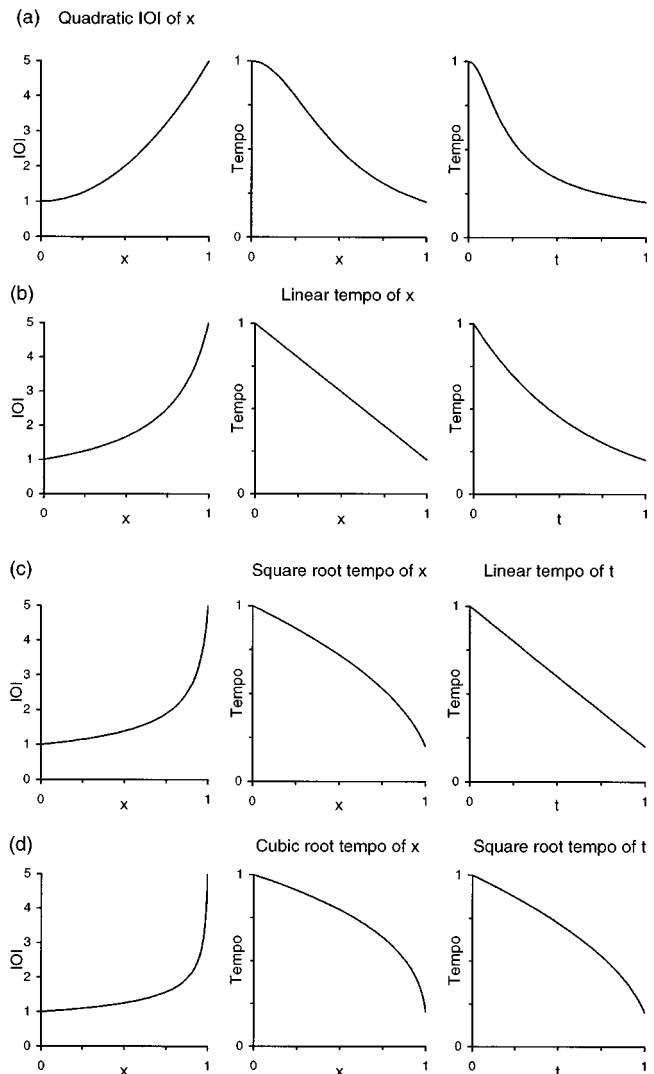
FIG. 1. Comparison of different methods of representing tempo changes during the final *ritardando* using the indicated four simple functions [(a)–(d)]. The columns show these functions plotted against alternative abscissas: IOI as a function of position x (left column), tempo as a function of position x (middle column), and tempo as a function of time t (right column).

expressed as tempo as a function of time. The choice of variables obviously affects the shape of the curve profoundly. A change of the independent variable from score position to time (mid- and right columns) results in a more concave or less convex curvature. For example, when the tempo is a square-root function of score position, it becomes a linear function of time. A quadratic relation between IOI and score position (top-left panel) has been used several times in the past (e.g., Todd, 1985; Repp 1992b; Friberg, 1995b). Note that this curve, when transformed into a curve showing tempo versus score position (top-middle panel), starts with a convex and ends with a concave curvature.

B. Previous models of tempo variations

Sundberg and Verrillo (1980) analyzed the characteristics of the final *ritardando* in music performances. They measured tone IOIs in 24 performed final *ritardandi* in recordings of baroque music and computed an average final *ritardando* profile for tempo versus time. Out of these data, they derived a model consisting of two phases, each of which

showed a linear decrease of tempo when expressed as a function of score position. The length of the second phase corresponded to the last musical motif of the piece.

Kronman and Sundberg (1987) found that the average final *ritardando* profile could be rather accurately approximated by one single square-root function, thus abandoning the two-phase model. They further related this function to what they assumed to be an accurate description of the decrease of the footstep frequency of a stopping runner, provided there was constant body deceleration and constant step length. This similarity suggested an interesting analogy between musical tempo and step frequency. It may be noted that the step frequency is equivalent to velocity if the step length is constant. However, Kronman and Sundberg used the *ritardando* data by Sundberg and Verrillo, expressed as instant tempo versus time, and compared these data with the deceleration model expressed as step frequency versus position. A simpler analogy would be to use time as the independent variable in both cases. If this is done, the tempo curve for the final *ritardando* becomes much less similar to the model, as in this case the step frequency comes out as a linear function of time.

Feldman *et al.* (1992) investigated curves of performed *accelerandi* and *ritardandi* in five examples that were selected by David Epstein from commercially available recordings. The authors developed a simple force model of physical motion that assumed tempo to be equivalent with velocity. They regarded smooth beginnings and endings important characteristics of such tempo changes, and therefore proposed that tempo should be expressed as a quadratic or cubic function of time. These functions correspond to a linear and a quadratic change of force with time, respectively. However, in the subsequent analysis, they used beat duration as a function of score position instead of tempo as a function of time, thus suggesting that these two completely different representations could be regarded as equivalent. They fitted their data, expressed in this new form (beat duration of score position), to linear, quadratic, or cubic functions. They found the two latter alternatives reasonably appropriate to approximate these data and falsely concluded that their force model neatly accounted for the observed tempo profiles.

Repp (1992a) measured the timing of 28 performances of Robert Schumann's *Träumerei*. The *accelerando–ritardando* shape of a salient, six-note motif was successfully modeled by expressing tone IOI as a quadratic function of score position. He also carried out a perceptual evaluation of this function applied to synthesized piano performances of the same music example (Repp, 1992b).

Todd (1985) presented a model of phrase-related tempo changes in music performances. In this model, tone IOIs were expressed as quadratic functions of score position. Later, he proposed a modified version (Todd, 1992, 1995) based on an analogy between velocity in physical motion and tempo in music performance, thus implying equivalence between physical position and score position. He simply assumed the deceleration and acceleration forces to be constant, which implied linear variations of tempo as a function of time (see also Longuet-Higgins and Lisle, 1989). It can be noted that this case corresponds to a square-root function of

TABLE I. Data on the dancers who performed the analyzed decelerations.

Dancer	Sex	Height (cm)	Weight (kg)
M1	Male	181	75
M2	Male	180	67
F1	Female	170	49
F2	Female	165	53

score position [Fig. 1(c) middle- and right panels], thus similar to the model presented by Kronman and Sundberg (1987).

Building on Todd's idea of a quadratic relation between tempo and score position, coauthor A.F. developed a model that related tempo changes to the hierarchical phrase structure (Friberg, 1995b). The model allowed for variations that typically can be observed between different experts' performances of the same piece. Thus, when tested against Repp's measurements of the 28 performances of *Träumerei*, the model successfully accounted for the tempo variation at the phrase level observed among these performances.

Summarizing, the models above have described the shape of the tempo variations as (1) a linear change of tempo versus score position, (2) as a quadratic change of IOI versus score position, or (3) as a linear change of tempo versus time. These models were based merely on assumptions regarding physical motion. Thus, no data were collected from real decelerations as performed by, e.g., human runners. This lack of reference to motion data was pointed out by Desain and Honing (1996), who also mentioned the likely influences of musical structure and global tempo on the final *ritardando*. Although human locomotion has been studied in several investigations (Margaria, 1976; Cavagna *et al.*, 1988; Alexander, 1995; Nilsson and Thorstensson, 1987; Ae *et al.*, 1992), the characteristics of stopping locomotion seem to have attracted little attention. Hence, it seemed necessary to perform actual measurements of runners' decelerations.

II. RUNNERS' DECELERATION

A. Methods

1. Deceleration measurements

Professional dancers, two males and two females, were used as subjects (Table I). Their task was to run at predetermined initial-step frequencies along a marked straight line and to stop their running at a marked point along this line. The subjects were not asked to think of any musical models for their running and deceleration; actually, music was not mentioned during the instruction of the subjects. Although the subjects were professional dancers, neither their running nor their decelerations appeared special in any sense.

The initial step frequencies were given in terms of acoustical click signals provided by a metronome connected to a loudspeaker. This signal was presented before the subjects started to run and continued during the first part of their running. Two step frequencies were selected, 2.9 and 4 Hz (interstep intervals 340 and 250 ms, respectively). The point at which the subjects were supposed to start the slowing down was either free, i.e., left to the subjects to decide, or

shown by a mark on the floor, 4 or 7 m from the end point. Each condition was recorded five times, but only two of the subjects used the free condition.

The experiment was carried out in a large hall. Stripes of sticky reflective tape were fastened to the floor perpendicular to the direction of running, 1-m apart at the beginning of the running path, and at 0.1 m along the final 10 m. Such tape stripes were also fastened to the subjects' ankles and hips as references. The footsteps were picked up by an audio microphone and also by a set of accelerometers placed on the floor at 2-m distances along the final 10 m of the running path. The audio and accelerometer signals were recorded on a TEAC PCM data recorder. The running was filmed by a video camera and recorded on a VHS recorder.

By displaying the video recording frame by frame, the step length could be determined with an accuracy of approximately ±3 cm. The audio and accelerometer recordings were analyzed using a waveform editing program (Soundswell Signal Workstation) allowing an accuracy of about ±5 ms in determining the time intervals between the impacts of the footsteps.

2. Rating experiment

Although the runners were all professional dancers, it seemed unrealistic to preclude that they invariably performed decelerations that completely corresponded to their artistic intentions. As it seemed unwise to base a model of final *ritardandi* on accidentally pathological examples of runners' decelerations, an evaluation experiment was run. Using the video recordings from the experimental session, an initial assessment of the aesthetical overall quality of the decelerations was carried out by a highly experienced teacher of eurhythmics at the Royal College of Music, Stockholm. The purpose of this pretest was to reduce the number of decelerations in the subsequent analyses.

Eight decelerations from each of the two step frequencies were selected. The selection was made so as to obtain a maximum variation with regard to subject, rating values obtained in the pretest, and deceleration-distance conditions. These 16 decelerations were copied into a video test tape, where each deceleration appeared three times. They were separated by 7-s pauses. The test took about 15 min and was preceded by eight practice trials. The tape was presented to six experienced experts in choreography and/or eurhythmics. The judges were asked to rate overall *aesthetic quality* of the final deceleration, taking into consideration *form* and *balance*. For each of the 48 decelerations, the judges put a mark on a 10-cm line on an answer sheet where the left end represented ''Extremely unaesthetic'' and the right end ''Extremely aesthetic.''

B. Results

1. Rating experiment

Table II summarizes the test result in terms of ratings averaged across replications and judges and the corresponding standard deviations. The table shows that the judges did not clearly prefer any particular step frequency or deceleration distance.

TABLE II. Ratings, averaged across repetitions and judges, of the aesthetical quality of the decelerations, listed in rank order.

Runner	Initial-step frequency (Hz)	Deceleration distance condition (m)	Mean rating (cm)	s.d. (cm)	Rank
M1	2.9	7	6.3	2.5	1
M1	2.9	4	6.3	2.2	2
M1	4	7	6.2	2.5	3
F2	2.9	free	5.9	2.5	4
F2	2.9	free	5.8	2.5	5
F2	4	free	5.8	1.9	6
F2	4	free	5.6	2.7	7
F1	2.9	free	5.3	2.4	8
F1	2.9	free	5	2.3	9
F2	4	4	4.8	2.1	10
F1	4	free	4.4	2.5	11
F1	4	free	4.2	2.3	12
M2	2.9	7	3.5	2.3	13
M2	4	7	2.7	1.8	14
M2	2.9	4	2.6	2	15
M2	4	4	1.5	1.8	16

Figure 2 shows the ordered-mean ratings for all the decelerations. The difference in mean rating was small between the stimuli that were rated high and greater between those which rated low. Thus, the curve showed a slight trend to a discontinuity between rank-order numbers 12 and 13. One male dancer, M2, produced all four lowest-rated decelerations. Most of these four decelerations exhibited irregularities in step-frequency patterns during the deceleration, as seen in the right-top graph in Fig. 3, and were omitted in the computation of average decelerations.

2. Deceleration patterns

Figure 3 shows instant-step frequency (inverse of interstep duration) and the associated step length for the two decelerations that the judges rated highest. To give an idea of the variation in the data, the two lowest-rated decelerations are also included in this figure. The decelerations mostly included six to ten steps. The step-frequency patterns varied widely among the 16 decelerations, some decreasing slightly,
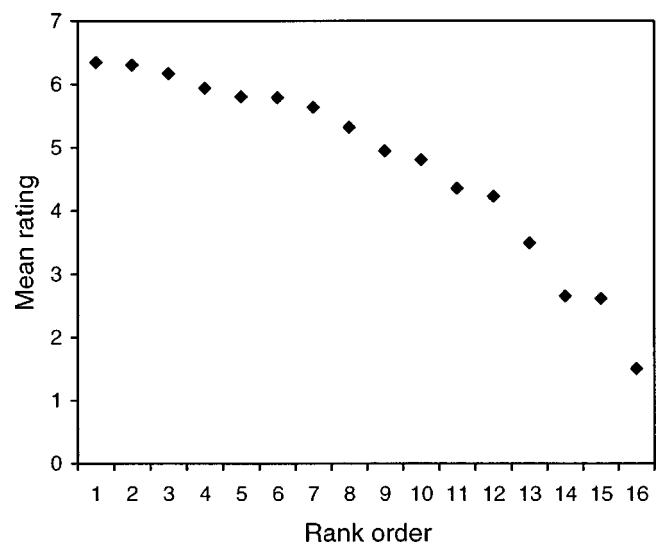
FIG. 2. Rank-ordered mean ratings obtained from the experiment where experts rated the aesthetical quality of runners' decelerations.
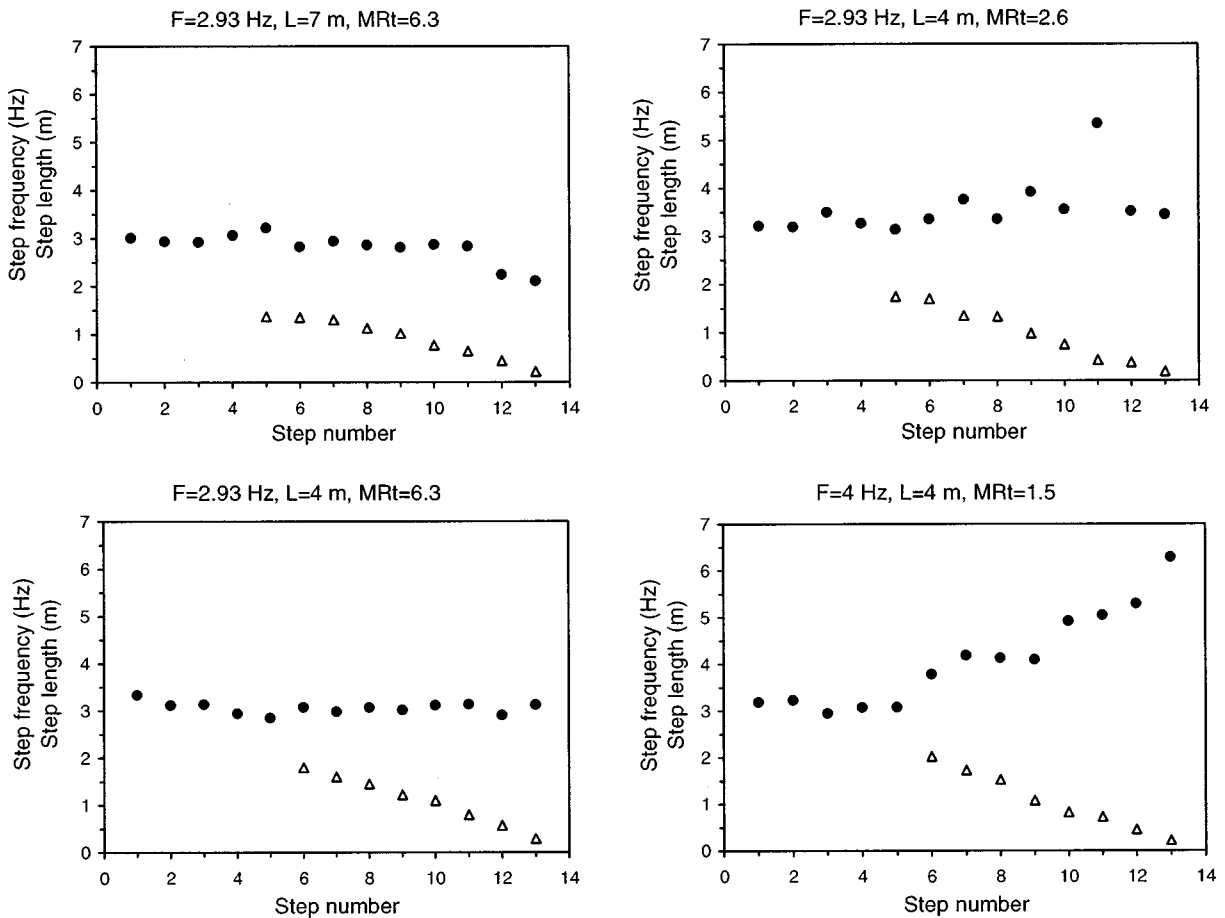
FIG. 3. Instant-step frequency (filled circles) and step-length (open triangles) patterns for the two highest- (left) and the two lowest- (right) rated decelerations. The initial values of step frequency (F), deceleration length (L), and the mean rating (MRt) of the deceleration are shown above each panel.

some remaining basically constant, and some even increasing toward the end of the deceleration, thus clearly negating the possibility that the change in step frequency serves as the model for the tempo change in final *ritardandi*. The step length, by contrast, decreased gradually toward the end of the deceleration in all cases. Thus, the slowing down was achieved mainly by decreasing the step length, an observation which is in good agreement with previous findings on the relation between step length and speed of locomotion (Alexander and Maloiy, 1984; Cavagna *et al.*, 1988).

Figure 4 shows velocity versus distance to the point of stop for the same decelerations as in Fig. 3. Instant velocity was estimated at each step by dividing the step length with the step duration. The position of each velocity estimation was taken as the middle value between two step positions. The number of velocity estimations ranged from six to eight points and the estimated deceleration distance ranged from 5.9 to 8.2 m in the 12 decelerations. The normalized velocity versus normalized position for all 16 decelerations are shown in the Appendix, Fig. A2.

As the number of velocity data for each deceleration was comparatively small, an average was computed for the 12 highest-ranked decelerations (mean ratings >4). Two average-velocity curves were computed: one curve with position and one curve with time as the independent variable. In both cases, each of the 12 velocity curves was normalized with respect to the first estimated-velocity value and with

respect to the associated position and time, respectively. Velocity values between data points were obtained by linear interpolation. The means were computed by sampling these interpolated normalized curves at 20 equidistant steps of position or time.

The resulting normalized mean velocity as a function of normalized position is shown in Fig. 5(a). The values of 0 and 1 on the abscissa correspond to the starting and the termination of the deceleration, respectively. The bars mark the 95%-confidence interval for the estimation of the mean at the sampled positions.

The mean-velocity pattern, when plotted as a function of normalized time, is very similar to that of the normalized mean *ritardando* curve of Sundberg and Verrillo (1980), see Fig. 5(b). This supports previous suggestions that there is equivalence between velocity and tempo (Todd, 1992, 1995; Feldman *et al.*, 1992). Note that, for reasons of comparison, the abscissa is normalized time. The match was obtained after scaling the abscissa of the velocity curve by a factor of 1.13. This value was found on a trial-and-error basis. The use of a scaling factor is motivated by the fact that, obviously, a *ritardando* curve can never reach a normalized tempo value of zero since it corresponds to an infinite note duration.

Kronman and Sundberg (1987) assumed that the deceleration force is constant during a deceleration of running (see also Todd, 1995). This implies that velocity is a straight line if time is used as the independent variable. As seen in Fig.
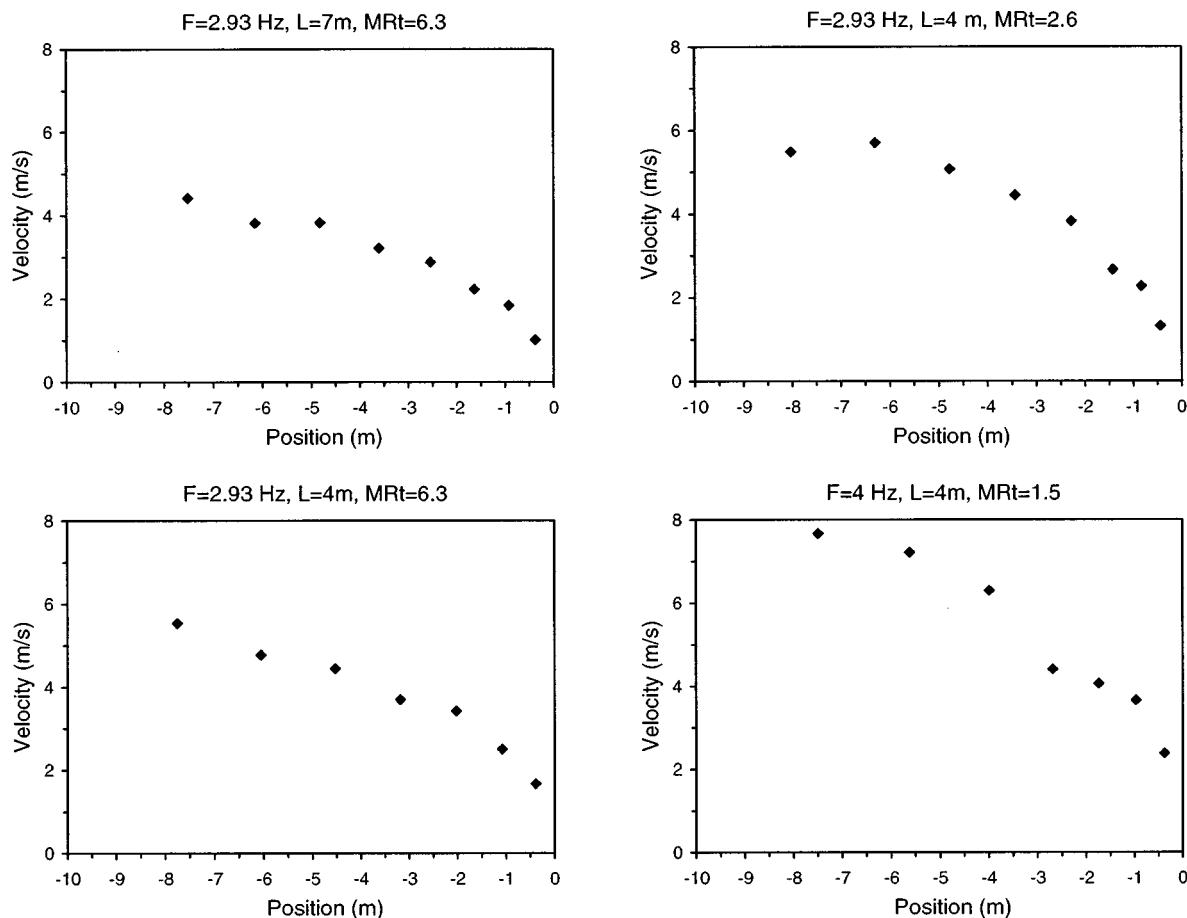
FIG. 4. Instant-velocity patterns for the decelerations shown in Fig. 3. The initial values of step frequency (F), deceleration length (L), and the mean rating (MRt) of the deceleration are shown above each panel.

5(b), this was not the case. However, the square of the velocity, i.e., the kinetic energy, is close to a straight-line function of time as shown in Fig. 5(c). Note that the straight-line approximation of the data point passes very close to the corners of the square in this figure. The close agreement between the data points and the line implies that the deceleration *power* was approximately constant throughout the entire deceleration. Individual velocity curves will be analyzed below in terms of how well our model fits the data.

C. Discussion of decelerations

An important question is to what extent the obtained velocity curves were specific to the experimental conditions in the recording session. Obviously we would have obtained quite different deceleration curves if the dancers had been running on a slippery surface, such as ice. The recordings were made in a gymnasium, where the floor has a comparatively large friction and thus should not have caused any abnormality in the deceleration data. Furthermore, in the rating experiment no preference was observed for any specific condition regarding step frequency or deceleration distance. Thus, our mean-velocity curve can be assumed to be reasonably representative for the stopping of running.

It could be argued that dancers are biased subjects in an experiment with the present aim, being prone to adopt the typical patterns of classical choreographic art. On the other hand, in the video recordings no tendency to use any special locomotion patterns could be seen. It could also be argued

that professional dancers are a typical subjects as they have been specially trained to move in synchrony with music. However, professional dancers share with almost anyone the experience of moving to music, since dancing is a very commonly enjoyed form of social life.

To rate the aesthetical quality of a runner's deceleration implies the task of giving a global assessment of a stimulus possessing many dimensions, such as coordination of limb movements, posture, etc. (Todd, 1983). In our case, this would have contributed to the comparatively high standard deviations of the ratings. The judges may have attributed different degrees of importance to various aspects of a given deceleration. Still, the rating experiment seemed to serve its main purpose, viz., to identify decelerations that appeared particularly unaesthetical to expert judges.

When plotted in rank order, the distribution of the ratings showed a slight trend to an elbow-like curve. It is interesting that a similar curve was found when, in a quite different experiment, experts rated hoarseness and other voice characteristics in children's voices (Sederholm *et al.*, 1993). In both these rating experiments, the notion of acceptability/ unacceptability of a multidimensional stimulus was probably relevant.

III. MODEL

A basis for the construction of our model for final *ritardandi* was the assumption that the deceleration power was constant in a runner's deceleration (*vide supra*). This implies

FIG. 6. The *ritardando* model with four different q values ($q=1,2,3,4$) and the quadratic IOI function. The final tempo was fixed at $v_{end}=0.3$. These five curves were used in the listening experiment.

FIG. 5. (a) Normalized mean velocity for the 12 highest-ranked decelerations as function of normalized score position. The bars mark the 95%-confidence interval. (b) Normalized mean velocity for the 12 highest-ranked decelerations as a function of normalized time (solid line) and mean normalized *ritardando* tempo versus normalized time according to Sundberg and Verrillo (1980). The former curve was obtained after scaling the time values by a factor of 1.13, see the text. (c) Squared normalized mean velocity for the 12 highest-ranked decelerations as a function of time. The line shows the best linear fit.

that the kinetic energy is a linear function of time and, since kinetic energy is proportional to velocity squared, velocity will be proportional to a square-root function of time. Let v be velocity (tempo), x be position (score position), then

$$v = \frac{dx}{dt} \sim \sqrt{t}. \tag{1}$$

Primarily for practical purposes discussed above, x was chosen as the independent variable. Integrating v with respect to t, solving for t, and substituting t in Eq. (1), we obtain

$$v(x) \sim x^{1/3}.$$

Thus, velocity (tempo) is proportional to the cubic root of position (score position). Reinspection of the individual *ritardandi* analyzed by Sundberg and Verrillo (1980) revealed variation with regard to the overall curvature. To account for this variation, a curvature parameter q was introduced

$$v(x) \sim x^{1/q}.$$

By changing the constant q, a number of different curvatures can be obtained, including the runners' mean deceleration ($q=3$) as well as the previously mentioned square-root function ($q=2$).

Unlike velocity in locomotion, the tempo never reaches zero in music, if tempo is defined as the inverse of tone IOI. This implies the need for a second parameter, the final tempo v_{end}. The resulting model of the tempo (v) as a function of score position (x) was defined as

$$v(x) = [1 + (v_{end}^q - 1)x]^{1/q}. \tag{2}$$

Here, tempo and v_{end} are normalized with respect to the pre-*ritardando* tempo v_{pre} and position is normalized with respect to total *ritardando* length measured in score units. Score position $x=0$ corresponds to the start position of the *ritardando* and $x=1$ to the onset of the last note. Thus, $v=1$ at $x=0$ and $v=v_{end}$ at $x=1$. Figure 6 shows the resulting tempo curves for four different q values. The values of $q=1$, $q=2$, and $q=3$ correspond to (a) a linear function of x, (b) a square-root function of x (i.e., a linear function of t), as pro-

posed earlier by Kronman and Sundberg, and Todd, and (c) the approximation of runners' deceleration, respectively.

The translation from the continuous curve to discrete tones can be realized by integrating the inverse of the tempo function in Eq. (2):

$$\int \frac{1}{v} = \int \frac{dt}{dx} = \int [1 + (v_{end}^q - 1)x]^{-1/q}.$$

Let $k = v_{end}^q - 1$. Then, we obtain time as a function of score position

$$t(x) = \frac{q(1+kx)^{(q-1)/q} - q}{(q-1)k}, \quad q > 1. \tag{3}$$

The integration constant was determined by setting $t(0) = 0$. The IOI of a tone is given by the time difference for the x values corresponding to the onset of the tone (x_1) to the onset of the following tone (x_2).

$$\begin{aligned} \text{IOI} &= t(x_2) - t(x_1) \\ &= \frac{q(1+kx_2)^{(q-1)/q} - q(1+kx_1)^{(q-1)/q}}{(q-1)k}. \end{aligned} \tag{4}$$

The advantage of using $t(x)$ to determine the tone durations is that it is independent of note values. For example, four sixteenth notes will add up exactly to the duration of one quarter note. It means that Eq. (4) can be applied on each voice in a polyphonic example and at the same time keep the synchrony. This is not the case if IOI is obtained by inverting the tempo value obtained from the continuous tempo curve at, e.g., the onset position of the tone.

The model [Eq. (2)] has the advantage that it is easy to transform, if time instead of position is preferred as the independent variable. Tempo as a function of time can be obtained by solving Eq. (3) for x and substituting the result in Eq. (2)

$$v(t) = [1 + (v_{end}^{q-1} - 1)t]^{1/(q-1)}.$$

Note that this equation is essentially the same as Eq. (2), with the value of q decreased by one.

A. Perceptual evaluation of the model

A listening experiment was performed to assess the preferred curvature value q in different music examples. The previously mentioned curve with IOI as a quadratic function of score position was included as an additional alternative.

1. Stimuli and procedure

Three different music examples were used, two excerpts from pieces by J. S. Bach and one sequence of two alternating notes a minor second apart, see Table III. In both Bach examples, the *ritardando* was applied to an unbroken sequence of notes of equal note values. These examples were chosen for evaluating the *ritardando* in musically realistic contexts, while the minor second example was chosen to attain a minimum of musical content without destroying the perception of the *ritardando* curve. When informally listening to the examples, the authors found that a simple tone repetition was not enough to differentiate the curvatures.

TABLE III. Music examples used in the listening experiment. The tempo before the *ritardando* (v_{pre}) and at the end (v_{end}), normalized with respect to v_{pre}, are also listed.

Music example	Abbreviation	v_{pre} (shortest notes/s)	v_{end}
J. S. Bach: Eng. Suite 2 Prel., last 5 meas.	E2P	6.48	0.3
J. S. Bach: Wohltemp. clav. I Prel. 1, last 5 meas.	WIP	4.47	0.4
minor second sequence (Db4–C4–Db4–C4–Db4 –C4–,...,Db4), 21 notes total	m2	5	0.4

Four different q values ($q = 1,2,3,4$) were used for the *ritardando* model [Eq. (2)]. For the phrasing curve with IOI as a quadratic function of score position, the expression

$$v(x) = \frac{1}{(1/v_{end} - 1)x^2 + 1}, \quad v_{end} > 0$$

was used, see Fig. 6.

The pre-*ritardando* tempo (v_{pre}), *ritardando* length, and final tempo (v_{end}) were fixed for each music example throughout the test (see Table III), and determined according to the advice of two professional musicians, Lars Frydén and Monica Thomasson, who listened to different alternatives. In all examples, the *ritardando* started at the first note onset occurring at least at 1.3 s, as measured in pre-*ritardando* note duration, preceding the last note.

When informally listening to the examples, it was found that the IOI of the penultimate note was important to the perceived magnitude of the *ritardando*. The method described above [Eq. (4)] for translation of the continuous-tempo function to discrete-note IOI did not allow specification of an exact value for the lengthening of the penultimate note (i.e., if the $v_{end} = 0.4$, the duration of the penultimate will *not* be DR $= 1/0.4$). Therefore, a second normalization was performed so that the IOI of the penultimate note was set to $1/(v_{end} * v_{pre})$.

Special attention also had to be paid to the last note. Its note value is sometimes the same as that of the preceding note, but sometimes considerably longer. In the latter case, no further prolongation of the last note is necessary. On the contrary, such long final notes can even be shortened in a real performance. In the test, the duration of the final note was simply set to 1.25 times the IOI of the penultimate note (m2 example). However, if the last note was already longer than this, it was left unchanged (E2P and WIP examples).

Lacking information about the relation between tempo and dynamics in final *ritardandi*, the music examples were played on sampler synthesis of a harpsichord (SampleCell). The *ritardando* model was implemented in the DIRECTOR MUSICES program (Friberg, 1995a) on a Macintosh computer. The examples were recorded on a DAT tape with some artificial reverberation (Yamaha REV7). All judges listened to the tape over earphones adjusted to a comfortable listening level.

The test tape contained 51 examples. The first six examples were selected from the following and were used for

practice trials only. The remaining 45 examples (5 curves×3 music examples×3 repetitions) were presented in random order. The entire test tape took 17 min.

The judges were asked to mark on a 10-cm-long visual analogue scale on an answering sheet how musical they found the performance of the *ritardando*. The endpoints of the line were labeled ''extremely good'' and ''extremely bad.'' The listeners were also instructed to try to ignore the performance of the music preceding the *ritardando* as well as the length of the final note, since these parameters did not change with tempo curvature. The rating values used in the subsequent analysis was defined as the length in mm from the extremely bad endpoint, i.e., the better *ritardando*, the higher the rating value.

2. Judges

A basic hypothesis was that the *ritardando* alludes to the stopping of locomotion and hence should be familiar not only to professional musicians playing classical repertoire. Therefore, 19 students were used as judges, all taking the course in music acoustics at the Royal Institute of Technology. After the test, they answered a questionnaire about their musical background. The questionnaire asked if they had experience performing music, if so, what instrument, how many years of performing, how many hours per week, and in which music styles. In addition, they could make any general comment about the test.

According to the answers from the questionnaire, most of the judges could be considered as amateur musicians. Nine judges reported that they had some experience of classical music. One of these had professional experience as a classical musician. Most judges found the test quite difficult, except the professional player. Thus, the task was difficult for listeners lacking previous experience with performance of *ritardandi* on a professional level.

3. Results

Using the judges' ratings as the dependent variable, the results were submitted to a repeated-measures analysis of variance performed by the SUPERANOVA 1.11 program for Macintosh. The within factors were 5 curves ×3 music examples×3 repetitions. Despite the reported dif-
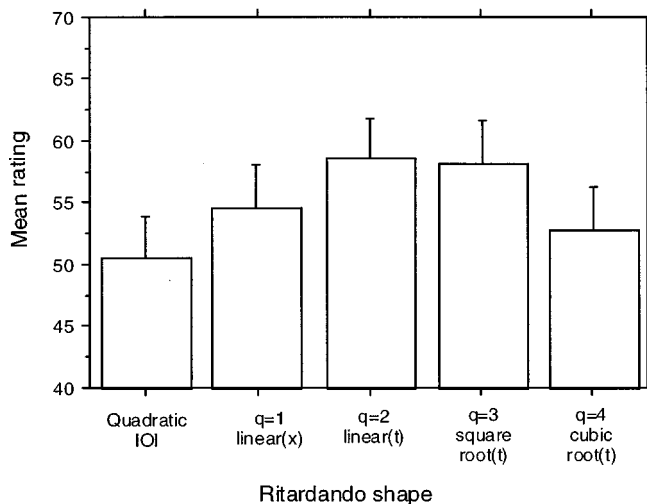
FIG. 7. Overall ratings, averaged across listeners, music examples, and repetitions, of the different curvatures used in the test. The bars indicate the positive parts of a 95%-confidence interval.

ficulty of the test, the main effect of curve was highly significant ($p < 0.0001$), indicating that the judges clearly could differentiate the curves.

The main effect of music example was significant ($p < 0.0001$); thus, the *ritardandi* were rated differently depending on the music examples. There was also a significant effect of repetition ($p < 0.015$). No interaction terms were significant. The main effect of music example and repetition disappeared when the m2 example was excluded from the analysis. The fact that there was a strong effect of repetition only in the case of the m2 example may indicate that this example had a strange musical content to which, however, the listeners gradually became accustomed.

The mean ratings for the different curvatures are shown in Fig. 7. They reveal that the two curvatures that received the highest ratings originated from the model with $q = 2$ and $q = 3$. The first value corresponds to the model supported by Kronman and Sundberg (1987) and by Todd (1992, 1995), while the second value corresponds to the curvature derived from runners' decelerations. Both for higher and lower q values and the quadratic IOI, the mean ratings were lower. This was confirmed by a highly significant contrast analysis resulting from a comparison of the cases $q = 2$ and $q = 3$ with the three remaining alternatives ($p < 0.0001$).

Figure 8, showing the means for each music example
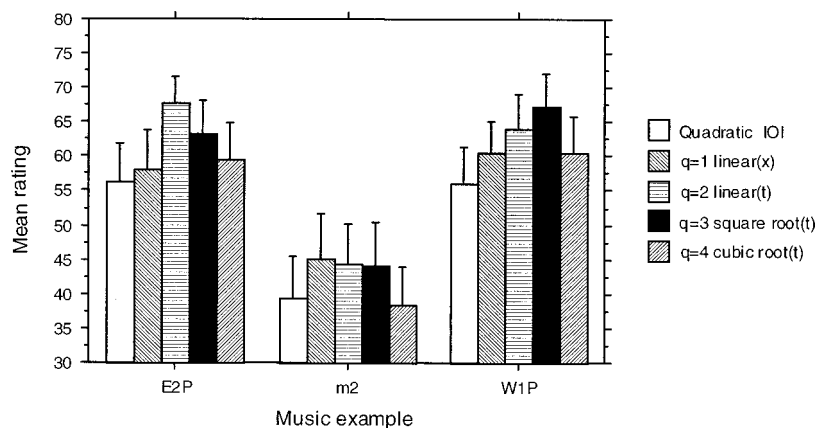
FIG. 8. Mean ratings for the interaction of music example and type of *ritardando* curve. The bars indicate the positive parts of a 95%-confidence interval.
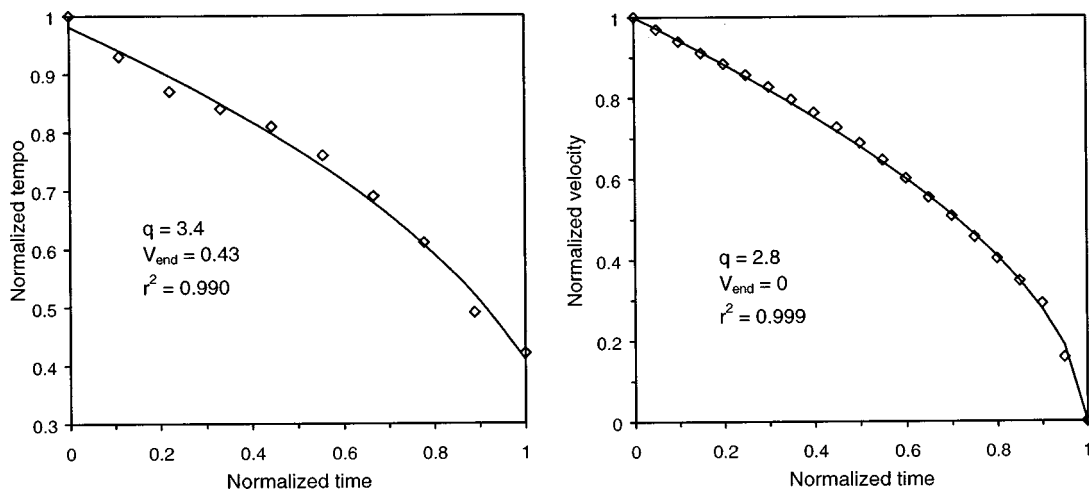
FIG. 9. Left panel: The model (solid line) fitted to the mean *ritardando* curve (diamonds) from Sundberg and Verrillo. Right panel: The model (solid line) fitted to the mean velocity curve (diamonds) of the runners' deceleration. Note that time rather than position is used as the independent variable. The model-parameter values used and the resulting determination coefficient are also shown.

and curve, offers a more detailed representation of the results. First, it can be noted that for all curves the minor second example was rated much lower than the other examples. Obviously, despite the instruction to concentrate on the *ritardando*, the judges were unable to disregard the musical context. Second, the maximum rating was obtained for the $q=2$ curve in the E2P example and for the $q=3$ curve in the WIP example. This suggests that the optimum curve is dependent on the music example. A contrast analysis comparing $q=2$ for E2P and $q=3$ for WIP with $q=3$ for E2P and $q=2$ for WIP showed a barely significant difference ($p<0.04$). Further testing with more-skilled listeners is needed to further confirm this hypothesis.

B. Matching the model to measurements

In a previous section, the runners' deceleration was found to fit well with the average *ritardando* curve. Here, the ability of the model to fit performed mean and individual *ritardandi* as well as runner's mean and individual decelerations will be examined.

The q and v_{end} parameters in the model, defined in Eq. (2), were varied by means of the solver function in Microsoft EXCEL 7.0, such that the sum of the squared distances between the model and the measured data was minimized. The normalization of measured *ritardandi* and decelerations were done relative to the first value. It means that a slight offset of the first value affects all remaining values. Therefore, an additional third parameter, v_{offset}, was varied in the optimizing process, which added a constant to the model.

1. Average curves

As an initial check of previous results, the model was fitted to the curves for the mean *ritardando* and the mean deceleration, see Fig. 9. The fit is good in both cases. In the case of the deceleration curve, however, this was expected, as the model was originally derived from this curve. Figure 9 also specifies the optimal values of the parameters q and v_{end}. For both cases, the q values were close to 3.

2. Individual ritardandi measured by Sundberg and Verrillo

The model was also fitted to individual *ritardandi* taken from the original raw data by Sundberg and Verrillo. In a *ritardando*, local lengthenings and shortenings of individual tones frequently occur, depending on musical context. Such local departures from the main *ritardando* curve increase the scatter in the fitted-parameter values. Therefore, to improve the reliability of the fitted-curvature data, only *ritardandi* with a smooth shape were selected, which contained a minimum of individual note departures. Thus, only the performances with at least six consecutive final notes with monotonically increasing IOIs were used. In this way, 12 final *ritardandi* were selected out of a possible total of 22, all by J. S. Bach, see Table IV. Apart from the present model, two other alternatives were tried. As note IOI is frequently assumed to be a quadratic function of score position, one alternative was a quadratic polynomial in which the three parameters were fitted to measured IOIs (henceforth, quadratic IOI). In the other alternative, a similar quadratic function was used to approximate the tempo rather than note IOI (henceforth, quadratic tempo). The fitted-model parameter values and the resulting determination coefficients (r^2) for the 12 examples are listed in Table IV. The model fitted to the 12 examples is plotted in the Appendix (Fig. A1). A comparison of the model and the two alternatives fitted to the first music example (WIP) is shown in Fig. 10. Notice that the quadratic IOI has the undesired property of an initial tempo increase. A more realistic model for the quadratic IOI would be to restrict the tempo to be decreasing. This would make for an even poorer fit.

As shown in Table IV, the mean q value ($q=2.8$) is very close to the initial value of $q=3$ that was derived from the runners' decelerations. Note that example WIP was also used in the listening experiment above. It received a q value of 2.5 that is just in the middle of the listeners' preference, as seen in Fig. 7. However, q varied substantially between examples. Indeed, two examples yielded $q=1.2$, i.e., the tempo decreased almost linearly with score position, and in three examples, q exceeded the value of four. Such low and high

TABLE IV. Model parameters (q, v_{end}, v_{offset}) producing the best fit of individual *ritardandi* for 12 music examples measured by Sundberg and Verrillo (1980). The number of notes included in the *ritardando* is listed in the second column. The resulting determination coefficients are given in the column marked Model. The two rightmost columns show the determination coefficients r^2 obtained for the two alternatives tried, the quadratic interonset interval (IOI), and the quadratic tempo (see the text).

Music examples	Notes	Fitted-model parameters			Determination coefficients (r^2)		
		q	v_{end}	v_{offset}	Model	Quadratic IOI	Quadratic tempo
W. clav I Prel. 1 (WIP)	10	2.5	0.32	0.005	0.982	0.927	0.975
W. clav II Prel. 1 (WP1)	8	2.1	0.37	0.0001	0.980	0.989	0.983
W. clav II Prel. 2 (WP2)	7	2.4	0.51	0.03	0.967	0.989	0.977
W. clav II Fug. 3 (WF3)	6	1.2	0.48	−0.03	0.969	0.951	0.968
W. clav II Fug. 5 (WF5a)	7	4.2	0.50	0.01	0.995	0.970	0.995
W. clav II Fug. 5 (WF5b)	8	2.6	0.37	−0.02	0.975	0.919	0.966
Eng. Suite 1 Allem. (E1A)	6	2.0	0.45	−0.03	0.982	0.943	0.978
Eng. Suite 2 Allem. (E2A)	11	3.7	0.37	0.02	0.975	0.927	0.980
Fr. Suite 4 Cour. (F4C)	6	4.2	0.50	0.02	0.991	0.959	0.986
Fr. Suite 6 Allem. (F6A)	7	2.4	0.45	0.02	0.981	0.965	0.979
Fr. Suite 6 Cour. (F6C)	7	5.0	0.46	−0.008	0.994	0.902	0.959
Italian Conc. Mvt. 3 (IC3)	7	1.2	0.34	−0.01	0.970	0.961	0.970
Mean		2.8	0.43	0.001	0.980	0.950	0.976
s.d.		1.2	0.07	0.02	0.01	0.03	0.01

values of q received low ratings in the listening test above (using other examples), yet were obviously acceptable in these performances. This supports the assumption above that the optimal *ritardando* curve depends on some characteristics of the music example, e.g., musical structure or tempo.

The final tempo v_{end} varied comparatively less, between 32% and 51% of the initial tempo. Desain and Honing (1996) suggested that the final tempo might be dependent on the global tempo. However, no indication of this was found in the present data. There was no correlation between the final tempo (v_{end}) and the pre-*ritardando* tempo ($\bar{T}$) as defined by Sundberg and Verrillo ($r = -0.02$).

Our model produced the highest mean correlation with the measurements (mean $r^2 = 0.98$). A *t*-test comparing the mean r^2 for the model and the mean r^2 for the quadratic IOI alternative yielded a significant difference ($p < 0.003$): this means that, on average, the model approximated the measured *ritardandi* better than the quadratic IOI.

The correlation was slightly better for the model than for the quadratic tempo, but this difference was not significant. With regard to the shortest *ritardandi*, consisting of no more than six notes, it could be argued that many slightly curved functions would offer a good fit. Longer *ritardandi*, on the other hand, often exhibited a more pronounced tempo decrease at the end than in the beginning. The model also accounted for such cases provided a relatively high value of q was used, see Fig. 11 (this example is not included in Table IV). The quadratic-tempo function, however, failed to produce the characteristic increased curvature toward the end of the *ritardando*.

3. Individual ritardandi measured by Feldman, Epstein, and Richards

Feldman *et al.* (1992) measured two *ritardandi* in performances of orchestral music. These *ritardandi* occurred within the pieces, i.e., not in a final position. Also, they were clearly longer than the final *ritardandi* considered above, and were measured at the beat level instead at the note level. The three functions presented above were fitted to their example, which had the smoother shape, see Fig. 12 (sample 1: A. Dvořák, Slavonic dance, op 48:8, measures 243–272). Despite the difference in style, length, and context, the result is similar to that observed for the *ritardando* shown in Fig. 11.
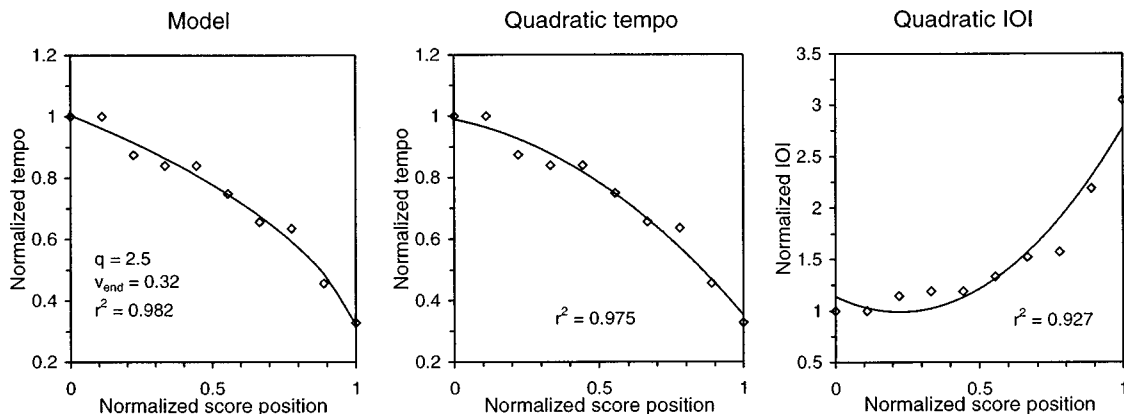
FIG. 10. Model (left), quadratic tempo (middle), and quadratic IOI (right) functions fitted to the *ritardando* data from music example WIP. The model parameters used are presented in Table IV.

FIG. 11. Model (left), quadratic tempo (middle), and quadratic IOI (right) functions fitted to a comparatively long *ritardando* measured in a performance of music example WP 19. This example was not included in Table IV. Note that the increased curvature in the end of the *ritardando* could not be modeled with a quadratic-tempo function.

Again, the model produced the best fit, slightly better than that of the quadratic-tempo function, especially in the end of the *ritardando*. The fit obtained with the quadratic IOI was the worst. It is noteworthy that Feldman *et al.* would have obtained much better fits if they had applied quadratic or cubic functions to tempo as a function of time (as they had suggested in the first part of their paper) rather than to IOI of score position.

4. Individual decelerations of runners

Table V presents the model and a quadratic-velocity function fitted to each of the 16 decelerations in Table II. The model fitted to the 16 examples is plotted in the Appendix (Fig. A2). According to the determination coefficients, also shown in Table V, the model matched the data better for the 12 highest-ranked decelerations. A two-tailed *t*-test revealed that the means of the determination coefficients r^2 differed significantly ($p < 0.02$) between the model and the quadratic-velocity function.

For the four decelerations that were discarded for reasons of low visual rating (Table V, rank 13–16), the determination coefficients for the model were significantly lower (two-tailed *t*-test, $p < 0.005$) than those of the group of 12, higher-rated decelerations (mean $r^2 = 0.975$ and 0.990, respectively). On the other hand, when fitting the quadratic function to these four decelerations, no significant change of r^2 was observed (mean $r^2 = 0.979$ and 0.978, respectively).

Thus, a high rating in the visual experiment corresponded to a good fit of the model, but this correspondence was not found if quadratic velocity was used.

IV. GENERAL DISCUSSION

In discussing the model proposed here for descriptions of final *ritardandi* and runners' decelerations, certain limitations should be kept in mind. The start of the final *ritardando* is difficult to identify in measurements, particularly in cases of a smooth onset. Perceptually a smooth onset of the *ritardando* is important, as mentioned. For example, informal listening tests revealed that the onset of the *ritardando* was far too abrupt when a linear tempo function of score position was applied. For the examples in Table IV, we identified the *ritardando* onset by means of a rigorously applied rule; that *all* tones after the onset must show a progressively decreasing tempo. This rule may yield delays of the point of onset in some cases, which leads to an underestimation of the value of *q*.

There are also other limitations. The perception of a final *ritardando* may depend not only on tempo changes, but also on dynamic changes. This parameter was not analyzed in the present investigation. Another important factor is its total length. What is considered an appropriate *ritardando* may also depend on the instrument played. In view of the analogies suggested by our findings between music and lo-
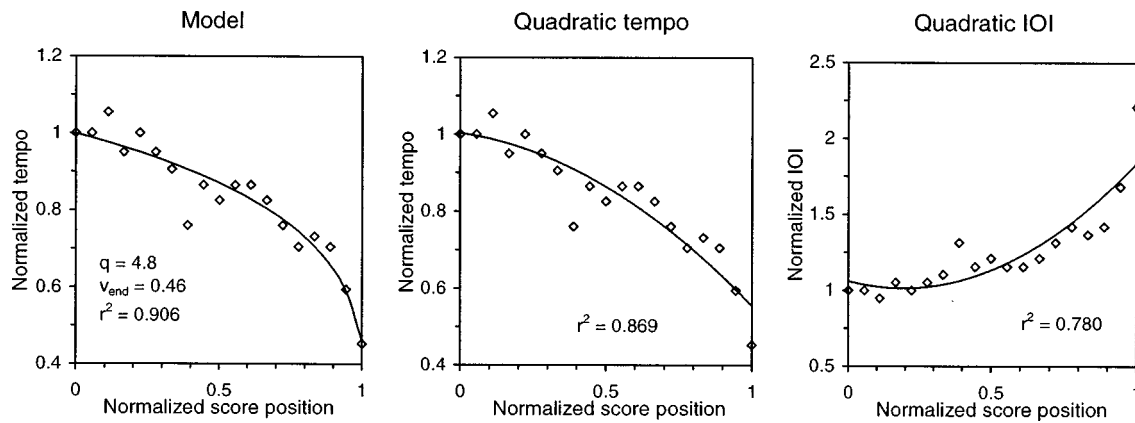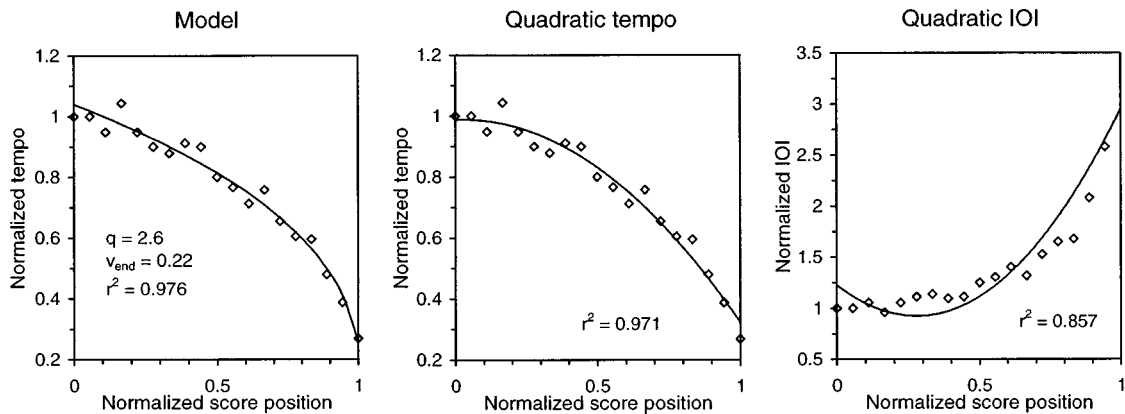

FIG. 12. Model (left), quadratic tempo (middle), and quadratic IOI (right) functions fitted to a *ritardando* measured by Feldman *et al.* (1992).

TABLE V. Model parameters (q, v_{end}, v_{offset}) producing the best fit of 16 individual decelerations produced by the dancers. The decelerations are listed in rank order according to the mean rating of aesthetic quality. The resulting determination coefficients are given in the column marked Model. The two rightmost columns show the determination coefficients r^2 obtained for the model and for the quadratic velocity alternative. The first 12 decelerations (Rank 1–12) were used for calculating the average deceleration pattern.

Deceleration	Fitted model parameters			Determination coefficient (r^2)	
Rank	q	v_{end}	v_{offset}	Model	Quadratic velocity
1	2.7	0.25	−0.02	0.989	0.975
2	2.7	0.33	−0.02	0.991	0.976
3	3.4	0.20	0.01	0.978	0.939
4	3.3	0.39	0.03	0.980	0.991
5	2.9	0.27	0.005	0.994	0.985
6	1.8	0.36	0.01	0.999	0.999
7	3.2	0.33	0.003	0.985	0.978
8	2.1	0.20	0.03	0.990	0.998
9	2.7	0.13	−0.006	0.996	0.962
10	2.7	0.31	0.003	0.988	0.976
11	3.4	0.32	0.01	0.995	0.981
12	2.7	0.21	−0.02	0.996	0.973
Mean (1–12)	2.8	0.27	0.004	0.990	0.978
s.d.	0.5	0.08	0.02	0.006	0.016
13	2.5	0.08	0.07	0.965	0.966
14	3.0	0.35	0.007	0.992	0.989
15	2.7	0.16	0.07	0.974	0.989
16	2.0	0.29	0.03	0.968	0.972
Mean (13–16)	2.6	0.22	0.05	0.975	0.979
s.d.	0.4	0.12	0.03	0.012	0.012

comotion, it would be tempting to explore possible musical equivalents of, e.g., inertia and its effect on the final *ritardando*.

It appeared that it was more difficult for the listeners to differentiate the tempo curves in a musically unnatural example. In selecting the music examples for the listening test, the authors frequently noted that the perceived character of the different curves was well exposed by real music examples but almost impossible to distinguish in unrealistic, simple examples, such as a sequence of tone repetitions. On the other hand, the tempo curve seems to originate from the paramount experience of locomotion. Maybe the musical unnaturalness of such examples distracts the listener's attention from the tempo curve. In any event, realistic musical examples seem crucial for a correct evaluation of any music performance model.

The quadratic IOI curve gave the poorest results, both in the listening experiment and in the curve fittings. This was surprising, since it had been successfully applied to describe tempo curves associated with phrasing (Todd, 1985; Repp, 1992b; Friberg, 1995b; Penel and Drake, 1998). Transformed to tempo as a function of score position, the quadratic IOI curve assumes a shape characterized by a gradual decrease of the curve steepness, as was illustrated in Fig. 1. If translated to velocity in locomotion, such a curve shape would imply that the runner refrains from spending energy on reduction of speed toward the end of the deceleration process, thus suggesting a continuation of the movement. This message appears quite appropriate at phrase endings; the music will continue beyond the phrase boundary. Indeed, according to informal listening tests the impression of an

approaching final stop disappeared when the quadratic IOI curve was used for final *ritardandi*; it was no more obvious that the last tone really was the last.

A factor of possible relevance to our results is musical style. The measurements and fittings in which the quadratic IOI was used mainly concerned romantic classical music, while the present final *ritardando* model was mostly tested on baroque music [except for sample 1 from Feldman *et al.* (1992), which was composed by Dvořák]. It is also possible that the poor success of the quadratic IOI alternative reflected that these two music styles are associated with different types of motion.

Surprisingly, we found two cases of $q = 1.2$ in the fittings of the individual *ritardandi*, i.e., the tempo decreased almost linearly with score position. Such a curve ($q = 1$) was rated low in the listening experiment (applied on different examples). Also, when applied in informal tests to a variety of music examples, this curve sounded musically unacceptable. As with the quadratic IOI one problem was that the piece did not appear to approach a final stop during the last part of the *ritardando*.

Why does our model work? The two cases $q = 2$ and $q = 3$, which received the highest ratings in the listening experiment, have a very simple form in terms of locomotion; the former implies that the braking force is constant while the latter implies that the braking power is constant. Such simple relations would facilitate prediction of the point of final stop.

The deceleration power was found to be approximately constant throughout the entire deceleration process. Thus, the dancers' velocity patterns appeared to be well planned, which should enable a spectator to predict the point of final stop. The similarity between the velocity curves and the tempo curves for the *ritardando* supports the hypothesis that the *ritardando* is an allusion to the stopping of running. Predictability of the instant at which the final tone appears in a piece of music is important not only to the players but probably also to the listeners. It is possible that the time of appearance of the final tone becomes predictable in music listening because of the similarity between the final *ritardando* and a runner's deceleration curve.

This investigation explored one possibility to analyze the relations between music and motion, but there are also other alternatives. For example, comparisons between hand-movement patterns, such as during conducting, and local tempo patterns might offer further interesting insights into the similarities between motion and music.

V. CONCLUSION

The mean instant velocity during runners' decelerations, perceived as aesthetically pleasing, can be accurately described by a square-root function of time. This implies that the runner is supplying a constant amount of deceleration power throughout the entire deceleration process. Such a deceleration pattern is strikingly similar to a curve representing the mean instant tempo versus time in final *ritardandi* of musical performances.

A model of the final *ritardando* was derived from runners' mean-deceleration curve, assuming constant decelera-

tion power. By introducing two main parameters, q for curvature and v_{end} for the end value, this model could well describe the average tempo curve in final *ritardandi*, the average velocity curve of runners' decelerations, as well as individual final *ritardandi*, and runners' individual decelerations. These findings substantiate the common assumption that locomotion and music are related.

A perceptual evaluation of the model indicated that listeners preferred q values equal to 2 and 3. The case of $q = 3$ corresponds to the average velocity of the runners' decelerations, while $q = 2$ corresponds to a previously proposed model for final *ritardandi* (Kronman and Sundberg, 1987) as well as to Todd's model for phrase-related tempo curves (Todd, 1992, 1995). However, in some individual *ritardandi* the curvature parameter q deviated from the values preferred in the listening experiment, thus suggesting influence of musical factors. Previous investigations have revealed that the tempo variation related to musical phrases can be described by expressing the IOI duration as a quadratic function of score position. This alternative yielded poor results, both in

the listening experiment and in the attempts to match individual measured *ritardandi*.

ACKNOWLEDGMENTS

APPENDIX

FIG. A1. The model (solid line) fitted to each of the 12 final *ritardandi* (diamonds) selected from the Sundberg and Verrillo investigation. The vertical axis represents normalized tempo and the horizontal axis, normalized score position. The model parameters used are presented in Table IV.
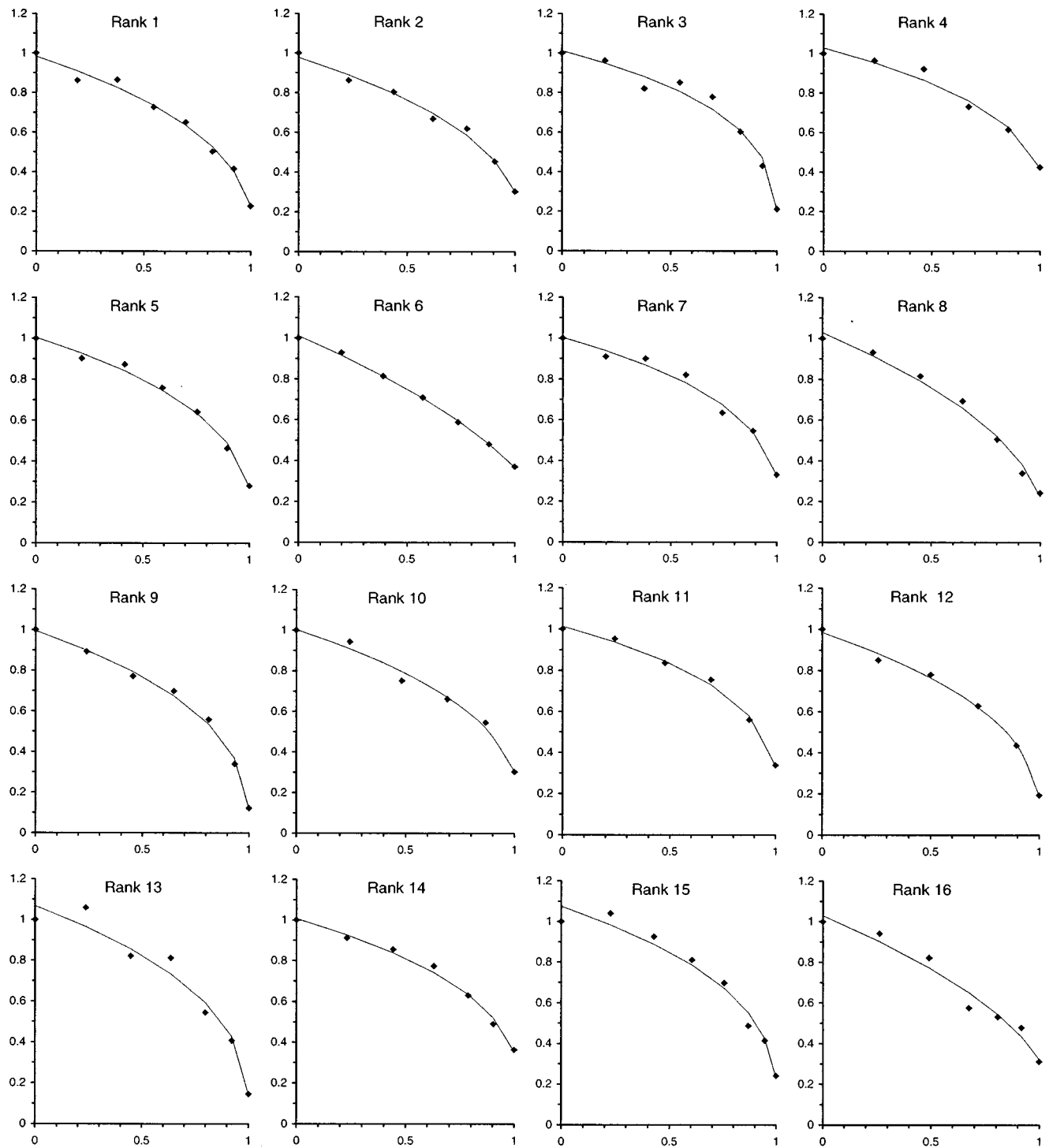
FIG. A2. The model (solid line) fitted to each of the 16 decelerations (diamonds) used in the visual rating experiment. The vertical axis represents normalized velocity and the horizontal axis, normalized position. The model parameters are presented in Table V.

Ae, M., Ito, A., and Suzuki, M. (**1992**). ''The men's 100 metres,'' New Studies Athlet. **7**(1), 47–52.

Alexander, R. McN. (**1995**). ''Simple models of human movement,'' Appl. Mech. Rev. **48**, 461–469.

Alexander, R. McN., and Maloiy, G. M. O. (**1984**). ''Stride length and stride frequencies of primates,'' J. Zool. **202**, 577–582.

Cavagna, G. A., Franzetti, P., Heglund, N. C., and Willems, P. (**1988**). ''The determinants of the step frequency in running, trotting and hopping in man and other vertebrates,'' J. Physiol. **399**, 81–92.

Desain, P., and Honing, H. (**1996**). ''Physical motion as a metaphor for timing in music: the final ritard,'' in *Proceedings of the 1996 International Computer Music Conference* (ICMA, San Francisco, CA), pp. 458–460.

Feldman, J., Epstein, D., and Whitman, R. (**1992**). ''Force dynamics of tempo change in music,'' Music Percept. **10**(2), 185–203.

Friberg, A. (**1995a**). ''A Quantitative Rule System for Musical Performance,'' Doctoral dissertation, Royal Institute of Technology, Sweden.

Friberg, A. (**1995b**). ''Matching the rule parameters of phrase arch to performances of '*Träumerei*': A preliminary study,'' in *Proceedings of the KTH Symposium on Grammars for Music Performance, May 27, 1995*, edited by A. Friberg and J. Sundberg (Speech, Music and Hearing, Royal Institute of Technology, Stockholm), pp. 37–44.

Kronman, U., and Sundberg, J. (**1987**). ''Is the musical *ritardando* an allusion to physical motion?'' in *Action and Perception in Rhythm and Music*, edited by A. Gabrielsson (Royal Swedish Academy of Music, Stockholm), Publication No. **55**, pp. 57–68.

Longuet-Higgins, H. C., and Lisle, E. R. (**1989**). ''Modelling music cogni-

tion,'' Contemp. Music Rev. **3**, 15–27.

Margaria, R. (**1976**). *Biomechanics and Energetics of Muscular Exercise* (Clarendon, Oxford).

Nilsson, J., and Thorstensson, A. (**1987**). ''Adaptility in frequency and amplitude of leg movements during human locomotion at different speeds,'' Acta Physiol. Scand. **129**, 107–114.

Penel, A., and Drake, C. (**1998**). ''Sources of timing variations in music performance: A psychological segmentation model,'' Psychol. Res. **61**, 12–32.

Repp, B. H. (**1992a**). ''Diversity and commonality in music performance: An analysis of timing microstructure in Schumann's '*Träumerei*,' '' J. Acoust. Soc. Am. **92**, 2546–2568.

Repp, B. H. (**1992b**). ''A constraint on the expressive timing of a melodic gesture: Evidence from performance and aesthetic judgement,'' Music Percept. **10(2)**, 221–242.

Repp, B. H. (**1993**). ''Music as motion: a synopsis of Alexander Truslit's (1938) 'Gestaltung und Bewegung in der Musik,' '' Psychol. Music **21**(1), 48–72.

Sederholm, E., McAllister, A., Sundberg, J., and Dahlkvist, J. (**1993**). ''Perceptual analysis of child hoarseness using continuous scales,'' Scand. J. Log. Phon. **18**, 73–82.

Shove, P., and Repp, B. H. (**1995**). ''Musical motion and performance: theoretical and empirical perspectives,'' in *The Practice of Performance: Studies in Musical Interpretation*, edited by J. Rink (Cambridge U.P., Cambridge), 55–83.

Sundberg, J. (**1988**). ''Computer synthesis of music performance,'' in *Generative Processes in Music*, edited by J. A. Sloboda (Clarendon, Oxford), 52–69.

Sundberg, J., Friberg, A., and Frydén, L. (**1992**). ''Music and locomotion. A study of the perception of tones with level envelopes replicating force patterns of walking,'' KTH Speech Transmission Laboratory Quarterly Progress and Status Report, **4/1992**, 109–122.

Sundberg, J., and Verrillo, V. (**1980**). ''On the anatomy of the ritard: A study of timing in music,'' J. Acoust. Soc. Am. **68**, 772–779.

Todd, J. T. (**1983**). ''Perception of gait,'' J. Exp. Psychol.: Human Percept. Performance **9**(1), 31–42.

Todd, N. P. McA. (**1985**). ''A model of expressive timing in tonal music,'' Music Percept. **3**, 33–58.

Todd, N. P. McA. (**1992**). ''The dynamics of dynamics: A model of musical expression,'' J. Acoust. Soc. Am. **91**, 3540–3550.

Todd, N. P. McA. (**1995**). ''The kinematics of musical expression,'' J. Acoust. Soc. Am. **97**, 1940–1949.

Truslit, A. (**1938**). *Gestaltung und Bewegung in der Musik* (Chr. Friedrich Vieweg, Berlin-Licherfelde).

Babinet's principle for elastic waves: A numerical test

José M. Carcione[a)]
Osservatorio Geofisico Sperimentale, P.O. Box 2011 Opicina, 34016 Trieste, Italy

Anthony F. Gangi[b)]
Department of Geology and Geophysics, Texas A&M University, College Station, Texas 77843-3114

Babinet's principle states that the diffracted fields from complementary screens are the negative of each other. In electromagnetics, Babinet's principle for infinitely thin perfectly conducting complementary screens implies that the sum, beyond the screen plane, of the electric and the magnetic fields (adjusting physical dimensions) equals the incident (unscreened) electric field. A test of the principle for the elastodynamic case was made using numerical calculations, and the results demonstrate that Babinet's principle holds quite well for complementary plane screens with contrasting boundary conditions; that is, the complementary screen of a stress-free screen is a rigid screen with openings where the original stress-free screen existed, and vice versa. The results are exact in an anisotropic SH case; for the P–SV case, the diffracted waves, PdP, SdS, PdS, and SdP satisfy the principle exactly, while the refracted waves, PdPrSc and SdPrSc, do not satisfy the principle at all (these waves are generally much smaller than the PdS and SdP waves). Diffracted surface waves also do not satisfy the principle. The numerical method is based on a domain-decomposition technique that assigns a different mesh to each side of the screen plane. The effects of the screens on wave propagation are modeled through the boundary conditions, requiring a special boundary treatment based on characteristic variables. The algorithm solves the velocity/stress wave equations and is based on a Fourier/Chebyshev differential operator. © *1999 Acoustical Society of America.* [S0001-4966(99)01403-4]

PACS numbers: 43.20.Bi, 43.20.Gp, 43.20.Px [DEC]

INTRODUCTION

Babinet's principle was originally used to relate the diffracted-light fields by complementary thin screens.[1] A complementary screen is a plane screen with opaque areas where the original plane screen had transparent areas. Roughly speaking, the principle states that behind the diffracting plane, the sum of the fields associated with a screen and with its complementary screen is just the field that would exist in the absence of any screen; that is, the diffracted fields from the two complementary screens are the negative of each other and cancel when summed. The principle was later extended to electromagnetic fields and perfectly conducting plane screens or diffractors.[2,3]

Gangi and Mohanty[4] investigated Babinet's principle for elastodynamic fields and nonplanar complementary screens by using the representation theorem (see, for example, Gangi[5]). They performed elastic-wave experiments using thin polystyrene sheets where wave propagation is practically two-dimensional. The experiments considered rigid complementary screens, stress-free complementary screens, and mixed rigid/stress-free complementary screens. The results did not provide conclusive evidence about the conditions for which the principle is valid, mainly due to the experimental errors and the fact that the ''rigid'' screen was not perfectly rigid.

To the best of our knowledge, no attempt has been made to test Babinet's principle by numerical-modeling techniques. The present work considers rigid and stress-free (weak) boundary conditions on the screens in order to reproduce the laboratory experiments performed by Gangi and Mohanty.[4] The numerical algorithm is based on a domain-decomposition technique,[6–8] where the implementation of the boundary conditions requires a special treatment based on characteristic variables. Then, the governing equations are solved by a grid method that uses the Chebyshev differential operator in the direction normal to the screen plane, and the Fourier differential operator parallel to the screen plane.

The principle is investigated in the isotropic case, as in Gangi and Mohanty,[4] and for SH propagation through the symmetry plane of a monoclinic medium and qP–qS propagation in a transversely isotropic solid whose symmetry axis is perpendicular to the screen plane. These numerical simulations provide an adequate test of the principle, in view of the different constitutive equations and wave-propagation modes.

Babinet's principle would be of value since it allows us to obtain the solution of the complementary problem from the solution of the original problem without any additional effort. Moreover, it provides a check of the solutions for problems that are self-complementary (e.g., the problem of a plane wave normally incident on a half plane). Finally, it adds to our knowledge of the complex phenomena of elastic-wave diffraction.

a)Electronic mail: carcione@gems755.ogs.trieste.it
b)Electronic mail: gangi@tamu.edu

I. 2-D ELASTODYNAMIC EQUATION OF MOTION

The elastodynamic solution makes use of the equations of momentum conservation and the stress/particle–velocity relations, that can be written as

$$\frac{\partial \mathbf{v}}{\partial t} = \mathbf{A} \frac{\partial \mathbf{v}}{\partial x} + \mathbf{B} \frac{\partial \mathbf{v}}{\partial z} + \mathbf{f}, \tag{1}$$

where the parameters $\mathbf{A}$, $\mathbf{B}$, $\mathbf{v}$, and $\mathbf{f}$ are explicitly given in the following subsections for the 2-D anisotropic case.

A. SH equation of motion

The particle–velocity/stress vector of the pure shear wave propagating in a monoclinic medium of arbitrary orientation (i.e., the normal to the isotropy plane makes an angle θ with the vertical z axis) is

$$\mathbf{v} = [v, \sigma_{xy}, \sigma_{zy}]^\mathsf{T}; \tag{2}$$

$$\mathbf{A} = \begin{bmatrix} 0 & \rho^{-1} & 0 \\ C_{66} & 0 & 0 \\ C_{46} & 0 & 0 \end{bmatrix}, \quad \mathbf{B} = \begin{bmatrix} 0 & 0 & \rho^{-1} \\ C_{46} & 0 & 0 \\ C_{44} & 0 & 0 \end{bmatrix}, \tag{3}$$

where ρ is the material density and C_{IJ} are elastic constants

$$C_{44} = c_{44} \cos^4 \theta + c_{66} \sin^4 \theta, \tag{4}$$

$$C_{66} = c_{44} \sin^4 \theta + c_{66} \cos^4 \theta, \tag{5}$$

$$C_{46} = (c_{44} + c_{66}) \cos^2 \theta \sin^2 \theta, \tag{6}$$

and the c_{IJ} are the elastic moduli in the principal axes system; i.e., when the z [or (3)] axis is the normal to the isotropy plane. Moreover,

$$\mathbf{f} = [f, 0, 0]^\mathsf{T} \tag{7}$$

is the body-force vector.

We recall that propagation in the plane of mirror symmetry of a monoclinic medium is the most general situation for which antiplane strain motion exists in all directions (the corresponding waves are also termed type-II S in the geophysical literature[9]). A detailed analysis of wave propagation of antiplane waves can be found in Carcione,[10] who studied the propagation of homogeneous plane waves in a viscoelastic medium.

B. qP–qS equation of motion

In a transversely isotropic medium, there are three wave solutions, two coupled modes denoted by qP and qS, representing the quasicompressional and quasishear modes, and the pure shear (SH) mode.[11] Since the medium has azimuthal symmetry, it is enough to consider qP–qS propagation in, say the (x,z) plane. The particle–velocity/stress vector and corresponding matrices are

$$\mathbf{v} = [v_x, v_z, \sigma_{xx}, \sigma_{zz}, \sigma_{xz}]^\mathsf{T}, \tag{8}$$

$$\mathbf{A} = \begin{bmatrix} 0 & 0 & \rho^{-1} & 0 & 0 \\ 0 & 0 & 0 & 0 & \rho^{-1} \\ c_{11} & 0 & 0 & 0 & 0 \\ c_{13} & 0 & 0 & 0 & 0 \\ 0 & c_{55} & 0 & 0 & 0 \end{bmatrix}, \tag{9}$$

$$\mathbf{B} = \begin{bmatrix} 0 & 0 & 0 & 0 & \rho^{-1} \\ 0 & 0 & 0 & \rho^{-1} & 0 \\ 0 & c_{13} & 0 & 0 & 0 \\ 0 & c_{33} & 0 & 0 & 0 \\ c_{55} & 0 & 0 & 0 & 0 \end{bmatrix}, \tag{10}$$

where c_{IJ} are the elastic moduli in the principal axes system and

$$\mathbf{f} = [f_x, f_z, 0, 0, 0]^\mathsf{T}. \tag{11}$$

II. BABINET'S PRINCIPLE FOR ELASTIC WAVES

Consider a screen S, and its complementary screen C, and assume that the total field in the presence of S is $\mathbf{v}_S$ and that related to C is $\mathbf{v}_C$. Babinet's principle as given by Gangi and Mohanty[4] states that the total fields on the opposite sides of the screens from the source satisfy

$$\mathbf{v}_S + \mathbf{v}_C = \mathbf{v}_0, \tag{12}$$

where $\mathbf{v}_0$ is the field in the absence of any screen. Equation (12) states that the diffraction fields for the complementary screens will be the negative of each other. Moreover, the total fields on the source side must satisfy

$$\mathbf{v}_S + \mathbf{v}_C = 2\mathbf{v}_0 + \mathbf{v}_R, \tag{13}$$

where $\mathbf{v}_R$ is the reflected (and diffracted) field by a screen composed of S and C if they have different boundary conditions, and it is just the reflected field if they have the same boundary condition.

III. SCREEN MODELING BY DOMAIN DECOMPOSITION

Consider a planar interface in an anisotropic medium, with the symmetry axis perpendicular to the interface plane. The medium may not necessarily be homogeneous. Assume the two-dimensional case, and refer to the upper and lower half-spaces with the labels I and II, respectively, with z increasing toward the upper medium.

The screen model is implemented in numerical modeling by using a domain-decomposition technique. Carcione[6] and Tessmer et al.[8] applied the method to model elastic waves across a welded interface between two elastic half-spaces and across an interface separating an acoustic layer from an elastic medium (where v_x need not be continuous). The boundary treatment is based on characteristics representing one-way waves propagating with the phase velocity of the medium. The wave equation is decomposed into outgoing- and incoming-wave modes perpendicular to the interface separating the two half-spaces. The outgoing waves are de-
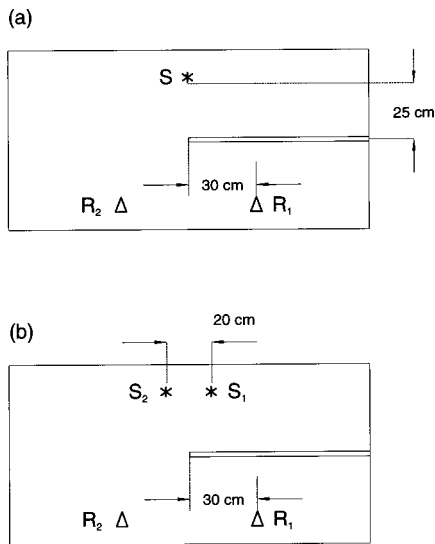
FIG. 1. Source–receiver configurations for the numerical experiments corresponding to the laboratory tests B (a) and A (b) performed by Gangi and Mohanty.[4] In (a), the fields detected by receiver R_1 and R_2 correspond to complementary screens if the medium is isotropic or transversely isotropic with its symmetry axis normal to the screen plane.

termined by the solution inside the corresponding half-space, while the incoming waves are calculated from the boundary conditions.

Most explicit time-integration schemes compute the operation $\mathbf{Mv} \equiv (\mathbf{v})^{\text{old}}$ where

$$\mathbf{M} = \mathbf{A}\frac{\partial}{\partial x} + \mathbf{B}\frac{\partial}{\partial z}. \tag{14}$$

The vector $(\mathbf{v})^{\text{old}}$ is then updated by the boundary treatment to give a new vector $(\mathbf{v})^{\text{new}}$ that takes into account the boundary conditions. The boundary equations are given in the Appendix.

The velocity–stress Eq. (1) is solved by a fourth-order Runge–Kutta time-integration algorithm. The spatial derivatives, that is, the operation with $\mathbf{M}$ on the field variables, are computed by using the Fourier method in the horizontal direction, and the Chebyshev method in the vertical directions, where nonperiodic boundary conditions are required. After an operation with $\mathbf{M}$, the field variables are updated by using the equations given in the Appendix. More details about the numerical technique can be found, for instance, in Carcione.[7,12]

IV. MODEL AND MODELING SETUP

The model simulates the laboratory tests performed by Gangi and Mohanty[4] in a homogeneous and elastic isotropic material (P–S propagation), and in addition, SH propagation through the symmetry plane of a monoclinic medium and qP–qS propagation in a transversely isotropic solid whose symmetry axis is perpendicular to the screen plane. The source–receiver configurations illustrated in Fig. 1(a) and (b) are used to test Babinet's principle. They correspond to configurations B and A in Gangi and Mohanty,[4] respectively.

The calculations use two meshes with $N_x = 375$ and $N_z = 81$ each, and a horizontal grid spacing of 4.7 mm. The

maximum vertical grid spacings are 7.1 and 7.35 mm, respectively. The source and receiver positions and the screen tip should be carefully determined, since a small difference can produce a big difference when comparing amplitudes of diffracted arrivals at the receivers. In number of grid points, the screen begins at the (horizontal) grid point 187. This means that the tip is in between points 186 and 187. Thus, taking this fact into account, source S in configuration B is applied at points 186 and 187, and sources S_1 and S_2, corresponding to configuration A, are located at grid points 208 and 165, respectively. Moreover, the positions of receivers R_1 and R_2 are in grid points 208 and 165, respectively. The vertical location of sources and receivers does not have a major influence on the calculations. The source emits a pulse of peak frequency $f_0 = 33$ KHz with a duration of approximately 68 μs. If time t is given in μs, the time history is

$$(1 - 2\alpha t^2)\exp(-\alpha t^2), \quad \alpha = 1/150.$$

A delay of 34.5 μs is applied to the pulse, to make it causal.

In order to better resolve the different events, a denser mesh is used for testing the principle with configuration B. In this case, $N_x = 625$, $N_z = 161$, with a horizontal grid spacing of 2.82 mm, and maximum vertical grid spacings of 3.55 and 3.65 mm, respectively. The source emits a pulse of peak frequency $f_0 = 52$ kHz with a duration of approximately 45 μs. The time history is obtained from the previous expression, with $\alpha = 2/75$. Causality requires a delay of 23.1 μs.

Open-radiation conditions and absorbing strips of width 18 grid points are implemented at the outer horizontal boundaries. At the sides, absorbing strips of the same width are used in order to eliminate wraparound effects caused by the Fourier operator. The solution is propagated to 900 ms with a time step of 0.3 μs and resampled to 1.2 μs.

V. TEST OF THE RECIPROCITY PRINCIPLE

A first numerical experiment tests the modeling algorithm by verifying the reciprocity principle.[13,14] Seismic reciprocity implies that sources and receivers can be interchanged under certain conditions. This relationship holds for an elastic medium with arbitrary boundary conditions, inhomogeneity, and anisotropy. In our experiments, the homogeneity is broken by the presence of the screen.

The test uses configuration A and compares the horizontal particle velocity v_x at R_1 caused by a vertical force at S_1, with the vertical particle velocity v_z at S_1 due to a horizontal source at R_1. The comparison is shown in Fig. 2, where the dotted line corresponds to the horizontal source. The matching is excellent, and provides a partial verification of the modeling algorithm.

VI. TEST OF BABINET'S PRINCIPLE

The following numerical experiments test the validity of Babinet's principle for complementary screens of the same type, i.e., both stress-free (weak) or both rigid, and for screens having different properties; that is, if the original screen is rigid (stress-free), the complementary screen may be stress-free (rigid). The qP–qS anisotropic case considers a crack embedded in a transversely isotropic medium.
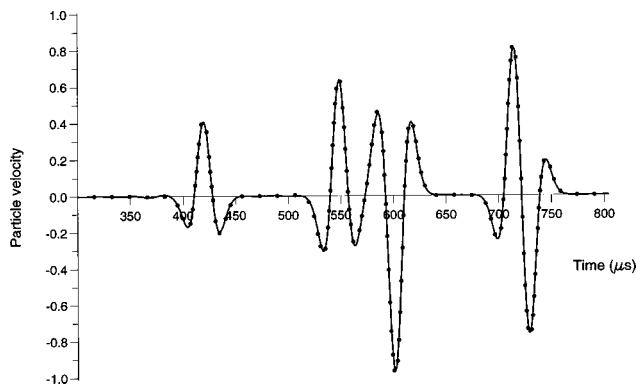
FIG. 2. Verification of the reciprocity principle using configuration A [Fig. 1(b)]. The test compares the horizontal-particle velocity v_x at R_1 caused by a vertical force at S_1 (continuous line) with the vertical-particle velocity v_z at S_1 due to a horizontal source at R_1 (dots).

A. The anisotropic SH case

We consider configuration B and a monoclinic medium with $C_{44} = \rho V_{44}^2$, $C_{66} = \rho V_{66}^2$, and $C_{46} = 0.5 \rho V_{44}^2$, where $V_{66} = 1300$ m/s, $V_{44} = 970$ m/s, and $\rho = 1$ g/cm^3 ($\theta \approx 45$ deg). Since the problem is not symmetric (the elliptical-wave surface is tilted with respect to the z-axis), the measurements at R_2 (R_1) in Fig. 1(a) do not provide the values corresponding to the complementary screen of the same type, when testing the principle at R_1 (R_2). Instead, the simulation with a complementary screen from grid point 1 to grid point 186 is required. The experiment consists of five simulations, two with rigid boundary conditions, with the screen at the left side and the right side of the plane, respectively, two with stress-free boundary conditions, and one unscreened.

Figure 3 compares scattered pulses (diffracted at the tip) at R_1 (580-μs onset) and R_2 (730-μs onset) for complementary screens of different type, i.e., stress-free and rigid. Figure 3(a) [(b)] corresponds to the weak screen at the right (left) side and the rigid screen at the left (right) side. The scattered field at receivers R_1 and R_2 for the rigid–left (weak–left) and weak–right (rigid–right) cases are obtained by subtracting the total field to the unscreened field (no screen present). As can be seen, there is an excellent match when the original screen is rigid (weak) and the complementary screen is weak (rigid), demonstrating that, in this case, Babinet's principle holds for screens of different type. This result is in agreement with the proof by Jones[3] in the purely acoustic case (pressure waves).

B. The elastic case

1. Isotropic media

The set of numerical experiments performed by Gangi and Mohanty[4] uses polystyrene (80 cm wide by 160 cm long) whose compressional and shear velocities are $V_P = Z_P/\rho = 1750$ m/s and $V_S = Z_S/\rho = 970$ m/s, respectively, with a density $\rho = 1$ g/cm^3. Figure 4(a) represents the particle velocity v_z recorded at receivers R_1 for a weak screen (broken line) and R_2 for a rigid screen (continuous line), corresponding to configuration B. P and S are the direct arrivals and d, r, and c denote diffracted, refracted, and critical, respectively. For instance, PdPrSc is the compressional wave
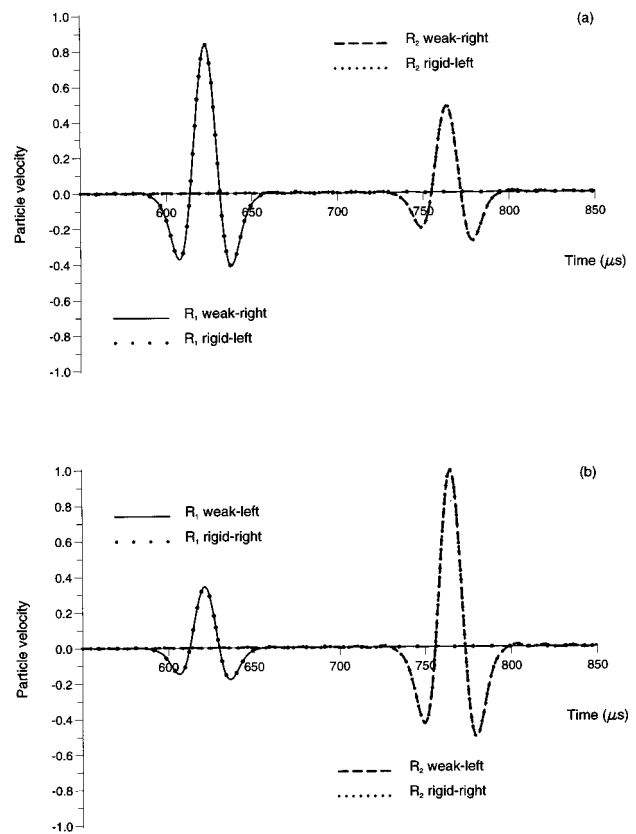
FIG. 3. Test of Babinet's principle for SH waves propagating in a monoclinic medium, corresponding to configuration B. The figure shows the scattered pulses at R_1 (580-μs onset) and R_2 (730-μs onset) for complementary screens of different type, i.e., stress-free and rigid. Figure 3(a) [(b)] corresponds to the weak screen at the right (left) side and the rigid screen at the left (right) side. The scattered field at receivers R_1 and R_2 for the rigid–left (weak–left) and weak–right (rigid–right) cases are obtained by subtracting the total field from the field obtained in the unscreened case (no screen present).

refracted along the screen plane and then incident at the receiver at the critical angle (i.e., a conical or lateral wave). Note that receiver R_1 records diffractions only. Figure 4(b) compares the unscreened field at R_2 (continuous line) to the field recorded at R_2 (rigid screen; direct arrivals plus diffractions) minus the field recorded at R_1 (weak screen; diffractions plus lateral waves). It is clear that Babinet's principle is not satisfied by the lateral wave PdPrSc, since this event is only recorded at R_1. This is evident in Fig. 5(a), which compares the scattered pulses at R_1 (continuous line) and R_2 (dotted line). As can be seen, there is no doubt that the PdP wave and the SdS wave (not visible in Fig. 4) satisfy the principle (for complementary screens of different type). Figure 5(b) represents the scattered pulse for weak complementary screens with the continuous line corresponding to R_1 and the dotted line to R_2. In this case, the principle is not satisfied.

Numerical experiments for configuration A are represented in Fig. 6, where (a) compares scattered events at R_1 (continuous line) and R_2 (dotted line) for complementary screens of the different type (weak screen and source S_1, and rigid screen and source S_2, respectively), and (b) compares scattered events for screens of equal type (weak screens for sources S_1 and S_2). The pulses correspond to the v_x compo-
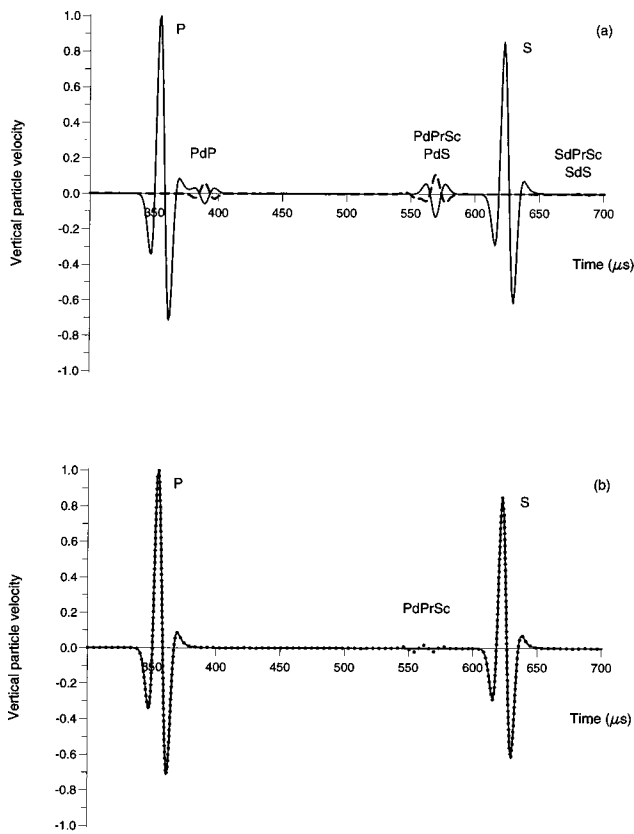
FIG. 4. Test of Babinet's principle for P–S waves propagating in an isotropic medium, where (a) shows the particle velocity v_z recorded at receivers R_1 for a weak screen (broken line) and R_2 for a rigid screen (continuous line), corresponding to configuration B. P and S are the direct arrivals and d, r, and c denote diffracted, refracted, and critical, respectively. (b) Compares the unscreened field at R_2 (continuous line) to the field recorded at R_2 (rigid screen; direct arrivals plus diffractions) minus the field recorded at R_1 (weak screen; diffractions plus lateral waves).

FIG. 5. Test of Babinet's principle for P–S waves propagating in an isotropic medium. (a) Compares the scattered pulses at R_1 (weak screen, continuous line) and R_2 (rigid screen, dotted line), while (b) represents the scattered pulse for weak complementary screens, with the continuous line corresponding to R_1 and the dotted line to R_2.

nent of the wave field. As before, the PdP wave satisfies the principle for the mixed case, as well as the SdP diffraction, not observed in configuration B. The mismatch is due to the presence of lateral waves. In particular, the SdPrSc event is much stronger than the SdS at receiver R_1. This can be appreciated in the snapshot displayed in Fig. 7, which shows the v_x component at 510 μs for a weak screen and source S_2. The PdPrSc and SdPrSc are the planar wavefronts below the screen, which are tangent to the PdS and SdS cylindrical wavefronts, respectively. The two larger cylindrical wavefronts correspond to the direct P and S waves, respectively.

2. Anisotropic media

A transversely isotropic medium is defined by the elastic constants $c_{11}=1.4\rho V_P^2$, $c_{33}=\rho V_P^2$, $c_{13}=0.08c_{33}$, and $c_{55}=\rho V_S^2$, with V_P and V_S as in the isotropic case. For illustration, Fig. 8 shows a polar representation of the energy (group) velocity corresponding to the qP (quasicompressional) and qS (quasishear) waves, where the vertical axis is the symmetry axis perpendicular to the plane of isotropy (by symmetry considerations, only one-quarter of the plane is displayed). Babinet's principle is tested in the presence of a crack, located between points 150 and 223. A snapshot of the v_z component at 510 μs can be seen in Fig. 9, with the crack

plane satisfying stress-free boundary conditions. Rayleigh waves traveling along this plane can be appreciated in the snapshot. Note the strong cuspidal triangle of the shear wave that triplicates in the direction of the receiver (see also Fig. 8). Figure 10(a) represents the particle velocity v_z for the crack (broken line) and the hole (continuous line), i.e., the "complementary crack," and Fig. 10(b) compares the unscreened field (continuous line) to the field obtained by substracting the two pulses represented in Fig. 10(a) (dotted line). Due to the particular source–receiver configuration, the diffractions are very close to the respective direct arrivals which generate them. The PdS diffraction can be clearly seen in Fig. 9 between the P and S waves. The stronger peak is the cusp of the shear wave, which due to triplication is followed by a weaker event arriving at approximately 550 μs. Figure 11 represents the scattered pulses, where the continuous line corresponds to the crack and the dotted line to the hole. The good matching between traces implies that Babinet's principle is satisfied also in the case of shear-wave triplication. The small differences may be due to the presence of weak lateral waves generated at the left tip of the crack.

VII. CONCLUSIONS

We have investigated Babinet's principle for elastic waves by using a numerical simulation technique. The method for solving wave propagation uses a domain-decomposition technique that assigns a different mesh to

FIG. 8. Polar representation of the energy (group) velocity corresponding to the qP (quasicompressional) and qS (quasishear) waves, where the vertical axis is the symmetry axis perpendicular to the plane of isotropy (from symmetry considerations, only one-quarter of the plane is displayed).

FIG. 6. Numerical experiments displaying the v_z component for configuration A, where (a) compares scattered events at R_1 (continuous line) and R_2 (dotted line) for complementary screens of different type (weak screen and source S_1, and rigid screen and source S_2, respectively), and (b) compares scattered events for screens of equal type (weak screens for sources S_1 and S_2).

each side of the screen plane. The use of the Chebyshev differential operator, to compute the spatial derivatives normal to the interface, allows the imposition of general boundary conditions. A first numerical experimental provides a partial verification of the modeling algorithm by testing the reciprocity principles in the presence of a stress-free screen.

In electromagnetics, Babinet's principle for infinitely thin perfectly conducting complementary screens implies

that the sum, beyond the screen plane, of the electric and the magnetic fields (adjusting physical dimensions) equals the incident (unscreened) electric field. In elastodynamics, the principle holds for the same field (particle velocity or stress), but for complementary screens satisfying different types of boundary conditions, i.e., if the original screen is weak (rigid), the complementary screen must be rigid (weak).

We have shown that Babinet's principle holds for screens embedded in anisotropic media, both for SH and qP–qS waves. Five simulations are required to test the principle for SH waves propagating in the plane of mirror symmetry of a monoclinic medium (the elliptical-wave surface is tilted with respect to the screen plane). The simulations indicate that Babinet's principle is satisfied also in the case of

FIG. 7. Snapshot of the v_x component at 510 μs for a weak screen and source S_2. The PdPrSc and SdPrSc are conical waves, which are tangent to the PdS and SdS cylindrical wavefronts, respectively. The two larger cylindrical wavefronts correspond to the direct P and S waves, respectively.
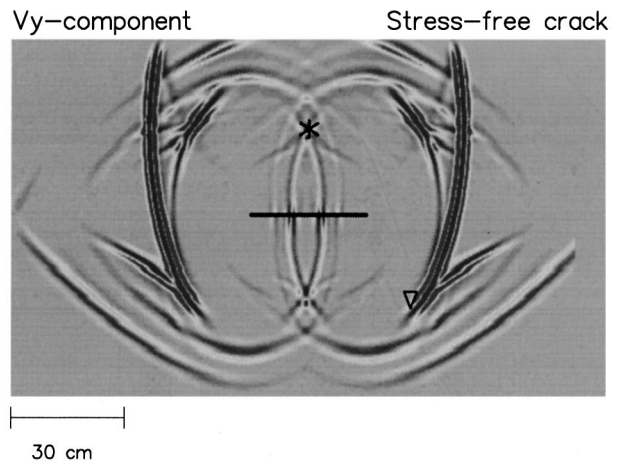
FIG. 9. Snapshot of the v_z component at 510 μs in a transversely isotropic medium, with the crack plane satisfying stress-free boundary conditions. Rayleigh waves traveling along this plane can be appreciated. The strong cuspidal triangle of the shear wave triplicates along the direction of the receiver.
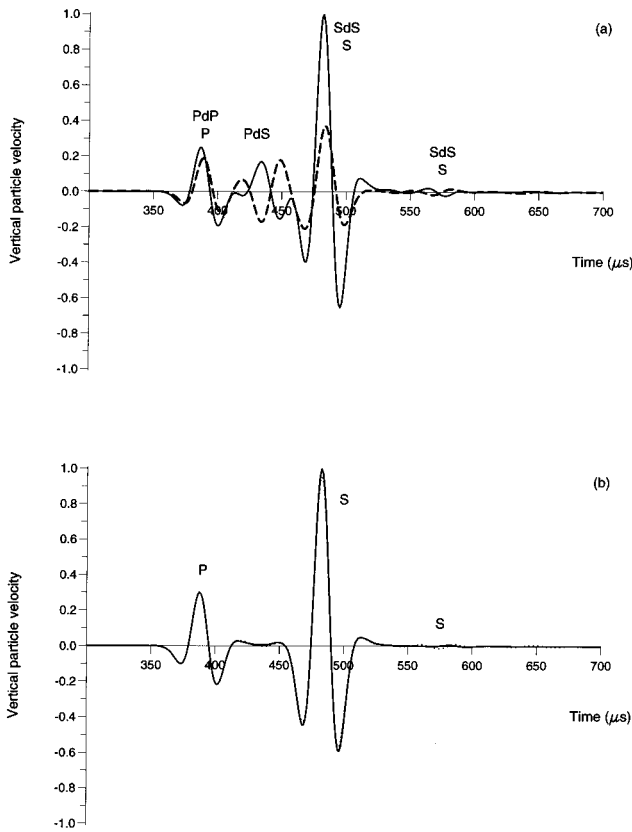
FIG. 10. Test of Babinet's principle for qP–qS waves propagating through a crack imbedded in a transversely isotropic medium. In (a), the particle velocity v_z corresponding to the crack (broken line) and the hole (continuous line) are represented. (b) Compares the unscreened field (continuous line) to the field obtained by subtracting the two pulses represented in (a) (dotted line).

shear-wave triplications (qS waves). Moreover, the experiments show that Babinet's principle holds for the near and far fields, and for an arbitrary pulse waveform and frequency spectrum. However, as expected, lateral and interface (e.g., Rayleigh) waves do not satisfy the principle.

Further research will involve the analysis of Babinet's principle for an inhomogeneous and/or viscoelastic background medium, screens separating a fluid and solid, and
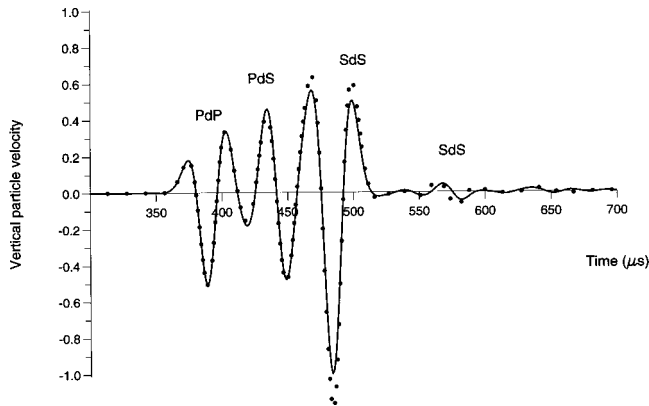
FIG. 11. Scattered pulses for the transversely isotropic case. The continuous line corresponds to the crack and the dotted line to the hole. The good matching between traces implies that Babinet's principle is also satisfied in the case of shear-wave triplication.

nonplanar screens. Moreover, a mathematical demonstration is required to prove that interface and lateral waves do not satisfy the principle.

APPENDIX: BOUNDARY EQUATIONS FOR ANISOTROPIC MEDIA

The following equations model the different boundary conditions between two half-spaces. In general, they were published for an isotropic medium. This Appendix extends the theory to a monoclinic medium for pure shear waves and to a transversely isotropic medium with the symmetry axis perpendicular to the screen plane for qP and qS waves.

1. The *SH* case

The domain-decomposition equations for SH waves resemble those of the acoustic case given in Carcione.[6] A similar analysis yields for a *welded* interface:

$$(v)_I^{new} = \tfrac{1}{2}\{(v)_{II}^{old} + (v)_I^{old} + Z_{44}^{-1}[(\sigma_{zy})_{II}^{old} + (\sigma_{zy})_I^{old}]\}, \tag{A1}$$

$$(\sigma_{zy})_I^{new} = \tfrac{1}{2}\{Z_{44}[(v)_{II}^{old} + (v)_I^{old}] + (\sigma_{zy})_I^{old} + (\sigma_{zy})_{II}^{old}\}, \tag{A2}$$

$$(\sigma_{xy})_{I(II)}^{new} = (\sigma_{xy})_{I(II)}^{old} - \frac{C_{46}}{C_{44}}[(\sigma_{zy})_{I(II)}^{old} - (\sigma_{zy})_{I(II)}^{new}], \tag{A3}$$

$$(v)_{II}^{new} = (v)_I^{new}, \quad (\sigma_{zy})_{II}^{new} = (\sigma_{zy})_I^{new}, \tag{A4}$$

where

$$Z_{44} = \sqrt{C_{44}\rho}. \tag{A5}$$

The relations for the *stress-free* case are

$$(v)^{new} = (v)^{old} \mp Z_{44}^{-1}(\sigma_{zy})^{old}, \tag{A6}$$

$$(\sigma_{zy})^{new} = 0, \tag{A7}$$

$$(\sigma_{xy})^{new} = (\sigma_{xy})^{old} - \frac{C_{46}}{C_{44}}(\sigma_{zy})^{old}, \tag{A8}$$

where the $-$ sign corresponds to half-space I and the $+$ sign to half-space II.

The updated variables for the *rigid* case are

$$(v)^{new} = 0, \tag{A9}$$

$$(\sigma_{zy})^{new} = (\sigma_{zy})^{old} \mp Z_{44}(v)^{old}, \tag{A10}$$

including Eq. (A8) and the same sign convention as before.

2. The qP–qS case

The characteristic waves for anisotropic media were obtained by Tessmer[15] and Carcione.[6,7] Carcione[6] obtained the boundary equations in the case of two *welded* isotropic media. Extension to the transversely isotropic case with the symmetry axis perpendicular to the interface yields

$$(v_x)_I^{new} = \frac{1}{2Z_S}\{Z_S(v_x)_I^{old} + Z_S(v_x)_{II}^{old} - (\sigma_{xz})_I^{old} + (\sigma_{xz})_{II}^{old}\}, \tag{A11}$$

$$(v_z)_{\mathrm{I}}^{\mathrm{new}} = \frac{1}{2Z_{\mathrm{P}}} \{ Z_{\mathrm{P}}(v_z)_{\mathrm{I}}^{\mathrm{old}} + Z_{\mathrm{P}}(v_z)_{\mathrm{II}}^{\mathrm{old}} - (\sigma_{zz})_{\mathrm{I}}^{\mathrm{old}} + (\sigma_{zz})_{\mathrm{II}}^{\mathrm{old}} \},$$

$$\text{(A12)}$$

$$(\sigma_{xx})_{\mathrm{I}}^{\mathrm{new}} = (\sigma_{xx})_{\mathrm{I}}^{\mathrm{old}} + \frac{c_{13}}{c_{33}} [(\sigma_{zz})_{\mathrm{I}}^{\mathrm{new}} - (\sigma_{zz})_{\mathrm{I}}^{\mathrm{old}}], \qquad \text{(A13)}$$

$$(\sigma_{zz})_{\mathrm{I}}^{\mathrm{new}} = \tfrac{1}{2} \{ Z_{\mathrm{P}}[(v_z)_{\mathrm{II}}^{\mathrm{old}} - (v_z)_{\mathrm{I}}^{\mathrm{old}}] + (\sigma_{zz})_{\mathrm{I}}^{\mathrm{old}} + (\sigma_{zz})_{\mathrm{II}}^{\mathrm{old}} \},$$

$$\text{(A14)}$$

$$(\sigma_{xz})_{\mathrm{I}}^{\mathrm{new}} = \tfrac{1}{2} \{ Z_{\mathrm{S}}[(v_x)_{\mathrm{II}}^{\mathrm{old}} - (v_x)_{\mathrm{I}}^{\mathrm{old}}] + (\sigma_{xz})_{\mathrm{I}}^{\mathrm{old}} + (\sigma_{xz})_{\mathrm{II}}^{\mathrm{old}} \},$$

$$\text{(A15)}$$

$$(v_x)_{\mathrm{II}}^{\mathrm{new}} = (v_x)_{\mathrm{I}}^{\mathrm{new}}, \qquad (v_z)_{\mathrm{II}}^{\mathrm{new}} = (v_z)_{\mathrm{I}}^{\mathrm{new}}, \qquad \text{(A16)}$$

$$(\sigma_{xx})_{\mathrm{II}}^{\mathrm{new}} = (\sigma_{xx})_{\mathrm{II}}^{\mathrm{old}} + \frac{c_{13}}{c_{33}} [(\sigma_{zz})_{\mathrm{II}}^{\mathrm{new}} - (\sigma_{zz})_{\mathrm{II}}^{\mathrm{old}}], \qquad \text{(A17)}$$

$$(\sigma_{zz})_{\mathrm{II}}^{\mathrm{new}} = (\sigma_{zz})_{\mathrm{I}}^{\mathrm{new}}, \qquad (\sigma_{xz})_{\mathrm{II}}^{\mathrm{new}} = (\sigma_{xz})_{\mathrm{I}}^{\mathrm{new}}, \qquad \text{(A18)}$$

where

$$Z_{\mathrm{P}} = \sqrt{c_{33}\rho} \quad \text{and} \quad Z_{\mathrm{S}} = \sqrt{c_{55}\rho}, \qquad \text{(A19)}$$

are the compressional and shear impedances along the z-axis, respectively. In the isotropic case, $c_{11} = c_{33}$ and $c_{13} = Z_{\mathrm{P}}^2 - 2Z_{\mathrm{S}}^2$.

The relations for the *stress-free* case are[15,7]

$$(v_x)^{\mathrm{new}} = (v_x)^{\mathrm{old}} \mp Z_{\mathrm{S}}^{-1}(\sigma_{xz})^{\mathrm{old}}, \qquad \text{(A20)}$$

$$(v_z)^{\mathrm{new}} = (v_z)^{\mathrm{old}} \mp Z_{\mathrm{P}}^{-1}(\sigma_{zz})^{\mathrm{old}}, \qquad \text{(A21)}$$

$$(\sigma_{xx})^{\mathrm{new}} = (\sigma_{xx})^{\mathrm{old}} + \frac{c_{13}}{c_{33}} [(\sigma_{zz})^{\mathrm{new}} - (\sigma_{zz})^{\mathrm{old}}], \qquad \text{(A22)}$$

$$(\sigma_{xz})^{\mathrm{new}} = 0, \qquad \text{(A23)}$$

$$(\sigma_{zz})^{\mathrm{new}} = 0, \qquad \text{(A24)}$$

where the $-$ sign corresponds to half-space I and the $+$ sign to half-space II.

The updated variables for the *rigid* case are[7]

$$(v_x)^{\mathrm{new}} = 0, \qquad \text{(A25)}$$

$$(v_z)^{\mathrm{new}} = 0, \qquad \text{(A26)}$$

$$(\sigma_{xx})^{\mathrm{new}} = (\sigma_{xx})^{\mathrm{old}} + \frac{c_{13}}{c_{33}} [(\sigma_{zz})^{\mathrm{new}} - (\sigma_{zz})^{\mathrm{old}}], \qquad \text{(A27)}$$

$$(\sigma_{xz})^{\mathrm{new}} = (\sigma_{xz})^{\mathrm{old}} \mp Z_{\mathrm{S}}(v_x)^{\mathrm{old}}, \qquad \text{(A28)}$$

$$(\sigma_{zz})^{\mathrm{new}} = (\sigma_{zz})^{\mathrm{old}} \mp Z_{\mathrm{P}}(v_z)^{\mathrm{old}}, \qquad \text{(A29)}$$

with the same sign convention as before.

[1] P. Epstein, Enzyl. d. Math. Wissensch., Bd. 5, Art. 24, SS. 510–511, Leipzig (1915).

[2] L. G. H. Huxley, *A Survey of the Principles and Practice of Wave Guides* (MacMillan, New York, 1947).

[3] D. S. Jones, *Acoustic and Electromagnetic Waves* (Oxford Science, New York, 1986).

[4] A. F. Gangi and B. B. Mohanty, ''Babinet's principle for elastic waves,'' J. Acoust. Soc. Am. **53**, 525–534 (1973).

[5] A. F. Gangi, ''A derivation of the seismic representation theorem using seismic reciprocity,'' J. Geophys. Res. **75**(11), 2088–2095 (1970).

[6] J. M. Carcione, ''Domain decomposition for wave propagation problems,'' J. Sci. Comput. **6**, 453–472 (1991).

[7] J. M. Carcione, ''Time-dependent boundary conditions for the 2-D linear anisotropic–viscoelastic wave equation,'' Numer. Meth. Part. Diff. Eqs. **10**, 771–791 (1994).

[8] E. Tessmer, D. Kessler, D. Kosloff, and A. Behle, ''Multi-domain Chebyshev–Fourier method for the solution of the equations of motion of dynamic elasticity,'' J. Comput. Phys. **100**, 355–363 (1992).

[9] R. D. Borcherdt, ''Reflection and refraction of type-II S waves in elastic and anelastic media,'' Bull. Seismol. Soc. Am. **67**, 43–67 (1977).

[10] J. M. Carcione, ''Wavefronts in dissipative anisotropic media,'' Geophysics **59**, 644–657 (1994).

[11] K. Helbig, *Foundations of Anisotropy for Exploration Seismics* (Pergamon, New York, 1994).

[12] J. M. Carcione, ''A 2-D Chebyshev differential operator for the elastic wave equation,'' Comput. Methods Appl. Mech. Eng. **130**, 33–45 (1996).

[13] D. Graffi, ''Sui teoremi di reciprocità nei fenomeni indipendenti dal tempo,'' Ann. Math. **18**, 173–200 (1939).

[14] L. Knopoff and A. F. Gangi, ''Seismic reciprocity,'' Geophysics **24**, 681–691 (1959).

[15] E. Tessmer, ''Seismische Modellierung unter Berücksichtigung der freien Oberfläche mithilfe spektralen Tschebyscheff-Methode,'' Ph.D. thesis, Hamburg University, 1990.

A generalized modal impulse response and Fourier transform approach to investigate acoustic transient Bessel beams and Bessel bullets

Peter R. Stepanishen[a)]

Department of Ocean Engineering, University of Rhode Island, Kingston, Rhode Island 02891

A generalized modal space–time impulse response and Fourier transform approach is developed to investigate the general properties of transient Bessel beam (TBB) fields which are generated using planar circular apertures. The approach is based on a modal decomposition of the aperture source distributions which are required to generate the space–time TBB fields. Numerical results are presented to illustrate the general space–time properties of the modal impulse responses and the modal source functions. The on-axis far field for the finite aperture is shown to be simply related to the lowest order term in the modal expansion. The space–time properties of the acoustic field for a particular type of band-limited TBB field which is designated as an acoustic Bessel bullet (BB) are then investigated. Some numerical results are presented to illustrate the space–time properties of acoustic BB fields generated from an infinite aperture. Analogous on-axis harmonic results from a finite aperture are presented. These latter results clearly indicate that the higher-order modes exhibit spatial rates of decay which are greater than the inverse range decay for the lowest order mode. © *1999 Acoustical Society of America.* [S0001-4966(99)01903-7]

PACS numbers: 43.20.Bi [ANN]

INTRODUCTION

In 1750 D'Alembert developed a general wave solution to the linearized small amplitude one-dimensional wave equation. The well-known solution consists of two traveling plane waves of arbitrary shape which travel in opposite directions with a constant wave speed. An important characteristic of the plane wave solution is that the wave exhibits no change in shape as it propagates with the small amplitude wave speed for the medium. For one-dimensional media, e.g., a string, the wave field may be compact in space at any time whereas for a three-dimensional media the plane wave field is obviously noncompact or localized in space.

During the last several decades there has been considerable interest in developing localized wave solutions for the three-dimensional wave equation which are localized or exhibit a compact space–time region. Brittingham developed the first localized wave (LW) solution to the homogeneous Maxwell's equation which he termed the focus wave mode (FWM).[1] The FWM solution corresponds to a Gaussian beam which propagates through space with local variations. A free parameter in the solution determines the overall characteristics of the field corresponding to a quasi-transverse plane wave at one extreme and a narrow spatially transverse pulse at the other extreme.

Ziolkowski subsequently used the FWM solution as a kernel for constructing new localized wave (LW) solutions.[2] Via the selection of an appropriate weighting function, Ziolkolski was able to obtain closed form expressions for the resultant integrals over the free parameter in the FWM solution. The resultant localized wave (LW) solution or modified power spectrum (MPS) pulse also included several parameters which allow a tailoring of the pulse shape. The modified power spectrum (MPS) pulse has received enormous attention in the literature,[3–10] as a result of potential applications in the areas of electromagnetics, optics and acoustics.

In a series of recent papers, Stepanishen[11–14] has developed a new class of localized waves using a combination of Fourier transform and space–time methods. These new localized waves were designated as acoustic bullets or acoustic transient Bessel beams (TBB). The space–time properties of these fields can be tailored via the selection of an inherent weighting function. Since the three-dimensional TBB field maintains its temporal and spatial shape as the acoustic bullet propagates in free space, the TBB field thus exhibits the same characteristic as the D'Alembert solution. It is noted that TBB fields include, as a special case, X waves,[15,16] which have received considerable interest in the acoustics, electromagnetic, and optics communities.

Although the exact TBB solution in all space cannot be generated from a finite planar aperture, the general characteristics of TBB fields can be realized in a limited space–time region via the use of an appropriate space–time source distribution. More specifically, an acoustic bullet with a smaller support region than the circular aperture can be launched from the finite aperture[12] as illustrated in Fig. 1. In the near-field region the field exhibits properties similar to those observed for the infinite aperture case, and in the far-field region the field generally exhibits an inverse range dependence. An impulse response approach to investigate the on-axis and far-field space–time properties of acoustic bullets or TBB fields was developed in a recent paper.[15] It is noted that the present definition of acoustic bullets differs from a previously introduced definition by Moses and

---

[a)]Electronic mail: stepanishen@oce.uri.edu
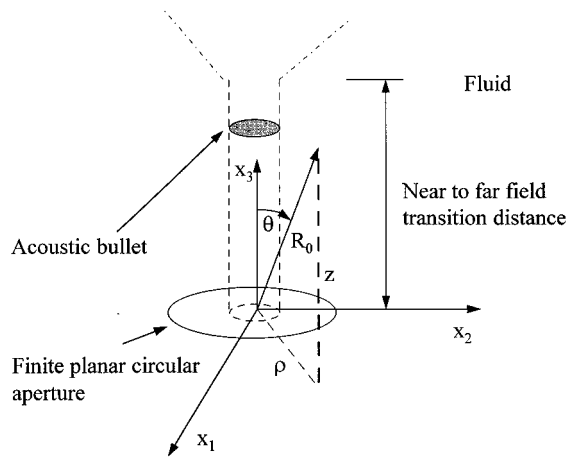
FIG. 1. An acoustic bullet launched from a finite planar aperture.

Prosser[17,18] who also used the term in addressing inverse initial value problems.

A generalized space–time modal impulse response and Fourier transform approach is developed in the present paper to investigate the properties of the space–time TBB fields which are generated using finite apertures. The generalized space–time modal impulse response and Fourier transform approach is developed in Sec. II from a modal decomposition of the aperture distributions which are required to generate the TBB fields. General properties and numerical results for the modal source functions and the modal impulse responses are presented and discussed. General modal expressions for the space–time and Fourier-transformed on-axis pressure field and angular-dependent far field are presented and discussed. The on-axis far field for the finite aperture is shown to be simply related to the lowest-order term in the modal expansion.

A particular type of acoustic bullet or TBB field which is designated as an acoustic Bessel bullet (BB) is investigated in Sec. III using the generalized modal impulse response and Fourier transform approach. In contrast to previously addressed baseband signals, an acoustic BB has a bandpass spectrum which is associated with a gated sinusoidal signal. Numerical results are first presented for the space–time properties of acoustic BB fields generated from an infinite aperture. Numerical results are then presented to illustrate the properties of the modal decomposition for quasi-sinusoidal on-axis acoustic BB fields generated from finite apertures. An interesting range-dependent modal stripping which occurs along the axis is observed. In contrast to the inverse range decay for the lowest-order mode which determines the on-axis far field, spatial rates of decay for the higher-order modes are noted to be greater than the ubiquitous spherical spreading loss due to a spatial redistribution of the modal energies.

I. GENERALIZED MODAL IMPULSE RESPONSE AND FOURIER TRANSFORM APPROACH

The acoustic wave equation for the axisymmetric pressure fields of interest $p(\rho,z,\tau)$ can be expressed in the normalized cylindrical coordinate system illustrated in Fig. 1 as

$$\left[\frac{1}{\rho}\frac{\partial}{\partial\rho}\left(\rho\frac{\partial}{\partial\rho}\right)+\frac{\partial^2}{\partial z^2}-\frac{\partial^2}{\partial\tau^2}\right]p(\rho,z,\tau)=0, \qquad (1)$$

where (ρ,z) are the normalized spatial coordinates and the normalized time is $\tau=c_0 t/a$ where t denotes the unscaled time variable, c_0 is the constant sound speed of the media, and a is the unscaled radius of the planar aperture of interest. TBB fields[12] which exhibit the properties of acoustic bullets in an unbounded free space can be simply expressed as follows:

$$p(\rho,z,\tau)=w(\tau)\otimes j(\rho,z,\tau), \qquad (2)$$

where $w(\tau)$ is an arbitrary weighting function which can be used to control the spectral properties of the field, $\otimes$ denotes the convolution operator, and

$$j(\rho,z,\tau)=\frac{1}{\pi[(\rho\sin\zeta)^2-(\tau-z\cos\zeta)^2]^{1/2}},$$
$$-\rho\sin\zeta+z\cos\zeta<\tau<\rho\sin\zeta+z\cos\zeta. \quad (3)$$

For the on-axis case where $\rho=0$ it is noted that

$$j(0,z,\tau)=\delta(\tau-z\cos\zeta), \qquad (4)$$

and the sifting property of the Dirac delta function $\delta(\ )$ then leads to the following result for the on-axis pressure:

$$p(0,z,\tau)=w(\tau-z\cos\zeta). \qquad (5)$$

In order to generate an acoustic TBB or bullet from a planar aperture it is first noted that a standard Green's function solution to the initial Neumann boundary value problem leads to the following well-known retarded time solution[19] for the pressure field:

$$p(\rho,z,\tau)=\int_0^\infty \rho_s\,d\rho_s\int_0^{2\pi}\left[\frac{\delta(\tau-R)}{2\pi R}\otimes a_z(\rho_s,0,\tau)\right]d\phi_s, \qquad (6)$$

where $R=\sqrt{\rho^2+\rho_s^2-2\rho\rho_s\cos\phi_s+z^2}$. The normal acceleration distribution $a_z(\rho,0,\tau)$ which is required to generate the acoustic bullet in the half space $z\geq0$ via Eq. (2) is readily obtained[12] via the linearized momentum equation, i.e.,

$$a_z(\rho,z,\tau)=\cos\zeta\frac{dw(\tau)}{d\tau}\otimes j(\rho,z,\tau). \qquad (7)$$

A space–time surface integral representation for the acoustic TBB field generated by the finite aperture of interest in Fig. 1 can now be obtained by combining Eqs. (6) and (7):

$$p(\rho,z,\tau)=\cos\zeta\int_0^1 \rho_s\,d\rho_s\int_0^{2\pi}d\phi_s\frac{1}{2\pi R}$$
$$\times\left\{\frac{dw(\tau)}{d\tau}\otimes j(\rho_s,0,\tau_s)\right\}_{\tau_s=\tau-R}, \qquad (8)$$

where the normalized radius of the aperture is unity. Since $w(\tau)$ can be removed outside the surface integral, it then follows that

1494 J. Acoust. Soc. Am., Vol. 105, No. 3, March 1999

Peter R. Stepanishen: Acoustic transient Bessel beams 1494

$$p(\rho,z,\tau) = \frac{dw(\tau)}{d\tau} \otimes h(\rho,z,\tau) \tag{9}$$

$$= w(\tau) \otimes \frac{dh(\rho,z,\tau)}{d\tau}, \tag{10}$$

where the generalized space–time impulse response $h(\rho,z,\tau)$ is defined as follows:

$$h(\rho,z,\tau) = \cos\zeta \int_0^1 \rho_s \, d\rho_s \int_0^{2\pi} d\phi_s \frac{1}{2\pi R} j(\rho_s,0,\tau_s)_{\tau_s=\tau-R}. \tag{11}$$

Rather than evaluate $h(\rho,z,\tau)$ directly from Eq. (11), an indirect modal decomposition approach is now employed. After expressing $j(\rho,0,\tau)$ as the following eigenfunction expansion,

$$j(\rho,0,\tau) = \sum_n v_n(\tau,\zeta) J_0(ka_n\rho), \tag{12}$$

where the $J_0(ka_n\rho)$ are zeroth-order Bessel functions of the first kind with $J_1(ka_n)=0$ which form a complete set of eigenfunctions on [0,1], it then follows from Eq. (11) that the generalized space–time impulse response $h(\rho,z,\tau)$ can be expressed as follows:

$$h(\rho,z,\tau) = \cos\zeta \sum_n v_n(\tau,\zeta) \otimes h_n(\rho,z,\tau), \tag{13}$$

where the generalized space–time modal impulse response $h_n(\rho,z,\tau)$ can be expressed as

$$h_n(\rho,z,\tau) = \int_0^1 \rho_s \, d\rho_s \int_0^{2\pi} d\phi_s \frac{\delta(\tau-R)}{2\pi R} J_0(ka_n\rho_s). \tag{14}$$

The pressure field of interest can now be expressed as follows:

$$p(\rho,z,\tau) = \cos\zeta \frac{dw(\tau)}{d\tau} \otimes \sum_n v_n(\tau,\zeta) \otimes h_n(\rho,z,\tau), \tag{15}$$

or, in a more concise form:

$$p(\rho,z,\tau) = \sum_n s_n(\tau,\zeta) \otimes h_n(\rho,z,\tau), \tag{16}$$

where

$$s_n(\tau,\zeta) = \cos\zeta \frac{dw(\tau)}{d\tau} \otimes v_n(\tau,\zeta). \tag{17}$$

Since the convolution operations are readily performed, $p(\rho,z,\tau)$ can be readily evaluated for a specified $w(\tau)$ once the $v_n(\tau)$ and $h_n(\rho,z,\tau)$ are known.

In light of the eigenfunction expansion in Eq. (12), it readily follows from the orthogonal properties of the $J_0(ka_n\rho)$ that $v_n(\tau)$ can now be expressed as

$$v_n(\tau,\zeta) = \frac{1}{N_n} \int j(\rho,0,\tau) J_0(ka_n\rho)\rho \, d\rho, \tag{18}$$

where $|\tau| < \sin\zeta$ and
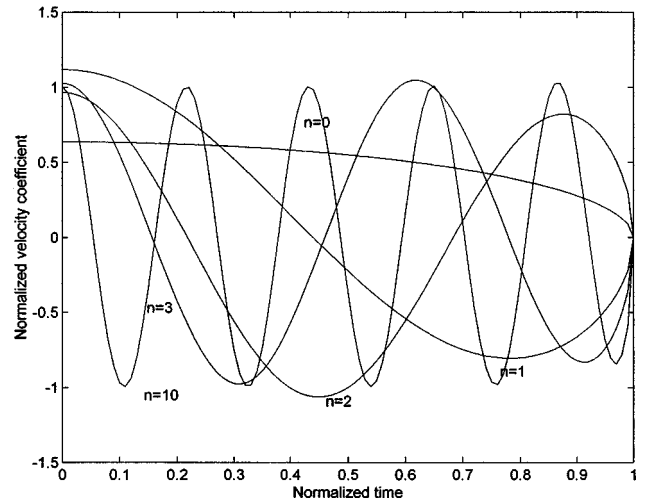
FIG. 2. Normalized velocity coefficients $\sin\zeta v_n(\tau,\zeta)$ vs $\tau/\sin\zeta$ for $n=0,1,2,3,10$.

$$N_n = \int_0^1 J_0^2(ka_n\rho)\rho \, d\rho = \frac{J_0^2(ka_n)}{2}. \tag{19}$$

After noting that some care must be exercised in establishing the limits of the integration in Eq. (18) it is apparent that:

$$v_n(\tau,\zeta) = \frac{1}{N_n} \int_{\tau/\sin\zeta}^1 \frac{1}{\pi[(\rho\sin\zeta)^2 - \tau^2]^{1/2}} J_0(ka_n\rho)\rho \, d\rho$$

$$= \frac{2}{\pi J_0^2(ka_n)\sin\zeta} \int_0^{\sqrt{1-(\tau/\sin\zeta)^2}} J_0$$

$$\times \left(ka_n \sqrt{y^2 + \left(\frac{\tau}{\sin\zeta}\right)^2}\right) dy. \tag{20}$$

It is readily apparent from Eq. (20) that $v_0(\tau,\zeta)$ can be simply expressed as

$$v_0(\tau) = \frac{2}{\pi\sin\zeta} \sqrt{1 - \left(\frac{\tau}{\sin\zeta}\right)^2}, \quad \left|\frac{\tau}{\sin\zeta}\right| < 1, \tag{21}$$

which, in the limit as $\sin\zeta \to 0$, leads to the expected result

$$\lim_{\sin\zeta \to 0} v_0(\tau,\zeta) = \delta(\tau). \tag{22}$$

It is noted that $\sin\zeta v_n(\tau,\zeta)$ is an even function of $\tau/\sin\zeta$ which is nonzero only over the range where $|\tau| < \sin\zeta$. Numerical results for the normalized velocity coefficients $\sin\zeta v_n(\tau,\zeta)$ vs $\tau/\sin\zeta$ are shown in Fig. 2 for $n=0,1,2,3,10$ and are applicable for all ζ. As n increases it is clear that $\sin\zeta v_n(\tau,\zeta)$ approaches a quasi-cosinusoidal signal with n zeros between 0 and $\tau/\sin\zeta=1$, i.e., $\sin\zeta v_n(\tau,\zeta) \to \cos((2n+1)/2)\pi\tau/\sin\zeta)$. The velocity coefficients $v_n(\tau,\zeta)$ thus exhibit the bandpass characteristics of a gated cosinusoidal function where the center frequency is observed to correspond to $(2n+1)/(4\sin\zeta)$ and the bandwidth is inversely related to the pulse duration, i.e., $1/\sin\zeta$. The normalized bandwidth is thus independent of ζ and proportional to $(2n+1)/4$.

In order to evaluate $p(\rho,z,\tau)$ using Eqs. (15) and (16), the generalized space–time modal impulse responses

$h_n(\rho,z,\tau)$ are also required. It is noted, however, that $h_n(\rho,z,\tau)$ has been previously evaluated[20] in closed form and may be expressed as follows for $\rho \geq 1$:

$$h_n(\rho,z,\tau) = \frac{\psi_e(\tau)}{\pi} \sum_m \varepsilon_m J_m(ka_n\rho)$$

$$\times J_m(ka_n\sqrt{\tau^2-z^2}) \frac{\sin(m\psi_e(\tau))}{m\psi_e(\tau)} \quad (23)$$

for $R_{\min} < \tau < R_{\max}$ where

$$R_{\min} = \sqrt{z^2+(\rho-1)^2}, \quad R_{\max} = \sqrt{z^2+(\rho+1)^2},$$

$$\psi_e(\tau) = \cos^{-1}\left(\frac{\tau^2-z^2+\rho^2-1}{2\rho\sqrt{\tau^2-z^2}}\right)$$

and $R = \sqrt{z^2+\rho^2}$. For $\rho \leq 1$, $h_n(\rho,z,\tau)$ may be expressed as follows:

$$h_n(\rho,z,\tau) = J_0(ka_n\rho)J_0(ka_n\sqrt{\tau^2-z^2}), \quad z \leq \tau \leq R_{\min}$$

$$= \frac{\psi_e(\tau)}{\pi} \sum_m \varepsilon_m J_m(ka_n\rho)J_m(ka_n\sqrt{\tau^2-z^2})$$

$$\times \frac{\sin(m\psi_e(\tau))}{m\psi_e(\tau)} \quad (24)$$

for $R_{\min} < \tau < R_{\max}$.

Several observations regarding the generalized modal impulse responses $h_n(\rho,z,\tau)$ are evident from Eqs. (23) and (24). First, it is noted that all the generalized modal impulse responses are causal with a finite time duration which varies between 0 and 2 which is the normalized travel time across the planar source. Second, the on-axis impulse response $h_n(0,z,\tau)$ is simply obtained and can be expressed as

$$h_n(0,z,\tau) = J_0(ka_n\sqrt{\tau^2-z^2}), \quad z \leq \tau \leq \sqrt{z^2+1}. \quad (25)$$

Third, it is noted that $h_n(\rho,z,\tau)$ for $\tau = z$ can be expressed as

$$h_n(\rho,z,z) = J_0(ka_n\rho), \quad 0 \leq \rho \leq 1$$

$$= 0, \quad 1 \leq \rho. \quad (26)$$

Finally, it is observed that:

$$h_n(\rho,z,\tau) = h_n(\rho,0,\sqrt{\tau^2-z^2}). \quad (27)$$

The generalized modal impulse responses for a fixed ρ and variable z are thus readily obtained from the generalized modal impulse response at $z=0$, i.e., $h_n(\rho,0,\tau)$, via a non-linear compression of the time axis.

In light of Eq. (27), numerical results for $h_n(\rho,0,\tau)$ are now presented to illustrate the general characteristics of the generalized modal impulse responses. Numerical results for $h_n(\rho,0,\tau)$ vs τ for $\rho = 0.0, 1.0, 2.0$ are shown in Figs. 3–6 for $n = 0,1,2,3$, respectively. The on-axis responses for $\rho=0$ simply correspond to the temporal equivalent of the spatial eigenfunctions with a time duration of 1.0 as noted from Eq. (25). The generalized modal impulse responses for $\rho = 1.0$ all start at $\tau = 0$ with an initial discontinuity which is equivalent to $\frac{1}{2}h_n(0,0,1)$ and they exhibit a time duration of 2.0. In contrast to the modal impulse responses for $\rho \leq 1$, $h_n(\rho,0,\tau)$ for $\rho > 1$ are nonzero for $\rho - 1 \leq \tau \leq \rho + 1$
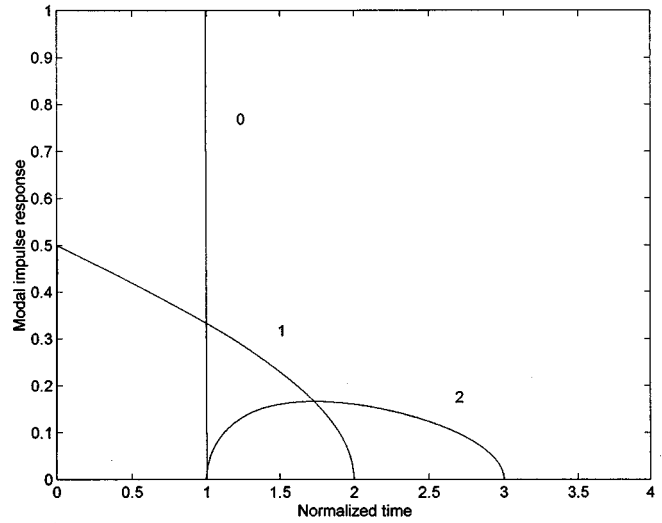
FIG. 3. The generalized impulse response $h_0(\rho,0,\tau)$ vs τ for $\rho=0,1,2$.

with a time duration of 2.0 and do not exhibit an initial discontinuity. The numerical results for $\rho = 2.0$ clearly illustrate these latter features. In general, it is also noted that the modal impulse responses become more oscillatory as n increases and more symmetrical as ρ increases.

As a complement to the preceding modal decomposition of the space–time field, an alternative frequency domain modal decomposition of acoustic TBB fields using a Fourier transform approach is now presented. After introducing the following definition of the Fourier transform pair for the pressure field

$$p(\rho,z,\tau) \Leftrightarrow P(\rho,z,\Omega), \quad (28)$$

where

$$P(\rho,z,\Omega) = \int_{-\infty}^{\infty} p(\rho,z,\tau)e^{-i\Omega\tau} d\tau, \quad (29)$$

$$p(\rho,z,\tau) = \frac{1}{2\pi}\int_{-\infty}^{\infty} P(\rho,z,\Omega)e^{i\Omega\tau} d\Omega, \quad (30)$$
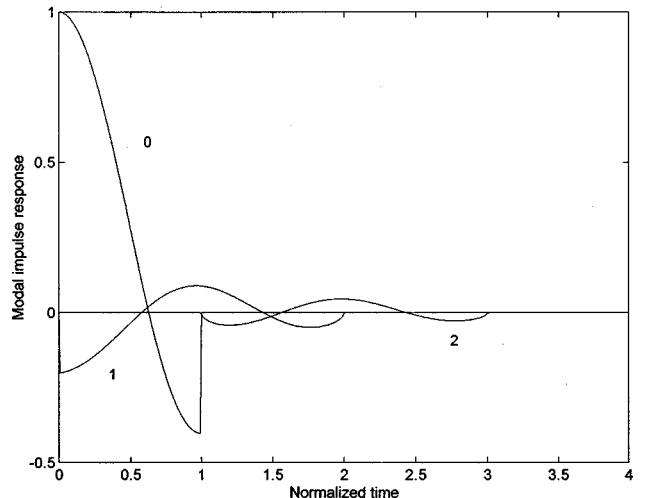
FIG. 4. The generalized impulse response $h_1(\rho,0,\tau)$ vs τ for $\rho=0,1,2$.

1496   J. Acoust. Soc. Am., Vol. 105, No. 3, March 1999

Peter R. Stepanishen: Acoustic transient Bessel beams   1496
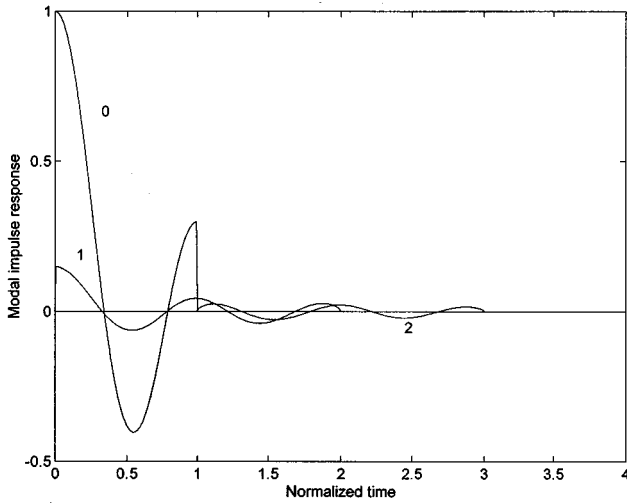
FIG. 5. The generalized impulse response $h_2(\rho,0,\tau)$ vs τ for $\rho=0,1,2$.

it is easily shown that the Fourier transform of Eq. (8) leads to the following Rayleigh surface integral representation for $P(\rho,z,\Omega)$:

$$P(\rho,z,\Omega)=i\Omega W(\Omega)\cos\zeta\int_0^1\rho_s\,d\rho_s\int_0^{2\pi}d\phi_s$$

$$\times\frac{e^{-i\Omega R}}{2\pi R}J_0(\Omega\sin\zeta\rho_s). \tag{31}$$

Since[11,12]

$$j(\rho,0,\tau)\Leftrightarrow J_0(\Omega\sin\zeta\rho), \tag{32}$$

it then follows from Eq. (12) that

$$J_0(\Omega\sin\zeta\rho)=\sum_n V_n(\Omega,\zeta)J_0(ka_n\rho), \tag{33}$$

where

$$V_n(\Omega,\zeta)=\frac{2}{J_0^2(ka_n)}\int_0^1 J_0(\Omega\sin\zeta\rho)J_0(ka_n\rho)\rho\,d\rho. \tag{34}$$
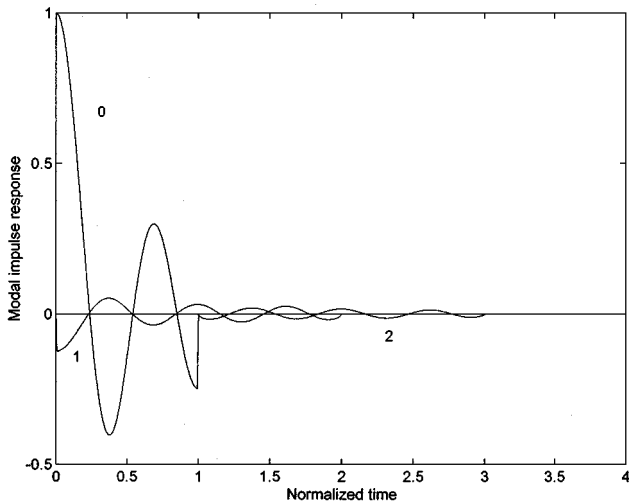
FIG. 6. The generalized impulse response $h_3(\rho,0,\tau)$ vs τ for $\rho=0,1,2$.

Thus, $P(\rho,z,\Omega)$ can be expressed as

$$P(\rho,z,\Omega)=\sum_n S_n(\Omega,\zeta)H_n(\rho,z,\Omega), \tag{35}$$

where

$$S_n(\Omega,\zeta)=\cos\zeta i\Omega W(\Omega)V_n(\Omega,\zeta) \tag{36}$$

and

$$H_n(\rho,z,\Omega)=\int_0^1\int_0^{2\pi}J_0(ka_n\rho_s)\frac{e^{-i\Omega R}}{2\pi R}\rho_s\,d\rho_s\,d\phi_s, \tag{37}$$

where

$$h_n(\rho,z,\tau)\Leftrightarrow H_n(\rho,z,\Omega), \tag{38}$$

$$s_n(\tau,\zeta)\Leftrightarrow S_n(\Omega,\zeta). \tag{39}$$

It is noted that Eq. (35) is simply the Fourier transform equivalent of Eq. (16).

A simple closed form expression for $V_n(\Omega,\zeta)$ is readily obtained after noting the following integral identity:[21]

$$\int\rho_s J_0(\alpha\rho_s)J_0(\beta\rho_s)\,d\rho_s$$

$$=\rho_s\frac{\beta J_0(\alpha\rho_s)J_1(\beta\rho_s)-\alpha J_0(\beta\rho_s)J_1(\alpha\rho_s)}{\beta^2-\alpha^2}. \tag{40}$$

It then follows, via the use of $J_1(ka_n)=0$, that

$$V_n(\Omega,\zeta)=\frac{2}{J_0(ka_n)}G_n(\Omega,\zeta), \tag{41}$$

where

$$G_n(\Omega,\zeta)\equiv\frac{\Omega\sin\zeta J_1(\Omega\sin\zeta)}{[(\Omega\sin\zeta)^2-ka_n^2]}. \tag{42}$$

It is noted that $V_n(\Omega,\zeta)$ is real, free of singularities, and an even function of Ω with a bandpass characteristic centered about $\Omega_n=ka_n/\sin\zeta\sim2\pi(2n+1)/(4\sin\zeta)$, which is to be expected in light of the results for $v_n(\tau,\zeta)$ in Fig. 2. For $\zeta=0$, it is obvious from Eq. (41) that

$$V_n(\Omega,0)=1,\quad n=0,$$

$$=0,\quad n>0. \tag{43}$$

The on-axis case is now explicitly addressed as a result of its importance in TBB fields. It is apparent from Eq. (35) that the on-axis pressure can simply be expressed as

$$P(0,z,\Omega)=\sum_n S_n(\Omega,\zeta)H_n(0,z,\Omega), \tag{44}$$

where

$$H_n(0,z,\Omega)=\int_0^1 J_0(ka_n\rho_s)\frac{e^{-i\Omega\sqrt{\rho_s^2+z^2}}}{\sqrt{\rho_s^2+z^2}}\rho_s\,d\rho_s$$

$$=\int_z^{\sqrt{z^2+1}}J_0(ka_n\sqrt{\tau^2-z^2})e^{-i\Omega\tau}\,d\tau. \tag{45}$$

The latter form is, of course, the Fourier transform of the on-axis impulse response in Eq. (27). For the piston or $n=0$ case it is also obvious that

$$H_0(0,z,\Omega) = -2je^{-i\Omega\alpha}\sin(\Omega\beta),\qquad(46)$$

where

$$\alpha = (\sqrt{z^2+1}+z)/2,\quad \beta = (\sqrt{z^2+1}-z)/2.$$

After utilizing the usual far-field approximation for R in Eq. (35) and then performing the integration over ϕ_s, the following expression for the Fourier transform of the far-field pressure is obtained:

$$P^f(R_0,\theta,\Omega) = \sum_n S_n(\Omega)H_n^f(R_0,\theta,\Omega),\qquad(47)$$

where

$$H_n^f(R_0,\theta,\Omega) = \frac{e^{-i\Omega R_0}}{2\pi R_0}\int_0^1 J_0(ka_n\rho)J_0(\Omega\sin\theta\rho_s)\rho_s\,d\rho_s.\qquad(48)$$

After again noting Eq. (40) it then follows via the use of $J_1(ka_n)=0$ that

$$H_n^f(R_0,\theta,\Omega) = \frac{e^{-i\Omega R_0}}{2\pi R_0}\pi J_0(ka_n)G_n(\theta,\Omega),\qquad(49)$$

where

$$G_n(\theta,\Omega) \equiv \frac{\Omega\sin\theta J_1(\Omega\sin\theta)}{[(\Omega\sin\theta)^2-ka_n^2]}.\qquad(50)$$

For $\theta=0$, it is further noted that

$$G_n(0,\Omega) = \tfrac{1}{2},\quad n=0,$$
$$= 0,\quad n\neq 0,\qquad(51)$$

and, for $\theta\neq 0$, the bandpass oscillatory nature of the Fourier transform $G_n(\theta,\Omega)$ is readily apparent from Eq. (50).

Although the space–time expressions for the modal impulse responses $h_n(\rho,z,\tau)$ can be used in the far field, simplified expressions for the far-field modal impulse responses can be easily developed from the preceding Fourier transform results. In light of Eqs. (15) and (49) it is now apparent that

$$p^f(R_0,\theta,\tau) = \sum_n s_n(\tau,\zeta)\otimes h_n^f(R_0,\theta,\tau),\qquad(52)$$

where the far field impulse response $h_n^f(R_0,\theta,\tau)$ is simply expressed as

$$h_n^f(R_0,\theta,\tau) = \frac{J_0(ka_n)}{2R_0}g_n(\theta,\tau-R_0),\qquad(53)$$

where

$$g_n(\theta,\tau)\Leftrightarrow G_n(\theta,\Omega).\qquad(54)$$

It then follows directly from Eq. (50) that

$$g_n(\theta,\tau) = \frac{1}{2\pi}\int_{-\infty}^{\infty}\frac{\Omega\sin\theta J_1(\Omega\sin\theta)}{[(\Omega\sin\theta)^2-ka_n^2]}e^{i\Omega\tau}d\Omega$$
$$= \frac{1}{\sin\theta}g_n\left(\frac{\tau}{\sin\theta}\right),\qquad(55)$$

where

$$g_n(\tau') = \frac{1}{2\pi}\int_{-\infty}^{\infty}\frac{\Omega J_1(\Omega)}{[(\Omega)^2-ka_n^2]}e^{i\Omega\tau'}d\Omega\qquad(56)$$

with $\tau'=\tau/\sin\theta$. The far-field impulse response $h_n^f(R_0,\theta,\tau)$ is thus simply expressed as

$$h_n^f(R_0,\theta,\tau) = \frac{J_0(ka_n)}{2R_0\sin\theta}g_n\left(\frac{\tau-R_0}{\sin\theta}\right).\qquad(57)$$

An important observation regarding the on-axis far field for TBB fields can now be noted. More specifically, for $\theta=0$ it is noted from the preceding development that

$$h_n^f(R_0,0,\tau) = \frac{1}{4R_0}\delta(\tau-R_0),\quad n=0,$$
$$= 0,\quad n\neq 0.\qquad(58)$$

It then follows from Eq. (52) that

$$p^f(R_0,0,\tau) = \frac{1}{4R_0}s_0(\tau-R_0,\zeta),\qquad(59)$$

which, in light of Eq. (17), can be expressed as

$$p^f(R_0,0,\tau) = \frac{1}{4R_0}\cos\zeta\frac{dw(\tau-R_0)}{d\tau}\otimes v_0(\tau,\zeta),\qquad(60)$$

where $v_0(\tau,\zeta)$ is specified in Eq. (21). *The on-axis far field is thus determined solely by the $n=0$ term in the modal expansion for the field.*

More generally, for $\theta\neq 0$ the $g_n(\tau')$ must be determined prior to using Eq. (57) to evaluate $p^f(R_0,\theta,\tau)$ via Eq. (52). In order to evaluate $g_n(\tau')$ the following transform pair is first observed:

$$iJ_1(\Omega)\Leftrightarrow j_1(\tau),\qquad(61)$$

where

$$j_1(\tau) = \frac{1}{\pi}\frac{\tau}{[1-\tau^2]^{1/2}},\quad |\tau|<1,$$
$$= 0,\quad |\tau|<1.\qquad(62)$$

Since

$$\frac{-i\Omega}{[\Omega^2-ka_n^2]}\Leftrightarrow c(\tau)=\cos(\tau)\ \tau\geqslant 0,\qquad(63)$$

it then follows from the convolution property of Fourier transforms that

$$g_n(\tau') = j_1(\tau')\otimes c(\tau').\qquad(64)$$

Although $c(\tau')$ is causal, $j_1(\tau')$ and $g_n(\tau')$ are noncausal with $g_n(\tau')=0$ for $|\tau'|>1$.

Since $g_n(\tau')$ is an even function of τ', numerical results for $g_n(\tau')$ vs τ' are shown in Fig. 7 for $\tau'>0$ and for n
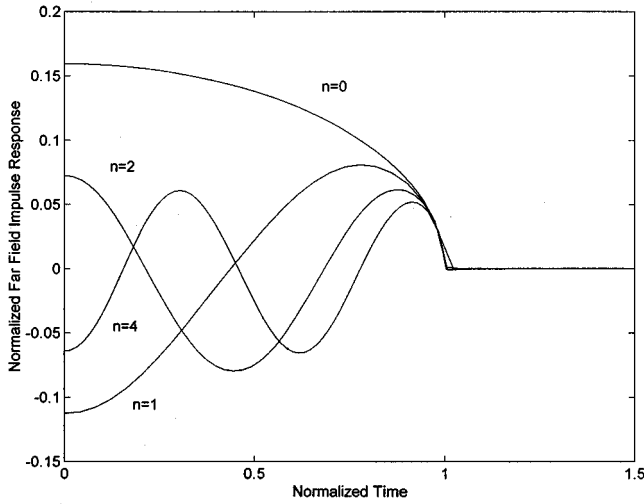
FIG. 7. $g_n(\tau')$ vs τ' for $n=0,1,2,3$ where $\tau'=\tau/\sin\zeta$.

$=0,1,2,3$. It is evident that $g_n(\tau')=0$ for $|\tau'|>1$ and the $g_n(\tau')$ exhibit an increasingly oscillatory behavior as n increases. More specifically, as n increases it is clear that $g_n(\tau')$ approaches a quasi-cosinusoidal signal with $2(n-1)$ zeros between $-1<\tau/\sin\theta<1$, i.e., $g_n(\tau')\propto(-1)^n\cos([(2n+1)/2]\pi\tau/\sin\theta)$. The far-field impulse response $h_n^f(R_0,0,\tau)$ thus exhibits the characteristics of a gated cosinusoidal function where the center frequency is observed to correspond to $(2n+1)/(4\sin\theta)$ and the bandwidth is inversely related to the pulse duration, i.e., $2/\sin\theta$. It then follows from Eq. (52) that the various frequency components in $s_n(\tau,\zeta)$ will be efficiently coupled to the far field at selected angles for which acoustic coincidence occurs, i.e., at a fixed θ' the acoustic coincidence frequency in $s_n(\tau,\zeta)$ will be $f_r^n=(2n+1)/(4\sin\theta')$. Finally, in light of Eqs. (41) and (49), it is not surprising that $h_n^f(R_0,\theta,\tau)$ and $v_n(\tau,\zeta)$ exhibit similar characteristics.

II. ACOUSTIC BESSEL BULLETS

In contrast to the analysis and results in the preceding section which are applicable for all TBB fields, a special type of band-limited TBB field, which was introduced in a recent paper[13] as an acoustic BB, is now addressed. Acoustic Bessel bullets are defined by the following gated sinusoidal weighting function $w(\tau)$:

$$w(\tau)=\sin(\Omega_b\tau), \quad 0\leq|\tau|\leq T=\frac{\pi N}{\Omega_b}, \quad (65)$$

where $w(\tau)$ is an odd noncausal time function, and Ω_b and $2T$ are the frequency and pulse duration which consists of N sinusoidal cycles. It is apparent from $W(\Omega)$, the Fourier transform of $w(\tau)$, that the relative bandwidth of the signal decreases as N increases.

The space–time properties of the acoustic BB fields generated by infinite planar apertures based on the above weighting function are readily investigated[13] via the use of Eq. (2) from which it follows that

$$p(\rho,z,\tau)=p(\rho,0,\tau-z\cos\zeta). \quad (66)$$

Since $w(\tau)$ is noncausal, $p(\rho,0,\tau)$ is a time-limited non-causal odd function with a time duration equivalent to $2T+2\rho\sin\zeta$ which is propagated in the z direction with the supersonic velocity $1/\cos\zeta$ and can be expressed as

$$p(\rho,0,\tau)=\int_{\tau_1}^{\tau_2}\frac{w(\tau-\tau')}{\pi[(\rho\sin\zeta)^2-(\tau')^2]^{1/2}}\,d\tau', \quad (67)$$

where the limits of integration are functions of τ. It is noted that $p(\rho,0,\tau)$ is an odd function of τ for all ρ and the on-axis pressure is simply expressed as

$$p(0,0,\tau)=\sin(\Omega_b\tau), \quad 0\leq|\tau|\leq T=\frac{\pi N}{\Omega_b}. \quad (68)$$

For the special case where $\rho\sin\zeta>\pi/\Omega_b$, $p(\rho,0,\tau)$ can be interpreted to consist of a turn-on transient extending from $-(\rho\sin\zeta+T)<\tau<(\rho\sin\zeta-T)$, a quasi-steady-state extending from $(\rho\sin\zeta-T)<\tau<(T-\rho\sin\zeta)$, and a turn-off transient extending from $(T-\rho\sin\zeta)<\tau<(T+\rho\sin\zeta)$. For $\rho\sin\zeta<T$ and $|\tau|\leq T-\rho\sin\zeta$ the pressure during the quasi-steady-state period can be described by the following expression:

$$p(\rho,0,\tau)=\int_{-\rho\sin\zeta}^{\rho\sin\zeta}\frac{w(\tau-\tau')}{\pi[(\rho\sin\zeta)^2-(\tau')^2]^{1/2}}\,d\tau', \quad (69)$$

which can be integrated to obtain[13]

$$p(\rho,0,\tau)=J_0(\Omega_b\rho\sin\zeta)\sin(\Omega_b\tau). \quad (70)$$

It is thus apparent that $p(\rho,0,\tau)$ may only consist of a turn-on and turn-off transient at the radial distances ρ_m where $J_0(\Omega_b\rho_m\sin\zeta)=0$.

The lateral extent of the BB defined by the weighting function in Eq. (65) may now be readily estimated for the preceding case and conditions via the use of the quasi-steady-state pressure in Eq. (70) which is also obviously valid for $\rho=0$. If the lateral extent of the BB is defined by the radial location ρ_n where the quasi-steady-state field is reduced to $1/\sqrt{2}$ of the peak on-axis field, it is then apparent that

$$\rho_n\approx\frac{1.1}{\Omega_b\sin\zeta}. \quad (71)$$

Clearly, the lateral extent of the BB can then be simply controlled via the carrier frequency Ω_b of the weighting function whereas the on-axis axial extent of the BB, i.e., $2T$, is also a function of N. Thus, the lateral and axial extent of the BB can be independently controlled via the selection of Ω_b and N or T.

A pressure map for $p(\rho,0,\tau)$ where $\Omega_b=73.18$ and $N=10$ is shown in Fig. 8 as a function of normalized time τ and normalized radial distance $\rho_r=\rho\sin\zeta$ for $0\leq\rho_r\leq0.5$. These results clearly illustrate the space–time dependence of $p(\rho,0,\tau)$ for the case of the infinite planar aperture. The on-axis result reproduces the weighting function as indicated in Eq. (68). A quasi-steady-state pressure is observed in the region centered about $\tau=0$. As ρ_r increases, the temporal extent of this region decreases as expected. It is noted that the quasi-steady-state results are in agreement with the ana-
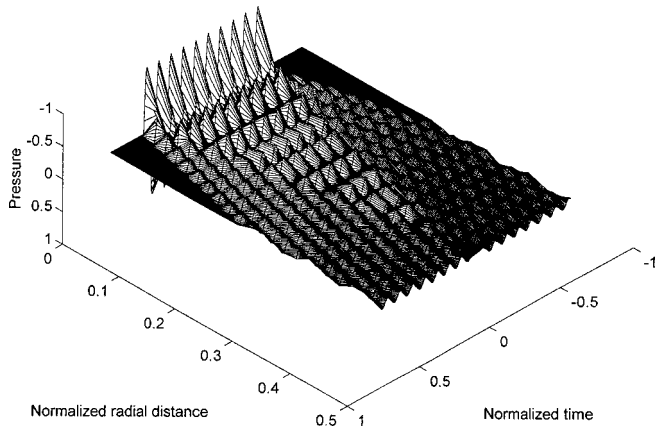
FIG. 8. Pressure map of $p(\rho,0,\tau)$ vs τ and $\rho_r=\rho\sin\zeta$ for $\Omega_b=73.18$ and $N=10$.

lytical result in Eq. (70). The lateral extent of the acoustic BB is also noted to be in general agreement with Eq. (71) and the axial extent is determined by $2T$.

In contrast to the preceding quasi-steady-state example a pressure map for $p(\rho,0,\tau)$ where $\Omega_b=73.18$ and $N=2$ is shown in Fig. 9 as a function of normalized time τ and normalized radial distance ρ_r for $0\leqslant\rho_r\leqslant0.5$. As a result of the shorter pulse duration of $2T$, the turn-on and turn-off transients are of increasing importance relative to the quasi-steady-state pressure contribution which only exists in the region where $0\leqslant\rho_r\leqslant T$. Equation (71) again provides a reasonable estimate of the lateral extent of the acoustic BB and the axial extent is again determined by the pulse duration $2T$. In the region where $\rho_r>T$ two distorted quasi-sinusoidal signals are readily observed in the pressure time history at each point. In general, the spectral content of the signals decreases as ρ_r increases further.

As a result of space limitations and the importance of the on-axis field, the present study is limited to illustrating the effect of a finite planar aperture on the on-axis quasi-steady-state field of acoustic BB fields. More specifically, if $T=NT_b\gg1$ is considered for a planar aperture, it is clear from the results in the preceding section that the pressure at each on-axis point is a quasi-steady-state sinusoidal oscillation. The amplitude and phase of the steady state pressure
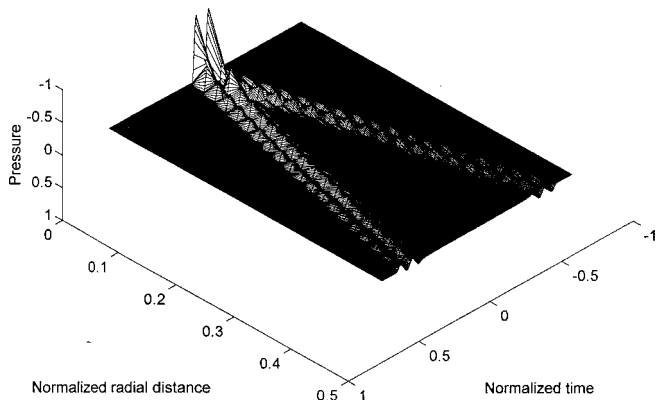
FIG. 9. Pressure map of $p(\rho,0,\tau)$ vs τ and $\rho_r=\rho\sin\zeta$ for $\Omega_b=73.18$ and $N=2$.
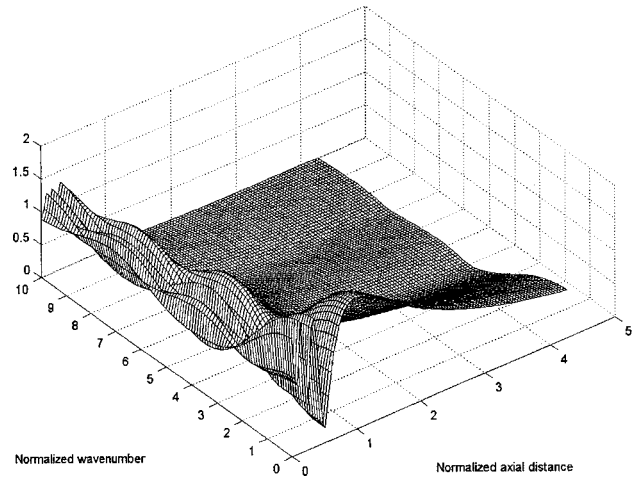
FIG. 10. A map of the generalized modal transfer function magnitude $|H_{ka_r}(0,z,\Omega_b)|$ vs ka_r and z/z_R for $\Omega_b=73.18$.

can thus be described by the preceding modal Fourier transform relationships, i.e.,

$$P(0,z,\Omega_b)=\sum_n S_n(\Omega_b,\zeta)H_n(0,z,\Omega_b), \qquad (72)$$

where

$$S_n(\Omega_b,\zeta)=\cos\zeta i\Omega_b\frac{2}{J_0(ka_n)}\frac{\Omega_b\sin\zeta J_1(\Omega_b\sin\zeta)}{[(\Omega_b\sin\zeta)^2-ka_n{}^2]}. \qquad (73)$$

Thus, the on-axis modal transfer functions $H_n(0,z,\Omega_b)$ are clearly of major importance in determining the properties of the axial field.

Consider now the following generalized modal transfer function $H_{ka_r}(0,z,\Omega_b)$ which is defined as follows:

$$H_{ka_r}(0,z,\Omega_b)=\int_z^{\sqrt{z^2+1}}J_0(ka_r\sqrt{\tau^2-z^2})e^{-i\Omega_b\tau}d\tau, \quad (74)$$

where ka_r is a normalized radial wave number. Clearly,

$$\lim_{ka_r\to ka_n}H_{ka_r}(0,z,\Omega_b)=H_n(0,z,\Omega_b). \qquad (75)$$

A map of $|H_{ka_r}(0,z,\Omega_b)|$ vs ka_r and z/z_R, where $z_R=\Omega_b/2\pi$ is the usual Rayleigh distance, is presented in Fig. 10 for $\Omega_b=73.18$ whereas a series of $|H_{ka_r}(0,z,\Omega_b)|$ vs z/z_R are shown in Fig. 11 for the various ka_r in Fig. 10. The results for $ka_r=0$ correspond to the $n=0$ case in Eq. (46).

The results in Figs. 10 and 11 illustrate several points of importance. First, $|H_{ka_r}(0,z,\Omega_b)|$ vs z/z_R exhibits a general oscillatory behavior followed by a monotonically decreasing response as z/z_R increases. The region of oscillatory behavior is a maximum for $ka_r=0$ and decreases as ka_r increases. In general, $|H_{ka_r}(0,z,\Omega_b)|\sim(z/z_R)^{-1}$; however, when $ka_r=ka_n$ with $n>0$, the transfer function $|H_{ka_n}(0,z,\Omega_b)|\sim(z/z_R)^{-2}$. This latter result is most clearly seen from the curves in Fig. 11 where the lowest curve of the two lowest dark stripes correspond to $ka_r=3.83$ and 7.02, i.e., ka_1 and ka_2. It is thus apparent that a mode stripping occurs along the axis. As z/z_R increases, the higher modes in the modal
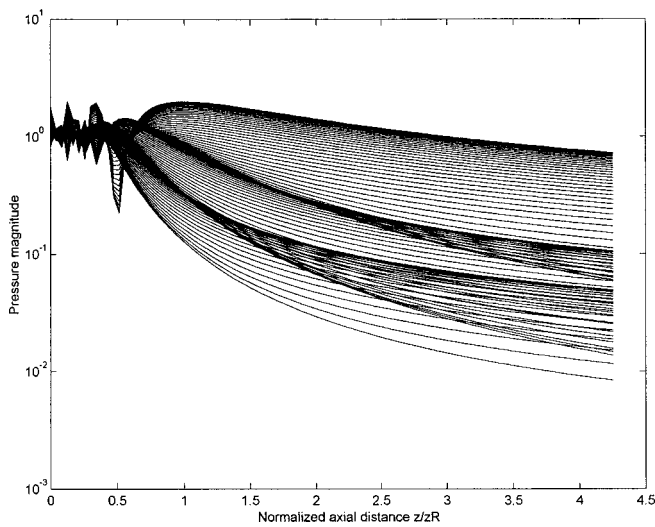
FIG. 11. The generalized modal transfer function magnitude $|H_{ka_r}(0,z,\Omega_b)|$ vs z/z_R for $\Omega_b=73.18$ and ka_r in the range $0 \leqslant ka_r \leqslant 10$.

expansion of the on-axis field are successively stripped from the on-axis field and redistributed to other spatial regions. Once again, it is obvious that the on-axis far field is controlled by the $n=0$ term in the modal expansion of Eq. (72).

Finally, the magnitude of the on-axis pressure $|P(0,z,\Omega_b)|$ vs z/z_R is shown in Fig. 12 for $\Omega_b=73.18$ and $\zeta=1$, 3, and 5 degrees. Several results of interest are apparent from the figure. First, it is noted that the location of the last maxima for a fixed ζ is a commonly used measure of the Rayleigh distance or near- to far-field transition distance for the case of a uniform piston where $\zeta=0$. It is obvious that the location of the last maxima for a fixed ζ is inversely related to ζ, i.e., as ζ increases the maxima moves closer to the planar aperture. Second, it is observed that the variation of the fluctuation in peak amplitude decreases as ζ increases. Third, it is observed that the on-axis field exhibits the expected inverse range dependence for $\zeta=1$ and 5 degrees; however, for $\zeta=3$ degrees, the on-axis decay corresponds to $(z/z_R)^{-2}$. The reason for the latter anomalous rate of decay
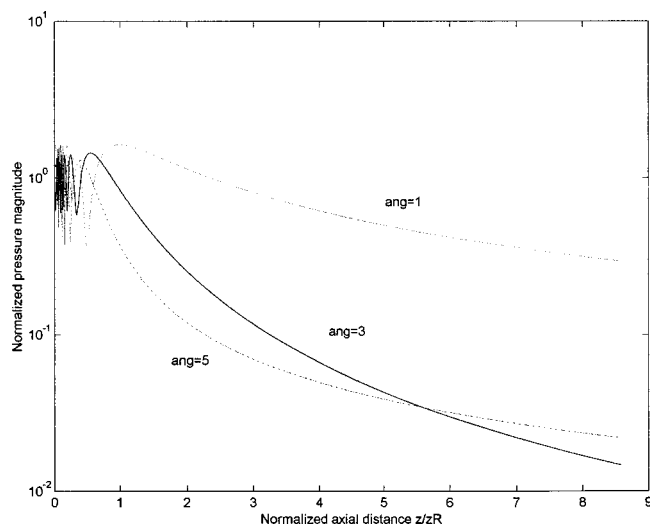
FIG. 12. The magnitude of the on-axis pressure $|P(0,z,\Omega_b)|$ vs z/z_R for $\Omega_b=73.18$ and $\zeta=1$, 3, and 5 degrees.

is that $S_0(\Omega_b,\zeta)$ and $V_0(\Omega_b,\zeta)$ are zero since $J_1(\Omega_b\sin\zeta)=0$ for $\zeta=3$ degrees. The $n \geqslant 1$ terms in the eigenfunction expansion thus control the spatial rate of decay of the field. Finally, it is noted that the on-axis anomalous rate of decay, which occurs here due to the spectrally pure excitation, would not occur for the pulsed case where the nonzero bandwidth associated with the finite pulse duration introduces frequency components for which $V_0(\Omega,\zeta) \neq 0$.

III. SUMMARY AND CONCLUSIONS

A generalized space–time modal impulse response and Fourier transform approach has been developed in the present paper to investigate the space–time properties of TBB fields which are generated using finite planar apertures. The generalized space–time modal impulse response approach results in a modal sum of convolution integrals for the pressure at each field point. The modal Fourier transform approach was simply obtained from the temporal Fourier transform of the field equations for the modal impulse response approach.

A key feature of the modal approach is the modal decomposition of the circular planar aperture distributions which are required to generate the TBB fields. Closed form expressions were presented for the associated modal impulse responses. General properties and numerical results for the modal source functions and the modal impulse responses were then presented and discussed. Relatively simple closed form expressions are developed for the modal Fourier transform decomposition of the on-axis field and the angular-dependent far-field transforms. In addition to providing a clear connection between the space–time and space–frequency properties of the field, the modal Fourier transform approach provides additional important insight into the nature of TBB fields. General modal expressions for the on-axis space–time pressure field and angular-dependent far field are presented and discussed. The on-axis far field for the finite aperture is shown to be simply related to the lowest-order term in the modal expansion.

The acoustic field for a particular type of TBB field which is designated as an acoustic BB, which has a bandpass spectrum, was briefly investigated using the generalized modal impulse response and Fourier transform approach. Numerical results were first presented for the space–time properties of acoustic BB fields generated from an infinite aperture. Analogous harmonic results were then presented for a finite aperture. An interesting range-dependent modal stripping along the axis of the aperture was observed. In contrast to the inverse range decay for the lowest-order mode which determines the on-axis far field, spatial rates of decay for the higher-order modes were noted to be greater than the ubiquitous spherical spreading loss due to a spatial redistribution of the modal energies.

It is now clear that the space–time modal impulse response approach can be simply used to determine the space–time properties of general TBB fields and acoustic BB fields in particular. Work in determining the transverse as well as the axial dependence of such fields for various weighting functions is in progress and will be reported shortly.[14] In

addition, it is equally clear that the basic space–time modal impulse response approach presented here can also be used to investigate the general properties of other localized waves, e.g., FWM and MPS wave fields, generated via planar apertures. A comparison of the properties of various localized wave fields is in progress and those results will also be reported in a later paper.

[1] J. N. Brittingham, ''Focus wave modes in homogeneous Maxwell's equations: transverse electric mode,'' J. Appl. Phys. **54**, 1179–1189 (1983).

[2] R. W. Ziolkowski, ''Exact solutions of the wave equation with complex source locations,'' J. Math. Phys. **26**, 861–863 (1985).

[3] R. W. Ziolkowski, ''Localized wave physics and engineering,'' Phys. Rev. A **44**(6), 3960–3984 (1991).

[4] I. M. Besieris, A. M. Shaarawi, and R. W. Ziolkowski, ''A bidirectional traveling plane wave representation of exact solutions of the scalar wave equation,'' J. Math. Phys. **30**, 1254–1269 (1989).

[5] J. V. Candy, R. W. Ziolkowski, and D. K. Lewis, ''Transient waves estimation: A multichannel deconvolution application,'' J. Acoust. Soc. Am. **88**, 2235–2247 (1990).

[6] J. V. Candy, R. W. Ziolkowski, and D. K. Lewis, ''Transient waves: Reconstruction and processing,'' J. Acoust. Soc. Am. **88**, 2248–2258 (1990).

[7] J. E. Hernandez, R. W. Ziolkowski, and S. R. Parker, ''Synthesis of the driving functions of an array for propagating localized wave energy,'' J. Acoust. Soc. Am. **92**, 550–562 (1992).

[8] R. W. Ziolkowski and D. K. Lewis, ''Verification of the localized wave transmission effect,'' J. Appl. Phys. **68**, 6083–6086 (1990).

[9] T. T. Wu, ''Electromagnetic missiles,'' J. Appl. Phys. **57**, 2370–2373 (1985).

[10] R. W. Ziolkowski, I. M. Besieris, and A. M. Shaarawi, ''Localized wave representations of acoustic and electromagnetic radiation,'' Proc. IEEE **79**(10), 1371–1378 (1991).

[11] P. R. Stepanishen and J. Sun, ''Acoustic bullets: Transient Bessel beams generated by planar apertures,'' J. Acoust. Soc. Am. **102**, 1955–1963 (1997).

[12] P. R. Stepanishen, ''Acoustic bullets/transient Bessel beams: Near to far field transition via an impulse response approach,'' J. Acoust. Soc. Am. **103**, 1742–1751 (1998).

[13] P. R. Stepanishen, ''Acoustic Bessel bullets,'' J. Sound Vib. (accepted for publication) (1999).

[14] P. R. Stepanishen, ''Transverse field characteristics of acoustic Bessel bullets,'' J. Acoust. Soc. Am. (in preparation) (1999).

[15] J. Lu and J. F. Greenleaf, ''Nondiffracting x waves-exact solutions to free-space scalar wave equation and their finite aperture realization,'' IEEE Trans. Speech Audio Process. **39**, 19–31 (1992).

[16] J. Lu and J. F. Greenleaf, ''Experimental verification of nondiffracting x waves,'' IEEE Trans. Ultrason. Ferroelectr. Freq. Control **39**(1), 441–446 (1992).

[17] H. E. Moses and R. T. Prosser, ''Initial conditions, sources, and currents for prescribed time-dependent acoustic and electromagnetic fields in three dimensions, part I: The inverse initial value problem, acoustic and electromagnetic bullets, expanding waves, and imploding waves,'' IEEE Trans. Antennas Propag. **AP-34**(2), 188–196 (1986).

[18] H. E. Moses and R. T. Prosser, ''Acoustic and electromagnetic bullets: Derivation of new exact solutions of the acoustic and Maxwell's equations,'' SIAM (Soc. Ind. Appl. Math.) J. Appl. Math. **50**(5), 1325–1340 (1990).

[19] P. R. Stepanishen, ''Transient radiation from pistons in an infinite planar baffle,'' J. Acoust. Soc. Am. **49**, 1626–1638 (1971).

[20] P. R. Stepanishen, ''Acoustic transients from planar axisymmetric vibrators using the impulse response approach,'' J. Acoust. Soc. Am. **70**, 1176–1181 (1981).

[21] I. S. Gradshetyn and I. M. Ryzhik, *Table of Integrals, Series, and Products* (Academic, Orlando, FL, 1980), 2nd ed.

A multiple microphone recording technique for the generation of virtual acoustic images

Yuvi Kahana, Philip A. Nelson, Ole Kirkeby, and Hareo Hamada[a]
Institute of Sound & Vibration Research, Southampton University SO17 1BJ, United Kingdom

A new recording technique based on multichannel digital signal processing is suggested. The system uses a dummy-head that is modeled as a rigid sphere with two pairs of microphones mounted on opposite sides of the sphere in the horizontal plane. Reversals—front back confusion, is a well-known phenomenon when localizing virtual acoustic images produced by either headphones or loudspeakers. Reproduction with two loudspeakers to the front of the listener causes rear virtual acoustic images to be perceived primarily at ''mirrored'' angles in the frontal hemisphere. The problem is tackled here by using a multichannel signal processing technique rather than by mimicking accurately the acoustomechanical properties of a human head. The acoustic signals which are recorded at the microphones are filtered by a 4×4 matrix of digital filters before being transmitted via four loudspeakers. The performance of the system is investigated by means of computer simulations, objective measurements, and also by subjective experiments in an anechoic environment, where the listeners are asked to localize the perceived angle of the signals which were prerecorded with the sphere dummy-head. Successful discrimination of reversals is achieved primarily due to the dominant role of the interaural time delay (ITD) for localization at low frequencies, but the accuracy with which listeners can localize virtual acoustic images is reduced in comparison to a conventional two-ear dummy-head (e.g., KEMAR) with a two-loudspeaker arrangement. The system is robust with respect to head rotations—virtual acoustic images do not disappear and localization ability improves when listeners use small head rotations. © *1999 Acoustical Society of America.* [S0001-4966(99)01103-0]

PACS numbers: 43.20.Fn, 43.20.Px, 43.60.Pt, 43.66.Qp [DEC]

INTRODUCTION

The perception of a virtual acoustic image by a listener is produced by ensuring that the sound pressures at the eardrums of the listener are equivalent to those produced by a real source at the desired position. The production of virtual acoustic images through the use of loudspeakers can be achieved either by reproduction of dummy-head recordings or by a synthesis of monophonic or stereophonic signals with a set of HRTFs (head-related transfer functions). In both cases, a common limitation is reversals. This phenomenon has been investigated previously, mainly for reproduction with headphones where sound sources in the frontal hemisphere were often perceived as being behind the listener; they appeared to be either elevated or closer to the listener than they were during the recording, or they appeared to be inside the head.[1–5] The reproduction of binaural recordings through loudspeakers, referred to as ''transaural audio'' (Cooper and Bauck[6]), overcomes the problem of externalization of virtual acoustic images but not the problem of reversals; reproduction with two loudspeakers in the front causes rear virtual acoustic images to be perceived primarily at ''mirrored'' angles in the frontal hemisphere (Damaske,[7] Nelson *et al.*[8]). The explanation for this ambiguity might be that the available commercial dummy-heads do not replicate exactly the individual form of the human head. Also, listeners use small head movements to distinguish between front and back, while binaural recording is undertaken with a fixed dummy-head position (Blauert,[1] Møller[9]).

The available commercial dummy-heads try to simulate different acoustomechanical properties of the human head such as the ear canals, pinnae, ear drums, etc. These have not yet been standardized, and different dummy-heads produce different performances (Kleiner,[10] Møller[11]). The dummy-head shape in this research is simplified to a sphere model in order to simulate the general diffraction around an average human head. Two pairs of microphones, whose diaphragms are flush mounted with the surface of a rigid sphere, are mounted on opposite sides of the sphere in the horizontal plane. The positioning of each microphone can be adjusted with respect to the ''interaural axis'' (as illustrated in Fig. 1); one microphone is moved slightly toward the ''front section'' and the other slightly to the ''rear,'' with a small distance between the microphones being provided to prevent spatial aliasing. The positions of the microphones (±10° with respect to the ''interaural axis'') correspond to slight head rotations of the listener in the reproduction space. Hill *et al.*[12] showed that the performance of a 4×4 virtual acoustic imaging system can be investigated by means of the rate of change of the interaural cross-correlation (IACC) function with respect to head rotation. Simulations demonstrated that the rate of change of the IACC that is produced by a real source cannot be replicated by a two-channel virtual acoustic imaging system. The four-channel system, with loudspeakers also placed behind the listener, can reproduce this change.

[a]Present address: Department of Information and Communication Engineering, Tokyo Denki University, Tokyo 101, Japan.
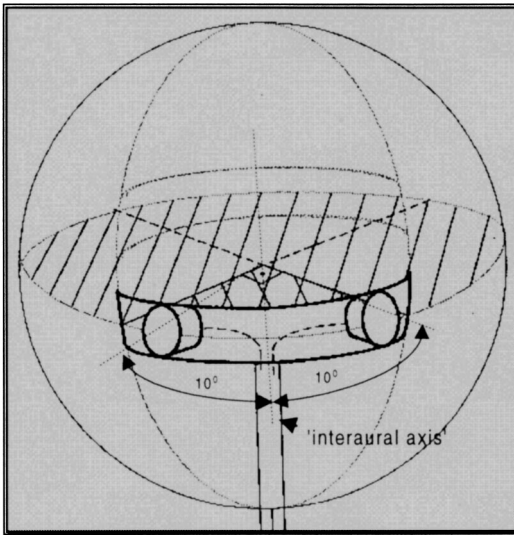
FIG. 1. A schematic drawing of the sphere model with a radius of 9.5 cm. Two pairs of Electret microphones are positioned at each side of the sphere. The ''front'' and ''rear'' microphones are positioned at ±10° with respect to the ''interaural axis.''

The subjective experiments which were based on synthesized signals from a monophonic source showed that the system is capable of resolving the problem of reversals found with the two-channel system, especially with slight head rotations.

It is commonly known that the sphere can not approximate an average human head over the whole audible frequency range, since at high frequencies the wavelength is comparatively short and the structure of the torso, head, and the pinnae become significant. However, the model can certainly be used as a reasonable approximation to a real head up to a frequency of a few kHz, since in terms of localization cues interaural time differences (ITD) are important at low frequencies (below approximately 1.5 kHz) and dominate interaural level differences (ILD) and spectral cues (Wightman and Kistler[13]). It has also been shown that ITDs for the above frequency range calculated with the sphere model in the horizontal plane were very similar to those of human heads with the same perimeter (Kuhn[14]). For higher frequencies, the ILD cues dominate, where the model of the sphere agrees with measurements with a dummy-head of sounds incident in the horizontal plane up to 2.5 kHz. Above this frequency, the pinna starts to affect localization at certain angles of incidence, and the ILD cues produce a large cone of confusion (Kuhn[15]). The spectral modification of the sound due to the pinna affects front/back and elevation localization at high frequencies from 4 up to 16 kHz (Hebrank and Wright[16]).

Recent studies[17–19] of sound field reproduction have demonstrated that a field can be reproduced, and approximate the original, by recording the acoustic signals at a finite number of positions in the original sound field. Then, the signals are processed via a matrix of linear filters in order to produce the inputs to a number of sources used for reproduction; in this case, four microphones and four loudspeakers. The solution presented here is an extension of the 2×2 cross-talk canceller, suggested initially by Atal and Schroeder.[20] A method of frequency domain deconvolution with regularization (Kirkeby et al.[21]) is used to calculate in the least-squares

sense the inverse filters through which the recorded signals are passed. These filters are designed to ensure that the recorded signals are accurately reproduced at the equivalent microphone positions on the surface of a sphere placed at the position of the listener's head.

This paper summarizes the results of the investigations of the new system. The results were obtained by calculating the inverse filters by using a classical model of the scattered sound field around a rigid sphere (Malecki[22]). This model was also used to calculate the sound field around the sphere when the input to the sources were filtered. Physical measurements were undertaken in order to validate the theoretical sphere model, and finally, subjective measurements were carried out in an anechoic environment to check whether listeners can discriminate reversals. The listeners were asked to localize the perceived angle of the recorded signal (which now appears as a virtual acoustic image). These results are compared with localization of real sources with the stimuli being speech and 1/3 octave band signals.

The results show that the measured acoustical characteristics of the sphere in the frequency and time domains were very similar to the theoretical model. The subjective measurements show that the system can deal successfully with the problem of reversals, thus reproducing the original recorded signals all around a single listener in an anechoic environment. The system is also robust with respect to head movements—the virtual acoustic images do not disappear and the localization ability improves when the listeners use small head rotations.

I. MULTICHANNEL SIGNAL PROCESSING THEORY

A. System description

Various methods for inverse filter design have been suggested and used for sound reproduction, both in the time and frequency domains. These include methods for designing adaptive finite impulse response (FIR) filters using sparse update algorithms (Nelson et al.,[18] Orduña-Bustamante[23]) and the method of fast deconvolution using regularization (Kirkeby et al.[21]) used in this research. This method is based on calculating the matrix of causal inverse FIR filters in the frequency domain. The calculation is undertaken using regularization, where the performance of the filters is optimized at a large number of discrete frequencies. Its main advantage is in calculating off-line very long filters (up to the DSP hardware limitations: 16 384 coefficients of each filter) at relatively high speeds (up to a few minutes with *Matlab* on a SGI workstation).

A diagram describing the signal processing problem of the sound reproduction system is shown in Fig. 2. By assuming that the system is working in discrete time, we can adopt the definition of the signals in the z-domain. It is assumed that the T microphones which record the sound field are restricted to the horizontal plane. The T observed signals described by the vector $\mathbf{u}(z)$. The objective is to reproduce these signals as closely as possible at the equivalent locations in the listener space. S sources are used to reproduce the field and their input signals are described by the vector $\mathbf{v}(z)$. These sources produce signals at R locations in the listening
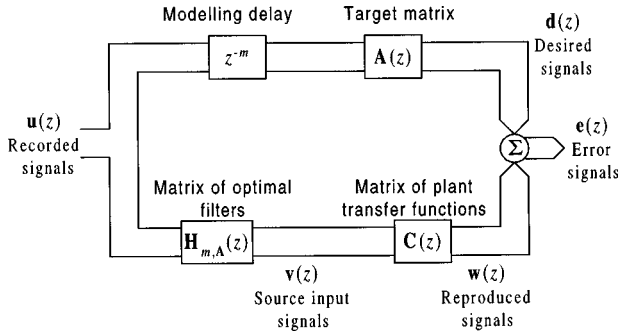
FIG. 2. A block diagram of a discrete-time multichannel sound reproduction system.

space, these signals comprising the vector $\mathbf{w}(z)$. For our purposes, we assume that the microphones are positioned at R locations in the listening space, which are equivalent to the T locations of the microphones in the recording space such that $T=R=4$. The R desired signals are described by the vector $\mathbf{d}(z)$, and the R performance error signals are described by the vector $\mathbf{e}(z)$.

The signal vectors can therefore be written as

$$\mathbf{u}(z)=\begin{bmatrix} U_1(z) \\ \vdots \\ U_T(z) \end{bmatrix} \quad \mathbf{v}(z)=\begin{bmatrix} V_1(z) \\ \vdots \\ V_S(z) \end{bmatrix} \quad \mathbf{w}(z)=\begin{bmatrix} W_1(z) \\ \vdots \\ W_R(z) \end{bmatrix},$$

$$\mathbf{d}(z)=\begin{bmatrix} D_1(z) \\ \vdots \\ D_R(z) \end{bmatrix} \quad \mathbf{e}(z)=\begin{bmatrix} E_1(z) \\ \vdots \\ E_R(z) \end{bmatrix}. \tag{1}$$

The matrices $\mathbf{A}(z)$, $\mathbf{C}(z)$, and $\mathbf{H}_{m,\mathbf{A}}(z)$ represent multichannel filters. $\mathbf{A}(z)$ is an $R\times T$ target matrix, $\mathbf{C}(z)$ is an $R\times S$ plant (electroacoustic) matrix, and $\mathbf{H}_{m,\mathbf{A}}(z)$ is an $S\times T$ matrix of inverse filters. The component z^{-m} delays all the elements of $\mathbf{u}$ by an integer number of m samples to ensure that the optimal filters are causal. These matrices have the following structures:

$$\mathbf{A}(z)=\begin{bmatrix} A_{11}(z) & \cdots & A_{1T}(z) \\ \vdots & \ddots & \vdots \\ A_{R1}(z) & \cdots & A_{RT}(z) \end{bmatrix},$$

$$\mathbf{C}(z)=\begin{bmatrix} C_{11}(z) & \cdots & C_{1S}(z) \\ \vdots & \ddots & \vdots \\ C_{R1}(z) & \cdots & C_{RS}(z) \end{bmatrix}, \tag{2}$$

$$\mathbf{H}_{m,\mathbf{A}}(z)=\begin{bmatrix} H_{11}(z) & \cdots & H_{1T}(z) \\ \vdots & \ddots & \vdots \\ H_{S1}(z) & \cdots & H_{ST}(z) \end{bmatrix}.$$

The error signals are defined as the difference between the desired signals and the reproduced signals,

$$\begin{bmatrix} E_1(z) \\ \vdots \\ E_R(z) \end{bmatrix}=\begin{bmatrix} D_1(z) \\ \vdots \\ D_R(z) \end{bmatrix}-\begin{bmatrix} W_1(z) \\ \vdots \\ W_R(z) \end{bmatrix}. \tag{3}$$

The goal is to design the matrix $\mathbf{H}_{m,\mathbf{A}}(z)$ which minimizes the magnitude of the vector of error signals, where $\mathbf{A}(z)$ and $\mathbf{C}(z)$ are given. From the block diagram shown in Fig. 2 and

Eqs. (1)–(3), we can derive the following relationships:

$$\mathbf{v}(z)=\mathbf{H}_{m,\mathbf{A}}(z)\mathbf{u}(z), \tag{4a}$$

$$\mathbf{d}(z)=z^{-m}\mathbf{A}(z)\mathbf{u}(z), \tag{4b}$$

$$\mathbf{w}(z)=\mathbf{C}(z)\mathbf{v}(z), \tag{4c}$$

and

$$\mathbf{e}(z)=\mathbf{d}(z)-\mathbf{w}(z). \tag{4d}$$

B. Optimal inverse filtering

The calculation of the optimal filters in the least-squares sense exposes some of the fundamental problems encountered with deconvolution of a multichannel system; these filters are constrained to be stable but not constrained to be either causal or finite duration. The goal is to find the signal vector $\mathbf{v}(e^{j\omega\Delta})$ which operates in discrete time on sampled input signals, and minimizes the sum of squared errors between the desired and reproduced signals.

The quadratic cost function that is to be minimized is given by

$$J(e^{j\omega\Delta})=\mathbf{e}^{H}(e^{j\omega\Delta})\mathbf{e}(e^{j\omega\Delta})+\beta\mathbf{v}^{H}(e^{j\omega\Delta})\mathbf{v}(e^{j\omega\Delta}). \tag{5}$$

The cost function thus consists of the sum of the squared errors $\mathbf{e}^{H}(e^{j\omega\Delta})\mathbf{e}(e^{j\omega\Delta})$ plus the sum of squared source input voltages $\mathbf{v}^{H}(e^{j\omega\Delta})\mathbf{v}(e^{j\omega\Delta})$ multiplied by a positive real number β, where $\mathbf{e}(e^{j\omega\Delta})$ and $\mathbf{v}(e^{j\omega\Delta})$ are vectors containing the Fourier transforms of the error signals and source input signals, respectively, and β is a regularization parameter. The latter quantifies the relative weighting in the cost function given to the "effort" used in minimizing the sum of squared errors. By varying β from zero to infinity, the solution changes gradually from minimizing only the performance error to minimizing only the effort cost. The optimal vector of source input signals $\mathbf{v}_{\text{opt}}(e^{j\omega\Delta})$ is given by

$$\mathbf{v}_{\text{opt}}(e^{j\omega\Delta})=[\mathbf{C}^{H}(e^{j\omega\Delta})\mathbf{C}(e^{j\omega\Delta})+\beta\mathbf{I}]^{-1}$$
$$\times\mathbf{C}^{H}(e^{j\omega\Delta})\mathbf{A}(e^{j\omega\Delta})\mathbf{u}(e^{j\omega\Delta}). \tag{6}$$

With no modeling delay ($m=0$) and according to Eq. (4a), the optimal filter matrix becomes in the z-domain,

$$\mathbf{H}_{0,\mathbf{A}}(z)=[\mathbf{C}^{T}(z^{-1})\mathbf{C}(z)+\beta\mathbf{I}]^{-1}\mathbf{C}^{T}(z^{1})\mathbf{A}(z). \tag{7}$$

The matrix of optimal inverse filters can be represented by $\mathbf{H}_{0,\mathbf{I}}$ (again, in a special case where $m=0$), which we define as the generalized cross-talk cancellation matrix, given by

$$\mathbf{H}_{0,\mathbf{I}}(z)=[\mathbf{C}^{T}(z^{-1})\mathbf{C}(z)+\beta\mathbf{I}]^{-1}\mathbf{C}^{T}(z^{1}). \tag{8}$$

This term is used whenever the target matrix is an identity matrix regardless of the value of m. As mentioned above, it is crucial to include a modeling delay with a sufficient length in order to ensure the best performance under the constraint of causality of all the filters.

II. SCATTERED SOUND FROM A WAVE IMPINGING ON A RIGID SPHERE

A. Frequency domain analysis

A rigid sphere was used as a model for the head in this research in order to simplify the analytical calculations of the
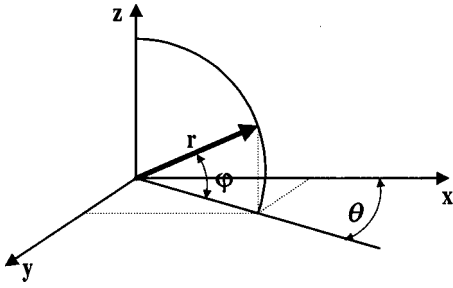
FIG. 3. Spherical coordinates used to define the general direction of a propagating plane wave [the formulation in Eqs. (9) and (10) was derived for propagation in the x direction, $\theta=0$, $\varphi=0$].

FIG. 4. Three dimensional map of the impulse response of the sphere. The front angles differ mainly in their delay and amplitude, while the rear angles are characterized by a second peak which is a result of an asymmetric propagation of the plane wave around the sphere.

sound field around a human head (later enabling us to compare these to measurements). When an acoustic wavefront meets an obstacle, reflection, diffraction, and scattering of the wave occur. For our purposes, we wish to evaluate the distribution of pressures on the surface of the sphere (to simplify, a plane wave is assumed to propagate. It is also restricted to the horizontal plane only, where the ears/transducers are placed). The total acoustic field around a sphere consists of two terms: the pressure due to the incident wave and the distribution of the pressure of the scattered wave. The general spherical coordinates for determining the acoustic field around a sphere are illustrated in Fig. 3, where the plane wave is propagating in the x direction ($\theta=0$, and $\varphi=0$). The equations given below for the complex pressure are based on those given by Malecki.[21] In the vicinity of the sphere, the total complex pressure, p_{tot}, can be written as

$$p_{\text{tot}}=p_0 \exp(j\omega t) \sum_{m=0}^{\infty} (-j)^{(m+1)}(2m+1)P_m(\cos\theta)$$

$$\cdot \frac{j_m(kr)n'_m(ka)-n_m(kr)j'_m(ka)}{j'_m(ka)-jn'_m(ka)}, \tag{9}$$

where p_0 is the amplitude of the pressure of the incident wave, ω the angular frequency, and k the wave number. The terms P_m denote Legendre polynomials, whilst j_m and n_m are spherical Bessel and Neumann functions, respectively. Finally, a is the radius of the sphere, r the distance from the origin of the sphere, and θ the direction of the incident wave.

On the surface of the sphere, this expression is reduced to the form

$$p_{\text{tot}}=p_0 \exp(j\omega t)$$

$$\times \sum_{m=0}^{\infty} \frac{(-j)^{(m+1)}(2m+1)(ka)^{-2}P_m(\cos\theta)}{j'_m(ka)-jn'_m(ka)}. \tag{10}$$

B. Time domain analysis

The analytical expressions presented above for the resultant sound field due to a sphere are in the frequency domain. In order to implement the digital filters, a time domain presentation is also required. Applying an inverse fast Fourier transform (FFT) to the frequency domain expression yields a noncausal impulse response with ripples due to the use of a rectangular window. Therefore, in order to overcome this problem (but with the penalty of attenuating the
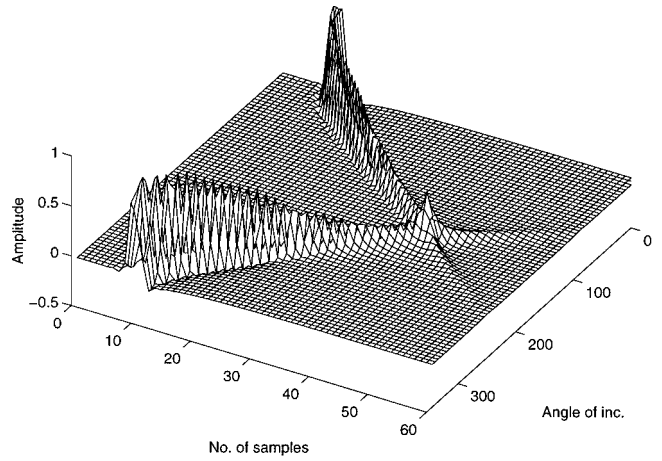
high frequencies), a half-Hanning window is implemented before using the inverse FFT. The method used to obtain the impulse responses around the sphere is as follows: the frequency response on the surface of the sphere is calculated for each angle of incidence (with a resolution of 5°) according to Eq. (10) in a discrete form. The sampling frequency is 48 kHz, and the Nyquist frequency is 24 kHz. The frequency is "mirrored" at the Nyquist frequency by appending the conjugate values. The new frequency response is multiplied by a half-Hanning window in the frequency domain. An inverse FFT is applied, followed by a cyclic shift to produce a delay at half of the number of the sampling points. It should be noted that this method gives only an approximation for the impulse response, although the distortion at high frequencies, which exceeds our frequency range demands, is not excessive. The map of the impulse response of the sphere is presented in Fig. 4. The left and right axes correspond to the time (number of samples) and the angle of incidence, respectively, whilst the vertical axis corresponds to the amplitude. The front angles differ mainly in their delay and amplitude, while the rear angles are characterized by a second peak whose amplitude is smaller than the first. This can be explained by the asymmetric propagation of the plane wave to these points: shorter, from one side of the sphere, and longer from the other. These appear mainly at angles close to 180°. A relatively high peak can be noticed at 180° because the two peaks have been superposed, due to symmetry of propagation from each side of the sphere.

C. Measurement of the sphere "HRTFs"

The equivalent "HRTFs" produced by the sphere were measured in order to give a comparison between the measured and the simulated responses in the time and frequency domains. This enabled the validation of the theoretical model, and the justification for the design of the inverse filters for the reproduction system. Four WM-063 Electret Condenser microphones were chosen carefully (out of 50) to have a minimal margin error of the magnitude and phase of

1000 Hz
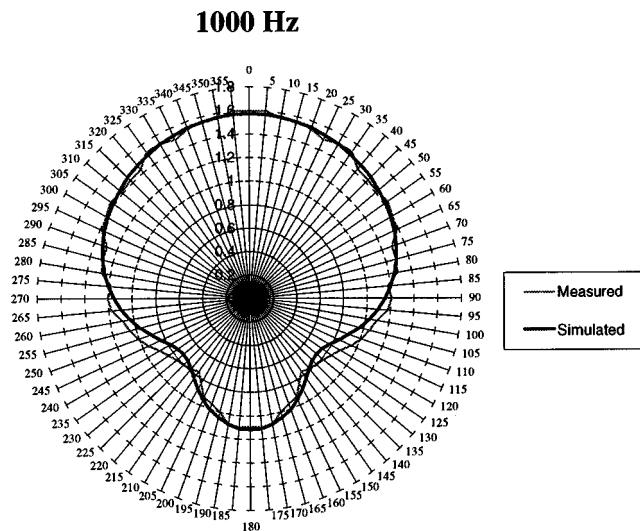
FIG. 5. Comparison of the measured and simulated directivity pattern on the surface of the sphere at 1 kHz (direction of incidence from the top). The results presented are shown after deconvolution of the loudspeaker and microphone responses.

the frequency response (the measured magnitude difference achieved was 1–2 dB and the phase difference was 1–2° over a frequency range of 4000 Hz). Four Celestion-1 loudspeakers were chosen using the same principles (out of 12) and the accuracy achieved was magnitude difference of 1 dB, and phase difference of less than 4° for the same frequency range. In order to measure the ''HRTF'' of the sphere, first the free-field impulse response was measured, which included mainly the response of the microphone and the loudspeaker. This measurement was deconvolved from the measurements of the impulse response when the microphone was placed in the slot at the circumference of the sphere. The sphere radius, 9.5 cm, was chosen as an average in response to anthropometric measurements (Burandt *et al.*[24]). The sphere was mounted 1.3 m above the floor on a fixed pivot through the middle of which the microphone cables were inserted. The loudspeakers were positioned 1.4 m from the

origin of the sphere. The microphones were connected to a four-channel Electret microphone amplifier, and to the MLSSA system (Rife and Vanderkooy[25]) in order to measure the impulse response with the sphere being rotated at 5° for each measurement. A 1024-point maximum length sequence was generated at a sampling rate of 48.19 kHz (this is the nearest sampling frequency to 48 kHz obtained with the MLSSA hardware). Each sequence was preaveraged and averaged for eight cycles. A few examples of the comparisons made between the measured (deconvolved) and simulated impulse response and frequency response are presented in Figs. 5–7, which show that the physical sphere has characteristics that are very close to the predictions of the theoretical model.

III. INVERSE FILTER DESIGN

A fixed set of inverse filters $H_{rs}(n)$ for implementing the cross-talk cancellation was calculated off-line following the initial measurement of the electroacoustic response of the reproduction system. (The examples presented in Figs. 10–13 demonstrate the best performance achieved with the regularization parameter β set to 0.0001.) The arrangement of the reproduction system used in the following example was ''asymmetric'' with loudspeakers at $-30°$, $30°$, $110°$, and $-110°$ and with the microphones at $-80°$, $80°$, $100°$, and $-100°$ (see Fig. 8). The sampling frequency was set to 48 kHz. Figure 9 shows in a matrix form (4×4) the electroacoustic impulse response. $C_{11}(n)$ corresponds to the impulse response measured at microphone number 1 due to loudspeaker number 1. $C_{12}(n)$ corresponds to the impulse response at the same microphone due to loudspeaker number 2, and so forth. The first 196 samples, which were the shortest delay between each of the loudspeakers and each of the microphones, were removed to ensure a stable inversion. The original measurement of the impulse response was made with 1024 samples, but since the impulse response here is relatively short, the data above sample 100 were just noise, so the impulse response was truncated to 128 samples. To
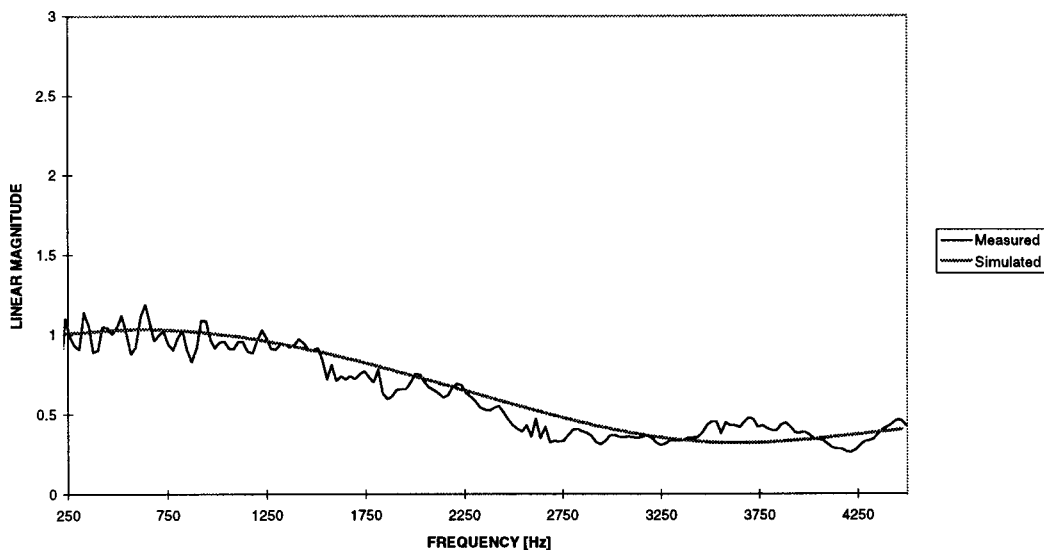
FIG. 6. Comparison of the measured and simulated frequency response of the sphere at 160°. The results presented are shown after deconvolution of the loudspeaker and microphone responses.
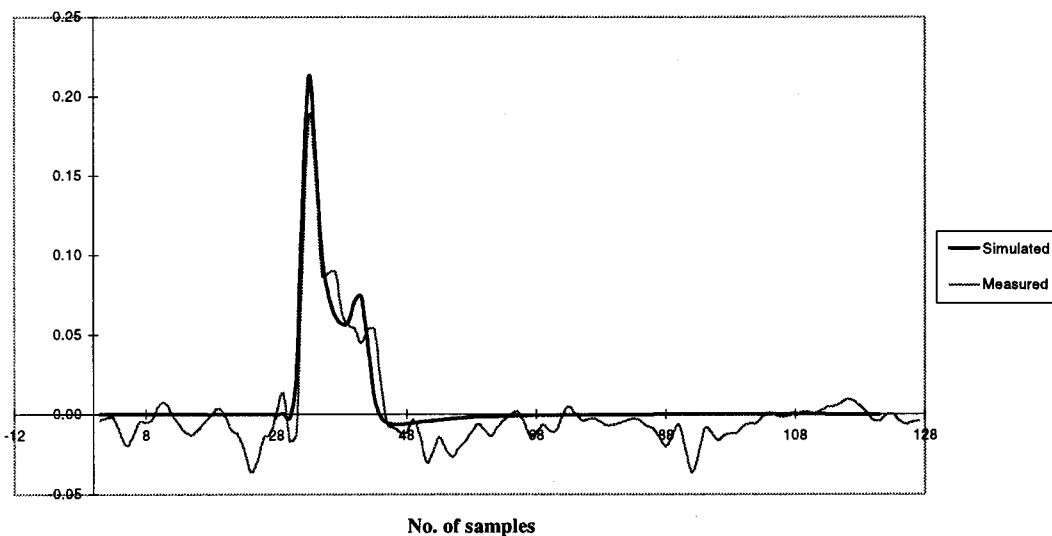
FIG. 7. Comparison of the measured and simulated impulse response of the sphere at 160°. The results presented are shown after deconvolution of the loudspeaker and microphone responses. The two peaks are a result of an asymmetric propagation of a plane wave around the sphere.

avoid ripples due to the rectangular truncation, a half-Hanning window was applied to the last 64 points. The shadow zone is clearly demonstrated in the off-diagonal elements, especially when a loudspeaker is in the opposite hemisphere of a microphone [e.g., $C_{23}(n)$, $C_{34}(n)$, etc.]. The inverse filters are presented in Fig. 10, where each filter is delayed by 512 coefficients to ensure that all the nonminimum phase components of the electroacoustic response are included and not truncated. The frequency response of the filters (in Fig. 11) reveals the limitations of implementing the filters in practice due to a boost at low and very high frequencies. It was of utmost importance to use a bandpass filter during the experiment, in order to protect the loudspeaker at low frequencies (below 180 Hz) and to cut frequencies above 5000 Hz (which were not in the scope of the experiment). The convolution in the time and frequency domains demonstrates the characteristics of the cross-talk cancellation network very well. Impulses appear only in the diagonal elements (in Fig. 12) and an almost flat response appears in the parallel elements in Fig. 13. An average attenuation of 15 dB is achieved at low frequencies, while at higher frequencies the attenuation reaches levels of -50 dB. It is important to state at this point that the performance in practice for the listeners was less efficient than as presented in the graphs due to hardware limitations (such as the response of the loudspeakers) and the differences between the HRTFs of the listeners and those of the sphere, but is nevertheless capable of producing virtual acoustic images of a reasonable clarity.

Due to the long filters obtained with deconvolution in the frequency domain, 1024 coefficients in this case, implementation can be undertaken only when appropriate advanced hardware is available. The measurements were made with the Yamaha Digital Audio Processor, which is capable of implementing 4×4 FIR filter matrix, whose elements can contain up to 16 384 coefficients, each at a sampling rate of 44.1 or 48 kHz.

IV. ANALYTICAL SIMULATION OF THE REPRODUCED SOUND FIELD IN THE NEAR VICINITY OF THE SPHERE

The form of the sound field reproduced in the region of the sphere is investigated following the implementation of the inverse filters. The aim of this presentation is to illustrate the reproduced pressure in the frequency domain not only at the positions of the microphones but also in the near vicinity of the sphere. The reproduced amplitude of the total pressure is calculated inside an area with the dimensions of $24 \times 24 \, \text{cm}^2$, and the radius of the sphere is 9.5 cm. The arrangement of the loudspeakers for this simulation is presented in Fig. 14. This area was divided into 100×100 points of calculation. The sound pressure (real and imaginary values) at each ear position ($\pm 10°$ with respect to the "interaural axis") was calculated at a single frequency with the sources which were modeled as plane waves and were not filtered. Later, all source inputs were filtered to produce "1" at one ear (ear no. 1 in Fig. 14) and "0" at the others (this is

FIG. 8. The "asymmetric" loudspeaker arrangements for reproduction in the experiment with virtual acoustic images.
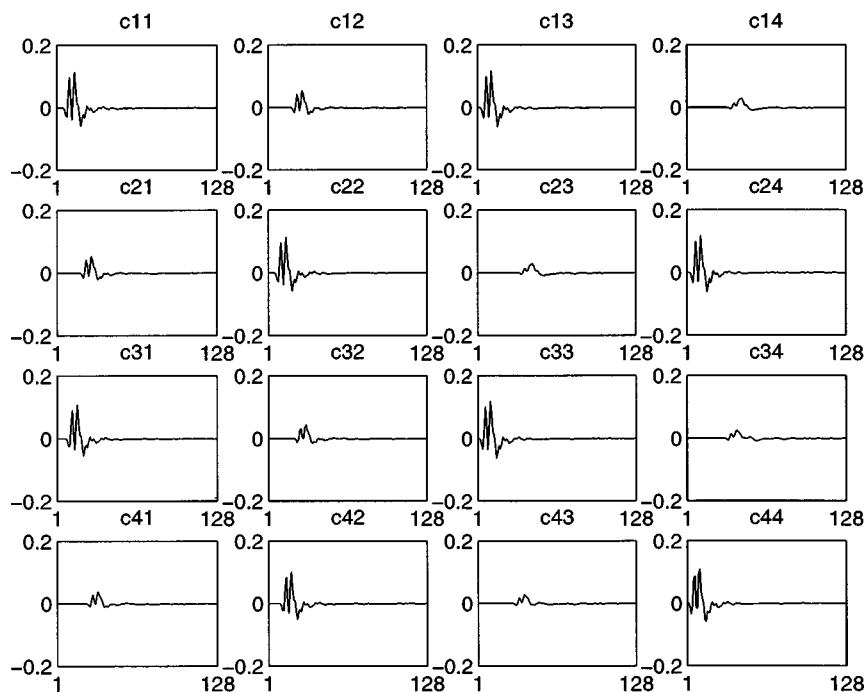
FIG. 9. The 16 elements of the electroacoustic matrix $C_{rs}(n)$, measured with the "asymmetric" loudspeaker arrangement (amplitude versus number of samples). The shadow zone is clearly demonstrated in the off-diagonal elements [e.g., $C_{23}(n)$, $C_{34}(n)$] when a loudspeaker is in the opposite hemisphere of a microphone.

accomplished by multiplying the vector $[1\ 0\ 0\ 0]^T$ with the cross-talk cancellation matrix **H**). We can notice the effect of the cross-talk cancellation on the robustness of head rotations: the zero pressure on the right side is maintained when the head is rotated, and on the left side a rapid change between "0" and "1" is achieved. Figure 15(a), (b), and (c) shows the sound field at 1, 2, and 4 kHz, respectively. These graphs demonstrate that the change of the sound pressures near the positions of the microphones due to head (sphere) rotations is similar for different frequencies.

V. SUBJECTIVE EVALUATION OF THE SYSTEM

A. The pilot study

A pilot study was carried out in order to investigate the performance of the system with respect to the following parameters:

Two loudspeaker arrangements: "asymmetric," and "symmetric" (as illustrated in Figs. 8 and 14, respectively).

Four HRTF databases:

(1) Direct measured elements of the impulse response
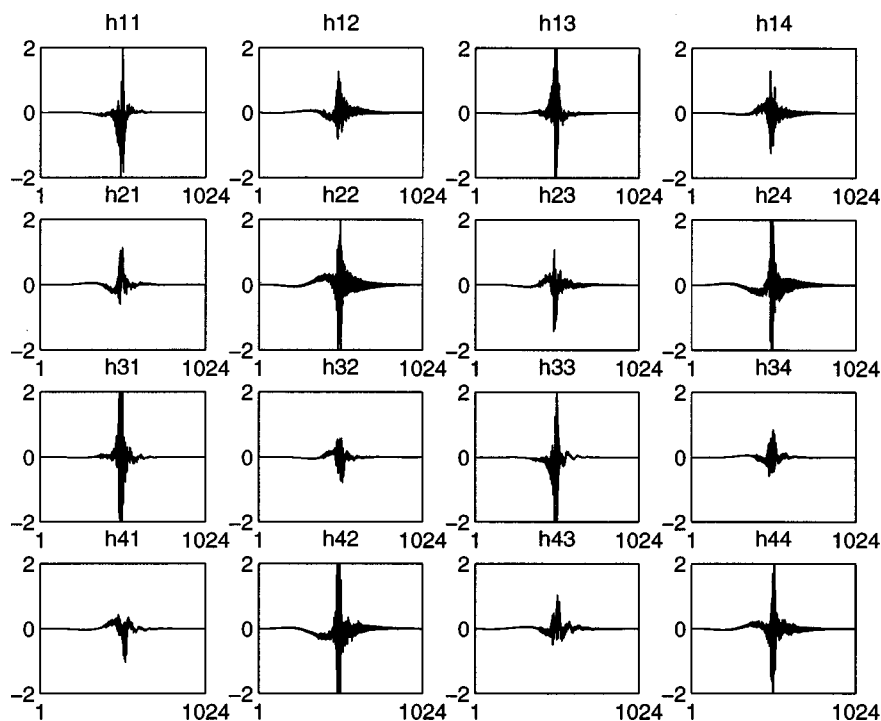
FIG. 10. The impulse responses of the filters $\mathbf{H}_{m,\mathbf{I}}(n)$ which deconvolve the matrix $\mathbf{C}(n)$ shown in Fig. 9, with the regularization parameter $\beta=0.0001$ (amplitude versus number of samples). Note that the main part of the energy of each filter is limited to its center, at the modeling delay—512 coefficients.
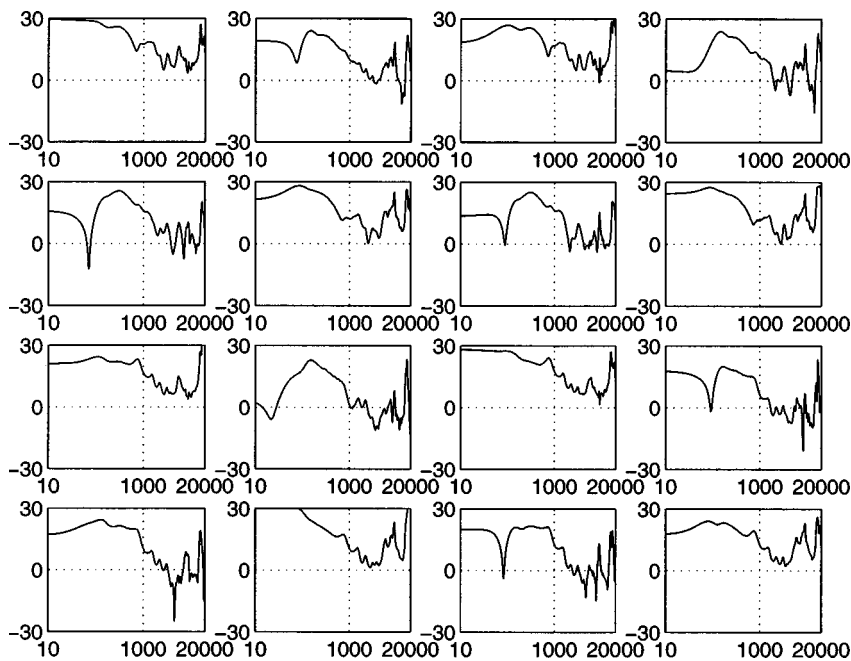
FIG. 11. The frequency responses of the filters $\mathbf{H}_{m,\mathbf{I}}(n)$ which deconvolve the matrix $\mathbf{C}(n)$ shown in Fig. 9, with the regularization parameter $\beta=0.0001$ (amplitude versus number of samples). Note the boost at low and very high frequencies [e.g. $H_{42}(n)$, $H_{24}(n)$] which might exceed the limitations of the performance of the loudspeakers.

matrix—$C_{rs}(n)$. The impulse response of each one of the 16 paths (4×4) was measured directly for each of the loudspeaker arrangements.

(2) Indirectly measured frequency response of the sphere. In this case 72 measurements were carried out, at a resolution of 5 deg. The elements of the matrix $C_{rs}(n)$ were found indirectly by interpolating the values in relation to the geometry of the four microphones and the four loudspeakers in the frequency domain.

(3) Analytical simulation of the frequency response of a sphere.

(4) The KEMAR dummy-head HRTF database.[26]

Three regularization parameters: ''too low,'' ''too high,'' and the best that was found.

The reproduction of virtual acoustic images with the ''symmetric'' arrangement sometimes caused similar effects to those obtained when listening to headphones: sound was localized closer to the head than it was recorded, or inside the head. Consequently, emphasis was placed on the ''asymmetric'' arrangement (the front and back pairs were in an asymmetric position with respect to the ''interaural axis''). With the investigation of the HRTF database, the best results were achieved with a set based on direct measurements of the impulse response between the loudspeakers and the microphones positioned in the sphere. Hence, this database was chosen to be implemented in the subjective experiment. All the other HRTFs worked well with a synthesis of virtual acoustic images, but did not work well with the cross-talk
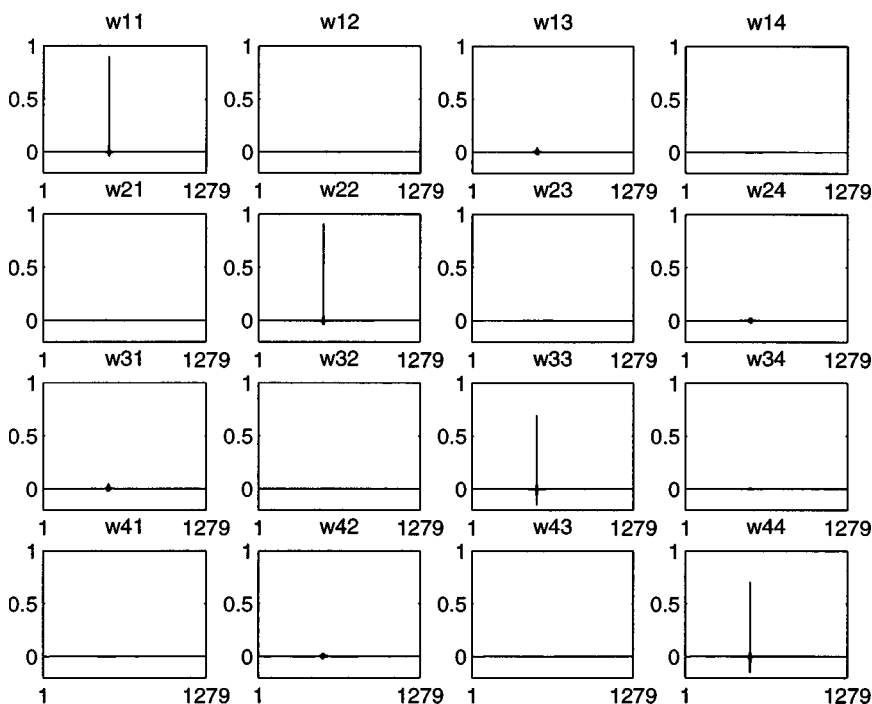
FIG. 12. The convolution $\mathbf{W}(n)$ of $\mathbf{C}(n)$ with $\mathbf{H}_{m,\mathbf{I}}(n)$, with the regularization parameter $\beta=0.0001$ (amplitude versus number of samples). The cross-talk is represented by the off-diagonal elements which are ideally zero. Note that the peaks occur at the modeling delay, at $n=512$.
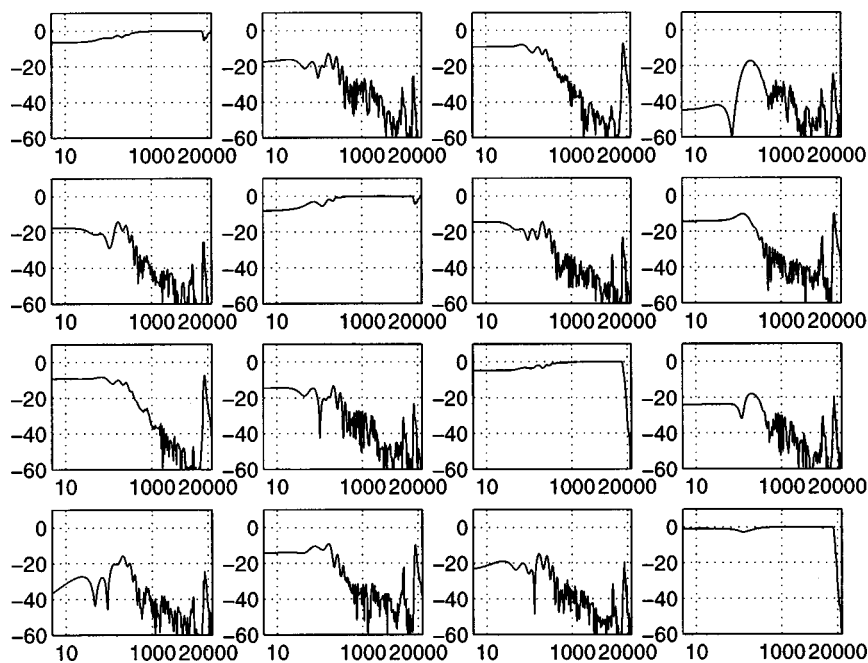
FIG. 13. The frequency response of the convolution $\mathbf{W}(f)$ of $\mathbf{C}(f)$ with $\mathbf{H}_{m,\mathbf{I}}(f)$, with the regularization parameter $\beta = 0.0001$ (reduction of the pressure in dB versus frequency in Hz). The diagonal elements are ideally 0 dB, and the off-diagonal elements are ideally minus infinity dB.

cancellation. Only a single microphone arrangement was used with a spacing of $\pm 10°$ (3.3 cm), which does not cause spatial aliasing at frequencies below ≈ 5200 Hz. A closer spacing was not chosen due to the physical dimensions of the microphones and the alignment problem with respect to the loudspeaker cone. It is important to point out a phenomenon that appeared when reproducing the sound using this system with four loudspeakers: with recorded sounds in the frontal hemisphere, the rear loudspeakers are not expected to emit substantial energy, yet it was found that a significant sound was heard from the rear as well. Therefore, localization was a harder task than expected, and it was found at this stage that a decision connecting front or back localization might be

FIG. 14. The ''symmetric'' loudspeaker arrangements used for the analytical simulation of the reproduced sound field in the vicinity of the sphere, and for reproduction in the pilot subjective experiment with virtual acoustic images.

connected to the ''color'' of the sound: ''brighter'' sound in the frontal hemisphere and ''darker'' sound in the rear (see Blauert,[1] Begault[4]).

B. The procedures used in the subjective experiment

The subjective experiment was carried out in the large anechoic chamber of the ISVR, and included ten volunteers whose audiometric profile had been previously checked to confirm that they had normal hearing. They were inexperienced with the task of localizing sounds in an anechoic environment and therefore we believe that the results of the localization experiments might have even been improved with trained localizers. The experiments with real sources and virtual acoustic images were carried out on different dates, the experiments with real sources lasting 20 min, and those with virtual acoustic images lasting 40 min.

The experiment with real sources was designed as a reference experiment, without using any processing of the signals. The goal was to investigate the ability of the listeners to localize different types of real (and later virtual) signals in the same environment. The listeners were introduced to their new environment (the anechoic chamber) and were seated in the center of a ''cage'' surrounded by a black acoustically transparent cloth. Marks indicating the azimuth angles were positioned at a resolution of 10° all around the cloth in the horizontal plane at the height of the loudspeakers which were at eye level. An angle of 0° was defined as being directly in front of the listener and 180° at the back. The arrangement of the ''cage'' and the nine loudspeakers in the anechoic chamber is shown in Fig. 16. Each signal was played for 10 sec, with the first and last 2 sec being used for fade-in and fade-out to eliminate ''clicks'' emanating directly from the loudspeakers. The loudspeakers were positioned only in the right hemisphere since the final goal was to investigate reversals, and testing sounds from sources all around the listeners would have made the tests much longer and would not have

FIG. 16. Loudspeaker arrangement for the experiment with real sources.

contributed significantly to the assessment of the system's performance. The signals that were chosen were: band-pass filtered speech (180–5000 Hz), and 1/3 octave band signals at 2000 and 4000 Hz. The listeners were asked to point with their hand or finger in the direction of the perceived angle and not to move their heads at all.

In the experiment with virtual acoustic images, only the ''asymmetric'' loudspeaker arrangement was used. The experimental apparatus included four Celestion-1 loudspeakers and two Yamaha P2160 power amplifiers. The DSP hardware was based on the Yamaha Digital Audio Processor with a Yamaha A-D converter type AD8X and a D-A converter type DA8X. Before commencing the experiment, the listeners were given instructions and an introduction to the experimental procedures. The signals were played randomly with respect to the type of signal and the angle of the virtual acoustic image. After a short break, the experiment was repeated with the listeners being told that they could rotate their heads slightly, a few degrees to each side, if they were not sure whether the sound was coming from the front or the back.

VI. RESULTS AND DISCUSSION

The results of the localization experiments are plotted in Figs. 17–20 as the perceived angle versus the presented angle. This presentation enables us to observe two characteristics of localization: the spread of the answers per each presented angle, and also a rough distinction between angles answered in the frontal and the rear hemispheres. The circle's area is proportional to the number of listeners who localized the same perceived angle.

Figure 17 presents a reference graph showing the results for a localization experiment in the anechoic chamber of virtual acoustic images which were synthesized with a KEMAR HRTF database (after Nelson et al.[8]). The loudspeaker's arrangement is $\pm 30°$ with respect to the listener. An angle of $0°$ was defined in this research for a source positioned to the right of the listener, $90°$ represents the source being in the front, etc. Reversals are clearly seen with 82% of the answers, for angles presented in the rear were localized in their

FIG. 15. The amplitude of the sound field around a sphere (24×24 cm^2) with four ''ears'' at (a) 1, (b) 2, and (c) 4 kHz when the cross-talk cancellation is implemented for a symmetric arrangement of loudspeakers (Fig. 14). The desired signals are ''1'' at the front left ear (1), and ''0'' at all the others (2,3,4). Black corresponds to a ratio of 0 and white corresponds to values equal to or greater than 1.
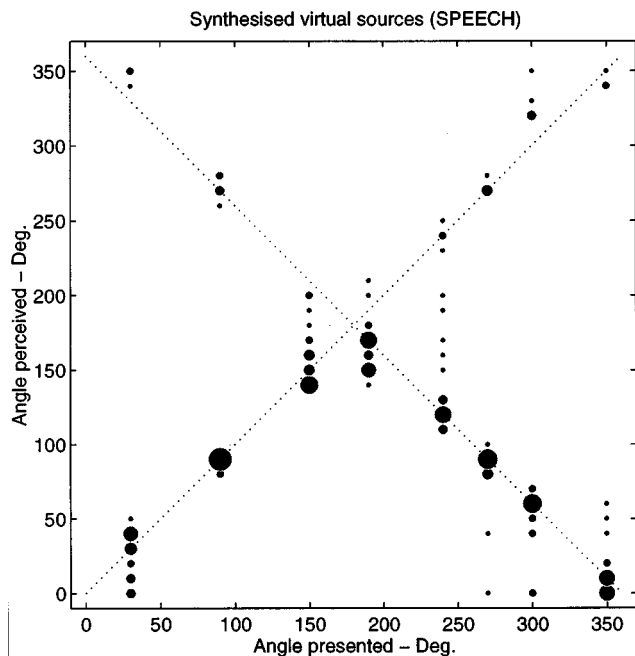
FIG. 17. Subjective experimental results in an anechoic environment for localization of synthesized virtual acoustic images with the HRTF database of KEMAR [after Nelson et al. (Ref. 8)].

mirror positions. It is also concluded that the number of confusion for sources presented in the front is minimal. Similar results were found by Hill et al.[12] By analyzing the data presented by Hill et al.,[12] it was found that 94% of the answers for rear images were localized in the front.

Figures 18–20 present the results of the subjective experiments in this research. Each figure includes three graphs that show the localization of real sources with fixed heads, and the localization of virtual acoustic images with fixed heads, and free heads. The overall performance of individuals varied from 97% correct answers with only 3% front/back reversals out of 90 signals for the listener with the best performance, to only 48% of correct answers for the listener with the worst performance. A general conclusion can be reached with respect to the localization of virtual acoustic images presented at 90°. Since no microphone was used to record at this angle, the estimates varied quite significantly (although this angle also proved problematic with real source localization). The listeners who localized these sources correctly, said that they achieved it by elimination: they had learned to localize sounds in the front and in the back by their "color," the front angles sounding "brighter" than the rear angles, which sounded "darker," with a 90° angle being localized by elimination. It also became apparent that the cross-talk performance at high frequencies was not very efficient (because of the limitations of the sphere model). The use of a band-pass filter helped to avoid localization of signals at angles where the loudspeakers were placed. This was particularly pronounced with speech containing affricates and fricatives (consonants such as "s" or "ts" and "f," respectively) emitted directly from the cone of the loudspeakers, while words without these consonants were correctly reproduced at the correct angles.

The results presented in Fig. 18(a) show how accurately
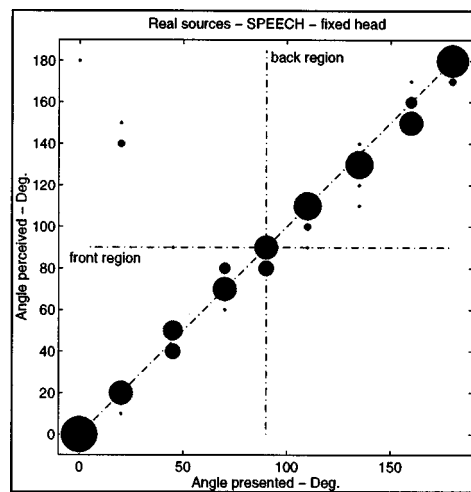
(a)
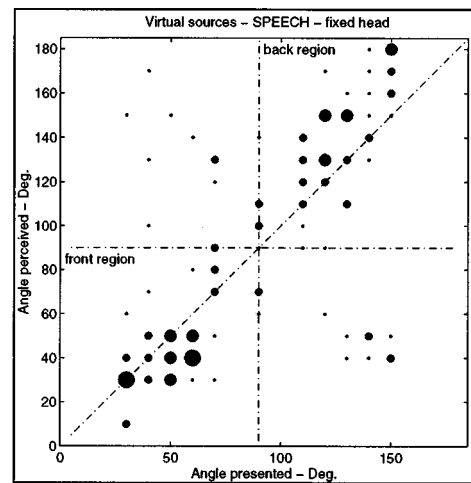
(b)
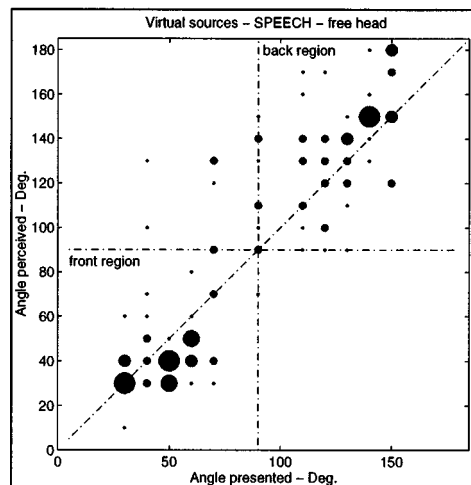
(c)

FIG. 18. (a) Subjective response in an anechoic environment for real sources using speech. The head of the listener is fixed. (b) Subjective response in an anechoic environment for virtual acoustic images using 180–5000 Hz band-pass filtered speech with the "asymmetric" loudspeaker arrangement. The head of the listeners is fixed. (c) As in (b), but the head of each listener is free for rotation.

(a)

(b)

(c)

(a)

(b)
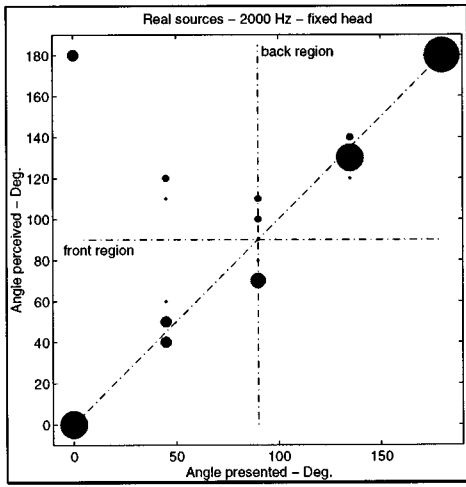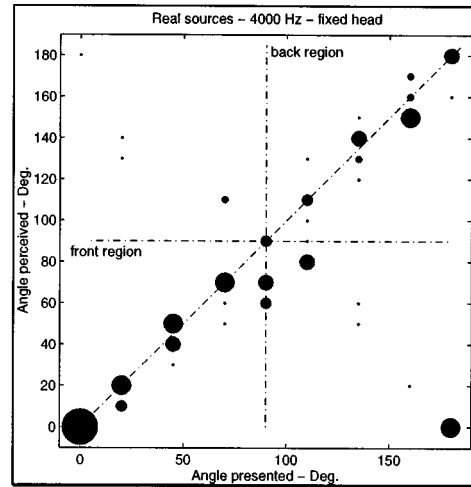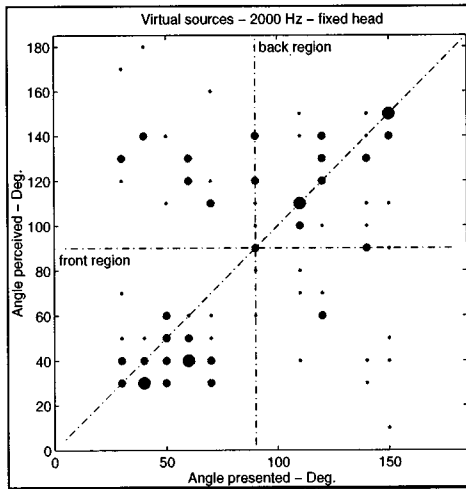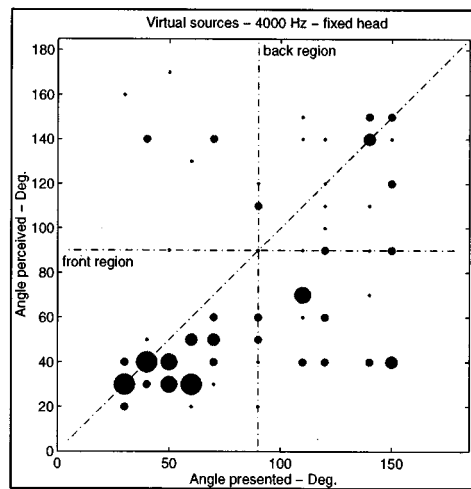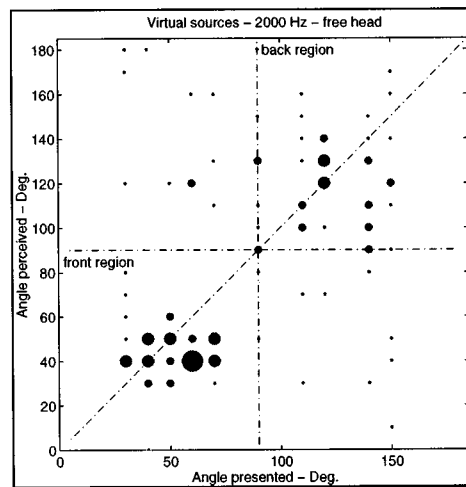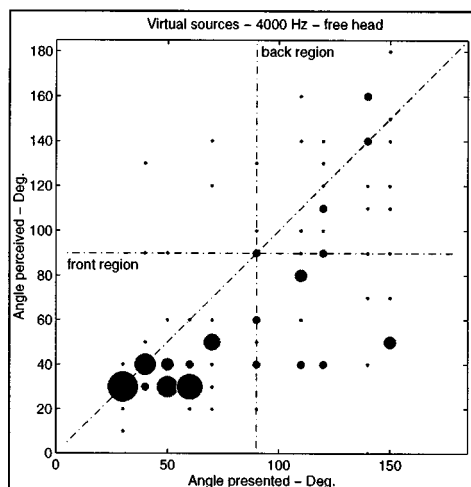
(c)

FIG. 19. (a) Subjective response in an anechoic environment for real sources using 1/3 octave band—2000 Hz. The head of the listener is fixed. (b) Subjective response in an anechoic environment for virtual acoustic images using 1/3 octave band—2000 Hz with the "asymmetric" loud-speaker arrangement. The head of the listeners is fixed. (c) As in (b), but the head of each listener is free for rotation.

FIG. 20. (a) Subjective response in an anechoic environment for real sources using 1/3 octave band—4000 Hz. The head of the listener is fixed. (b) Subjective response in an anechoic environment for virtual acoustic images using 1/3 octave band—4000 Hz with the "asymmetric" loud-speaker arrangement. The head of the listeners is fixed. (c) As in (b), but the head of each listener is free for rotation.
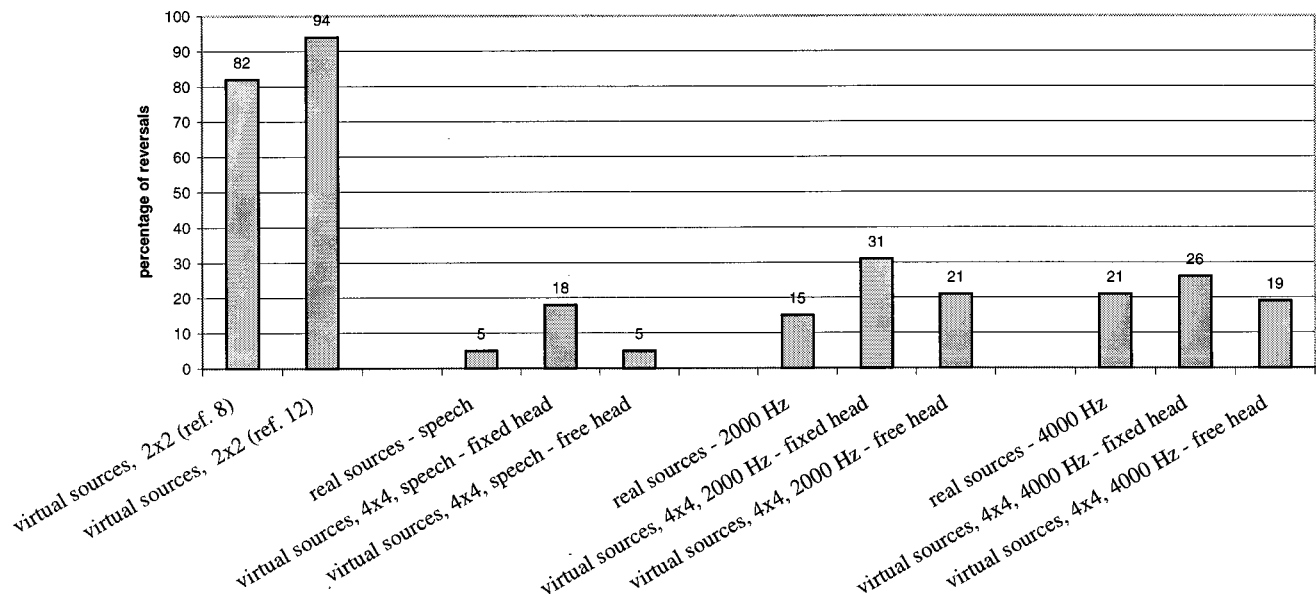
FIG. 21. The percentage of reversals when listening through loudspeakers. High rate of confusion is noticed for the conventional system with two loudspeakers in the front. Discrimination of reversals is achieved with the 4×4 system, especially when the head of the listeners is free for rotation.

listeners can localize real sources in an anechoic environment without rotating their heads, with only a small percentage of reversals (5%). Figure 18(b) and (c) present the localization performance of virtual acoustic images, without and with head rotations, respectively. In both graphs the majority of the answers are in the lower left and upper right quadrants (no reversals zones). When the listeners didn't rotate their heads, the percentage of reversals was 18%, which then reduced to only 5% when they used head rotations to discriminate front from back. This means that for the majority of listeners, sound that was recorded (as opposed to synthesized) at a specific angle with the sphere dummy-head, was reproduced at that angle (or in the region of that angle). Two important features of localization appear in this graph: the accuracy of localization for each angle (reaching values of ±30°) is less than that achieved with real sources or with synthesized virtual acoustic images with two loudspeakers,[8] and a wide spread at an angle of 90° shows accuracy decreasing at angles in that region.

Figures 19(a) and 20(a) show that the ability to localize 1/3 octave band signals at 2000 Hz (18% of reversals) and 4000 Hz (21% of reversals) with real sources in the anechoic chamber without rotating the head is reduced compared to localization of speech signals (5% of reversals) under the same conditions. The performance of localization of virtual acoustic images is presented in Figs. 19(b), 19(c), and 20(b) and 20(c), and although more confusion appears (between 20% and 30% of reversals), these are comparable with the confusion that appears with real sources.

Figure 21 summarizes the percentage of reversals. It first shows the high rate of reversals appear with two examples[8,12] of conventional 2×2 systems (82% and 94% of reversals of rear virtual acoustic images). The figure also shows the percentage of reversals when listening to the proposed 4×4 system, and the results are compared with localization with real sources. It can be seen that discriminating reversals with the proposed virtual imaging system is successful, when the listeners rotate their head, and when the performance is compared to localization with real sources.

Similar results were obtained by Hill et al.,[12] who synthesized (as opposed to recorded as in this research) 3 kHz band limited noise signals from a monophonic source. The subjective experiments' results showed that when listeners used slight head rotations, they succeeded in discriminating front from back signals.

VII. CONCLUSIONS

A new sound reproduction system is suggested that is based on multichannel digital signal processing and uses a four-ear dummy-head modeled as a rigid sphere. Physical acoustic measurements of the sphere validated the theoretical model in the frequency and time domains. Analytical simulations of the sound field with the cross-talk cancellation being implemented demonstrate the principle of reversal discrimination obtained by the concept of "four ears." The subjective experiments showed clearly that the system can deal successfully with the problem of reversals, thus reproducing the original recorded signals all around a single listener in an anechoic environment. The most successful results were obtained with speech signals. More confusion tends to appear with third octave bands at 2000 and 4000 Hz signals, although when compared to the experiment with real sources, the overall performance of the system still shows remarkably successful results. The system is also robust with respect to head movements—the performance is improved when the listeners rotate their heads. The main disadvantage of the system is that the sound field around a listener's head is more complex than in a two-loudspeaker arrangement, and therefore the image of a virtual acoustic image is less clear. Consequently, the accuracy of localization of each presented virtual acoustic source is reduced in comparison to the two-loudspeaker arrangement.

[1] J. Blauert, *Spatial Hearing: The Psychophysics of Human Sound Localization* (MIT, Cambridge, MA, 1983).

[2] F. L. Wightman and D. J. Kistler, ''Headphone simulation of free-field listening I and II: Psychophysical validation,'' J. Acoust. Soc. Am. **85**, 858–878 (1989).

[3] H. Møller, ''Fundamentals of binaural technology,'' Appl. Acoust. **36**, 171–218 (1992).

[4] D. R. Begault, *3-D Sound for Virtual Reality and Multimedia* (AP Professional, Cambridge, MA, 1994).

[5] S. Weinrich, ''The problem of front-back localization in binaural hearing,'' Scand. Audiol. **11**, Suppl. 15 (1982).

[6] D. H. Cooper and J. Bauck, ''Prospects for transaural recording,'' J. Audio Eng. Soc. **37**, 3–19 (1989).

[7] P. Damaske, ''Head-related two-channel stereophony with loudspeaker reproduction,'' J. Acoust. Soc. Am. **50**, 1109–1115 (1971).

[8] P. A. Nelson, F. Orduña-Bustamante, D. Engler, and H. Hamada, ''Experiments on a system for the synthesis of virtual acoustic sources,'' J. Audio Eng. Soc. **44**(11), 996–1007 (1996).

[9] H. Møller, M. F. Sørensen, C. B. Jensen, and D. Hammershøi, ''Binaural technique: Do we need individual recordings?'' J. Audio Eng. Soc. **44**, 451–469 (1996).

[10] M. Kleiner, ''Problems in the design and use of 'dummy-heads,' '' Acustica **41**, 183–193 (1978).

[11] H. Møller, C. B. Jensen, and M. F. Sørensen, ''Evaluation of artificial heads in listening tests,'' 102nd Audio Eng. Soc. Convention, Munich, Germany, preprint 4404 (1997).

[12] P. A. Hill, P. A. Nelson, O. Kirkeby, and H. Hamada, ''Resolution of front back confusion in virtual acoustic imaging systems,'' J. Acoust. Soc. Am. (submitted).

[13] F. L. Wightman and D. J. Kistler, ''The dominant role of low-frequency interaural time differences in sound localization,'' J. Acoust. Soc. Am. **91**, 1648–1661 (1992).

[14] G. F. Kuhn, ''Model for the interaural time differences in the azimuthal plane,'' J. Acoust. Soc. Am. **62**, 157–167 (1977).

[15] G. F. Kuhn, ''Physical acoustics and measurements pertaining to directional hearing,'' in *Directional Hearing*, edited by W. A. Yost and G. Gourevitch (Springer-Verlag, New York, 1987).

[16] J. Hebrank and D. Wright, ''Spectral cues used in the localization of sound sources on the median plane,'' J. Acoust. Soc. Am. **56**(6), 1829–1834 (1974).

[17] P. A. Nelson, ''Active control of acoustic fields and the reproduction of sound,'' J. Sound Vib. **177**(4), 447–477 (1994).

[18] P. A. Nelson, F. Orduña-Bustamante, and H. Hamada, ''Multichannel signal processing techniques in the reproduction of sound,'' J. Audio Eng. Soc. **44**(11), 973–989 (1996).

[19] O. Kirkeby, P. A. Nelson, F. Orduña-Bustamante, and H. Hamada, ''Local sound field reproduction using digital signal processing,'' J. Acoust. Soc. Am. **100**(3), 1584–1593 (1996).

[20] B. S. Atal and M. R Schroeder, ''Apparent sound source translator,'' U.S. Patent No. 3,236,949 (1962).

[21] O. Kirkeby, P. A. Nelson, H. Hamada, and F. Orduña-Bustamante, ''Fast deconvolution of multi-channel systems using regularization,'' IEEE Trans. Speech Audio Process. **6**, 189–194 (1998).

[22] I. Malecki, *Physical Foundations of Technical Acoustics* (Pergamon, Warszawa, 1969).

[23] F. Orduña-Bustamante, Ph.D. dissertation, ISVR, University of Southampton, 1995.

[24] U. Burandt, C. Posselt, S. Ambrozis, M. Hosenfeld, and V. Knauff, ''Anthropometric contribution to standardizing mannequins for artificial-head microphones and to measuring headphones and ear protectors,'' Appl. Ergonomics **22**, 373–378 (1991).

[25] D. Rife and J. Vanderkooy, ''Transfer-function measurement with maximum-length sequences,'' J. Audio Eng. Soc. **37**(6), 419–444 (1989).

[26] B. Gardner and K. Martin, *KEMAR HRTF measurements*, MIT's Media Lab, http://sound.media.mit.edu/KEMAR.html.

An advanced boundary element/fast Fourier transform axisymmetric formulation for acoustic radiation and wave scattering problems

Stephanos V. Tsinopoulos
Department of Mechanical and Aeronautical Engineering, University of Patras, GR-26 500 Patras, Greece and Institute of Chemical Engineering and High Temperature Chemical Processes-FORTH, GR-26 500, Patras, Greece

John P. Agnantiaris
Department of Mechanical and Aeronautical Engineering, University of Patras, GR-26 500 Patras, Greece

Demosthenes Polyzos[a)]
Department of Mechanical and Aeronautical Engineering, University of Patras, GR-26 500 Patras, Greece and Institute of Chemical Engineering and High Temperature Chemical Processes-FORTH, GR-26 500, Patras, Greece

An advanced boundary element/fast Fourier transform (BE/FFT) methodology for solving axisymmetric acoustic wave scattering and radiation problems with non-axisymmetric boundary conditions is reported. The boundary quantities of the problem are expanded in complex Fourier series with respect to the circumferencial direction. Each of the expanding coefficients satisfies a surface integral equation which, due to axisymmetry, is reduced to a line integral along the surface generator of the body and an integral over the angle of revolution. The first integral is evaluated through Gauss quadrature by employing a two-dimensional boundary element methodology. The integration over the circumferencial direction is performed simultaneously for all the Fourier coefficients through the FFT. The singular and hyper-singular integrals are computed directly by employing highly accurate three-dimensional integration techniques. The accuracy of the proposed boundary element methodology is demonstrated by means of representative numerical examples. © *1999 Acoustical Society of America.* [S0001-4966(99)01803-2]

PACS numbers: 43.20.Fn [ANN]

INTRODUCTION

The boundary element method (BEM) is a well-known and powerful numerical tool, successfully used in recent years to solve various types of engineering problems in acoustics.[1] A remarkable advantage it offers as compared to other numerical methods such as the finite difference (FDM) and the finite element method (FEM) is the reduction of the dimensionality of the problem by one. Thus, three-dimensional problems are accurately solved by discretizing only two-dimensional surfaces surrounding the domain of interest. In the case where the problem is characterized by an axisymmetric geometry, the BEM reduces further the dimensionality of the problem, requiring just a discretization along a meridional line of the body. These advantages in conjunction with the automatic accounting of the radiation conditions, when infinite or semi-infinite domains are treated, render the BEM ideal for analyzing axisymmetric radiation and wave scattering problems. One can find details concerning the application of the BEM to wave propagation and scattering problems in the books of Manolis and Beskos[2] and Rego Silva.[3]

The departure point of any frequency domain axisymmetric boundary element formulation, dealing with acoustic exterior problems, in existence until now in the literature is the transformation of the integral representation of the problem into cylindrical coordinates. Then, due to the axisymmetric nature of the free space Green's function, a surface integral is reduced to an integral defined on a meridional line of the body and an integral over the angle of revolution. The latter integral, when singularity occurs, is computed in terms of elliptic integrals. Otherwise, the integration is performed numerically by means of Gauss quadrature. The integral along the meridional line is computed numerically by employing a two-dimensional boundary element methodology. When the boundary conditions of the problem are axisymmetric, the analysis is straightforward. In the case of non-axisymmetric boundary conditions, a Fourier series expansion of the boundary quantities with respect to the circumferencial direction is necessary, in order to decompose the problem to a series of pure axisymmetric problems. Here one can mention the works of Meyer *et al.*,[4] Seybert *et al.*,[5] Martinez,[6] Sarkissian,[7] Juhl,[8] Soenarko,[9] Grannel *et al.*,[10] and Wang *et al.*[11]

The main problem with the above described boundary element methodology is the time consuming evaluation of the circumferencial integrals, which have to be computed separately for each Fourier component of the problem. However, the very recent works of Kuijpers *et al.*[12] in acoustics and Ozkan and Mengi[13] in elastodynamics revealed that the

---

[a)]Electronic mail: Polyzos@tech.mech.upatras.gr

computational effort can be drastically reduced by performing the circumferencial integration, simultaneously for all the Fourier harmonics, through the fast Fourier transform (FFT) algorithm.[14]

In this work an advanced BEM formulation, appropriately combined with the FFT and the nonperiodic FFT[15] algorithms for solving axisymmetric radiation and scattering problems in frequency domain acoustics, is presented. The proposed formulation has been implemented to solve the standard Helmholtz boundary integral equation,[3] its normal derivative[3] as well as the linear combination of them, known in the literature as the composite boundary integral equation of Burton and Miller.[16] The boundary quantities of the problem are expanded in discrete complex Fourier series with respect to the circumferencial direction. Each Fourier coefficient satisfies a surface integral equation which, due to axisymmetry, is reduced to an integral equation containing a line integral along a surface generator of the body and an integral over the angle of revolution. The first integral is evaluated through Gauss quadrature by applying a two-dimensional boundary element methodology. The integration over the angle of revolution is performed simultaneously for all the Fourier coefficients through the FFT, with obvious computational gains. The singular and hyper-singular integrals are computed directly with high accuracy by means of three-dimensional integration techniques.

A brief review of the integral equations, most commonly used for solving acoustic problems, as well as the special axisymmetric form of those equations, are presented in a unified way in Sec. I. Section II is subdivided into three parts. In part A, the proposed boundary element formulation is described. Parts B and C deal with the evaluation of nonsingular and singular integrals, respectively. Also in part C, the computational efficiency of the proposed technique concerning the direct evaluation of singular integrals is demonstrated via appropriate numerical tests. Finally, in Sec. III three representative numerical examples exhibit the accuracy of the present formulation.

The methodology presented here can be thought of as an improved and advanced extension of the work of Ozkan and Mengi[13] to acoustic problems because it employs quadratic boundary elements instead of constant ones used in their work, evaluates the singular integrals by means of the highly accurate direct algorithms of Guiggiani et al.[17] appropriately modified for the present axisymmetric case, and performs the integration over the angle of revolution by utilizing an automatically determined number of FFT points. By comparison of the present work to that of Kuijpers et al.,[12] the formulation proposed here can be considered more efficient, as far as it is concerned with the singular integration used, and more general, because it deals not only with the standard Helmholtz boundary integral equation,[3] but also solves effectively the composite one.[16] Finally, the use of complex Fourier series, instead of real ones, renders the present BE/FFT methodology easily extendable to electromagnetic and elastic problems, as it is evident by the recent works of Tsinopoulos et al.[18,19]

I. INTEGRAL EQUATIONS—AXISYMMETRIC FORMULATION

The integral equations mostly employed by the BEM, to solve acoustic wave scattering or radiation problems, are briefly presented in the following. Consider a three-dimensional (3-D) body of volume V, enclosed by a surface S on which a unit normal vector $\mathbf{n}$, pointing into V, is defined. The body is submerged into an infinite linear acoustic medium. When a harmonic acoustic wave ϕ^i impinges upon the body, the resulting scattering problem admits a frequency domain integral equation, which for smooth boundaries has the following general form:

$$
\begin{aligned}
\frac{1}{2}&\left[\varepsilon_0\phi(\mathbf{x},\omega)+\varepsilon_1\frac{\partial\phi(\mathbf{x},\omega)}{\partial\mathbf{n_x}}\right]\\
&+\int_S\left[\varepsilon_0\frac{\partial G(\mathbf{x},\mathbf{y},\omega)}{\partial\mathbf{n_y}}+\varepsilon_1\frac{\partial^2 G(\mathbf{x},\mathbf{y},\omega)}{\partial\mathbf{n_x}\,\partial\mathbf{n_y}}\right]\phi(\mathbf{x},\omega)\,dS_\mathbf{y}\\
&=\varepsilon_0\phi^i(\mathbf{x},\omega)+\varepsilon_1\frac{\partial\phi^i(\mathbf{x},\omega)}{\partial\mathbf{n_x}}\\
&+\int_S\left[\varepsilon_0 G(\mathbf{x},\mathbf{y},\omega)+\varepsilon_1\frac{\partial G(\mathbf{x},\mathbf{y},\omega)}{\partial\mathbf{n_x}}\right]\frac{\partial\phi(\mathbf{x},\omega)}{\partial\mathbf{n_y}}\,dS_\mathbf{y},\quad(1)
\end{aligned}
$$

where $\mathbf{x}$ and $\mathbf{y}$ are position vectors representing a field and source point, respectively, ω is the circular frequency, ϕ and $\partial\phi/\partial\mathbf{n}$ stand for the velocity potential and the normal component of the particle velocity on the surface S of the body, respectively, and G represents the free space Green's function. When a radiation problem is considered, the incident terms in Eq. (1) are omitted.

Providing different values for the constants ε_0 and ε_1 in Eq. (1), three different integral equations may be obtained. When $\varepsilon_0=1$ and $\varepsilon_1=0$, Eq. (1) corresponds to the standard Helmholtz integral equation.[3] For the case where $\varepsilon_0=1$ and $\varepsilon_1=i/K$, with K being the wave number, one obtains the composite integral equation proposed by Burton and Miller,[16] while, when $\varepsilon_0=0$ and $\varepsilon_1=1$, the hyper-singular integral equation is obtained. The composite integral equation has the advantage of providing unique solution at any frequency, while the hyper-singular one is suitable for treating radiation and scattering problems dealing with bodies of zero thickness.[3] In the latter case the velocity potential ϕ and the normal component of the particle velocity $\partial\phi/\partial\mathbf{n}$ are substituted by their jump values $\Delta\phi$ and $\Delta\partial\phi/\partial\mathbf{n}$ across the surface S of the thin body.

Consider the body to be axisymmetric with respect to the X_3 axis of a rectangular coordinate system (X_1,X_2,X_3) and an associated cylindrical coordinate system (ρ,φ,z) with $z\equiv X_3$, as shown in Fig. 1. Transforming Eq. (1) into the cylindrical coordinate system and omitting, for reasons of simplicity, the dependence of all quantities on the circular frequency ω, one obtains

1518   J. Acoust. Soc. Am., Vol. 105, No. 3, March 1999

Tsinopoulos et al.: Acoustic BE/FFT axisymmetric formulation   1518
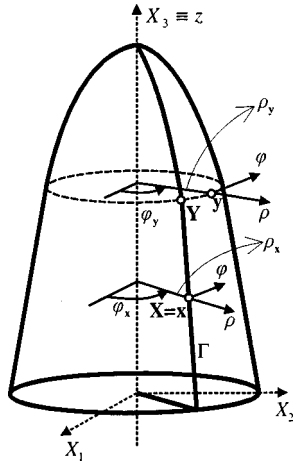
FIG. 1. The axisymmetric body and its coordinate systems.

$$\frac{1}{2}\left[\varepsilon_0\phi(\mathbf{x})+\varepsilon_1\frac{\partial\phi(\mathbf{x})}{\partial\mathbf{n_x}}\right]+\int_\Gamma\rho_\mathbf{y}\int_0^{2\pi}\left[\varepsilon_0\frac{\partial G(\mathbf{x},\mathbf{y})}{\partial\mathbf{n_y}}\right.$$

$$\left.+\varepsilon_1\frac{\partial^2 G(\mathbf{x},\mathbf{y})}{\partial\mathbf{n_x}\,\partial\mathbf{n_y}}\right]\phi(\mathbf{y})\,d\varphi_\mathbf{y}\,d\Gamma_\mathbf{y}$$

$$=\varepsilon_0\phi^i(\mathbf{x})+\varepsilon_1\frac{\partial\phi^i(\mathbf{x})}{\partial\mathbf{n_x}}+\int_\Gamma\rho_\mathbf{y}\int_0^{2\pi}\left[\varepsilon_0 G(\mathbf{x},\mathbf{y})\right.$$

$$\left.+\varepsilon_1\frac{\partial G(\mathbf{x},\mathbf{y})}{\partial\mathbf{n_x}}\right]\frac{\partial\phi(\mathbf{y})}{\partial\mathbf{n_y}}\,d\varphi_\mathbf{y}\,d\Gamma_\mathbf{y}, \tag{2}$$

where $\rho_\mathbf{y}$ and $\varphi_\mathbf{y}$ are the polar coordinates of the source point $\mathbf{y}$ and Γ is a surface generator of the body. When a scattering problem is under consideration, the incident terms are expanded into discrete complex Fourier series with respect to the polar angle φ, as follows:

$$\left\{\begin{array}{c}\phi^i(\mathbf{x})\\ \dfrac{\partial\phi^i(\mathbf{x})}{\partial\mathbf{n_x}}\end{array}\right\}=\sum_{n=-n_c}^{n_c}\left\{\begin{array}{c}\phi_n^i(\rho_\mathbf{x},z_\mathbf{x})\\ v_n^i(\rho_\mathbf{x},z_\mathbf{x})\end{array}\right\}e^{in\varphi_\mathbf{x}}, \tag{3}$$

where ϕ_n^i and v_n^i are the Fourier coefficients and n_c is the minimum number of harmonics required for the accurate expansion of the incident field. This cutoff harmonic n_c is determined numerically, at the point $\mathbf{x}\varepsilon\Gamma$ with the maximum ρ, in order to have a coefficient $\phi_{n_c}^i(\mathbf{x})$ no less than $10^{-2}\phi_0$, where ϕ_0 is the amplitude of the incident wave. The Fourier coefficients are related to the expanded functions through the integrals

$$\left\{\begin{array}{c}\phi_n^i(\rho_\mathbf{x},z_\mathbf{x})\\ v_n^i(\rho_\mathbf{x},z_\mathbf{x})\end{array}\right\}=\frac{1}{2\pi}\int_0^{2\pi}\left\{\begin{array}{c}\phi^i(\mathbf{x})\\ \dfrac{\partial\phi^i(\mathbf{x})}{\partial\mathbf{n_x}}\end{array}\right\}e^{-in\varphi_\mathbf{x}}\,d\varphi_\mathbf{x}. \tag{4}$$

The above equations represent the Fourier transform formula and the coefficients ϕ_n^i and v_n^i can be computed by using the FFT algorithm.[20] In the case of radiation problems, a similar procedure is followed for the Fourier expansion of the boundary excitations.

Expanding now the boundary velocity potential and normal velocity fields into discrete complex Fourier series with respect to φ, one obtains

$$\left\{\begin{array}{c}\phi(\mathbf{x})\\ \dfrac{\partial\phi(\mathbf{x})}{\partial\mathbf{n_x}}\end{array}\right\}=\sum_{n=-n_c}^{n_c}\left\{\begin{array}{c}\phi_n(\rho_\mathbf{x},z_\mathbf{x})\\ v_n(\rho_\mathbf{x},z_\mathbf{x})\end{array}\right\}e^{in\varphi_\mathbf{x}}. \tag{5}$$

The fields are expanded into complex Fourier series, instead of real ones, in order to avoid the split of the problem into symmetric and antisymmetric modes. Although the two formulations are mathematically equivalent, the expansion based into the complex Fourier series is conceptually simpler and more attractive for a numerical implementation, especially in problems employing vector and tensor fields such as elastic ones.[13,21]

Inserting now the expansions of Eqs. (3) and (5) into Eq. (2) and invoking orthogonality arguments, one obtains the following integral equation for the nth Fourier boundary velocity potential and normal velocity coefficients:

$$\frac{1}{2}\left[\varepsilon_0\phi_n(\mathbf{X})+\varepsilon_1 v_n(\mathbf{X})\right]+\int_\Gamma\rho_\mathbf{Y}\left[\varepsilon_0\frac{\partial G^{(n)}(\mathbf{X},\mathbf{Y})}{\partial\mathbf{n_Y}}\right.$$

$$\left.+\varepsilon_1\frac{\partial^2 G^{(n)}(\mathbf{X},\mathbf{Y})}{\partial\mathbf{n_X}\,\partial\mathbf{n_Y}}\right]\phi_n(\mathbf{Y})\,d\Gamma_\mathbf{Y}$$

$$=\varepsilon_0\phi_n^i(\mathbf{X})+\varepsilon_1 v_n^i(\mathbf{X})+\int_\Gamma\rho_\mathbf{Y}\left[\varepsilon_0 G^{(n)}(\mathbf{X},\mathbf{Y})\right.$$

$$\left.+\varepsilon_1\frac{\partial G^{(n)}(\mathbf{X},\mathbf{Y})}{\partial\mathbf{n_X}}\right]v_n(\mathbf{Y})\,d\Gamma_\mathbf{Y}, \tag{6}$$

where all the kernels G, $\partial G/\partial\mathbf{n_Y}$, $\partial G/\partial\mathbf{n_X}$, $\partial^2 G/\partial\mathbf{n_X}\,\partial\mathbf{n_Y}$ presented in the above equation have a representation of the form

$$F^{(n)}(\mathbf{X},\mathbf{Y})=\int_0^{2\pi}F(\mathbf{X},\mathbf{Y},\varphi)e^{in\varphi}\,d\varphi \tag{7}$$

with $\mathbf{X}(\rho_\mathbf{x},z_\mathbf{x})$, $\mathbf{Y}(\rho_\mathbf{y},z_\mathbf{y})$ being the field and source point, respectively, belonging to the same surface generator Γ of the axisymmetric body (see Fig. 1), from which the circumferential angle $\varphi=\varphi_\mathbf{y}-\varphi_\mathbf{x}$ is measured.

The integral equation (6) in conjunction with the appropriately expanded boundary conditions form a well-posed boundary value problem for each Fourier coefficient ϕ_n and v_n and can be solved numerically by employing the boundary element method.

II. NUMERICAL IMPLEMENTATION

The present section deals with the numerical implementation of the axisymmetric formulation described in the previous section.

A. Boundary element formulation

The surface generator Γ is discretized into E Three-noded quadratic isoparametric boundary elements with length being smaller than or equal to one-fourth of the wavelength of the disturbance. Corners or nodal points belonging on the axis of symmetry z, corresponding to $\rho=0$, are treated by partially discontinuous elements.[22] Let the total number of the nodal points be equal to L. Then, adopting a global numbering for all the L nodes by associating to each pair

(element e, local node a) a number β, and writing the integral equation (6) for a node indicated by the position vector $\mathbf{X}^k$, one has

$$\frac{1}{2}[\varepsilon_0\phi_n^k + \varepsilon_1 v_n^k] + \sum_{\beta=1}^{L} [\varepsilon_0 H_{\beta k}^{(n)} + \varepsilon_1 Q_{\beta k}^{(n)}]\cdot\phi_n^\beta$$

$$= \varepsilon_0\phi_n^{i(k)} + \varepsilon_1 v_n^{i(k)} + \sum_{\beta=1}^{L} [\varepsilon_0 T_{\beta k}^{(n)} + \varepsilon_1 W_{\beta k}^{(n)}]\cdot v_n^\beta. \tag{8}$$

The integrals H, Q, T, W, appearing in the above equation, can be expressed as

$$F_{\beta k}^{(n)} = \int_{-1}^{1} \rho_{\mathbf{Y}^e(\xi_1)} f_{\beta k}^{(n)} N^\alpha(\xi_1) J_{\xi_1}\, d\xi_1 \Bigg|_{e\,\alpha\to\beta} \tag{9}$$

and

$$f_{\beta k}^{(n)} = \int_0^{2\pi} U(\mathbf{X}^k, \mathbf{Y}^e(\xi_1),\varphi) e^{in\varphi}\, d\varphi \tag{10}$$

with U representing the kernels $\partial G/\partial\mathbf{n}_{\mathbf{Y}^e(\xi_1)}$, $\partial^2 G/\partial\mathbf{n}_{\mathbf{X}^k}\partial\mathbf{n}_{\mathbf{Y}^e(\xi_1)}$, G, $\partial G/\partial\mathbf{n}_{\mathbf{X}^k}$ when F corresponds to the integrals H, Q, T, W, respectively.

In Eqs. (9) and (10) N^α ($\alpha=1,2,3$) are the shape functions of a line quadratic element and J_{ξ_1} is the Jacobian of the transformation from the global to the local co-ordinate system ξ_1. Collocating Eq. (8) to all nodal points L and applying the boundary conditions one obtains the following final linear system of algebraic equations for the nth harmonic:

$$\mathbf{A}^{(n)}\cdot\mathbf{x}^{(n)} = \mathbf{b}^{(n)}, \tag{11}$$

where the vectors $\mathbf{x}^{(n)}$ and $\mathbf{b}^{(n)}$ contain all the unknown and known Fourier coefficients, respectively. This system can be solved by the well-known LU decomposition algorithm.[20]

As it has already been mentioned, one of the advantages of the present formulation is that the integrals in Eq. (10), when $\beta\neq k$ (nonsingular case), are evaluated simultaneously for all harmonics n by employing the FFT algorithm with great computational gains, especially if a large number of harmonics must be taken into account. Details are given in the part B of the present section. However, when $\beta=k$ all integrals of Eq. (9) become singular. The integrals T, H, and W exhibit a weak singularity, while the integral Q is hypersingular and must be handled in the sense of Hadamard finite part.[23] For the singular integration a special treatment is required and an advanced technique, combining direct evaluation of 3-D singular integrals and the FFT algorithm, is proposed in Sec. II C.

B. Evaluation of nonsingular integrals

Integrals (9), on the generator Γ, are evaluated by using a standard Gauss quadrature, employing Λ_{ek} integration points, with Λ_{ek} given by the expression

$$\Lambda_{ek} = 1 + \mathrm{INT}\left[\zeta_1\left(\frac{D_{ek}}{l_e}\right)^{-\zeta_2}\right], \tag{12}$$

where INT indicates the next lower integer and D_{ek} is the minimum distance between the point $\mathbf{X}^k$ and the integration
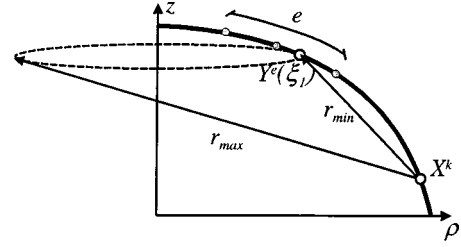
FIG. 2. The minimum and maximum distances between a field point and source points over the circumference.

element e of length l_e. The above formula, which is similar to that proposed by Bu[24] for 3-D integration, has been established in the present work by giving values to the dimensionless variable D/l greater than 5×10^{-3}, in order to evaluate the aforementioned nonsingular integrals with accuracy of 0.01%. The constants ζ_1, ζ_2 are equal to $\zeta_1=1.95$, $\zeta_2=1.00$ and $\zeta_1=2.35$, $\zeta_2=1.06$ when integrals with kernels of order $O(1/r)$ and $O(1/r^3)$, respectively, are treated and the minimum value of Λ_{ek} is equal to 4.

The integrals of Eq. (10), over the angle of revolution φ, are computed by application of the FFT methodology. In the present work the FFT algorithm of IMSL[20] is employed in the computations. The interval $[0, 2\pi]$ is divided into M equal parts, each of which represents an angle $\Delta\varphi=2\pi/M$. In accordance to the requirement of a conventional FFT algorithm, M should be a power of 2, i.e., $M=2^p$, $p\varepsilon N$. According to discrete Fourier transform theory, the integrals of Eq. (10) can be written as

$$f_{\beta k}^{(n)} = \frac{2\pi}{M}\sum_{m=0}^{M-1} U(\mathbf{X}^k,\mathbf{Y}^e(\xi_1),\varphi_m) e^{i2\pi(nm/M)}, \tag{13}$$

where all the kernels are now defined on each angle $\varphi_m = m\Delta\varphi$.

The efficient computation of integral (13) requires an optimum choice for the FFT points M. According to a recent study made by Kuijpers $et\ al.$,[12] the required number of FFT points depends on the minimum ($r_{\min}$) and maximum ($r_{\max}$) distances (see Fig. 2) between the field point $\mathbf{X}^k$ and the source points $\mathbf{y}(\mathbf{Y}^e(\xi_1),\varphi_m)$ and the wave number K of the excitation. Thus, through a curve-fitting procedure, they proposed a formula for the optimum selection of the FFT points, in order to evaluate weakly singular integrals with accuracy of 0.1%. In the present work, utilizing the aforementioned parameters, a new formula is proposed. This formula is valid for the evaluation of both weakly and hyper-singular integrals with accuracy of 0.01% and is given by the following relation:

$$M=2^p,$$

$$p = \mathrm{INT}\Bigg\{ a_1 + a_2\, \mathrm{Log}_{10}\Bigg[a_3(Kr_{\max})^{a_4}$$

$$\times\left(1-\left(\frac{r_{\min}}{r_{\max}}\right)^{a_5}\right)^{a_6} + a_7\left(\frac{r_{\max}}{r_{\min}}\right)^{a_8} + a_9\Bigg]\Bigg\}, \tag{14}$$

where INT indicates the next lower integer, the coefficients a_i for both weakly and hypersingular kernels are given in Table I, and the minimum value of M is equal to 16. Equa-

TABLE I. Coefficients a_i, for weak and hyper-singular kernels.

Coefficient	Weakly singular	Hyper-singular
a_1	8.456	7.766
a_2	3.502	2.794
a_3	10.90	63.64
a_4	0.682	0.835
a_5	3.455×10^{-5}	3.067×10^{-5}
a_6	0.567	0.739
a_7	2.306×10^{-2}	2.674×10^{-2}
a_8	1.00	1.247
a_9	2.593×10^{-2}	4.807×10^{-2}

FIG. 3. The 3-D boundary element geometry for singular integration in Cartesian (X_1, X_2, X_3) and local (ξ_1, ξ_2) coordinate systems.

tion (14) has been derived through a curve-fitting procedure of a database, which contains the required FFT points for the evaluation of the integrals with accuracy of 0.01%. This database has been constructed for dimensionless variables $r_{\max}/r_{\min}$ and $K r_{\max}$ lying in the intervals [1, 500] and [0, 200], respectively. It should be noticed here that the interval corresponding to the ratio $r_{\max}/r_{\min}$ is less than that considered by Kuijpers *et al.*[12] ([1, 2000]). This is because, in their work, the FFT algorithm is also used to deal with singular integration, where the field and the source point get very close to each other, thus providing large values for the ratio $r_{\max}/r_{\min}$, while in the present work, the conventional FFT methodology is applied only when nonsingular integrals are treated. Finally, as it is evident in Sec. III, Eq. (14) provides accurate results for a wide frequency range.

C. Evaluation of singular integrals

As it has already been mentioned, in the case when $\beta = k$ the kernels of integrals in Eq. (9) become singular, with the integrals T, H, and W being weakly singular $O(1/r)$ while the integral Q is hyper-singular $O(1/r^3)$. A special integration technique to treat these integrals is proposed here, which is of a different sense compared to others appearing so far in the literature for axisymmetric formulations. Its main novelty is that it takes into account the singular behavior around the field point in a 3-D sense, in contrast with the so far proposed acoustic axisymmetric integration schemes where the singularity is taken into account only along the line generator Γ. For example, in the formulation proposed by Kuijpers *et al.*,[12] the singularity over the circumference is treated by simply increasing the FFT points of a conventional FFT algorithm.

According to the present methodology, a 3-D boundary element $abcd$ is created around the singularity (see Fig. 3). The created element, on the circumferencial direction, has an initial maximum width equal to the length l_e of the corresponding line element on the generator Γ. The width of the created element corresponds to a constant polar angle $2\varphi_e = l_e/\rho_{\max}$, where $\rho_{\max}$ is the maximum ρ-cylindrical coordinate of the corresponding line element. Next, the interval [0, 2π] is divided into M equal parts defined by the angle $\Delta\varphi = 2\pi/M$. The number M is determined by using the relation (14) with $r_{\max} = 2\rho_{\mathbf{X}^k}$ and $r_{\min} = \rho_{\mathbf{X}^k}\sqrt{2(1-\cos(\varphi_e))}$. The final width of the created element is obtained by taking into account that the angle φ_e must be an integer multiple of the
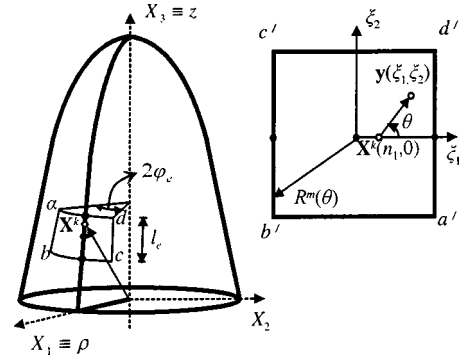
step angle $\Delta\varphi$. Under this constraint, the angle φ_e becomes equal to $j\Delta\varphi$, with j being an integer such that $j \leq M/2$ and is given by the following relation:

$$j = 1 + \text{INT}\left(\frac{\varphi_e}{\Delta\varphi}\right). \tag{15}$$

At this point the integrals of Eq. (10) are split into two integrals, one over the φ direction into the created element $(-j\Delta\varphi, j\Delta\varphi)$ and a second one over the remaining circumferential integration region $(j\Delta\varphi, 2\pi - j\Delta\varphi)$, as

$$f_{kk}^{(n)} = f_{kk}^{(n)(1)} + f_{kk}^{(n)(2)}, \tag{16}$$

where

$$f_{kk}^{(n)(1)} = \int_{-j\Delta\varphi}^{j\Delta\varphi} U(\mathbf{X}^k, \mathbf{Y}^e(\xi_1), \varphi)e^{in\varphi}\, d\varphi, \tag{17}$$

$$f_{kk}^{(n)(2)} = \int_{j\Delta\varphi}^{2\pi - j\Delta\varphi} U(\mathbf{X}^k, \mathbf{Y}^e(\xi_1), \varphi)e^{in\varphi}\, d\varphi. \tag{18}$$

The integrals $F_{kk}^{(n)(1)}$ given by Eqs. (9) and (17) are treated as surface integrals over the created 3-D element and they are directly evaluated as in a conventional 3-D BEM formulation. For this purpose a local variable ξ_2 is introduced, which describes the polar angle φ through the following linear relation

$$\varphi(\xi_2) = j\Delta\varphi\xi_2, \quad \xi_2 \in [-1, \ 1]. \tag{19}$$

Thus, the integrals $F_{kk}^{(n)(1)}$ in the local $\xi_1 - \xi_2$ plane are written as

$$F_{kk}^{(n)(1)} = \int_{-1}^{1}\int_{-1}^{1}\rho_{\mathbf{Y}^e(\xi_1)}U(\mathbf{X}^k, \mathbf{y}(\xi_1, \xi_2))$$
$$\times e^{in\varphi(\xi_2)}N^\alpha(\xi_1)J_\varphi J_{\xi_1}\, d\xi_1\, d\xi_2, \tag{20}$$

where $J_\varphi = j\Delta\varphi$ is the Jacobian of the transformation of Eq. (19). Transforming now the integrals (20) into a local polar coordinate system (see Fig. 3) and applying the methodology proposed by Guiggiani *et al.*[17] for the direct treatment of the hyper-singular integral Q, appropriately modified for the present axisymmetric case, one obtains

$$T_{kk}^{(n)(1)} = \sum_{m=1}^{l} \int_{\theta_1^m}^{\theta_2^m} \int_0^{R^m(\theta)} T^m(R,\theta)\, dR\, d\theta, \tag{21}$$

$$H_{kk}^{(n)(1)} = \sum_{m=1}^{l} \int_{\theta_1^m}^{\theta_2^m} \int_0^{R^m(\theta)} H^m(R,\theta)\, dR\, d\theta, \tag{22}$$

$$W_{kk}^{(n)(1)} = \sum_{m=1}^{l} \int_{\theta_1^m}^{\theta_2^m} \int_0^{R^m(\theta)} W^m(R,\theta)\, dR\, d\theta, \tag{23}$$

$$Q_{kk}^{(n)(1)} = \sum_{m=1}^{l} \int_{\theta_1^m}^{\theta_2^m} \int_0^{R^m(\theta)} \left(Q^m(R,\theta) \right.$$
$$\left. - \frac{{}^2q^m(\theta)}{R^2} - \frac{{}^1q^m(\theta)}{R} \right) dR\, d\theta$$
$$+ \sum_{m=1}^{l} \int_{\theta_1^m}^{\theta_2^m} \left\{ {}^1q^m(\theta) \ln \left| \frac{R^m(\theta)}{\beta^m(\theta)} \right| - {}^2q^m(\theta) \right.$$
$$\left. \times \left[\frac{\gamma(\theta)}{(\beta^m(\theta))^2} + \frac{1}{R^m(\theta)} \right] \right\} d\theta, \tag{24}$$

where T^m, H^m, W^m, and Q^m are the integrands of Eq. (20) expressed in the local polar coordinate system, while all the remaining parameters in Eqs. (21)–(24) are given in the Appendix. If $(n_1, 0)$ are the coordinates of the singular point $\mathbf{X}^k$ in the local coordinate system (ξ_1, ξ_2), then the summation index l takes the value 1 when $-1 < n_1 < 1$ and the value 2 when $n_1 = \pm 1$. It should be noticed here that the integrals of Eqs. (21)–(24) are regular and can be easily computed for each harmonic n, through standard Gauss quadrature, with 6×6 integration points.

The remaining integrals $f_{kk}^{(n)(2)}$ of Eq. (18) are computed through a nonperiodic FFT algorithm simultaneously for all harmonics n. According to this algorithm, the integration is done again in the interval $[0, 2\pi]$, as in a conventional FFT algorithm, except that now the fundamental kernels U are set equal to 0 when they are defined at the interval $(-j\Delta\varphi, j\Delta\varphi)$. The error resulting by the latter procedure is taken into account and an appropriate correction is imposed. Details about this nonperiodic FFT algorithm can be found in Ref. 15, pp. 577–584.

In order to demonstrate the efficiency of the present integration technique, a test problem concerning the accuracy and the computational speed for the evaluation of weakly singular integrals is presented. The present singular integration technique is compared to the one used in the work of Kuijpers et al.,[12] which is the only one appearing so far in the literature in the context of acoustic BE/FFT methodology. In that work, the integrands of the integrals $H^{(n)}$ and $T^{(n)}$ in Eq. (9) are evaluated by means of a conventional FFT algorithm. As it is well known, these integrands are complex functions. Their real part, near the singular point, exhibits a logarithmic behavior, while the imaginary part is regular. The weakly singular real part is handled by using a Gauss–log quadrature technique, while the regular imaginary part is computed separately through a Gauss–Legendre quadrature.

The test problem concerns a sphere of radius a subjected to a plane incidence, propagating vertically to the axis of symmetry z. The dimensionless frequency of the problem is
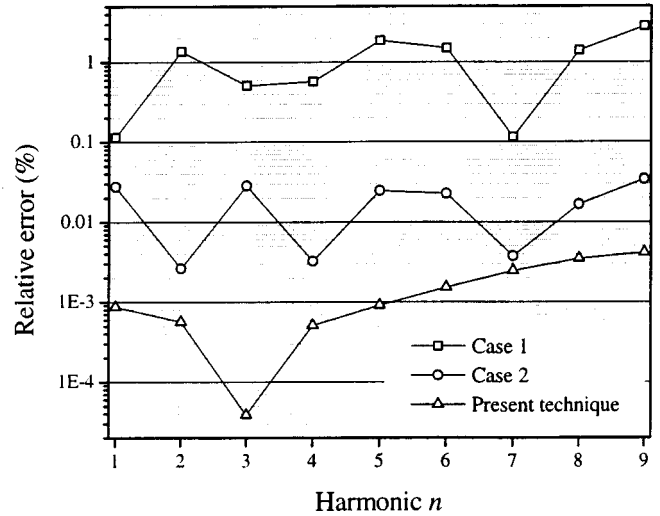
FIG. 4. Relative percent error of the magnitude of the $T^{(n)}$ integral versus positive harmonic number at $Ka = 5$.

$Ka = 5$ and the line elements of the discretized generator have a length equal to one-fourth of the wavelength. The integrals $T^{(n)}$ are computed for the node with coordinates $(a, 0)$ in the $\rho - z$ plane through, first, the present singular integration technique and, second, the one used in Kuijpers et al.,[12] with two possible combinations for the number of integration points. The first case (case 1) refers to the use of two integration points for both the Gauss–log and Gauss–Legendre quadratures. The second case (case 2) uses 16 points for the Gauss–log and 3 points for the Gauss–Legendre quadrature. The combination of integration points in case 1 corresponds to the minimum requirement for both quadratures. The combination in case 2 corresponds, first, to a maximum choice of integration points, that can be found by the authors, for the Gauss–log quadrature and, second, to a choice of integration points for the Gauss–Legendre quadrature, which provides convergence. The relative percent error of the magnitude of the $T^{(n)}$ integrals as a function of each positive harmonic n is shown in Fig. 4. The total CPU time needed for the evaluation of the above integrals for all harmonics was 2.05×10^{-2} s for the present technique, 1.72×10^{-2} s for case 1, and 3.24×10^{-1} s for case 2. All the calculations were done in a 233 MHz Pentium II PC.

The same test problem is solved when the dimensionless frequency of the problem is $Ka = 50$. Here, case 1 remains the same. However, in case 2, the number of integration points for both the Gauss–log and the Gauss–Legendre quadratures is 4. This choice is imposed by the fact that when more than four integration points are used for the Gauss–log quadrature, the dimensionless variable r_{max}/r_{min}, in the formula for the automatic selection of FFT points, used in Kuijpers et al.,[12] exceeds the limits of operation. Figure 5 shows the relative percent error of the magnitude of the $T^{(n)}$ integrals as a function of each positive harmonic n. The total CPU time for the present test was 1.40×10^{-1} s for the present technique, 1.93×10^{-1} s for case 1, and 4.95×10^{-1} s for case 2.
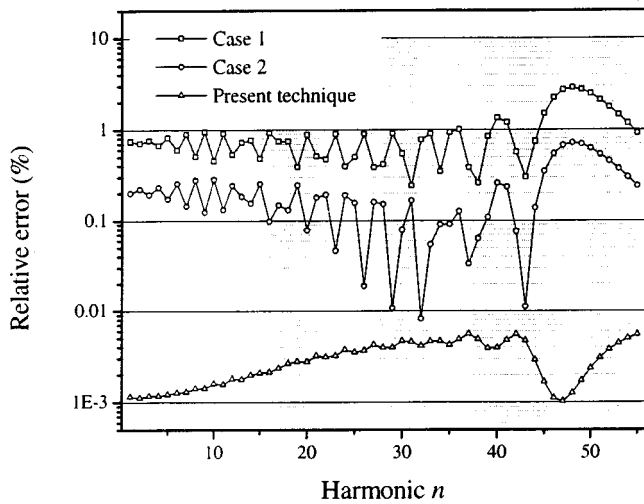
FIG. 5. Relative per cent error of the magnitude of the $T^{(n)}$ integral versus positive harmonic number at $Ka = 50$.

As it is evident, the accuracy provided by the proposed technique is better than that provided by cases 1 and 2, for both intermediate ($Ka = 5$) and high ($Ka = 50$) frequencies. The computational speed of the present integration is comparable to that of case 1 and higher than that of case 2.

III. NUMERICAL EXAMPLES

Three benchmark problems are solved in order to demonstrate the high accuracy of the proposed BE/FFT formulation. The first problem deals with the radiation from a sphere of radius a pulsating with uniform radial velocity. The problem is solved by using the integral equation (1) with $\varepsilon_0 = 1$, $\varepsilon_1 = 0$ (standard) and with $\varepsilon_0 = 1$, $\varepsilon_1 = i/K$ (composite). The line generator is discretized in 14 elements. The magnitude of the acoustic pressure p on the surface of the sphere is plotted in Fig. 6 as function of the dimensionless frequency Ka. The analytical solution, as given in Rego Silva,[3] is also plotted for comparison. It can be seen that both integral equations, solved with the proposed axisymmetric formula-
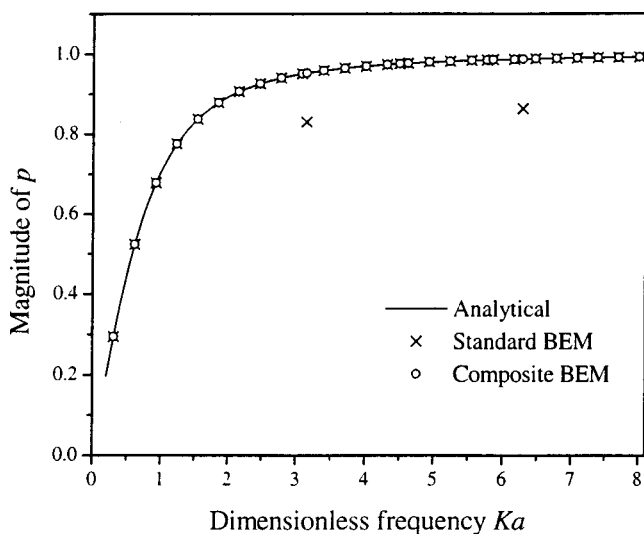
FIG. 6. Magnitude of the acoustic pressure p on the surface of a pulsating sphere versus dimensionless frequency Ka.
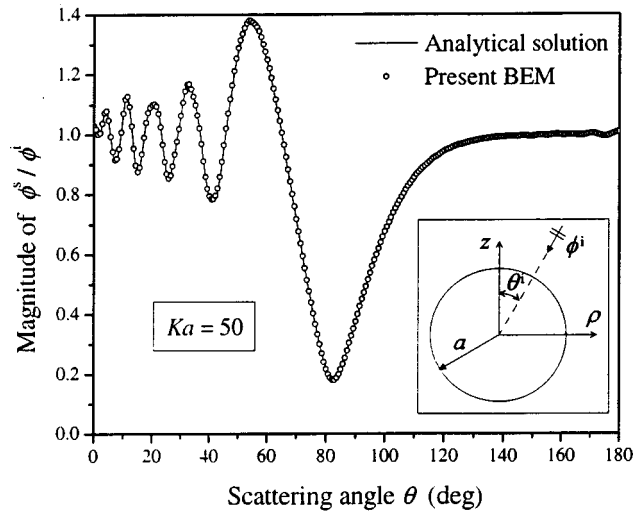
FIG. 7. Magnitude ratio of scattered to incident velocity potentials on the surface of a rigid sphere versus scattering angle for $Ka = 50$.

tion, provide results in excellent agreement with the analytical solution, except at the two fictitious eigenfrequencies ($Ka = \pi$ and 2π) appearing in the frequency range considered, when the standard integral equation is used.

The second example concerns the scattering of a plane acoustic wave from a rigid sphere with radius a, for a high dimensionless frequency $Ka = 50$. The incident wave propagates in a direction $\theta^i = 30°$, measured from the symmetry axis z, in the $\rho - z$ plane. This problem is solved by utilizing the standard integral equation, in order to show the great accuracy of the proposed axisymmetric formulation when non-axisymmetric boundary conditions are considered. The line generator is discretized in 126 elements and a total number of 61 harmonics are analyzed. The magnitude ratio of the scattered ϕ^s to the incident ϕ^i velocity potentials, on the boundary of the sphere, in the $\rho - z$ plane is calculated. The results are shown in Fig. 7 as a function of a scattering angle θ, measured from the incident propagation direction. The analytical solution as given in Skudrzyk[25] is also plotted and
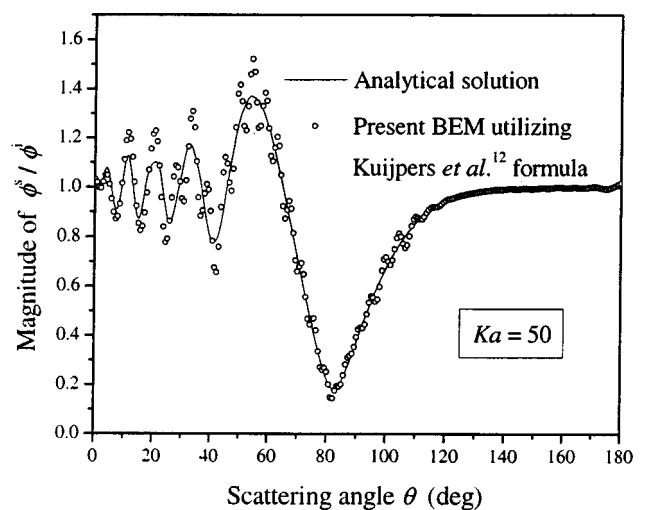
FIG. 8. Magnitude ratio of scattered to incident velocity potentials on the surface of a rigid sphere versus scattering angle for $Ka = 50$, with use of Kuijpers et al.'s[12] formula for nonsingular integrals.
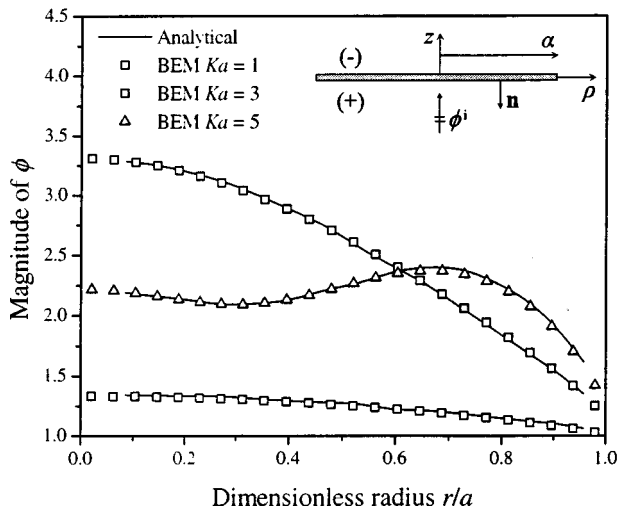
FIG. 9. Magnitude of total velocity potential versus dimensionless radius of a rigid disk for $Ka = 1,3,5$.

the excellent agreement between the present results and the analytical solution is evident.

For comparison reasons, the above scattering problem is solved again by using, instead of Eq. (14), the formula proposed in Kuijpers et al.[12] for the evaluation of nonsingular integrals. The results are shown in Fig. 8 and as it is apparent the solution presents significant instabilities, although the variables r_{max}/r_{min} and $K(r_{max}-r_{min})$ of the formula do not exceed the limits of operation at this particular frequency.

Finally, the scattering problem of an incident plane wave from a rigid thin circular disk of radius a is solved. The incident wave is propagating along the z axis. This problem demonstrates the accuracy of the present BE/FFT formulation when thin scatterers are analyzed. In this case integral equation (1) with $\varepsilon_0 = 0$, $\varepsilon_1 = 1$ is used and the line generator of the disk is discretized in eight elements. The magnitude of the total velocity potential ϕ on the bright $(+)$ side of the disk surface versus the dimensionless radius r/a of the disk is shown in Fig. 9 for $Ka = 1,3,5$. The results are compared to the analytical solution of Leitner[26] and the agreement is excellent.

IV. CONCLUSIONS

An advanced BE/FFT formulation is developed for the solution of acoustic scattering and radiation problems (with arbitrary boundary conditions) dealing with any kind of body of revolution. The proposed formulation is general, efficient, and it provides accurate results at any frequency. Its main contributions are that (i) it proposes a new technique for the evaluation of singular and hyper-singular integrals, based on a combination of three-dimensional BEM analysis and a nonperiodic FFT quadrature and (ii) it determines automatically the required number of FFT and Gauss points for the evaluation of circumferencial and line integrals, respectively, with a desired accuracy.

APPENDIX: EXPLICIT EXPRESSIONS OF THE FUNCTIONS IN THE SINGULAR INTEGRATION

Here the kernels $^1q^m(\theta)$, $^2q^m(\theta)$ as well as the functions $R^m(\theta)$, $\beta^m(\theta)$, and $\gamma^m(\theta)$ appearing in the integrals (21)–(24) are derived and given explicitly.

First some fundamental expansions used in Guiggiani's et al.[17] methodology are properly modified for the needs of the present analysis. The departure point is the Taylor's expansion of a vector function $\mathbf{f}(\xi_1,\xi_2)$ at the neighborhood of the singular point $\mathbf{X}^k(n_1,0)$ (see Fig. 3), i.e.,

$$\mathbf{f}(\xi_1,\xi_2) = \mathbf{f}(\boldsymbol{\xi}) = \mathbf{f}(\boldsymbol{\eta}) + \boldsymbol{\nabla}_{\boldsymbol{\xi}}\mathbf{f}(\boldsymbol{\xi})|_{\boldsymbol{\xi}=\mathbf{n}} \cdot (\boldsymbol{\xi}-\mathbf{n})$$
$$+ \tfrac{1}{2}\boldsymbol{\nabla}_{\boldsymbol{\xi}}\boldsymbol{\nabla}_{\boldsymbol{\xi}}\mathbf{f}(\boldsymbol{\xi})|_{\boldsymbol{\xi}=\mathbf{n}} \cdot (\boldsymbol{\xi}-\mathbf{n}) \otimes (\boldsymbol{\xi}-\mathbf{n}) + \cdots,$$
$$(A1)$$

where

$$\boldsymbol{\nabla}_{\boldsymbol{\xi}} = \frac{\partial}{\partial\xi_1}\hat{\boldsymbol{\xi}}_1 + \frac{\partial}{\partial\xi_2}\hat{\boldsymbol{\xi}}_2 \qquad (A2)$$

Introducing a polar coordinate system in the parametric plane ξ_1,ξ_2 with the origin at the point $\mathbf{X}^k(n_1,0)$, i.e.,

$$\xi_1 = n_1 + R\cos\theta, \quad \xi_2 = 0 + R\sin\theta, \qquad (A3)$$

it is easy to see that the expansion (A1) is also written

$$\mathbf{f}(\xi_1,\xi_2) = \mathbf{f}(\mathbf{n}) + R\left(\frac{\partial\mathbf{f}}{\partial\xi_1}\bigg|_{\boldsymbol{\xi}=\mathbf{n}}\cos\theta + \frac{\partial\mathbf{f}}{\partial\xi_2}\bigg|_{\boldsymbol{\xi}=\mathbf{n}}\sin\theta\right)$$
$$+ \frac{1}{2}R^2\left(\frac{\partial^2\mathbf{f}}{\partial\xi_1^2}\bigg|_{\boldsymbol{\xi}=\mathbf{n}}\cos^2\theta + \frac{\partial^2\mathbf{f}}{\partial\xi_2^2}\bigg|_{\boldsymbol{\xi}=\mathbf{n}}\sin^2\theta\right.$$
$$+ 2\frac{\partial^2\mathbf{f}}{\partial\xi_1\partial\xi_2}\bigg|_{\boldsymbol{\xi}=\mathbf{n}}\cos\theta\sin\theta\right) + O(R^3). \quad (A4)$$

Any vector $\mathbf{y}(\xi_1,\xi_2)$ belonging in the created 3-D element (see Fig. 3) has the following form:

$$\mathbf{y}(\xi_1,\xi_2) = \rho_{\mathbf{Y}(\xi_1)}\cos\varphi(\xi_2)\hat{\mathbf{x}}_1 + \rho_{\mathbf{Y}(\xi_1)}\sin\varphi(\xi_2)\hat{\mathbf{x}}_2$$
$$+ z_{\mathbf{Y}(\xi_1)}\hat{\mathbf{x}}_3, \qquad (A5)$$

where

$$\rho_{\mathbf{Y}(\xi_1)} = \rho^l N^l(\xi_1), \quad z_{\mathbf{Y}(\xi_1)} = z^l N^l(\xi_1). \qquad (A6)$$

Applying now the expansion (A4) to the vector $\mathbf{y}(\xi_1,\xi_2) - \mathbf{X}(n_1,0)$ and taking into account relations (A5) and (A6) as well as the expression

$$\frac{d\varphi}{d\xi_2} = j\Delta\varphi = J_\varphi \qquad (A7)$$

one obtains

$$\mathbf{y}(\xi_1,\xi_2) - \mathbf{X}(n_1,0) = R\left\{ \left(\rho^l \left. \frac{dN^l(\xi_1)}{d\xi_1} \right|_{\xi_1=n_1} \cos\theta \right) \hat{\mathbf{x}}_1 + (\rho^l N^l(n_1) J_\varphi \sin\theta) \hat{\mathbf{x}}_2 \right.$$

$$\left. + \left(z^l \left. \frac{dN^l(\xi_1)}{d\xi_1} \right|_{\xi_1=n_1} \cos\theta \right) \hat{\mathbf{x}}_3 \right\} + \frac{1}{2} R^2 \left\{ \left(\rho^l \left. \frac{d^2 N^l(\xi_1)}{d\xi_1^2} \right|_{\xi_1=n_1} \cos^2\theta - \rho^l N^l(n_1) J_\varphi^2 \sin^2\theta \right) \hat{\mathbf{x}}_1 \right.$$

$$\left. + \left(2\rho^l \left. \frac{dN^l(\xi_1)}{d\xi_1} \right|_{\xi_1=n_1} J_\varphi \sin\theta \cos\theta \right) \hat{\mathbf{x}}_2 + \left(z^l \left. \frac{d^2 N^l(\xi_1)}{d\xi_1^2} \right|_{\xi_1=n_1} \cos^2\theta \right) \hat{\mathbf{x}}_3 \right\} + O(R^3). \tag{A8}$$

Relation (A8) can be written in a compact symbolic way as

$$\mathbf{y} - \mathbf{X} = R\mathbf{A}(\theta) + R^2 \mathbf{B}(\theta) + O(R^3), \tag{A9}$$

which is the foundation stone in the integration technique proposed by Guiggiani et al.[17] for the direct evaluation of hyper-singular integrals. Based on (A4) and taking into account relation (A9), the following asymptotic expressions concerning the hyper-singular term l/r^3, the Jacobian vector $\mathbf{J}(\xi_1,\xi_2)$, the shape functions $N^\alpha(\xi_1)$, and the function $e^{in\varphi(\xi_2)}$ can be easily obtained:

$$\frac{1}{r^3} = \frac{1}{R^3 A^3(\theta)} - \frac{3A_i(\theta)B_i(\theta)}{R^2 A^5(\theta)} + O\left(\frac{1}{R}\right) = \frac{{}^3S(\theta)}{R^3} + \frac{{}^2S(\theta)}{R^2} + O\left(\frac{1}{R}\right), \tag{A10}$$

where $A = |\mathbf{A}|$, $r = |\mathbf{y} - \mathbf{X}|$, i represents summation,

$$\mathbf{J}(\xi_1,\xi_2) = \frac{\partial \mathbf{y}}{\partial \xi_2} \times \frac{\partial \mathbf{y}}{\partial \xi_1} = \left[\left(z^i \left. \frac{dN^i(\xi_1)}{d\xi_1} \right|_{\xi_1=n_1} \rho^l N^l(n_1) J_\varphi \right) \hat{\mathbf{x}}_1 - \left(\rho^i \left. \frac{dN^i(\xi_1)}{d\xi_1} \right|_{\xi_1=n_1} \rho^l N^l(n_1) J_\varphi \right) \hat{\mathbf{x}}_3 \right]$$

$$+ R\left[\left(z^i \left. \frac{d^2 N^i(\xi_1)}{d\xi_1^2} \right|_{\xi_1=n_1} \rho^l N^l(n_1) + \rho^i \left. \frac{dN^i(\xi_1)}{d\xi_1} \right|_{\xi_1=n_1} z^l \left. \frac{dN^l(\xi_1)}{d\xi_1} \right|_{\xi_1=n_1} \right) J_\varphi \cos\theta \hat{\mathbf{x}}_1 \right.$$

$$+ \left(z^i \left. \frac{dN^i(\xi_1)}{d\xi_1} \right|_{\xi_1=n_1} \rho^l N^l(n_1) J_\varphi^2 \sin\theta \right) \hat{\mathbf{x}}_2 - \left(\rho^i \left. \frac{d^2 N^i(\xi_1)}{d\xi_1^2} \right|_{\xi_1=n_1} \rho^l N^l(n_1) \right.$$

$$\left. \left. + \left(\rho^i \left. \frac{dN^i(\xi_1)}{d\xi_1} \right|_{\xi_1=n_1} \right)^2 \right) J_\varphi \cos\theta \hat{\mathbf{x}}_3 \right] + O(R^2) = {}^0\mathbf{J} + R^1 \mathbf{J} + O(R^2), \tag{A11}$$

$$J(\xi_1,\xi_2) = |\mathbf{J}(\xi_1,\xi_2)| = \rho_{\mathbf{Y}(\xi_1)} J_\varphi J_{\xi_1}, \tag{A12}$$

$$N^\alpha(\xi_1) = N^\alpha(n_1) + R \left. \frac{dN^\alpha(\xi_1)}{d\xi_1} \right|_{\xi_1=n_1} \cos\theta + O(R^2)$$

$$= N_0^\alpha + R N_l^\alpha(\theta) + O(R^2), \tag{A13}$$

$$e^{in\varphi(\xi_2)} = 1 + R(in J_\varphi \sin\theta) + O(R^2)$$

$$= {}^0e + R^1 e + O(R^2). \tag{A14}$$

Thus the kernels ${}^1q^m(\theta)$ and ${}^2q^m(\theta)$ have the asymptotic expressions

$${}^1q^m(\theta) = \frac{1}{4\pi} \{ [{}^0e N_1^\alpha \cdot {}^0J_i \mathbf{n}_i(n_1) + {}^1e N_0^\alpha \cdot {}^0J_i \mathbf{n}_i(n_1)$$

$$+ {}^0e N_0^\alpha \cdot {}^1J_i \mathbf{n}_i(n_1)] \cdot {}^3S(\theta)$$

$$+ {}^0e N_0^\alpha \cdot {}^0J_i \mathbf{n}_i(n_1) \cdot {}^2S(\theta) \} \tag{A15}$$

$${}^2q^m(\theta) = \frac{1}{4\pi} \{ {}^0e N_0^{\alpha 0} J_i \mathbf{n}_i(n_1) \cdot {}^3S(\theta) \}, \tag{A16}$$

where $\mathbf{n}_i$ are the components of the unit normal vector at the singular point.

Finally, the function $R^m(\theta)$ stands for the parametric representation of the square boundary element $a'b'c'd'$ of the $\xi_1-\xi_2$ plane (see Fig. 3), while the functions $\beta^m(\theta)$ and $\gamma^m(\theta)$ are given by the relations

$$\beta^m(\theta) = \frac{1}{A(\theta)}, \tag{A17}$$

$$\gamma^m(\theta) = \frac{A_i B_i}{A^4}. \tag{A18}$$

[1] Boundary Element Methods in Acoustics, edited by R. D. Ciskowski and C. A. Brebbia (Computational Mechanics Publications, Southampton, and Elsevier Applied Science, London, 1991).

[2] G. D. Manolis and D. E. Beskos, Boundary Element Methods in Elasto-dynamics (Unwin–Hyman, London, 1988).

[3] J. J. do Rego Silva, ''Acoustic and Elastic Wave Scattering using Boundary Elements,'' in Topics in Engineering Vol. 18, edited by C. A. Brebbia and J. J. Connor (Computational Mechanics Publications, Southampton, 1994), Chaps. 2, 3, pp. 7–68.

[4] W. L. Meyer, W. A. Bell, M. P. Stallybrass, and B. T. Zinn, ''Prediction of the sound field radiated from axisymmetric surfaces,'' J. Acoust. Soc. Am. 36, 631–638 (1979).

[5] A. F. Seybert, B. Soenarko, F. J. Rizzo, and D. J. Shippy, ''A special integral equation formulation for acoustic radiation and scattering for axisymmetric bodies and boundary conditions,'' J. Acoust. Soc. Am. **80**, 1241–1247 (1986).

[6] R. Martinez, ''A boundary integral formulation for thin-walled shapes of revolution,'' J. Acoust. Soc. Am. **87**, 523–531 (1990).

[7] A. Sarkissian, ''Radiation or scattering from multiple axisymmetric cylinders,'' J. Acoust. Soc. Am. **91**, 3121–3125 (1992).

[8] P. Juhl, ''An axisymmetric integral equation formulation for free space non-axisymmetric radiation and scattering of a known incident wave,'' J. Sound Vib. **163**(3), 397–406 (1993).

[9] B. Soenarko, ''A boundary element formulation for radiation of acoustic waves from axisymmetric bodies with arbitrary boundary conditions,'' J. Acoust. Soc. Am. **93**(2), 631–639 (1993).

[10] J. J. Grannel, J. J. Shirron, and L. S. Couchman, ''A hierarchic *p*-version boundary element method for axisymmetric acoustic scattering and radiation,'' J. Acoust. Soc. Am. **95**, 2320–2329 (1994).

[11] W. Wang, N. Atalla, and J. Nicolas, ''A boundary integral approach for acoustic radiation of axisymmetric bodies with arbitrary boundary conditions valid for all wave numbers,'' J. Acoust. Soc. Am. **101**(3), 1468–1478 (1997).

[12] A. H. W. M. Kuijpers, G. Verbeek, and J. W. Verheij, ''An improved acoustic Fourier boundary element method using fast Fourier transform integration,'' J. Acoust. Soc. Am. **102**, 1394–1401 (1997).

[13] G. Ozkan and Y. Mengi, ''On the use of FFT algorithm for the circumferential coordinate in boundary element formulation of axisymmetric problems,'' Int. J. Numer. Methods Eng. **40**, 2385–2412 (1997).

[14] J. W. Cooley and J. W. Tukey, ''An algorithm for the machine calculation of complex Fourier series,'' Math. Comput. **19**, 297–301 (1965).

[15] W. H. Press, S. A. Teukolsky, W. T. Vetterling, and B. P. Flannery, *Numerical Recipes in FORTRAN, The Art of Scientific Computing* (Cambridge U.P., Cambridge, 1994), 2nd ed.

[16] A. J. Burton and G. F. Miller, ''The application of integral equation methods to the solution of some exterior boundary-value problem,'' Proc. R. Soc. London, Ser. A **323**, 201–210 (1971).

[17] M. Guiggiani, G. Krishnasamy, T. J. Rudolphi, and F. J. Rizzo, ''A General Algorithm for the Numerical Solution of Hypersingular Boundary Integral Equations,'' J. Appl. Mech. **59**, 604–614 (1992).

[18] S. V. Tsinopoulos, S. E. Kattis, and D. Polyzos, ''An advanced BE/FFT methodology for solving electromagnetic wave scattering problems with axisymmetric dielectric particles,'' Engineering Analysis with Boundary Elements (accepted for publication).

[19] S. V. Tsinopoulos, S. E. Kattis, D. Polyzos, and D. E. Beskos, ''An advanced Boundary Element Method for axisymmetric elastodynamic analysis,'' Comput. Meth. Appl. Mech. Eng. (accepted for publication).

[20] *IMSL, IMSL Math/Library User's Manual*, Version 3.0 (Visual Numerics, Inc., Houston, TX, 1994).

[21] H. C. Wang and P. K. Banerjee, ''Generalized axisymmetric elastodynamic analysis by boundary element method,'' Int. J. Numer. Methods Eng. **30**, 115–131 (1990).

[22] C. Patterson and M. A. Sheikh, ''Interelement continuity in the Boundary Element Method,'' in *Topics in Boundary Element Research Vol. I*, edited by C. A. Brebbia (Springer-Verlag, Berlin, 1984), Chap. 6, pp. 123–141.

[23] J. Hadamard, *Lectures on Cauchy's Problem in Linear Partial Differential Equations* (Dover, New York, 1952).

[24] S. Bu, ''Infinite Boundary Elements for the dynamic analysis of machine foundations,'' Int. J. Numer. Methods Eng. **40**, 3901–3917 (1997).

[25] E. Skudrzyk, *The Foundations of Acoustics* (Springer-Verlag, New York, 1971).

[26] A. Leitner, ''Diffraction of sound by a circular disk,'' J. Acoust. Soc. Am. **21**, 331–334 (1949).

Wave propagation in a viscoelastic medium containing fluid-filled microspheres

A. M. Baird and F. H. Kerr
*Defence Evaluation and Research Agency, Winfrith Technology Centre, Dorchester, Dorset DT2 8XJ,
United Kingdom*

D. J. Townend
*Defence Evaluation and Research Agency, Ively Road, Farnborough, Hampshire GU 14 0LX,
United Kingdom*

Effective medium techniques have been developed by many authors to model the acoustic propagation through layers of visco-elastic materials which contain fluid-filled or elastic cavities. This paper extends such work to the case of materials containing air-filled microspheres whose thin glassy shell separates the interior air from the surrounding polymer. Such composites have been found particularly useful in conditions of high hydrostatic loading where the presence of the reinforcing shells delays the onset of the hole collapse and the consequent degradation in the acoustic performance of the composite. In the present paper, a model is presented which includes the effect of shell wall thickness variability but excludes the depth dependency—the latter will be presented in a sequel. Theoretical predictions are compared with experimentally measured values of transmission loss for both stiff and soft polymer substrates and, in each case, good agreement with experimental data is shown. © *1999 Acoustical Society of America.* [S0001-4966(99)06203-7]

PACS numbers: 43.20.Gp, 43.20.Bi [DEC]

INTRODUCTION

Analytical theories of transmission phenomena are important for predicting the acoustic properties of novel anechoic materials, particularly those composites which are used in modern underwater sound applications. Typically, such materials are composed of an elastic or visco-elastic polymer into which air is introduced either by means of macrovoids (large, molded holes), microvoids (small air perforations, irregularly distributed), or in the form of microspheres (essentially microvoids which are separated from the matrix substrate by a thin glassy shell wall). They function principally by two means; first, by means of the scattering and absorption of energy by the inclusions and, second, by impedance principles whereby either the sound transmission can be significantly reduced by creating a large mismatch in the characteristic impedance at the boundary between adjacent media or reflectivity can be reduced by the close matching of the two impedances at the interfaces. By careful selection of the component materials, a multilayered structure can be designed to provide optimal performance in the required regime of interest while satisfying the appropriate constraints of cost, weight, thickness, and other relevant factors. For such design purposes, a reliable mathematical model of the acoustic performance is clearly fundamental.

Within the literature, countless papers have been published on acoustic and elastic wave propagation through materials containing inclusions. Very useful overviews of this work can be found in Refs. 1–3, each of which contains an extensive bibliography listing the most important contributions to the subject. Essentially, the papers can be divided into two categories: those concerned with scattering by a single inclusion and those attempting to characterize the composite scattering material (i.e., matrix and inclusions) by assigning some bulk properties to the medium and thereafter treating it as a uniform ''effective'' medium.

For spherical inclusions, much has been written on the scattering of a plane harmonic wave by an elastic, rigid, or fluid inclusion which is embedded in an elastic or fluid matrix; see, for example, Refs. 4 and 5. Extensions to a distribution of such inclusions can be found in Refs. 6–11 with many other references cited in the review papers mentioned earlier. Scattering by elastic shells has also been well researched, although, until recently, the published results were mainly confined to the ultrasonics literature concerning propagation through suspensions and emulsions (e.g., Refs. 12, 13) or to a single elastic shell in a fluid medium (e.g., Refs. 14, 15). Notable exceptions have been presented in Refs. 16–18 in which the scattering matrix was assumed to be elastic, and the multiple scattering by a distribution of scatterers was treated in the same manner as for the simpler spherical inclusions.

For a single spherical shell, though, the most comprehensive treatment is the all-encompassing study of Anson and Chivers[19] in which the matrix, shell, and inner core can be fluid or elastic and the model takes account of viscous and thermal effects in each of the constituent phases. This leads to a system of 12 simultaneous equations for the various wave coefficients to satisfy the requirements of continuity of normal and tangential velocities and stresses and of temperature and heat flux at the two surfaces of the shell. These are presented in the form of a matrix which is solved by Gaussian elimination methods after performing a number of algebraic manipulations to ensure numerical stability.

The present work is aimed at describing the main mechanisms associated with the scattering and transmission

process rather than presenting a far-reaching study in which the underlying physics are buried within the extremely detailed algebra. In particular, the contributions from thermal waves have been ignored since these are considered negligible for the types of material combinations considered here. The research has been developed primarily for predicting the performance of materials which could be used realistically for sonar applications and has recently been extended to take account of the various parameters which typically characterize the environment, i.e., temperature, depth, and ambient sound speed. This has been supported by a comprehensive testing program, involving small scale laboratory experiments and deep water trials carried out at sea. Such tests have enabled us to validate the modeling techniques which are presented in this paper and in its two sequels.

Essentially, an effective medium approach is taken in which the composite material is characterized by a homogeneous medium whose visco-elastic properties are determined from theoretical techniques depending on the overall geometry (e.g., thickness, void fraction, inclusion size, etc.) and knowledge of various parameters which describe the constituent parts (e.g., the shear modulus, density, and bulk modulus of each of the phases). Clearly, for materials containing microvoids or macrovoids, the geometry changes with depth as the cavities decrease in size and the layer becomes thinner and stiffer; for polymers containing microspheres, the pressure dependency is much more involved with the presence of the reinforcing shells resulting in a nonlinear change in performance as depth increases. Further, as is well known,[20] the frequency-dependent visco-elastic moduli in the matrix polymer vary with temperature. It is important, therefore, that these properties are all described accurately prior to their use in the acoustic propagation model.

The present paper is concerned only with the modeling of sound propagation through the various types of air-filled polymers; the constituent materials' properties and the geometry are assumed to have been determined *a priori*. Enhancements to incorporate pressure and temperature dependence will be described in the sequels. Further, since effective media techniques are now well established for polymers containing simple fluid-filled cavities and elastic inclusions (as discussed in the following section), the work concentrates on their application to shell-reinforced materials.

An initial model is described for the situation where the scatterers are identical; this can be considered as an extension of the single scattering theory developed by Gaunaurd and Überall[8] or of the multiple scattering approach of Varadan *et al.*[9] for simple spherical inclusions but with greater algebraic complexity caused by the presence of the shell walls. As with the theories in Refs. 8 and 9, and indeed in various other models, the techniques make use of the lowest order components of the field scattered by a single inclusion in a visco-elastic polymer. The model is then enhanced very easily to incorporate the case of a nonuniform distribution of inclusion sizes by averaging the scattering coefficients, taking account of an appropriate probability density function defined over all possible inclusion sizes.

I. EFFECTIVE MEDIUM SOLUTIONS

Problems involving the modeling of wave propagation in a cavity-filled medium are generally recognized as being impossible to solve analytically as infinite orders of rescattering would have to be considered along with the need to satisfy continuity conditions for stresses and displacements across each of the cavity boundaries when, in many cases, the exact location of each of the cavities (with respect to some chosen origin) is unknown. Often, however, the analysis can be simplified by replacing the composite medium by a homogeneous ''effective'' medium which can be characterized by an appropriate choice of effective parameters. In this way, the problem of predicting the transmission loss through a layer containing air-filled scatterers would be approximated by that of predicting the transmission of sound through a layer of homogeneous material, and the solution to this latter problem can be found in many standard textbooks, e.g., Ref. 21.

For a low concentration of sparsely distributed scatterers, when multiple scattering effects are negligible, single scattering approaches can often be used reliably. If the dimensions of the cavities are sufficiently small (e.g., where the cavities take the form of microvoids in a foam matrix) so that the resonant frequencies lie outwith the frequency band of interest, then a nonresonant model such as that of Kuster and Toksöz[7] can be employed. Otherwise, resonance effects should be included by means of a dynamic (frequency-dependent) model similar to that developed by Gaunaurd and Überall in Ref. 8. For higher void fractions, a multiple scattering approach must be used, for example, that of Waterman and Truell[10] which accounts for first orders of rescattering but not higher orders, or that developed more exactly by Varadan *et al.*[9] in which the effective wave numbers in the low frequency limit are obtained from simple dispersion relations using a *T*-matrix formulation to express the scattered field coefficients in terms of the exciting fields at each of the scatterers and hence to obtain the total field at any point within the matrix.

In effect, all of these models provide a means of obtaining a set of frequency-dependent estimates for ''averaged'' wave numbers and densities as a function of the material properties of the constituent media, the dimensions of the cavities, and the void fraction. The subsequent use of these averaged properties within a layered-medium model for wave propagation then yields frequency-dependent predictions for reflection and transmission coefficients which depend on the effective parameters as well as on the thickness of the individual layers and the angle of incidence of the incoming wave.

II. THE SINGLE INCLUSION PROBLEM

Since the ''many-inclusion'' problem depends intrinsically on the wave scattered by a single spherical inclusion which is embedded in a visco-elastic polymer, we shall consider the ''single-inclusion'' problem first. For this, the basic geometry is shown in Fig. 1 and represents the most general case.
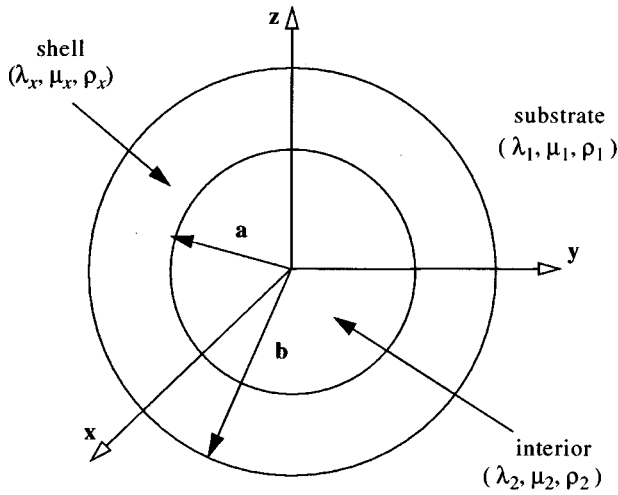
FIG. 1. The scattering geometry.

As shown, a spherical elastic shell of inner radius a and outer radius b contains an interior elastic core and is assumed to be embedded in a visco-elastic polymer. The three media are assumed to be isotropic and therefore can each be characterized by a pair of Lamé parameters (λ_i and μ_i) and by the material density ρ_i. In these, and in other expressions, the subscript 1 will denote the properties of the surrounding matrix substrate, the subscript x will describe the shell properties, and the subscript 2 will be used to describe the properties associated with the internal medium. Additionally, ϵ will denote the volume fraction of the shell, i.e., $\epsilon = (1 - a^3/b^3)$.

For the particular case of interest to acoustic materials designers, the central core is air, the shell is formed from a polymer in its glassy regime (i.e., $|\lambda_1| \sim |\mu_1|$), and the substrate is typically a polymer which is operating in its rubbery regime (i.e., $|\lambda_1| \gg |\mu_1|$). For the sake of completeness, however, the most general case will be investigated in detail, the simpler case of fluid-filled shells can be derived from the resulting analysis by setting the shear modulus in the core equal to zero.

If we assume that the motion is sinusoidal with time dependence of the form $e^{-i\omega t}$, then the field equations for linear visco-elasticity are defined by the Kelvin–Voigt model as

$$(\lambda + 2\mu)\nabla\nabla\cdot\mathbf{u} - \mu\nabla\times\nabla\times\mathbf{u} = -\rho\omega^2\mathbf{u}, \tag{1}$$

where λ and μ are the complex Lamé parameters of the visco-elastic medium, ρ is the density, ω is the angular frequency, and $\mathbf{u}$ denotes the displacement. As is customary in the solution of elastic problems, $\mathbf{u}$ is expressed in terms of a scalar potential ϕ representing longitudinal (i.e., compressional) motion and a vector potential $\mathbf{\Psi}$ which represents the shear component of the motion so that

$$\mathbf{u} = \nabla\phi + \nabla\times\mathbf{\Psi}. \tag{2}$$

The two potentials satisfy the scalar and vector Helmholtz equations

$$\nabla^2\phi + k_d^2\phi = 0; \quad k_d = \omega/c_d; \quad c_d^2 = (\lambda + 2\mu)/\rho \tag{3}$$

and

$$\nabla^2\mathbf{\Psi} + k_s^2\mathbf{\Psi} = 0; \quad k_s = \omega/c_s; \quad c_s^2 = \mu/\rho. \tag{4}$$

Further, for the spherical geometry, the vector potential can be written in terms of the two scalar Debye potentials ψ and χ as

$$\mathbf{\Psi} = r\psi\mathbf{e}_r + \nabla\times(r\chi\mathbf{e}_r), \tag{5}$$

the $\mathbf{e}_r$ denoting the unit basis vector in the radial direction.[22] Substitution into Eq. (4) illustrates that ψ and χ satisfy the scalar wave equation with wave number k_s.

The incident field is now assumed to be a plane dilatational wave which propagates along the z axis with a corresponding scalar potential given by

$$\phi_{\text{inc}} = \phi_0 e^{i(k_{d1}z - \omega t)}$$

$$= \phi_0 e^{-i\omega t}\sum i^n(2n+1)j_n(k_{d1}r)P_n(\cos\theta), \tag{6}$$

where the Rayleigh expansion has been used to express the field in terms of orthogonal spherical harmonics and k_{d1} is the longitudinal wave number in the substrate (using the subscript convention described earlier). This incident wave excites compressional and shear motions in both the shell and the interior medium and also results in scattered waves of both types within the substrate itself.

The various wave potentials may be expressed in terms of spherical Bessel functions and Legendre polynomials in the usual way. In the interior of the inclusion, only Bessel functions of the first kind are permitted because of the requirement for finiteness at the origin. In the far field, the radiation condition dictates that the scattered potentials contain only spherical Hankel functions of the first kind, corresponding to outgoing waves. Finally, in the shell, there are no restrictions and the fields are therefore linear combinations of spherical Bessel functions of the first and second kind. A complete description of these is given below where the A_n to H_n are constants which are uniquely determined by the boundary conditions. It should be noted that the ψ component of shear is not present because of the requirement for azimuthal symmetry:

$$\phi_{\text{inc}} = \phi_0 e^{-i\omega t}\sum i^n(2n+1)j_n(k_{d1}r)P_n(\cos\theta), \tag{7}$$

$$\phi_{\text{sc}} = \phi_0 e^{-i\omega t}\sum i^n(2n+1)A_n h_n(k_{d1}r)P_n(\cos\theta), \tag{8}$$

$$\chi_{\text{sc}} = \phi_0 e^{-i\omega t}\sum i^n(2n+1)B_n h_n(k_{s1}r)P_n(\cos\theta), \tag{9}$$

$$\phi_x = \phi_0 e^{-i\omega t}\sum i^n(2n+1)[E_n j_n(k_{dx}r)$$
$$+ F_n n_n(k_{dx}r)]P_n(\cos\theta), \tag{10}$$

$$\chi_x = \phi_0 e^{-i\omega t}\sum i^n(2n+1)[G_n j_n(k_{sx}r)$$
$$+ H_n n_n(k_{sx}r)]P_n(\cos\theta), \tag{11}$$

$$\phi_2 = \phi_0 e^{-i\omega t} \sum i^n (2n+1) C_n j_n(k_{d2} r) P_n(\cos\theta), \quad (12)$$

$$\chi_2 = \phi_0 e^{-i\omega t} \sum i^n (2n+1) D_n j_n(k_{s2} r) P_n(\cos\theta). \quad (13)$$

Given the azimuthal symmetry, a complete set of boundary conditions are obtained from the continuity of the radial and tangential components of the displacement (u_r and u_θ) and the continuity of the normal components of radial and tangential stress (τ_{rr} and $\tau_{r\theta}$) at the interior and exterior shell radii. In applying these boundary conditions, the stress and displacement components are given in terms of the Debye potentials as

$$u_r = \frac{\partial}{\partial r}\left(\phi + \frac{\partial}{\partial r}(r\chi)\right) + k_s^2 r\chi, \quad (14)$$

$$u_\theta = \frac{1}{r}\frac{\partial}{\partial\theta}\left(\phi + \frac{\partial}{\partial r}(r\chi)\right), \quad (15)$$

$$\tau_{rr} = -\lambda k_d^2 \phi + 2\mu\frac{\partial}{\partial r}\left[\frac{\partial}{\partial r}\left(\phi + \frac{\partial}{\partial r}(r\chi)\right) + k_s^2 r\chi\right], \quad (16)$$

$$\tau_{r\theta} = \mu\frac{\partial}{\partial\theta}\left[2\frac{\partial}{\partial r}\frac{1}{r}\left(\phi + \frac{\partial}{\partial r}(r\chi)\right) + k_s^2\chi\right]. \quad (17)$$

The resulting eight simultaneous equations can be written conveniently in matrix form as

$$
\begin{bmatrix}
d_{11}^{(n)} & d_{12}^{(n)} & d_{13}^{(n)} & d_{14}^{(n)} & d_{15}^{(n)} & d_{16}^{(n)} & d_{17}^{(n)} & d_{18}^{(n)} \\
d_{21}^{(n)} & d_{22}^{(n)} & d_{23}^{(n)} & d_{24}^{(n)} & d_{25}^{(n)} & d_{26}^{(n)} & d_{27}^{(n)} & d_{28}^{(n)} \\
d_{31}^{(n)} & d_{32}^{(n)} & d_{33}^{(n)} & d_{34}^{(n)} & d_{35}^{(n)} & d_{36}^{(n)} & d_{37}^{(n)} & d_{38}^{(n)} \\
d_{41}^{(n)} & d_{42}^{(n)} & d_{43}^{(n)} & d_{44}^{(n)} & d_{45}^{(n)} & d_{46}^{(n)} & d_{47}^{(n)} & d_{48}^{(n)} \\
d_{51}^{(n)} & d_{52}^{(n)} & d_{53}^{(n)} & d_{54}^{(n)} & d_{55}^{(n)} & d_{56}^{(n)} & d_{57}^{(n)} & d_{58}^{(n)} \\
d_{61}^{(n)} & d_{62}^{(n)} & d_{63}^{(n)} & d_{64}^{(n)} & d_{65}^{(n)} & d_{66}^{(n)} & d_{67}^{(n)} & d_{68}^{(n)} \\
d_{71}^{(n)} & d_{72}^{(n)} & d_{73}^{(n)} & d_{74}^{(n)} & d_{75}^{(n)} & d_{76}^{(n)} & d_{77}^{(n)} & d_{78}^{(n)} \\
d_{81}^{(n)} & d_{82}^{(n)} & d_{83}^{(n)} & d_{84}^{(n)} & d_{85}^{(n)} & d_{86}^{(n)} & d_{87}^{(n)} & d_{88}^{(n)}
\end{bmatrix}
\begin{bmatrix}
A_n \\ B_n \\ C_n \\ D_n \\ E_n \\ F_n \\ G_n \\ H_n
\end{bmatrix}
$$

$$
= \begin{bmatrix}
r_1^{(n)} \\ r_2^{(n)} \\ r_3^{(n)} \\ r_4^{(n)} \\ r_5^{(n)} \\ r_6^{(n)} \\ r_7^{(n)} \\ r_8^{(n)}
\end{bmatrix}, \quad (18)
$$

where the matrix elements are listed in the Appendix. For the zeroth order coefficients, only the four equations expressing the continuity of u_r and τ_{rr} at the interfaces are needed, resulting in a 4×4 system for the coefficients A_0, C_0, E_0, and F_0. These and the general nth order terms can then be found by applying Cramer's rule.

For most applications, we are interested in the case where the wavelength of the various modes is long compared to the dimensions of the microspheres. Under these circumstances, the scattering coefficients may be approximated by replacing each of the terms in the matrix system by their low frequency asymptotic expansions. With the exception of the zeroth order term, resonance effects in the A_n coefficients will be assumed to occur at sufficiently high frequencies to allow only the first nonvanishing terms in the corresponding expressions to be significant. However, it is known that the A_0 coefficient can exhibit monopole resonances at low frequencies, so additional terms have been retained here.

Assuming that the shell fraction ϵ is small, low frequency expansions for the first three scattering coefficients are given by

$$A_0 = \left(\frac{y_{d1}^3}{3i}\right)\frac{\alpha_1 - \dfrac{y_{d1}^2}{10}\alpha_2 - \dfrac{x_{d2}^2}{10}\alpha_3 - \dfrac{y_{dx}^2}{9}\epsilon\left(K_x + \dfrac{4}{3}\mu_x\right)}{\beta_1 + \dfrac{y_{d1}^2}{2}\beta_2 - \dfrac{x_{d2}^2}{10}\beta_3 - \dfrac{y_{dx}^2}{9}\epsilon\left(K_x + \dfrac{4}{3}\mu_x\right)}; \quad (19)$$

$$A_1 = \left(\frac{y_{d1}^3}{9i}\right)\left[1 - \frac{\rho_x}{\rho_1}\epsilon - \frac{\rho_2}{\rho_1}(1-\epsilon)\right], \quad (20)$$

and

$$A_2 = \left(\frac{2y_{d1}^3}{9i}\right)\frac{\epsilon\alpha_{x,2}\left(\dfrac{\mu_x}{\mu_1} - 1\right) + (1-\epsilon)\alpha_{x,x}\left(\dfrac{\mu_2}{\mu_1} - 1\right)}{\epsilon\alpha_{x,2}\alpha_{1,x} + (1-\epsilon)\alpha_{x,x}\alpha_{1,2}}, \quad (21)$$

where the x_{mj} and y_{mj} are as given in the Appendix and

$$\alpha_1 = K_2 - K_1 + \epsilon\frac{(K_1 + \frac{4}{3}\mu_x)}{(K_x + \frac{4}{3}\mu_x)}(K_x - K_2), \quad (22)$$

$$\beta_1 = K_2 + \frac{4}{3}\mu_1 + \frac{4}{3}\epsilon\frac{(\mu_x - \mu_1)}{(K_x + \frac{4}{3}\mu_x)}(K_x - K_2), \quad (23)$$

$$\alpha_2 = K_2 - \frac{5}{3}K_1 - \frac{8}{9}\mu_1$$
$$+ \epsilon\frac{(\frac{5}{3}K_1 + \frac{4}{3}\mu_x + \frac{8}{9}\mu_1)}{(K_x + \frac{4}{3}\mu_x)}(K_x - K_2), \quad (24)$$

$$\beta_2 = (1 + \tfrac{2}{3}iy_{d1})$$
$$\times\left[K_2 + \frac{4}{3}\mu_1 + \frac{4}{3}\epsilon\frac{(\mu_x - \mu_1)}{(K_x + \frac{4}{3}\mu_x)}(K_x - K_2)\right]$$
$$- \frac{2}{3}(1 + iy_{d1})\left[K_1 + \frac{4}{3}\mu_1 - \epsilon\frac{(K_1 + \frac{4}{3}\mu_1)}{(K_x + \frac{4}{3}\mu_x)}\right.$$
$$\times (K_x - K_2)\right], \quad (25)$$

$$\alpha_3 = \frac{5}{3}K_2 - K_1 + \frac{8}{9}\mu_2 + \epsilon\frac{(K_1 + \frac{4}{3}\mu_x)}{(K_x + \frac{4}{3}\mu_x)}$$
$$\times (K_x - \frac{5}{3}K_2 - \frac{8}{9}\mu_x), \quad (26)$$

$$\beta_3 = \frac{5}{3}K_2 + \frac{4}{3}\mu_1 + \frac{8}{9}\mu_2 + \frac{4}{3}\epsilon\frac{(\mu_x - \mu_1)}{(K_x + \frac{4}{3}\mu_x)}$$

$$\times (K_x - \frac{5}{3}K_2 - \frac{8}{9}\mu_2), \tag{27}$$

$$\alpha_{m,n} = \frac{4}{3}\left(\frac{9K_m}{8\mu_m} + 1\right) + \frac{\mu_n}{\mu_m}\left(\frac{K_m}{\mu_m} + 2\right), \tag{28}$$

with K_m denoting the bulk modulus for the different materials. The frequency-dependent terms in A_0 enable that coefficient to be compared directly with the corresponding term in the work of Gaunaurd and Überall[8] for elastic inclusions in a visco-elastic medium. Therefore the scattering model described in the following section is properly established as an extension of that theory.

III. THE MULTIPLE SPHERE PROBLEM: GU TYPE APPROACH

As discussed in the Introduction, there are various techniques for constructing a homogenized medium to represent the matrix-plus-inclusions composite within much wider and more intricate modeling scenarios. The model developed by Gaunaurd and Überall[8] (GU) offers a simple approach for spherical scatterers which can easily be extended to the microspheres problem.

Within the GU theory (itself an extension of the static modeling of Kuster and Toksöz[7] and Kerner[6]), a collection of N spherical scatterers are assumed to be contained inside a representative sphere V_0 of radius $R = R_0 b$ where b denotes the outer radius of the inclusions (which are all considered, initially, to be identical). The modelling objective is to replace V_0 by a sphere of homogeneous material whose parameters should be determined in such a way that under excitation by a plane longitudinal incident wave, the low frequency displacement field due to scattering by the single effective sphere should be approximately equal to that due to scattering by the original composite material of the same volume. The following assumptions are made:

(i) the inclusions are randomly distributed throughout V_0,
(ii) the observation point is sufficiently far from V_0 that the center of each inclusion can be regarded as being at the center of V_0,
(iii) multiple scattering effects are negligible so that the exciting field on each scatterer can be regarded as that produced by the original incident wave.

Clearly, condition (iii) holds only for a low concentration of scatterers.

In the case of identical scatterers of radius b, the third of the above conditions leads to the equation

$$\mathbf{u}^*(\mathbf{r}, \mathbf{r}_0) = N\mathbf{u}^{sc}(\mathbf{r}, \mathbf{r}_0), \tag{29}$$

where the left hand side is the field scattered by the effective sphere centred at $\mathbf{r}_0$ and $\mathbf{u}^{sc}$ is the field scattered by an inclusion which is assumed to be centred at $\mathbf{r}_0$. In agreement with condition (ii), we must also assume that the observation point $\mathbf{r}$ is far from V_0 so that $\mathbf{u}^*$ and $\mathbf{u}^{sc}$ can be represented by their far field asymptotic expansions.

From Eq. (8), it is easily deduced that the scattered dilatational potential can be approximated in the far field by

$$\mathbf{u}^{sc}(\mathbf{r}, \mathbf{r}_0) = \nabla\phi_{sc}, \tag{30}$$

where

$$\phi_{sc} = -i\phi_0\frac{e^{i(k_{d1}r - \omega t)}}{k_{d1}r}\sum (2n+1)A_nP_n(\cos\theta). \tag{31}$$

For the effective sphere, the scattering vector $\mathbf{u}^*$ can obviously be represented in the same way by

$$\mathbf{u}^*(\mathbf{r}, \mathbf{r}_0) = \nabla\phi^*, \tag{32}$$

where

$$\phi^* = -i\phi_0\frac{e^{i(k_{d1}r - \omega t)}}{k_{d1}r}\sum (2n+1)A_n^*P_n(\cos\theta). \tag{33}$$

In that expression, the effective scattering coefficients A_n^* can be obtained as a function of the matrix parameters and the (as yet undetermined) parameters of the effective medium by solving the system in Eq. (18) with the shell fraction set equal to 1, the two radii equal to R and the shell and interior parameters equal to the corresponding effective parameters K^*, μ^*, and ρ^*. Therefore, Eq. (29) becomes:

$$\sum (2n+1)A_n^*P_n(\cos\theta) \approx N\sum (2n+1)A_nP_n(\cos\theta). \tag{34}$$

Now, as has been described by others (e.g., Refs. 8 and 16), it is sufficient to consider only the first three terms in the partial wave expansions to extract the effective properties of interest. This is justifiable on physical grounds since these terms are proportional to the volume of the scattering object, whereas the higher order terms are negligible. Thus by termwise comparison of the two series in Eq. (34), we obtain

$$\tilde{A}_n^*(k_{d1}R_0b)^3 = N\tilde{A}_n(k_{d1}b)^3, \quad n = 0,1,2, \tag{35}$$

where $\tilde{A}_n^*$ and $\tilde{A}_n$ denote the coefficients of $(k_{d1}b)^3$ in A_n^* and A_n, respectively. Hence, upon noticing that

$$\phi = \frac{Nb^3}{R^3} \tag{36}$$

defines the volume concentration of scatterers in the volume V_0, we obtain the system

$$\tilde{A}_n^* = \phi\tilde{A}_n, \quad n = 0,1,2 \tag{37}$$

from which the three effective parameters are easily found. From knowledge of these, the complex effective wave numbers are obtained from the relationships

$$(k_d^*)^2 = \frac{\omega^2\rho^*}{K^* + \frac{4}{3}\mu^*} \quad \text{and} \quad (k_s^*)^2 = \frac{\omega^2\rho^*}{\mu^*}, \tag{38}$$

and then the real effective speeds and attenuation values follow from

$$k_d^* = \frac{\omega}{c_d^*} + i\alpha_d^* \quad \text{and} \quad k_s^* = \frac{\omega}{c_s^*} + i\alpha_s^*. \tag{39}$$

Note, incidentally, that although we have restricted the matching process to the scattered dilatational potential, the analogous equations which would arise from matching the shear coefficients B_1 and B_2 with those from the effective scattered shear wave are actually identical to lowest order in $k_{d1}b$ to those obtained in Eq. (37). (There is no B_0 term.) The same equations arise for the case of an incident shear wave although, again, we have no monopole term. We may conclude therefore that all of the required effective parameters can be obtained from Eq. (37) and that the corresponding results for incident and effective shear waves are in complete agreement with those found in the following paragraphs.

A. The monopole term A_0

From the first of the equations in Eq. (37), we obtain

$$\frac{K^* - K_1}{K^* + \frac{4}{3}\mu_1} = \phi \frac{\alpha_1 - \frac{y_{d1}^2}{10}\alpha_2 - \frac{x_{d2}^2}{10}\alpha_3 - \frac{y_{dx}^2}{9}\epsilon\left(K_x + \frac{4}{3}\mu_x\right)}{\beta_1 + \frac{y_{d1}^2}{2}\beta_2 - \frac{x_{d2}^2}{10}\beta_3 - \frac{y_{dx}^2}{9}\epsilon\left(K_x + \frac{4}{3}\mu_x\right)}, \tag{40}$$

which completely specifies the bulk modulus. Note that, when the scattering medium is very large as in the present case, the frequency-dependent terms in the approximation of $\widetilde{A}_0^*$ may be neglected since the resonances in the effective sphere can then be considered as fictitious. (This point has been justified on physical grounds by Gaunaurd in Ref. 8 and is acceptable on mathematical grounds also since, when the radius of the effective sphere is sufficiently large, the cubic approximations to the spherical Bessel functions are no longer of higher accuracy than their ''static'' values.)

For the case of air-filled glassy inclusions in a rubbery matrix, the expression for K^* simplifies and can be approximated by

$$K^* = \frac{K_1^R\left[1 - \phi + \frac{3K_2^R}{4\mu_1^R} \frac{\mu_x^R}{\mu_1^R}\epsilon' - \left(\frac{\omega}{\omega_{mbt}}\right)^2 - i\Delta_0\right]}{1 + \left(\frac{3K_2^R}{4\mu_1^R} \frac{\mu_x^R}{\mu_1^R}\epsilon'\right)(1-\phi) + \frac{3K_1^R}{4\mu_1^R}\phi(1-\epsilon') - \left(\frac{\omega}{\omega_{mbt}}\right)^2\left[1 + \frac{\phi}{2}\left(1 + \frac{3\rho_2 K_1^R}{5\rho_1 K_2^R}\right)\right] - i\Delta_1}, \tag{41}$$

where ϵ' is the reduced volume fraction of the shell given by

$$\epsilon' = \frac{\epsilon K_x^R}{K_x^R + \frac{4}{3}\mu_x^R} \tag{42}$$

and the superscript R denotes that the real part of the complex modulus should be used. The damping terms Δ_0 and Δ_1 are defined by

$$\Delta_0 = \left(\frac{\omega}{\omega_{mbt}}\right)^2\frac{\omega}{\omega_k} + \delta_1(1-\phi) + \delta_x\frac{\mu_x^R}{\mu_1^R}\epsilon' \tag{43}$$

and

$$\Delta_1 = \left(\frac{\omega}{\omega_{mbt}}\right)^2\frac{\omega}{\omega_k} + \delta_1 + \delta_x\frac{\mu_x^R}{\mu_1^R}\epsilon'(1-\phi), \tag{44}$$

where δ_1 and δ_x denote the loss tangents for the matrix substrate and the shell, respectively, and ω_{mbt} is the familiar Meyer–Brendel–Tamm resonance frequency given by

$$\omega_{mbt} = \frac{2}{b}\sqrt{\frac{\mu_1^R}{\rho_1}}. \tag{45}$$

Finally, ω_k is a constant defined by

$$\omega_k = \frac{1}{b}\sqrt{\frac{K_1^R}{\rho_1}}, \tag{46}$$

which has no physical significance in this context.

In constructing the above expression for K^*, we have cast the result in a form based on the static modulus derived by Kerner[6] but with additional frequency and damping terms. Inspection reveals that the main effect of the shell is a stiffening of the composite through terms proportional to $\epsilon'\mu_x^R/\mu_1^R$. In fact, apart from some changes to the damping constant, the effect of the shell is equivalent to increasing the air pressure by an amount proportional to $4\epsilon'\mu_x^R/3$.

Finally, it is worth remarking that the static bulk modulus for this composite material is a by-product of these calculations which is given by

$$K^* = \frac{K_1^R\left[1 - \phi + \frac{3K_2^R}{4\mu_1^R} \frac{\mu_x^R}{\mu_1^R}\epsilon'\right]}{1 + \left(\frac{3K_2^R}{4\mu_1^R} \frac{\mu_x^R}{\mu_1^R}\epsilon'\right)(1-\phi) + \frac{3K_1^R}{4\mu_1^R}\phi(1-\epsilon')}. \tag{47}$$

B. The dipole term A_1

The second equation in Eq. (37), i.e., the $n=1$ case, leads to the expression

$$1 - \frac{\rho^*}{\rho_1} = \phi\left[1 - \frac{\rho_x}{\rho_1}\epsilon - \frac{\rho_2}{\rho_1}(1-\epsilon)\right] \tag{48}$$

from which the effective density is readily obtained as

$$\rho^* = \rho_1 + \phi[\rho_1 - \rho_x \epsilon - \rho_2(1-\epsilon)]. \tag{49}$$

Examination of this expression indicates that the effective density is determined by a law of mixtures applied to the constituent parts including the shell.

C. The quadrupole term A_2

Finally, the $n=2$ case in Eq. (37) leads to the expression

$$
\frac{6\mu_1\left(\dfrac{\mu^*}{\mu_1}-1\right)}{6\dfrac{\mu^*}{\mu_1}(K_1+2\mu_1)+(9K_1+8\mu_1)}
$$

$$
= \phi\frac{\epsilon\alpha_{x,2}\left(\dfrac{\mu_x}{\mu_1}-1\right)+(1-\epsilon)\alpha_{x,x}\left(\dfrac{\mu_2}{\mu_1}-1\right)}{\epsilon\alpha_{x,2}\alpha_{1,x}+(1-\epsilon)\alpha_{x,x}\alpha_{x,2}} \tag{50}
$$

from which the complex effective shear modulus is easily obtained.

IV. THE MULTIPLE SPHERE PROBLEM: SIZE DISTRIBUTION

The above analysis was based on the assumption that the microspheres are identical in geometry; in practice, this is not generally true. Indeed, a sample of microspheres are likely to differ in volume as well as in shell thickness. So, since the dynamic properties derived earlier depend on the shell fraction and volume, the effective medium solutions must be enhanced to account for this variability.

Consider the case of an arbitrary distribution of inclusions where the number of inclusions per unit volume with outer radius b_i, inner radius a_j, and shell fraction $\epsilon_{i,j}=1-a_j^3/b_i^3$ is denoted by $n_{i,j}$. So the total concentration of microspheres is given by

$$\phi = \frac{4\pi}{3}\sum_{i,j} n_{i,j}b_i^3 = \frac{4\pi}{3}b^3\sum_{i,j} n_{i,j}, \tag{51}$$

where b represents the average outer radius of the microspheres.

Next, consider the three multipoles described previously. The summation of these coefficients over the distribution of microspheres will contain a volume term proportional to b_i^3 and some function of the relative shell wall thickness $\epsilon_{i,j}$. So if we write $A_{n,i,j}$ to denote the scattering coefficient which is appropriate to the ijth microsphere, then Eq. (35) will become

$$\tilde{A}_n^*(k_{d1}R_0 b)^3 = V\sum_{i,j} n_{i,j}\tilde{A}_{n,i,j}(k_{d1}b_i)^3, \quad n=0,1,2, \tag{52}$$

where V is the volume of the effective sphere. Therefore

$$\tilde{A}_n^* = \frac{V}{(R_0 b)^3}\sum_{i,j} n_{i,j}\tilde{A}_{n,i,j}b_i^3 = \phi\tilde{A}_n, \quad n=0,1,2, \tag{53}$$

where the $\tilde{A}_n$ are now given by the averaged quantities

$$\tilde{A}_n = \frac{\sum_{i,j} n_{i,j}\tilde{A}_{n,i,j}b_i^3}{\sum_{i,j} n_{i,j}b_i^3}, \quad n=0,1,2. \tag{54}$$

So knowledge of the full distribution of shell thicknesses and radii is required for the most general case.

To simplify the above, we introduce a normalized size distribution function $\bar{n}_{i,j}$ defined by

$$\bar{n}_{i,j} = \frac{\dfrac{4\pi}{3}n_{i,j}b_i^3}{\phi} = \frac{\dfrac{4\pi}{3}n_{i,j}b_i^3}{\dfrac{4\pi}{3}b^3\Sigma_{i,j}n_{i,j}}. \tag{55}$$

Then Eq. (53) becomes

$$\tilde{A}_n^* = \phi\sum_{i,j} \bar{n}_{i,j}\tilde{A}_{n,i,j}, \quad n=0,1,2. \tag{56}$$

As before, the dipole and quadrupole terms $\tilde{A}_1$ and $\tilde{A}_2$ can be approximated by their static limits and the monopole term by a low frequency expansion. Then the dipole equation becomes

$$
1 - \frac{\rho^*}{\rho_1} = \phi\frac{\sum_{i,j} n_{i,j}b_i^3\left[1 - \dfrac{\rho_x}{\rho_1}\epsilon_{i,j} - \dfrac{\rho_2}{\rho_1}(1-\epsilon_{i,j})\right]}{\Sigma_{i,j}n_{i,j}b_i^3}
$$

$$
= \frac{4\pi}{3}\sum_{i,j} n_{i,j}b_i^3\left[1 - \frac{\rho_x}{\rho_1}\epsilon_{i,j} - \frac{\rho_2}{\rho_1}(1-\epsilon_{i,j})\right], \tag{57}
$$

which leads to the expression

$$\rho^* = \rho_1(1-\phi) + \rho_2\phi\sum_{i,j} \bar{n}_{i,j}(1-\epsilon_{i,j}) + \rho_x\phi\sum_{i,j} \bar{n}_{i,j}\epsilon_{i,j} \tag{58}$$

for the effective density. For the shear modulus, the appropriate equation becomes

$$
\frac{6\mu_1\left(\dfrac{\mu^*}{\mu_1}-1\right)}{6\dfrac{\mu^*}{\mu_1}(K_1+2\mu_1)+(9K_1+8\mu_1)} = \phi\sum_{i,j} \bar{n}_{i,j}M_{1,i,j}, \tag{59}
$$

where

$$
M_{1,i,j} = \frac{\epsilon_{i,j}\alpha_{x,2}\left(\dfrac{\mu_x}{\mu_1}-1\right)+(1-\epsilon_{i,j})\alpha_{x,x}\left(\dfrac{\mu_2}{\mu_1}-1\right)}{\epsilon_{i,j}\alpha_{x,2}\alpha_{1,x}+(1-\epsilon_{i,j})\alpha_{x,x}\alpha_{1,2}}. \tag{60}
$$

It is readily seen that, apart from in the normalized weighting terms $\bar{n}_{i,j}$, these volume averaged coefficients contain no dependence on the radii, only on the shell fraction.

For the monopole case, however, the analysis is more complicated as for the identical inclusions. Indeed, the equation for the bulk modulus is now given by

$$\frac{K^* - K_1}{K^* + \frac{4}{3}\mu_1} = \phi\sum_{i,j} \bar{n}_{i,j}M_{0,i,j}, \tag{61}$$

where

1533   J. Acoust. Soc. Am., Vol. 105, No. 3, March 1999

Baird *et al.*: Wave propagation in a viscoelastic medium   1533

$$M_{0,i,j}$$

$$= \frac{\alpha_{1,i,j} - \dfrac{y_{d1,i}^2}{10}\alpha_{2,i,j} - \dfrac{x_{d2,j}^2}{10}\alpha_{3,i,j} - \dfrac{y_{dx,i}^2}{9}\epsilon_{i,j}\left(K_x + \dfrac{4}{3}\mu_x\right)}{\beta_{1,i,j} + \dfrac{y_{d1,i}^2}{2}\beta_{2,i,j} - \dfrac{x_{d2,j}^2}{10}\beta_{3,i,j} - \dfrac{y_{dx,i}^2}{9}\epsilon_{i,j}\left(K_x + \dfrac{4}{3}\mu_x\right)},$$

$$(62)$$

the $\alpha_{m,i,j}$ and $\beta_{m,i,j}$ depending on the shell fraction and the normalized wave numbers on the radii.

Once again, knowledge of the effective parameters enables us to compute a pair of effective wave numbers which, together with the effective density, will provide a complete characterization of the effective medium.

Finally, in this section, we return to the case of air-filled inclusions in a visco-elastic polymer. Therefore, we shall set the $\epsilon_{i,j}$ equal to zero and the shell parameters equal to those of the interior with, clearly, $\mu_x = \mu_2 = 0$. Further, the void fraction will be given by Eq. (51) but with $\bar{n}_i \equiv \bar{n}_{i,j}$ describing a normalized distribution over all radii b_i.

Immediately, it is seen that Eq. (58) becomes

$$\rho^* = \rho_1(1-\phi) + \rho_2\phi\sum_i \bar{n}_i = \rho_1(1-\phi) + \rho_2\phi, \qquad (63)$$

so that the effective density depends only on the overall void fraction and not on the size distribution of the inclusions. Further, as the $M_{1,i,j}$ in Eq. (60) is also independent of radius, it follows from Eq. (59) that the effective shear modulus, given by

$$\frac{6\mu_1\left(\dfrac{\mu^*}{\mu_1} - 1\right)}{6\dfrac{\mu^*}{\mu_1}(K_1 + 2\mu_1) + (9K_1 + 8\mu_1)} = \frac{-6\mu_1\phi}{(9K_1 + 8\mu_1)}, \quad (64)$$

is also dependent on the overall air fraction only. However, the effective bulk modulus is now given by:

$$\frac{K^* - K_1}{K^* + \tfrac{4}{3}\mu_1} = \phi\sum_{i,j} \bar{n}_i M_{0,i}, \qquad (65)$$

where

$$M_{0,i} = \frac{\alpha_1 - \dfrac{y_{d1,i}^2}{10}\alpha_2 - \dfrac{y_{d2,i}^2}{10}\alpha_3}{\beta_1 + \dfrac{y_{d1,i}^2}{2}\beta_2 - \dfrac{y_{d2,i}^2}{10}\beta_3} \qquad (66)$$

and the α_j and β_j are given in Eqs. (22)–(27) with ϵ set equal to zero there. Therefore the effective bulk modulus (and, consequently, the effective longitudinal wave number) depends intrinsically upon the distribution of radius sizes.

Clearly, the results in this section provide an extension to the work of Gaunaurd and Barlow in Ref. 23 in which the visco-elasticity of the polymer matrix was modeled by interpreting the longitudinal and shear speeds in the matrix as being complex with the viscosity represented by the imaginary "loss factor." This is in every way compatible with the present derivation in which the dependence of the matrix wave numbers on complex moduli is assumed to be inherent in the Kelvin–Voigt equation (1).

V. THE MULTIPLE SPHERE PROBLEM: VARADAN APPROACH

As mentioned earlier, various other techniques have been developed for constructing a representative effective medium. One such model is that of Varadan et al.[9] which includes multiple scattering. In the case of inclusions which are small on a wavelength scale and which are largely air-filled, it has been found that this approach gives very similar results to the GU model described above.

A comprehensive account of the model derivation can be found in Ref. 9 and need not be repeated here. It is sufficient to note that at low frequency, the effective compressional and shear wave numbers are given by

$$\left(\frac{\tilde{k}_d}{k_{d1}}\right)^2 = \frac{(1 - 9\phi\tilde{A}_1 i)(1 - 3\phi\tilde{A}_0 i)\left[1 - \dfrac{9}{2}\phi i\tilde{A}_2\left(\dfrac{K_1}{\mu_1} + 2\right)\right]}{\left[1 + 15\phi i\tilde{A}_2(1 - 3\phi i\tilde{A}_0) - \dfrac{9}{2}\phi i\tilde{A}_2\left(\dfrac{K_1}{\mu_1} + 2\right)\right]}$$

$$(67)$$

and

$$\left(\frac{\tilde{k}_s}{k_{s1}}\right)^2 = \frac{(1 - 9\phi i\tilde{A}_1)\left[1 - \dfrac{9}{2}\phi i\tilde{A}_2\left(\dfrac{K_1}{\mu_1} + 2\right)\right]}{\left[1 + 6\phi i\tilde{A}_2\left(\dfrac{9K_1}{8\mu_1} + 1\right)\right]}, \qquad (68)$$

which, after routine algebraic manipulation, are shown to be identically equal to the complex effective wave numbers defined in Eq. (38). Therefore, if the effective density is defined as in Eq. (58) and the scattering coefficients as in Eq. (54), then the effective bulk modulus and shear modulus are obtained from the relations

$$\mu^* = \frac{\rho^*\omega^2}{(k_s^*)^2} \quad \text{and} \quad K^* + \frac{4\mu^*}{3} = \frac{\rho^*\omega^2}{(k_d^*)^2}, \qquad (69)$$

and thus the material is characterized exactly as before but without the need to define an effective sphere of indeterminate radius.

VI. EXPERIMENTAL RESULTS

As an illustration of the performance of the model, the predicted and measured acoustic properties of various composite materials were compared using stiff substrate and soft substrate samples as defined by their relative shear moduli. In the case of the stiff substrate material, various samples were fabricated using 5%, 9%, 13%, and 17% concentration (by volume) of microspheres to form a single 1-cm layer of the composite material in each case.

For the soft substrate, a single sample of thickness 2.5 cm was manufactured to contain a 10% (by volume) concentration of microspheres. Subsequent measurement using a parametric array system at the UK Defence Evaluation and

TABLE I. Physical constants for polymer-microspheres experimental samples.

		Stiff polymer	Soft polymer
Bulk modulus of substrate (Pa):		3×10^9	3×10^9
Density of substrate (kg/m³):		1090	935
Dynamic shear modulus coefficients:	$A0$	6.675 69	5.939 78
	$A1$	3.954×10^{-2}	2.6618×10^{-1}
	$A2$	9.39×10^{-3}	-3.613×10^{-2}
	$A3$	3.85×10^{-3}	4.1×10^{-3}
Dynamic loss tangent (tan delta) coefficients:	$B0$	9.792×10^{-2}	5.251×10^{-2}
	$B1$	5.9×10^{-4}	1.9374×10^{-1}
	$B2$	6.89×10^{-2}	-6.209×10^{-2}
	$B3$	-9.25×10^{-3}	8.19×10^{-3}
Bulk modulus of shell (Pa):		2.1×10^9	2.1×10^9
Density of shell (kg/m³):		1700	1700
Shear modulus of shell (Pa):		1.26×10^9	1.26×10^9
Loss tangent of shell:		0.1	0.1
Bulk modulus of air at 1 atm (Pa):		1.4×10^5	1.4×10^5
Density of air at 1 atm (kg/m³):		1.28	1.28
Average shell fraction:		2.5×10^{-2}	2.5×10^{-2}
Average outer shell radius (m):		5×10^{-5}	5×10^{-5}

Research Agency (DERA) furnished values of transmission loss over a range of frequencies from 5 to 130 kHz.

The physical properties of the matrix materials, including dynamic shear modulus and loss tangent—both derived from measurements taken on a Dynamical Mechanical Thermal Analyzer (DMTA)—are set out in Table I. Note that the frequency-dependent shear modulus and loss tangent coefficients were obtained by fitting a third order polynomial to the DMTA measurements which had been transformed to a frequency scale by the use of WLF (Williams–Landel–Ferry) shifting techniques as outlined in Ref. 20. Specifically, the moduli are given by:

$$\log \mu_1^R = A0 + A1 \times \log f + A2 \times (\log f)^2 + A3 \times (\log f)^3 \tag{70}$$

and

$$\delta_1 = B0 + B1 \times \log f + B2 \times (\log f)^2 + B3 \times (\log f)^3, \tag{71}$$

where f denotes the frequency in Hz.

For the purposes of this paper, and in order to illustrate the nature of the effect, a Rayleigh distribution function for the shell fraction chosen to be independent of the inclusion size has been assumed. Although chosen on heuristic grounds, initial measurements indicate that this distribution is not far from reality for the grade of microspheres used in the samples described here. The average shell wall fraction of the distribution was chosen to match the measured value shown in Table I. The distribution function is given by

$$n(\epsilon) = \frac{n_0 \pi \epsilon}{2 \bar{\epsilon}^2} \exp\left(-\frac{\pi}{4} (\epsilon/\bar{\epsilon})^2 \right). \tag{72}$$

For both materials, the model predictions were obtained from the effective wave numbers given in Eq. (38) where the effective moduli were approximated by their low frequency expansions as given in Eqs. (19)–(21). The accuracy of these expansions was checked by comparing the results to those calculated by numerical evaluation of the exact scattering coefficients, and excellent agreement was obtained in each case with the ''approximate'' parameters requiring much less computing time than the full numerical values.

Figures 2 to 5 display experimentally measured transmission loss values together with the model predictions for the stiff samples. As can been seen from the figures, the
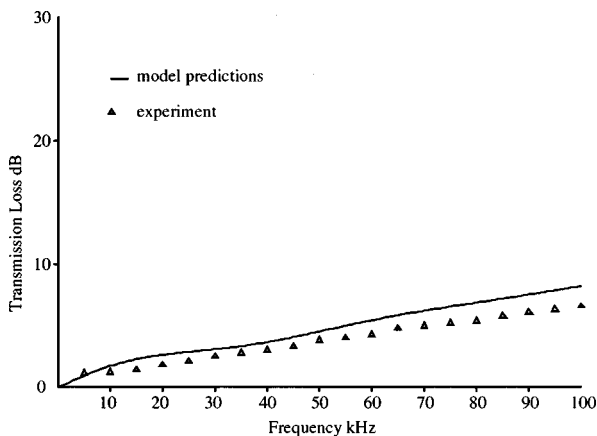
FIG. 2. Stiff substrate, 1 cm thick, with 5% microspheres.
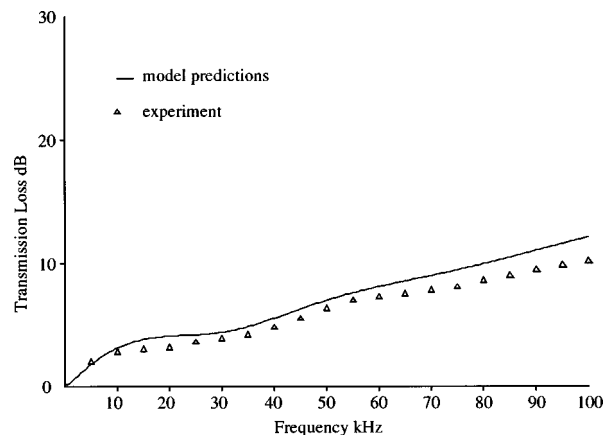
FIG. 3. Stiff substrate, 1 cm thick, with 9% microspheres.
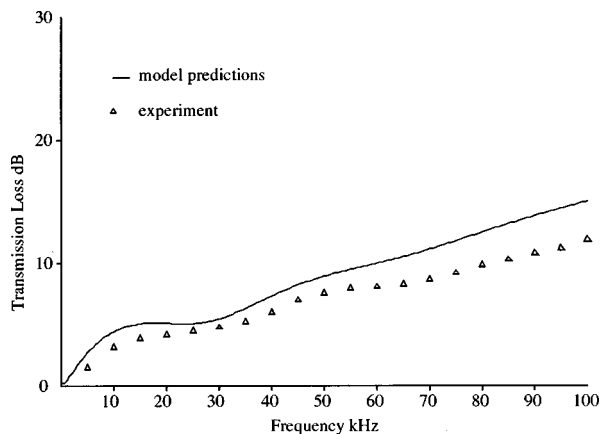
FIG. 4. Stiff substrate, 1 cm thick, with 13% microspheres.

FIG. 6. Soft substrate, 2.5 cm thick, with 10% microspheres.

comparison with measured values is good at all void fractions, particularly at frequencies of less than 40 kHz. There is a 2–3 dB discrepancy at higher frequencies which is probably due to the polynomial fit to the measured dynamic data being less accurate in this region. The magnitude of the discrepancy increases with void fraction; however, this is to be expected since the transmission loss gradually increases as the void fraction is increased and, as a consequence, the sample becomes more compliant.

Figure 6 presents the results for the soft polymer sample. For this material, the substrate polymer was chosen so that the dynamic shear modulus was typically around 10^6 Pa. With this value, terms of the form $\epsilon(\mu_x/\mu_1)$ dominate the denominators of the expressions for the monopole and quadrupole terms as set out in Eqs. (19) and (21). Consequently, the acoustic performance actually depends on the average of ϵ^{-1} rather than ϵ, thus emphasizing the importance of including the size variability in the model. Indeed, this is seen clearly in the figure where the model results are compared to those which would be generated by assuming that the shells are identical with a thickness equal to the average value given in Table I. Clearly, the predictions obtained by including the size distribution are much closer to the measured data. In particular, at the high frequency end, the results of the enhanced model are within a factor of 2 of the measured values, whereas, for the case of uniform shell size, the model

results underestimate the transmission loss by a factor of 10. Although more detailed data on the actual shell wall distribution would almost certainly improve the accuracy of the model predictions, it is fair to say that the current prediction is probably correct to within the limits of experimental error.

VII. SUMMARY AND CONCLUSIONS

Composite materials for sound reduction applications are often constructed by introducing a known volume of air-filled cavities into an elastic or visco-elastic polymer. Traditionally, this has been achieved through molding (to produce regular holes) or by gas-blowing (to generate an irregular distribution of tiny air-filled microvoids). More recently, however, successful materials have been developed by novel means through the introduction of glassy microspheres whose thin stiff shell separates the air from the surrounding polymer. These are particularly useful at depth where the presence of the reinforcing shells delays the onset of the performance degradation which is characteristic of all air-filled materials when exposed to hydrostatic loading.

Theoretical techniques have been developed elsewhere (Refs. 8 and 9) to model the acoustic propagation through visco-elastic materials containing fluid-filled or elastic cavities. This paper extends such work to the case of air-filled microspheres and presents a model which includes the effect of shell wall variability within the scattering approach. Model predictions are compared with experimentally measured values of transmission loss for both stiff and soft polymer substrates and, in each case, good agreement with experimental data is shown. The results confirm also that the effect of shell wall variability is important in the case of soft polymer substrates.

For materials design purposes, however, it is important to be able to predict the acoustic performance of such materials under the conditions in which they would most likely be used; for example, in various temperatures, depths, and sonar environments. As mentioned in the Introduction, the visco-elastic moduli vary as a function of temperature and the materials geometry changes with pressure. Indeed, it is their superior behavior at high pressures which gives recommendation to the shell-reinforced materials for use at depths

FIG. 5. Stiff substrate, 1 cm thick, with 17% microspheres.

where the simple air-filled materials would be ineffective due to total hole collapse.

The current work has recently been extended to incorporate such considerations. For example, a new approach to pressure-dependency modeling has recently been developed which extends the treatment of deformation for simple spherical holes so that predictions can be made of the depth-dependent behavior of a visco-elastic layer containing a distribution of microspheres. Further, a novel treatment of the temperature dependency has been formulated to provide an analytical means of generating frequency-dependent moduli without the need for the graphical manipulation techniques of the WLF approach in Ref. 20. Future papers will present the theoretical development and demonstrate the validity by comparisons with experimental data, thus providing a unified approach to the modeling of propagation through air-filled materials in arbitrary underwater environments.

APPENDIX

The components of the matrix system of Eq. (18) are listed below. For convenience, the notation for the wave numbers

$$y_{dm} = k_{dm}b; \quad x_{dm} = k_{dm}a; \quad y_{sm} = k_{sm}b; \quad x_{sm} = k_{sm}a$$

has been defined such that the m denotes the appropriate subscript corresponding to the matrix, the shell, or the interior medium:

$$d_{11}^{(n)} = y_{d1}h_n'(y_{d1}),$$

$$d_{12}^{(n)} = n(n+1)h_n(y_{s1}),$$

$$d_{13}^{(n)} = 0, \quad d_{14}^{(n)} = 0,$$

$$d_{15}^{(n)} = -y_{dx}j_n'(y_{dx}),$$

$$d_{16}^{(n)} = -y_{dx}n_n'(y_{dx}),$$

$$d_{17}^{(n)} = -n(n+1)j_n(y_{sx}),$$

$$d_{18}^{(n)} = -n(n+1)n_n(y_{sx}),$$

$$d_{21}^{(n)} = h_n(y_{d1}),$$

$$d_{22}^{(n)} = y_{s1}h_n'(y_{s1}) + h_n(y_{s1}),$$

$$d_{23}^{(n)} = 0, \quad d_{24}^{(n)} = 0,$$

$$d_{25}^{(n)} = -j_n(y_{dx}),$$

$$d_{26}^{(n)} = -n_n(y_{dx}),$$

$$d_{27}^{(n)} = -y_{sx}j_n'(y_{sx}) - j_n(y_{sx}),$$

$$d_{28}^{(n)} = -y_{sx}n_n'(y_{sx}) - n_n(y_{sx}),$$

$$d_{31}^{(n)} = \left[n(n+1) - \frac{y_{s1}^2}{2}\right]h_n(y_{d1}) - 2y_{d1}h_n'(y_{d1}),$$

$$d_{32}^{(n)} = n(n+1)[y_{s1}h_n'(y_{s1}) - h_n(y_{s1})],$$

$$d_{33}^{(n)} = 0, \quad d_{34}^{(n)} = 0,$$

$$d_{35}^{(n)} = -\frac{\rho_x}{\rho_1}\frac{y_{s1}^2}{y_{sx}^2}\left\{\left[n(n+1) - \frac{y_{sx}^2}{2}\right]\right.$$
$$\left. \times j_n(y_{dx}) - 2y_{dx}j_n'(y_{dx})\right\},$$

$$d_{36}^{(n)} = -\frac{\rho_x}{\rho_1}\frac{y_{s1}^2}{y_{sx}^2}\left\{\left[n(n+1) - \frac{y_{sx}^2}{2}\right]\right.$$
$$\left. \times n_n(y_{dx}) - 2y_{dx}n_n'(y_{dx})\right\},$$

$$d_{37}^{(n)} = -\frac{\rho_x}{\rho_1}\frac{y_{s1}^2}{y_{sx}^2}n(n+1)[y_{sx}j_n'(y_{sx}) - j_n(y_{sx})],$$

$$d_{38}^{(n)} = -\frac{\rho_x}{\rho_1}\frac{y_{s1}^2}{y_{sx}^2}n(n+1)[y_{sx}n_n'(y_{sx}) - n_n(y_{sx})],$$

$$d_{41}^{(n)} = y_{d1}h_n'(y_{d1}) - h_n(y_{d1}),$$

$$d_{42}^{(n)} = \left[n(n+1) - 1 - \frac{y_{s1}^2}{2}\right]h_n(y_{s1}) - y_{s1}h_n'(y_{s1}),$$

$$d_{43}^{(n)} = 0, \quad d_{44}^{(n)} = 0,$$

$$d_{45}^{(n)} = -\frac{\rho_x}{\rho_1}\frac{y_{s1}^2}{y_{sx}^2}[y_{dx}j_n'(y_{dx}) - j_n(y_{dx})],$$

$$d_{46}^{(n)} = -\frac{\rho_x}{\rho_1}\frac{y_{s1}^2}{y_{sx}^2}[y_{dx}n_n'(y_{dx}) - n_n(y_{dx})],$$

$$d_{47}^{(n)} = -\frac{\rho_x}{\rho_1}\frac{y_{s1}^2}{y_{sx}^2}\left\{\left[n^2 + n - 1 - \frac{y_{sx}^2}{2}\right]\right.$$
$$\left. \times j_n(y_{sx}) - y_{sx}j_n'(y_{sx})\right\},$$

$$d_{48}^{(n)} = -\frac{\rho_x}{\rho_1}\frac{y_{s1}^2}{y_{sx}^2}\left\{\left[n^2 + n - 1 - \frac{y_{sx}^2}{2}\right]\right.$$
$$\left. \times n_n(y_{sx}) - y_{sx}n_n'(y_{sx})\right\},$$

$$d_{51}^{(n)} = 0, \quad d_{52}^{(n)} = 0,$$

$$d_{53}^{(n)} = x_{d2}j_n'(x_{d2}),$$

$$d_{54}^{(n)} = n(n+1)j_n(x_{s2}),$$

$$d_{55}^{(n)} = -x_{dx}j_n'(x_{dx}), \quad d_{56}^{(n)} = -x_{dx}n_n'(x_{dx}),$$

$$d_{57}^{(n)} = -n(n+1)j_n(x_{sx}),$$

$$d_{58}^{(n)} = -n(n+1)n_n(x_{sx}),$$

$$d_{61}^{(n)} = 0, \quad d_{62}^{(n)} = 0,$$

$$d_{63}^{(n)} = j_n(x_{d2}),$$

$$d_{64}^{(n)} = x_{s2}j_n'(x_{s2}) + j_n(x_{s2}),$$

$$d_{65}^{(n)} = -j_n(x_{dx}),$$

$$d_{66}^{(n)} = -n_n(x_{dx}),$$

$$d_{67}^{(n)} = -x_{sx}j_n'(x_{sx}) - j_n(x_{sx}),$$

$$d_{68}^{(n)} = -x_{sx}n_n'(x_{sx}) - n_n(x_{sx}),$$

$$d_{71}^{(n)} = 0, \quad d_{72}^{(n)} = 0,$$

$$d_{73}^{(n)} = \left[n(n+1) - \frac{x_{s2}^2}{2} \right] j_n(x_{d2}) - 2x_{d2}j_n'(x_{d2}),$$

$$d_{74}^{(n)} = n(n+1)[x_{s2}j_n'(x_{s2}) - j_n(x_2)],$$

$$d_{75}^n = -\frac{\rho_x}{\rho_2} \frac{x_{s2}^2}{x_{sx}^2} \left\{ \left[n(n+1) - \frac{x_{sx}^2}{2} \right] \right.$$
$$\left. \times j_n(x_{dx}) - 2x_{dx}j_n'(x_{dx}) \right\},$$

$$d_{76}^{(n)} = -\frac{\rho_x}{\rho_2} \frac{x_{s2}^2}{x_{sx}^2} \left\{ \left[n(n+1) - \frac{x_{sx}^2}{2} \right] \right.$$
$$\left. \times n_n(x_{dx}) - 2x_{dx}n_n'(x_{dx}) \right\},$$

$$d_{77}^{(n)} = -\frac{\rho_x}{\rho_2} \frac{x_{s2}^2}{x_{sx}^2} n(n+1)[x_{sx}j_n'(x_{sx}) - j_n(x_{sx})],$$

$$d_{78}^{(n)} = -\frac{\rho_x}{\rho_2} \frac{x_{s2}^2}{x_{sx}^2} n(n+1)[x_{sx}n_n'(x_{sx}) - n_n(x_{sx})],$$

$$d_{81}^{(n)} = 0, \quad d_{82}^{(n)} = 0,$$

$$d_{83}^{(n)} = x_{d2}j_n'(x_{d2}) - j_n(x_{d2}),$$

$$d_{84}^{(n)} = \left[n(n+1) - 1 - \frac{x_{s2}^2}{2} \right] j_n(x_{s2}) - x_{s2}j_n'(x_{s2}),$$

$$d_{85}^{(n)} = -\frac{\rho_x}{\rho_2} \frac{x_{s2}^2}{x_{sx}^2} [x_{dx}j_n'(x_{dx}) - j_n(x_{dx})],$$

$$d_{86}^{(n)} = -\frac{\rho_x}{\rho_2} \frac{x_{s2}^2}{x_{sx}^2} [x_{dx}n_n'(x_{dx}) - n_n(x_{dx})],$$

$$d_{87}^{(n)} = -\frac{\rho_x}{\rho_2} \frac{x_{s2}^2}{x_{sx}^2} \left\{ \left[n^2 + n - 1 - \frac{x_{sx}^2}{2} \right] \right.$$
$$\left. \times j_n(x_{sx}) - x_{sx}j_n'(x_{sx}) \right\},$$

$$d_{88}^{(n)} = -\frac{\rho_x}{\rho_2} \frac{x_{s2}^2}{x_{sx}^2} \left\{ \left[n^2 + n - 1 - \frac{x_{sx}^2}{2} \right] \right.$$
$$\left. \times n_n(x_{sx}) - x_{sx}n_n'(x_{sx}) \right\},$$

$$r_1^{(n)} = -y_{d1}j_n'(y_{d1}),$$

$$r_2^{(n)} = -j_n(y_{d1}),$$

$$r_3^{(n)} = -\left\{ \left[n(n+1) - \frac{y_{s1}^2}{2} \right] j_n(y_{d1}) - 2y_{d1}j_n'(y_{d1}) \right\},$$

$$r_4^{(n)} = -[y_{d1}j_n'(y_{d1}) - j_n(y_{d1})],$$

$$r_5^{(n)} = 0, \quad r_6^{(n)} = 0, \quad r_7^{(n)} = 0, \quad r_8^{(n)} = 0.$$

[1] G. C. Gaunaurd, ''Elastic and acoustic resonance wave scattering,'' Appl. Mech. Rev. **42**, 143–192 (1989).

[2] A. L. Anderson and L. D. Hampton, ''Acoustics of gas-bearing sediments. I. Background,'' J. Acoust. Soc. Am. **67**, 1865–1889 (1980).

[3] Z. Hashin, ''Analysis of composite materials—A survey,'' J. Appl. Mech. **50**, 481–505 (1983).

[4] C. F. Ying and R. Truell, ''Scattering of a plane longitudinal wave by a spherical obstacle in an isotropically elastic fluid,'' J. Acoust. Soc. Am. **27**, 1086–1097 (1956).

[5] N. G. Einspruch and R. Truell, ''Scattering of a plane longitudinal wave by a spherical fluid obstacle in an elastic medium,'' J. Acoust. Soc. Am. **32**, 214–219 (1960).

[6] E. H. Kerner, ''The elastic and thermo-elastic properties of composite media,'' Proc. Phys. Soc. LXIX (8-B), 808–813 (1956).

[7] G. T. Kuster and M. N. Toksöz, ''Velocity and attenuation of seismic waves in two-phase media: part 1. Theoretical formulations,'' Geophysics **39**, 587–606 (1974).

[8] G. C. Gaunaurd and H. Überall, ''Resonance theory of the effective properties of perforated solids,'' J. Acoust. Soc. Am. **71**, 282–295 (1982).

[9] V. K. Varadan, Y. Ma, and V. V. Varadan, ''A multiple scattering theory for elastic wave propagation in discrete random media,'' J. Acoust. Soc. Am. **77**, 375–385 (1985).

[10] P. C. Waterman and R. Truell, ''Multiple scattering of waves,'' J. Math. Phys. **2**, 513–537 (1961).

[11] M. C. Davis, ''Attenuation of sound in highly concentrated suspensions and emulsions,'' J. Acoust. Soc. Am. **65**, 387–391 (1979).

[12] C. C. Church, ''The effects of an elastic solid surface layer on the radial pulsations of gas bubbles,'' J. Acoust. Soc. Am. **97**, 1510–1521 (1994).

[13] Z. Ye, ''On sound scattering and attenuation of Albunex® bubbles,'' J. Acoust. Soc. Am. **100**, 2011–2028 (1996).

[14] R. R. Goodman and R. Stern, ''Reflection and transmission of sound by elastic spherical shells,'' J. Acoust. Soc. Am. **31**, 338–344 (1962).

[15] G. C. Gaunaurd and A. Kalnins, ''Resonances in the sonar cross-sections of coated spherical shells,'' Int. J. Solids Struct. **18**, 1083–1102 (1982).

[16] A. K. Mal and S. K. Bose, ''Dynamic moduli of a suspension of imperfectly bonded spheres,'' Proc. Cambridge Philos. Soc. **76**, 587–600 (1974).

[17] M. C. Junger, ''Dilatational waves in an elastic solid containing lined, gas-filled spherical cavities,'' J. Acoust. Soc. Am. **69**, 1573–1576 (1981).

[18] S. K. Datta, H. M. Ledbetter, Y. Shindo, and A. H. Shah, ''Phase velocity and attenuation of plane elastic waves in a particle-reinforced composite medium,'' Wave Motion **10**, 171–182 (1988).

[19] L. W. Anson and R. C. Chivers, ''Ultrasonic scattering from spherical shells including viscous and thermal effects,'' J. Acoust. Soc. Am. **93**, 1687–1699 (1993).

[20] J. D. Ferry, *Viscoelastic Properties of Polymers* (Wiley, New York, 1961).

[21] L. Brekhovskikh, *Waves in Layered Media*, 2nd ed. (Academic, London, 1980).

[22] A. C. Eringen and E. S. Suhubi, *Elastodynamics: Vol. II, Linear Theory* (Academic, New York, 1975), pp. 719–720.

[23] G. C. Gaunaurd and J Barlow, ''Matrix viscosity and cavity-size distribution effects on the dynamic effective properties of perforated elastomers,'' J. Acoust. Soc. Am. **75**, 23–34 (1984).

Acoustic eigenfrequencies in a spheroidal cavity with a concentric penetrable sphere

Gerassimos C. Kokkorakis and John A. Roumeliotis[a)]
Department of Electrical and Computer Engineering, National Technical University of Athens,
Athens 15773, Greece

The acoustic eigenfrequencies f_{nsm} in a spheroidal cavity containing a concentric penetrable sphere are determined analytically, for both Dirichlet and Neumann conditions in the spheroidal boundary. Two different methods are used for the evaluation. In the first, the pressure field is expressed in terms of both spherical and spheroidal wave functions, connected with one another by well-known expansion formulas. In the second, a shape perturbation method, this field is expressed in terms of spherical wave functions only, while the equation of the spheroidal boundary is given in spherical coordinates. The analytical determination of the eigenfrequencies is possible when the solution is specialized to small values of $h = d/(2R_2)$, $(h \ll 1)$, with d the interfocal distance of the spheroidal boundary and $2R_2$ the length of its rotation axis. In this case exact, closed-form expressions are obtained for the expansion coefficients $g_{nsm}^{(2)}$ and $g_{nsm}^{(4)}$ in the resulting relation $f_{nsm}(h) = f_{ns}(0)[1 + h^2 g_{nsm}^{(2)} + h^4 g_{nsm}^{(4)} + O(h^6)]$. Analogous expressions are obtained with the use of the parameter $v = 1 - (R_2/R_2')^2$, $(|v| \ll 1)$, with $2R_2'$ the length of the other axis of the spheroidal boundary. Numerical results are given for various values of the parameters. © *1999 Acoustical Society of America.* [S0001-4966(99)05803-8]

PACS numbers: 43.20.Ks [ANN]

INTRODUCTION

Calculation of eigenfrequencies in acoustic cavities of various shapes is an important problem with many applications in room acoustics,[1] acoustic levitation[2,3] and high accuracy measurements of sound speed in gases.[4] The shape of the boundaries severely limits the possibility for analytical solution of such problems. For complicated geometries numerical techniques are used. Analytical, perturbational methods were used elsewhere, in order to obtain the acoustic eigenfrequencies in a spherical cavity with an eccentric inner sphere, for both Dirichlet and Neumann boundary conditions, in the case of small eccentricity between the two spheres,[5] or for a small inner sphere.[6,7] In spheroidal cavities calculation is more complex, due to the complexity of spheroidal functions. In Refs. 8 and 9 the eigenfrequencies of a prolate spheroidal cavity were calculated, for Dirichlet and Neumann boundary conditions, too. The same is valid also in Refs. 10 and 11 for concentric spheroidal–spherical cavities, by analytical, perturbational methods. In this last case not only the prolate but also the oblate spheroidal boundaries are examined.

In the present paper the acoustic cavity, shown in Fig. 1, is examined also for both Dirichlet and Neumann conditions in its spheroidal boundary, which has major and minor semi-axes R_2 and R_2', respectively, and interfocal distance d. It contains a concentric penetrable sphere with radius R_1. This cavity is a perturbation of the concentric spherical one with radii R_1 and R_2. Only the prolate spheroidal boundary is shown, but corresponding formulas for the oblate one are obtained immediately. The length of the rotation axis in each case is $2R_2$, while that of the other axis is $2R_2'$.

The acoustic eigenfrequencies in the former cavity are determined by two different methods. In the first of them the pressure field is expressed in terms of both spherical and spheroidal wave functions, while use is made of the well-known expansion formulas connecting these functions.[12] In the second method we use shape perturbation. In this case the pressure field is expressed in terms of spherical wave functions only, while the equation of the spheroidal boundary is given in spherical coordinates r and θ. In both cases, after the satisfaction of the boundary conditions, we obtain an infinite determinantal equation for the evaluation of the eigenfrequencies. In the special case of small $h = d/(2R_2)$, $(h \ll 1)$ we are led to an exact evaluation, up to the order h^4, for the elements of the infinite determinant and, finally, for the determinant itself. It is then possible to obtain the eigenfrequencies in the form $f_{nsm}(h) = f_{ns}(0)[1 + h^2 g_{nsm}^{(2)} + h^4 g_{nsm}^{(4)} + O(h^6)]$. The expansion coefficients $g_{nsm}^{(2)}$ and $g_{nsm}^{(4)}$ are independent of h and are given by exact, closed-form expressions, while $f_{ns}(0)$ are the eigenfrequencies of the corresponding spherical cavity with $h = 0$.

The main advantage of such an analytical solution lies in its general validity for each small value of h and for all modes, while numerical techniques require repetition of the evaluation for each different h, with accuracy deteriorating quickly for higher order modes.

Analogous expansions are obtained by using the parameter $v = 1 - (R_2/R_2')^2$, $(|v| \ll 1)$.

Our method can be applied also in the corresponding exterior (scattering) problem.

The cases of the Dirichlet and Neumann conditions in the spheroidal boundary are examined in Secs. I and II, re-

[a)]Electronic mail: iroumel@cc.ece.ntua.gr
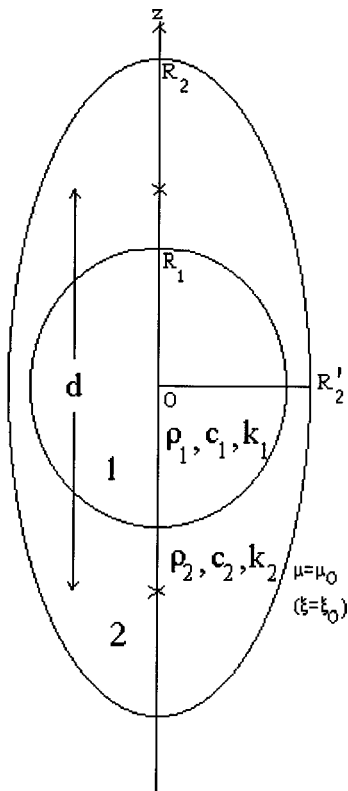
FIG. 1. Geometry of the cavity.

spectively. Finally, Sec. III includes numerical results and discussion.

I. DIRICHLET BOUNDARY CONDITIONS

As shown in Fig. 1, the density, the sound speed and the wave number are ρ_1, c_1, k_1 and ρ_2, c_2, k_2 inside the penetrable sphere (region 1) and between it and the spheroidal boundary (region 2), respectively. The materials of both regions are considered as fluids or fluidlike, i.e., they do not support shear waves.

Let p_1 and p_2 be the acoustic pressure fields in regions 1 and 2, respectively. These fields, which satisfy the scalar Helmholtz equation, have the following expressions:

$$p_1 = \sum_{n=0}^{\infty} \sum_{m=0}^{n} j_n(k_1 r) P_n^m(\cos \theta)[C_{nm} \cos m\varphi$$
$$+ D_{nm} \sin m\varphi], \tag{1}$$

$$p_2 = \sum_{n=0}^{\infty} \sum_{m=0}^{n} [j_n(k_2 r) - E_n n_n(k_2 r)] P_n^m(\cos \theta)$$
$$\times [A_{nm} \cos m\varphi + B_{nm} \sin m\varphi]. \tag{2}$$

In Eqs. (1), (2) r, θ, φ are the spherical coordinates with respect to O, j_n and n_n are the spherical Bessel functions of the first and second kind, respectively, and P_n^m is the associated Legendre function of the first kind.

By satisfying the boundary conditions at $r = R_1$

$$p_1 = p_2, \quad \frac{1}{\rho_1 c_1} \frac{\partial p_1}{\partial(k_1 r)} = \frac{1}{\rho_2 c_2} \frac{\partial p_2}{\partial(k_2 r)}, \tag{3}$$

and using the orthogonal relations for the associated Legendre[13] and the trigonometric functions we obtain the following expression for E_n

$$E_n = \frac{j_n(x_1) j_n'(w_1) - q j_n(w_1) j_n'(x_1)}{n_n(x_1) j_n'(w_1) - q j_n(w_1) n_n'(x_1)}, \tag{4}$$

where

$$w_1 = k_1 R_1, \quad x_1 = k_2 R_1, \quad q = \frac{\rho_1 c_1}{\rho_2 c_2}, \tag{5}$$

and the primes denote derivatives with respect to the argument.

In order to satisfy the remaining boundary condition $p_2 = 0$ at the spheroidal boundary, denoted by $\mu = \mu_0$, we follow two different methods. In the first of them we expand the spherical wave functions, appearing in Eq. (2), into concentric spheroidal ones by the formula[12]

$$z_n^{(\sigma)}(k_2 r) P_n^m(\cos \theta)$$

$$= \frac{2}{2n+1} \frac{(n+m)!}{(n-m)!} \sum_{\ell=m,m+1}^{\infty} {}' \frac{i^{\ell-n}}{N_{m\ell}}$$

$$\times d_{n-m}^{m\ell} S_{m\ell}(c,\eta) R_{m\ell}^{(\sigma)}(c,\xi), \quad c = k_2 d/2. \tag{6}$$

In Eq. (6) $\xi = \cosh \mu$, η are the spheroidal coordinates (φ is common in both systems), $z_n^{(\sigma)}$ ($\sigma = 1 - 4$) is the spherical Bessel function of any kind, $R_{m\ell}^{(\sigma)}$ is the corresponding radial spheroidal function of the same kind, $S_{m\ell}$ and $d_{n-m}^{m\ell}$ are the angular spheroidal function of the first kind and its expansion coefficients, while

$$N_{mn} = 2 \sum_{r=0,1}^{\infty} {}' \frac{(d_r^{mn})^2 (r+2m)!}{(2r+2m+1)r!}. \tag{7}$$

The prime over the summation symbols in Eqs. (6) and (7) indicates that when $n - m$ is even/odd these summations start with the first/second value of their summation index and continue only with values of the same parity with it.

We substitute from Eq. (6) into Eq. (2) satisfying the boundary condition $p_2 = 0$ at $\mu = \mu_0 (\xi = \xi_0)$ and we next use the orthogonal properties of the angular spheroidal[12] and the trigonometric functions, to obtain finally the following infinite set of linear homogeneous equations for the expansion coefficients A_{nm} (or B_{nm})

$$\sum_{n=m,m+1}^{\infty} {}' \alpha_{\ell nm} A_{nm} = 0, \quad \ell \geq m, m+1, \tag{8}$$

where

$$\alpha_{\ell nm} = \frac{2i^{-n}(n+m)!}{(2n+1)(n-m)!}$$

$$\times d_{n-m}^{m\ell} [R_{m\ell}^{(1)}(c, \cosh \mu_0) - E_n R_{m\ell}^{(2)}(c, \cosh \mu_0)]. \tag{9}$$

In Eqs. (8) and (9) ℓ and n are both even or odd, starting with that value of m or $m+1$, which has the same parity with them. So, Eq. (8) separates into two distinct subsets, one with ℓ, n even and the other with ℓ, n odd.

We next substitute $R_{m\ell}^{(1)}$ and $R_{m\ell}^{(2)}$ from Eq. (7) of Ref. 10 into Eq. (9) and set each one of the two determinants

$\Delta(\alpha_{\ell nm})$ (one with ℓ, n even and the other with ℓ, n odd) of the coefficients $\alpha_{\ell nm}$ in Eq. (8) equal to 0. So, we obtain two determinantal equations of the same form for the evaluation of the eigenfrequencies, which are treated simultaneously under the symbol $\Delta(\alpha_{\ell nm})$. By dividing $\alpha_{\ell nm}$ by the product $2i^{-n}\tanh^m\mu_0(d^{m\ell}_{\ell-m})^2(n+m)/[(2n+1)(n-m)!]$, as in Ref. 10, we do not change the roots of the determinantal equation. We next use the symbol $\alpha_{\ell n}$ for the resulting coefficient, deleting the subscript m for simplicity, and replace $c=k_2d/2$ by its equal one $c=x_2h$, where $x_2=c\cosh\mu_0=k_2R_2$ and $h=d/(2R_2)$. For large values of h the determinantal equation can be solved only numerically, but for small h ($h\ll1$) an analytical solution is possible. In this last case we can set up to the order h^4,

$$\alpha_{nn}=D^{(0)}_{nn}+h^2D^{(2)}_{nn}+h^4D^{(4)}_{nn}+O(h^6),$$

$$\alpha_{n\pm2,n}=h^2D^{(2)}_{n\pm2,n}+h^4D^{(4)}_{n\pm2,n}+O(h^6), \quad (10)$$

$$\alpha_{n\pm4,n}=h^4D^{(4)}_{n\pm4,n}+O(h^6).$$

Exact expressions for the various D's used in our calculations are given in Eqs. (A1)–(A5) of the Appendix.

Relations (10) allow a closed-form evaluation of the determinant $\Delta(\alpha_{\ell n})=\Delta(\alpha_{\ell nm})$, up to the order h^4, in steps exactly the same with those in Ref. 10, which will not be repeated here.

The resonant wave numbers $k_2=k_2(h)$, as well as $x_2=x_2(h)=k_2(h)R_2$ have also expansions of the form

$$k_2(h)=k^{(0)}_2+h^2k^{(2)}_2+h^4k^{(4)}_2+O(h^6), \quad (11)$$

$$x_2(h)=x^{(0)}_2+h^2x^{(2)}_2+h^4x^{(4)}_2+O(h^6),$$

$$x^{(\rho)}_2=k^{(\rho)}_2R_2, \quad \rho=0,2,4, \quad (12)$$

where $k^{(0)}_2\equiv k^0_2$ and $x^{(0)}_2\equiv x^0_2$ correspond to the concentric spherical cavity with radii R_1 and R_2 ($h=0$).

The expressions of $x^{(2)}_2$ and $x^{(4)}_2$ in terms of D's are exactly the same as in Ref. 10 and are given by the formulas

$$x^{(2)}_2=-\left[\frac{dD^0_{nn}(x^0_2)}{dx_2}\right]^{-1}D^{(2)}_{nn}(x^0_2), \quad (13)$$

$$x^{(4)}_2=-\left[\frac{dD^0_{nn}(x^0_2)}{dx_2}\right]^{-1}\left[\frac{(x^{(2)}_2)^2}{2}\frac{d^2D^0_{nn}(x^0_2)}{dx_2^2}+x^{(2)}_2\frac{dD^{(2)}_{nn}(x^0_2)}{dx_2}\right.$$

$$+D^{(4)}_{nn}(x^0_2)-\frac{D^{(2)}_{n+2,n}(x^0_2)D^{(2)}_{n,n+2}(x^0_2)}{D^0_{n+2,n+2}(x^0_2)}$$

$$\left.-\frac{D^{(2)}_{n,n-2}(x^0_2)D^{(2)}_{n-2,n}(x^0_2)}{D^0_{n-2,n-2}(x^0_2)}\right], \quad (14)$$

where $D^{(0)}_{nn}\equiv D^0_{nn}$. As it is evident from Eq. (8), the various subscripts in Eq. (10) and so also in Eqs. (13), (14) should be equal or greater than $m\geq0$. In the opposite case the corresponding α's and D's are equal to zero and so disappear.

In Eqs. (13) and (14) we have used the relations $x_1=\tau x_2$, $w_1=\tau x_2c_2/c_1$, where $\tau=R_1/R_2=$ constant, so x_2 is the only variable.

Formulas (13) and (14) are also valid for the oblate cavity, with the only difference that $D^{(2)}$'s change their signs

and R_2 is the minor semiaxis of the oblate boundary. So, $x^{(2)}_2$ changes its sign, while $x^{(4)}_2$ remains the same.

The eigenfrequencies for the problem of two concentric spheres with radii R_1 and R_2, used in Eqs. (13), (14), are given by the equation [Eq. (A1) in the Appendix] $D^0_{nn}=0$, or

$$\frac{j_n(x^0_2)}{n_n(x^0_2)}=E_n(x^0_2), \quad x^0_1=\tau x^0_2, \quad w^0_1=\tau x^0_2\frac{c_2}{c_1}, \quad \tau=\frac{R_1}{R_2}. \quad (15)$$

By using Eqs. (15), (A1), (A22) from the Appendix and the Wronskian[13] $j_n(x^0_2)n'_n(x^0_2)-j'_n(x^0_2)n_n(x^0_2)=1/(x^0_2)^2$, we obtain

$$\frac{dD^0_{nn}(x^0_2)}{dx_2}=-\frac{1}{(x^0_2)^2n_n(x^0_2)}-n_n(x^0_2)\frac{dE_n(w^0_1,x^0_1)}{dx_2}. \quad (16)$$

Equations (16) and (A2) substituted in (13) give $x^{(2)}_2$. The expression for $x^{(4)}_2$ is much more lengthy, but is obtained immediately from Eqs. (13), (14), (16), (A1)–(A5) and (A22)–(A24).

By setting Eq. (12) in the form $x_2(h)=x^0_2[1+h^2g^{(2)}+h^4g^{(4)}+O(h^6)]$ we obtain the eigenfrequencies in the cavity of Fig. 1 by the expression

$$f_{nsm}(h)=f_{ns}(0)[1+h^2g^{(2)}_{nsm}+h^4g^{(4)}_{nsm}+O(h^6)],$$

$$n=0,1,2,\ldots, \quad s=1,2,3,\ldots, \quad m=0,1,2,\ldots,n, \quad (17)$$

where $f_{ns}(0)=c_2(x^0_2)_{ns}/(2\pi R_2)$ are the eigenfrequencies of the concentric spherical cavity, $x^0_2=(x^0_2)_{ns}$ are the successive positive roots of Eqs. (15) and $g^{(2),(4)}=x^{(2),(4)}_2/x^0_2[g^{(2),(4)}_{nsm}=(x^{(2),(4)}_2)_{nsm}/(x^0_2)_{ns}]$.

We next apply the second method for the determination of the eigenfrequencies. This is a shape perturbation method with no use of spheroidal wave functions. Equations (1)–(5) are also valid in this case. In order to satisfy the remaining boundary condition $p_2=0$, at the spheroidal surface, we express the equation of this surface in terms of r and θ, as in Ref. 14

$$r=\frac{R_2}{\sqrt{1-v\sin^2\theta}}, \quad (18)$$

where[11]

$$v=1-\left(\frac{R_2}{R'_2}\right)^2=\mp h^2-h^4+O(h^6). \quad (19)$$

The upper/lower sign in Eq. (19) corresponds to the prolate ($v<0$)/oblate ($v>0$) spheroidal boundary.

We expand Eq. (18) into power series in h, thus obtaining up to the order h^4

$$r=R_2\left[1\mp\frac{h^2}{2}\sin^2\theta-\frac{h^4}{2}\sin^2\theta\left(1-\frac{3}{4}\sin^2\theta\right)+O(h^6)\right]. \quad (20)$$

By using Eq. (20) we get the following expansion[11] ($x_2=k_2R_2$):

$$j_n(k_2r) = j_n(x_2) \mp \frac{h^2}{2} x_2 j_n'(x_2) \sin^2\theta - \frac{h^4}{2} x_2 \sin^2\theta$$

$$\cdot \{ j_n'(x_2) - \tfrac{1}{4}[3j_n'(x_2) + x_2 j_n''(x_2)]\sin^2\theta \}$$

$$+ O(h^6), \tag{21}$$

and a similar one for $n_n(k_2r)$.

We next substitute the former expansions into Eq. (2) satisfying the boundary condition at the spheroidal surface and we use the orthogonal properties of the associated Legendre[13] and the trigonometric functions, concluding finally to the following infinite set of linear homogeneous equations for the expansion coefficients A_{nm} (or B_{nm}), up to the order h^4:

$$\alpha_{n-4,n}A_{n-4,m} + \alpha_{n-2,n}A_{n-2,m} + \alpha_{nn}A_{nm} + \alpha_{n+2,n}A_{n+2,m}$$

$$+ \alpha_{n+4,n}A_{n+4,m} = 0, \quad n \geq m. \tag{22}$$

The third subscript m is omitted from the various α's in Eq. (22), for simplicity. Their expressions are also given by the general expansions (10), but with different D's, which are given in Eqs. (A6)–(A9) of the Appendix. As it is evident from Eq. (2), the first subscripts of A's (and B's) should be always equal or greater than $m \geq 0$. In the opposite case A's (and B's) are equal to zero and disappear. The same is valid also for the corresponding α's and D's.

If m has the same/opposite parity with n, i.e., $n-m$ is even/odd, the first subscript of the α's in Eq. (22) starts from the minimum value $m/m+1$ and continues with the values $m+2/m+3$, $m+4/m+5$, etc. So, Eq. (22) separates into two distinct subsets, one with n even and the other with n odd. Setting each one of the determinants of the coefficients α, in these subsets, equal to zero, we obtain two determinantal equations of the same form for the evaluation of the eigenfrequencies, which are treated simultaneously. The rest steps are exactly the same as with the first method. So, Eqs. (11)–(17) are also valid here with identical final results as in that method [$x_2^{(2)}$ is obtained from Eqs. (13), (16) and (A7), while $x_2^{(4)}$ from Eqs. (13), (14), (16), (A6)–(A9) and (A22)–(A24)], as it is expected for the same problem. This consists a very good check for their correctness.

The problem can be also solved, from the beginning, by using the eccentricity parameter v instead of h. In this case the expansion of the general quantity y with respect to v is

$$y = y(v) = y^0 + vy_v^{(1)} + v^2 y_v^{(2)} + O(v^3), \tag{23}$$

while its expansion with respect to h is

$$y = y(h) = y^0 + h^2 y_h^{(2)} + h^4 y_h^{(4)} + O(h^6). \tag{24}$$

By using Eq. (19) into (23), as well as the relation

$$v^2 = h^4 + O(h^6) \tag{25}$$

we finally obtain[11]

$$y_v^{(1)} = \mp y_h^{(2)}, y_v^{(2)} = \mp y_h^{(2)} + y_h^{(4)}. \tag{26}$$

These last expressions are unique for both the prolate and the oblate cavity (v includes the sign), because $y_h^{(2)}$ simply changes its sign in these two cases.

By using the limiting value $\rho_1 \to 0$ ($q \to 0$), with c_1 finite, in Eq. (4), we obtain $E_n = j_n(x_1)/n_n(x_1)$, corresponding to a soft inner sphere. In the special case with $\rho_1 = \rho_2$ and $c_1 = c_2$, $q = 1$, $w_1 = x_1$ and $E_n = 0$. Use of the small argument formulas for the various Bessel functions[13] in Eq. (4) as $R_1 \to 0$, gives also $E_n = 0$. The last two cases correspond to a simple spheroidal cavity, i.e., in the absence of the inner sphere. In all three cases the various results become identical with the corresponding ones in Refs. 10 and 11. For $E_n = 0$, Eq. (16) is replaced by $dD_{nn}^0(x_2^0)/dx_2 = j_n'(x_2^0)$.

II. NEUMANN BOUNDARY CONDITIONS

Equations (1)–(5) are also valid in this case. In order to satisfy the boundary condition $\partial p_2/\partial\mu = 0$ ($\partial p_2/\partial\xi = 0$) at $\mu = \mu_0$ ($\xi = \xi_0$), according to the first method, we follow steps identical to those for the Dirichlet case. So, we use again formulas (6) and (7) and conclude finally to the infinite set (8), with the difference that $\alpha_{\ell nm}$ is now given by the expression

$$\alpha_{\ell nm} = \frac{2i^{-n}(n+m)!}{(2n+1)(n-m)!}$$

$$\times d_{n-m}^{m\ell} \left[\frac{\partial R_{m\ell}^{(1)}(c, \cosh\mu_0)}{\partial\mu} - E_n \frac{\partial R_{m\ell}^{(2)}(c, \cosh\mu_0)}{\partial\mu} \right]. \tag{27}$$

The remarks after Eq. (9) are again valid in this case. We next substitute $\partial R_{m\ell}^{(1)}/\partial\mu$ and $\partial R_{m\ell}^{(2)}/\partial\mu$ from Eq. (33) of Ref. 10 into Eq. (27) and follow the same procedure as in the Dirichlet case. So, we obtain again Eqs. (10)–(14) and (17) but with different expressions for the various expansion coefficients, which are given in Eqs. (A12)–(A15) of the Appendix. In place of Eq. (15) we now have

$$\frac{j_n'(x_2^0)}{n_n'(x_2^0)} = E_n(x_2^0), \quad x_1^0 = \tau x_2^0, \quad w_1^0 = \tau x_2^0 \frac{c_2}{c_1}, \tag{28}$$

while, by using Eqs. (28), (A12), (A22) and the Wronskian $j_n'(x_2^0)n_n''(x_2^0) - j_n''(x_2^0)n_n'(x_2^0) = [(x_2^0)^2 - n(n+1)]/(x_2^0)^4$, we obtain in place of Eq. (16)

$$\frac{dD_{nn}^0(x_2^0)}{dx_2} = -\frac{(x_2^0)^2 - n(n+1)}{(x_2^0)^3 n_n'(x_2^0)} - x_2^0 n_n'(x_2^0) \frac{dE_n(w_1^0, x_1^0)}{dx_2}. \tag{29}$$

Equations (29) and (A13) substituted in (13) give $x_2^{(2)}$. The expression for $x_2^{(4)}$ is much more lengthy, but is obtained immediately from Eqs. (13), (14), (29), (A12)–(A15) and (A22)–(A24).

According to the second method, the boundary condition at the spheroidal surface is expressed as $\hat{u} \cdot \nabla p_2 = 0$, with $\hat{u}$ the normal unit vector there, where[11]

TABLE I. Dirichlet conditions, $\tau = R_1/R_2 = 0.2(0.5)$, $\rho_2/\rho_1 = 0.820$, $c_2/c_1 = 0.787$.

	n	m	s 1	2	3	4
$(x_2^0)_{ns}$	0		3.177 90(3.559 71)	6.501 60(7.210 62)	9.936 19(10.366 79)	13.365 58(14.325 24)
	1		4.486 10(4.711 36)	7.745 53(8.862 57)	11.066 88(12.032 23)	14.494 62(15.773 77)
	2		5.761 16(5.865 33)	9.088 70(10.073 77)	12.345 25(13.870 28)	15.656 05(17.058 48)
	3		6.987 53(7.031 11)	10.414 10(11.145 51)	13.694 39(15.437 97)	16.949 25(18.601 91)
$g_{nsm}^{(2)}$	0	0	0.344 06(0.428 86)	0.360 30(0.313 11)	0.366 44(0.409 89)	0.358 75(0.364 37)
	1	0	0.199 71(0.244 14)	0.204 75(0.242 79)	0.213 32(0.189 74)	0.219 74(0.264 96)
		1	0.399 43(0.488 28)	0.409 49(0.485 57)	0.426 65(0.379 48)	0.439 48(0.529 93)
	2	0	0.237 73(0.269 14)	0.238 29(0.320 50)	0.242 98(0.225 86)	0.251 36(0.290 21)
		1	0.285 28(0.322 96)	0.285 94(0.384 60)	0.291 58(0.271 04)	0.301 63(0.348 25)
		2	0.427 92(0.484 45)	0.428 92(0.576 90)	0.437 37(0.406 56)	0.452 44(0.522 37)
	3	0	0.244 36(0.261 26)	0.244 16(0.326 41)	0.244 99(0.288 47)	0.249 00(0.238 21)
		1	0.266 57(0.285 01)	0.266 36(0.356 08)	0.267 26(0.314 70)	0.271 64(0.259 87)
		2	0.333 22(0.356 27)	0.332 94(0.445 10)	0.334 07(0.393 37)	0.339 55(0.324 84)
		3	0.444 29(0.475 02)	0.443 93(0.593 47)	0.445 43(0.524 49)	0.452 73(0.433 11)
$g_{nsm}^{(4)}$	0	0	0.287 40(0.380 06)	0.454 87(0.258 68)	0.500 62(1.697 56)	0.472 91(0.779 97)
	1	0	0.172 25(0.222 26)	0.312 11(0.188 53)	0.439 25(0.430 22)	0.446 97(1.412 77)
		1	0.315 19(0.463 98)	0.422 44(0.315 38)	0.525 28(0.563 89)	0.538 78(1.234 51)
	2	0	0.008 16(0.164 49)	0.073 86(−0.986 60)	0.237 85(−0.508 26)	0.301 96(−0.184 46)
		1	0.234 09(0.297 28)	0.333 31(0.340 12)	0.470 29(0.213 73)	0.568 60(1.321 73)
		2	0.330 57(0.453 67)	0.383 07(0.513 66)	0.465 10(0.192 64)	0.532 06(1.147 67)
	3	0	0.040 08(0.177 55)	0.024 64(0.109 70)	0.159 16(−1.073 90)	0.366 18(0.305 79)
		1	0.110 71(0.217 35)	0.125 24(0.211 68)	0.249 18(−0.650 71)	0.427 43(0.414 20)
		2	0.266 72(0.318 24)	0.333 72(0.447 47)	0.426 93(0.195 64)	0.537 91(0.639 27)
		3	0.340 52(0.424 66)	0.370 07(0.606 64)	0.415 51(0.195 52)	0.477 79(0.680 55)

TABLE II. Neumann conditions, $\tau = R_1/R_2 = 0.2(0.5)$, $\rho_2/\rho_1 = 0.820$, $c_2/c_1 = 0.787$.

	n	m	s 1	2	3	4
$(x_2^0)_{ns}$	0		0 (0)	4.593 68(5.321 42)	8.076 78(8.539 48)	11.565 52(12.299 21)
	1		2.0785 7(2.065 35)	5.935 43(6.584 94)	9.276 24(10.483 81)	12.682 46(13.641 99)
	2		3.341 69(3.329 69)	7.284 93(7.708 81)	10.613 20(12.050 94)	13.911 58(15.272 41)
	3		4.514 05(4.506 37)	8.582 49(8.834 41)	11.968 13(13.250 97)	15.248 40(17.063 92)
$g_{nsm}^{(2)}$	0	0	- (-)	0.352 66(0.409 12)	0.365 22(0.314 75)	0.364 96(0.439 78)
	1	0	0.027 51(0.023 60)	0.189 10(0.254 63)	0.203 83(0.189 61)	0.214 25(0.237 87)
		1	0.484 29(0.491 39)	0.408 48(0.541 61)	0.420 08(0.388 18)	0.435 34(0.482 28)
	2	0	0.182 70(0.181 15)	0.231 60(0.299 20)	0.237 17(0.288 05)	0.245 22(0.224 55)
		1	0.257 92(0.256 54)	0.282 16(0.363 85)	0.286 50(0.347 41)	0.295 37(0.270 29)
		2	0.483 60(0.482 68)	0.433 84(0.557 81)	0.434 47(0.525 50)	0.445 82(0.407 52)
	3	0	0.212 60(0.211 25)	0.239 93(0.289 24)	0.242 25(0.329 32)	0.245 21(0.229 13)
		1	0.242 78(0.241 35)	0.263 22(0.317 19)	0.264 97(0.360 01)	0.267 92(0.250 27)
		2	0.333 31(0.331 62)	0.333 07(0.401 04)	0.333 11(0.452 08)	0.336 04(0.313 68)
		3	0.484 21(0.482 08)	0.449 50(0.540 80)	0.446 69(0.605 54)	0.449 58(0.419 36)
$g_{nsm}^{(4)}$	0	0	- (-)	0.388 61(0.331 51)	0.509 44(0.556 64)	0.497 98(2.139 97)
	1	0	0.002 79(−0.001 42)	0.230 09(0.250 39)	0.390 53(0.186 52)	0.463 00(1.218 65)
		1	0.353 85(0.377 20)	0.368 74(0.516 54)	0.488 42(0.220 76)	0.549 29(1.239 80)
	2	0	−0.045 04(0.008 38)	0.000 61(0.068 21)	0.143 08(−1.642 10)	0.296 70(−0.031 19)
		1	0.204 57(0.205 67)	0.279 89(0.377 77)	0.401 47(0.228 16)	0.535 14(0.525 47)
		2	0.354 56(0.361 04)	0.358 28(0.573 67)	0.424 37(0.284 77)	0.507 73(0.583 57)
	3	0	0.037 14(0.059 73)	0.007 27(0.251 12)	0.066 14(−0.701 53)	0.256 99(−0.292 88)
		1	0.104 04(0.118 83)	0.101 13(0.297 71)	0.169 40(−0.350 43)	0.335 23(−0.122 20)
		2	0.257 61(0.256 91)	0.300 40(0.418 80)	0.378 67(0.377 97)	0.484 26(0.210 74)
		3	0.356 50(0.356 31)	0.358 23(0.558 40)	0.392 42(0.508 95)	0.447 05(0.168 60)
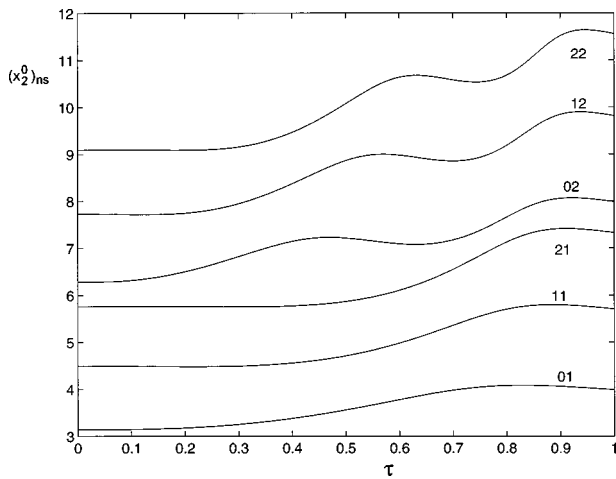
FIG. 2. Eigenfrequencies of a spherical cavity with a penetrable sphere; $\rho_2/\rho_1=0.820$, $c_2/c_1=0.787$—Dirichlet conditions.

$$\hat{u}=\left(1-\frac{h^4}{8}\sin^2 2\theta\right)\hat{u}',$$

$$\hat{u}'=\hat{r}+\frac{h^2}{2}\sin 2\theta(\pm 1+h^2\cos^2\theta)\hat{\theta}+O(h^6). \tag{30}$$

So

$$\hat{u}\cdot\nabla p_2=\hat{u}'\cdot\nabla p_2=\frac{\partial p_2}{\partial r}+\frac{h^2}{2}\sin 2\theta(\pm 1$$

$$+h^2\cos^2\theta)\frac{1}{r}\frac{\partial p_2}{\partial\theta}=0. \tag{31}$$

We next substitute from Eq. (2) into (31), thus obtaining the equation
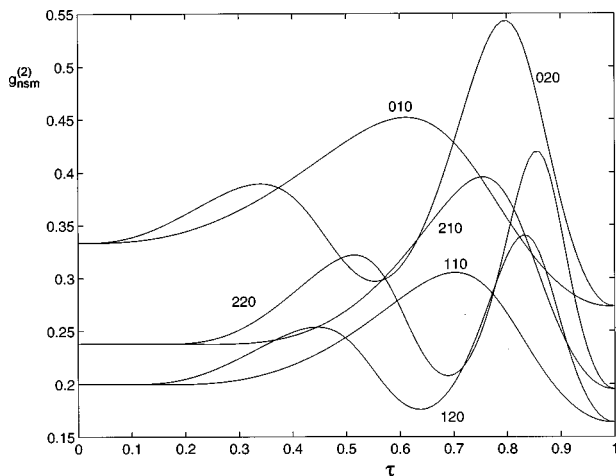
FIG. 3. First order expansion coefficients for eigenfrequencies in a spheroidal cavity with a penetrable sphere; $\rho_2/\rho_1=0.820$, $c_2/c_1=0.787$—Dirichlet conditions.
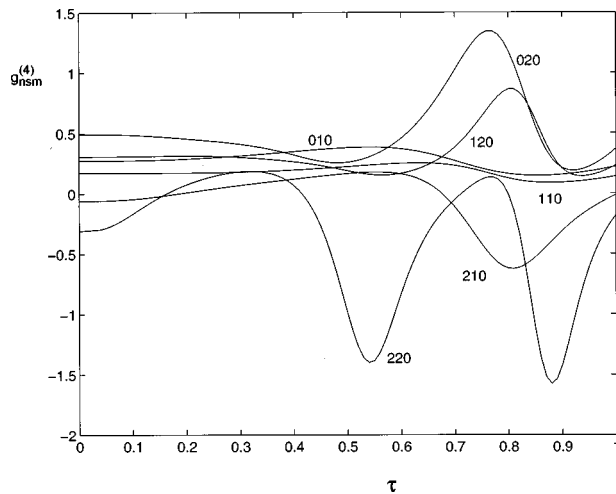
FIG. 4. Second order expansion coefficients for eigenfrequencies in a spheroidal cavity with a penetrable sphere; $\rho_2/\rho_1=0.820$, $c_2/c_1=0.787$—Dirichlet conditions.

$$\sum_{n=0}^{\infty}\sum_{m=0}^{n}\left\{[j_n'(k_2 r)-E_n n_n'(k_2 r)]P_n^m(\cos\theta)\right.$$

$$+\frac{h^2}{2}\sin 2\theta(\pm 1+h^2\cos^2\theta)\frac{1}{k_2 r}[j_n(k_2 r)-E_n n_n(k_2 r)]$$

$$\left.\cdot\frac{dP_n^m(\cos\theta)}{d\theta}\right\}[A_{nm}\cos m\varphi+B_{nm}\sin m\varphi]=0. \tag{32}$$

By using Eq. (20) we get expansions similar to Eq. (21) for $j_n'(k_2 r)$ and $n_n'(k_2 r)$, but with one more prime in each one of their Bessel functions. We also obtain the expansion[11]

$$\frac{j_n(k_2 r)}{k_2 r}=\frac{j_n(x_2)}{x_2}\mp\frac{h^2}{2}\left[-\frac{j_n(x_2)}{x_2}+j_n'(x_2)\right]\sin^2\theta$$

$$+\frac{h^4}{2}\left\{\left[\frac{j_n(x_2)}{x_2}-j_n'(x_2)\right]\sin^2\theta\right.$$

$$+\frac{1}{4}\left[-\frac{j_n(x_2)}{x_2}+j_n'(x_2)+x_2 j_n''(x_2)\right]\sin^4\theta\right\}$$

$$+O(h^6) \tag{33}$$

and a similar one for $n_n(k_2 r)/k_2 r$.

We next substitute the former expansions into Eq. (32) and we use the orthogonal properties of the associated Legendre and the trigonometric functions, thus obtaining again the set (22), certainly with different α's and so D's, which are given in Eqs. (A16)–(A19) of the Appendix.

The rest steps are identical with those in the first method, i.e., we obtain again Eqs. (10)–(14), (17) and (28), (29) with identical as their final results [$x_2^{(2)}$ is obtained from Eqs. (13), (29) and (A17), while $x_2^{(4)}$ from Eqs. (13), (14), (29), (A16)–(A19) and (A22)–(A24)], as is expected for the same problem. This is a very good check for their correctness.

The parameter v, instead of h, can be also used in this case by keeping in mind Eqs. (19) and (23)–(26).

By using the limiting value $\rho_1\rightarrow\infty$ $(q\rightarrow\infty)$, with c_1 finite, in Eq. (4), we obtain $E_n=j_n'(x_1)/n_n'(x_1)$, corresponding
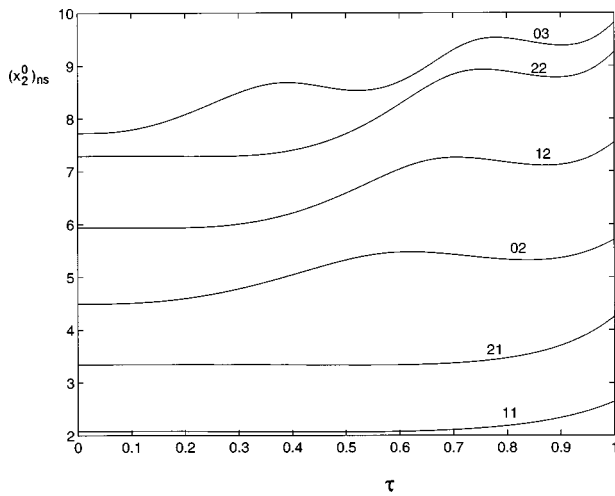
FIG. 5. Eigenfrequencies of a spherical cavity with a penetrable sphere; $\rho_2/\rho_1 = 0.820$, $c_2/c_1 = 0.787$—Neumann conditions.

FIG. 7. Second order expansion coefficients for eigenfrequencies in a spheroidal cavity with a penetrable sphere; $\rho_2/\rho_1 = 0.820$, $c_2/c_1 = 0.787$—Neumann conditions.

to a hard inner sphere. So, the various results become identical with the corresponding ones in Refs. 10 and 11. The same is valid also for a simple spheroidal cavity, where $E_n = 0$. In this last case Eq. (29) is replaced by $dD_{nn}^0(x_2^0)/dx_2 = x_2^0 j_n''(x_2^0)$.

III. NUMERICAL RESULTS AND DISCUSSION

In Table I the roots $(x_2^0)_{ns}$ ($n = 0-3$, $s = 1-4$) of Eq. (15) as well as the corresponding values of $g_{nsm}^{(2)}$ and $g_{nsm}^{(4)}$ are given in the Dirichlet case, for $\tau = R_1/R_2 = 0.2, 0.5, \rho_2/\rho_1 = 0.820, c_2/c_1 = 0.787$. In Table II the roots $(x_2^0)_{ns}$ of Eq. (28) are given, as well as g's in the Neumann case, for the same τ's and the values of the parameters as before. The value $(x_2^0)_{01} = 0$ corresponds to the smallest eigenvalue $k_2^0 = k_1^0 = 0$ (with constant eigenfunction) of the Helmholtz equation under Neumann conditions. As $(x_2^0)_{01} = 0$, also $f_{01}(0) = 0$ and $f_{010}(h) = 0$, so the values of $g_{010}^{(2)}$ and $g_{010}^{(4)}$ do not matter.

Both tables are referred to the prolate cavity. For the oblate one $g^{(2)}$'s simply change their signs, while $g^{(4)}$'s re-

FIG. 6. First order expansion coefficients for eigenfrequencies in a spheroidal cavity with a penetrable sphere; $\rho_2/\rho_1 = 0.820$, $c_2/c_1 = 0.787$—Neumann conditions.
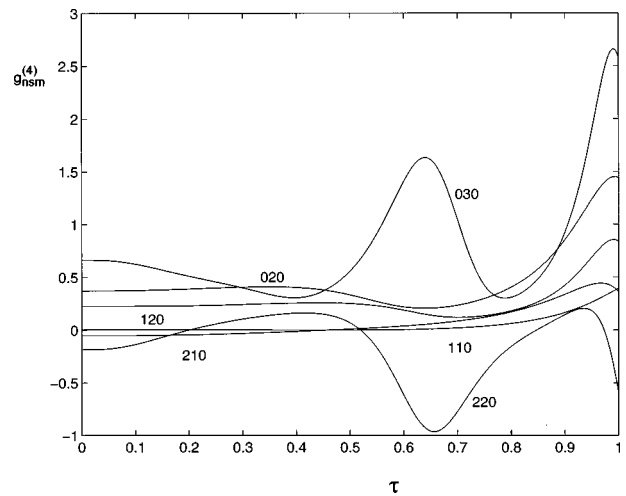
main unchanged. (The same will be valid also in Figs. 3, 4, 6 and 7, which follow.)

For the values of the parameters used, all $g^{(2)}$'s in both tables are positive. Keeping in mind Eq. (17), this means that the eigenfrequencies of the prolate/oblate cavity are greater/smaller than those of the corresponding spherical one, up to the order h^2.

From the former tables and many other available results, it is evident that $(x_2^0)_{ns}$ ($n \geq 0, s \geq 1$) and so also $f_{ns}(0)$ for Neumann conditions are smaller than the corresponding ones for Dirichlet conditions. The same is valid for $f_{nsm}(h)$, as can be easily proved for the results given in these tables, in the case with $h \ll 1$.

In Fig. 2 we plot the roots $(x_2^0)_{ns}$ ($n = 0-2, s = 1, 2$) of Eq. (15) versus τ, for a concentric spherical cavity with radii R_1 and R_2 and Dirichlet conditions. The various numbers designating the curves in this and the rest of the figures correspond to the subscripts of the ordinate. For $\tau \to 0 (R_1 \to 0)$, $E_n \to 0$ and so $(x_2^0)_{ns}$ tend to the zeros of $j_n(x_2^0)$, corresponding to a simple spherical cavity with parameters ρ_2, c_2. For $\tau \to 1 (R_1 \to R_2)$, $x_1^0 \to x_2^0$, so Eq. (15) is reduced to $j_n(w_1^0) = j_n(x_2^0 c_2/c_1) = 0$ corresponding to a simple spherical cavity with parameters ρ_1, c_1 and $(x_2^0)_{ns}$ in this case are equal with those for $\tau \to 0$, multiplied by c_1/c_2.

In Figs. 3 and 4 we plot $g_{nsm}^{(2)}$ and $g_{nsm}^{(4)}$, respectively, versus τ, for the cavity of Fig. 1 with Dirichlet conditions. For $\tau \to 0$ the various g's tend to the corresponding ones for a simple spheroidal cavity[11] with parameters ρ_2, c_2, by taking in mind Eqs. (26). So, $g^{(2)}$'s are independent of s in this case, as it was proved in Ref. 11 and is seen in Fig. 3. For $\tau \to 1$ (for the prolate cavity is necessary that $h \to 0$, as $\tau \to 1$) the same remarks as before are valid for g's, where now the simple spheroidal cavity has parameters ρ_1, c_1. Also in this case $g^{(2)}$'s are independent of s, as is seen in Fig. 3, and are equal with those for $\tau \to 0$, multiplied by ρ_2/ρ_1. This can be proved easily by using the result[11] $g_{nsm}^{(2)} = F$ [F is given in Eq. (A10)] for $\tau \to 0$, as well as Eqs. (13), (16), (A7), (15), the Wronskian following it and (A22) for $\tau \to 1$, i.e., with $x_1^0 \to x_2^0$ and $j_n(w_1^0) = 0$.

In Fig. 5 the roots $(x_2^0)_{ns}$ $(n=0-2, s=1-3)$ of Eq. (28) are plotted versus τ, for a concentric spherical cavity with radii R_1 and R_2 and Neumann conditions $[(x_2^0)_{01}=0$, as in Table II]. For $\tau \to 0$, $(x_2^0)_{ns}$ tend to the zeros of $j_n'(x_2^0)$, corresponding to a simple spherical cavity with parameters ρ_2, c_2. For $\tau \to 1$, Eq. (28) is reduced to $j_n'(w_1^0) = j_n'(x_2^0 c_2/c_1) = 0$ (for a simple spherical cavity with ρ_1, c_1) and $(x_2^0)_{ns}$ are equal with the corresponding ones for $\tau \to 0$, multiplied by c_1/c_2.

In Figs. 6 and 7 we plot $g_{nsm}^{(2)}$ and $g_{nsm}^{(4)}$, respectively, versus τ, for the cavity of Fig. 1 with Neumann conditions. For $\tau \to 0$ the various g's tend to the corresponding ones for a simple spheroidal cavity[11] with parameters ρ_2, c_2 [we keep in mind Eqs. (26)]. So, $g_{oso}^{(2)}(s \geq 2)$ are independent of s in this case, as is seen in Fig. 6. For $\tau \to 1$ the same remarks are valid for g's in a simple spheroidal cavity with parameters ρ_1, c_1. So $g_{oso}^{(2)}$ are independent of s also in this case (Fig. 6).

APPENDIX

The expressions for the various D's appearing in Eq. (10) and used in our calculations are the following (the upper/lower sign corresponds to the prolate/oblate cavity):

1. Dirichlet boundary conditions

A. First method (use of spheroidal wave functions)

$$D_{nn}^0 = u_{nn},\tag{A1}$$

$$D_{nn}^{(2)} = \pm \frac{x_2^2}{2(2n+1)}\left[\frac{(n+m+1)(n+m+2)}{(2n+3)^2}u_{n+2,n}\right.$$
$$\left. - \frac{(n-m-1)(n-m)}{(2n-1)^2}u_{n-2,n}\right],\tag{A2}$$

$$D_{nn}^{(4)} = x_2^4 \frac{(n+m+1)(n+m+2)}{(2n+1)(2n+3)^2(2n+7)}$$
$$\times \left[\frac{1-4m^2}{(2n-1)(2n+3)^2}u_{n+2,n}\right.$$
$$\left. + \frac{(n+m+3)(n+m+4)}{8(2n+5)^2}u_{n+4,n}\right]$$
$$- x_2^4 \frac{(n-m-1)(n-m)}{(2n-5)(2n-1)^2(2n+1)}$$
$$\cdot \left[\frac{1-4m^2}{(2n-1)^2(2n+3)}u_{n-2,n}\right.$$
$$\left. - \frac{(n-m-3)(n-m-2)}{8(2n-3)^2}u_{n-4,n}\right],\tag{A3}$$

$$D_{n+2,n}^{(2)} = \pm x_2^2 \frac{(n+m+1)(n+m+2)}{2(2n+3)^2(2n+5)}u_{n+2,n},$$

$$D_{n,n+2}^{(2)} = \mp x_2^2 \frac{(n-m+1)(n-m+2)}{2(2n+1)(2n+3)^2}u_{n,n+2},\tag{A4}$$

where

$$u_{vs} = j_v(x_2) - E_s n_v(x_2).\tag{A5}$$

B. Second method (shape perturbation)

$$D_{nn}^0 = u_{nn},\tag{A6}$$

$$D_{nn}^{(2)} = \mp x_2 F u_{nn}',\tag{A7}$$

$$D_{nn}^{(4)} = x_2 G(3u_{nn}' + x_2 u_{nn}'') - x_2 F u_{nn}',\tag{A8}$$

$$D_{n+2,n}^{(2)} = \pm x_2 \frac{(n+m+1)(n+m+2)}{2(2n+3)(2n+5)}u_{n+2,n+2}',$$

$$D_{n,n+2}^{(2)} = \pm x_2 \frac{(n-m+1)(n-m+2)}{2(2n+1)(2n+3)}u_{nn}',\tag{A9}$$

where

$$F = \frac{n^2+m^2+n-1}{(2n-1)(2n+3)},\tag{A10}$$

$$G = \frac{(n+m+1)(n+m+2)(n+m+3)(n+m+4)}{8(2n+1)(2n+3)^2(2n+5)}$$
$$+ \frac{(n-m-1)(n-m)(n+m+1)(n+m+2)}{2(2n-1)^2(2n+3)^2}$$
$$+ \frac{(n-m-3)(n-m-2)(n-m-1)(n-m)}{8(2n-3)(2n-1)^2(2n+1)},\tag{A11}$$

while the number of primes over u_{vs}, in any case, denotes the number of primes over $j_v(x_2)$ and $n_v(x_2)$ (i.e., the order of their derivatives with respect to their argument x_2) in Eq. (A5).

2. Neumann boundary conditions

A. First method (use of spheroidal wave functions)

$$D_{nn}^0 = x_2 u_{nn}',\tag{A12}$$

$$D_{nn}^{(2)} = \mp \left[x_2 u_{nn}' - mu_{nn}\right.$$
$$- x_2^3 \frac{(n+m+1)(n+m+2)}{2(2n+1)(2n+3)^2}u_{n+2,n}'$$
$$\left. + x_2^3 \frac{(n-m-1)(n-m)}{2(2n-1)^2(2n+1)}u_{n-2,n}'\right],\tag{A13}$$

$$D_{nn}^{(4)} = x_2^2 \frac{(n+m+1)(n+m+2)}{2(2n+1)(2n+3)^2}\left\{-x_2 u_{n+2,n}' + mu_{n+2,n}\right.$$
$$+ \frac{2x_2^3}{2n+7}\cdot\left[\frac{1-4m^2}{(2n-1)(2n+3)^2}u_{n+2,n}'\right.$$
$$\left.\left. + \frac{(n+m+3)(n+m+4)}{8(2n+5)^2}u_{n+4,n}'\right]\right\}$$

$$-x_2^2 \frac{(n-m-1)(n-m)}{2(2n-1)^2(2n+1)} \left\{ -x_2 u'_{n-2,n} + m u_{n-2,n} \right.$$

$$+ \frac{2x_2^3}{2n-5} \cdot \left[\frac{1-4m^2}{(2n-1)^2(2n+3)} u'_{n-2,n} \right.$$

$$\left. \left. - \frac{(n-m-3)(n-m-2)}{8(2n-3)^2} u'_{n-4,n} \right] \right\}, \tag{A14}$$

$$D_{n+2,n}^{(2)} = \pm x_2^3 \frac{(n+m+1)(n+m+2)}{2(2n+3)^2(2n+5)} u'_{n+2,n},$$

$$D_{n,n+2}^{(2)} = \mp x_2^3 \frac{(n-m+1)(n-m+2)}{2(2n+1)(2n+3)^2} u'_{n,n+2}. \tag{A15}$$

B. Second method (shape perturbation)

$$D_{nn}^0 = x_2 u'_{nn}, \tag{A16}$$

$$D_{nn}^{(2)} = \mp x_2^2 F u''_{nn} \mp M u_{nn}, \tag{A17}$$

$$D_{nn}^{(4)} = x_2^2 G[3u''_{nn} + x_2 u'''_{nn}] + \frac{L}{2(2n+1)}[u_{nn} + x_2 u'_{nn}]$$

$$- x_2^2 F u''_{nn} - M u_{nn}, \tag{A18}$$

$$D_{n+2,n}^{(2)} = \pm \frac{(n+m+1)(n+m+2)}{2(2n+3)(2n+5)}[x_2^2 u''_{n+2,n+2}$$

$$- 2(n+3)u_{n+2,n+2}], \tag{A19}$$

$$D_{n,n+2}^{(2)} = \pm \frac{(n-m+1)(n-m+2)}{2(2n+1)(2n+3)}[x_2^2 u''_{nn} + 2n u_{nn}],$$

where

$$M = \frac{1}{2n+1}\left[\frac{(n+1)(n^2-m^2)}{2n-1} - \frac{n((n+1)^2-m^2)}{2n+3} \right], \tag{A20}$$

$$L = \frac{(n-m)(n+m+1)}{2n+1}\left[\frac{(n+1)(n+m)}{2n-1} + \frac{n(n-m+1)}{2n+3} \right]$$

$$\times \left(\frac{n+m}{2n-1} - \frac{n-m+1}{2n+3} \right)$$

$$- \frac{n((n+1)^2-m^2)(n+m+2)(n+m+3)}{(2n+3)^2(2n+5)}$$

$$+ \frac{(n+1)(n-m-2)(n-m-1)(n^2-m^2)}{(2n-3)(2n-1)^2}. \tag{A21}$$

3. Two useful derivatives

The following two derivatives of E_n are very useful in Eqs. (13), (14), for the evaluation of $x_2^{(2)}$ and $x_2^{(4)}$ in any case, i.e., for Dirichel and Neumann conditions and for both methods. Various recurrence relations and Wronskians for spherical Bessel functions[13] have been used for their evaluation:

$$\frac{dE_n}{dx_2} = -\left\{ \tau x_1^2\left(1-\frac{\rho_1}{\rho_2}\right)[j'_n(w_1)]^2 + q^2\tau j_n^2(w_1) \right.$$

$$\left. \times \left[x_1^2 - \frac{\rho_2}{\rho_1}w_1^2 - n(n+1)\left(1-\frac{\rho_2}{\rho_1}\right) \right] \right\} \bigg/ (x_1^4 Q^2), \tag{A22}$$

$$\frac{d^2E_n}{dx_2^2} = -\frac{2\tau^2}{x_1^4 Q^2}\left\{ x_1\left(1-\frac{\rho_1}{\rho_2}\right)j'_n(w_1)[j'_n(w_1) + w_1 j''_n(w_1)] \right.$$

$$+ q^2\frac{c_2}{c_1}j_n(w_1)j'_n(w_1)\cdot\left[x_1^2 - \frac{\rho_2}{\rho_1}w_1^2 - n(n+1) \right.$$

$$\left. \times \left(1-\frac{\rho_2}{\rho_1}\right) \right] + q^2 j_n^2(w_1)\left(x_1 - \frac{w_1}{q}\right) \bigg\}$$

$$- 2\tau\frac{dE_n}{dx_2}\left(\frac{2}{x_1} + \frac{Q_1 + Q_2 c_2/c_1}{Q} \right), \tag{A23}$$

where

$$Q = n_n(x_1)j'_n(w_1) - q j_n(w_1)n'_n(x_1),$$

$$Q_1 = n'_n(x_1)j'_n(w_1) - q j_n(w_1)n''_n(x_1), \tag{A24}$$

$$Q_2 = n_n(x_1)j''_n(w_1) - q j'_n(w_1)n'_n(x_1),$$

while $x_1 = \tau x_2$, $w_1 = \tau x_2 c_2/c_1$ and $\tau = R_1/R_2$.

[1] P. M. Morse and K. U. Ingard, *Theoretical Acoustics* (McGraw–Hill, New York, 1968).

[2] M. Barmatz, ''Overview of containerless processing technologies,'' Proceedings of the Symposium of Materials Processing in the Reduced Gravity Environment of Space, Boston, MA, Nov. 1981 (Elsevier, New York, 1982), pp. 25–37.

[3] M. Barmatz and P. Collas, ''Acoustic radiation potential on a sphere in plane, cylindrical, and spherical standing wave fields,'' J. Acoust. Soc. Am. **77**, 928–945 (1985).

[4] M. R. Moldover, J. B. Mehl, and M. Greenspan, ''Gas-filled spherical resonators: Theory and experiment,'' J. Acoust. Soc. Am. **79**, 253–272 (1986).

[5] J. D. Kanellopoulos and J. G. Fikioris, ''Acoustic resonant frequencies in an eccentric spherical cavity,'' J. Acoust. Soc. Am. **64**, 286–297 (1978).

[6] J. A. Roumeliotis, J. D. Kanellopoulos, and J. G. Fikioris, ''Acoustic resonance frequency shifts in a spherical cavity with an eccentric inner small sphere,'' J. Acoust. Soc. Am. **90**, 1144–1148 (1991).

[7] J. A. Roumeliotis and J. D. Kanellopoulos, ''Acoustic eigenfrequencies and modes in a soft-walled spherical cavity with an eccentric inner small sphere,'' J. Franklin Inst. **329**, 727–735 (1992).

[8] C. T. M. Chang, ''Natural resonant frequency of a prolate acoustical resonator,'' J. Acoust. Soc. Am. **49**, 611–614 (1971).

[9] P.-T. Chen, ''Variational formulation of interior cavity frequencies for spheroidal bodies,'' J. Acoust. Soc. Am. **100**, 2980–2988 (1966).

[10] G. C. Kokkorakis and J. A. Roumeliotis, ''Acoustic eigenfrequencies in concentric spheroidal–spherical cavities,'' J. Sound Vib. **206**, 287–308 (1997).

[11] G. C. Kokkorakis and J. A. Roumeliotis, ''Acoustic eigenfrequencies in concentric spheroidal-spherical cavities: Calculation by shape perturbation,'' J. Sound Vib. **212**, 337–355 (1998).

[12] C. Flammer, *Spheroidal Wave Functions* (Stanford U.P., Stanford, CA, 1957).

[13] M. Abramowitz and I. A. Stegun, *Handbook of Mathematical Functions* (Dover, New York, 1972).

[14] Y. Mushiake, ''Backscattering for arbitrary angles of incidence of a plane electromagnetic wave on a perfectly conducting spheroid with small eccentricity,'' J. Appl. Phys. **27**, 1549–1556 (1956).

Three-pass mufflers with uniform perforations

A. Selamet and V. Easwaran

The Ohio State University, Department of Mechanical Engineering and Center for Automotive Research,
206 West 18th Avenue, Columbus, Ohio 43210

A. G. Falkowski

Chrysler Corporation, Detroit, Michigan 48227

A quasi-one-dimensional approach is presented to analyze three-pass mufflers with perforated elements using numerical decoupling. The approach is further developed to include mufflers with ducts extended into the end cavities. Theoretical predictions are compared with experiments for three different muffler configurations, one fabricated and two commercially available mufflers, and shown to agree reasonably well. The effect of porosity, length of the end cavities, and expansion chamber diameter are studied. Also, the effect of ducts extending into the end cavities are investigated. © *1999 Acoustical Society of America.* [S0001-4966(99)01703-8]

PACS numbers: 43.20.Mv, 43.50.Gf [ANN]

LIST OF SYMBOLS

A	cross-sectional area
c_0	speed of sound
d	duct diameter
D	d/dx
f	frequency; as defined in Eq. (4)
i	imaginary unit, $\sqrt{-1}$
k_0	wave number, ω/c_0
M	Mach number
$\mathbf{n}$	unit vector normal to the control surface
p	pressure
t	time; perforate thickness
T	transfer matrix
TR	rank reduced transfer matrix as defined by Eq. (63)
u	axial velocity
$\mathbf{u}$	velocity vector
U	velocity of moving medium
v	radial velocity
x	axial coordinate

Greek symbols

Γ	control surface
δ	end correction length
ζ	specific impedance of perforate
λ	eigenvalue
ρ	density
Υ	diagonal matrix composed of eigenvalues
ϕ	porosity/open-area ratio
Φ	vector of generalized coordinates/transformation vector
Ψ	matrix of eigenvectors
ω	angular frequency, $2\pi f$
Ω	control volume

Subscripts

0	mean value
LEC	left end chamber
REC	right end chamber

Superscripts

$\sim$	perturbed quantity
$'$	d/dx
h	perforate
T	transpose

INTRODUCTION

Perforated tube elements are widely used in resonators and mufflers to suppress engine exhaust noise. Typical examples include concentric tube resonators and cross-flow elements. The flow through the tubes can be either straight-through or reversed. Aero-acoustic analysis of perforated elements in the form of a series expansion for the straight-through silencer elements was first presented by Sullivan and Crocker.[1] A segmentation method developed by Sullivan[2,3] later lumped the effect of perforations into a number of discrete planes with solid pipes present in between. This was followed up by Jayaraman and Yam[4] who developed a decoupling method to obtain a closed form analytical solution.

Thawani and Jayaraman demonstrated the use of this method[5] by analyzing straight-through resonators in the absence of flow. Rao and Munjal[6] extended the analysis of Jayaraman and Yam by allowing the Mach numbers in the inner perforated duct and the outer casing to be different. Munjal *et al.*[7] then developed a decoupling procedure by extracting the roots of the characteristic polynomial of the system numerically. Later, Peat[8] presented another numerical decoupling approach where the eigenvalues and the eigenvectors were obtained rather than the roots of the characteristic polynomial, thereby removing the numerical instability problems associated with other methods described thus far. Gogate and Munjal[9] extended the analysis of Munjal *et al.*[7] to include open-ended two-pass perforated mufflers. Re-
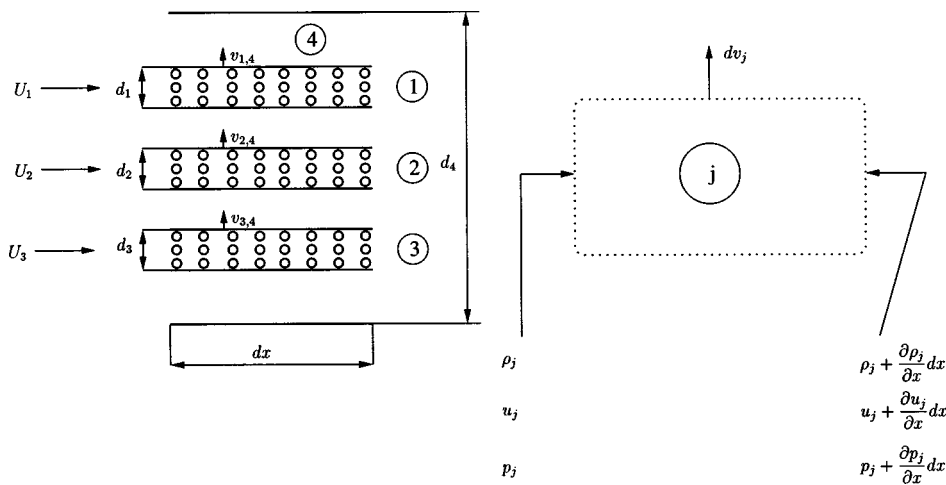
FIG. 1. Three-duct perforated element.

cently, Dokumaci[10] presented a matrizant approach for the analysis of perforated duct mufflers and included the gradient of the mean flow in the analysis which was later extended to include multiple duct perforated pipe arrangement with identical perforated pipes.[11] All of these studies, except Ref. 10, are limited to concentric tube resonators, plug mufflers, or two-pass mufflers (two perforated ducts plus an expansion chamber).

As many of the commercially available mufflers implement three passes (three perforated ducts plus an expansion chamber), such configurations have been of more recent interest. Ross[12] attempted the analysis of the three-pass muffler using the finite element method, but only demonstrated the results for the case where the middle pipe was just pass through (not perforated). Recently, Dickey et al.[13] presented a time-domain computational analysis of a multi-pass perforated muffler, and illustrated the results for a three-pass muffler. The corresponding frequency domain analysis of this muffler was later presented by Munjal,[14] via a decoupling method, which was also refined to include the extended-tube three-pass perforated element muffler.[15] This decoupling approach was shown by Peat[8] to lead to numerical instability problems, especially near transmission loss peaks.

The present study has developed a quasi-one-dimensional theoretical model for the analysis of a three-pass perforated duct muffler based on the transfer matrix method and the numerical decoupling of Peat.[8] The method is then generalized to include the analysis of three-pass mufflers where the ducts extend into the end cavities. A prototype three-pass muffler was built and the transmission loss was measured in an impedance tube facility for this prototype muffler, as well as for two production mufflers. Experimental results are shown to be in reasonable agreement with the theoretical predictions.

Following this introduction, the general theoretical approach is discussed in Sec. I for the analysis of the three-pass muffler. The ''numerical decoupling'' of the differential equations is described in Sec. II, the boundary conditions for the expansion chamber and the end cavities in Sec. III, and a transfer matrix solution in Sec. IV. The results are presented in Sec. V, followed by concluding remarks in Sec. VI.

I. THEORY

The derivation of governing equations follows, in general, that of Sullivan[2,3] and Peat.[8] The mean flow in the chamber (designated by 4 in Fig. 1), however, is assumed to be zero. In addition, the thicknesses of the walls of the perforated tubes (designated by 1–3 in Fig. 1) are assumed to be negligible compared to the diameter of the chamber, and the gradient of the mean flow is neglected.

Consider four control volumes, each of length dx, as shown in Fig. 1. For simplicity, the tube and the chamber are assumed to be circular. Integrating the continuity equation,

$$\frac{\partial \rho}{\partial t} + \boldsymbol{\nabla} \cdot \rho \mathbf{u} = 0, \tag{1}$$

over a finite control volume Ω and applying the divergence theorem yields

$$\frac{\partial}{\partial t} \int_{\Omega} \rho \, d\Omega + \int_{\Gamma} \rho \mathbf{u}_j \cdot \mathbf{n} \, d\Gamma = 0, \quad j = 1,2,3,4, \tag{2}$$

where $\mathbf{u}$ is the velocity vector, ρ is the density, Γ is the control surface, and $\mathbf{n}$ is the unit vector normal to the surface Γ. Applying Eq. (2) to each of the four control volumes yields

$$\frac{\partial \rho_j}{\partial t} + u_j \frac{\partial \rho_j}{\partial x} + \rho \frac{\partial u_j}{\partial x} + \rho f_j = 0, \quad j = 1,2,3,4, \tag{3}$$

where

$$f_j = \frac{4 v_{j,4}}{d_j}, \quad j = 1,2,3;$$

$$f_4 = -\frac{4(d_1 v_{1,4} + d_2 v_{2,4} + d_3 v_{3,4})}{d_4^2 - (d_1^2 + d_2^2 + d_3^2)}; \tag{4}$$

$v_{j,4}$ is the radial velocity of duct j; d_1, d_2, d_3 are the diameters of the perforated tubes; and d_4 is the diameter of the chamber or the external housing.

Similarly, integrating the momentum equation

$$\frac{\partial \mathbf{u}_j}{\partial t} + \mathbf{u}_j \cdot \nabla \mathbf{u}_j = -\frac{1}{\rho} \nabla p_j \tag{5}$$

over the finite control volume Ω gives

$$\int_\Omega \frac{\partial \mathbf{u}_j}{\partial t} d\Omega + \frac{1}{2} \int_\Gamma \mathbf{u}_j \cdot \mathbf{u}_j \mathbf{n} \, d\Gamma + \int_\Omega \frac{1}{\rho} \nabla p_j \, d\Gamma = 0,$$

$$j = 1,2,3,4, \tag{6}$$

where p_j is the pressure in duct j. The x component of Eq. (6) is then

$$\frac{\partial u_j}{\partial t} + u_j \frac{\partial u_j}{\partial x} + \frac{1}{\rho} \frac{\partial p_j}{\partial x} = 0, \quad j = 1,2,3,4. \tag{7}$$

Equations (3) and (7) are linearized by substituting $\rho = \rho_0 + \tilde{\rho}$, $u_j = U_j + \tilde{u}_j$, and $p_j = p_0 + \tilde{p}_j$ and retaining only the first-order terms, where U_j is the mean velocity in duct j, the symbol "~" denotes a fluctuating component, and the subscript 0 is the steady-state component. This yields

$$\frac{\partial \tilde{\rho}}{\partial t} + U_j \frac{\partial \tilde{\rho}}{\partial x} + \rho_0 \frac{\partial \tilde{u}_j}{\partial x} + \rho_0 f_j = 0, \quad j = 1,2,3,4, \tag{8}$$

for the continuity equation and

$$\rho_0 \frac{\partial \tilde{u}_j}{\partial t} + \rho_0 U_j \frac{\partial \tilde{u}_j}{\partial x} + \frac{\partial \tilde{p}_j}{\partial x} = 0, \quad j = 1,2,3,4, \tag{9}$$

for the momentum equation. Similarly, from isentropic relationship

$$\frac{\tilde{p}}{\tilde{\rho}} = c_0^2. \tag{10}$$

For uniform perforations in a duct of constant cross section, at any position along the perforate,[1]

$$v_{j,4} = \frac{\tilde{p}_j - \tilde{p}_4}{\rho_0 c_0 \zeta_j}, \quad j = 1,2,3, \tag{11}$$

where c_0 is the speed of sound and ζ_j is the specific acoustic impedance of the perforate of duct j, given in terms of the

mean flow, duct geometry, and the perforate geometry.[1–3,8,16] Substituting the expressions for f_j and $\tilde{\rho}$ given, respectively, by Eqs. (4) and (10), in Eq. (8) and employing Eq. (11) yields

$$\frac{1}{c_0^2} \frac{\partial \tilde{p}_j}{\partial t} + \frac{U_j}{c_0^2} \frac{\partial \tilde{p}_j}{\partial x} + \rho_0 \frac{\partial \tilde{u}_j}{\partial x} + \frac{4}{d_j} \left(\frac{\tilde{p}_j - \tilde{p}_4}{c_0 \zeta_j} \right) = 0, \quad j = 1,2,3, \tag{12}$$

and (for $j=4$)

$$\frac{1}{c_0^2} \frac{\partial \tilde{p}_4}{\partial t} + \rho_0 \frac{\partial \tilde{u}_4}{\partial x}$$

$$-\frac{4}{d_4^2 - (d_1^2 + d_2^2 + d_3^2)} \sum_{m=1}^{3} \frac{d_m}{c_0 \zeta_m} (\tilde{p}_m - \tilde{p}_4) = 0. \tag{13}$$

Upon operating Eqs. (12) and (13) with $\partial/\partial t$ and subtracting from it the corresponding Eq. (9) (after operating it with $\partial/\partial x$) yields

$$\frac{1}{c_0^2} \frac{\partial^2 \tilde{p}_j}{\partial t^2} + \frac{2U_j}{c_0^2} \frac{\partial^2 \tilde{p}_j}{\partial t \partial x} - (1 - M_j^2) \frac{\partial^2 \tilde{p}_j}{\partial x^2}$$

$$+ \frac{4}{c_0 \zeta_j d_j} \left(\frac{\partial \tilde{p}_j}{\partial t} - \frac{\partial \tilde{p}_4}{\partial t} \right) + \frac{4M_j}{\zeta_j d_j} \left(\frac{\partial \tilde{p}_j}{\partial x} - \frac{\partial \tilde{p}_4}{\partial x} \right) = 0 \tag{14}$$

for the perforated ducts ($j = 1$ to 3), and

$$\frac{1}{c_0^2} \frac{\partial^2 \tilde{p}_4}{\partial t^2} - \frac{\partial^2 \tilde{p}_4}{\partial x^2}$$

$$+ \frac{4}{d_4^2 - (d_1^2 + d_2^2 + d_3^2)} \left(\frac{d_1}{\zeta_1} \frac{\partial \tilde{p}_1}{\partial t} + \frac{d_2}{\zeta_2} \frac{\partial \tilde{p}_2}{\partial t} + \frac{d_3}{\zeta_3} \frac{\partial \tilde{p}_3}{\partial t} \right)$$

$$- \frac{4}{d_4^2 - (d_1^2 + d_2^2 + d_3^2)} \left(\frac{d_1}{\zeta_1} + \frac{d_2}{\zeta_2} + \frac{d_3}{\zeta_3} \right) \frac{\partial \tilde{p}_4}{\partial t} = 0 \tag{15}$$

for the chamber ($j=4$). Substituting for the time harmonic motion

$$\tilde{p}(x,t) = p(x) \exp(i\omega t) \tag{16}$$

in Eqs. (14) and (15) yields

$$\begin{bmatrix} D^2 + \alpha_1 D + \alpha_4 & 0 & 0 & \alpha_7 D + \alpha_{10} \\ 0 & D^2 + \alpha_2 D + \alpha_5 & 0 & \alpha_8 D + \alpha_{11} \\ 0 & 0 & D^2 + \alpha_3 D + \alpha_6 & \alpha_9 D + \alpha_{12} \\ \alpha_{13} & \alpha_{14} & \alpha_{15} & D^2 + \alpha_{16} \end{bmatrix} \begin{Bmatrix} p_1 \\ p_2 \\ p_3 \\ p_4 \end{Bmatrix} = \begin{Bmatrix} 0 \\ 0 \\ 0 \\ 0 \end{Bmatrix} \tag{17}$$

where

$$\alpha_j = \frac{-2M_j}{1 - M_j^2} \left[\frac{2}{\zeta_j d_j} + ik_0 \right], \quad j = 1,2,3, \tag{18}$$

$$\alpha_{j+3} = \frac{1}{1 - M_j^2} \left(k_0^2 - \frac{4ik_0}{\zeta_j d_j} \right), \quad j = 1,2,3, \tag{19}$$

$$\alpha_{j+6} = \frac{4M_j}{(1 - M_j^2) \zeta_j d_j}, \quad j = 1,2,3, \tag{20}$$

$$\alpha_{j+9} = \frac{4ik_0}{(1 - M_j^2) \zeta_j d_j}, \quad j = 1,2,3, \tag{21}$$

$$\alpha_{j+12} = \frac{4ik_0 d_j / \zeta_j}{d_4^2 - (d_1^2 + d_2^2 + d_3^2)}, \quad j = 1,2,3, \tag{22}$$

$$\alpha_{16} = (k_0^2 - \alpha_{13} - \alpha_{14} - \alpha_{15}), \tag{23}$$

$k_0 = 2\pi f/c_0$ is the wave number, and f is the frequency. Equation (17) is decoupled[8] and solved as shown next.

II. NUMERICAL DECOUPLING

Let

$$y_1 = p_1', \quad y_2 = p_2', \quad y_3 = p_3', \quad y_4 = p_4',$$
$$y_5 = p_1, \quad y_6 = p_2, \quad y_7 = p_3, \quad y_8 = p_4, \tag{24}$$

$$[B] = \begin{bmatrix} -\alpha_1 & 0 & 0 & -\alpha_7 & -\alpha_4 & 0 & 0 & -\alpha_{10} \\ 0 & -\alpha_2 & 0 & -\alpha_8 & 0 & -\alpha_5 & 0 & -\alpha_{11} \\ 0 & 0 & -\alpha_3 & -\alpha_9 & 0 & 0 & -\alpha_6 & -\alpha_{12} \\ 0 & 0 & 0 & 0 & -\alpha_{13} & -\alpha_{14} & -\alpha_{15} & -\alpha_{16} \\ 1 & 0 & 0 & 0 & 0 & 0 & 0 & 0 \\ 0 & 1 & 0 & 0 & 0 & 0 & 0 & 0 \\ 0 & 0 & 1 & 0 & 0 & 0 & 0 & 0 \\ 0 & 0 & 0 & 1 & 0 & 0 & 0 & 0 \end{bmatrix} \tag{27}$$

and superscript T denotes the transpose. Let

$$\{y\} = [\Psi]\{\Phi\}, \tag{28}$$

where $[\Psi]$ is a matrix whose columns are the eigenvectors of matrix $[B]$, and $\{\Phi\}$ is a transformation vector or a vector of generalized coordinates. Substituting Eq. (28) in Eq. (25) then gives

$$\{\Phi'\} = [\Psi]^{-1}[B][\Psi]\{\Phi\} \equiv [\Upsilon]\{\Phi\}, \tag{29}$$

where $[\Upsilon]$ is a diagonal matrix composed of the eigenvalues λ of the matrix $[B]$. Substituting the solution of Eq. (29),

$$\{\Phi\} = \lfloor c_1 e^{\lambda_1 x}, c_2 e^{\lambda_2 x}, c_3 e^{\lambda_3 x}, c_4 e^{\lambda_4 x},$$
$$c_5 e^{\lambda_5 x}, c_6 e^{\lambda_6 x}, c_7 e^{\lambda_7 x}, c_8 e^{\lambda_8 x}, \rfloor^T, \tag{30}$$

in Eq. (28) yields

$$\{y\} = [\Psi]\lfloor c_1 e^{\lambda_1 x}, c_2 e^{\lambda_2 x}, c_3 e^{\lambda_3 x}, c_4 e^{\lambda_4 x},$$
$$c_5 e^{\lambda_5 x}, c_6 e^{\lambda_6 x}, c_7 e^{\lambda_7 x}, c_8 e^{\lambda_8 x} \rfloor^T. \tag{31}$$

Substituting Eq. (31) in Eq. (24), replacing p_j' by $\rho_0 c_0 u_j$ [using Eq. (9)], and then rearranging the equation gives

$$\{p\} = [\Lambda(x)]\{c\}, \tag{32}$$

where

$$\{p\} = \lfloor p_1, \quad \rho_0 c_0 u_1, \quad p_2, \quad \rho_0 c_0 u_2,$$
$$p_3, \quad \rho_0 c_0 u_3, \quad p_4, \quad \rho_0 c_0 u_4 \rfloor^T, \tag{33}$$

where the symbol $(')$ denotes d/dx. Substituting Eq. (24) in Eq. (17) then yields

$$\{y'\} = [B]\{y\}, \tag{25}$$

where

$$\{y\} = \lfloor y_1, \quad y_2, \quad y_3, \quad y_4, \quad y_5, \quad y_6, \quad y_7, \quad y_8 \rfloor^T, \tag{26}$$

$$\{c\} = \lfloor c_1, \quad c_2, \quad c_3, \quad c_4, \quad c_5, \quad c_6, \quad c_7, \quad c_8 \rfloor^T, \tag{34}$$

and

$$[\Lambda(x)] = \begin{bmatrix} \Psi_{51} e^{\lambda_1 x} & \Psi_{52} e^{\lambda_2 x} & \cdots & \Psi_{58} e^{\lambda_8 x} \\ \dfrac{-\Psi_{11} e^{\lambda_1 x}}{ik_0 + M_1\lambda_1} & \dfrac{-\Psi_{12} e^{\lambda_2 x}}{ik_0 + M_1\lambda_2} & \cdots & \dfrac{-\Psi_{18} e^{\lambda_8 x}}{ik_0 + M_1\lambda_8} \\ \Psi_{61} e^{\lambda_1 x} & \Psi_{62} e^{\lambda_2 x} & \cdots & \Psi_{68} e^{\lambda_8 x} \\ \dfrac{-\Psi_{21} e^{\lambda_1 x}}{ik_0 + M_2\lambda_1} & \dfrac{-\Psi_{22} e^{\lambda_2 x}}{ik_0 + M_2\lambda_2} & \cdots & \dfrac{-\Psi_{28} e^{\lambda_8 x}}{ik_0 + M_2\lambda_8} \\ \Psi_{71} e^{\lambda_1 x} & \Psi_{72} e^{\lambda_2 x} & \cdots & \Psi_{78} e^{\lambda_8 x} \\ \dfrac{-\Psi_{31} e^{\lambda_1 x}}{ik_0 + M_3\lambda_1} & \dfrac{-\Psi_{32} e^{\lambda_2 x}}{ik_0 + M_3\lambda_2} & \cdots & \dfrac{-\Psi_{38} e^{\lambda_8 x}}{ik_0 + M_3\lambda_8} \\ \Psi_{81} e^{\lambda_1 x} & \Psi_{82} e^{\lambda_2 x} & \cdots & \Psi_{88} e^{\lambda_8 x} \\ \dfrac{-\Psi_{41} e^{\lambda_1 x}}{ik_0 + M_4\lambda_1} & \dfrac{-\Psi_{42} e^{\lambda_2 x}}{ik_0 + M_4\lambda_2} & \cdots & \dfrac{-\Psi_{48} e^{\lambda_8 x}}{ik_0 + M_4\lambda_8} \end{bmatrix}. \tag{35}$$

III. BOUNDARY CONDITIONS

The schematic of two typical three-pass perforated element mufflers (i) where the perforated ducts do not extend into the end chambers and (ii) where the perforated ducts extend into the end chambers are shown in Figs. 2 and 3, respectively. Two different segments can be identified: (i) expansion chamber and (ii) end chambers. Boundary conditions for these segments are discussed in this section.
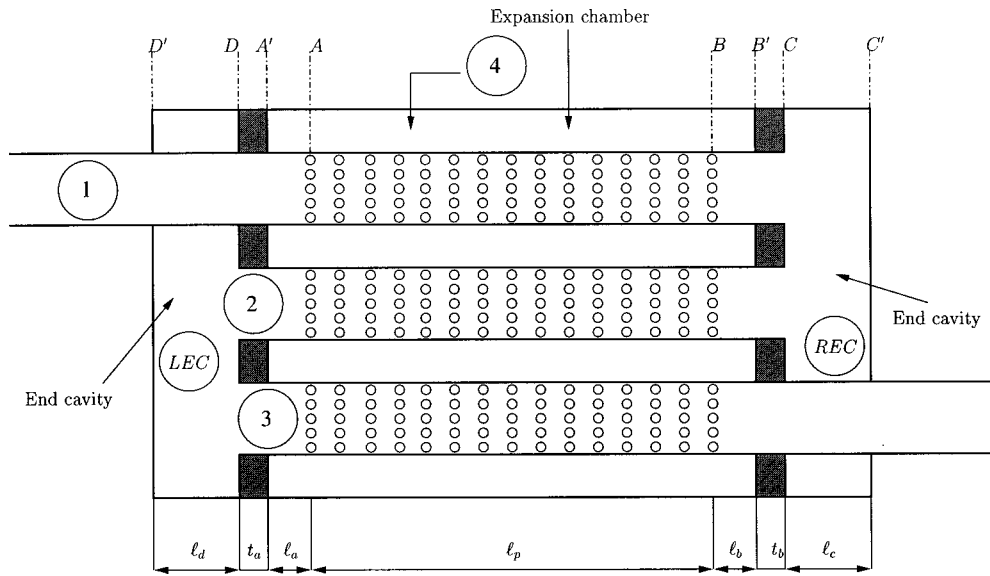
FIG. 2. A typical three-pass perforated muffler.

A. Expansion chamber

At sections A' and B', because of the rigid walls the velocity $u_4 = 0$. Therefore,

$$\rho_0 c_0 u_4|_A = -i \tan(k_0 \ell_a) p_4,$$

and

$$\rho_0 c_0 u_4|_B = i \tan(k_0 \ell_b) p_4. \qquad (36)$$

B. End cavities—No extensions

At the junction C in the right end chamber (REC) (see Fig. 2)

$$p_1 = p_2 = p_{\mathrm{REC}}, \quad A_1 u_1 + A_2 u_2 = A_{\mathrm{REC}} u_{\mathrm{REC}},$$

and

$$i \tan(k_0 \ell_c) p_{\mathrm{REC}} = \rho_0 c_0 u_{\mathrm{REC}}, \qquad (37)$$

where A_1, A_2, and A_{REC} are the cross-sectional areas of ducts 1, 2, and the end chamber (at C), respectively. Also,

$$\left\{ \begin{array}{c} p_1 \\ \rho_0 c_0 u_1 \end{array} \right\}_B = \left[\begin{array}{cc} \cos k_0 \ell_{b1} & i \sin k_0 \ell_{b1} \\ i \sin k_0 \ell_{b1} & \cos k_0 \ell_{b1} \end{array} \right] \left\{ \begin{array}{c} p_1 \\ \rho_0 c_0 u_1 \end{array} \right\}_C \qquad (38)$$

and

$$\left\{ \begin{array}{c} p_2 \\ \rho_0 c_0 u_2 \end{array} \right\}_B = \left[\begin{array}{cc} \cos k_0 \ell_{b2} & i \sin k_0 \ell_{b2} \\ i \sin k_0 \ell_{b2} & \cos k_0 \ell_{b2} \end{array} \right] \left\{ \begin{array}{c} p_2 \\ \rho_0 c_0 u_2 \end{array} \right\}_C, \qquad (39)$$

where $\ell_{b1} = \ell_b + t_b + \delta_1$, $\ell_{b2} = \ell_b + t_b + \delta_{2C}$, and

$$\delta_1 = 0.425 d_1 \left(1.0 - 1.25 \frac{d_1}{\sqrt{d_4^2 - d_3^2}} \right),$$

$$\delta_{2C} = 0.425 d_2 \left(1.0 - 1.25 \frac{d_2}{\sqrt{d_4^2 - d_3^2}} \right) \qquad (40)$$

are the end corrections for the expansion of ducts 1 and 2, respectively, into the end chamber at C. The end correction
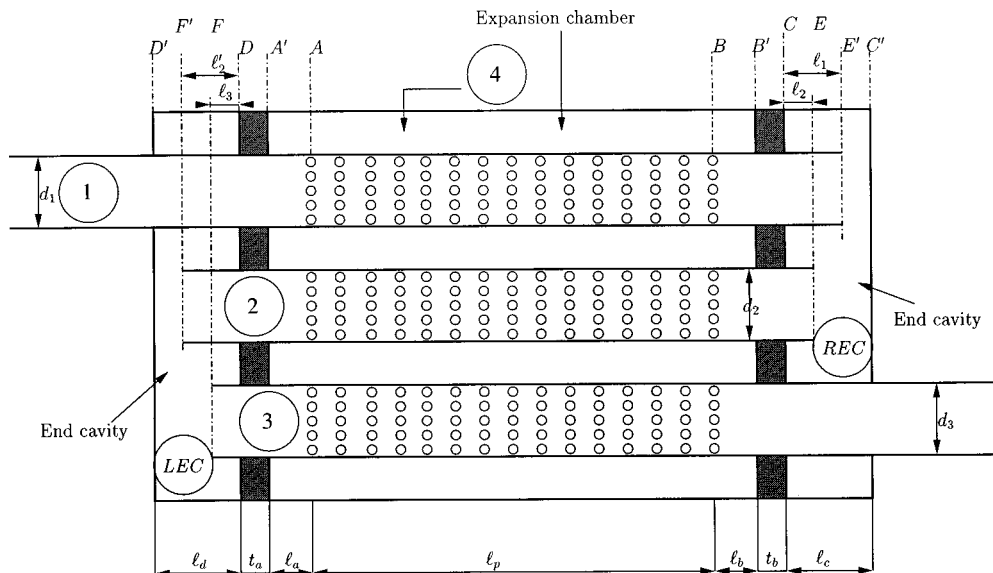
FIG. 3. A typical three-pass perforated muffler with ducts extending into the end cavities.

lengths are added to account for the lumped inertance at the ends of ducts 1 and 2 (at location C) and correspond to the lumped inertance of a duct terminating into an infinite flange.[17]

Combining Eqs. (37)–(39) gives

$$\left\{ \begin{array}{c} p_1 \\ \rho_0 c_0 u_1 \end{array} \right\}_B = [Q] \left\{ \begin{array}{c} p_2 \\ \rho_0 c_0 u_2 \end{array} \right\}_B, \tag{41}$$

where

$$[Q] = \begin{bmatrix} \cos(k_0 \ell_{b1}) & i \sin(k_0 \ell_{b1}) \\ i \sin(k_0 \ell_{b1}) & \cos(k_0 \ell_{b1}) \end{bmatrix}$$

$$\times \begin{bmatrix} 1 & 0 \\ i \dfrac{A_{REC}}{A_1} \tan(k_0 \ell_c) & -\dfrac{A_2}{A_1} \end{bmatrix}$$

$$\times \begin{bmatrix} \cos(k_0 \ell_{b2}) & i \sin(k_0 \ell_{b2}) \\ i \sin(k_0 \ell_{b2}) & \cos(k_0 \ell_{b2}) \end{bmatrix}^{-1}. \tag{42}$$

Similarly, applying boundary conditions at junction D in the left end chamber (LEC) leads to

$$\left\{ \begin{array}{c} p_2 \\ \rho_0 c_0 u_2 \end{array} \right\}_A = [R] \left\{ \begin{array}{c} p_3 \\ \rho_0 c_0 u_3 \end{array} \right\}_A, \tag{43}$$

where $[R]$ can be obtained from $[Q]$ by replacing (i) ℓ_b by $-\ell_a$, (ii) t_b by $-t_a$, (iii) ℓ_c by $-\ell_d$, (iv) A_1 by A_2 and A_2 by A_3, (v) δ_1 by $-\delta_3$ and δ_2 by $-\delta_4$, and (vi) the subscript REC by LEC, as

$$[R] = \begin{bmatrix} \cos(k_0 \ell_{a1}) & -i \sin(k_0 \ell_{a1}) \\ -i \sin(k_0 \ell_{a1}) & \cos(k_0 \ell_{a1}) \end{bmatrix}$$

$$\times \begin{bmatrix} 1 & 0 \\ -i \dfrac{A_{LEC}}{A_2} \tan(k_0 \ell_d) & -\dfrac{A_3}{A_2} \end{bmatrix}$$

$$\times \begin{bmatrix} \cos(k_0 \ell_{a2}) & -i \sin(k_0 \ell_{a2}) \\ -i \sin(k_0 \ell_{a2}) & \cos(k_0 \ell_{a2}) \end{bmatrix}^{-1}, \tag{44}$$

where $\ell_{a1} = \ell_a + t_a + \delta_{2D}$, $\ell_{a2} = \ell_a + t_a + \delta_3$, and

$$\begin{aligned} \delta_{2D} &= 0.425 d_2 \left(1.0 - 1.25 \frac{d_2}{\sqrt{d_4^2 - d_1^2}} \right), \\ \delta_3 &= 0.425 d_3 \left(1.0 - 1.25 \frac{d_3}{\sqrt{d_4^2 - d_1^2}} \right), \end{aligned} \tag{45}$$

are the end corrections for the expansion of ducts 2 and 3, respectively, into the end cavity at D.

C. End cavities—With extensions

A typical three-pass muffler where the inlet, center, and the outlet ducts extend into the end chamber is illustrated in Fig. 3. An enlarged view of its right end chamber is shown in Fig. 4.
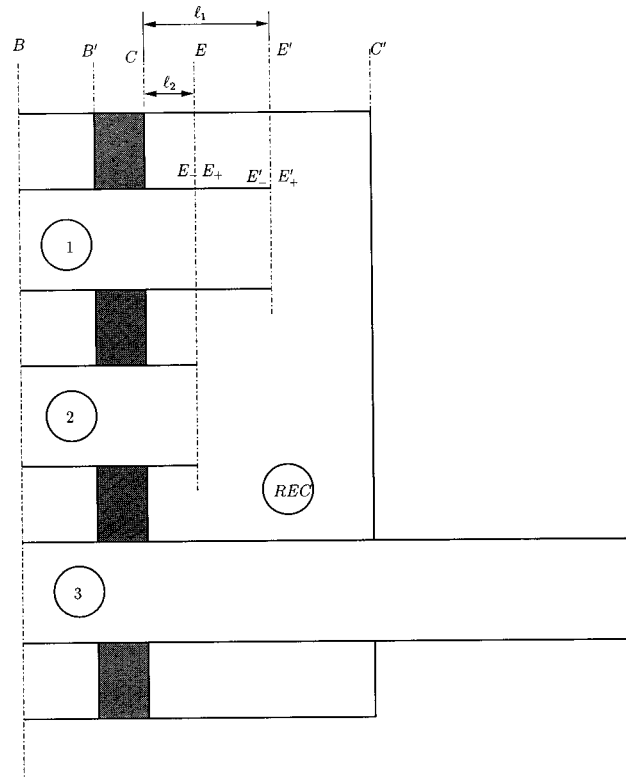
FIG. 4. An enlarged view of right end chamber.

1. Case I ($\ell_1 \geqslant \ell_2$)

At location E' (see Fig. 4)

$$p_1|_{E'} = p_{REC}|_{E'_-} = p_{REC}|_{E'_+} \tag{46}$$

and

$$A_1 \rho_0 c_0 u_1|_{E'} + (A_{REC} - A_1) \rho_0 c_0 u_{REC}|_{E'_-}$$
$$= A_{REC} \rho_0 c_0 u_{REC}|_{E'_+}. \tag{47}$$

Because of the rigid ends at locations C and C', $u_{REC} = 0$. Hence,

$$\left. \frac{\rho_0 c_0 u_{REC}}{p_{REC}} \right|_{E'_+} = i \tan k_0 (\ell_c - \ell_1) \tag{48}$$

and

$$\left. \frac{\rho_0 c_0 u_{REC}}{p_{REC}} \right|_{E_-} = -i \tan k_0 \ell_2. \tag{49}$$

Combining Eqs. (46)–(48) gives

$$\left\{ \begin{array}{c} p_1 \\ \rho_0 c_0 u_1 \end{array} \right\}_{E'} = \begin{bmatrix} 1 & 0 \\ i \dfrac{A_{REC}}{A_1} \tan k_0 (\ell_c - \ell_1) & -\dfrac{(A_{REC} - A_1)}{A_1} \end{bmatrix}$$

$$\times \left\{ \begin{array}{c} p_{REC} \\ \rho_0 c_0 u_{REC} \end{array} \right\}_{E'_-}. \tag{50}$$

At location E,

$$p_{REC}|_{E_+} = p_{REC}|_{E_-} = p_2|_E \tag{51}$$

and

$$(A_{\text{REC}}-A_1)\rho_0 c_0 u_{\text{REC}}\big|_{E_+}$$

$$=(A_{\text{REC}}-A_1-A_2)\rho_0 c_0 u_{\text{REC}}\big|_{E_-}+A_2\rho_0 c_0 u_2\big|_E. \qquad (52)$$

Combining Eqs. (49), (51), and (52) yields

$$\left\{\begin{array}{c} p_{\text{REC}} \\ \rho_0 c_0 u_{\text{REC}} \end{array}\right\}_{E_+}=\left[\begin{array}{cc} 1 & 0 \\ -i\left(\dfrac{A_{\text{REC}}-A_1-A_2}{A_{\text{REC}}-A_1}\right)\tan k_0\ell_2 & \dfrac{A_2}{A_{\text{REC}}-A_1} \end{array}\right]$$

$$\times\left\{\begin{array}{c} p_2 \\ \rho_0 c_0 u_2 \end{array}\right\}_E. \qquad (53)$$

Also, the state variables p_{REC} and u_{REC} at either ends of the duct segment $E-E'$ are related by

$$\left\{\begin{array}{c} p_{\text{REC}} \\ \rho_0 c_0 u_{\text{REC}} \end{array}\right\}_{E'_-}=\left[\begin{array}{cc} \cos k_0(\ell_1-\ell_2) & -i\sin k_0(\ell_1-\ell_2) \\ -i\sin k_0(\ell_1-\ell_2) & \cos k_0(\ell_1-\ell_2) \end{array}\right]$$

$$\times\left\{\begin{array}{c} p_{\text{REC}} \\ \rho_0 c_0 u_{\text{REC}} \end{array}\right\}_{E_+}. \qquad (54)$$

In view of Eqs. (50), (53), and (54),

$$\left\{\begin{array}{c} p_1 \\ \rho_0 c_0 u_1 \end{array}\right\}_{E'}=\left[\begin{array}{cc} 1 & 0 \\ i\dfrac{A_{\text{REC}}}{A_1}\tan k_0(\ell_c-\ell_1) & -\dfrac{(A_{\text{REC}}-A_1)}{A_1} \end{array}\right]$$

$$\times\left[\begin{array}{cc} \cos k_0(\ell_1-\ell_2) & -i\sin k_0(\ell_1-\ell_2) \\ -i\sin k_0(\ell_1-\ell_2) & \cos k_0(\ell_1-\ell_2) \end{array}\right]$$

$$\times\left[\begin{array}{cc} 1 & 0 \\ -i\left(\dfrac{A_{\text{REC}}-A_1-A_2}{A_{\text{REC}}-A_1}\right)\tan k_0\ell_2 & \dfrac{A_2}{A_{\text{REC}}-A_1} \end{array}\right]$$

$$\times\left\{\begin{array}{c} p_2 \\ \rho_0 c_0 u_2 \end{array}\right\}_E. \qquad (55)$$

In the presence of ducts extending into the end cavities, Eqs. (38) and (39) become

$$\left\{\begin{array}{c} p_1 \\ \rho_0 c_0 u_1 \end{array}\right\}_B=\left[\begin{array}{cc} \cos k_0\ell_{b3} & i\sin k_0\ell_{b3} \\ i\sin k_0\ell_{b3} & \cos k_0\ell_{b3} \end{array}\right]\left\{\begin{array}{c} p_1 \\ \rho_0 c_0 u_1 \end{array}\right\}_{E'}$$

$$(56)$$

and

$$\left\{\begin{array}{c} p_2 \\ \rho_0 c_0 u_2 \end{array}\right\}_B=\left[\begin{array}{cc} \cos k_0\ell_{b4} & i\sin k_0\ell_{b4} \\ i\sin k_0\ell_{b4} & \cos k_0\ell_{b4} \end{array}\right]\left\{\begin{array}{c} p_2 \\ \rho_0 c_0 u_2 \end{array}\right\}_E,$$

$$(57)$$

respectively, where $\ell_{b3}=\ell_b+t_b+\ell_1+\delta_1$ and $\ell_{b4}=\ell_b+t_b+\ell_2+\delta_2$, and δ_1 and δ_2 are end corrections for the expansion of ducts 1 and 2 into the chamber at E' and E. Thus, in view of Eqs. (56), (57), and (53), the matrix $[Q]$ defined by Eq. (41) becomes

$$[Q]=\left[\begin{array}{cc} \cos k_0\ell_{b3} & i\sin k_0\ell_{b3} \\ i\sin k_0\ell_{b3} & \cos k_0\ell_{b3} \end{array}\right]$$

$$\times\left[\begin{array}{cc} 1 & 0 \\ i\dfrac{A_{\text{REC}}}{A_1}\tan k_0(\ell_c-\ell_1) & -\dfrac{(A_{\text{REC}}-A_1)}{A_1} \end{array}\right]$$

$$\times\left[\begin{array}{cc} \cos k_0(\ell_1-\ell_2) & -i\sin k_0(\ell_1-\ell_2) \\ -i\sin k_0(\ell_1-\ell_2) & \cos k_0(\ell_1-\ell_2) \end{array}\right]$$

$$\times\left[\begin{array}{cc} 1 & 0 \\ -i\left(\dfrac{A_{\text{REC}}-A_1-A_2}{A_{\text{REC}}-A_1}\right)\tan k_0\ell_2 & \dfrac{A_2}{A_{\text{REC}}-A_1} \end{array}\right]$$

$$\times\left[\begin{array}{cc} \cos k_0\ell_{b4} & i\sin k_0\ell_{b4} \\ i\sin k_0\ell_{b4} & \cos k_0\ell_{b4} \end{array}\right]^{-1}. \qquad (58)$$

2. Case II ($\ell_1<\ell_2$)

Following the procedure illustrated for Case I, it can be shown that

$$\left\{\begin{array}{c} p_2 \\ \rho_0 c_0 u_2 \end{array}\right\}_E=\left[\begin{array}{cc} 1 & 0 \\ i\dfrac{A_{\text{REC}}}{A_2}\tan k_0(\ell_c-\ell_2) & -\dfrac{(A_{\text{REC}}-A_2)}{A_2} \end{array}\right]$$

$$\times\left[\begin{array}{cc} \cos k_0(\ell_2-\ell_1) & -i\sin k_0(\ell_2-\ell_1) \\ -i\sin k_0(\ell_2-\ell_1) & \cos k_0(\ell_2-\ell_1) \end{array}\right]$$

$$\times\left[\begin{array}{cc} 1 & 0 \\ -i\left(\dfrac{A_{\text{REC}}-A_1-A_2}{A_{\text{REC}}-A_2}\right)\tan k_0\ell_1 & \dfrac{A_1}{A_{\text{REC}}-A_2} \end{array}\right]$$

$$\times\left\{\begin{array}{c} p_1 \\ \rho_0 c_0 u_1 \end{array}\right\}_{E'}. \qquad (59)$$

Equation (59) can also be obtained from Eq. (55) by switching subscripts 1 and 2, and E and E'. The matrix $[Q]$ is then given by

$$[Q] = \begin{bmatrix} \cos k_0 \ell_{b3} & i \sin k_0 \ell_{b3} \\ i \sin k_0 \ell_{b3} & \cos k_0 \ell_{b3} \end{bmatrix}$$

$$\times \begin{bmatrix} 1 & 0 \\ -i\left(\dfrac{A_{REC} - A_1 - A_2}{A_{REC} - A_2}\right)\tan k_0 \ell_1 & \dfrac{A_1}{A_{REC} - A_2} \end{bmatrix}^{-1}$$

$$\times \begin{bmatrix} \cos k_0(\ell_2 - \ell_1) & -i \sin k_0(\ell_2 - \ell_1) \\ -i \sin k_0(\ell_2 - \ell_1) & \cos k_0(\ell_2 - \ell_1) \end{bmatrix}^{-1}$$

$$\times \begin{bmatrix} 1 & 0 \\ i\dfrac{A_{REC}}{A_2}\tan k_0(\ell_c - \ell_2) & -\dfrac{(A_{REC} - A_2)}{A_2} \end{bmatrix}^{-1}$$

$$\times \begin{bmatrix} \cos k_0 \ell_{b4} & i \sin k_0 \ell_{b4} \\ i \sin k_0 \ell_{b4} & \cos k_0 \ell_{b4} \end{bmatrix}^{-1}. \tag{60}$$

The matrix $[R]$ defined by Eq. (43) may now be obtained from $[Q]$ following the procedure similar to that illustrated in Sec. III B. In the absence of ducts extending into the end chambers, Eqs. (58) and (60) can readily be shown to reduce to Eq. (42).

IV. TRANSFER MATRIX SOLUTION

The transfer matrix $[T]$ is defined as

$$\{p\}_{x_A} = [T]\{p\}_{x_B}, \tag{61}$$

which relates the state vector $\{p\}$ at A to that at B. By substituting $x = x_A$ and $x = x_B$ in Eq. (32) gives

$$[T] = [\Lambda(x_A)][\Lambda(x_B)]^{-1}. \tag{62}$$

Equation (61) subject to appropriate boundary conditions is the solution of the coupled Eq. (17), which is illustrated next.

Substituting Eq. (36) in Eq. (61) yields

$$\begin{Bmatrix} p_1 \\ \rho_0 c_0 u_1 \\ p_2 \\ \rho_0 c_0 u_2 \\ p_3 \\ \rho_0 c_0 u_3 \end{Bmatrix}_A = [TR] \begin{Bmatrix} p_1 \\ \rho_0 c_0 u_1 \\ p_2 \\ \rho_0 c_0 u_2 \\ p_3 \\ \rho_0 c_0 u_3 \end{Bmatrix}_B, \tag{63}$$

where $[TR]$ is the rank reduced transfer matrix given in terms of the elements of $[T]$ by

$$TR_{mn} = T_{mn} - \frac{(T_{8n} + i \tan(k_0 \ell_a)T_{7n})(T_{m7} + i \tan(k_0 \ell_b)T_{m8})}{T_{87} + i \tan(k_0 \ell_b)T_{88} + i \tan(k_0 \ell_a)(T_{77} + i \tan(k_0 \ell_b)T_{78})}, \quad m,n = 1,\ldots,6. \tag{64}$$

Substituting Eqs. (41) and (43) in Eq. (63) yields

$$\begin{Bmatrix} p_1 \\ \rho_0 c_0 u_1 \end{Bmatrix}_A = [T_{overall}] \begin{Bmatrix} p_3 \\ \rho_0 c_0 u_3 \end{Bmatrix}_B, \tag{65}$$

where

$$[T_{overall}] = [TR_{13}] - ([TR_{11}][Q] + [TR_{12}])([TR_{21}][Q]$$
$$+ [TR_{22}] - [R][TR_{31}][Q] - [R][TR_{32}])^{-1}$$
$$\times ([TR_{23}] - [R][TR_{33}]) \tag{66}$$

is the overall 2×2 transfer matrix. Transmission loss (TL) is then evaluated by[18]

$$TL = 20 \log_{10}\left[\frac{1}{2}\sqrt{\frac{A_1}{A_3}}\left|T_{11} + T_{12} + T_{21} + T_{22}\right|\frac{1 + M_1}{1 + M_3}\right]. \tag{67}$$

Computer programs were developed in $C++$ to predict the transmission loss of a three-pass muffler with and without the perforated ducts extending into the end cavity. The results obtained from the approach described in Secs. II–IV are presented next.

V. RESULTS AND DISCUSSION

A. Prototype muffler

A prototype three-pass muffler with a clear cast acrylic external housing of diameter $d_4 = 0.1651$ m and with three perforated brass pipes (forming the three passes) of inner diameter $d_1 = d_2 = d_3 = 0.0489$ m and thickness $t = 0.0008$ m was fabricated to facilitate controlled experiments. End cavities of lengths $\ell_c = 0.15$ m and $\ell_d = 0.102$ m were separated from the central section by aluminum baffles of thickness $t_a = t_b = 0.0127$ m. An interior duct porosity of $\phi = 0.045$ was obtained by drilling 448 holes of $d_h = 0.00234$ m diameter in each duct over the central region such that $\ell_p = 0.27432$ m and $\ell_a = \ell_b = 0.02794$ m. The dimensions of the fabricated prototype were chosen to duplicate a Chrysler production muffler. The three perforated brass tubes are held in position by two identical baffles as shown in Fig. 5. The transmission loss characteristics of the fabricated prototype are measured in an impedance tube setup. The details of the setup are described elsewhere.[19]

Figure 6 compares the theoretical predictions (depicted by solid line) and experimental results (depicted by solid symbols) for the fabricated prototype. The experimental results agree reasonably well with the theoretical results up to about 900 Hz. Higher-order acoustic modes start propagating beyond this frequency, limiting the present analysis. Note, this frequency is somewhat lower than the limit for the first diametral mode in a circular duct $[f_{\text{first diametral mode}}$

1555   J. Acoust. Soc. Am., Vol. 105, No. 3, March 1999

Selamet et al.: Three-pass mufflers   1555
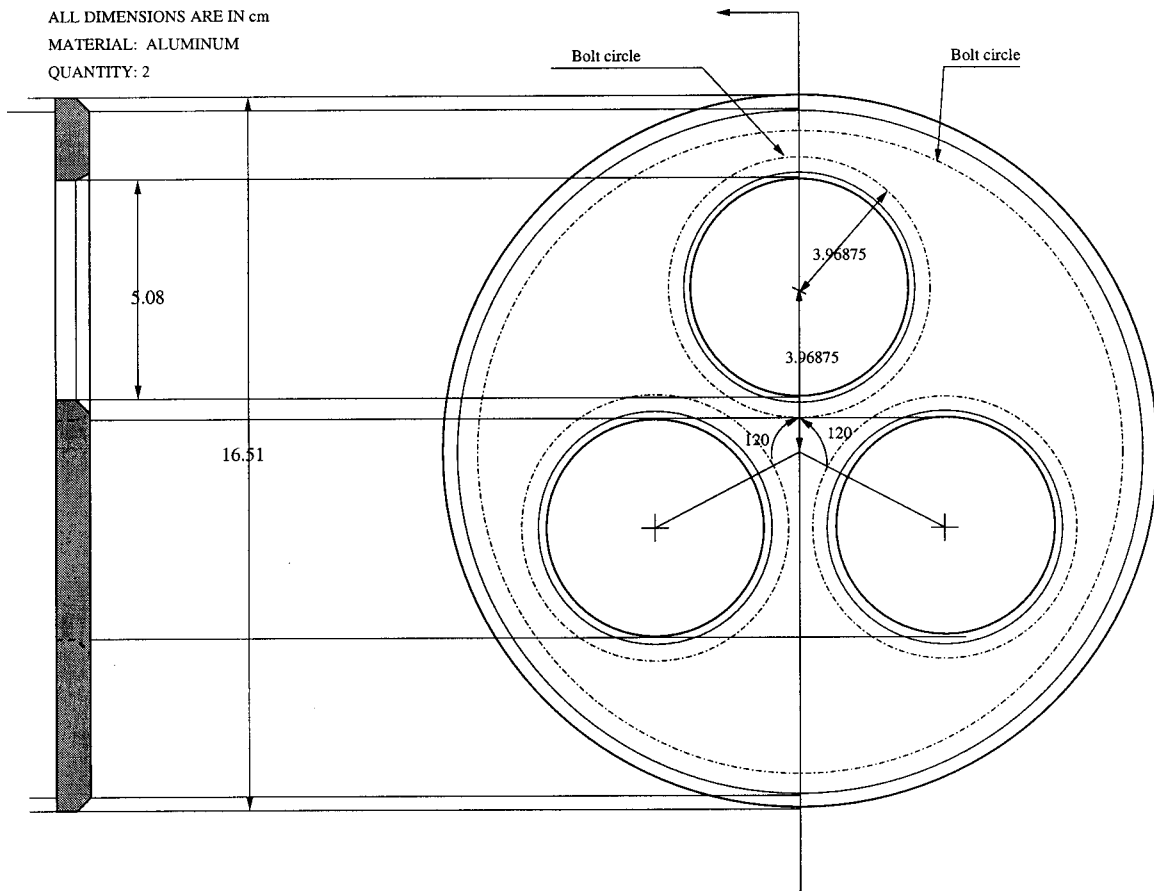
FIG. 5. Schematic of the baffle plate.
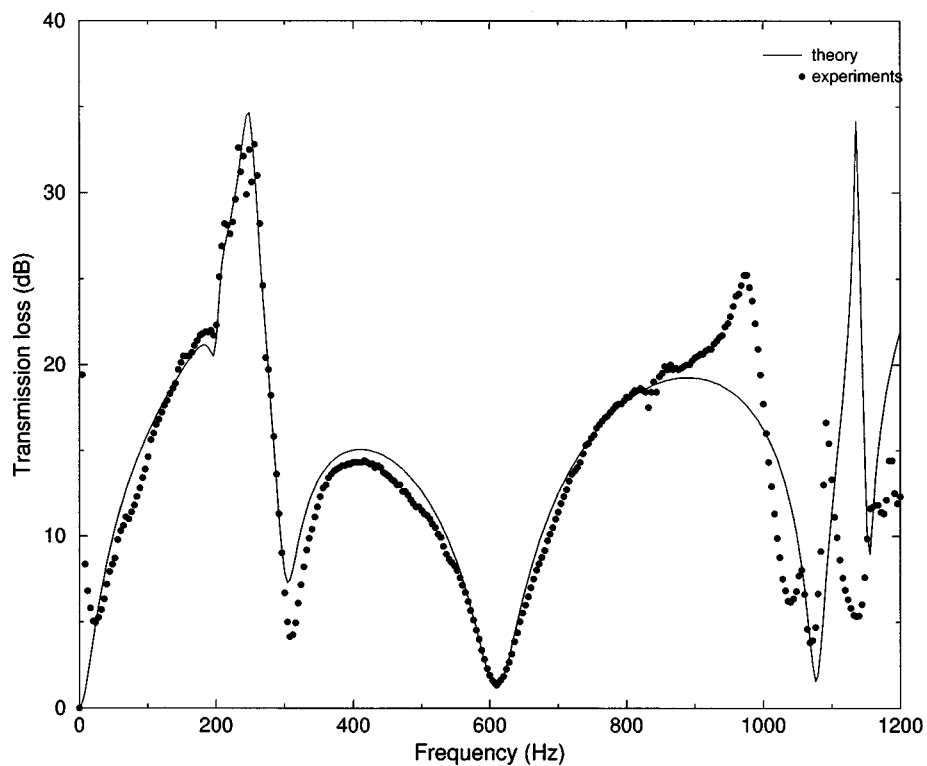
FIG. 6. Transmission loss of the three-pass perforated muffler: theory versus experiments. $\ell_p=0.274$ m, $\ell_a=\ell_b=0.0279$ m, $\ell_c=0.15$ m, $\ell_d=0.102$ m, $t_a=t_b=0.0127$ m, $d_1=d_2=d_3=0.0489$ m, $d_4=0.1651$ m, $d_h=0.00\,234$ m, $t=0.0008$ m, $\phi=0.045$, $\rho=1.18$ kg/m^3, $c_0=343.7$ m/s, and $M=0$.

$=1.84c_0/\pi d_{max}\approx1220\,\text{Hz}$, for d_{max} (chamber)$=0.1651$ m and a sound speed of 344 m/s]. This limit, however, shifts to higher frequencies as the speed of sound increases or as the gas temperature rises (since the speed of sound varies in direct proportion to the square root of the gas temperature). At very low frequencies (<50 Hz), the impedance tube termination is not fully anechoic and results in some discrepancy between theoretical predictions and experimental results. The overall behavior resembles that of a simple expansion chamber of length $\ell=\ell_p+\ell_a+\ell_b$ (because of the central section, with troughs occurring at frequency intervals of $c_0/2\ell\approx520\,\text{Hz}$, and peaks at odd multiples of the frequency $c_0/4\ell\approx260\,\text{Hz}$), with a superimposed resonance near 240 Hz, contributed by the presence of the two end cavities. Note, the perforate impedance for quiescent medium,[1-3]

$$\zeta=[6\times10^{-3}+ik_0(t+0.75d_h)]/\phi, \qquad (68)$$

was used in Fig. 6. Here, t is the duct thickness and d_h is the perforate diameter. This same impedance is used in all the figures that follow.

B. Production mufflers

The transmission loss characteristics of two production three-pass mufflers used in Chrysler vehicles were measured in the impedance tube setup. The mufflers were later cut open to obtain the geometric details. The expansion chamber and the end cavities of both mufflers are elliptical in cross section. For theoretical treatment, elliptical cross sections were replaced by circular ducts of equal cross-sectional area.

The theoretical and experimental results for the first muffler are shown in Fig. 7. As in Fig. 6, the muffler shows an expansion chamber behavior with a superimposed resonance at about 250 Hz. The resonance may be attributed to the combined effect of the end cavities. Theoretical results compare reasonably well up to about 700 Hz, a frequency dictated primarily by the propagation of higher-order modes. Discrepancy between theory and experiments may also be attributed to the fact that the exact geometry and the louver size and its distribution are not known *a priori*; only a rough estimate of the physical dimensions of the muffler has been used in the computations. Also, the cross-sectional area of the inlet and outlet ducts are not exactly uniform as assumed by the theoretical model.

The inlet and center perforated ducts of the second muffler extend into the right and the left end chambers, respectively. The two baffle plates of this muffler have two holes each, approximately 0.0254 m in diameter. Since the present theoretical method cannot handle baffle holes (which would couple the expansion chamber and the end cavities directly), these holes were plugged before the muffler was mounted in the impedance tube setup. Theoretical and experimental results for this muffler are compared in Fig. 8. As in Figs. 6 and 7, two resonant peaks occur at low frequencies, due mainly to the presence of the end cavities. The agreement between the theory and experiments is reasonable at low frequencies. Similar to the muffler of Fig. 7, the discrepancy between theory and experiments may partially be attributed to the fact that the exact geometry, and the pore size and its distribution are not known *a priori*; only a rough estimate of the physical dimensions of the muffler has been used in the computations. The theory assumes that there is a common length ℓ_p over which the inlet, center, and the outlet ducts are perforated. This particular muffler, however, has perforations which are nonuniformly distributed. Therefore, an average perforated length has been used in the computations.
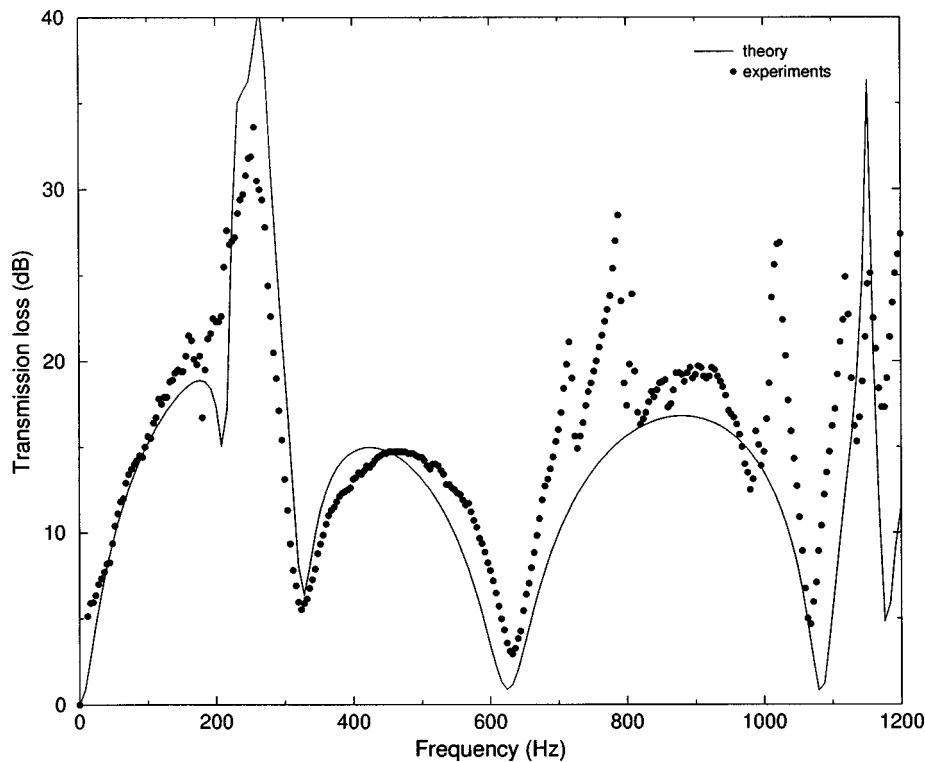
FIG. 7. Transmission loss of a Chrysler muffler theory versus experiments. $\ell_p=0.28$ m, $\ell_a=0.02$ m, $\ell_b=0.03$ m, $\ell_c=0.102$ m, $\ell_d=0.152$m, $t_a=t_b=0.011$ m, $d_1=d_2=d_3=0.0489$ m, $d_4=0.164$ m, $d_h=0.00\,249$ m, $t=0.0008$ m, $\phi=0.09$, $\rho=1.18$ kg/m^3, $c_0=344.57$ m/s, and $M=0$.

1557   J. Acoust. Soc. Am., Vol. 105, No. 3, March 1999

Selamet *et al.*: Three-pass mufflers   1557
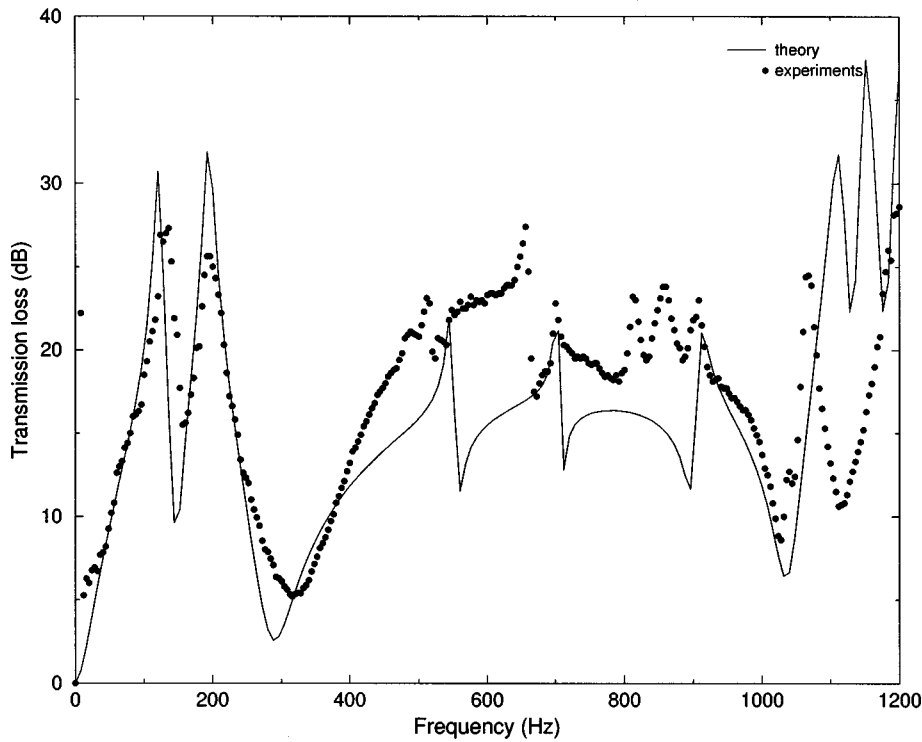
FIG. 8. Transmission loss of a Chrysler muffler theory versus experiments. $\ell_p = 0.105$ m, $\ell_a = 0.025$ m, $\ell_b = 0.05$ m, $\ell_c = 0.25$ m, $\ell_d = 0.148$ m, $\ell_1 = 0.205$ m, $\ell_2 = 0$ m, $\ell'_2 = 0.112$ m, $\ell_3 = 0$ m, $t_a = t_b = 0.015$ m, $d_1 = 0.0482$ m, $d_2 = 0.0424$ m, $d_3 = 0.0475$ m, $d_4 = 0.157$ m, $d_h = 0.00\,249$ m, $t = 0.0008$ m, $\phi = 0.09$, $\rho = 1.18$ kg/m^3, $c_0 = 344.57$ m/s, and $M = 0$.

This may also contribute to the differences between the theoretical predictions and the experimental results.

C. Parametric study

Similar to Ref. 14, the variations of the parameters which affect the performance of the three-pass muffler are studied in this section. The prototype muffler is used as the baseline case in all the comparisons that follow (see solid lines in Figs. 9–14).

The sensitivity of the three-pass muffler to variations in duct porosity is shown in Fig. 9. The effect of porosity is marginal until about 600 Hz (beyond which expansion chamber behavior dominates). At frequencies greater than 600 Hz the transmission loss is greater for the muffler with lower duct porosities. At low frequencies (<300 Hz), where the resonances are due to the end cavity, the effect is just the opposite. These frequency limits depend, to a large extent, on the geometry of the muffler.
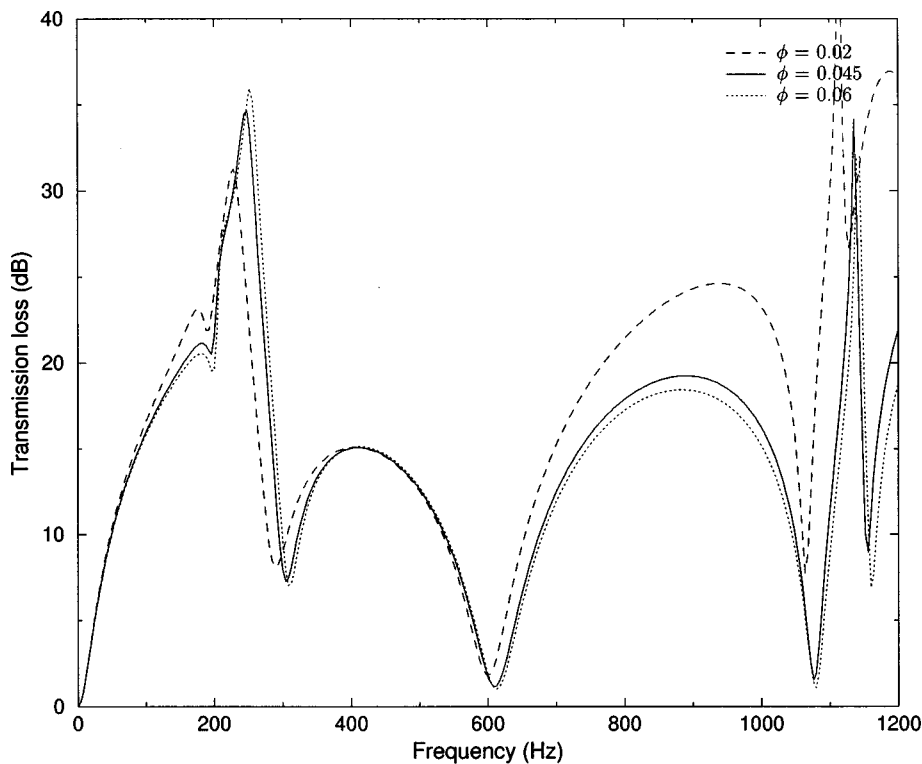
FIG. 9. Effect of porosity on the performance of a three-pass muffler. $\ell_p = 0.274$ m, $\ell_a = \ell_b = 0.0279$ m, $\ell_c = 0.15$ m, $\ell_d = 0.102$ m, $t_a = t_b = 0.0127$ m, $d_1 = d_2 = d_3 = 0.0489$ m, $d_4 = 0.1651$ m, $d_h = 0.00\,234$ m, $t = 0.0008$ m, $\rho = 1.18$ kg/m^3, $c_0 = 343.7$ m/s, and $M = 0$.
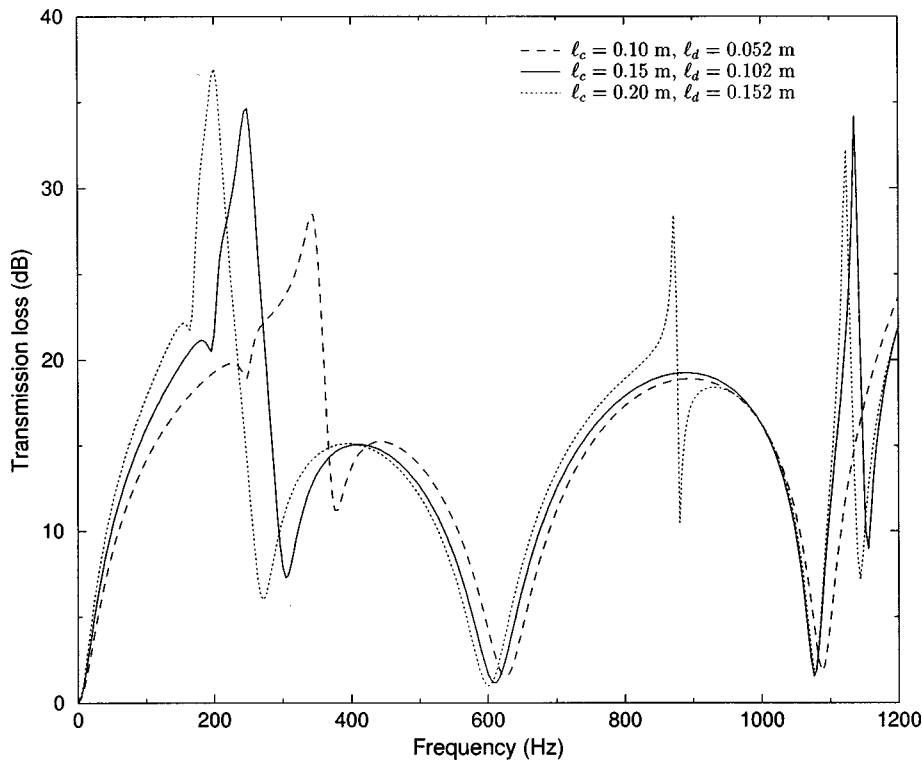
FIG. 10. Effect of the length of end cavity on the performance of a three-pass muffler. $\ell_p = 0.274$ m, $\ell_a = \ell_b = 0.0279$ m, $t_a = t_b = 0.0127$ m, $d_1 = d_2 = d_3 = 0.0489$ m, $d_4 = 0.1651$ m, $d_h = 0.00234$ m, $t = 0.0008$ m, $\phi = 0.045$, $\rho = 1.18$ kg/m^3, $c_0 = 343.7$ m/s, and $M = 0$.

Figure 10 shows the effect of the length of the end cavities on the transmission loss characteristics. Increasing the length of the end cavities shifts the peaks in the transmission loss to lower frequencies. As noted in Figs. 5–9, the end cavities contribute to the resonant peaks, since they, together with the perforated ducts, constitute approximately a Helmholtz resonator. It is well known that the resonance frequency of a Helmholtz resonator is inversely proportional to the square root of the length of the cylindrical cavity, which

in this case is the length of end cavities for fixed cross-sectional area. This explains the shift observed in Fig. 10. Figure 11 compares the muffler of the baseline case with a muffler whose end chambers are identical (only ℓ_c is varied and made equal to ℓ_d). Since the total length of the end cavity for the latter case is reduced, the resonance peaks shift to higher frequencies. The effect, however, is marginal beyond 400 Hz where the simple expansion chamber behavior dominates. The effect of the length of expansion chamber is
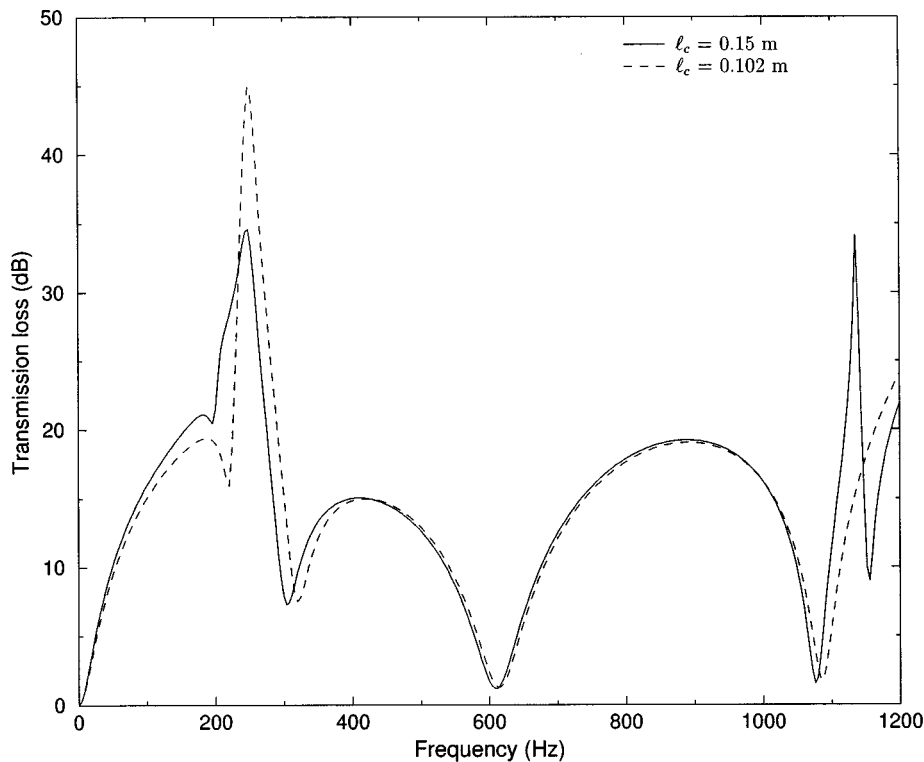
FIG. 11. Effect of the length (ℓ_c) of one of the end cavities on the performance of a three-pass muffler. $\ell_p = 0.274$ m, $\ell_a = \ell_b = 0.0279$ m, $\ell_d = 0.102$ m, $t_a = t_b = 0.0127$ m, $d_1 = d_2 = d_3 = 0.0489$ m, $d_4 = 0.1651$ m, $d_h = 0.00234$ m, $t = 0.0008$ m, $\phi = 0.045$, $\rho = 1.18$ kg/m^3, $c_0 = 343.7$ m/s, and $M = 0$.
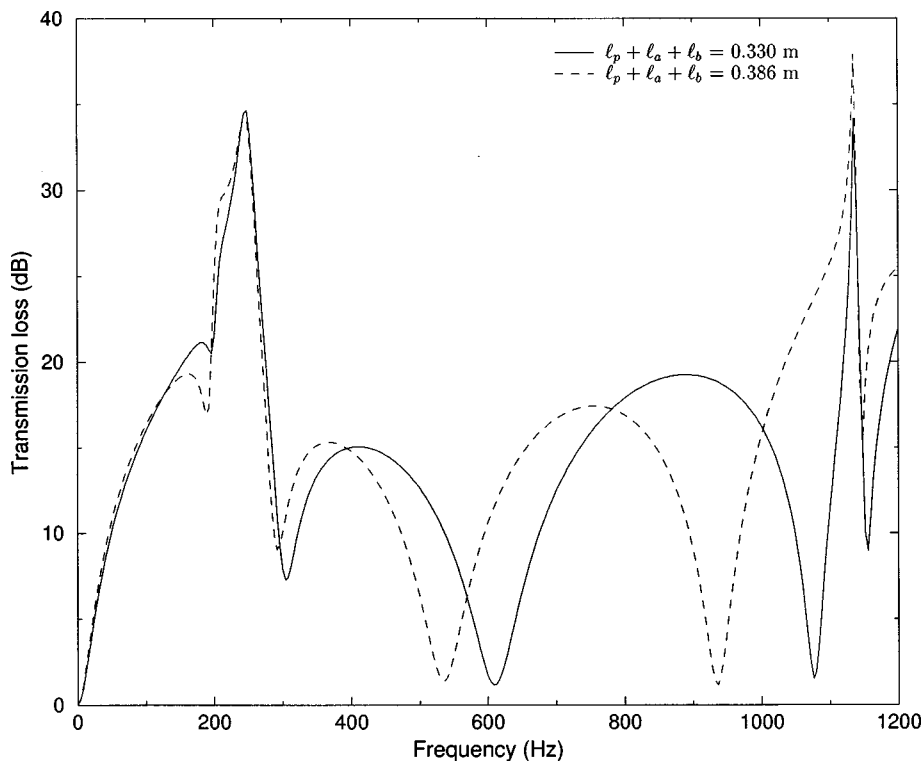
FIG. 12. Effect of the length (ℓ_c) of the expansion chamber on the performance of a three-pass muffler. $\ell_a = \ell_b = 0.0279$ m, $\ell_c = 0.15$ m, $\ell_d = 0.102$ m, $t_a = t_b = 0.0127$ m, $d_1 = d_2 = d_3 = 0.0489$ m, $d_4 = 0.1651$ m, $d_h = 0.00\,234$ m, $t = 0.0008$ m, $\phi = 0.045$, $\rho = 1.18$ kg/m^3, $c_0 = 343.7$ m/s, and $M = 0$.

shown in Fig. 12. Increase in the expansion chamber length $\ell_p + \ell_a + \ell_b$ (ℓ_a and ℓ_b were retained the same) shifts the peaks and troughs to lower frequencies. The effect is minimal at low frequencies (below 300 Hz) where end cavities dominate.

The effect of increase in the diameter of the expansion chamber is shown in Fig. 13. An increase in the diameter increases the transmission loss at higher frequencies (>600 Hz). The presence of the middle chamber (expansion cham-

ber), as discussed earlier, results in a simple expansion chamber behavior. The troughs for a simple expansion chamber occur at frequency intervals of $f = c_0/2\ell \approx 520$ Hz. It is well known that the transmission loss for a simple expansion chamber increases with increase in the diameter ratio. This explains the behavior observed at frequency >520 Hz. At lower frequencies, the Helmholtz behavior of the end chamber becomes important. Increase in the expansion chamber diameter increases the diameter of the end cavities and, since

FIG. 13. Effect of the diameter of the expansion chamber on the performance of a three-pass muffler. $\ell_p = 0.274$ m, $\ell_a = \ell_b = 0.0279$ m, $\ell_c = 0.15$ m, $\ell_d = 0.102$ m, $t_a = t_b = 0.0127$ m, $d_1 = d_2 = d_3 = 0.0489$ m, $d_h = 0.00\,234$ m, $t = 0.0008$ m, $\phi = 0.045$, $\rho = 1.18$ kg/m^3, $c_0 = 343.7$ m/s, and $M = 0$.
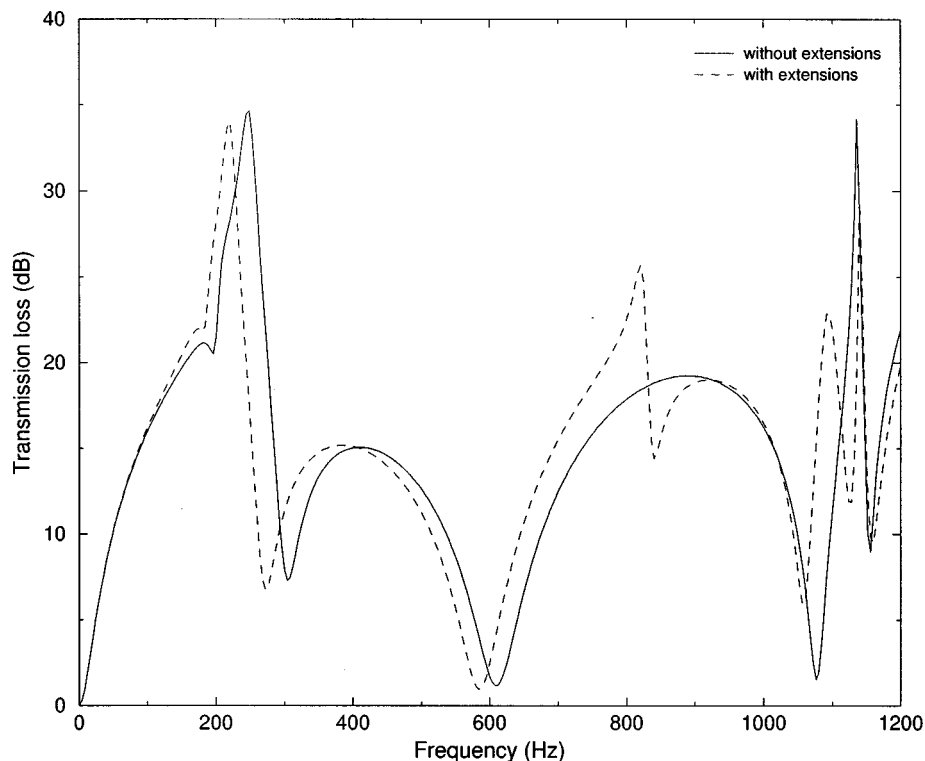
FIG. 14. Effect of the duct extensions into the end cavities on the performance of a three-pass muffler. $\ell_p = 0.274$ m, $\ell_a = \ell_b = 0.0279$ m, $\ell_c = 0.15$ m, $\ell_d = 0.102$ m, $t_a = t_b = 0.0127$ m, $d_1 = d_2 = d_3 = 0.0489$ m, $d_4 = 0.1651$ m, $d_h = 0.00234$ m, $t = 0.0008$ m, $\phi = 0.045$, $\rho = 1.18$ kg/m^3, $c_0 = 343.7$ m/s, and $M = 0$. For the muffler with extensions into the end cavity, $\ell_1 = 0.076$ m, $\ell_2 = 0$ m, $\ell_2' = 0.126$ m, and $\ell_3 = 0$ m.

the Helmholtz resonance frequency is inversely proportional to the square root of the cavity cross-sectional area for a given length (which in the present case is the cross-sectional area of the end cavity), the resonant peaks shift to lower frequencies when the diameter of the end cavity is increased. Also, as the diameter of the expansion chamber increases, the expansion chamber behavior becomes more pronounced.

Figure 14 shows the effect of ducts extending into the end chambers. The presence of duct extensions in the end cavity shifts the peaks and troughs to lower frequencies; the effect, however, is marginal. Also, an additional peak is introduced at about 800 Hz.

VI. CONCLUDING REMARKS

A quasi-one-dimensional approach is presented to analyze three-pass mufflers with perforated ducts using the ''numerical decoupling.'' The approach is further developed to include mufflers with ducts extended into the end cavities. Theoretical and experimental results are first compared for a fabricated prototype three-pass muffler. This is followed by a similar comparison for two production mufflers. Theoretical results compare reasonably well with experiments. Duct porosity is shown to have only a marginal effect until about 600 Hz beyond which the transmission loss is greater for a muffler with lower duct porosity. Increasing the length of the end cavities is found to shift the transmission loss peaks to lower frequencies. The effect is similar when the diameter of the expansion chamber is increased. Increase in the expansion chamber diameter is also shown to increase the transmission loss at frequencies greater than 600 Hz and at some lower frequencies. Finally, the presence of duct extensions in the end cavity is shown to shift the peaks and troughs to lower frequencies; the effect, however, is marginal.

[1] J. W. Sullivan and M. J. Crocker, ''Analysis of concentric-tube resonators having unpartitioned cavities,'' J. Acoust. Soc. Am. **64**, 207–215 (1978).
[2] J. W. Sullivan, ''A method of modeling perforated tube muffler components. I: theory,'' J. Acoust. Soc. Am. **66**, 772–778 (1979).
[3] J. W. Sullivan, ''A method of modeling perforated tube muffler components. II: applications,'' J. Acoust. Soc. Am. **66**, 779–788 (1979).
[4] K. Jayaraman and K. Yam, ''Decoupling approach to modeling perforated tube muffler components,'' J. Acoust. Soc. Am. **69**, 390–396 (1981).
[5] P. T. Thawani and K. Jayaraman, ''Modelling and applications of straight-through resonators,'' J. Acoust. Soc. Am. **73**, 1387–1389 (1983).
[6] K. N. Rao and M. L. Munjal, ''A generalized decoupling method for analyzing perforated element mufflers,'' in *Proceedings of the 1984 Nelson Acoustic Conference*, Wisconsin (1984).
[7] M. L. Munjal, K. N. Rao, and A. D. Sahasrabudhe, ''Aeroacoustic analysis of perforated muffler components,'' J. Sound Vib. **114**, 173–188 (1987).
[8] K. S. Peat, ''A numerical decoupling analysis of perforated pipe silencers,'' J. Sound Vib. **123**, 199–212 (1988).
[9] G. R. Gogate and M. L. Munjal, ''Analytical and experimental aeroacoustic studies of open-ended three-duct perforated elements used in mufflers,'' J. Acoust. Soc. Am. **97**, 2919–2927 (1995).
[10] E. Dokumaci, ''Matrizant approach to acoustic analysis of perforated multiple pipe mufflers carrying mean flow,'' J. Sound Vib. **191**, 505–518 (1995).
[11] E. Dokumaci, ''A subsystem approach for acoustic analysis of mufflers having identical perforated pipes,'' J. Sound Vib. **193**, 985–1001 (1995).

[12] D. F. Ross, ''A finite element analysis of perforated component acoustic systems,'' J. Sound Vib. **79**, 133–143 (1981).

[13] N. S. Dickey, A. Selamet, and J. M. Novak, ''Multi-pass perforated tube silencers: a computational approach,'' J. Sound Vib. **211**, 435–448 (1998).

[14] M. L. Munjal, ''Analysis of a flush-tube three-pass perforated element muffler by means of transfer matrices,'' Int. J. Acoust. Vib. **2**, 63–68 (1997).

[15] M. L. Munjal, ''Analysis of extended-tube three-pass perforated element muffler by means of transfer matrices,'' in *Proceedings of the Fifth International Congress on Sound and Vibration*, Adelaide, South Australia, 15–18 December 1997, Vol. III, pp. 1701–1714.

[16] M. L. Munjal, *Acoustics of Ducts and Mufflers* (Wiley, New York, 1987).

[17] U. Ingard, ''On the theory and design of acoustic resonators,'' J. Acoust. Soc. Am. **25**, 27–38 (1953).

[18] A. Selamet and V. Easwaran, ''Wave propagation and attenuation in Herschel–Venturi tubes,'' J. Acoust. Soc. Am. **101**, 936–942 (1997).

[19] A. Selamet, N. S. Dickey, and J. M. Novak, ''The Herschel–Quincke tube: a theoretical, computational, and experimental investigation,'' J. Acoust. Soc. Am. **96**, 3177–3185 (1994).

A spatially averaged impulse response for an unfocused piston transducer

Charles J. Daly[a)] and N. A. H. K. Rao

Chester F. Carlson Center for Imaging Science, Rochester Institute of Technology, Rochester, New York 14623

Fourier–Bessel theory is used to derive a closed-form solution for the spatially averaged velocity-potential impulse response associated with one-way diffraction from an unfocused piston transducer of radius a. The derivation provides additional insight into the problem of diffraction from an unfocused piston transducer. © *1999 Acoustical Society of America.*
[S0001-4966(99)03403-7]

INTRODUCTION

Computation of a spatially integrated or spatially averaged impulse response is the first step when correcting for diffraction effects in attenuation measurements with ultrasound.[1] Williams[2] makes the case for spatial integration, while Harris[3] makes the case for spatial averaging. The two cases differ by a multiplicative factor only, and we do not dwell on the difference here. The spatially averaged impulse response for an unfocused piston transducer is amenable to closed-form solution. Hence, piston transducers have been researched for over fifty years.[1] Indeed, Huntington *et al.*,[4] Williams,[2,5] Seki *et al.*,[6] Bass,[7] Rhyne,[8] and Rogers and Van Buren[9] all derived closed-form spatially averaged one-way diffraction corrections. Khimunin[10] and Benson and Kiyohara[11] tabulated extensive numerical results, and more recently, Harris,[3] Cassereau *et al.*,[12] and Chen *et al.*[13] have continued the work of the early researchers.

In this paper, Fourier–Bessel theory[14] is used to present a novel derivation of the spatially averaged impulse response for an unfocused piston transducer. The derivation leads to additional insight into the problem of diffraction from an unfocused piston transducer.

I. DERIVATION AND DISCUSSION

With c and $J_n(x)$ denoting the speed of sound and an nth-order Bessel function of the first kind, respectively, the arccos diffraction formulation in *integral form* is

$$h_1(\rho,z,t)$$
$$= \begin{cases} ac \int_0^\infty J_0(\tau\rho)J_1(\tau a)J_0(\tau\sqrt{(ct)^2-z^2})d\tau, & ct>z, \\ 0, & ct<z, \end{cases} \tag{1}$$

and in *closed form* involves eponymous arccos terms. The integral and closed-form results were derived analytically by Oberhettinger[15] in 1961. A decade later, Stepanishen derived the closed-form solution geometrically and interpreted it as

a)Electronic mail: cjd6905@rit.edu or narpci@rit.edu

an impulse response.[16] Hence, the arccos diffraction formulation is also known as the velocity-potential impulse response.

Equation 1 assumes a piston transmitter of radius a and a *point* receiver. The spatially averaged impulse response in the case of a *finite* piston receiver of radius $b \leq a$ is

$$\langle h_1(z,t)\rangle_b = \frac{1}{\pi b^2}\left[2\pi \int_0^b h_1(\rho,z,t)\rho \, d\rho \right]. \tag{2}$$

Rhyne[8] derived a closed-form expression for $\langle h_1(z,t)\rangle_b$ with $b=a$ by integrating the closed-form arccos diffraction formulation directly, and Cassereau *et al.*[12] generalized Rhyne's result by doing the same for $0<b<\infty$.

These results can be placed in new perspective by spatially averaging the integral form of the arccos diffraction formulation [Eq. (1)] and interpreting the result as a Fourier–Bessel or Hankel transform

$$\langle h_1(z,t)\rangle_b = \frac{1}{\pi b^2}\left[2\pi ac \int_{\rho=0}^b \int_{\tau=0}^\infty J_0(\tau\rho)J_1(\tau a) \right.$$
$$\left. \times J_0(\tau\sqrt{(ct)^2-z^2})\rho \, d\rho \, d\tau \right],$$

$$= \frac{1}{\pi b^2}\left[2\pi abc \int_{\tau=0}^\infty \tau^{-1}J_1(\tau b)J_1(\tau a) \right.$$
$$\left. \times J_0(\tau\sqrt{(ct)^2-z^2})d\tau \right],$$

$$= \frac{1}{\pi b^2}\left[2\pi abc \int_{\tau=0}^\infty \tau^{-2}J_1(\tau b) \right.$$
$$\left. \times J_1(\tau a)J_0(\gamma\tau)\tau \, d\tau \right],$$

$$= \frac{c}{\pi b^2}\mathcal{H}\{2\pi\tau^{-1}bJ_1(\tau b)\tau^{-1}aJ_1(\tau a)\}, \tag{3}$$

where $\gamma = \sqrt{(ct)^2-z^2}$, and $\mathcal{H}$ denotes the Hankel transform with conjugate variables γ and τ. The convolution theorem for Hankel transforms allows Eq. (3) to be written

$$\langle h_1(z,t)\rangle_b = \frac{c}{\pi b^2} \, \mathrm{cyl}\!\left(\frac{\gamma}{2b}\right) \underset{\gamma}{*} \mathrm{cyl}\!\left(\frac{\gamma}{2a}\right), \tag{4}$$

where $\mathrm{cyl}(r)$ is defined in Ref. 17. Gaskill derived a closed-form solution to Eq. (4) via graphical convolution. With $\alpha = (\gamma^2 + a^2 - b^2)/(2\gamma a)$, and $\beta = (\gamma^2 + b^2 - a^2)/(2\gamma b)$, the solution is

$$\langle h_1(z,t)\rangle_b$$

$$= \begin{cases} c, & \gamma < a-b, \\[6pt] \dfrac{ca^2}{\pi b^2}[\cos^{-1}(\alpha) - \alpha\sqrt{1-\alpha^2}] \\[6pt] \quad + \dfrac{c}{\pi}[\cos^{-1}(\beta) - \beta\sqrt{1-\beta^2}], & a-b \le \gamma \le a+b, \\[6pt] 0, & \gamma > a+b. \end{cases}$$

$$\tag{5}$$

Equation (5) reduces to Rhyne's result when $b=a$, and, with the exception of a multiplicative constant, Eq. (5) appears to be the same as the result derived by Cassereau *et al.*

Even though it was derived under the assumption $b \le a$, Eq. (5) is completely general. That is, a and b can simply be interchanged in Eq. (5) if $b>a$. Reasons for this will be discussed in the next section. Algebraic manipulation of γ reveals that, for a fixed b, the spatially averaged velocity-potential impulse response $\langle h_1(z,t)\rangle_b$ is compressed in time as z increases.[12,1]

Equation (5) was used to compute $\langle h_1(z,t)\rangle_b$ for six values of b at two depths: $z=3$ cm and $z=9$ cm. The speed of sound was set at $c=1540$ m/s, and the diameter of the piston transmitter was set at $2a=13$ mm; the radius of the receiver b is annotated in each of the plots. The transmitter was assumed to have an infinitely broadband or Dirac response;[12] the excitation was assumed to be an impulse; and the sampling frequency was set at $f_S = 36$ MHz. The results are shown in Figs. 1 and 2.

Spatially averaged velocity-potential impulse responses for the case $b=a/1000$ are shown in Fig. 1(a) and (b) and are consistent with point-receiver theory.[16] In particular, the case $b=a/1000$ approximates an on-axis *point receiver*, and point-receiver theory predicts that the velocity-potential impulse response for an on-axis point receiver is a rectangular pulse with a pulse width that is compressed in time with increasing depth. The spatially averaged results obtained using Eq. (5) with $b=a/1000$ are consistent with this predic-
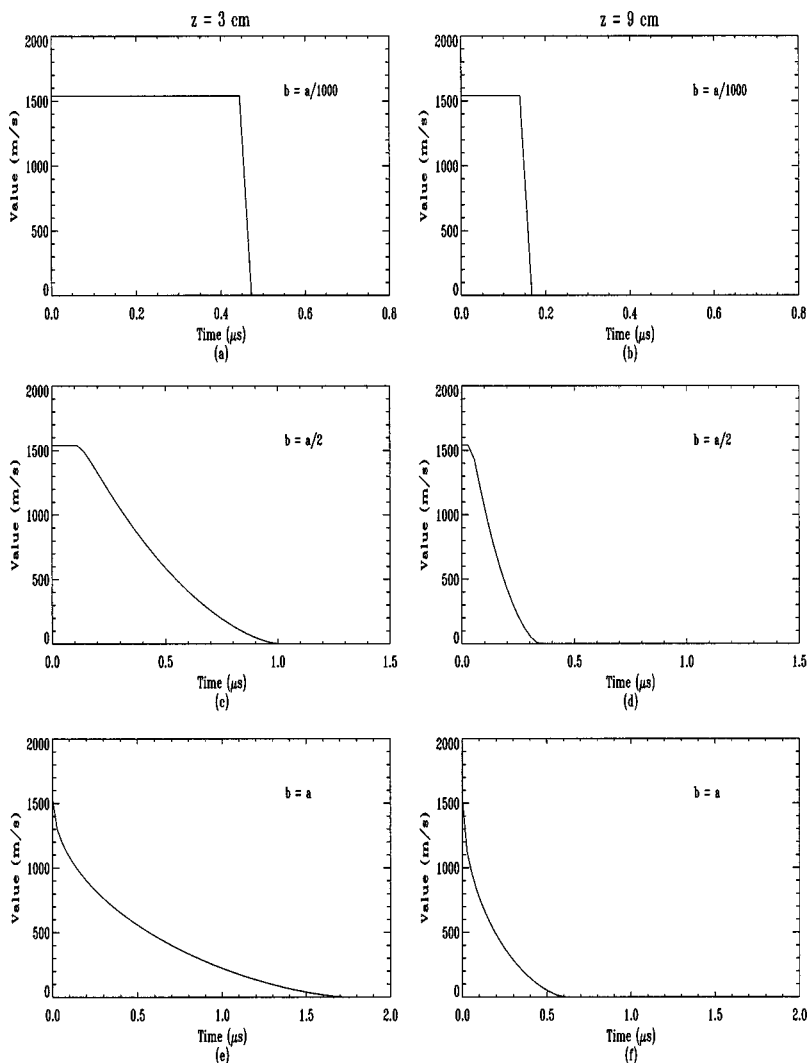
FIG. 1. Spatially averaged velocity-potential impulse responses.
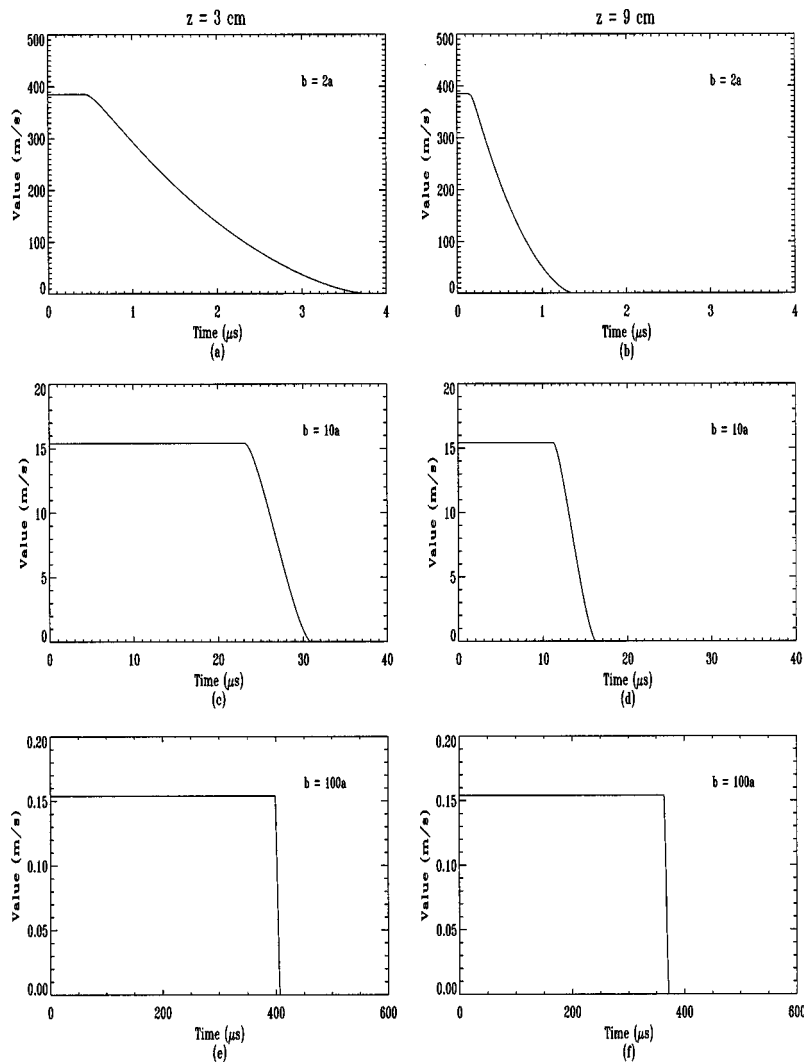
FIG. 2. More spatially averaged velocity-potential impulse response.

tion. Figure 1(c) and (d) reveal that the pulse-like nature of the spatially averaged impulse response decays as b is increased.

Figure 1(e) and (f) show spatially averaged impulse responses for the case $b=a$, and the results are consistent with those presented by Rhyne.[8] Figure 2(a)–(f) reveal that a pulse-like behavior begins to re-emerge in the spatially averaged impulse responses as b becomes larger than a. This behavior will be discussed in the next section. Finally, the graphs in both Fig. 1 and Fig. 2 confirm the prediction that, for a fixed b, the spatially averaged velocity-potential impulse response is compressed in time as z increases.

II. FURTHER INSIGHTS

Additional insight can be gained by considering Eqs. (4) and (5). First, the generality of Eq. (5) is due to the commutativity of convolution in Eq. (4) which, in this context, may be interpreted as a mathematical manifestation of Helmholtz's reciprocity theorem.[18] Consequently, a and b can simply be interchanged in Eq. (5) if $b>a$.

Furthermore, point-receiver theory complemented with Helmholtz's reciprocity theorem can be used to predict that the spatially averaged velocity-potential impulse response will resemble a rectangular pulse when $b \gg a$. That is, the

impulse response will be a rectangular pulse when the transmitter, relative to the receiver, approximates an on-axis *point transmitter*. The graphs in Fig. 2 show that the spatially averaged impulse response becomes more pulse-like as b is increased. Thus, the prediction is theoretically confirmed and the behavior of the impulse responses for $b>a$ explained.

Second, Eq. (5) is well known in optics. Gaskill calls it the *cylinder-function cross correlation* (Ref. 17, pp. 302–304), while Bracewell gives the name *chat* function (Ref. 19, pp. 187–192) to the special case that results when $b=a$. Bracewell coined this term because the shape of the graph of Eq. (5) as a function of γ for $b=a$ resembles a Chinese farmer's hat. Thus, insights and results developed in optics for Eq. (5) may benefit researchers in ultrasound.

Finally, the graph that results from plotting Eq. (5) as a function of time t for $b=a$ is strikingly similar to the celebrated *brachistochrone*;[20–22] compare Fig. 1(e) and (f) and Fig. 3. Indeed, the form of Eq. (5) for the case $b=a$ is similar to the equation for the brachistochrone; Eq. (5) for the case $b=a$ is

$$\langle h_1(z,t)\rangle_a = \frac{2c}{\pi}\left[\arccos\left(\frac{\gamma}{2a}\right) - \frac{\gamma}{2a}\sqrt{1 - \frac{\gamma^2}{4a^2}}\right], \qquad (6)$$

and, with the parameterization
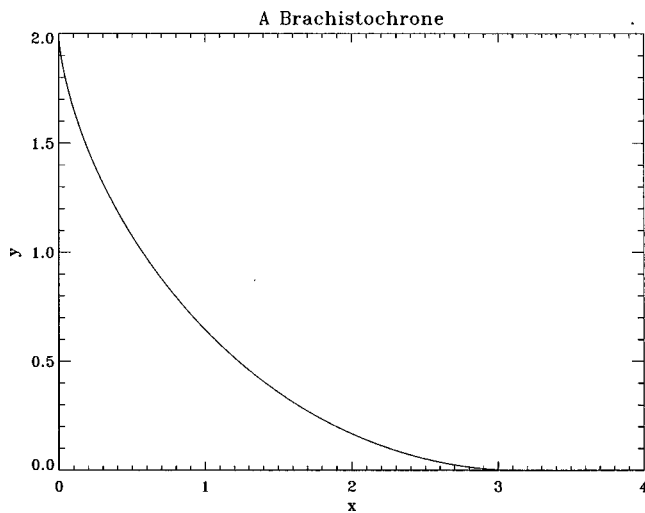
FIG. 3. A brachistochrone.

$$x = a(\theta - \sin \theta) \tag{7a}$$

and

$$y = a(1 + \cos \theta), \tag{7b}$$

where $0 \leq \theta \leq \pi$, the equation for the brachistochrone is

$$x = a \arccos\left(\frac{y-a}{a}\right) - a\sqrt{1 - \left(\frac{y-a}{a}\right)^2}. \tag{8}$$

Note the similarity between Eq. (6) and Eq. (8). The graphical and functional similarities just noted are not surprising when one considers the physical origins of and mathematical solutions to the brachistochrone and diffraction problems.

Specifically, both problems can be formulated in terms of Hamilton's physical principle of least action.[23,21,24] Thus, both are mathematically amenable to solution via the calculus of variations. More rigorous comparison of these two problems may lead to deeper understanding of diffraction from piston transducers and transducers involving other geometries.

III. CONCLUSION

Fourier–Bessel theory was used to present a novel derivation of the spatially averaged velocity-potential impulse response associated with one-way diffraction from an unfocused piston transducer of radius a. The derivation also led to insights which may be of theoretical and practical interest to researchers in ultrasound.

[1] G. Harris, ''Review of transient field theory for a baffled planar piston,'' J. Acoust. Soc. Am. **70**, 10–19 (1981).

[2] A. Williams, Jr., ''Integrated signal on circular piston receiver centered in a piston beam,'' J. Acoust. Soc. Am. **48**, 285–289 (1970).

[3] G. Harris, ''Transient field of a baffled planar piston transducer having an arbitrary vibration amplitude distribution,'' J. Acoust. Soc. Am. **70**, 186–204 (1981).

[4] H. Huntington, A. Emslie, and V. Hughes, ''Ultrasonic delay lines. I,'' J. Franklin Inst. **245(1)**, 16–23 (1948).

[5] A. Williams, Jr., ''The piston source at high frequencies,'' J. Acoust. Soc. Am. **23**, 1–6 (1951).

[6] H. Seki, A. Granato, and R. Truell, ''Diffraction effects in the ultrasonic field of a piston source and their importance in the accurate measurement of attenuation,'' J. Acoust. Soc. Am. **28**, 230–238 (1956).

[7] R. Bass, ''Diffraction effects in the ultrasonic field of a piston source,'' J. Acoust. Soc. Am. **30**, 602–605 (1958).

[8] T. Rhyne, ''Radiation coupling of a disk to a plane and back or a disk to disk: An exact solution,'' J. Acoust. Soc. Am. **61**, 318–324 (1977).

[9] P. Rogers and A. Van Buren, ''An exact expression for the Lommel diffraction correction integral,'' J. Acoust. Soc. Am. **55**, 728–728 (1974).

[10] A. Khimunin, ''Numerical calculation of the diffraction corrections for the precise measurement of ultrasound absorption,'' Acustica **27**, 173–181 (1972).

[11] G. Benson and O. Kiyohara, ''Tabulation of some integral functions describing diffraction effects in the ultrasonic field of a circular piston source,'' J. Acoust. Soc. Am. **55**, 184–185 (1974).

[12] D. Cassereau, D. Guyomar, and M. Fink, ''Time deconvolution of diffraction effects—Application to calibration and prediction of transducer waveforms,'' J. Acoust. Soc. Am. **84**, 1073–1085 (1988).

[13] X. Chen, K. Schwarz, and K. Parker, ''Acoustic coupling from a focused transducer to a flat plate and back to the transducer,'' J. Acoust. Soc. Am. **95**, 3049–3054 (1994).

[14] A. Papoulis, *Systems and Transforms with Applications in Optics* (McGraw-Hill, New York, 1968), Chaps. 5 and 9.

[15] F. Oberhettinger, ''On transient solutions of the 'baffled piston' problem,'' J. Res. Natl. Bur. Stand., Sect. B **65B**(1), 1–5 (1961).

[16] P. Stepanishen, ''Transient radiation from pistons in an infinite planar baffle,'' J. Acoust. Soc. Am. **49**, 1627–1638 (1971).

[17] J. Gaskill, *Linear Systems, Fourier Transforms, and Optics* (Wiley, New York, 1978).

[18] L. Kinsler and A. Frey, *Fundamentals of Acoustics* (Wiley, New York, 1982), 3rd ed.

[19] R. Bracewell, *Two-Dimensional Imaging* (Prentice-Hall, Englewood Cliffs, NJ, 1995).

[20] R. Courant and F. John, *Introduction to Calculus and Analysis*, Vol. I (Interscience, New York, 1965).

[21] H. Goldstein, *Classical Mechanics* (Addison-Wesley, Reading, MA, 1950).

[22] G. Thomas, Jr., *Calculus* (Addison-Wesley, Reading, MA, 1969).

[23] M. Born and E. Wolf, *Principles of Optics* (Pergamon, New York, 1980), 6th ed.

[24] P. Morse and K. Ingard, *Theoretical Acoustics* (McGraw-Hill, New York, 1968).

Experimental study of a fractal acoustical cavity

B. Hébert, B. Sapoval,[a) and S. Russ

Laboratoire de Physique de la Matière Condensée, Ecole Polytechnique-CNRS, 91128 Palaiseau, France

The resonance properties of a prefractal cavity are studied in an acoustical transmission experiment. Resonance frequencies and quality factors are measured and compared to theory. All the delocalized modes are detected, and their measured eigenfrequencies closely fit numerical predictions. Most of the localized modes appear to be missing in the experimental spectra because of their weak coupling with the acoustic excitation and detection. The measurement of the quality factor of the acoustic resonances confirms the existence of increased damping due to the irregular shape of the cavity. This constitutes the first experimental evidence for the damping power of fractal structures. © *1999 Acoustical Society of America.* [S0001-4966(99)04503-8]

PACS numbers: 43.20.+g, 43.55.+p, 61.43.Hv [ANN]

INTRODUCTION AND THEORETICAL PREDICTIONS

Geometrical irregularities are present in many natural and artificial systems, and their vibrational properties are of general interest. Current empirical knowledge about resonators indicates that perturbations of a resonator geometry may modify not only its frequency spectrum but also the resonances quality factors. Experimental observation and numerical calculation of the low-frequency modes of fractal drums have been already published.[1,2] The fractal language makes it possible to express extreme geometrical irregularity or geometrical disorder by simple models.[3,4] The study of the acoustic properties of a fractal cavity may then help to understand the acoustical properties of strongly irregular systems in general. This paper presents the first experimental study of a prefractal cavity. It follows a theoretical study which suggested the existence of localization and increased damping in such systems.[5] We call prefractal a physical system which displays in its geometry a *finite* range of scale invariance. A prefractal cavity is then smooth under some characteristic length, often called the smaller cutoff length, while in a mathematical fractal cavity the smaller cutoff length is null and the object is rough at all scales. Here this smaller smooth length is of the order 1 cm while the size of the cavity is a few tens of cm.

In the experiment, the lower 15 or so acoustic resonances of a shallow cavity with typical diameter of order 30 cm are detected in the range 300 to 2500 Hz and their frequencies are compared to numerical predictions. The measurement of the energy dissipation through the quality factors confirms the existence of increased damping due to geometrical irregularity. Several modes predicted by theory are not observed in this experiment. These missing modes are localized modes which are confined near the irregular frontier of the cavity. Consequently, their coupling to the experimental excitation and detection is weak. This is why they are not observed as we show below.

The geometry of the base of the cylindrical cavity studied here is shown in Fig. 1. The cavity is closed by two parallel horizontal plates distant of 5 cm so that the vertical

height is irrelevant in the frequency range of interest. The figure shows the contour of the base of the cylinder with sizes of the order of tens of cm. This shape has been chosen for several reasons. First, it is not too difficult to build. Second, the eigenmodes can be computed readily using our standard method.[2,6] In addition, this shape presents no geometrical symmetry, and the eigenmodes are not degenerate.

In the following, we restrict ourselves to linear acoustics and consider the limit of weak losses. In this way, the amplitude distribution is well approximated by the zero-loss modes of an infinitely rigid cavity. We consider an eigenmode N at frequency ω_N with a pressure distribution:

$$p_N(x,y,z,t) = p_0 V^{1/2} \Psi_N(x,y,z) \cos(\omega_N t), \tag{1}$$

where p_0 is the peak acoustic pressure and V is the volume of the cavity. In the following, we use everywhere functions $\Psi_N(x,y,z)$ which are normalized in the volume of the cavity V by the relation

$$\int \int \int_V dv \, \Psi_N^2(x,y,z) = 1. \tag{2}$$

For sound velocity c, the acoustic pressure obeys the Helmholtz equation $\Delta P = (1/c^2)(\partial^2 P/\partial t^2)$ with the condition that the normal derivative $(\nabla P)_n = 0$ (Neumann boundary condition). This condition corresponds to a perfectly reflecting surface with no phase change. The eigenmodes $\Psi_N(x,y,z)$ are solutions of the eigenvalue equation $\Delta \Psi_N = -(\omega_N^2/c^2)\Psi_N$. As the experimental cavity is shallow (height $L_z = 5$ cm) only the so-called higher-order modes exist within the experimental frequency range. These eigenmodes take the form $\Psi_N(x,y,z) = (L_z)^{-1/2}\Psi_n(x,y)$, where L_z is the height of the cavity. (Then the index N and n correspond respectively to 3D and 2D functions.) The functions $\Psi_n(x,y)$ satisfy the two-dimensional eigenvalue equation $\Delta \Psi_n = -(\omega_n^2/c^2)\Psi_n$ and are normalized over the cross section. The eigenfrequencies ω_N remain unchanged: $\omega_N = \omega_n$.

Systems in which the perimeter only is fractal, like a fractal drum or a fractal cavity, are called ''surface fractals'' and their vibrations ''fractinos.''[2] The two-dimensional modes of the prefractal geometry are then ''Neumann frac-

---

[a)Electronic mail: bernard.sapoval@polytechnique.fr
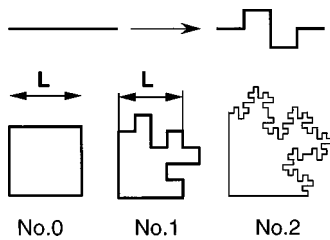
FIG. 1. Geometry of the base of the cylindrical prefractal cavity. This geometry is obtained by substituting two adjacent sides of the square by the generator shown at the top of the figure and by reiterating the process once. The side of the square has a length L and the area L^2 is kept constant by the transformation. The fractal which is generated this way has a fractal dimension equal to 3/2.

TABLE I. Results of the numerical computation of the properties of the prefractal cavity (No. 2 in Fig. 1). The mode of index $n=0$ is the trivial mode of uniform pressure. For this mode the formal value of Λ_0/L (for the trivial state) is equal to 1/10, because $\Psi_0^2(x,y)=1/L^2$ and the perimeter of the cavity is equal to $10L$.

Mode index n	Frequency ($c/2L$ units)	Λ_n/L	Participation ratio S_n/L^2	Amplitude sensitivity (arb. units)
0	0.00 000	0.100 000	1.00 000	
1	0.58 910	0.057 883	0.31 067	$5.519e-2$
2	0.75 484	0.065 382	0.33 962	$2.238e-1$
3	1.09 158	0.064 684	0.27 935	$7.917e-2$
4	1.30 855	0.037 871	0.10 546	$8.076e-5$
5	1.41 363	0.065 756	0.28 032	$5.773e-3$
6	1.62 054	0.073 745	0.37 089	$1.386e-2$
7	2.02 414	0.071 256	0.23 029	$7.952e-2$
8	2.12 723	0.053 850	0.26 484	$1.819e-2$
9	2.19 563	0.057 096	0.18 639	$1.707e-2$
10	2.38 734	0.055 200	0.36 047	$3.029e-2$
11	2.61 450	0.028 737	0.03 063	$6.320e-5$
12	2.61 352	0.028 632	0.05 139	$8.990e-7$
13	2.61 395	0.028 631	0.04 382	$5.300e-6$
14	2.67 935	0.061 661	0.24 670	$7.754e-4$
15	2.71 453	0.052 465	0.14 829	$1.637e-2$
16	2.93 055	0.051 903	0.16 457	$1.640e-2$
17	3.00 412	0.061 955	0.24 945	$5.550e-4$
18	3.15 946	0.058 272	0.22 662	$1.196e-2$
19	3.21 682	0.040 803	0.05 986	$1.844e-3$
20	3.28 241	0.034 162	0.03 162	$6.175e-4$
21	3.30 723	0.035 245	0.04 277	$7.379e-4$
22	3.49 220	0.050 780	0.05 543	$3.803e-2$
23	3.60 769	0.070 307	0.22 336	$4.327e-3$
24	3.71 762	0.077 729	0.28 223	$1.774e-1$

tinos.'' The Neumann fractinos of our geometry have been numerically calculated using the method developed in Refs. 2 and 6. The computation is made on a discretized grid which uses 160 segments in the length L of Fig. 1. This induces only a negligible error on the numerical values of the lower eigenfrequencies, as discussed in Ref. 2. For each mode n, the frequency ω_n, the amplitude distribution, the localization volume, and the quality factor Q_n have been computed.

Localization effects correspond to the more or less strongly uneven distribution of the vibration amplitude in the resonator. To characterize mathematically the localization or the confinement of each mode Ψ_n, we compute an existence surface S_n defined by[7]

$$S_n = \left[\int dx\, dy\, |\Psi_n|^4 \right]^{-1}. \tag{3}$$

Whenever the relative existence volume S_n/L^2 or "participation ratio" of state n is found to be significantly smaller than 1, this particular mode is called "localized." It was found in Refs. 5 and 6 that a number of modes of fractal cavities are confined at the boundary, the amplitude in the inner part of the resonators being small. The values of the participation ratios S_n/L^2 for our cavity are given in Table I. For states $n=4, 11, 12, 13, 19, 20, 21$, and 22, the existence surface is only a small fraction of the total surface of the resonator. Note that for the delocalized cosine functions of a square or rectangular cavity, the value of the participation ratio is equal to 2/3 {inverse of the integral of $[(2/L)^{1/2} \cos(\pi x/L)]^4$} for modes uniform in one direction and to 4/9 for the others. The spatial location of the confined modes is linked to the Neumann boundary condition for which the boundary region is free to vibrate. Eigenmodes can then have a maximum amplitude at the boundary. This is illustrated in Fig. 2, which pictures the amplitude distribution of the delocalized mode $n=14$ and of the localized mode $n=11$. Visual comparison reveals the strength of the localization effect which enters the category of weak localization. This term is used in the same general sense describing enhanced backscattering in random media. Here localization is a consequence of the partially destructive interference of waves reflected by the irregular boundary.[6]

The quality factors of prefractal cavities have been recently calculated[5] and it was predicted that the boundary layer damping is increased by the geometrical irregularity of the frontier. Acoustical losses in a rigid cavity are due to heat conduction and to viscous dissipation. Away from the walls, these losses are small at audio frequencies and are neglected here.[8–10] Energy dissipation takes place at the cavity walls on a small boundary layer with a thickness of the order of 10^{-4} cm, much smaller than the smaller cutoff length of the geometry.[9,11] To calculate the losses, we consider that the walls present a small but finite specific admittance $\varepsilon(\omega)$. This admittance can be that of the real fluid boundary layer or more simply, the admittance of a suitable sound absorbing material of small thickness, covering the lateral cavity walls. The calculations in Ref. 5 were aimed at the study of the geometrical dependence of the damping by irregular walls. The results of this work neglected on purpose the role of the horizontal covers of the cavities. In the present work, these contributions cannot be neglected and the results are generalized below.

The quality factor Q_N of a resonator for a mode N is the ratio of the stored energy to the losses per cycle W_N:

$$Q_N = 2\pi E_N / W_N. \tag{4}$$

Along the same lines as discussed in Ref. 5, one can take into account the losses on the lateral walls and the losses on the covers by writing
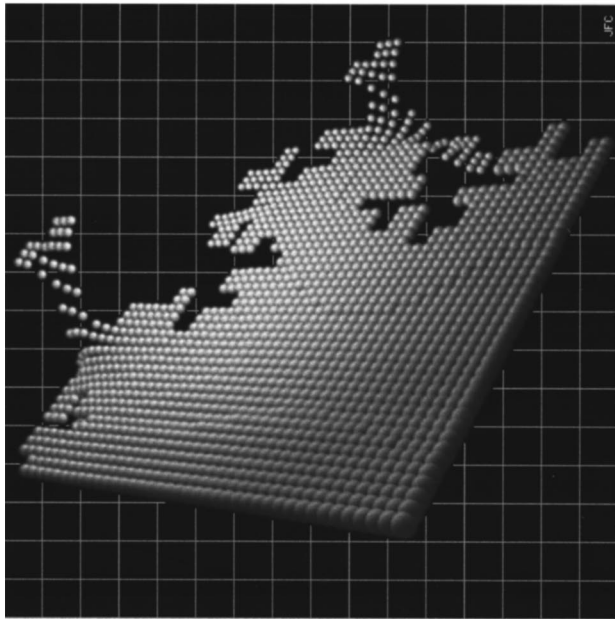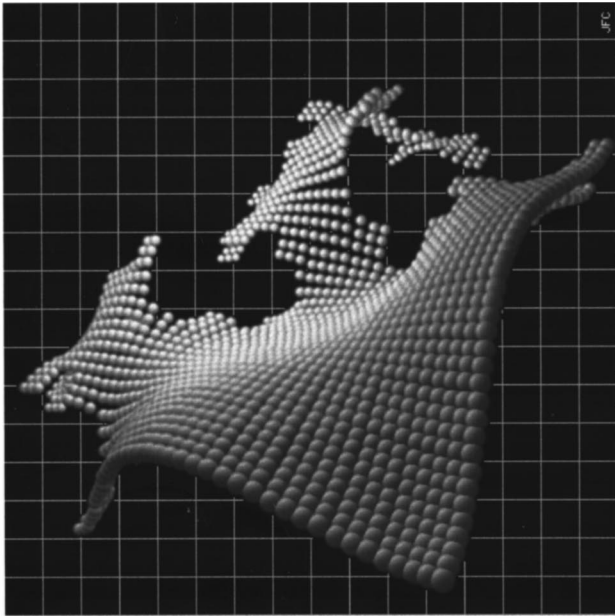
FIG. 2. Comparison between localized and delocalized modes: at the top, mode $n=14$, with a participation ratio of order 0.25; at the bottom, mode $n=11$, with a participation ratio of order 0.030. Mode $n=11$ is clearly strongly localized the irregular frontier of the cavity. The computer imaging is due to J. F. Colonna.

$$1/Q_N = (c/\omega_N)\left\{[\operatorname{Re}\varepsilon_{\mathrm{lat}}(\omega_n)]\int\int_{\mathrm{lat}.s} ds|\Psi_N^2(x,y,z)|\right.$$

$$\left. +2[\operatorname{Re}\varepsilon_{\mathrm{cov}}(\omega_n)]\int\int_{\mathrm{cov}.s} ds|\Psi_N^2(x,y,z)|\right\}, \quad (5)$$

where $\varepsilon_{\mathrm{lat}}(\omega_N)$ and $\varepsilon_{\mathrm{cov}}(\omega_N)$ are, respectively, the specific admittances of the lateral walls and of the covers; the integrals are taken respectively over the lateral and cover surfaces. For the modes $\Psi_N(x,y,z)=(L_z)^{-1/2}\Psi_n(x,y)$, the second integral is simply equal to $(L_z)^{-1}$. The above equation can then be written

$$\frac{1}{Q_N} = \frac{1}{Q_n} = \frac{c}{\omega_n}\left\{[\operatorname{Re}\varepsilon_{\mathrm{lat}}(\omega_n)]\int\int_{\mathrm{lat}.S} ds|\Psi_N^2(x,y,z)|\right.$$

$$\left. +[\operatorname{Re}\varepsilon_{\mathrm{cov}}(\omega_n)](2/L_z)\right\}. \quad (6)$$

For the same mode the first integral can be expressed as

$$\int\int_{\mathrm{lat}.S} ds|\Psi_N^2(x,y,z)| = \int_{\mathrm{perimeter}} dl|\Psi_n^2(x,y)|, \quad (7)$$

where the right side integral is over the perimeter of a cross section. Finally, the quality factor is given by

$$1/Q_n = (c/\omega_n)\{[\operatorname{Re}\varepsilon_{\mathrm{lat}}(\omega_n)](\Lambda_n^{-1}) + [\operatorname{Re}\varepsilon_{\mathrm{cov}}(\omega_n)]$$

$$\times(2L_z^{-1})\}, \quad (8)$$

with

$$\frac{1}{\Lambda_n} = \int_{\mathrm{perimeter}} dl|\Psi_n^2(x,y)|. \quad (9)$$

The length $\Lambda_n/[\operatorname{Re}\varepsilon_{\mathrm{lat}}(\omega_n)]$ is a ''damping length'' given by the curvilinear integral over the perimeter of the cavity.[5] For delocalized modes $|\Psi_n^2(x,y)|$ is of order of L^{-2} and the larger the perimeter, the smaller Λ_n and the stronger the damping. For localized modes, the larger the amplitude at the boundary, the lower the value of the length Λ_n and also the lower the quality factor.[5]

These equations then simply express that the dissipation which takes place at the cavity walls increases with the local pressure amplitude and the effective perimeter of the region where the mode exists. Theoretical values of Λ_n have been computed from the eigenmodes amplitude distribution. They are given in Table I. One can note that the more localized modes are predicted to exhibit stronger damping as Λ_n is smaller. This can be explained qualitatively by the fact that, for these modes, the amplitude at the boundary is larger, because of their normalization in a smaller volume. The integral (9) is then increased correspondingly, and Λ_n is smaller. This argument can be made quantitative for the strongly localized modes.[5]

Relations (8) and (9) are general and can be applied to any geometry. In order to compare the irregular cavity with a ''smooth'' equivalent, the resonances of a rectangular cavity built of the same material with the same height were studied. The dimensions of this rectangular cavity have been chosen in order to have resonances in the same frequency range as our prefractal system, with no degeneracy. The modes of rectangular cavities are known. Theory relating to the rectangular cavity is recalled in the Appendix. The experimental measurement of the quality factors of the rectangular cavity resonances permits us to calibrate the value of the admittances $\varepsilon(\omega)$ of the lateral walls.

If one neglects the difference between the specific contributions of the heat and viscous losses,[8] $[\operatorname{Re}\varepsilon_{\mathrm{lat}}(\omega_n)] = [\operatorname{Re}\varepsilon_{\mathrm{cov}}(\omega_n)] = [\operatorname{Re}\varepsilon(\omega_n)]$ and the product $Q_n \times[\operatorname{Re}\varepsilon(\omega_n)]$ is only a function of the pressure distribution through Λ_n. It depends on the geometry of the resonator only, independently of the physical characteristics of the walls. The numerical values of $Q_n\times[\operatorname{Re}\varepsilon(\omega_n)]$ for both the
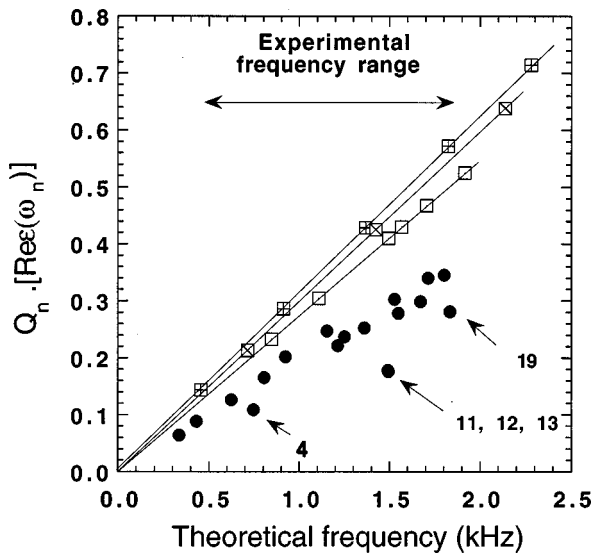
FIG. 3. Theoretical values of $Q_n[\text{Re }\varepsilon(\omega_n)]$ for the rectangular (squares) and prefractal cavity (circles). The values for the rectangular cavity are obtained from Eq. (A4). The values for the prefractal cavity are obtained from Eq. (5), using Table I. The Q-factors for the prefractal cavity are predicted to be smaller than for the rectangular cavity, especially for the localized states indicated by arrows.

rectangular and the prefractal cavities are shown in Fig. 3. Damping is then predicted to increase with "fractalization" even for the delocalized modes. For these modes, the damping is roughly proportional to the perimeter. The localized modes, $n=4$, 11, 12, 13, and 19, are predicted to be even more damped.

I. EXPERIMENTS

The experiment is an acoustic transmission experiment. It is represented schematically in Fig. 4. The prefractal cavity is built in aluminium, with dimensions corresponding to $L=30.4$ cm. The smaller flat segment (smaller cutoff) of the structure is equal to $l=(30.4/16)=1.875$ cm. The rectangular cavity has dimensions $L_x=24.0$ cm and $L_y=37.5$ cm. Both cavities have the same height $L_z=5$ cm. The cavities are excited by a pure sine signal through a loudspeaker MSP-30 connected to a low-frequency generator (Schlumberger 4417). The excitation frequency is scanned linearly with time. The modulation speed and the range of frequen-
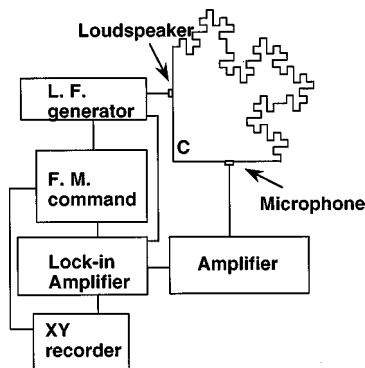
FIG. 4. Scheme of the experimental setup. The distances from the loudspeaker and the microphone to the corner C are respectively 18.9 and 16.4 cm.

cies can both be varied. The acoustic signal is detected by a microphone EM110, sensitive to the local pressure on the cavity wall. Both microphone and loudspeaker have been chosen small in order to minimize the perturbation of the geometry. They are coupled to the cavity through a cylindrical hole, 1 cm in diameter, situated at half-height. The positions of the loudspeaker and of the microphone are indicated in the figure. The microphone signal is amplified and filtered. A homemade synchronous detector measures its in-phase and quadrature components. This permits one to detect both the absorption and the dispersion components of the cavity transmission.

Two sets of transmission experiments were performed with the rectangular and the prefractal cavities. In the first set, the lateral aluminum cavity walls were bare. In the second set, the lateral cavity walls were covered with a fabric, serving as absorbent material, in order to increase the wall admittance $[\text{Re }\varepsilon_{\text{lat}}(\omega_n)]$. The goal of this second set of experiments was to control better the dissipation process due to acoustic losses on the irregular lateral walls. One should note that, in order to obtain only modes which are uniform in the vertical direction, the height of the cavity should be kept smaller than the half-wavelength, 17 cm at 1 kHz. Consequently, the dissipation due to the cover is far from being negligible in Eq. (8). This is the reason why we have to increase the participation of the lateral walls to damping by covering the lateral walls with a more absorbing material. Since increasing the dissipation broadens the resonances, the absorbent material was chosen to cause only a moderate increase of the dissipation, so that individual quality factors could still be measured. The theoretical equations in the Appendix are used to calculate the real part of the wall admittance from the measurements on the rectangular cavity. This allows the prediction of the Q-factors of the resonances of the fractal cavity, which can be compared to experiment. In the following, we first discuss the spectra and then the damping measurements.

II. FREQUENCY SPECTRA

Transmission experiments have been performed both with the rectangular and the prefractal cavity between 400 and 2000 Hz. The transmission spectra of both cavities with bare aluminium walls are shown in Fig. 5. The spectrum of the rectangular cavity gives eigenfrequencies which fit Eq. (A2). The mode indexes of the fractal cavity resonances have been attributed by comparison with the eigenfrequency values given in Table I using $L=30.4$ cm and $c=340$ m/s. When the lateral walls of the cavities were covered with absorbent material, the spectra were essentially the same.

Several facts are observed. First, for a given value of the phase relation between excitation and detection, the transmission spectrum is not an absorption spectrum. Some peaks are "up," others "down." This corresponds to the fact that, on a trace going from the loudspeaker to the microphone, one crosses an even or odd number of node lines. Depending of this number, the signal phase is shifted by 180 degrees. The $n=2$, 3, and 14 resonances present a dispersion component that can only be annihilated if the particular mode is isolated, by delicate tuning of the phase between the loud-
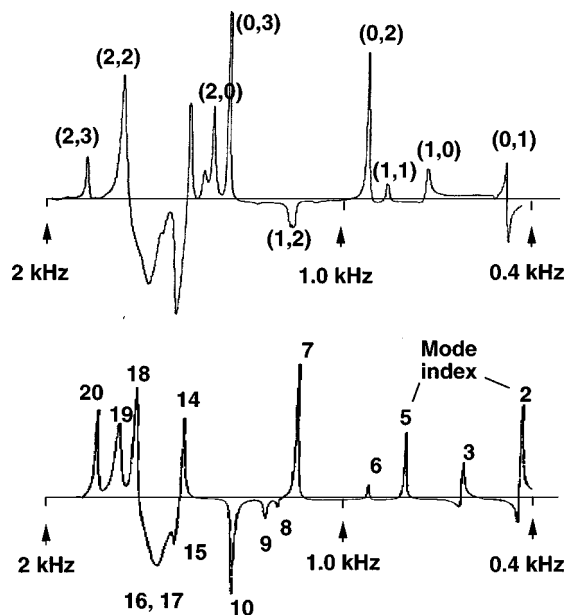
FIG. 5. Experimental transmission spectra of the rectangular (top) and fractal (bottom) cavities. The mode indexes (μ,μ') of the rectangular cavity and the mode indexes n of the prefractal cavity are indicated. Note that the fractino modes $n=4$, 11, 12, and 13 are "missing." These modes are localized (see Table I). They are weakly coupled to the excitation and the detection because of their localization near the irregular frontier and subsequent weakness at the loudspeaker and microphone location. As seen in Table I or Fig. 6, their intrinsic sensitivity A_n, defined in Eq. (10), is predicted to be much smaller than that of the modes that are detected.

FIG. 6. Intrinsic sensitivity (in arbitary units) calculated using Eq. (10) as a function of the mode index. The localized modes are indicated by the arrows. Modes $n=4$, 11, 12, and 13, which have a small intrinsic sensitivity, are not found in the experimental spectrum at the bottom of Fig. 5.

speaker sine excitation and the detected signal. This is due to the fact that the impedance matching (in amplitude and phase) is different for the different modes that are detected.

Second, modes $n=4$, 11, 12, and 13, which are localized on the irregular region of the frontier, are missing. They are not detected, because the loudspeaker and the microphone are not located in their region of existence. To understand why localized modes can be "missed" in our experiment, one has to discuss the experimental sensitivity.

The transmission amplitude of a mode n for given values of the excitation voltage and signal amplification chain depends on several factors: the acoustic pressures at the excitation (loudspeaker) and detection (microphone) locations, the impedances matching, and the quality factor of the mode. There is no reason for the transmission amplitude to be constant. It is, however, clear that the higher the amplitudes at excitation and detection, the higher the transmission. One can then, knowing the acoustic pressure distribution in space for each mode n, compute an "intrinsic" sensitivity A_n which is the product of the acoustic pressure at the loudspeaker location $\Psi_{n,LS}$ and the acoustic pressure at the microphone location $\Psi_{n,\mu P}$:

$$A_n = |\Psi_{n,LS} \times \Psi_{n,\mu P}|. \tag{10}$$

The two factors depend on the pressure distribution and are found to be comparatively very small for states localized at the irregular frontier (see Fig. 4). The values of A_n computed from the numerical values of the amplitude of the normalized amplitudes of vibrations are listed in Table I and are shown in Fig. 6. They display a very large dispersion. One

observes that, *because of the location of the excitation and detection at the smooth part of the cavity where the values of both $\Psi_{n,LS}$ and $\Psi_{n,\mu P}$ are small*, the localized modes can be missed in an experiment where the signal-to-noise ratio is finite (see below). Note also that localized modes are more damped,[5] which should decrease even more the experimental sensitivity. All the modes with a value $A_n > 10^{-4}$ were detected in the experiment. The mode $n=19$, although localized, according to Table I, was detected because of its relatively high amplitude sensitivity.

The fact that the experimental amplitudes do not reproduce the distribution of the intrinsic sensitivity indicates that the quality factors and the impedance matching also play a role in the intensity of the transmitted signal, but a detailed study of these effects is beyond the scope of the present work. Note that, at the emission, it is the loudspeaker *velocity* which is imposed whereas the microphone measures the acoustic pressure proportional to $\Psi_{n,\mu P}$. Then the emission depends really on the local acoustic velocity of the mode. This is the local normal derivative of the acoustic pressure. This derivative is linked to $\Psi_{n,LS}$ by the local impedance of the mode at the loudspeaker location.

The experimental resonance frequencies of the fractal cavity are compared with the numerical predictions in Fig. 7. The agreement is good. Slight differences between the two can be attributed to several possible causes: small temperature variations, shifts due to finite Q values, or the role of the small loudspeaker and microphone apertures.

III. RESONANCES DAMPING

Quality factors were studied for both cavities with walls either bare or covered by absorbing material. We have measured carefully the Q-factors from the absorption and dispersion spectra for each resonance that could be isolated in the spectra. For the rectangular cavity, the measured resonances correspond respectively to $(\mu=1,\ \mu'=0)$; $(\mu=1,\ \mu'=1)$;
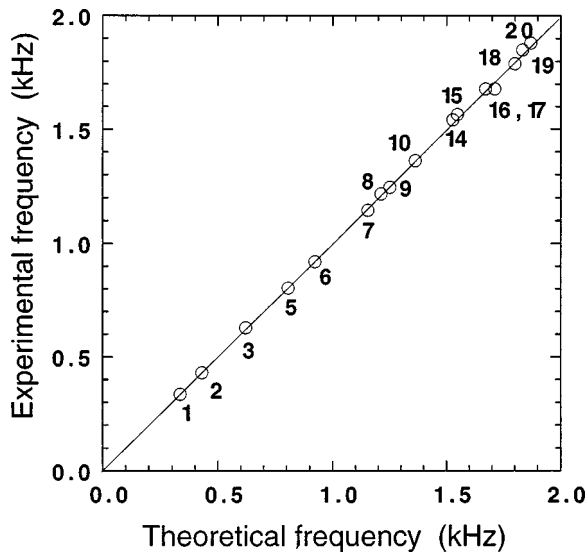
FIG. 7. Comparison between the experimental eigenfrequencies and their theoretical values for the observed (nonlocalized) modes of the prefractal cavity with bare walls. The theoretical resonance frequencies were obtained from the data of Table I using $c = 340$ m/s.

$(\mu = 0, \mu' = 2)$; $(\mu = 1, \mu' = 2)$; and $(\mu = 0, \mu' = 3)$. For the prefractal cavity, we have studied carefully the modes $n = 3, 5, 6, 7$, and 10, not modes $n = 8$ and 9, because they are too close in frequency. Higher modes are also insufficiently resolved for measurement of the individual Q-factors. The transmitted signals of the mode $n = 5$ are shown as an example in Fig. 8. Note that the signal-to-noise ratio is of order 100. The signal-to-noise ratio is then expected to be of order 1 for the localized modes $n = 4, 11, 12$, and 13 from the values of the intrinsic sensitivity listed in Table I, explaining that they are not detected.
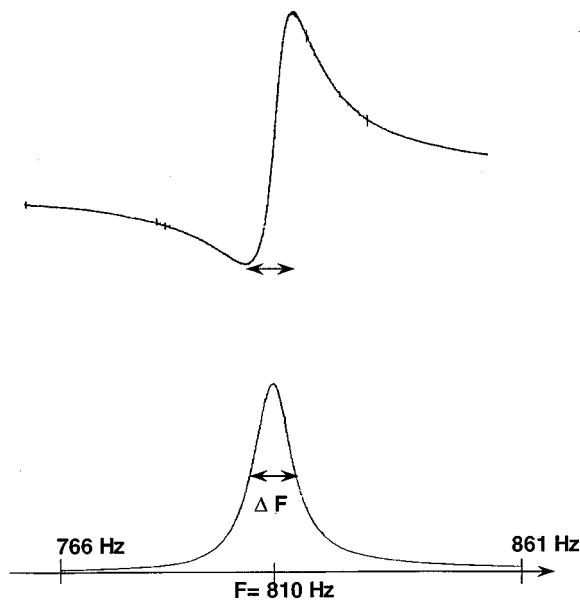
FIG. 8. Experimental determination of the quality factor. Top: dispersion signal of mode $n = 5$, bottom: absorption signal of the same mode. The Q-factor is equal to the ratio $F_n / \Delta F_n$ of the resonance frequency to the width at half-height of the absorption signal or to the peak distance of the dispersion curve.
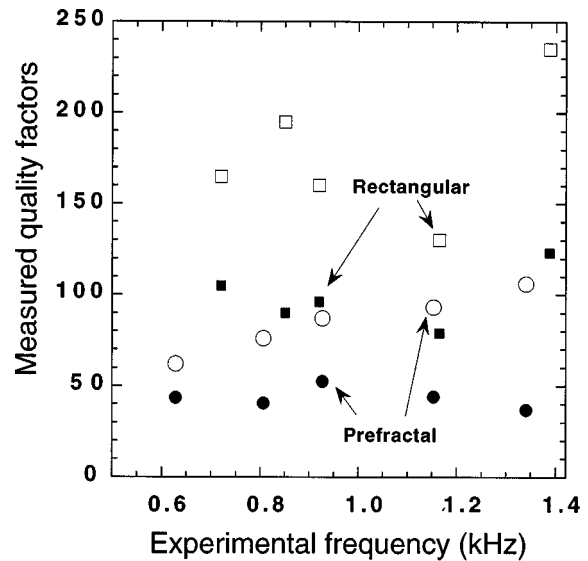
FIG. 9. Measured quality factors. Squares correspond to the rectangular cavity and circles to the prefractal cavity. Both in the cases of bare walls, represented by empty symbols, or with walls covered with absorbent fabric, represented by filled symbols, the Q-factors are smaller by a factor of order 2 for the prefractal cavity.

The experimental values of the quality factors for the individual resonances are given in Fig. 9. The measured values confirm that the prefractal cavity is more damped than the smooth rectangular cavity by a factor of order 2. The results are reminiscent of the theoretical prediction displayed in Fig. 3.

The following discussion proceeds in three steps. First, we compare the quality factors of the bare rectangular cavity with known results. Second, we calibrate the admittance of the fabric that we use to increase the damping on the lateral walls. Finally, we use this measurement, made on the rectangular cavity, to predict the quality factors of the fractal cavity and compare with experiment.

First we assume, for simplicity, that both viscous and thermal losses contribute equally to the different modes dissipation, so than we can write $[\mathrm{Re}\, \varepsilon_{\mathrm{lat}}(\omega_n)] = [\mathrm{Re}\, \varepsilon_{\mathrm{cov}}(\omega_n)] = [\mathrm{Re}\, \varepsilon(\omega_n)]$. The equations (A4) used to describe the properties of the bare walls rectangular cavity should be approximately verified with the value $[\mathrm{Re}\, \varepsilon(\omega_n)]$ of the order of $\approx 10^{-3}$ at 1 kHz found in the literature.[8] Using this value in Eq. (A4), one predicts Q-factors of the order of 270 for the rectangular bare cavity with rigid aluminum walls. This value has the same order of magnitude but is somewhat larger than the experimental values which are found in the range 150 to 200. This indicates the existence of additional damping sources in the experiment, such as the possible contribution to damping of the seal between the upper cover and the main body of the cavity.

Since the additional damping should not be modified by the coverage of the lateral walls, the rectangular cavity resonances can be used to calibrate the value of the *difference* between the admittance of the fabric and that of the bare walls. This difference $\Delta[\mathrm{Re}\, \varepsilon_{\mathrm{lat}}(\omega_n)] = [\mathrm{Re}\, \varepsilon_{\mathrm{lat}}(\omega_n)]_{\mathrm{fabric}} - [\mathrm{Re}\, \varepsilon_{\mathrm{lat}}(\omega_n)]_{\mathrm{bare}}$ can be measured using Eq. (A4). For example, for a mode $\mu \neq 0$, $\mu' \neq 0$, one can write
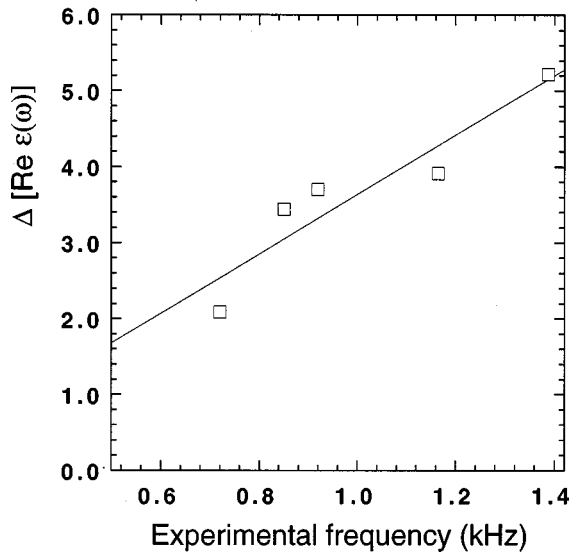
FIG. 10. Experimental frequency dependence of $\Delta[\text{Re } \varepsilon(\omega)]$. This is the real part of the difference between the specific admittance of the absorbing walls and the bare walls. These experimental values are obtained from the measurement of the Q-factors of the rectangular cavity resonances with the use of Eq. (11), or equivalent equations deduced from Eq. (A4) in the cases $(\mu \neq 0, \ \mu' = 0)$ and $(\mu = 0, \ \mu' \neq 0)$. The line represents the best linear fit between these values.

$$\Delta[\text{Re } \varepsilon_{\text{lat}}(\omega_n)] = [Q_{\text{fabric}}^{-1} - Q_{\text{bare}}^{-1}](\omega_n/c)$$
$$\times [L_x L_y/4(L_x + L_y)]. \qquad (11)$$

Note that by this procedure, the contributions of the covers and the additional contribution are automatically eliminated from the determination of $\Delta[\text{Re } \varepsilon_{\text{lat}}(\omega_n)]$. The values of $\Delta[\text{Re } \varepsilon_{\text{lat}}(\omega)]$, calculated by this procedure from the data in Fig. 9, are shown in Fig. 10.

Using the experimental value for $\Delta[\text{Re } \varepsilon_{\text{lat}}(\omega)]$, one can predict the values of the fractal Q-factors and compare them with experiment by using a relation that follows simply from Eq. (8):

$$Q_{\text{fabric}}^{-1} = [Q_{\text{bare}}^{-1}]_{\text{exp}} + (c/\omega_n)\Delta[\text{Re } \varepsilon_{\text{lat}}(\omega)] \cdot \Lambda_n^{-1}. \qquad (12)$$

In other words, it is assumed that for each cavity, the contribution of the covers and of the additional damping remains the same when the damping on the lateral walls is modified by the presence of the sound absorbing fabric. The comparison between the fractal Q-factors computed from Eq. (12) and experiment is shown in Fig. 11. The theoretical values have been calculated using the linear fit of $\Delta[\text{Re } \varepsilon_{\text{lat}}(\omega)]$ shown in Fig. 10. Taking into account that the accuracy of the measurement of Q factors is around $\pm 5\%$, the agreement between theory and experiment can be considered satisfactory.

These results constitute the first experimental evidence of the existence of increased damping in fractal acoustic cavities. More detailed theoretical and experimental study should include a specific calculation of the contribution of heat and viscous losses to each mode and an increase in the experimental sensitivity, including experiments with excitation and detection located in the region of existence of the localized modes at the fractal boundary.
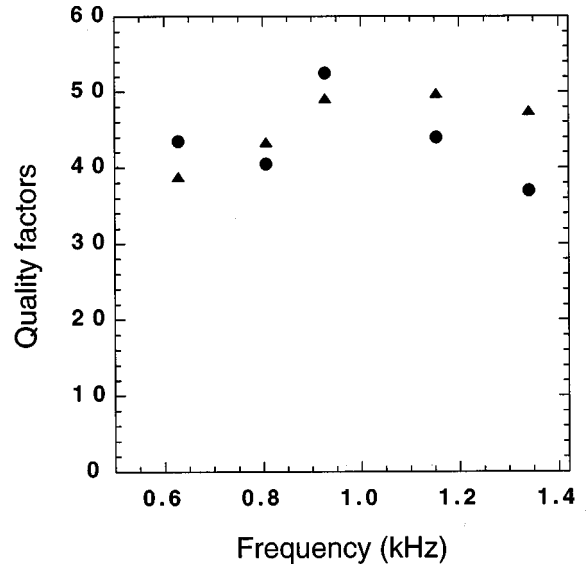
FIG. 11. Comparison between theoretical (triangles) and experimental Q-factors (circles) for the prefractal cavity with absorbing lateral walls. The theoretical values are obtained from Eq. (12) using the Λ_n values given in Table I and the linear fit in Fig. 10.

IV. CONCLUSION

We have presented the first experimental study of a pre-fractal cavity. The observed frequency spectrum agrees with numerical predictions. The fact that most of the localized modes are not detected is due to their very weak coupling with the experimental excitation and detection and the existence of a finite signal-to-noise ratio. The weak coupling is a direct consequence of the confinement of these modes near the irregular frontier. In that sense, the experimentally ''missing'' modes confirm the existence of a strong localization effect. The measurement of the quality factor of several resonances gives the first experimental confirmation of the increased damping power of fractal structures as compared to more regular geometrical structures.[12] In particular, a cavity with a larger number of iterations of the frontier geometry should be more damped than the case that we have studied. Although our results on damping are obtained in the case of weak losses, they may have possible applications to room acoustics. They also can be considered a rationale to better understand the dependence of the properties of anechoic chambers on geometry.

The idea to study fractal resonators arises from the suggestion that there could exists in nature a ''self-stabilization'' of fractal structures due to their increased damping power.[1,4] For example, self-stabilization could be the cause of the existence of fractal sea-coasts by limiting erosion through increased damping of waves. Of course, the present result is only one step towards this uncertain goal, but it can be considered as a positive step in that direction.

1573   J. Acoust. Soc. Am., Vol. 105, No. 3, March 1999

Hébert et al.: Damping in fractal cavities   1573

his help in the realization of the experiment. Remarks by unknown referees of the *Journal of Acoustical Society of America* are gratefully acknowledged.

APPENDIX: DAMPING OF A RECTANGULAR CAVITY

The 2D modes of rectangular cavities have been known since Rayleigh. They can be labeled by two positive integers μ and μ'. The normalized modes take the form

$$\Psi_{\mu\neq 0,\mu'=0}(x,y)=(2/L_xL_y)^{1/2}\cos(\mu x/L_x),$$

$$\Psi_{\mu=0,\mu'\neq 0}(x,y)=(2/L_xL_y)^{1/2}\cos(\mu' y/L_y), \quad\quad (A1)$$

$$\Psi_{\mu\neq 0,\mu'\neq 0}(x,y)=2/(L_xL_y)^{1/2}\cos(\mu x/L_x)\cos(\mu' y/L_y).$$

Their frequency is given by

$$\omega_{\mu,\mu'}=\pi c[(\mu/L_x)^2+(\mu'/L_y)^2]^{1/2}, \quad\quad (A2)$$

where L_x is the width and L_y the length. Using Eqs. (8) and (9), the damping lengths Λ are found to be

$$(\Lambda_{\mu\neq 0,\mu'=0})^{-1}=2(L_x+2L_y)/L_xL_y,$$

$$(\Lambda_{\mu=0,\mu'\neq 0})^{-1}=2(2L_x+L_y)/L_xL_y, \quad\quad (A3)$$

$$(\Lambda_{\mu\neq 0,\mu'\neq 0})^{-1}=4(L_x+L_y)/L_xL_y$$

$$(Q_{\mu\neq 0,\mu'=0})^{-1}=(c/\omega_{\mu\neq 0,\mu'=0})\{[\text{Re }\varepsilon_{\text{lat}}(\omega_{\mu\neq 0,\mu'=0})]$$
$$\times(2(L_x+2L_y)/L_xL_y)$$
$$+[\text{Re }\varepsilon_{\text{cov}}(\omega_{\mu\neq 0,\mu'=0})](2L_z^{-1})\},$$

$$(Q_{\mu=0,\mu'\neq 0})^{-1}=(c/\omega_{\mu=0,\mu'\neq 0})\{[\text{Re }\varepsilon_{\text{lat}}(\omega_{\mu=0,\mu'\neq 0})]$$
$$\times(2(2L_x+L_y)/L_xL_y)$$
$$+[\text{Re }\varepsilon_{\text{cov}}(\omega_{\mu=0,\mu'\neq 0})](2L_z^{-1})\},$$
$$(A4)$$

$$(Q_{\mu\neq 0,\mu'0})^{-1}=(c/\omega_{\mu\neq 0,\mu'\neq 0})\{[\text{Re }\varepsilon_{\text{lat}}(\omega_{\mu\neq 0,\mu'\neq 0})]$$
$$\times(4(L_x+L_y)/L_xL_y)$$
$$+[\text{Re }\varepsilon_{\text{cov}}(\omega_{\mu\neq 0,\mu'\neq 0})](2L_z^{-1})\}.$$

If the admittances of the lateral walls and the covers are equal to $\varepsilon(\omega_n)$, the products $Q_n[\text{Re }\varepsilon(\omega_n)]$ are situated on the three linear curves as shown in Fig. 3.

[1] B. Sapoval, Th. Gobron, and A. Margolina, ''Vibrations of fractal drums,'' Phys. Rev. Lett. **67**, 2974–2977 (1991).

[2] B. Sapoval and Th. Gobron, ''Vibrations of strongly irregular or fractal resonators,'' Phys. Rev. E **47**, 3013–3024 (1993).

[3] B. B. Mandelbrot, *The Fractal Geometry of Nature* (Freeman, San Francisco, 1982).

[4] B. Sapoval, *Fractals* (Aditech, Paris, 1990); *Universalités et Fractales* (Flammarion, Paris, 1997).

[5] B. Sapoval, O. Haeberlé, and S. Russ, ''Acoustical properties of; irregular and fractal cavities,'' J. Acoust. Soc. Am. **102**, 2014–2019 (1997).

[6] S. Russ, B. Sapoval, and O. Haeberlé, ''Irregular and fractal resonators with Neumann boundary conditions: Density of states and localization,'' Phys. Rev. E **55**, 1413 (1997).

[7] See, for example, D. J. Thouless, ''Electrons in disordered systems and the theory of localization'' Phys. Rep. **13**, 93–142 (1974).

[8] P. M. Morse and K. Uno Ingard, *Theoretical Acoustics* (Princeton U.P., Princeton, NJ, 1968).

[9] A. D. Pierce, *Acoustics: An Introduction to its Physical Principles and Applications* (McGraw–Hill, New York, 1981).

[10] M. Bruneau, *Introduction aux théories de l'acoustique* (Université du Maine éditeur, Le Mans, 1983).

[11] M. Bruneau, C. Garing, and H. Leblond, ''Quality factor and boundary-layer attenuation of low order modes in acoustic cavities,'' J. Phys. (Paris) **46**, 1079–1085 (1985).

[12] S. Russ and B. Sapoval, ''Anomalous viscous damping of vibrations of fractal percolation clusters,'' Phys. Rev. Lett. **73**, 1570–1573 (1994).

Oscillations in harmonics generated by the interaction of acoustic beams

Mark D. Cahill and Andrew C. Baker[a]

Department of Physics, University of Bath, Bath BA2 7AY, United Kingdom

A numerical model of nonlinear propagation is used to investigate two cases of monochromatic ultrasonic beams interacting at small angles in a nonlinear medium. Two finite Young's slits are seen to produce fringes at harmonic frequencies of the source in places where the source frequency is absent, which can be seen as a combination of harmonic generation near the source, and in the beam. Two intersecting beams with shaded edges are seen to produce similar fringes in the near field, with an oscillatory structure. Algebraic solutions to a simplified model, using the weak-field Khokhlov–Zabolotskaya equation, are invoked to illustrate the origin of the oscillations, and of the far-field directivity, providing an alternative view of the fringes due to Young's slits. It is seen that two weakly interacting beams can produce fringes of second harmonic where the source frequency has low amplitude, if the beams coincide at the point of observation, or if a boundary condition is imposed on the second harmonic where the beams coincide. © *1999 Acoustical Society of America.* [S0001-4966(99)03103-3]

PACS numbers: 43.25.Cb, 43.25.Jh [MAB]

INTRODUCTION

It has been established that when a sound wave of finite amplitude passes through a nonlinear medium, the wave tends to steepen in such a way as to produce harmonics of the source frequency, and for the case of waves whose components are approximately collinear, the Khokhlov–Zabolotskaya–Kuznetsov (KZK) equation[1] has been found to describe this phenomenon. This equation has been shown to possess solutions which exhibit what have come to be known as ''fingers''[2]—fringes at harmonic frequencies, which appear between the regions of constructive interference in the source frequency, and these have been observed experimentally.[3,4]

What might be considered surprising about this phenomenon is the assumption that, since (in a first approximation) harmonics are necessarily generated where the fundamental is nonzero, and since the harmonics due to the self-action of a plane wave have motion parallel to that wave, then the harmonic fringes should in some sense follow those of the source frequency. This is compounded by the observation of Westervelt[5] that the wave equation which he derived, and to which the KZK equation approximates in the case of near-collinearity, a nondissipative medium, and weak nonlinearity,[6] possesses a solution which is proportional to a quantity (related to the energy density) quadratic in the fundamental beam, and which thus vanishes where the fundamental and its derivatives vanish. A similar conclusion is reached by Jiang and Greenleaf[7] for a dissipative medium.

Many studies have been published which show that fingers nevertheless do appear (see also, for example, Refs. 6 and 8), and the purpose of this paper is to elucidate the mechanisms of their production by means of two simple, if idealized, examples. In the process, the phenomenon of oscillation[9] of harmonics is explored, and seen to be both a cause of fingers in the near field, and a limiting factor on those in the far field.

The KZK equation,

$$\frac{\partial^2 p'}{\partial \sigma\, \partial \tau} = \alpha r_0 \frac{\partial^3 p'}{\partial \tau^3} + \frac{1}{4}\nabla_\perp^2 p' + \frac{r_0}{2 l_d}\frac{\partial^2 p'^2}{\partial \tau^2}, \tag{1}$$

assumes that the beam can be regarded as propagating approximately in one direction, along the z axis, in the absence of vorticity.

It is most convenient to perform the general analysis in terms of dimensionless quantities; τ is the dimensionless retarded time coordinate

$$\tau = \omega t - kz, \tag{2}$$

p' is a dimensionless measure of the overpressure,

$$p' = (P - p_0)/P_0, \tag{3}$$

P being the pressure, p_0 is the ambient pressure, and P_0 is here taken to be the amplitude of the pressure at the source, and the wave has a characteristic wavelength $\lambda = 2\pi/k$, frequency $f = \omega/2\pi$, and speed c (the medium is assumed nondispersive). The Rayleigh distance,

$$r_0 = \pi a^2/\lambda, \tag{4}$$

where a is a characteristic radius of the beam near the source, is itself a characteristic distance in the direction of propagation, and defines the dimensionless coordinate

$$\sigma = \frac{z}{r_0}. \tag{5}$$

The first term on the rhs is the absorption, with coefficient

$$\alpha = \alpha_0 f^2, \tag{6}$$

[a]Now working at Christian Michelsen Research AS, Fantoftvegen 38, Postboks 6031, 5020 Bergen, Norway.
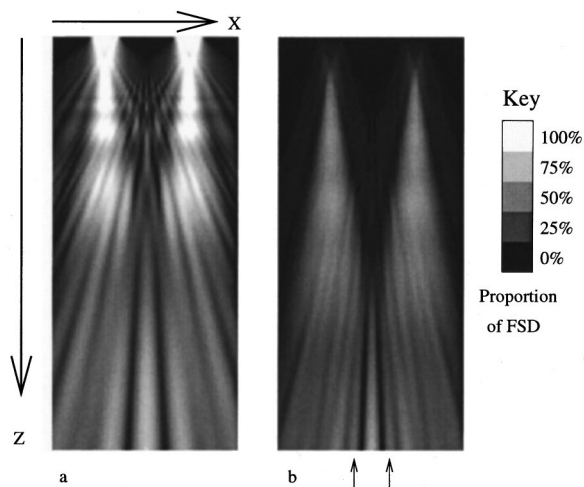
FIG. 1. Amplitude plot of Young's fringes, showing a region 33 mm wide, the beams propagating down the page for 150 mm. The images are expanded ×2 horizontally. (a) Fundamental, full scale deflection (FSD)=1 MPa, (b) second harmonic, FSD=0.5 MPa. Two fingers are indicated by arrows.

$$\alpha_0 = 2.5 \times 10^{-14} \ \mathrm{Np \, m^{-1} \, Hz^{-2}} \tag{7}$$

in water, the second term is diffraction, with

$$\nabla_\perp^2 = \frac{\partial^2}{\partial x'^2} + \frac{\partial^2}{\partial y'^2}, \tag{8}$$

$$(x', y') = (x, y)/a, \tag{9}$$

and the last term describes the nonlinear distortion, with the ''shock wave formation distance''

$$l_d = \frac{c^2 \rho_0}{\beta k P_0} \tag{10}$$

the approximate distance at which, neglecting attenuation, a plane wave of given amplitude forms a shock wave, β being 3.5 in water.

The numerical tool used to solve this is the Bergen code,[10,11] which solves the KZK equation as a set of diffusion equations, one for each temporal harmonic of the beam, weakly coupled by the nonlinear term. This is done using finite difference algorithms and with coordinates appropriate to a spherically diverging beam.

I. NUMERICAL RUNS

Specific examples of acoustic interactions are given in the following sections, and specific dimensional parameters are given. These can be related to the dimensionless quantities of the general equations by Eqs. (2)–(10).

A. Young's slits

Figure 1(a) shows the fundamental beam due to two slits of width 5 mm and length 20 mm, separated by 10 mm, the beam propagating down the page, through water for a distance of 150 mm. The image is a cross section through the center of the beam, perpendicular to the slits, and one sees the usual fringes fanning out towards the bottom of the image. The amplitude of the initial wave, P_0 is 1 MPa, and the frequency is 2.25 MHz, under which conditions the system is
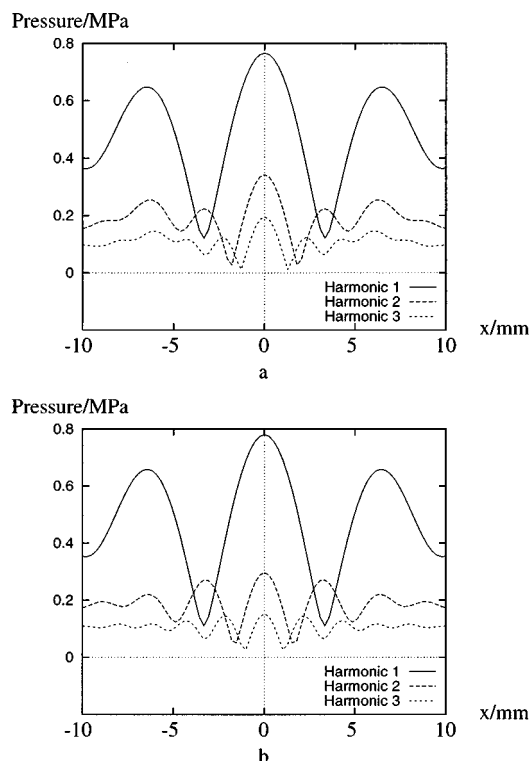
FIG. 2. Amplitude of the first three harmonic components in a cross section of the beam from Young's slits, corresponding to the bottom of Fig. 1: (a) fully interacting field and (b) field due to each slit separately calculated and then superposed.

strongly nonlinear, so that in addition to the fringes of the fundamental, one also sees fringes at harmonic frequencies. Figure 1(b) is the second harmonic field produced by the nonlinear interaction. In addition to the second harmonic seen within each fringe of the fundamental, it also clearly possesses ''fingers'' between these fringes. This is hardly surprising, since we see that in the region just below the slits, the fundamental possesses maxima, which are effectively sources of the second harmonic. Two such sources might be expected to produce an interference pattern with twice the transverse spatial frequency found in the fundamental, simply because the second harmonic has half of the wavelength of the fundamental. From this oversimplified point of view, then, the fingers are the result not of nonlinear interaction of the beams, one from each slit, but of the superposition of the beams, each with its compliment of the second harmonic, and higher harmonics, produced prior to the interaction.

Figure 2(a) shows a cross section of the beam at $z = 150$ mm, $y = 0$, i.e., across the bottom of the images. It includes the third harmonic, which also shows fringes; for each fringe of the fundamental there are two corresponding fringes of the second harmonic, and three of the third, just as would be expected from a superposition of two noninteracting sources. Figure 2(b), however, shows the pattern produced by adding the fields of two such noninteracting slits, calculated using the same model. The two patterns are very similar, but there is a visible difference—the interacting beams have slightly stronger second and third harmonic fringes where there is a fundamental fringe, and the fingers (located at the fundamental minima) are slightly diminished.
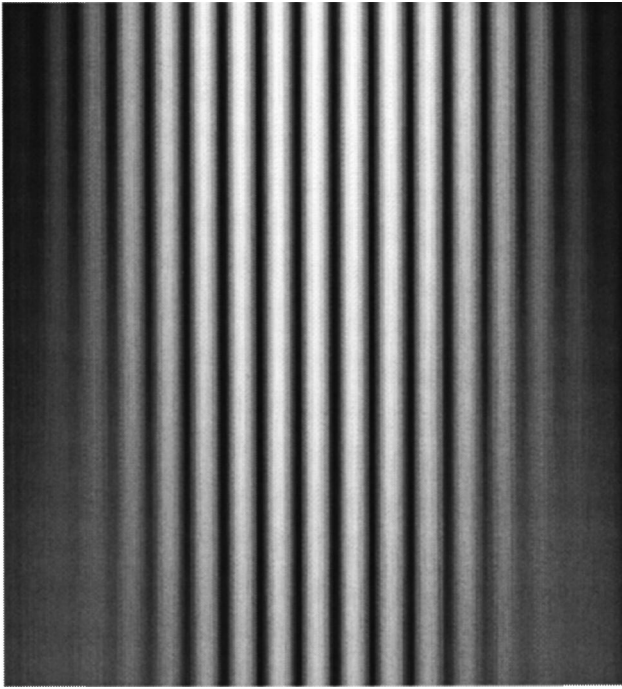
FIG. 3. Fundamental amplitude due to cosine grating (intersecting beams) in plane $y=0$. Beam propagates down the page from grating at the top. FSD=1 MPa. Region shown is 67 by 150 mm^2, expanded $\times 2$ horizontally.

The nonlinear interaction of the beams acts to *diminish* the fingers. This also is not surprising, if we consider that some of the harmonic generation will take place where the beams are interacting, so that there will be increased generation of harmonics where there is constructive interference of the fundamental, and where there is destructive interference of the fundamental there will be less harmonic generation, than in the case of the noninteracting slits. It is known[2] that for a circular source the fingers diminish as $1/r$, while the lobes corresponding to those of the fundamental diminish more slowly, as $\ln(r)/r$, being continuously ''pumped'' by the (itself diminishing) fundamental.

B. Cosine grating

While Young's slits are a familiar system, their spatial spectrum still has a complex structure, making it difficult to see clearly the spatial properties of harmonic generation. A simpler system is now considered in which the interacting beams cross at the origin and possess shaded edges, which limit the width of their spatial spectra. The source function

$$p' = \cos(Kx')f(x',y') \tag{11}$$

for $K>10$ has a spatial spectrum in the x direction with two clearly defined lobes, at $k_x = \pm K/a$, for a reasonably smooth $f(x',y')$, that is, it represents two beams crossing at an angle

$$2\theta = \frac{2K}{ka}. \tag{12}$$

First consider the case

$$f(x',y') = \exp(-5(x'^2 + y'^2)^2), \tag{13}$$

a   b
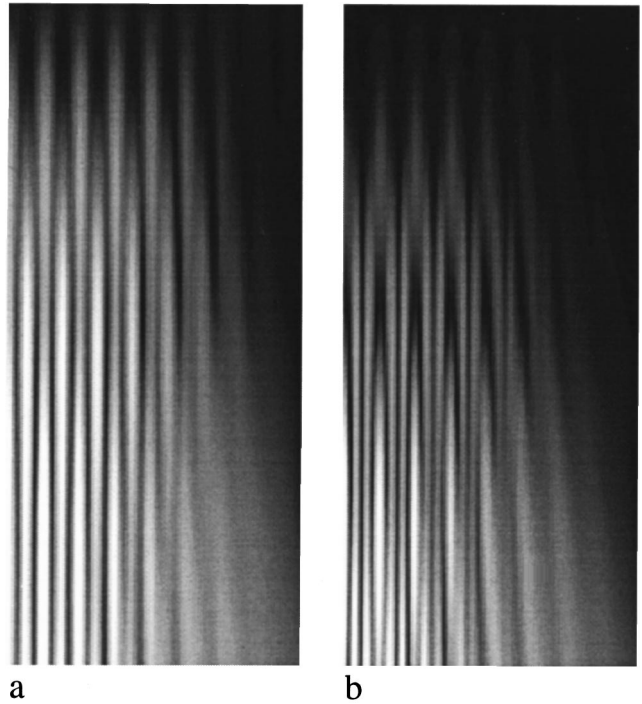
FIG. 4. Amplitude plots for cosine grating (intersecting beams), as in Fig. 3, but for (a) second harmonic, FSD=0.25 MPa and (b) third harmonic, FSD=0.167 Mpa. Beam propagates down the page from grating at the top, with the top left-hand corner being at the center of the source. Region shown is 33 by 150 mm^2, expanded $\times 2$ horizontally.

which is flatter than a Gaussian profile, and take $K=10\pi$, the pressure $P_0=1$ MPa, frequency $f=2.25$ MHz, and dimension of the source $a=4$ cm.

Figure 3 shows the resulting evolution of the fundamental in the near field, as it propagates 15 cm down the page, from the grating at the top of the figure, in the plane $y'=0$, perpendicular to the grating. Across the top the source falls off, while down the page at the sides, the fringes become less distinct as the two beams separate. Figure 4(a) shows the second harmonic. The left half of the image has been cut off, so that the top left-hand corner corresponds to the center of the grating, but the scale is the same as in Fig. 3. As the beam propagates downwards, fringes of second harmonic appear, as expected, where the fundamental has the greatest amplitude. At 4 cm from the source, however, fingers start to appear between these principal fringes, and at 8 cm from the source these fingers are brighter than the principal fringes. Figure 4(b) shows the same thing occurring in the third harmonic—principal fringes appear at the maxima of the fundamental, to be outshone by two intermediate fingers 7 cm from the source. The oscillations continue, with the principal fringes brightest 11 cm from the source, and (just discernibly) the fingers brightest at the bottom of the image.

To see what is happening here, consider Fig. 5. This shows the spatial spectrum of the second harmonic (in the x direction, for $y=0$), from Fig. 4(a), as a function of z, the beam propagating into the page. To the right of the figure is a band with spatial frequency twice that of the fundamental. This grows smoothly, as might be expected. To the left, however, is a band centered on $k_t=0$ which, while initially grow-
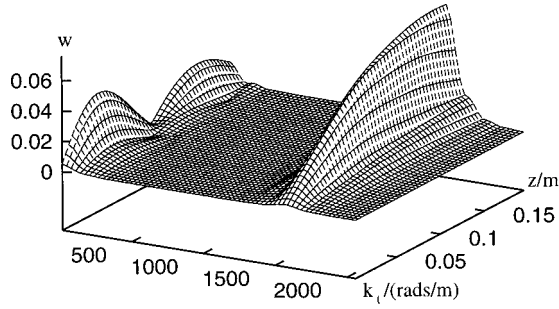
FIG. 5. Amplitude of the transverse Fourier transform of the second harmonic, as a function of z, the distance from a cosine grating. The units of k_t are rad/m, the fundamental having a maximum at $k_t = K/a = 785$ rad/m, which generates second harmonic components at $\pm K/a \pm K/a$.

ing twice as fast as the right-hand band, proceeds to oscillate. The initial behavior is what one might expect, since the self-action of each component of the fundamental (at $k_t = \pm K/a$) will create the right-hand bands, and the interaction of the two will create one with zero spatial frequency, and will be seen in some sense to be associated with the fingers.

Oscillations have been noted before in harmonic generation,[9,12] where they were seen to be due to beating between the generated harmonic field and the field due to the boundary conditions, and this will be seen to be the case here as well.

II. ANALYSIS

A. The weak-field approximation

The previous example involved a strong field, in a dissipative medium. In order to gain a clearer understanding of the origin of the oscillations in Figs. 4 and 5, consider Eq. (1) in the limit of negligible absorption, α, and adopt the quasi-linear approximation, in which we need only consider fields due to the self-action of the fundamental field.

Equation (1) becomes the Khokhlov–Zabolotskaya (KZ) equation

$$\frac{\partial^2 p'}{\partial \sigma \, \partial \tau} = \frac{1}{4} \nabla_{\perp}^2 p' + \frac{r_0}{2 l_d} \frac{\partial^2 p'^2}{\partial \tau^2}, \tag{14}$$

and, adopting the Fourier decomposition

$$p' = \frac{1}{2i} \sum_{n=-\infty}^{\infty} W_n(x', \sigma) e^{in\tau}, \tag{15}$$

$$W_n = -W_{-n}^*, \tag{16}$$

$$W_0 = 0 \tag{17}$$

(the normalization is appropriate to the computer program), we find

$$\frac{\partial W_n(\sigma)}{\partial \sigma} = -\frac{i}{4n} \nabla_{\perp}^2 W_n + \frac{r_0 n}{4 l_d} \sum_{m=-\infty}^{\infty} W_{n-m} W_m. \tag{18}$$

If the source includes only the fundamental W_1, with

$$W_1(x', 0) = \cos(Kx') \exp(-2x'^2), \tag{19}$$

independent of y, then in the quasi-linear approximation,[2]

$$\frac{\partial W_1(x', \sigma)}{\partial \sigma} = -\frac{i}{4} \frac{\partial^2 W_1}{\partial x'^2}, \tag{20}$$

$$\frac{\partial W_2(x', \sigma)}{\partial \sigma} = -\frac{i}{8} \frac{\partial^2 W_2}{\partial x'^2} + \frac{r_0}{2 l_d} W_1^2. \tag{21}$$

Decomposing W_n into its transverse spatial spectrum,

$$W_n(x', \sigma) = \int_{-\infty}^{\infty} e^{-i k_x x'} \omega_n(k_x, \sigma) dk_x, \tag{22}$$

then

$$\frac{\partial \omega_1(k_x, \sigma)}{\partial \sigma} = \frac{i k_x^2}{4} \omega_1(k_x, \sigma), \tag{23}$$

$$\frac{\partial \omega_2(k_x, \sigma)}{\partial \sigma} = \frac{i k_x^2}{8} \omega_2(k_x, \sigma)$$

$$+ \frac{r_0}{2 l_d} \int_{-\infty}^{\infty} \omega_1(k_x - k_x', \sigma) \omega_1(k_x', \sigma) dk_x', \tag{24}$$

and

$$\omega_1(k_x, 0) = \sqrt{\frac{1}{32\pi}} \left[\exp\left(-\frac{(k_x + K)^2}{8} \right) \right.$$

$$\left. + \exp\left(-\frac{(k_x - K)^2}{8} \right) \right], \tag{25}$$

so that

$$\omega_1(k_x, \sigma) = \sqrt{\frac{1}{32\pi}} \left[\exp\left(-\frac{(k_x + K)^2}{8} \right) \right.$$

$$\left. + \exp\left(-\frac{(k_x - K)^2}{8} \right) \right] \exp(i k_x^2 \sigma / 4), \tag{26}$$

which has the inverse transform

$$W_1(x', \sigma) = \frac{1}{2\sqrt{1 - 2i\sigma}} \left[\exp\left(\frac{(4ix' + K)^2}{8(1 - 2i\sigma)} - \frac{K^2}{8} \right) \right.$$

$$\left. + \exp\left(\frac{(4ix' - K)^2}{8(1 - 2i\sigma)} - \frac{K^2}{8} \right) \right]. \tag{27}$$

The two terms in the square brackets are clearly the two diverging beams, whose amplitudes at $x' = \mp K\sigma/2$, decrease as $1/\sqrt[4]{1 + 4\sigma^2}$. The wave is described in Eq. (1) with a retarded time coordinate, so the greater part of the phase of each component is implicit in the representation; however, the first terms on the rhs of the differential equations (23) and (24) impose a phase lag on the wave due to its having a component in the transverse (x) direction, proportional to the square of k_x. This is due to the relation $\mathbf{k}^2 = \omega^2/c^2$, $\mathbf{k}$ and ω being the dimensional angular frequencies, in the parabolic approximation $k_x \ll 1$ [see the discussion introducing Eq. (1)].

B. Near-field oscillations

Now applying Eq. (26) to Eq. (24), and evaluating the convolution, one finds

$$\frac{\partial \omega_2(k_x,\sigma)}{\partial \sigma} = \frac{ik_x^2}{8}\omega_2(k_x,\sigma) + \frac{r_0}{32l_d\sqrt{\pi(1-2i\sigma)}}$$
$$\times \left[\exp\left(-\frac{(k_x+2K)^2}{16}\right) \right.$$
$$+ \exp\left(-\frac{(k_x-2K)^2}{16}\right)$$
$$\left. + 2\exp\left(-\frac{k_x^2}{16} + \frac{iK^2\sigma}{2(1-2i\sigma)}\right) \right] e^{ik_x^2\sigma/8}, \tag{28}$$

which, confining attention for now to the region near the grating with

$$K^2\sigma^2 \ll 1, \quad \sigma \ll 1, \tag{29}$$

is

$$\frac{\partial \omega_2(k_x,\sigma)}{\partial \sigma} \approx \frac{ik_x^2}{8}\omega_2(k_x,\sigma) + \frac{r_0}{32\sqrt{\pi}l_d}$$
$$\times \left[\exp\left(-\frac{(k_x+2K)^2}{16}\right) \right.$$
$$+ \exp\left(-\frac{(k_x-2K)^2}{16}\right)$$
$$\left. + 2\exp\left(-\frac{k_x^2}{16} + \frac{iK^2\sigma}{2}\right) \right] e^{ik_x^2\sigma/8}. \tag{30}$$

All three components in the square brackets represent Gaussians with greater width than those in Eq. (26), corresponding in configuration space to a source narrower than the width of the fundamental. The first two terms are due to the convolution of each term of Eq. (26) with itself, and are centered on $k_x = \mp 2K$, with a phase lag $ik_x^2\sigma/8$, as might be expected, but the third, which is due to the convolution of each beam with the other, and so represents the interaction of the two, while centered on $k_x = 0$, has an additional phase lag $iK^2\sigma/2$. This additional lag is directly attributable to that in the beams of the fundamental, which each possess a lag appropriate to a mode with $k_x = K$, and it is this which can be seen as the cause of the oscillations.

Imposing the condition that there is no second harmonic at the grating

$$\omega_2(k_x,0) = 0, \tag{31}$$

Eq. (30) has the solution

$$\omega_2(k_x,\sigma) \approx \frac{r_0}{32l_d\sqrt{\pi}}\left[\left(\exp\left(-\frac{(k_x+2K)^2}{16}\right) \right. \right.$$
$$\left. + \exp\left(-\frac{(k_x-2K)^2}{16}\right) \right)\sigma$$
$$\left. + \frac{4i}{K^2}(1-e^{iK^2\sigma/2})\exp\left(-\frac{k_x^2}{16}\right) \right] e^{ik_x^2\sigma/8}. \tag{32}$$

In configuration space, and given the approximation (29), this is
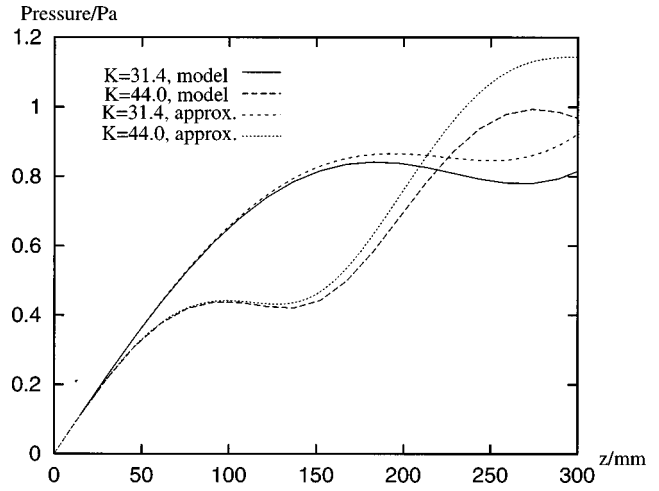
FIG. 6. Comparison of predictions from the numerical model, and from the algebraic approximation equation (33), for the axial variation of the amplitude of the second harmonic, for $K=10\pi$ and $K=14\pi$.

$$W_2(x',\sigma) \approx \frac{r_0}{8l_d}e^{-4x'^2}\left[2e^{iK^2\sigma/2}\cos(2Kx')\sigma \right.$$
$$\left. + \frac{8}{K^2}e^{iK^2\sigma/4}\sin\left(\frac{K^2\sigma}{4}\right) \right]. \tag{33}$$

Figures 6 and 7 compare this approximation with the results of model runs. Here a is taken as 8 cm, the (ideally infinite) length of the slits is taken to be 80 cm, $\alpha = 0$, $P_0 = 1$ kPa, and all other parameters are as before. Figure 6 shows the amplitude of the beam along the central lobe ($x' = 0$) for two values of K, while Fig. 7 compares the complex components for $K = 10\pi$. While the approximation becomes invalid after a couple of cycles, it reproduces the oscillations and phase variation of the first cycle well.

The first two terms in the square brackets of Eq. (32) vary as σ, while the third oscillates, being proportional to $(1-e^{iK^2\sigma/2})$. This is the difference between a component generated in the beam, which rotates in phase due to the lag $iK^2\sigma/2$ mentioned above, and a term due to the boundary
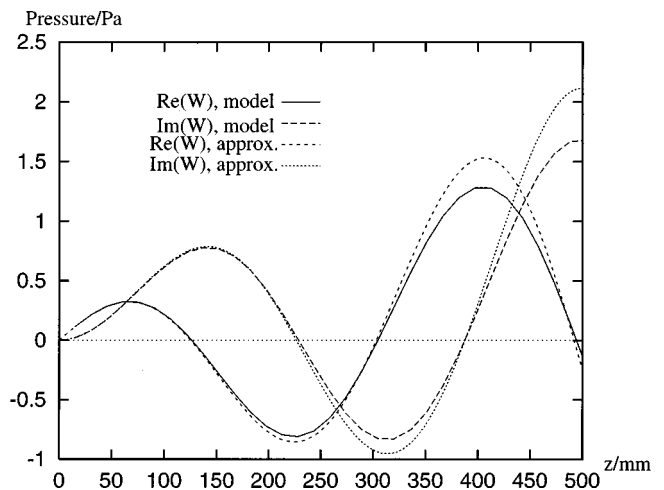
FIG. 7. Comparison of predictions by the numerical model, and by the algebraic approximation equation (33), for the axial variation of the complex components of the second harmonic. $K = 10\pi$.
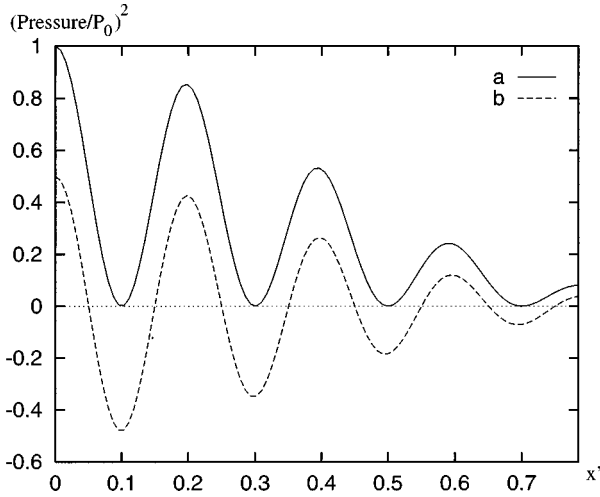
FIG. 8. Illustrating a mechanism for the production of fingers; (a) the square of the source function $W_1(x',0)$, for $K = 10\pi$, to which the second harmonic is initially proportional and (b) the same function with an offset of half the envelope $\exp(4x'^2)$. (b) Possesses fingers at $x' = 0.1, 0.3, \ldots$.

condition (31), which propagates with the natural phase. These interfere to produce the sine in the second term of Eq. (33), and describe an oscillation like that seen in Fig. 5.

Regarding the production of fingers, for very small $K^2\sigma$, the coefficient of the third Gaussian (the cross term) in Eq. (32) is approximately 2σ, so that

$$\omega_2(k_x,\sigma) \approx \frac{r_0\sigma}{32l_d\sqrt{\pi}}\left[\left(\exp\left(-\frac{(k_x+2K)^2}{16}\right)\right.\right.$$
$$\left.\left.+\exp\left(-\frac{(k_x-2K)^2}{16}\right)\right)+2\exp\left(-\frac{k_x^2}{16}\right)\right],$$
(34)

which, up to a Gaussian envelope, is the Fourier transform of $\cos^2(Kx')$ [see Eq. (19)], which has zero amplitude where W_1 is zero. By $\sigma = 2\pi/K^2$, however, the coefficient of the cross term is zero (the field due to the boundary condition cancels that generated by the beam), and Eq. (32) then resembles the Fourier transform of $\cos(2Kx')$. The situation is illustrated by Fig. 8; the cross term is proportional to the envelope (being centered about $k_x = 0$), and its cancellation produces a field with negative values where there is no fundamental field, which are the fingers.

C. Fingers in the far field

An exact solution to the perturbative cosine grating will now be found, which will reveal another mechanism, by which the $k_x = 0$ component can manifest itself as a single finger, rather than the multiple fingers seen in the near field. Instead of using inequalities (29), write the solution to Eq. (28) in integral form as

$$\omega_2(k_x,\sigma) = e^{ik_x^2\sigma/8}\frac{r_0}{32l_d\sqrt{\pi}}\int_{\sigma_0}^{\sigma}\frac{d\sigma'}{\sqrt{1-2i\sigma'}}$$

$$\times\left[\exp\left(-\frac{(k_x+2K)^2}{16}\right)+\exp\left(-\frac{(k_x-2K)^2}{16}\right)\right.$$

$$\left.+2\exp\left(-\frac{k_x^2}{16}+\frac{iK^2\sigma'}{2(1-2i\sigma')}\right)\right],$$
(35)

where the lower bound of the integration σ_0 will be set to 0 at the end of the calculation, to implement the boundary condition equation (31). Delaying the evaluation of this until after the inverse Fourier transform has been performed,

$$W_2(x',\sigma) = \frac{r_0}{8l_d\sqrt{1-2i\sigma}}\int_{\sigma_0}^{\sigma}\frac{d\sigma'}{\sqrt{1-2i\sigma'}}$$

$$\times\left[\exp\left(\frac{(4ix'+K)^2}{4(1-2i\sigma)}-\frac{K^2}{4}\right)\right.$$

$$+\exp\left(\frac{(4ix'-K)^2}{4(1-2i\sigma)}-\frac{K^2}{4}\right)$$

$$\left.+2\exp\left(-\frac{4x'^2}{1-2i\sigma}+\frac{K^2}{4}\left(\frac{1}{1-2i\sigma'}-1\right)\right)\right],$$
(36)

we eventually find

$$W_2(x',\sigma) = \frac{r_0}{8l_d}\left\{\frac{i}{\sqrt{1-2i\sigma}}(\sqrt{1-2i\sigma}-\sqrt{1-2i\sigma_0})\right.$$

$$\times\left[\exp\left(\frac{(4ix'+K)^2}{4(1-2i\sigma)}-\frac{K^2}{4}\right)\right.$$

$$\left.+\exp\left(\frac{(4ix'-K)^2}{4(1-2i\sigma)}-\frac{K^2}{4}\right)\right]$$

$$\left.+\mathrm{cr}(K,x',\sigma,\sigma_0)-\mathrm{cr}(K,x',\sigma,\sigma)\right\},$$
(37)

where the function cr, due to the cross term, is

$$\mathrm{cr}(K,x',\sigma,\tau) = \frac{K}{\sqrt{1-2i\sigma}}\exp\left(-\frac{4x'^2}{1-2i\sigma}-\frac{K^2}{4}\right)$$

$$\times\left[\frac{2\sqrt{1-2i\tau}}{iK}\exp\left(\frac{K^2}{4(1-2i\tau)}\right)\right.$$

$$\left.+\sqrt{\pi}\,\mathrm{erf}\left(\frac{iK}{2\sqrt{1-2i\tau}}\right)\right],$$
(38)

and

$$\mathrm{erf}(y) = \frac{2}{\sqrt{\pi}}\int_0^y \exp(-y'^2)dy'.$$
(39)

The terms other than the cross term in Eq. (37) are the self-action of each beam. Note that for finite σ_0, $x' = \mp K\sigma/2$, large σ, they tend to a constant—decreased amplitude as the beam spreads is cancelled by growth due to generation from
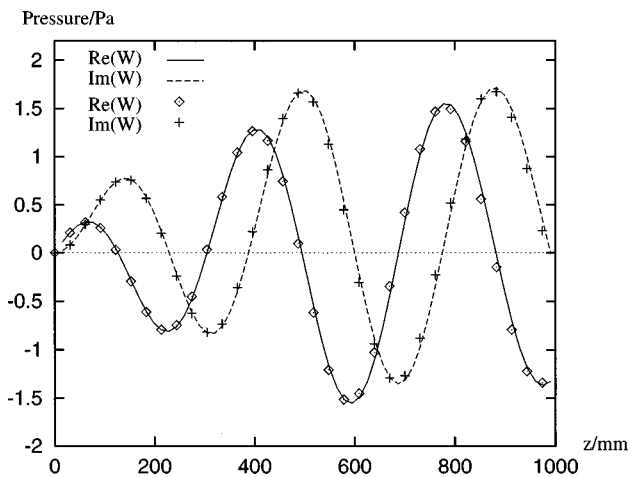
FIG. 9. Comparison of predictions by the numerical model (curves), and by the exact solution equation (37) (points), for the axial variation of the complex components of the second harmonic. $K = 10\pi$, $P_0 = 1$ kPa.

the fundamental. The analogous behavior for a three-dimensional problem is $\omega_2 \sim \ln(z)/z^2$ as noted at the end of Sec. I A.

While Eq. (37) is not easy to evaluate, packages such as Maple are quite capable of tabulating and plotting it. Figure 9 compares the axial behavior of the exact solution, with the model run of Figs. 6 and 7, and Fig. 10 compares them in a cross section of the beam 274 mm from the grating, a point where the fingers are stronger than the principal fringes. The slight deviation of the model from theory for large z in Fig. 9 may be due to the finite length of the slits in the model run. Otherwise, the fit is exact enough to confirm the accuracy of the Bergen code, and incidentally to reassure one that the algebra is correct.

Turning to the cross term,

$$cr(K,x',\sigma,\sigma) - cr(K,x',\sigma,\sigma_0), \qquad (40)$$
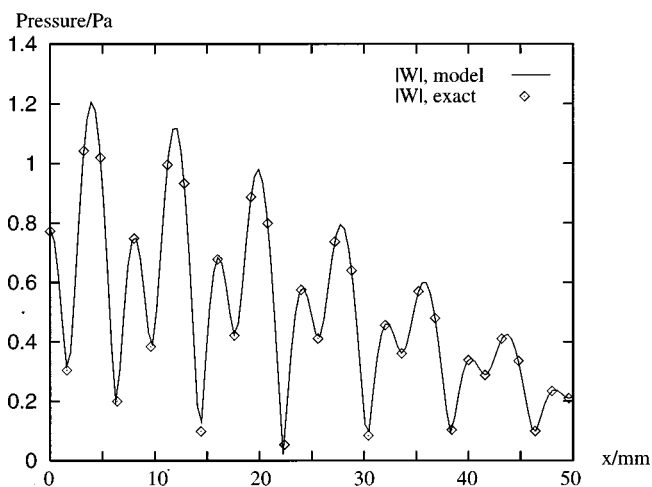
FIG. 10. Comparison of predictions by the numerical model (curves), and by the exact solution equation (37) (points), for the transverse variation of the magnitude of the second harmonic at $z = 274$ mm. Note that the fingers are stronger than the principal fringes. $K = 10\pi$, $P_0 = 1$ kPa.
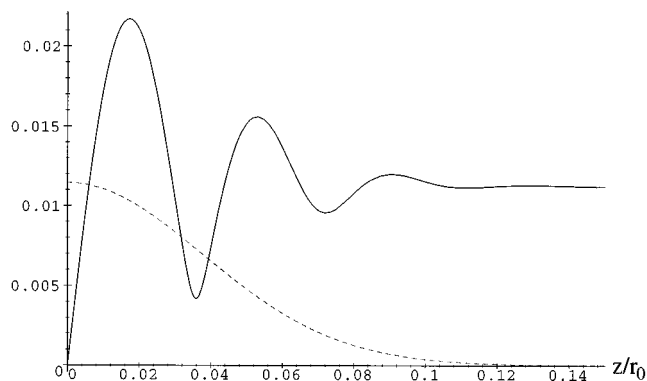
FIG. 11. Amplitude of the cross-term equation (40), on axis ($x = 0$) for $K = 6\pi$: boundary condition equations (31) (continuous line) and (41) (dashed line).

for very large σ (finite x' and σ_0) this tends to $-2i \times \exp(-K^2/4)$, which is to say that there is a constant term in the limit proportional to the overlap of the directivities of the beams. Insofar, then, as the fundamental beams propagate in different directions, this limit is negligible. Setting $\sigma_0 = 0$, in accord with Eq. (31), the continuous line in Fig. 11 shows that the amplitude of the term oscillates at first, then settles down to an almost constant value for moderate values of σ, eventually falling off as $1/\sqrt[4]{1 + 4\sigma^2}$. As the principal fringes diverge, this term propagates down the z axis, to form a finger.

The solution (27) is defined for negative σ, and while it would be difficult to create such a beam, it is still meaningful to ask what second harmonic field it would generate, if the second harmonic were set to zero at some point before the intersection of the beams. With this in mind, the dashed line in Fig. 11 shows the amplitude of the cross term assuming

$$\omega_2(k_x, -10) = 0, \qquad (41)$$

i.e., with $\sigma_0 = -10$. With this boundary condition, the second harmonic is effectively zero outside the region in which both fundamental beams are present—just the behavior described by Westervelt. To see how these two cases differ, consider Figs. 12 and 13, which show the complex components of the cross term for each boundary condition. In the "Westervelt" case, Fig. 12, there is a substantial imaginary component of the second harmonic at the origin. In order to
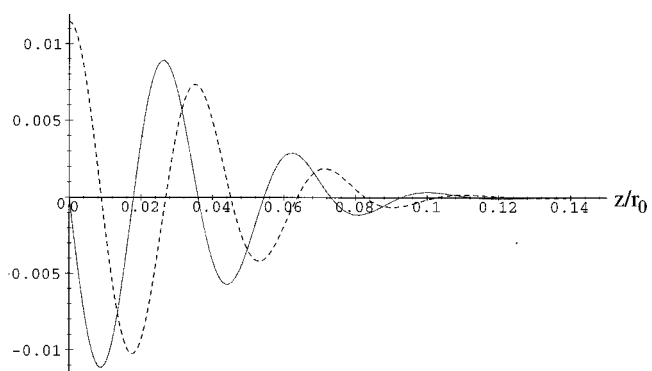
FIG. 12. Axial components of the cross term for boundary condition equation (41): real component (continuous line) and imaginary component (dashed line).
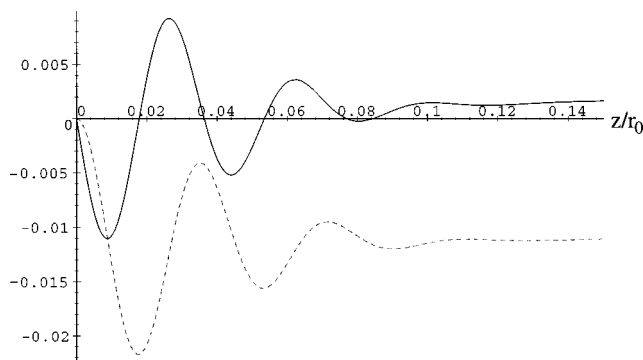
FIG. 13. Axial components of the cross term for boundary condition equation (31): real component (continuous line) and imaginary component (dashed line).

set this to zero for the boundary condition at $\sigma_0 = 0$, a component must be subtracted, whose evolution is seen in Fig. 13 to produce a large negative imaginary component beyond the region of interaction of the beams [which slowly rotates into the real component due to the factor $1/\sqrt{1-2i\sigma}$ in Eq. (38)]. The far-field finger is thus seen to be a direct result of the boundary condition, Eq. (31). It is the "free wave" of Naze Tjøtta and Tjøtta.[9]

III. DISCUSSION

It has been seen in the previous two sections that the development of fingers in the near and far fields of a simple system can be attributed to the difference between the spatial frequencies of freely propagating waves of the second harmonic, and of the source function due to the interaction of noncollinear beams. In the near field, the mismatch causes this component to stop growing, as it becomes out of phase with its source, which shifts the fringe pattern to produce fingers of opposite phase. In the far field, this mismatch can be seen as the reason that the generated component (the "Westervelt component") does not propagate beyond the region of interaction of the beams—it is a commonplace result of scattering theory that "off-shell" modes, i.e., modes which do not satisfy the free-field equation, do not propagate (see Ref. 13, Chap. 5, Sec. 2), and the fact that the phase of the source function rotates with respect to a free field propagating in the same direction indicates that it is the source of an off-shell field. The component which cancels this off-shell field at the boundary, however, is itself on-shell, and it is this which propagates. The effect of boundary conditions on generated harmonics was explored more fully in Refs. 14 and 15. On the other hand, components of the two beams which are collinear produce a source field which is on-shell, and so generates a component of the second harmonic which propagates.

The objection might rightly be raised that by imposing the boundary condition equation (19), appropriate to a source, and then considering the beams as originating before that point, one is describing an artificially symmetrical arrangement, which might not be representative of more realistic systems. Fortunately, Darvennes and Hamilton[16] have considered a system in which the boundary conditions possess two distinct Gaussian sources in three dimensions, whose beams then cross, subject to the KZ equation. Their Eq. (24), describing the far-field behavior, contains two terms, one proportional to the product of the directivities of the source, and varying as $\ln(z)/z$ [the counterpart of the constant limit $-2i\exp(-K^2/4)$ above], due to collinear components in the beams, and the other a bilinear function of the beams at the boundary, as must the "free field" component be, if at the boundary it is to cancel the Westervelt component, itself bilinear in the fundamental beams.

Finally, to revisit the Young's fringes, although Figs. 1 and 2 refer to beams with finite amplitude and absorption, one can envisage the second harmonic in a low-amplitude system as being composed of three fields—the first generated by the interaction of collinear modes in the two beams, the second due to the local interaction of noncollinear modes (bearing in mind that the beams overlap through most of the half-space $z > 0$), and the third attributable to the boundary condition, which requires cancellation at $z = 0$ of the field generated by local interaction of the fundamental field. In practice, however, the distinction between these is ambiguous, both because it depends on the choice of boundary, and because sources of modes which violate only slightly the free-field equation must act for a considerable distance before drifting out of phase with their generated waves. In the far field, the first component will create fringes of second harmonic coinciding with those of the fundamental, but its continuous generation, in the absence of propagation of the second component, may be expected to generate fingers, as in the near field of the cosine grating. Given the complex spatial spectrum, it is not surprising that oscillations are not apparent in the amplitude of the fingers, but detailed examination of the field does show that the second harmonic in the fingers has opposite phase from that in the principal fringes. Note that between fringes of the fundamental, its transverse derivative is nonzero, and so Westervelt's argument[5] (see the Introduction) does not deny the existence of fingers.

While the solutions derived above are for simple systems, it may be possible to approximate the boundary condition equation (31) experimentally, by inserting a frequency-dependent attenuator at the intersection of two beams of sound. If the attenuator is thin on the scale $2r_0/K^2$ of the oscillations, and effectively removes the generated harmonics from two intersecting beams, then one would expect a weak far-field finger to be observed.

The analytic solution obtained may also be of use for testing numerical models of nonlinear propagation.

In summary, far from being anomalous, the nonlinear production of harmonic fields in regions where there is little fundamental field is a natural consequence of the imposition of zero amplitude on the harmonics in regions where the fundamental is nonzero, the continuous local production of on-shell harmonics, and suppression of off-shell harmonics.

ACKNOWLEDGMENTS

[1] V. P. Kuznetsov, ''Equations of nonlinear acoustics,'' Sov. Phys. Acoust. **16**, 467–470 (1971).

[2] J. Berntsen, J. Naze Tjøtta, and S. Tjøtta, ''Near field of a large acoustic transducer. Part IV: Second harmonic and sum frequency radiation,'' J. Acoust. Soc. Am. **75**, 1383–1391 (1984).

[3] J. A. TenCate, ''An experimental investigation of the nonlinear pressure field produced by a plane circular piston,'' J. Acoust. Soc. Am. **94**, 1084–1089 (1993).

[4] C. R. Reilly and K. J. Parker, ''Finite-amplitude effects on ultrasound beam patterns in attenuating media,'' J. Acoust. Soc. Am. **86**, 2339–2348 (1989).

[5] P. J. Westervelt, ''Scattering of sound by sound,'' J. Acoust. Soc. Am. **29**, 934–935 (1957).

[6] J. Berntsen, J. Naze Tjøtta, and S. Tjøtta, ''Interaction of sound waves. Part IV: Scattering of sound by sound,'' J. Acoust. Soc. Am. **86**, 1968–1983 (1989).

[7] Z-Y. Jiang and J. F. Greenleaf, ''The nonlinear interaction of two plane waves in a viscous medium,'' J. Acoust. Soc. Am. **99**, 2783–2790 (1996).

[8] S. Nachef, D. Cathignol, J. Naze Tjøtta, A. M. Berg, and S. Tjøtta, ''Investigation of a high-intensity sound beam from a plane transducer—Experimental and theoretical results,'' J. Acoust. Soc. Am. **98**, 2303–2323 (1995).

[9] J. Naze Tjøtta and S. Tjøtta, ''Interaction of sound waves. Part I: Basic equations and plane waves,'' J. Acoust. Soc. Am. **82**, 1425–1428 (1987).

[10] J. Berntsen, ''Numerical Calculation of Finite Amplitude Sound Beams'' in *Frontiers of Nonlinear Acoustics: Proceedings of the 12th ISNA*, edited by M. F. Hamilton and D. T. Blackstock (Elsevier Science, New York, 1990), pp. 191–196.

[11] A. C. Baker, A. M. Berg, A. Sahin, and J. Naze Tjøtta, ''The nonlinear pressure field of plane, rectangular apertures: Experimental and theoretical results,'' J. Acoust. Soc. Am. **97**, 3510–3517 (1995).

[12] M. A. Foda, ''Nonlinear propagation and distortion of two plane waves interacting at arbitrary angles,'' Acustica **82**, 213–219 (1996).

[13] O. V. Rudenko and S. I. Soluyan, *Theoretical Foundations of Nonlinear Acoustics*, translated from Russian by R. T. Beyer (Consultants Bureau, New York, 1977).

[14] J. Naze Tjøtta and S. Tjøtta, ''Interaction of sound waves. Part III: Two real beams,'' J. Acoust. Soc. Am. **83**, 487–495 (1988).

[15] J. Naze Tjøtta, J. A. TenCate, and S. Tjøtta, ''Effects of boundary conditions on the nonlinear interaction of sound beams,'' J. Acoust. Soc. Am. **89**, 1037–1049 (1991).

[16] C. M. Darvennes and M. F. Hamilton, ''Scattering of sound by sound from two Gaussian beams,'' J. Acoust. Soc. Am. **87**, 1955–1964 (1990).

Theory of the backscattering of sound by phase-matched nonlinear interaction

Dmitrii Kouznetsov[a] and Augusto García-Valenzuela[b]

Centro de Instrumentos, Universidad Nacional Autónoma de México, Ap. 70-186, Cd. Universitaria, 04510, D. F., México

The nonlinear interaction of noncollinear acoustical waves is considered. Conditions of the resonant backscattering of one wave from the lattice produced by the other two are formulated in analogy with the four-wave mixing known in optics. The efficiency of the phase-matched interaction of acoustical waves is calculated in the resonant approximation for a gas media. Such approximation is constructed on the basis of the expansion of the sound equations preserving up to cubic terms. The amplitude of the backscattered wave is expressed as the product of the efficiency, the amplitudes of three waves, the wave number of the backscattered wave, and the size of the region of interaction. Such backscattering is proposed as an acoustical remote probe. The distance to the interaction region and the amplitude of initial waves are limited by nonlinear degradation of waves due to the second-order nonlinearity. For acoustical waves with wave number 10 m^{-1}, sources of size 1 m, and about 100 m to the interaction region, the amplitude of the backscattered wave can be about 10^{-10} of the atmospheric pressure. At the detection with a signal-to-noise ratio about of 10, the resolution of such method on the wind velocity may be about 1 m/s. © *1999 Acoustical Society of America.* [S0001-4966(99)04103-X]

PACS numbers: 43.25.Jh [MAB]

INTRODUCTION

Acoustic remote probes are efficient tools in atmospheric physics. Usually one registers a signal scattered from turbulent inhomogeneities of the atmosphere.[1,2] To get efficient phase-matched scattering, one uses waves of different origin, such as radiowaves and acoustical waves with appropriate relation of wave numbers.[3,4]

We propose an alternative technique which uses the interaction of only acoustical waves; here we present the deduction of formulas which appeared in Ref. 5 without proof. In this reference, the present results were proposed to be used as an acoustic remote probe. We briefly discuss such a proposal as well.

In a homogeneous isotropic medium, we need two acoustical waves to write a lattice, and one probe wave to be reflected from this lattice. Such processes are widely used in optics, where it is known as four-wave mixing.[6,7] It takes place for all types of nonlinearities, even in a gain medium.[8] Efficient interaction occurs at the phase-matching condition. This condition depends neither on the nature of waves nor on the type of nonlinearity. Here we deal with acoustical waves in a gas; the medium is isotropic and nondispersive, which simplifies the equations.

We should mention that recently J. Berntsen *et al.* published a series of papers (see Ref. 9 and references therein) in which they analyzed the interaction of Gaussian acoustical beams in the second-order approximation. However, effects of four-wave mixing mentioned above appear only in the third order. To keep equations simple we work here with plane waves. The consideration of these effects with well-defined beams could be a continuation of the present work.

The possible geometry of a phase-matched backscattering experiment is shown in Fig. 1. Let sources 1 and 2 emit two strong sound beams which produce a lattice within the region of interaction. Here we are interested in the case in which a third wave (the probe beam) emited by source 3 is backscattered from this lattice. In this case the reflected wave can be registered by a detector located at source 3.

We assume that the frequency of the third source is given. So, we need to calculate, for the given geometry, the frequencies of sources 1 and 2, and the placement of the window of frequency selection of the detector (Sec. I). Then, for the case of resonance, we need to calculate the efficiency of the nonlinear interaction (Sec. II). Finally, we need to estimate the maximum amplitude of sound, which could be registered with such a scheme (Sec. III), and, as an example, estimate the sensitivity of such a method to the wind velocity.

I. PHASE-MATCHING CONDITION

Consider three plane waves emitted by sources 1, 2, and 3 as shown in Fig. 1. Let the corresponding wave vectors be **p**, **q**, **k**.

To have resonant interaction, we need to satisfy the conditions of phase synchronism:

$$\mathbf{p} - \mathbf{q} + \mathbf{k} = \mathbf{r}, \quad \omega_{\mathbf{p}} - \omega_{\mathbf{q}} + \omega_{\mathbf{k}} = \omega_{\mathbf{r}}, \tag{1}$$

where **r** is the wave vector of some scattered wave, and the ω's are the corresponding frequencies. Such conditions are well known in optics.[6,7] They are refered as ''phase-matching conditions,'' or ''phase synchronism conditions.''

[a] Electronic mail: kusnecov@aleph.cinstrum.unam.mx
[b] Electronic mail: garciaa@aleph.cinstrum.unam.mx
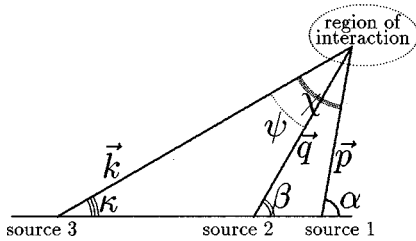
FIG. 1. Geometry of a nonlinear acoustical remote probe based on the backscattering due to four-wave interaction.

For acoustical waves in isotropic and nondispersive media, $\omega_\mathbf{k} = v_s / |\mathbf{k}|$, where the velocity of sound v_s is the same for all wave vectors.

Note that the phase synchronism conditions are satisfied for the collinear second-harmonic generation. If we set $\mathbf{q} = 0$ and $\mathbf{p} = \mathbf{k} = \mathbf{r}/2$, Eqs. (1) hold. We see that only one incident wave is necessary for the phase-matched interaction, but no backscattering is possible in this case. In a dispersionless and isotropic medium we need to have at least three different waves to generate a wave with its wave vector anti-collinear to one of the incident waves.

For the purpose of an acoustical remote probe, we assume that all initial wave vectors have positive vertical components: all waves are produced by ground level sources and no initally counter-propagating waves can be realized.

Consider the condition that the wave vector $\mathbf{r}$ of the scattered sound is anti-collinear to one of inital wave vectors $\mathbf{k}$ (backscattering). Then Eqs. (1) imply that $\mathbf{p}$, $\mathbf{q}$, $\mathbf{k}$, $\mathbf{r}$ are in the same plane. Therefore, the problem becomes two-dimensional. Using the angles α, β, κ defined in Fig. 1, we can represent these vectors in Cartesian coordinates:

$$\mathbf{p} = \{p \cos(\alpha), p \sin(\alpha)\},$$

$$\mathbf{q} = \{q \cos(\beta), q \sin(\beta)\},$$

$$\mathbf{k} = \{k \cos(\kappa), k \sin(\kappa)\}, \tag{2}$$

$$\mathbf{r} = \{-r \cos(\kappa), -r \sin(\kappa)\}.$$

(The last equality implies that $\mathbf{k}$ and $\mathbf{r}$ are anti-collinear.) We assume that the wave number of the probe beam, k, and the angles α, β, κ are given. These angles are defined by the location of the sources of sound and the region from which we want to get the backscattered signal.

The question is: for given α, β, κ and k, what frequencies should sources 1 and 2 emit so that the resonant scattered wave goes back to source 3?

Since the velocity of sound is constant, we have $r = p - q + k$. Substituting Eqs. (2) into the first of Eqs. (1), we get

$$p \cos(\alpha) - q \cos(\beta) + k \cos(\kappa) = -(p - q + k) \cos(\kappa), \tag{3}$$

$$p \sin(\alpha) - q \sin(\beta) + k \sin(\kappa) = -(p - q + k) \sin(\kappa). \tag{4}$$

From this system, we may readily express p and q in terms of the wave number k and the angles α, β, κ:

$$p = \frac{2k \sin(\beta - \kappa)}{\sin(\alpha - \beta) + \sin(\alpha - \kappa) - \sin(\beta - \kappa)}, \tag{5}$$
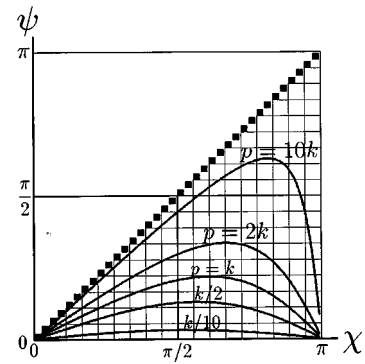
FIG. 2. Wave number p of one of two phase-matched waves which provide the effective backscattering of the wave with given wave number k as a function of angles χ and ψ between $\mathbf{k}$, $\mathbf{p}$ and between $\mathbf{k}$, $\mathbf{q}$, respectively [formula (7)].

$$q = \frac{2k \sin(\alpha - \kappa)}{\sin(\alpha - \beta) + \sin(\alpha - \kappa) - \sin(\beta - \kappa)}. \tag{6}$$

Note the rotational invariance: the frequencies $\omega_1 = v_s p$ and $\omega_2 = v_s q$ which give rise to the effective backscattering depend on the differences between the angles only. So, to represent wave numbers p, q graphically, we define $\chi = \alpha - \kappa$, $\psi = \beta - \kappa$ (see Fig. 1) and plot

$$p = p(\chi, \psi) = \frac{2k \sin(\psi)}{\sin(\chi - \psi) + \sin(\chi) - \sin(\psi)}$$

$$= \frac{k \sin(\psi/2)}{\sin(\chi/2 - \psi/2) \cos(\chi/2)}, \tag{7}$$

$$q = q(\chi, \psi) = \frac{2k \sin(\chi)}{\sin(\chi - \psi) + \sin(\chi) - \sin(\psi)}$$

$$= \frac{k \sin(\chi/2)}{\sin(\chi/2 - \psi/2) \cos(\psi/2)}. \tag{8}$$

Equilines of $p(\chi, \psi)$, $q(\chi, \psi)$, and $r(\chi, \psi) = p(\chi, \psi) - q(\chi, \psi) + k$ are plotted in Figs. 2, 3, and 4 respectively. The line of small black squares represents infinite values at $\chi = \psi$. Thus, sources 1 and 2 cannot have the same location. Note the symmetry: $r(\pi - \psi, \pi - \chi) = k^2 / r(\chi, \psi)$.

Equations (7) and (8) tell us the frequencies that sources 1 and 2 should emit in order to have synchronism and produce effective backscattering. Function $r(\chi, \psi)$ expresses the
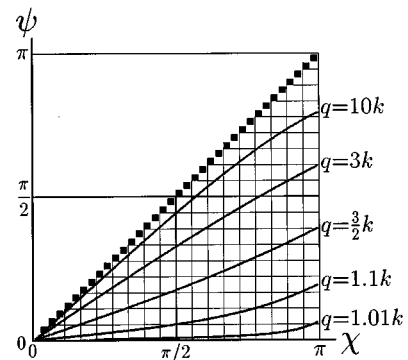
FIG. 3. Wave number q of the second phase-matched wave as a function of the angles χ and ψ [formula (8)].
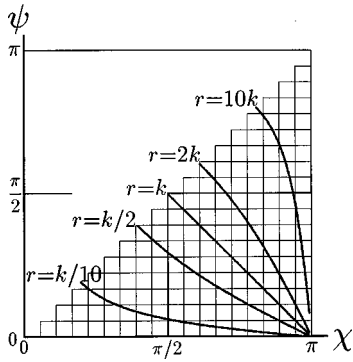
FIG. 4. Wave number $r = p - q + k$ of the reflected wave [formulas (7) and (8)].

wave number of the backscattered wave. To estimate its amplitude, we need first to calculate the efficiency of such backscattering. This is the subject of the following section.

II. SOUND EQUATIONS

Now we should calculate the efficiency of the resonant four-wave interaction of acoustical waves starting from the fundamental equations of sound propagation. In the numbered equations of this section, we use neither the assumption of backscattering ($\mathbf{k}\downarrow\uparrow\mathbf{r}$), nor that vectors $\mathbf{p}$, $\mathbf{q}$, $\mathbf{r}$ are coplanar, but we will return to these assumptions to plot figures.

Sound propagation in a fluid such as the atmosphere is described by Euler's equation and the continuity equation.[10,11]

$$\rho \frac{\partial \mathbf{v}}{\partial t} + \rho(\mathbf{v}\cdot\boldsymbol{\nabla})\mathbf{v} + \boldsymbol{\nabla}P = 0, \quad \frac{\partial \rho}{\partial t} + \mathbf{v}\cdot\boldsymbol{\nabla}\rho + \rho\boldsymbol{\nabla}\cdot\mathbf{v} = 0. \quad (9)$$

Here ρ is the density of the fluid, $\mathbf{v}$ is the wave velocity, P is the pressure, and t is time. Operator $\boldsymbol{\nabla}$ differentiates with respect to the vector $\mathbf{x}$ of spatial coordinates. We assume that the process is adiabatic, and

$$P = P_0\left(\frac{\rho}{\rho_0}\right)^\gamma, \quad (10)$$

where P_0 and ρ_0 are the pressure and density in the absence of waves. To be more concrete, we assume that $\gamma = \text{const.}$[12] For a monoatomic gas, $\gamma = 5/3$; for a diatomic gas with a rigid molecule (the case of the atmosphere), $\gamma = 7/5$. We assume that the vibrational degrees of freedom are not excited for air at room temperature. For the limit of multiatomic gas with soft molecules, $\gamma \approx 1$. Note that the generalization to the case of any smooth function $P(\rho)$ is straightforward.

It is convenient to define the normalized variables $\tau = t/v_s$, $\mathbf{u} = \mathbf{v}/v_s$, where

$$v_s = \sqrt{\gamma \frac{P_0}{\rho_0}} \quad (11)$$

is the velocity of sound. Let $\rho = \rho_0(1 + \eta)$, where η is treated as a new variable. We assume that $|\eta| \ll 1$. Then

$$\frac{1}{1 + \eta} = 1 - \eta + \eta^2 + \cdots, \quad (12)$$

$$\boldsymbol{\nabla}(1 + \eta)^\gamma = \gamma\boldsymbol{\nabla}\eta + \gamma(\gamma - 1)\eta\boldsymbol{\nabla}\eta + \tfrac{1}{2}\gamma(\gamma - 1)$$
$$\times (\gamma - 2)\eta^2\boldsymbol{\nabla}\eta + \cdots. \quad (13)$$

Now we can rewrite (9) in the new variables:

$$\frac{\partial \eta}{\partial \tau} + \boldsymbol{\nabla}\cdot\mathbf{u} = -\eta\boldsymbol{\nabla}\cdot\mathbf{u} - \mathbf{u}\cdot\boldsymbol{\nabla}\eta, \quad (14)$$

$$\frac{\partial \mathbf{u}}{\partial \tau} + \boldsymbol{\nabla}\eta = -(\mathbf{u}\cdot\boldsymbol{\nabla})\mathbf{u} - (\gamma - 2)\eta\boldsymbol{\nabla}\eta$$
$$- \frac{(\gamma - 2)(\gamma - 3)}{2}\eta^2\boldsymbol{\nabla}\eta - \cdots. \quad (15)$$

Searching for an approximate solution to the above equations we use the perturbation series:

$$\eta = \eta^{(1)} + \eta^{(2)} + \eta^{(3)} + \cdots,$$
$$\mathbf{u} = \mathbf{u}^{(1)} + \mathbf{u}^{(2)} + \mathbf{u}^{(3)} + \cdots. \quad (16)$$

Let the first-order approximation be the superposition of the three plane waves emitted by the three sources:

$$\eta^{(1)} = A + B + C + A^* + B^* + C^*,$$
$$\mathbf{u}^{(1)} = \hat{p}A + \hat{q}B + \hat{k}C + \hat{p}A^* + \hat{q}B^* + \hat{k}C^*, \quad (17)$$

where

$$A = a\exp(i\mathbf{p}\cdot\mathbf{x} - ip\tau), \quad B = b\exp(i\mathbf{q}\cdot\mathbf{x} - iq\tau),$$
$$C = c\exp(i\mathbf{k}\cdot\mathbf{x} - ik\tau), \quad (18)$$

and $\hat{p} = \mathbf{p}/p$, $\hat{q} = \mathbf{q}/q$, $\hat{k} = \mathbf{k}/k$. In what follows, we also use $\hat{r} = \mathbf{r}/r$ and treat a, b, c as constants. It is easy to see that $\eta^{(1)}$ and $\mathbf{u}^{(1)}$ satisfy the linearized equations

$$\frac{\partial \eta^{(1)}}{\partial \tau} + \boldsymbol{\nabla}\cdot\mathbf{u}^{(1)} = 0, \quad \frac{\partial \mathbf{u}^{(1)}}{\partial \tau} + \boldsymbol{\nabla}\eta^{(1)} = 0. \quad (19)$$

Four-wave mixing is due to the third-order terms, but first we need to construct the second-order approximation. To get the equations for $\eta^{(2)}$ and $\mathbf{u}^{(2)}$, we substitute the first-order approximations in the right-hand part of Eqs. (14) and (15), and keep only quadratic terms:

$$\frac{\partial \eta^{(2)}}{\partial \tau} + \boldsymbol{\nabla}\cdot\mathbf{u}^{(2)} = -\boldsymbol{\nabla}\cdot(\mathbf{u}^{(1)}\eta^{(1)}), \quad (20)$$

$$\frac{\partial \mathbf{u}^{(2)}}{\partial \tau} + \boldsymbol{\nabla}\eta^{(2)} = -(\mathbf{u}^{(1)}\cdot\boldsymbol{\nabla})\mathbf{u}^{(1)} - (\gamma - 2)\eta^{(1)}\boldsymbol{\nabla}\eta^{(1)}. \quad (21)$$

We take the divergence of (21) and subtract (20) differentiated with respect to τ. It gives

$$\nabla^2\eta^{(2)} - \frac{\partial^2\eta^{(2)}}{\partial\tau^2} = -\boldsymbol{\nabla}\cdot((\mathbf{u}^{(1)}\cdot\boldsymbol{\nabla})\mathbf{u}^{(1)}$$
$$+ (\gamma - 2)\eta^{(1)}\boldsymbol{\nabla}\eta^{(1)})$$
$$+ \frac{\partial}{\partial\tau}\boldsymbol{\nabla}\cdot(\eta^{(1)}\mathbf{u}^{(1)}). \quad (22)$$

After solving this equation, we can get $\mathbf{u}^{(2)}$, upon integrating (21) with respect to τ. Similarly we find the equation to third order:

$$\nabla^2 \eta^{(3)} - \frac{\partial^2 \eta^{(3)}}{\partial \tau^2} = -\boldsymbol{\nabla} \cdot ((\mathbf{u}^{(2)} \cdot \boldsymbol{\nabla}) \mathbf{u}^{(1)} + (\mathbf{u}^{(1)} \cdot \boldsymbol{\nabla}) \mathbf{u}^{(2)})$$

$$+ (\gamma - 2) \nabla^2 \left(\eta^{(2)} \eta^{(1)} + \frac{\gamma - 3}{6} \eta^{(1)3} \right)$$

$$+ \boldsymbol{\nabla} \cdot \left(\frac{\partial}{\partial \tau} (\eta^{(2)} \mathbf{u}^{(1)} + \eta^{(1)} \mathbf{u}^{(2)}) \right). \quad (23)$$

Equations (22) and (23) are inhomogeneous Helmholtz equations where the right-hand side represent sources. Direct substitution of (17) in (22) results in many terms. Fortunately, we have no need to consider all these terms, but only those that yield resonating contributions to the third-order approximation.

As we shall see, the amplitude of the acoustical waves should be much less than the atmospheric pressure. The nonlinear income per wavelength is small; so, only the resonant terms are important.

The resonant terms arise from the product AB^*C, proportional to $\exp(i r \mathbf{x} - i r \tau)$, and from its complex conjugate. Thus, on the right-hand side of (22) we may keep only terms containing the products AB^*, AC, B^*C and their complex conjugate. Such resonant approximation is used commonly in optics to calculate the efficiency of harmonics generation.[6,7]

In this resonant approximation we get from (22)

$$\nabla^2 \eta^{(2)} - \frac{\partial^2 \eta^{(2)}}{\partial \tau^2}$$

$$= ((\hat{k} \cdot \hat{p} + \gamma - 2)|\mathbf{k} + \mathbf{p}|^2 + (1 + \hat{p} \cdot \hat{k})(p+k)^2) AC$$

$$+ ((\hat{p} \cdot \hat{q} + \gamma - 2)|\mathbf{p} - \mathbf{q}|^2 + (1 + \hat{p} \cdot \hat{q})(p-q)^2) AB^*$$

$$+ ((\hat{k} \cdot \hat{q} + \gamma - 2)|\mathbf{k} - \mathbf{p}|^2 + (1 + \hat{k} \cdot \hat{q})(k-q)^2) B^*C$$

$$+ \text{c.c.}, \quad (24)$$

where ''c.c.'' denotes the complex conjugate terms.

To calculate the contribution from each source term in (24) to $\eta^{(2)}$, consider equation

$$\nabla^2 \eta^{(2)} - \frac{\partial^2 \eta^{(2)}}{\partial \tau^2} = Q \exp(i \mathbf{s} \cdot \mathbf{x} - i \Omega \tau), \quad (25)$$

where $Q = \text{const}$. One can readily check that

$$\eta^{(2)} = \frac{Q}{\Omega^2 - |\mathbf{s}|^2} \exp(i \mathbf{s} \mathbf{x} - i \Omega \tau) \quad (26)$$

is a solution of (25). To solve (24), we apply (26) as solution of (25) with $\mathbf{s} = \mathbf{k} + \mathbf{p}$, $\Omega = k + p$; $\mathbf{s} = \mathbf{p} - \mathbf{q}$, $\Omega = p - q$; $\mathbf{s} = \mathbf{k} - \mathbf{p}$, $\Omega = k - p$; and their complex congutations. We write no additional solution of the homogeneous equation, since it would not contribute to the resonant third-order terms.

Calculating the corresponding contributions to $\eta^{(2)}$ as indicated above, we get

$$\eta^{(2)} = \xi_b AC + \xi_c AB^* + \xi_a B^*C + \text{c.c.}, \quad (27)$$

where

$$\xi_b = \frac{|\mathbf{k} + \mathbf{p}|^2 (\hat{p} \cdot \hat{k} + \gamma - 2) + (\hat{p} \cdot \hat{k} + 1)(p+k)^2}{(p-k)^2 - |\mathbf{p} - \mathbf{k}|^2}$$

$$= \frac{(k+p)^2 (2\hat{p} \cdot \hat{k} + \gamma - 2)}{2(pk - \mathbf{p} \cdot \mathbf{k})} - \hat{p} \cdot \hat{k} - \gamma + 2, \quad (28)$$

$$\xi_c = \frac{|\mathbf{p} - \mathbf{q}|^2 (\hat{p} \cdot \hat{q} + \gamma - 2) + (\hat{p} \cdot \hat{q} + 1)(p-q)^2}{-(q-p)^2 + |\mathbf{q} - \mathbf{p}|^2}$$

$$= \frac{(p+q)^2 (2\hat{p} \cdot \hat{q} + \gamma - 2)}{-2(pq - \mathbf{p} \cdot \mathbf{q})} - \hat{p} \cdot \hat{q} - \gamma + 2, \quad (29)$$

$$\xi_a = \frac{|\mathbf{k} - \mathbf{q}|^2 (\hat{k} \cdot \hat{q} + \gamma - 2) + (\hat{k} \cdot \hat{q} + 1)(k-q)^2}{-(q-k)^2 + |\mathbf{q} - \mathbf{k}|^2}$$

$$= \frac{(k-q)^2 (2\hat{q} \cdot \hat{k} + \gamma - 2)}{-2(qk - \mathbf{q} \cdot \mathbf{k})} - \hat{q} \cdot \hat{k} - \gamma + 2, \quad (30)$$

where we used $(p+k)^2 - |\mathbf{p} + \mathbf{k}|^2 = 2(pk - \mathbf{p} \cdot \mathbf{k})$ in Eq. (28), and similar expressions in Eqs. (29) and (30). Substituting $\eta^{(2)}$ and $\eta^{(1)}$ into (21) yields

$$\frac{\partial \mathbf{u}^{(2)}}{\partial \tau} = -i(\xi_c + \gamma - 2 + \hat{p} \cdot \hat{k})(\mathbf{p} + \mathbf{k}) AC$$

$$- i(\xi_b + \gamma - 2 + \hat{p} \cdot \hat{q})(\mathbf{p} - \mathbf{q}) AB^*$$

$$- i(\xi_a + \gamma - 2 + \hat{k} \cdot \hat{q})(\mathbf{k} - \mathbf{q}) CB^* + \text{c.c.} \quad (31)$$

The integration with respect to τ adds the factors $i/(k+p)$, $i/(p-q)$, and $i/(k-q)$ to the terms with AC, AB^*, and CB^*, respectively. Using Eqs. (28)–(30), we get

$$\mathbf{u}^{(2)} = \boldsymbol{\mu}_b AC + \boldsymbol{\mu}_c AB^* + \boldsymbol{\mu}_a B^*C + \text{c.c.}, \quad (32)$$

where

$$\boldsymbol{\mu}_b = \frac{(2\hat{p} \cdot \hat{k} + \gamma - 1)(k+p)(\mathbf{p} + \mathbf{k})}{2(kp - \mathbf{p} \cdot \mathbf{k})}, \quad (33)$$

$$\boldsymbol{\mu}_c = \frac{(2\hat{p} \cdot \hat{q} + \gamma - 1)(p-q)(\mathbf{p} - \mathbf{q})}{-2(pq - \mathbf{p} \cdot \mathbf{q})}, \quad (34)$$

$$\boldsymbol{\mu}_a = \frac{(2\hat{k} \cdot \hat{q} + \gamma - 1)(k-q)(\mathbf{k} - \mathbf{q})}{-2(kq - \mathbf{k} \cdot \mathbf{q})}. \quad (35)$$

Using the above results we may calculate the resonant contribution to $\eta^{(3)}$ from (23). Direct substitution of $\eta^{(2)}$ and $\mathbf{u}^{(2)}$ on the right-hand side of (23) also results in many terms. We keep only those with AB^*C, and rewrite (23) in the following form:

$$\nabla^2 \eta^{(3)} - \frac{\partial^2 \eta^{(3)}}{\partial \tau^2} = F r^2 AB^*C + \text{c.c.}$$

$$= Fab^*c r^2 \exp(i r \mathbf{x} - i r \tau) + \text{c.c.}, \quad (36)$$

where

$$F = \xi_b (\hat{q} \cdot \hat{r} + \gamma - 2) + \xi_c (\hat{k} \cdot \hat{r} + \gamma - 2) + \xi_a (\hat{p} \cdot \hat{r} + \gamma - 2)$$

$$+ \boldsymbol{\mu}_b \cdot (\hat{q} + \hat{r}) + \boldsymbol{\mu}_c \cdot (\hat{k} + \hat{r}) + \boldsymbol{\mu}_a \cdot (\hat{p} + \hat{r})$$

$$+ (\gamma - 2)(\gamma - 3). \quad (37)$$

While we treat *a*, *b*, and *c* as constants, the product Fab^*cr^2 does not depend on coordinates, so, (37) has the solution

$$\eta^{(3)} = (\mathbf{r} \cdot \mathbf{x}) F \frac{ab^*c}{2i} \exp(i\mathbf{r}\mathbf{x} - ir\tau) + \text{c.c.} \quad (38)$$

This solution corresponds to the case in which the nonlinear interaction generates the wave with wave vector **r**, and its amplitude is proportional to the length of interaction. We assume that this third wave is absent at the origin of coordinates. The origin of coordinates corresponds to the beginning of the region of interaction, if we approximate it with an abrupt function. For more accurate calculus, one should define the smooth spatial structure of *a*, *b*, and *c* and construct the paraxial approximation of Eq. (36) with given *F* = const. We write a closed expression for this *F* below.

The phase-matching conditions enable us to simplify the scalar products with the $\boldsymbol{\mu}$'s that appear upon substitution of Eqs. (33)–(35) into Eq. (37). Since $\mathbf{p} + \mathbf{k} = \mathbf{q} + \mathbf{r}$ and $p + k = q + r$, we have for $\boldsymbol{\mu}_b \cdot (\mathbf{q} + \mathbf{r})$ that $(\mathbf{p} + \mathbf{k}) \cdot (\hat{q} + \hat{r}) = (\mathbf{q} + \mathbf{r}) \cdot (\hat{q} + \hat{r}) = q + r + q\hat{q} \cdot \hat{r} + r\hat{p} \cdot \hat{r} = (q + r)(1 + \hat{p} \cdot r)$, with similar expressions for $\boldsymbol{\mu}_c \cdot (\mathbf{k} + \mathbf{r})$ and $\boldsymbol{\mu}_a \cdot (\mathbf{p} + \mathbf{r})$. Substituting the ξ's from (28)–(30) and some algebra, we get

$$
\begin{aligned}
F = & \frac{(p+k)^2 (2\hat{p} \cdot \hat{k} + \gamma - 1)(2\hat{q} \cdot \hat{r} + \gamma - 1)}{2(pk - \mathbf{p} \cdot \mathbf{k})} \\
& - \frac{(p-q)^2 (2\hat{p} \cdot \hat{q} + \gamma - 1)(2\hat{k} \cdot \hat{r} + \gamma - 1)}{2(pq - \mathbf{p} \cdot \mathbf{q})} \\
& - \frac{(k-q)^2 (2\hat{k} \cdot \hat{q} + \gamma - 1)(2\hat{p} \cdot \hat{r} + \gamma - 1)}{2(kq - \mathbf{k} \cdot \mathbf{q})} \\
& - (\hat{p} \cdot \hat{k})(\hat{q} \cdot \hat{r}) - (\hat{k} \cdot \hat{q})(\hat{k} \cdot \hat{r}) - (\hat{q} \cdot \hat{p})(\hat{p} \cdot \hat{r}) \\
& - (\hat{p} \cdot \hat{k} + \hat{q} \cdot \hat{r} + \hat{k} \cdot \hat{q} + \hat{k} \cdot \hat{r} + \hat{q} \cdot \hat{p} + \hat{p} \cdot \hat{r})(\gamma - 2) \\
& + (\gamma - 2)(3 - 2\gamma). \quad (39)
\end{aligned}
$$

This is our main result: The efficiency of the phase-matched four-wave interaction is expressed in terms of the wave vectors and the adiabatic constant γ.

Note the symmetry of (39). Under the phase-matching conditions, *F* is invariant with respect to each of following transformations:

(A) $\hat{p} \leftrightarrows \hat{k}$, $p \leftrightarrows k$,

(B) $\hat{p} \leftrightarrows \hat{q}$, $p \leftrightarrows -q$,

(C) $\hat{p} \leftrightarrows \hat{r}$, $p \leftrightarrows -r$,

(D) $\hat{q} \leftrightarrows \hat{k}$, $q \leftrightarrows -k$,   (40)

(E) $\hat{q} \leftrightarrows \hat{r}$, $q \leftrightarrows r$,

(F) $\hat{k} \leftrightarrows \hat{r}$, $k \leftrightarrows -r$.

To see the invariance of *F* with respect to (C), (E), and (F), note that the phase-matching condition leads to $pk - \mathbf{p} \cdot \mathbf{k} = qr - \mathbf{q} \cdot \mathbf{r}$, and similar expressions for the other denominators in (39).
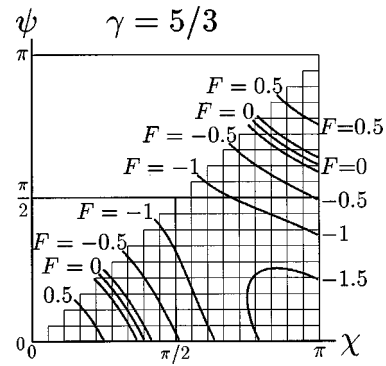
FIG. 5. Efficiency *F* of backscattering as function of the angles χ and ψ [formula (39)] for a monoatomic gas, $\gamma = 5/3$.

Now let us return to our original problem on the backscattering of the wave *C*: Let **k** and **r** be anticollinear. Then the efficiency *F* depends only on the angles χ and ψ, defined in Sec. I. So, we treat it as $F = F(\chi, \psi)$. This function is represented in Fig. 5 for a monoatomic gas, in Fig. 6 for diatomic gas (case of the atmosphere), and in Fig. 7 for a multiatomic gas.

Note the symmetry: $F(\chi, \psi) = F(\pi - \psi, \pi - \psi)$. It follows from the symmetries (40) and the symmetry of the wave numbers as functions of χ, ψ, discussed in Sec. I.

The level $F = 0$ corresponds to the absence of backscattering. To make it noticeable we plot also levels $F = \pm 0.1$; so, in Figs. 5 and 6 the level $F = 0$ appears as a triple line. The disappearance of backscattered waves at some values of angles χ, ψ can be interpreted as the destructive interference of waves reflected by the lattices produced by each pair of incident waves.

The efficiency of the backscattering depends on the constant γ. Thus, the four-wave mixing gives also an extravagant acoustical method to measure the mean number of atoms in the molecules of the gas: location of the $F = 0$ line is very different in Figs. 5–7.

III. NUMERICAL ESTIMATIONS

The fundamental result of the previous section expresses the amplitude of the phase-matched reflected wave in terms of the wave numbers of the incident waves and the angles between their wave vectors; it increases with the wave number. So, the efficiency of this effect is limited by the maximal

FIG. 6. Efficiency *F* of backscattering as function of the angles χ and ψ [formula (39)] for diatomic gas, $\gamma = 7/5$.

FIG. 7. Efficiency F of backscattering as function of the angles χ and ψ [formula (39)] for extremally multiatomic gas, $\gamma = 1$.

FIG. 8. Deformation of the initial waveform of the monochromatic acoustical wave due to higher-harmonics generation: initial waveform $H(x,0) = H_0 \cos(kx)$ (thin line) and deformed waveform $H(x,\tau)$ at $\tau = 0.95\tau_{\rm dis}$ [thick line, formula (48)].

$$H\left(x + \frac{\gamma+1}{2}H(x,0)\tau, \tau\right) = H(x,0). \tag{48}$$

Note that here x has the sense of the local space coordinate of the wave as it is moving. This solution (and the initial equations) become invalid if H' becomes infinite. The distance traveled as this takes place is defined in nonlinear acoustics as the discontinuity distance. We denote it $\tau_{\rm dis}$. Note that we may interpret τ as the distance of propagation.

To estimate value of $\tau_{\rm dis}$, we take the derivative of (48) with respect to x:

$$H'\left(x + \frac{\gamma+1}{2}H(x,0)\tau, \tau\right)\left(1 + \frac{\gamma+1}{2}H'(x,0)\tau\right) = H'(x,0). \tag{49}$$

Hence,

$$H'\left(x + \frac{\gamma+1}{2}H(x,0)\tau, \tau\right) = \frac{H'(x,0)}{1 + [(\gamma+1)/2]H'(x,0)\tau}. \tag{50}$$

The denominator becomes zero at $[(\gamma+1)/2]H'(x,0)\tau = -1$. If the initial wave is monochromatic, $H(x,0) = H_0 \cos(kx)$, then the shock waves appear at $\tau = \tau_{\rm dis} = 2/[(\gamma+1)kH_0]$. The solution (48) is plotted in Fig. 8 by the thick line at $\tau = 0.95\tau_{\rm dis}$. To compare, we plot in the same graph the initial wave $H(x,0) = H_0 \cos(kx)$ with a thin line.

At values of τ larger than $\tau_{\rm dis}$ the solution becomes invalid. This gives the natural limit to the amplitude. For example, if the distance of propagation $L \approx 100$ m, and the wave number $k \approx 10\,\mathrm{m}^{-1}$, then the amplitude of waves cannot be greater than $H_{\max} = 2/[(\gamma+1)kL] \approx 10^{-3}$.

If we make the initial amplitude greater than $H_{\max}$, shock waves appear at the distance $\tau_{\rm dis}$. They consume the energy of the wave before it reaches the region of interaction (Fig. 1). At the given initial amplitude, the length of adiabatic propagation can be doubled, if we take $H(-x, \tau_{\rm dis})$ as the initial condition.

In what follows we collect the results of previous sections to estimate the amplitude of the signal reflected by the four-wave interaction in the atmosphere for the case of Fig. 1. From here on we retain the orders of magnitude only.

Suppose that all wave numbers p, q, k, and r are of the same order of magnitude. So, we may write k instead of p, q, r. Suppose that all distances of propagation are of the same order of magnitude, L. Then, since $2/(\gamma+1) \approx 1$, the initial amplitudes should be about

wave number that can propagate without significant absorption. For air at 20 °C and a water fraction of 5×10^{-3}, the absorption coefficient reaches $3 \times 10^{-4}\,\mathrm{m}^{-1}$ at $k = 10\,\mathrm{m}^{-1}$ (see, for example, Ref. 12); so, the natural limit for the wave numbers where we still can neglect absorption at a few hundred meters is $k \approx 10\,\mathrm{m}^{-1}$.

Another important concern is regarding the nonlinear degradation of plane waves as they travel to the region of interaction. This process begins with the phase-matched second-harmonic generation, discussed in Sec. I. To estimate this effect, consider the case of one-dimensional propagation.

In analogy with Ref. 10, we rewrite Eqs. (14) and (15) as

$$\dot{\eta} + u' + (\eta u)' = 0, \tag{41}$$

$$\dot{u} + \eta' + uu' + (\gamma-2)\eta\eta' = 0, \tag{42}$$

where $\eta = \eta(x,\tau)$ and $u = u(x,\tau)$; the prime indicates the derivative with respect to the first argument, and the dot denotes the derivative with respect to the last one. Note that we define neither prime as the derivative with respect to x, nor the dot as the derivative with respect to τ, because below, we use this notation also for the case when the first argument is not simply x.

Here we keep only the quadratic terms with respect to the amplitude of the wave: the second-order contribution is largest. We search the solution of Eqs. (41) and (42) as the sum of counter-propagating waves H and J:

$$\eta = H(x-\tau, \tau) + J(x+\tau, \tau), \tag{43}$$

$$u = H(x-\tau, \tau) - J(x+\tau, \tau). \tag{44}$$

Substituting Eqs. (43) and (44) into (41) and (42), we get

$$\dot{H} + \dot{J} + 2HH' + 2JJ' = 0, \tag{45}$$

$$\dot{H} - \dot{J} + HH' + JJ' - H'J - HJ'$$
$$+ (\gamma-2)(HH' + JJ' + H'J + HJ') = 0. \tag{46}$$

Adding these two equations and neglecting the nonlinear interaction with the counter-propagating wave J, we get

$$2\dot{H} + (\gamma+1)HH' = 0. \tag{47}$$

The solution of this equation can be written as[13]

$$H_i \approx \frac{1}{kL}. \tag{51}$$

At larger amplitudes, shock waves appear: The tangent of the front of acoustical waves becomes infinite; definitely, we are out of our approximation. Of course, physically, the gradient of density remains finite, but so high that the diffusion of molecules of the gas causes strong dissipation, and waves lose their power before they reach the region of interaction.

Suppose that the transversal size of all sources is D. During propagation, each beam becomes larger due to diffraction. At distance L, its size becomes

$$l \approx \frac{L}{kD}, \tag{52}$$

where we assume that $l \ll L$.

Due to the expansion of each beam, the amplitude of each wave becomes D/l times less, and the amplitude of the interacting waves is about

$$H \approx \frac{D}{l} H_i \approx \frac{D^2}{L^2}. \tag{53}$$

The amplitude of the backscattered sound is about

$$H_r \approx F k l H^3 \approx F \frac{D^5}{L^5}, \tag{54}$$

where F is the angular factor calculated in Sec. II.

If the reflected signal is detected with an antenna of the same size D, an additional factor kD should be used to calculate the amplitude in the focus; so, the amplitude at the receiver should be about

$$H_D \approx F \frac{kD^6}{L^5}. \tag{55}$$

For example, if $F \approx 1$, $k \approx 10\,\text{m}^{-1}$, $D \approx 1$ m, and $L \approx 100$ m, we have that the amplitude of the signal at the detector should be about 10^{-9}. This means that the receiver should be able to detect sound of pressures about $10^{-9} P_0 \approx 10^{-4}\,\text{N/m}^2 \approx 10^{-3}\,\mu\text{m Hg}$. The resolution of detectors is limited by thermal noise pressure. Pressure resolutions of $10^{-3}\,\mu\text{mHg}$ have been reported,[14] and it is still far from the theoretical limit.[15]

From Sec. I we know the frequency of the backscattered signal. Thus, a narrow spectral filter can be used to improve the signal to noise ratio. This makes it possible to extend the distance to the region of interaction for a few hundreds meters more for the same size of sources.

In Ref. 5 we presented some additional speculations about the nonplanar geometry of waves, which causes the partial focusing of the backscattered wave and increases the amplitude of registered signal for an order of magnitude.

Finally, let us estimate the sensitivity of such a probe to the wind velocity. The angular deviation ϕ of an acoustical beam by a wind of velocity v follows from the analysis in Chap. 8 of Ref. 11. Roughly, $\phi \approx v/v_s$. At the region of interaction, of size l, such angular deviation causes a drastic dephasement of the interacting waves when $kl\phi \approx \pi$. Taking l from Eq. (52), we find the wind velocity that causes such dephasement, $v \approx \pi v_s/(kl) \approx \pi v_s D/L$. The limit δv of resolution will be better by the signal-to-noise ratio factor ν:

$$\delta v \approx \pi \frac{v_s}{\nu} \frac{D}{L}. \tag{56}$$

For example, for $D \approx 1$ m and $L \approx 10$ m as in the previous example, and taking $v_s \approx 340$ m/s, and $\nu \approx 10$, we have $\delta v \approx 1$ m/s.

Note that wind parallel to the plane of Fig. 1 causes bending of the reflected beam; however, in this case, the beam still lies within the same plane. Such bending can be corrected (and, therefore, measured) by the adjustment of wave numbers p and q. As for the bending caused by the orthogonal component of wind, it cannot be compensated in such a manner, and the detector should be displaced from the location of source 3, giving us the measure of the component of the wind orthogonal to the plane Fig. 1.

IV. CONCLUSIONS

The resonant nonlinear interaction of acoustic waves is analyzed. Wave numbers of two waves which result in the efficient backscattering of the third wave (Fig. 1) are calculated (Figs. 2 and 3) as functions of angles between the wave vectors. The efficiency of this process is calculated and presented graphically for various values of the adiabatic constant γ (Figs. 5–7).

The possible application of the phase-matched four-wave interaction as a remote acoustic probe is suggested. The nonlinear degradation of acoustical waves limits the values of the wave number, initial amplitude and the distance of propagation in such probe. For wave numbers of about 10 m^{-1}, with sources of size of about 1 m and a distance to the intersection of 100 m, the relative pressure (relative to the atmospheric pressure) in the backscattered wave can be about 10^{-10}. The frequency of the backscattered signal is calculated (Fig. 4), so angular and spectral filters can be used.

The qualitative calculation of the distribution of amplitude in the backscattered beam should imply the consideration of the transversal (and, maybe, longitudinal) structure of incident beams. Such calculations are a possible continuation of this work.

The resolution on the measurement of the velocity of wind is estimated to be in the order of 1 m/s. The complete analysis of an acoustical remote probe based on four-wave interaction in moving media can be made using the proper transformation of the wave vectors and also could become a subject for future investigations.

[1] L. G. McAllister, ''Acoustic sounding of the lower troposphere,'' J. Atmos. Terr. Phys. **30**, 1439–1440 (1968).

[2] D. Atlas, ''Indirect probing techniques,'' Bull. Am. Meteorol. Soc. **43**, 457–466 (1962).

[3] M. A. Kallistratova and A. Kon, *Radio-Acoustic Remote Probe of the Atmosphere* (MOCKBA, Hayka, 1985), pp. 4–195 (in Russian).

[4] G. T. Peters, H. Timmerman, and H. Hinzpeter, ''Temperature sounding in the planetary boundary layer by RASS-system: Analysis and results,'' Int. J. Remote Sens. **4**, 49–63 (1983).

[5] D. Kouznetsov and A. García-Valenzuela, ''Backscattering of sound by nonlinear interaction in gas media and its possible application to a remote sensing acoustical probe,'' Meteorologische Zeitschrift, N.F. **7**, 237–240 (1998).

[6] R. W. Boyd, *Nonlinear Optics* (Academic, New York, 1992).

[7] A. Newell and J. Moloney, *Nonlinear Optics* (Adison–Wesley, New York, 1961).

[8] T. I. Kuznetsova and D. Yu. Kuznetsov, ''Condition for the appearence of a negative image in an optical signal amplifier,'' Kvantovaya Electronica **11**, 2145–2384 (1984) [Sov. J. Quantum Electron. **14**, 1457–1460 (1984)].

[9] J. Berntsen, J. N. Tjøtta, and S. Tjøtta, ''Interaction of sound waves. Part IV: Scattering of sound by sound,'' J. Acoust. Soc. Am. **86**, 1968–1983 (1989).

[10] P. Morse and K. U. Ingard, *Theoretical Acoustics* (Princeton U.P., Princeton, NJ, 1986).

[11] L. A. Landau and E. M. Lifshitz, *Fluid Mechanics* (Academic, New York, 1986).

[12] A. D. Pierce, *Acoustics: An Introduction to its Physical Principles and Applications* (McGraw–Hill, New York, 1981), Chap. 10, pp. 508–565.

[13] D. G. Crighton, A. P. Dowling, J. E. F. Williams, M. Heckl, and F. G. Leppington, *Modern Methods in Analytical Acoustics* (Springer-Verlag, Berlin, 1992), Chap. 3, Sec. 4, p. 637.

[14] H. L. Chau and K. D. Wise, ''Scaling limits in batch-fabricated silicon pressure sensors,'' IEEE Trans. Electron Devices **ED-34**, 850–858 (1987).

[15] R. R. Spencer, B. M. Fleischer, P. W. Barth, and J. B. Angell, ''A theoretical study of transducer noise in piezoresistive and capacitive silicon pressure sensors,'' IEEE Trans. Electron Devices **ED-35**, 1289–1297 (1987).

Subarctic frontal effects on long-range acoustic propagation in the North Pacific Ocean

E. C. Shang and Y. Y. Wang

Cooperative Institute for Research in Environmental Sciences, University of Colorado/NOAA,
Environmental Technology Laboratory, Boulder, Colorado 80303-3328

Acoustic propagation along the Hawaiian–Aleutian path at low frequency (65 Hz) for the acoustic thermometry of ocean climate (ATOC) has been simulated using the implicit finite difference parabolic equation (IFD-PE). This simulation is based upon the Semtner–Chervin model with one-half-degree resolution. The adiabaticity has been assessed, and it was found that significant mode coupling takes place at the sub-arctic front area (44.8 ° N). Due to the range-dependent double channel, two characteristic ranges were identified in this area: (i) the modal degeneration range R_m^D and (ii) the modal scattering range R_m^S. At range R_m^D, mode m and mode n (usually, $n=m+1$) are degenerated, the modal wave numbers of mode m and mode n become equal, and mode n then takes the shape of mode m. Therefore, there is no *real repopulation* (modal scattering), but a modal name change takes place at this range. The modal name change can cause a miscalculation of the adiabatic travel time. At range R_m^S, however, real repopulation does take place. Numerical simulations illustrate that R_m^D and R_m^S are separated by about 10 km at lower modes ($m<5$) and are merged at higher modes.   © *1999 Acoustical Society of America.* [S0001-4966(99)06603-5]

PACS numbers: 43.30.Bp [SAC-B]

INTRODUCTION

Acoustic propagation along the Hawaiian–Aleutian path at 65 Hz for the acoustic thermometry of ocean climate (ATOC)[1] has been simulated using the implicit finite difference parabolic equation (IFD-PE) code[2] for propagation and the KRAKEN code[3] for local mode calculation. These simulations are based on the Semtner–Chervin model with a one-half-degree resolution for the February realization.[4]

The Hawaiian–Aleutian path crosses the sub-Arctic front near 44.8 °N. It is known that the ocean front usually
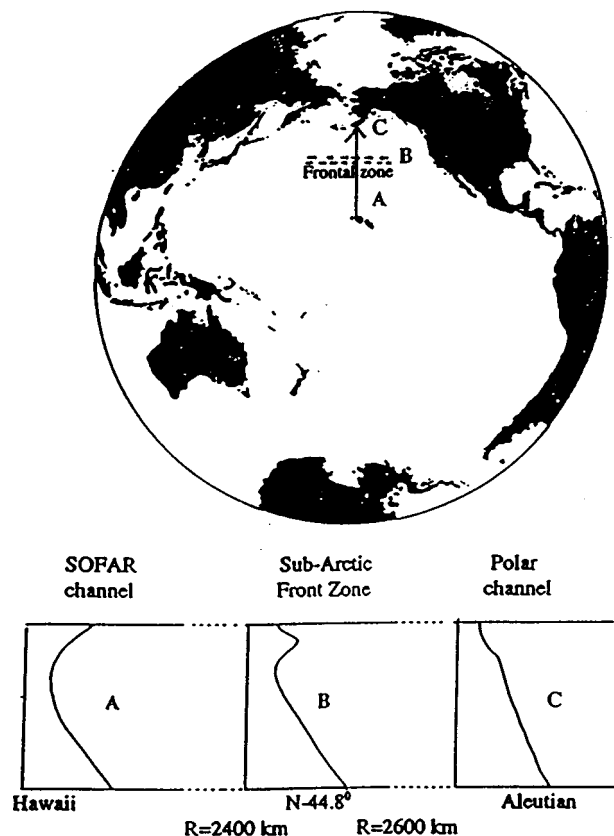
FIG. 1. The acoustic path from Hawaii northward is shown by the arrow (top panel), and the SSP types at three sections of the path (bottom panel).
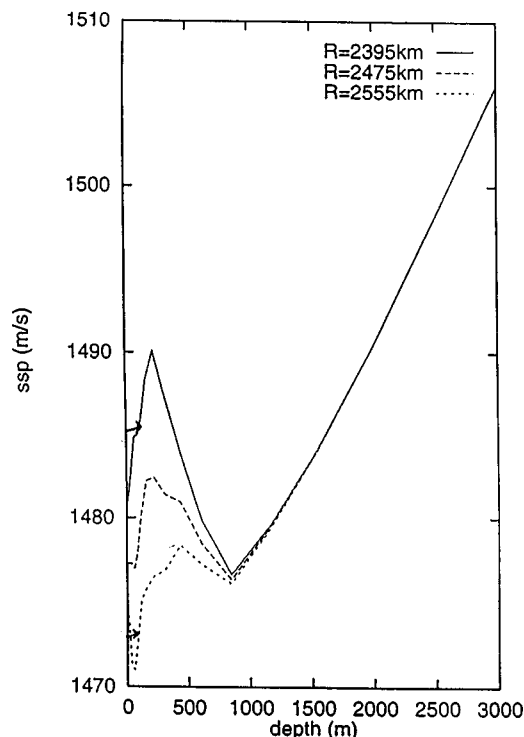
FIG. 2. The range-dependent double-channel SSPs from $R=2395$ to $R=2555$ km due to the sub-Arctic front.

(a) R = 2475 km

(d) R = 2520 km
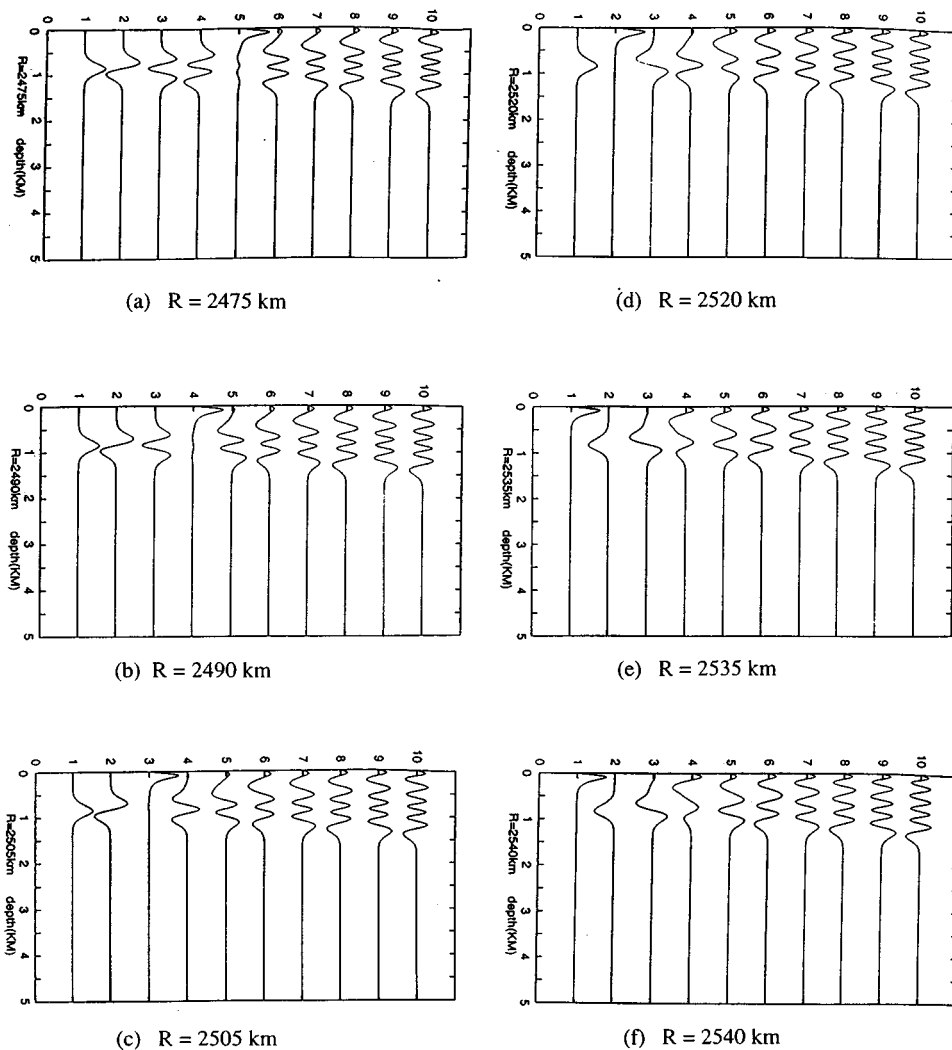
(b) R = 2490 km

(e) R = 2535 km

FIG. 3. The local modes ($m = 1-10$) at different ranges ($f = 65$ Hz), (a) $R = 2475$ km, (b) $R = 2490$ km, (c) $R = 2502$ km, (d) $R = 2520$ km, (e) $R = 2535$ km, (f) $R = 2540$ km.

(c) R = 2505 km

(f) R = 2540 km

has sharp spatial variety and can cause significant mode coupling.[5,6] However, for the Semtner–Chervin model, the influence of the front on acoustic propagation is not only mode coupling but also mode degeneration, due to the range-dependent double channel feature.

The entire path of the acoustic propagation can be divided into the following three sectors (see Fig. 1):

(i)   Sector A. *The SOFAR channel:* from Hawaii northward to range $R = 2400$ km,
(ii)   Sector B. *The range-dependent double channel:* a transition area from $R = 2400$ km to $R = 2600$ km, the sub-Arctic front zone,
(iii) Sector C. *The Polar channel:* after $R = 2600$ km, north to the Aleutian Islands.

Part of the range dependency of the double channel is shown in Fig. 2. In this letter, the following effects caused by this range-dependent double channel are discussed:

(i)   Modal degeneration and modal name change,
(ii)   Modal travel time miscalculation due to name change.

I. MODAL DEGENERATION AND NAME CHANGE

Suppose the acoustic source is near Hawaii. In this event, what happens is that when the acoustic wave propa-

gates from the SOFAR channel into the frontal zone, some modes will be trapped in the upper-surface duct. For our acoustic frequency $f = 65$ Hz, only one mode can be supported by the upper duct. The mode-trapping process begins at the higher mode and ends at mode 1 along this range-dependent double channel. Figure 3(a)–(f) illustrate the trapping process from mode 5 (at $R = 2475$ km) to mode 1 (at $R = 2540$ km).

Between the two ranges where the two adjacent modes
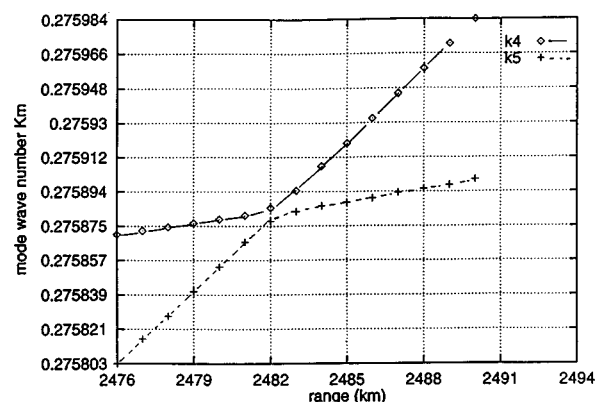
FIG. 4. Modal wave number k_4 and k_5 as a function of range. The modal degeneration range $R_{45}^D = 2482$ km.
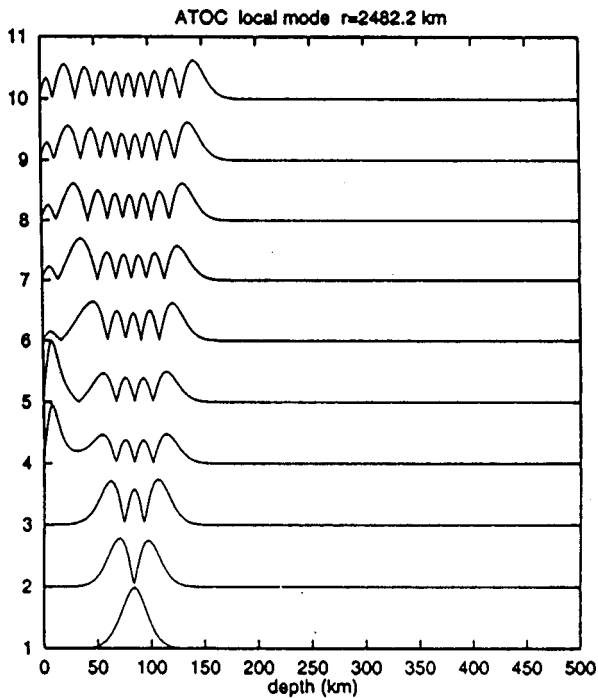
FIG. 5. At $R_{45}^D = 2482$ km, $|U_4(z)| = |U_5(z)|$.

FIG. 7. At $R_{12}^D = 2530$ km, $|U_1(z)| = |U_2(z)|$.

are sequentially trapped into the upper duct, there is a *modal degeneration* point. For example, mode 5 is trapped at range $R_5 = 2475$ km [see Fig. 3(a)] and mode 4 is trapped at range $R_4 = 2490$ km [see Fig. 3(b)]. Between these two ranges, there is a point at $R_{45}^D = 2482$ km where mode 4 and mode 5 are *degenerated*, which means that at this point we have $k_4 = k_5$ and $|U_4(z)| = |U_5(z)|$ (see Figs. 4 and 5). The same thing occurs for mode 1 and mode 2 at $R_{12}^D = 2530$ km (see Figs. 6 and 7). As shown in Fig. 3(a) and (b), after mode 4 is trapped in the upper duct, the ''original'' mode 4 is now named ''mode 5.'' Similarly, in Fig. 3(d) and (e), after mode 1 is trapped in the upper duct, the original mode 1 is now named ''mode 2.'' This process is referred to as the ''*modal name change*.'' Let us set mode 1 as the incident field; the modal degeneration range $-r_1^D$, the modal scattering range $-r_1^S$, and the ''energy distribution'' are shown in Fig. 8. As we can see, there is no real energy repopulation but a name change takes place at r_1^D. The energy repopulation takes

place after r_1^S. Numerical value of r_m^D and r_m^S are listed in Table I.

II. MODAL TRAVEL TIME MISCALCULATION DUE TO NAME CHANGE

The conventional adiabatic modal travel time calculation is given by[7]

$$t_m^{\text{Ad}} = \int_0^R dr \left\{ C_m(r) \int U_m^2(z;r)/c_0^2(z)dz \right\}. \tag{1}$$

When a modal name change takes place on the propagation path, Eq. (1) can give an incorrect modal travel time. For example, if we know that the received signal of mode 2 at range $R = 2555$ km is adopted from mode 1 at range R_{12}^D

FIG. 6. Modal wave number k_1 and k_2 as a function of range. The modal degeneration range $R_{12}^D = 2530$ km.
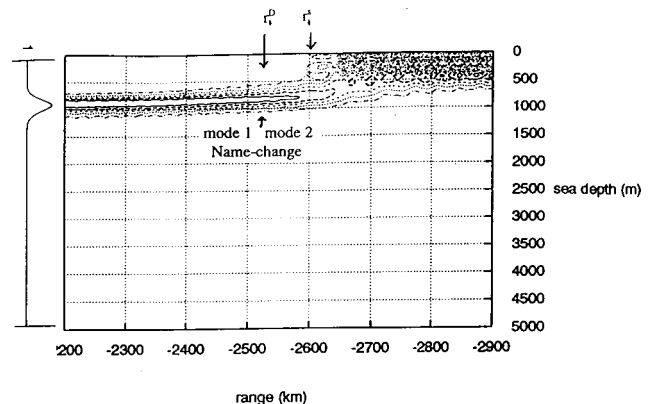
FIG. 8. The modal degeneration range $-r_1^D$, the modal scattering range $-r_1^S$, and the ''energy distribution'' for mode 1 as the incident field.

TABLE I. Ranges of modal degeneration and scattering.

| | Range | | Phase velocity | | | |
m	R_m^{trap} (km)	R_m^D (km)	C_m^{trap} (m s^{-1})	C_m^D (m s^{-1})	R_m^S (km)	$(R_m^S - R_m^D)$ (km)
1	2535		1476.68		2585	55
		>2530		>1477.04		
2	2520		1477.73		2550	37
		>2513		>1478.30		
3	2505		1478.77		2535	37
		>2498		>1479.32		
4	2490		1479.82		2515	33
		>2482		>1480.35		
5	2475		1480.86		2495	25
		>2470		⋯		
6	2460		1482.09		2475	10
		>2465		⋯		
7	2450		1482.92		2460	⋯
		⋯		⋯		
8	2440		1483.75			

$= 2530$ km, and is not the continuation of mode 2 due to modal name change, then the modal travel time of mode 2 should be corrected as

$$t_m^{\text{Ad-Nc}} = \int_0^{R_{12}^D} dr \left\{ C_1(r) \int U_1^2(z)/c_0^2(z) dz \right\} + \int_{R_{12}^D}^R dr \left\{ C_2(r) \int U_2^2(z)/c_0^2(z) dz \right\}. \quad (2)$$

Our numerical results illustrate that the modal travel time with name-change correction given by Eq. (2) is very close to the modal travel time calculated by using the decomposed PE field.[8] Some numerical results are listed in Tables II and Table III.

TABLE II. Comparison of modal travel time calculation (short distance).[a]

m	$R_{(m-1)m}^D$ (km)	t_m^{Ad} (s)	$t_m^{\text{Ad-Nc}}$ (s)	t_m^{PE} (s)
2	2530	108.346	108.353	108.351
3	2520	108.325	108.334	108.333
5	2485	108.297	108.303	108.306

[a]Source at $R_0 = 2395$ km; receiver at $R = 2555$ km; propagation distance=160 km.

TABLE III. Comparison of modal travel time calculation (long distance).[a]

m	$R_{(m-1)m}^D$ (km)	t_m^{Ad} (s)	$t_m^{\text{Ad-Nc}}$ (s)	t_m^{PE} (s)
2	2530	1726.659	1726.853	1726.849

[a]Source at $R_0 = 0$ km; receiver at $R = 2555$ km; propagation distance=2555 km.

III. SUMMARY

The specific set of SSP given by the Semtner–Chervin model in the frontal zone has a strong range-varying double-duct structure which causes interesting effects in terms of modes moving from one duct to the other, and with mode degeneration (two modes with identical wave numbers) occurring at specific ranges followed by a modal name change. These modal features must be taken into account when using mode processing for long-range propagation crossing such a frontal zone.

[1] W. Munk, P. Worcester, and C. Wunsch, *Ocean Acoustic Tomography* (Cambridge U.P., Cambridge, 1995).
[2] D. Lee and G. Botseas, ''An implicit finite difference (IFD) computer model for solving the parabolic equation,'' NUSC Tech. Report 6659, New London Laboratory, New London, CT (1982).
[3] M. Porter, ''The KRAKEN normal mode program,'' Report, SACLANT Undersea Center, La Specia, Italy (1988).
[4] A. Semtner and R. Chervin, ''A simulation of the global ocean circulation with resolved eddies,'' J. Geophys. Res. **93**(C12), 15502–15522 (1988).
[5] E. C. Shang, Y. Y. Wang, and T. Georges, ''Dispersion and repopulation of Heard–Ascension modes,'' J. Acoust. Soc. Am. **96**, 2371–2379 (1994).
[6] G. Jin, J. Lynch, C.-S. Chiu, and J. Miller, ''A theoretical and simulation study of acoustic normal mode coupling effects due to the Barents Sea Polar Front, with applications to acoustic tomography and matched-field processing,'' J. Acoust. Soc. Am. **100**, 193–205 (1996).
[7] R. Koch, C. Penland, P. Vidmar, and K. Hawker, ''On the calculation of normal mode group velocity and attenuation,'' J. Acoust. Soc. Am. **73**, 820–825 (1983).
[8] E. C. Shang and Y. Y. Wang, ''Acoustic travel time computation based on PE solution,'' J. Comput. Acoust. **1**, 91–100 (1993).

A long-range and variable focus phase-conjugation experiment in shallow water

W. S. Hodgkiss, H. C. Song, and W. A. Kuperman

Marine Physical Laboratory, Scripps Institution of Oceanography, University of California, San Diego, La Jolla, California 92093-0701

T. Akal and C. Ferla

SACLANT Undersea Research Center, La Spezia, Italy

D. R. Jackson

Applied Physics Laboratory, University of Washington, Seattle, Washington 98105

A second phase-conjugation experiment was conducted in the Mediterranean Sea in May 1997 extending the results of the earlier time-reversal mirror experiment [Kuperman *et al.*, J. Acoust. Soc. Am. **103**, 25–40 (1998)]. New results reported here include (1) extending the range of focus from the earlier result of 6 km out to 30 km, (2) verifying a new technique to refocus at ranges other than that of the probe source [Song *et al.*, J. Acoust. Soc. Am. **103**, 3234–3240 (1998)], and (3) demonstrating that probe-source pulses up to 1 week old can be refocused successfully. © *1999 Acoustical Society of America.* [S0001-4966(99)02603-X]

INTRODUCTION

A recent experiment[1] first demonstrated an acoustic time-reversal mirror (TRM) in the ocean. A TRM[2,3] also referred to as the process of phase conjugation in the frequency domain,[4–8] focuses sound from a source–receive array (SRA) back to the probe source (PS) which ensonified the SRA. The SRA receives the probe-source field, time reverses it (phase conjugation in the frequency domain), and then uses the time-reversed data as the excitation for an array of sources which are collocated with the receiving hydrophones. If the ocean environment does not change significantly during the two-way travel time, the phase-conjugate field will refocus, regardless of the complexity of the medium, with the caveat that excessive loss in the system degrades the process. The focus is both spatial and temporal, recombining the multipaths from the first part of the transmission.[9] Since this process offers an approach to compensate for multipath interference and other distortion through a complex medium, it may be applicable to various adaptive sonar and communication concepts.

This paper describes a second phase-conjugation experiment conducted in May 1997. The new results reported in this paper include: (1) extending the range of focus from the earlier result of 6 km out to 30 km, (2) validating a new technique to refocus at ranges other than that of the probe source, and (3) demonstrating that probe-source pulses 1 day, 2 days, and as much as 1 week old can be successfully refocused.

I. EXPERIMENTAL GEOMETRY

The second TRM experiment was performed off the west coast of Italy in May 1997 at the same location as the previous experiment.[1]

Figure 1 is a schematic of the experiment, and indicates
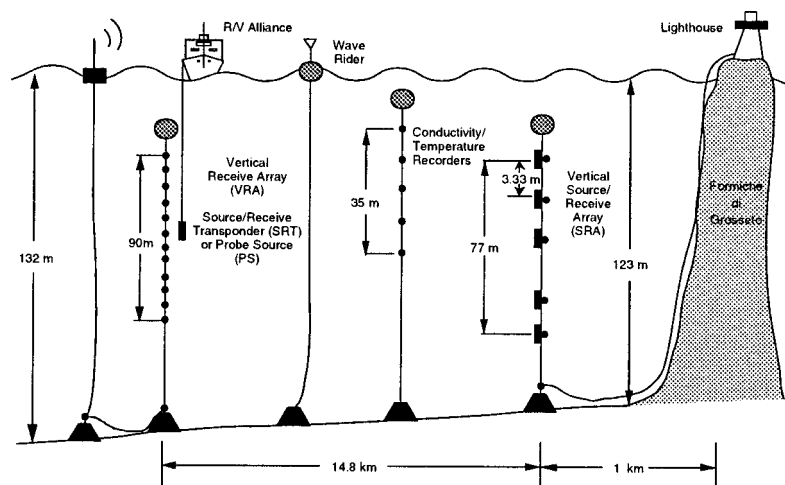
FIG. 1. Experimental setup for the May 1997 phase-conjugation experiment.
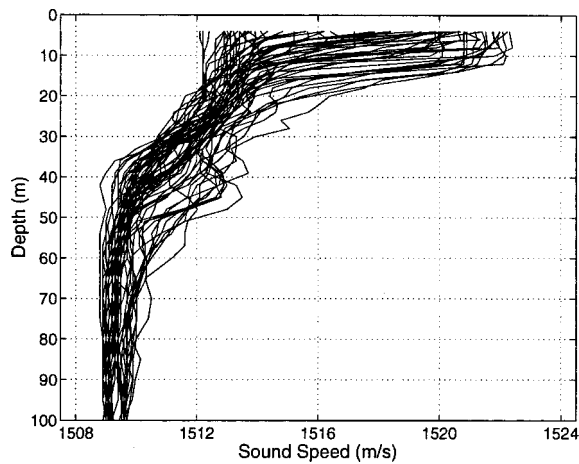
FIG. 2. Sound-speed profiles derived from CTDs for the period 11–24 May 1997.

FIG. 3. The range-dependent bathymetry obtained from an echo sounder and the bottom sound-speed structure determined from earlier experiments are shown along with a sound-speed profile averaged over the period 12–14 May 1997. The range is relative to the SRA. The sound speed in the sediment layer is smaller than in the water column, such that the top and bottom sound speeds are assumed to be 1460 and 1490 m/s, respectively. The depths of the SRA elements are also included.

the types of environmental measurements that were made. The TRM was implemented by a 77-m source–receive array (SRA), in 123-m-deep water, which was hardwired to the Isola di Formica di Grosseto. The SRA consisted of 23 hydrophones with 23 collocated slotted cylinder sources with a nominal resonance frequency of 445 Hz. The sources were operated at a nominal source level of 160 dB. The received signals were digitized, time reversed, and after being converted back to analog form, retransmitted. A flextensional probe source (PS) was deployed from the NATO research vessel ALLIANCE. The probe source, together with a receiving hydrophone, also was used as a transponder in some parts of the experiment. The ALLIANCE also deployed a 48-element vertical receive array (VRA) spanning 90 m which, for most of the experiment, was located 14.8 km from the SRA. The VRA radio telemetered all individual element data back to the ALLIANCE. For the runs in which we simultaneously varied the range of the PS and the VRA, the VRA was suspended from the ALLIANCE to ensure its being very close to the probe source (within 60 m). Additional hardware details can be found in Appendix B of Ref. 1.

Figure 2 shows a collection of sound-speed profiles obtained from a conductivity–temperature–depth (CTD) probe, which provides an indication of the sound-speed variability over the duration of the experiment. Note the increase in sound speed of the surface layer due to surface warming. The range-dependent bathymetry obtained from an echo sounder and the bottom sound-speed structure determined from earlier experiments[1,10] are shown in Fig. 3, along with the mean sound-speed profile over the period 12–14 May 1997. Note that the sound speed in the sediment layer (the thickness of which varies with range from the SRA) is smaller than the sound speed in the water column.

II. LONG-RANGE SHALLOW-WATER PHASE CONJUGATION

The previous experiment[1] contained TRM results at only 6.3 km. Here, we present results out to 30 km. For these runs, the VRA and the PS were both suspended from the ALLIANCE. Just from the size of the ship, the difference between their ranges to the SRA was within 60 m. Figure 4

shows the results for PS at an 81-m depth for five different ranges from the SRA: 4.5, 7.7, 15, 20, and 30 km. As expected, the temporal focus remains compact while the spatial focus broadens with range due to mode stripping. The latter can be seen more quantitatively in Fig. 5(a). Note, however, that there is a significant sidelobe around a 40-m depth at a 15-km range, as shown in Fig. 4(c). Also, in Fig. 4(a) the focus appears to occur at 85 m, which is below the PS depth. The depth axes in Fig. 4 are based upon the assumed array-element depths for a perfectly vertical receive array, although the VRA was suspended from the freely drifting ALLIANCE [except in the case of Fig. 4(f)]. In fact, the ALLIANCE was drifting at approximately 1/2 kt during the period of Fig. 4(a), 1/3 kt during the period of Fig. 4(b), and there was almost no drifting of the ship during the periods of Fig. 4(c)–(e). Incorporating a nonvertical shape of the array resulting from the ship drifting could bring the focus of Fig. 4(a) back to the PS depth. We also note that the mainlobes of the focus have longer tails towards the bottom for ranges greater than $R = 15$ km. This is due to the contribution of lower-order modes excited for a deep PS source (81-m depth) in a strongly downward-refracting environment.

Simulations using the environment of Fig. 3 as an input confirm that the focal structure is consistent with theory.[1] The broader mainlobes around the PS depth in Fig. 5(a) when $R = 20$ and $R = 30$ km are due to backpropagated noise components in the vicinity of 460 Hz (close to the carrier frequency of 445 Hz), which are embedded in the data received by the SRA. The simulations also predict the sidelobe around the 40-m depth at the 15-km range. As described below, this sidelobe is due to the nonoptimum spatial coverage of the source–receive array (SRA) in this particular environment.

There are two issues in spatial sampling: array aperture and element spacing. We used a 23-element SRA spaced 3.33 m, i.e., approximately λ at the frequency 445 Hz. The uppermost element is at a 25-m depth and the SRA spans 77

m of a 123-m water depth. Here, λ spacing is sufficient for a vertical array due to the waveguide nature of the channel.[11]

Figure 6 shows simulation results for various SRA configurations, clearly demonstrating that the sidelobe can be removed by lowering the SRA 10 m towards the bottom. As can be seen, element spacing is not the issue. The results indicate that in a strongly downward-refracting environment, it is better to sample the field in the lower part of the water column. For a different sound-speed profile, however, the sidelobe disappears as shown in Fig. 4(f) (also at 15-km range), which was obtained 10 days later than Fig. 4(c).

Figures 7 and 8 show the experimental results for the PS at a 47-m depth at various ranges. We note from Fig. 2 that this depth undergoes considerably more sound-speed structure variability than the deep probe-source position. An attempt to simulate the double peaks at the 30-km range using

a simple time-invariant environment as above had little success. In addition, the structure of the double peaks changes significantly over the 15-min period (the duration of this portion of the experiment). The spatial and temporal variability of the sound-speed structure at this time is under investigation. Figure 7(a) also suggests that the array shape was not vertical due to drifting of the ship, as pointed out in Fig. 4(a).

To summarize, the TRM is still quite effective at 30 km—particularly for the deeper probe source, which is in the more stable part of the water column. This focal property of the waveguide TRM is quite impressive. The focal region has a vertical extent of about 25 m (3 dB down from peak) at a range of 30 km, which corresponds to 20% of the waveguide depth at a range of about 250 waveguide depths. Although we did not map out the radial extent of the focus, Fig. 9 is a simulation using the environmental parameters which
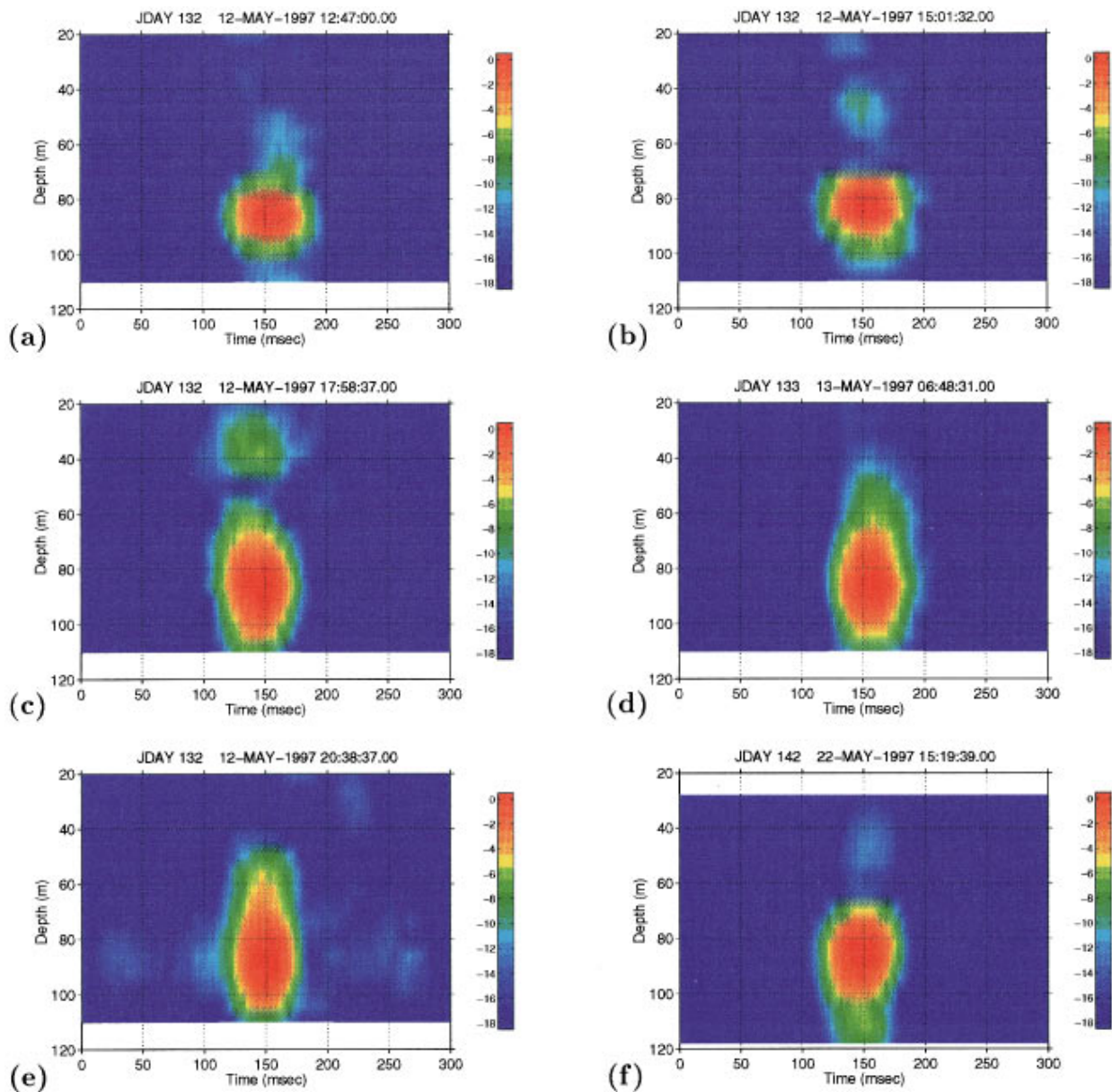
FIG. 4. Experimental results for 50-ms, 445-Hz center frequency probe-source (PS) pings at 81-m depth and various ranges, R, between the PS and the source–receive array (SRA). (a) $R=4.5$, (b) $R=7.7$ km, (c) $R=15$ km. (d) $R=20$ km. (e) $R=30$ km. (f) $R=15$ km. The vertical receive array (VRA) is within 60 m of the PS. Both the VRA and PS were suspended from the ALLIANCE except in (f), which was from another run where the rf-telemetered VRA was at 15-km range. Note the different depth coverage of the VRA in (f) in comparison with (a)–(e).
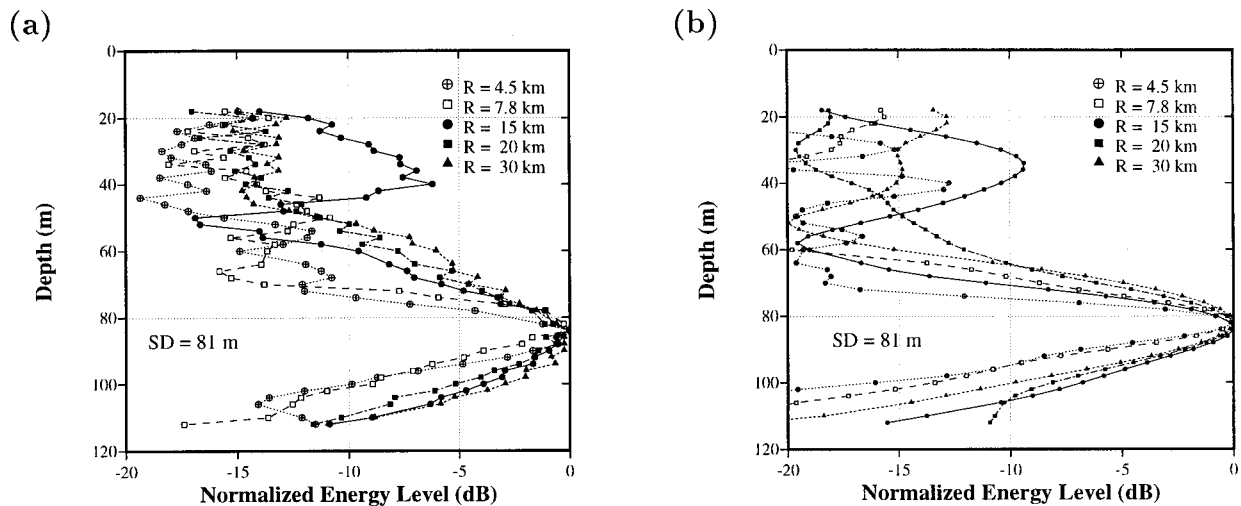
FIG. 5. The energy over a 0.3-s time window of the pulse received on the VRA as a function of depth for various ranges. The depth of the PS was 81 m. (a) Experimental results. (b) Simulation results using the environment shown in Fig. 3. Note the sidelobe at around 40-m depth and 15-km range in both cases.

have successfully described this process, indicating that the radial size of the focal region (depth of field) is on the order of 800 m (3 dB down from the peak) at a 30-km range and 300 m at a 5-km range.

III. TRM WITH VARIABLE-RANGE FOCUSING

Here, we present results which experimentally confirm a technique to change the range focus of a TRM[12] based on the frequency-range invariant of the interference pattern in a waveguide. The technique involves retransmitting the data at a shifted frequency according to the desired change in focal range. The expression which governs this shift is

$$(\Delta\omega/\omega) = \beta(\Delta R/R), \tag{1}$$
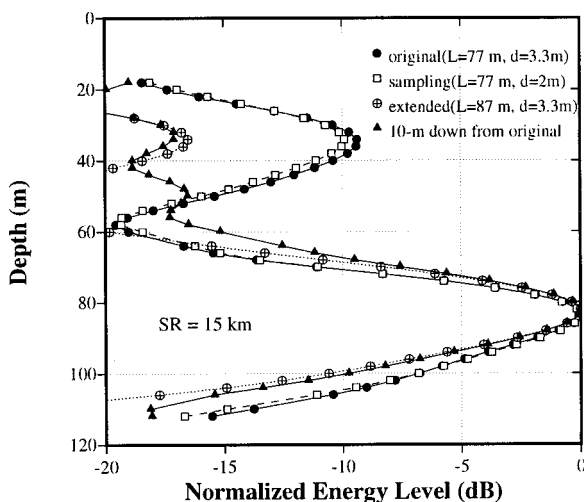
FIG. 6. Energy over 0.3-s time window of the simulated data at 15-km range as a function of depth for various SRA configurations. The original SRA spans 77 m of a 123-m water depth with the top element at 25-m depth and the element spacing of 3.3 m ($L=77$ m, $d=3.3$ m) as shown with solid circles. The line with squares is obtained with the same aperture but more dense sampling ($d=2$ m). The result from extending the aperture towards the bottom ($L=87$ m) is displayed with open circles. Last, the line with solid triangles shows the result with the original aperture ($L=77$ m) but shifted down 10 m (i.e., the top element at 35-m depth).

where R is the horizontal distance of the SRA from the PS. The invariant β is determined by the properties of the medium, and is approximately equal to 1 in a shallow-water acoustic waveguide. In a mildly range-dependent waveguide, the value of β varies with range R.

During the experiment, the frequency shift was implemented in near real-time by a simple fast Fourier transform (FFT) bin shift of the probe-source data received by the SRA prior to retransmission. In the following results, the nominal PS range is 15 km. Figure 10(a) shows the focusing for the PS at a depth of 47 m when the VRA was 500-m inbound of the probe source; Fig. 10(b) shows the focusing using a theoretically predicted −15-Hz shift to refocus the pulse at the SRA ($\beta=1$). The results for the PS at a depth of 82 m are shown in Fig. 11 when the VRA was 700-m outbound of the PS. A +30-Hz frequency shift brought the focus back, as shown in Fig. 11(b). In Fig. 12(a), the VRA was 600-m inbound of the probe source, which resulted in considerable defocusing. Figure 12(b)–(d) show frequency shifts of 20, 25, and 32 Hz with the best focus resulting from the 32-Hz shift. It is interesting to note that this latter result corresponds to $\beta=1.4$, and in essence, this procedure is a way of determining β.

To summarize, it is possible to shift the focal range on the order of 10% of the nominal range of the probe source. The theory on which this shift is dependent is valid only over a frequency range in which the mode shapes do not change significantly. Frequency shifts of greater than about 10% violate this condition. A practical limitation also comes from the transducer characteristics of the SRA, the resonance of which is around 445 Hz with a 3-dB bandwidth of approximately 35 Hz, as shown in Fig. B1 in Ref. 1. Therefore, it is difficult to excite the pulse at a carrier frequency more than 10% offset from the original resonance frequency.

From the results presented above, temporal compression appears to be a robust property of the TRM focus since it occurs even when spatial focusing is absent. In this particular environment, our narrow-band 50-ms pulse (22 cycles at 445 Hz) is dispersed to about 75 ms one-way duration for the PS
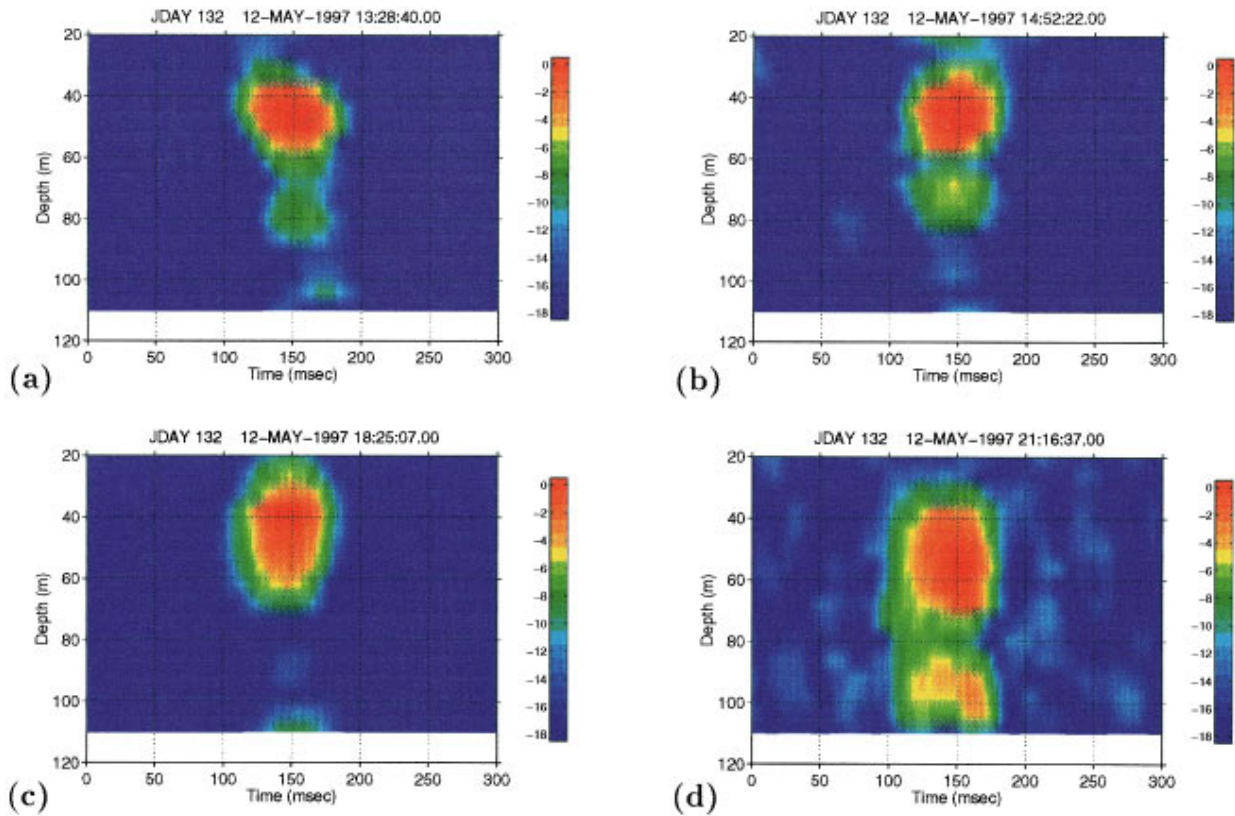
FIG. 7. Experimental results for 50-ms, 445-Hz center frequency probe-source (PS) pings at 47-m depth and various ranges, R, between the PS and the source–receive array (SRA). (a) $R=3.7$ km. (b) $R=7.8$ km. (c) $R=15$ km. (d) $R=30$ km. The vertical receive array (VRA) is within 60 m of the PS. Both the VRA and PS were suspended from the ALLIANCE. Note the double peaks at the 30-km range.

at a 15-km range from the SRA [see Fig. 13(a)]. The VRA results show that the retransmissions have been compressed roughly to the original pulse duration. A shorter-duration pulse, however, would have displayed more significant spreading when not in focus than in the immediate vicinity of the focal spot. Note also that the out-of-focus ranges considered here are within 10% of the nominal focal range.

IV. TRM WITH LONG-TIME MEMORY

Clearly, for a time-independent medium, one can use stored probe pulses to focus on specific locations.[3] However,

the temporal variability of the ocean is expected to limit such a procedure. In the previous experiment,[1] we found that a single probe-source pulse received at the SRA could be used to provide a stable focus for up to 3 h (the total duration of that portion of the experiment). In the May 1997 experiment, we found that probe pulses up to 1 week old still produced a significant focus at the original probe-source location.

Figure 13(a) shows the original probe-source pulse as received by the SRA (on Julian day 132 at 17:42:05 Z) for the PS at a depth of 81 m, and Fig. 13(b) shows the time-
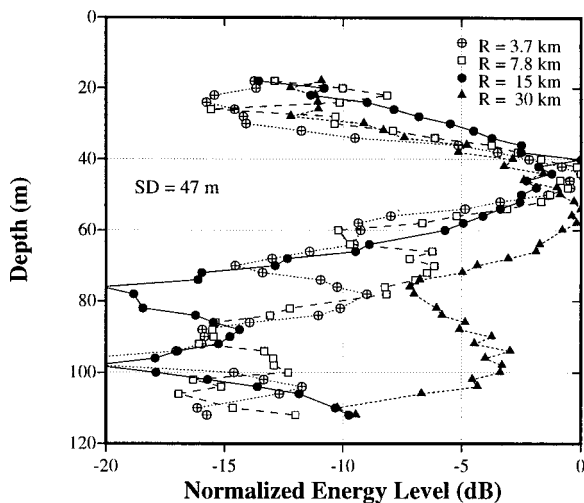
FIG. 8. The energy over a 0.3-s time window of the pulse received on the VRA as a function of depth for various ranges. The depth of the PS was 47 m. Note the double peaks at the 30-km range.
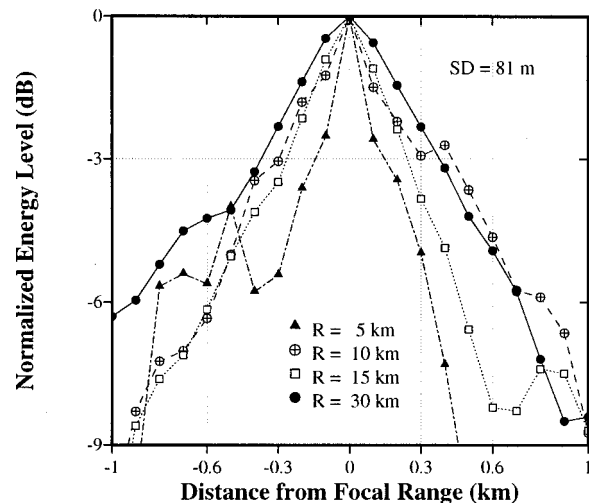
FIG. 9. Simulated results of the energy over 0.3-s time window of the pulse received on the VRA as a function of range with respect to the focal range for various source ranges: 5, 10, 15, and 30 km.
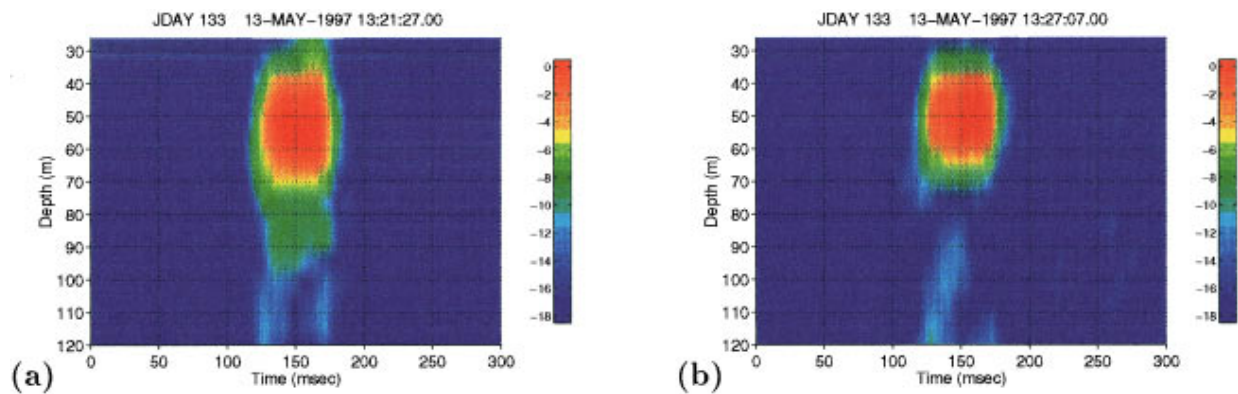
FIG. 10. Experimental results for the PS at a depth of 47 m. (a) Out-of-focus results on the VRA when the VRA is 500-m inbound of the PS. (b) Same as (a) except a −15-Hz frequency shift has been applied to the data at the SRA prior to retransmission. Note that the focus is improved significantly.
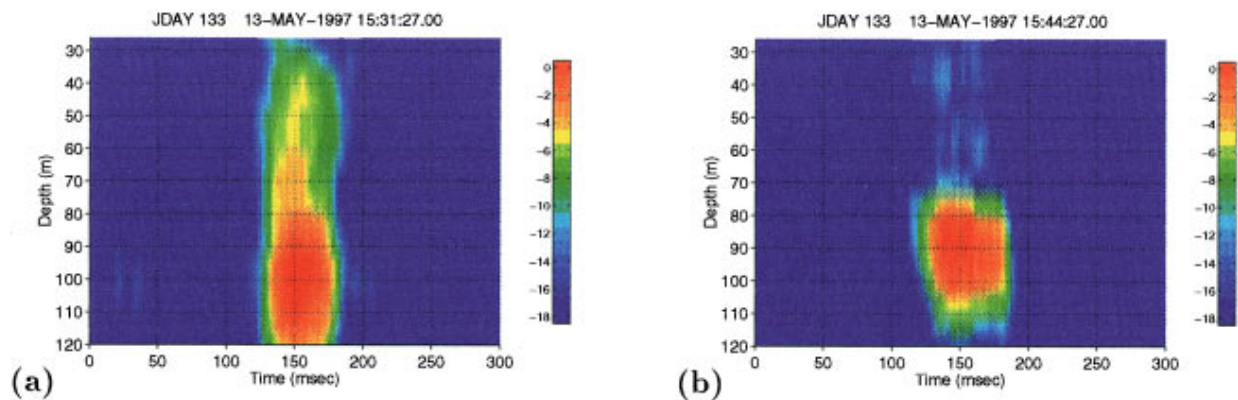
FIG. 11. Experimental results for the PS at a depth of 82 m. (a) Out-of-focus results on the VRA when the VRA is 700-m outbound of the PS. (b) Same as (a) except a +30-Hz frequency shift has been applied to the data at the SRA prior to retransmission. Note that the focus is brought back onto the VRA.
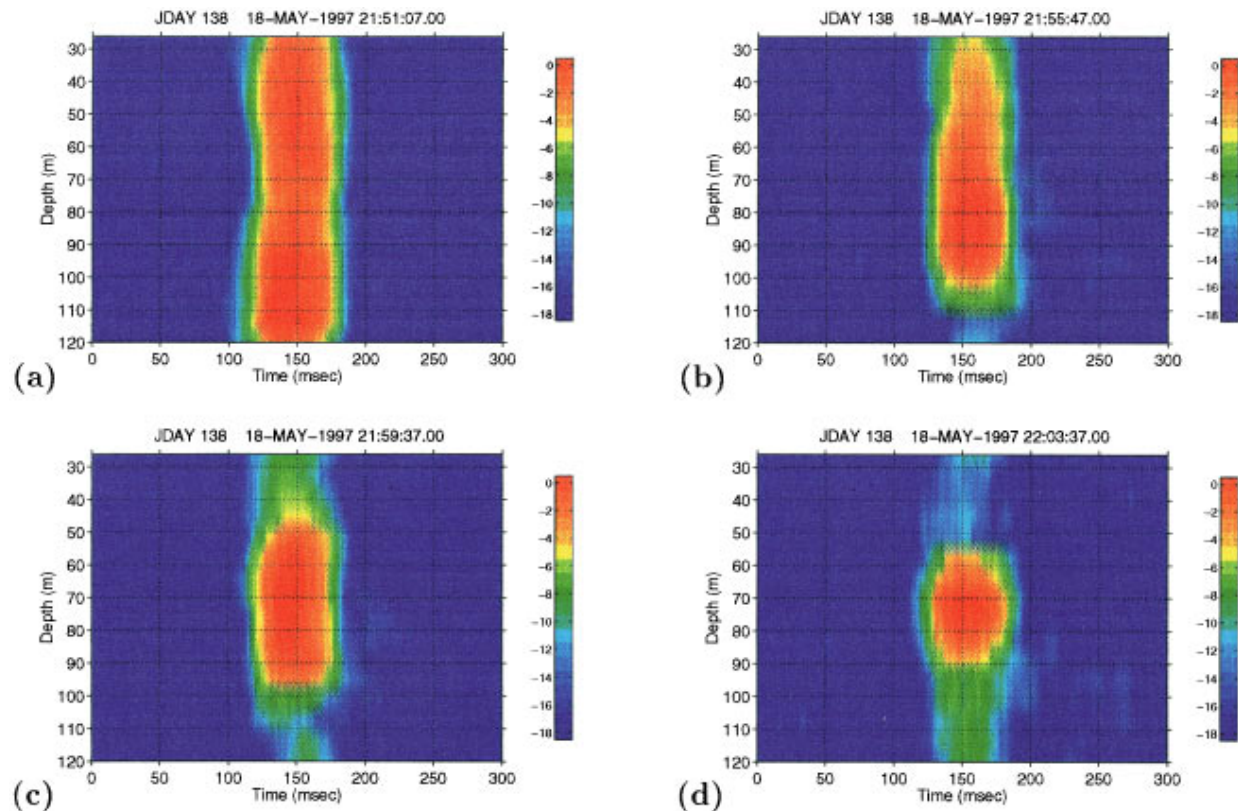
FIG. 12. Experimental results for the PS at a depth of 68 m. (a) Out-of-focus results on the VRA when the VRA is 600-m inbound of the PS. (b) −20-Hz frequency shift. (c) −25-Hz frequency shift. (d) −32-Hz frequency shift. The −32-Hz shift in (d) shows the best focus, which corresponds to $\beta = 1.4$.
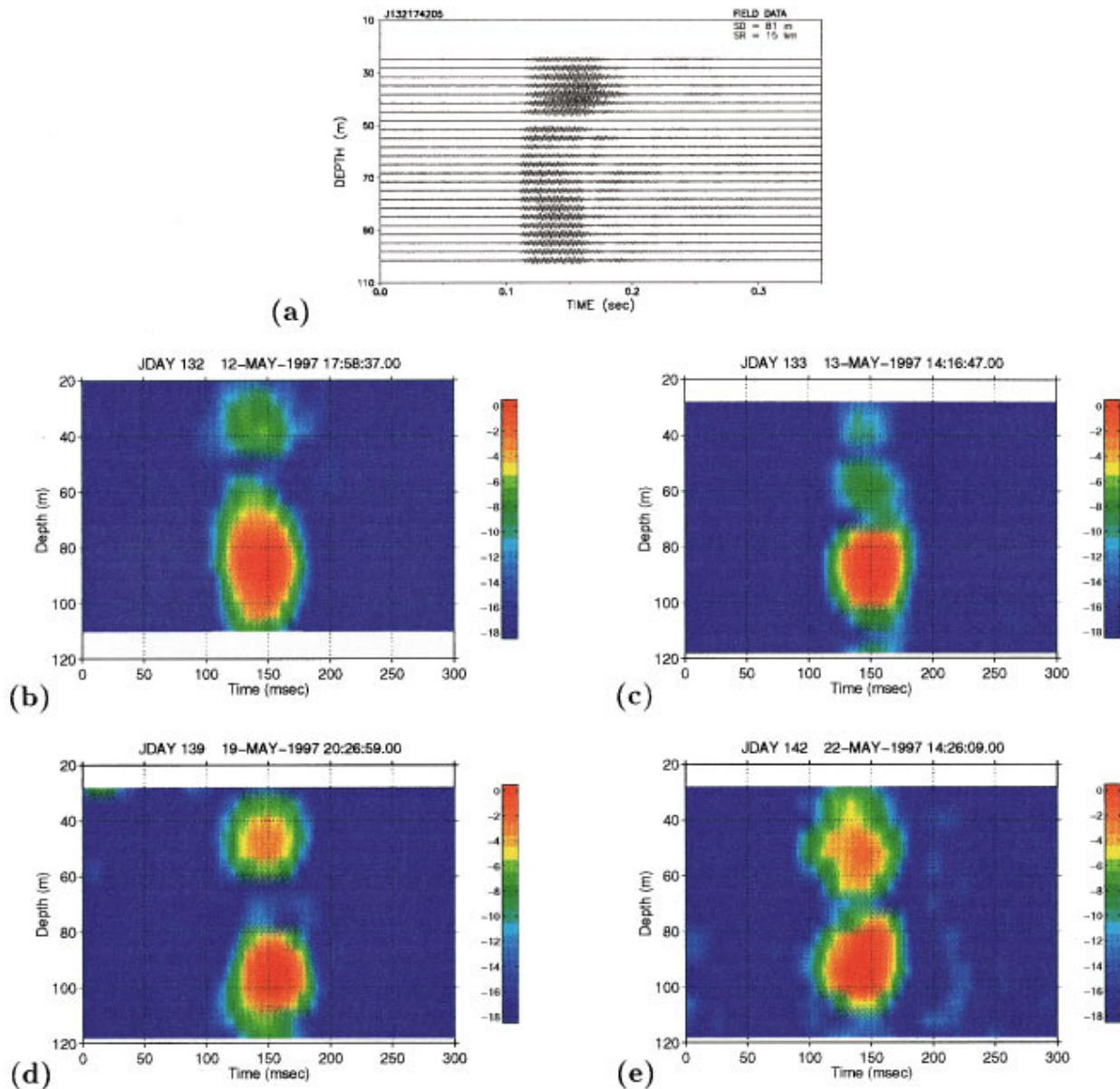
FIG. 13. Experimental results using an old ping which was received by the SRA on JD 132 at 17:42:05 Z. (a) The pulse data received on the SRA for the PS at depth of 81 m. (b) The original data received on the VRA from the time-reversed transmission of the pulse shown in (a) when the PS and VRA were at the same range of 15.2 km. (c) The results on the VRA from the retransmission of (a) 1 day later. The VRA was 400-m inbound of the PS. (d) The results on the VRA from the retransmission of (a) with a −16-Hz frequency shift 1 week later. The VRA was 300-m inbound of the PS. (e) The results on the VRA from the retransmission of (a) 10 days later. The VRA was 300-m inbound of the PS. Note the different depth coverage of (b) from (c)–(e) because the VRA was suspended from the ALLIANCE at that time.
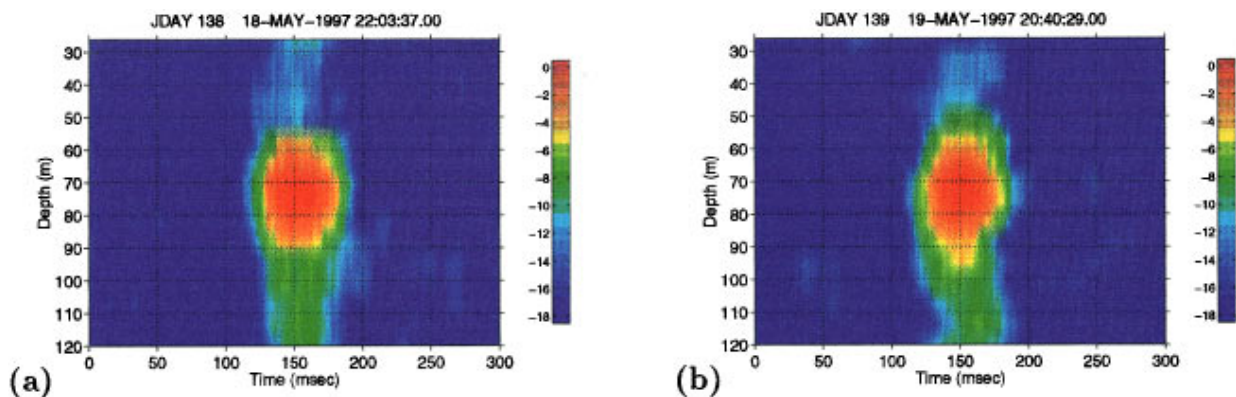
FIG. 14. Experimental results using an old ping which was received by the SRA on JD 138 at 21:48 Z. (a) The original data received on the VRA when the VRA was 600-m inbound of the PS. (b) The data on the VRA 1 day later from the same ping used for (a). In both cases, a −32-Hz frequency shift was applied to the ping received by the SRA prior to retransmission.

reversed pulse received on the VRA just a short time later (16 min). Figure 13(c)–(e) show the results on the VRA for the Fig. 13(a) pulse retransmitted 1 day, 1 week, and 10 days later. Note the different depth coverage of Fig. 13(b) from the others because the VRA was suspended from the ALLIANCE at that time, not moored as in the other cases. The biggest environmental change that occurred during this experiment was a gradual warming of the surface layer, resulting in an increase in sound speed near the surface as indicated in Fig. 2. Therefore, the results from a deep probe source will be less sensitive to these environmental variations over the period than will be the case for a shallow source.

It is surprising that a 1-day-old ping apparently shows better focusing, as seen in Fig. 13(c). Although the focus is significantly degraded after a week along with the appearance of a side-lobe in the upper water column, the TRM clearly retains a memory. Furthermore, it might be possible to enhance the focus with techniques related to that of the last section. In Fig. 13(d), a -16-Hz frequency shift was applied prior to retransmission of the pulse in Fig. 13(a) where the VRA was 300-m inbound of the PS. In fact, the mismatch in environmental parameters such as sound speed and water depth can be compensated by shifting the frequency.[13] Figure 14 shows the results for the PS at a depth of 68 m using a day-old ping which was received by the SRA on JD 138 at 21:48 Z along with the original result from the same ping (15 min later). The results in this section suggest that the repetition rate required to keep a stable focus may be less than originally suspected.

V. SUMMARY AND CONCLUSIONS

We have demonstrated that a time-reversal mirror can produce significant focusing out to long ranges in a shallow-water environment—30 km in water depths on the order of 125 m. Furthermore, we have confirmed experimentally that the range of focus can be varied up to about 10% around the nominal focal range. Finally, we have demonstrated that a time-reversal mirror can have substantial memory. In this experiment, probe-source pulses up to 1 week old were successfully refocused.

[1] W. A. Kuperman, W. S. Hodgkiss, H. C. Song, T. Akal, C. Ferla, and D. R. Jackson, ''Phase conjugation in the ocean: Experimental demonstration of an acoustic time-reversal mirror,'' J. Acoust. Soc. Am. **103**, 25–40 (1998).

[2] M. Fink, ''Time Reversal Mirrors,'' in *Acoustical Imaging*, edited by J. P. Jones (Plenum, New York, 1995), Vol. 21, pp. 1–15.

[3] M. Fink, ''Time Reversed Acoustics,'' Phys. Today **50**, 34–40 (March 1997).

[4] B. Y. Zel'dovich, N. F. Pilipetsky, and V. V. Shkunov, *Principles of Phase Conjugation* (Springer-Verlag, Berlin, 1985).

[5] D. R. Jackson and D. R. Dowling, ''Phase conjugation in underwater acoustics,'' J. Acoust. Soc. Am. **89**, 171–181 (1991).

[6] D. R. Dowling and D. R. Jackson, ''Narrow-band performance of phase-conjugate arrays in dynamic random media,'' J. Acoust. Soc. Am. **91**, 3257–3277 (1992).

[7] D. R. Dowling, ''Phase-conjugate array focusing in a moving medium,'' J. Acoust. Soc. Am. **94**, 1716–1718 (1993).

[8] D. R. Dowling, ''Acoustic pulse compression using passive phase-conjugate processing,'' J. Acoust. Soc. Am. **95**, 1450–1458 (1994).

[9] A. Parvulescu, ''Matched-signal (Mess) processing by the ocean,'' J. Acoust. Soc. Am. **98**, 943–960 (1995).

[10] J. P. Hermand and M. Siderius, ''Yellow Shark '95: Experimental and inversion results for broadband acoustic propagation over a soft clay bottom,'' J. Acoust. Soc. Am. **102**, 3142 (1997).

[11] A. B. Baggeroer, W. A. Kuperman, and H. Schmidt, ''Matched field processing: source localization in correlated noise as an optimum parameter estimation problem,'' J. Acoust. Soc. Am. **83**, 571–587 (1988).

[12] H. C. Song, W. A. Kuperman, and W. S. Hodgkiss, ''A time reversal mirror with variable range focusing,'' J. Acoust. Soc. Am. **103**, 3234–3240 (1998).

[13] G. A. Grachev, ''Theory of acoustic field invariants in layered waveguide,'' Acoust. Phys. **39**(1), 33–35 (1993).

Physics of 3-D scattering from rippled seabeds and buried targets in shallow water

Henrik Schmidt[a)]
SACLANT Undersea Research Centre, I-19138 La Spezia, Italy

Jaiyong Lee
Massachusetts Institute of Technology, Cambridge, Massachusetts 02139

A new wave theory model providing consistent modeling of seabed insonification, three-dimensional target scattering, and rough seabed reverberation has been used to investigate the spatial and temporal characteristics of the multistatic scattering and reverberation from rippled, shallow water seabeds. It is shown that the highly polarized—close to monochromatic—spectral characteristics of ripple fields are associated with a reverberation environment which is highly sensitive to both the frequency and insonification aspect relative to the ripples. The study suggests that significant gains in detection performance for buried objects can be achieved by band-limiting the processing to frequencies below an environmentally dependent ''cut-off'' frequency. The study also confirms theoretically the intuitive advantage of insonifying the seabed along the ripple direction to reduce monostatic reverberation. © *1999 Acoustical Society of America.*
[S0001-4966(99)00903-0]

INTRODUCTION

The detection and classification of targets buried in the seabed have traditionally been performed using high-frequency sonars operating at grazing angles above critical, where the acoustic field is propagating in the vertical direction in the bottom and therefore only undergoes losses associated with the seabed transmission and the bottom attenuation. However, in shallow water such an approach is severely limited in terms of coverage, and a significant research effort has recently been focused on the potential of detecting and classifying buried objects using sonars with subcritical incidence on the seabed.

Most of this work has focused on the high frequencies (10–100 kHz) of traditional bottom sonars, with the scientific issues being associated with the fundamental physics of the bottom interaction. Here, one of the most important issues has been the identification of mechanisms for subcritical bottom penetration, including rough seabed scattering,[1] and porous media effects.[2] Other research has focused on the seabed reverberation environment, which is obviously a critical factor in regard to sonar performance.[3,4] Other related work has been associated with the issues of the actual scattering process for buried targets.[5]

It is well known that lower frequencies have better penetration properties, in part because of the lower attenuation, but more importantly, in the context of subcritical target detection, lower frequencies have a deeper evanescent ''tail'' at subcritical incidence.[6] As a consequence, a significant research effort has recently been directed toward lower frequencies. Thus, for example, SACLANTCEN has directed a series of bottom interaction experiments involving penetra-

tion, reverberation, and target scattering measurements, using a parametric sonar with secondary frequencies in the range 2–12 kHz. The results of this effort are beginning to emerge. Thus, a recent modeling and analysis effort has led to a new understanding of the dominant penetration mechanisms in this frequency regime.[7] The analysis suggests that below approximately 5 kHz the evanescent coupling is the dominant mechanism, while at higher frequencies scattering from the seabed roughness dominates.

One of the models used in Ref. 7 was the new OASES-3D scattering and reverberation model, developed at the Massachusetts Institute of Technology,[4,8] and this model accurately reproduced the experimental data. Because this model inherently decomposes the field into its coherent and scattered components, it provided a direct measure of the relative contribution of the two mechanisms. Since OASES-3D inherently computes the coherent and scattered fields throughout the waveguide, the agreement with the penetration data suggested that the same model could be applied to investigate the spatial and temporal properties of the three-dimensional scattered and reverberant field in shallow water waveguides, and the principal results of this analysis are described in the following.

It should be stressed that the conclusions of this study concern only the *ripple-induced reverberation* properties. Thus, for example, at low frequencies the evanescent bottom penetration becomes significant, and scattering and reverberation from bedrock roughness and volume inhomogeneities such as buried rocks and boulders may become important, countering the effect of the spatial filtering provided by the seabed ripples. Also, the present study assumes the ripple field to have insignificant low wave number roughness, the presence of which would increase the low-frequency reverberation levels. Another effect that will affect the signal–reverberation ratio is the frequency dependence of the sonar

---

[a)]On leave from Department of Ocean Engineering, Massachusetts Institute of Technology, Cambridge, MA 02139.

footprint. The present study assumes a constant sonar footprint, whereas the insonified area for parametric sonars will be approximately inversely proportional to the frequency squared, countering the predicted decay of the ripple scattering. However, the 6 dB per octave added to the low-frequency behavior of the reverberation is insignificant compared to the rapidly decaying ripple contribution. On the other hand, the beamwidth effect may be important in combination with the other low-frequency reverberation mechanisms.

The evaluation of the relative significance of these various mechanisms affecting low-frequency bottom reverberation requires a series of well controlled experiments incorporating different bottom types, seabed roughness statistics, and source–receiver geometries. The GOATS'98 experiment carried out jointly between SACLANTCEN and MIT in May 1998 includes measurements of the full three-dimensional reverberant field, which according to the models described here will be significantly different for the various scattering and reverberation mechanisms.

I. SCATTERING AND REVERBERATION MODEL

The three-dimensional version of the OASES propagation model has been combined with a perturbational approach to allow full wave-theory modeling of the three-dimensional field associated with bottom-interaction of narrow-beam sonars such as the TOPAS parametric source.[9] The new OASES-3D model handles consistently both the coherent component of the full waveguide field, including the evanescent bottom penetration, and the scattering and reverberation produced by anisotropic seabed roughness.[4] Even though the modeling approach treats the scattered field deterministically, and therefore coherently, we will maintain the traditional scattering theory terminology, with the field in the absence of scatters being referred to as the *coherent* field, and the field perturbation being denoted the *scattered* field.

As a first step, the standard OASES code is applied to compute the field in a waveguide with smooth interfaces. Subsequently, the interface scattering is computed using the perturbation approach to rough elastic interface scattering developed by Kuperman and Schmidt.[10,11] The original perturbation theory is based on a 2-D Fourier transform formulation for rough interfaces of infinite extent. For computational reasons this approach is only feasible for evaluation of the scattered field in plane geometry with one-dimensional roughness.[11] However, many sonar problems are characterized by a sonar ''footprint'' or ''patch'' of limited extent, as is the case, for example, for the TOPAS, and an alternative implementation of the perturbation theory has therefore been devised by LePage,[12] in effect representing the insonified roughness patch by a *virtual source distribution*. The field produced by this source distribution can then be very efficiently evaluated by wave number integration models, such as OASES, using azimuthal Fourier synthesis.[13]

It should be pointed out that traditional perturbation approaches are most often applied to directly predict the field statistics by formal averaging. In contrast, the approach used in OASES-3D uses a spatial realization of the roughness statistics, or a directly measured roughness patch, to generate a single field realization. However, the model is sufficiently efficient to allow for computing the field statistics using Monte Carlo ensemble averaging.

A. Coherent field modeling

The coherent component of the field, including the evanescent bottom field, is computed by the OASES code,[8] using standard wave number integration for solving the fluid–elastic wave equations in stratified waveguides.[6]

For arbitrary fluid–elastic stratifications, this theory decomposes the wave field in each layer ℓ into compression and shear potentials,

$$\chi_\ell = \{\phi_\ell, \psi_\ell, \Lambda_\ell\}, \tag{1}$$

where χ_ℓ is a generic potential representing the compressional potential ϕ_ℓ and the two scalar shear potentials ψ_ℓ and Λ_ℓ, representing horizontally (SH) and vertically (SV) polarized shear waves, respectively.[13] Obviously, in a fluid medium, χ_ℓ represents the compressional potential alone. For propagation and scattering in a horizontally stratified medium, it is convenient to introduce a coordinate system $(\mathbf{x}, z)$ where the vertical coordinate z is represented by a separate scalar, while the horizontal coordinates are represented in vector form $\mathbf{x} = (x, y)$.

Away from physical sources the seismoacoustic field potentials of time dependence $\exp(-j\omega t)$ must satisfy homogeneous Helmholtz equations of the form

$$[\nabla^2 + k_\ell^2]\chi_\ell(\mathbf{x}, z) = 0, \tag{2}$$

where k_ℓ represents the appropriate medium wave numbers.

In addition, the field must satisfy the boundary conditions at all interfaces z_ℓ in the stratification, as well as the source conditions. Assuming the *physical sources* are limited to a single depth, z_s, a dummy interface is added at this depth, and the interface conditions may be written in the operator form

$$B_\ell \chi_{\ell;\ell+1}(\mathbf{x}, z_\ell) = -f_s(\mathbf{x})\delta_{\ell s}, \quad \ell = 1, 2, \ldots, N, \tag{3}$$

where $\delta_{\ell s}$ is the Kronecker delta, having unit value at the source interface, and zero at all other interfaces. N is the total number of physical and dummy interfaces in the stratification. The differential matrix operator B_ℓ represents the derivatives relating the physical parameters involved in the boundary conditions to the potentials.[10] Thus, Eq. (3) represents the continuity of the pertinent displacements and stresses at all physical interfaces, and discontinuity conditions imposed by the physical source distribution $f_s(\mathbf{x})$.

For problems with source distributions of finite horizontal extent, Eqs. (2) and (3) are most conveniently solved in cylindrical coordinates. Here, the Helmholtz Eq. (2) has solutions in the form of an azimuthal Fourier series of Hankel transform integrals,

$$\chi_\ell(r, z, \theta) = \sum_{m=0}^{\infty} \begin{Bmatrix} \cos m\theta \\ \sin m\theta \end{Bmatrix} \int_0^{\infty} dk_r\, k_r J_m(k_r r)$$
$$\times [\tilde{\chi}_{m;\ell}^+(k_r)e^{jk_z z} + \tilde{\chi}_{m;\ell}^-(k_r)e^{-jk_z z}], \tag{4}$$

where r, z are the depth and range coordinates, and k_r is the horizontal wave number. The depth-dependence of the field

is represented by the exponentials, with k_z being the vertical wave number, defined as

$$k_z = \begin{cases} \sqrt{k_\ell^2 - k_r^2}, & k_r \le k_\ell, \\ j\sqrt{k_r^2 - k_\ell^2}, & k_r > k_\ell, \end{cases} \tag{5}$$

where $k_\ell = \omega/c_\ell$ is the medium wave number for layer ℓ. In this form, the integral representation clearly separates the field into waves *propagating* vertically in the layer ($k_r \le k_\ell$), and waves which are exponentially growing or decaying, the *evanescent* waves ($k_\ell \le k_r$), separated by the critical wave number $k_r = k_\ell$. The amplitudes $\chi_{m;\ell}^{\pm}(k_r)$ are found by matching the boundary conditions of continuous particle motion and stresses (pressure) at all interfaces in the stratification. Since these boundary conditions must be satisfied at all ranges r, they must be satisfied at each wave number component, in accordance with *Snell's Law*. Assembled for all interfaces, these conditions are expressed in matrix form as

$$\widetilde{B}_\ell(k_r)\widetilde{\chi}_{m;\ell,\ell+1}^{\pm}(k_r) = -\widetilde{f}_{s;m}(k_r)\delta_{\ell s}, \quad \ell = 1,2,\dots,N. \tag{6}$$

This equation is formally obtained as the Fourier–Hankel transform of the spatial boundary conditions, Eq. (3). At the depth of the source z_s, the right-hand side represents the discontinuity of the Hankel transforms of the particle motion and pressure due to the presence of the source. Note that the global coefficient matrix $\widetilde{B}_\ell$ in Eq. (6) is independent of the Fourier order m, which has obvious computational advantages when solving for many Fourier orders. As shown by Schmidt and Glattetre,[13] this is achieved by expressing the boundary conditions, and therefore the source term $\widetilde{f}_{s;m}$ in terms of the following combinations of the azimuthal expansion coefficients for the displacements and stresses:

$$\widetilde{f}_{s;m}(k_r)^T \approx \Delta[(\tilde{u}^m + \tilde{v}^m), (\tilde{u}^m - \tilde{v}^m), \tilde{w}^m, \tilde{\sigma}_{zz}^m, (\tilde{\sigma}_{zr}^m + \tilde{\sigma}_{z\theta}^m),$$
$$(\tilde{\sigma}_{zr}^m - \tilde{\sigma}_{z\theta}^m)]. \tag{7}$$

It should be pointed out that the wave-field amplitude solutions to Eq. (6) are *exact*, whereas the numerical evaluation of the wave number integrals in Eq. (4) will exhibit truncation and discretization errors. On the other hand, these errors can be reduced to insignificance by the standard wave number-integration contour deformation and sampling procedures.[6]

The OASES propagation model directly implements Eqs. (4) and (6), and consequently inherently decomposes the field into its propagating and evanescent components.

B. Perturbation scattering theory

Following the computation of the coherent field by wave number integration, the scattering by rough interfaces can be consistently handled using the method of small perturbations developed by Kuperman and Schmidt.[10] For arbitrary fluid–elastic stratifications, this theory decomposes the wave field into coherent and scattered components of the field potentials in layer number ℓ, as illustrated in Fig. 1,

$$\chi_\ell = \langle \chi_\ell \rangle + s_\ell = \begin{cases} \phi_\ell = \langle \phi_\ell \rangle + p_\ell \\ \psi_\ell = \langle \psi_\ell \rangle + q_\ell, \\ \Lambda_\ell = \langle \Lambda_\ell \rangle + r_\ell \end{cases} \tag{8}$$
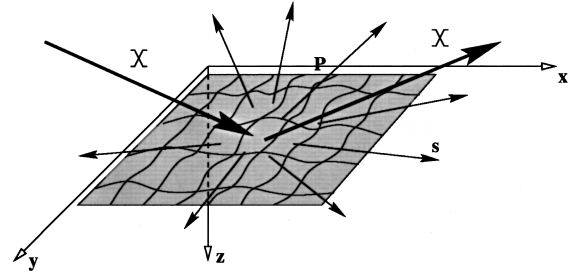
FIG. 1. Rough interface patch in stratified waveguide, insonified by a seismoacoustic field.

where χ_ℓ again is a generic potential representing the compressional potential and shear potentials in layer ℓ.

The coherent field satisfies the Helmholtz equation, Eq. (2), and a boundary condition similar to Eq. (3), but with a modified boundary operator B_ℓ. The self-consistent modification is important for evaluating coherent scattering losses.[10] However, for evaluating the scattered field, the unperturbed conditions may be applied for the coherent field in what is equivalent to the *Born approximation*.

Similarly, the scattered potentials satisfy homogeneous Helmholtz equations

$$[\nabla^2 + k_\ell^2]s_\ell(\mathbf{x},z) = 0, \tag{9}$$

and a set of boundary conditions, which according to the perturbation theory are of the form,

$$B_\ell s_{\ell;\ell+1}(\mathbf{x},z_\ell) = -f_v(\mathbf{x})\delta_{\ell v}, \quad \ell = 1,2,\dots,N, \tag{10}$$

where the distribution function $f_v(\mathbf{x})$ is given by[10–12]

$$f_v(\mathbf{x}) = \left[\overbrace{\gamma_v(\mathbf{x})\frac{\partial B_v}{\partial z}}^{\text{elevation}} + \overbrace{\nabla\gamma_v(\mathbf{x})\circ b_v}^{\text{rotation}} \right]\langle \chi_{v;v+1}(\mathbf{x},z_v)\rangle. \tag{11}$$

Here, $\gamma_v(\mathbf{x})$ is the roughness elevation of interface v at depth z_v. B_v is the same boundary operator as above, while b_v represents the rotation of the boundary conditions due to the roughness slope.

Obviously, Eq. (10) is totally equivalent to Eq. (3), with the physical source distribution $f_s(\mathbf{x})$ replaced by the distribution function $f_v(\mathbf{x})$ at the depth of the rough interface. Thus, $f_v(\mathbf{x})$ represents a *virtual source distribution*, the amplitude and phase distributions of which are determined by the coherent field and the roughness through Eq. (11).

1. Wave number representation

For horizontal stratifications with rough interfaces of infinite extent, the perturbation theory proceeds by transforming the boundary equations (10) into the wave number domain, yielding for the wave number spectrum of the scattered field,[11]

$$\widetilde{s}_{\ell;\ell+1}^{\mp}(\mathbf{q}) = -\widetilde{B}_\ell^{-1}(\mathbf{q})\frac{\delta_{\ell v}}{2\pi}\int d^2\mathbf{k}\,\widetilde{\gamma}_v(\mathbf{q}-\mathbf{k})$$
$$\times\left[\frac{\partial\widetilde{B}_v(\mathbf{k})}{\partial z} + j(\mathbf{q}-\mathbf{k})\widetilde{b}_v(\mathbf{k})\right]\langle\widetilde{\chi}_{v;v+1}^{\mp}(\mathbf{k})\rangle,$$
$$\ell = 1,2,\dots,N. \tag{12}$$
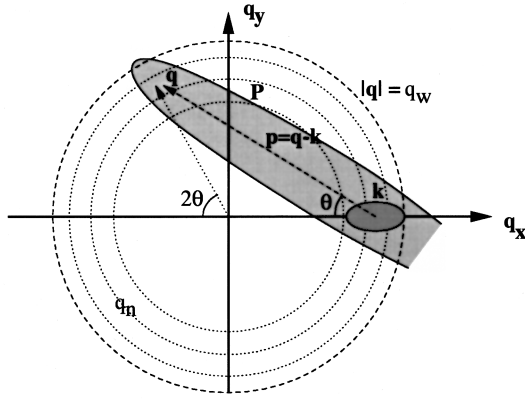
FIG. 2. Graphical representation of the scattering wave number kernel. The scattered field is a convolution in the wave number plane of the incident field by the anisotropic roughness wave number spectrum.

For random, spatially homogeneous interface roughness, the roughness statistics are given by the spatial correlation function $N_v(\Delta \mathbf{r})$ or its Fourier transform, the normalized roughness power spectrum $P_v(\mathbf{p})$, and the roughness variance $\langle \gamma_v^2 \rangle$

$$N_v(\Delta \mathbf{r}) = \langle \gamma_v(\mathbf{r}) \gamma_v(\mathbf{r} + \Delta \mathbf{r}) \rangle, \tag{13}$$

$$\langle \gamma_v^2 \rangle P_v(\mathbf{p}) = \frac{1}{2\pi} \int d^2 \Delta \mathbf{r} N_v(\Delta \mathbf{r}) e^{-j\mathbf{p} \cdot \Delta \mathbf{r}}. \tag{14}$$

Then, the following expression is achieved for the spatial correlation function for the scattered field[11]

$$
C_S(\mathbf{r}_1, z_1, \mathbf{r}_2, z_2) = \frac{\langle \gamma_v^2 \rangle}{(2\pi)^3} \int d^2 \mathbf{p} P_v(\mathbf{p})
$$
$$
\times \left[\int d^2 \mathbf{q} A_m(z_1, \mathbf{q}, \mathbf{q} + \mathbf{p}) e^{j\mathbf{q} \cdot \mathbf{r}_1} \right]
$$
$$
\times \left[\int d^2 \mathbf{q} A_n(z_2, \mathbf{q}, \mathbf{q} + \mathbf{p}) e^{j\mathbf{q} \cdot \mathbf{r}_2} \right]^\dagger,
$$
$$\tag{15}$$

where $(\mathbf{r}_1, z_1)$ and $(\mathbf{r}_1, z_1)$ are the coordinates of receivers in layers m and n, respectively, and $A_{\ell}(z, \mathbf{q}, \mathbf{k})$ is the scattering kernel

$$A_{\ell}(z, \mathbf{q}, \mathbf{k}) = e_{\ell}(z, \mathbf{q}) \tilde{T}_{v;\ell}^*(\mathbf{q}, \mathbf{k}) \langle \tilde{\chi}_{v;v+1}^{\mp}(\mathbf{k}) \rangle.$$

Here $e_{\ell}(z, \mathbf{q})$ contains the exponentials representing the up- and down-going scattered wave field in layer ℓ, and $\tilde{T}_{v;\ell}$ is a generalized *transition matrix* for the field in layer ℓ produced by scattering from rough interface number v,

$$\tilde{T}_{v;\ell}(\mathbf{q}, \mathbf{k}) = -\tilde{B}_{\ell}^{-1}(\mathbf{q}) \frac{\delta_{\ell v}}{2\pi} \left[\frac{\partial \tilde{B}_v(\mathbf{k})}{\partial z} + j(\mathbf{q} - \mathbf{k}) \tilde{b}_v(\mathbf{k}) \right],$$
$$\ell = 1, 2, \dots, N. \tag{16}$$

The scattering integrals of both Eqs. (12) and (15) are of a form convolving a medium dependent boundary operator term by the roughness spectrum at the difference wave number. This *Bragg scattering* condition is illustrated graphically in Fig. 2. An incident field with a wave number spectrum centered around the wave vector $\mathbf{k}$ is convolved with an an-

isotropic roughness spectrum with skewness θ, creating a scattered field composed of wave vectors $\mathbf{q}$ within the lightly shaded envelope in Fig. 2, representing the roughness spectrum. The modal structure of the waveguide, represented by the inverse boundary operator $\tilde{B}_{\ell}^{-1}(\mathbf{q})$ in Eq. (16), is indicated by the circles in Fig. 2. Thus, the resulting scattered field will have a modal structure in all directions, but shaded by the roughness spectrum centered at the incident wave number.

Even though in the following the wave number representation of the scattered field statistics is not used directly, the *Bragg scattering* condition is convenient for interpreting the numerical results, and diagrams similar to Fig. 2 will be used extensively in the following to explain the spatial and temporal *super sensitivity* of the reverberation environment associated with rippled seabeds.

2. Finite roughness patch

For realistic two-dimensionally rough interfaces, the convolution integrals in the correlation function, Eq. (15), become four dimensional. Even though a normal-mode expansion of Eq. (15) has recently been developed, yielding orders of magnitude in computational savings,[14] the full numerical evaluation of the three-dimensional field statistics through Eq. (15) is computationally prohibitive. Consequently, numerical implementations have been limited to plane or axisymmetric problems with one-dimensional roughness.[11,14]

For a finite size roughness patch or sonar footprint, the scattered field can instead be represented by a spatial integral over the patch P,

$$s_{\ell}(\mathbf{x}; z) = \int_P G_{\ell}(\mathbf{x}, \mathbf{x}_v; z, z_v) d^2 \mathbf{x}_v, \tag{17}$$

where $G_{\ell}(\mathbf{x}, \mathbf{x}_v; z, z_v)$ is a *generalized Green's function* satisfying the standard Helmholtz equation, and the boundary conditions,

$$B_{\ell}(\mathbf{x}) G_{\ell; \ell+1}(\mathbf{x}, \mathbf{x}_v; z, z_v) = -\delta(\mathbf{x} - \mathbf{x}_v) f_v(\mathbf{x}) \delta_{\ell v},$$
$$\ell = 1, 2, \dots, N, \tag{18}$$

with the virtual source distribution $f_v(\mathbf{x})$ given by Eq. (11). This equation is obviously of a form identical to the coherent equation, Eq. (3), and can therefore be solved in cylindrical coordinates using the Fourier–Hankel transform, with solutions of the form of Eq. (4). Inserting these solutions into Eq. (17), and reversing the order of integration, then yields for the scattered field,

$$s_{\ell}(r, z, \theta) = \sum_{m=0}^{\infty} \begin{Bmatrix} \cos m\theta \\ \sin m\theta \end{Bmatrix} \int dq_r q_r J_m(q_r r)$$
$$\times \left[\int_P \tilde{G}_{\ell}^m(q_r, z, r_v, \theta_v) r_v dr_v d\theta_v \right]. \tag{19}$$

As was the case for the coherent field produced by the physical sources, the scattered field can then be computed using the three-dimensional version of OASES,[13] with the physical source kernels being replaced by the virtual source equivalents, obtained as the Fourier–Hankel transforms of Eq. (11).

The details of this transformation are described by Fan.[15]

The Fourier series in Eq. (19) converges very fast for orders larger than the dimensionless size ka of the patch, due to the asymptotic behavior of the virtual source kernels

$$\tilde{G}_{\nearrow}^m(q_r,z,r_v,\theta_v) \sim J_m(q_r r_v) \rightarrow 0, \quad \text{for } m > q_r r_v, \quad (20)$$

and the truncation of the azimuthal Fourier series is therefore easily determined *a priori*. Thus, the number of significant terms in the series depends only on the patch size, with the typical number being equal to a few times the *patch size* in wavelengths. In contrast, the number of terms in the numerical evaluation of each of the two dimensions of the equivalent Fourier transform in Cartesian coordinates is determined by the *receiver range*. For finite size patches, the virtual source range is typically much shorter than the receiver ranges, which is the key to the numerical superiority of the cylindrical form.

C. Target modeling

Even though the present paper primarily focuses on the reverberation environment, the implications of the results have to be seen in the context of a potential target signal, and a generic target modeling capability has therefore been implemented into OASES-3D.

Using a 3-D adaptation of the approach of Ingenito,[16] the target is represented by a *virtual source* with a radiation pattern determined by convolving the incident field by a target scattering function. The present 3-D implementation is very similar to the one recently presented by Makris,[17] who rigorously derived the Fourier–Hankel representation of the 3-D waveguide field for a finite size spherical target, and then formally investigated the validity of representing the target as a *point scatterer*. Here, instead, the point-scatter assumption is directly adopted and the Fourier–Hankel transform of the scattered field is performed numerically, in a form which is directly compatible with the OASES infrastructure, totally consistent with the handling of rough interface scattering. In this *single-scattering* approach, the stratification is ignored in the actual scattering process, with the target assumed to be in an infinite medium. Thus, for an incident plane wave of wave number k_r and horizontal azimuthal angle θ_0, the target scattering is represented by a *shaded point source* term,[16]

$$\chi(R,\theta,q_r) = \frac{\exp jkR}{R} S^{\pm}(\theta,q_r,\theta_0,k_r), \quad (21)$$

where $S^{\pm}(\theta,q_r,\theta_0,k_r)$ is the scattering function, with the $\pm$ representing the up- and downward propagating components. The scattering function is represented in terms of the horizontal wave numbers k_r and q_r of the incident and scattered field, respectively, instead of the more common representation in terms of vertical angles. However, using the wave number form we can directly obtain the scattering function for evanescent incident and scattered field components by analytical continuation, which is crucial to the modeling of scattering by buried targets.

For simple objects the scattering function can be determined analytically. Thus, for spheres, the expansion of the

scattering function in terms of spherical harmonics is well established.[16] The scattering function in the evanescent regime $q_r, k_r > k$ is handled by simple analytical continuation. For general targets the scattering function can be determined numerically, e.g., using finite-element approaches.[18]

For a target in a stratified waveguide, Eq. (21) must be transformed into a wave number integral representation of the form of Eq. (4) to be able to express the boundary conditions in the wave number domain, Eq. (6). For the point source, corresponding to the $\exp(jkR)/R$ term in Eq. (21), this transformation is provided by the *Sommerfeld–Weil* integral, with the kernel $j\exp(jq_z|z-z_t|)/q_z$ at depth z.[6] Applying the *stationary phase* or *far-field* approximation, the corresponding wave number kernel for the scattered field is achieved by simply shading the kernel of the Sommerfeld–Weil integral by the scattering function,

$$\tilde{\chi}_{\nearrow}(z,\theta,q_r) = j\frac{e^{jq_z|z-z_t|}}{q_z} S^{\pm}(\theta,q_r,\theta_0,k_r). \quad (22)$$

The wave number integral representation of the target scattering then follows as

$$\chi_{\nearrow}(r,z,\theta) = \sum_{m=0}^{\infty} \begin{Bmatrix} \cos m\theta \\ \sin m\theta \end{Bmatrix} \int_0^{\infty} dq_r \, q_r J_m(q_r r) j^{m+1}$$
$$\times \frac{e^{jq_z|z-z_t|}}{q_z} \tilde{S}_m^{\pm}(q_r,\theta_0,k_r), \quad (23)$$

where $j^m \tilde{S}_m^{\pm}(q_r,\theta_0,k_r)$ is the Fourier–Hankel transform of the scattering function in Eq. (22). The right-hand side of the global boundary condition equation, Eq. (6), representing the Fourier expansion terms for the scattered field, then follows as the discontinuity in pressure and particle velocity above and below the nominal target depth z_t, associated with the wave number kernels

$$\tilde{\chi}_{m;\nearrow}(q_r,z) = j^{m+1} \frac{e^{jq_z|z-z_t|}}{q_z} \tilde{S}_m^{\pm}(q_r,\theta_0,k_r). \quad (24)$$

For incident fields of finite spectral width, the scattering function in Eq. (24) is replaced by an integral over the incident wave number k_r of the scattering function weighted by the spectral density of the incident field.

The solution of Eq. (6), followed by the wave number integration, Eq. (4), then directly yields the target scattering in all layers.

The validity of the single-scattering approach for targets near interfaces is obviously at issue, but as shown by Fawcett,[5] the approach appears sufficiently accurate for objects buried in sedimentary bottoms. However, the single-scatter approximation may be inadequate when modeling the temporal details of the scattered signals. Here the late multiples may be of lower amplitude than the primary response, but separated enough in time to provide important classification information. Another related issue, in particular for objects close to the seabed interface, is the treatment of the target as a *point scatterer*, which is a key feature of this approach. The validity of this approximation was rigorously addressed by Makris,[17] who concluded that the point scatterer approximation for the sphere is valid for ranges in ex-
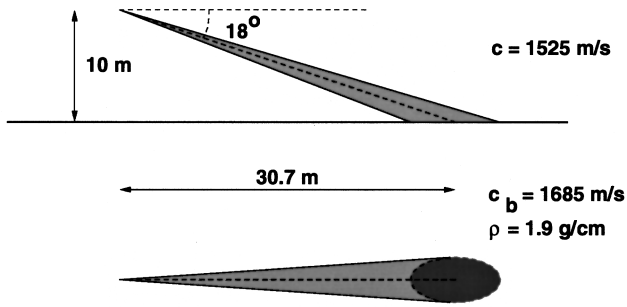
FIG. 3. Geometry configuration for seabed reverberation modeling. A parametric sonar is used to insonify a seabed patch of approximately 10×5 m, at a nominal grazing angle of $18°$.

cess of a sphere diameter from the centroid. It is uncertain how this translates to the handling of transmission through the seabed interface from shallow-buried targets. However, it is hypothesized that by including the evanescent components of both the incident and scattered fields, the correct physics of the primary interaction with buried targets is adequately
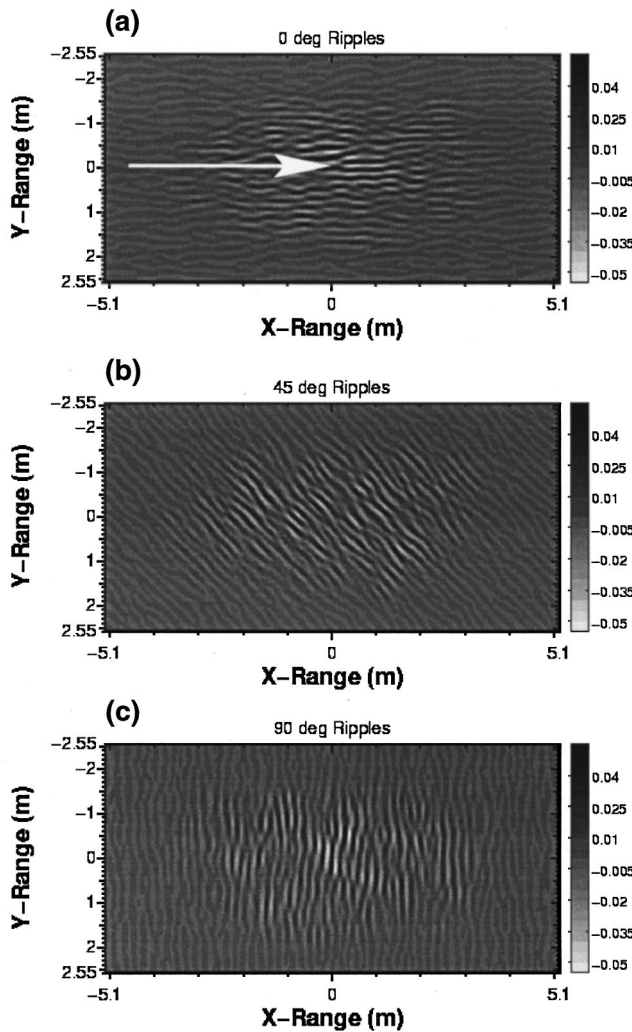
FIG. 4. Rippled seabeds used for analysis. The ripples are shaded by the footprint of the sonar beam, incident at $18°$ grazing angle in the direction indicated by the arrow. The ripple fields are realizations of the same spectral statistics, but with different skew angles relative to the incident beam: (a) 0; (b) 45; (c) $90°$.
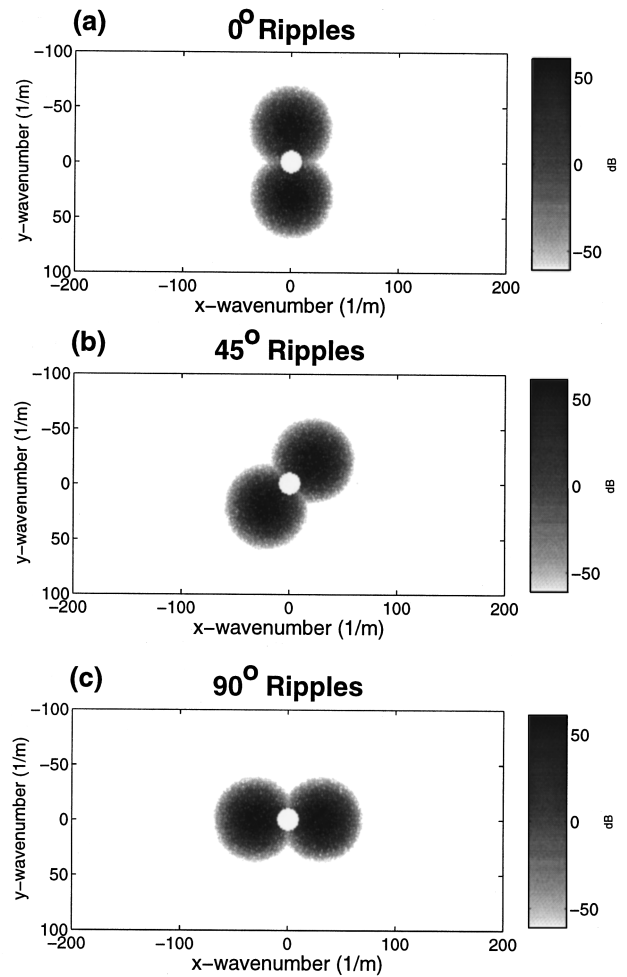
FIG. 5. Wave number spectra in dB of rippled seabeds shown in Fig. 4. Ripple aspect angles: (a) 0; (b) 45; (c) $90°$.

represented, at both super- and subcritical sonar scenarios. In any case, all the approximations made here must ultimately be assessed by comparison to results of ''exact'' numerical models and, more importantly, experiments.

II. 3-D SCATTERING AND REVERBERATION

The new scattering and reverberation model has previously been applied to investigate the mechanisms responsible for sonar penetration into rippled seabeds in the 1–10 kHz frequency regime.[7] This study showed excellent agreement between the penetration predicted by OASES-3D and the predictions of a Helmholtz–Kirchhoff approach,[19] and the agreement with the experimental data was excellent, both qualitatively and quantitatively. The analysis concluded that two mechanisms were primarily responsible for the subcritical penetration. At frequencies up to 5–7 kHz, the direct evanescent coupling is the controlling mechanism. This was confirmed by direct OASES[8] modeling using both plane wave and finite beam insonification of the seabed.

At higher frequencies, both scattering models showed a dominance of the roughness scattering contribution. Further, the modeling showed a sharp ''cut-off'' in the scattering contribution below 3 kHz. A detailed analysis of this phenomenon showed that the unexpectedly sharp low-frequency cut-
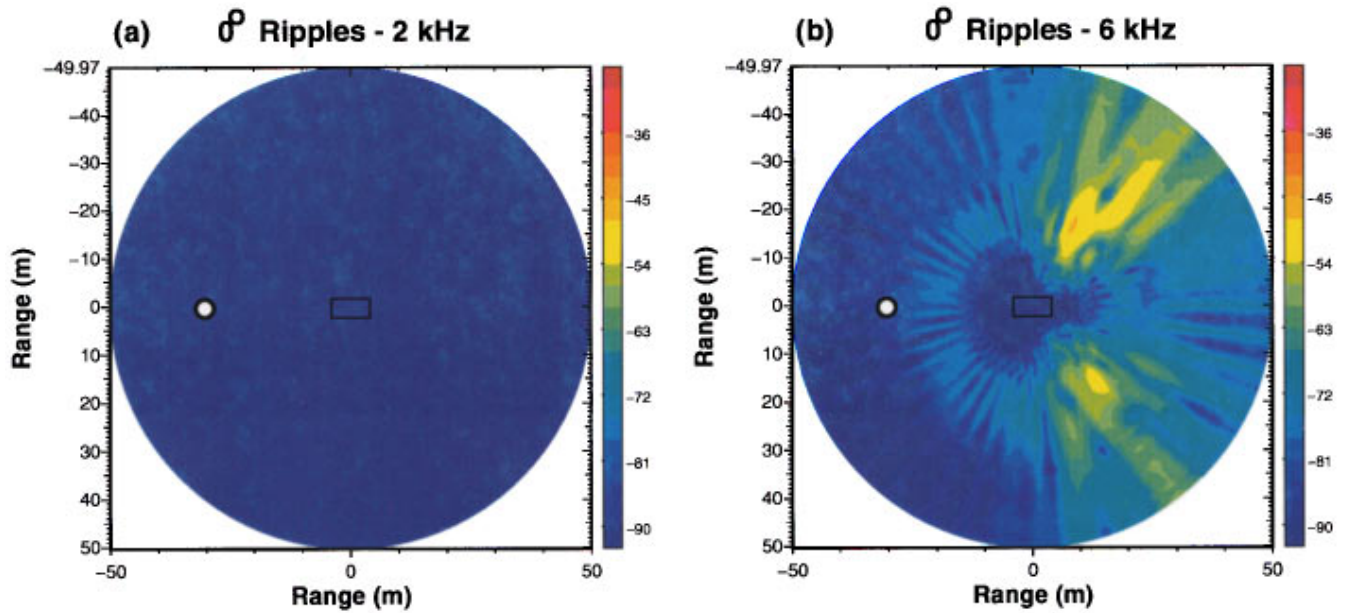
FIG. 6. 3-D scattering from rippled sand bottom insonified by narrow-beam sonar incident at a 0° aspect angle relative to the ripple axis. The incident field is a plane wave of 0 dB amplitude and 18° grazing angle. The plots show pressure level contours in dB at (a) 2 and (b) 6 kHz, in a horizontal plane 10 m above the seabed, centered at the sonar footprint. The small circles indicate the position of the source and monostatic receiver for a sonar with nominal 18° grazing angle incidence. The rectangle at the origin indicates the position and size of the roughness patch.

off is associated with the particular spectral characteristics of seabed ripples. Most scattering work in the past has been assuming Gaussian or power-law spectra of the seabed roughness,[20] which, when adopted here, resulted in a much more gradual frequency dependence of the scattering contribution.

This understanding then led to the hypothesis that the reverberant field in the water column would exhibit a similarly sharp low-frequency cut-off. Such a phenomenon, in combination with the low-frequency enhancement of the evanescent penetration and scattering by buried objects, in turn suggests that significant gains can be achieved in subcritical detection performance by operating below the environmentally determined "cut-off" frequency. The present study primarily focuses on the first hypothesis, i.e., the frequency dependence of the reverberation environment and its dependence on the ripple characteristics. A parallel study is dealing with the systems issues associated with the target detection problem.[21]

A. Environmental model

The environmental model is identical to the one used for the penetration study.[7] As a characteristic subcritical incidence scenario, we consider the geometry shown in Fig. 3. The water sound speed is 1525 m/s, while the bottom is sand represented by a fluid half-space with compressional velocity 1685 m/s and density 1.9 g/cm^3. The corresponding critical grazing angle is 25.17°. The seabed is insonified by a narrow-beam sonar at a nominal grazing angle of 18°. The sonar footprint is approximately 10×5 m.

Three different realizations of the ripple statistics are being considered, as shown in Fig. 4. They are being generated by the ripple model developed by Pouliquen et al.,[19]

based on statistics observed during the penetration experiment. The short correlation length L of the ripples is 20 cm and the root-mean-square (RMS) roughness height is 2.5 cm. Three different skewness angles are considered, 0°, 45°, and 90°. The associated roughness wave number spectra are shown in Fig. 5. Note the strongly polarized, almost monochromatic nature of the roughness spectra, and the filtering of the low-wave number components, inherent to this seabed model.[19] The very small amount of low- and high-wave number components of this roughness model is critical to the physics of the reverberation, as will be discussed in the following.

The roughness patches are shaded by a Hanning window consistent with the spatial width of the incident beam. The perturbation theory is linear in both the roughness γ_v and the coherent field χ_v in Eq. (11). Consequently, within the limits
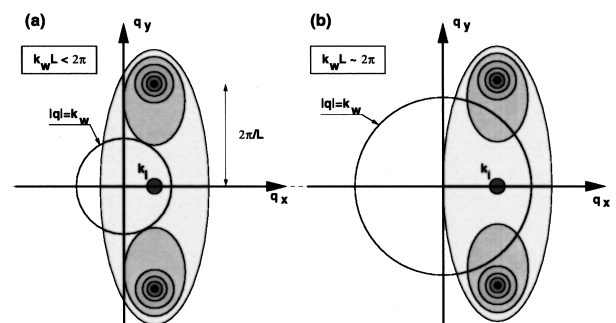
FIG. 7. Bragg scattering conditions for ripples of aspect angle 0° relative to incident field. The shading indicates the level of the roughness power spectrum, centered at the incident wave number k_i. The short correlation length of the ripples is L, and the water wave number is k_w. (a) Low frequency ($k_w L < 2\pi$). (b) Medium frequency ($k_w L \approx 2\pi$).
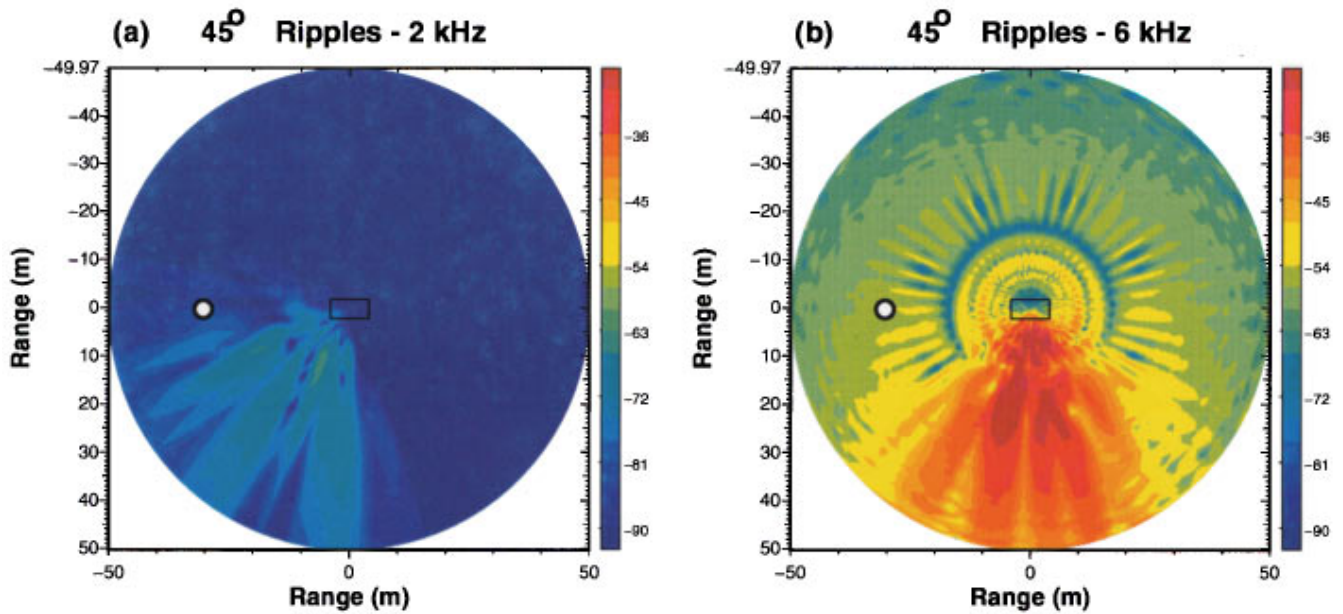
FIG. 8. 3-D scattering from rippled sand bottom insonified by narrow-beam sonar incident at a 45° aspect angle relative to the ripple axis. The incident field is a plane wave of 0 dB amplitude and 18° grazing angle. The plots show pressure level contours in dB at (a) 2 and (b) 6 kHz, in a horizontal plane 10 m above the seabed, centered at the sonar footprint. The small circles indicate the position of the source and monostatic receiver for a sonar with nominal 18° grazing angle incidence. The rectangle at the origin indicates the position and size of the roughness patch.

of the perturbation theory, the roughness shading is equivalent to a shading of the incident beam.

Even though OASES is capable of simulating the actual spectral content of the incident beam, it is much more computationally efficient to use the patch shading in combination with an incident plane wave, and the effect on the scattered field has been found to be insignificant. All the results shown in the following are therefore generated using a plane wave of unit amplitude (0 dB) incident at the nominal 18° grazing.

B. Reverberant field

The spatial and temporal distribution of the scattered field has been computed in the band 1–10 kHz, and covering ranges out to 50 m from the center of the footprint.

For the case of 0° ripples [Fig. 4(a)], Fig. 6 shows the cw power level in dB in a horizontal plane at the source depth, 10 m above the seabed, at a frequency of 2 (a), and 6 kHz (b). The dimensionless correlation length of the ripples at the two frequencies is $k_w L = 2 \pi f L / c = 1.6$ and 4.9, respectively. The dynamic range of the contour levels is 60 dB, with red indicating high field values, and blue, low. The small circle indicates the position of the source and a monostatic receiver for 18° nominal incidence. Note the extremely low reverberation levels at the low frequency, and the predominantly forward scattering at 6 kHz.

The explanation for this behavior is illustrated in Fig. 7 showing the wave number diagram similar to Fig. 2, but consistent with the specific ripple statistics. Thus, the gray shading indicates schematically the power spectrum of Fig. 5(a), centered at the incident wave number k_i corresponding to 18°. The circles indicate the medium wave number at the two frequencies, separating the *propagating* ($q_r < k_w$) and *evanescent* components of the scattered field in the water column. At low frequencies ($k_w L < 2 \pi$) most of the rough-

ness power is outside the circle and the associated scattering is therefore evanescent in the water column and not reaching the receiver at 10 m altitude.

At the higher frequency, the acoustic wavelength is of the same order of magnitude as the ripple correlation length ($k_w L \approx 2 \pi$), and the "tails" of the power spectrum enter the propagating spectrum, producing the "splitting" in the forward scattered field observed in Fig. 6(b). The backscattering even at this high frequency is obviously still rather insignificant, consistent with Fig. 7(b).

Figures 8 and 9 show the corresponding results for the 45° ripple aspect angle in Fig. 4(b). Again, the scattered field in the source plane is consistent with the Bragg conditions, with an overall increase in scattering at the higher frequency where more of the roughness power enters the propagating regime bounded by the circle $|q_r| = k_w$. The overall scattering, including the monostatic backscattering, is obviously in-
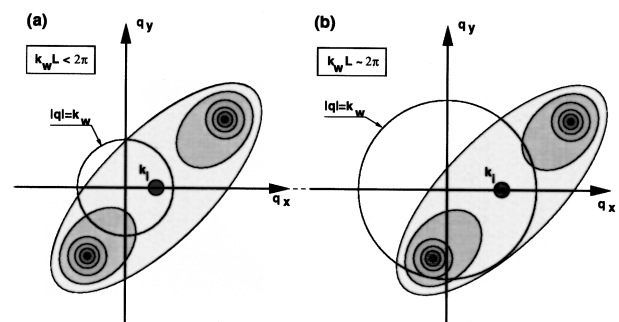
FIG. 9. Bragg scattering conditions for ripples of aspect angle 45° relative to incident field. The shading indicates the level of the roughness power spectrum, centered at the incident wave number k_i. The short correlation length of the ripples is L, and the water wave number is k_w. (a) Low frequency ($k_w L < 2 \pi$). (b) Medium frequency ($k_w L \approx 2 \pi$).
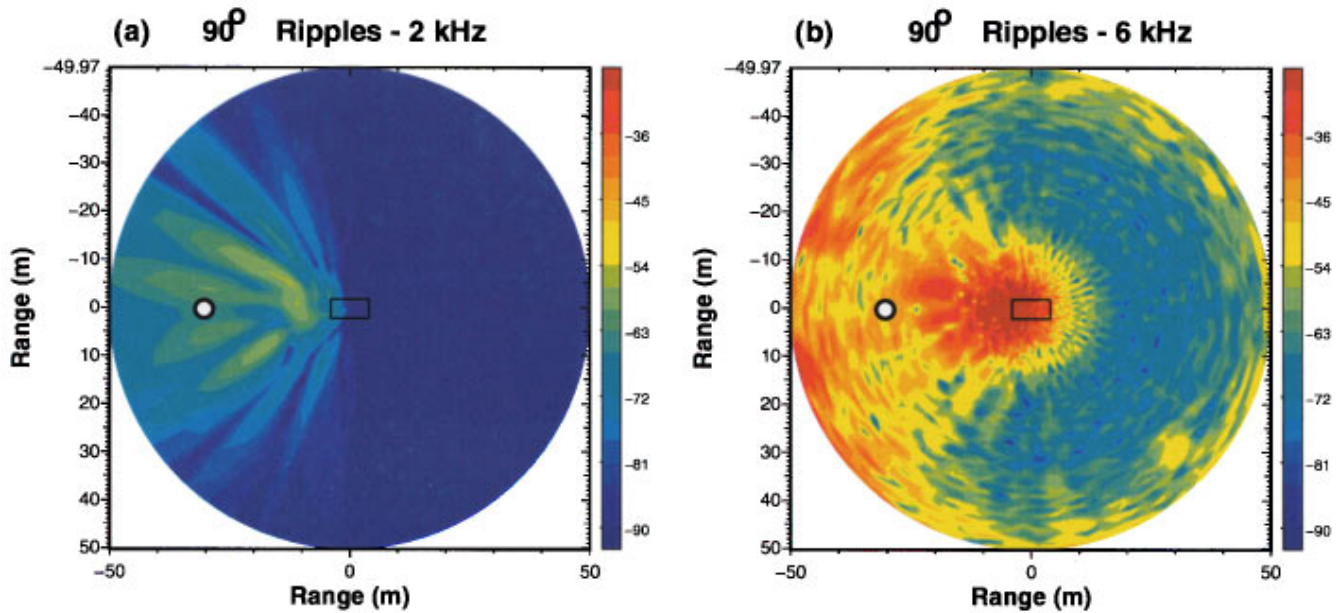
FIG. 10. 3-D scattering from rippled sand bottom insonified by narrow-beam sonar incident at a 90° aspect angle relative to the ripple axis. The incident field is a plane wave of 0 dB amplitude and 18° grazing angle. The plots show pressure level contours in dB at (a) 2 and (b) 6 kHz, in a horizontal plane 10 m above the seabed, centered at the sonar footprint. The small circles indicate the position of the source and monostatic receiver for a sonar with nominal 18° grazing angle incidence. The rectangle at the origin indicates the position and size of the roughness patch.

creased significantly compared to the case where the insonification is parallel to the ripples.

Finally, Figs. 10 and 11 show the result for the ripples being insonified at 90°. Here the difference between the two frequencies is particularly dramatic, with a very strong backscattering observed at 6 kHz. Note also the insignificant forward scattering in this case, the reason for which is that the forward lobe of the power spectrum is in the evanescent regime, as illustrated in Fig. 11. Also, the Bragg diagrams show that for this case a maximum in the backscattering can be expected for a frequency for which $2\pi/L = 2k_i$, which translates to a frequency of $f = 4.22$ kHz.

C. Target scattering

The implications of the temporal and spatial characteristics of the ripple reverberation become particularly evident when compared to the scattering produced by a seabed target. To illustrate this, OASES-3D has been applied to com-

FIG. 11. Bragg scattering conditions for ripples of aspect angle 90° relative to incident field. The shading indicates the level of the roughness power spectrum, centered at the incident wave number k_i. The short correlation length of the ripples is L, and the water wave number is k_w. (a) Low frequency ($k_wL < 2\pi$). (b) Medium frequency ($k_wL \approx 2\pi$).

pute the 3-D scattered field produced by a solid sphere of radius 30 cm, buried flush at the center of the sonar footprint, and insonified by a plane wave of 18° incidence. Analogous to the reverberation results above, Fig. 12 shows the scattered power in dB in a horizontal plane 10 m above the seabed, centered at the target and covering ranges out to 50 m. The spatial structure of the target scattering is obviously significantly different from the reverberation. Thus, the target scattering at 6 kHz, corresponding to $ka \approx 6.7$, shown in Fig. 12(b), is dominated by steep scattering angles, with a sharp drop in scattered power beyond a range of approximately 22 m, corresponding to the critical angle of 25.17°. At shorter ranges, the target scattering path corresponds to waves propagating in the bottom, while at longer ranges the coupling of the target scattering back into the water column is occurring through evanescent coupling, or ''tunneling.'' For $r > 22$ m a radial interference pattern is evident, being associated with interference between the ''tunneled'' direct arrival and a second diffracted (creeping wave) arrival from the target, as discussed later in relation to the temporal response. Another characteristic feature at the higher frequency is the strong forward lobe, even in the evanescent regime.

The corresponding result at 2 kHz ($ka \approx 2.2$) is shown in Fig. 12(a). Here the critical angle transition is much less distinct, and the scattering at the longer ranges is significantly higher than at higher frequencies. The reason for this is obviously the slower decay of the evanescent ''tail'' at subcritical angles, yielding improved penetration,[7] as well as more efficient energy tunneling back into propagating waves in the water column.

The most striking difference between the target scattering and the reverberation is of course the opposite frequency dependencies. Thus, from a monostatic as well as bistatic point of view, the target scattering beyond the ''critical''
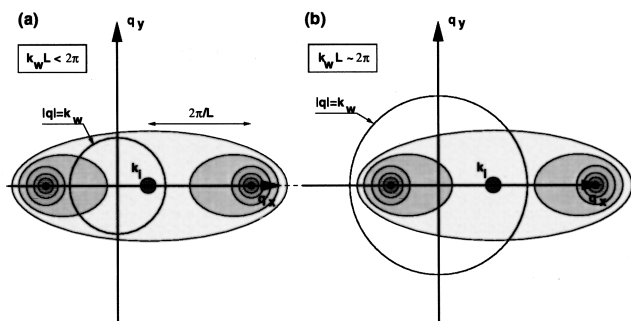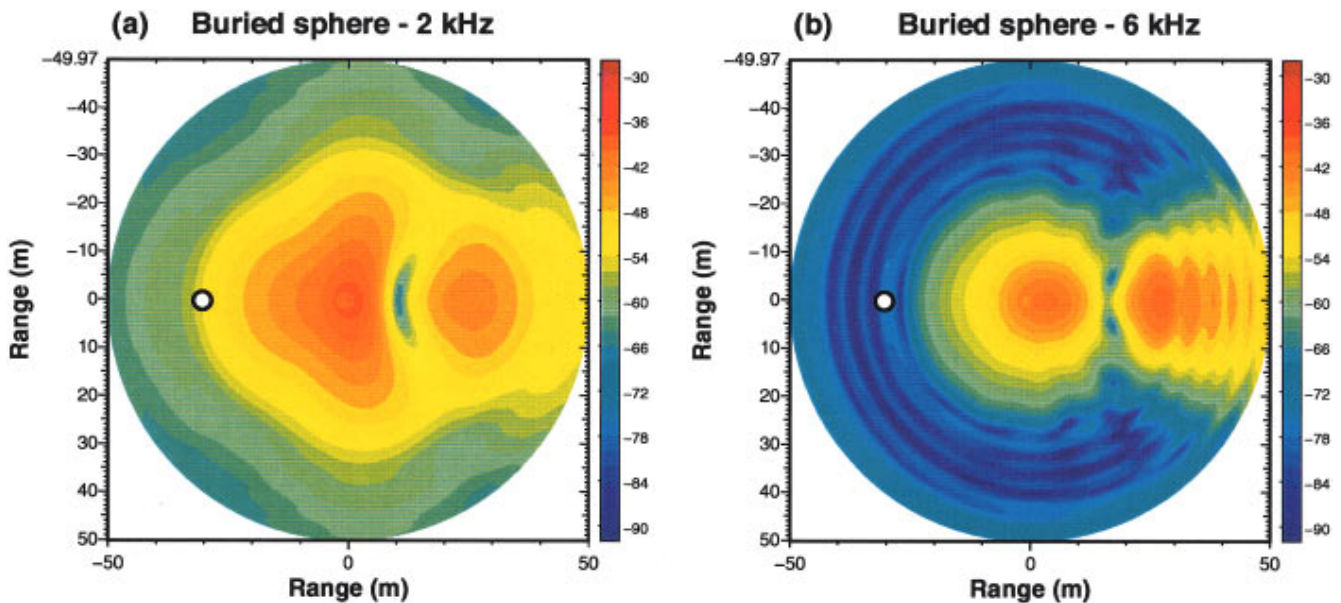
FIG. 12. 3-D scattering from 30 cm radius sphere buried flush in sand bottom insonified by a plane wave of 0 dB amplitude and 18° grazing angle. The plots show pressure level contours in dB at (a) 2 kHz ($ka \simeq 2.2$) and (b) 6 kHz ($ka \simeq 6.7$), in a horizontal plane 10 m above the seabed, centered at the sonar footprint. The small circles indicate the position of the source and monostatic receiver for a sonar with nominal 18° grazing angle incidence.

cone is increasing with decreasing frequency, in contrast to the reverberation, which increases dramatically with increasing frequency.

D. Monostatic backscatter

Even though the present study has been aimed at the physics of the 3-D scattering important to multi- and bistatic sonar concepts, there are still significant operational advantages in operating in a monostatic configuration, and here the particular spectral characteristics of the sand ripples have some interesting implications as well.

For a monostatic receiver, the results of the target and reverberation modeling for the subcritical incidence, 18°, are summarized in Fig. 13, showing the backscattering power versus frequency for the three different ripple polarizations as the solid curve (0°), the dashed curve (45°), and the dotted curve (90°). The monostatic backscattering power of the flush-buried sphere is shown as a dashed-dotted curve. Note that in contrast to the backscattering strength of a free floating target, which is approximately constant above $ka \simeq 1$, the backscattering strength of the flush-buried target has a distinct maximum at $ka \simeq 1$, associated with the frequency dependence of the evanescent excitation and scattering.

The dotted curve shows a clear maximum in the backscattering from the footprint at approximately 4 kHz, consistent with the Bragg condition as discussed above. Also, Fig. 13 shows a very strong dependence of the monostatic reverberation on the ripple aspect angle. Thus, at frequencies below 5 kHz, the reverberation from the 90° ripples is close to 60 dB higher than from the 0° ripples, and 20–30 dB higher than the backscattering power of the 45° ripples. At frequencies above 5–7 kHz, the differences reduce to 10–20 dB.

Figure 13 clearly illustrates the opposite frequency dependence of the buried target field and the reverberation for monostatic receivers. This in turn suggests that significant gains may be achieved in subcritical detection performance by limiting the bandwidth to frequencies below the ripple-induced "cut-off" frequency.

Of course, Fig. 13 shows results in terms of target and reverberation power, and does therefore not account for any time-domain processing gain. To investigate the performance implications of the sonar bandwidth for buried targets, the model has been used to simulate the temporal response at a monostatic receiver. Figure 14 shows the time series of the
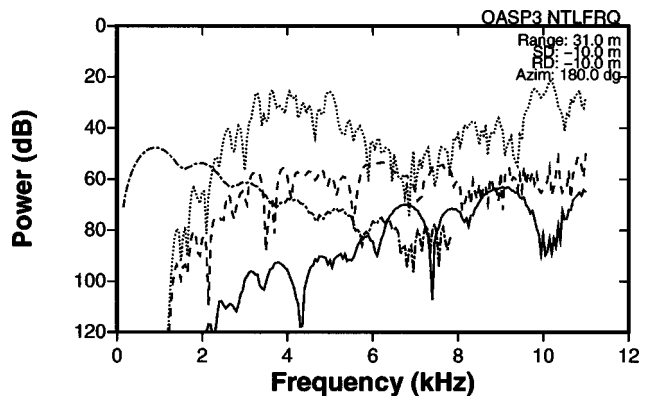
FIG. 13. Frequency dependence of monostatic reverberation power for ripple aspect 0 (solid curve), 45 (dashed curve), and 90° (dotted curve), corresponding to the footprints (a), (b), and (c) in Fig. 4, respectively. The incident field is a plane wave of 0 dB amplitude and grazing angle 18°. The monostatic receiver is at 10 m altitude and 31 m range, as indicated by the small circles in Figs. 6–10. The dashed-dotted curve shows the monostatic target return for a sphere of 30 cm radius buried flush in a smooth seabed.
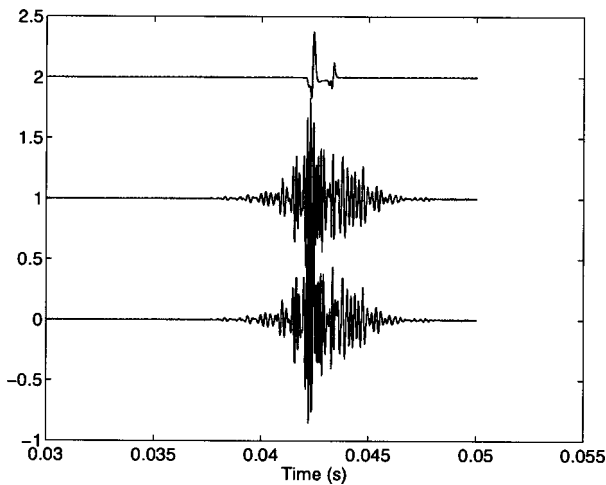
FIG. 14. OASES simulation of time series of acoustic pressure at a monostatic receiver at nominally 18° grazing angle. The upper trace shows the target signal, while the center trace shows the seabed reverberation for a ripple aspect of 45° aspect. The lower trace shows the total signal. All traces are plotted on the same scale.

pressure signal, band-limited to 0.5–10.5 kHz. The source pulse is a replica of a Ricker wavelet with center frequency 8 kHz, commonly used for the TOPAS secondary.[7] The incident field is again a unit amplitude 18° grazing angle plane wave. The upper trace shows the pure target signal at a receiver 10 m above the seabed at 30.77 m horizontal range, corresponding to the nominal 18° grazing angle. Note the double target arrival. The first arrival is the direct target return, generated by evanescent ''tunneling'' of energy back into the subcritical scattering angles. The second arrival is a diffracted arrival generated by a ''creeping wave'' traveling around the spherical target. The second trace shows the simulated reverberation time series for a ripple aspect angle of 45°. Finally, the lower trace shows the total received field, where the target signal is obviously totally dominated by the reverberation.

To illustrate how the different spectral characteristics of the target and the reverberation may be explored for detection, Fig. 15 shows the spectrograms corresponding to the time series in Fig. 14. The upper plot shows contours of the spectrogram of the pure target signal, while the middle and lower plots show the spectrograms of the reverberation and the total field, respectively. Here it becomes evident that the only significant information about the presence of a buried target in this scenario is at frequencies below the reverberation ''cut-off'' frequency of 2–3 kHz. This suggests that improved detection performance can be achieved by band-limiting the processing frequencies as opposed to using the full band. The investigation of this hypothesis and the associated sonar processing issues is the subject of a parallel research effort at SACLANTCEN.[21]

Along the same line, the ripple orientation relative to the insonification is obviously extremely critical to the detection problem. Thus, as can be observed in Fig. 13, by insonifying along the direction of the ripples, the bandwidth associated with positive target-to-reverberation ratio is obviously increased significantly, from 2 to 6 kHz, compared to the case where the insonification is perpendicular to the ripples. Also,

the ripple ''wavelength'' is a critical parameter. Thus, larger scale ripples encountered in deeper water will shift the reverberation ''cut-off'' to a lower frequency, while shorter near-shore ripples will be associated with less low-frequency reverberation.

To take advantage of such environmental reverberation dependencies in an operational scenario, the sonar system must be closely tied to the environmental assessment and have adaptive capabilities which allow the platform to select optimal insonification and reception geometries.

III. CONCLUSION

A new wave theory model providing consistent modeling of seabed insonification, three-dimensional target scattering, and rough seabed reverberation has been used to investigate the spatial and temporal characteristics of the multistatic acoustic field associated with narrow-beam sonars for seabed target detection and classification.

The reverberation environment associated with hydrodynamically induced ripple structures in water of 10–20 m depth is found to be strongly frequency dependent in the 1–10 kHz regime, with the most distinct feature being a very sharp drop in the reverberation below a ''cut-off'' frequency, which for sand ripples of 20 cm wavelength is approximately 2 kHz.

This low-frequency ''cut-off'' feature is a result of the specific, highly polarized, roughness spectrum associated with sand ripples. Thus, the wave number spectrum of the ripple fields in this study has insignificant low-wave number components. In contrast, the traditional power-law roughness spectra used for characterizing seabeds have their maximum spectral content at the low wave numbers, resulting in a more gradual reverberation decay toward lower frequencies.

In addition to the drastic drop in reverberation observed at low frequencies, the analysis also demonstrates theoretically that enhanced subcritical backscattering from buried objects is achieved at frequencies below 4–5 kHz. The combined effects suggest that *enhanced detection performance can be achieved by limiting the processing bandwidth to frequencies below typically 3–4 kHz, in contrast to traditional sonar philosophy of expanding bandwidth to achieve enhanced processing gain against reverberation.*

Also, the analysis suggests, that at low frequencies in particular, a dramatic, up to 60 dB, reduction in reverberation power can be achieved by insonifying the seabed along the ripple direction.

These results in turn suggest the development of new *environmentally adaptive sonar technology* that takes optimum advantage of the strong temporal and spatial sensitivity of the seabed interaction.

However, it should be stressed that these conclusions concern only the *ripple-induced reverberation* properties. Thus, for example, it must be assumed that real ripple fields are superimposed on a finite isotropic seabed roughness which will counter the drastic low-frequency cutoff in the reverberation power predicted here, with the resultant frequency dependence of the reverberation becoming less dramatic. The relative role of such isotropic roughness components is the object of a continued modeling and experimental
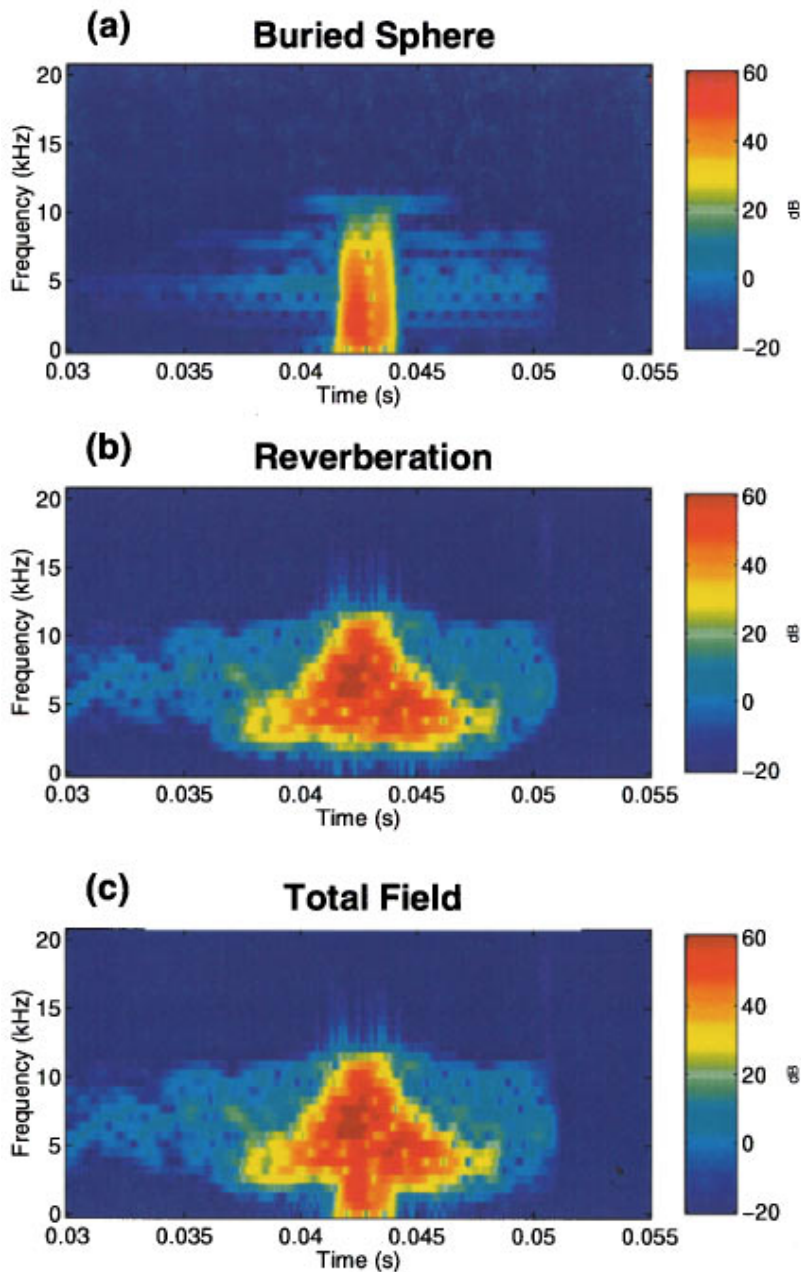
FIG. 15. Spectrograms of monostatic receiver time series simulated by OASES-3D. (a) Target signal alone. (b) Reverberation for 45° ripple aspect. (c) Total signal.

analysis effort, but unfortunately the low-wave number roughness components of real seabeds are not easily determined. On the other hand, even though the absolute reverberation levels are affected by such roughness components, the conclusions of this study are qualitatively unchanged. Also, the spatial filtering provided by the seabed ripples is countered by scattering from bedrock roughness and volume inhomogeneities such as buried rocks and boulders, which may become significant at low frequencies. Another effect that will affect the signal–reverberation ratio is the frequency dependence of the sonar footprint. The present study assumed a constant sonar footprint, whereas the insonified area for parametric sonars will be approximately inversely proportional to the frequency squared, countering the predicted decay of the ripple scattering.

The evaluation of the relative significance of these various mechanisms affecting low-frequency bottom reverbera-tion requires a series of well controlled experiments incorporating different bottom types, seabed roughness statistics, and source–receiver geometries. The GOATS'98 experiment carried out jointly between SACLANTCEN and MIT in May 1998 included measurements of the full three-dimensional reverberant field, which according to the models described here were significantly different for the various scattering and reverberation mechanisms.

[1] E. I. Thorsos, D. R. Jackson, J. E. Moe, and K. L. Williams, ''Modeling of subcritical penetration into sediments due to interface roughness,'' in *High Frequency Acoustics in Shallow Water*, edited by N. G. Pace, E. Pouliquen, O. Bergem, and A. P. Lyons, SACLANTCEN Conference Proceedings series CP-45, 1997.

[2] N. P. Chotiros, ''Biot model of sound penetration in water saturated sand,'' J. Acoust. Soc. Am. **97**, 199–214 (1995).

[3] K. L. Williams and D. R. Jackson, ''Bottom bistatic scattering: Experimental results and model comparison for a carbonate sediment,'' in *High Frequency Acoustics in Shallow Water*, edited by N. G. Pace, E. Pouliquen, O. Bergem, and A. P. Lyons, SACLANTCEN Conference Proceedings series CP-45, 1997.

[4] H. Schmidt, J. Lee, H. Fan, and K. LePage, ''Multistatic bottom reverberation in shallow water,'' in *High Frequency Acoustics in Shallow Water*, edited by N. G. Pace, E. Pouliquen, O. Bergem, and A. P. Lyons, SACLANTCEN Conference Proceedings series CP-45, 1997.

[5] J. A. Fawcett, ''Scattering from an elastic cylinder buried beneath a rough water/basement interface,'' in *High Frequency Acoustics in Shallow Water*, edited by N. G. Pace, E. Pouliquen, O. Bergem, and A. P. Lyons, SACLANTCEN Conference Proceedings series CP-45, 1997.

[6] F. Jensen, W. A. Kuperman, M. B. Porter, and H. Schmidt, *Computational Ocean Acoustics* (AIP Press, New York, 1994).

[7] A. Maguer, E. Bovio, W. L. Fox, E. Pouliquen, and H. Schmidt, ''Mechanisms for subcritical penetration into a sandy bottom: Experimental and modeling results,'' SACLANT Undersea Research Centre, SR 287, La Spezia, Italy, 1998.

[8] H. Schmidt, OASES, Version 2.1, user guide and reference manual. Technical report, Massachusetts Institute of Technology, 1997.

[9] *Simrad TOPAS PS 040 Operator Manual*, Bentech Subsea AS, Stjørdal, Norway.

[10] W. A. Kuperman and H. Schmidt, ''Self-consistent perturbation approach to rough surface scattering in stratified elastic media,'' J. Acoust. Soc. Am. **86**, 1511–1522 (1989).

[11] H. Schmidt and W. A. Kuperman, ''Spectral representations of rough interface reverberation in stratified ocean waveguides,'' J. Acoust. Soc. Am. **97**(4), 2199–2209 (1995).

[12] K. LePage, ''Elastic scattering in oceanic waveguides,'' Ph.D. Thesis, Massachusetts Institute of Technology, June 1992.

[13] H. Schmidt and J. Glattetre, ''A fast field model for three-dimensional wave propagation in stratified environments based on the global matrix method,'' J. Acoust. Soc. Am. **78**, 2105–2114 (1985).

[14] B. Tracey and H. Schmidt, ''Seismo-acoustic field statistics in shallow water,'' IEEE J. Ocean Eng. **22**, 317–331 (1997).

[15] H. Fan, ''Wave theory modeling of three-dimensional seismo-acoustic reverberation in ocean waveguides,'' Ph.D. Thesis, Massachusetts Institute of Technology, September 1995.

[16] F. Ingenito, ''Scattering from objects in a stratified medium,'' J. Acoust. Soc. Am. **82**, 2051–2069 (1987).

[17] N. C. Makris, ''A spectral approach to 3-D object scattering in layered media applied to scattering from submerged spheres,'' J. Acoust. Soc. Am. **104**, 2105–2113 (1998).

[18] J. Fawcett, ''Finite element modelling of three-dimensional scattering from azimuthally-symmetric elastic shells,'' SACLANT Undersea Research Centre, SR 273, La Spezia, Italy, 1998.

[19] E. Pouliquen, A. Lyons, and N. G. Pace, ''Penetration of acoustic waves into sandy seafloors at low grazing angles: The Helmholtz-Kirchhoff approach,'' SACLANT Undersea Research Centre, SR 290, La Spezia, Italy, 1998.

[20] E. I. Thorsos and D. R. Jackson, ''The validity of the perturbation approximation for rough surface scattering using a Gaussian roughness spectrum,'' J. Acoust. Soc. Am. **86**, 261–277 (1989).

[21] W. L. Fox and A. Maguer, ''Detection of buried objects at low grazing angles: Preliminary experimental results,'' SR 293, SACLANT Undersea Research Centre, La Spezia, Italy, 1998.

Kronecker autoregressive and spherical harmonic ambient noise models

Alain C. Barthelemy[a)]

Northrop Grumman Norden Systems, Inc., 10 Norden Place, P.O. Box 5300, MS C121, Norwalk, Connecticut 06856

Peter K. Willett[b)]

University of Connecticut, Electrical and Systems Engineering, 260 Glenbrook Road, Box U-157, Storrs, Connecticut 06268-3157

This paper develops two new models for ambient noise processes which exist in the deep ocean. The first model, termed the Kronecker autoregressive model, extends existing ideas regarding the use of linear models on uniform line arrays. The paper shows that the novel parametrization accurately models physical noise processes for uniformly sampled volumetric arrays. A new proof is presented which shows that for the case of purely sinusoidal signals, the Kronecker form provides an exact model, suggesting its use for colored noise sources. The second model uses a form of the spherical harmonic expansion to develop an original linear matricial model. Additionally, this paper presents a new algorithm needed for computing the weighting coefficients involved with this model. © *1999 Acoustical Society of America.* [S0001-4966(99)05103-6]

PACS numbers: 43.30.Nb [SAC-B]

INTRODUCTION

Numerous experimental and analytical studies describe underwater ambient noise mathematically, by computing spatial correlation functions theoretically,[1–5] experimentally, with at-sea measurements,[5–7] and numerically, by modeling ocean noise statistics.[8]

These studies indicate that nonisotropic additive ambient sensor noise exists in the ocean. In the deep ocean, ambient noise exhibits a frequency-dependent, vertical directionality: at low frequencies, distant shipping causes an increased noise about the horizontal; at high frequencies, wave action imparts an increased noise about the vertical.[2,4] A mixed spectral acoustic environment[9] exists, consisting of discrete frequency sources (tonals) and continuous frequency sources (colored noise). Direction finders exhibit high false alarm rates in the presence of spatially colored ambient noise. Standard methods applied in practice exhibit serious degradations in terms of bias, angular resolution, spurious peaks, nondetection of weak sources, and estimate of the number of sources.[10] To combat the effects of colored noise, prewhitening algorithms have been developed.[11–13]

Although some mathematical models for spatial noise correlations accurately represent physical phenomena, they may not be amenable for expression in terms of a vector parametrization. The work by LeCadre[7,11,12] demonstrates that a linear model, namely an autoregressive (AR) parametrization of the noise approximately equals the physical results in the case of a uniform line array. Indeed, since an array with regularly spaced elements provides spatially uniform data samples (and assume temporally regular data), an AR model seems appropriate. Many authors choose the AR parametrization in their work, for example, Nagesha and Kay,[14] Ye and DeGroat,[15] and Tewfik.[16] In fact, Tewfik[16] makes a strong statement, paraphrased here, regarding the utility of the AR model:

> Fortunately, it has been established in Ref. 11 that noise processes that result from known background underwater noise fields have power spectra that can be adequately modeled by low-order rational AR models.

However, the uniform line array AR parametrization suffers two significant drawbacks, in that its geometry represents a subset of the important volumetric, or general, case (see Ref. 13) and the requirement for uniform sampling constrains the use of AR models.

For the case of an arbitrarily oriented volumetric array when correlation exists due to a nonisotropic noise environment, physical correlation models become paramount. Ambient noise due to natural phenomena and human causes exists in the ocean. Two excellent references by Burdic (Ref. 1, pp. 297–302) and Wenz[5] describe common sources of acoustic ambient noise in the ocean. Wenz identifies many physical sources of ambient noise such as thermal agitation from molecular movement of the medium, hydrodynamic sources from bubbles, water droplets, surface waves, and turbulence, and oceanic traffic from ships. Wenz characterizes each of these sources on a composite plot (Ref. 5, p. 1952, Fig. 13) showing relative sound pressure spectrum level versus frequency band (and for the case of wind-related effects, for several wind intensities).

The physical source component of interest for this paper includes high-frequency hydrodynamic sources due to surface waves caused by wind. These waves in turn generate oscillating bubbles, adding to the effect. The lower frequency sound generated by distant oceanic traffic in shipping lanes constitutes the principal human contribution.
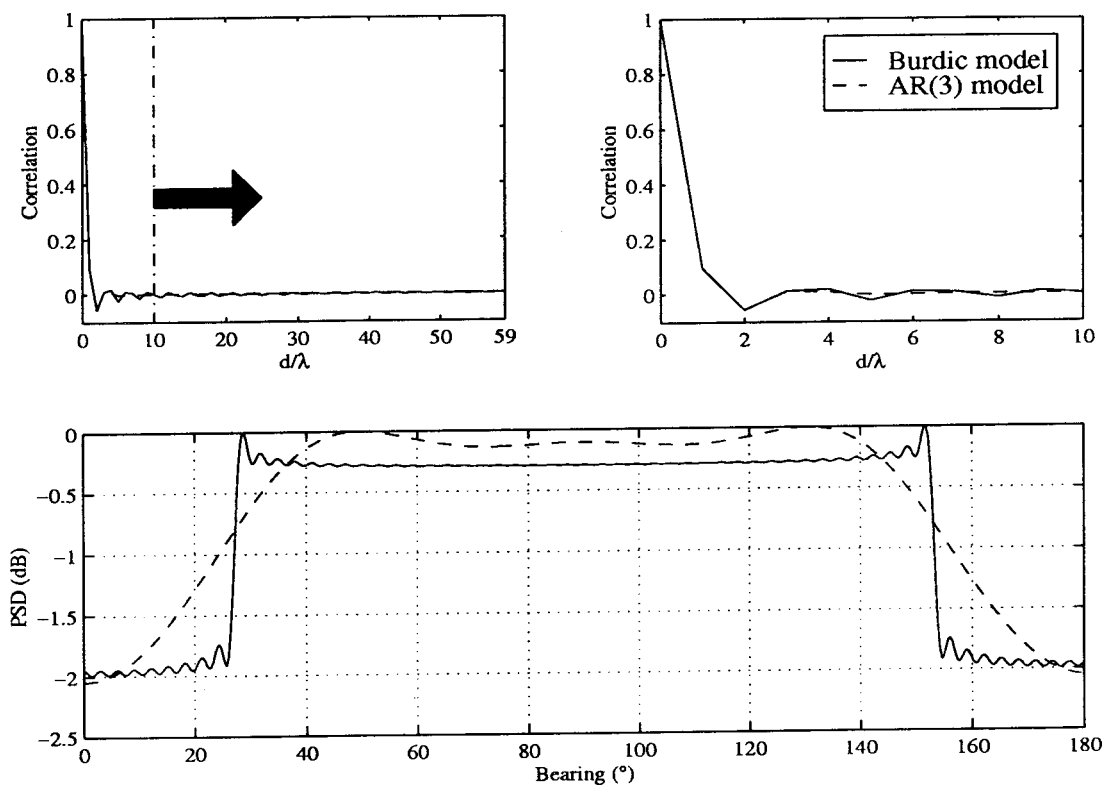
FIG. 1. Correlation sequence (with zoom-in) and power spectral density for isotropic (white) noise as modeled by Burdic (solid lines) and an AR(3) model approximation (dotted line). The array contains 60 elements and has 0.45 wavelength spacing.

Burdic (Ref. 1, pp. 306–314) formulates the physical properties mathematically, by identifying the correlation properties of three types of angular noise distributions of ambient noise: isotropic, surface, and impulsive. Burdic[1] makes the important assumption that the cross correlation between any two sensors depends only on the distance between them, not on their relative orientation in space. The Cox[2] model generalizes Burdic's work[1] by incorporating the orientation into the correlation computation.

Previous ambient noise models[11,12] worked only for uniform line arrays, primarily for noise sources broadside to the uniform line array, or consisted of complicated mathematical models derived from physical principles.[1,2] These models were not amenable to generalized volumetric array geometries, and not amenable to algorithm development, say, to develop a prewhitening algorithm (see Refs. 13, 17, and 18). Additionally, it is unclear whether new techniques, such as the relative entropy functional,[19] will be easy to generalize to general volumetric arrays.[20]

This work generalizes the use of AR models to volumetric, uniformly sampled arrays through the use of a novel parametrization, termed the Kronecker AR model. The work proves that such a model generates spatial densities which approximate physical ambient noise processes. The work develops the complex AR model and shows how it may be used for nonbroadside ambient noise sources. This paper performs a novel application of two information theoretic criteria to show the low dimensionality associated with such a model. The paper applies the Levinson–Durbin–Wiggins algorithm[21] to prove the validity of such a model. As further validation of the model, a new proximity metric is defined which compares the Kronecker AR model with physically generated ones.

This work develops an original linear matrix parametrization based on the spherical harmonic expansion which is applicable to general volumetric arrays. This model provides a simple parametrization in terms of real weighting coefficients. As part of this model, a new computational algorithm is presented which computes model parameters for arbitrary orders in the expansion.

The format of this paper is as follows. In Sec. I we describe the novel parametrizations and extensions to previous work for the case of uniformly sampled and volumetric arrays. In Sec. II we summarize the results of this work.

I. AMBIENT NOISE MODELS

A. Uniformly sampled arrays

A qualitative comparison between Burdic's models[1] and AR processes with real coefficients provides justification for the use of AR models. The Levinson algorithm (Ref. 22, pp. 161–171) is used to compute the AR coefficients from Burdic's correlation estimates[1] and the form of the power spectral density from (Ref. 22, p. 111) is used. Figure 1 plots the correlations and power spectral densities (PSDs) obtained from Burdic's model[1] for isotropic noise as solid lines. The dotted line in the figure depicts results for an AR processes of order 3. The figure represents results for a 60-element array with 0.45-wavelength spacing, temporal frequency of interest 500 Hz, and speed of propagation 1498 m/s (a more
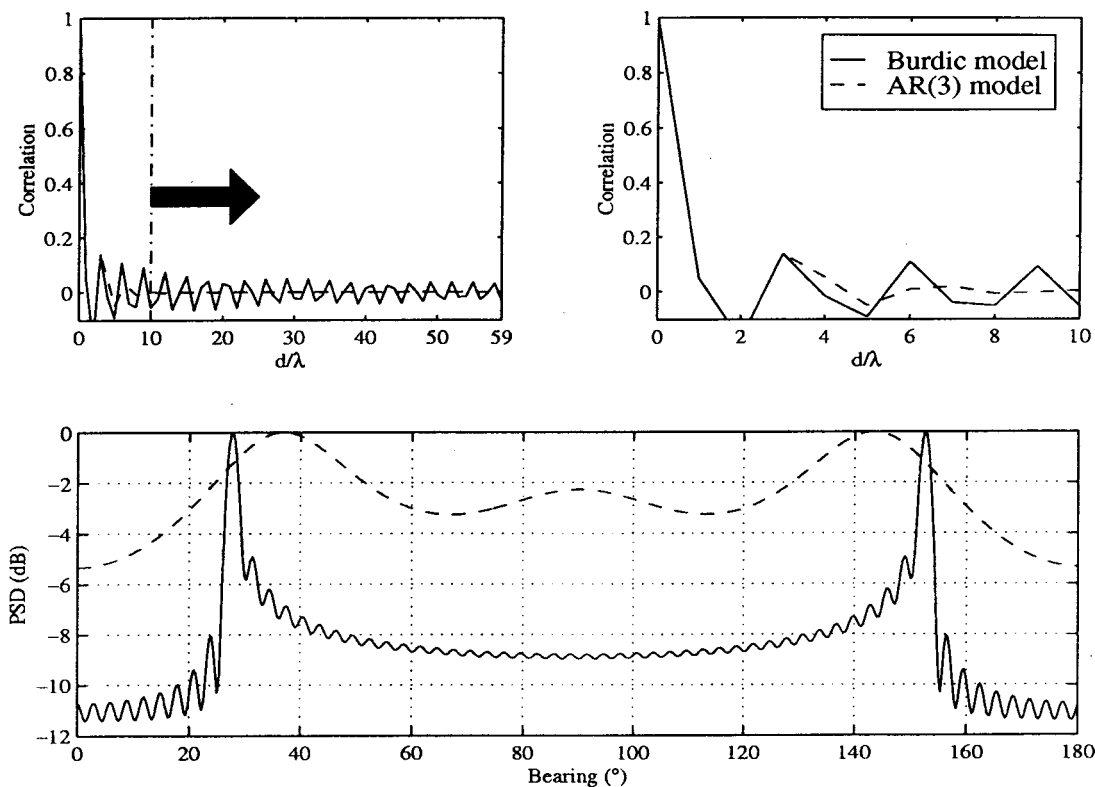
FIG. 2. Correlation sequence (with zoom-in) and power spectral density for impulsice (possibly due to distant shipping) noise as modeled by Burdic (solid lines) and an AR(3) model approximation (dotted line). The array contains 60 elements and has 0.45 wavelength spacing.

illustrative figure results from spacing of slightly less than 0.5 wavelength). Figure 2 illustrates similar results for noise due to distant shipping (impulsive noise) with a half-wavelength array. Figure 3 illustrates results for noise due to surface waves. All three figures illustrate a workable degree of fit for AR models with typical noise.

Figure 4 depicts plots of two AR model order selection criteria versus search index for the correlations due to surface noise from a single line array with 12 sensors. The two criteria use the forms from Kay's book (Ref. 22, pp. 234–237). Figure 5 shows a similar plot for correlations due to shipping noise. Clearly, both criteria estimate a low model order in the vicinity of 2 for both types of noise.

Next we explore the relationship between autoregressive coefficients and steered colored or extended noise sources. This relationship is necessary for relating complex AR coefficients and direction-of-arrival angle for the extended noise sources.

For simplicity of exposition, employ a quarter wavelength uniform line array with a single impinging extended noise source arriving from direction-of-arrival angle θ. Assume that $\theta=90$ degrees represents broadside to the array. A first-order autoregressive process models the ambient noise with the coefficient

$$a_1 = -0.7. \tag{1}$$

Since this coefficient is purely real, the spatial density of the resulting process is broadside to the array as depicted in Fig. 6.

Now to model the same AR(1) source as one arriving from $\theta=45$ degrees rather than broadside, use the equation

$$\tilde{a}_1 = a_1 e^{j2\pi d \cos\theta} = 0.4240 - 0.5570j, \tag{2}$$

where d represents intersensor spacing, here $d=\lambda/2$. Figure 7 represents the spatial density of this process.

Figures 1–7 demonstrate the effectiveness of unidimensional AR models for modeling correlation and spectral density properties of ambient ocean noise. A natural approach suggests the use of multidimensional AR models for uniform planar or uniform volumetric arrays.

For planar arrays, the aim of this research is to model the noise impinging on this $M \times N/M$ array as a multidimensional AR process of maximum order $(M,N/M)$. The validity of the uniform line array model enforces this assumption. To test the validity of this model on a typical array, perform the following operations:

(1) Compute the Cox[2] shipping noise correlation coefficients for the array.
(2) Compute the power spectra of the correlation coefficients via the two-dimensional discrete Fourier transform (DFT).
(3) Use the Levinson–Wiggins–Robinson algorithm[21] to compute the two-dimensional AR coefficients.
(4) For a selected AR order, compute the associated correlations.
(5) From these correlations, compute the PSD from the AR coefficients via the spatial Wiener–Khintchine theorem (Ref. 23, p. 117).
(6) Compare the two power spectra.

Figure 8 depicts the PSDs obtained for a 3×12 planar array. Notice that the Cox[2] model assumes that the noise fields are uniform in azimuth ϕ. The nomenclature 4-D re-
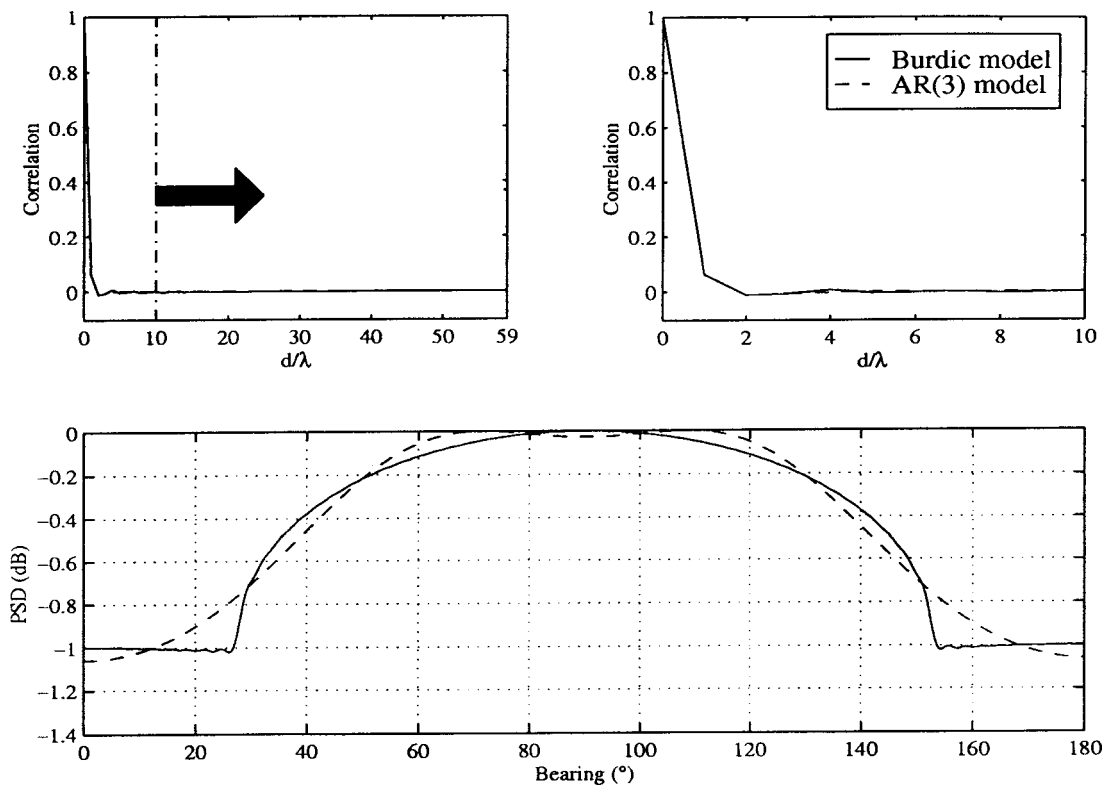
FIG. 3. Correlation sequence (with zoom-in) and power spectral density for surface-generated (possibly due to wind and wave action) noise as modeled by Burdic (solid lines) and an AR(3) model approximation (dotted line). The array contains 60 elements and has 0.45 wavelength spacing.

fers to the Wiener–Khintchine result, while the reduced AR order depicts results for an order of (3,2). The reduced AR model displays a good fit with the physical one (''good'' implying that the model is suitable and meets the expectations of this paper).

A similar analysis is performed here for arrays with volumetric aperture. As an example, consider a $2\times2\times12$ uniform volumetric array. Figure 9 depicts the reduced AR order power spectral density for order (3,2,2). Again this spectrum contains the expected shape for noise due to distant shipping.

Although the multi-dimensional AR model approach seems alluring, for very large volumetric arrays where the total number of sensors often reaches into the tens or hundreds, however, the required estimation order of AR parameters becomes prohibitive. Two approaches reduce associated problem dimensionality: reduction of region of support for AR models, and the use of Kronecker matrix product.
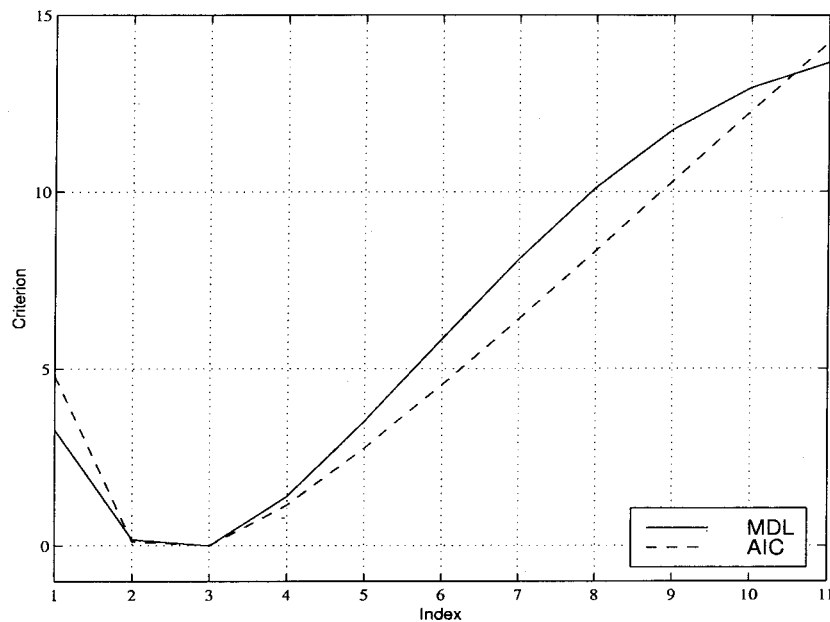
FIG. 4. The AIC and MDL model order selection criteria for surface noise impinging on a single line 12-sensor array. The minimum of both curves is at 3, which represents the estimated AR model order. The MDL measure employs 1000 data snapshots. Both curves are scaled and normalized.
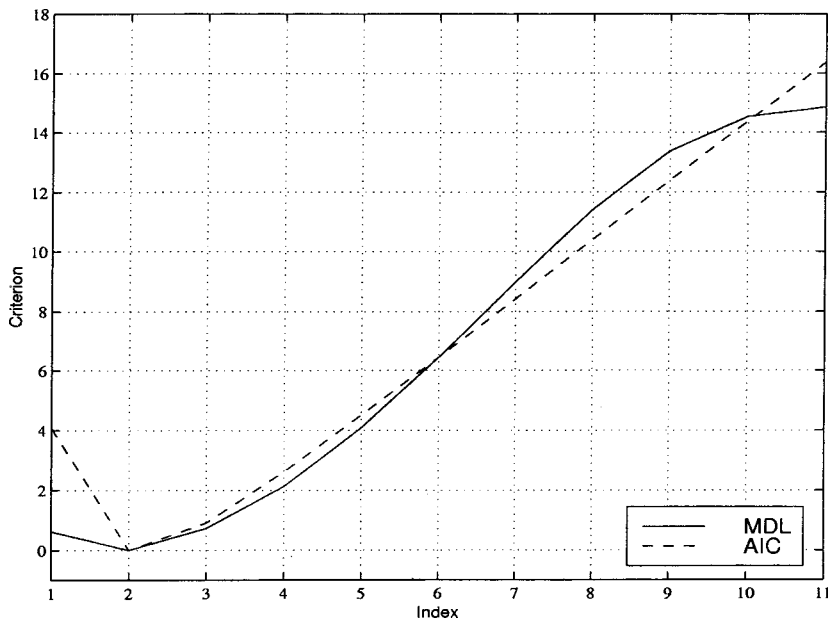
FIG. 5. The AIC and MDL model order selection criteria for shipping noise impinging on a single line 12-sensor array. The minimum of both curves is 2, which represents the estimated AR model order. The MDL measure employs 1000 data snapshots. Both curves are scaled and normalized.

Given a uniform planar array with M lines of N/M sensors per line, N represents the total number of elements. To restrict the region of support, reduce this region by the bound (p_x, p_z), where $p_x \leq N/M$ and $p_z \leq M$. For the uniform cuboid case, represent the bounded coefficient region by (p_x, p_y, p_z), where $p_z p_y \leq M$ and $p_x \leq N/M$.

Two problems exist with the reduced order parametrization for the planar and volumetric cases. The total number of coefficients to estimate still equals $p_x p_y$ and $p_x p_y p_z$, respectively, which may represent a large number of parameters. The second problem involves the functional relationship between the coefficients and the correlation matrix derived from them, which makes it difficult to form a vector parametrization of the total correlation matrix derived from the coefficients. A Kronecker product model provides a functional relationship while simultaneously reducing the number of parameters. Reference 24 describes an argument demon-

strating that for sinusoidal signals, the Kronecker model equals the classical model exactly. This relationship suggests that an extension to colored noise sources is feasible.

Notice that for uniformly spatially sampled multiple line arrays, the Cox[2] model generates noise correlation matrices with block Toeplitz structure. Denoting this matrix by $\mathbf{Q}$, for an M line by N/M sensors per line array, the matrix assumes the structure

$$\mathbf{Q} = \underbrace{\begin{bmatrix} \overbrace{\mathbf{Q}_{11}}^{N/M \times N/M} & \mathbf{Q}_{21}^H & \cdots & \mathbf{Q}_{M1}^H \\ \mathbf{Q}_{21} & \ddots & \ddots & \vdots \\ \vdots & \ddots & \ddots & \mathbf{Q}_{21}^H \\ \mathbf{Q}_{M1} & \cdots & \mathbf{Q}_{21} & \mathbf{Q}_{11} \end{bmatrix}}_{N \times N}, \tag{3}$$
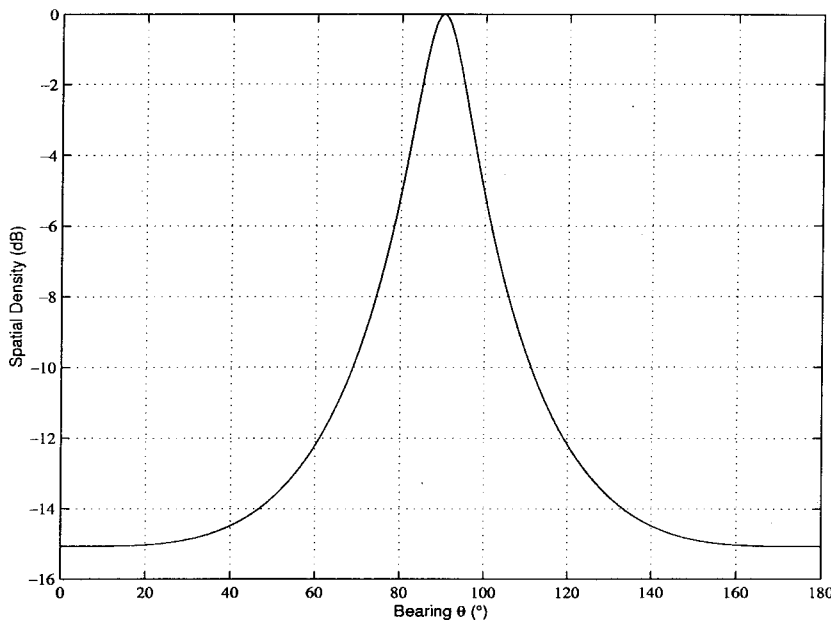
FIG. 6. Spatial density of ambient noise, modeled as a first-order autoregressive process, plotted versus bearing. Since the coefficient, $\mathbf{a}_1 = -0.7$ is real, the ambient noise modeled by this process has its peak broadside to the array.
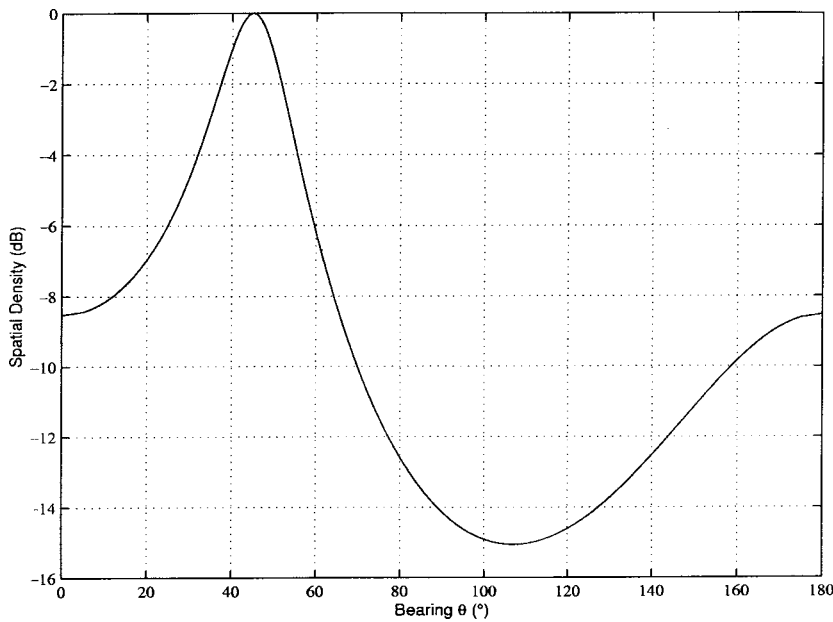
FIG. 7. Spatial density of ambient noise, modeled as a first-order autoregressive process impinging from 45 degrees, plotted versus bearing. In this case, since the coefficient $\mathbf{a}_1 = 0.4240 - 0.5570j$ is complex, the ambient noise modeled by this process has its peak off-broadside to the array at 45 degrees.

where $\mathbf{Q}_{ij}$, $\forall i,j = 1,2,...,M$ represents a set of $N/M \times N/M$ Toeplitz and symmetric ($\mathbf{Q}_{ij} = \mathbf{Q}_{ij}^T$) block elements. The index across lines applies for planar or cuboid geometry, as long as sequential indexing exists. For example, the matrix $\mathbf{Q}_{ij}$ represents the cross-correlation matrix between lines i and j across all N/M sensors, while the diagonal blocks when $i = j$ represent the autocorrelation matrices of each ith line.

Thus, to construct this matrix with the Kronecker product, use matrices of dimension

$$\underbrace{\mathbf{Q}}_{N \times N} = \underbrace{\mathbf{Q}_\uparrow}_{M \times M} \otimes \underbrace{\mathbf{Q}_\swarrow}_{N/M \times N/M} , \tag{4}$$

where the arrows denote orientation on a planar array (xz plane, z vertical, array parallel to x direction) and the symbol $\otimes$ represents the Kronecker product (see Appendix A for a brief discussion of the Kronecker product). For volumetric

arrays, to preserve the overall size of the matrix, measure the cross-sectional grid, and partition the parametrization properly.

Since the Gohberg–Semencul relation[25] directly parametrizes the inverse of each Toeplitz subblock ($\mathbf{Q}_\uparrow^{-1}, \mathbf{Q}_\rightarrow^{-1}, \mathbf{Q}_\swarrow^{-1}$) in terms of AR coefficients, the partitioning into Toeplitz matrix elements of the block matrix provides the desired total parametrization. Equally important, by employing the Kronecker product, problem dimensionality reduces dramatically. The nomenclature p_x, p_y, p_z denotes the respective AR orders for each matrix ($\mathbf{Q}_\uparrow, \mathbf{Q}_\rightarrow, \mathbf{Q}_\swarrow$). Hence for the planar case, the term $p_x p_y$ represents the reduced AR order from above, while $p_x + p_y$ represents the Kronecker reduced order. For the three axis case, model order reduces to $p_x + p_y + p_z$. Thus, the Kronecker product model meets our criteria for a low-order functional surface to optimize over.

Application of the Levinson–Wiggins–Robinson[21] algo-
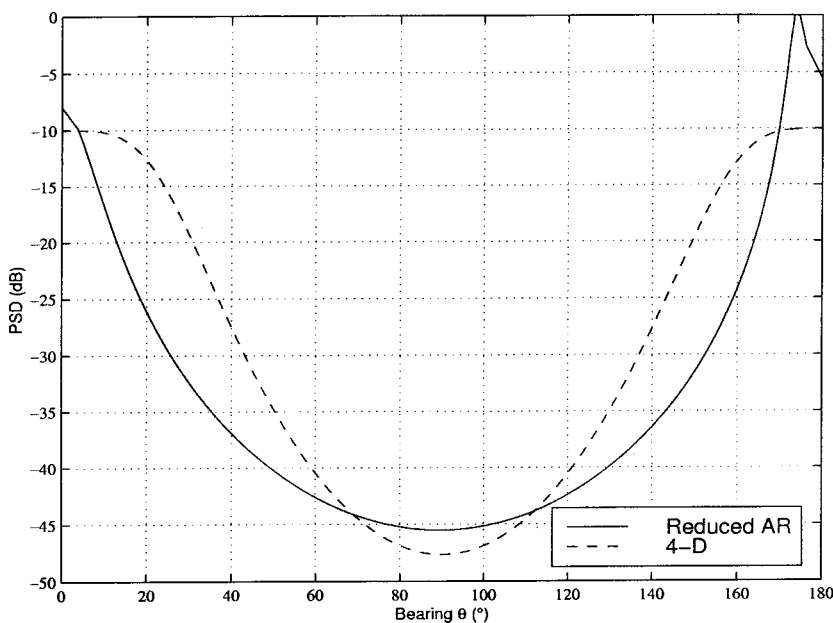
FIG. 8. Cox shipping noise model power spectral density comparisons between Fourier transform and AR(3,2) process for a 3×12 planar array.
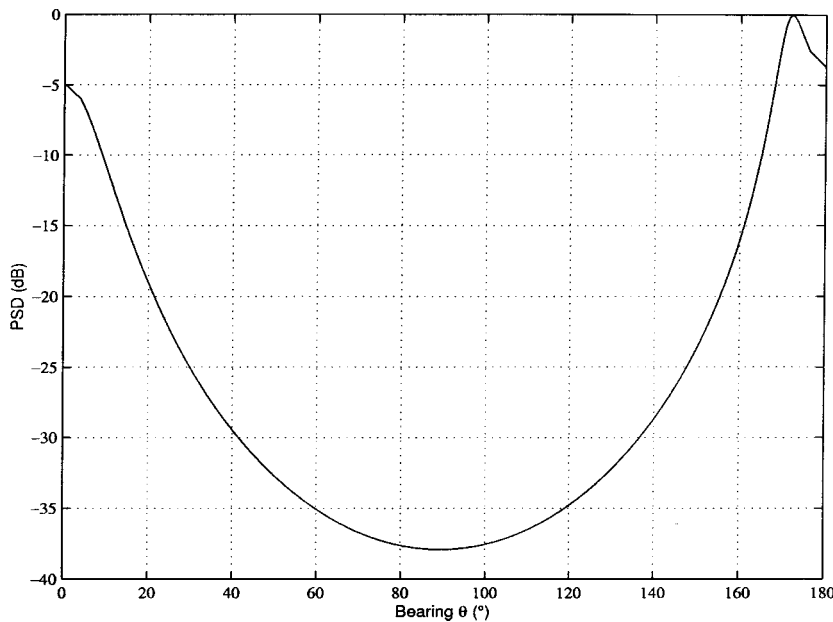
FIG. 9. The AR(3,2,2)-modeled noise due to distant shipping on a $2\times2\times12$ volumetric array.

rithm (LWR) lends further credence to this approach. First examine the planar case. Given a model with orders $p_x=5$ and $p_z=3$ for a 4×12 array form the matrix $\mathbf{Q}=\mathbf{Q}_z\otimes\mathbf{Q}_x$ where the parameter vector $\mathbf{a}_z^T=[1\ a_1\ a_2\cdots a_{p_z}]$ parametrizes $\mathbf{Q}_z$ via the Gohberg–Semencul formula[25] and so on for $\mathbf{Q}_x$ with $\mathbf{a}_x$. The LWR algorithm computes the matrix of multidimensional AR coefficients $\mathbf{A}$ of the size $N/M\times M$ from the matrix $\mathbf{Q}$. Interestingly, the matrix $\mathbf{A}$ contains the outer product of the parameter vectors. Specifically, the matrix assumes the form $\mathbf{A}_T=\mathbf{a}_z^T\mathbf{a}_x$. In the three-axis case, the nonzero elements of the coefficient matrix assume a cubic shape as depicted in Fig. 10.

A proximity metric provides a qualitative measure of the fit between an AR noise model and a physically generated one. The following approach defines this metric (without loss of generality, employ a uniform planar array).

(1) Using the Cox[2] formula, compute the noise correlation matrix $\mathbf{Q}$ due to surface noise or distant shipping for an N total sensor planar array with M parallel lines.

(2) Again using the Cox[2] formula, determine the vector of correlation coefficients (first row of matrix $\mathbf{Q}_\uparrow$) $\mathbf{q}_\uparrow$ for a single vertical line array of M sensors.

(3) Obtain the correlation sequence for the horizontal line of sensors $\mathbf{q}_\rightarrow$ with the Cox[2] formula.

(4) Use the Levinson–Durbin algorithm[22] to compute the vector of AR coefficients $\mathbf{a}_\uparrow$ and $\mathbf{a}_\rightarrow$ for the two sequences $\mathbf{q}_\uparrow$ and $\mathbf{q}_\rightarrow$.

(5) Use the Gohberg–Semencul formula[25] to obtain $\mathbf{Q}_\uparrow$ and $\mathbf{Q}_\rightarrow$ from $\mathbf{a}_\uparrow$ and $\mathbf{a}_\rightarrow$.

(6) Form the estimate of the noise correlation matrix via the Kronecker product $\hat{\mathbf{Q}}=\mathbf{Q}_\uparrow\otimes\mathbf{Q}_\rightarrow$ and normalize $\hat{\mathbf{Q}}=N\hat{\mathbf{Q}}/\mathrm{trace}\,(\hat{\mathbf{Q}})$.

(7) Define the proximity measure as a function of vertical and horizontal AR order

$$\epsilon(p_\uparrow,p_\rightarrow)=\|\hat{\mathbf{Q}}-\mathbf{Q}\|_F.\tag{5}$$

Figure 11 depicts a graph of the proximity measure for surface-generated noise versus possible AR orders in the horizontal and vertical. Figure 12 depicts the graph versus only $p_\rightarrow$ for a fixed choice of $p_\uparrow=4$. The Cox[2] model for shipping noise generates similar results in both cases. As expected, the proximity measure decreases as the order of the AR model increases. The AR model provides a good fit.

B. General volumetric arrays

The Cox[2] model generalizes the Burdic[1] expressions and computes the correlation coefficients for both surface-wave-generated noise and distant shipping (impulsive) noise. This model describes these coefficients for any sensor array of arbitrary known geometry. When employing a two- or three-dimensional uniform array, the model generates noise correlation matrices with block-Toeplitz structure.[22] Cox[2] defines a normalized directional density function for azimuthally uniform (uniform across ϕ) fields $F(\theta,\omega)$ and expands it into spherical harmonics,
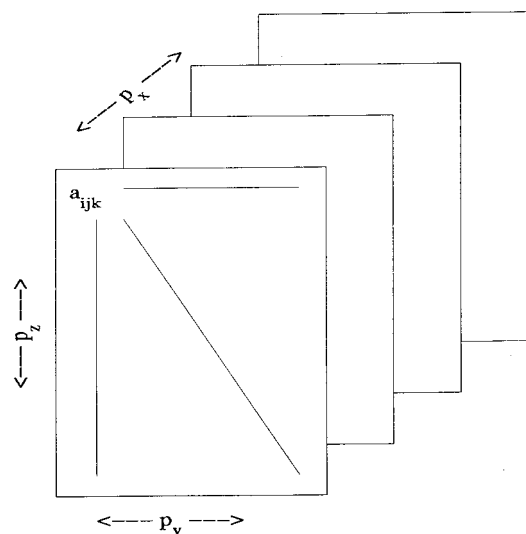
FIG. 10. Three-dimensional matrix of Levinson–Wiggins–Robinson coefficients for an $AR(p_x,p_y,p_z)$ model.
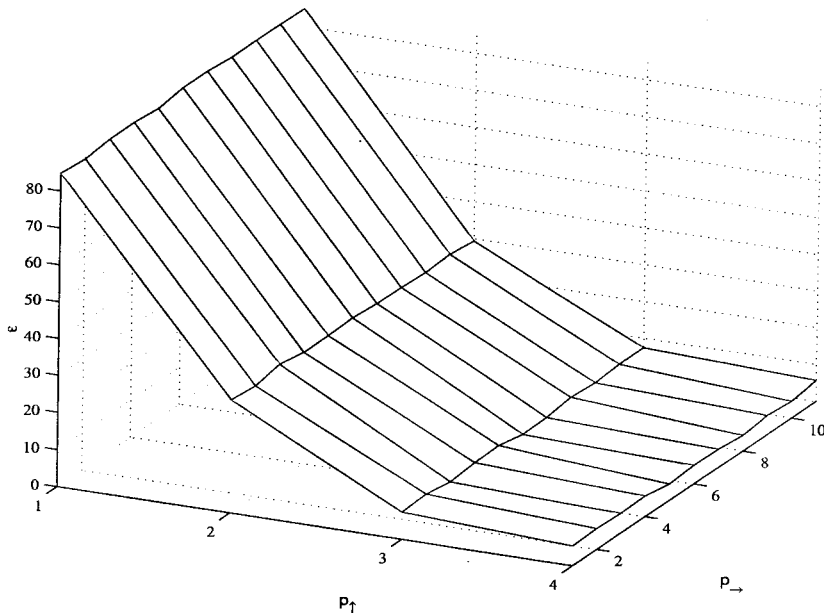
FIG. 11. Proximity measure versus AR orders in two-directions for AR models of surface-generated noise.

$$F(\theta,\omega) = \sum_{l=0}^{\infty} c_l(\omega) P_l(\cos \theta), \qquad (6)$$

where $c_l(\cdot)$ represents the coefficient for the lth term in the expansion, $P_l(\cdot)$ the Legendre polynomial of the first kind (Ref. 26, pp. 332–334). Cox[2] provides the coefficients, derived by curve-fitting to ocean acoustic data. The correlation $\mathbf{Q}_{mn}(d,\omega,\gamma)$ (normalized element of noise correlation matrix) between two sensors m and n separated by distance d with angle relative to the vertical γ at frequency ω equals

$$\mathbf{Q}_{mn} = \sum_{l=0}^{\infty} i^l c_l(\omega) P_l(\cos \gamma) j_l(\omega d/c), \qquad (7)$$

where $j_l(\cdot)$ represents the lth-order spherical Bessel function of the first kind (Ref. 26, p. 437) and i represents a complex number.

Appendix B presents a technique for obtaining the necessary coefficients $c_l(\cdot)$ for the shipping noise model. These values appear in Cox's paper (Ref. 2, Table I, p. 1297). Finite precision effects cause some of his values to disagree with the values computed in Appendix B.

For distant shipping noise, part of the spherical harmonic expansion involves the expression relating even powers of $\sin \theta$ to the Legendre polynomials

$$\sin^{2n} \theta = \sum_{k=0}^{n} a_{2k} P_{2k}(\cos \theta), \qquad (8)$$

where Appendix B describes an algorithm for computing the coefficients a_{2k} for $k=0,1,...,n$ and $P_{2k}(\cdot)$ represents the Legendre polynomials of the first kind. Given these results, for noise due to distant shipping, Cox[2] shows that the fol-
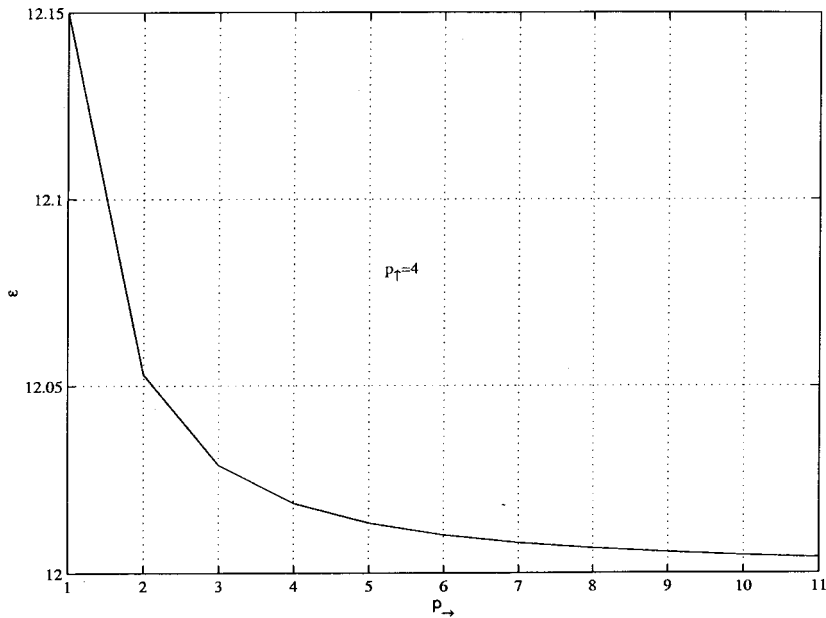
FIG. 12. Proximity measure versus AR orders in the horizontal where $p_\uparrow = 4$ for surface-generated noise.

lowing form represents the fourth-order directional density function (independent of ω),

$$F_8(\theta) = 0.04 + \frac{0.96}{0.40635} \sin^8 \theta$$

$$= 1.0 + 2.3625 \left[\sum_{k=1}^{4} a_{2k} P_{2k}(\cos \theta) \right], \qquad (9)$$

where the unusual constants are due to normalization. To plug this expansion into the one in Eq. (7) relate the coefficients

$$c_0 = 1, \quad c_{2k} = 2.3625 a_{2k}, \qquad (10)$$

for $k = 1, 2, ..., 4$. This provides the following relation for the correlation matrix of noise due to distant shipping

$$\mathbf{Q}_{\mathrm{SHIP},mn} = \sum_{l=0}^{4} i^{2l} c_{2l}(\omega) P_{2l}(\cos \gamma) j_{2l}(\omega d/c), \qquad (11)$$

where for the fourth-order case $c_0 = 1.0000$, $c_2 = -1.7455$, $c_4 = 1.0876$, $c_6 = -0.3491$, and $c_8 = 0.0470$. Notice that the parametrization always normalizes c_0 to unity.

For noise due to surface wave action, Cox[2] uses a four-term harmonic model of the form

$$F_{\mathrm{SEA}}(\theta) = 0.1 + 0.9 \left[\frac{\sin 2\theta}{4 \sin(\theta/2)} \right]^2 \qquad (12)$$

and represents it in terms of Legendre polynomials by employing the relation

$$\left(\frac{\sin(n\zeta)}{n \sin \zeta} \right) = \frac{1}{n} \left[1 + \frac{2}{n} \sum_{j=1}^{n-1} (n-j)\cos(2j\zeta) \right]. \qquad (13)$$

Since this represents a cosine series, use an expression such as Ref. 26, Eqs. 8.7.3, p. 335 or 22.3.13, p. 776, which relates cosine series to Legendre polynomials, to convert it to the form

$$\left[\frac{\sin 2\theta}{4 \sin(\theta/2)} \right]^2 = \frac{1}{6} + \frac{3}{10} P_1(\cos \theta) + \frac{1}{3} P_2(\cos \theta)$$

$$+ \tfrac{1}{5} P_3(\cos \theta), \qquad (14)$$

so that the normalized directional density function

$$F_{\mathrm{SEA}}(\theta) = 1.0 + 3.6 \left[\sum_{n=1}^{3} a_n P_n(\cos \theta) \right], \qquad (15)$$

where $a_1 = \frac{3}{10}$, $a_2 = \frac{1}{3}$, and $a_3 = \frac{1}{5}$. To plug this expansion into the one in Eq. (7) relate the coefficients

$$c_0 = 1, \quad c_k = 3.6 a_k, \qquad (16)$$

for $k = 1, 2, 3$. This provides the following relation for the correlation matrix of noise due to surface noise,

$$\mathbf{Q}_{\mathrm{SEA},mn} = \sum_{l=0}^{3} i^l c_l(\omega) P_l(\cos \gamma) j_l(\omega d/c), \qquad (17)$$

where for the third-order case $c_0 = 1.0000$, $c_1 = 1.0800$, $c_2 = 1.2000$, and $c_3 = 0.7200$. This parametrization also normalizes c_0 to unity.

The coefficients c_i parametrize the entire noise correlation matrix for both the surface and the shipping noise cases. Although the coefficients operate on each element of the correlation matrix independently, a matrix form of the expansions exist. This section develops the matrix form and forms a vector parametrization of the expansion. Kneipfer[4] developed an efficient method for computing the Cox[2] parametrizations by computing only unique elements of each of the matrices. This section exploits some of his formulation.

The following form represents the desired expansion for the shipping noise correlation matrix in terms of the coefficients c_{2i} for $i = 0, 1, ..., 4$:

$$\mathbf{Q}_{\mathrm{SHIP}} = \sum_{i=0}^{4} c_{2i} \mathbf{Z}_{2i} + \mathbf{A}. \qquad (18)$$

Reference 24 examines the computation of the $\mathbf{Z}_{2i}$ and $\mathbf{A}$ matrices.

II. SUMMARY

This paper has presented novel, low-dimensional parametrizations for ambient noise fields for both uniform and general volumetric sensor arrays. Previously developed methods modeled only the noise for uniform line arrays with primarily broadside ambient noise fields or provided parametrizations based on the spherical harmonic expansion which were not amenable to vector parametrization. This paper used information-theoretic criteria to show that only low-order models were necessary. Previous works on model order had stated only qualitative results. The paper showed that multi-dimensional AR models approximate physically generated noise spectra, and presented a new model based on the Kronecker product which reduces parametrization order associated with them. This paper developed a new proof which shows the equivalence between the Kronecker signal model and the exact classical signal model. Such a model has never been employed before in the literature. The paper developed a novel noise model based on a matricial form of the spherical harmonic expansion and provided an algorithm for computing the associated weighting coefficients. The previously derived forms of this expansion did not allow for simple vector parametrization, nor did they state how the coefficients were computed.

A main result of this work involves the comparison between both noise parametrizations. The Kronecker AR version of the algorithm is only applicable in the case where uniform spatial sampling exists. Arrays of this type include uniform line arrays (equal intersensor spacing), and uniform planar and cuboid arrays (equal intersensor and interline spacing). This geometrical constraint limits the utility of this version of the algorithm. This model, however, does provide a low-dimensional parametrization and extensibility (via complex AR coefficients) to nonbroadside ambient noise sources. The ability to identify nonbroadside extended noise sources would prove useful if a direction-finding algorithm was trying to identify the direction-of-arrival of such an extended source. Once the algorithm estimated the appropriate complex AR coefficient, an estimate of the direction-of-arrival angle could be obtained. Although the paper has dem-

onstrated that such a model is a good representation of distant shipping and surface-wave-generated noise, other noise spatial densities may exist where the model might not be appropriate.

The linear matrix form of the spherical harmonic expansion model is applicable to any array with arbitrary geometry, providing great extensibility. This model also provides a low-dimensional parametrization. In this paper the model was shown to provide good approximations to distant shipping and surface-wave-generated noise. Noise densities may exist where an alternate parametrization might be necessary.

ACKNOWLEDGMENTS

APPENDIX A: PROPERTIES OF THE KRONECKER PRODUCT

This Appendix describes a useful property of the Kronecker product.

Definition 1: Given the $M \times M$ matrix $\mathbf{A}$ and the $N/M \times N/M$ matrix $\mathbf{B}$, define the $N \times N$ Kronecker product matrix $\mathbf{C} = \mathbf{A} \otimes \mathbf{B}$ as

$$C = \begin{bmatrix} a_{11}B & \cdots & a_{1M}B \\ \vdots & \ddots & \vdots \\ a_{M1}B & \cdots & a_{MM}B \end{bmatrix}, \tag{A1}$$

where a_{ij} represents the $(i,j\text{th})$ element of matrix $\mathbf{A}$.

Lemma 1: If $\mathbf{A}^{-1}$ and $\mathbf{B}^{-1}$ exist, then

$$\mathbf{C}^{-1} = \mathbf{A}^{-1} \otimes \mathbf{B}^{-1}. \tag{A2}$$

APPENDIX B: DERIVATION OF THE COX COEFFICIENTS

This Appendix derives an original algorithm for computing the coefficients necessary for the spherical harmonic expansion of physically derived shipping noise. This algorithm is based on solving a matrix equation of the form $\mathbf{Ax} = \mathbf{b}$ whose elements are derived from orthogonal polynomial expansions appearing in Ref. 26. Results from the pseudocode description are presented for two expansion orders and compared with similar results appearing in Ref. 2. The significant contribution of this algorithm is that the coefficients may be derived for any arbitrary model order. When compared to Cox's results,[2] this algorithm provides slightly different answers, which may be an artifact of round-off error.

For low-frequency noise, functions of the form $\sin^{2n} \theta$ represent attractive models. The expansion of these functions into Legendre polynomials $P_n(\cos \theta)$ of the first kind requires coefficients a_{2k}. The expansion assumes the form

$$\sin^{2n} \theta = \sum_{k=0}^{n} a_{2k} P_{2k}(\cos \theta). \tag{B1}$$

This Appendix addresses computation of these coefficients by equating two known relations in (B2) and (B4). The explicit expansion for Legendre polynomials takes the form

$$P_l(x) = \frac{1}{2^l} \sum_{i=0}^{\lfloor l/2 \rfloor} (-1)^i \binom{l}{i} \binom{2l-2i}{l} x^{l-2i}, \tag{B2}$$

where

$$\binom{m}{n} = \frac{m!}{n!(m-n)!}. \tag{B3}$$

The second relation represents powers of $\sin \theta$ in terms of binomial coefficients

$$\sin^{2n} \theta = (\sin^2 \theta)^n = (1 - \cos^2 \theta)^n$$

$$= \sum_{m=0}^{n} (-1)^m \binom{n}{m} \cos^{2m} \theta. \tag{B4}$$

The pseudocode description formulates the problem as

$$\mathbf{Ay'} = \mathbf{b}, \tag{B5}$$

where $\mathbf{A}$ is a matrix of Legendre coefficients, $\mathbf{y'}$ represents the desired coefficients to be computed using Gaussian elimination, and $\mathbf{b}$ is a vector of binomial coefficients. Assume that N represents the maximum desired order of the expansion (Cox[2] uses $N=4$ and 10).

(1) Initialize result matrix $\mathbf{Y}$:

$$\mathbf{Y} = \mathbf{0}_{(N+1) \times N} \tag{B6}$$

(2) Initialize matrix of Legendre coefficients:

$$\mathbf{A} = \mathbf{0}_{(N+1) \times (N+1)} \tag{B7}$$

(3) Compute Legendre coefficients

for $n = 0 \rightarrow N$

for $l = 0 \rightarrow n$

$$\mathbf{A}_{(n+1-l),(n+1)} = \frac{(-1)^l}{4^n} \binom{2n}{l} \binom{4n-2l}{2n}$$

end l

end n $\qquad$ (B8)

(4) Compute vector of binomial coefficients;

for $m = 1 \rightarrow N$

$$\mathbf{b} = \mathbf{0}_{(m+1) \times 1}$$

for $n = 0 \rightarrow m$

$$\mathbf{b}_{(n+1),1} = (-1)^n \binom{m}{n}$$

end n $\qquad$ (B9)

1627   J. Acoust. Soc. Am., Vol. 105, No. 3, March 1999

A. C. Barthelemy and P. K. Willett: Ambient noise models   1627

and compute matrix of results, where each column of this matrix represents a vector of coefficients

$$\mathbf{A}_{(1\rightarrow m+1),(1\rightarrow m+1)}\mathbf{y}' = \mathbf{b} \tag{B10}$$

and fill in the mth column of the result matrix $\mathbf{Y}$

$$\mathbf{Y}_{(1\rightarrow m+1),m} = \mathbf{y}'$$

end m $\qquad$ (B11)

(5) Return result for specific order

$$\mathbf{y} = \mathbf{Y}_{(1\rightarrow N),N}. \tag{B12}$$

Table BI represents results obtained from this algorithm for $N=4$ and 10. The following MATLAB function which implements this pseudocode aids in its understanding.

TABLE BI. The coefficients a_{2k} for $k=0,1,...,10$, in the expansion of $\sin^{2n}\theta$ in terms of Legendre polynomials up to the tenth order where $n=10$. These results differ slightly from those appearing in Cox's paper; this may be due to finite precision effects.

Order k	$N=4$	$N=10$
0	4.0635e-01	2.7026e-01
1	−7.3882e-01	−5.8752e-01
2	4.6034e-01	5.7107e-01
3	−1.4776e-01	−4.0735e-01
4	1.9891e-02	2.2501e-01
5	0	−9.6837e-02
6	0	3.2023e-02
7	0	−7.8842e-03
8	0	1.3639e-03
9	0	−1.4813e-04
10	0	7.6068e-06

```
function y = COX_COEFF(maxm);
  % Alain Barthelemy 28 January 1994
  % This program computes the coefficients in the expansion
  % for Reference (1), Equation 76.
  % The program utilizes an explicit expansion for Legendre Polynomials
  % and the binomial expansion for powers of sin(theta).
  % It formulates the problem as Ax=b, where the x's are the desired coefficients.
  % References:
  % (1) Cox, H., ``Spatial Correlation in Arbitrary Noise Fields with Application
  %      to Ambient Sea Noise'', JASA 54/5, 1973.
  % (2) Kneipfer, R., ``A MATLAB Program for Predicting the Performance of
  %      Multiline Towed Arrays'', NUWC-NL Technical Report 10, 167, 15 August 1992.
  % (3) Abramowitz, M. and Stegun, I., ``Handbook of Mathematical Functions
  %      with Formulas, Graphs, and Mathematical Tables'', Applied Mathematics
  %      Series 55, National Bureau of Standards, December 1972.
  % maxm is the maximum order of the expansion.

  result = zeros(maxm+1,maxm);% Initialize matrix for results
  A = zeros(maxm+1,maxm+1); % Initialize matrix of Legendre coefficients
  for n = 0:maxm,
    for l = 0:n,
      A(n+1-l,n+1) = (((-1)^l)/(4^n))*COMBINATION(2*n,l)*COMBINATION(4*n-2*l,2*n);
    end;
  end;
  for m = 1:maxm,
    b = zeros(m+1,1);
    for n = 0:m,
      b(n+1) = ((-1)^n)*COMBINATION(m,n); % Vector of binomial coefficients
    end;
    % Matrix of results
    % Each column of this matrix represents a vector of coefficients
    result(1:m+1,m) = A(1:m+1,1:m+1)\b;
  end;
  y = result(:,maxm);
  return;
  % %%%%%%%%%%%%%%%%%%%%%%%%%%%%%%%%%%
  % Function to compute combinations
  function y = COMBINATION(m,n);
    % Computes the number of combinations
    y = FACTORIAL(m)/(FACTORIAL(n)*FACTORIAL(m-n));
  return;
  % %%%%%%%%%%%%%%%%%%%%%%%%%%%%%%%%%%
```

```
% Function to compute factorial
function y = FACTORIAL(n);
  y = prod(1:n);
return;
```

[1] W. S. Burdic, *Underwater Acoustic System Analysis* (Prentice-Hall, Englewood Cliffs, NJ, 1984).

[2] H. Cox, J. Acoust. Soc. Am. **54**, 1289–1301 (1973).

[3] B. F. Cron and C. H. Sherman, J. Acoust. Soc. Am. **34**, 1732–1736 (1962).

[4] R. R. Kneipfer, *A MATLAB Program for Predicting the Performance of Multiline Towed Arrays* (Naval Undersea Warfare Center, New London, CT, 1992).

[5] G. M. Wenz, J. Acoust. Soc. Am. **34**, 1936–1956 (1962).

[6] R. J. Urick, *Principles of Underwater Sound* (McGraw–Hill, New York, 1975).

[7] J.-P. Le Cadre, *Experimentation sur des signaux d'antenne remorquee d'une methode d'estimation des parametres de correlation du bruit* (Groupe d'Etudes et de Recherches de Detection Sous-Marine, Toulon, France, 1985).

[8] R. J. Webster, IEEE J. Ocean Eng. **19**, 134–137 (1994).

[9] S. Kay and V. Nagesha, *Proceedings of ICASSP* (IEEE, New York, 1993), pp. IV-232–IV-235.

[10] M. Wax and T. Kailath, IEEE Trans. Acoust., Speech, Signal Process. **ASSP-33**, 387–392 (1985).

[11] J.-P. Le Cadre, *Contribution a l'Utilisation des Methodes Parametriques en Traitement d'Antenne* (L'Universite Scientifique et Medicale de Grenoble, Grenoble, France, 1987).

[12] J.-P. Le Cadre, IEEE Trans. Acoust., Speech, Signal Process. **ASSP-37**, 965–983 (1989).

[13] A. C. Barthelemy, *Volumetric Array Prewhitening* (Univ. of Connecticut, Storrs, CT, 1996).

[14] V. Nagesha and S. Kay, *Proceedings of ICASSP* (IEEE, New York, 1993), pp. IV-240–IV-243.

[15] H. Ye and R. D. DeGroat, IEEE Trans. Signal Process. **43**, 938–949 (1995).

[16] A. H. Tewfik, IEEE Trans. Signal Process. **39**, 1933–1942 (1991).

[17] A. C. Barthelemy and P. K. Willett, *Proceedings of ICASSP* (IEEE, New York, 1995), pp. 3543–3546.

[18] A. C. Barthelemy and P. K. Willett, *Conference Record, Twenty-seventh Asilomar Conference* (IEEE, New York, 1993), pp. 243–247.

[19] J.-P. Le Cadre, SIAM (Soc. Ind. Appl. Math.) J. Math. Anal. (accepted for publication).

[20] J.-P. Le Cadre, private communication (1995).

[21] R. A. Wiggins and E. A. Robinson, J. Geophys. Res. **70**, 1885–1891 (1965).

[22] S. M. Kay, *Modern Spectral Estimation: Theory and Application* (Prentice-Hall, Englewood Cliffs, NJ, 1988).

[23] S. Lawrence Marple, Jr., *Digital Spectral Analysis with Applications* (Prentice-Hall, Englewood Cliffs, NJ, 1987).

[24] A. C. Barthelemy and P. K. Willett, IEEE Trans. Signal Process. **46**, 281–293 (1998).

[25] B. Cernuschi-Frias, IEEE Trans. Signal Process. **39**, 190–192 (1991).

[26] M. Abramowitz and I. A. Stegun, *Handbook of Mathematical Functions: With Formulas, Graphs and Mathematical Tables* (Dover, New York, 1972).

Viscosity measurement with laser-generated and detected shear waves

R. Daniel Costley,[a] Vimal V. Shah,[b] Christopher B. Winstead, and J. P. Singh
Diagnostic Instrumentation and Analysis Laboratories, Mississippi State University,
205 Research Boulevard, Starkville, Mississippi 39759-9734

Krishnan Balasubramaniam
Department of Aerospace Engineering, Mississippi State University, P.O. Box A, Mississippi State,
Mississippi 39762

A technique is described in which laser-generated shear waves can be used to measure the viscosity of liquids. The technique involves measuring the shear wave reflection coefficient at a solid–liquid interface. To accommodate this procedure, a wedge was designed to launch laser-generated shear waves into the material at nearly normal incidence to the solid–liquid interface. The reflected laser-generated shear waves are detected at a second interface with a laser interferometer. The angle of incidence at this second interface is at an angle greater than the critical angle. The purpose of this arrangement is to maximize the out-of-plane displacement at this second interface so that detection with the interferometer can be more easily accomplished. Calculations that support the design of the wedge and experiment are outlined and experimental results are presented and discussed. This technique would be most applicable in those situations in which conventional techniques are not suitable, such as those involving high temperature and hostile environments. © *1999 Acoustical Society of America.* [S0001-4966(99)03803-5]

PACS numbers: 43.35.Cg, 43.35.Yb, 43.35.Zc [HEB]

INTRODUCTION

Laser-generated ultrasound has great potential in applications where it is difficult or impractical to use a contact transducer. These applications include those in high temperature and corrosive environments.[1–3] This study deals with developing a technique to measure the viscosity of high temperature, and possibly corrosive liquids, such as molten glasses and metals. However, the work presented here is part of a feasibility study, and the experiments have been conducted at room temperature. Future advances and modifications of the technique will adapt it to more hostile environments.

The technique, as explained in more detail in subsequent sections, involved measuring the amplitude of laser-generated shear waves reflected from a solid–liquid interface. This information was used to determine the reflection coefficient, which can be correlated to the viscosity of the liquid. Very few works have dealt directly with laser-generated shear waves. This is probably because the laser is not an efficient shear wave generator, and because in-plane displacements are more difficult to detect than out-of-plane displacements.

Lasers are typically inefficient generators of ultrasound, especially in the thermoelastic regime. Approximately 6% of the energy of an incident light pulse at 1064 nm is absorbed on a clean aluminum surface, the rest being reflected.[1] Not all of the absorbed energy is converted into ultrasound. Of the energy that is converted into ultrasound in aluminum, approximately 21% is contained within the shear wave, 77% is contained within the Rayleigh wave, and 2% is contained in the compressional wave.[4]

When a shear wave reflects from a surface at normal incidence, the particle motion is entirely within the plane of the surface. Laser interferometers have been developed which can measure these in-plane displacements so that shear waves can be detected directly.[5] In a separate study, a similar interferometer was used to study laser-generated shear waves.[6] Laser-generated shear waves have also been detected with other transducers. Hutchins and Wilkins[7] used electromagnetic transducers to detect laser-generated shear waves and determine their polarization. In a precursor to the work presented here, laser-generated shear waves were detected with piezoelectric shear wave transducers.[8]

The effect of fluid viscosity on reflected horizontally polarized shear waves has been investigated elsewhere.[9–11] Due to the viscosity of a fluid, shear waves can be transmitted into viscous liquid. However, these waves are highly attenuated and rapidly dampen. The capability of the fluid media to convey these waves diminishes the amplitude of the reflected shear waves propagating back into the solid. Thus, the amplitude of these reflected shear waves depends on the capacity of the liquid to transmit them, or its viscosity. The magnitude of the decrease and its relation with the fluid properties will be discussed in the following section.

As mentioned in a preceding paragraph, an earlier study was conducted in which the viscosity of calibration liquids was correlated to the reflection coefficient of laser-generated shear waves.[8] The shear waves were launched with a pulsed Nd:YAG laser into an aluminum wedge and detected using a

piezoelectric transducer. This paper describes the results obtained with a totally noncontact system, generating the shear waves with a pulsed laser, and detecting the reflected shear waves with a laser interferometer.[12,13] As part of this project, a wedge was designed so that the laser-generated shear waves are incident to the solid–liquid interface at nearly normal incidence. This causes the relative particle motion between the solid and liquid to be parallel to one another, which is a shearing type motion. The reflection of shear waves at this angle is therefore the most sensitive to viscosity since viscosity is a resistance to shear.

After the shear waves reflect off the solid–liquid interface, they are incident on the surface of detection at greater than the critical angle. This allows for the largest possible out-of-plane displacement. These displacements can then be detected with the more common Mach–Zehnder or Michelson interferometers. This type of arrangement has been used with both aluminum and graphite wedges.

In the following section, the analysis of shear wave reflection from a solid–liquid interface is outlined. Several results from this analysis are presented. The motion of the surface at a solid–air interface is then considered. Results from these two analyses form the basis for the design of the shear wave wedge, an apparatus used to detect laser-generated shear waves. The experimental configuration is described in the following section. In the final section, experimental results obtained with the shear wave wedge are correlated to the viscosity of various calibration liquids.

I. REFLECTION OF SV WAVES

The reflection of shear waves from a solid–liquid interface is affected by the viscosity and density of the liquid, as well as by the properties of the solid. Earlier work has exploited horizontally polarized shear waves (SH waves).[10,11] These are shear waves whose particle motion is parallel to the solid–liquid interface. When these types of shear waves are incident on an interface, only shear waves are transmitted and reflected.[14] However, laser-generated shear waves are vertically polarized, which means that a component of their particle motion is perpendicular to the interface. The exception to this is when the angle of incidence of the vertically polarized shear wave (SV wave) is 0 deg, as measured from the normal to the interface. In this case, the two types of shear waves are indistinguishable for an isotropic solid.

A. Theory

The solution for the reflection coefficient for SH waves from a solid–liquid interface is simpler than that for SV waves since just one type of wave is transmitted and reflected. However, the solution involving SV waves is straightforward, although it involves allowing for the existence of transmitted and reflected compressional waves (P waves). The solution outlined in this section follows the procedures presented in textbooks on wave propagation.[14,15] The geometry used in the solution is depicted graphically in Fig. 1 where ρ_1 and ρ_2 represent the density of the solid and liquid, respectively, ζ and η represent the bulk and shear viscosities of the liquid, respectively, λ and μ are the Lamé
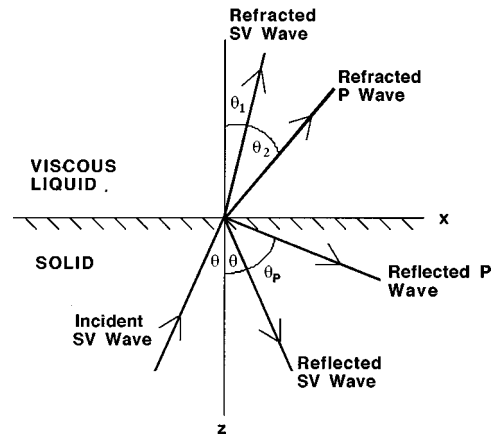
FIG. 1. A graphical representation of a vertically polarized shear wave (SV wave) reflecting from a stress-free surface when the angle of incidence is less than the critical angle. The particle motion of the SV waves is perpendicular to its direction of propagation, but in the plane of the figure. The particle motion of the compressional wave (P wave) is parallel to its direction of propagation.

constants for the solid. In this solution, it is assumed that the displacements are a function of the spatial variables x and z, and time, t. The relevant displacement-boundary conditions are the continuity of the x- and z-components of displacement at the interface, u and w, respectively. In addition, the normal and shear stresses, σ_{zz} and σ_{xz}, must be continuous across the interface. In the solid, these stresses are written

$$\sigma_{zz} = \lambda \frac{\partial u}{\partial x} + (\lambda + 2\mu) \frac{\partial w}{\partial z},$$

$$\sigma_{xz} = \mu \left(\frac{\partial u}{\partial z} + \frac{\partial w}{\partial x} \right). \tag{1}$$

If one assumes linear acoustics and harmonic waves of angular frequency ω (and using the $\exp(-i\omega t)$ convention), the stresses in the liquid can be written

$$\sigma_{zz} = (\rho_2 c_0^2 - i\omega\zeta) \frac{\partial u}{\partial x} - 2i\omega\eta \frac{\partial w}{\partial z},$$

$$\sigma_{xz} = -i\omega\eta \left(\frac{\partial u}{\partial z} + \frac{\partial w}{\partial x} \right), \tag{2}$$

where c_0 is the longitudinal bulk wave speed in the liquid and $i = \sqrt{(-1)}$.

In both the solid and the liquid, the displacements can be expressed in terms of potential functions ϕ and ψ using the Helmholtz decomposition (for the plane-strain case)[14,15]

$$u = \frac{\partial \phi}{\partial x} - \frac{\partial \Psi}{\partial z}; \quad w = \frac{\partial \phi}{\partial z} + \frac{\partial \Psi}{\partial x}. \tag{3}$$

Displacements in the solid and fluid, and their potentials, are distinguished by the use of the subscripts s or f, respectively. In the solid, the potentials can be written

$$\phi_s = P_s e^{ik_p(x \sin \theta_p + z \cos \theta_p)},$$

$$\psi_s = I_s e^{ik(x \sin \theta - z \cos \theta)} + S_s e^{ik(x \sin \theta + z \cos \theta)}, \tag{4}$$

where $k = \omega/\beta$, $k_p = \omega/\alpha$ and β and α represent the shear- and compressional-wave speeds in the solid, respectively.

The refracted P and SV waves in the viscous liquid are represented by

$$\phi_f = P_f e^{ik_2(x \sin \theta_2 - z \cos \theta_2)},$$
$$\psi_f = S_f e^{ik_1(x \sin \theta_1 - z \cos \theta_1)}, \tag{5}$$

where $k_2 = \omega/c_0$, $k_1 = \omega/c_1$, c_1 is the shear wave speed in the fluid and[16]

$$c_1^2 = -i\omega \frac{\eta}{\rho_f}. \tag{6}$$

The expressions for the potentials can be substituted into the expressions for the displacements, which can then be substituted into the expressions for the stresses. These equations can be used to represent the boundary conditions at $z = 0$. The result of this exercise is four equations which can be written in matrix form:

$$
\begin{vmatrix}
-\dfrac{\beta}{\alpha} \sin \theta_p & \cos \theta & \dfrac{\beta}{c_1} \cos \theta_1 & \dfrac{\beta}{c_0} \sin \theta_2 \\[2mm]
-\dfrac{\beta}{\alpha} \cos \theta_p & -\sin \theta & \dfrac{\beta}{c_1} \sin \theta_1 & -\dfrac{\beta}{c_0} \cos \theta_2 \\[2mm]
\left(\dfrac{\beta}{\alpha}\right)^2 \sin 2\theta_p & -\cos 2\theta & -\dfrac{i\omega\eta}{\mu}\left(\dfrac{\beta}{c_1}\right)^2 \cos 2\theta_1 & -\dfrac{i\omega\eta}{\mu}\left(\dfrac{\beta}{c_0}\right)^2 \sin 2\theta_2 \\[2mm]
\left(\dfrac{\beta}{\alpha}\right)^2 \dfrac{\lambda+2\mu}{\mu} \cos^2 \theta_p & \sin 2\theta & -\dfrac{i\omega\eta}{\mu}\left(\dfrac{\beta}{c_1}\right)^2 \sin 2\theta_1 & -\dfrac{\rho_f c_0^2 - i\omega(\zeta + 2\eta \cos \theta_2)}{\mu}\left(\dfrac{\beta}{c_0}\right)^2
\end{vmatrix}
\begin{pmatrix}
\dfrac{P_s}{I_s} \\[2mm]
\dfrac{S_s}{I_s} \\[2mm]
\dfrac{S_f}{I_s} \\[2mm]
\dfrac{P_f}{I_s}
\end{pmatrix}
=
\begin{pmatrix}
\cos \theta \\
\sin \theta \\
\cos 2\theta \\
\sin 2\theta
\end{pmatrix}. \tag{7}
$$

The displacement in the solid can be represented in terms of the incident SV wave, reflected SV wave, and reflected P wave. In the solid, the x-component of the displacement turns out to be

$$u = u^I + u^S + u^P,$$
$$= ik \cos \theta [I e^{ik(x \sin \theta - z \cos \theta)} - S e^{ik(x \sin \theta + z \cos \theta)}]$$
$$+ ik_p \sin \theta_p P e^{ik_p(x \sin \theta_p + z \cos \theta_p)}. \tag{8}$$

The superscripts and coefficients I, S, and P refer to the incident SV wave, the reflected SV wave, and the P wave, respectively. A similar expression exists for the z component of the displacement. The total displacement is represented by

$$\mathbf{u} = (u^I + u^S + u^P)\hat{e}_x + (w^I + w^S + w^P)\hat{e}_z,$$
$$= \mathbf{u}^I + \mathbf{u}^S + \mathbf{u}^P, \tag{9}$$

where $\hat{e}_x$ and $\hat{e}_z$ are unit vectors in the x and z directions, respectively, and $\mathbf{u}^I = u^I \hat{e}_x + w^I \hat{e}_z$, etc. The reflection coefficient for SV waves is defined as

$$R_s = \frac{|\mathbf{u}^S|}{|\mathbf{u}^I|} = \left|\frac{S_s}{I_s}\right|, \tag{10}$$

while the reflection coefficient for SV waves to P waves turns out to be

$$R_P \equiv \frac{|\mathbf{u}^P|}{|\mathbf{u}^I|} = \frac{\beta}{\alpha}\left|\frac{P_s}{I_s}\right|. \tag{11}$$

B. Solid–viscous liquid interface

It is evident from Eq. (7) that the bulk viscosity, ζ, couples with the transmitted P wave. Due to its nature, the volume viscosity affects mainly the P wave inside the fluid.[17] Since the second viscosity has little effect on the waves re-

flected in the solid, it can be neglected. Contrary to the bulk viscosity, the shear viscosity couples with both the incident and reflected P and SV waves. Therefore, the reflected SV wave, as well as the mode-converted P wave, are sensitive to the shear viscosity of the liquid.

By referring to Eqs. (7)–(11), it can be seen that the reflection coefficient is a function of the angle of incidence and the frequency of the SV wave, the properties of the solid, and the properties of the liquid. The reflection coefficients for SV and P waves as a function of angle of incidence up to the critical angle of the SV wave are plotted in Fig. 2. For all the examples in this section, the solid is aluminum and the liquid is glycerin unless otherwise noted. At $0°$, the reflection coefficient is 0 for the P wave and nearly 1 for the SV wave.
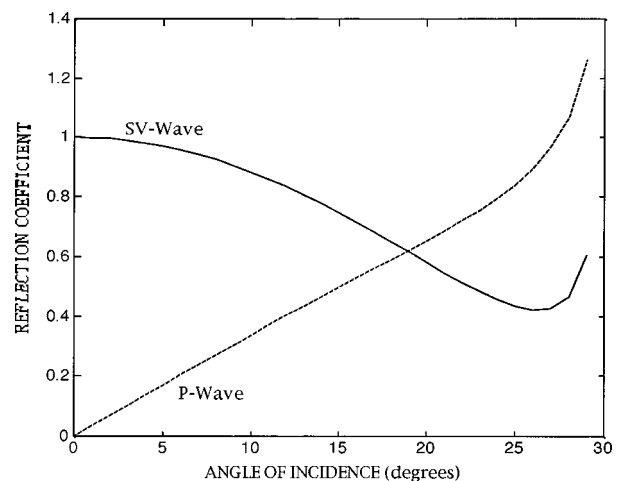
FIG. 2. Reflection coefficient of SV to SV and P waves as a function of angle of incidence at 1.0 MHz. The solid is aluminum, with density 2700 kg/m^3, shear (SV) wave speed 3100 m/s, and compressional (P) wave speed 6300 m/s. The liquid is glycerin, with a shear viscosity of 12 poise.
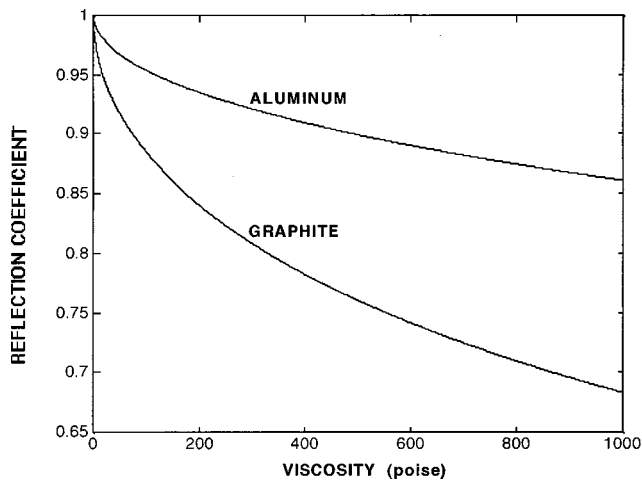
FIG. 3. Reflection coefficient for 1.0 MHz shear waves at normal incidence off a solid–liquid interface for two different solids. The hypothetical liquid has the same density and sound speed as glycerin, which is a 1260 kg/m^3 and 1920 m/s, respectively.

FIG. 5. SV-to-P wave reflection coefficient, R_P, as a function of viscosity for different angles of incidence and frequencies. The solid is aluminum and the liquid is a hypothetical liquid with the same density and speed of sound as glycerin, and whose viscosity is varied from 0 to 300 poise.

This agrees with the results from the reflection of SH waves.

The reflection coefficient as a function of the viscosity of the liquid for two different solids is presented in Fig. 3. The curves are for a shear wave at normal incidence, so that no P waves are generated. The density and sound speed of the hypothetical liquid were the same as for glycerin: 1260 kg/m^3 and 1920 m/s. As can be seen in the figure, the reflection coefficient for an aluminum–liquid interface is less sensitive to changes in viscosity than for a graphite–liquid interface. This is due to the lower shear wave impedance of graphite. Also, the reflection coefficients for both solids are more sensitive to changes in viscosity at lower viscosities than at higher viscosities, where the magnitude of the slope decreases.

The reflection coefficient for SV waves is plotted in Fig. 4 as a function of liquid viscosity for three different angles of incidence (0, 10, and 20°) and two different frequencies (0.5 and 5.0 MHz). For each of the three angles, the higher fre-

quency results in a curve with a steeper slope. Thus, the higher frequency would make for a more sensitive determination of viscosity. Also, the figure shows that R_s decreases as the angle of incidence increases, in agreement with Fig. 2.

The reflection coefficient for SV to P waves, R_P, is plotted for two different angles of incidence and two frequencies in Fig. 5. As in Fig. 4, the higher frequency curves have a steeper slope. However, neither curve is very steep, indicating that the reflected compressional wave is not a good indicator of liquid viscosity. In addition, the lower magnitude of this reflection coefficient means that it would be more difficult to detect. Also, note that R_P increases as the angle of incidence increases, again in agreement with Fig. 2. This is to be expected since, as will be seen in the next section, the interface has more out-of-plane motion at the higher angles of incidence.

In addition to solid and fluid properties, frequency and angle of incidence play significant roles in the magnitude of the reflection coefficients. When designing a system to determine viscosity, it would be desirable that the angle of incidence be at or near normal to the interface. At these angles, the reflection coefficient for SV waves is less sensitive to angle. At angles greater than 10° the effect of angle of incidence is more pronounced than the effect of viscosity. In this case, the angle of incidence would have to be determined accurately. In addition, a near-normal angle of incidence will allow for the maximum amplitude of the reflected SV wave.

C. Solid–air interface

When an SV wave is incident on a solid–air interface, both an SV wave and a longitudinal wave (P wave) are reflected when the angle of incidence is less than the critical angle. It is assumed that neither SV or P waves are transmitted into the air and the solid surface is stress free. The critical angle is defined as the angle of incidence for which the reflected P wave propagates parallel to the surface. For an angle larger than the critical angle, which is approximately

FIG. 4. SV wave reflection coefficient, R_S, as a function of viscosity for different angles of incidence and frequencies. The solid is aluminum and the liquid is a hypothetical liquid with the same density and speed of sound as glycerin, and whose viscosity is varied from 0 to 300 poise.

FIG. 6. In-plane and out-of-plane displacements on a stress-free, graphite surface due to an incident SV wave. The critical angle is at 38 deg, where the discontinuity occurs.

FIG. 7. Directivity pattern for laser-generated shear waves in aluminum.

D. Shear wave wedge

The characteristics of laser-generated shear waves discussed in the last section guided the design of a wedge that could be used in the detection of reflected, laser-generated shear waves. These characteristics include their directivity, their reflection from the solid–liquid interface, and their interaction with the solid–air interface. The wedge is depicted in Fig. 8. As shown in the figure, the angle of the wedge is made equal to the critical angle. This causes the narrow lobe of the laser-generated shear wave to be incident at nearly 90° at the solid–liquid interface. The reflection coefficient of an SV wave at a solid–viscous liquid interface should be more sensitive to changes in shear viscosity if its angle of incidence is near normal. Intuitively, this seems correct since the shear viscosity is a resistance to a shear type, or in-plane, motion. This angle of incidence also allows for the maximum amplitude of the reflected SV wave.

The interferometer beam is located within 5 mm of the spot where the pulsed laser strikes the surface of the wedge. Thus, the angle at which the reflected shear wave is incident at the detector is at a slightly larger angle than the critical angle. As can be seen from Fig. 6, this will produce the largest possible out-of-plane displacement. Thus, it is not necessary, or even advantageous, to use an in-plane detector. These two criteria, normal incidence at the solid–liquid interface and incidence at greater than the critical angle at the solid–air interface where the signal is being detected, were used to design the apparatus used to measure the viscosity of liquids in contact with the appropriate wedge surface.

38° in graphite and 30° in aluminum, the wave number of the P wave is complex so that it becomes an evanescent-type wave.

Another consequence of SV waves is that, for non-normal incidence, they produce components of displacement that are parallel (in-plane) and normal (out-of-plane) to the surface of the interface. The relative magnitudes of these two components were computed by considering a graphite solid half space, again following procedures presented in several textbooks.[14,15] The surface of the half space was stress free. The situation is similar to that of Fig. 1, except that the viscous liquid is replaced by vacuum, or air. The angle of incidence of the SV wave was varied from 0 to 90°. The results of this calculation, which are independent of frequency, were plotted in Fig. 6. As can be seen in the figure, at normal incidence (0°), the total displacement is parallel to the interface (in-plane). The in-plane component starts out negative at 0°, increases to zero, changes sign, and continues to increase up to the critical angle, which in this case is approximately 38°. Both components of displacements have a discontinuity at this point. The out-of-plane displacement increases to a maximum when the angle is just a few degrees greater than the critical angle. In order to detect an SV wave incident on a stress-free interface, it would be advantageous for the angle of incidence to coincide with this maximum.

The ultrasound was generated by a pulsed laser on a stress-free surface. Expressions for the directivity patterns of shear waves produced by pulsed-laser sources in the thermoelastic regime have been derived and presented elsewhere.[2,3] They are basically a function of the material properties, specifically Poisson's ratio, and are independent of frequency. Figure 7 shows the directivity pattern for shear waves for a thermoelastic source in aluminum. A distinctive feature of the directivity is the narrow lobe directed at an angle of approximately 30° to the surface normal. We have empirically determined, for several different materials, that the angle at which the maximum occurs corresponds to the critical angle for SV wave reflection from a stress-free surface.

FIG. 8. Schematic of wedge for laser-generated shear wave measurements. The laser pulse and the detection beam are generally separated by less than 5 mm.

II. EXPERIMENTAL CONFIGURATION

The experimental configuration consisted of an Nd:YAG pulsed laser, a laser interferometer, and a solid wedge as described in the last section. A small plastic container was attached to one side of the wedge to contain the different viscous liquids. The laser beams from the pulsed laser and the interferometer struck the wedge on the opposite side from the viscous liquid, as seen in Fig. 8. A cylindrical lens was used to focus the pulsed-laser beam into a line source. The dimensions of the line source were typically 5 by 1 mm, with some variation between different sets of measurements. The distance between the line source and the interferometer beam was approximately 1–2 mm, again with some variation between sets of measurements. The one-way travel distance of the laser-generated shear waves was approximately 15–20 mm. This was determined by measuring with a ruler from the spot where the lasers hit the wedge along a line that was perpendicular to the viscous-fluid side of the wedge. The distance was also confirmed with time-of-flight measurements.

Because of their close proximity, and to avoid interference problems, it was decided that the pulsed laser and interferometer laser should not be of the same color light. The pulsed laser was an Nd:YAG operating at a wavelength of 1064 nm. The interferometer laser was a frequency–doubled diode-pumped Nd:YAG operating at a wavelength of 532 nm. The interferometer used in this research was a Mach–Zehnder type.[18] It has a bandwidth of approximately 10 MHz and a noise limit of approximately 0.1 nm for a transient pulse. The output of the interferometer electronics is a voltage signal that is proportional to the velocity of the surface at the point of detection.

Voltage waveforms produced by laser-generated shear waves in aluminum and graphite wedges are shown in Fig. 9. The air signal was taken with air in place of the viscous liquid, as shown in Fig. 8. The signals were also averaged to improve the signal-to-noise ratio. All of the signals were averages of at least 100 waveforms.

The shear wave reflection coefficient was calculated as the ratio of the peak-to-peak amplitudes of the viscous-liquid signal to the air signal. Since air has negligible viscosity compared to the viscous liquids, the amplitude of the air signal served to represent the amplitude of the incident signal. In doing this, it was assumed that losses due to geometrical spreading and attenuation in the medium were the same in both the air signal and the viscous-liquid signal. In practice, four air signals and four viscous-liquid signals, as shown in Fig. 9, were acquired, and 16 different reflection coefficients were calculated. These were then averaged, this averaged value was then plotted in Fig. 10. A standard deviation was calculated for each averaged reflection coefficient. The error bars in Fig. 10 represent the average of the s.d.'s calculated for a given experiment. The signals were not converted to units of displacement (e.g., nm) since the voltage signals serve perfectly well for calculating the reflection coefficient ratio.

The work reported in this paper uses broadband ultrasonic signals due to the generation by the laser pulse. The reflection coefficient from a solid–viscous liquid interface is
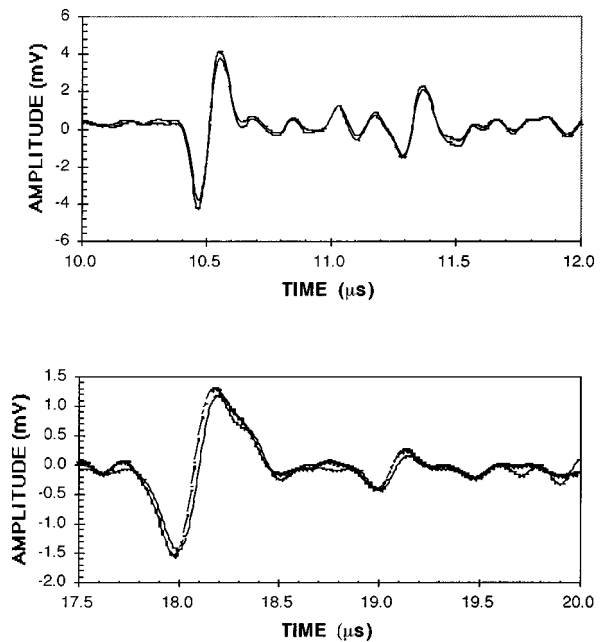
FIG. 9. Reflected, laser-generated shear waves detected in (a) aluminum (at 10.5 μs) and (b) graphite (at 18.0 μs) wedges with laser interferometer. In each case, the larger amplitude signal (black line) was the reference acquired with an air-backed wedge. The smaller amplitude signal (gray line) was acquired when the wedge was backed with a viscous liquid.

frequency dependent, as shown in Fig. 4. However, for a given set of measurements, the pulse duration and the size of the laser spot were constant. Thus, the frequency content of the signals was assumed to be similar and the frequency dependence was neglected. A more detailed analysis on this frequency dependence, along with simulations of broadband
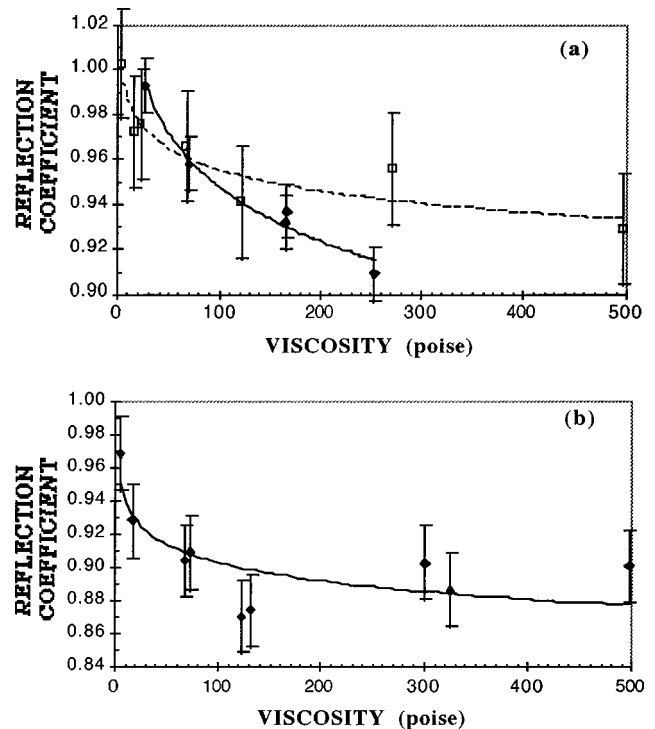
FIG. 10. Viscosity measured with laser-generated SV waves on (a) aluminum and (b) graphite wedges for several different calibration liquids. The solid and dashed lines are second-order polynomial fits to the data.

reflections of shear waves from a solid–liquid interface, has been reported elsewhere.[19]

The differences in laser-pulse energy that generated the air and viscous-liquid signals were neglected in calculating the reflection coefficient. The variations in signal amplitude due to variations in the pulsed-laser energy were minimized by adjusting the Q-switch delay of the pulsed laser so that energy output of the laser was at its most stable operating point. Even then, the energy per pulse varied by approximately 10%. Some of this variation was accounted for by signal averaging and the averaging procedure used in calculating the reflection coefficients.

The aluminum and graphite wedges were used to measure the shear wave reflection coefficient from several different viscous liquids. The liquids were certified viscosity standards available through Canon. For each liquid, the viscosity was tabulated at several temperatures. All of the measurements were taken at room temperature, which varied between 20 and 23 °C, and it was assumed that the liquids were at that temperature. The viscosity of the liquid at the recorded room temperature was determined by interpolating along an exponential fit between the tabulated viscosity values. The viscosity of these liquids was plotted against the measured reflection coefficients in Fig. 10. The curves plotted along with the data are trendlines to aid the reader to follow a given set of measurements, and do not represent the theoretical solution.

III. RESULTS AND DISCUSSION

The plots in Fig. 10 represent the results from three sets of measurements, two with the aluminum wedge and one with the graphite wedge. It can be seen that the data has the same trend as the theoretical curve from Fig. 3, but closer scrutiny shows that the data points do not lie exactly on the theoretical curves.

The two sets of measurements taken on the aluminum wedge are plotted in Fig. 10(a). The waveforms shown in Fig. 9(a) are from the set represented by the solid diamonds in Fig. 10(a). This set of data shows a greater change in the reflection coefficient with viscosity than does the set represented by the open squares. This change in ''slope'' is probably due to differences in the frequency contents of the signals. It can be seen from Fig. 9 that the signals are broadband, transient pulses. However, the pulse width was slightly different for the two sets. The peak-to-peak distance of the liquid signal in Fig. 9(a) was 86 ns. The peak-to-peak distance of a representative signal from the open square set of data was 113 ns. This represents a lower frequency than the filled-diamond data. The fast-Fourier transforms of the signals support this conclusion. The differences in the frequency content were probably due to small differences in the thickness of the line source. The theoretical results from Fig. 4 show that a lower frequency results in a lower slope.

It can also be seen from Fig. 10(a) that the reflection coefficient of the open squares is less than that of the solid diamonds at the lower viscosities (less than 70 poise). This could be due to differences in the angle of incidence of the SV wave at the solid–liquid interface. Figures 2 and 4 show that, for a given frequency and viscosity, the SV wave re-

flection coefficient decreases as the angle of incidence increases (up to 20°). This would mean that the signals corresponding to the open-square data had a larger angle of incidence, as well as a lower frequency.

The results of an experiment conducted with the same viscous liquids and a graphite wedge are plotted in Fig. 10(b). The results show the same trend in the data that was observed with the aluminum wedge; however, there is at least as much scatter. It was suggested in Sec. I.B that the viscosity could be measured with more resolution with a graphite wedge because of its lower shear impedance. However, this seems to be offset by the attenuation of high-frequency ultrasound in the graphite. Since the higher frequencies attenuate significantly more than the lower frequencies, the frequency content of the signal is reduced. This effect lowers the resolution of the viscosity measurements. The frequency dependence of the reflection coefficient for graphite is even more pronounced than that of aluminum, which is shown in Fig. 4.

IV. SUMMARY AND CONCLUSIONS

A solid wedge was designed to determine the viscosity of liquids using laser-generated shear waves. The shear waves were generated with a pulsed laser and detected with a laser interferometer on the same side of the wedge. The shear waves traveled through the wedge where they reflected from the solid–liquid interface. The reflected wave traveled back to the original side, where it was detected with the laser interferometer. The angle between the two surfaces was such that the reflected shear wave would create the maximum out-of-plane displacement at the detector.

The obvious advantage of such a system is that it is noncontact. This would be especially useful when making measurements at high temperatures. One application of interest is the measurement of glass viscosity in its molten state. Most commercially available piezoelectric transducers used in this application would dipole at these temperatures (1000–1800 °C). In order to use piezoelectric transducers for this application, they would have to be protected from this harsh environment. Mounting it on a water-cooled buffer rod is one solution to this problem.[20] However, in many cases, operators of these facilities do not like this solution because of the possibility of waters leaks, which can contaminate the material being processed or create a hazardous situation. Also, cooling may act as a heat sink which cannot be tolerated by many high-temperature processes, as is found in the production of ceramic fibers.[21] The technique described in this paper would eliminate the need for water cooling.

Admittedly, the proposed technique has several disadvantages. These include (a) the need for a special wedge, (b) the relatively high cost of instrumentation, (c) the use of lasers and hence the associated safety issues, and (d) the reduced sensitivity and stability of the interferometric reception of ultrasonic waves when compared with piezoelectric sensors. Another limitation is the lack of resolution, i.e., the reflection coefficient at 5 MHz changes from 1 to 0.84 over a viscosity range of 300 P, as shown in Fig. 4. In spite of these limitations, this method still has the potential to be used in applications where traditional methods cannot be deployed.

These applications include those in hostile environments, inaccessible regions, and, as discussed above, situations where water cooling is not appropriate.

ACKNOWLEDGMENT

[1] C. B. Scruby, R. J. Dewhurst, D. A. Hutchins, and S. B. Palmer, ''Laser Generation of Ultrasound in Metals,'' in *Research Techniques in Nondestructive Testing,* Vol. 5, edited by R. S. Sharpe (Academic, London, 1982), Chap. 8, pp. 281–327.

[2] C. B. Scruby and L. E. Drain, *LASER ULTRASONICS: Techniques and Applications* (Hilger, New York, 1990), Chap. 1.

[3] D. A. Hutchins, ''Ultrasonic Generation by Pulsed Lasers,'' in *Physical Acoustics*, Vol. 18, edited by W. P. Mason and R. N. Thurston (Academic, New York, 1988), pp. 21–23.

[4] L. R. F. Rose, ''Point-Source Represention for Laser-Generated Ultrasound,'' J. Acoust. Soc. Am. **75**, 723–732 (1984).

[5] J.-P. Monchalin, J.-D. Aussel, R. Heon, C. K. Jen, A. Bouldreault, and R. Bernier, ''Measurements of In-Plane and Out-of-Plane Ultrasonic Displacements by Optical Heterodyne Interferometry,'' J. Nondestruct. Eval. **8**(2), 121–133 (1989).

[6] S. Y. Zhang, M. Paul, S. Fassbender, U. Schleichert, and W. Arnold, ''Experimental Study of Laser-Generated Shear Waves Using Interferometry,'' Res. Nondestruct. Eval. **2**(3), 143–156 (1990).

[7] D. A. Hutchins and D. E. Wilkins, ''Polarized Shear Waves Using Laser Line Sources and Electromagnetic Acoustic Transducer Detection,'' Appl. Phys. Lett. **47**(8), 789–791 (1985).

[8] R. D. Costley, V. Shah, K. Balasubramaniam, and J. P. Singh, ''Shear Wave Wedge for Laser Ultrasonics,'' in *Review of Progress in Quantitative Nondestructive Evaluation*, Vol. 15, edited by D. O. Thompson and D. E. Chimenti (Plenum, New York, 1996), pp. 601–605.

[9] W. P. Mason, W. O. Baker, H. J. McSkimin, and J. H. Heiss, ''Measurement of Shear Elasticity and Viscosities of Liquids at Ultrasonic Frequencies,'' Phys. Rev. **75**(6), 936–946 (1949).

[10] S. H. Sheen, H. T. Chien, and A. C. Raptis, ''An In-Line Ultrasonic Viscometer,'' in *Review of Progress in Quantitative Nondestructive Evaluation*, Vol. 14, edited by D. O. Thompson and D. E. Chimenti (Plenum, New York, 1995), pp. 1151–1158.

[11] V. Shah, K. Balasubramaniam, R. D. Costley, and J. P. Singh, ''Measurement of Viscosity in Liquids Using Reflection Coefficient ...Phase Difference Method,'' in *Review of Progress in Quantitative Nondestructive Evaluation*, Vol. 15, edited by D. O. Thompson and D. E. Chimenti (Plenum, New York, 1996), pp. 2067–2071.

[12] R. D. Costley, C. Winstead, V. Shah, K. Balasubramaniam, and J. P. Singh, ''Viscosity Measurement with Laser Ultrasonics,'' in *Review of Progress in Quantitative Nondestructive Evaluation*, Vol. 16, edited by D. O. Thompson and D. E. Chimenti (Plenum, New York, 1996), pp. 539–545.

[13] J. P. Singh, K. Balasubramaniam, R. D. Costley, V. V. Shah, and C. Winstead, U.S. Patent 5,686,661 (1997).

[14] J. D. Achenbach, *Wave Propagation in Elastic Solids* (North-Holland, Amsterdam, 1973), Chaps. 5 and 2.

[15] A. Bedford and D. S. Drumheller, *Introduction to Elastic Wave Propagation* (Wiley, New York, 1994).

[16] C. B. Officer, *Introduction to the Theory of Sound Transmission* (McGraw-Hill, New York, 1958), Chap. 6.

[17] T. A. Litovitz and C. M. Davis, ''Structural and Shear Relaxation in Liquids,'' in *Physical Acoustics*, Vol. 2, edited by W. P. Mason (Academic, New York, 1964), Chap. 5.

[18] D. A. Bruttomesso, L. J. Jacobs, and R. D. Costley, ''Development of an Interferometer for Acoustic Emission Testing,'' J. Eng. Mech. **119**, 2303–2316 (1993).

[19] V. V. Shah and K. Balasubramaniam, ''Effect of Viscosity on Ultrasound Wave Reflection from a Solid/Liquid Interface,'' Ultrasonics **34**, 817–824 (1996).

[20] V. Shah, K. Balasubramaniam, R. D. Costley, and J. P. Singh, ''Sensor Development for High Temperature Viscosity Measurement,'' in *Review of Progress in Quantitative Nondestructive Evaluation*, Vol. 18, edited by D. O. Thompson and D. E. Chimenti (Plenum, New York, 1998), pp. 853–858.

[21] J. Righi, U.S. Patent 5,163,620 (1992).

Ultrasonic *in-situ* determination of the regression rate of the melting interface in burning metal rods

Martin Veidt and Theodore A. Steinberg

Department of Mechanical Engineering, University of Queensland, Brisbane, Queensland, 4072, Australia

Results of tests in which metallic rods are burned in oxygen enriched atmospheres often include the determination of the regression rate of the melting interface for the burning test specimen. This regression rate is used as an indication of a metallic material's relative flammability and its general ability to sustain burning under the test conditions. This paper reports on the development and first application of an ultrasonic measurement system that enables *in situ* measurement of the regression rate of the melting interface in burning metal rods. All other methods currently used for determining this parameter are based on posttest, visual interrogation, which is costly and often inaccurate. The transducer and associated equipment used to drive and record the transducer's output signal are described and typical results for iron rods burning in pure oxygen at different gauge pressures are given along with a comparison of these results with regression rates obtained from visual interrogation. The excellent sensitivity, accuracy and reliability of the new ultrasonic transducer are demonstrated, thus indicating the transducer's great potential. © *1999 Acoustical Society of America.* [S0001-4966(99)00702-X]

PACS numbers: 43.35.Zc [HEB]

INTRODUCTION

The burning characteristics of metallic materials are important in the design, fabrication, and subsequent use of many industrial systems and processes when operations are in environments that support combustion. Initial work investigated the pyrophoric behavior of metallic materials under ambient conditions and was often focused on fire safety in relation to mining activities.[1,2] The use of metallic particulates as additives to enhance a propellant's performance also spurred interest in the burning properties of various metallic materials.[3–5] Another motivation for understanding the combustion characteristics of metallic materials has arisen as a result of costly component and system failures. Both aerospace (government and civilian) and industrial (air separation plants, turbine blade producers, medical component manufacturers, valve manufacturers, etc.) organizations are experiencing incidents involving burning metallic materials, typically in pressurized oxygen systems, that often resulted in serious system failures.[6–8]

These incidents motivated both NASA and The American Society for Testing and Materials (ASTM) to develop and incorporate standard tests to determine a metallic material's tendency to burn in oxygen-enriched atmosphere.[9,10] These test methods are very similar to one another and typically require five standardized samples (0.32-cm-diam rod) to be tested. The burning characteristics that are typically reported from these tests include the threshold pressure and the regression rate of the melting interface. The threshold pressure is the lowest pressure that will just support combustion of the test sample and the regression rate is the rate at which the melting interface (the surface between the unburned rod and the molten mass) moves up the test sample as it is burned. Both the threshold pressure and the regression rate are used as indicators of a metallic material's flammability in oxygen-enriched environments. The regression rate is used as an indication of a metallic material's relative flammability when different metallic materials burn at the same test pressure and as an indication of a metallic material's general ability to sustain burning under the test conditions.

With the exception of only two methods, all reported methods for determining the regression rate are based on posttest visual interrogation of either a video or film recording of the burning test sample. This method is expensive and time intensive, since the recording must be obtained on a reviewable medium and an individual must develop and implement the procedure to obtain the regression rate from this medium. In addition, quantification of the regression rate by visual techniques has other, more important, problems such as accuracy and reproducibility. The major sources of errors are related to inaccuracies in the determination of the correct scale factor used posttest when viewing the visual record, variations in the speed of the recording, and human errors associated with determining the melting interface due to contrast problems and obscuration of the melting surface by condensed-phase products.

The two methods, which have been reported to determine the regression rate without relying on posttest analysis of a visual recording, were both developed and used at NASA White Sands Test Facility (WSTF). The first technique relied upon the response of thermopiles (many thermocouples) put at the end of copper tubes, which were placed along the walls of the combustion chamber.[11] The second technique relied on a gravimetric transducer, which was recording the changing mass of a burning sample as a function of time.[12] Both techniques are no longer used, mainly due to their inefficiency, the associated reliability and accuracy problems, and extended maintenance requirements.

This paper reports on the development and application of an ultrasonic measurement system to directly determine realtime regression rate data of the melting interface for
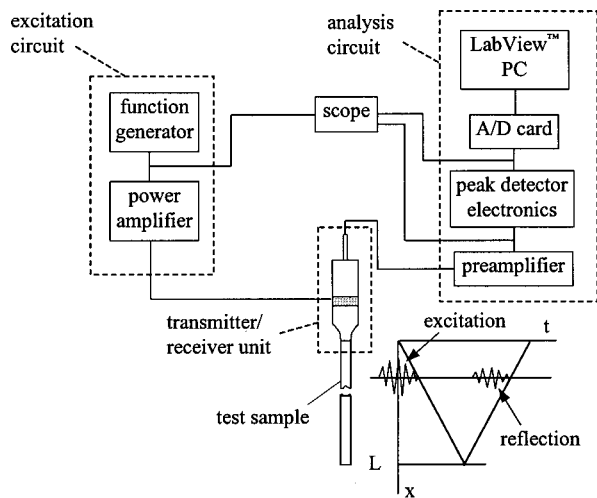
FIG. 1. Sketch of the ultrasonic measurement system and measurement concept.

burning metal rods, thus eliminating all of the problems described above. It provides a description of the developed transducer and the associated equipment used to drive and record the transducer's output signal. Results from the first applications of the transducer for burning iron rods are given along with comparisons to regression rates calculated by standard visual techniques.

I. ULTRASONIC MEASUREMENT SYSTEM

In Fig. 1 the basic measurement concept is illustrated. The transmitting transducer, which is coupled to the test sample, emits an ultrasonic pulse of known center frequency that travels down the rod as a longitudinal stress wave (velocity $c_0 = \sqrt{E/\rho}$, where E is the Young's modulus and ρ is the density of the material). The receiver detects the pulse after it is reflected from the end of the rod. The peak detector electronics determines the time of flight for the pulse and this measurement, together with the known propagation velocity c_0, which is determined from a precombustion measurement, enables real-time automatic calculation of the changing rod length as a function of time (the regression rate). Thus, the major components of the measurement system shown in Fig. 1 and described in detail below are (a) the ultrasonic transmitter/receiver unit, (b) the excitation circuit and (c) the signal conditioning and analysis circuit.

Figure 2 shows a schematic and photograph of the ultrasonic transmitter/receiver unit, which consists of two piezoelectric parts: a ringducer (transmitter, Ferroperm, PZ 27, outer diameter 10 mm, inner diameter 6 mm, thickness 2 mm) and a pinducer (receiver, ValpeyFisher, VP 1093, aperture 1.3 mm). A transducer design using separate transmitter/receiver elements rather than a conventional, single-element pulse echo arrangement proved to be necessary to have sufficient signal strength on one side and good detector sensitivity on the other in the extremely harsh environmental conditions for burning metal rods. The bronze collar, shown in the photograph, isolates the transducer from the burning metal sample preventing ignition and providing temperature stability. It is also used to hold and align the sample in the
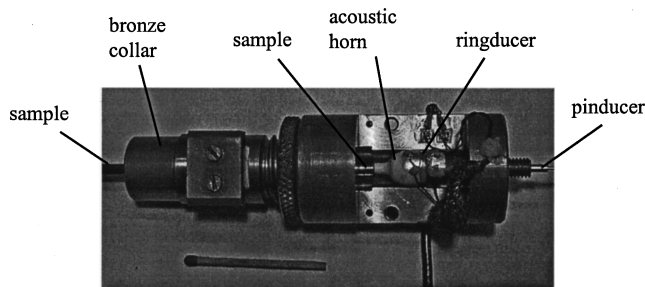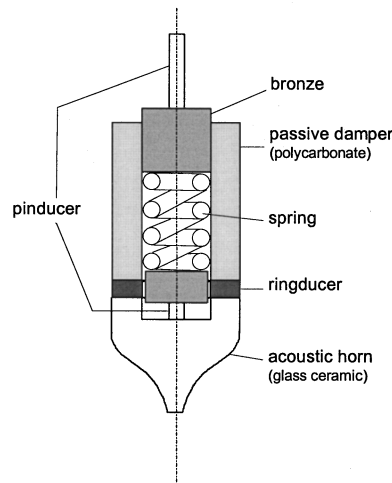
FIG. 2. Schematic and photograph of ultrasonic transmitter/receiver unit.

axial and lateral directions. The ringducer is sandwiched between an acoustic horn manufactured from glass ceramic and a passive damper element from polycarbonate. The pinducer is held in good contact with the sonic funnel by spring loading using the polycarbonate damper element and the bronze collar as support structures.

The electronics to drive the ringducer and receive and analyze the signal from the pinducer are shown in Fig. 1. The excitation path of these electronics consist of an arbitrary function generator and a high-power amplifier. The arbitrary function generator creates a narrow-band excitation pulse of the required center frequency, which results in the propagation of longitudinal waves in the sample rod and allows for the unambiguous identification of the reflected pulse. For 0.32-cm-diam, 180-cm-long iron rods a three cycle, 300-kHz sinusoidal burst fulfills these requirements. It results in an interrogation length of approximately 6 cm, which is sufficient considering that a steady-state regression rate is usually reached within the first centimeter of burning. The major effects which restrict the unambiguous identification of the reflected pulse for shorter rod lengths are the ringing of the ringducer on one hand and the internal reflections within the transducer unit itself on the other. The high-power amplifier conditions the excitation signal to a peak-to-peak level of approximately 100 V, which results in sufficiently strong excitation signals that can be clearly delineated from the acoustic noise generated from the combustion process. In the detection path, an ultrasonic preamplifier is used to condition the signal, an in-house built electronic circuit, which is de-
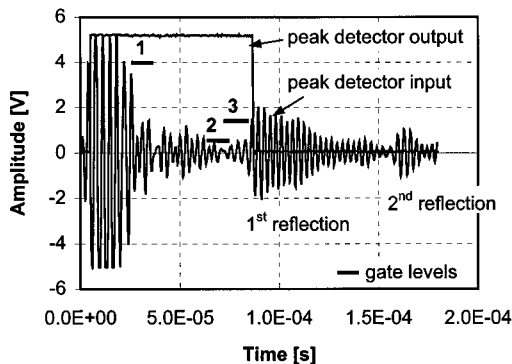
FIG. 3. Precombustion ultrasonic transducer output when attached to a 0.32-cm-diam, 18-cm-long iron rod and corresponding peak detector output signal.

FIG. 4. Ultrasonic transducer output during combustion of a 0.32-cm-diam iron rod burning in pure oxygen at a gauge pressure of 0.69 MPa (100 psia).

scribed in detail below, allows for the real-time measurement of the time-of-flight, and a PC, running LabView™ data acquisition and analysis software, is used for data processing, storage and display. A digitizing oscilloscope is used to monitor the signals and is an important tool for pretest adjustments and fine tuning of the test system.

The new ultrasonic system has been commissioned for a combustion system with associated control software, connections, viewports, video equipment and test procedures that have been described previously.[13]

Figure 3 shows the precombustion signal received when the transducer is used on a 0.32-cm-diam, 18-cm-long iron rod. The second area of high amplitude in the peak detector input signal shown on the figure represents the arrival of the first reflection of the longitudinal wave from the end of the rod. Electronically, the time-of-flight of the induced stress wave that is directly related to the rod length is detected using three voltage level detectors with the gatings indicated. The first one is set up to detect a large signal level and to set the output voltage of the circuit to approximately +5 V as shown. The second one detects a certain period of low voltage level signal without changing the output voltage of the circuit. The third one detects the next large (relative) voltage peak and sets the output voltage back to zero. Since a high–low–high sequence is required, the correct sequential detection is ensured. As stated, the width of the rectangular peak detector output signal, shown in Fig. 3, represents a multiple-length of the rod (in this case two times). These ''signal widths,'' or multiples of the rod length, are electronically measured using a 20-MHz counter circuit and transferred to the PC at a rate of approximately 8 Hz for posttest calculation of the regression rate of the melting interface of the burning rod.

II. EXPERIMENTS, RESULTS AND DISCUSSION

As stated, Fig. 3 depicts the output from the transducer prior to a test. This data is used to calculate the velocity, c_0, of longitudinal waves in the rod, which then allows the calculation of the rod's changing length during a test. Since the regression rate of the melting interface is large compared to the heat transfer rate within the rod, any temperature increase is restricted to a small length at the end of the burning rod. Consequently, the temperature dependence of c_0 has not to
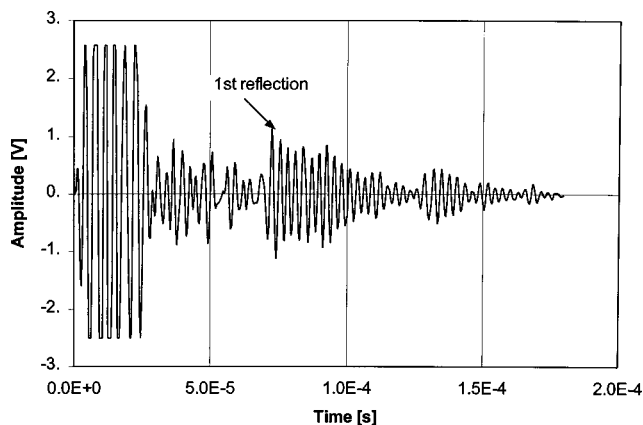
be considered in a first-order calculation of the regression rate. During the burning of a sample, the transducer's output retains the same pattern except the reflections begin to move to the left as the rod becomes shorter. One such output from the transducer during burning of a 0.32-cm-diam commercially pure iron rod in 0.69 MPa (100 psia) oxygen is shown in Fig. 4, where it is noted that the first reflection has been shifted towards the left. Figure 4 would have an associated rectangular peak detector output signal of about +5 V similar to the one shown in Fig. 3, except it would be of smaller width. This decrease in width is a direct multiple of the change in rod length between the time the two signals were recorded. Figure 5 shows the changing rod length with time as determined real-time by the transducer and associated electronics as described above. The slope of a best-fit line to these data points represents the mean regression rate of the melting interface for the burning iron.

The slope of the line fitted to the points shown in Fig. 5 was calculated to be 4.07 mm/s and this is taken to be the mean regression rate of the melting interface of this 0.32-cm-diam commercially pure iron rod in 0.69 MPa (100 psia) oxygen. The video record obtained for this burning iron was
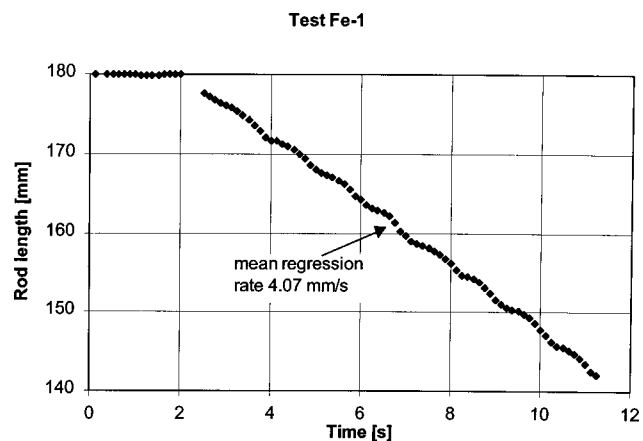
FIG. 5. Real-time changing rod length during combustion of a 0.32-cm-diam iron rod in 0.69 MPa (100 psia) oxygen pressure. The slope fitted to the data points represents the mean regression rate of the melting interface for the burning iron rod. The periodic variations of the instantaneous regression rates are related to the growth and detachment of individual drops of molten mass.

TABLE I. Regression rates of burning 0.32-cm-diam iron rods in pure oxygen at different gauge pressures.

Test	Oxygen pressure [MPa]	Measured regression rate pressure (mm/s)	
		Ultrasonic system	Visual interrogation
Fe-0	~0.6	3.82±0.08[a]	–
Fe-1	0.69	4.07±0.08	4.0±0.3
Fe-2	0.69	4.06±0.08	4.1±0.3
Fe-3	0.69	4.07±0.08	4.0±0.3
Fe-4	0.5	3.77±0.08	3.8±0.2
Fe-5	0.5	3.64±0.07	4.1±1.1
Fe-6	0.5	3.60±0.07	4.0±1.1

[a]The various factors that contribute to the reported uncertainties of the ultrasonic measurement system are discussed and quantified in the Appendix.

interrogated visually and a regression rate of the burning rod by this method was determined to be 4.0 mm/s. Obviously there is excellent agreement between the regression rate obtained by the ultrasonic transducer and the visual interrogation method. Published values for the regression rate of the melting interface for a burning iron rod in 0.69 MPa (100 psia) oxygen were found in the literature.[14,15] The reported regression rate of about 4.2 mm/s is also in excellent agreement with the regression rate calculated by the new ultrasonic transducer.

In Table I the results of the measured regression rates for 0.32-cm-diam commercially pure iron rods burning in pure oxygen are summarized. The values of the calculated mean regression rates using the new ultrasonic measurement system are in excellent agreement with values determined using conventional visual interrogation. The system enables reliable identification of even small variations, which may result, for example, from slight changes in the applied oxygen pressure between individual tests. It is important to mention that the calculation of the regression rates using the new system requires almost no time compared to the conventional posttest visual interrogation technique. The various factors that contribute to the reported uncertainties of the ultrasonic measurement system are discussed and quantified in the Appendix.
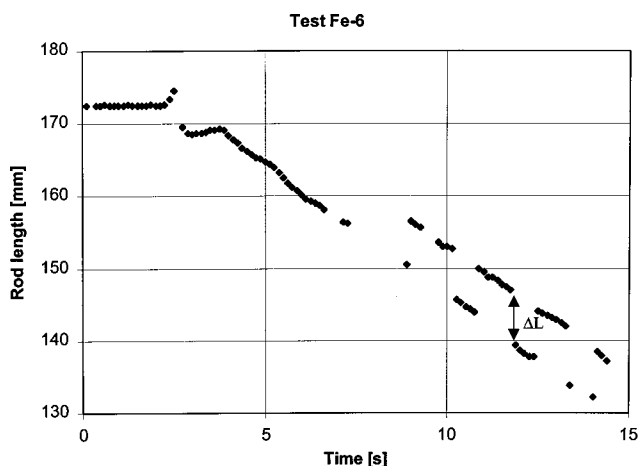
FIG. 6. Changing rod length raw data during combustion of a 0.32-cm-diam iron rod in 0.5 MPa (72.5 psia) oxygen pressure. The two parallel data sets result from the peak detector electronics locking on to different cycles of the reflected pulse.

A characteristic feature, which is present in Fig. 5, is the periodic variations in the measured instantaneous regression rates, which is the result of the growth and detachment of individual drops of molten mass. This effect has been reported in the literature,[14–16] but it has never been documented with such clarity, thus demonstrating the outstanding sensitivity of the new ultrasonic measurement system.

It is the authors' contention that regression rates calculated with this ultrasonic transducer will be more reliable and accurate than similar rates calculated visually. In general, most of the errors described above that are present during the visual interrogation process are completely eliminated when the ultrasonic transducer is used. No scale factors and no playback of recordings are necessary, thus no distance, parallax, or recording speed errors are present. In addition, there are no restrictions on access time to the burning rod, which is normally limited by the viewports of the recording system, and the combustion phenomena is not important in the calculation of the regression rate, i.e., ambiguities due to contrast problems and the obscuration of the melting surface by condensed-phase products are irrelevant.

In Fig. 6 the rod length versus time raw data for experiment Fe-6 are presented. It shows the effect when the amplitude of the reflected wave varies in time in such a way that the peak detector electronics locks on to different cycles of the reflected pulse. This results in unsteady rod length data as indicated by the two different data samples, which are vertically shifted by $\Delta L = c_0 T$, where $T = 3.3 \mu s$ is the period of the 300-kHz excitation signal. The figure shows that the data can be used to calculate the regression rate, since although the absolute length of the burning rod varies, the slope of the curves, i.e., the regression rates are the same. In the Appendix further details are given on the accuracy of the new measurement technique.

III. CONCLUSIONS

A new ultrasonic measurement system has been developed which is capable of quantifying the regression rate of the melting interface for a burning metallic rod. The regression rates for burning iron rods in pure oxygen at different gauge pressures provided by the ultrasonic transducer compare excellently with published values and regression rates determined from standard posttest visual interrogation of a recorded image. In addition, the new measurement system has proven to be much more cost effective and significantly more sensitive and accurate than the visual techniques typically used to obtain this parameter.

ACKNOWLEDGMENTS

APPENDIX: UNCERTAINTY ANALYSIS

The major factor which determines the accuracy of the ultrasonic measurement system is the ratio between the individual wave propagation components that define the width of

1641   J. Acoust. Soc. Am., Vol. 105, No. 3, March 1999

M. Veidt and T. A. Steinberg: Ultrasonic in situ determination   1641
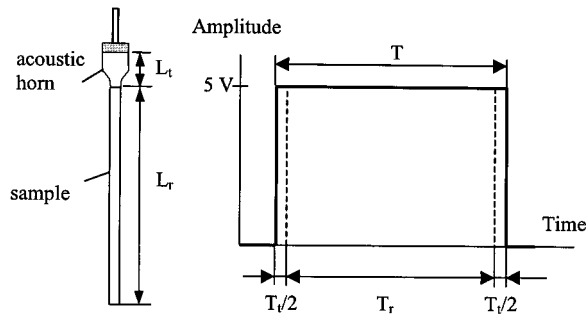
FIG. A1. Sketch of the wave propagation segments that contribute to the width of the rectangular peak detector output signal.

the rectangular peak detector output signal. As illustrated in Fig. A1, the pulse width is not only controlled by the time the pulse needs to travel along the rod, but also by the time required for the propagation within the transducer unit. Therefore, the assumption that a constant value of c_0 can be used to calculate the instantaneous rod length during the entire combustion period is strictly not correct.

In the initial, precombustion test, which is used to determine c_0, the time T_t is approximately 4% of the total time T if the rod length is 180 mm and the wave velocities within the metallic rod and the glass ceramic acoustic horn are assumed to be $c_r = 5$ mm/μs and $c_t = 12$ mm/μs, respectively. The velocity c_0 determined from the measurement is:

$$c_0 = \frac{2L_r}{T} = 4.8 \quad \text{mm}/\mu\text{s}. \tag{A1}$$

In comparison, T_t is approximately 6% if the rod is 120 mm long or, in other words, the instantaneous rod length is calculated to be

$$L_r = \frac{c_0 T}{2} = 122.4 \quad \text{mm} \tag{A2}$$

if the c_0 value from above is used, which over estimates the real length by 2%.

In conclusion, considering an interrogation length of approximately 60 mm and typical wave propagation velocities for metallic samples, the maximum uncertainty for the measured rod lengths is less than 2%.

[1] F. P. Bowden, ''The development of combustion and explosion in liquids and solids,'' in *Fourth Symposium on Combustion* (Williams and Wilkins, Baltimore, 1953), pp. 161–172.

[2] H. Titman, ''A review of experiments on the ignition of inflammable gases by fictional sparking,'' Trans. Inst. Min. Eng. **115**, 535–557 (1955).

[3] D. A. Gorden, ''Combustion characteristics of metal particles,'' in *Solid Propellant Rocket Research*, edited by M. Summerfield (Academic, New York, 1960), pp. 271–278.

[4] G. H. Markstein, ''Combustion of metals,'' AIAA J. **1**, 560–562 (1963).

[5] R. Friedman and A. Macek, ''Ignition and combustion of aluminum particles in hot ambient gasses,'' Combust. Flame **6**, 9–19 (1965).

[6] C. E. Cataldo, ''LOX/GOX related failures during space shuttle main engine development,'' NASA TM-82424 (NASA, Washington, DC, 1981).

[7] D. W. G. Dicker and R. K. Wharton, ''A review of incidents involving the use of high-pressure oxygen from 1982 to 1985 in Great Britain,'' in *Flammability and Sensitivity of Materials in Oxygen-Enriched Atmosphere, III, ASTM STP 986*, edited by D. W. Schroll (American Society for Testing and Materials, Philadelphia, 1988), pp. 318–327.

[8] J. A. Daniel, R. C. Christianson, J. M. Stoltzfus, and M. A. Rucker, ''A hazards analysis method for oxygen systems including several case studies,'' in *Flammability and Sensitivity of Materials in Oxygen-Enriched Atmospheres, VI, ASTM STP 1197*, edited by D. Janoff and J. Stoltzfus (American Society for Testing and Materials, Philadelphia, 1993), pp. 360–372.

[9] ''Standard test method for determining the combustion behavior of metallic materials in oxygen-enriched atmospheres,'' in *ASTM STANDARD GO124-94* (American Society for Testing and Materials, Philadelphia, 1994).

[10] ''Flammability, odor, offgassing, and compatibility requirements and test procedures for materials in environments that support combustion,'' *NHB 8060.1C* (National Aeronautics and Space Administration, Washington, DC, 1991).

[11] T. A. Steinberg, M. A. Rucker, and H. D. Beeson, ''Promoted combustion of nine structural metals in high-pressure gaseous oxygen; a comparison of ranking methods,'' in *Flammability and Sensitivity of Materials in Oxygen-Enriched Atmospheres, IV, ASTM STP 1040*, edited by J. M. Stoltzfus, F. Benz, and J. Stradling (American Society for Testing and Materials, Philadelphia, 1989), pp. 54–75.

[12] S. Sircar, H. Gabel, J. M. Stoltzfus, and F. Benz, ''The analysis of metals combustion using a real-time gravimetric technique,'' in *Flammability and Sensitivity of Materials in Oxygen-Enriched Atmospheres, V, ASTM STP 1111*, edited by J. M. Stoltzfus and K. McIlroy (American Society for Testing and Materials, Philadelphia, 1991), pp. 313–325.

[13] T. A. Steinberg and B. C. Scown, ''New test capabilities for the evaluation of material flammability in oxygen-enriched atmospheres,'' in *Flammability and Sensitivity of Materials in Oxygen-Enriched Atmospheres, VII, ASTM STP 1267*, edited by D. Janoff, B. Royals, and M. Gunaji (American Society for Testing and Materials, Philadelphia, 1995), pp. 57–67.

[14] J. Sato, K. Sato, and T. Hirano, ''Fire spread mechanisms along steel cylinders in high pressure oxygen,'' Combust. Flame **51**, 279–287 (1983).

[15] J. Sato and T. Hirano, ''Behavior of fire spreading along high-temperature mild steel and aluminum cylinders in oxygen,'' in *Flammability and Sensitivity of Materials in Oxygen-Enriched Atmospheres, II, ASTM STP 910*, edited by M. A. Benning (American Society for Testing and Materials, Philadelphia, 1986), pp. 118-134.

[16] F. J. Benz, R. C. Shaw, and J. M. Homa, ''Burn propagation rates of metals and alloys in gaseous oxygen,'' in *Flammability and Sensitivity of Materials in Oxygen-Enriched Atmospheres, II, ASTM STP 910*, edited by M. A. Benning (American Society for Testing and Materials, Philadelphia, 1986), pp. 135–152.

1642   J. Acoust. Soc. Am., Vol. 105, No. 3, March 1999

M. Veidt and T. A. Steinberg: Ultrasonic *in situ* determination   1642

Study on the longitudinal–torsional compound transducer with slanting slots

Lin Shuyu

Applied Acoustics Institute, Shaanxi Teachers University, Xian, Shaanxi, 710062, People's Republic of China

The longitudinal–torsional compound transducer with slanting slots is studied. The compound transducer is composed of a sandwiched longitudinal ultrasonic transducer and a transmission cylinder with slanting slots. The equivalent circuit for the longitudinal–torsional vibrating system is derived. Based on the equivalent circuit, the input mechanical impedance and the resonance-frequency equation for the compound system are obtained. The effect of the slanting angle of the slanting slots, the position of the slanting slots, and the geometrical length of the slanting slots on the resonance frequency of the compound longitudinal–torsional system is analyzed theoretically and experimentally. Experiments show that the measured resonance frequencies are in good agreement with the predicted results. © *1999 Acoustical Society of America.* [S0001-4966(99)02303-6]

INTRODUCTION

As science and technology develop, some traditional ultrasonic technologies such as ultrasonic soldering, ultrasonic machining, and ultrasonic fatigue testing have found widespread applications in the fields of industry, electronics, and material science. At the same time, new ultrasonic technologies such as the ultrasonic motor and ultrasonic surgery have been paid increasing attention. Corresponding to this development, the key parts of ultrasonic equipment, i.e., the ultrasonic transducer and the vibrating system, have become an important research subject recently. Apart from the traditional single vibrational mode ultrasonic transducer, such as the longitudinal, the torsional, and the flexural transducers,[1–4] some compound transducers such as longitudinal–torsional and longitudinal–flexural transducers have found newer applications.[5–8]

For the creation of torsional and longitudinal–torsional vibration, two methods can be used. One is by means of the conversion of longitudinal into torsional vibration,[9] and the other is by using the tangentially polarized piezoelectric ceramics.[10] In the first method, the conversion of longitudinal into torsional vibration is by means of two sandwiched longitudinal transducers, which are attached on the sides of a transmission cylinder. The torsional vibration in the cylinder can be created by choosing the phase of the input voltages of the transducer. In this case, the total input electric power can be large and the system can be used in high-power ultrasonic applications. However, since the volume of the vibrating system is large and the efficiency of conversion of longitudinal into torsional vibration is low, the system has not been widely used. Another method to create the torsional and longitudinal–torsional vibration by means of conversion of longitudinal into torsional vibration is by using a drilling tool with spiral slots, which is attached to the output end of a longitudinal-sandwiched transducer. In this case, the vibration system can create longitudinal–torsional compound vi-

bration. Since the geometrical shape of the transmission cylinder is complex, the computation and design of this kind of transducer is difficult. The vibrational characteristics cannot be studied analytically. Even if the numerical methods such as the finite element method are used, the analysis is still complex and cumbersome.

For the creation of torsional and longitudinal–torsional vibration by means of the tangentially polarized piezoelectric ceramics, the design theory is well developed.[11] In this case, the torsional-sandwiched transducer is composed of the tangentially polarized piezoelectric-ceramic tubes and the front and back metal cylinders, and the longitudinal–torsional compound transducer is composed of the longitudinally and tangentially polarized piezoelectric ceramic tubes and the front and back metal cylinders. Although this kind of transducer is similar to the sandwiched longitudinal transducer in appearance, the concrete manufacture of the transducer is complex, especially for the processing of the tangentially polarized piezoelectric ceramic ring. Since the polarization is along the circumferential direction, large sectors are difficult to polarize and electrical breakdown may happen. In this case, an entire polarization is difficult to achieve. To overcome these difficulties, the piezoelectric ceramic sectors must be small and the lateral dimension (such as the diameter of the segmented ceramic ring and the wall thickness of ring) is limited. This gives rise to the problem that the power capacity and the efficiency of the transducer is also limited. Therefore, this kind of transducer is mostly used in ultrasonic motor and other low-power applications rather than high-power ultrasonic applications. On the other hand, for the longitudinal–torsional compound transducers, since the sound speeds of longitudinal and torsional vibrations are different, the longitudinal and torsional vibrations are difficult to resonate at the same frequency. Although the simultaneous resonance of longitudinal and torsional vibrations can be achieved by properly choosing the shape and dimension
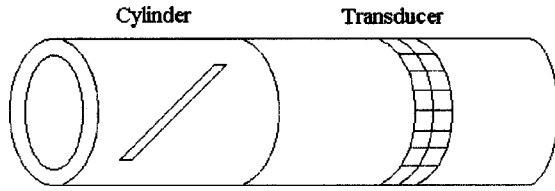
FIG. 1. Longitudinal–torsional compound transducer with slanting slots.

of the transducer,[12] the computation is complex.

To avoid these problems in computing and processing the torsional and longitudinal–torsional transducer, a new type of longitudinal–torsional compound transducer with slanting slots was developed and used in ultrasonic motors.[13] In this paper, this kind of transducer is studied theoretically and experimentally, an equivalent circuit model used for the analysis and design of the compound transducer is given, and the effect of the slanting slots on the resonance frequency is analyzed.

I. EQUIVALENT CIRCUIT MODEL FOR THE COMPOUND TRANSDUCER

The longitudinal–torsional compound transducer with slanting slots is shown in Fig. 1. In the figure, the right part is the sandwiched longitudinal transducer and the left part is the transmission cylinder with slanting slots. As there are slanting slots on the transmission cylinder, the longitudinal vibration created by the sandwiched longitudinal transducer will be partially converted into torsional vibration. Therefore, longitudinal and torsional vibrations will coexist in the transmission cylinder and at its output end, longitudinal–torsional compound vibration will be produced. It is obvious that the characteristics of the slanting slots, such as the slanting angle, the position, and the dimensions, will affect the performance of the compound transducer.

According to traditional design theory for the transducer, the compound transducer can be designed by two methods. First, the transducer can be a vibrator of one wavelength; the longitudinal transducer and the transmission cylinder are vibrators of half wavelength, respectively. Second, the compound transducer can be a vibrator of half wavelength; the longitudinal transducer and the transmission cylinder are vibrators of quarter wavelength, respectively. In this paper, the compound transducer is designed as a vibrator of one wavelength, the longitudinal transducer and the transmission cylinder with slanting slots are vibrators of half wavelength.

In Fig. 2, the half-wavelength transmission cylinder with
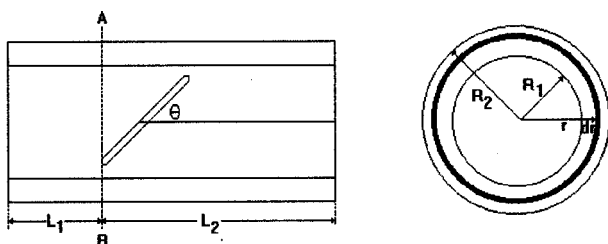
FIG. 2. The half-wavelength transmission cylinder with slanting slots.

slanting slots is shown. Its length and outer and inner radiuses are L, R_2, and R_1, respectively. In the figure, θ is the slanting angle of the slanting slots, L_1 is the distance between the input end of the cylinder and the slanting slots. L_2 is the length of the rest of the cylinder. Since the creation of torsional vibration is by means of the slanting slots, the vibration in the part before the slanting slots may be regarded as longitudinal vibration, while the vibration in the remaining part of the cylinder (whose length is L_2) is a longitudinal–torsional compound vibration. For simplicity, the slanting slots are assumed to be very thin, and their width can be regarded as infinitesimal. Therefore, the slanting slots can be treated as a geometrical line with finite length, and the slanting slots have no effect on the mass of the cylinder. However, the slots alter the vibrational mode of the cylinder, and apart from longitudinal vibration, torsional vibration is created in the cylinder. In Fig. 2, the dotted line AB is the dividing line between the cylinder in longitudinal vibration and the cylinder in longitudinal–torsional compound vibration. On the left side of the dividing line, the acting force in the cylinder is the longitudinal force F, while on the right side of the dividing line, there are two kinds of forces acting on it: one is the longitudinal force component F_L, the other is the shearing force component F_T. From Fig. 2, these two force components can be expressed as

$$F_L = F \cos \theta, \tag{1}$$

$$F_T = F \sin \theta. \tag{2}$$

Based on the theory of longitudinal and flexural vibration, the longitudinal force component in the cylinder will create longitudinal vibration, while the shearing force component will create torsional vibration. The torsional moment M of shearing force component can be obtained as

$$M = \int \int_s rf \, ds, \tag{3}$$

where $s = \pi(R_2^2 - R_1^2)$ is the cross-sectional area of the cylinder, $ds = 2\pi r \, dr$, r is the radius of any position in the cylinder as shown is Fig. 2, and f is the shearing force acting on the unit cross-sectional area in the cylinder on the divided surface. From the above analysis, the shearing force on the unit cross-sectional area can be expressed as

$$f = \frac{F \sin \theta}{\pi(R_2^2 - R_1^2)}; \tag{4}$$

substituting Eq. (4) into Eq. (3) yields

$$M = F \sin \theta \frac{2(R_2^3 - R_1^3)}{3(R_2^2 - R_1^2)}. \tag{5}$$

If the wall thickness of the cylinder is small and the average radius of the cylinder is large, we can get the relation of $R_1 = R_2 = R$ approximately; the above equation can be rewritten as

$$M = F \sin \theta \cdot R. \tag{6}$$

On the other hand, if the cylinder is solid, $R_1 = 0$, the torsional moment M can be expressed as
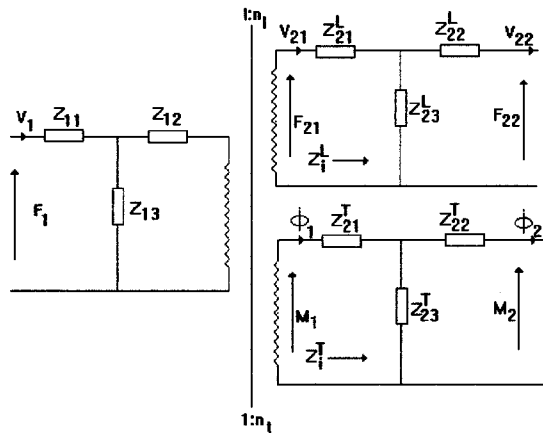
FIG. 3. The equivalent-circuit model for the longitudinal–torsional compound cylinder.

$$M = F \sin\theta \cdot 2/3R_2. \tag{7}$$

In general cases, the transmission cylinder is between these two limiting cases. Based on the above analysis, it is obvious that the slanting slots create both longitudinal and torsional vibrations in the cylinder; the vibration in the back part of the cylinder whose length is L_2 is a longitudinal–torsional compound one.

Based on one-dimensional longitudinal and torsional theory and the above analysis, the equivalent circuit model for the longitudinal–torsional compound cylinder can be obtained as shown in Fig. 3. Where F_1 and V_1 are the longitudinal force and velocity at the input end of the cylinder, F_{21}, V_{21}, and F_{22}, V_{22} are the longitudinal forces and velocities at the dividing surface and the output end of the cylinder with slanting slots, respectively, $M_1, \dot\varphi_1$ and $M_2, \dot\varphi_2$ are the torsional moments and angular velocities at the dividing surface and the output end of the cylinder, n_L and n_T are the conversion coefficients between longitudinal vibration and torsional vibration, their expressions can be given as

$$n_L = \cos\theta, \tag{8}$$

$$n_T = \frac{M}{F} = \sin\theta \frac{2(R_2^3 - R_1^3)}{3(R_2^2 - R_1^2)}. \tag{9}$$

When the slanting angle of the slanting slots is zero, $n_L = 1, n_T = 0$. It is obvious that in this case there is no torsional vibration in the cylinder, and this is consistent with the observed result. In Fig. 3, $Z_{11}, Z_{12}, Z_{13}, Z_{21}^L, Z_{22}^L, Z_{23}^L$ and $Z_{21}^T, Z_{22}^T, Z_{23}^T$ are the series and parallel impedances of the cylinder before and after the dividing line in longitudinal and torsional vibrations, respectively. Their expressions are as follows:

$$Z_{11} = Z_{12} = jZ_1 \tan\left(\frac{k_L L_1}{2}\right), \tag{10}$$

$$Z_{13} = \frac{Z_1}{j \sin(k_L L_1)}, \tag{11}$$
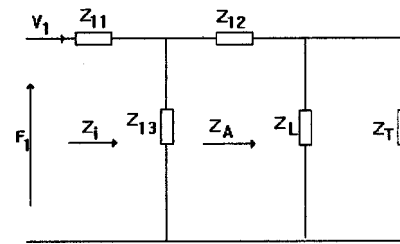
FIG. 4. The simplified equivalent-circuit model for the longitudinal–torsional compound cylinder with slanting slots.

$$Z_{21}^L = Z_{22}^L = jZ_2 \tan\left(\frac{k_L L_2}{2}\right), \tag{12}$$

$$Z_{23}^L = \frac{Z_2}{j \sin(k_L L_2)}, \tag{13}$$

$$Z_{21}^T = Z_{22}^T = jZ_2^T \tan\left(\frac{k_T L_2}{2}\right), \tag{14}$$

$$Z_{23}^T = \frac{Z_2^T}{j \sin(k_T L_2)}, \tag{15}$$

where $Z_1 = \rho C_L S_1$, $Z_2 = \rho C_L S_2$, $C_L = (E/\rho)^{1/2}$ is the sound speed of longitudinal vibration in a slender rod, S_1 and S_2 are the cross-sectional areas of the cylinder before and after the dividing line, and S_1 may be equal to S_2. $Z_2^T = \rho C_T I_P$, $C_T = (G/\rho)^{1/2}$ is the sound speed of torsional vibration in a slender rod, $G = E/2(1 + \sigma)$ is the rigidity modulus. $I_P = (\pi/2)(R_2^4 - R_1^4)$ is the moment of the cross section, $k_L = \omega/C_L$, $k_T = \omega/C_T$, k_L and k_T are the wave numbers of longitudinal and torsional vibrations. When the longitudinal–torsional compound cylinder is without external load, its two output ends in Fig. 3 are short circuited. From Fig. 3, the input mechanical impedances Z_i^L and Z_i^T for the longitudinal and torsional vibrations in the cylinder after the dividing line can be obtained,

$$Z_i^L = \frac{F_{21}}{V_{21}} = \frac{F_L}{V_{21}} = jZ_2 \tan(k_L L_2), \tag{16}$$

$$Z_i^T = \frac{M_1}{\dot\varphi_1} = \frac{M}{\dot\varphi_1} = jZ_2^T \tan(k_T L_2). \tag{17}$$

After the above transformation, Fig. 3 can be reduced to the following form as shown in Fig. 4, where $Z_L = Z_i^L/n_L^2$, $Z_T = Z_i^T/n_T^2$, Z_L and Z_T are two reflected mechanical impedances of the longitudinal and torsional vibration components in the cylinder before the dividing line. From Fig. 4, the compound mechanical impedance at the dividing line, which is also the load impedance of the cylinder in longitudinal vibration, can be derived as

$$Z_A = \frac{Z_L \cdot Z_T}{Z_L + Z_T}. \tag{18}$$

Substituting the expressions of Z_L and Z_T into Eq. (18) yields

$$Z_A = j \frac{9(R_2^2 - R_1^2)^2 Z_2 Z_2^T \tan(k_L L_2)\tan(k_T L_2)}{4Z_2 \sin^2(\theta)(R_2^3 - R_1^3)^2 \tan(k_L L_2) + 9Z_2^T \cos^2(\theta)(R_2^2 - R_1^2)^2 \tan(k_T L_2)}. \tag{19}$$

Based on the impedance-transformation theory of transmission line, the input impedance Z_i of the cylinder can be obtained

$$Z_i = jZ_1 \tan(k_L L_1 + \alpha), \tag{20}$$

where α is a parameter that is determined by the frequency, slanting angle, shape, and dimensions of the cylinder after the dividing line; it can be expressed as

$$\tan \alpha = \frac{Z_A}{jZ_1} = \frac{9(R_2^2 - R_1^2)^2 Z_2 Z_2^T \tan(k_T L_2)\tan(k_L L_2)}{Z_1[4Z_2 \sin^2(\theta)(R_2^3 - R_1^3)^2 \tan(k_L L_2) + 9Z_2^T \cos^2(\theta)(R_2^2 - R_1^2)^2 \tan(k_T L_2)]}. \tag{21}$$

When the material, shape, and dimension of the cylinder before and after the dividing line are the same, $Z_1 = Z_2$, Eq. (21) can be simplified as

$$\tan \alpha = \frac{9(R_2^2 - R_1^2)^2 Z_2^T \tan(k_T L_2)\tan(k_L L_2)}{4Z_2 \sin^2(\theta)(R_2^3 - R_1^3)^2 \tan(k_L L_2) + 9Z_2^T \cos^2(\theta)(R_2^2 - R_1^2)^2 \tan(k_T L_2)}. \tag{22}$$

From Eq. (20), when the input mechanical impedance Z_i is equal to zero, the longitudinal–torsional compound cylinder with slots resonate. Its resonance frequency equation can be obtained as

$$k_L L_2 + \alpha = n\pi \quad (n = 1,2,3,...), \tag{23}$$

where n is a positive integer; it represents the vibrational mode of the cylinder. When $n = 1$, the cylinder resonates at the fundamental mode.

From the above analysis and the expressions of the derived parameters, it can be seen that the slanting slots create torsional vibration in the cylinder when the cylinder with slots is excited by a sandwiched longitudinal ultrasonic transducer. It is obvious that the slanting slots play an important role in the conversion of longitudinal into torsional vibration; its position, shape, and dimension affect the vibrational characteristics of the cylinder. In the next sections, the effect of the slanting slots on the longitudinal–torsional compound cylinder will be studied.

II. THE EFFECT OF THE SLANTING ANGLE OF THE SLOTS ON THE RESONANCE FREQUENCY OF THE CYLINDER

It can be seen from the above analysis that the slanting slots in the cylinder alter the vibrational mode, and torsional vibration is created. The slanting angle, the shape, and dimensions of the slanting slots affect the vibration of the cylinder. In general cases, the concrete slots have finite geometrical dimensions, such as finite width and length. However, when the slots are wide and long, they not only alter the vibrational mode of the cylinder, but also alter the mass and shape of the cylinder. In this case, the analysis of the cylinder with large slots is difficult.

As mentioned above, the width of the slots is considered as infinitesimal. In this case, the slanting slots can be treated as ideally geometrical lines with finite length. They do not affect the mass and shape of the cylinder; their sole role is that the vibrational mode of the cylinder is changed. Resonance frequency is an important parameter for ultrasonic vibrating systems. From the above analysis, it can be seen that

the resonance-frequency Eq. (23) of the cylinder with slanting slots is a transcendental one about the material parameter, the slanting angle, the shape, and dimension of the cylinder. Therefore, the analytic expression of the resonance frequency with these parameters is impossible to find.

In the following analysis, the slanting angle of the slanting slots is considered as a parameter; the relation between the input mechanical impedance and the phase length of the cylinder is studied. When this is done, the effect of the slanting angle on the resonance frequency of the cylinder can be analyzed and explained. In order to study the relation between the input mechanical impedance and the frequency and geometrical dimensions of the cylinder, we introduce the concept of phase length, which is defined as the product of the wave number and the length of the cylinder. In this paper, there are three kinds of phase lengths, i.e., $k_L L_1$, $k_L L_2$, and $k_T L_2$. On the other hand, to simplify the theoretical analysis, the following transformation should be done. The relation between the Young's modulus and the rigidity modulus is expressed as

$$G = \frac{E}{2(1+\sigma)}, \tag{24}$$

where σ is Poisson's ratio of the cylinder material. Using Eq. (24), the torsional phase length $k_T L_2$ can be expressed as

$$k_T L_2 = [2(1+\sigma)]^{1/2} k_L L_2. \tag{25}$$

When Eq. (25) is substituted into the expression of the input mechanical impedance of the cylinder, it can be found that the input mechanic impedance Z_i is a function of phase length $k_L L_1$, $k_L L_2$ and the slanting angle of the slanting slots. Figure 5(a) and (b) are the theoretically computed relation between the normalized input impedance Z_i/Z_1 and the phase length $k_L L_2$. In Fig. 5(a) and (b), the phase length $k_L L_1$ is given an arbitrary constant, while the slanting angle of the slanting slots is changed as a parameter. For every given slanting angle, a curve describing the relation between the normalized input mechanical impedance and the phase length $k_L L_2$ can be plotted. Figure 5(a) describes the relation between the impedance and the phase length when the slant-
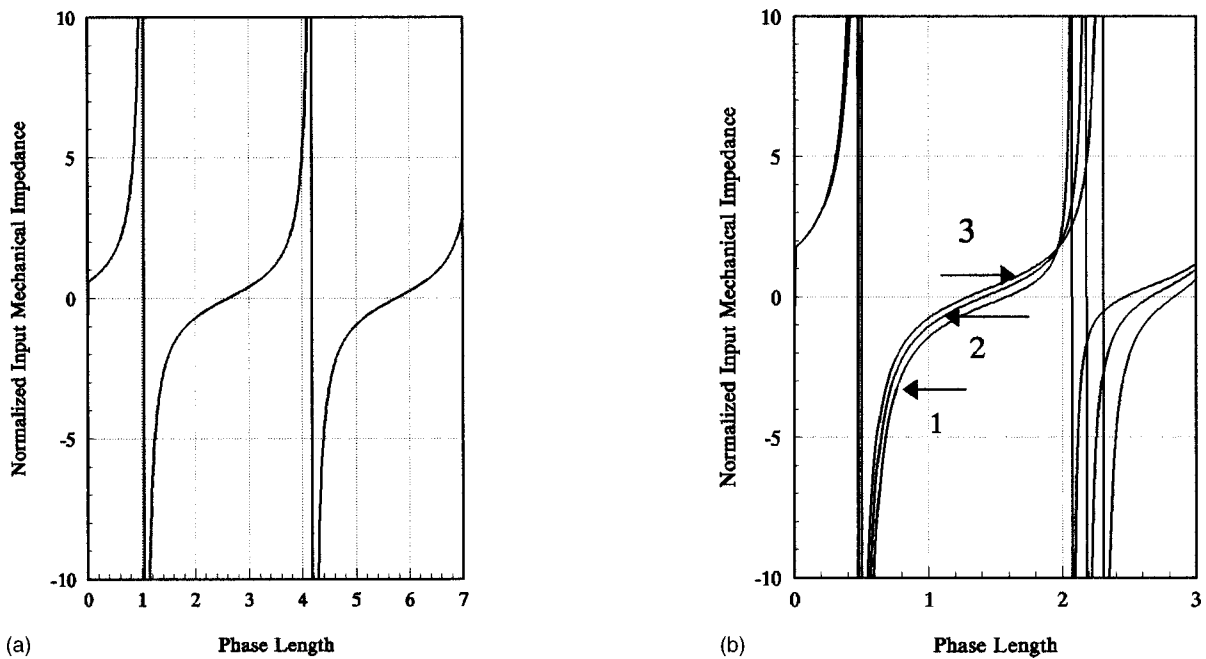
FIG. 5. (a) The theoretically computed relation between the normalized input mechanical impedance and the phase length when the slanting angle is zero. (b) The theoretically computed relation between the normalized input mechanical impedance and the phase length when the slanting angle is 30, 45, and 60 deg.

ing angle is zero. In Fig. 5(b), curves 1, 2, and 3 correspond to the relations between the impedance and the phase length when the slanting angle equals 30, 45, and 60 deg, respectively.

It can be seen from Fig. 5(a) and (b) that the slanting slots alter the vibrational characteristics of the cylinder with slanting slots, and the vibrational mode of the cylinder is increased. It is obvious that apart from the comparatively low resonance frequency, a resonance frequency higher than

the first resonance frequency is created. Based on theoretical analysis and experimental observation, it can be concluded that the lower frequency corresponds to the resonant vibration of the cylinder in longitudinal vibration, while the higher resonance frequency corresponds to the resonant vibration of the cylinder in torsional vibration. It should be pointed out that since the vibration of the cylinder is a longitudinal–torsional compound vibration, the resonant vibration corresponding to the lower resonance frequency is a
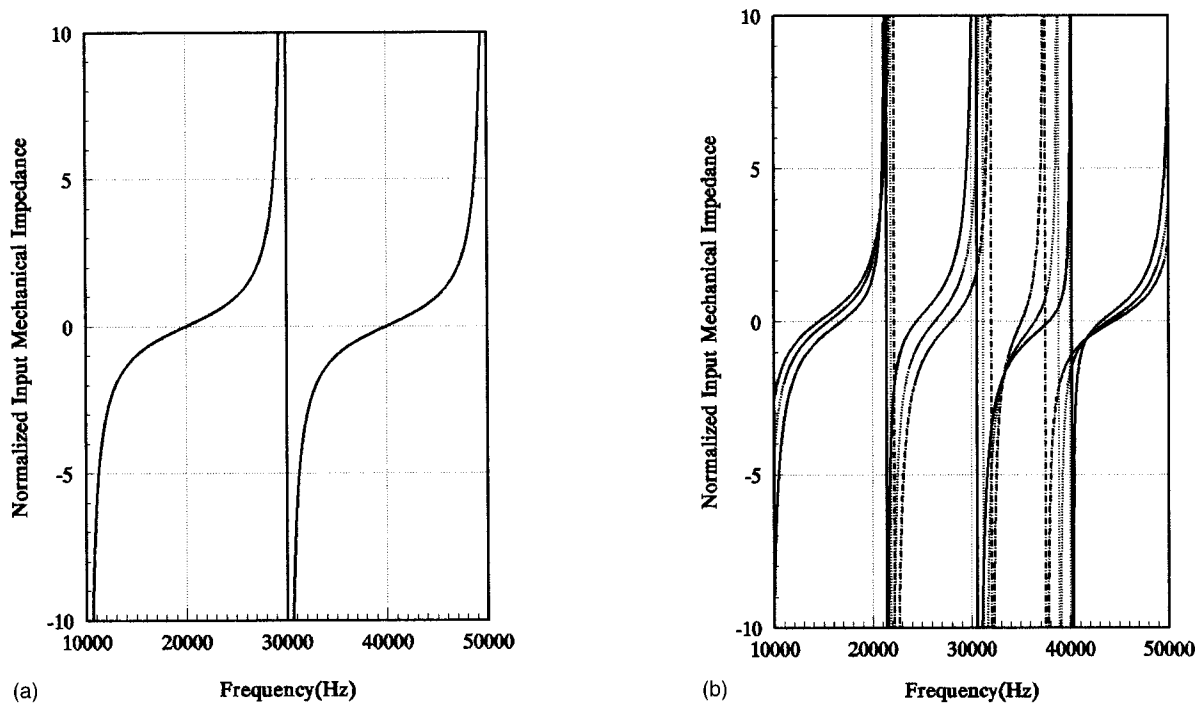
FIG. 6. (a) The theoretically computed curve between the normalized input mechanical impedance and the frequency when the slanting angle is zero. (b) The theoretically computed curve between the normalized input mechanical impedance and the frequency when the slanting angle is 30, 45, and 60 deg.

compound vibration in which the longitudinal vibration dominates the torsional vibration, while the resonant vibration corresponding to the higher resonance frequency is a compound vibration in which the torsional vibration dominates the longitudinal vibration.

On the other hand, it can also be seen that the slanting slots alter the resonance frequency of the cylinder. When the slanting angle is increased, the lower resonance frequency is decreased, while the higher resonance frequency is increased. This can be explained as follows. For the lower resonance frequency, the longitudinal vibration is dominant; when the slanting angle is increased, the torsional vibration becomes stronger, and the energy for the torsional vibration is increased. Compared with the longitudinal vibration, the torsional vibration is a lateral vibration. When the energy for the lateral vibration is increased, the resonance frequency for the longitudinal vibration is decreased. This is consistent with Rayleigh's frequency correction for the longitudinal vibration when the lateral vibration is considered. For the higher resonance frequency, the torsional vibration is dominant. When the slanting angle is increased, the longitudinal vibration becomes weaker, and the longitudinal energy is also decreased. Therefore, the resonance frequency for the torsional vibration is increased. Figure 6(a) and (b) show the relation between the normalized input mechanical impedance and the frequency when the slanting angle is chosen as a parameter. In Fig. 6(a), the slanting angle is zero, while in Fig. 6(b), the solid line, the dotted line, and the line of dashes and solid lines correspond to the slanting angle of 30, 45, and 60 deg, respectively.

From the above analysis and the computed curves, it can be seen that for higher vibrational modes of the longitudinal–torsional compound cylinder, there are also two kinds of resonance frequency: one is for the longitudinally dominated vibration, and the other is for the torsionally dominated vibration. In other words, the slanting slots alter the vibrational characteristics of the cylinder, its vibrational mode is increased, and the vibration of the cylinder with slanting slots becomes a complex compound vibration.

III. THE EFFECT OF THE POSITION OF THE SLANTING SLOTS ON THE RESONANCE FREQUENCY OF THE CYLINDER IN LONGITUDINAL–TORSIONAL COMPOUND VIBRATION

Based on the above analysis, the slanting slots alter the vibrational characteristics of the cylinder. It is obvious that the position of the slanting slots will definitely alter the characteristics of the cylinder. It can be seen from Fig. 2 that L_1 is the distance between the input end of the cylinder and the dividing line; it is also the distance between the slanting slots and the input end of the cylinder. Figure 7 is the theoretically computed curve between the normalized input mechanical impedance and the frequency. When the normalized input mechanical impedance becomes zero, the resonance frequency of the cylinder can be found. In Fig. 7, the total length of the cylinder is kept a constant, i.e., $L = L_1 + L_2$ is a constant, and the slanting angle is also kept a constant. The distance L_1 between the slots and the input end of the cylinder is chosen as a parameter. In Fig. 7, the solid line, the
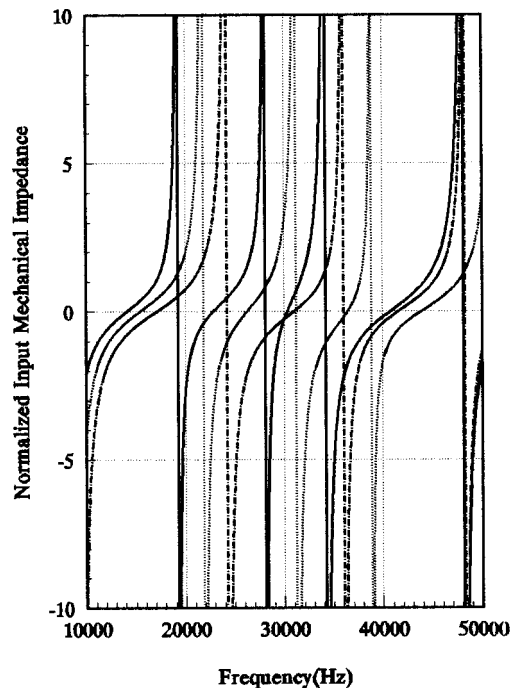
FIG. 7. The theoretically computed curve between the normalized input mechanical impedance and the designed frequency of the cylinder when the position of the slanting slot changes.

dotted line, and the line of dashes and solid lines represent three different relation curves when the distance L_1 is 0.03, 0.05, and 0.07 m, respectively.

From Fig. 7 it can be seen that when the distance L_1 between the slots and the input end of the cylinder is increased, the lower resonance frequency is increased, and the higher resonance frequency is also increased. This can be explained as follows. When the distance L_1 is increased and the length L of the cylinder is kept a constant, the torsional vibration in the cylinder is decreased and its vibration energy is also decreased; this will definitely cause the resonance frequency of the longitudinal vibration in the cylinder to rise. For the higher resonance frequency (that is, the resonance frequency of the torsional vibration in the cylinder, since the torsional vibration is created in the cylinder after the dividing line), when the length L_1 is increased, while the total length of the cylinder is a constant, the length L_2 of the cylinder with the slanting slots is decreased; therefore, the resonance frequency of the torsional vibration is increased according to the one-dimensional theory of a slender rod in torsional vibration.

IV. THE EFFECT OF THE LENGTH OF SLOTS ON THE RESONANCE FREQUENCY OF THE CYLINDER IN LONGITUDINAL–TORSIONAL COMPOUND VIBRATION

Since the slanting slots are assumed to be ideally geometrical lines with finite length, their effect on the mass of the vibrating system can be ignored. However, the length of slots will alter the vibrational characteristics of the cylinder. When the slanting angle is kept a constant, the length L_2 can be regarded as the substitute of the length of slots. In the
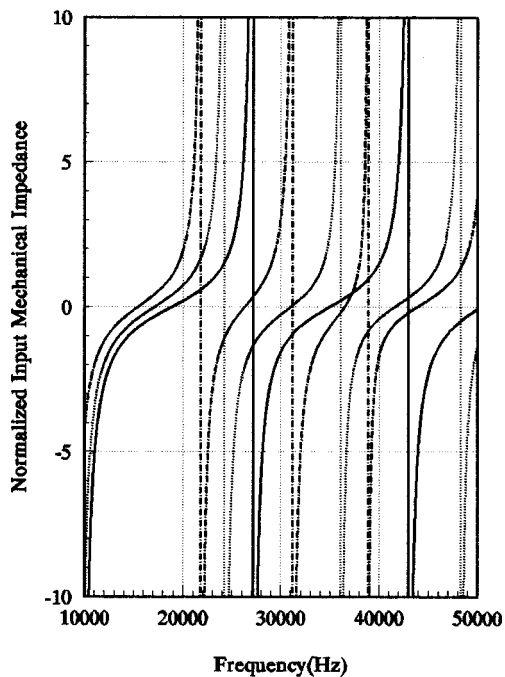
FIG. 8. The theoretically computed curve between the normalized input mechanical impedance and the frequency of the cylinder in longitudinal–torsional compound vibration when the length of the slanting slot changes.

following, the relation between the resonance frequency and the length L_2 is studied. Figure 8 is the theoretically computed curve between the normalized input mechanical impedance and the frequency when the length L_2 is chosen as a parameter. In Fig. 8, the length $L=L_1+L_2$ and the slanting angle are still kept constants. Three values of L_2, i.e., $L_2 =0.035$, 0.055, and 0.075 m, are used in the computation; they correspond to the solid line, the dotted line, and the line of dashes and solid lines, respectively.

From Fig. 8 it can be seen that when the length of slots is increased, the lower resonance frequency of the cylinder is decreased and the higher resonance frequency is also decreased. This can be explained as follows. When the length L_2 is increased, the torsional vibration is increased; therefore, the resonance frequency of the longitudinal vibration will decrease. For the higher resonance frequency, when the length L_2 is increased, the resonance frequency for the torsional vibration is decreased according to one-dimensional vibrational theory in that the resonance frequency is in inverse proportion to its length.

V. EXPERIMENTAL RESULTS

To verify the derived conclusions, some cylinders with slanting slots were designed and machined. The width of the slots is about 1 mm. The material of the cylinder is steel. Its

material parameters are as follows: $C_L=5000$ m/s, $\sigma =0.28$. The resonance frequencies of the vibrating system that is composed of the sandwiched longitudinal transducer and the cylinder with slanting slots are measured using the transmission-line method that is commonly used in the measurement of piezoelectric ceramic vibrators. The measured results are listed in Table I, where f_0 is the theoretically computed and designed resonance frequency of the cylinder, f_{mt} is the measured resonance frequency of the designed sandwiched transducer, f_{mc} is the measured resonance frequency for the compound system of the sandwich longitudinal transducer and the cylinder, and f_{0c} is the computed resonance frequency of the cylinder with slanting slots.

In the experiments, the resonance frequency of the cylinder with slanting slots is not measured directly. The resonance frequencies of the sandwiched longitudinal transducers and the compound system are measured. According to traditional theory of transducer measurement, for a compound vibrating system consisting of a transducer and a transmission cylinder, if the resonance frequencies of the transducer and the transmission cylinder are almost the same, then the resonance frequency of the compound vibrational system is also approximately equal to the resonance frequency of the transducer or the transmission cylinder. In this paper, the reverse method is used. The resonance frequency of the cylinder with slanting slots is determined by measuring the resonance frequencies of the transducer and the compound vibrating system. The equation used to calculate the resonance frequency of the cylinder is

$$f_{0c}=f_{mc}^2/f_{mt}. \tag{26}$$

From Table I it can be seen that the measured resonance frequencies of the transducer and the compound system are almost the same; therefore, the resonance frequency of the cylinder is approximately equal to the resonance frequency of the transducer or the compound system. From the measured results, it is obvious that the measured results are consistent with the predicted results, and the theoretically derived relations between the resonance frequency and the slanting angle, the position, and the length of the slots are also verified. As for the frequency-measurement error, the following factors should be taken into account. First, the standard values of the material used in the computation are different from the actual material parameter. Second, the resonance frequency of the cylinder is obtained indirectly from the measured resonance frequency of the sandwiched longitudinal transducer and the compound system. However, this error is small; it does not affect the verified relations that are derived in the theoretical analysis.

TABLE I. The measured resonance frequencies for the longitudinal–torsional compound system of the sandwiched transducer and the cylinder.

R_1 (mm)	R_2 (mm)	L_1 (mm)	L_2 (mm)	θ (deg)	f_0 (Hz)	f_{mt} (Hz)	f_{mc} (Hz)	f_{0c} (Hz)
10	20	65	50	30	20 000	19 877	19 763	19 649
10	20	65	50	45	18 720	19 012	18 608	18 213
10	20	85	30	45	20 770	19 967	19 917	19 868

VI. CONCLUSIONS

In this paper, the longitudinal–torsional compound system with slanting slots is studied. The equivalent circuit model for the cylinder with slanting slots is derived and the resonance-frequency equation is also obtained. The effect of the slanting angle, the position, and the length of slanting slots on the resonance frequency of longitudinal–torsional cylinder is analyzed. To sum up the above analysis, the following conclusions are obtained:

(1) The slanting slots can alter the vibrational modes and characteristics of the cylinder, and the longitudinal–torsional compound vibration in the cylinder is produced.

(2) For every vibration mode, such as the fundamental mode, there are two kinds of resonance frequency; they correspond to the longitudinally dominated and torsionally dominated vibrations, respectively.

(3) When the slanting angle of slots is increased, the resonance frequency for the longitudinally dominated vibration is decreased, while the resonance frequency for the torsionally dominated vibration is increased.

(4) When the distance between the slots and the input end of the cylinder is increased, the resonance frequency for the longitudinally dominated vibration is increased and the resonance frequency for the torsionally dominated vibration is also increased.

(5) When the length of slots is increased, the resonance frequency for the longitudinally dominated vibration is decreased, and the resonance frequency for the torsionally dominated vibration is also decreased.

[1] E. A. Neppiras, ''The pre-stressed piezoelectric sandwiched transducer,'' Ultrasonics International 1973 Conference Proceedings, p. 295.

[2] L. Shuyu and Z. Fucheng, ''Study of vibrational characteristics for piezoelectric sandwich ultrasonic transducers,'' Ultrasonics **32**, 39–42 (1994).

[3] H. Nagashima and S. Ueha, ''Study of longitudinal–torsional composite vibrator system,'' J. Acoust. Soc. Jpn. **45**(2), 94–100 (1989).

[4] J. A. Gallego-Juarez, G. Rodriguez-Corral, and L. Gaete-Garreton, ''An ultrasonic transducer for high power applications in gases,'' Ultrasonics **16**, 267–271 (1978).

[5] K. Nakamura, M. Kurosawa, and S. Ueha, ''Design of a hybrid transducer type ultrasonic motor,'' IEEE Trans. Ultrason. Ferroelectr. Freq. Control **40**, 395–401 (1993).

[6] S. Ueha, H. Nagashima, and M. Masuda, ''Longitudinal–torsional composite transducer and its applications,'' Jpn. J. Appl. Phys., Part 1 **26-2**, 188–190 (1987).

[7] Y. Watanabe, Y. Tsuda, and E. Mori, ''A longitudinal–flexural complex-mode ultrasonic high-power transducer system with one-dimensional construction,'' Jpn. J. Appl. Phys., Part 1 **32**, 2430–2434 (1993).

[8] O. Ohnishi, O. Myohga, and T. Ucnikawa, ''Piezoelectric ultrasonic motor using longitudinal–torsional composite vibration of a cylinder resonator,'' Ultrasonics Symposium 1989, pp. 739–743.

[9] L. D. Rozenberg, *Sources of High-Intensity Ultrasound* (Plenum, New York, 1969), Vol. 2.

[10] L. Shuyu, ''Torsional vibration of coaxially segmented, tangentially polarized piezoelectric ceramic tubes,'' J. Acoust. Soc. Am. **99**, 3476–3480 (1996).

[11] L. Shuyu, ''Study of the sandwiched piezoelectric ultrasonic torsional transducer,'' Ultrasonics **32**(6), 461–465 (1994).

[12] L. Shuyu, ''Sandwiched piezoelectric ultrasonic transducers of longitudinal–torsional compound vibrational modes,'' IEEE Trans. Ultrason. Ferroelectr. Freq. Control **44**, 1189–1197 (1997).

[13] J. Tsujino, R. Suzuki, and M. Talenchi, ''Load characteristics of ultrasonic rotary motor using a longitudinal–torsional vibration converter with diagonal slots. Large torque ultrasonic rotary motor,'' Ultrasonics **34**(2–5), 265–269 (1996).

Elastic contact problem of the piezoelectric material in the structure of a bolt-clamped Langevin-type transducer

Kazunari Adachi, Masaharu Tsuji, and Hiroshi Kato

Department of Electrical and Information Engineering, Faculty of Engineering, Yamagata University, 4-3-16 Jonan, Yonezawa, Yamagata, 992-8510 Japan

Bolt-clamped Langevin-type transducers (BLTs) are widely used in various fields of industrial application of high-power ultrasonics. One of the most crucial points in designing a transducer of this type is estimation of the bearing stress imposed by clamping on the interface between the metal block and the piezoelectric element. This *prestress*, which compensates for low tensile strength of the piezoelectric materials used, must be larger than the dynamic vibratory stress at the interface between the components in high-amplitude operation. Precise estimation of it is virtually impossible, owing to an intricate elastic contact problem. However, with the use of the unique finite-element-analysis system developed by one of the authors, approximate solutions of the problem have been obtained. A BLT design based on the results of the prestress calculations is proposed. The results of its experimental verification have also been reported. © *1999 Acoustical Society of America.* [S0001-4966(99)03503-1]

INTRODUCTION

Bolt-clamped Langevin-type transducers (BLTs) are widely used as efficient vibratory sources in various fields of industrial application of high-power ultrasonics. The transducers of this type can steadily generate high-amplitude ultrasonic vibrations. Figure 1 illustrates a typical construction of the BLT, in which piezoelectric elements are sandwiched by two metal blocks and clamped with a screw bolt.

Since the elements are usually made of polarized lead zirconate titanate (PZT) ceramic, appropriate static compressional-bearing stress needs to be imposed on them by clamping, so as to compensate for their weakness to tensile stress. This *prestress* must be larger than the dynamic vibratory stress at the interface between the components in high-amplitude operation; otherwise, mechanical loss owing to unstable contact between them drastically decreases the efficiency of the BLT, and the thermal stress due to excessive heat generation may cause fracture in the elements. Estimation of the prestress exerted by clamping is thus one of the the most crucial points in designing a BLT. However, precise estimation of it is virtually impossible, since that involves an intricate elastic contact problem with piezoelectricity to be taken into account. Research on the optimized design of this type of transducers has been done less enthusiastically for this reason.

Fortunately, Adachi *et al.* have already devised a simple and practical numerical method which allows us to obtain approximate solutions of the elastic contact problems for nonpiezoelectric elastic materials with the use of finite elements.[1] By applying this method, we can easily estimate the prestress distribution as well as the vibratory one. Hence, the authors have decided to expand the method so that it can be applied to piezoelectric materials.

In this paper, a common finite-element formulation of piezoelectric systems is summarized first before its application to the ''*clamping problem*'' of BLTs is explained. Next,

the specifications of the finite-element-analysis system developed by the authors for this research are also briefly described. The authors then propose a BLT design based on the results of the prestress calculations, and finally show some measured characteristics of the newly designed BLT as the experimental verification of the numerical method.

I. FINITE-ELEMENT FORMULATION OF PIEZOELECTRIC SYSTEMS AND ITS APPLICATION TO THE CLAMPING PROBLEM OF BLTs

To begin with, a standard formulation of piezoelectric finite elements is given for a comprehensible explanation of the clamping analysis using them, though there has been some preceding research[2–4] on such elements since the late 1960s.

If the electro–magnetic interaction can be ignored, the relationships among the relevant physical properties of a linear nondissipative piezoelectric system can be expressed in the forms[5]

$$\mathbf{T} = \mathbf{c}^E \mathbf{S} - \mathbf{e}^t \mathbf{E}, \tag{1}$$

$$\mathbf{D} = \mathbf{e}\mathbf{S} + \boldsymbol{\epsilon}^S \mathbf{E}, \tag{2}$$

where $\mathbf{T}$, $\mathbf{S}$, $\mathbf{D}$, and $\mathbf{E}$ denote the stress, strain, electric-displacement, and electric-field vectors, respectively, of the system, and $\mathbf{c}^E (= \mathbf{c}^{Et})$, $\mathbf{e}$, and $\boldsymbol{\epsilon}^S (= \boldsymbol{\epsilon}^{St})$ are the matrices of elastic, piezoelectric, and dielectric constants, respectively, of the material. We should note here that $\mathbf{T}$ and $\mathbf{S}$ are *the vector representation of the stress and strain tensors in the engineering notation*. Here, the superscript *t* means the transpose of the matrix.

The strain $\mathbf{S}$ and the electric-field vector $\mathbf{E}$ are obtained by

$$\mathbf{S} = \mathbf{L}\mathbf{x}, \tag{3}$$

$$\mathbf{E} = -\operatorname{grad} \psi, \tag{4}$$
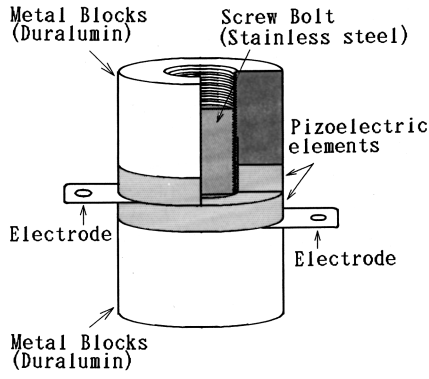
FIG. 1. A bolt-clamped Langevin-type transducer.

where $\mathbf{L}$ is a linear spatial partial differential operator,[6] and $\mathbf{x}$ and ψ are the particle displacement and the electric potential.

In accordance with the standard discretization procedure of the finite element method,[6] the particle displacement $\mathbf{x}$ and velocity $\mathbf{v}$ of the system can be expressed in the forms

$$\mathbf{x} = \mathbf{N}_d \mathbf{u}, \tag{5}$$

$$\mathbf{v} = \dot{\mathbf{x}} = \mathbf{N}_d \dot{\mathbf{u}}, \tag{6}$$

where $\mathbf{u}$ and $\mathbf{N}_d$ are the nodal displacement vector and the *shape function* matrix for the particle displacement, respectively, and the dot means temporal differentiation.

Similarly,

$$\psi = \mathbf{N}_p \boldsymbol{\phi}, \tag{7}$$

where $\boldsymbol{\phi}$ and $\mathbf{N}_p$ are the nodal electric-potential vector and the *shape function* vector for the electric potential, respectively.

Using Eqs. (3), (4), (5), and (7), $\mathbf{S}$ and $\mathbf{E}$ are thus approximated as

$$\mathbf{S} = \mathbf{B}\mathbf{u}, \tag{8}$$

$$\mathbf{E} = -\mathbf{A}\boldsymbol{\phi}, \tag{9}$$

where $\mathbf{B} = \mathbf{L}\mathbf{N}_d$ and $\mathbf{A} = \mathbf{N}_p$.

From Eqs. (1), (2), (6), (8), and (9), we obtain

$$U = \frac{1}{2} \int \mathbf{S}^t \mathbf{T} \, dV,$$

$$= \frac{1}{2} \int (\mathbf{u}^t \mathbf{B}^t \mathbf{c}^E \mathbf{B} \mathbf{u} + \mathbf{u}^t \mathbf{B}^t \mathbf{e}^t \mathbf{A} \boldsymbol{\phi}) dV. \tag{10}$$

$$H = \frac{1}{2} \int \mathbf{D}^t \mathbf{E} \, dV,$$

$$= \frac{1}{2} \int (-\mathbf{u}^t \mathbf{B}^t \mathbf{e}^t \mathbf{A} \boldsymbol{\phi} + \boldsymbol{\phi}^t \mathbf{A}^t \boldsymbol{\epsilon}^S \mathbf{A} \boldsymbol{\phi}) dV. \tag{11}$$

$$T = \frac{1}{2} \int \rho \mathbf{v}^t \mathbf{v} \, dV,$$

$$= \frac{1}{2} \int \rho \dot{\mathbf{u}}^t \mathbf{N}_d^t \mathbf{N}_d \dot{\mathbf{u}} \, dV, \tag{12}$$

in which U, H, and T are the total elastic, electrical, and kinetic energies of the system, respectively, and the integrations are conducted over the volume.

In Eqs. (10), (11), and (12), let

$$\mathbf{M} = \int \rho \mathbf{N}_d^t \mathbf{N}_d \, dV, \quad \mathbf{K} = \int \mathbf{B}^t \mathbf{c}^E \mathbf{B} \, dV,$$

$$\mathbf{P} = \int \mathbf{B}^t \mathbf{e} \mathbf{A} \, dV, \quad \mathbf{G} = \int \mathbf{A}^t \boldsymbol{\epsilon}^S \mathbf{A} \, dV,$$

where $\mathbf{M}$, $\mathbf{K}$, $\mathbf{P}$ and $\mathbf{G}$ are called the mass, elastic, piezoelectric, and dielectric matrices, respectively, of the system, we have

$$U = \tfrac{1}{2} \mathbf{u}^t \mathbf{K} \mathbf{u} + \tfrac{1}{2} \mathbf{u}^t \mathbf{P} \boldsymbol{\phi}, \tag{13}$$

$$H = -\tfrac{1}{2} \mathbf{u}^t \mathbf{P} \boldsymbol{\phi} + \tfrac{1}{2} \boldsymbol{\phi}^t \mathbf{G} \boldsymbol{\phi}, \tag{14}$$

$$T = \tfrac{1}{2} \dot{\mathbf{u}}^t \mathbf{M} \dot{\mathbf{u}}. \tag{15}$$

The work exerted by forces and electric charges externally applied to the system can also be given in the discretized form

$$W = \mathbf{u}^t \mathbf{f} + \boldsymbol{\phi}^t \mathbf{q}, \tag{16}$$

where $\mathbf{f}$ and $\mathbf{q}$ denote the force and electric charge vectors, respectively.

Now, we can obtain the Lagrangian $\mathcal{L}$ of the system from Eqs. (13), (14), (15), and (16) as

$$\mathcal{L} = U - H - T - W,$$

$$= \tfrac{1}{2} \mathbf{u}^t \mathbf{K} \mathbf{u} + \mathbf{u}^t \mathbf{P} \boldsymbol{\phi} - \tfrac{1}{2} \boldsymbol{\phi}^t \mathbf{G} \boldsymbol{\phi} - \tfrac{1}{2} \dot{\mathbf{u}}^t \mathbf{M} \dot{\mathbf{u}} - \mathbf{u}^t \mathbf{f} - \boldsymbol{\phi}^t \mathbf{q}. \tag{17}$$

Lagrange's equations of motion of the system are

$$\frac{d}{dt} \left(\frac{\partial \mathcal{L}}{\partial \dot{u}_i} \right) - \frac{\partial \mathcal{L}}{\partial u_i} = 0, \tag{18}$$

$$\frac{d}{dt} \left(\frac{\partial \mathcal{L}}{\partial \dot{\phi}_i} \right) - \frac{\partial \mathcal{L}}{\partial \phi_i} = 0, \tag{19}$$

where t is time, u_i and ϕ_i denote the components of the vectors $\mathbf{u}$ and $\boldsymbol{\phi}$, respectively, and the subscript i indicates each component.

Substitute Eq. (17) into Eq. (18) and Eq. (19), we obtain a set of simultaneous equations of the types

$$\mathbf{M}\ddot{\mathbf{u}} + \mathbf{K}\mathbf{u} + \mathbf{P}\boldsymbol{\phi} = \mathbf{f}, \tag{20}$$

$$\mathbf{P}^t \mathbf{u} + \mathbf{G}\boldsymbol{\phi} = \mathbf{q}. \tag{21}$$

For static cases, i.e., $\ddot{\mathbf{u}} = 0$, we have

$$\mathbf{K}\mathbf{u} + \mathbf{P}\boldsymbol{\phi} = \mathbf{f}, \tag{22}$$

$$\mathbf{P}^t \mathbf{u} + \mathbf{G}\boldsymbol{\phi} = \mathbf{q}. \tag{23}$$

These equations are the general finite-element formulation of static deformation of linear piezoelectric systems.

If there is no electric charge inflow, putting $\mathbf{q} = 0$ in Eq. (23) and substituting it into Eq. (22), we obtain

$$(\mathbf{K} + \mathbf{P}\mathbf{G}^{-1}\mathbf{P}^t)\mathbf{u} = \mathbf{f}. \tag{24}$$

Let $\mathbf{K}' = \mathbf{K} + \mathbf{P}\mathbf{G}^{-1}\mathbf{P}^t$ in Eq. (24), we have

$$\mathbf{K}'\mathbf{u} = \mathbf{f}. \tag{25}$$
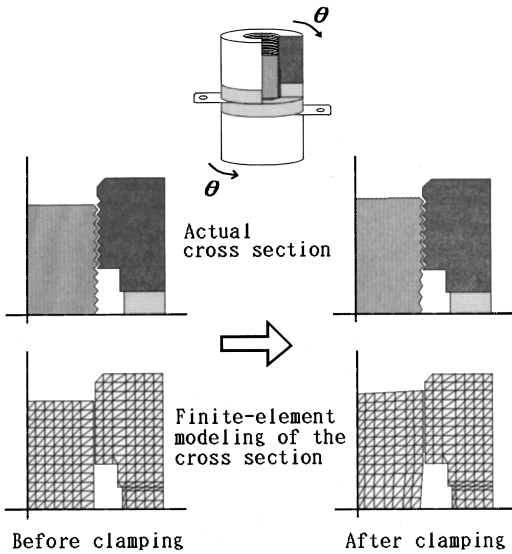
FIG. 2. A schematic explanation on the clamping process in assembling a BLT and its representation in the finite-element analysis.

Equation (25) is similar to the equation which depicts linear static deformation of an ordinary elastic system. However, in the case of clamping, internal, not external, forces exist in the system. Thus, to derive the equations that give the solution of the problem, Eq. (25) should be rewritten in an appropriate form.

Such a process of mathematical transformation seems complicated, but its underlying concept is actually quite simple. Figure 2, which illustrates the clamping process in assembling a BLT, also gives a schematic explanation of the concept. The figure shows only one-quarter of the BLT because of its symmetry. From a static viewpoint, revolution of the metal blocks for clamping can be considered as hooking each turn of thread of the male screw of the bolt to the corresponding one of the female screw of the block. In the finite-element analysis, therefore, the clamping process can be regarded as the operation of combining every pair of nodes which represents the points brought into contact with each other by clamping.

The finite-element modeling, carried out separately for all the components involved, allows us to calculate the static-bearing stress—including the prestress—at the interfaces between the components. If the static deformation is caused only by clamping, the resulting pair of internal forces exerted on each pair of nodes must have the same magnitude but opposite directions in the modeling. The vector difference in displacement between the coupled nodes is equal to the positional difference between them before the deformation.

These relationships can be rigorously represented by the mathematical forms

$$\begin{pmatrix} \mathbf{K}_{11} & \mathbf{K}_{12} & \mathbf{K}_{13} \\ \mathbf{K}_{21} & \mathbf{K}_{22} & \mathbf{K}_{23} \\ \mathbf{K}_{31} & \mathbf{K}_{32} & \mathbf{K}_{33} \end{pmatrix} \begin{pmatrix} \mathbf{u}_1 \\ \mathbf{u}_2 \\ \mathbf{u}_3 \end{pmatrix} = \begin{pmatrix} \mathbf{f}_1 \\ \mathbf{f}_2 \\ 0 \end{pmatrix}, \tag{26}$$

$$\mathbf{u}_2 - \mathbf{u}_1 = \mathbf{d}_x, \tag{27}$$

$$\mathbf{d}_x = \mathbf{x}_1 - \mathbf{x}_2, \tag{28}$$

and

$$\mathbf{f}_1 = -\mathbf{f}_2, \tag{29}$$

where $\mathbf{u}_1$ and $\mathbf{f}_1$ are the nodal-displacement and internal-force vectors, respectively, for nodes $\mathbf{x}_1$ to be coupled with nodes $\mathbf{x}_2$ by clamping; $\mathbf{u}_2$ and $\mathbf{f}_2$ those for $\mathbf{x}_2$; $\mathbf{u}_3$ the displacement vector for the other nodes; $\mathbf{K}_{ij}$ ($i,j=1,2,3$) the partitions of the matrix $\mathbf{K}'$ corresponding to those of vectors $\mathbf{f}$ and $\mathbf{u}$; and $\mathbf{d}_x$ the vector difference in coordinates between nodes $\mathbf{x}_1$ and $\mathbf{x}_2$. The vectors $\mathbf{x}_1$ and $\mathbf{x}_2$ have the same number of components, each of which is one of the coordinates of a node in contact with the other, and $\mathbf{u}_1$, $\mathbf{u}_2$, $\mathbf{f}_1$, and $\mathbf{f}_2$ are the vectors whose components correspond accordingly to those of $\mathbf{x}_1$ and $\mathbf{x}_2$.

Upon substitution of Eqs. (27), (28), and (29) into Eq. (26), we obtain

$$\begin{pmatrix} \mathbf{K}_{11} & \mathbf{K}_{12} & \mathbf{K}_{13} \\ \mathbf{K}_{21} & \mathbf{K}_{22} & \mathbf{K}_{23} \\ \mathbf{K}_{31} & \mathbf{K}_{32} & \mathbf{K}_{33} \end{pmatrix} \begin{pmatrix} \mathbf{u}_1 \\ \mathbf{u}_1 + \mathbf{d}_x \\ \mathbf{u}_3 \end{pmatrix} = \begin{pmatrix} \mathbf{f}_1 \\ -\mathbf{f}_1 \\ 0 \end{pmatrix}. \tag{30}$$

Transposing all the unknowns to the left-hand side of these simultaneous equations and the known d_x to the right-hand side, we have

$$\begin{pmatrix} \mathbf{K}_{11}+\mathbf{K}_{12} & -\mathbf{E} & \mathbf{K}_{13} \\ \mathbf{K}_{21}+\mathbf{K}_{22} & \mathbf{E} & \mathbf{K}_{23} \\ \mathbf{K}_{31}+\mathbf{K}_{32} & \mathbf{O} & \mathbf{K}_{33} \end{pmatrix} \begin{pmatrix} \mathbf{u}_1 \\ \mathbf{f}_1 \\ \mathbf{u}_3 \end{pmatrix} = \begin{pmatrix} -\mathbf{K}_{12}\mathbf{d}_x \\ -\mathbf{K}_{22}\mathbf{d}_x \\ -\mathbf{K}_{32}\mathbf{d}_x \end{pmatrix}. \tag{31}$$

By solving Eq. (31) for $\mathbf{u}_1$, $\mathbf{u}_3$, and $\mathbf{f}_1$, we can easily obtain the stress distribution in the system, as well as the deformed shape of it, using the well-known relationship between the components of nodal displacement and that of the stress in each element.

Strictly speaking, however, analysis of the clamping effect is a finite-deformation problem which requires nonlinear treatment of the system, since the deformation caused by clamping is ''*visible*'' in most cases. Hence, it should be noted that this method is valid only if the deformation is relatively small, as compared with the size of the whole system of interest.

In the calculations actually conducted by the authors, the screw threads are not precisely modeled with finite elements, but each turn of thread is represented by a node, as shown in Fig. 2. In addition, each nodal displacement at the threads is assumed to be coupled with its corresponding one only in the direction along the axis of the bolt. In other words, it is assumed that the initial axial-positional gap between each pair of nodes at the threads is equal to their difference in axial displacement caused by clamping, while their radial-positional gap has nothing to do with their displacements. This assumption is introduced so that the modeling will closely approximate the mechanical property of the screw joint. The revolution angle of the blocks for clamping can be formulated as the initial axial-positional gap divided by the pitch of the screw.

The finite-element-analysis system developed for this research can deal not only with the clamping problem but also usual static deformation, modal vibration, and harmonic forced-vibration problems for any two-dimensional piezo-
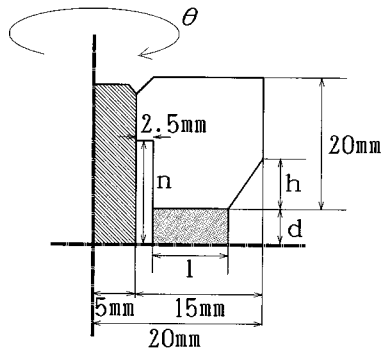
FIG. 3. Geometrical parameters set for optimum design of the BLT as shown in Fig. 1.

electric system including axisymmetric ones. Furthermore, it can also solve the problems of "*modal vibration control*" [7] of such piezoelectric systems. The platform on which the analysis system can work is 4.3BSD UNIX (or any compatible operating system). X-window system (X11R4 or a more recent version) is also necessary for the graphic displays. The system is composed of some programs and Bourn Shell scripts. The source codes of the programs are written in FORTRAN 77 and C.

II. NUMERICAL SEARCH FOR AN OPTIMIZED BLT DESIGN IN TERMS OF THE PRESTRESS AT THE INTERFACE

The low-aspect-ratio configuration of the BLT as shown in Fig. 1 has the advantage of maintaining a large area of the
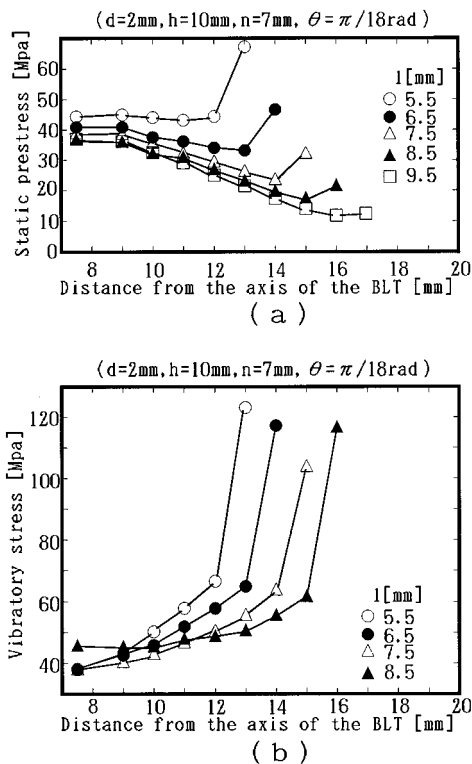
FIG. 4. The normal component of the static prestress imposed by the clamping (a) and that of the dynamic vibratory stress at the lowest-resonance frequency of the BLT (b) at the interface between the metal (duralumin) block and the piezoelectric ceramic (C-21) element as functions of the distance from the axis of the transducer, with the difference between the outer and inner radii of the element l as a parameter.
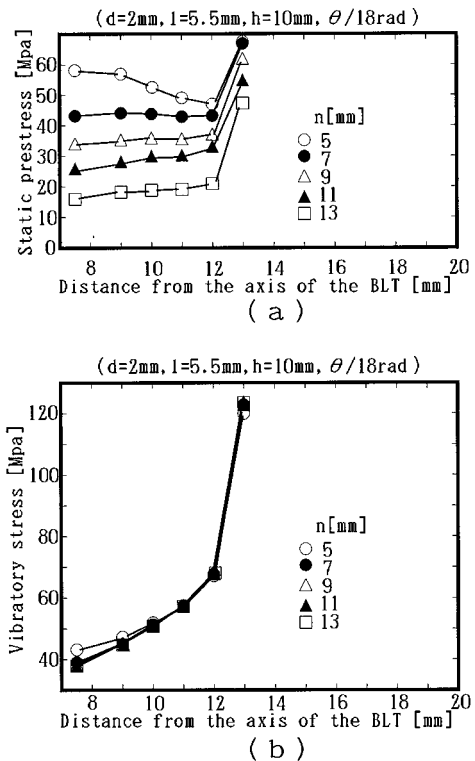
FIG. 5. Same as in Fig. 4, but with the unthreaded length of the screw hole n as a parameter.

radiating face and sufficient volume ratio of the piezoelectric ceramic elements that excite the vibration while realizing high-resonance frequency. However, constructing such a "*stumpy*" BLT poses quite a practical problem. The most serious difficulty is how to impose enough prestress all over the area of the interface between the metal block and the piezoelectric ceramic element. No conventional designing method has yet guaranteed that. Hence, the mechanical quality factor Q—the efficiency, in other words—of a BLT of this shape type inevitably tends to be very low as a transducer used for high-power ultrasonic applications. The authors thus tried to find out the optimum shape of the BLT in terms of the prestress by repetition of the finite-element simulation for many shape types of the transducer.

Figure 3 shows the geometrical parameters set for seeking the optimum shape of the BLT in terms of the prestress. Here, it should be noted that the tapered portion defined by the parameters l and h are introduced and θ denotes the revolution angle of the metal (duralumin) blocks for clamping. In the seeking process, the authors maintained the condition that the maximum tensile stress at the threads of the screws should not exceed 500 MPa. In addition to the static prestress imposed by the clamping, the dynamic vibratory stress at the interface in the lowest-resonance vibration was also calculated for every case on the assumption that the amplitude at the outer circumference of its end surfaces was $10\,\mu m_{0-p}$. All the analyses were done for only one-quarter of the transducer because of its symmetry. The electrodes were assumed to be electrically short-circuited; in other words, the BLT was assumed to be driven by an ideal voltage source and their thickness was ignored in the calculation, though they

（d=2mm, h=10mm, n=7mm, $\theta = \pi/18$rad ）
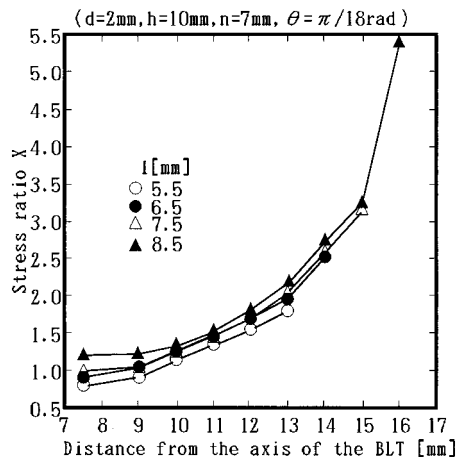
FIG. 6. Distribution of the ratio of the normal component of the dynamic vibratory stress to that of the static prestress at the interface between the metal block and the piezoelectric ceramic element, with the difference between the outer and inner radii of the element l as a parameter.

（d=2mm, l=5.5mm, n=4mm, $\theta = \pi/18$rad ）

FIG. 8. Same as in Fig. 6, but with the length of the tapered portion h as a parameter.

are indispensable for its actual operation. The piezoelectric elements and the screw bolt were assumed to be made of C-21 (Fuji Ceramics Co. Ltd.) and stainless steel, respectively.

Let us look at some numerical results of the analyses. Figure 4 shows the normal components of both the static prestress and the vibratory stress at the interface as functions of the distance from the axis of the transducer, with the difference between the outer and inner radii of the piezoelectric ceramic element l as a parameter. When the difference gets narrow, the prestress shows a very sharp rise near the outer circumference of the interface, while the distribution of the normal component of the vibratory stress just shifts its steep slope towards the axis. Figure 5 shows the effect of the unthreaded length of the screw hole n on the stress distributions. Though the change in the unthreaded length does not affect the vibratory stress, its increase suppresses the prestress, especially on the inside edge of the interface. This means that we can control the relative magnitude of the prestress in the vicinity of the inner circumference by changing the length.

The authors carried out similar analyses for the other

geometrical parameters defined in Fig. 3. Figures 6, 7, 8, and 9 give some of the results in a more comprehensible form than Figs. 4 and 5. These graphs show the distributions of the ratio of the normal component of the vibratory stress to that of the static prestress at the interface when the thickness of the piezoelectric element d is maintained at 2 mm. If the stress ratio X exceeds unity (the vibratory stress is larger than the static prestress), the contact between the piezoelectric element and the metal block becomes unstable. We find that the stress ratio at a point on the interface becomes larger as it approaches the outer circumference in any case. In addition, as a result of the simulations, the change in the element thickness d was found to have no significant influence on the distribution.

From the numerous results of the simulation, the authors finally selected $d=2$ mm, $l=5.5$ mm, $h=10$ mm, and $n=11$ mm as the optimum values of the parameters. It was also found that the maximum tensile stress at the threads of the screws is 485 MPa while maintaining the stress ratio X below unity over the interface when the value of θ is set at $\pi/8$.

III. EXPERIMENTAL VERIFICATION

Two geometrically identical BLTs of the optimum shape found in the numerical analyses of the previous section were

（d=2mm, l=5.5mm, h=10mm, $\theta = \pi/18$rad ）

FIG. 7. Same as in Fig. 6, but with the unthreaded length of the screw hole n as a parameter.

（d=2mm, l=5.5mm, h=10mm, n=11mm ）
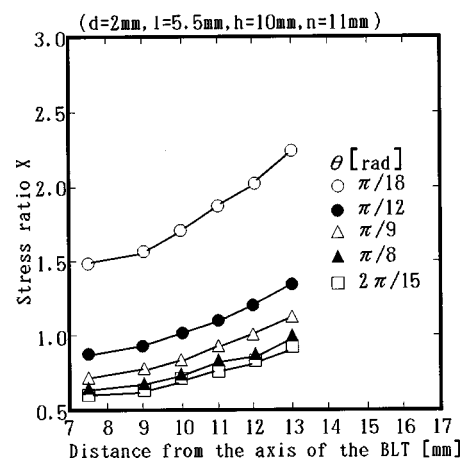
FIG. 9. Same as in Fig. 6, but with the revolution angle of the metal blocks for clamping θ as a parameter.

TABLE I. Measured characteristics of two experimental BLTs and the calculated values. Q, f_0, Y_{m0}, C_d, k_{vn}, and A denote the mechanical quality factor, lowest-resonance frequency, motional admittance at the resonance, clamped capacitance, electromechanical-coupling factor, and force factor, respectively, of the BLT.

	BLT1	BLT2	Calculated
Q	665.9	564.5	⋯
f_0 [kHz]	40.75	41.15	41.95
Y_{m0} [mS]	32.46	31.64	⋯
C_d [nF]	3.956	4.554	3.211
k_{vn}	0.219	0.218	0.184
A [N/V]	2.87	2.77	0.666

manufactured for experimental evaluation of the design. Their measured and calculated characteristics are tabulated in Table I. The voltage applied to the BLTs for the measurement was $1\,V_{rms}$ except for the force factor A, which was evaluated at $10\,V_{p-p}$. The measurement system was the same as Adachi *et al.* had used before.[1] The authors also observed their resonance frequencies and Q values at higher applied voltages, namely 10 and $20\,V_{rms}$. When the voltage is $20\,V_{rms}$, the vibration amplitude at the end surfaces of the two transducers can be estimated approximately at $10\,\mu m_{0-p}$ from the measured parameters. Table II shows the results.

Thanks to the optimum design which realizes the appropriate prestress distribution at the interface, the Q values of the experimental transducers are maintained fairly high even in high-amplitude operation at a frequency over 40 kHz in spite of their low-aspect-ratio shape. Since precise measurement of the prestress at the interface is virtually impossible, direct comparison between the calculated and measured prestress distribution cannot be presented here. However, the high Q values can be considered as indirect proof of the success of the transducer design aided by the numerical method.

The reason for the large discrepancy on the force factor A may be attributed to numerical round-off error owing to the small values of the electromechanical-coupling factor k_{vn} from which the values of A are derived in the calculation, though we find a good agreement between the calculation and the measurement for the resonance frequency.

IV. CONCLUSIONS

The authors developed a simple and practical finite-element analysis system, with which we can obtain approximate solutions of intricate elastic contact problems of piezoelectric systems within the limit of linearity, and thus predict the static prestress exerted by clamping the bolt on the interface between the metal block and the piezoelectric element in a BLT. Using this system, optimum design of a BLT with a low-aspect-ratio shape was tried, and the measured high-Q values of the experimental BLTs of the design support the effectiveness of the design procedure using this analysis system.

ACKNOWLEDGMENTS

TABLE II. The measured values of the mechanical quality factor Q and lowest-resonance frequency f_0 of the BLTs in high-amplitude operation.

	BLT1		BLT2	
Applied voltage	10 [V]	20 [V]	10 [V]	20 [V]
Q	573.2	302	499.2	272.7
f_0 [kHz]	40.73	40.60	41.23	41.17

[1] K. Adachi, Y. Konno, and S. Masaki, ''Development of Bolt-Clamped Langevin-Type Transducer with High Mechanical Quality Factor for Excitation of Large Torsional Vibration,'' Jpn. J. Appl. Phys., Part 1 **33**, 1182–1188 (1994).

[2] R. Holland and E. P. Eer Nisse, ''Design of Resonant Piezoelectric Devices,'' Research Monograph No. 56 (MIT, Cambridge, MA, 1969).

[3] H. Allik and T. J. R. Hughes, ''Finite Element Method for Piezoelectric Vibration,'' Int. J. Numer. Methods Eng. **2**, 151–157 (1970).

[4] J. N. Decarpigny *et al.*, ''In-air Analysis of Piezoelectric Tonpilz Transducers in a Wide Frequency Band using a Mixed Finite Element-Plane Wave Method,'' J. Acoust. Soc. Am. **78**, 1499–1507 (1985).

[5] G. S. Kino, Acoustic Waves: Devices, Imaging, and Analog Signal Processing (Prentice-Hall, Englewood Cliffs, NJ, 1987), p. 546.

[6] O. C. Zienkiewicz, *The Finite Element Method* (McGraw-Hill, UK, Maidenhead, 1977), 3rd ed., Chap. 2.

[7] K. Adachi *et al.*, ''Modal Vibration Control of Large Ultrasonic Tools with the Use Wave-trapped Horns,'' J. Acoust. Soc. Am. **87**, 208–214 (1990).

A hybrid method for the vibration analysis of complex structural-acoustic systems

R. S. Langley[a)]
Department of Engineering, University of Cambridge, Cambridge CB2 1PZ, United Kingdom

P. Bremner
Vibro-Acoustic Sciences, Inc., 12555 High Bluff Drive, Suite 310, San Diego, California 92130

A new method is presented for the analysis of complex dynamic systems which is based on partitioning the system degrees of freedom into a ''global'' set and a ''local'' set. The global equations of motion are formulated and solved in a standard deterministic manner, although due account is taken of the presence of the local degrees of freedom via an approach which is analogous to fuzzy structure theory. The local equations of motion are formulated and solved by using statistical energy analysis (SEA) with due account being taken of power input from the global degrees of freedom. The method can be considered to encompass a number of existing analysis techniques and to form a flexible framework within which a number of detailed modeling strategies can be devised. A simple rod system provides an initial application, and it is shown that the method yields very good results from low to high frequency excitation. © *1999 Acoustical Society of America.* [S0001-4966(99)00502-0]

PACS numbers: 43.40.At, 43.40.Cw, 43.40.Hb [CBB]

INTRODUCTION

The analysis of the response of a coupled structural-acoustic system to external excitation becomes increasingly difficult with increasing excitation frequency. The main reason for this lies in the fact that the wavelength of the system deformation reduces with increasing frequency, and it therefore becomes difficult to devise a precise mathematical model that can adequately capture the complex response pattern. In the context of the finite element method,[1] it is generally considered that approximately eight elements must be used to adequately resolve each structural wavelength, and this can and does lead to unfeasibly large models at high frequencies. Another difficulty is that the system response becomes increasingly sensitive to geometrical imperfections as the wavelength of the response decreases, so that even a very detailed deterministic mathematical model based on the nominal system properties may not yield a reliable response prediction.

Given the difficulties involved in developing a detailed mathematical model of high-frequency vibration, there has been much research effort directed at the development of alternative, more approximate techniques. Foremost amongst these is statistical energy analysis (SEA),[2] in which the system is modeled as a collection of subsystems, each of which is assigned a single response variable corresponding to the vibrational energy. The conditions required for the successful application of SEA have been the subject of considerable previous work (see, for example Ref. 3), and it is generally recognized that, in addition to other conditions, each subsystem must ideally contain a number of resonant modes over the analysis band of interest. One implication of this condition is that the wavelength of the subsystem deforma-tion must be of the same order as, or less then, the dimensions of the subsystem. In some cases this requirement may be only partially met: for example, in-plane waves in a plate are generally of much longer wavelength than bending waves, so that while the bending motion might meet the SEA requirement, the in-plane motion might not. While such difficulties can, in some cases, be overcome by employing problem specific modeling techniques within SEA (as, for example, in Ref. 4), it is true to say that a general approach is lacking. The problem of the existence of both short and long wavelength deformations within a structure is likely to become more severe with *decreasing* frequency, in the sense that all wavelengths will be sufficiently short at a sufficiently high frequency. This creates a difficult mid-frequency zone between low-frequency finite element modeling and high-frequency SEA modeling.

A relatively new approach to the vibration analysis of complex systems is offered by fuzzy structure theory.[5–7] In this approach the system is considered to be comprised of a master structure to which is connected a set of uncertain or fuzzy attachments. In practical terms the master structure might represent a ship hull, while the fuzzy attachments might be internal systems consisting of items such as piping and mechanical or electrical equipment. A key result of fuzzy structure theory is that the attached items act mainly to provide damping to the master structure, and, furthermore, the level of this damping is (surprisingly) independent of the dissipation factor of the attachments.[6] As yet, fuzzy structure theory has only been applied to relatively simple systems; as discussed in what follows, some of the principles of fuzzy structure theory are adopted in the present work to develop a hybrid deterministic/SEA analysis method for a general structural-acoustic system.

A third approach to the analysis of high-frequency vibrations in complex systems has been developed by Belyaev

---

and his co-workers,[8–10] in which the response is considered to be comprised of a ''smooth'' function and a set of local modes defined within each subsystem. A differential equation of motion is developed which governs the smooth function and also makes an allowance for the presence of the local modes; in agreement with the findings of fuzzy structure theory, the local modes act primarily to add damping to the system. This methodology has been applied to the longitudinal vibration of an extended structure, in which the governing equation of motion was that of a rod.[9]

In what follows a new technique is presented for the vibration analysis of complex systems which contains elements of each of the three methods outlined above: SEA, fuzzy structure theory, and the Belyaev smooth function approach. The system response is partitioned into two components, corresponding to long wavelength and short wavelength deformations. The long wavelength component is modeled deterministically, while the short wavelength component is modeled by using SEA. The interaction between the two components is considered in some detail, and it is shown that results similar to those yielded by fuzzy structure theory are obtained. Two analogies with the previously mentioned work can be drawn: the long wavelength deformation can be identified with the master structure in fuzzy structure theory, or alternatively with the smooth response in the Belyaev approach.

The equations of motion of a general structural-acoustic system are developed in Sec. I, and division of the response into two components (referred to as the ''global'' and ''local'' components) is described. The prediction of the global response is described in Sec. II and the application of SEA to the prediction of the local response is described in Sec. III. A summary of the approach is presented in Sec. IV, and an example application is given in Sec. V.

I. EQUATIONS OF MOTION

A. General form of the EOM for builtup systems

The equations of motion (EOM) of a general builtup system which is composed of a number of subsystems such as beams, plates, shells, and acoustic volumes can be formulated by using the Lagrange–Rayleigh–Ritz approach, in which the system response is expressed in terms of a complete set of admissible functions.[11] With this approach, the three components of the system displacement $\mathbf{u} = (u_1 \quad u_2 \quad u_3)^T$ at a general location $\mathbf{x} = (x_1 \quad x_2 \quad x_3)^T$ are written in the form

$$\mathbf{u}(\mathbf{x},t) = \sum_{n=1}^{\infty} q_n(t)\boldsymbol{\phi}_n(\mathbf{x}), \tag{1}$$

where $\boldsymbol{\phi}_n(\mathbf{x})$ represents the nth admissible function, and $q_n(t)$ is the associated degree of freedom (or ''generalized coordinate'') which constitutes the time-dependent amplitude of the admissible function. Many different types of admissible function may be selected—for example, each function may extend smoothly over the whole system, or, alternatively, each function may be restricted to a limited region of the system, as in the finite element method;[1] the main stipulation is that the functions must have an appropri-

ate degree of continuity and must form a complete set under the prescribed natural boundary conditions.[11] The equations of motion which govern the amplitudes q_n follow from the application of Lagrange's equation, and have the well-known form[11]

$$\mathbf{M\ddot{q}} + \mathbf{C\dot{q}} + \mathbf{Kq} = \mathbf{F}, \tag{2}$$

where $\mathbf{M}$, $\mathbf{C}$, and $\mathbf{K}$ are respectively the mass, damping, and stiffness matrices, and the vector $\mathbf{F}$ contains the generalized forces. The mnth entry of the mass matrix can, in general, be written in the form[11]

$$M_{mn} = \sum_{r=1}^{N_S} \int_{V_r} \rho_r(\mathbf{x})\boldsymbol{\phi}_m^T(\mathbf{x})\boldsymbol{\phi}_n(\mathbf{x})\,d\mathbf{x}, \tag{3}$$

where the summation covers each subsystem (for example, beam, plate, shell, or acoustic volume) which forms part of the complete system, and $\rho_r(\mathbf{x})$ is the volume density of the rth subsystem. The mnth entry of the stiffness matrix can be formulated by writing the strain–displacement and stress–strain relations for the rth subsystem as follows:

$$\boldsymbol{\epsilon}_r = \boldsymbol{\Delta}_r \mathbf{u}, \tag{4}$$

$$\boldsymbol{\sigma}_r = \mathbf{D}_r \boldsymbol{\epsilon}_r. \tag{5}$$

Here $\boldsymbol{\sigma}_r$ and $\boldsymbol{\epsilon}_r$ are respectively the stress and strain vectors, and $\mathbf{D}_r$ is the constitutive matrix. The term $\boldsymbol{\Delta}_r$ which appears in Eq. (4) is a matrix of differential operators (in the spatial coordinates $\mathbf{x}$) which acts on the system displacements $\mathbf{u}$ to produce the strain $\boldsymbol{\epsilon}_r$. It can be noted that, with the correct identification of the relevant symbols, Eqs. (4) and (5) are applicable to any type of subsystem, ranging, for example, from a bending beam to a three-dimensional elastic continuum: in the first case the stress and strain are scalars which correspond to the beam bending moment and curvature, whereas, in the second case Eqs. (4) and (5) correspond to the standard three-dimensional elasticity relations in which both the stress and strain have six components (three direct terms and three shear terms). With the notation introduced in Eqs. (4) and (5), the mnth component of the stiffness matrix can now be written in the form[11]

$$K_{mn} = \sum_{r=1}^{N_S} \int_{V_r} (\boldsymbol{\Delta}_r \boldsymbol{\phi}_m)^T \mathbf{D}_r \boldsymbol{\Delta}_r \boldsymbol{\phi}_n \,d\mathbf{x}. \tag{6}$$

The damping matrix $\mathbf{C}$ which appears in Eq. (2) cannot, in general, be expressed in a simple form analogous to either Eq. (3) or (6): the physical causes of damping are various and complex, and a purely theoretical estimate of $\mathbf{C}$ may be significantly in error. For this reason it is usual to adopt a semi-empirical approach to the evaluation of $\mathbf{C}$, in which either Rayleigh damping is assumed, or a loss factor model of the damping is employed. In the first case it is assumed that $\mathbf{C}$ is a linear combination of $\mathbf{M}$ and $\mathbf{K}$, so that Eq. (2) can be diagonalized by a transformation to modal coordinates. In the second case, it is assumed that each subsystem is hysteretically damped, so that the contribution of the rth subsystem to $\mathbf{C}$ is directly proportional to the contribution of this subsystem to $\mathbf{K}$: if the damping varies significantly from subsystem to subsystem, then this can lead to a damping matrix $\mathbf{C}$ which is *not* a linear combination of $\mathbf{M}$ and $\mathbf{K}$.

Further aspects of the damping model adopted are discussed in the following sections.

The final term which appears in Eq. (2) is the generalized force vector **F**; this vector has the components

$$F_m(t) = \sum_{r=1}^{N_S} \int_{V_r} \mathbf{p}_r(\mathbf{x},t)^T \boldsymbol{\phi}_m(\mathbf{x}) \, d\mathbf{x}, \tag{7}$$

where $\mathbf{p}_r(\mathbf{x},t)$ represents the distributed loading which acts on subsystem r. The distributed loading may be random in both space and time, and this will lead to random (and generally correlated) generalized forces. In this case Eq. (2) is most easily solved in the frequency domain by using spectral analysis techniques.[12] More generally, a frequency domain solution to Eq. (2) is also the preferred approach for harmonic forcing, and thus the frequency domain is considered exclusively in what follows. The Fourier transform of Eq. (2) yields

$$[-\omega^2 \mathbf{M} + i\omega \mathbf{C} + \mathbf{K}]\mathbf{q} = \mathbf{Dq} = \mathbf{F}, \tag{8}$$

where ω is the circular frequency and **D** is termed the dynamic stiffness matrix of the system. It should be noted that the terms **q** and **F** which appear in Eq. (8) are complex frequency-dependent quantities which represent the Fourier transforms of the generalized coordinates and generalized forces; for harmonic excitation, these quantities represent the complex amplitudes of the response and forcing.

Equations (3) and (6)–(8) constitute the equations of motion of a general builtup system. These equations allow for a wide range of potential modeling techniques via the choice of the admissible functions $\boldsymbol{\phi}_n(\mathbf{x})$; in fact, the equations encompass all possible energy based formulations ranging from the Rayleigh quotient to the h- and hp-versions of the finite element method. The choice of a suitable set of admissible functions depends to a large extent on the nature of the structure to be analyzed (including the nature of the excitation) and the computational resources which are available. As discussed in the Introduction, particular problems arise when considering medium- to high-frequency vibrations of complex structures: in this case the structural deformation can have a very short wavelength, meaning that an unfeasible number of admissible functions may be needed to capture the detailed behavior of the system. In what follows, a method is presented whereby the admissible functions are partitioned into "long-" and "short-" wavelength functions, and the response associated with the short-wavelength functions is computed by using statistical, rather than deterministic, techniques.

B. Wave number partitioning and global modes

In what follows the admissible functions which appear in Eq. (1) are partitioned into two sets which are nominally referred to as "global" and "local" admissible functions, so that the equation is modified to read

$$\mathbf{u}(\mathbf{x},t) = \sum_{n=1}^{N_g} q_n^g(t) \boldsymbol{\phi}_n^g(\mathbf{x}) + \sum_{n=1}^{N_l} q_n^l(t) \boldsymbol{\phi}_n^l(\mathbf{x}), \tag{9}$$

where the suffices g and l are used respectively to denote the global and local sets. The partitioning is made on the following general basis: the global admissible functions are intended to capture the "long wavelength" deformations of the structure while the local admissible functions are intended to capture the "short wavelength" deformations. As explained in what follows, a statistical energy analysis (SEA) model of the response associated with the local admissible functions is employed in the present work to eliminate the need for a detailed deterministic model.

The somewhat vague definition of the global and local admissible functions can perhaps be clarified by considering the particular example of a three-dimensional beam framework comprised of closed section beam members. At a specified frequency, a single beam within the framework can propagate three types of elastic wave: bending, torsional, and axial waves. The torsional and axial waves generally have a much longer wavelength than the bending waves, and structural deformations on this scale would be included in the set of "global" admissible functions, while the "local" admissible functions would encompass the bending wavelength. The use of the terminology "global" and "local" is related to the fact that the modal density of a single beam is relatively low for axial and torsional modes in comparison with bending modes.[13] Over a given frequency band, the beam may have a theoretical mode count of, say, 0.1 for axial modes and, say, 4.0 for bending modes; this implies that the beam is unlikely to exhibit an axial mode within the frequency band, although axial motion may contribute to a mode of the whole structure—that is, a "global" mode (simplistically, a ten-element framework would have an "axial" mode count of unity). In contrast, the beam is highly likely to exhibit a number of bending modes within the frequency band, and, when the beam is *in situ*, these modes could contribute to either localized ("local") or extended modes of the complete framework.

From a practical point of view, the "global" admissible functions could consist of a relatively coarse mesh finite element model which is able to capture the longer wavelength deformations of the structure. The "local" admissible functions could then be employed to enhance this model and capture the short wavelength deformation—were the hierarchical (or hp-version) finite element method employed, then the local admissible functions could be identified in principle with the internal or hierarchical shape functions. The precise way in which the partitioning represented by Eq. (9) is implemented is an open issue—the main feature of the following analysis is that the response encompassed by the "local" admissible functions is modeled by using SEA, so that all aspects of the dynamics not covered by this approach should be incorporated within the global admissible functions.

Having partitioned Eq. (1) in the form of Eq. (9), it follows that the system equations of motion, Eq. (8), can be partitioned as follows

$$\begin{pmatrix} \mathbf{D}_{gg} & \mathbf{D}_{gl} \\ \mathbf{D}_{gl}^T & \mathbf{D}_{ll} \end{pmatrix} \begin{pmatrix} \mathbf{q}^g \\ \mathbf{q}^l \end{pmatrix} = \begin{pmatrix} \mathbf{F}^g \\ \mathbf{F}^l \end{pmatrix}. \tag{10}$$

Without loss of generality, the global coordinates $\mathbf{q}^g$ can be selected (or transformed) so that the matrix partition $\mathbf{D}_{gg}$ is diagonal, providing a Rayleigh damping model is assumed

R. S. Langley and P. Bremner: Complex structural-acoustic systems

for the response in these coordinates. In this case the global admissible functions $\phi_n^g(\mathbf{x})$ can be interpreted as ''global modes,'' although it should be noted that the true modes of the system cannot be modeled solely in terms of $\mathbf{q}^g$ but also require a contribution from $\mathbf{q}^l$. If $\mathbf{D}_{gg}$ is a diagonal matrix, then the nth diagonal entry will have the form

$$(\mathbf{D}_{gg})_{nn} = \omega_n^2(1 + i\,\eta_n) - \omega^2, \tag{11}$$

where ω_n and η_n are the natural frequency and loss factor associated with the nth ''global mode,'' and it has been assumed that the mode shape $\phi_n^g(\mathbf{x})$ is scaled to unit generalized mass.

The matrix partition $\mathbf{D}_{gl}$ which appears in Eq. (10) governs the coupling between the global and local degrees of freedom, and this has contributions from the three matrices $\mathbf{M}$, $\mathbf{C}$, and $\mathbf{K}$ which appear in Eq. (8). It will be assumed in what follows that each local admissible function is identified with a single subsystem, so that the admissible function is everywhere zero except within this subsystem. Under this assumption the dominant contribution to $\mathbf{D}_{gl}$ can be identified by considering the integrals which appear in Eqs. (3) and (6). In order to do this, it is helpful to focus on the coupling between global mode m and local coordinate n (defined over subsystem r), and to define the following integrals:

$$M_{nn}^{ll} = \int_{V_r} \rho(\mathbf{x}) \phi_n^{lT}(\mathbf{x}) \phi_n^l(\mathbf{x})\, d\mathbf{x}, \tag{12}$$

$$K_{nn}^{ll} = \int_{V_r} (\boldsymbol{\Delta}_r \phi_n^l)^T \mathbf{D}_r \boldsymbol{\Delta}_r \phi_n^l\, d\mathbf{x}, \tag{13}$$

$$M_{mn}^{gl} = \int_{V_r} \rho(\mathbf{x}) \phi_m^{gT}(\mathbf{x}) \phi_n^l(\mathbf{x})\, d\mathbf{x}, \tag{14}$$

$$K_{mn}^{gl} = \int_{V_r} (\boldsymbol{\Delta}_r \phi_m^g)^T \mathbf{D}_r \boldsymbol{\Delta}_r \phi_r^l\, d\mathbf{x}. \tag{15}$$

By definition, the global admissible functions are of long wavelength relative to the local admissible functions, and hence it follows that $O(\boldsymbol{\Delta}_r \phi_m^g)/O(\phi_m^g) \ll O(\boldsymbol{\Delta}_r \phi_n^l)/O(\phi_n^l)$. Now if the local coordinate is resonant, so that $O(\omega^2 M_{nn}^{ll}) = O(K_{nn}^{ll})$, then it follows from Eqs. (12)–(15) that $O(K_{mn}^{gl}) \ll O(\omega^2 M_{mn}^{gl})$. Given that the influence of the damping matrix $\mathbf{C}$ will generally be small, it can be concluded that, under the stated conditions, the dominant contribution to $\mathbf{D}_{gl}$ will arise from inertial coupling so that

$$\mathbf{D}_{gl} \approx -\omega^2 \mathbf{M}_{gl}, \tag{16}$$

where $\mathbf{M}_{gl}$ is the appropriate partition of $\mathbf{M}$. It can be noted that certain choices of global and local admissible functions can render Eq. (16) exact; if, for example, the local admissible functions are taken to be the blocked modes of a subsystem (i.e., the modes obtained under clamped boundary conditions) and the global admissible functions are expressed in terms of static or ''constraint'' modes,[14] then by definition the two sets of functions are stiffness orthogonal, and all coupling occurs through the mass matrix.

As discussed in what follows, the precise form of the partition $\mathbf{D}_{ll}$ which appears in Eq. (10) is not required under the present formulation. The system response is sought by reexpressing Eq. (10) in the form

$$(\mathbf{D}_{gg} - \mathbf{D}_{gl}\mathbf{D}_{ll}^{-1}\mathbf{D}_{gl}^T)\mathbf{q}^g = \mathbf{F}^g - \mathbf{D}_{gl}\mathbf{D}_{ll}^{-1}\mathbf{F}^l, \tag{17}$$

$$\mathbf{D}_{ll}\mathbf{q}^l = \mathbf{F}^l - \mathbf{D}_{gl}^T\mathbf{q}^g. \tag{18}$$

Equation (17) follows by eliminating $\mathbf{q}^l$ from the first row of Eq. (10), while Eq. (18) follows immediately from the second row of Eq. (10). The rationale behind Eqs. (17) and (18), and the method of solution, is described in the following sections. In this regard, Eq. (17) is referred to as the global equation of motion, while Eq. (18) is described as the local equation of motion.

II. SOLUTION OF THE GLOBAL EQUATION OF MOTION

A. The modified dynamic stiffness matrix: Fuzzy structures

The left side of Eq. (17) contains a modification to the global dynamic stiffness matrix $\mathbf{D}_{gg}$ which arises from the presence of the local degrees of freedom. The mnth component of this additional matrix can be expressed in the form

$$(\mathbf{D}_{gl}\mathbf{D}_{ll}^{-1}\mathbf{D}_{gl}^T)_{mn} = \sum_{j=1}^{N_l} \sum_{k=1}^{N_l} (\mathbf{D}_{gl})_{mj}(\mathbf{D}_{ll}^{-1})_{jk}(\mathbf{D}_{gl})_{nk}, \tag{19}$$

where the summations are taken over the local coordinates. This expression can be considerably simplified by making a number of assumptions regarding the nature of the local admissible functions. Firstly, as is commonly done in SEA, it can be assumed that the local coordinates are weakly coupled, so that $\mathbf{D}_{ll}$ is nearly diagonal and can be approximated as being diagonal for the present purposes. If the local admissible functions are further taken to be mode shapes of the uncoupled (or ''blocked'') subsystems (scaled to unit generalized mass), then Eq. (19) simplifies to

$$(\mathbf{D}_{gl}\mathbf{D}_{ll}^{-1}\mathbf{D}_{gl}^T)_{mn} = \sum_{j=1}^{N_l} (\mathbf{D}_{gl})_{mj}(\mathbf{D}_{gl})_{nj}[\omega_j^2(1 + i\,\eta_j) - \omega^2]^{-1}, \tag{20}$$

where ω_j and η_j represent the natural frequency and loss factor of local mode j. If the complete system contains N_S subsystems, and subsystem r has N_r modes, then Eq. (20) can be rewritten in the form

$$(\mathbf{D}_{gl}\mathbf{D}_{ll}^{-1}\mathbf{D}_{gl}^T)_{mn} = \sum_{r=1}^{N_S} \sum_{k=1}^{N_r} (\mathbf{D}_{gl})_{mj(k,r)}(\mathbf{D}_{gl})_{nj(k,r)}$$
$$\times [(\omega_k^r)^2(1 + i\,\eta_k^r) - \omega^2]^{-1}, \tag{21}$$

where ω_k^r and η_k^r represent the natural frequency and loss factor of local mode k of subsystem r, and the symbol $j(k,r)$ is used to indicate the position of this mode in the total sequence of local modes. It follows from Eqs. (14) and (16) that the product which appears within the summation in Eq. (21) can be written as

$$(\mathbf{D}_{gl})_{mj(k,r)}(\mathbf{D}_{gl})_{nj(k,r)} = \omega^4 j_{rmn}^2(k), \tag{22}$$

where

$$j_{rmn}^2(k) = \int_{V_r} \int_{V_r} \rho(\mathbf{x})\rho(\mathbf{x}') \boldsymbol{\phi}_m^{gT}(\mathbf{x})$$

$$\times \mathbf{R}_r(\mathbf{x},\mathbf{x}',k) \boldsymbol{\phi}_n^g(\mathbf{x}') \, d\mathbf{x}\, d\mathbf{x}', \qquad (23)$$

$$\mathbf{R}_r(\mathbf{x},\mathbf{x}',k) = \boldsymbol{\phi}_{j(k,r)}^l(\mathbf{x}) \boldsymbol{\phi}_{j(k,r)}^{lT}(\mathbf{x}'). \qquad (24)$$

The function $\mathbf{R}_r$ which appears in Eq. (24) can be viewed as a form of modal correlation coefficient for the local modes in subsystem r; if the final term on the right of Eq. (21) is a smooth function of ω_k^r, then it is admissible to average $\mathbf{R}_r$ over a group of local modes k—in this case a good approximation to $\mathbf{R}_r$ can be obtained by employing a high-frequency asymptotic estimate of $\boldsymbol{\phi}_{j(k,r)}^l$, such as a simple standing wave system.[15] The dimensionless term j_{rmn}^2 which appears in Eq. (23) can be interpreted as a form of ''joint acceptance function''[16] between the global modes and the local modes in subsystem r.

The use of Eq. (22) in Eq. (21) leads to the following result for the additional dynamic stiffness matrix arising from the presence of the local modes

$$(\mathbf{D}_{gl}\mathbf{D}_{ll}^{-1}\mathbf{D}_{gl}^T)_{mn} = \omega^4 \sum_{r=1}^{N_S} \sum_{k=1}^{N_r} j_{rmn}^2(k)$$

$$\times [(\omega_k^r)^2(1+i\eta_k^r) - \omega^2]^{-1}. \qquad (25)$$

This expression can be further simplified by considering the properties of the final summation which appears on the right-hand side; in order to do this it is helpful to consider separately the contribution arising from the resonant local modes ($\omega_k^r \approx \omega$) and from the inertia dominated local modes ($\omega_k^r \ll \omega$), and this is done in the following subsections. The contribution arising from stiffness dominated local modes ($\omega_k^r \gg \omega$) is not considered here, as this will normally be negligible.

1. Contribution from the resonant modes

In considering the contribution to Eq. (25) arising from the local modes which are near to resonance ($\omega_k^r \approx \omega$), the term $j_{rmn}^2(k)$ can reasonably be assumed to be independent of k, at least over the restricted range of the resonant modes; Eq. (25) can then be simplified by considering the properties of the following sum:

$$S_r = \sum_{k=1}^{N_r} [(\omega_k^r)^2(1+i\eta_k^r) - \omega^2]^{-1}. \qquad (26)$$

Langley[17] has shown that for a one-dimensional subsystem the sum has the following bounds:

$$(\pi\nu_r/2\omega)\tanh(\pi m_r/2) \leqslant -\operatorname{Im}(S_r)$$

$$\leqslant (\pi\nu_r/2\omega)\coth(\pi m_r/2), \quad (27)$$

$$\left| \operatorname{Re}(S_r) - \frac{\pi\nu_r}{2\omega}\gamma \right| \leqslant \frac{\pi\nu_r}{2\omega}\left[\frac{\sin(\pi m_r)}{\cosh(\pi m_r) - \cos(\pi m_r)} \right], \qquad (28)$$

where ν_r is the modal density of subsystem r and $m_r = \omega\eta_r\nu_r$ is the subsystem modal overlap factor (in which η_r

is the average loss factor). The term γ which appears in Eq. (28) is dependent on the nature of the dispersion relation of the subsystem: $\gamma=0$ for a nondispersive system, while $\gamma=-1$ for bending waves in a beam. If the system modal overlap is high, then Eqs. (27) and (28) lead to the results

$$\operatorname{Im}(S_r) \approx -(\pi\nu_r/2\omega), \qquad (29)$$

$$\operatorname{Re}(S_r) \approx (\pi\nu_r/2\omega)\gamma. \qquad (30)$$

Although Eqs. (27) and (28) were derived for a one-dimensional subsystem, the equations also give an approximate indication of the range of variation in S_r for a two-dimensional system such as a plate—the main difference is that the natural frequencies of a two-dimensional system have a pseudo-random spacing, whereas those of a one-dimensional system have a simple deterministic spacing. Lyon[18] has considered various aspects of the statistics of S_r for the two-dimensional case: on the assumption that the occurrence of natural frequencies forms a Poisson random process, it can be shown that $\operatorname{E}[\operatorname{Im}(S_r)]=-(\pi\nu_r/2\omega)$, in agreement with Eq. (29), and also that $\operatorname{E}[\operatorname{Re}(S_r)]=0$. Furthermore, the ratio of the standard deviation to the mean for the imaginary part of the sum is given by $\sigma/\mu=1/\sqrt{\pi m_r}$, so that the coefficient of variation reduces with increasing modal overlap.

On the basis of the above discussion, it is clear that the simplest approximation to S_r (which will be strictly valid at high modal overlap) is to employ Eq. (29) for the imaginary part and to approximate the real part to zero. Equation (25) then becomes

$$(\mathbf{D}_{gl}\mathbf{D}_{ll}^{-1}\mathbf{D}_{gl}^T)_{mn} = -i\frac{\pi\omega^3}{2}\sum_{r=1}^{N_S} j_{rmn}^2\nu_r, \qquad (31)$$

where j_{rmn}^2 represents the average value of $j_{rmn}^2(k)$. This result implies that the local modes act to damp the global modes; by considering a diagonal component $m=n$ of the above result, it is clear that the local modes produce an effective loss factor of the form

$$\eta_m^{\text{eff}} = \frac{\pi\omega}{2}\sum_{r=1}^{N_S} j_{rmm}^2\nu_r. \qquad (32)$$

This extremely simple result is in full agreement with recent work on fuzzy structure theory:[5–7] such work is concerned with the effect of ''fuzzy'' or uncertain attachments on the dynamics of a master structure—the fuzzy attachments are normally considered to be a set of oscillators having random properties. One of the key results of fuzzy structure theory is that, under the appropriate conditions, the fuzzy attachments add damping to the master structure to a degree which depends on the modal density of the attachments but not on the loss factor of the attachments. This result is mirrored in Eq. (32): in the present analysis the local modes take on the role of the fuzzy structure and the global modes act as the master structure.

A fundamental feature of fuzzy structure theory is that there is no need to model the fuzzy attachments in detail. This is also a feature of the present work, in that Eq. (32) contains only the asymptotic modal density of the local system rather than detailed natural frequency information. The fact that fuzzy structure theory has generally been applied to

random point attachments implies that the nature of the coupling to the master structure is described in terms of random point impedances, and in this case there is no equivalent of the term j_{rmn}^2 which appears in the present work. As shown in Eq. (23), this term requires detailed knowledge of the global modes together with an average measure of the local mode shapes expressed through the function $\mathbf{R}_r$. Hence, as in fuzzy structure theory, the present approach does not require a detailed model of the local system either in terms of the mode shapes or the natural frequencies. In one sense the present method can be viewed as an application of the principles of fuzzy structure theory to distributed attachments, consisting of the local mode dynamics.

2. Contribution from the inertia dominated modes

The contribution to Eq. (25) arising from inertia dominated local modes ($\omega_k^r \ll \omega$) can be written in the form

$$(\mathbf{D}_{gl}\mathbf{D}_{ll}^{-1}\mathbf{D}_{gl}^T)_{mn} = -\omega^2 \sum_{r=1}^{N_S} \sum_{k=1}^{N_r'} j_{rmn}^2(k), \tag{33}$$

where N_r' represents the number of inertia dominated modes. The result yielded by Eq. (33) will be determined by the k dependency of the coefficient $j_{rmn}^2(k)$; it is shown in Sec. V, for example, that a significant *negative* effective mass results from Eq. (33) if the subsystem is an elastic rod.

B. Evaluation of the modified forcing vector

1. General considerations

The global equation of motion, Eq. (17), contains a forcing term on the right-hand side which arises from the generalized forces acting on the local coordinates. The mth component of this force can be written as

$$(\mathbf{D}_{gl}\mathbf{D}_{ll}^{-1}\mathbf{F}^l)_m = \sum_{j=1}^{N_l} \sum_{k=1}^{N_l} (\mathbf{D}_{gl})_{mj}(\mathbf{D}_{ll}^{-1})_{jk}F_k^l. \tag{34}$$

Following the same line of development as in the previous subsection, this equation can be rewritten in the form

$$(\mathbf{D}_{gl}\mathbf{D}_{ll}^{-1}\mathbf{F}^l)_m = \sum_{r=1}^{N_S} \sum_{k=1}^{N_r} (\mathbf{D}_{gl})_{mj(k,r)}F_{j(k,r)}^l$$
$$\times [(\omega_k^r)^2(1+i\eta_k^r)-\omega^2]^{-1}, \tag{35}$$

where only the diagonal entries of $\mathbf{D}_{ll}$ have been retained. An approximate evaluation of the summation which appears in Eq. (35) is complicated by the fact that the sign of both $(\mathbf{D}_{gl})_{mj(k,r)}$ and $F_{j(k,r)}^l$ can oscillate with the summation index k; this problem can be circumvented by considering the modulus squared of the generalized force, which has the approximate form

$$|(\mathbf{D}_{gl}\mathbf{D}_{ll}^{-1}\mathbf{F}^l)_m|^2 = \omega^4 \sum_{r=1}^{N_S} \sum_{k=1}^{N_r} j_{rmm}^2(k)$$
$$\times |F_{j(k,r)}^l/[(\omega_k^r)^2(1+i\eta_k^r)-\omega^2]|^2, \tag{36}$$

where Eq. (22) has been employed, and cross-product terms between the various local modes k have been taken to aver-

age to zero. This result will hold if the local mode generalized forces $F_{j(k,r)}^l$ are uncorrelated, which is a standard assumption within statistical energy analysis. As in the case of Eq. (25), both the resonant and the inertia dominated local modes will contribute to the summation which appears in Eq. (36). By analogy with the analysis contained in Secs. II A 1 and II A 2, the summation can be evaluated approximately to yield the result

$$|(\mathbf{D}_{gl}\mathbf{D}_{ll}^{-1}\mathbf{F}^l)_m|^2 = \sum_{r=1}^{N_S} \langle|F_{j(k,r)}^l|^2\rangle_k \left\{ \left\langle \frac{j_{rmm}^2}{2\eta_k^r} \right\rangle_k \omega\pi\nu_r \right.$$
$$\left. + \sum_{k=1}^{N_r'} j_{rmm}^2(k) \right\}, \tag{37}$$

where $\langle\ \rangle_k$ denotes an average over the local modes. The generalized force $\mathbf{D}_{gl}\mathbf{D}_{ll}^{-1}\mathbf{F}^l$ which appears in Eq. (17) can now be reconstructed from Eq. (37), although it should be noted that this result does not contain any phase information. The resonant and inertia dominated contributions to Eq. (37) are in quadrature, but the phase of these terms relative to the global generalized forces $\mathbf{F}^g$ is not as yet fully determined; this issue is considered further in Sec. II B 2.

Equations (36) and (37) are based on the assumption that the cross-product terms which arise when Eq. (35) is squared will average to zero. As stated previously, this result will hold if the local mode generalized forces are uncorrelated, and this will be highly dependent on the nature of the applied loading. For rain-on-the-roof forcing (often assumed in SEA[2]), the generalized forces are, in fact, uncorrelated, while for other types of loading it is possible that cross-correlation terms can have a significant effect, in which case Eqs. (36) and (37) will yield a poor estimate of the modified force vector. An alternative approach to the calculation of the modified force vector, which does not rely on the assumption of uncorrelated local mode generalized forces, is presented in Sec. II B 3.

2. Rain-on-the-roof forcing

In the special case of rain-on-the-roof forcing, the correlation between the global generalized force and the additional generalized force which appears in Eq. (17) can readily be established. Rain-on-the-roof forcing is defined such that the temporal Fourier transform of the distributed load $\mathbf{p}_r$ which appears in Eq. (7) has the property

$$E[\mathbf{p}_r(\mathbf{x},\omega)\mathbf{p}_r^{*T}(\mathbf{x}',\omega)] = \mathbf{S}\delta(\mathbf{x}-\mathbf{x}'), \tag{38}$$

where $E[\ ]$ represents the expected value, $\mathbf{S}$ is a correlation matrix, and δ is the Dirac delta function. Now, following Eq. (35), the mth component of the force which appears on the right of Eq. (17) has the form

$$F_m^g - (\mathbf{D}_{gl}\mathbf{D}_{ll}^{-1}\mathbf{F}^l)_m = F_m^g - \sum_{r=1}^{N_S} \sum_{k=1}^{N_r} (\mathbf{D}_{gl})_{mj(k,r)}F_{j(k,r)}^l$$
$$\times [(\omega_k^r)^2(1+i\eta_k^r)-\omega^2]^{-1}, \tag{39}$$

where

$$F_m^g = \sum_{r=1}^{N_S} \int_{V_r} \mathbf{p}_r^T(\mathbf{x}) \boldsymbol{\phi}_m^g(\mathbf{x}) \, d\mathbf{x}, \tag{40}$$

$$F_{j(k,r)}^l = \int_{V_r} \mathbf{p}_r^T(\mathbf{x}) \boldsymbol{\phi}_{j(k,r)}^l(\mathbf{x}) \, d\mathbf{x}. \tag{41}$$

The correlation between the two terms which appear on the right of Eq. (39) is determined by the correlation between F_m^g and $F_{j(k,r)}^l$; in this regard it follows from Eqs. (38), (40), and (41) that

$$E[F_m^g F_{j(k,r)}^{l*}] = \int_{V_r} \boldsymbol{\phi}_m^{gT}(\mathbf{x}) \mathbf{S} \boldsymbol{\phi}_{j(k,r)}^l(\mathbf{x}) \, d\mathbf{x}. \tag{42}$$

In most practical applications it is not restrictive to assume that $\mathbf{S}$ is diagonal and proportional to ρ_r, in which case it follows from Eqs. (14) and (16) that

$$E[F_m^g F_{j(k,r)}^{l*}] = -(\alpha/\omega^2)(\mathbf{D}_{gl})_{mj(k,r)}, \tag{43}$$

where α is some constant. It follows that the correlation between the two force components which appear in Eq. (39) has a similar form to the right-hand side of Eq. (21), and the analysis methods outlined in Secs. II A 1 and II A 2 can therefore be employed to evaluate this quantity.

3. Alternative method of evaluating the modified forcing vector

As discussed previously, the method outlined in Sec. II B 1 for calculating the modified forcing vector is based on the assumption that the local mode generalized forces are uncorrelated. If this is not a valid assumption, then an alternative approach can be developed by writing Eq. (34) in the form

$$(\mathbf{D}_{gl} \mathbf{D}_{ll}^{-1} \mathbf{F}^l)_m = \sum_{j=1}^{N_l} (\mathbf{D}_{gl})_{mj} q_j^{lB}, \tag{44}$$

$$\mathbf{q}^{lB} = \mathbf{D}_{ll}^{-1} \mathbf{F}^l. \tag{45}$$

Here $\mathbf{q}^{lB}$ can be interpreted as the ''blocked'' local mode response, i.e., the local mode response obtained from Eq. (10) when the global response $\mathbf{q}^q$ is enforced to be zero. It follows from Eqs. (14) and (16) that Eq. (44) can be expressed in the form

$$(\mathbf{D}_{gl} \mathbf{D}_{ll}^{-1} \mathbf{F}^l)_m$$
$$= \sum_{r=1}^{N_S} \sum_{k=1}^{N_r} \left\{ -\omega^2 \int_{V_r} \rho(\mathbf{x}) \boldsymbol{\phi}_m^{gT}(\mathbf{x}) \boldsymbol{\phi}_{j(k,r)}^l(\mathbf{x}) \, d\mathbf{x} \right\} q_{j(k,r)}^{lB}, \tag{46}$$

and by taking the summation over k inside the integral this result can be rewritten as

$$(\mathbf{D}_{gl} \mathbf{D}_{ll}^{-1} \mathbf{F}^l)_m = \sum_{r=1}^{N_S} -\omega^2 \int_{V_r} \rho(\mathbf{x}) \boldsymbol{\phi}_m^{gT}(\mathbf{x}) \mathbf{u}_r^B(\mathbf{x}) \, d\mathbf{x}, \tag{47}$$

$$\mathbf{u}_r^B(\mathbf{x}) = \sum_{k=1}^{N_r} q_{j(k,r)}^{lB} \boldsymbol{\phi}_{j(k,r)}^l(\mathbf{x}). \tag{48}$$

The term $\mathbf{u}_r^B(\mathbf{x})$ represents the ''blocked'' local response of subsystem r; if some estimate of this quantity is available, then Eq. (47) can be used to yield the modified forcing vector (a specific example of this approach is given in Sec. V A 2).

C. Calculation of the global response

Explicit expressions for those terms in the global equation of motion, Eq. (17), which arise from the presence of the local modes are presented in Eqs. (31), (33), (37), and (47). Given these terms, the equations of motion can be solved to yield the global response vector $\mathbf{q}^g$; if the excitation is random, then Eq. (17) yields the transfer function of the global response, and standard spectral analysis techniques can be used to obtain the response spectra and mean squared values.[12]

It is well known that uncertainties in the properties of a system can have a significant effect on the dynamic response; such uncertainties are normally allowed for in statistical energy analysis (SEA) by considering the mean and variance of the response of an ensemble of random systems. In the present work, uncertainties can affect the global mode response both directly through uncertainties in the matrix $\mathbf{D}_{gg}$ and indirectly through uncertainties in the local mode terms described by Eqs. (31), (33), (37), and (47). If necessary, the effect of uncertainties in $\mathbf{D}_{gg}$ can be incorporated into the present analysis by using the stochastic finite element method[19] to formulate the global admissible functions. Uncertainty in the local mode terms poses a more difficult problem, although some mention of the implications of Poisson natural frequency spacing has already been made in Sec. II A, and ongoing work in fuzzy structure theory is addressing issues of this kind.[20]

III. SOLUTION OF THE LOCAL EQUATIONS OF MOTION

A. Statistical energy analysis formulation

The ''local'' coordinate equation of motion is given by Eq. (18), where it can be recalled that the coordinates $\mathbf{q}^l$ relate to the short wavelength local modes in each of the N_S subsystems, so that the dimension of $\mathbf{q}^l$ may be extremely large. In preference to a deterministic approach, a solution to Eq. (18) can be sought by employing statistical energy analysis (SEA), in which each subsystem is assigned a single degree of freedom corresponding to the vibrational energy of the local modes. The SEA equations are developed by considering power balance for each subsystem, and this leads to a set of N_S equations in the form[2]

$$\omega \eta_r E_r + \omega \sum_{s=1}^{N_S} \eta_{rs} \nu_r \left(\frac{E_r}{\nu_r} - \frac{E_s}{\nu_s} \right) = P_r, \quad r = 1, 2, \ldots, N_S, \tag{49}$$

where η_r, ν_r, E_r, and P_r are respectively the loss factor, modal density, energy, and external power input to subsystem r, and η_{rs} is termed the coupling loss factor between subsystem r and subsystem s.

The subsystem energies E_r are normally considered to be averages over a specified frequency band, and ensemble

averaging over a set of random systems is normally presupposed in deriving the coupling loss factors.[2] SEA was originally formulated for broadband rain-on-the-roof forcing; subsequent work has shown that the method can be applied more generally, providing the results are interpreted correctly. Most notably, (i) at high statistical overlap (i.e., ensemble mixing of the subsystem natural frequencies) the response tends to become ergodic, and the ensemble average response predicted at a single frequency is in close agreement with the frequency band average obtained for a single realization, and (ii) for reverberant systems the ensemble-averaged response is insensitive to the difference between point loading and rain-on-the-roof forcing. Thus the restrictions on both the spatial and spectral nature of the loading can be relaxed under the appropriate conditions, as discussed in detail in Ref. 2.

In relating Eq. (49) to Eq. (18), it can be noted that the coupling loss factors are not normally derived directly from the dynamic stiffness matrix $\mathbf{D}_{ll}$, but rather are based on an independent analysis which often involves a consideration of elastic wave transmission between the various subsystems. Within the context of the present approach, care is needed to ensure that the coupling loss factors employed in Eq. (49) are fully consistent with the local admissible functions which are adopted. Consider, for example, a modeling strategy in which the complete set of admissible functions for a subsystem is taken to consist of the blocked modes and the static (or ''constraint'') modes. The blocked modes are defined as the modes of vibration obtained under clamped boundary conditions, while the static modes are the shapes obtained by (statically) deflecting one point on the boundary and holding all other boundary points fixed.[14] The blocked modes are by definition uncoupled from each other and inertially coupled to the static modes. A one-dimensional subsystem has a finite number of static modes, each of which has a smooth (long wavelength) distribution through the structure, and such modes would generally be included in the set of ''global'' admissible functions. In this case the local degrees of freedom (the blocked modes) of any subsystem are coupled only to the global degrees of freedom so that $\mathbf{D}_{ll}$ is strictly a diagonal matrix; this means that the coupling loss factors which appear in Eq. (49) should be set to zero. (The blocked modes are of course *indirectly* coupled via the global admissible functions, but this coupling is already allowed for within the present methodology, and the use of nonzero coupling loss factors would doubly account for this effect. This aspect is illustrated by the numerical example considered in Sec. V.) In contrast, a two-dimensional subsystem has an infinite number of static modes (since there are an infinite number of boundary points), and these can be combined to produce a limited number of smooth (long wavelength) functions and an infinite number of shorter wavelength functions—only the smooth functions would be included in the set of global admissible functions. In this case the local degrees of freedom consist of the blocked modes *and* the short wavelength static modes, so that $\mathbf{D}_{ll}$ contains coupling terms, both within and across subsystems. Furthermore, the short wavelength static modes are commensurate with the short wavelength elastic waves which are employed in a

wave calculation of the coupling loss factors, and in this case it can be argued that the conventional coupling loss factors should be included in Eq. (49). To summarize the position, it is important to ensure that the coupling loss factors which are employed in Eq. (49) are consistent with the form of the matrix $\mathbf{D}_{ll}$, and this is determined by the choice of the global and local admissible functions.

The power input which appears in Eq. (49) arises from both of the forcing terms which appear on the right of Eq. (18). The power input by the first term can be estimated by using standard methods, which are normally based on the impedance of an infinite subsystem;[2] the second term on the right of Eq. (18) is nonstandard, however, since this term will result in a power input to the subsystem from the global modes, and this issue is considered in detail in the following subsection.

B. Power input from the global modes

The power input from the global modes to the local modes can be estimated by considering initially the power input to a single local mode in a particular subsystem. In doing this, it is consistent with standard SEA methods to neglect the coupling between the local modes: this is equivalent to calculating the power input to an uncoupled (or ''blocked'') subsystem, and it is normally argued that the power input is not significantly affected by coupling between the subsystems. If the coupling to other local modes is neglected, then it follows from Eq. (18) that the equation of motion for local mode k of subsystem r has the form

$$[(\omega_k^r)^2(1+i\,\eta_k^r)-\omega^2]q_{j(k,r)}^l=F_{j(k,r)}^l-(\mathbf{D}_{gl}^T\mathbf{q}^g)_{j(k,r)},$$
(50)

where the index $j(k,r)$ is as defined in Secs. II A and II B. Considering initially the case $F_{j(k,r)}^l=0$, the time averaged power input to the mode to can be written as

$$P_{r,k}^g=\tfrac{1}{2}\,\mathrm{Re}\{-i\,\omega q_{j(k,r)}^l(\mathbf{D}_{gl}^T\mathbf{q}^g)_{j(k,r)}^*\}$$
$$=\frac{1}{2}\,\mathrm{Re}\left\{\frac{i\,\omega|(\mathbf{D}_{gl}^T\mathbf{q}^g)_{j(k,r)}|^2}{(\omega_k^r)^2(1+i\,\eta_k^r)-\omega^2}\right\}.$$
(51)

The power input to the complete set of modes in subsystem r is therefore given by

$$P_r^g=\sum_{k=1}^{N_r}\frac{1}{2}\,\mathrm{Re}\left\{\frac{i\,\omega|(\mathbf{D}_{gl}^T\mathbf{q}^g)_{j(k,r)}|^2}{(\omega_k^r)^2(1+i\,\eta_k^r)-\omega^2}\right\}.$$
(52)

This result can be simplified by employing the same techniques as were used to simplify Eqs. (21) and (23): the denominator can be averaged over k and the sum over k can then be performed by employing Eq. (29). This procedure yields

$$P_r^g=\frac{\omega^4\pi\nu_r}{4}\sum_{m=1}^{N_g}\sum_{n=1}^{N_g}j_{rmn}^2q_mq_n^*,$$
(53)

where j_{rmn}^2 is given by Eq. (25) and the summations cover the complete set of global modes. In considering the units of the various terms which appear in Eq. (53), it can be noted that j_{rmn}^2 is dimensionless while the generalized coordinates q_m have units of length$\times$(mass)$^{1/2}$ (since the mode shapes

are scaled to unit generalized mass), so that P_r^g correctly has units of power. As would be anticipated, it can be seen that the power input to the local modes, given by Eq. (53), is equal to the power dissipated from the global modes via the fuzzy damping terms, Eq. (31).

Thus far the case $F_{j(k,r)}^l = 0$ has been considered; if $F_{j(k,r)}^l \neq 0$, then power is input to the subsystem via the local forcing, and also there is the possibility of interaction between the local and global forcing terms which appear on the right of Eq. (50). The power input by the local forcing, P_r^l say, can be computed by using standard SEA procedures,[2] while any modification to the power input arising from interaction between the two forcing terms will depend upon their relative phase. If the two terms are considered to be uncorrelated, then the total power input is given by $P_r = P_r^g + P_r^l$; more generally, whatever the correlation between the two terms, the total power input will always fall within the bounds $P_r^g + P_r^l - (P_r^g P_r^l)^{1/2} \leq P_r \leq P_r^g + P_r^l + (P_r^g P_r^l)^{1/2}$. These bounds are narrow if either $P_r^g \ll P_r^l$ or $P_r^l \ll P_r^g$—the former case will apply to a weakly coupled subsystem (in the SEA sense[2]) which has direct excitation, while the latter case will apply to any subsystem which is not directly excited. Given that weak coupling is often cited as a necessary condition for the successful application of SEA, it can be concluded that the present approach will yield a close estimate of the total power input under the normal SEA restrictions.

C. Calculation of the local response

The response in the local modes can be calculated by solving the SEA equations, Eq. (49), to yield the subsystem energy levels. The power input which appears in Eq. (49) includes the power arising from the global modes, which can be estimated from Eq. (53) once the global mode responses q_m have been calculated by using the method described in Sec. II. Equation (49) represents the standard form of the SEA equations: within the framework of the present analysis methodology this equation could readily be replaced with recent variants of the method, such as wave intensity analysis[21] or vibrational conductivity techniques.[22] Furthermore, whereas Eq. (49) yields an estimate of the mean subsystem energies, approximate methods are also available whereby the variance of the subsystem energies can be estimated[2]—again, such methods can readily be incorporated into the present analysis scheme.

IV. SUMMARY OF THE ANALYSIS PROCEDURE

The present analysis approach is based on partitioning the response of the system into ''global'' and ''local'' components: the main distinguishing feature between these two components lies in the wavelength of the associated system response. The global component is intended to capture long wavelength deformations, whereas the local component relates to short wavelength deformations. Within this general framework it is possible to envisage a wide range of detailed modeling strategies regarding the precise way in which the partitioning is implemented, and no one fixed scheme is put forward here. The solution method consists of a deterministic model of the global response and a statistical energy analysis model of the local response, with due allowance for the coupling which exists between the two types of response.

The global equations of motion are given by equation (17), which includes a contribution to the dynamic stiffness matrix and the forcing vector arising from the presence of the local response. The contribution to the dynamic stiffness matrix is detailed in Sec. II A, and a simple approximate closed form expression for this term is given by Eqs. (31) and (33). These results are based on a number of assumptions, the most notable being that the local modes have a high degree of modal overlap; in this case the main effect of the local mode dynamics is to add damping and an effective mass to the global modes, in-line with fuzzy structure theory. If the adopted assumptions are invalid, then Eqs. (19)–(21) provide a more accurate model of the effect of the local modes. The additional forcing term which appears in Eq. (17) is detailed in Sec. II B, and in this case a simple closed-form approximate expression for the forcing is given by Eq. (37) or (47). It can be stressed that with the present approach the global mode response can be found *before* the local response is known, so that the analysis method is direct rather than iterative.

The local mode response is computed by using SEA, Eq. (49). This equation includes an input power term which arises from the presence of the global modes, and an expression for this power is given by Eq. (53). This expression involves the global mode response, which must be computed from Eq. (17) prior to considering the local mode response, although again the analysis method is direct rather than iterative. It can be noted that the term ''local'' response does *not* necessarily imply that the short-wavelength responses of the various subsystems are considered to be uncoupled—the SEA equations include the effect of coupling between the various subsystems, and fully allow for the fact that power can be transmitted throughout the whole structure by the action of the local modes alone.

V. EXAMPLE APPLICATION

A. A hybrid rod element

The foregoing analysis is illustrated in what follows by application to a number of simple structures consisting of elastic rods—this choice of system allows an insight into the role of the various terms which appear in the hybrid analysis method, without introducing undue mathematical complexity. Each rod is modeled by using a single hierarchical finite element; with this approach the axial displacement of the generic rod element (having Young's modulus E_Y, density ρ, length L, and cross-sectional area A) which is shown in Fig. 1 is written in the form

$$u(x,t) = q_1(t)(1-x/L) + q_2(t)(x/L)$$

$$+ \sqrt{\frac{2}{\rho A L}} \sum_{n=1}^{\infty} q_{n+2}(t) \sin\left(\frac{n\pi x}{L}\right). \tag{54}$$

Here q_1 and q_2 represent the nodal displacements of the element (i.e., the displacements at the two end points) and q_{n+2} represents the amplitude of the nth ''internal'' or hierarchical shape function. The internal shape functions are
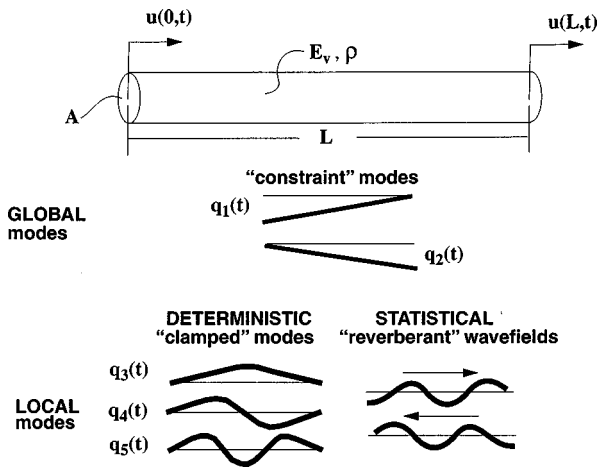
FIG. 1. Schematic of a single rod element showing the nodal displacement and internal hierarchical shape functions for deterministic analysis and the alternative wave field model for statistical analysis.

taken to be the modes of a clamped rod, $\sqrt{2/\rho AL}\,\sin(n\pi x/L)$, where the scaling factor $\sqrt{2/\rho AL}$ is introduced to enforce unit generalized mass. It can readily be shown that the non-zero entries of the upper triangle of the element mass matrix are as follows:

$$M_{11}=M_{22}=\rho AL/3, \tag{55}$$

$$M_{12}=\rho AL/6, \tag{56}$$

$$M_{1,n+2}=\sqrt{2\rho AL}/n\pi, \tag{57}$$

$$M_{2,n+2}=-(-1)^{n}\sqrt{2\rho AL}/n\pi, \tag{58}$$

$$M_{n+2,n+2}=1. \tag{59}$$

Similarly, the nonzero entries of the upper triangle of the element stiffness matrix have the form

$$K_{11}=K_{22}=E_{Y}A/L, \tag{60}$$

$$K_{12}=-E_{Y}A/L, \tag{61}$$

$$K_{n+2,n+2}=\omega_{n}^{2}, \tag{62}$$

where $\omega_{n}=(n\pi/L)\sqrt{E_{Y}/\rho}$ is the nth natural frequency of the clamped rod.

The wave number partitioning scheme which is outlined in Sec. I B requires the generalized coordinates of the rod element to be subdivided into a global set $\mathbf{q}^{g}$ and a local set $\mathbf{q}^{l}$. If the nodal displacements and the first s clamped modes are included in $\mathbf{q}^{g}$, then this set will contain $s+2$ coordinates, while the local set will contain the remaining clamped modes. As described in Sec. II, the equations of motion which govern the global coordinates must be modified to allow for the presence of the local set, and this is done through the inclusion of an additional dynamic stiffness matrix (Sec. II A) and an additional force vector (Sec. II B). Furthermore, the global response injects power into the local response (Sec. III B). These items are considered in the following subsections.

1. The modified "global" dynamic stiffness matrix

It can be shown from Eqs. (19), (20), and (55)–(59) that the additional dynamic stiffness matrix ($\Delta\mathbf{D}$ say) for the

present element is zero apart from the 2×2 subblock which relates to the nodal displacements. These nonzero components have the form

$$(\Delta\mathbf{D})_{11}=(\Delta\mathbf{D})_{22}=-2\omega^{4}\rho AL\sum_{n=s+1}^{\infty}\left(\frac{1}{n\pi}\right)^{2}$$
$$\times[\omega_{n}^{2}(1+i\eta_{n})-\omega^{2}]^{-1}, \tag{63}$$

$$(\Delta\mathbf{D})_{12}=2\omega^{4}\rho AL\sum_{n=s+1}^{\infty}(-1)^{n}\left(\frac{1}{n\pi}\right)^{2}$$
$$\times[\omega_{n}^{2}(1+i\eta_{n})-\omega^{2}]^{-1}. \tag{64}$$

As discussed in Sec. II A, the summations which appear in Eqs. (63) and (64) yield both a resonant and a nonresonant contribution. Taken together, these two contributions give

$$(\Delta\mathbf{D})_{11}=(\Delta\mathbf{D})_{22}=iE_{Y}Ak_{0}+2\omega^{2}\rho AL\sum_{n=s+1}^{\infty}\left(\frac{1}{n\pi}\right)^{2}, \tag{65}$$

$$(\Delta\mathbf{D})_{12}=-2\omega^{2}\rho AL\sum_{n=s+1}^{\infty}(-1)^{n}\left(\frac{1}{n\pi}\right)^{2}, \tag{66}$$

where $k_{0}=\omega\sqrt{\rho/E_{Y}}$ is the wave number associated with the vibration frequency ω: this term arises by putting $n\pi=k_{0}L$ for the resonant contribution to Eq. (63). In addition, it has been noted that the modal density of the rod is given by $\nu=Lk_{0}/\pi\omega$.[13] The resonant contribution which appears in Eq. (65) should only be included if the excitation frequency is encompassed by the resonant frequencies of the local modes: i.e., for $\omega<\omega_{s+1}$ the local modes are not resonant, and the term $iE_{Y}Ak_{0}$ should be excluded.

If $s=0$, so that all of the clamped modes are included in the local coordinate set $\mathbf{q}^{l}$, then the summations which appear in Eqs. (65) and (66) can be evaluated to yield respectively $\frac{1}{6}$ and $-\frac{1}{12}$. In this case the total effective dynamic stiffness matrix for the global coordinates has the form $(\mathbf{D}+\Delta\mathbf{D})_{11}=(\mathbf{D}+\Delta\mathbf{D})_{22}=iE_{Y}Ak_{0}$ and $(\mathbf{D}+\Delta\mathbf{D})_{12}=0$, where the static terms arising from the stiffness matrix $\mathbf{K}$ have been neglected on the grounds that $k_{0}\gg(1/L)$ for high frequencies, so that $E_{Y}Ak_{0}\gg E_{Y}A/L$. The term $iE_{Y}Ak_{0}$ can be recognized as the dynamic stiffness of a semi-infinite rod; it is well known that the dynamic behavior of a damped one-dimensional system approaches that of an infinite or semi-infinite system at high frequencies,[13] and it is reassuring to note that the present approach can reproduce this result under the appropriate conditions—namely high modal overlap, so that the summations which appear in Eqs. (63) and (64) can justifiably be evaluated by using the methods outlined in Sec. II.

2. The modified "global" forcing vector

In the examples which follow, the applied forcing is taken to be a harmonic point load of complex amplitude P applied at a position x_{0} on the rod element. The generalized force produced on the nth internal generalized coordinate (i.e., the generalized coordinate associated with the nth clamped mode) can in this case be written as

$$F_n = P\sqrt{2/\rho AL}\,\sin(n\pi x_0/L). \tag{67}$$

As discussed in Sec. II B, the generalized forces which act on the local coordinate set $\mathbf{q}^l$ produce an addition to the force vector which acts on the global coordinate set $\mathbf{q}^g$. Two methods of computing this additional force are outlined in Secs. II B 1 and II B 3; for the present loading case the generalized forces acting on the local modes are highly correlated, and thus the method described in Sec. II B 3 must be adopted. The "blocked" local response $\mathbf{u}^B(\mathbf{x})$ of the element can readily be calculated by considering the response of a point loaded clamped-clamped rod, and Eq. (47) then yields

$$(\mathbf{D}_{gl}\mathbf{D}_{ll}^{-1}\mathbf{F}^l)_1 = P[\sin k_c(L-x_0)/\sin k_c L]$$
$$- P[1-(x_0/L)], \tag{68}$$

$$(\mathbf{D}_{gl}\mathbf{D}_{ll}^{-1}\mathbf{F}^l)_2 = P(\sin k_c x_0/\sin k_c L) - P(x_0/L), \tag{69}$$

where $k_c = k_0 - i\eta k_0/2$ is the complex wave number of the system. If the modal overlap is high, then Eqs. (68) and (69) simplify to

$$(\mathbf{D}_{gl}\mathbf{D}_{ll}^{-1}\mathbf{F}^l)_1 = P\exp(-ik_c x_0) - P[1-(x_0/L)], \tag{70}$$

$$(\mathbf{D}_{gl}\mathbf{D}_{ll}^{-1}\mathbf{F}^l)_2 = P\exp[-ik_c(L-x_0)] - P(x_0/L). \tag{71}$$

It can be noted that the final term on the right of Eqs. (70) and (71) will exactly cancel the "direct" generalized force acting on the nodal coordinates. Furthermore, the first term on the right of Eqs. (70) and (71) could have been predicted directly by employing a ray tracing argument, in the sense that the term represents the nodal force produced by the elastic wave which is generated at the point load. Finally, it should be noted that $\mathbf{u}^B(\mathbf{x})$ represents the *total* blocked response of the element, in the sense that *all* of the hierarchical generalized coordinates contribute to this result; some of these coordinates might, however, be included in the global set of coordinates rather then the local set, and in this case the contribution of these terms should be subtracted from Eqs. (70) and (71).

3. Power input from the global response

The power input from the global response to the local response is given by Eq. (53). For the present rod element this expression takes the form

$$P^g = E_Y A k_0 \omega(|q_1|^2 + |q_2|^2)/2. \tag{72}$$

This result can be identified as the power dissipated through the effective damping terms which appear in Eqs. (65); Eq. (72) is also equivalent to the power transmitted to a semi-infinite rod by an imposed end motion q, and this is consistent with comments made in Sec. V A 1 regarding the physical interpretation of the dynamic stiffness terms.

B. The response of two coupled rods

A schematic of a structure which consists of two end-coupled rods is shown in Fig. 2. The Young's modulus, mass density, cross-sectional area, and length of rod i are denoted by E_{Yi}, ρ_i, A_i, and L_i, respectively, and the following nondimensional parameters are introduced to describe the system:
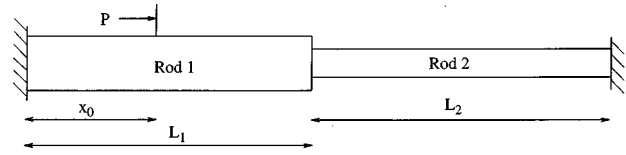
FIG. 2. Schematic of two coupled rods, with axial load P applied to rod 1.

$$\Omega = \omega\nu_1 = (\omega L_1/\pi)\sqrt{\rho_1/E_{Y1}}, \tag{73}$$

$$\nu_R = \nu_2/\nu_1 = (L_2/L_1)\sqrt{E_{Y1}\rho_2/E_{Y2}\rho_1}, \tag{74}$$

$$D_R = E_{Y2}A_2 k_2/E_{Y1}A_1 k_1 = \sqrt{E_{Y2}\rho_2/E_{Y1}\rho_1}, \tag{75}$$

$$L_R = L_2/L_1. \tag{76}$$

The nondimensional frequency Ω gives the approximate mode count for rod 1 (i.e., the number of modes which resonate below ω), while the term D_R is the dynamic stiffness ratio of two semi-infinite rods which have the same physical properties as the finite rods. It can readily be shown that the elastic wave transmission coefficient from rod 1 to rod 2, T_{12}, and the associated power transmission coefficient τ_{12} are given by

$$T_{12} = 2/(1+D_R), \tag{77}$$

$$\tau_{12} = 4D_R/(1+D_R)^2, \tag{78}$$

so that D_R gives a direct indication of the strength of coupling between the rods—a value of D_R close to unity represents strong coupling. The modal overlap factors for the two rods can be written in terms of the nondimensional parameters in the form $m_1 = \omega\eta_1\nu_1 = \eta_1\Omega$ and $m_2 = \eta_2\Omega\nu_R$, where η_1 and η_2 are the system loss factors.

Rod 1 is considered to be subjected to a point load of complex amplitude P acting at location x_0, and the response of the system is expressed in terms of the following nondimensional vibrational energies:

$$\hat{E}_1 = E_1/E_{1R}, \tag{79}$$

$$\hat{E}_2 = E_2/E_{1R}, \tag{80}$$

$$E_{1R} = |P|^2 L_1/(E_1 A_1). \tag{81}$$

Here E_1 and E_2 are the vibrational energies (defined as twice the kinetic energy) of the two rods, and E_{1R} is a reference energy. The response of the system is calculated by three methods: (i) the hybrid method described in Secs. I–IV, (ii) conventional statistical energy analysis, and (iii) the dynamic stiffness method.[23] The last method is an exact approach which provides a benchmark against which the performance of the other two methods can be assessed. The three example systems summarized in Table I are considered in the following subsections; in all cases the loss factors are taken to be

TABLE I. Nondimensional parameters employed in the three example systems.

Example	ν_R	D_R	τ_{12}	L_R
1	12.3	0.1	0.331	1.23
2	0.117	10.0	0.331	1.17
3	1.72	0.447	0.854	0.77
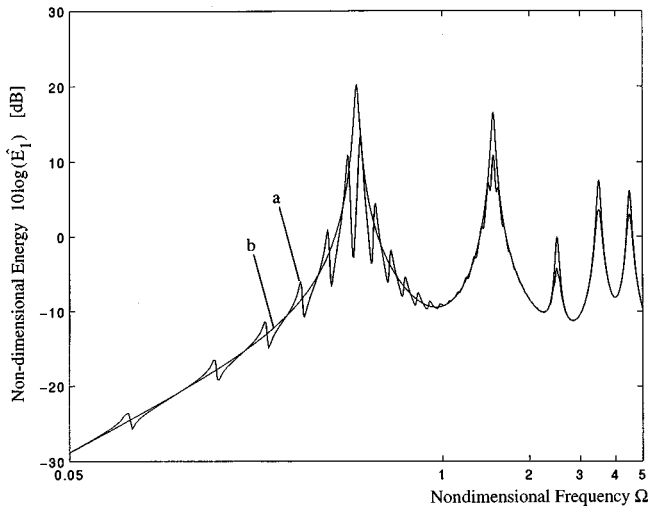
FIG. 3. Nondimensional energy in rod 1 for the first example system: (a) exact result for the coupled system and (b) exact result for the uncoupled system.

$\eta_1 = \eta_2 = 0.03$, rod 1 is driven at the point $x_0/L_1 = 0.37$, and the outer ends of the rods are taken to be clamped.

1. Example 1: $\nu_R = 12.3$

In this case rod 2 has a relatively high modal density and acts as a "fuzzy attachment" to rod 1. This phenomenon is illustrated in Fig. 3, where exact dynamic stiffness results for the energy in rod 1 are shown for both the coupled (rod 2 present) and uncoupled (rod 2 absent) case. It is clear that rod 2 provides additional damping to the modes of rod 1—the rapid undulations in the coupled result at low frequencies are caused by the individual modes of rod 2: as the frequency increases, the modal overlap of rod 2 exceeds unity and the effect of individual modes is no longer visible.

The hybrid modeling technique has been applied to the present system by taking the global degrees of freedom to include the first 10 hierarchical terms for rod 1 and the first 12 hierarchical terms for rod 2. This approach captures the clamped modes of rod 1 which lie below $\Omega = 10$ and the clamped modes of rod 2 which lie below $\Omega = 1$. For frequencies $\Omega > 1$, the "global" degrees of freedom of rod 2 must be augmented with a "local" set, and this introduces a modification to the global equations of motion, as detailed in Sec. V A 1. Once the global equations of motion have been solved, the power input to the local response is calculated according to Sec. V A 3, and the corresponding vibrational energy is then found by employing a single subsystem SEA model. The results obtained by using this approach are compared in Figs. 4 and 5 with exact dynamic stiffness results and also with the results of a conventional SEA calculation. The results for rod 1 are shown in Fig. 4: as would be expected, the current method yields results which are nearly identical to the exact results for frequencies up to $\Omega = 1$. Beyond this frequency the present approach does not capture the effect of the individual modes of rod 2, but rather yields a smooth result which is a very good approximation to the exact response. The SEA result does not capture the individual resonant peaks associated with rod 1, and hence the
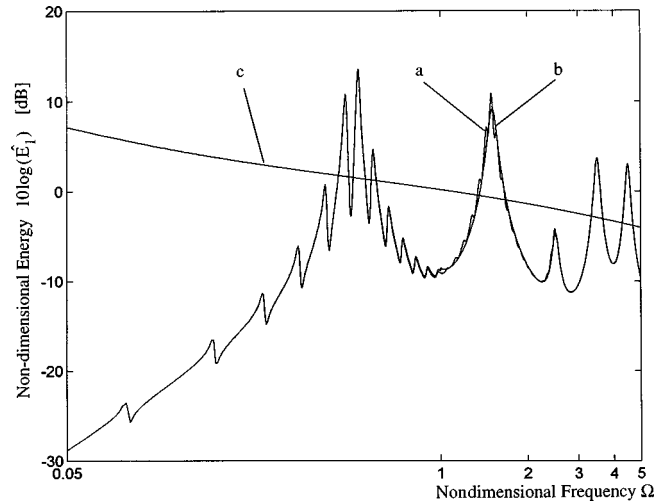
method yields only an approximation to the mean level of the response. Very similar trends are shown in Fig. 5 for the case of rod 2.

The use of 10 and 12 hierarchical shape functions for rods 1 and 2, respectively, was chosen to yield an accurate response prediction for frequencies below $\Omega = 1$. The response above this frequency is affected little by reducing the number of terms included in the global set of degrees of freedom—for example, it has been found that near exact results can be obtained over the range $1 < \Omega < 5$ by employing six hierarchical terms for rod 1 and no hierarchical terms for rod 2. Allowing for the fact that the outer end of each rod is clamped, this leads to seven global degrees of freedom; in contrast, a conventional hierarchical model of the system

FIG. 4. Nondimensional energy in rod 1 for the first example system: (a) exact result given by the dynamic stiffness method, (b) the present hybrid method, and (c) conventional SEA. Note that curves (a) and (b) are indistinguishable at lower frequencies.
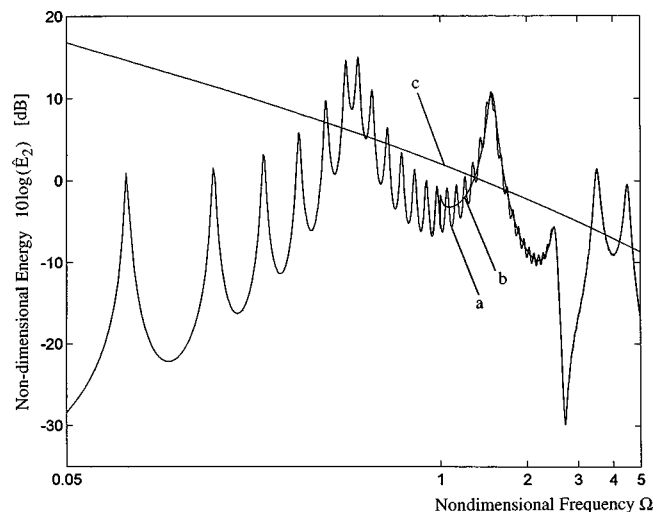
FIG. 5. Nondimensional energy in rod 2 for the first example system: (a) exact result given by the dynamic stiffness method, (b) the present hybrid method, and (c) conventional SEA. Note that curves (a) and (b) are indistinguishable at lower frequencies.
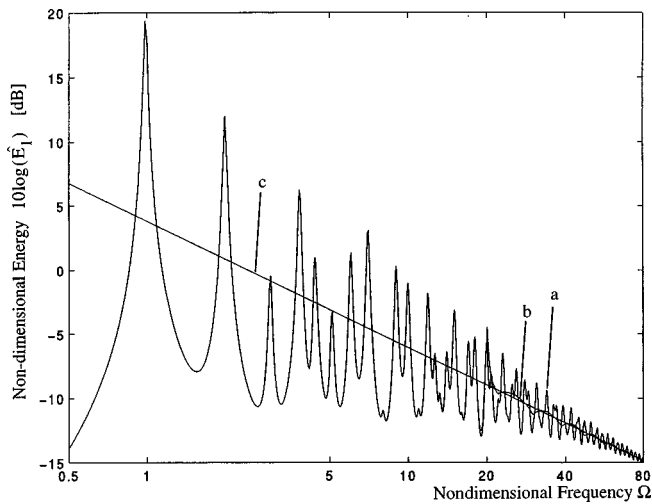
FIG. 6. Nondimensional energy in rod 1 for the second example system: (a) exact result given by the dynamic stiffness method, (b) the present hybrid method, and (c) conventional SEA. Note that curves (a) and (b) are indistinguishable at lower frequencies.

FIG. 7. Nondimensional energy in rod 2 for the second example system: (a) exact result given by the dynamic stiffness method, (b) the present hybrid method, and (c) conventional SEA. Note that curves (a) and (b) are indistinguishable at lower frequencies.

over this frequency range would require around 70 degrees of freedom to capture all of the relevant modes of each rod.

2. Example 2: $\nu_R = 0.117$

In this example the excitation is applied to a rod of high modal density which is coupled to a rod of much lower modal density. The number of hierarchical terms employed in the hybrid method is 20 for rod 1 and 10 for rod 2, which covers the clamped modes below $\Omega = 20$ for rod 1 and below $\Omega = 85$ for rod 2. The frequency range considered is $0 < \Omega < 80$, so that the response of rod 1 must be augmented with a "local" response for $20 < \Omega < 80$; the local response modifies the global dynamic stiffness matrix as described in Sec. V A 1, and contributes to the global force vector in accordance with Sec. V A 2. The local response is driven by the global response (Sec. V A 3), and a single subsystem SEA model is employed to compute the resulting vibrational energy.

The vibrational energy in rod 1 is shown in Fig. 6: the present method yields a near exact prediction of the energy for $\Omega < 20$ and an accurate smoothed approximation for $20 < \Omega < 80$. The standard SEA prediction is also in good agreement with the exact results for this rod. This is to be expected, since rod 1 is weakly coupled to rod 2, and behaves very much like a driven uncoupled subsystem which has high modal overlap, thus meeting the conditions for the successful application of SEA. The vibrational energy of rod 2 is shown in Fig. 7, where it can be seen that the present method again yields a good prediction over the whole frequency range. For $\Omega > 20$ the method captures the individual modes of rod 2 but smoothes the effect of the modes of rod 1 (which are accounted for via the "local" response of rod 1). The standard SEA result shown in Fig. 7 is clearly biased; this is due to the fact that the *coupled* system does not meet the requirements of the method—rod 2 has a low modal overlap, and the forcing consists of a single point load rather than rain-on-the-roof excitation (which has a strong effect on the response of the driven subsystem at the coupling point).
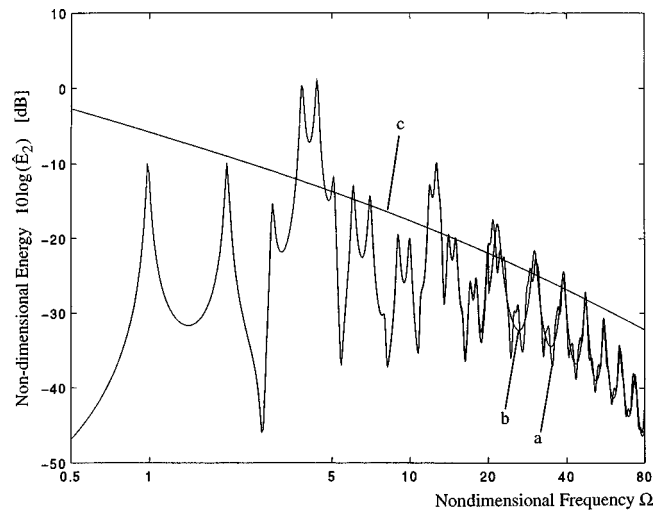
The results shown in Figs. 6 and 7 for $\Omega > 20$ are not affected by a reduction in the number of hierarchical terms included in the set of global degrees of freedom for rod 1. If *no* hierarchical terms are included for rod 1, then the global degrees of freedom consist of the displacement of node 2 and the ten hierarchical terms for rod 2, giving an 11-degrees-of-freedom system. In contrast, a conventional hierarchical finite element model of the system would require around 95 degrees of freedom to fully capture the modes of vibration which lie below $\Omega = 80$.

3. Example 3: $\nu_R = 1.723$

This example concerns two rods which have similar modal densities: 7 and 12 hierarchical terms are employed, respectively, for rods 1 and 2, and this captures the modes of vibration which lie below $\Omega = 8$. For $\Omega > 8$ the global degrees of freedom of each rod are augmented with a local set which constitutes an SEA subsystem. As explained in Sec. III A, the two SEA subsystems are not directly coupled for the present case, since the hierarchical functions which are employed correspond to the *blocked* modes of each rod. This implies that the coupling loss factors which appear in Eq. (44) are set to zero.

Computed results for the energy of the system are shown in Figs. 8 and 9. It is clear that the present method gives a very accurate response prediction for $\Omega < 8$ and a good smoothed approximation for $\Omega > 8$. The SEA result which is shown in Fig. 9 clearly contains a bias which is not evidenced in the present approach. The cause of this bias can be traced to the occurrence of low modal overlap and the consideration of point loading, rather than rain-on-the-roof forcing. For $\Omega > 8$ the results yielded by the present method are not affected by the number of hierarchical terms employed in the global analysis, so that the same results are yielded by a single degree-of-freedom model (consisting of the displacement of the middle node) which contains *no* hierarchical terms. In contrast, a conventional hierarchical finite element
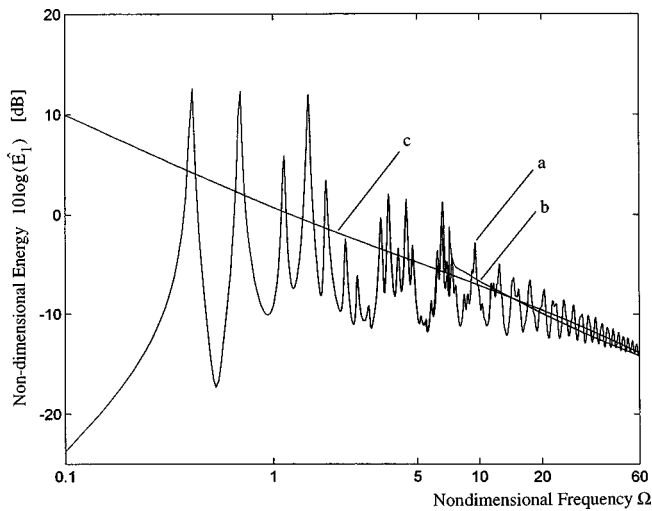
FIG. 8. Nondimensional energy in rod 1 for the third example system: (a) exact result given by the dynamic stiffness method, (b) the present hybrid method, and (c) conventional SEA. Note that curves (a) and (b) are indistinguishable at lower frequencies.

model of the system would require around 105 degrees of freedom to fully capture the modes which lie below $\Omega=60$.

VI. CONCLUSIONS

A hybrid method has been presented for the dynamic analysis of complex systems. As detailed in Sec. I, the method is based on partitioning the degrees of freedom into a "global" set and a "local" set: the treatment of these two sets has been discussed in Secs. II and III, respectively, and a summary of the approach has been given in Sec. III. The method has been found to yield good results for a relatively simple system comprising two coupled rods, and the application of the method to more complex systems is now required.

In some ways the present method represents a unification of a number of disparate existing analysis methods: the finite element method, statistical energy analysis, fuzzy
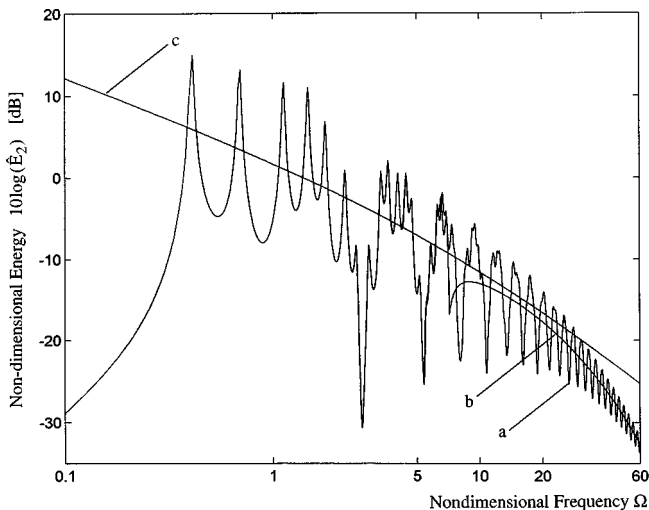
FIG. 9. Nondimensional energy in rod 2 for the third example system. (a) exact result given by the dynamic stiffness method, (b) the present hybrid method, and (c) conventional SEA. Note that curves (a) and (b) are indistinguishable at lower frequencies.

structure theory, and the Belyaev "smooth function" approach. The partitioning scheme which forms the basis of the method has been presented in a general, nonprescriptive way, and in this sense the method forms a flexible framework within which many detailed modeling strategies may be devised.

ACKNOWLEDGMENTS

[1] O. C. Zienkiewicz and R. L. Taylor, *The Finite Element Method: Basic Concepts and Linear Applications*, 3rd ed. (McGraw Hill, London, 1989).

[2] R. H. Lyon and R. G. DeJong, *Theory and Application of Statistical Energy Analysis*, 2nd ed. (Butterworth-Heinemann, Boston, 1995).

[3] F. J. Fahy, "Statistical energy: a critical overview," Philos. Trans. R. Soc. London, Ser. A **346**, 431–447 (1994).

[4] W. B. Rockwood, L. K. H. Lu, P. Warner, and R. G. DeJong, "Statistical energy analysis applied to structure-borne noise in marine structures," in *Statistical Energy Analysis, Proceedings of the Winter Annual Meeting of the American Society of Mechanical Engineers*, December 1987, edited by K. H. Hsu, D. J. Nefske, and A. Akay (NCA-Vol. 3), pp. 73–79 (1987).

[5] C. Soize, "A model and numerical method in the medium frequency range for vibroacoustic predictions using the theory of structural fuzzy," J. Acoust. Soc. Am. **94**, 849–865 (1993).

[6] A. D. Pierce, V. W. Sparrow, and D. A. Russell, "Fundamental structural-acoustic idealizations for structures with fuzzy internals," J. Vibration Acoust. **117**, 339–348 (1995).

[7] M. Strasberg and D. Feit, "Vibration damping of large structures induced by attached small resonant structures," J. Acoust. Soc. Am. **99**, 335–344 (1996).

[8] A. K. Belyaev and V. A. Palmov, "Integral theories of random vibration of complex structures," in *Random Vibration-Status and Recent Developments*, edited by I. Elishakoff and R. H. Lyon (Elsevier, Amsterdam, 1986).

[9] A. K. Belyaev, "Dynamic simulation of high-frequency vibration of extended complex structures," Mechanics of Structures and Machines **20**, 155–168 (1992).

[10] A. K. Belyaev, "High frequency vibration of extended complex structures," Probabilistic Engineering Mechanics **8**, 15–24 (1993).

[11] L. Meirovitch, *Elements of Vibration Analysis*, 2nd ed. (McGraw-Hill, New York, 1986).

[12] Y. K. Lin, *Probabilistic Theory of Structural Dynamics* (McGraw-Hill, New York, 1967).

[13] L. Cremer, M. Heckl, and E. E. Ungar, *Structure-borne Sound* (Springer-Verlag, Berlin, 1987), 2nd ed.

[14] R. R. Craig, *Structural Dynamics: An Introduction to Computer Methods* (Wiley, New York, 1981).

[15] V. V. Bolotin, *Random Vibrations of Elastic Systems* (Martinus Nijhoff, The Hague, 1984), Chap. 4.

[16] E. J. Richards and D. J. Mead (editors), *Noise and Acoustic Fatigue in Aeronautics* (Wiley, London, 1968), Chap. 14.

[17] R. S. Langley, "Spatially averaged frequency response envelopes for one- and two-dimensional structural components," J. Sound Vib. **178**, 483–500 (1994).

[18] R. H. Lyon, "Statistical analysis of power injection and response in structures and rooms," J. Acoust. Soc. Am. **45**, 545–565 (1967).

[19] A. Der Kiureghian and J-B. Ke, "The stochastic finite element method in structural reliability," Probabilistic Engineering Mechanics **3**, 83–91 (1988).

[20] R. L. Weaver, "Mean and mean-squared responses of a prototypical master/fuzzy structure," J. Acoust. Soc. Am. **101**, 1441–1449 (1997).

[21] R. S. Langley, ''A wave intensity technique for the analysis of high frequency vibrations,'' J. Sound Vib. **159**, 483–502 (1992).

[22] D. J. Nefske and S. H. Sung, ''Power flow finite element analysis of dynamic systems: basic theory and application to beams,'' Journal of Vibration, Stress and Reliability in Design **111**, 94–100 (1989).

[23] R. S. Langley, ''Analysis of power flow in beams and frameworks using the direct-dynamic stiffness method,'' J. Sound Vib. **136**, 439–452 (1990).

Vibration of unsymmetrically laminated thick quadrilateral plates

K. M. Liew
Centre for Advanced Numerical Engineering Simulations (CANES), School of Mechanical and Production Engineering, Nanyang Technological University, Singapore 639798

W. Karunasena
Department of Civil and Environmental Engineering, James Cook University of North Queensland, Townsville, Queensland 4811, Australia

S. Kitipornchai and C. C. Chen
Department of Civil Engineering, The University of Queensland, Queensland 4072, Australia

The problem of free vibration of arbitrary quadrilateral unsymmetrically laminated plates subject to arbitrary boundary conditions is considered. The Ritz procedures supplemented by the simple polynomial shape functions are employed to derive the governing eigenvalue equation. The displacements are approximated by a set of polynomials which consist of a basic boundary function that impose the various boundary constraints. A first-order shear deformable plate theory is employed to account for the effects of the transverse shear deformation. The numerical accuracy of the solution is verified by studying the convergence characteristics of the vibration frequencies and also by comparison with existing results. The new results of this study include the sensitivity of the vibration responses to variations in the lamination, boundary constraints and thickness effects, and also their interactions. These numerical values are presented for a typical graphite/epoxy material, in tabular and graphical forms. © *1999 Acoustical Society of America.* [S0001-4966(99)04403-3]

INTRODUCTION

In recent years, we have witnessed an increasing use of laminated composite materials for manufacturing plate components due to its high strength-to-weight ratio and better corrosion resistance as well as the advantages of composite tailoring. Because of the increasing use of fibrous composite materials in flight vehicle structures, an improved understanding of the vibration behavior of composite panels is required.

It is known that the matrix material used in fiber-reinforced composites is of relatively low shearing stiffness when compared to the fibers. In order to achieve a more reliable prediction of the vibration responses for the composite laminates, the effect of transverse shear deformation has to be incorporated in the mathematical modeling. The importance of transverse shear deformation for the analysis of composite laminates was well documented.[1–4] Modeling of this effect via refined plate theories is normally adopted to account for the transverse shear strain distribution through the thickness dimension. Among the researchers, Yang, Norris, and Stavsky (YNS)[5] were the earliest to consider the effects of shear deformation in vibration analysis of composite laminated plates. For vibration analysis, the first-order YNS shear deformation theory is normally sufficient. Although the theory assumes a constant shear stress distribution through the thickness, it gives reasonably accurate vibration frequencies when used in conjunction with a shear correction factor on the shear modulus.

Considerable work has been devoted to the study of free vibration of plates.[6–9] For predicting the vibration responses, the possibility of variation in stacking sequences for laminated panels is an important factor to be considered in the mathematical modeling. This has led to the development of lamination plate theories to incorporate the different fiber orientations and possible stacking sequences. The other important factor to be considered is the variation of boundary conditions which is normally accommodated either by an approximate method or a numerical technique. Researchers[10–13] have attempted to investigate various aspects of the vibration behavior of composite laminates by varying the boundary conditions, thickness, and stacking sequences. These analyses have been carried out using different approximate techniques and shear deformation theories.

This paper describes an analysis method for vibration of unsymmetrically laminated composite plates with the inclusion of transverse shear deformation using the YNS shear deformation theory. The solution employs the Ritz method,[14] in which a set of polynomials is used as the admissible displacement and rotation functions, for determining the vibration frequencies. The analysis method is capable of handling unsymmetric composite laminates of different boundary conditions, an arbitrary quadrilateral geometry, and anisotropic material properties. Thus we believe an analytical tool, with such capabilities as what we propose, is of great value for preliminary design of composite structures. A set of results for the vibration frequency parameters of unsymmetrically laminated plates of quadrilateral shape subject to different boundary conditions and laminations is presented.
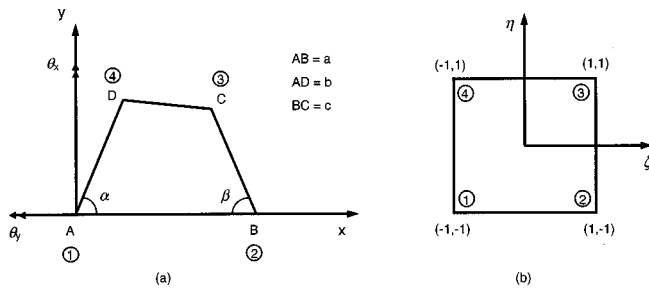
FIG. 1. Geometry and coordinate systems: (a) actual quadrilateral plate and (b) basic square plate.

I. MATHEMATICAL FORMULATIONS

A. Preliminary definition

Consider an arbitrary flat quadrilateral plate of uniform thickness h, composed of any number of anisotropic plies oriented alternately at angles θ and $-\theta$. The Cartesian coordinate system $x-y$ is located at the middle plane of the plate and the geometry of the plate is defined by side lengths a, b, c and two angles α and β, as shown in Fig. 1(a). The material of each ply is assumed to possess a plane of elastic symmetry parallel to the $x-y$ plane.

In this study, the plate under consideration is subjected to different combinations of free, simply supported, and clamped boundary conditions. The plate, as shown in Fig. 1, is described by a symbolism defining the boundary conditions at their four edges, for instance, SCSF means a plate whose edges at AB, BC, CD, and AD are simply supported, clamped, simply supported, and free, respectively. The problem is to determine the natural frequencies of the plate.

B. Energy functional

Employing the first-order shear deformation plate theory,[5] the displacement field for free vibration can be written as

$$\bar{u}=u(x,y,t)+z\grave{e}_x(x,y,t), \tag{1a}$$

$$\bar{v}=v(x,y,t)+z\grave{e}_y(x,y,t), \tag{1b}$$

$$\bar{w}=w(x,y,t), \tag{1c}$$

where $\bar{u}$, $\bar{v}$, and $\bar{w}$ are the displacement components in the x, y, and z directions, respectively, u and v are the in-plane displacements of the mid-plane, and θ_x and θ_y are the rotations about the y and x axes, respectively. The strain–displacement and stress–strain relations for any ply in the (x,y) system are given by

$$\epsilon=\mathbf{L}\mathbf{U}, \quad \sigma=\mathbf{Q}\epsilon, \tag{2}$$

where

$$\mathbf{U}^T=\langle \mu \quad v \quad w \quad \theta_x \quad \theta_y \rangle, \tag{3}$$

$$\epsilon^T=\langle \epsilon_{xx} \quad \epsilon_{yy} \quad \gamma_{yz} \quad \gamma_{xz} \quad \gamma_{xy} \rangle, \tag{4}$$

$$\sigma^T=\langle \sigma_{xx} \quad \sigma_{yy} \quad \sigma_{yz} \quad \sigma_{xz} \quad \sigma_{xy} \rangle, \tag{5}$$

$$\mathbf{L}=\begin{bmatrix} \partial_x & 0 & 0 & z\partial_x & 0 \\ 0 & \partial_y & 0 & 0 & z\partial_y \\ 0 & 0 & \partial_y & 0 & 1 \\ 0 & 0 & \partial_x & 1 & 0 \\ \partial_y & \partial_x & 0 & z\partial_y & z\partial_x \end{bmatrix}, \tag{6}$$

$$\mathbf{Q}=\begin{bmatrix} Q_{11} & Q_{12} & 0 & 0 & Q_{16} \\ Q_{12} & Q_{22} & 0 & 0 & Q_{26} \\ 0 & 0 & Q_{44} & Q_{45} & 0 \\ 0 & 0 & Q_{45} & Q_{55} & 0 \\ Q_{16} & Q_{26} & 0 & 0 & Q_{66} \end{bmatrix}, \tag{7}$$

in which σ_{ij} and ϵ_{ij} are the stress and strain components, respectively, and $\tilde{a}_{ij}=2\mathring{a}_{ij}$; Q_{ij} are the elements of the plane-stress reduced constitutive matrix of the ply material which are obtained from the transform matrix considering fiber orientation and the material properties (Young's moduli, Poisson's ratios, and shear moduli), E_1, E_2, v_{12}, v_{21}, G_{12}, G_{13}, G_{23} of each ply; and ∂_x and ∂_y indicate the partial differentiation with respect to x and y, respectively. The energy functional π of the entire plate can be written in terms of the maximum strain energy $U_{\max}$ and maximum kinetic energy $T_{\max}$ as

$$\pi=U_{\max}-T_{\max}, \tag{8}$$

where

$$U_{\max}=\frac{1}{2}\int_V \epsilon^T Q\epsilon \, dV, \tag{9}$$

$$T_{\max}=\frac{1}{2}\Omega^2 \int_V \rho U_1^T U_1 \, dV, \tag{10}$$

$$U_1^T=\langle \bar{u} \quad \bar{v} \quad \bar{w} \rangle, \tag{11}$$

in which ρ denotes density of the ply material per unit volume, V represents the total volume of the plate, and Ω and U_1 are angular frequency and displacement amplitude for a vibrating plate with harmonic motion, respectively.

C. Geometric mapping

For the convenience in numerical integration and application of boundary conditions, the actual quadrilateral plate in the $x-y$ plane is mapped into a 2×2 basic square plate in the $\zeta-\eta$ plane [as shown in Fig. 1(b)] using the coordinate transformation defined by

$$x=\sum_{i=1}^4 N_i x_i, \quad y=\sum_{i=1}^4 N_i y_i, \tag{12}$$

where x_i and y_i are the coordinates of the ith corner of the quadrilateral plate in the $x-y$ plane. The mapping functions N_i are defined by

$$N_i=\tfrac{1}{4}(1+\zeta\zeta_i)(1+\eta\eta_i), \quad i=1,2,3,4, \tag{13}$$

where ζ_i and η_i are the coordinates of the ith corner of the basic square plate in the $\zeta-\eta$ plane.

TABLE I. Values of θ_j in Eq. (21) for different edge boundary conditions.

Supporting condition for jth edge	θ_j				
	ϕ_{x1}	ϕ_{y1}	ϕ_{z1}	φ_{x1}	φ_{y1}
Clamped (C)	1	1	1	1	1
Free (F)	0	0	0	0	0
Simply supported (S^*)	0	0	1	0	0
Simply supported (S) with edge ∥ to x axis	0	1	1	1	0
Simply supported (S) with edge ∥ to y axis	1	0	1	0	1

Using the chain rule of differentiation, the first derivatives of any quantity ( ) in the two coordinate systems are related by

$$\begin{Bmatrix} \partial_x( ) \\ \partial_y( ) \end{Bmatrix} = \mathbf{J}^{-1} \begin{Bmatrix} \partial_\zeta( ) \\ \partial_\eta( ) \end{Bmatrix}, \tag{14}$$

where

$$\mathbf{J} = \begin{bmatrix} \partial_\zeta x & \partial_\zeta y \\ \partial_\eta x & \partial_\eta y \end{bmatrix} \tag{15}$$

in which $\mathbf{J}$ denotes the Jacobian matrix of the geometric mapping. Equations (14) and (15) will be used later to transform the $x-y$ domain integrals in Eqs. (9) and (10) into the $\zeta-\eta$ domain integrals.

D. The polynomial shape functions

For the laminated plate, the displacement and rotation components may be expressed by a set of polynomial shape functions in the $\zeta-\eta$ plane as

$$u(\zeta, \eta) = \sum_{q=0}^{p_1} \sum_{r=0}^{q} a_i \phi_{xi}(\zeta, \eta) = \sum_{i=1}^{m_1} a_i \phi_{xi}(\zeta, \eta) = \mathbf{a}^T \Phi_x, \tag{16a}$$

$$v(\zeta, \eta) = \sum_{q=0}^{p_2} \sum_{r=0}^{q} b_i \phi_{yi}(\zeta, \eta) = \sum_{i=1}^{m_2} b_i \phi_{yi}(\zeta, \eta) = \mathbf{b}^T \Phi_y, \tag{16b}$$

$$w(\zeta, \eta) = \sum_{q=0}^{p_3} \sum_{r=0}^{q} c_i \phi_{zi}(\zeta, \eta) = \sum_{i=1}^{m_3} c_i \phi_{zi}(\zeta, \eta) = \mathbf{c}^T \Phi_z, \tag{16c}$$

$$\theta_x(\zeta, \eta) = \sum_{q=0}^{p_4} \sum_{r=0}^{q} d_i \psi_{xi}(\zeta, \eta) = \sum_{i=1}^{m_4} d_i \psi_{xi}(\zeta, \eta)$$
$$= \mathbf{d}^T \Psi_x, \tag{16d}$$

$$\theta_y(\zeta, \eta) = \sum_{q=0}^{p_5} \sum_{r=0}^{q} e_i \psi_{yi}(\zeta, \eta) = \sum_{i=1}^{m_5} e_i \psi_{yi}(\zeta, \eta) = \mathbf{e}^T \Psi_y, \tag{16e}$$

where p_s ($s = 1,2,3,4,5$) is the degree of the mathematically complete two-dimensional polynomial space; a_i, b_i, c_i, d_i, and e_i are the unknown coefficients to be varied with the subscript i given by

$$i = \frac{(q+1)(q+2)}{2} - (q-r); \tag{17}$$

$\mathbf{a}$, $\mathbf{b}$, $\mathbf{c}$, $\mathbf{d}$, and $\mathbf{e}$ are the unknown coefficient vectors having a_i, b_i, c_i, d_i, and e_i as respective elements; m_s ($s = 1,2,3,4,5$) are, respectively, the dimensions of $\mathbf{a}$, $\mathbf{b}$, $\mathbf{c}$, $\mathbf{d}$, and $\mathbf{e}$ given by

$$m_s = \tfrac{1}{2}(p_s + 1)(p_s + 2), \tag{18}$$

and Φ_x, Φ_y, Φ_z, Ψ_x, and Ψ_y are the shape function vectors whose elements are given by

$$\phi_{xi} = f_i \phi_{x1}, \tag{19a}$$

$$\phi_{yi} = f_i \phi_{y1}, \tag{19b}$$

$$\phi_{zi} = f_i \phi_{z1}, \tag{19c}$$

$$\psi_{xi} = f_i \psi_{x1}, \tag{19d}$$

$$\psi_{yi} = f_i \psi_{y1}, \tag{19e}$$

where

$$f_i = \zeta^{q-r} \eta^r, \tag{20}$$

and ϕ_{x1}, ϕ_{y1}, ϕ_{z1}, ψ_{x1}, and ψ_{y1} are the basic functions corresponding to u, v, w, θ_x, and θ_y, respectively. The basic functions consist of the products of boundary expressions of the laminated plate to ensure the automatic satisfaction of geometric boundary conditions.

Four types of boundary conditions can be considered when analyzing plates using a first-order shear deformation plate theory. These are free edge (F), clamped edge (C), the first kind of simply supported edge (S), and the second kind of simply supported edge (S*). The S condition requires the transverse and lateral displacement and the tangential rotation to be zero while the S* condition requires only the transverse displacement along the support to be zero. A detailed definition of the four types of boundary conditions for isotropic plates is available elsewhere.[14]

The basic functions for the displacements and bending slopes can be expressed by a single expression

$$\prod_{j=1}^{4} [\Gamma_j(\zeta, \eta)]^{\theta_j}, \tag{21}$$

where Γ_j is the boundary expression of the jth supporting edge in the $\zeta-\eta$ plane and Θ_j, depending on the support edge conditions, is determined from Table I.

TABLE II. Comparison of frequency parameter $\lambda = \omega a^2 \sqrt{\rho/(Eh^2)}$ of a square simply supported isotropic plate ($\nu = 0.3$, $h/a = 0.1$).

Sources	Mode sequence No.				
	1	2	3	4	5
$p_s = 4$	5.770	13.804	27.561	33.205	46.581
$p_s = 6$	5.769	13.764	26.040	32.689	43.567
$p_s = 8$	5.769	13.764	25.738	32.295	43.169
$p_s = 9$	5.769	13.764	25.734	32.294	42.421
$p_s = 10$	5.769	13.764	25.734	32.284	42.420
3D elasticity solution (Ref. 10)	5.780	13.805	25.867	32.491	42.724
Reddy's FEM solution (Ref. 11)	5.793	14.081	27.545	35.050	49.693
CPT solution (Ref. 15)	5.973	14.934	29.867	38.829	53.868

E. Eigenvalue problem

Transforming the integration domain of the integrals in Eqs. (9) and (10) to the $\zeta - \eta$ plane and substituting Eq. (16) in the resulting expressions, the energy function π in Eq. (8) can be written as

$$\pi = \tfrac{1}{2}\mathbf{q}^T(\mathbf{K} - \Omega^2\mathbf{M})\mathbf{q} \tag{22}$$

in which

$$\mathbf{q}^T = \langle \mathbf{a}^T \quad \mathbf{b}^T \quad \mathbf{c}^T \quad \mathbf{d}^T \quad \mathbf{e}^T \rangle \tag{23}$$

$$\mathbf{K} = \int_{\bar{A}} \begin{bmatrix} K_{aa} & K_{ab} & K_{ac} & K_{ad} & K_{ae} \\ & K_{bb} & K_{bc} & K_{bd} & K_{be} \\ & & K_{cc} & K_{cd} & K_{ce} \\ \text{symmetric} & & & K_{dd} & K_{de} \\ & & & & K_{ee} \end{bmatrix} |\mathbf{J}| d\bar{A}, \tag{24}$$

$$\mathbf{M} = \int_{\bar{A}} \begin{bmatrix} M_{aa} & M_{ab} & M_{ac} & M_{ad} & M_{ae} \\ & M_{bb} & M_{bc} & M_{bd} & M_{be} \\ & & M_{cc} & M_{cd} & M_{ce} \\ \text{symmetric} & & & M_{dd} & M_{de} \\ & & & & M_{ee} \end{bmatrix} |\mathbf{J}| d\bar{A}. \tag{25}$$

Here $\mathbf{K}$ and $\mathbf{M}$ represent the stiffness and mass matrices of the plate, respectively, and $\bar{A}$ denotes the area of the basic square plate. Details of the submatrices of $\mathbf{K}$ and $\mathbf{M}$ are given in the Appendix.

Setting the first variation of the energy functional in Eq. (22) to zero gives the governing eigenvalue problem

$$(\mathbf{K} - \Omega^2\mathbf{M})\mathbf{q} = 0. \tag{26}$$

In the numerical analysis, the Gauss quadrature method is employed to evaluate the integrals appearing in Eqs. (24) and (25) after making use of Eq. (14) to calculate the derivatives with respect to x and y. Standard eigenvalue solvers may be used to compute the natural frequencies of laminated quadrilateral plates by solving the general eigenvalue problem defined in Eq. (26).

II. NUMERICAL RESULTS AND DISCUSSIONS

The laminated plates under consideration are composed of any number of plies that have the same geometric and material properties, and lie in an unsymmetric stacking sequence. For example, a four-ply laminate is arranged in a manner of $(\theta/-\theta/\theta/-\theta)$. A high-modulus graphite/epoxy is used to study the vibration behavior of the unsymmetrically laminated composite plates. Each ply is a unidirectional fiber reinforced composite possessing the dimensionless material properties of: $E_1/E_2 = 40$; $G_{12}/E_2 = G_{13}/E_2 = 0.6$; $G_{23}/E_2 = 0.5$; and $v_{12} = 0.25$ (for all examples considered here, otherwise the material properties will be specified).

A. Convergence and comparison studies

As a check on the numerical accuracy of the analysis method, natural frequency parameters were first obtained for a moderately thick isotropic plate with relative thickness ratio $h/a = 0.10$. The present results are compared with the values from 3-D linear elasticity analysis[10] and the Reddy's FEM solution[11] in Table II. The present solutions have been computed using values of p_s increasing from 4 to 10 which is equivalent to a variation in matrix size from 75×75 to 330×330. Clearly the eigenvalues of lower modes converge relatively faster than the higher modes, and $p_s = 10$ is needed to give convergent eigenvalues. In general, the present results are in close agreement with those values given by Srinivas et al.[10] and Reddy[11] for isotropic plates.

A further verification on the numerical accuracy of the present method is shown in Table III. The fundamental frequency parameters for a simply supported three-ply orthotropic square laminated plate are given together with the values of 3-D linear elasticity analysis.[10] A convergence study was again carried out by varying the number of degree of polynomials p_s for the laminated plate with various degree of orthotropy E_1/E_2. It is obvious that a degree p_s of less than 4 (the determinant size is 75×75) is more than enough to furnish the convergent results since only the fundamental frequency parameters are of interest in this comparison. The results obtained from the present analysis are seen to be in close agreement with the 3-D elasticity solutions.[10]

Table IV presents nondimensional frequency parameters for a four-ply unsymmetrically laminated square plate with stacking sequence (45 deg/−45 deg/45 deg/−45 deg) of relative thickness ratio $h/a = 0.10$. A degree $p_s = 10$ (the determinant size is 330×330) is used for this computation. The results of the first ten frequency parameters for six different combinations of boundary conditions (SSSS, SSCS, CSCS, FSFS, FSSS, FSCS) of laminated plates from various

TABLE III. Comparison of nondimensional fundamental frequency $\omega h\sqrt{\rho_2/(E_x)_2}$ of a simply supported three-ply orthotropic square plate ($h_1:h_2:h_3=0.1:0.8:1$, $h/a=0.1$).

Sources	$(E_x)_1/(E_x)_2$				
	1	2	3	4	5
$p_s=2$	0.0501	0.0605	0.0839	0.1122	0.1345
$p_s=4$	0.0474	0.0573	0.0796	0.1065	0.1278
$p_s=6$	0.0474	0.0573	0.0796	0.1065	0.1278
3D elasticity solution (Ref. 10)	0.0474	0.0570	0.0772	0.0981	0.1120
CPT (Ref. 16)	0.0497	0.0606	0.0853	0.1153	0.1390

sources are presented. The table includes the closed form solutions of Bert and Chen,[12] results of classical plate theory by Jones et al.,[16] and finite element solutions of Reddy.[11] The present results are in good agreement with those closed form[12] and finite element solutions.[11] However, they do not correlate well with those values from the classical plate theory since the effects of shear deformation were not considered in their formulation.[16]

B. Parametric studies

Tables V–IX present results for the first six nondimensional frequency parameters for a four-ply unsymmetrically laminated quadrilateral plate with different boundary conditions. Five sets of boundary conditions are considered, namely CFFF, SCFF, CCFF, CCCF, and CCCC, respectively. The plate geometry is defined by parameters given as follows: $b/a=0.9$, $c/a=0.7$, $\alpha=65$ deg, and $\beta=75$ deg as shown in Fig. 1. The results for the plates are given with the relative thickness ratio h/a ranging from 0.01 (a thin laminate) to 0.20 (a moderately thick laminate) and fiber orientation angle θ ranging from 0° to 90°.

The effect of boundary conditions on vibration responses of laminated plates has also been examined. Tables V–IX show that an increasing boundary constraint induces a higher vibration response. In Table IX, close agreement is seen between the solutions from the present paper and those from finite element package ANSYS using $20\times20\times10$ mesh and SOLID46 element. A higher constraint has higher plate stiffness and thus results in a higher physical frequency of vibration. For instance, it is clearly evident that the CFFF plate possesses a lower vibration frequency than the CCFF plate and the CCCC plate, e.g., compare Tables V, VII, and IX. The frequency parameters for the CCCC plate are the highest among all the plates investigated. Since the CCCC plate has more boundary kinematic constraints than the CCFF and CFFF plates, it is expected that imposing more boundary kinematic constraints tends to induce a higher frequency of vibration.

It is of interest to investigate the effects of transverse shear deformation by considering plates with different relative thickness ratios h/a. It is obvious that as the plate thickness increases, a significant decrease in vibration frequency occurs due to shear flexibility. These results (Tables V–IX) clearly indicate that the effect of transverse shear deformation becomes more pronounced for higher modes of vibration. For example, we compare this to the cantilevered four-ply quadrilateral laminated plate with $\theta=90°$ as tabulated in

TABLE IV. Comparison of frequency parameter $\lambda=\omega a^2\sqrt{\rho/(E_2 h^2)}$ of four-ply laminated square plates [(45 deg/−45 deg/45 deg/−45 deg), $h/a=0.1$].

Mode No.	Edge boundary conditions					
	SSSS	SSCS	CSCS	FSFS	FSSS	FSCS
1	18.4633[a] 18.46[b] 18.609[c] 23.53[d]	19.4146	20.4821	6.2645	10.0492	10.3573
2	34.4144[a]	34.9489	35.0258	15.4105	24.1490	25.3702
3	34.8739[a] 34.87[b] 35.405[c]	36.4707	38.0732	23.7974	26.3117	26.3228
4	34.8739[a]	50.8870	51.2703	29.5499	32.4374	41.1690
5	50.5204[a] 50.52[b]	54.2742	54.2743	30.9739	40.9123	42.4812
6	54.2741[a] 54.27[b] 54.360[c]	55.6697	56.9964	32.3327	40.9990	47.1965
7	54.2741[a] 54.27[b]	61.2240	67.2011	34.4144	47.1970	51.8856
8	67.1731[a] 67.17[b] 67.637[c]	67.1871	68.5613	45.9121	51.8856	57.4100
9	67.1731 67.17[b]	67.8609	75.5939	47.1525	57.1046	57.6118
10	68.8290	75.5874	77.4117	47.7045	58.6215	58.6218

[a]Present solution.
[b]Navier solution (Ref. 12).
[c]FEM solution (Ref. 11).
[d]CPT solution (Ref. 16).

TABLE V. Variation of frequency parameter $\lambda = \omega a^2 \sqrt{\rho/(E_2 h^2)}$ with nondimensional thickness h/a for a four-ply laminated quadrilateral cantilever (CFFF) plate $(\theta/-\theta/\theta/-\theta)$ having $b/a = 0.9$, $c/a = 0.7$, $\alpha = 65$ deg, $\beta = 75$ deg.

θ	h/a	Mode sequence No.					
		1	2	3	4	5	6
0°	0.01	2.2563	8.1953	11.8461	23.3086	31.0204	45.8713
	0.05	2.2418	7.9392	11.5733	22.1499	26.3208	29.5124
	0.10	2.2122	7.4888	10.9171	13.1604	20.0256	23.7195
	0.15	2.1712	6.9560	8.7736	10.0738	15.8130	17.7714
	0.20	2.1209	6.3990	6.5802	9.1861	11.8597	15.4305
30°	0.01	3.5351	17.4442	22.3211	47.1132	58.7759	78.9316
	0.05	3.3895	16.2671	20.1569	41.0384	41.6310	49.8356
	0.10	3.2226	14.4623	17.1527	20.4950	31.1102	33.7266
	0.15	3.0700	12.6339	13.6496	14.5047	20.7402	27.3062
	0.20	2.9257	10.2263	11.0133	12.3504	15.5628	22.6110
45°	0.01	6.1402	26.2006	30.5065	67.4438	72.9078	86.5239
	0.05	5.7917	22.9487	26.8472	54.8328	59.0032	63.7771
	0.10	5.3312	18.6221	21.5916	31.8562	40.0761	43.2858
	0.15	4.8904	15.2228	17.3656	21.2290	30.6122	32.4749
	0.20	4.4804	12.7182	14.2885	15.9558	24.2648	24.6639
60°	0.01	9.1317	26.1052	42.9302	62.2516	72.1352	106.8625
	0.05	8.6596	22.8392	36.1535	50.5121	56.6187	79.4564
	0.10	7.7657	18.1898	26.9628	37.0135	40.5321	50.5277
	0.15	6.8271	14.7235	20.7487	28.8910	30.9310	33.5532
	0.20	6.8271	14.7235	20.7487	28.8910	30.9310	33.5532
90°	0.01	12.5558	19.3126	33.8502	55.3454	69.9477	78.9487
	0.05	11.7455	17.4554	30.1719	36.8467	45.8967	52.4128
	0.10	10.0151	14.2899	18.4233	24.4072	32.6693	35.8728
	0.15	8.3122	11.5068	12.2822	19.8149	24.6878	26.9986
	0.20	6.9440	9.2117	9.4085	16.5385	19.8701	21.5538

TABLE VI. Variation of frequency parameter $\lambda = \omega a^2 \sqrt{\rho/(E_2 h^2)}$ with nondimensional thickness h/a for a four-ply laminated quadrilateral SCFF plate $(\theta/-\theta/\theta/-\theta)$ having $b/a = 0.9$, $c/a = 0.7$, $\alpha = 65$ deg, $\beta = 75$ deg.

θ	h/a	Mode sequence No.					
		1	2	3	4	5	6
0°	0.01	13.8460	17.8158	30.0756	53.1808	61.7054	83.9846
	0.05	12.9312	15.8825	27.7375	46.9823	49.8065	58.4074
	0.10	10.9234	13.0366	24.1572	29.2037	33.2656	41.2432
	0.15	8.9012	10.9968	19.4691	21.0072	25.4842	32.7146
	0.20	7.3089	9.5930	14.6019	18.3458	20.7853	26.4601
30°	0.01	15.0008	28.9744	51.1799	68.2917	91.0909	107.0619
	0.05	13.6157	23.8238	42.2318	54.1084	73.9337	78.3244
	0.10	11.2917	18.5858	33.4827	37.9725	44.6419	52.0581
	0.15	9.3255	15.2421	27.0967	28.6788	29.9363	38.6305
	0.20	7.8639	12.9677	21.7057	22.7869	23.5750	30.5150
45°	0.01	14.2253	33.1021	59.3108	74.3919	103.3488	132.5401
	0.05	12.8510	27.3612	49.1983	60.1734	77.4813	77.9251
	0.10	10.7888	21.7209	36.1281	38.7829	44.7335	53.1769
	0.15	9.0808	17.7841	25.7833	27.6090	34.4751	39.3143
	0.20	7.7783	14.9569	19.3219	22.0684	27.6496	30.9389
60°	0.01	11.3138	33.3563	49.0644	77.8675	96.3661	107.8581
	0.05	10.3479	29.5224	42.3633	57.8389	63.5807	76.5789
	0.10	8.9845	24.3936	28.8783	32.7126	46.5415	54.0519
	0.15	7.8309	19.2256	20.1305	25.6278	35.3447	40.2143
	0.20	6.9017	14.3983	16.8525	20.7428	28.0896	31.4680
90°	0.01	4.3641	18.6107	38.8560	49.8370	64.2270	68.5829
	0.05	4.2726	17.7055	34.8301	41.1501	43.5695	55.2468
	0.10	4.1131	16.0223	20.5750	28.7493	33.6621	38.0649
	0.15	3.9199	13.7167	14.2353	23.3082	25.3766	26.6132
	0.20	3.7096	10.2875	12.6024	19.0324	19.0545	21.9154

TABLE VII. Variation of frequency parameter $\lambda = \omega a^2 \sqrt{\rho/(E_2 h^2)}$ with nondimensional thickness h/a for a four-ply laminated quadrilateral CCFF plate ($\theta/-\theta/\theta/-\theta$) having $b/a = 0.9$, $c/a = 0.7$, $\alpha = 65$ deg, $\beta = 75$ deg.

θ	h/a	Mode sequence No.					
		1	2	3	4	5	6
0°	0.01	16.2181	19.3708	35.4926	60.9359	68.0647	92.2907
	0.05	14.7060	17.6086	32.5252	51.9527	55.5002	58.3557
	0.10	11.8966	15.0074	27.8684	29.1779	36.1104	44.4848
	0.15	9.5337	12.8859	19.4519	23.7358	27.4953	33.7148
	0.20	7.8395	11.2333	14.5889	20.3530	22.2436	27.1379
30°	0.01	17.5281	33.1535	59.3769	73.5924	103.0377	114.5025
	0.05	15.5668	26.8011	48.7010	56.7692	79.3287	84.2004
	0.10	12.6714	20.8756	37.0807	39.5471	45.1375	53.4121
	0.15	10.3826	17.0056	28.2004	30.0708	30.7386	39.3700
	0.20	8.7069	14.2808	21.9574	23.1596	24.9881	30.9649
45°	0.01	17.9685	40.8303	65.5348	89.9501	112.2603	141.7445
	0.05	15.5734	32.8326	52.2516	68.9487	80.9073	93.7450
	0.10	12.6329	25.0122	37.0189	46.7172	48.4525	53.9696
	0.15	10.4315	19.7239	27.7908	31.1349	36.2706	39.5705
	0.20	8.8049	16.1139	22.0856	23.3369	28.7354	31.0545
60°	0.01	16.5152	44.0349	58.1094	91.5423	110.6112	124.3205
	0.05	14.4972	36.3630	46.9534	68.7853	82.1525	88.5825
	0.10	11.9760	27.3179	33.9424	48.0579	55.2884	58.2165
	0.15	10.0206	21.2974	25.9053	36.2377	40.4972	41.3746
	0.20	8.5348	17.3436	20.8220	28.8297	30.5240	32.1720
90°	0.01	14.2579	29.5475	54.3926	70.2148	79.2786	91.5496
	0.05	13.2857	26.7113	45.2776	53.0904	60.3084	61.0317
	0.10	11.3989	21.9543	30.1542	32.3052	37.4387	43.1905
	0.15	9.5711	17.9172	20.1028	24.4090	28.8181	33.4063
	0.20	8.0963	14.8976	15.0771	19.5923	23.3279	25.5129

TABLE VIII. Variation of frequency parameter $\lambda = \omega a^2 \sqrt{\rho/(E_2 h^2)}$ with nondimensional thickness h/a for a four-ply laminated quadrilateral CCCF plate ($\theta/-\theta/\theta/-\theta$) having $b/a = 0.9$, $c/a = 0.7$, $\alpha = 65$ deg, $\beta = 75$ deg.

θ	h/a	Mode sequence No.					
		1	2	3	4	5	6
0°	0.01	17.6973	34.1609	59.7968	68.0236	91.7802	96.6534
	0.05	16.5700	31.5583	51.7301	54.6482	69.3039	83.0134
	0.10	14.3393	26.8563	36.0348	42.3832	44.2622	48.2187
	0.15	12.2501	22.5476	27.4426	28.2555	35.8438	37.0344
	0.20	10.5648	19.0786	21.1916	22.1921	29.5662	30.0301
30°	0.01	26.3791	59.7396	75.8855	107.1104	129.2748	159.1530
	0.05	23.1584	49.2694	58.4055	82.7382	91.7070	106.8977
	0.10	18.6825	36.6229	40.3126	57.7555	60.1870	67.1212
	0.15	15.1416	28.1949	30.0146	43.2144	43.7882	47.8056
	0.20	12.5351	22.6918	23.7432	34.1207	34.3637	36.8416
45°	0.01	35.2908	76.0432	87.7724	143.2751	149.1184	163.7034
	0.05	29.5709	58.0057	65.3167	98.0825	102.1905	108.4718
	0.10	22.1908	39.9198	43.6071	62.3605	65.0708	67.8583
	0.15	17.0677	29.6423	31.8339	44.7680	46.6648	48.5036
	0.20	13.6710	23.4241	24.9368	34.6805	36.1925	37.5879
60°	0.01	42.9179	72.3946	107.8570	120.3575	154.8198	187.3991
	0.05	34.1284	53.6813	74.2079	84.6497	100.4231	120.5027
	0.10	23.8396	36.6540	46.9332	56.2842	62.9365	72.7234
	0.15	17.7255	27.5221	33.6805	41.7413	45.1242	51.1581
	0.20	13.9939	22.0168	26.1735	33.0744	35.0002	39.2784
90°	0.01	43.4300	68.7582	82.5915	101.8683	127.5584	143.7919
	0.05	32.7566	47.4887	59.1411	72.5697	75.7385	84.2147
	0.10	22.4246	30.5186	37.8693	40.9431	47.5062	54.3330
	0.15	16.5342	22.5906	25.2462	31.0756	35.0580	39.2727
	0.20	13.0084	18.0414	18.9346	24.8554	27.8639	30.7196

TABLE IX. Variation of frequency parameter $\lambda = \omega a^2 \sqrt{\rho/(E_2 h^2)}$ with nondimensional thickness h/a for a four-ply laminated quadrilateral CCCC plate $(\theta/-\theta/\theta/-\theta)$ having $b/a = 0.9$, $c/a = 0.7$, $\alpha = 65$ deg, $\beta = 75$ deg.

θ	h/a	Mode sequence No.					
		1	2	3	4	5	6
0°	0.01	66.3495	90.0324	116.4425	148.5115	154.1021	191.4730
	0.05	47.1823	61.9749	81.0273	91.1540	107.5743	109.9071
	0.10	30.4523	41.2417	54.8355	54.9536	57.0321	67.0205
	0.15	22.3313	31.3377	36.6357	39.2099	43.9170	48.2761
	0.20	17.7211	25.3115	27.4768	30.5112	35.4955	37.7389
30°	0.01	69.9690	113.4161	153.8890	169.3880	219.6646	240.6992
	0.05	51.6977	78.8926	96.9603	113.0431	128.9760	145.9206
	0.10	34.2667	51.5109	58.6595	72.5893	76.6762	84.1318
	0.10[a]	33.7214	48.2861	59.7392	⋯	76.4849	⋯
	0.15	24.9896	37.5799	41.3285	52.5940	53.7613	58.2197
	0.20	19.5157	29.4261	31.7441	41.0000	41.2449	44.3261
	0.20[a]	19.3151	27.8423	32.7428	37.9514	41.7162	⋯
45°	0.01	71.2040	134.6393	142.0045	219.0485	224.3553	236.8315
	0.05	53.3544	90.6412	93.5954	131.3998	136.5774	138.6236
	0.10	35.4820	56.3467	57.7407	77.7898	81.1901	81.7483
	0.10[a]	34.3553	52.3320	58.4081	73.1138	77.8335	⋯
	0.15	25.6655	39.9508	40.8639	54.2171	56.6539	57.2051
	0.20	19.8951	30.7762	31.4564	41.3947	43.2748	43.8418
	0.20[a]	19.5410	29.1283	32.2272	39.8901	42.2981	⋯
60°	0.01	70.1182	117.1055	151.1298	184.9894	206.8792	256.9287
	0.05	51.6900	80.3975	96.2806	116.1955	126.4063	146.0168
	0.10	34.2223	51.9518	58.4403	72.4923	76.5185	84.7863
	0.10[a]	32.5711	50.7552	55.5471	70.1423	77.1372	⋯
	0.15	24.9457	37.8020	41.1987	51.9979	54.1098	58.7674
	0.20	19.4832	29.5817	31.6604	40.2859	41.7437	44.7770
	0.20[a]	18.9789	28.9711	31.0564	39.2440	42.5898	⋯
90°	0.01	71.6008	87.0326	112.9384	148.7590	182.1487	194.0421
	0.05	48.3066	60.9233	81.4380	98.1799	103.3688	109.9078
	0.10	30.4750	41.4449	54.8299	54.9539	59.1779	65.1740
	0.15	22.2888	31.5762	36.6359	39.4922	44.2076	47.5391
	0.20	17.6919	25.4841	27.4769	30.6821	35.4071	37.4117

[a]FEM solution from ANSYS.

Table V. The fundamental frequency decreases by about half as the thickness ratio increases from 0.01 to 0.20. However, the frequency for the sixth mode (a higher mode) decreases to about a quarter subject to the same thickness condition.

It is also worthwhile to examine the variation of frequency parameters of laminates by increasing the number of plies. Figures 2–5 present results for laminates with various fiber orientation angles and stacking in an unsymmetric manner. Laminates subjected to CCCC, CCFF, S*S*S*S*, and CFCF boundary conditions with stacking sequence $(\theta/-\theta/\theta/-\theta/...)$ are considered. The graphs in Figs. 2–5 show that the fundamental frequency parameter increases initially and reaches a maximum value as the number of plies increases, except when θ is 0 or 90 deg. It is easy to demonstrate this phenomenon by referring to Fig. 2. It can be seen that the fundamental frequency parameter increases and reaches a maximum value of about 32 when number of plies is at about 7 (or 8) for $\theta = 15$ deg. When the number of plies reaches 7 (or 8), the analysis of this laminate can be treated as a single layer anisotropic plate.

III. CONCLUDING REMARKS

This paper considers the vibration analysis of arbitrary quadrilateral unsymmetrically laminated composite plates
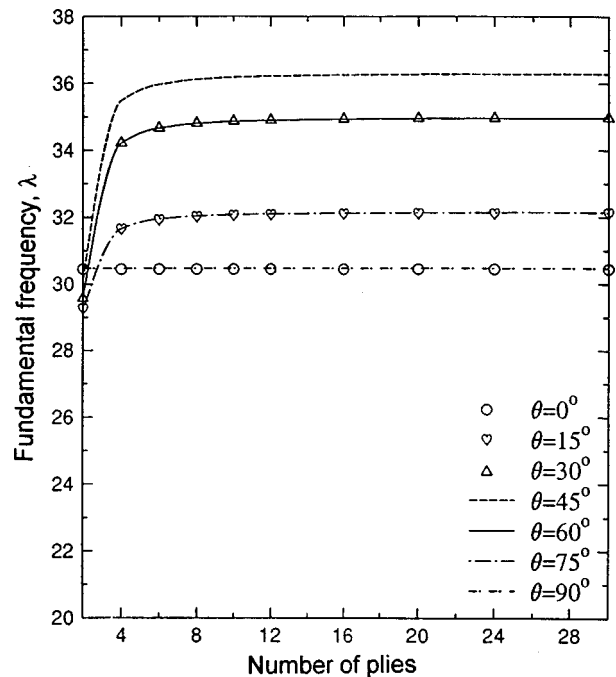
FIG. 2. Effect of number of plies on the fundamental frequency $\lambda = \omega a^2 \sqrt{\rho/(E_2 h^2)}$ of the laminated CCCC quadrilateral plate $(\theta/-\theta/\theta/-\theta/.../\theta/-\theta)$ having $h/a = 0.1$, $b/a = 0.9$, $c/a = 0.7$, $\alpha = 65$ deg, $\beta = 75$ deg.
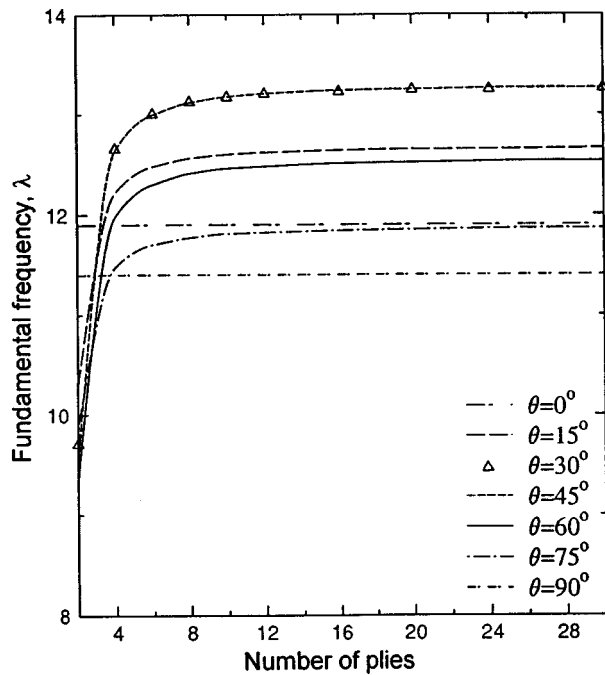
FIG. 3. Effect of number of plies on the fundamental frequency $\lambda = \omega a^2 \sqrt{\rho/(E_2 h^2)}$ of the laminated CCFF quadrilateral plate ($\theta/-\theta/\theta/-\theta/... /\theta/-\theta$) having $h/a = 0.1$, $b/a = 0.9$, $c/a = 0.7$, $\alpha = 65$ deg, $\beta = 75$ deg.

with various boundary conditions. The analysis has been performed using the Ritz method with polynomials as its admissible displacement and rotation functions. This analysis method is extremely versatile because a basic function is employed which easily accommodates various boundary conditions. The significance of the transverse shear deformation has been investigated. This effect was incorporated in the mathematical model using the YNS first-order shear deformation theory.
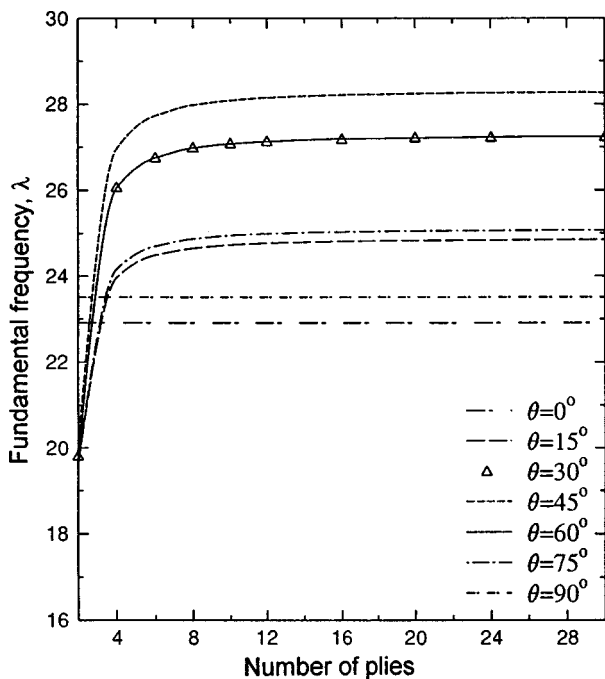
FIG. 4. Effect of number of plies on the fundamental frequency $\lambda = \omega a^2 \sqrt{\rho/(E_2 h^2)}$ of the laminated S*S*S*S* quadrilateral plate ($\theta/-\theta/\theta/ -\theta/.../\theta/-\theta$) having $h/a = 0.1$, $b/a = 0.9$, $c/a = 0.7$, $\alpha = 65$ deg, $\beta = 75$ deg.
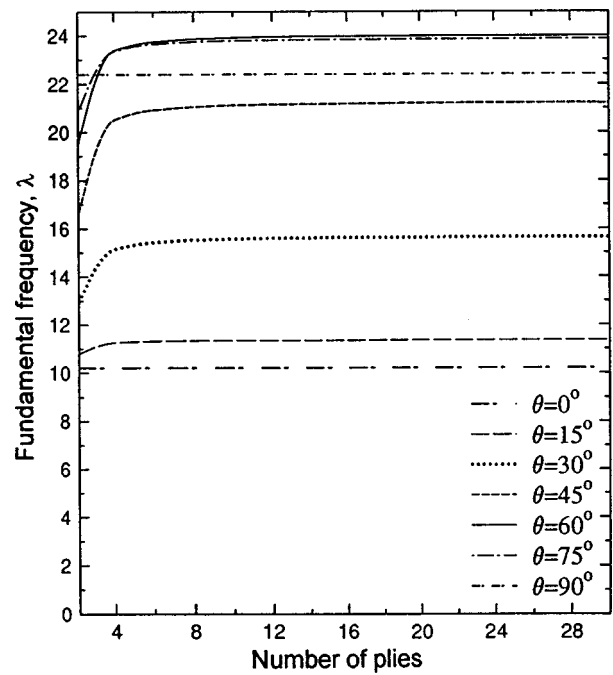
FIG. 5. Effect of number of plies on the fundamental frequency $\lambda = \omega a^2 \sqrt{\rho/(E_2 h^2)}$ of the laminated CFCF quadrilateral plate ($\theta/-\theta/\theta/-\theta/... /\theta/-\theta$) having $h/a = 0.1$, $b/a = 0.9$, $c/a = 0.7$, $\alpha = 65$ deg, $\beta = 75$ deg.

The vibration analysis of several plate problems has been presented and the results compared with established solutions from available literature. Close agreement has been obtained for the comparison studies, verifying the accuracy and applicability of the present analysis method. As a closing remark, it is important to point out that, although only a few plate examples has been presented in this study, the method is readily applicable to solving a wide range of quadrilateral unsymmetrically laminated plates of arbitrary shape. As an approximate technique, the method has the advantage of not exhibiting any mesh distortion sensitivity, therefore modeling accurately the quadrilateral geometry without boundary losses.

APPENDIX: SUBMATRICES OF STIFFNESS AND MASS MATRICES

The elements in the stiffness matrices $\mathbf{K}$ and mass matrices $\mathbf{M}$, respectively, can be further expanded as

$$K_{aa} = \partial_x \phi_x (A_{11} \partial_x \phi_x^T + A_{16} \partial_y \phi_x^T)$$
$$+ \partial_y \phi_x (A_{16} \partial_x \phi_x^T + A_{66} \partial_y \phi_x^T), \tag{A1a}$$

$$K_{ab} = \partial_x \phi_x (A_{12} \partial_y \phi_y^T + A_{16} \partial_x \phi_y^T)$$
$$+ \partial_y \phi_x (A_{26} \partial_y \phi_y^T + A_{66} \partial_x \phi_y^T), \tag{A1b}$$

$$K_{ac} = K_{bc} = 0, \tag{A1c}$$

$$K_{ad} = \partial_x \phi_x (B_{11} \partial_x \psi_x^T + B_{16} \partial_y \psi_x^T)$$
$$+ \partial_y \phi_x (B_{16} \partial_x \psi_x^T + B_{66} \partial_y \psi_x^T), \tag{A1d}$$

$$K_{ae} = \partial_x \phi_x (B_{12} \partial_y \psi_y^T + B_{16} \partial_x \psi_y^T)$$
$$+ \partial_y \phi_x (B_{26} \partial_y \psi_y^T + B_{66} \partial_x \psi_y^T), \tag{A1e}$$

$$K_{bb} = \partial_y \phi_y (A_{22} \partial_y \phi_y^T + A_{26} \partial_x \phi_y^T)$$
$$+ \partial_x \phi_y (A_{26} \partial_y \phi_y^T + A_{66} \partial_x \phi_y), \quad \text{(A1f)}$$

$$K_{bd} = \partial_y \phi_y (B_{12} \partial_x \psi_x^T + B_{26} \partial_y \psi_x^T)$$
$$+ \partial_x \phi_y (B_{16} \partial_x \psi_x^T + B_{66} \partial_y \psi_x^T), \quad \text{(A1g)}$$

$$K_{be} = \partial_y \phi_y (B_{22} \partial_y \psi_y^T + B_{26} \partial_x \psi_y^T)$$
$$+ \partial_x \phi_y (B_{26} \partial_y \psi_y^T + B_{66} \partial_x \psi_y^T), \quad \text{(A1h)}$$

$$K_{cc} = \partial_y \phi_x (A_{44} \partial_y \phi_z^T + A_{45} \partial_x \phi_z^T)$$
$$+ \partial_x \phi_z (A_{45} \partial_y \phi_z^T + A_{55} \partial_x \phi_z^T), \quad \text{(A1i)}$$

$$K_{cd} = (A_{45} \partial_y \phi_z + A_{55} \partial_x \phi_z) \psi_x^T, \quad \text{(A1j)}$$

$$K_{ce} = (A_{44} \partial_y \phi_z + A_{45} \partial_x \phi_z) \psi_y^T, \quad \text{(A1k)}$$

$$K_{dd} = \partial_x \psi_x (D_1 \partial_x \psi_x^T + D_{16} \partial_y \psi_x^T)$$
$$+ \partial_y \psi_x (D_{16} \partial_x \psi_x^T + D_{66} \partial_y \psi_x^T) + A_{55} \psi_x \psi_x^T, \quad \text{(A1l)}$$

$$K_{de} = \partial_x \psi_x (D_{12} \partial_y \psi_y^T + D_{16} \partial_x \psi_y^T)$$
$$+ \partial_y \psi_x (D_{26} \partial_y \psi_y^T + D_{66} \partial_x \psi_y^T) + A_{45} \psi_x \psi_y^T, \quad \text{(A1m)}$$

$$K_{ee} = \partial_y \psi_y (D_{22} \partial_y \psi_y^T + D_{26} \partial_x \psi_y^T)$$
$$+ \partial_x \psi_y (D_{26} \partial_y \psi_y^T + D_{66} \partial_x \psi_y^T) + A_{44} \psi_y \psi_y^T, \quad \text{(A1n)}$$

$$M_{aa} = E_1 \phi_x \phi_x^T, \quad \text{(A2a)}$$

$$M_{ad} = E_2 \phi_x \psi_x^T, \quad \text{(A2b)}$$

$$M_{bb} = E_1 \phi_y \phi_y^T, \quad \text{(A2c)}$$

$$M_{be} = E_2 \phi_y \psi_y^T, \quad \text{(A2d)}$$

$$M_{cc} = E_1 \phi_z \phi_z^T, \quad \text{(A2e)}$$

$$M_{dd} = E_3 \psi_x \psi_x^T, \quad \text{(A2f)}$$

$$M_{ee} = E_3 \psi_y \psi_y^T, \quad \text{(A2g)}$$

$$M_{ab} = M_{ac} = M_{ae} = M_{bc} = M_{bd} = M_{cd} = M_{ce} = M_{de} = 0. \quad \text{(A2h)}$$

In the above, A_{ij}, B_{ij}, and C_{ij} are effective laminate stiffness coefficients given by

$$(A_{ij}, B_{ij}, D_{ij}) = \int_{-h/2}^{h/2} (1, z, z^2) Q_{ij} \, dz, \quad i, j = 1, 2, 6,$$
$$\text{(A3a)}$$

$$A_{ij} = k_{ij}^2 \int_{-h/2}^{h/2} Q_{ij} \, dz, \quad i, j = 4, 5, \quad \text{(A3b)}$$

and E_i are the effective inertia coefficients given by

$$(E_1, E_2, E_3) = \int_{-h/2}^{h/2} (1, z, z^2) \rho \, dz, \quad \text{(A4)}$$

where $k_{ij}^2 = 5/6$ are the transverse shear correction coefficients. Note that for antisymmetric angle-ply laminates A_{16}, A_{26}, A_{45}, B_{11}, B_{12}, B_{22}, D_{16}, B_{26}, and E_2, are identically zero.

[1] J. N. Reddy, ''A review of the literature on finite-element modelling of laminated composite plates and shells,'' Shock Vib. Digest **17**(4), 3–8 (1985).

[2] C. W. Bert, ''Research on dynamic behaviour of composite and sandwich plates, V: Part I,'' Shock Vib. Digest **23**(6), 3–14 (1991).

[3] C. W. Bert, ''Research on dynamic behaviour of composite and sandwich plates, V: Part II,'' Shock Vib. Digest **23**(7), 9–21 (1991).

[4] K. M. Liew, Y. Xiang, and S. Kitipornchai, ''Research on thick plate vibration: a literature survey,'' J. Sound Vib. **180**(1), 163–176 (1995).

[5] P. C. Yang, C. H. Norris, and Y. Stavsky, ''Elastic wave propagation in heterogeneous plates,'' Int. J. Solid Struct. **2**(4), 665–684 (1966).

[6] A. W. Leissa, ''Vibration of plates,'' NASA SP-160, Washington (1969).

[7] A. W. Leissa, ''Recent research in plate vibrations, 1973–76: complicating effects,'' Shock Vib. Digest **10**(12), 21–35 (1978).

[8] A. W. Leissa, ''Plate vibration and research, 1976–1980: complicating effects,'' Shock Vib. Digest **13**(10), 19–36 (1981).

[9] A. W. Leissa, ''Recent studies in plate vibrations, 1981–1985, part II: complicating effects,'' Shock Vib. Digest **19**(3), 10–24 (1987).

[10] S. Srinivas, C. V. J. Rao, and A. K. Rao, ''An exact analysis for vibration of simply-supported homogeneous and laminated thick rectangular plates,'' J. Sound Vib. **12**(2), 187–199 (1970).

[11] J. N. Reddy, ''Free vibration of antisymmetric, angle-ply laminated plates including transverse shear deformation by the finite element method,'' J. Sound Vib. **66**(4), 565–576 (1979).

[12] C. W. Bert and T. L. C. Chen, ''Effect of shear deformation on vibration of antisymmetric angle-ply laminated rectangular plates,'' Int. J. Solid Struct. **14**(3), 465–473 (1978).

[13] Y. Xiang, S. Kitipornchai, and K. M. Liew, ''Buckling and vibration of thick laminates on pasternak foundations,'' J. Engng Mech. **122**(1), 54–63 (1996).

[14] K. M. Liew, Y. Xiang, S. Kitipornchai, and C. M. Wang, ''Vibration of thick skew plates based on Mindlin shear deformation plate theory,'' J. Sound Vib. **168**(1), 39–69 (1993).

[15] K. M. Liew, K. Y. Lam, and S. T. Chow, ''Free vibration analysis of rectangular plates using orthogonal plate function,'' Comput. Struct. **34**(1), 79–85 (1990).

[16] R. M. Jones, H. S. Morgan, and J. M. Whitney, ''Buckling and vibration of antisymmetrically laminated angle-ply rectangular plates,'' J. Appl. Mech. **40**(2), 1143–1144 (1973).

A numerical method for vibro-acoustic problems with incompatible finite element meshes using B-spline functions

M. Guerich[a) and M. A. Hamdi

LG2mS/AVI, UPRA CNRS N: 6066, Université de Technologie de Compiègne, B.P. 529,
60205 Compiegne Cedex, France

This paper describes a new method for computing fluid–structure coupling with incompatible finite element meshes using uniform cubic B-spline functions (UCBFs). A modal approach is used which has the advantage of computing the individual structural and fluid mode shapes, using independent meshes. In order to compute the fluid–structure coupling for the incompatible meshes, it is necessary to interpolate the structure and fluid mode shapes over a common geometric mesh. This mesh is defined by the shell itself which is also interpolated by UCBF using a minimum number of geometric control nodes. New structural and fluid meshes are first derived from the geometric mesh by defining two different element multiplicities. An extrapolation algorithm is then developed to deduce the values of fluid and structure functions (displacement and pressure) over the two new meshes. The UCBFs are finally used to interpolate mode shapes of fluid and structure from the two previous meshes into a common mesh. Having the two new functions on the same common mesh provides the fluid–structure coupling for incompatible meshes. The method is illustrated for 2-D and 3-D coupled problems corresponding to shells of revolution, plates, and 3-D shells. © *1999 Acoustical Society of America.* [S0001-4966(99)03302-0]

PACS numbers: 43.40.Ey, 43.40.Rj [CBB]

LIST OF SYMBOLS

C_{ijkl}	Elasticity tensor of the structure
ρ_s	Structural mass density
ρ_1	Mass density of the internal fluid
ρ_2	Mass density of the external fluid
p_1	Acoustic pressure in the internal fluid
p_2	Acoustic pressure in the external fluid
c	Speed of sound in the fluid
ω	Circular frequency
$k = \omega/c$	Wave number
V_s^i	Domain of the ith substructure
∂V_s^i	Boundary of the ith substructure
Γ	Interface separating two substructures
λ	Lagrange multiplier
F	Mechanical excitation
V_a^i	Domain of the internal fluid
V_a^e	Domain of the external fluid
S_0	Fixed part of the structure
S_1	Internal surface
S_2	External surface
n_i	The ith component of the unique outward unit normal vector **n**
S_f	Part of the structure when mechanical forces are imposed
K,M	Stiffness and mass matrices of the structure
H,Q	Internal fluid matrices
D	Acoustic admittance of the external surface S_2
C	Coupling operator between the internal fluid and the structure
B	Coupling operator between the external fluid and the structure
A	Auto-influence acoustic matrix
δ	Vector of the generalized displacements
ψ	Vector of the generalized pressures
α	Vector or matrix of control variables
φ	Basic B-spline function
S_l^j	The ''length'' or the ''surface'' corresponding to mode shape j and the iteration l.
N	Basis interpolation function
$\langle \rangle$	Raw vector
$\{\,\}$	Vector
$[\,]$	Matrix
ξ_g, η_g	Geometric reduced parameters
ξ_s, η_s	Structural reduced parameters
ξ_f, η_f	Fluid reduced parameters

INTRODUCTION

The analysis of the vibratory behavior of a structure in contact with a fluid most often requires taking into account the problem of fluid–structure interaction. In this case, the added mass and stiffness of the fluid can modify the vibratory behaviors of the structure. The resolution of such problems consists of solving the equations of motion of the structure and the fluid which are coupled via the interaction surface by two conditions. For inviscid fluid, these two conditions correspond to the continuity of the normal component of the displacement and the stress vector through the fluid–structure interface.

[a)Present address: STRACO, 20 rue du Fonds Pernant, 60471 Compiegne Cedex, France.

Coupled problems can be classified into two major categories: (a) internal coupling problems such as vibration of tanks filled with liquids or gases where the fluid occupies the domain limited by the structure, and (b) external coupling problems such as the vibrations of submersibles where the structure is submerged in an infinite fluid domain.

In the case of internal coupling, the most used formulations are those based on the finite element method, which requires the discritization of the structure and the domain occupied by the fluid. These formulations are only distinguished from each other by the choice of variables in the fluid domain; these variables can be the fluid particle displacement field, the pressure, the displacement potential, or both the pressure and potential at the same time.[1,2] For this particular case, the formulations should distinguish whether the fluid is described by the displacement field or by a scalar field, in which case the formulation obviously calls for an integration over the fluid–structure interaction surface.

In both cases, the structure and the fluid meshes could be different either because the wavelengths in the structure and in the fluid are different, or because the two models have been independently defined. The numerical treatment of this integral can be complicated in the case of incompatible meshes especially for three-dimensional problems.

The fluid–structure coupling using incompatible meshes is seldom discussed in the literature. A method called least common mesh (LCM) has been proposed,[3] and was used for the computation of added mass in fluid–structure problems.[4] Its main drawback is its limitation to planar surfaces. Recently a method of fluid–structure coupling with boundary grid operator has been proposed.[5] It is based on the projection of fluid–structure information over a virtual grid, which could be a structural mesh, a fluid boundary mesh, or a virtual one. However, this approach presents the disadvantage of isoparametric discretization which provides, after projection, significant loss of coupling information especially in the case of complex geometries. Parallel to our work, a procedure which consists of transferring information from a given mesh to another one has been proposed.[6] This procedure is based on a local projection of each node of one of the two meshes over the other by means of mesh transfer matrices. This method presents the advantage of modal method such as the reduction of the system size, but has the same disadvantage of the method used in Ref. 5, that is, loss of coupling informations.

The method proposed herein has the advantage of avoiding the usual isoparametric discretization through an independence between the geometry, the structural displacement, and the pressure in the fluid. The resolution of some vibroacoustic applications using two- or three-dimensional (2-D or 3-D) structures shows a good performance of the proposed method based on uniform cubic B-spline functions (UCBF).

I. INCOMPATIBLE MESHES FOR COUPLED STRUCTURES

Coupled structures are generally composed of several subcomponents or substructures. The finite element meshes for each substructure are not necessarily the same, either because the finite element models have been defined inde-
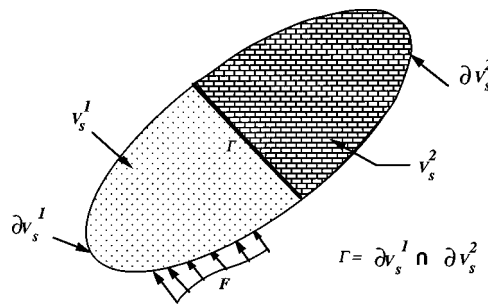
FIG. 1. Decomposition into two substructures.

pendently, or because of the independence of the wavelength of each substructure (heterogeneous structures, structures of different dimensions).

Here, the use of incompatible meshes in the case of the linear dynamic of coupled structures is presented to show how to extend it to the case of coupling fluid–structure system. The dynamic analysis of a structure composed of two substructures is then considered (Fig. 1). The unknown used to describe the linear dynamic of the two coupled substructures is the displacement in every point of the system.

The couple of displacement vectors (w^1, w^2) satisfies the following variational equation:[7]

$$\delta\left\{\frac{1}{2}\left(K_1(w^1, w^1) + K_2(w^2, w^2)\right) - \frac{\omega^2}{2}\left(M_1(w^1, w^1)\right.\right.$$
$$\left.\left. + M_2(w^2, w^2)\right)\right\} = L_1(F, w^1), \tag{1}$$

where $K_l(w^l, w^l)$ and $M_l(w^l, w^l)$ are respectively the stiffness and mass matrices of the lth substructure, given by

$$K_l(w^l, w^l) = \int_{V_S}(\sigma^l ij(w^l)\varepsilon^l ij(w^l))dV^l, \tag{2}$$

$$M_l(w^l, w^l) = \int_{V_S}\rho_s^1 w_i^1 w_i^1\, dV^l, \tag{3}$$

Here $\sigma^l ij$ is the Cauchy stress tensor related to the strain tensor $\varepsilon^l mn$:

$$\sigma^l ij = C^l ijmn\varepsilon^l mn$$
$$\varepsilon^l mn = \frac{1}{2}\left(\frac{\partial w^l m}{\partial x_n} + \frac{\partial w^l n}{\partial x_m}\right). \tag{4}$$

Also, $L_1(w^1, F)$ is the linear operator due to the mechanical excitation F acting on the first boundary of the substructure domain ∂V_s^1,

$$L_1(w^1, F) = \int_{\partial V_S^1} F_i \partial w_i^1\, d(\partial V_s^1). \tag{5}$$

The additional kinematic condition, $w^1 = w^2$, must be satisfied on Γ, so this strong kinematic condition could be replaced by its weak form,[8,9]

$$\int_\Gamma \lambda(w^1 - w^2)d\Gamma = 0, \tag{6}$$

where λ is the Lagrange multiplier.

Several papers[9,10] dealt with the coupling of substructures using the above technique to solve incompatible mesh problems.

This method extends easily to the resolution of fluid–structure coupling with incompatible meshes by considering the fluid as a special elastic medium with the following constitutive law relating the pressure p to the displacement w_f of the fluid:

$$p = -\rho_f c^2 \operatorname{div} w_f. \tag{7}$$

This requires the use of a displacement–displacement formulation for the structure and for the fluid. The following formulation of the coupled problem is thus obtained:[11]

$$\delta\left\{ \frac{1}{2}\left(K_S(w_s,w_s)+K_f(w_f,w_f)\right)-\frac{\omega^2}{2}\left(M_S(w_s,w_s)\right.\right.$$

$$\left.\left. +M_f(w_f,w_f)\right)+L_a(w_s,w_f)\right\} = L(w_s,F), \tag{8}$$

where the irrotationality of the fluid displacement must be satisfied in the fluid domain V_a^i.[11] Here,

$$\operatorname{curl} \mathbf{w}_f = \mathbf{0} \quad \text{in} \quad V_a^i, \tag{9}$$

where w_s is the displacement of the structure, K_s and M_s are the stiffness and mass matrices of the structure, K_f and M_f are the stiffness and mass matrix of the fluid, and

$$L_a(w_s,w_f) = \int_\Gamma \lambda(w_s-w_f)n\,d\Gamma. \tag{10}$$

The problem can be summarized by finding (w_s,w_f) $\in \mathscr{A}$ solution of the variational equation (8), where the admissible space $\mathscr{A}$ is defined by

$$\mathscr{A} = \{\mathbf{w}_s \text{ kinematically admissible}, \ \mathbf{w}_f;$$

$$\operatorname{curl} \mathbf{w}_f = \mathbf{0} \quad \text{in} \quad V_a^i\}. \tag{11}$$

This formulation described as a *nonstandard* formulation[2] has the disadvantage of requiring the discretization of the constant $\operatorname{curl} \mathbf{w}_f = \mathbf{0}$, which is a complex numerical problem.[11]

In this paper, the standard variational formulation using the structural displacement and the fluid pressure as variables is preferred for solving fluid–structure problems with incompatible meshes.

II. FORMULATION IN TERMS OF DISPLACEMENT FOR THE STRUCTURE AND THE PRESSURE FOR THE FLUID

This formulation will be presented for the harmonic oscillations of a linear elastic structure V_s, initially at rest, containing an inviscid compressible fluid V_a^i, and immersed in an infinite fluid domain V_a^e initially at rest. The structure is excited by a harmonic surface load $\mathbf{F}$ acting on the external surface $\mathbf{S}_2$ (Fig. 2).

The governing equations of coupled internal/external problem are recalled in terms of the displacement vector for the structure and of the pressure for the fluid.[1,2]

Elasto-dynamic equation of the structure:
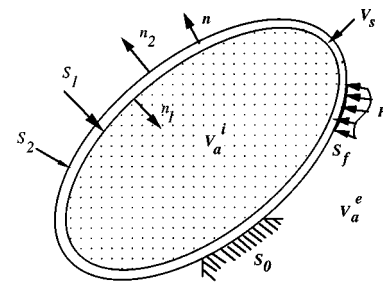
FIG. 2. Internal fluid structure interaction.

$$\frac{\partial}{\partial x_j}(\sigma_{ij}) + \rho_s \omega^2 w_i = 0 \quad \text{in} \quad \mathbf{V_s}. \tag{12}$$

Helmholtz equation for the fluid:

$$(\nabla^2+k^2)p_1=0 \quad \text{in} \quad V_a^i, \tag{13a}$$

$$(\nabla^2+k^2)p_2=0 \quad \text{in} \quad V_a^e. \tag{13b}$$

Kinematic boundary condition:

$$w_i=0 \quad \text{on} \quad S_0. \tag{14}$$

Kinematic coupling conditions (first coupling condition):

$$\frac{\partial p_1}{\partial n}-\rho_1\omega^2 w=0 \quad \text{on} \quad S_1, \tag{15}$$

$$\frac{\partial p_2}{\partial n}-\rho_2\omega^2 w=0 \quad \text{on} \quad S_2. \tag{16}$$

Equilibrium of dynamic forces (second coupling condition):

$$\sigma_{ij}n_j+p_1n_i=0 \quad \text{on} \quad S_1, \tag{17}$$

$$\sigma_{ij}n_j+p_2n_i=0 \quad \text{on} \quad S_2. \tag{18}$$

Mechanical boundary condition:

$$\sigma_{ij}n_j=F_i \quad \text{on} \quad S_f. \tag{19}$$

Sommerfeld's radiation condition for the external fluid:

$$\lim_{r\to\infty} r\left(\frac{\partial p_2}{\partial r}-ikp_2\right)=0. \tag{20}$$

To use the finite element method, a weak form of these equations is required. The variational formulation of the fluid–structure coupling is obtained[1,2] by introducing a space $\mathcal{C}_w$ of smooth functions w defined in $\mathbf{V_s}$ and a space $\mathcal{C}_p$ of smooth functions p, defined in $V_a^i \cup V_a^e (p_1,p_2 \in \mathcal{C}_p)$. The mixed boundary and finite element variational formulation is then given by[12]

$$\delta\{\tfrac{1}{2}(K(w,w)-\omega^2 M(w,w))-C(p_1,w)+\tfrac{1}{2}C(p_2,w)$$

$$+B(p_2,w)+\tfrac{1}{2}A(w,w)+\tfrac{1}{2}(H(p_1,p_1)-Q(p_1,p_1))$$

$$+\tfrac{1}{2}D(p_2,p_2)\}=L(F,\delta w), \tag{21}$$

where $K(w,w)$ and $M(w,w)$ are the stiffness and mass matrices of the structure, $C(p_1,w)$ is the coupling operator between the internal fluid and the structure given by

$$C(p_1,w)=\int_{S_2} p_1 w \, dS_2, \tag{22}$$

while $C(p_2,w)$ and $B(p_2,w)$ are the coupling operators between the external fluid and the structure given by

$$C(p_2,w)=\int_{S_1} p_2 w \, dS_1, \tag{23a}$$

$$B(p_2,w)=-\int_{S_2}\int_{S_2} w(X) \frac{\partial G(X,Y)}{\partial n_Y} p_2(Y) dS_2 \times dS_2. \tag{23b}$$

Here $G(X,Y)=\exp(ikr)/(-4\pi r)$ is the free space Green's function which satisfies the Helmholtz equation (13b) and the Sommerfeld's condition (20).

Then $A(w,w)$ is the auto-influence acoustic operator given by

$$A(w,w)=\rho_2\omega^2 \int_{S_2}\int_{S_2} w(X) G(X,Y) w(Y) dS_2 \times dS_2, \tag{24}$$

$H(p_1,p_1)$ and $Q(p_1,p_1)$ are the internal fluid matrices (corresponding to the kinetic energy and the energy of compression), given by

$$H(p_1,p_1)=\frac{1}{\rho_1\omega^2} \int_{V_a^i} |\operatorname{grad} p_1|^2 \, dV_a^i \tag{25}$$

and

$$Q(p_1,p_1)=\frac{1}{\rho_1 c^2} \int_{V_a^i} p_1^2 \, dV_a^i, \tag{26}$$

$L(F,\delta w)$ is a linear operator due to mechanical forces given by

$$L(F,\delta w)=\int_{S_f} F_i \delta w_i \, dS_f, \tag{27}$$

and $D(p_2,p_2)$ is the acoustic admittance of the external surface S_2 given by

$$D(p_2,p_2)=\frac{1}{\rho_2\omega^2} \int_{S_2}\int_{S_2} w(X) \frac{\partial G(X,Y)}{\partial n_Y}$$
$$\times p_2(Y) \, dS_2 \times dS_2. \tag{28}$$

The variational equation (21) is not valid for $\omega=0$. However, this singularity could be solved knowing that for $\omega=0$, $H(p_1,p_1)=0$ and $D(p_2,p_2)=0$ for a closed cavity and a closed surface S_2.

The discritization of this formulation yields to the following matrix equation:

$$\begin{bmatrix} K-\omega^2 M & -C & \left(B+\dfrac{C}{2}\right) \\[2mm] -C^t & \dfrac{H}{\rho_1\omega^2}-\dfrac{Q}{\rho_1 c^2} & 0 \\[2mm] \left(B+\dfrac{C}{2}\right)^t & 0 & \dfrac{D}{\rho_2\omega^2} \end{bmatrix} \begin{Bmatrix} W \\ P_1 \\ P_2 \end{Bmatrix} = \begin{Bmatrix} F \\ 0 \\ 0 \end{Bmatrix}, \tag{29}$$

where W is the nodal displacement vector of the structure, P_1 is the pressure vector in the volume V_a^i, and P_2 is the pressure on the external surface S_2. The resolution of this system gives the nodal displacement vector of the structure W and the nodal pressure vectors P_1 and P_2 of both the internal and external fluids.

The high number of physical degrees of freedom, which can be incorporated in a finite element model of fluid–structure interaction (about ten thousands), make their use difficult.[6] A modal method is thus preferred for the low frequency response of the coupled system. It has the advantage of computing separately the mode shapes for fluid and for the structure and leads to a linear algebraic system of small size. For this reason, the modal method is frequently used in several applications of fluid–structure interaction problems such as coupling between elastic plates and acoustical cavities,[13–15] the study of acoustic comfort in automobile passenger compartments,[16–18] and other academic applications.[19,20]

The modal method consists of representing the displacement w over the modal basis of the structure and the internal pressure p_1 over of the modes of the internal cavity,

$$w=\sum_{i=1}^{m} \delta_i W_i, \tag{30}$$

$$p_1=\sum_{j=1}^{n} \psi_j P_{1,j}, \tag{31}$$

where W_i and $P_{1,j}$ are respectively the ith structural mode of the structure and the jth cavity mode of the internal fluid and δ_i and ψ_j are the generalized coordinates.

Thus the system (29) reduces to

$$\begin{bmatrix} K_r-\omega^2 M_r & -C_r & \left(\hat{B}_r+\dfrac{\hat{C}_r}{2}\right) \\[2mm] -C_r^t & \dfrac{H_r}{\rho_1\omega^2}-\dfrac{Q_r}{\rho_1 c^2} & 0 \\[2mm] \left(\hat{B}_r+\dfrac{\hat{C}_r}{2}\right)^t & 0 & \dfrac{D}{\rho_2\omega^2} \end{bmatrix} \begin{Bmatrix} \delta \\ \psi \\ P_2 \end{Bmatrix} = \begin{Bmatrix} F_r \\ 0 \\ 0 \end{Bmatrix}, \tag{32}$$

where C_r is the coupling matrix projected on both the structure and the fluid modes and $\hat{B}_r$, and $\hat{C}_r$ are the coupling matrices projected only on the structure modes.

The problem of fluid–structure coupling with incompatible meshes consists of computing the reduced coupling operator C_r, $\hat{C}_r$, and $\hat{B}_r$. Here, we restrict our presentation to the computation of the matrix C_r.
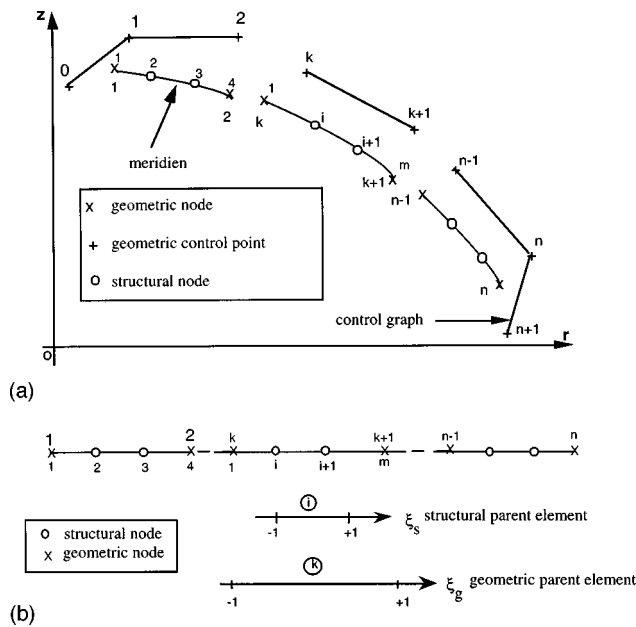
FIG. 3. The meridian and its control graph (physical and parametric meshes).

FIG. 4. A geometric element and its virtual control graph.

The component $C_r(i,j)$ of the reduced coupling operator C_r is given by

$$C_r(i,j) = \int_{S_1} w^i . p^j . dS_1, \tag{33}$$

where w^i represents the normal component of the displacement corresponding to the ith structural mode and p^j represents the boundary value of the pressure corresponding to the jth cavity mode. The reduced coupling operator is then computed using B-spline interpolation.

III. B-SPLINE INTERPOLATION: FINITE ELEMENT APPROACH

The choice of B-spline interpolation[21–27] is motivated by the following properties:

(i)   locality of the interpolation,
(ii)   continuity $C^{3'}$ inside an element, and C^2 between elements, and
(iii) a new discritization approach of the shell surface by super-elements (a set of elements).

The interpolation procedures are explained in detail in Refs. 25 and 28 for the case of shells of revolution and in Refs. 25, 27, and 29 for the case of shells of arbitrary shapes.

For shells of revolution, the meridian is divided into one or more several super-elements which are further divided into several geometric sections. Each section represents a geometric element and each subsection represents a structural/fluid element (Fig. 3).

The finite element B-spline approach allows us to interpolate geometric (resp. physical) variables f over one geometric (resp. structural or fluid) element i using the following equation:

$$f_i(\xi) = \sum_{k=i-1}^{i+2} \alpha_k \varphi_k(\xi); \quad \xi \in [-1, +1], \tag{34}$$

where α_k for $k = i-1$ to $i+2$ are the control variables of the function f over the element or subelement i and φ_k is a basic B-spline function.[21,23] These variables satisfy the following interpolation conditions on the nodes of each element,[25]

$$f_i(-1) = f_i, \quad i = 1,2,...,n-1,$$
$$f_{n-1}(1) = f_n, \tag{35}$$

when n is the number of geometric nodes.

To solve for control variables, two additional conditions should by defined at the ends of a super-element. These could be computed by either imposing zero second parametric derivatives (natural B-splines),

$$f_1^{(2)}(-1) = 0, \quad f_{n-1}^{(2)}(+1) = 0 \tag{36}$$

for C^0 interpolation, or by imposing first parametric derivatives,

$$f_1^{(1)}(-1) = \tfrac{1}{4}(\alpha_2 - \alpha_1),$$
$$f_{n-1}^{(1)}(+1) = \tfrac{1}{4}(\alpha_{n+1} - \alpha_{n-1}) \tag{37}$$

for C^1 interpolation between super-elements.

For shells of arbitrary shapes, the surface is divided into one or several super-elements which is in turn divided into several geometric elements. Each square, defined by the tensor product of two sections, represents a geometric element, while a subsquare represents fluid/structure element (Fig. 4).

Two-dimensional finite element B-spline approach allows us to interpolate geometric (resp. physical) variables F over one geometric (resp. structural or fluid) element (i,j) using the following equation,

$$f_{i,j}(\xi,\eta) = \sum_{k=i-1}^{i+2}\sum_{l=j-1}^{j+2} \alpha_{k,l}\varphi_k(\xi)\varphi_1(\eta);$$

$$(\xi,\eta) \in [-1,+1]\times[-1,+1], \tag{38}$$

where $\alpha_{k,l}$ for $k=i-1$ to $i+2$ and $l=j-1$ to $j+2$ are the control variables of the function F over the element or subelement (i,j). These variables satisfy the interpolation conditions on the nodes of each element. In mathematical terms, these conditions consist of determining the set $\mathcal{P}$ of poles,

$$\mathcal{P}=\{\alpha_{i,j};\ i=0,...,m+1;\ j=0,...,n+1\}, \tag{39}$$

from the data of the set $\mathcal{F}$ of interpolated values,

$$\mathcal{F}=\{f_{i,j};\ i=1,...,m;\ j=1,...,n\}. \tag{40}$$

There are $m\times n$ data for $(m+2)\times(n+2)$ unknowns. In order to have a closed problem, edge conditions are necessary. Two types of conditions exist: the multiple-point method which consists of multiplying the edge control points[25] and the virtual point method.[25,27] It should be noted that the first method has the disadvantage of producing edge squares having fairly small dimensions as compared to the internal squares. Consequently, the virtual point method has been adopted for the case of arbitrary shapes with zero conditions at the edges of super-element of the second parametric derivatives (natural B-splines).

IV. COMPUTATION OF THE REDUCED MATRIX

The variational formulation (21) naturally calls out for an integral on the fluid–structure interaction surface regardless of the studied problem (internal, external, or internal/external at the same time). The numerical treatment of this integral with incompatible meshes is formulated in a different way than when using a Lagrange multiplier as described previously. The problem is difficult especially for the case of three-dimensional structures.

A modal method is used to compute the mode shapes of both the structure and the fluid. Their domains are discritized by finite elements via two-mesh schemes which can be different (structure:mesh 1, fluid:mesh 2).

The problem then reduces to the computation of the integral

$$C_r(i,j) = \int_{S_1} w^i.p^j.\,dS_1.$$

In order to compute this integral, it is necessary to reproduce the structural mode w^i and the acoustic mode p^j over a common geometric mesh. It is the shell itself which is modeled using B-spline interpolation from few modes (mesh 3). A new structure B-spline mesh (mesh 1b) and a new fluid B-spline mesh (mesh 2b) are then deduced from mesh 3 by introducing two elementary multiplicity factors. These factors are computed subsequently according to convergence criterion. The latter is based on the relative error between
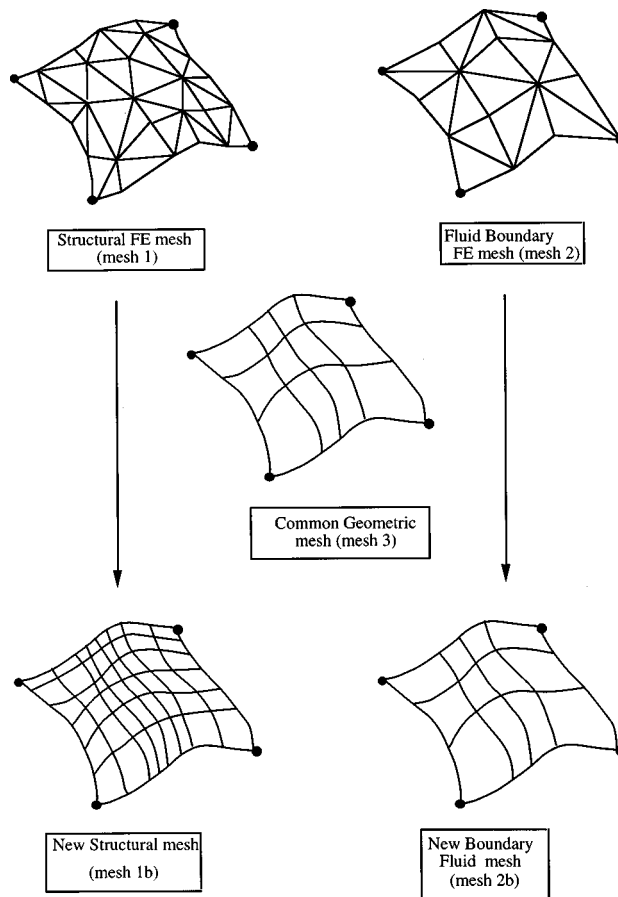
FIG. 5. Extrapolation algorithm, different meshes.

two successive iterations on the "length" of the mode shape in the case of axisymmetric shells, and on the "surface" of the mode shape in the case of shells of arbitrary shapes. The multiplicity factors could be computed automatically in order to satisfy the following criterion:

$$\frac{|S_{l-1}^j - S_l^j|}{S_{l-1}^j} < \epsilon, \tag{41}$$

where ϵ is a given relative error and S_l^j is the "length" for axisymmetric shell or the "surface" for shell of arbitrary shapes corresponding to the mode j and iteration l,

$$S_l^j = \int_s \sqrt{1+\left(\frac{\partial \tilde{f}_j}{\partial s}\right)^2}\,ds, \tag{42}$$

$$S_l^j = \int_S \sqrt{1+\left(\frac{\partial \tilde{f}_j}{\partial s}\right)^2}\cdot\sqrt{1+\left(\frac{\partial \tilde{f}_j}{\partial t}\right)^2}\,dS, \tag{43}$$

where t and s are the local parametric coordinates over the modal surface. The function $\tilde{f}$ holds for the normal displacement or for the pressure.

The convergence curves derived from (41) are monotonic. This allows us to have only one multiplicity coefficient for a given ϵ.[30] This is due to the local nature of the criterion which describes the variation of the "length" or the "surface" defined on the common geometry.

After the automatic construction of the structure submesh (1b) and the fluid submesh (2b), extrapolation algo-

rithms have been developed to obtain the values of the structural displacement and the fluid pressure over the two new submeshes (Fig. 5).

These algorithms must solve the following mathematical problem:

Let $\mathcal{M}$ and $\tilde{\mathcal{M}}$ be two different but neighboring clusters of nodes:

$$\mathcal{M}=\{(N_i); \quad i=1,2,...,n\}$$

$$=(\text{nodes of the initial finite element mesh}),$$

$$\tilde{\mathcal{M}}=\{(N_i); \quad j=1,2,...,\tilde{n}\}$$

$$=(\text{nodes of the new submeshes 1b or 2b}).$$

The problem consists of the extrapolation of the displacement vector from mesh 1 to submesh 1b and the pressure from mesh 2 to submesh 2(b), respectively.

Several algorithms have been developed for shells of revolution[28,30] and for shells of arbitrary shapes.[29,30]

An extrapolation algorithm is presented here for the case of shells of arbitrary shapes.

For each node i of the B-spline submesh the following steps should be carried out:

(1) calculating the distances between the node i to all the other nodes of the initial mesh;
(2) ordering these nodes with respect to increasing distances;
(3) choosing the nearest 3 nodes k, l, and m to the node i; and
(4) interpolating the value of the function at node i using values at nodes k, l, and m.

Two cases could appear:

(i) If the three nodes are lined up, a linear interpolation using an average weighted by the distances is used, referring to the two nearest nodes k and l,

$$\tilde{F}_i=\frac{F_k d_{i,l}+F_l d_{i,k}}{d_{i,l}+d_{i,k}}, \tag{44}$$

where $d_{i,l}$ is the distance between the nodes i and l, and F_k is the value of the function F at the node k.

(ii) If the three nodes are not lined up, a projection of the node i on the plan P formed by these three nodes is done. Let h be the result of this projection. Two other cases can arise:

If h is merged with the node i, a linear interpolation is done using an average weighted by the distances, referring to the nearest two nodes k and l [Eq. (44)].

If h is not merged with the node i, the center of gravity g of the three nodes is calculated, and a linear interpolation weighted by the volumes is used:

$$\tilde{F}_i=\frac{F_l V_l+F_k V_k+F_m V_m}{V_l+V_k+V_m}, \tag{45}$$

where V_l is the volume of the tetrahedron which tops are the nodes g, m, k, i, V_k is the volume of the tetrahedron which tops are the nodes g, m, l, i, and V_m is the volume of the tetrahedron which tops are the nodes g, l, k, i.

Now that the modes of the structure and fluid have been defined over the two submeshes (1b) and (2b), the coupling

operator C_r can be computed. For the case of shells of revolution, B-spline interpolation of functions of one parameter[28] is used [Eq. (34)] and for the case of shells of arbitrary shapes the tensor product B-spline interpolation[27,29] is used [Eq. (38)].

For the computation of the integral

$$C_r(i,j)=\int_{S_1} w^i.p^j.\,dS_1 \tag{46}$$

it is necessary to evaluate the elementary vector dS_1, the displacement and the pressure over a same common geometric mesh (mesh 3).

The geometrical coordinates x, y, and z of a geometric element ig, jg, are given by

$$x_{ig,jg}(\xi_g,\eta_g)=\langle N(\xi_g)\rangle[\chi]^t[X_{ig,jg}][\chi]\{N(\eta_g)\}, \tag{47}$$

$$y_{ig,jg}(\xi_g,\eta_g)=\langle N(\xi_g)\rangle[\chi]^t[Y_{ig,jg}][\chi]\{N(\eta_g)\}, \tag{48}$$

$$z_{ig,jg}(\xi_g,\eta_g)=\langle N(\xi_g)\rangle[\chi]^t[Z_{ig,jg}][\chi]\{N(\eta_g)\}. \tag{49}$$

The matrices $[X_{ig,jg}]$, $[Y_{ig,jg}]$, and $[Z_{ig,jg}]$, which are the matrices of coordinates of the control nodes of the (ig,jg)th geometric element, are defined by

$$[X_{ig,jg}]=\begin{bmatrix} X_{ig-1,jg-1} & X_{ig-1,jg} & X_{ig-1,jg+1} & X_{ig-1,jg+2} \\ X_{ig,jg-1} & X_{ig,jg} & X_{ig,jg+1} & X_{ig,jg+2} \\ X_{ig+1,jg-1} & X_{ig+1,jg} & X_{ig+1,jg+1} & X_{ig+1,jg+2} \\ X_{ig+2,jg-1} & X_{ig+2,jg} & X_{ig+2,jg+1} & X_{ig+2,jg+2} \end{bmatrix}, \tag{50}$$

$X_{ig,jg}$, $Y_{ig,jg}$, and $Z_{ig,jg}$ are the coordinates of the control node $V_{ig,jg}$,

$$[\chi]=\frac{1}{48}\begin{bmatrix} -1 & 3 & -3 & 1 \\ 3 & -3 & -3 & 3 \\ -3 & -15 & 15 & 3 \\ 1 & 23 & 23 & 1 \end{bmatrix}, \tag{51}$$

Here $(\xi_g,\eta_g)\in[-1,+1]\times[-1,+1]$ are local geometric parameters,

$$\langle N(\xi_g)\rangle=\langle \xi_g^3 \quad \xi_g^2 \quad \xi_g \quad 1\rangle \tag{52}$$

and $\{N(\eta_g)\}$ has the same expression of $\langle N(\xi_g)\rangle^t$.

The B-spline functions are used again to interpolate the physical variables (displacement and pressure) corresponding to the structural and fluid mode shapes.

The displacement of the (is,js)th element for the ith structure mode is given by

$$w^i_{is,js}=\langle N(\xi_s)\rangle[\chi]^t[W^i_{is,js}][\chi]\{N(\eta_s)\}; \tag{53}$$

$N(\xi_s)$ is the same as $N(\xi_g)$ by replacing g by s, $[W^i_{is,js}]$ has the same expression as $[X_{ig,jg}]$, and $W^i_{is,js}$ is the (is,js)th control variable of the structural displacement corresponding to the ith structure mode.

The pressure of the (if,jf)th fluid element for the jth fluid mode is given by

$$p^j_{if,jf}=\langle N(\xi_f)\rangle[\chi]^t[P^j_{if,jf}][\chi]\{N(\eta_f)\}; \tag{54}$$

$N(\xi_f)$ is the same as $N(\xi_g)$ by replacing g by f, $[P^j_{if,jf}]$ has the same expression as $[X_{ig,jg}]$ by replacing X by W and g

by s, and $P^j_{if,jf}$ is the (if, jf)th control variable of the pressure layout on the fluid–structure interaction surface corresponding to the jth fluid mode.

The summation over all super-elements leads to

$$C_r(i,j) = \sum_{isg=1}^{Nsegt} \left\{ \int_{isg} w^i \cdot p^j \cdot dS \right\}, \qquad (55)$$

where $Nsegt$ denotes the total number of super elements.

For each super-element, the sum must be done over all the geometrical elements. Because each superelement isg is made of $M_{isg} \times N_{isg}$ nodes, the integral will be

$$C_r(i,j) = \sum_{isg=1}^{Nsegt} \left\{ \sum_{ig=1}^{Misgt} \sum_{jg=1}^{Nisg} \left(\int_{ig,jg} w^i_{ig,jg} \cdot p^j_{ig,jg} \cdot dS_{ig,jg} \right) \right\}. \qquad (56)$$

The summation and the numerical integration are done either on a structure or a fluid element according to the corresponding meshes. Supposing that the structural mesh is the finest one, the (i,j)th term of the reduced coupling matrix can be written as

$$C_r(i,j) = \sum_{isg=1}^{Nsegt} \left\{ \sum_{ig=1}^{Misg} \sum_{jg=1}^{Nisg} \left(\sum_{is=1}^{Ms} \sum_{js=1}^{Ms} I_{is,js} \right) \right\}, \qquad (57)$$

where

$$I_{is,js} = \int_{is,js} w^i_{is,js} p^j_{if,jf} \, dS_{ig,jg}. \qquad (58)$$

This integral can also be written using local coordinates:

$$I_{is,js} = \frac{1}{M_s^2} \int_{-1}^{+1} \int_{-1}^{+1} w^i_{is,js}(\xi_s, \eta_s) p^j_{if,jf}(\xi_f, \eta_f)$$
$$\times J_{ig,jg}(\xi_g, \eta_g) d\xi_s \, d\eta_s, \qquad (59)$$

where

$$J_{ig,jg}(\xi_g, \eta_g) = \det \left(\left\{ \begin{array}{c} \frac{\partial x_{ig,jg}}{\partial \xi_g} \\ \frac{\partial y_{ig,jg}}{\partial \xi_g} \\ \frac{\partial z_{ig,jg}}{\partial \xi_g} \end{array} \right\} \times \left\{ \begin{array}{c} \frac{\partial x_{ig,jg}}{\partial \eta_g} \\ \frac{\partial y_{ig,jg}}{\partial \eta_g} \\ \frac{\partial z_{ig,jg}}{\partial \eta_g} \end{array} \right\} \right) \qquad (60)$$

is the determinant of the Jacobean matrix corresponding to the geometrical application and M_s is the multiplicity factor of the B-spline structure mesh.

Structural and fluid modes are now continuous over the geometric common mesh. This solves completely the difficulties induced by incompatible meshes.

V. VALIDATION AND EVALUATION OF THE PERFORMANCE OF THE PROPOSED METHOD

A. Shells of revolution (2D problems)

A steel spherical shell of radius "a" filled with water (considered as compressible fluid) and excited with an external pressure $P_2(\theta) = \frac{1}{2}(3\cos^2\theta - 1)$. We intend to compute the pressure over the shell surface, $20\log(P)$, where P is the
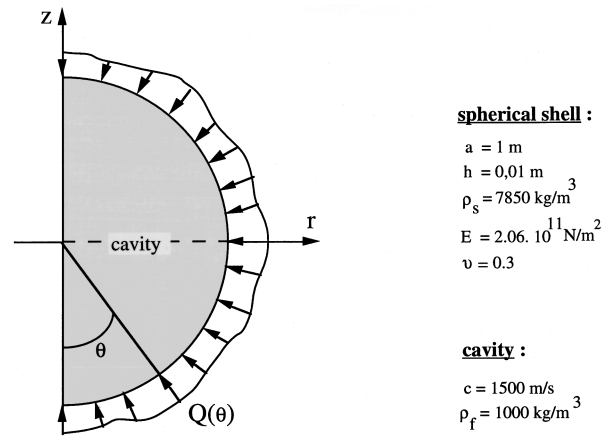
FIG. 6. Description of the spherical shell and its excitation.

pressure averaged over all nodes of the boundary of the fluid, and the vibrational energy, $10\log(E_v)$, where E_v is the sum of kinetic and deformation energies. The frequency range (0–5000 Hz) is considered. This corresponds to the dimensionless wave number range $ka = 0$ to 20 (see Fig. 6).

In order to compute the above physical quantities, the meridian of the spherical shell is discritized into 88 axisymmetric finite elements with four degrees of freedom (DOF) per node (radial, vertical, and circular displacements: U_r, U_z, U_θ, and one rotation around the curvilinear abscissa $\partial w/\partial s$ where w is the normal displacement).

As a first step the fluid cavity is discritized into axisymmetric linear triangular elements, with the constraint that at the boundary the fluid elements coincide with the structural elements. The number of elements along the vertical side is equal to 88 [Fig. 7(a)].

For the computation of the coupling operator, a geometric B-spline mesh (mesh 3) is obtained using nine nodes equally spaced on the meridian of the spherical shell. The results are compared to those using a boundary element method (BEM).[31]

Figure 8 shows that the results using the proposed method in the case of compatible meshes (SPL-COM) are in
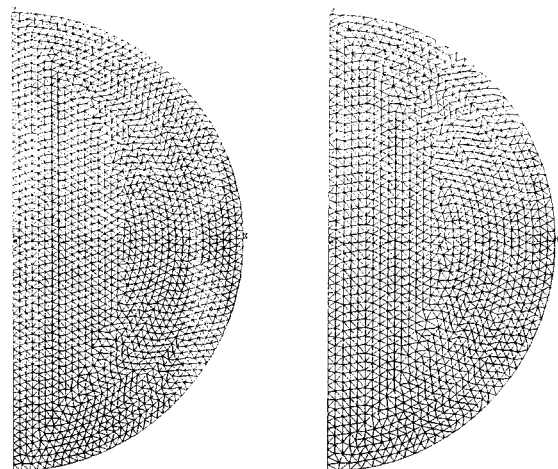
FIG. 7. Compatible and incompatible fluid meshes for spherical cavity.
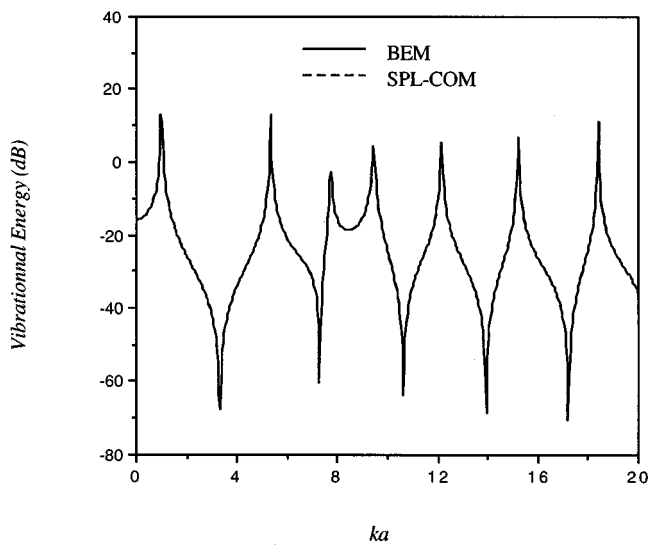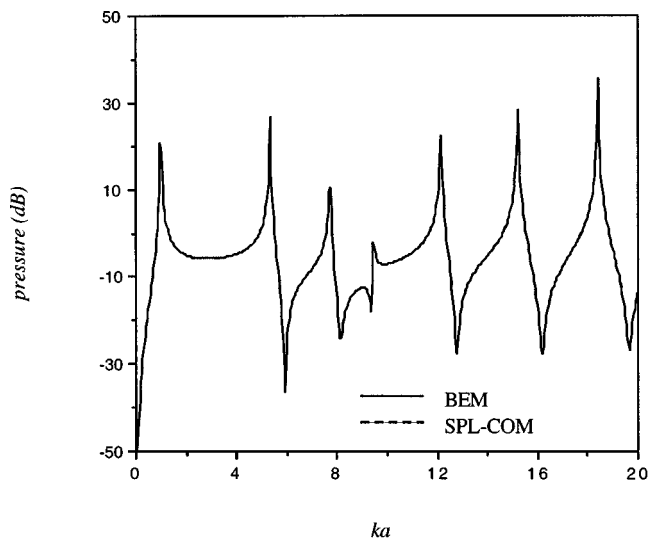
FIG. 8. Comparison between results of spherical shell obtained by the proposed method with compatible meshes (SPL-COM) and those obtained by BEM.

FIG. 9. Comparison between results of spherical shell obtained by the proposed method with incompatible meshes (SPL-INC) and those obtained by BEM.

very good agreement with those resulting from BEM.[31] This validates the proposed B-spline coupling operator procedure for compatible meshes for a 2D problem.

In a second step, an incompatible fluid mesh is used for the cavity by taking 64 elements over the meridian and 64 elements along the vertical side [Fig. 7(b)]. Figure 9 shows the very good agreement between the results using the proposed method in the case of incompatible meshes (SPL-INC) and those obtained by BEM.[31]

In order to study the performance of the proposed technique, the number of boundary nodes of the B-spline cavity mesh (mesh 2b) is fixed to 65 while the number of nodes of the B-spline structural mesh (mesh 1b) is decreased from 89 to 9. The performance of the method is thus evaluated by computing the relative error curves with respect to the results obtained using incompatible meshes with 89 nodes for the mesh 1b and 65 nodes for the mesh 2b. This evaluation is made to corresponding to low, medium, and high frequencies
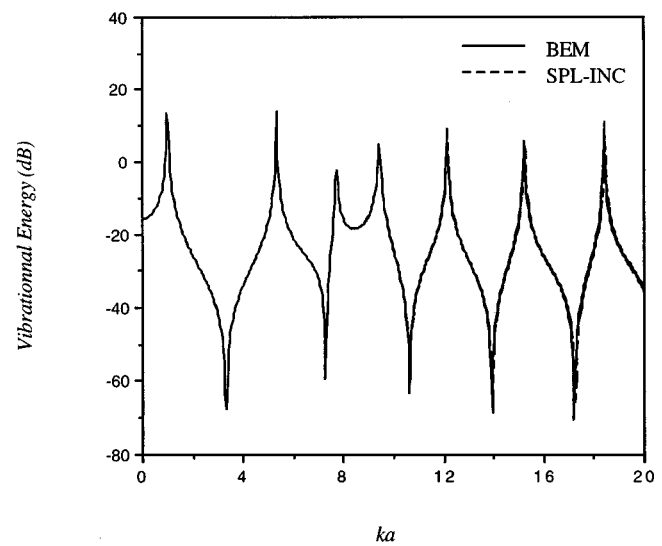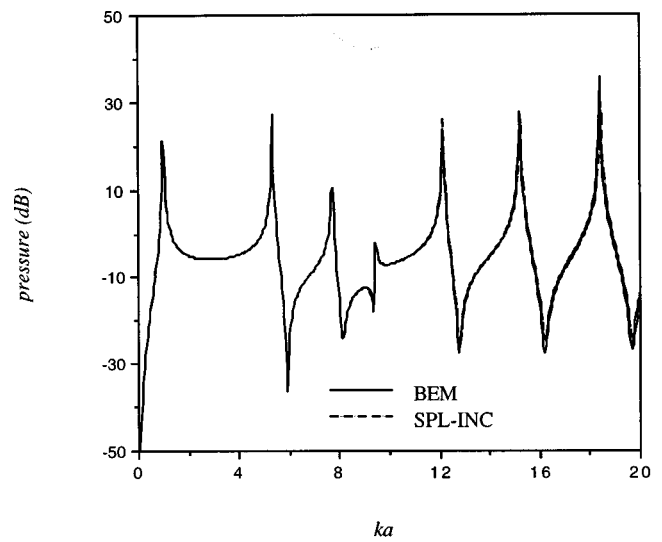
(100, 1000, and 4000 Hz, which corresponds to the following values of ka: 0.42, 4.2, and 16.75). Results given in Fig. 10 show that the maximum error obtained with a mesh 1b of 9 nodes and mesh 2b of 65 nodes is about 0.8%. From this first evaluation, 9 structural nodes (mesh 1b) are adequately chosen to yield sufficiently low errors. Having the number of structural nodes fixed to 9, the number of fluid nodes (mesh 2b) is then decreased from 65 to 9. The error curves are given by Fig. 11. Despite some flips, global convergence tendency is observed with errors less than 1.5%. It should be noted that the flips in Fig. 11 are due to errors induced by modifying both the structure (9 instead to 89) and the fluid number of nodes (from 65 to 9).

This very simple case shows the high accuracy of the proposed method to solve 2D coupled problems. It has been shown that the results of the B-spline coupling operator procedure can be attained with a minimum number of nine control nodes that could be used both for the computation of the

convergence curve (ka=0.42)

convergence curve (ka=4.20)

convergence curve (ka=16.75)
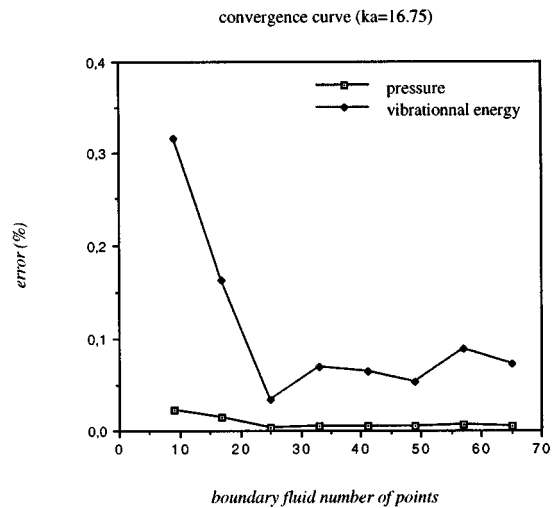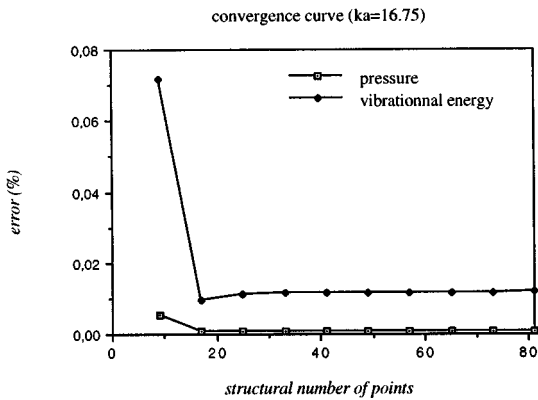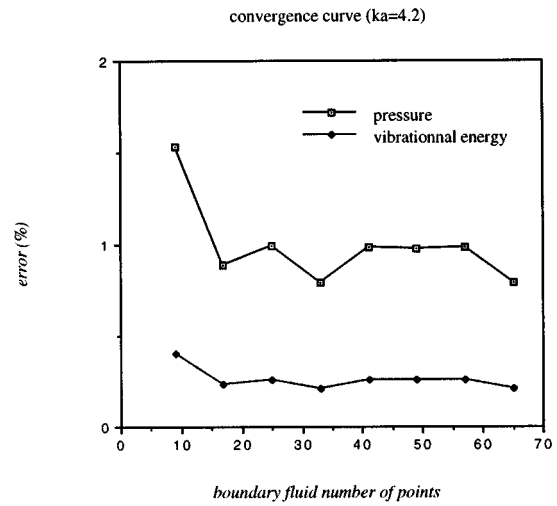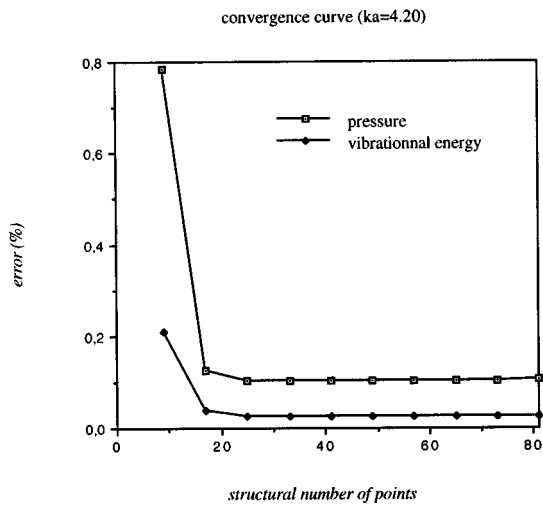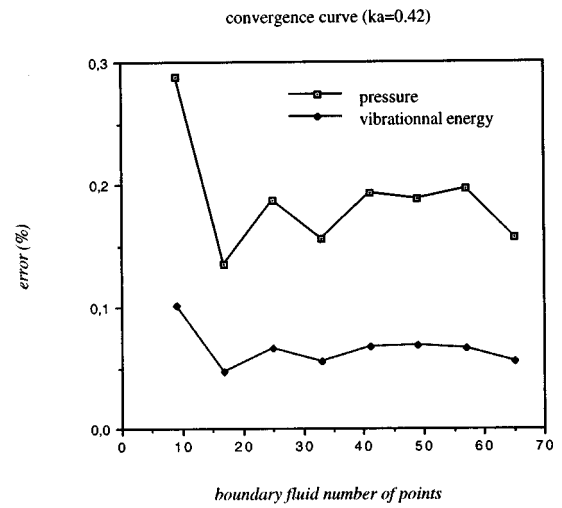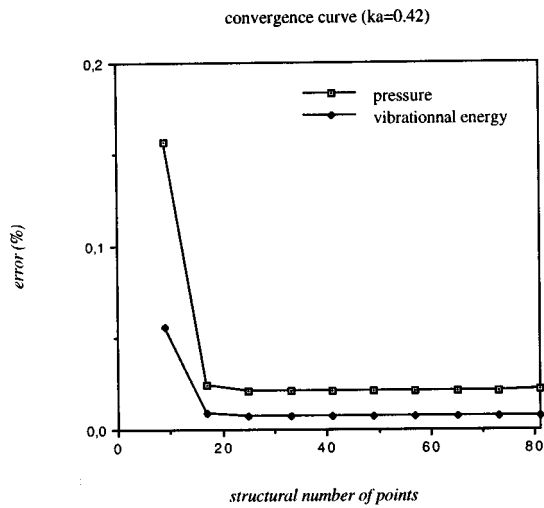
FIG. 10. Convergence error curves with a B-spline fluid mesh of 65 points.

coupling operators and the representation of the mechanical excitation $P_2(\theta)$.

B. Shells of arbitrary shapes (3D problems)

1. Plate–cavity interaction

In this section, the frequency response of a cubic cavity backed by an elastic plate[13–15] is studied. This plate is excited by a constant pressure $P_{ext} = 2$ Pa (Fig. 12). The frequency range (0–1000 Hz) is considered. This corresponds

convergence curve (ka=0.42)

convergence curve (ka=4.2)

convergence curve (ka=16.75)

FIG. 11. Convergence error curves with a B-spline structural mesh of nine points.

to the dimensionless wave number range $ka = 0$ to 3.5. We intend to compute the following physical quantities:

(i)   the transmission loss factor: $TL = 20 \log_{10}(P_{ext}/P_{bot})$, where P_{bot} is the internal pressure on the bottom of the cavity; and
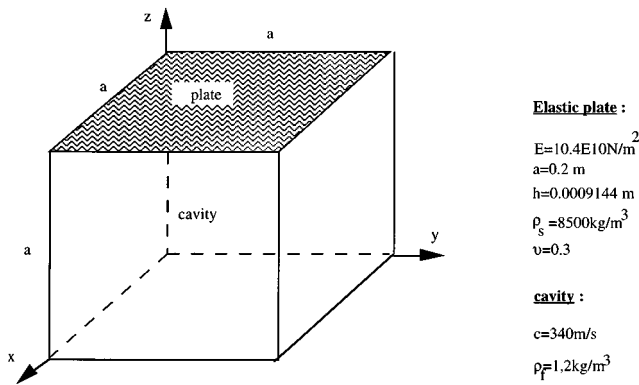
FIG. 12. Description of the plate–cavity coupling system.

Elastic plate :

$E = 10.4 \text{E} 10 \text{N/m}^2$
$a = 0.2$ m
$h = 0.0009144$ m
$\rho_s = 8500 \text{kg/m}^3$
$\upsilon = 0.3$

cavity :

$c = 340 \text{m/s}$
$\rho_f = 1,2 \text{kg/m}^3$

FIG. 13. Comparison between results of the plate–cavity system obtained by the proposed method with compatible meshes (SPL-COM) and those obtained by BEM.

(ii) the dimensionless displacement $W = 20 \log_{10}(W_c/a)$, where W_c is the central displacement of the elastic plate.

A structural finite element mesh of 14×14 elements of four nodes and three DOF per node (displacement w and the rotations θ_x and θ_y) has been considered. The cavity is meshed, in a first step, by a solid mesh of $14 \times 14 \times 14$ elements of eight nodes and one DOF per node for the compatible case, and, in a second step, by a solid mesh of $6 \times 6 \times 6$ elements of eight nodes and one DOF per node for the incompatible case.

For the computation of the coupling operator, a geometric B-spline mesh (mesh 3) is obtained using a cluster of 5×5 nodes.

The results are compared to those using a boundary element method (BEM)[15,32] which used compatible meshes and was validated by analytical results.

Figure 13 shows that the results using the proposed method in the case of compatible meshes (SPL-COM) are in very good agreement with those resulting from BEM.[15,32]

Figure 14 shows, once again, that the results using the proposed method in the case of incompatible meshes (SPL-INC) are in very good agreement with those resulting from BEM.[15,32]

This example validates the coupling between a 2-D structure (plate) and a 3D cavity.[33]

2. Experimental car compartment model

This example extracted from Refs. 34, 35 corresponds to a simplified model of a car compartment. This model is made of nine aluminum panels having 3-mm thickness and two rigid lateral panels closing an air cavity. The coupled system is harmonically excited by a point vertical force of 1 N applied to node B in the frequency range 50 to 200 Hz (Fig. 15). We intend to compute the transfer function at node B,

$$\Gamma = 20 \log_{10}\left(\frac{\gamma}{F}\right), \tag{61}$$

where γ is the acceleration at node B and F is the unit force at node B.

In order to compute the transfer function, the structure is discretized by 360 3D finite elements with four nodes and six DOF per node (three displacements and three rotations).
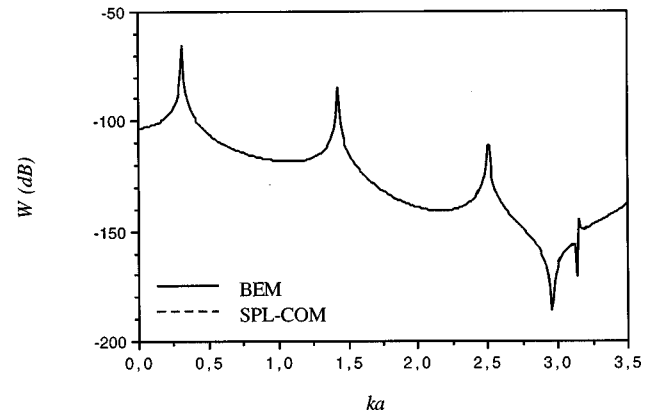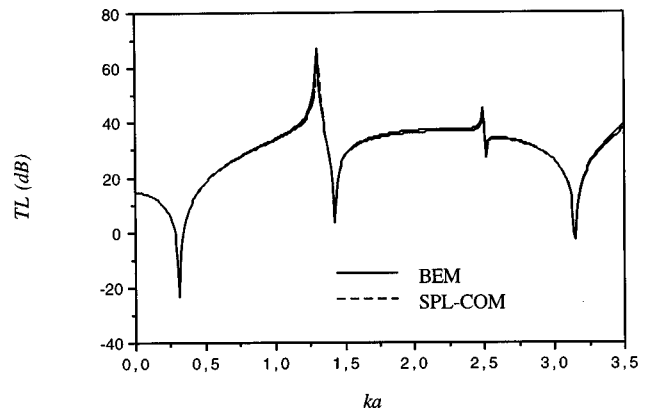
The cavity is discretized by solid finite elements of six and eight nodes and with one DOF per node. The meshes of the structure and of the cavity are incompatibles (Fig. 16).

For the computation of the coupling operator, a geometric B-spline mesh (mesh 3) is obtained using nine super-elements. Each super-element is discretized using 5×5 equidistant nodes.

In Refs. 34 and 35, the characteristics of the material used on the two lateral panels are not given and the problem presented in these references is not coupled. The results obtained by the proposed method are thus compared with those obtained by I-DEAS vibroacoustics[32] package using a boundary element method. We used 884 boundary elements to model the internal fluid and 384 3D finite elements with four nodes and six DOF per node for the structural mesh. These two meshes are compatibles.

Figure 17 shows a good agreement between the results obtained by the present method (SPL-IN) and those obtained by I-DEAS vibro-acoustics for all frequencies except in the narrow range located around 170 Hz. In fact, a high coupling phenomenon is present in this band due to the fact that two modes of the structure and of the fluid are fairly close (174 and 171 Hz, respectively). It is thus necessary to refine the computation of the coupling operator in this band. This can be done by reducing the mesh size of the fluid (the mesh size
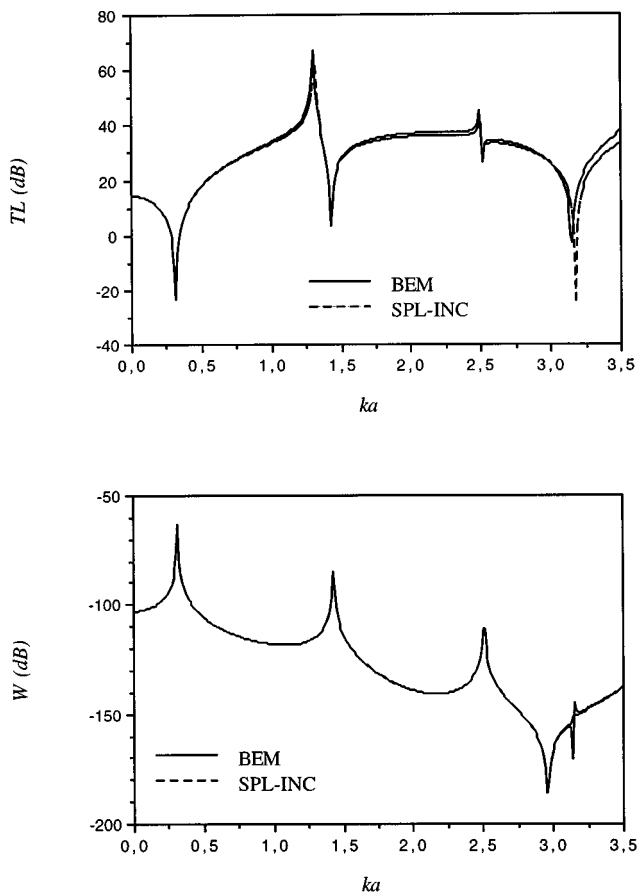
FIG. 14. Comparison between results of the plate–cavity system obtained by the proposed method with incompatible meshes (SPL-INC) and those obtained by BEM.

of the structure is the same in the proposed method and in I-DEAS).

This example confirms the validity of the method for the incompatible meshes in the case of 3-D coupled problems,[36] especially in the case of complex shape shells.

VI. CONCLUSION

An original numerical method for vibro-acoustic problems with incompatible finite element meshes is presented. This method uses a modal approach which has the advantage of computing separately structural and acoustical mode shapes using different meshes for the structure and for the fluid. The proposed method uses a uniform cubic B-spline interpolation which has the following advantages: (a) locality
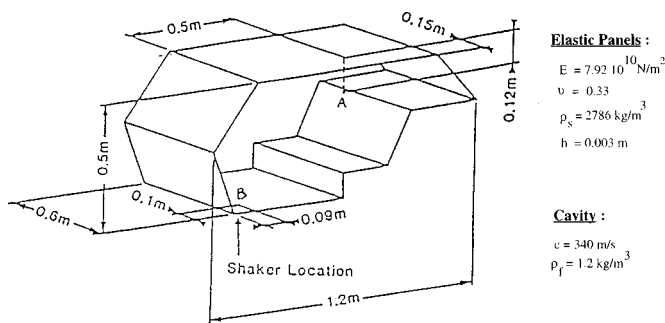
FIG. 15. Description of the car compartment model.

structural mesh

fluid mesh
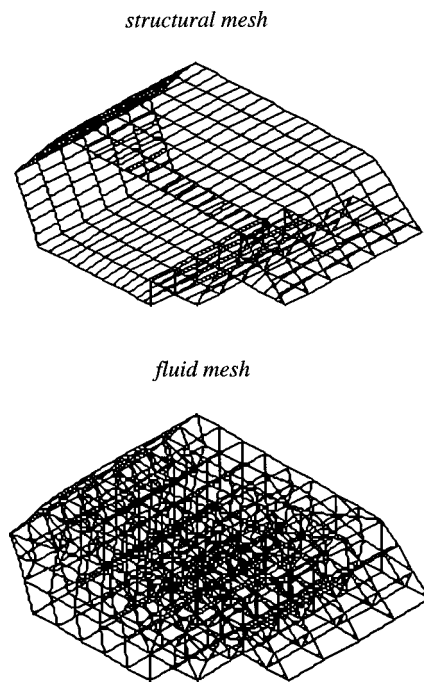
FIG. 16. Fluid and structure incompatible meshes for the car compartment model.

of the interpolation, (b) continuity C^3 inside elements and C^2 between elements, and (c) a new discritization approach of the shell surface by super-elements which allows vibro-acoustic analyses of arbitrary shapes structures.

The method is illustrated by solving 2-D and 3-D coupled problems corresponding to shells of revolution, plates, and 3-D shells. The 2-D case study concerned a spherical shell filled with water and excited with an external pressure. In this case, the mean square value of the pressure over the shell surface and the averaged vibrational energy have been computed in the 0–5000-Hz frequency range. The results obtained by the present method are in good agreement with those obtained by the boundary element method. This simple case shows the high accuracy of the proposed method for solving 2-D coupled problems. It has been shown that the results can be attained with a minimum number of nine control nodes which could be used both for the computation of the coupled operators and the representation of the mechanical excitation.

To illustrate the 3-D coupled problem, two case studies were considered. The first dealt with elastic plate–cubic cav-
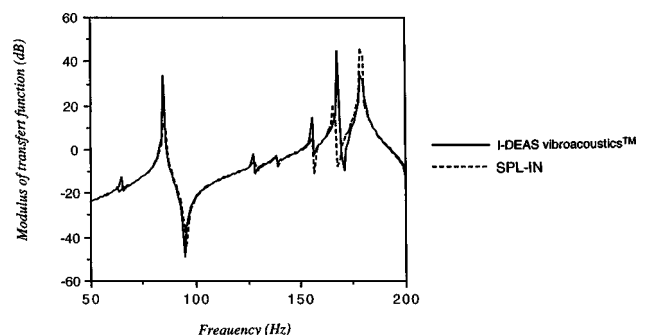
FIG. 17. Comparison between results of the car compartment model obtained by the proposed method with incompatible meshes (SPL-INC) and those obtained by I-DEAS vibroacoustics.

ity interaction problem with constant pressure applied on the plate. In this particular case the transmission loss factor and the dimensionless displacement over the plate were obtained. Here also, the results obtained by the proposed method are in good agreement with those obtained by analytical computations. This example validates the coupling between 2-D structure (plate) and a 3-D cavity. The second 3-D case study dealt with a simplified car compartment model as excited by a vertical force point. The corresponding transfer function between acceleration and force at the excitation point has been derived. The results obtained by the proposed method and by I-DEAS vibroacoustics™ code are in good agreement, confirming the validity of the method in the case of complex shape shells.

In perspective and in continuation of the present work, the focus of future works will be oriented towards the following subject areas: (i) extension of the method to mechanical coupling problems as a whole, namely to the method of subdomains with incompatible meshes, (ii) use of nonuniform B-spline functions for the purpose of eliminating the constraint of the regularity of the B-spline mesh size, and (iii) grouping all these developments in one computation code for solving problems of fluid–structure coupling using incompatible meshes.

ACKNOWLEDGMENTS

[1] C. Lesueur, *Rayonnement Acoustique des Structures* (Interactions fluide-structure), Collection de la DER, EDF (Eyrolles, 1988) (in French).

[2] J. P. Morand and R. Ohayon, *Fluid-structure Interactions* (Wiley, New York, 1995).

[3] A. Adobes, ''pour le calcul des intégrales des produits de fonctions de forme,'' rapport interne, DER, EDF (1989) (in French).

[4] M. Guerich, ''Calcul de l'opérateur de couplage fluide-structure pour des maillages incompatibles par la méthode du P.P.C.M, DEA, ENIT, TUNISIE, 1990 (similar to the Master's) (in French).

[5] P. Lamary, ''Une méthode de couplage élasto-acoustique par opérateur de grille frontière pour discrétisation acoustique et structure non coincidents, Doct. Mécanique Appliquée, Acoustique et Matériaux, Compiègne, 1991 (in French).

[6] J. P. Coyette and Y. D. Pelerin, ''An efficient coupling procedure for handling large size interior structural-acoustic problems,'' Proceeding of the ISMA19: Tools for Noise and Vibration Analysis, Leuven, Belgium, September 1994, Vol. 2, pp. 729–738.

[7] C. Farhat and F. X. Roux, ''A Method of Finite Element Tearing and Interconnecting and its Parallel Solution algorithm,'' Int. J. Numer. Methods Eng. **32**, 1205–1227 (1991).

[8] C. Farhat and M. Geradin, ''A Hybrid Formulation of a Component Mode Synthesis Method,'' AIAA/ASME/AHS/ASC, Structures, Structural Dynamics and Materials Conference, Dallas, 13–15 April 1992.

[9] C. Farhat and M. Geradin, ''On a Component Mode Synthesis Method and its Application to Incompatible Substructures,'' Comput. Struct. **51**(5), 459–473 (1994).

[10] P. Le Tallec and T. Sassi, ''Domain Decomposition with Nonmatching Grids,'' Cahier des Mathématiques et de la décision, No. 9115, CEREMADE, Univ. Paris Dauphine, 1991.

[11] M. A. Hamdi, Y. Ousset, and G. Verchery, ''A Displacement Method for the Analysis of Vibrations of Coupled Fluide-Structure Systems,'' Int. J. Numer. Methods Eng. **13**, 139–150 (1978).

[12] H. Defosse, M. A. Hamdi, and L. Mebarek, ''Coupling of Integral and Finite Element Methods for Solving Vibroacoustic Problems,'' in Proceeding of International Conference on Acoustic and Dynamic Environment of Space Transportation Systems, Jouy-en-Josas, France, 8–11 February 1994, pp. 55–70.

[13] L. Cheng and C. Lesueur, ''Influence des amortissements sur la réponse vibroacoustique: étude théorique d'une plaque axcitée acoustiquement et couplée à une cavité,'' J. Acoust. **2**, 105–118 (1989) (in French).

[14] J. Pan and D. A. Bies, ''The effect of fluid-structural coupling on sound waves in an enclosure—Theoretical part,'' J. Acoust. Soc. Am. **87**, 691–707 (1990).

[15] R. W. Guy, ''The Transmission of Sound through a Cavity-Backed Finite Plate,'' J. Sound Vib. **27**(2), 207–233 (1972).

[16] S. H. Sung and D. J. Nefske, ''Component Mode Synthesis of a Vehicle Structural-Acoustic System Model,'' AIAA J. **6**, 1021–1026 (1986).

[17] C. Zhang and D. L. Brown, ''Interior noise investigation of a passenger car by means of a mixed vibro-acoustics modal analysis,'' Proceedings of ISMA'19, Tools for Noise and Vibration Analysis, Leuven, Belgium, 12–14 September 1994, Vol. 2, pp. 551–564.

[18] J. A. Wolf, Jr., ''Modal Synthesis for Combined Structural-Acoustic Systems,'' AIAA J. **15**, 743–745 (1977).

[19] J. L. Guyader, ''Analyse modale du comportement vibroacoustique des structures: Mécanisme de réduction du bruit généré,'' Rev. Acoust. **79**, 27–37 (1986) (in French).

[20] J. Pan, ''The forced response of an acoustic-structural coupled system,'' J. Acoust. Soc. Am. **91**, 949–956 (1992).

[21] C. De Boor, ''Package for calculating with B-splines,'' SIAM (Soc. Ind. Appl. Math.) J. Numer. Anal. **14**(3), 441–472 (1977).

[22] W. M. Newman and R. F. Sproul, *Principles of Interactive Computer Graphics*, 2nd ed. (McGraw-Hill, New York, 1979).

[23] C. De Boor, *A Practical Guide to Splines, Applied Mathematical Sciences*, Vol. 27 (Springer-Verlag, New York, 1878) (4th ed., 1987).

[24] W. Cheney and D. Kincaid, *Numerical Mathematics and Computing*, 2nd ed. (Brooks/Cole, Monterey, California, 1985).

[25] B. A. Barsky, ''End conditions and boundary conditions for uniform B-spline curve and surface representations,'' Computers in Industry **3**, 17–29 (1982).

[26] G. Farin, *Curves and Surfaces for Computer Aided Geometric Design—A Practical Guide* (Academic, New York, 1988).

[27] B. A. Barsky and D. P. Greenberg, ''Determining a set of B-spline control vertices to generate an interpolating surface,'' Comput. Graph. Image Process. **14**, 203–226 (1980).

[28] M. Guerich and M. A. Hamdi, ''Computation of fluid-structure coupling operator on incompatible meshes with Uniform Cubic B-spline function,'' in Proceedings of ISMA'19, Tools for Noise and Vibration Analysis, Leuven, Belgium, 12–14 September 1994, Vol. 3, pp. 1177–1188.

[29] M. Guerich and M. A. Hamdi, ''Etude d'un problème couplé plaque-cavité en maillages incompatibles par les fonctions B-splines cubiques uniformes,'' Proceedings of StruCoMe 94, Paris, France, 22–24 November 1994, pp. 131–144 (in French).

[30] M. Guerich, ''Une méthode numérique pour la résolution des problèmes de couplage fluide-structure en maillages incompatibles par les fonctions B-splines Cubiques Uniformes,'' Doc. UTC, Mécanique Appliquée Acoustiques et Matériaux, Compiègne, September 1995 (in French).

[31] Ph. Jean, ''Une méthode variationnelle par équations intégrales pour la résolution numérique des problèmes de couplage élasto-acoustique,'' Doct. Mécanique Appliquée, Acoustique et Matériaux, Compiègne, 1985 (in French).

[32] SDRC, *User Manual of I-DEAS Vibro-acoustics*, April 1995.

[33] M. Guerich and M. A. Hamdi, ''Finite Element Analysis using incompatible meshes with uniform cubic B-Spline functions,'' in Proceedings of the Euro. Noise '95: An international INCE Symposium, Lyon, France, 22–24 March 1995, Vol. 2, pp. 555–560.

[34] Sh. Suzuki, ''Application in the Automotive Industry,'' in *Boundary Element Methods in Acoustics*, edited by R. D. Ciskowski and C. A. Brebbia (Computational Mechanics Publications, Southampton, UK, 1991), Chap. 7, pp. 131–146.

[35] Sh. Suzuki, S. Maruyama, and H. Ido, ''Boundary element analysis of cavity noise problems with complicated boundary conditions,'' J. Sound Vib. **130**(1), 79–91 (1989).

[36] M. Guerich and M. A. Hamdi, ''Modelisation of a fluid structure interaction problem by a finite element method on incompatible meshes (automobile application),'' 3ème Congrès de mécanique, Faculté des Sciences de Tétouan, Maroc, 22–25 April 1997, pp. 415–420.

Repulsion phenomena in the phase-velocity dispersion curves of circumferential waves on elastic cylindrical shells

G. Maze, F. Léon, and J. Ripoche
LAUE URA CNRS 1373, University of Le Havre, 76610 Le Havre, France

H. Überall[a)]
LAUE URA CNRS 1373, University of Le Havre, 76610 Le Havre, France
and Department of Physics, Catholic University of America, Washington, DC 20064

The complex eigenfrequencies of a fluid-immersed evacuated infinite cylindrical shell, when plotted in the complex frequency plane, can be grouped into families corresponding to different types of circumferential waves. The dispersion curves versus frequency of the phase velocities of these circumferential waves are analogous to those of the Lamb waves on a plate $A_0, A_1, \ldots$ and S_0, $S_1, \ldots$, but contain an additional branch reminiscent of the fluid-borne Scholte–Stoneley wave. This branch together with the A_0-analog forms an interacting pair of dispersion curves A_{0+} (upper branch) and A_{0-} (lower branch) which exhibit a repulsion phenomenon near the ambient fluid sound speed. Results of a recent numerical study of this phenomenon are here explained by perturbation theory, showing that during repulsion the wave character gets exchanged so that at frequencies above repulsion A_{0+} is a flexural and A_{0-} a fluid-borne wave, and vice versa below repulsion. © *1999 Acoustical Society of America.* [S0001-4966(99)00902-9]

INTRODUCTION

The dispersion curves for the infinite set of Lamb wave modes of vibration for an elastic plate *in vacuo*, of both symmetric or compressional $(S_0, S_1, S_2, \ldots)$, and antisymmetric or flexural type $(A_0, A_1, A_2, \ldots)$ are well known, see, e.g., Ref. 1. Only the S_0 and A_0 waves exist all the way down to zero frequency, while the higher-order waves exhibit lower-cutoff frequencies. For cylindrical shells, the S_i and A_i $(i \geq 1)$ curves are only slightly changed by the curvature, and this is even true for the S_0 wave, the change depending, of course, on the shell thickness or the ratio b/a of inner-to-outer shell radius. For metal shells with external fluid loading, however, an additional fluid-borne (or Scholte–Stoneley type) circumferential wave arises, which also exists for plates fluid loaded on one side as discussed by Grabowska[2] and Talmant.[3]

This wave, which was called the A wave,[3,4] is coupled to the (flexural) A_0 wave in such a way that their two interacting dispersion curves approach and then repel each other near the coincidence frequency (the frequency where the phase velocities of both these waves are near the sound velocity in the ambient water), rather than crossing each other as their shape away from coincidence would lead us to expect.[5]

Earlier studies of the corresponding acoustic phenomenon, there referred to as a ''bifurcation'' of the dispersion curves, have been carried out empirically for the case of evacuated, water-immersed spherical metal shells.[4,6] We shall find it useful here to adopt the notation of Ref. 6, namely A_{0+} for the upper and A_{0-} for the lower dispersion curve of the interacting pair of fluid-borne and flexural

waves. The repulsion phenomenon of A_{0+} and A_{0-} dispersion curves was studied numerically in previous work[7] for an evacuated, fluid-immersed cylindrical shell, both as a function of frequency and of the inner-to-outer shell radius ratio b/a (shell thickness). We here use a perturbative approach in order to describe, starting from the characteristic equation of the fluid-loaded shell, the shape of the resonance frequency curves plotted versus b/a in the vicinity of the near-crossover point. Our analysis demonstrates the interchange of the physical nature of the curves during this passage. Additionally, we also calculate the backscattering amplitudes of an incident sound wave from the shell, and we exhibit the resonances caused by the flexural, fluid-borne, and compressional waves as they appear in the amplitudes of the backscattered waves as a function of shell thickness. Qualitative explanations for the appearance of these resonance features are provided on the basis of the imaginary parts of the calculated resonance frequencies.

I. CALCULATION OF COMPLEX RESONANCE FREQUENCIES AND DISPERSION CURVES

We shall here investigate the circumferential waves (or ''surface waves'') on evacuated, water-immersed infinite cylindrical stainless steel shells of various wall thicknesses, with density $\rho = 7900 \text{ kg/m}^3$, compressional wave velocity $c_L = 5790 \text{ m/s}$, and shear wave velocity $c_T = 3100 \text{ m/s}$. An earlier calculation,[8] which we shall extend here, has furnished complex resonance frequencies for this object as shown in Fig. 1 (from Refs. 8(a) and (b), plotted in the complex $k_1 a$ plane where k_1 is the incident wave vector and a is the outer cylinder radius. This is done for various ratios b/a from 0.5 to 0.99 as indicated. For each value of b/a, the complex resonance frequencies are seen to fall into three

a)Visiting Professor.
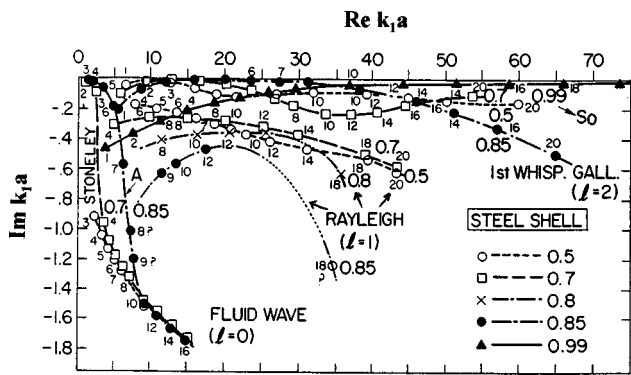
FIG. 1. Complex resonance frequencies plotted in the $k_1 a$ plane for air-filled, water-loaded steel shells of various wall thicknesses. The notation of "Rayleigh" and "Whispering Gallery" waves follows that for a solid cylinder, Ref. 9 (from Ref. 8).

FIG. 2. Phase velocity dispersion curves versus $k_1 a$ of circumferential waves on air-filled, water-loaded cylindrical steel shells of various thicknesses (from Ref. 8).

families connected by curves, along which the resonance frequencies are indicated by dots labeled by the mode number n. The families are labeled by $\ell = 0$, 1, and 2 or, following similar pictures for the case of solid elastic cylinders,[9] are designated by "Stoneley wave" $\ell = 0$ (also known as Scholte–Stoneley wave), "Rayleigh wave" $\ell = 1$, and "First Whispering Gallery wave" $\ell = 2$ (higher-order Whispering Gallery waves being present but not entered into the figure). As shown earlier,[10] the mentioned resonance frequency families originate physically from the corresponding circumferential wave types as they form standing waves with n wavelengths spanning the circumference of the cylinder. The phase velocity c_ℓ^p of the ℓth surface wave can be obtained by the formula[11]

$$c_\ell^p / c = \mathrm{Re}\ (k_1 a)_{n\ell} / n, \qquad (1)$$

$(k_1 a)_{n\ell}$ being the complex resonance frequencies and c the sound velocity in water. The dispersion curves of c_ℓ^p / c are plotted versus $k_1 a$ in Fig. 2 (from Ref. 8, where the Stoneley dispersion curve on a shell was obtained for the first time). Values of compressional (c_L), shear (c_T), and Rayleigh wave speed c_R divided by c are indicated on the right. An alternative nomenclature for the surface waves with the dispersion curves shown would be, in analogy with the Lamb-type plate waves, S_0 for the $\ell = 2$ wave, A_0 for the $\ell = 1$ wave, and A for the $\ell = 0$ Scholte–Stoneley wave. Below, we shall instead use the notation[6] A_{0+} and A_{0-} for $\ell = 0$ and 1 since this remains unambiguous when passing through the region of repulsion.

While for the case of the spherical shell the A_{0+} and A_{0-} dispersion curves have been well separated,[6] this is not the case for the cylindrical shell data in Fig. 2 where the coincidence region in the lower left-hand portion does not furnish sufficient detail. The present investigation clarifies this point, and analyzes in detail the repulsion phenomenon of the A_{0+} and A_{0-} wave dispersion curves in this region.

We first consider the resonance frequencies $(k_1 a)_{n\ell}$ for $\ell = 1$ (i.e., the flexural wave, A_0), and for $\ell = 0$ (i.e., the fluid-borne Scholte–Stoneley wave, A) only, for a given mode number n, as a function of the shell radius ratio b/a ($b/a = 0$ being the solid cylinder, and $b/a = 1$ an infinitesimally thin shell). The complex values $(k_1 a)_{n\ell}^*$ are written as
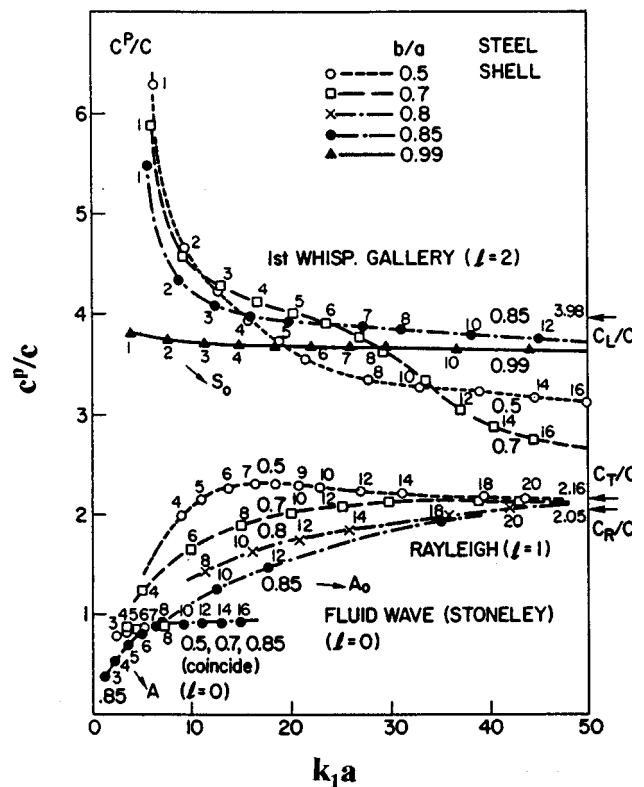
$$(k_1 a)_{n\ell}^* = (k_1 a)_{n\ell} - \tfrac{1}{2} i \Gamma_{n\ell}, \qquad (2)$$

$\Gamma_{n\ell}$ being the width of the corresponding resonance, and $\tfrac{1}{2}\Gamma_{n\ell}$ and $(k_1 a)_{n\ell}$ are plotted versus b/a in the lower and upper parts of Fig. 3(a)–(c) for $n = 4$–6, respectively. In this representation, the points again divide into the families A_0 ($\ell = 1$) and A ($\ell = 0$), here denoted by R (Rayleigh) and S (Scholte), respectively. Although for $n = 4$ and below (not illustrated) it is not clear from the figures whether the real parts of the two families do or do not cross over and the imaginary parts do or do not repel each other at certain well-defined values of b/a, it appears that for $n = 5$, 6 and also above (not illustrated), a clear repulsion takes place for the real parts, and a clear intersection for the imaginary parts. By dashed lines we indicate the behavior of the family A_0 for the shell in vacuum (i.e., the unperturbed case); here, the Stoneley family A is absent, as is Γ_{n1}. The dotted line will be described later.

The perturbation is provided by the water loading, which not only causes the presence of the Stoneley wave (interacting with the A_0 wave), but which also generates the repulsion phenomenon. The latter appears more clearly in the dispersion curves, obtained from Eq. (1) and plotted versus $k_1 a$ in Fig. 4(a)–(c) for $b/a = 0.5$, 0.7, and 0.9, respectively. These can be compared with the lower portion of Fig. 2, where now the details have become clarified. We shall here use the notation A_{0+} (upper curve) and A_{0-} (lower curve) for the two distinct dispersion curves. The dashed curve shows again the corresponding A_0 dispersion curve for a shell in vacuo, where it is similar to the A_0 Lamb wave curve
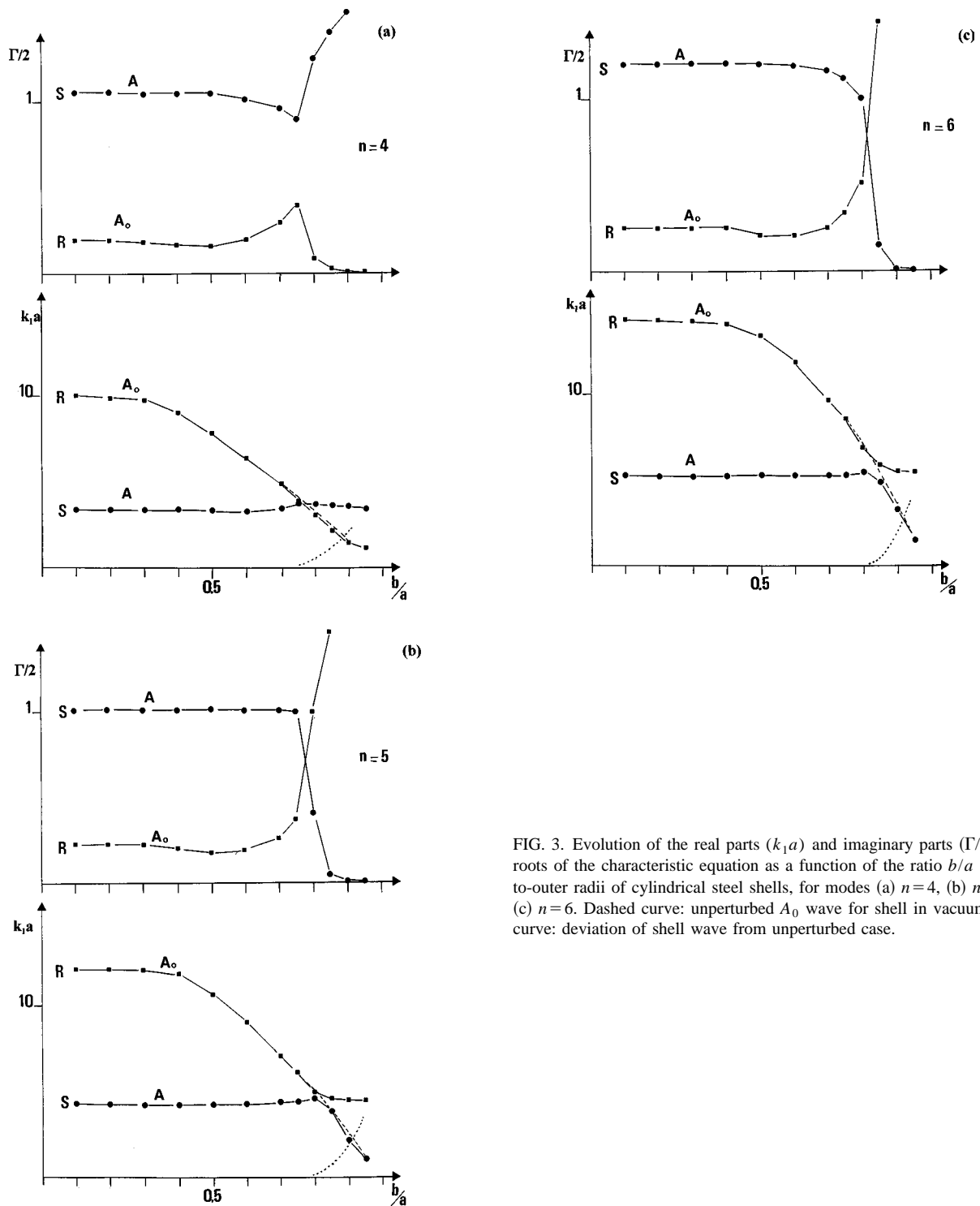
FIG. 3. Evolution of the real parts $(k_1 a)$ and imaginary parts $(\Gamma/2)$ of the roots of the characteristic equation as a function of the ratio b/a of inner-to-outer radii of cylindrical steel shells, for modes (a) $n=4$, (b) $n=5$, and (c) $n=6$. Dashed curve: unperturbed A_0 wave for shell in vacuum; dotted curve: deviation of shell wave from unperturbed case.

on a plate in vacuo, i.e., it tends to zero for $k_1 a \rightarrow 0$. In the present fluid-loaded case, the figure shows, however, the repulsion phenomenon of the dispersion curves for these two waves, which had been previously noted for the spherical shell.[4,6] For frequencies above coincidence, the A_{0+} wave plays the role of the flexural A_0 wave, while below coincidence this function is taken over by the A_{0-} wave. Above coincidence, the A_{0-} wave flattens out and stays below c up to the highest frequencies, thus playing the role of the Stoneley wave, while below coincidence, the A_{0+} wave has become more horizontal, thus taking over the role of the Stone-

ley wave. This portion of the A_{0+} wave had not been found in the below-coincidence region by Ref. 8, but it had earlier been obtained by Murphy et al.,[12] this reference being the first work in which resonances of a cylindrical shell had been studied; see, e.g., Fig. 4 of Ref. 8(b). It is seen that, although first attempting to intersect, the dispersion curves finally repel each other, and the nature of the two curves has become interchanged after the failed intersection: descending from the high-frequency side in Fig. 4, the A_{0+} wave resembles the flexural A_0 wave and the A_{0-} resembles the fluid-borne wave (which is called the A wave in the nomenclature of Ref.
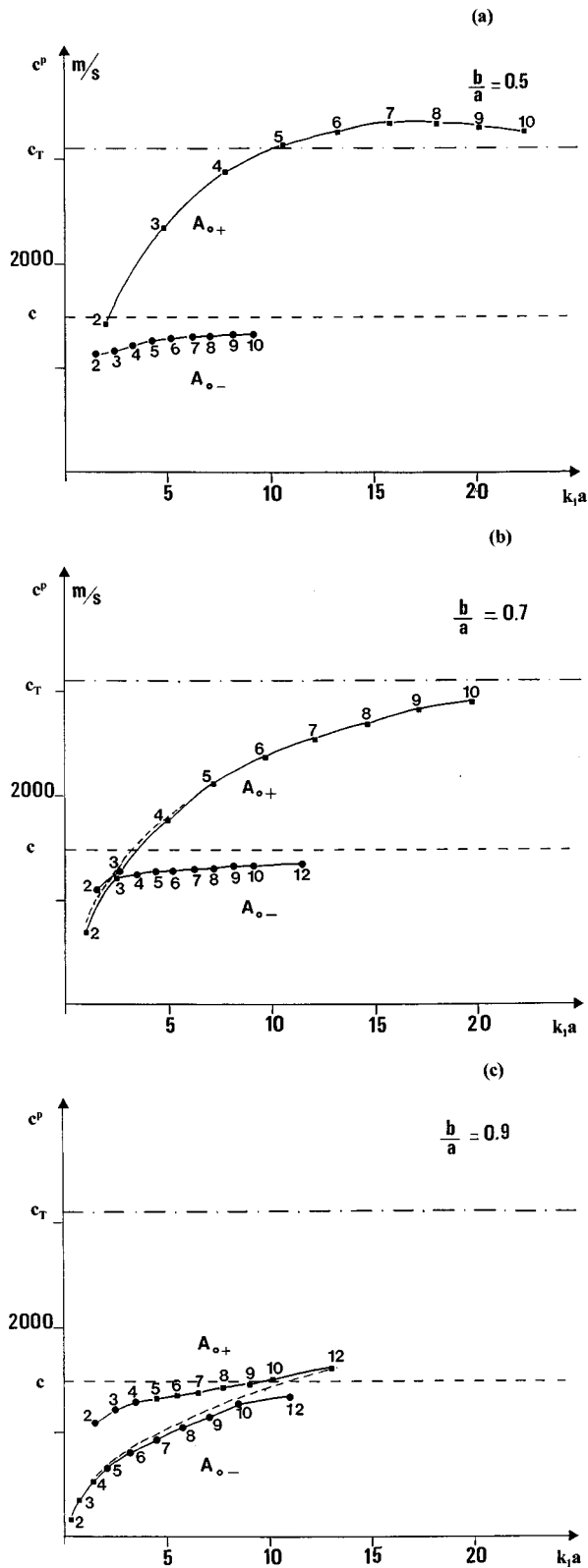
FIG. 4. Phase velocity dispersion curves for cylindrical steel shells with (a) $b/a = 0.5$, (b) $b/a = 0.7$, and (c) $b/a = 0.9$. Dashed curve: unperturbed A_0 wave for shell in vacuum.

4), but below the near-intersection the A_{0-} wave resembles the flexural A_0 while the A_{0+} wave resembles the fluid-borne wave. Below, it will be shown that such a resemblance is not only based on the appearance of the dispersion curves, but that there is an actual exchange of the character of the waves

going along in accordance with this. Note that an analogous phenomenon takes place in the dispersion curves of waves in a plate (in vacuo,[13] fluid loaded,[13] or coated;[14] see also Ref. 15).

II. PERTURBATION THEORY OF THE REPULSION PHENOMENON

This approach will be applied to Fig. 3, and we have to consider two limiting cases in order to identify the perturbation:

(1) If b/a is not too close to unity, we consider the ratio $\rho \equiv \rho_w / \rho_{st} = 1/7.9$ as the perturbation. The limit $\rho \to 0$ is the unperturbed case (shell in vacuo) and we know the corresponding flexural-wave values $(k_1 a)_{n1}^{(0)}$ (the superscript 0 denoting the unperturbed values), (see the dashed curves in Fig. 3), while $(k_1 a)_{n0}^{(0)}$ of the Stoneley wave do not exist.

(2) If b/a is close to unity, the shell is very thin. Let us call

$$b/a = \beta, \quad \zeta = 1 - \beta, \tag{3}$$

and for $\beta \to 1$ or $\zeta \to 0$, the mass of the shell is small compared to the mass of the entrained fluid. Here, ζ is the perturbation and $\zeta \to 0$ is the unperturbed case, i.e., the object is a vacuum bubble in water. From Eq. (1) and Fig. 4 it can be seen that in this limit, $\mathrm{Re}\,(k_1 a)_{n0}^{(0)} \to 0$.

The complex resonance frequencies were here calculated as the poles in the acoustic scattering amplitude. The far-field scattering amplitude at angle θ is given by its modulus as[16]

$$|F^\infty| = \frac{2}{(\pi k_1 a)^{1/2}} \left| \sum_{n=0}^{\infty} \varepsilon_n \frac{D_n^{[1]}}{D_n} \cos n\theta \right|. \tag{4}$$

With the abbreviations $x = k_1 a$, $y = \beta x$, $y_{L,T} = \beta x_{L,T}$, where $x_{L,T} = x c / c_{L,T}$, one has a 7×7 determinant

$$D_n = \begin{vmatrix} \frac{1}{2} \rho x_T^2 H_n(x) & M_{1j} \\ nH_n(x) - xH_{n+1}(x) & M_{2j} \\ 0 & M_{3j} \\ \vdots & \vdots \\ 0 & M_{7j} \end{vmatrix}, \tag{5}$$

$j = 2, \dots 7$, where we take M_{nj} from Ref. 16 and set $\alpha = 0$ for normal incidence. To obtain $D_n^{[1]}$, we replace the first two elements in the first column of Eq. (5) by

$$-\tfrac{1}{2} \rho x_T^2 J_n(x), \quad -[nJ_n(x) - xJ_{n+1}(x)].$$

Expanding, one has

$$D_n = \tfrac{1}{2} \rho x_T^2 H_n(x) \Delta_n^{(1)}(x) - [nH_n(x) - xH_{n+1}(x)] \Delta_n^{(2)}(x), \tag{6}$$

with the subdeterminants $\Delta_n^{(1),(2)}$ being real for real x, the two elements with H_n, H_{n+1} in Eq. (5) being the only complex functions in D_n. Setting $D_n = 0$ corresponds to the characteristic equation of the shell which furnishes the complex resonance frequencies.

In the limit $\rho \to 0$, this equation becomes

$$-[nH_n(x) - xH_{n+1}(x)] \Delta_n^{(2)} = 0. \tag{7}$$

Vanishing of the first factor, or $H'_n(x) = 0$, furnishes the external circumferential or Franz waves[17] that circumnavigate a rigid cylinder, while $\Delta_n^{(2)}(x) = 0$ furnishes the mentioned real flexural wave frequencies $x_{n1}^{(0)}$.

In the approach to the limit $\zeta \to 0$ ($\beta \to 1$ and $y_{LT} \to x_{LT}$) we subtract M_{5j} from M_{1j}, and M_{6j} from M_{3j}, and M_{7j} from M_{4j} without changing the determinant. We then expand $M_{1j} - M_{5j}$, etc. in a Taylor series in ζ, obtaining the limiting expressions

$$\Delta_n^{(1)}(x) = \zeta^2 \overline{\Delta}_n^{(1)}(x) + \cdots, \quad \Delta_n^{(2)}(x) = \zeta^3 \overline{\Delta}_n^{(2)}(x) + \cdots, \tag{8}$$

so that close to this limit, one has

$$D_n(x) = \zeta^2 \{ \tfrac{1}{2} \rho x_T^2 H_n(x) \overline{\Delta}_n^{(1)}(x)$$
$$- \zeta [n H_n(x) - x H_{n+1}(x)] \overline{\Delta}_n^{(2)}(x) \}. \tag{9}$$

The limiting form of the characteristic equation is thus

$$\tfrac{1}{2} \rho x_T^2 H_n(x) \overline{\Delta}_n^{(1)}(x) = 0. \tag{10}$$

Vanishing of the first term, $H_n(x) = 0$, furnishes the complex resonance frequencies of the external Franz waves that circumnavigate a cylindrical vacuum bubble, while $\overline{\Delta}_n^{(1)}(x) = 0$ furnishes the Stoneley resonance frequencies $x_{n0}^{(0)}$ around the bubble; for these, we have found above that $\mathrm{Re}\,(x)_{n0}^{(0)} = 0$.

Let us call

$$\mathcal{H}_n(x) = [n H_n(x) - x H_{n+1}(x)] / H_n(x). \tag{11}$$

Near the thin-shell limit $\zeta \to 0$, the characteristic equation $D_n(x) = 0$ then becomes, from Eq. (9),

$$\overline{\Delta}_n^{(1)}(x) - \frac{\zeta}{\rho} \frac{2}{x_T^2} \mathcal{H}_n(x) \overline{\Delta}_n^{(2)}(x) = 0. \tag{12}$$

Starting from $x_{n0}^{(0)}$, the perturbation solution is for the Stoneley frequencies:

$$x_{n0}^* = x_{n0}^{(0)} + \delta_{n0}. \tag{13}$$

Inserting in Eq. (12) and Taylor expanding, we find

$$x_{n0}^* = x_{n0}^{(0)} + \frac{\zeta}{\rho} \mathcal{H}_n(x_{n0}^{(0)}) \frac{2 \overline{\Delta}_n^{(2)}(x_{n0}^{(0)})}{x_T^2 \overline{\Delta}_n^{(1)'}(x_{n0}^{(0)})}, \tag{14}$$

which furnishes the behavior of x_{n0}^* with ζ (and ρ) near the thin-shell limit $\zeta \to 0$. The curves x_{n0} thus tend linearly to zero as $b/a \to 1$, with a slope that increases with n. All this is evident in Fig. 3, verifying the downturn of the Stoneley (A) wave curve as it passes the point of repulsion and thus guaranteeing the repulsion of the curves denoted A_0 and A to the left of the repulsion point in all portions of Fig. 3, and hence also in all portions of Fig. 4 (where we use the notation A_{0+} and A_{0-} for each entire curve). Figure 3 seems to indicate that also $\mathrm{Im}\,x_{n0}^{(0)} = 0$ so that the curves for x_{n0} likewise tend to zero for $\zeta \to 0$, as observed.

For thicker shells, we consider the limit $\rho \to 0$ in which the flexural-wave frequencies $x_{n1}^{(0)}$ are known. The characteristic equation is then

$$\overline{\Delta}_n^{(2)}(x) - \frac{\rho}{2\zeta} \mathcal{H}_n^{-1}(x) x_T^2 \overline{\Delta}_n^{(1)} = 0, \tag{15}$$

and expanding around the flexural-wave roots,

$$x_{n1}^* = x_{n1}^{(0)} + \delta_{n1}, \tag{16}$$

we find

$$x_{n1}^* = x_{n1}^{(0)} + \frac{\rho}{\zeta} \mathcal{H}_n^{-1}(x_{n1}^{(0)}) \frac{x_T^2 \overline{\Delta}_n^{(1)}(x_{n1}^{(0)})}{2 \overline{\Delta}_n^{(2)'}(x_{n1}^{(0)})}, \tag{17}$$

which furnishes the behavior of x_{n1}^* with ρ (and ζ) for the case of light fluid loading. The same equation describes, however, the behavior of the deviation $\delta_n \equiv \mathrm{Re}\,\delta_{n1} = x_{n1} - x_{n1}^{(0)}$ of the flexural-wave curve from that of the corresponding curve (dashed) where no fluid loading was assumed, as a function of b/a. In fact, this behavior is predicted by Eq. (17) as proportional to $1/\zeta$ for b/a not too close to unity. In Fig. 3, we have entered as *dotted* curves the values of δ_n as read from the points of Fig. 3, to the right of the point of repulsion, always interpreting the upper curves as A. The resulting dotted curves indeed show a shape close to the predicted $1/\zeta$ dependence, which also holds for the imaginary parts if one does not push too close to the $b/a \to 1$ limit. Thus, the apparent correctness of this perturbation treatment is evident for the above-repulsion portion of Figs. 3 and 4. This leads to the inescapable conclusion, noted before, that the repulsion also inverts the character of the A_0 and the A curves on the two sides of the point of repulsion, as compared to the character of the A_0 curve with no fluid loading (dashed).

III. INFLUENCE OF THE A_0 AND A RESONANCES ON THE SPECTRA OF SCATTERING AMPLITUDES

Two types of spectra can be plotted numerically: the far-field form function which represents the acoustic pressure, and the spectrum "Im/Re" (the ratio of imaginary and real parts of the scattering amplitude) which is the tangent of the phase of acoustic pressure.[18] Figure 5 presents such spectra for evacuated, water-immersed stainless-steel cylindrical shells, with values of the thickness parameter $b/a = 0.5$, 0.7, 0.8, and 0.9. On these figures, the resonances of the $\ell = 1$ (flexural) family are marked by squares, those of the $\ell = 0$ (Scholte–Stoneley) family by round dots, and those of the first Whispering Gallery wave ($\ell = 2$) by a star; the other resonances have not been entered. For b/a values 0.5 and 0.7, resonances appear in the form function and in the Im/Re spectrum that can be attributed to the $\ell = 1$ family, and none to the $\ell = 0$ family (disregarding those with $\ell = 2$). For the $b/a = 0.8$ shell, resonances are attributable to the $\ell = 1$ family except the $n = 5$ resonance, belonging to the $\ell = 0$ family. For the $b/a = 0.9$ shell, the resonances belong to the $\ell = 0$ family, except that of the $n = 4$ mode which belongs to the $\ell = 1$ family. For associating a spectral feature with a resonance, we must call upon the imaginary part of the root of the characteristic equation, i.e., the quantity Γ. With large imaginary parts, the resonance width becomes large which causes the resonance to be prone to escaping detection. In the case of the $b/a = 0.9$ shell, the first detected resonance is of
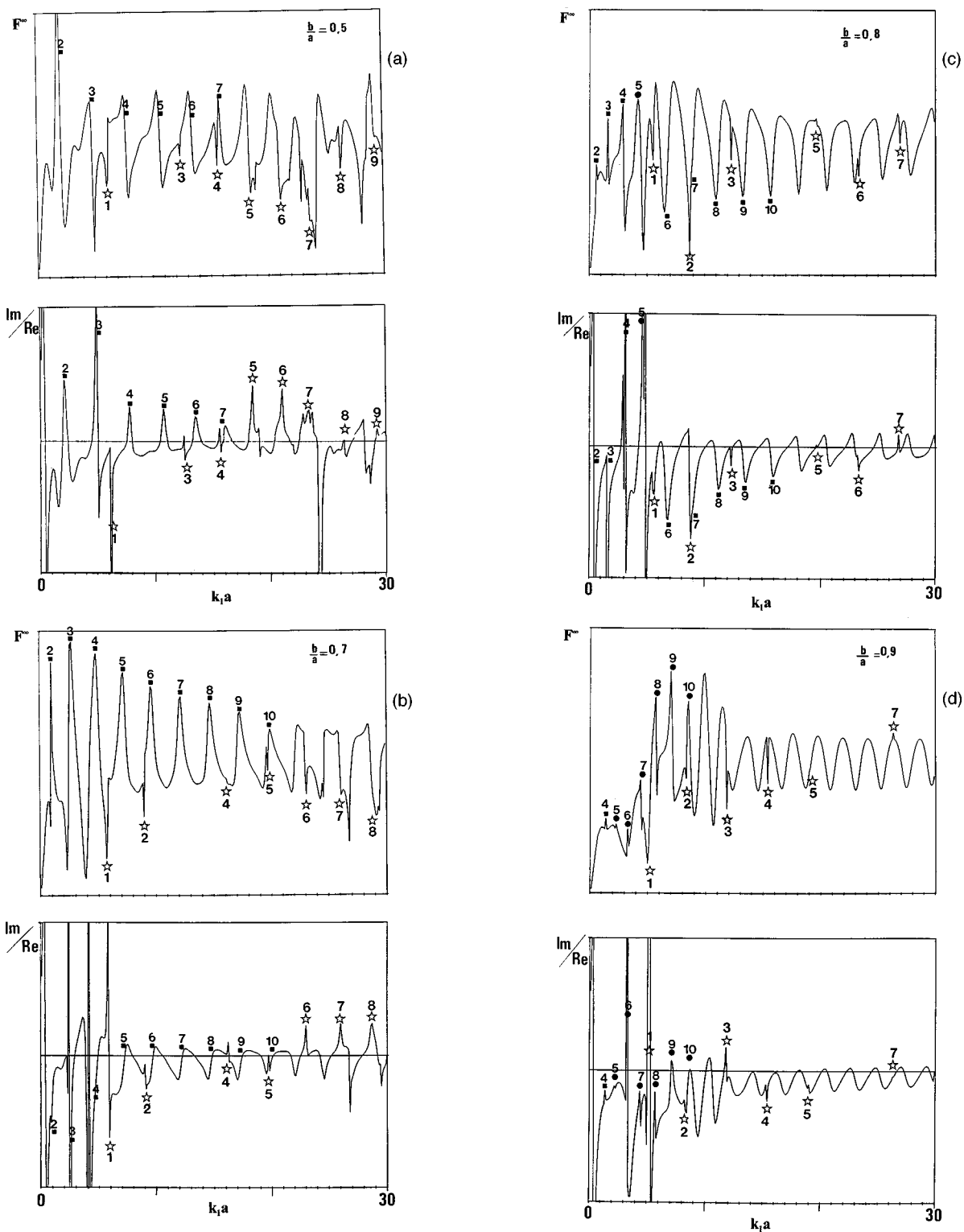
FIG. 5. Spectra of the form function F_∞ and of Im/Re for cylindrical steel shell with (a) $b/a = 0.5$, (b) $b/a = 0.7$, (c) $b/a = 0.8$, and (d) $b/a = 0.9$.

mode number $n = 4$; those with smaller mode numbers are not apparent since their imaginary part now is too small, which is tantamount to a lack of coupling to the water. For b/a increasing beyond 0.9, all the observed modes belong to the $\ell = 0$ family, the first of these growing bigger and bigger since the coupling of the lower modes is too weak. We should also note that for a given value of b/a, the more a modal resonance grows, the more its imaginary part will grow. This has the consequence that the $\ell = 0$ family resonances detected in the spectra will become wider and wider, i.e., they will be of less and less influence. These two last remarks explain the observed fact[19] that for the Scholte–Stoneley wave, the resonances are visible only within a "frequency window" which shifts to higher frequencies as b/a tends to unity. The flexural wave is, for the usual materials, strongly coupled to the liquid and only forms resonances of

large width, which makes them harder to observe.[20] Its phase velocity tends towards that of the Rayleigh wave on a liquid/solid interface with increasing frequency of the incident wave. The Whispering Gallery waves (stars in Fig. 5) are more weakly coupled to the liquid, which increases their detectability. However, the coupling increases as a function of the frequency. A minimum in this coupling can be observed at low frequency, which renders these resonances very narrow in the neighborhood of this minimum.[20]

As a final remark, we should note that the $\ell=1$ wave is observed here via its resonances only for sufficiently thick shells. For thin shells with b/a larger than 0.9 [see Fig. 5(d)], this wave which then becomes the A_0 plate wave, is no longer observable by the resonance method, and only the $\ell=0$ (Scholte–Stoneley or A) wave and the $\ell=2$ (S_0) wave are observable, as recently shown by us.[21]

IV. CONCLUSION

The numerical results presented above allow us to show the presence of the two resonance families A_0 and A, and to trace their characteristics (resonance frequency and width) as a function of the ratio b/a. A numerical study of the resonance frequencies and widths demonstrates that for increasing values of b/a, the A_0 curve first follows that of the corresponding flexural resonance frequencies of a shell *in vacuo*, while the A-wave resonances are almost independed of b/a (Fig. 3). The two curves for the real parts of the resonance frequencies approach each other, but instead of intersecting, they repel each other, the A wave now following the vacuum-flexural wave curve while the A_0 wave continues independent of b/a. (In Fig. 4, the notation A_{0+}, A_{0-} is used for each of the continuous dispersion curves.) The nature of the waves gets interchanged when the dispersion curves pass through the repulsion region. This is demonstrated analytically by a perturbation-theoretical approach, proving that after passing through the point of repulsion with increasing b/a, the A wave then takes over the role which the A_0 wave used to play for the thinner shells in the unperturbed case of no fluid loading. A parallel consideration of the phase velocity dispersion curves for the A_{0+} and A_{0-} waves demonstrates the repulsion phenomenon in an alternate fashion, and the simultaneous exchange of flexural wave-fluid wave character is already evident here from the appearance of the dispersion curves.

Note added in proof: In a forthcoming paper (K. Motegi and K. Toda, ''Interaction between two leaky Lamb wave modes propagating in a water-loaded bilayer consisting of a piezoelectric ceramic plate and a glass plate,'' Ultrasonics, in press) the authors discuss the cross-over of dispersion curves with simultaneous repulsion of absorption curves, or vice versa, analogous to our discussion following Eq. (2), providing additional insight into the mathematical reasons for these phenomena.

[1] L. M. Brekhovskikh, *Waves in Layered Media* (Academic, New York, 1960), Fig. 26.

[2] A. Grabowska, ''Propagation of elastic wave in solid layer-liquid system,'' Arch. Acoust. **4**, 57–64 (1979).

[3] M. Talmant, ''Rétrodiffusion d'une impulsion ultrasonore brève par une coque cylindrique à paroi mince,'' Ph.D. thesis, University of Paris VII, 1987.

[4] M. Talmant, H. Überall, R. D. Miller, M. F. Werby, and J. W. Dickey, ''Lamb waves and fluid-borne waves on water-loaded, air-filled thin spherical shells,'' J. Acoust. Soc. Am. **86**, 278–289 (1989).

[5] See, e. g., H. Überall, A. Gérard, J. Duclos, M. El H. Khelil, X. L. Bao, and P. K. Raju, ''Acoustic scattering resonances: Relation to external and internal surface waves,'' Appl. Mech. Rev. **49**, S63–S71 (1996), Fig. 5.

[6] G. S. Sammelmann, D. H. Trivett, and R. H. Hackman, ''The acoustic scattering by a submerged, spherical shell. I. The bifurcation of the dispersion curve for the antisymmetric Lamb wave,'' J. Acoust. Soc. Am. **85**, 114–124 (1989).

[7] G. Maze, F. Léon, J. Ripoche, A. Klauson, J. Metsaveer, and H. Überall, ''Nature de l'onde d'interface de Scholte sur une coque cylindrique,'' Acustica **81**, 201–213 (1995).

[8] a) J. V. Subrahmanyam, ''Creeping wave analysis through frequency plane for an obliquely incident plane wave on an elastic scatterer,'' Ph.D. thesis, Catholic Unversity of America, Washington, DC, 1983; b) M. Talmant, G. Quentin, J. L. Rousselot, J. V. Subrahmanyam, and H. Überall, ''Acoustic resonances of thin cylindrical shells and the resonance scattering theory,'' J. Acoust. Soc. Am. **84**, 681–688 (1988).

[9] J. V. Frisk, J. W. Dickey, and H. Überall, ''Surface wave modes on elastic cylinders,'' J. Acous. Soc. Am. **58**, 996–1008 (1975).

[10] H. Überall and G. C. Gaunaurd, ''The physical content of the singularity expansion method,'' Appl. Phys. Lett. **39**, 362–364 (1981).

[11] A. Derem and J. L. Rousselot, ''Résonances acoustiques du cylindre élastique infini et leur relation avec les ondes de surface,'' Rev. Cethedec **67**, 1–34 (1981).

[12] J. D. Murphy, E. D. Breitenbach, and H. Überall, ''Resonance scattering of acoustic waves from cylindrical shells,'' J. Acoust. Soc. Am. **64**, 677–683 (1978); see also E. D. Breitenbach, H. Überall, and K. B. Yoo, ''Resonant acoustic scattering from elastic cylindrical shells,'' J. Acoust. Soc. Am. **74**, 1267–1273 (1983).

[13] H. Überall, B. Hosten, M. Deschamps, and A. Gérard, ''Repulsion of phase-velocity dispersion curves and the nature of plate vibrations,'' J. Acoust. Soc. Am. **96**, 908–917 (1994).

[14] V. Kinra, private communication.

[15] C. W. Farnell and E. L. Adler, ''Elastic wave propagation in thin layers,'' Phys. Acoust. **9**, 35–127 (1972).

[16] F. Lecroq, F. Léon, D. Décultot, and G. Maze, ''Diffusion d'une onde acoustique par un tube limité par des disques plans: études théoriques et expérimentales,'' Acustica **74**, 51–62 (1991).

[17] H. Überall, R. D. Doolittle, and J. V. McNicholas, ''Use of sound pulses for a study of circumferential waves,'' J. Acoust. Soc. Am. **39**, 564–578 (1966).

[18] G. Maze, ''Acoustic scattering from submerged cylinders MIIR Im/Re: Experimental and theoretical study,'' J. Acoust. Soc. Am. **89**, 2559–2566 (1991).

[19] A Gérard, J. L. Rousselot, J. L. Izbicki, G. Maze, and J. Ripoche, ''Résonances d'ondes d'interface de coques cylindriques minces imergées: détermination et interprétation,'' Rev. Phys. Appl. **23**, 289 (1988).

[20] G. Maze and J. Ripoche, ''Methode d'isolement et d'identification des résonances (MIIR) de cylindres et de tubes soumis á une onde acoustique plane dans l'eau,'' Rev. Phys. Appl. **18**, 319 (1983).

[21] A. C. Ahyi, P. Pernod, O. Gatti, V. Latard, A. Merlen, and H. Überall, ''Expermental demonstration of the pseudo-Rayleigh (A_0) wave,'' J. Acoust. Soc. Am. **104**, 2727–2732 (1998).

The mobility functions and their application in calculating power flow in coupled cylindrical shells

R. S. Ming, J. Pan, and M. P. Norton

Department of Mechanical and Materials Engineering, The University of Western Australia, Nedlands, WA 6907, Australia

The mobility functions of semi-infinite and finite cylindrical shells are useful in calculating the structural wave power flows in coupled pipeline systems. However, their expressions and characteristics are not available in the existing literature. In this paper, the mobility functions of elastic cylindrical *in vacuo* shells have been numerically studied and applied to estimate both the input power and the power flow in coupled finite cylindrical shell systems. © *1999 Acoustical Society of America.* [S0001-4966(99)02402-9]

PACS numbers: 43.40.Ey [CBB]

INTRODUCTION

Elastic cylindrical shells have many industrial and defense applications. The determination of vibrational energy transmission between coupled cylindrical shells is an important subject in the area of noise and vibration control. Several methods are available for the calculation of the energy transmission. One of them is the mobility method[1–5] in which the vibrational energy transmission across a structural joint is expressed in terms of mobility functions. The mobility functions of beams, plates, walls, and floors have been extensively studied.[6,7] However, the mobility of elastic cylindrical shells received scant attention, perhaps due to the complexity involved in solving and interpreting the dispersion equations. Franken[8] obtained the input modal impedance of a simply supported cylindrical shell, but his analysis did not include bending stiffness of the shell and it has limitations for the estimation of input power in practical applications. Heckl[9] and Fuller[10] have derived the analytic expressions for evaluating the input radial force mobility of an infinite elastic cylindrical shell. Harari[11] developed the general expressions for evaluating the transmission loss based on the structural impedances of finite and semi-infinite cylindrical *in vacuo* shells. However, detailed analysis of the structural impedances was not presented. It is difficult to use these general expressions to give a physical interpretation of the vibrational transmissions resulting from different types of excitations.

In this paper, an analysis is presented to calculate the input, cross, and transfer mobilities of an elastic cylindrical shell subjected to different types of excitations. The analysis is limited to homogenous thin-walled *in vacuo* shells and frequencies such that the rotational kinetic energy of vibration and transverse deformation of the shell wall may be ignored. For infinite cylindrical shells, the analysis is an extension of the work by Fuller.[10] For finite and semi-infinite cylindrical shells, the mobilities are calculated based on the motion equations[12,13] and the boundary conditions. Numerical results are presented and their physical interpretations are discussed for a steel cylindrical *in vacuo* shell with the thickness to radius ratios of 0.05 and 0.01 in the $n=0$, 1, and 2 circumferential modes. The results are then applied to analyze the vibrational energy transmission between two coupled finite cylindrical shells when one of them is excited by an external point radial force.

I. BASIC EQUATIONS

Consider a uniform thin cylindrical shell of thickness h and mean radius a. The midsurface of the shell is described in an (x, θ) cylindrical coordinate, as shown in Fig. 1. If u, v, and w represent the components of displacement in the axial, circumferential, and radial directions, respectively, the equation of motion for an element of the shell can be written as[12,13]

$$\left[a^2 \frac{\partial^2}{\partial x^2} + \frac{1-\mu}{2} \frac{\partial^2}{\partial \theta^2} - \frac{\rho(1-\mu^2)}{E} a^2 \frac{\partial^2}{\partial t^2} \right.$$
$$\left. + \beta^2 \frac{1-\mu}{2} \frac{\partial^2}{\partial \theta^2} \right] u + \left[\frac{1+\mu}{2} a \frac{\partial^2}{\partial x \partial \theta} \right] v + \left[a\mu \frac{\partial}{\partial x} \right.$$
$$\left. - \beta^2 a^3 \frac{\partial^3}{\partial x^3} + \beta^2 \frac{1-\mu}{2} a \frac{\partial^3}{\partial x \partial \theta^2} \right] w = -\frac{a^2 p_x}{K}, \quad \text{(1a)}$$

$$\left[\frac{1+\mu}{2} a \frac{\partial^2}{\partial x \partial \theta} \right] u + \left[\frac{1-\mu}{2} a^2 \frac{\partial^2}{\partial x^2} + \frac{\partial^2}{\partial \theta^2} - \frac{\rho(1-\mu^2)}{E} a^2 \frac{\partial^2}{\partial t^2} \right.$$
$$\left. + 3\beta^2 a^2 \frac{1-\mu}{2} \frac{\partial^2}{\partial x^2} \right] v$$
$$+ \left[\frac{\partial}{\partial \theta} - \frac{3-\mu}{2} \beta^2 a^2 \frac{\partial^3}{\partial x^2 \partial \theta} \right] w = -\frac{a^2 p_\phi}{K}, \quad \text{(1b)}$$

$$\left[a\mu \frac{\partial}{\partial x} - \beta^2 a^3 \frac{\partial^3}{\partial x^3} + \beta^2 \frac{1-\mu}{2} a \frac{\partial^3}{\partial x \partial \theta^2} \right] u$$
$$+ \left[\frac{\partial}{\partial \theta} - \frac{3-\mu}{2} \beta^2 a^2 \frac{\partial^3}{\partial x^2 \partial \theta} \right] v + \left[1 + \beta^2 \nabla^4 \right.$$
$$+ \frac{\rho(1-\mu^2)}{E} a^2 \frac{\partial^2}{\partial t^2} + \beta^2 \left(1 + 2 \frac{\partial^2}{\partial \theta^2} \right) \right] w = \frac{a^2 p_r}{K}, \quad \text{(1c)}$$
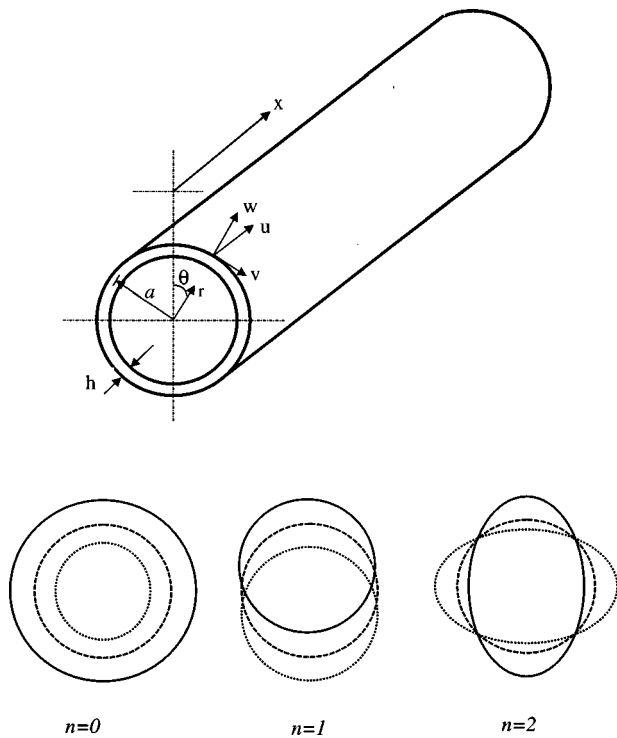
FIG. 1. Coordinate system and modal shapes.

where μ is the Poisson's ratio, E is the Young's modulus, ρ is the material density, $\beta^2 = h^2/12a^2$, $\nabla^2 = a^2(\partial^2/\partial x^2) + \partial^2/\partial\theta^2$ is a Laplacian-type operator, $K = Eh/(1-\mu^2)$ is the extensional rigidity, and p_x, p_ϕ, and p_r are the orthogonal components of mechanical excitation per unit area which act on the shell in the axial, circumferential, and radial directions, respectively. At cross section x, the effective transverse force S_x, the bending moment M_x, the extensional stress N_x, and the effective shear stress T_x can be expressed as[12]

$$S_x = D\left(\frac{\partial^3 w}{\partial x^3} + \frac{2-\mu}{a^2}\frac{\partial^3 w}{\partial x\,\partial\theta^2} - \frac{1}{a}\frac{\partial^2 u}{\partial x^2} + \frac{1-\mu}{2a^3}\frac{\partial^2 \mu}{\partial\theta^2}\right.$$
$$\left. - \frac{3-\mu}{2a^2}\frac{\partial^2 v}{\partial x\,\partial\theta}\right), \tag{2a}$$

$$M_x = D\left(\frac{\partial^2 w}{\partial x^2} + \frac{\mu}{a^2}\frac{\partial^2 w}{\partial\theta^2} - \frac{1}{a}\frac{\partial u}{\partial x} - \frac{\mu}{a^2}\frac{\partial v}{\partial\theta}\right), \tag{2b}$$

$$N_x = K\left(\frac{\partial u}{\partial x} + \frac{\mu}{a}\frac{\partial v}{\partial\theta} + \frac{\mu}{a}w\right) - \frac{D}{a}\frac{\partial^2 w}{\partial x^2}, \tag{2c}$$

$$T_x = \frac{1-\mu}{2}\left(\frac{K}{a}\frac{\partial u}{\partial\theta} + \left(K - \frac{D}{a^2}\right)\frac{\partial v}{\partial x} + \frac{D}{a^2}\frac{\partial^2 w}{\partial x\,\partial\theta}\right), \tag{2d}$$

where $D = Eh^3/(1-\mu^2)$ is the bending rigidity of the shell.

The displacement components of the wave propagating in the positive axial direction can be expressed in the following forms:[14]

$$u = \sum_{n=0}^{\infty} u_n = \sum_{n=0}^{\infty}\sum_{s=1}^{m} U_{ns}\cos(n\theta)\exp(-ik_{ns}x + i\omega t + i\pi/2), \tag{3a}$$

$$v = \sum_{n=0}^{\infty} v_n = \sum_{n=1}^{\infty}\sum_{s=1}^{4} V_{ns}\sin(n\theta)\exp(-ik_{ns}x + i\omega t), \tag{3b}$$

$$w = \sum_{n=0}^{\infty} w_n = \sum_{n=0}^{\infty}\sum_{s=1}^{m} W_{ns}\cos(n\theta)\exp(-ik_{ns}x + i\omega t), \tag{3c}$$

where k_{ns} is the axial wave number, $\omega = 2\pi f$ is the radian frequency, n is the circumferential modal number, subscript s corresponds to the axial wave number solutions, $m = 3$ for $n = 0$ and $m = 4$ for $n > 0$. For the axial symmetrical mode ($n = 0$), there are six axial wave number solutions for finite and infinite cylindrical shells. For $n > 0$, however, eight axial wave number solutions are possible, and in this case, four possible axial waves could propagate simultaneously in both positive and negative directions. For every n and s pair, the coefficients U_{ns}, V_{ns}, and W_{ns} are coupled among each other.

Substituting Eq. (3) into (1) gives

$$\begin{bmatrix} L_{11} & L_{12} & L_{13} \\ L_{21} & L_{22} & L_{23} \\ L_{31} & L_{32} & L_{33} \end{bmatrix}\begin{bmatrix} U_{ns} \\ V_{ns} \\ W_{ns} \end{bmatrix} = \frac{a^2}{K}\begin{bmatrix} -p_x \\ -p_\phi \\ p_r \end{bmatrix}, \tag{4}$$

where

$$L_{11} = (k_{ns}a)^2 + \frac{1-\mu}{2}(1+\beta^2)n^2 - \Omega^2,$$

$$L_{12} = L_{21} = \frac{1+\mu}{2}nk_{ns}a,$$

$$L_{13} = L_{31} = \beta^2(k_{ns}a)^3 + \left(\mu - \frac{1-\mu}{2}\beta^2 n^2\right)k_{ns}a,$$

$$L_{22} = \frac{1-\mu}{2}(1+3\beta^2)(k_{ns}a)^2 + n^2 - \Omega^2,$$

$$L_{23} = L_{32} = \frac{3-\mu}{2}\beta^2 n(k_{ns}a)^2 + n,$$

$$L_{33} = \beta^2(k_{ns}a)^4 + 2n^2\beta^2(k_{ns}a)^2 + 1 - \Omega^2 + \beta^2(1-n^2)^2,$$

$\Omega = \omega a/c_L$ is the nondimensional frequency, and c_L is the extensional phase speed of the shell material. For free vibration where p_x, p_ϕ, and p_r are zeros, the determinant of the matrix L on the right-hand side of Eq. (4) is zero. The coefficients U_{ns} and V_{ns} can be expressed in terms of W_{ns} by solving two of the three free vibration equations,

$$U_{ns} = \alpha_{uns}W_{ns}, \quad V_{ns} = \alpha_{vns}W_{ns}, \tag{5}$$

where α_{uns} and α_{vns} are complex numbers.

II. MOBILITY FUNCTIONS

A. Infinite cylindrical shells

Fuller[10] has demonstrated that the input radial force mobility of an infinite cylindrical shell can be calculated by using the method of residues. His analysis can be applied to calculating other types of the structural mobility of an infi-

nite cylindrical shell. For example, the input axial force mobility (the ratio of the axial velocity component to the axial force component at the same position) for the circumferential mode of n at $x=0$ can be expressed as

$$Y_{UN}^n = \frac{i\omega u_n}{F_N^n} = \frac{\Omega^2}{\omega\rho h a} \sum_{s=1}^{4} R_{ns}^{UN} \tag{6}$$

where F_N^n is the external axial force component applied around the circumference $x=0$ for the circumferential mode of n; R_{ns}^{UN} is the residue at the pole corresponding to the circumferential mode n and the axial wavenumber s, i.e.,

$$R_{ns}^{UN} = \frac{L_{22}L_{33} - L_{23}L_{32}}{(\det|L|)'}, \tag{7}$$

where $\det|L|$ is the determinant of the coefficient matrix in Eq. (4) and the prime denotes the derivative with respect to $k_{ns}a$.

The cross mobility Y_{VS}^n, the ratio of the circumferential velocity component to the radial force F_S^n acting around the circumference at $x=0$ for the circumferential mode of n, can be expressed as

$$Y_{VS}^n = \frac{i\omega v_n}{F_S^n} = \frac{\Omega^2}{\omega\rho h a} \sum_{s=1}^{4} R_{ns}^{VS}, \tag{8}$$

where

$$R_{ns}^{VS} = \frac{L_{21}L_{13} - L_{11}L_{23}}{(\det|L|)'}. \tag{9}$$

B. Semi-infinite cylindrical shells

Although a cut of an infinite cylindrical shell at $x=0$ physically results in two semi-infinite cylindrical shells and each is excited by half of the total external force, the structural mobility of a semi-infinite cylindrical shell at the end is not just twice that of an infinite cylindrical shell because the boundary conditions at the excitation position are different. For semi-infinite cylindrical shells, no restrictions are imposed on the displacement or the velocity at the end, whereas for infinite cylindrical shells symmetry and continuity demand that some velocity components must vanish at the excitation position. For the calculation of a radial force associated mobility, the bending moment, the extensional stress, and the effective shear stress are assumed to be zeros at the end of semi-infinite cylindrical shells, while these stress resultants are nonzero and could be transmitted across the excitation position in infinite cylindrical shells.

The mobility function of a semi-infinite cylindrical shell cannot be formulated by using the method of residues. It may be determined from the motion equation and the boundary conditions. Due to the complexity, however, it does not appear feasible to seek analytic expressions of the structural mobility. Thus a numerical evaluation needs to be introduced.

If the expressions in Eq. (3) are adopted to represent the displacement components of a semi-infinite cylindrical shell, the stress and moment resultant vector at the end $x=0$ can be expressed as

$$Q = [S_x \quad M_x \quad N_x \quad T_x]^T = \sum_{n=0}^{\infty} J_n G_n W_n. \tag{10}$$

For $n>0$, $W_n = [W_{n1}, W_{n2}, W_{n3}, W_{n4}]^T$ and G_n is a 4×4 matrix:

$$G_n(1,s) = \frac{iD}{a^3} \left((k_{ns}a)^3 + (2-\mu)n^2 k_{ns}a \right.$$
$$\left. + \left((k_{ns}a)^2 - \frac{1-\mu}{2}n^2 \right)\alpha_{uns} + \frac{3-\mu}{2}nk_{ns}a\,\alpha_{vns} \right),$$

$$G_n(2,s) = -\frac{D}{a^2} \left((k_{ns}a)^2 + \mu n^2 + k_{ns}a\,\alpha_{uns} + n\mu\alpha_{vns} \right),$$

$$G_n(3,s) = \frac{K}{a} \left(k_{ns}a\,\alpha_{uns} + \mu n\alpha_{vns} + \mu + \beta^2(k_{ns}a)^2 \right),$$

$$G_n(4,s) = -\frac{1-\mu}{2}\frac{K}{a} \left(n\alpha_{uns} + (1-\beta^2) \right.$$
$$\left. \times k_{ns}a\,\alpha_{vns} - n\beta^2 k_{ns}a \right), \quad s=1,2,3,4$$

and

$$J_n = \begin{pmatrix} \cos(n\theta) & 0 & 0 & 0 \\ 0 & \cos(n\theta) & 0 & 0 \\ 0 & 0 & \cos(n\theta) & 0 \\ 0 & 0 & 0 & \sin(n\theta) \end{pmatrix}.$$

For $n=0$, $W_0 = [W_{01}, W_{02}, W_{03}]^T$; J_0 is a 3×3 unit matrix and G_0 is 3×3 matrix where the elements can be calculated from the above equations by neglecting $G_0(m,4)$ and $G_0(4,m)$ $(m=1,2,3,4)$.

For the calculation of the mobility functions associated with a radial force, only one external radial force is assumed to act on the end, that is, the external force vector is $F = [F_S,0,0,0]^T$. For each circumferential mode, the coefficient vector W_n can be determined by solving the matrix equation $Q_n = F_n$ at $x=0$. Then the displacement or velocity at any position of the shell can be determined. The input and cross mobilities at the end and also the transfer mobilities at different positions with reference to the force acting on the end can be calculated from the ratios of the corresponding velocity components to the external force. For the calculation of the axial force associated mobilities, however, the external force vector is assumed to be $F = [0,F_N,0,0]^T$.

C. Finite cylindrical shells

For a finite cylindrical shell of length l, the response may be expressed in the superposition of eight possible waves. For example, the radial component of displacement can be written as

$$w = \sum_{n=0}^{\infty} \left[\sum_{s=1}^{m} W_{ns} \exp(-ik_{ns}x) + \sum_{s=m+1}^{2m} W_{ns} \right.$$

$$\left. \times \exp(ik_{n(s-m)}(x-l)) \right] \cos(n\theta)\exp(i\omega t). \qquad (11)$$

Similar expressions can be written for the axial and circumferential components of displacement. From Eqs. (2), (5), and (11) the stress and moment resultant vector at the ends, $x=0$ and $x=l$, can be expressed as

$$Q|_{x=0} = [S_x \quad M_x \quad N_x \quad T_x]^T|_{x=0}$$

$$= \sum_{n=0}^{\infty} J_n[G_n, -G_n]A_n^0 X_n, \qquad (12a)$$

$$Q|_{x=l} = [S_x \quad M_x \quad N_x \quad T_x]^T|_{x=l}$$

$$= \sum_{n=0}^{\infty} J_n[G_n, -G_n]A_n^l X_n, \qquad (12b)$$

where

$$A_n^0 = \begin{pmatrix} E_m & 0 \\ 0 & B_m \end{pmatrix}, \quad A_n^l = \begin{pmatrix} B_m & 0 \\ 0 & E_m \end{pmatrix},$$

$$B_m = \begin{pmatrix} \exp(-ik_{n1}l) & 0 & 0 & 0 \\ 0 & \exp(-ik_{n2}l) & 0 & 0 \\ 0 & 0 & \cdots & 0 \\ 0 & 0 & 0 & \exp(-ik_{nm}l) \end{pmatrix},$$

E_m is an $m \times m$ unit matrix ($m=3$ for $n=0$ and $m=4$ for $n>0$), $X_0 = [W_{01}, W_{02}, ..., W_{06}]^T$ and $X_n = [W_{n1}, W_{n2}, ..., W_{n8}]^T$ ($n>0$). X_n can be determined by solving the matrix equations resulting from the end boundary conditions. For the calculation of the mobility functions of a finite cylindrical shell, the free end condition is usually assumed at $x=0$ and a desired external force vector is assumed to act on it. The boundary conditions at the other end ($x=l$) will depend on the practical considerations. After X_n is determined, the components of displacement at any position of the shell can be calculated and then the mobility functions can be evaluated from the ratios of the corresponding velocity components to the external force.

III. VIBRATIONAL ENERGY TRANSMISSION

For coupled cylindrical shells, the power flow through the coupling boundary can be expressed in terms of mobility functions. If one of the cylindrical shells (subsystem 1) is excited by an external force vector, $F_e = [F_{Se}, M_e, F_{Ne}, F_{Te}]^T$, at cross section x_e, the velocity vector $D = [\dot{w} \quad \dot{\phi} \quad \dot{u} \quad \dot{v}]^T$ as well as the stress and moment resultant vector Q of the receiving cylindrical shell (subsystem 2) at the coupling boundary can be expressed as[5]

$$D = Y_2(Y_1 + Y_2)^{-1} Y_e F_e, \qquad (13)$$

$$Q = (Y_1 + Y_2)^{-1} Y_e F_e, \qquad (14)$$

where Y_e is a transfer mobility matrix between the force acting position x_e and the coupling boundary, and Y_1 and Y_2
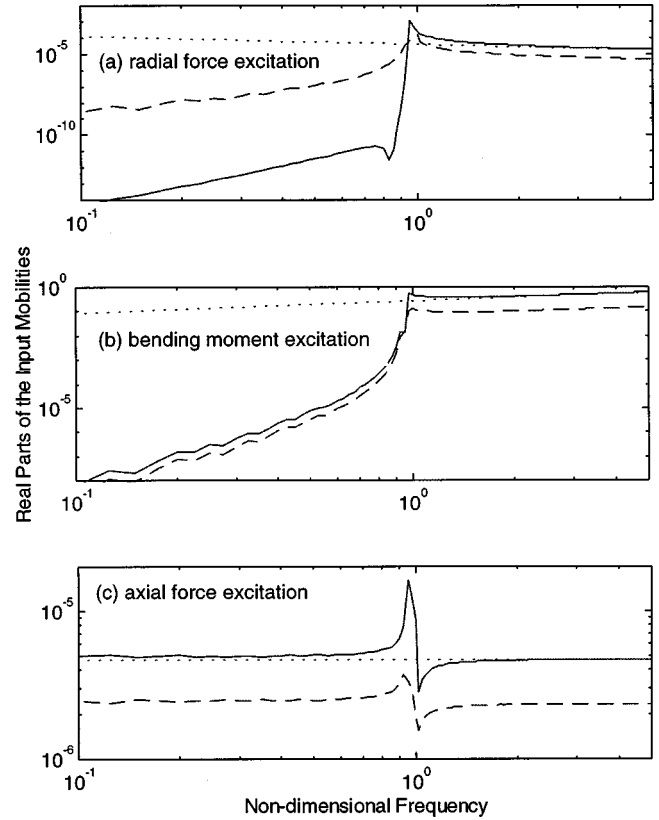
FIG. 2. The real parts of the input mobilities for a steel cylindrical *in vacuo* shell of $h/a = 0.05$ for $n=0$. ———: Semi-infinite shell; – – –: infinite shell; ---: semi-infinite plate.

are the mobility matrices of subsystems 1 and 2 at the coupling boundary, respectively. The power flow across the boundary is given by

$$P = \frac{1}{2} \text{Re}\left\{ \int_{-\pi}^{\pi} Q^T D^* a \, d\theta \right\}$$

$$= \frac{a\pi}{2} \sum_{n=0}^{\infty} \text{Re}\{ F_{en}^T Y_e^{nT} (Y_1^{nT} + Y_2^{nT})^{-1}$$

$$\times Y_2^{n*} (Y_1^{n*} + Y_2^{n*})^{-1} Y_e^{n*} F_{en}^* \}, \qquad (15)$$

where $F_{en} = [F_{Sen}, M_{en}, F_{Nen}, F_{Ten}]^T$ and $F_e = J_n F_{en}$. If $F_e = F_0 \delta(x - x_e)\delta(\theta)$ is a point radial force acting on the position $(x, \theta) = (x_e, 0)$, $M_{en} = F_{Nen} = F_{Ten} = 0$, $F_{Sen} = aF_0/\pi$ ($n>1$), and $F_{Se0} = aF_0/2\pi$.

IV. NUMERICAL RESULTS

A. Mobility functions

Steel cylindrical shells with the wall thickness-to-radius ratios of $h/a = 0.05$ and 0.01 are taken as examples to evaluate the structural mobilities. To illustrate the structural mobilities in a broad frequency range, the analysis is made in a nondimensional frequency range with steps of $\Delta\Omega = 0.025$.

Figures 2–7 show the comparisons of the input mobilities of infinite and semi-infinite cylindrical *in vacuo* shells of $h/a = 0.05$ vibrating in the $n=0$, 1, and 2 circumferential modes, respectively. Also shown for comparison are the real and imaginary parts of the input mobilities of a semi-infinite
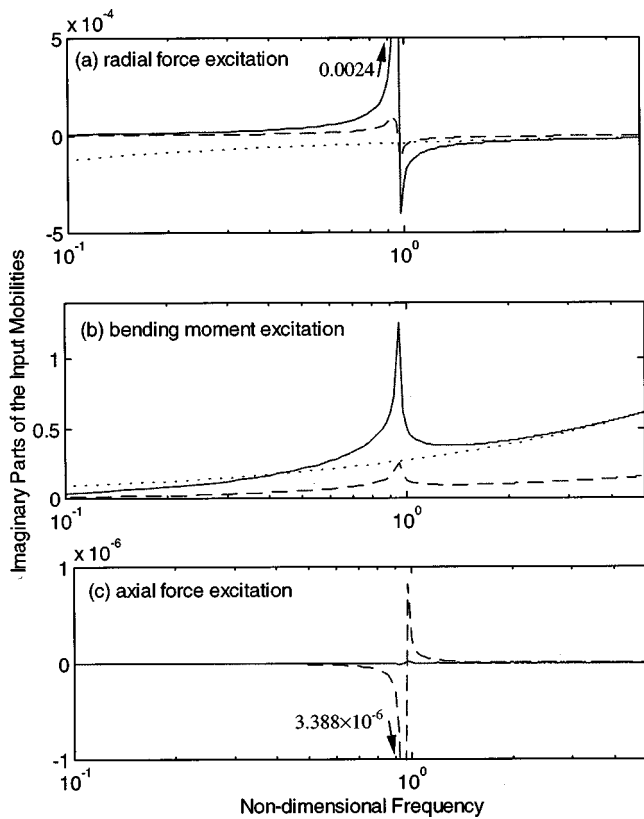
FIG. 3. The imaginary parts of the input mobilities for a steel cylindrical *in vacuo* shell of $h/a = 0.05$ for $n = 0$. ———: Semi-infinite shell; −−−: infinite shell; ---: semi-infinite plate.

FIG. 4. The real parts of the input mobilities for a steel cylindrical *in vacuo* shell of $h/a = 0.05$ for $n = 1$. ———: Semi-infinite shell; −−−: infinite shell; ---: semi-infinite plate.

homogeneous plate with the same thickness and material properties as those of the shells. The plate has a width of $2\pi a$ and is simply supported along the two edges. All the real parts of the input mobilities are positive while the imaginary parts could be negative, depending on frequency and the type of excitation. The magnitudes of both the real and imaginary parts of the input mobilities of the semi-infinite shell are larger than but not exactly twice as those of the infinite one at most frequencies except for the real part of the $n = 0$ input radial force mobility at frequencies below the ring frequency [see Fig. 2(a)] and for the imaginary part of the $n = 0$ input axial force mobility [see Fig. 3(d)]. For the case of a radial force excitation, the real part of the input mobility increases with increasing the circumferential modal number n or frequency at frequencies below the ring frequency. Besides the sharp peak at the ring frequency, peaks or troughs also appear at the cut-on frequencies. At the ring frequency, the real part of the input mobility reaches its maximum value while the imaginary part of the input mobility jumps from a positive value to a negative value. At frequencies above the ring frequency the imaginary part of the input mobility is negative and its magnitude decreases with increasing frequency. At frequencies above twice the ring frequency, however, the input mobility of the semi-infinite shell can be approximated by that of the semi-infinite plate. For $n > 0$, the approximation error of the real part increases with increasing frequency and n. This is because the effect of Poisson's ratio was not considered in the plate but in the shell and it becomes stronger as n increases. When the shells
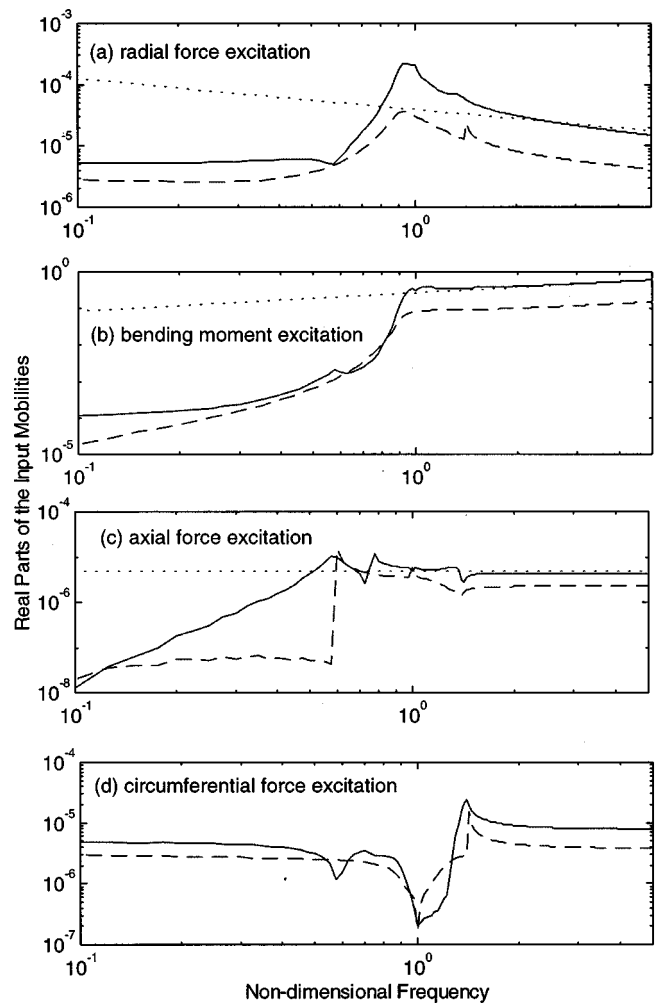
vibrate in the breathing circumferential mode, the real part of the input mobility of the semi-infinite shell is much lower than that of the infinite shell at frequencies below the ring frequency. This is because the axial and rotational components of displacement at the end of the semi-infinite cylindrical shell are not restricted and relatively large while those at the excitation position of the infinite cylindrical shell are required to be zeros due to the symmetry. Therefore, a larger percentage of the external radial force is required to balance the stress resulted from the axial and rotational vibration and a smaller radial component of the displacement is produced for the breathing mode in the semi-infinite cylindrical shell.

For the bending moment excitation, the real part of the input mobility increases with increasing frequency and the circumferential modal number n, especially at frequencies below the ring frequency. The imaginary part of the input mobility is positive and also increases with increasing frequency, but it is insensitive to the change of the circumferential number except at the ring frequency where a peak appears in both the real and imaginary part curves of the input mobility. At frequencies above the ring frequency, the input mobility of a semi-infinite cylindrical shell can be approximated by that of a semi-infinite plate having the same
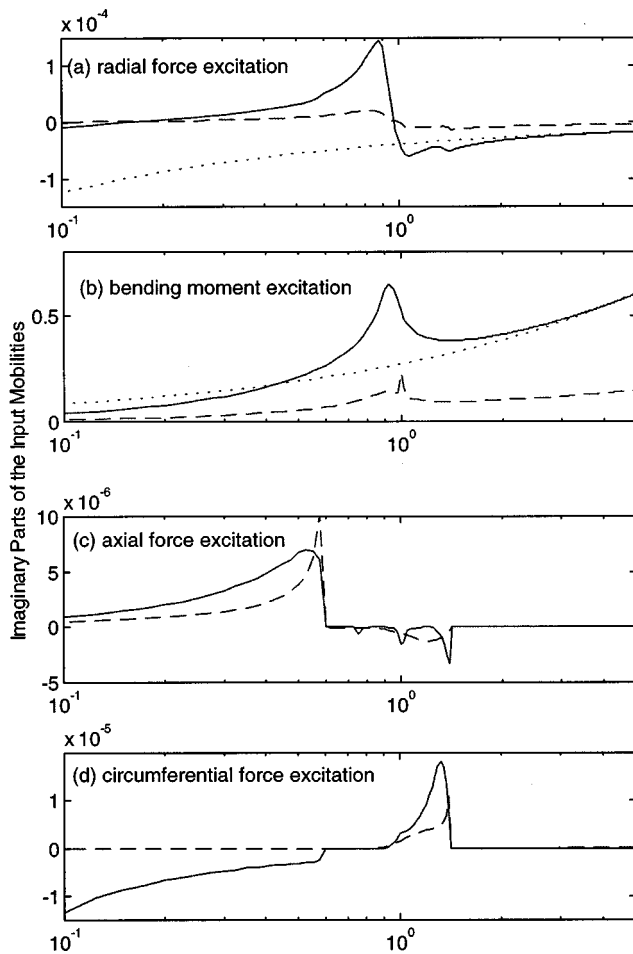
FIG. 5. The imaginary parts of the input mobilities for a steel cylindrical *in vacuo* shell of $h/a = 0.05$ for $n = 1$. ———: Semi-infinite shell; – – –: infinite shell; ---: semi-infinite plate.

FIG. 6. The real parts of the input mobilities for a steel cylindrical *in vacuo* shell of $h/a = 0.05$ for $n = 2$. ———: Semi-infinite shell; – – –: infinite shell; ---: semi-infinite plate.

thickness and material properties. Of all the input mobilities, the input bending moment mobility is the largest. This indicates that for cylindrical shells the bending moment excitation is the most effective source and it should be considered first in noise and vibration control.

For an axial force excitation, the imaginary part of the input mobility is very small at all frequencies except at the ring frequency for $n = 0, 2$. The real part of the input mobility decreases with increasing circumferential modal number n and it is negligibly small for infinite shells but increases with increasing frequency for semi-infinite shells for $n > 0$ at frequencies far below the ring frequency. At frequencies close to the ring frequency, peaks and troughs are present in the mobility curves. At frequencies above the ring frequency, the real parts of the input mobilities become constants and that of a semi-infinite cylindrical shell can be approximated with a negligible positive error by the longitudinal wave mobility of a semi-infinite plate, of which the imaginary value is zero. The approximation error increases with increasing n. The reason is the same as that explained for the case of radial force excitation. Of all the input mobilities, the input axial force mobility is the smallest except for the breathing mode ($n = 0$) at frequencies below the ring frequency.

For a circumferential force excitation, the real part of the input mobility has a trough rather than a peak at the ring
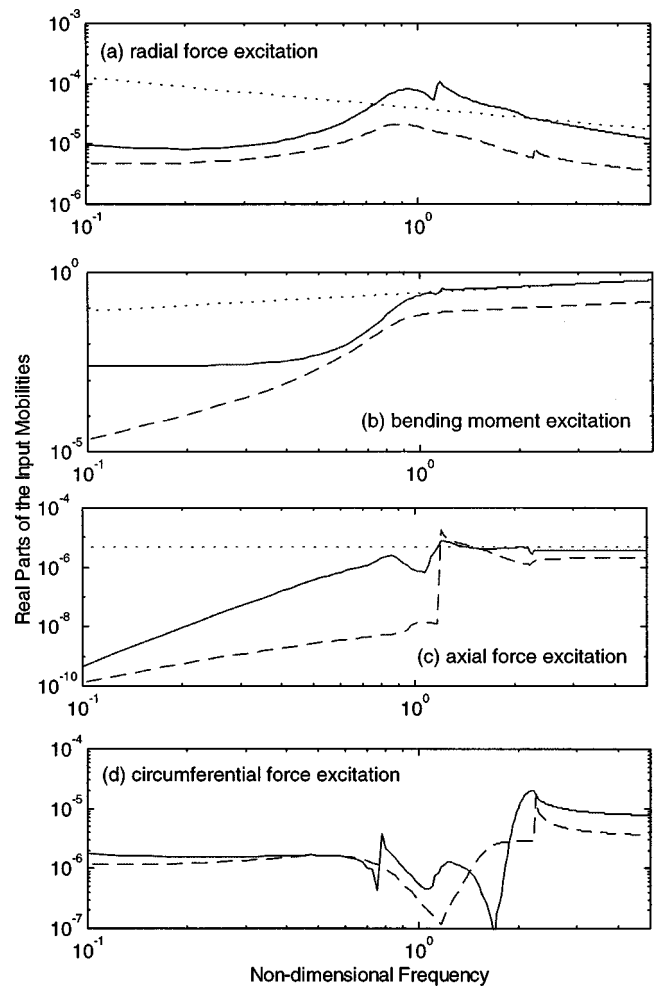
frequency and it is nearly constant at frequencies below half or above twice the ring frequency. The imaginary part of the input mobility increases with increasing frequency. The peaks of the imaginary part curves appear rather than at the ring frequency. At frequencies far below the ring frequency the magnitude of the imaginary part of the input mobility of a semi-infinite cylindrical shell is much larger than that of an infinite cylindrical shell. The input circumferential force mobility is smaller than the input radial force mobility.

Figures 8 and 9 show the comparisons of the input and cross mobilities of a semi-infinite cylindrical shell of $h/a = 0.05$ for $n = 0, 1, 2$, respectively. The real part of cross mobility Y_{US}^n (the ratio of the axial velocity component u_n to the radial force component F_S^n for the circumferential mode of n) is positive at frequencies below the ring frequency and then becomes negative except for the real part of Y_{US}^0, which is negative at all but the ring frequency [the absolute value of the real part of Y_{US}^0 is shown in Fig. 8(a)]. The real part of cross mobility Y_{VS}^n (the ratio of the circumferential velocity component $\dot{v}_n$ to the radial force component F_S^n for the circumferential mode of n), however, has a comparable magnitude but different signs than that of Y_{US}^n at most frequencies. At frequencies below the ring frequency for $n > 0$, the imaginary part of cross mobility Y_{US}^n is negative and very small in
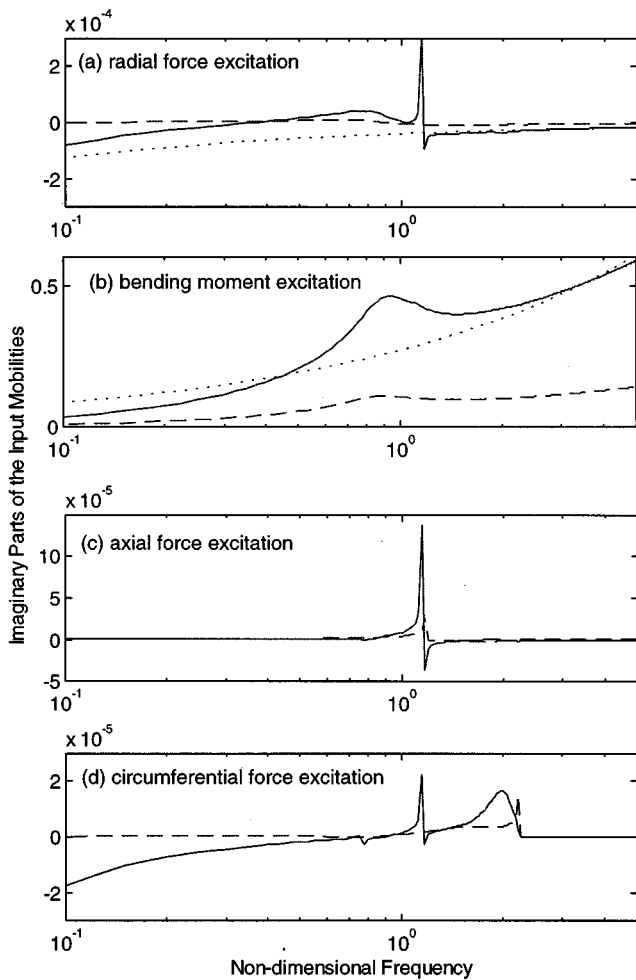
FIG. 7. The imaginary parts of the input mobilities for a steel cylindrical *in vacuo* shell of $h/a = 0.05$ for $n = 2$. ———: Semi-infinite shell; – – –: infinite shell; ---: semi-infinite plate.

FIG. 8. The real parts of the input and cross radial force mobilities for a steel semi-infinite cylindrical *in vacuo* shell of $h/a = 0.05$ for $n = 0,1,2$. ———: Input mobility Y_{WS}; – – –: cross mobility Y_{US}; ---: cross mobility Y_{VS}.

comparison to that of cross mobility Y_{VS}^n, which is positive. At frequencies above the ring frequency, both real and imaginary parts of Y_{US}^n and Y_{VS}^n can be negligible in comparison with those of the input mobility Y_{WS}^n. This figure indicates that the cross mobilities need to be considered only at frequencies below the ring frequency for the calculation of power flow in coupled shells.

Figures 10 and 11 show the comparisons of the real and imaginary parts of the input radial force mobilities of finite and semi-infinite cylindrical shells. The finite and semi-infinite cylindrical shells have the same radius (100 mm) and the same material properties. In order to assess the effect of the shell wall thickness on the structural mobility, two different shell wall thicknesses (1 and 5 mm) are chosen, resulting in different wall thickness-to-radius ratios of 0.01 and 0.05. For the finite cylindrical shells, the length-to-radius ratio of 10 is chosen and the dissipation loss factor is assumed to be a constant of 0.005. The free-free end conditions are assumed. It can be seen that for a semi-infinite cylindrical shell the change of shell wall thickness does not lead to the change of the mobility curve shapes. However, a thinner shell wall results in a larger mobility (both real and imaginary parts), but the mobility ratio is not equal to the wall thickness ratio. For finite cylindrical shells, both the real and
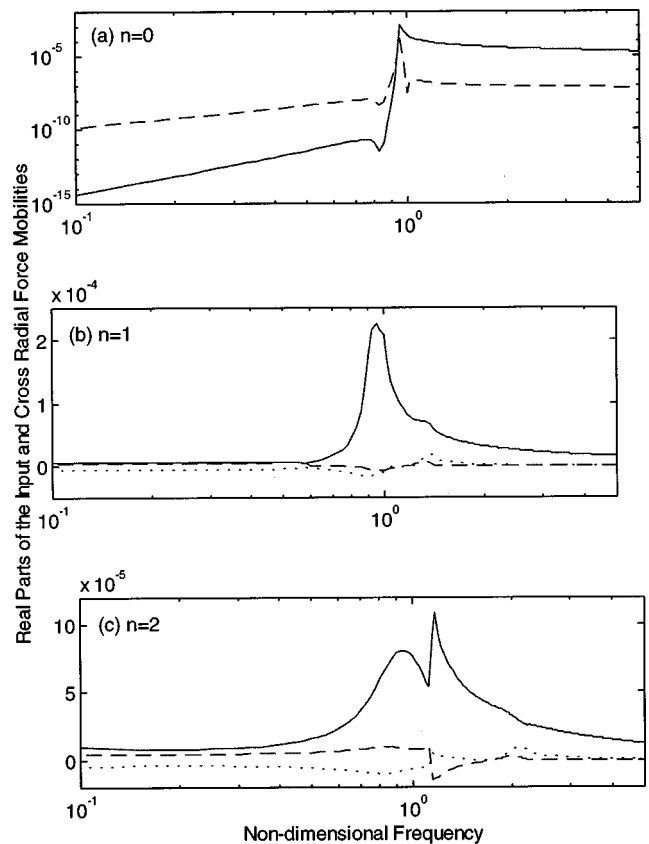
imaginary parts of the mobility fluctuate and the fluctuation decreases with increasing frequency or with decreasing the shell wall thickness. At frequencies above the ring frequency, the mobility of a semi-infinite cylindrical shell is a good approximation of the frequency-averaged mobility of a finite cylindrical shell. At frequencies below the ring frequency, the mobility of a semi-infinite cylindrical shell is larger than the frequency-averaged mobility of a finite cylindrical shell except for the breathing mode of $n = 0$ where the input mobility of the finite shell is smooth and much higher than that of the semi-infinite cylindrical shell.

Figures 12 and 13 show the comparisons of the real and imaginary parts of the $n = 1$ input radial force mobilities of finite cylindrical shells with different shell lengths and different dissipation loss factors. It is shown that the increase of shell length or the dissipation loss factor results in not only the reduction of the fluctuation but also the increase of the frequency-averaged mobility level, especially at frequencies below the ring frequency. It may be concluded from Figs. 10–13 that for finite cylindrical shells the level and the fluctuation (the magnitude and the upper frequency limit) of the mobility functions will depend on the shell wall thickness and shell length as well as the dissipation loss factor.

Figures 14 and 15 show the comparisons of the real and imaginary parts of the $n = 1$ input radial force mobilities of finite cylindrical shells of $h/a = 0.05$, $\eta = 5 \times 10^{-3}$, and $L/a = 10$ with different end conditions. Different boundary
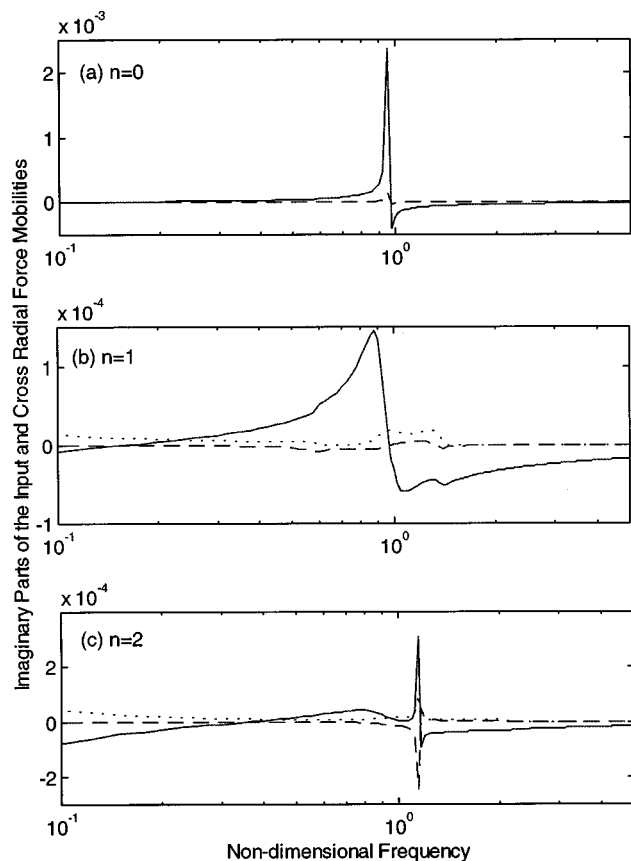
FIG. 9. The imaginary parts of the input and cross radial force mobilities for a steel semi-infinite cylindrical *in vacuo* shell of $h/a = 0.05$ for $n = 0,1,2$. ——: Input mobility Y_{WS}; – – –: cross mobility Y_{US}; ---: cross mobility Y_{VS}.

FIG. 10. The real parts of the input radial force mobilities for the semi-infinite steel cylindrical shells of $h/a = 0.05$ (– – – –) and $h/a = 0.01$ (---) and for the finite steel cylindrical shells ($L/a = 10$; $\eta = 5 \times 10^{-3}$) of $h/a = 0.05$ (——) and $h/a = 0.01$ (– – –) with free-free end conditions.

conditions result in different mobility curve shapes because of different natural frequencies. A large difference in the mobility curve shapes mainly appears at frequencies below and close to the ring frequency. For the free-simply supported and the free-clamped end conditions, the difference is negligible at frequencies far below the ring frequency but is visible at frequencies above the ring frequency. For the free-free and the free-clamped end conditions, however, the difference is large at frequencies far below the ring frequency but is negligible at frequencies above the ring frequency. The boundary end conditions will not affect the mobility levels. It was shown in the calculation that the effects of the boundary end conditions on the mobility functions is significant only for lightly damped short finite cylindrical shells.

B. Power flow in coupled cylindrical shells

Consider that two thin-walled cylindrical *in vacuo* shells are coupled at their ends. The uncoupled end of each shell is assumed to be simply supported. One of the shells (subsystem 1) is excited by a point radial force at the position of 0.6 m away from the coupling boundary. The physical and material properties of the coupled cylindrical shells are shown in Table I. Based on the consideration that the dissipation loss factor is typically of order 10^{-4} to 10^{-3} for a homogeneous cylindrical shell, 10^{-3} to 10^{-2} for a built-up cylindrical shell with bolted joints, and of order 10^{-2} to
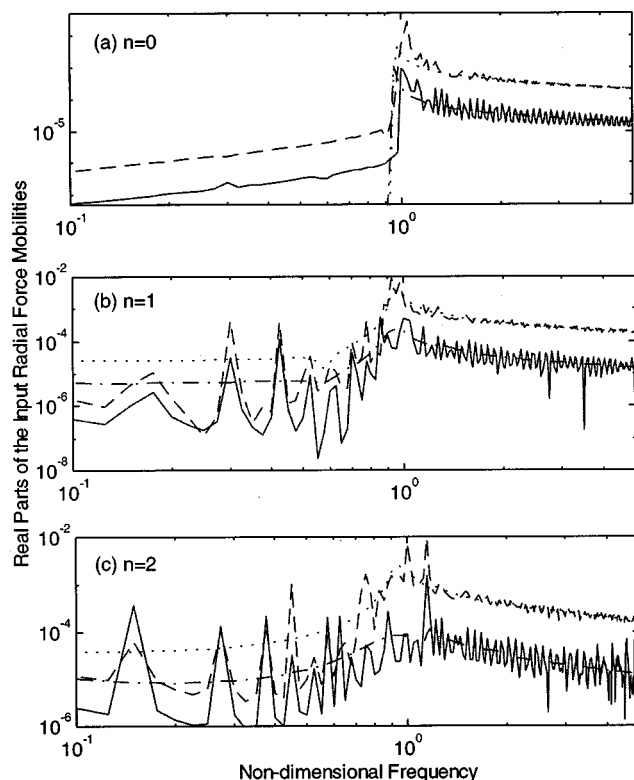
10^{-1} for an operational cylindrical shell containing machinery,[15] the dissipation loss factor of 5×10^{-3} is assumed in this study except for case D. The input power and the power flow in the coupled cylindrical shells are estimated using both the traveling wave method and the mobility method. For the traveling wave method, every displacement component of each shell is assumed to be the superposition of eight wave components [see Eq. (11)]. The wave amplitudes are determined from Eq. (5) and the equations resulting from the conditions in the source location and the coupling boundary. Then the stress and moment resultant vector at coupling boundary is determined from Eq. (2). For the mobility method, the velocity vector and the stress/moment vector are expressed in terms of mobility functions [see Eqs. (13) and (14)]. The input power is calculated using the input mobility of an infinite cylindrical shell and the power flow is calculated from Eq. (15) by using the mobility functions of a semi-infinite cylindrical shell. Figure 16 shows the comparison of the input powers into the subsystem 1 in case A calculated using the traveling wave method and the mobility method. It can be seen that the input power increases first with increasing frequency to reach a maximum value at the ring frequency and then decreases with increasing frequency. Except for the breathing mode of $n = 0$ at frequencies below the ring frequency, the input power calculated using the traveling wave method fluctuates. The mobility method, which uses the mobilities of an infinite cylindrical shell instead of those of a finite cylindrical shell, can give an accurate frequency average estimation of the input power at frequencies
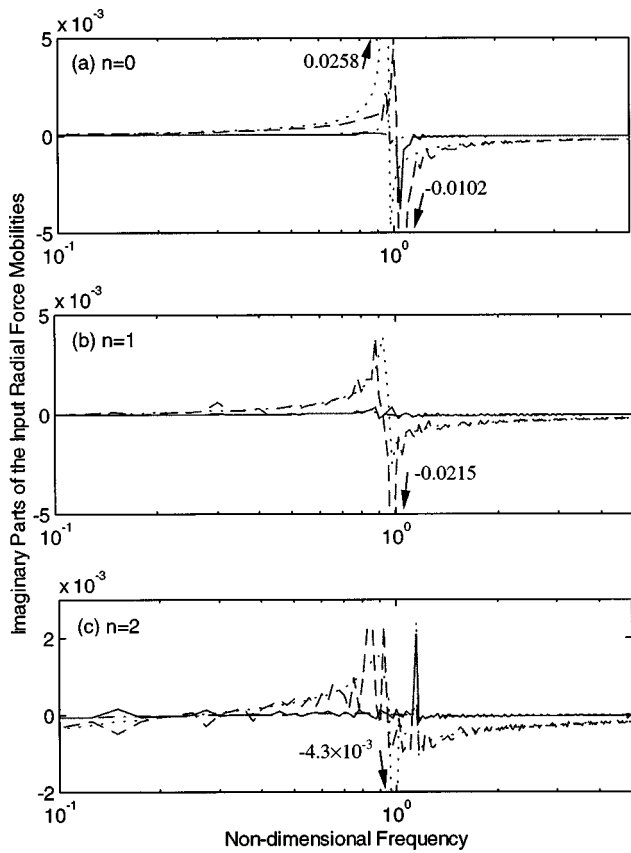
FIG. 11. The imaginary parts of the input radial force mobilities for the semi-infinite steel cylindrical shells of $h/a=0.05$ (----) and $h/a=0.01$ (---) and for the finite steel cylindrical shells ($L/a=10$; $\eta=5\times10^{-3}$) of $h/a=0.05$ (———) and $h/a=0.01$ (---) with free-free end conditions.

above the ring frequency but will give an overestimation resulting in a positive estimation error, which decreases with increasing frequency, at frequencies below the ring frequency. However, it was shown in the calculation that the fluctuation magnitude of input power into a finite cylindrical shell and the estimate error for using the mobility method
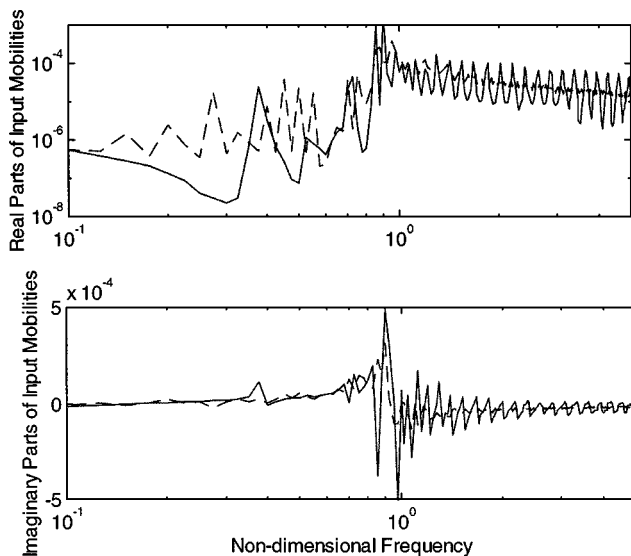
FIG. 12. The $n=1$ input radial force mobilities for the finite steel cylindrical shells of $h/a=0.05$ and $\eta=5\times10^{-3}$ with free-free end conditions. ———: $L/a=5$; ---: $L/a=20$.
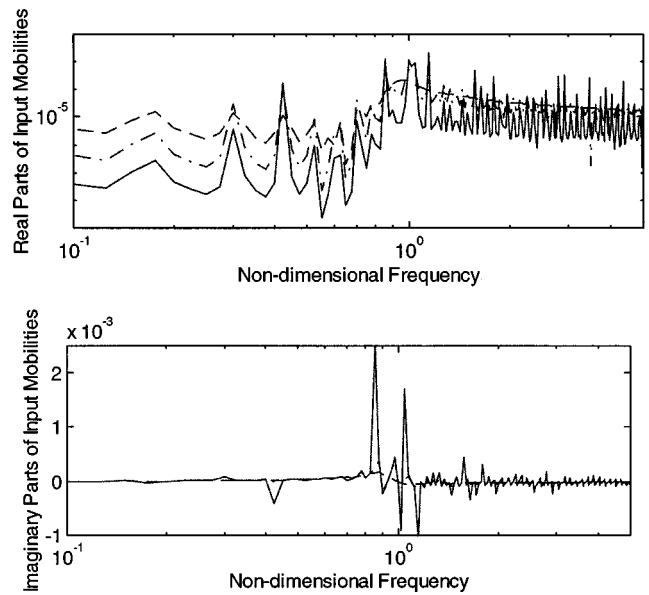
FIG. 13. The $n=1$ input radial force mobilities for the finite steel cylindrical shells of $h/a=0.05$ and $L/a=10$ with free-free end conditions. ———: $\eta=5\times10^{-4}$; ---: $\eta=5\times10^{-3}$; ----: $\eta=5\times10^{-2}$.

decrease with decreasing the shell wall thickness or with increasing the shell length and the dissipation loss factor.

Figures 17 and 18 show the comparison of the power flows across the coupling boundary between two finite cylindrical shells, which are calculated using the traveling wave method and the mobility method, respectively. Similar to the
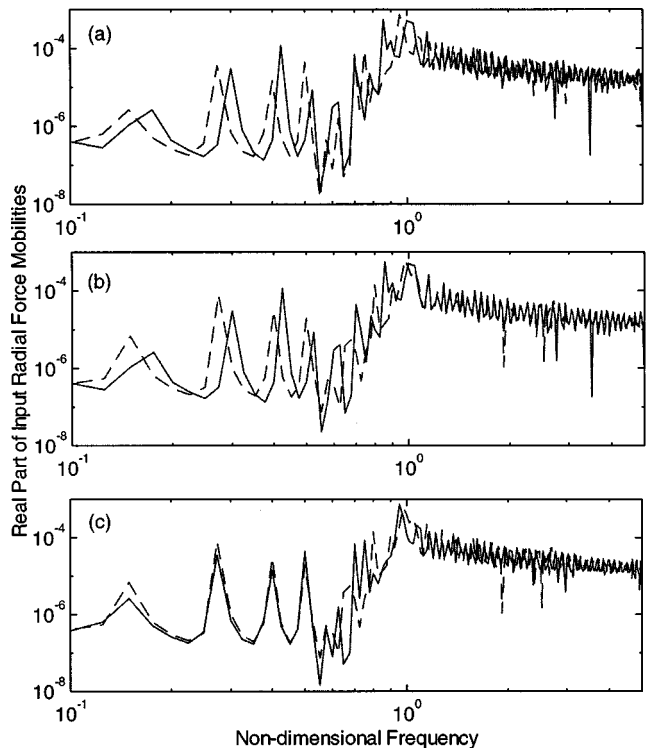
FIG. 14. The real parts of the $n=1$ input radial force mobilities for the finite steel cylindrical shells of $h/a=0.05$, $\eta=5\times10^{-3}$ and $L/a=10$ with different end conditions. (a) ———: free-free; ---: free-simply supported; (b) ———: free-free; ---: free-clamped; (c) ———: free-simply supported; ---: free-clamped.

1710   J. Acoust. Soc. Am., Vol. 105, No. 3, March 1999

Ming *et al.*: Coupled cylindrical shells   1710

FIG. 15. The imaginary parts of the $n=1$ input radial force mobilities for the finite steel cylindrical shells of $h/a=0.05$, $\eta=5\times10^{-3}$ and $L/a=10$ with different end conditions. (a) ———: free-free; –––: free-simply supported; (b) ———: free-free; –––: free-clamped; (c) ———: free-simply supported; –––: free-clamped.

FIG. 16. The input powers of a radial force excited finite steel cylindrical *in vacuo* shell of $h/a=0.05$; $L/a=10$ and $\eta=5\times10^{-3}$ for $n=0,1,2$. ———: Calculated using the traveling wave method; –––: calculated using the mobility functions of an infinite cylindrical shell.

input powers, the power flows between finite cylindrical shells fluctuate and their levels increase with increasing frequency at frequencies below the ring frequency but decrease with increasing frequency at frequencies above the ring frequency. The mobility method, which uses the mobility functions of a semi-infinite cylindrical shell instead of those of a finite cylindrical shell, overestimates the actual power flows and the estimation error depends on frequency, the circumferential number n, the dissipation loss factor, the wall thickness, and the length of the cylindrical shell. If the receiving cylindrical shell is longer, thinner, or of a larger dissipation

loss factor, the accuracy of the mobility method will be higher, especially for a lower circumferential number and at frequencies above the ring frequency. For a practical pipe system, the dissipation loss factor is usually of order 10^{-3} to 10^{-2}. The mobility method could give a reasonably accurate estimation of the power flows even at low frequencies if the length-to-radius ratio of the receiving pipe is larger than 10.

V. CONCLUSIONS

In this paper, the mobility functions of finite and semi-infinite elastic cylindrical shells of $h/a=0.01$ and 0.05 have been investigated and subsequently used to estimate the power flows in coupled cylindrical shells. For semi-infinite

TABLE I. Physical and material properties of the coupled cylindrical shells.

Case	Subsystem	Young's modulus (N/m²)	Poisson's ratio	Density (kg/m³)	Loss factor	Length (m)	Thickness (mm)	Radius (m)
A	1	2.1×10^{11}	0.3	7800	5×10^{-3}	1.0	5	0.1
	2	2.1×10^{11}	0.3	7800	5×10^{-3}	1.0	5	0.1
B	1	2.1×10^{11}	0.3	7800	5×10^{-3}	1.0	5	0.1
	2	2.1×10^{11}	0.3	7800	5×10^{-3}	4.0	5	0.1
C	1	2.1×10^{11}	0.3	7800	5×10^{-3}	1.0	1	0.1
	2	2.1×10^{11}	0.3	7800	5×10^{-3}	1.0	1	0.1
D	1	2.1×10^{11}	0.3	7800	1×10^{-4}	1.0	1	0.1
	2	2.1×10^{11}	0.3	7800	1×10^{-4}	1.0	1	0.1
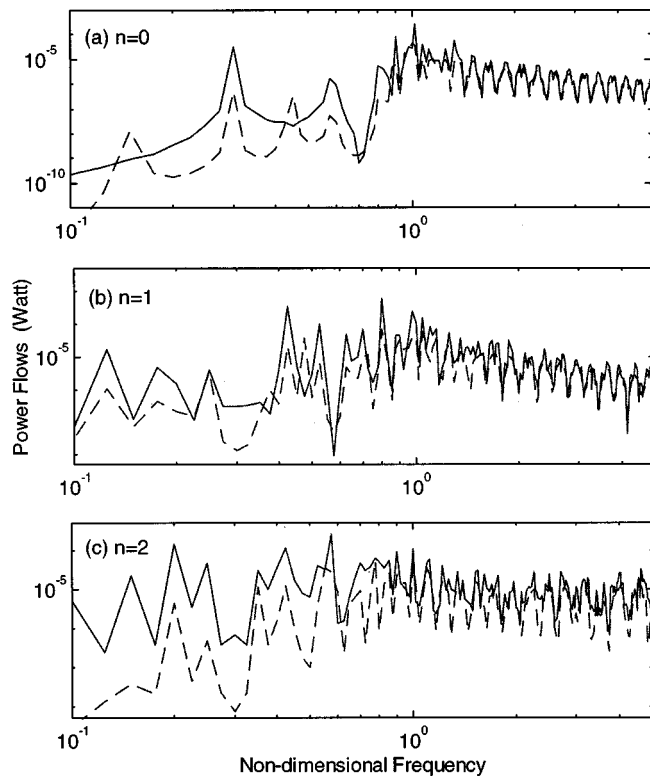
FIG. 17. The power flows between two coupled finite steel cylindrical *in vacuo* shells (case A) for $n = 0,1,2$. $---$: Calculated using the traveling wave method; $———$: calculated using the mobility functions of semi-infinite cylindrical shells.

and infinite elastic cylindrical *in vacuo* shells, the structural mobility is a function of frequency, the circumferential modal number, the excitation type, and also the shell wall thickness. The smaller the shell wall thickness, the larger the structural mobility. Peaks or troughs are present in the input mobility curves at the ring and cut-on frequencies. The real part of the input mobility is always positive, but the imaginary part of the input mobility (except for the input bending moment mobility) could be negative depending on the wavetype and the frequency range of interest. The cross mobility is usually negligible at frequencies above the ring frequency in comparison with the corresponding input mobility. The input mobility of a semi-infinite cylindrical shell is greater than that of an infinite cylindrical shell except for the breathing circumferential mode at frequencies below the ring fre-
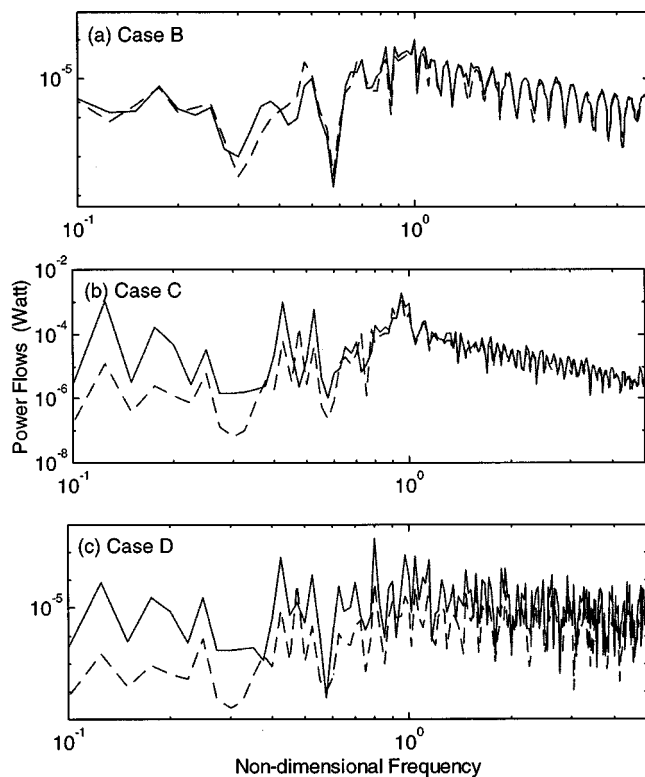
FIG. 18. The power flows between two coupled finite steel cylindrical *in vacuo* shells for $n = 0,1,2$. $---$: Calculated using the traveling wave method; $———$: calculated using the mobility functions of semi-infinite cylindrical shells: (a) case B; (b) case C; (c) case D.

quency, and it can be predicted on the basis of a semi-infinite plate model at frequencies above the ring frequency.

For finite cylindrical shells, the input mobility fluctuates and its level is a function of the dissipation loss factor, the shell length, and the shell wall thickness. The fluctuation decreases with increasing frequency, the dissipation loss factor, the shell length, or with decreasing the shell wall thickness. The boundary conditions affect the mobility curve shapes because of different natural frequencies, but they do not affect the mobility levels. For a finite cylindrical shell with a dissipation loss factor of order 10^{-3} and a length to radius ratio of not less than 10, the frequency averaged mobility can be approximated with a negligible error by the mobility of a semi-infinite cylindrical shell at frequencies above the ring frequency. At frequencies far below the ring frequency, however, the frequency-averaged mobility of a finite cylindrical shell is usually smaller than the mobility of a semi-infinite cylindrical shell unless the dissipation loss factor of the finite shell is very high (on an order of 10^{-2}) or the shell length is reasonably great (the shell length-to-radius ratio is larger than 40).

Both the input power and the power flow in a coupled finite cylindrical shell system can be estimated using the mobility method, which uses the mobility functions of a semi-infinite or infinite cylindrical shell instead of those of a finite cylindrical shell. The estimation error is a function of frequency, the circumferential number n, the dissipation loss factors, the wall thicknesses, and the shell lengths of the finite cylindrical shells. The mobility method gives only a frequency-averaged input power. For a coupled cylindrical shell system with dissipation loss factors of order 10^{-3}, the mobility method can give a reasonably accurate estimation of the power flows at frequencies above the ring frequency. At low frequencies, however, the mobility method overesti-

mates the power flows and the accuracy is usually poor unless the dissipation loss factor or the shell length-to-radius ratio of the receiving cylindrical shell is large.

ACKNOWLEDGMENTS

[1] J. M. Cuschieri, ''Excitation and response of piping systems,'' J. Acoust. Soc. Am. **83**, 641–646 (1988).

[2] J. M. Cuschieri, ''Vibration transmission through periodic structures using mobility power flow method,'' J. Sound Vib. **143**(1), 65–74 (1990).

[3] J. M. Cuschieri, ''Structural power flow analysis using a mobility approach of an L-shaped plate,'' J. Acoust. Soc. Am. **87**, 1159–1165 (1990).

[4] B. L. Clarkson, ''Estimation of the coupling loss factor of structural joints,'' J. Mech. Eng. Sci., Part C **205**, 17–22 (1991).

[5] N. H. Farag and J. Pan, ''Dynamic response and power flow in two dimensional coupled beam structures under in-plane loading,'' J. Acoust. Soc. Am. **99**, 2930–2937 (1996).

[6] L. Cremer, M. Heckl, and E. E. Ungar, *Structure-borne Sound* (Springer-Verlag, New York, 1973).

[7] R. S. Ming and B. M. Gibbs, ''Experimental study of rotational mobilities of concrete floors,'' Proc. Inst. Acoust. **15**(3), 303–310 (1990).

[8] P. A. Franken, ''Input impedances of simple cylindrical structures,'' J. Acoust. Soc. Am. **32**, 473–477 (1960).

[9] M. Heckl, ''Vibrations of point-driven cylindrical shells,'' J. Acoust. Soc. Am. **34**, 1553–1557 (1962).

[10] C. R. Fuller, ''The input mobility of an infinite circular cylindrical elastic shell filled with fluid,'' J. Sound Vib. **87**(3), 409–427 (1983).

[11] A. Harari, ''Wave propagation in cylindrical shells with finite regions of structural discontinuity,'' J. Acoust. Soc. Am. **62**, 1196–1205 (1977).

[12] W. Flugge, *Stresses in Shells* (Springer-Verlag, New York, 1973).

[13] A. W. Leissa, ''Vibration of Shells,'' NASA SP-288, 1973.

[14] C. R. Fuller, ''The effects of wall discontinuities on the propagation of flexural waves in cylindrical shells,'' J. Sound Vib. **75**(2), 207–228 (1981).

[15] M. C. Junger and D. Feit, *Sound, Structures and Their Interaction* (MIT, Cambridge, MA, 1972).

Minimizing the sound power radiated by a cube as a function of the size of constrained layer damping patches

Daniel H. Kruger and J. Adin Mann III
Department of Aerospace Engineering and Engineering Mechanics, 2019 Black Engineering Building, Iowa State University, Ames, Iowa 50011

In cases where a structure's excitation cannot be altered, the sound radiation from the structure must be minimized by modifying the structure within given design constraints. In this work small modifications of an existing structure are considered, rather than a complete design of complex material geometries and properties, or active control methods. Sound power radiated by a cube as a function of normal surface velocity was written using the boundary element method (BEM) [K. A. Cunefare and G. H. Koopman, J. Vib. Acoust. **113**, 387–394 (1991)]. The normal surface velocity of a square plate was measured using a laser vibrometer. The plate was measured with no damping and with eight areas of constrained layer damping material. A cube was simulated by placing various combinations of measured plate velocity distributions on the sides of the cube. In this case, the BEM power function was minimized using a finite difference modification of the gradient method and by the method of simulated annealing. Sound power of the cube was reduced by as much as 8 dB while applying constrained layer damping material to only 0.93% of the cube's surface area when one side of the cube was vibrating. The sound power radiated by the cube was reduced by 7.8 dB by covering just 4.06% of the total surface area of the cube when all six sides of the cube were vibrating. © *1999 Acoustical Society of America.* [S0001-4966(98)02809-4]

PACS numbers: 43.40.Rj [CBB]

INTRODUCTION

Reducing the sound radiated by structures with outer surfaces consisting mainly of thin metal sheets or plates is of great interest to many working in structural acoustics. Examples of such structures are washing machines, refrigerators, or even a car body. Much of the current work consists of implementing active control measures, or performing a major redesign of the shape or structural properties of the machine being studied.[1,2] The primary objective of this paper is to reduce the sound radiated by structures through passive control measures that are added to an existing structure. Typically, the existing structure has been designed for performance specifications other than low noise levels and cannot be dramatically redesigned. A further objective is to show that significant reductions in the sound power radiated by such a structure can be achieved through the application of small patches of constrained layer damping material. This is supported by Lall *et al.*[3] who show that the damping loss factor of a plate can be maximized as a function of the size and location of a damping patch.

Previous work by Spalding and Mann[4] and Kruger *et al.*[5] demonstrated that the structural intensity can be used to identify locations on a structure where constrained layer damping patches are effective. This paper will demonstrate a method to then optimize the size of the damping patches. Finally, it is a goal of this work to show that there is an optimal amount of constrained layer damping material that should be used within designated constraints. Specifically, once the radiated sound power is minimized within a specified maximum area of damping material, applying more damping than the optimal amount can actually cause the radiated sound power levels to increase above the minimum.

In the work presented in this paper, the sound power radiated by a structure is written as a quadratic function of the normal surface velocity using the boundary element method (BEM).[1,2] Next, two gradient methods for minimizing the radiated sound power as a function of one or more structural parameters are developed for the case where the dependence of normal surface velocity as a function of structural parameters is measured experimentally. The two gradient methods prove to be inadequate to solve all the optimization examples, especially the case where several structural parameters are simultaneously optimized. Therefore, the method of simulated annealing was applied to this optimization problem. While the optimized function used in this paper could not be fully determined analytically, this work does establish a fully general optimization process once the dependence of the normal surface velocity on structural parameters can be determined analytically.

Finally, the results of studies performed using the optimization techniques to minimize the radiated sound power of a cube are presented. The studies minimize the radiated sound power as a function of the area of a constrained layer damping patch placed inside the surface of a vibrating cubic structure. Velocity fields for this cube were constructed by assembling the measured surface velocity of a clamped thin square plate under various damping conditions.

I. OPTIMIZED FUNCTION

The radiated sound power is to be optimized (minimized) as a function of structural parameters. Without an efficient method to directly express the radiated sound power as a function of a structural parameter, for example, damping patch size and location, a hybrid method was used. Since the
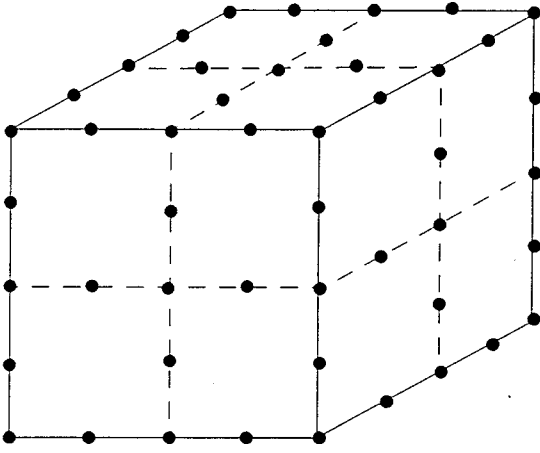
FIG. 1. Pictorial diagram of a boundary element discretization for a cubic structure.

radiated sound power as a function of a structure's normal velocity is readily determined by the boundary element method (BEM), the following function was defined for this work,

$$W(v(a)),\qquad(1)$$

where the radiated sound power, W, is a function of the normal surface velocity, v, and the normal surface velocity is a function of the structural parameter(s) a. This hybrid function was chosen because the calculation of the normal surface velocity as a function of structural parameters, $v(a)$, is not thoroughly developed for discrete constrained layer damping patches of arbitrary shape, location, and size. Therefore, defining the sound power with Eq. (1) and using approximate expressions for $v(a)$ allows us to develop the framework to implement gradient and simulated annealing optimization processes. Once the capability exists to accurately determine $v(a)$, then this can be added to the established optimization framework for completely general problems to be solved. In the meantime, the optimization method developed in this paper are limited by the approximate determination of $v(a)$.

II. BOUNDARY ELEMENT METHOD

All elements of the method for writing the sound power radiated by a structure in terms of its normal surface velocity via the boundary element method (BEM) have been covered extensively in previous papers.[1,2] Thus, only a brief description of the BEM and its adaptation to passive noise control methods will be presented. The main points of the gradient method are also documented extensively in the literature.[6] Therefore, only the basic ideas and modifications made for the purpose of optimizing with respect to a structural parameter, such as constrained layer damping material, will be discussed. Modeling the effects of constrained layer damping is not addressed in this work.

The basic procedure in the BEM is to divide the surface of a structure into individual boundary elements as shown in Fig. 1. In this research, the boundary elements consist of eight nodes, each with quadratic shape functions. Once the structure's surface is discretized, the radiated sound power of

the structure, W, can be written as a quadratic function of a column vector $\{V\}$ which consists of the complex normal surface velocity at each node,

$$W(V)=\tfrac{1}{4}\{V\}H[B]\{V\},\qquad(2)$$

where H denotes the complex conjugate of the transpose and $[B]$ is a matrix of coefficients. The calculation of $[B]$ is fully covered by Cunefare and Koopmann.[1]

The $[B]$ matrix relates the normal velocity of the structure to the sound power radiated by the structure using information about the geometry of the structure, the frequency, and the three-dimensional acoustic free space Green's function. The matrix of coefficients $[B]$ is calculated from the BEM.

Several characteristics of the $[B]$ matrix are important to note. First of all, it is not a function of the surface velocity $\{V\}$. Further, $[B]$ is not a function of the material of the vibrating structure. Thus, once a $[B]$ matrix is calculated for a given structural geometry, the sound power radiated for that structure can be calculated for any surface velocity placed on that structure at a given frequency. This fact is used extensively in the optimization process. In reality, changes in the velocity pattern of a structure are the result of structural changes, such as variations in material or the application of damping and stiffening materials. Thus, the frequency of a given velocity pattern, such as a mode of the structure, can change. It has been verified that the same $[B]$ matrix can be used for a structure whose velocity pattern is being altered by some form of structural modification, as long as the frequency of the velocity pattern does not vary by more than ten percent of the original value.[7,8] This limit is chosen because changes in sound power that result from frequency changes of 10% begin to exceed reductions in power resulting from altered velocity patterns.

III. THE GRADIENT METHOD

Gradient optimization methods were first investigated for the optimization problem. The gradient method begins with computing a direction of search vector, $\{P\}_j$, which is calculated from the gradient of the sound power expressed in Eq. (2) with respect to velocity,

$$\{P\}_j^V=-\frac{\partial W}{\partial\{V\}}=-\frac{1}{2}\,([B])\{V\}_j,\qquad(3)$$

where the subscript j denotes the iteration number. This vector points in the opposite direction of the gradient of the sound power (as a function of velocity), since the gradient always points toward changes in the velocity vector which will increase the value of the sound power. Then the power W is rewritten as a function of the direction of search vector and a step size parameter θ,

$$W_{\theta_j}=W(\{V\}_j+\theta_j\{P\}_j).\qquad(4)$$

The quantity θ_j represents how far the velocity should be modified in the direction of search in order to change the value of the sound power in the direction of a minimum.

It is now desired to calculate the value of θ_j which minimizes the power function denoted in Eq. (2). Since the power

as a function of velocity resulting from the BEM is quadratic, the value of θ_j which minimizes Eq. (4) is found by taking the first derivative of that equation with respect to θ_j and setting it equal to zero, as shown below:

$$\frac{\partial}{\partial \theta_j} \left[W(\{V\}_j + \theta_j \{P\}_j) \right] = 0. \tag{5}$$

Then Eq. (5) is solved for θ_j, and the new velocity and sound power are calculated. Both the velocity and sound power are subject to constraints and convergence criteria that are described in the next sections.

When optimizing the sound radiation with respect to physical structural parameters, it is necessary to compute the direction of search vector as a function of the structural parameter of interest. We have already presented an analytical expression for the sound power as a function of surface normal velocity in Eq. (2). Initially we will assume that an analytical relationship for the velocity vector as a function of some set of structural parameters also exists. Further, these two functions can then be combined to form an equation for the sound power as a function of the set of structural parameters, Eq. (1). Then, a direction of search vector for this power function, D_j, can be written as a multiplication of the gradients of the two separate functions,

$$D_j = -\left\{ \frac{\partial W}{\partial a_i} \right\}_j = -\left\{ \frac{\partial W}{\partial V} \right\}_j \left[\frac{\partial V}{\partial a_i} \right]_j, \tag{6}$$

where j is the iteration number and the a_i represents a set of structural parameters. For example, a set a_i could consist of parameters describing the location, size, and thickness of one or more damping patches added to the structure's surface. The rest of the gradient method can then be carried out as previously described.

In many cases, however, an analytic relationship between surface velocity and a set of structural parameters is not currently known. Application of small constrained layer damping patches is currently one of these cases. A future goal is to express this relationship analytically. Until then, we will use measurements to determine the result of applying constrained layer damping material. Because of this, some modifications of the gradient method will be made next.

The following optimization process was developed for the situation when the normal velocity on the surface of the structure is only known at discrete values of the structural parameters that are to be modified. These velocities are obtained, for example, by performing a series of measurements as a set of structural parameters is varied. Once these measurements are completed, the derivative of velocity with respect to the structural parameters is approximated using a finite difference relationship,

$$\left\{ \frac{\partial V}{\partial a_i} \right\}_k = \frac{\{V\}_{k+1} - \{V\}_k}{(\Delta a_i)_k}, \tag{7}$$

where the subscript k denotes the kth value of structural parameter a_i, and the subscript i denotes the ith structural parameter in the set a_i at which the surface normal velocity is known. The gradient of the radiated sound power with respect to the normal surface velocity is also needed at the

same values of the velocity that are known for the discrete values of the structural parameters. This gradient, however, can be calculated exactly,

$$\left\{ \frac{\partial W}{\partial V} \right\}_k = \frac{1}{2} [B]\{V\}_k. \tag{8}$$

The two vectors can be multiplied together to get a total derivative of radiated sound power with respect to change in structural parameter for each structural parameter via

$$\left\{ \frac{\partial W}{\partial a_i} \right\}_k = \left\{ \frac{\partial W}{\partial V} \right\}_k^T \left\{ \frac{\partial V}{\partial a_i} \right\}_k. \tag{9}$$

If the derivative of a particular structural parameter is negative, then it is recommended that the size of the parameter be increased, otherwise no further modification is desired. Note that this method could be used for any structural parameter, and would not have to be done via the finite difference method if a continuous analytical expression existed for the velocity as a function of the structural parameter of interest.

The researchers noted that the method outlined above, now denoted as structural optimization method one (SOM1), easily halted for even very small local minima in the discrete function of power as a function of the structural parameters. To prevent this, structural optimization method two (SOM2) was developed. In addition to calculating the quantities in Eqs. (6)–(8), a second velocity gradient is calculated between values two points apart,

$$\left\{ \frac{\partial V}{\partial a_i} \right\}_{k,2} = \frac{\{V\}_{k+2} - \{V\}_k}{\Delta a_i}. \tag{10}$$

Then a value of $\{\partial W/\partial a_i\}_{k,2}$ is calculated similarly to Eq. (9) for each structural parameter varied and is compared to the result of SOM1. SOM2 increments the size of the structural parameter by one step if the result of Eq. (9) is the most negative derivative. If the result of Eq. (9) indicates that the size of the structural parameter currently represents a local minima for sound power, SOM2 checks ahead two points to see if that derivative is negative. If so, SOM2 increases the size of the structural parameter by two discrete values. If both derivatives are positive, it is assumed that the method has reached a significant minima in the value of sound power with respect to that structural parameter.

IV. A HEURISTIC EXPLANATION OF SIMULATED ANNEALING

If the radiated sound power is simultaneously minimized with respect to more than one structural parameter, gradient methods quickly prove to be inadequate. Combinatorial optimization methods, on the other hand, are particularly suited for minimizing a function of many parameters which are allowed to vary simultaneously.[9] Of all the methods of combinatorial optimization available, simulated annealing was chosen because of its ability to avoid small local minima on route to a global minimum. The following paragraphs are a heuristic description of the simulated annealing process and how it was applied to our problem.

The optimization method of simulated annealing is analogous to the behavior of interacting atoms in a metallic

FIG. 2. Flowchart of optimization by simulated annealing.

radiated power of the structure is analogous to the energy level sustained in the metal at a given temperature. Therefore, the parameter DW is analogous to the change in the radiated sound power. The process assumes that, occasionally, the structure must be allowed to radiate at a higher power level in order to find the set of values which the structural parameters must assume in order for the minimum radiated power value to be found. This is analogous to the higher energy state allowed from time to time in the annealing process. The final physical parameter, the structural parameter being optimized, in our case the damping patch size, is a random variable at which the radiated sound power is evaluated.

At the start of the algorithm, the structure has an initial temperature P_0 and an initial radiated power W_0. Selection of P_0 for practical power minimization situations will be discussed later in Sec. VII. Then, a new value of radiated power, W_{J+1}, is calculated for a random value of the optimization variable, damping patch size, also discussed in Sec. VII.

The next step is to compare W_{J+1} to the previous power value radiated by the structure, W_J, by calculating DW_J. If it is the first iteration, then $J=0$ and W_J is W_0. If DW_J is less than zero, W_{J+1} is automatically accepted as the new power level. If it is lower than any power value so far, W_{Best} is also updated. However, on the other hand, if DW_J is greater than zero, the higher power W_{J+1} can still be accepted if the Boltzmann probability function of the value of DW_J is within a certain problem dependent range. Typically, this range is chosen so that the probability of a nonimproving solution is high at the start and is drastically reduced near the end of the annealing process when P is low.

After a new candidate W_{J+1} is either accepted or rejected, based on the two criteria described in the previous paragraph, the algorithm checks to see if thermal equilibrium is reached. This step is essential to reduce the probability that nonimproving power values will be accepted in future iterations. After equilibrium is achieved by one of two criteria, the temperature parameter P is reduced. The first equilibrium condition is met if a certain number, say ten, of improved (lower) values of W_{J+1} have been successively accepted. In this case, the system must be allowed to cool since the system must have started at values of the design parameters where the radiated power (energy level) was quite large compared to the rest of the design space. The counter for acceptances is then reset to zero. The second equilibrium criterion is met if an arbitrary number, say 30, of nonimproving W_{J+1} candidates have been rejected. The system needs to cool, though very slowly, because a large number of rejections indicates that the structure is nearing its lowest possible radiated power value. The counter for rejections is then reset to zero.

Once the structure has reached equilibrium and been allowed to cool, the last step is to check to see if the convergence criteria for the radiated sound power have been reached. The first criterion for convergence is whether or not W_{Best} is below a specified value, W_{Min}. The second criterion is whether or not P is below a specified value, P_{Min}. If both criteria are met, the process is ended. If neither criterion is

solid in thermal equilibrium at temperature T.[9] When T is high enough for the metal to be a liquid, atoms in the solid have a random arrangement and a higher energy level, W. As T is reduced, the atoms become more ordered and the energy of the solid is generally reduced. However, W occasionally increases in a cooling metal in nature.[10] The rate at which energy may occasionally be allowed to increase is estimated by the Boltzmann probability function

$$Prob = \exp(-DW/kT), \qquad (11)$$

where DW is the change in energy, k is Boltzmann's constant, and T is the current temperature.[10] Thus, as T is reduced, the probability that a higher energy level, W, will be achieved is reduced, just as in nature. If the material is allowed to cool slowly enough, the atoms comprising it form a very ordered crystalline solid with a minimum energy state. This is nearly exactly what is done in the annealing process for manufactured alloys. If the cooling occurs too quickly, flaws in the ordering of the atoms occur, resulting in a slightly higher final energy state and a weakened metallic solid, and the process is called quenching.

The steps for extending this analogy to an algorithm for the minimization of the radiated sound power by a structure as a function of several structural parameters[11] is outlined in Fig. 2. In the algorithm, the temperature T and Boltzmann constant k are combined into one temperature parameter which will be called P. The parameter P is analogous to the temperature of the metallic solid in the annealing process. These parameters, T, k, and P, are not analogous to physical parameters in the structural acoustic problem, but are parameters which control the optimization process. However, the

FIG. 3. Pictorial diagram of experimental clamped plate measurement situation.

FIG. 4. Pictorial diagram of cubic velocity pattern construction from individual plate measurements.

met, a no value is returned from the decision box, the algorithm heads back to the top, J is incremented by one, and the whole process is begun again. If the W criterion is met but the P criterion is not, a no value is also returned in the hope that additional reduction over the amount hoped for will be achieved before the temperature parameter P is cooled below P_{Min}. If the P criterion is met, the algorithm is always considered to have converged, since it is very unlikely that further reduction in power will occur if the system has been allowed to cool slowly enough. Selection of appropriate cooling rates will be discussed in Sec. VII.

V. MEASURING THE SURFACE NORMAL VELOCITY

The relationship between the normal surface velocity and the structural parameters, $V(a)$ in Eq. (1), was determined from experimental data. The structural optimization studies involved the application of constrained layer damping material. All of the studies were carried out using data from a series of nine experimental measurements. In all nine of these measurements, the normal velocity of a thin square aluminum plate with clamped boundary conditions on all four sides was measured using a laser vibrometer. The square plate measured 60.96 cm on a side, and was 3.175 mm thick. A total of 225 evenly spaced measurement points was used to sample the plate. This grid was chosen so that measurement points corresponded to the nodes for a plate discretized into 49 boundary elements.

The first of the nine measurements was performed with an undamped plate. The plate was point driven by a shaker in the lower left-hand corner of the plate, as shown in Fig. 3. In the second measurement, a constrained layer damping patch consisting of 3M Scotchdamp viscoelastic damping material number SJ 2015 type 1205 constrained by a 0.3-mm-thick aluminum layer was applied to the back side of the plate. The size of this patch was 5.08 cm by 5.08 cm, about 0.69% of the total plate area. Figure 3 shows the location of the damping patch, in the lower right corner of the plate, centered 21.6 cm from the closest sides. This location was chosen using the measured structural intensity.[4,5] For measurements three through nine, the size of the damping patch was uniformly increased by 0.69% of the total plate area while
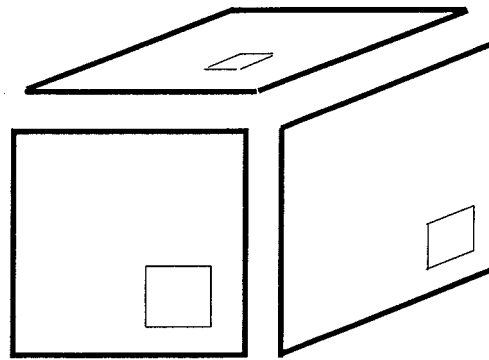
keeping the patch square, until a maximum of 5.56% of the plate area was covered for measurement nine. This limit was chosen arbitrarily as a low number.

The normal surface velocity was measured with a Polytec OFV 1102 laser vibrometer. The plate was excited by a B&K 4809 shaker attached to the plate through a PCB 208 A02 force transducer. The signals from the force transducer and the laser vibrometer were amplified by an Ithaco 453 amplifier and filtered by a Krohn-Hite model 30 low pass elliptical filter (148 dB per octave rolloff). The signals were sampled at 2048 Hz by a Concurrent computer. The Fourier transform of each signal was calculated and the frequency response function was calculated at each frequency. Thus, the final data that was obtained was the velocity per unit input force at each measurement location.

VI. VELOCITY DISTRIBUTIONS ON THE CUBE

In the first three studies, the velocity patterns for a cubic structure were constructed by assembling six of the velocity distributions from the square plate measurements, one for each side of the cube, as shown in Fig. 4. This allows the cube to have any one of the nine square plate velocity distributions on a particular side of the cube. A tenth possible velocity pattern was zero velocity at every node to allow any side of the cube to remain rigid. This cube does not exactly model a real cube, because the vibrational coupling between the sides of the box is ignored. However, this structure is only a test problem used for the purposes of evaluating and demonstrating the optimization procedures developed in this work. Application of the techniques to real structures with vibration coupling will proceed exactly as described in this paper. Any structural coupling will alter the structure's velocity, therefore changing the outcome of the optimization, but it is hypothesized that the optimization procedures will not be changed.

Recall from Sec. II that a given $[B]$ matrix is only good for a particular frequency. However, the frequency of each mode changed less than 1% with the application of damping material, so it was only necessary to calculate one $[B]$ matrix for each mode.

Figure 5 shows the magnitude of the measured velocity per unit force measured via the frequency response function for the third vibration mode of the undamped square plate.
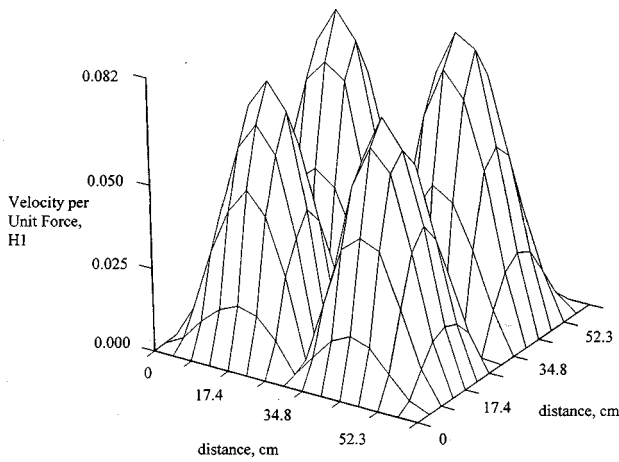
FIG. 5. First measured plate mode shape; magnitude of velocity per unit force frequency response function is displayed.

Damped and undamped plate mode shapes occurring at $ka = 1.2$ for mode three were used in this study for two reasons. First, large reductions in sound power were calculated from the mode three velocity patterns for certain damping patch sizes. Second, plots of the discrete power values calculated from the mode three velocity patterns indicated both local and absolute minima that would adequately test the effectiveness of the optimization techniques.

VII. SIMULATED ANNEALING IMPLEMENTATION

A computer code was written to perform simulated annealing. One of the main features of the program, other than those described in Fig. 2, was the ability for the user to input the W_0, W_{Min}, P_0, and P_{Min} parameters. Also, the program lets the user select how many sides of the cubic structure on which the size of a constrained layer damping patch will be allowed to vary, as well as a cooling rate for the annealing process, called DP. Then the program allows the user to designate the initial size of the damping patch on each of the sides allowed to vary. The algorithm was not allowed to select damping patch sizes outside the measured range. The undamped velocity is assigned to the sides which are not allowed to vary. Finally, the program allows the user to select the probability of a nonimproving solution by entering a minimum value of the Boltzmann probability function in Eq. (11). The name of this parameter is Probmin. All damping solutions corresponding to values of Probmin that are less than the minimum value are rejected by the algorithm.

As soon as all of the parameters are entered, the program utilizes a random number generator that achieves a random number between zero and one by using the internal clock of the computer and three linear congruential generators in series.[12] Based on the value of the random number, the program chooses which of the sides allowed to vary will be changed for the calculation of the next function value. Then, another random number is chosen, and the program decides how much to increase or decrease the size of the damping patch on the side of the cube allowed to vary. It should also be noted that the simulated annealing process does not use a direction of search vector, therefore no derivative, such as in Eq. (6), is needed.

The simulated annealing process requires that the sound power be calculated at arbitrary values over a continuous range of the structural parameter. Since the sound power is being calculated from the normal surface velocity, then the normal surface velocity must be calculated over a continuous range of the structural parameter. However, for this work the velocity is only known at the discrete values of the structural parameter, damping size, for which measurements were performed. In order to develop a continuous function for the normal velocity, the normal velocity at each measurement location is curve fit as a function of the structural parameter. The curve fit parameters are then used to estimate the surface velocity at the specified value of the structural parameter. In the event that the velocity can be determined explicitly as a function of the structural parameter, then this step is not required. Otherwise, the simulated annealing process is completely general.

Selecting appropriate values of W_0, W_{Min}, P_0, P_{Min}, Probmin, and DP is essential for the simulated annealing algorithm to converge. The parameter W_0 is the easiest because it is just the initial amount of sound power radiated by a structure before any modifications have been made. Then, W_{Min} is determined by the amount of reduction desired. Specifically, if 5 dB of reduction is desired, then W_{Min} is set to be 5 dB smaller than W_0.

There are many ways of choosing the parameter P_0 and each is dependent on the specific problem simulated annealing is being applied to. In this work, P_0 was set to be about 10% greater than W_0 to allow the algorithm to occasionally accept slightly higher solutions for the radiated power than the initial value W_0 at the start of the optimization. Then, P_{Min} was chosen in the same fashion as W_{Min}.

Choosing a successful cooling rate, DP, can prove rather tricky in practice. If function evaluations are expensive or time consuming, a faster cooling rate is needed to reduce the number of evaluations performed. If the number of evaluations is less of a concern, a slower cooling rate is more likely to result in the lowest possible radiated sound power.

The choice of the Probmin parameter is the least definite of all the parameters mentioned. In general, it is desired that the simulated annealing algorithm have a high probability of accepting a higher value of radiated sound power when the temperature parameter P is still high and to have a low probability when P is nearly completely cooled. For results presented in this work, a value of 0.98 was used as the minimum accepted value calculated by the Boltzmann probability equation in the algorithm. This number was arrived at as a result of trial and error. It was found that the algorithm took an unnecessarily high number of function evaluations to converge when the process was nearly cooled if Probmin was about 10% lower. Also, the algorithm got stuck in a local minimum too quickly if the value was more than 1.5% higher.

VIII. RESULTS AND DISCUSSION

The results from the two gradient and simulated annealing optimization processes are presented for several test cases. The results will show the advantages and limitations of each optimization process.
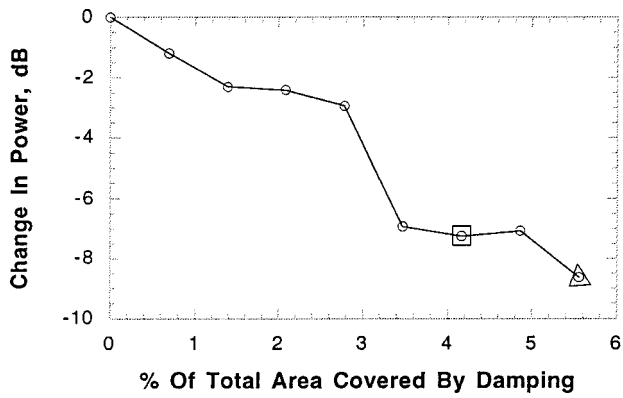
FIG. 6. Change in radiated sound power of a cube with five sides rigid as a function of the size of the constrained layer damping patch on the top side. The square indicates where SOM1 converged while the triangle indicates where SOM2 converged.

FIG. 7. Change in radiated sound power of a cube with five sides having undamped plate velocity as a function of the size of the constrained layer damping patch on the top side. The square indicates where SOM1 converged while the triangle indicates where SOM2 converged.

A. Study one

In the first structural optimization study, five sides of the cube were held rigid, while the velocity was allowed to vary on only one side of the cube. The change in sound power radiated by the cube as a function of the percentage of the area of the one side of the box covered by damping is shown in Fig. 6. The radiated sound power was calculated for Fig. 6 at each of the values of damping for which data is available in order to demonstrate the performance of the structural optimization methods. Typically this curve would not be known as the optimization is performed.

Note that the largest change in power occurred at about 3% of the surface area in Fig. 6. Structural optimization method one (SOM1) converged at the point with a square around it in Fig. 6. This point corresponds to a reduction in power of 7.25 dB with a damping patch size of 4.17% of the surface area. SOM2 converged at the constraint boundary, a point with a triangle around it in Fig. 6. A reduction in radiated sound power of 8.63 dB was obtained while using the maximum possible amount of damping material on one side of the cube.

B. Study two

For the second structural optimization study, the undamped plate velocity was initially placed on all six sides of the cube. Again, the size of the damping patch, and thus the velocity pattern, on one side of the cube was allowed to vary. Figure 7 shows the change in sound power radiated as a function of the percentage of plate area covered by constrained layer damping material. This time, SOM1 converged at a power reduction of 0.68 dB for a damping patch area of about 1.39% of the total area of the top side of the cube, denoted by the point with a square around it in Fig. 7. SOM2 converged at a power reduction of 7.32 dB for a damping patch size of 3.47% of the total area, which was the absolute power minimum for this data. Note that neither method converged at the constraint boundary in this case, but SOM1 missed the most significant reduction.

Once again, the largest change in the sound power occurred at about 3%, shown in Fig. 7. Figure 6 shows that further increases in the damping patch area resulted in fur-

ther slight reductions in the radiated sound power in the previous experiment. Conversely, Fig. 7 shows that the radiated sound power increases sharply from the minimum value if the damping patch area is increased beyond 3.47%.
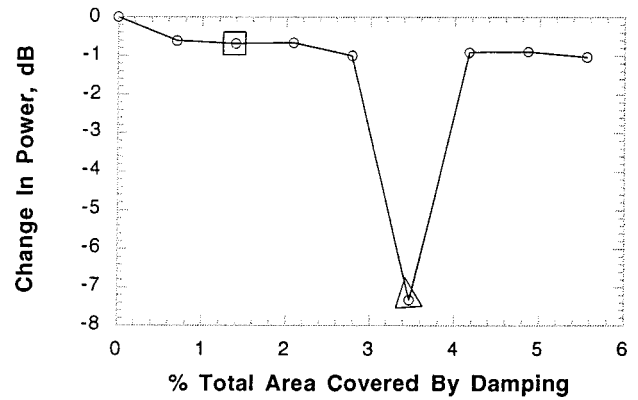
Figures 5 and 8(a)–(c) show the magnitude of the measured velocity per unit force for the undamped plate and three damping patch sizes. Note that the velocity magnitude is reduced as the damping patch area is increased for the plate. Thus, in the first experiment, power is reduced to a minimum as the surface velocity amplitude is decreased, while in the second experiment, the power begins to increase sharply above the minimum value as velocity is further decreased. These results indicate that the acoustic coupling between vibrating areas of the structure can have a significant influence on the reduction of sound radiation. Therefore, care must be used when damping material is applied to only a limited area of a complex structure.

C. Study three

In the third study, the undamped plate velocity was again used as the initial velocity pattern on all six sides of the plate. This time, the damping patch size was allowed to vary independently on two sides of the cube. The reduction of the radiated sound power as a function of the percentage of the area of each side covered by the constrained layer damping patch is shown in Fig. 9. Positive values indicate a power reduction. The multiple peaks in Fig. 9 indicate that a few local minima exist within the constraint boundary when the velocity is varied on two sides of the cube. Note that the absolute minimum within the constraint boundary (the highest peak) occurs on the boundary of maximum area for both damping patches. This value corresponds to a reduction of 2.12 dB in sound power for equal damping patch sizes of 5.56% of the plate area on both sides of the cube. SOM1 was not used because it had difficulty bypassing local minima in studies one and two. SOM2 located a significant reduction in power of 1.86 dB. This reduction resulted from damping patches of 1.39% of the total area on the top of the cube and 3.47% on the front of the cube. Neither method found the absolute minimum in this experiment.

(a)

(b)

(c)
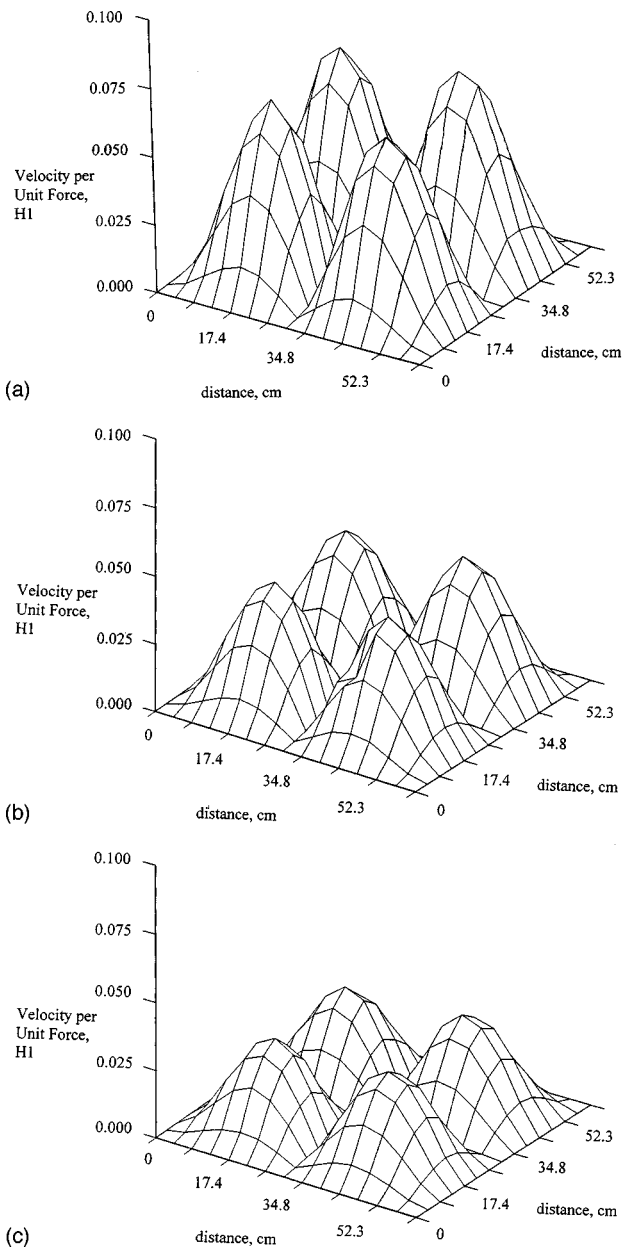
FIG. 8. Measured mode 3 magnitude of the frequency response function; $ka = 1.2$. Constrained layer damping patch covering (a) 2.08%, (b) 3.47%, and (c) 5.56% of the plate area; 5.56% is the maximum amount area.

At this point it is clear that gradient methods of optimization are not capable of reliably finding the minimum sound radiation for applying damping patches to a vibrating structure because the functional dependence is complex. These results motivated the investigation of the simulated annealing optimization technique.

When comparing Figs. 7 and 9, one might expect the data in Fig. 7 would match the data in Fig. 9 when only one patch was varied (i.e., one patch has an area of zero in Fig. 9). However, the data in Fig. 7 was for a patch on a different side than the two patches used for Fig. 9. Clearly the relationship between the sound power and the damping patch size depends on the side that the damping patch is applied to. This variation is caused by acoustic coupling which strongly controls the sound radiation from this cube in the frequency range studied. Since the vibration pattern applied to each
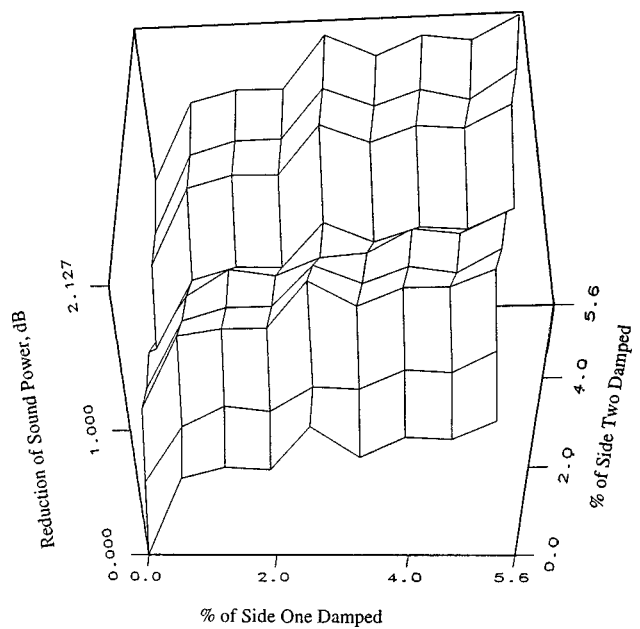
FIG. 9. Reduction in sound power radiated by a cube with four sides having undamped plate velocity and various sizes of damping patch on the top and front sides as a function of a percentage of the plate area covered by constrained layer damping material on the top and front sides.

side is not a perfectly symmetric 2,2 mode, then the acoustic coupling seen by each side varies, therefore varying the impact of damping on each side. Further discussion about the impact of acoustic coupling on the optimization process is described by Kruger[7] and Kruger and Mann.[8]

D. Study four

In the fourth study, the method of simulated annealing was used to optimize the sound power radiated by the cube as a function of the area of constrained layer damping patches on two sides of the cube. Once again, the other four sides of the cube vibrated with the undamped plate velocity. In the first part of the study, the simulated annealing program was run five times with the same initial conditions; since the process is random, five different results are possible. The parameter W_{Min} was set 2.0 dB lower than W_0 in all five cases. The cooling rate DP was set so that the algorithm had to cool at least five times for W_{Min} to be reached. The results are shown in Table I. The parameters $d1$ and $d2$ in Table I refer to the area, in square cm, of the square damping patches on the two sides of the cube. Because the annealing process is random, several runs are performed in order to ensure that the minimum, or a solution close to the minimum, has been found.

The maximum value for each of these parameters is 206.5 cm^2 and the minimum is 0.0 cm^2. Case five obtained the best result, achieving 2.11 dB with a 205.8 cm^2 damping patch on the top side of the cube and a 205.2 cm^2 damping patch on the front side of the cube. The total area covered by both of the patches is 1.84% of the total surface area of the cube and is very near the absolute minimum of 2.12 dB indicated in Fig. 9.

In cases two, four, and five, the program found reductions in the radiated sound power greater than or equal to the

TABLE I. Results of study four.

Case	Start d1 (cm²)	Start d2 (cm²)	Finish d1 (cm²)	Finish d2 (cm²)	N	Reduction (dB)
1	154.8	154.8	147.1	157.7	124	1.84
2	154.8	154.8	205.2	130.3	120	2.00
3	154.8	154.8	127.1	174.2	27	1.89
4	154.8	154.8	112.3	194.2	23	2.01
5	154.8	154.8	205.8	205.2	11	2.11
Average	154.8	154.8	159.4	172.3	57	1.89

2.0 dB specified before the process cooled. In cases one and three, the final power reductions are less than 2.0 dB because the process cooled before the algorithm found damping patch sizes that produced velocities which resulted in reductions in sound power radiated by the cube of 2.0 dB or greater. Even though both cases had the same cooling rate, case three cooled in much fewer function evaluations than case one. Some general characteristics of the simulated annealing process account for this behavior. First, simulated annealing alternately rejects a higher power, accepts a lower power, or accepts a higher power without reaching the number of each of these required for thermal equilibrium and subsequent cooling. This causes the program to use a lot more function evaluations with the same cooling rate, as in case one. Second, the program can randomly choose new powers that are too high and are rejected several times in a row so that thermal equilibrium is reached and the process cools in a minimum number of function evaluations without finding a lower power, as in case three.

Notice the average values reported at the bottom of Table I. The average reduction is determined by calculating the reduction in the radiated sound power when the average of the calculated damping areas are used. The average values of the five cases tend to be meaningless because the radiated sound power corresponding to the average values of damping patch size may not be a local minimum. In fact, it may be higher than any of the power values from the cases comprising the average. Also, the annealing process is random in that five searches started with exactly the same set of initial parameters and obtained five different results. Consequently, the best of the results or the result with damping areas that are most practical to implement should be used.

E. Study five

In the fifth study, the method of simulated annealing was used to optimize the sound power radiated by the cube as a function of the area of square constrained layer damping patches on three sides of the cube. The other three sides of the cube were given the undamped plate velocity. The result is a three-dimensional design space. A total of eight cases were explored in this study so that the annealing process could be started near each of the eight corners of the design space. A value of W_{min} was chosen to be 2.75 dB less than the power radiated by the undamped box. The cooling rate was the same as in study four. The results are shown in Table II. The parameters $d1$, $d2$, and $d3$ refer to the size of the three damping patches in square cm. Case eight resulted in the maximum reduction, 3.11 dB, with the constrained layer damping patches only covering 1.89% of the total cube surface area. This best value is assumed to be very close to the absolute minimum because several searches were done with a sufficiently slow cooling rate. The exact absolute minimum was not calculated due to the excessive number of function evaluations required.

Another characteristic of the method of simulated annealing was noted as a result of this study. Specifically, if a search requires many function evaluations, as in case one where 252 evaluations were required, it may be appropriate to give up on the search and restart the simulated annealing process in some other portion of the design space.

Like study four, using the average of each area to calculate the radiated sound power, Table II, produces less reduction than the most effective cases. Thus, the most effective damping patch configuration which is also capable of

TABLE II. Results of study five.

Case	Start d1 (cm²)	Start d2 (cm²)	Start d3 (cm²)	Finish d1 (cm²)	Finish d2 (cm²)	Finish d3 (cm²)	N	Reduction (dB)
1	51.6	51.6	51.6	202.6	75.5	161.9	252	2.64
2	51.6	51.6	154.8	138.1	116.1	192.9	166	2.81
3	51.6	154.8	51.6	109.7	127.1	89.7	92	2.64
4	51.6	154.8	154.8	56.1	19.4	187.1	67	2.44
5	154.8	51.6	51.6	200.7	53.5	151.9	188	2.78
6	154.8	51.6	154.8	110.3	71.6	185.8	98	2.64
7	154.8	154.8	51.6	113.5	134.8	53.5	60	2.71
8	154.8	154.8	154.8	114.8	169.0	138.7	57	3.11
Average	103.2	103.2	103.2	131.0	108.4	143.9	122	2.68

being realistically implemented, for example, with manufacturing constraints, should be chosen.

F. Study six

In the sixth study, the method of simulated annealing was used to optimize the sound power radiated by the cube as a function of the area of square constrained layer damping patches on the four, five, and six sides of the cube. The purpose of this study was to demonstrate that the simulated annealing algorithm was successful when damping was placed on four or more sides of the cube.

When the damping patch size was allowed to vary on four sides of the cube, a maximum reduction of 4.32 dB was achieved in 188 function evaluations. The value of W_{Min} was 4.15 dB less than the power radiated by the undamped cube. The total area covered by these four patches was 2.76% of the total surface area of the cube, only 73% of the total area that could be covered.

For the case where the damping patch size was allowed to vary on five sides of the cube, a maximum reduction of 5.45 dB was achieved in 34 function evaluations. The value of W_{min} was designated 5.25 dB less than the maximum power radiated by the cube. At convergence, the patches covered 3.80% of the total surface area of the cube, only 81% of the total area that could be covered.

In the last case, the damping patch size was allowed to vary on all six sides of the cube. A maximum reduction of 7.80 dB was located in 38 function evaluations when W_{Min} was set 7.5 dB below the level of power radiated by the undamped box. These square patches of constrained layer damping material covered just 4.06% of the surface area of the cube, only 72% of the total area that could be covered. This is just 0.26% more than the previous case, but the radiated sound power was reduced by an additional 2.35 dB. Also note that, as in all cases, the maximum amount of area that could be covered with damping material was not the optimum solution.

IX. CONCLUSIONS

Several important conclusions were reached. First, it was shown that it is possible to achieve large reductions in the radiated sound power for a cubic structure while modifying only a small percentage of the total surface area of the structure. For example, reductions of over 7 dB were found for structural modifications to areas as small as 0.58% of the total structure surface area when 0.93% of the total surface area could be modified. Not only do these possible reductions exist, an effective method of determining the optimal sizes of structural modifications to attain the reductions was developed in this work.

The gradient optimization methods were effective when only one structural parameter was being varied, and did find significant reductions when two structural parameters were varied. However, neither gradient method found the maximum reduction when two structural parameters were varied.

The method of simulated annealing was much more effective for optimizing the sound power radiated by the cubic structure as a function of the area covered by multiple damping patches placed on the surface of a structure when the proper set of initial parameters was chosen. Specifically, any minimum can be found if the cooling rate of the process is slow enough to allow the algorithm to fully explore the design space before cooling is complete. Simulated annealing does not guarantee that the exact absolute minimum will be found every time. Therefore, the benefit of a result that is very close to the absolute minimum of a function must be carefully weighed against the cost of the number of function evaluations required to obtain that result. The number of function evaluations required to obtain a desired amount of reduction in the radiated sound power can often be reduced by starting the program in some other area of the design space if the algorithm is taking a long time to converge.

The multiple solutions from the simulated annealing optimization method also have the advantage of providing several alternatives. The best can be chosen based on other design criteria such as ease of manufacturing, the structure's strength and rigidity, or robustness of the solution to manufacturing tolerances.

The results also show that, given some limit, the greatest possible structural modification is not always the most effective at reducing the radiated sound power. In one instance, the maximum reduction in sound power occurred while less than half of the possible surface was covered by a constrained layer damping patch. In another, the size of a damping patch which achieved maximum reduction was only about three-fifths of the total possible. Increasing the size of this patch further resulted in significantly lower reductions compared to the optimal solution.

The structural optimization methods described in this paper achieved significant power reductions when the structure's surface velocity as a function of the size of a constrained layer damping patch was approximated from experimentally measured values. The methods used in this paper can also be used for the case where the analytical expressions of normal structural velocity as a function of structural parameters are known.

[1] K. A. Cunefare and G. H. Koopmann, ''A boundary element approach to optimization of active noise control sources on three-dimensional structures,'' J. Vib. Acoust. **113**, 387–394 (1991).

[2] K. A. Cunefare and G. H. Koopmann, ''Acoustic design sensitivity for structural radiators,'' J. Vib. Acoust **114**, 178–186 (1992).

[3] A. R. Lall, N. T. Asnani, and B. C. Nakra, ''Vibration and damping analysis of rectangular plate with partially covered constrained viscoelastic layer,'' J. Vib. Acoust. Stress Reliability Design **109**, 241–247 (1987).

[4] A. B. Spalding and J. A. Mann III, ''Placing small constrained layer damping patches on a plate to attain global or local velocity changes,'' J. Acoust. Soc. Am. **97**, 3617–3624 (1995).

[5] D. H. Kruger, J. A. Mann III, and T. Wiegandt, ''Placing constrained layer damping patches using reactive shearing intensity measurements,'' J. Acoust. Soc. Am. **101**, 2075–2082 (1997).

[6] A. E. Bryson, Jr. and Y. C. Ho, *Applied Optimal Control,* Rev. print. (Hemisphere, New York, 1975).

[7] H. K. Kruger, ''Minimizing the radiated sound power with minimal structural modification,'' Ph.D. dissertation, Iowa State University, 1995.

[8] H. K. Kruger and J. A. Mann III, ''Minimizing the sound power radiated by a structure using velocity constraints,'' submitted to J. Acoust. Soc. Am.

[9] S. Kirkpatrick, C. Gelatt, and M. Vecchi, ''Optimization by simulated annealing,'' Science **220**(4598), 671–680 (1983).

[10] N. Metropolis, A. Rosenbluth, M. Rosenbluth, A. Teller, and E. Teller, ''Equation of state calculations by fast computing machines,'' J. Chem. Phys. **21**, 1080–1092 (1953).

[11] G.-S. Chen, R. J. Bruno, and M. Salama, ''Optimal placement of active/passive members in truss structures using simulated annealing,'' AIAA J. **29** (8), 1327–1334 (1991).

[12] W. Press, B. Flannery, S. Teukolsky, and W. Vetterling, *Numerical Recipes* (Cambridge U.P., Cambridge, 1989).

A wave field extrapolation approach to acoustical modeling in enclosed spaces

A. J. Berkhout, D. de Vries, J. Baan, and B. W. van den Oetelaar
Laboratory of Acoustics, Department of Applied Physics, Delft University of Technology, P.O.B. 5046, 2600 GA, Delft, The Netherlands

In practice, impulse responses in enclosed spaces are calculated with algorithms that are based on the ray tracing model, the mirror image source model, or a mixture of both. Using those algorithms, however, the wave character of sound propagation is not properly taken into account and complex boundaries cannot be included. This paper presents an alternative approach adopted from the seismic imaging field. The proposed model is based on the concept of wave field extrapolation. Absorption properties of the boundaries can be specified in detail by means of reflection matrices. Propagation between boundaries is formulated by propagation matrices. Impulse responses along an array of receivers are numerically simulated by executing a sequence of matrix multiplications that can be interpreted as generalized spatial convolutions. Diffraction phenomena due to the finiteness and irregularity of the boundaries are correctly taken into account. The proposed algorithm is illustrated on a two-dimensional configuration. Results are compared with those of conventional models and with measured data. A discussion on computing time is included. In addition, the proposed algorithm leads to new directions in the analysis of measurements in enclosed spaces. The proposed algorithm implies a new concept for dereverberation of recordings that are made in complex acoustic surroundings, using microphone arrays. © *1999 Acoustical Society of America.* [S0001-4966(99)03203-8]

PACS numbers: 43.55.Ka, 43.55.Fw [JDQ]

INTRODUCTION

In this paper a new approach to the simulation of impulse responses in enclosed spaces is presented. Traditionally, impulse responses are measured or simulated at a few individual receiver positions that are supposed to be representative for the listeners area. In this way, the results can only be analyzed and interpreted in a statistical way. When, however, closely spaced receiver arrays are used instead of individual receivers, deterministic wave field analysis becomes possible which enables a significant increase of insight in the temporal and spatial properties of the acoustic field.[1,2] An example of such a multi-trace impulse response data set, measured in a rectangular room, is shown in Fig. 1. The parameter ''offset'' along the horizontal axis denotes the lateral receiver position with respect to the array center.

For the simulation of multi-trace impulse responses, algorithms are available that are based on ray tracing, mirror source imaging, or a mixture of both concepts. Ray (or cone) tracing[3,4] is an approach in which the wavefronts are spatially sampled by a distribution of discrete rays. In the algorithms available until now, diffraction effects at boundary edges and irregularities are not properly taken into account. This means that an incomplete version of measured impulse responses is obtained. In the mirror image source model (MISM) each reflection is interpreted as the direct signal of a source that has been mirrored in the reflecting boundaries, where each boundary is described by simple acoustic mirrors. Except for rectangular enclosures,[5] a ''visibility test''[6] is needed for each reflection in order to verify whether the related mirror image source can indeed be ''seen'' by the receiver: the connecting line between source and receiver has to intersect the last reflecting wall within its geometrical dimensions. This test is not only very time consuming, but it also causes a discontinuity in being ''seen'' or ''not seen'' of reflected wavefronts, thus discarding the diffraction phenomena physically occuring at the edges of finite boundaries. Pierce[7] has presented a theory on edge diffraction which could be added to the MISM in order to improve its accuracy.

In this paper, an alternative approach to acoustic modeling is proposed. It is derived from a multi-scattering algorithm that is successfully applied in seismic imaging.[8] This so-called WRW (W stands for Wave propagation, R for Reflection) algorithm is based on wave theory, which means that it fully takes the wave character of sound propagation into account.

I. WAVE FIELD PROPAGATION IN TERMS OF MATRIX MULTIPLICATION

In this section the underlying theory is summarized. For an extensive treatment of the theory and the derivation of the mathematical expressions, the reader is referred to Ref. 9.

According to Huygens' principle, the propagation of a wave through a medium can be qualitatively described by adding the contributions of all secondary sources positioned along a wavefront. This implies that the wave field in a source-free volume V can be described by a distribution of secondary sources along the boundary surface S of V [see Fig. 2(a)]. Mathematically, this property can be quantitatively described by the Kirchhoff–Helmholtz integral, formulated in the space-frequency domain as
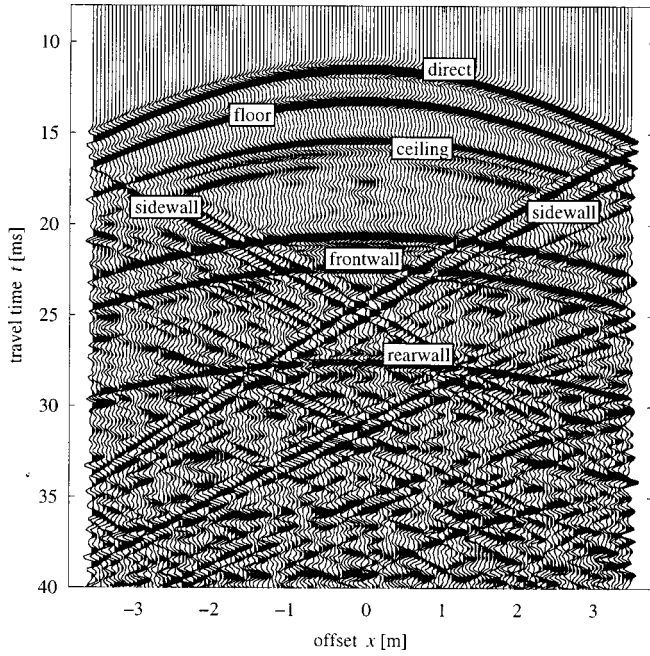
FIG. 1. Multitrace impulse response of a rectangular room.

$$P(\vec{r}_A,\omega) = \frac{1}{4\pi} \oint \left[j\omega\rho_0 V_n(\vec{r}_S,\omega) \frac{e^{-jk\Delta r}}{\Delta r} \right.$$

$$\left. + P(\vec{r}_S,\omega) \frac{1+jk\Delta r}{\Delta r} \cos\varphi \frac{e^{-jk\Delta r}}{\Delta r} \right] dS,$$

$$\text{for } \vec{r}_A \in V, \tag{1}$$

where $\Delta r = |\vec{\Delta r}| = |\vec{r}_A - \vec{r}_S|$ is the distance from a secondary source point $\vec{r}_S$ at the surface S to the reconstruction point A at position $\vec{r}_A$ inside V, and φ is the angle between the vector $\vec{\Delta r}$ and the inward pointing normal vector $\vec{n}$. The wave number k is defined as the ratio between angular frequency ω and propagation velocity c, ρ_0 is the air density, and V_n is the particle velocity in the direction of $\vec{n}$. The first term under the integral in Eq. (1) represents the field of a secondary monopole distribution on surface S, each monopole having the strength of the local normal velocity due to the primary source distribution. The second term represents the field of a secondary dipole distribution, each dipole having the strength of the local pressure due to the primary source distribution. A degenerated form of a closed surface is an infinite plane surface S between source and receiver domain, say, the plane z_0 at $z=0$ parallel to the x and y axes. In this case the Kirchhoff–Helmholtz integral can be simplified, yielding the Rayleigh integrals. The Rayleigh I integral describes the pressure field in the lower half-space as reconstructed by a distribution of monopoles on the acquisition plane z_0 (i.e., using velocity information only). The Rayleigh II integral describes the pressure field in the lower half-space as reconstructed by a distribution of dipoles on z_0 (i.e., using pressure information only). In this paper, only the Rayleigh II integral is used; for the three-dimensional situations it can be formulated as

(a) Kirchhoff-Helmholtz
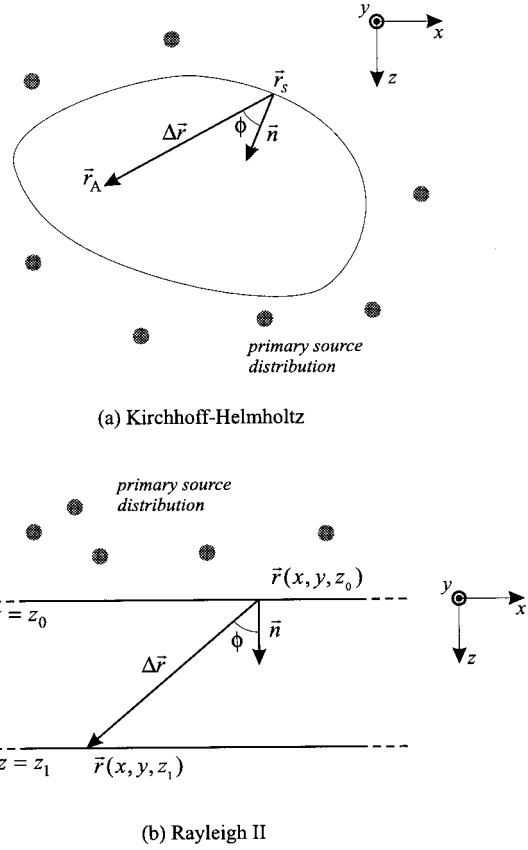
(b) Rayleigh II

FIG. 2. Illustration of the Kirchhoff–Helmholtz and the Rayleigh II integrals.

$$P(\vec{r}_1,\omega) = \frac{jk}{2\pi} \int_{-\infty}^{\infty} \int_{-\infty}^{\infty} P(\vec{r}_0,\omega)$$

$$\times \left[\frac{1+jk\Delta r}{jk\Delta r} \right] \cos\varphi \frac{e^{-jk\Delta r}}{\Delta r} dx\, dy, \tag{2}$$

$\vec{r}_0$ and $\vec{r}_1$ being related to the planes z_0 and z_1, respectively. Using this equation, the wave field at any position $\vec{r}_1$ in the lower half-space can be synthesized if the pressure field at the recording plane z_0 is known. This statement forms the basis of wave field extrapolation that is presented in the next section. We now consider the configuration of Fig. 2(b) and use the Rayleigh II integral, Eq. (2), for forward wave field extrapolation from the plane $z=z_0$ to the plane $z=z_1$:

$$P(x_1,y_1,z_1,\omega) = \int_{-\infty}^{\infty} W(x_1-x,y_1-y,\Delta z,\omega)$$

$$\times P(x,y,z_0,\omega) dx\, dy, \tag{3}$$

where

$$W(x_1-x,y_1-y,\Delta z,\omega) = \frac{jk}{2\pi} \left[\frac{1+jk\Delta r}{jk\Delta r} \right] \cos\varphi \frac{e^{-jk\Delta r}}{\Delta r}, \tag{4}$$

$\Delta z = |z_1-z_0|$, and $\cos\varphi = \Delta z/\Delta r$. Equation (4) can be recognized as a convolution integral along the x and the y axes.

In practice, the continuous integral kernel $W(x_1-x,y_1-y,\Delta z,\omega)$ in Eq. (4) has to be replaced by a discrete propagation matrix $\mathbf{W}^+(z_1,z_0)$ containing the dis-
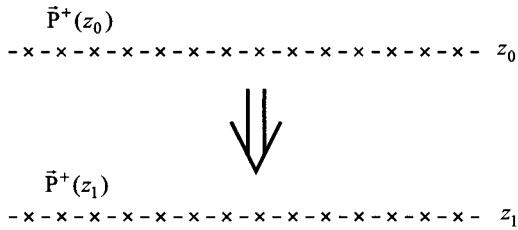
(a) spatial configuration

(b) system representation

FIG. 3. Downward wave propagation between two parallel planes, given by $z=z_0$ and $z=z_1$.

crete extrapolation operators for all relevant combinations of $\vec{r}_0$ and $\vec{r}_1$ at z_0 and z_1, respectively. The superscript "+" denotes that the matrix describes downward propagation into the $+z$ direction. The convolution integral, Eq. (3), is now replaced by a matrix multiplication (see Fig. 3):

$$\vec{P}^+(z_1) = \mathbf{W}^+(z_1, z_0)\vec{P}^+(z_0), \tag{5}$$

where the vectors $\vec{P}^+(z_0)$ and $\vec{P}^+(z_1)$ describe the discrete versions of the downgoing pressure fields at z_0 and z_1, respectively. Note that one column of propagation matrix $\mathbf{W}^+(z_1, z_0)$ represents the pressure field at z_1 due to a unit dipole at z_0. For two plan-parallel planes (Fig. 3), $\mathbf{W}^+(z_1, z_0)$ forms a Toeplitz matrix: all elements on any diagonal are equal.

Similarly, when the primary sources are positioned in the lower half-space at $z > z_1$, then sound waves are upward propagating into the $-z$ direction, generating the pressure fields $\vec{P}^-(z_1)$ at z_1 and $\vec{P}^-(z_0)$, at z_0, respectively. The propagation from z_1 to z_0 is described by a discrete propagation matrix $\mathbf{W}^-(z_0, z_1)$ containing the extrapolation operators for all relevant combinations of $\vec{r}_1$ and $\vec{r}_0$ at z_1 and z_0, respectively. The superscript "−" denotes that the matrix describes upward propagation into the $-z$ direction. The convolution integral, Eq. (3), is now replaced by a matrix multiplication (see Fig. 4):

$$\vec{P}^-(z_0) = \mathbf{W}^-(z_0, z_1)\vec{P}^-(z_1). \tag{6}$$

Note the large similarity between Eqs. (5) and (6). Note also that $\mathbf{W}^+(z_1, z_0) = [\mathbf{W}^-(z_0, z_1)]^T$.

II. WAVE FIELD PROPAGATION AND REFLECTION IN TERMS OF MATRIX MULTIPLICATION: THE WRW MODEL

A. One reflecting surface

In a homogeneous medium, Eqs. (5) and (6) give an adequate description of sound propagation. However, if a reflecting boundary is reached, two mechanisms enter the propagation model: reflection and transmission. Let z_1 be

such a boundary, having a reflectivity matrix for downward incident waves $\mathbf{R}^+(z_1)$. Then an upward traveling reflected wave field is generated:

$$\vec{P}^-(z_1) = \mathbf{R}^+(z_1)\vec{P}^+(z_1). \tag{7}$$

Note that Eq. (7) represents the reflection process in terms of a spatial convolution. If the reflecting boundary is locally reacting, then $\mathbf{R}^+(z_1)$ is a diagonal matrix, holding the reflection coefficients for each grid point at z_1. For the configuration of Fig. 5(a), where z_1 is positioned below the source plane z_s and the detector plane z_d, not only the *downward* traveling direct sound is recorded at the detector plane, but also an *upward* traveling reflected wave. Note that the source plane and detector plane may contain any distribution of point, line, and plane sources and detectors, respectively.

Using the matrix $\mathbf{W}^+(z_d, z_s)$ which describes the downward propagation of the direct sound from z_s to z_d, the matrix $\mathbf{W}^+(z_1, z_s)$ which describes the downward propagation
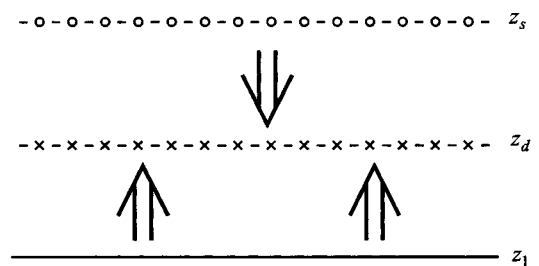
(a) geometrical configuration: one reflector at z_1
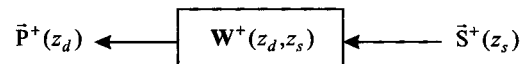
(b) direct wave field at z_d
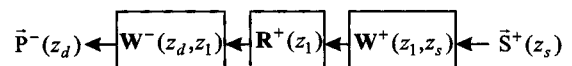
(c) reflected wave field at z_d

FIG. 5. Propagation and reflection in the case of one reflector.

1727   J. Acoust. Soc. Am., Vol. 105, No. 3, March 1999

Berkhout *et al.*: Wave field extrapolation for modeling   1727

of the direct sound to the reflector, and the matrix $\mathbf{W}^-(z_d,z_1)$ which describes the upward propagation of the reflected wave from z_1 to z_d, we may write for the recorded pressure field at z_d

$$\vec{P}(z_d)=\vec{P}^+(z_d)+\vec{P}^-(z_d)$$

$$=\mathbf{W}^+(z_d,z_s)\vec{S}^+(z_s)$$

$$+[\mathbf{W}^-(z_d,z_1)\mathbf{R}^+(z_1)\mathbf{W}^+(z_1,z_s)]\vec{S}^+(z_s),\quad(8)$$

where the elements of vector $\vec{S}^+(z_s)$ represent the primary source distribution at z_s. The process of propagation and reflection is illustrated by the block diagrams of Fig. 5(b) and (c). Note that in the field of seismic exploration, sources and receivers are generally placed at the earth's surface z_0. For this situation, the upward traveling reflected field from all reflecting depth levels are of interest (only one reflecting bounce at each depth level):

$$\vec{P}^-(z_0)=\sum_{m=1}^{\infty}[\mathbf{W}^-(z_0,z_m)\mathbf{R}^+(z_m)\mathbf{W}^+(z_m,z_0)]\vec{S}^+(z_0).\quad(9)$$

This model for primary reflections is known in the seismic literature as the WRW model.[10]

B. Two reflectors

Figure 6(a) shows a configuration where sources and detectors are placed between two parallel reflecting surfaces at z_1 and z_2. Now, at the detector plane z_d, direct sound from the sources at z_s and primary reflections from the two reflectors will be recorded, but also multiple reflections that have propagated several times upward and downward between the two reflectors. In Fig. 6(b), the process of direct sound propagation is represented as a block diagram. The direct sound field $\vec{P}_{\mathrm{dir}}$ at depth level z_d, generated by the source distribution $\vec{S}$ in source plane z_s, is given by

(a) geometrical configuration: two reflectors at z_1 and z_2

(b) direct wave field at z_d

(c) reflected wave field at z_d
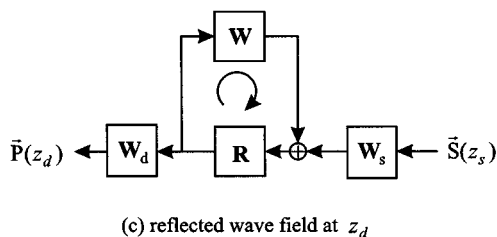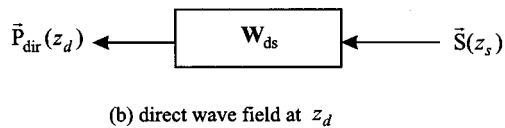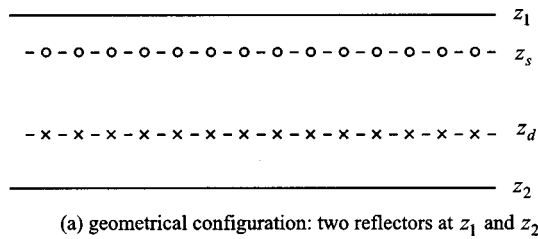
FIG. 6. Propagation and reflection in the case of two reflectors.

$$\vec{P}_{\mathrm{dir}}=\mathbf{W}_{ds}\vec{S},\quad(10)$$

where $\mathbf{W}_{ds}$ is a shorter notation for matrix $\mathbf{W}^+(z_d,z_s)$. The block diagram of Fig. 6(c) describes the generation of primaries and multiples at depth level z_d in terms of propagation and reflection matrices. From the diagram it can easily be derived that the primary reflections can be written as

$$\vec{P}_1=[\mathbf{W}_d\mathbf{R}\mathbf{W}_s]\vec{S}\quad(11a)$$

and the kth-order multiple reflections as

$$\vec{P}_k=[\mathbf{W}_d(\mathbf{R}\mathbf{W})^k\mathbf{R}\mathbf{W}_s]\vec{S}.\quad(11b)$$

The matrix $\mathbf{W}_s$ in Eqs. (11a) and (11b) consists of two submatrices, $\mathbf{W}_{1s}^-=\mathbf{W}^-(z_1,z_s)$ and $\mathbf{W}_{2s}^+=\mathbf{W}^+(z_2,z_s)$, describing the propagation between the source plane and the two reflectors:

$$\mathbf{W}_s=\begin{pmatrix}\mathbf{W}_{1s}^-\\\mathbf{W}_{2s}^+\end{pmatrix}.\quad(12a)$$

In a similar way, matrix $\mathbf{W}_d$ consists of two submatrices $\mathbf{W}_{d1}^+=\mathbf{W}^+(z_d,z_1)$ and $\mathbf{W}_{d2}^-=\mathbf{W}^-(z_d,z_2)$, describing the propagation from the reflectors to the detector plane:

$$\mathbf{W}_d=(\mathbf{W}_{d1}^+\quad\mathbf{W}_{d2}^-).\quad(12b)$$

The reflectivity matrix $\mathbf{R}$ in Eqs. (11a) and (11b) has a diagonal structure, where the diagonal contains two submatrices $\mathbf{R}_1^-=\mathbf{R}^-(z_1)$ and $\mathbf{R}_2^+=\mathbf{R}^+(z_2)$, describing the reflective properties of the two reflectors (walls):

$$\mathbf{R}=\begin{pmatrix}\mathbf{R}_1^-&\mathbf{0}\\\mathbf{0}&\mathbf{R}_2^+\end{pmatrix}.\quad(13)$$

Finally, the interwall propagation matrix $\mathbf{W}$ in Eq. (11b) is given by

$$\mathbf{W}=\begin{pmatrix}\mathbf{W}_{11}&\mathbf{W}_{12}\\\mathbf{W}_{21}&\mathbf{W}_{22}\end{pmatrix},\quad(14)$$

where submatrix $\mathbf{W}_{21}$ describes the propagation from wall 1 to wall 2 and submatrix $\mathbf{W}_{12}$ the propagation from wall 2 to wall 1. Note that $\mathbf{W}_{12}$ equals $\mathbf{W}_{21}^T$. Each diagonal submatrix describes the effect of wave propagation in the wall itself, e.g., caused by a bending wave field. In this paper we will set the diagonal matrices to zero, considering wave propagation between the walls only.

Summation of all orders of reflection given by Eq. (11b) yields a Neumann series:

$$\vec{P}_{\mathrm{refl}}=\sum_{k=1}^{\infty}[\mathbf{W}_d(\mathbf{R}\mathbf{W})^{k-1}\mathbf{R}\mathbf{W}_s]\vec{S}$$

$$=[\mathbf{W}_d[\mathbf{I}-\mathbf{R}\mathbf{W}]^{-1}\mathbf{R}\mathbf{W}_s]\vec{S}$$

$$=[\mathbf{G}_d\mathbf{R}\mathbf{W}_s]\vec{S},\quad(15a)$$

where $\mathbf{I}$ is the unity matrix and multiple scattering operator $\mathbf{G}_d$ is defined by

$$\mathbf{G}_d=\mathbf{W}_d[\mathbf{I}-\mathbf{R}\mathbf{W}]^{-1}.\quad(15b)$$

Note that Eq. (15a) may also be written as

$$\vec{P}_{\mathrm{refl}}=[\mathbf{W}_d\mathbf{R}\mathbf{G}_s]\vec{S}\quad(15c)$$

with

$$\mathbf{G}_s = [\mathbf{I} - \mathbf{WR}]^{-1}\mathbf{W}_s. \tag{15d}$$

From the foregoing it follows that the total wave field, including the direct sound, is given by

$$\vec{P} = [\mathbf{W}_{ds} + \mathbf{G}_d\mathbf{R}\mathbf{W}_s]\vec{S} \tag{16a}$$

or

$$\vec{P} = [\mathbf{W}_{ds} + \mathbf{W}_d\mathbf{R}\mathbf{G}_s]\vec{S}. \tag{16b}$$

C. Enclosed space with *N* reflecting boundaries

Recently it has been proposed to measure impulse responses along a closely spaced microphone array.[2] Results of such measurements can be well simulated by using the matrix multiplication equations as given in Sec. II B. Now, the propagation matrices $\mathbf{W}_s$ and $\mathbf{W}_d$ consist of submatrices describing the propagation from the sources to all N boundaries, and from these boundaries to the detectors, respectively:

$$\mathbf{W}_s = (\mathbf{W}_{1s} \quad \mathbf{W}_{2s} \quad \ldots \quad \mathbf{W}_{Ns})^T,$$
$$\mathbf{W}_d = (\mathbf{W}_{d1} \quad \mathbf{W}_{d2} \quad \ldots \quad \mathbf{W}_{dN}). \tag{17a}$$

The diagonal of reflection matrix $\mathbf{R}$ contains submatrices specifying the reflective properties of all N boundaries:

$$\mathbf{R} = \begin{pmatrix} \mathbf{R}_1 & \mathbf{0} & \cdot & \cdot & \mathbf{0} \\ \mathbf{0} & \mathbf{R}_2 & & & \cdot \\ \cdot & & \cdot & & \cdot \\ \cdot & & & \cdot & \cdot \\ \mathbf{0} & \cdot & \cdot & \cdot & \mathbf{R}_N \end{pmatrix}. \tag{17b}$$

The $N \times N$ elements of interwall propagation matrix $\mathbf{W}$ are submatrices describing the propagation between all boundaries:

$$\mathbf{W} = \begin{pmatrix} \mathbf{W}_{11} & \mathbf{W}_{12} & \cdot & \cdot & \mathbf{W}_{1N} \\ \mathbf{W}_{21} & \mathbf{W}_{22} & \cdot & \cdot & \mathbf{W}_{2N} \\ \cdot & & \cdot & & \cdot \\ \cdot & & & \cdot & \cdot \\ \mathbf{W}_{N1} & \mathbf{W}_{N2} & \cdot & \cdot & \mathbf{W}_{NN} \end{pmatrix}. \tag{17c}$$

Note that in the situation of an enclosed space surrounded by reflectors with various orientations, the meaning of ''upward'' and ''downward'' disappears, and therefore the superscripts '' + '' and '' − '' have been deleted. As mentioned before, in this paper we take the $\mathbf{0}$ matrix for the diagonal matrices $\mathbf{W}_{ii}$. Further, note that $\mathbf{W}_{ij} = \mathbf{W}_{ji}^7$. In Fig. 8 the propagation paths, as defined by the elements of propagation matrix $\mathbf{W}$, are visualized for the configuration of Fig. 7.

The expressions for the primary and multiple reflections in an enclosed space given by Eq. (15) imply a new concept for dereverberation of recordings made in complex sound fields using a microphone array. By inversion of operator $\mathbf{G}_d$ [Eq. (15b)] and multiplication of the result with propagation operator $\mathbf{W}_d$ [Eq. (12b)], a prediction-error operator $\mathbf{F}$ is designed, which is a symmetric matrix with unit diagonal elements:
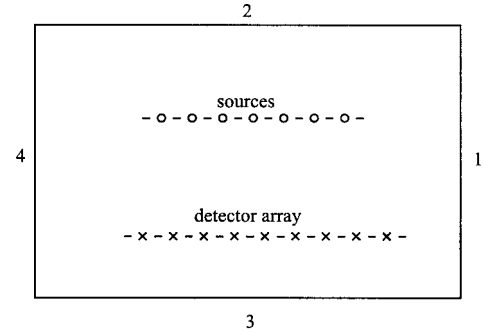
FIG. 7. Geometry, sources, and detector array for a 2-D rectangular enclosure.

$$\mathbf{F} = \mathbf{W}_d[\mathbf{I} - \mathbf{RW}]\mathbf{W}_d^{-1}. \tag{18}$$

Application of this operator to the complex reflection part of the impulse response given by Eq. (15a) yields the much simpler primary response of the hall as given by Eq. (11a):

$$\vec{P}_1 = \mathbf{F}\Delta\vec{P} = [\mathbf{W}_d\mathbf{R}\mathbf{W}_s]\vec{S}. \tag{19}$$

A similar procedure can be derived from Eqs. (15c) and (15d). How the matrix inversion can be performed in a stable and efficient way, and how the primary response can be optimally used for further processing, is a topic of present research.

(a) elements of the upper triangular part of interwall propagation matrix **W**

(b) elements of the lower triangular part of interwall propagation matrix **W**
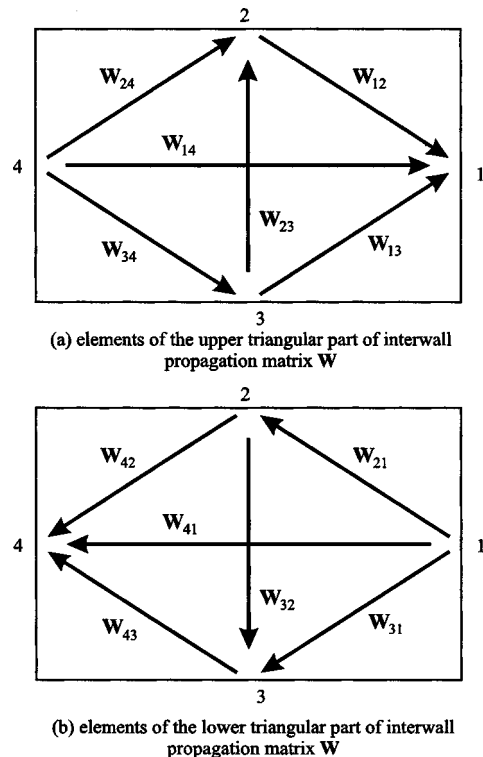
FIG. 8. Propagation paths represented in the triangular submatrices of propagation matrix **W**.
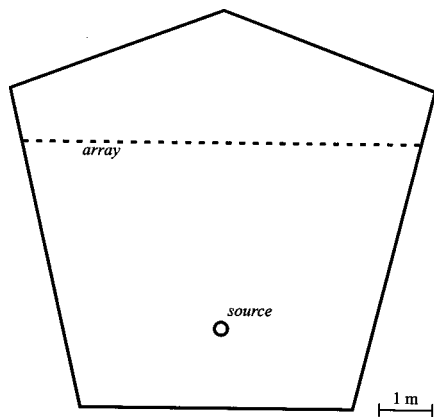
FIG. 9. Geometry of a two-dimensional enclosure used in the simulations.

III. NUMERICAL SIMULATION WITH THE WRW MODEL

From Eqs. (15a) and (15b) it can be easily derived that the modeling equations for the reflections can be written in an iterative way:

$$\vec{Q}^{(i)} = \mathbf{R}\mathbf{W}_s\vec{S} + \mathbf{R}\mathbf{W}\vec{Q}^{(i-1)}, \tag{20a}$$

$$\vec{P}_{\text{refl}} = \mathbf{W}_d\vec{Q}, \tag{20b}$$

with $\vec{Q}^{(0)} = \vec{0}$. Equations (20a) and (20b) are used to numerically simulate the response of a two-dimensional enclosure. Figure 9 shows the geometry of the enclosure and the position of the source and the microphone array. Calculations were done in the space-frequency domain. Then, the results were multiplied with the spectrum of an appropriate source signal. An inverse Fourier transform was applied to represent the results in the space–time domain. For comparison, re-

sponses have also been simulated with the mirror image source model (MISM).

Figure 10(a) shows the impulse responses along the microphone array simulated with the WRW model. Figure 10(b) shows the corresponding responses as simulated with the MISM. It is clearly seen that in the latter model, diffraction due to the finite dimensions of the boundaries is not taken into account: the transition between an image source being ''seen'' and ''not seen'' is abrupt, resulting in a sudden ending of reflected wave fronts. In reality, each ending of a boundary forms a secondary line source generating a diffraction wave appearing as a hyperbola in the space–time domain. Diffraction is properly taken into account by the WRW model. The difference between the results of the two models is shown in Fig. 10(c). It is seen that the diffracted waves mainly appear as ''extensions'' of the reflected wave fronts; other parts of the hyperbolic wave fronts are heavily masked by interference. The performance of the MISM can be significantly improved when the model is extended with a diffraction algorithm according to the theory given by Pierce.[7] Figure 11(a) again shows the WRW model results. Figure 11(b) gives the responses as simulated with the extended version of the MISM. Figure 11(c) gives the difference between the results of the WRW model and the extended MISM. Comparison with Fig. 10(c) shows that the extension of the MISM has significantly reduced the differences with the results of the WRW model. However, bear in mind that only first-order diffractions are simulated by the MISM extension: it is, in practice, not feasible to take reflections and diffractions of diffractions into account. Therefore, even the extended MISM is physically incomplete.
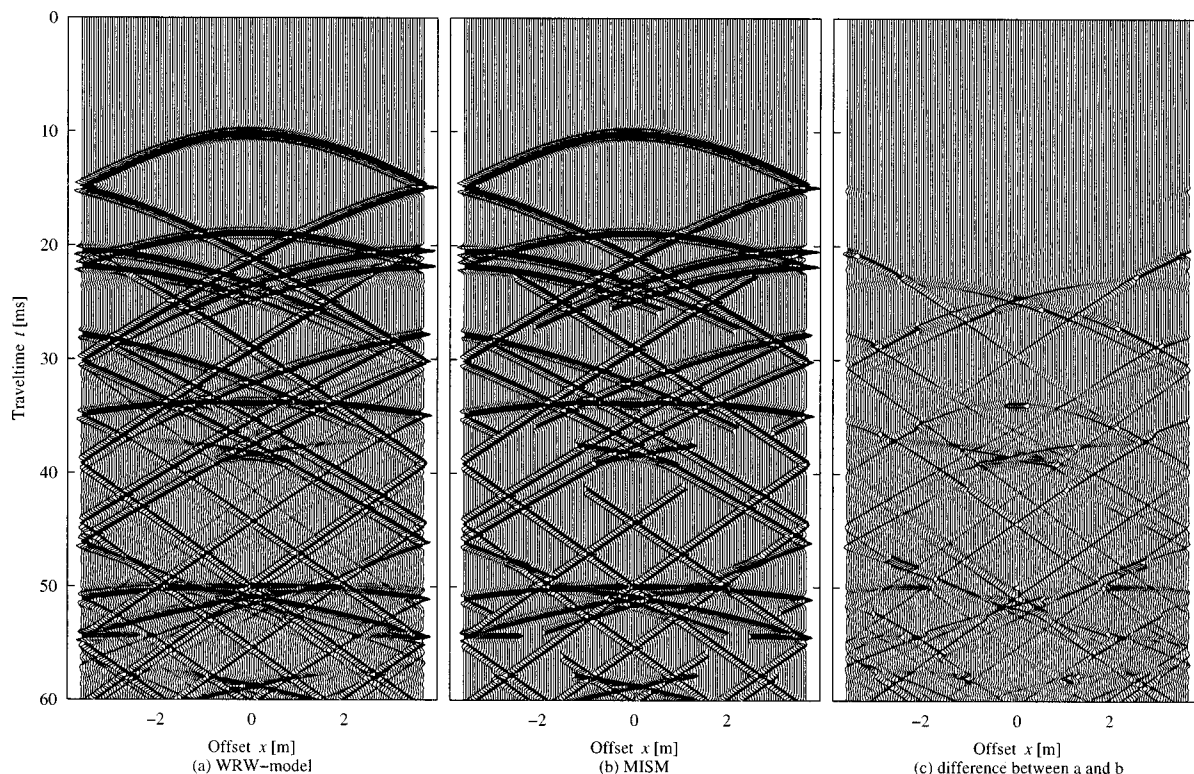
FIG. 10. A comparison of results simulated with the WRW model and the MISM.
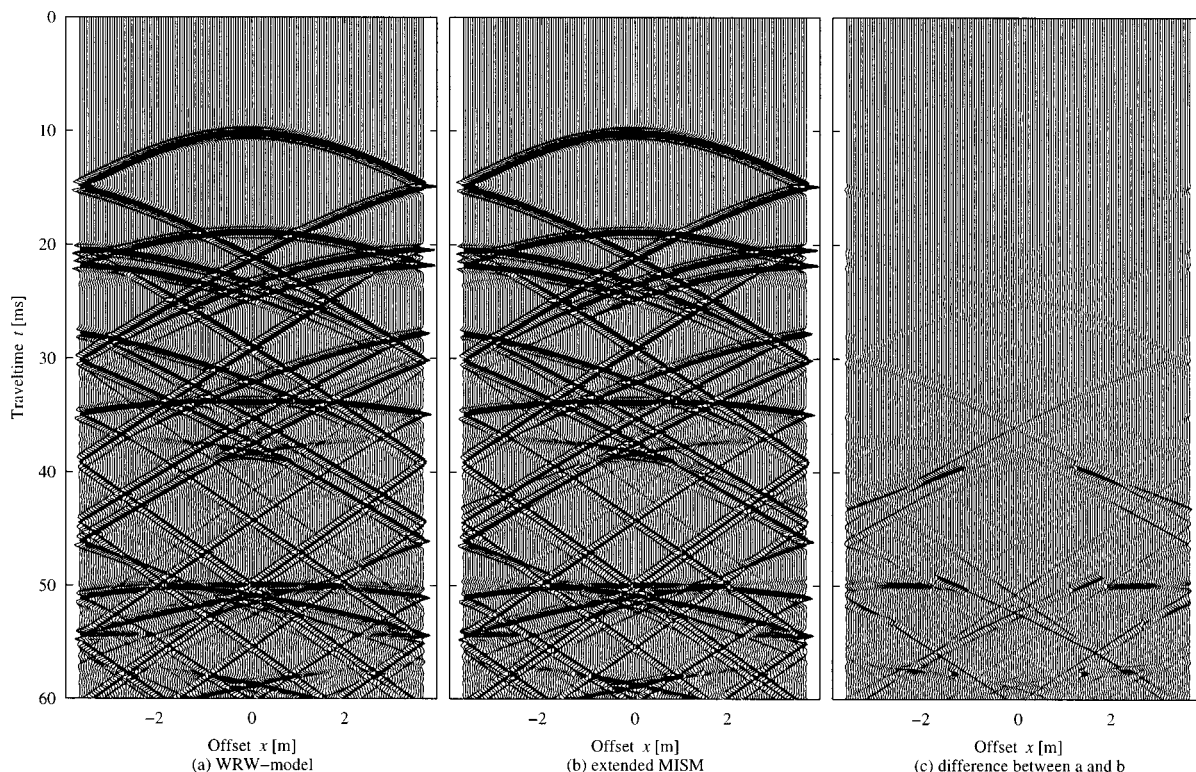
FIG. 11. A comparison of results simulated with the WRW model and the extended MISM.

IV. COMPARISON OF THE WRW MODEL RESULTS WITH MEASUREMENTS

In order to test the validity of the two-dimensional WRW model regarding reflection and diffraction effects at finite surfaces, impulse responses on a simple source–reflector configuration were measured in an anechoic chamber. A loudspeaker (VIFA-M 110) was positioned in front of a rectangular reflector (width 2.40 m, height 1.20 m). Responses were measured with a microphone array containing 148 microphone positions with 0.05-m interspacing, oriented parallel to the reflector. Source and array were positioned at the same height as the horizontal center line of the reflector, such that there is vertical symmetry. The configuration is depicted in Fig. 12. Figure 13(a) shows the measured result. After the direct wave front, the reflected sound arrives at the array. In addition to the specularly reflected wave front, two hyperbolic diffraction wave fronts which have larger curvature are seen, generated by the left and right edges of the

reflector. (The diffraction wave fronts generated by the upper and lower reflector boundaries, which are not included in the two-dimensional WRW model, are almost coinciding with the specular reflection, thus slightly broadening the corresponding wave front.) Some weaker phenomena appear due to the partially anechoic chamber. Figure 13(b) shows the measured result after elimination of these phenomena by filtering techniques described by Baan et al.,[11] which can be better compared with the data simulated with the two-dimensional WRW model shown in Fig. 13(c). It is seen that the direct wave front, the reflected wave front (not mixed up with diffraction effects from upper and lower boundaries, as in the measurements), and the diffractions from the left and right boundaries are in good agreement with the measured data. Other than in the simulation of the 2-D room with interconnected boundaries, Figs. 10(a) and 11(a), the hyperbolic diffraction wavefronts now show up entirely; it is clearly seen that they smoothly join the reflected wavefront as an apparent extension.

V. SOME REMARKS ON COMPUTING TIME

Based on the WRW model, impulse responses are calculated in the space-frequency domain applying the iterative solution given in Eqs. (20a) and (20b). For all relevant frequencies each iteration represents one complete order of reflections, requiring a computing time Δt_{WRW}. Hence, if N orders of reflections are included, the total computing time (neglecting the short time needed to calculate the direct sound) equals

$$T_{\mathrm{WRW}} = N \Delta t_{\mathrm{WRW}}. \tag{21a}$$

FIG. 12. Geometry of the measurement setup in the anechoic chamber.
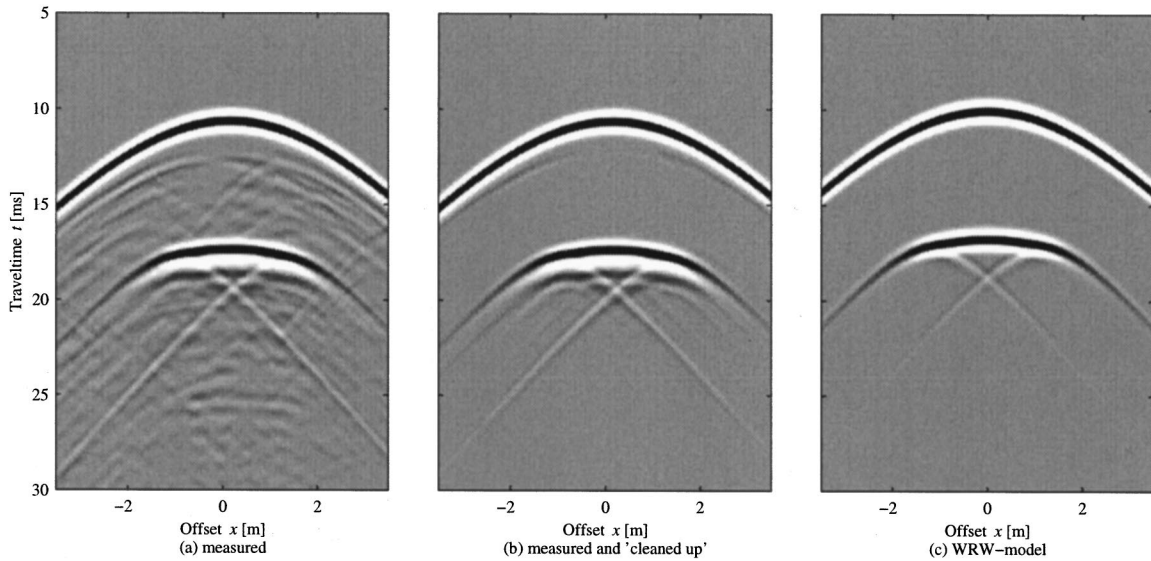
FIG. 13. Measured results compared to simulations with the WRW model.

If the traditional MISM or its extended version is used in practical situations, the visibility at the receivers of each mirror image source has to be tested, followed by calculation of the response in case of visibility. Since the computing time for the response is very small in comparison with the visibility test, an equal computing time Δt_{MISM} can be assigned to each possible mirror image source. If the room considered has M boundaries, the number of possible mirror image sources corresponding with reflections of order k equals $M(M-1)^{k-1}$, thus increasing exponentially with increasing order. Hence, again taking N orders of reflections into account and neglecting the direct sound, the total computing time equals

$$T_{MISM} = \sum_{k=1}^{N} M(M-1)^{k-1} \Delta t_{MISM}. \tag{21b}$$

It can be seen from Eq. (21b) that, depending on the values of Δt_{WRW} and Δt_{MISM}, for a certain value of N the required computing time for the WRW model will become shorter than for MISM. For the 2-D simulations in an enclosure with five boundaries, using a SUN Ultra 2200 workstation, Δt_{WRW} is of the order 10^2 s and Δt_{MISM} of the order 10^{-3} s. This means that the WRW algorithm is faster than the MISM for $N > 9$. Vorländer[12] developed a version of the MISM where the visible mirror image sources are identified by a fast ray-tracing procedure. Here, computing time increases with the third power of the reflection order, such that for the simple 2-D configuration treated here it is faster than the WRW model up to $N > 20$, i.e., all orders of interest. However, it should be noted that the physical shortcomings inherent to the MISM also hold for Vorländer's hybrid approach.

In practice, we deal with 3-D enclosures. Therefore, the WRW model should be extended to three dimensions, which means a substantial increase of Δt_{WRW}: instead of lines, the transmission between spatially sampled planes has to be calculated. In this context it is interesting to pay attention to computing times associated with boundary element method (BEM) algorithms.[13] The BEM has conceptual similarities

with the WRW model: reflectivity-related admittance values are specified on mesh points at the enclosure boundaries and transmission functions between the boundary points are calculated and processed in order to determine boundary pressure and velocity distributions. From these distributions, the pressure field at a detector array can be calculated using Eq. (1). The computing time, on a similar workstation as used in our simulations, of a fast iterative frequency domain BEM algorithm is reported to be of the order $10^{-5}P^2$ s per frequency component, where P is the total number of boundary mesh points.[14] Hence, for a full-scale concert hall where the number of mesh points is of the order 10^6, application of BEM appears not a practical option.

At present we are investigating solutions to reduce the computing time for the 3-D WRW model. The use of parallel computers and spatial sampling of the boundaries in relation with the frequency considered are possible solutions. In addition, we are investigating a fast numerical method to directly invert the matrix $(\mathbf{I} - \mathbf{RW})$ in Eq. (15b).

VI. CONCLUSIONS

(1) A qualitative model has been proposed for the acoustic impulse response of enclosures. The so-called WRW model gives ample physical insight in the complex propagation and reflection processes.

(2) An iterative version of the WRW model has been used for numerical simulation purposes. Our experience is very positive with respect to physical accuracy.

(3) The WRW model allows the formulation of a prediction-error operator that can be used to dereverberate recordings made in a hall with a microphone array.

[1] A. J. Berkhout, M. M. Boone, and P. J. M. Valks, "Multichannel impulse responses for outdoor noise propagation," J. Acoust. Soc. Am. **98**, 1169–1177 (1995).

[2] A. J. Berkhout, D. de Vries, and J. J. Sonke, "Array technology for acoustic wave field analysis in enclosures," J. Acoust. Soc. Am. **102**, 2757–2770 (1997).

[3] M. Vorländer, "Ein Strahlverfolgungs-Verfahren zur Berechnung von

Schallfeldern in Räumen,'' Acustica **65**, 138–148 (1988).

[4] B.-I. L. Dalenbäck, ''Room acoustic prediction based on a unified treatment of diffuse and specular reflection,'' J. Acoust. Soc. Am. **100**, 899–909 (1996).

[5] H. Kuttruff, *Room Acoustics*, 3rd ed. (Elsevier Applied Science, London, 1991), Chap. IV.

[6] J. Borish, ''Extension of the image model to arbitrary polyhedra,'' J. Acoust. Soc. Am. **75**, 1827–1836 (1984).

[7] A. D. Pierce, *Acoustics. An Introduction to Its Physical Principles and Applications* (Acoustical Society of America, New York, 1991), 2nd ed., Chap. 9.

[8] A. J. Berkhout and D. J. Verschuur, ''Estimation of multiple scattering by iterative inversion, Part I: Theoretical considerations,'' Geophysics **62**, 1586–1595 (1997).

[9] A. J. Berkhout, *Applied Seismic Wave Theory* (Elsevier, Amsterdam, 1987), Chap. VIII.

[10] A. J. Berkhout, ''A unified approach to acoustical reflection imaging, Part I: The forward model,'' J. Acoust. Soc. Am. **93**, 2005–2017 (1993).

[11] J. Baan and D. de Vries, ''Array technology for discrimination between specular and non-specular reflections in enclosed spaces,'' preprint AES 104th Convention, Amsterdam (1998).

[12] M. Vorländer, ''Simulation of the transient and steady state sound propagation in rooms using a new combined sound particle—image source algorithm,'' J. Acoust. Soc. Am. **86**, 172–178 (1989).

[13] R. D. Ciskowski and C. A. Brebbia, eds., *Boundary Element Methods in Acoustics* (Comp. Mechanics/Elsevier Applied Science, London, 1991).

[14] A. P. Berkhoff, private communication (1998).

Acoustic-impulse spectroscopy in Cu–Zn alloys

Rebekah Min-Fang Hsu

Room C408, Department of Physics, Foo Yin Institute of Technology, Ta-liao, Kaohsiung Hsien 831, Taiwan, Republic of China

Ching-Shuei Wur and Chang-Shew Jan

Department of Physics, National Cheng Kung University, Tainan 701, Taiwan, Republic of China

An electro-optical design was developed as the impulse spectrometer to identify the composition of the binary Cu–Zn alloys. The acoustic emission (AE) of Cu–Zn alloys was investigated using the Michelson interferometer as the detector. AE signals were detected from the impulse method with a one-dimensional simplified model. It is reported that the Cu component percentage in the family of the Cu–Zn alloys could be related to the bandwidth of frequency spectrum. Therefore, their composition can be recognized by observing the AE information in dynamics. © *1999 Acoustical Society of America.* [S0001-4966(99)02203-1]

PACS numbers: 43.58.−e, 43.58.Gn [SLE]

INTRODUCTION

The acoustic-impulse (AI) methodology is commonly applied in our daily life. For example, at the supermarket we tap on a watermelon and listen to the echo to determine the ripeness of the watermelon. In order to identify a false coin, we would drop it on the hard ground and listen to its sound. Although we commonly use these skills, a sophisticated application of the AI method has not been as well developed as other nondestructive testing or evaluation in ultrasonics. The pioneering scientific work for the AI technique was done by Schroeer, Rowand, and Kamm in 1970.[1] Although their goal to detect cracks was not reached, AI technology for identifying specimen fatigue was developed and the quantitative analysis of material composition using the AI method was promising. The advent of the space shuttle has prompted considerable attention to develop a structured health-monitoring system for detecting and locating structural damage. From experience gained in the machinery diagnostic field, one would expect the vibration signature of the structure to provide useful information. Both the frequency-response functions and time-domain parameters are typical signals in determining the location and extent of structural damage. Most prior work in damage-location algorithms was reviewed by Zimmerman and Kaouk.[2] The survey of acoustic monitoring and damage-assessment methods was discussed by Dimorogonas.[3]

Acoustic emission (AE) is the stress or pressure wave generated during dynamic processes in materials.[4] There are many mechanisms,[5] such as crack nucleation and propagation, multiple dislocation slip, twinning, and grain boundary sliding, etc. AE waveforms can carry information about the fine structure of the source event. The occurrence of multiple reflections within the specimen and ringing within the detecting transducer can obscure the nature of the source waveform. Fortunately, the frequency analysis of the detected waveform could provide information about the source event and about the vibration in the transmission properties of the structure under testing. In general, AE is irreversible (Kaiser effect, 1950[6]) and random. When a small mechanical impulse enters the specimen, the strain is elastic. The spontaneous emission of sound pulses depends on the structure of the material. The binary Cu–Zn alloys are polycrystalline solids. A δ-impulse could simplify the frequency responses by reducing them to a Gaussian process.

The acoustic emission during martensitic transformation in β_1 Cu–Zn alloy was studied by Esmail and Grabec.[7] The slowly growing banded martensite is distinguishable by dilatometric changes at very low amplitude, high-repetition-rate acoustic emission. The burst-type martensite is accompanied by high-amplitude, low-repetition-rate emission burst. Our previous study[8] revealed that the acoustic emission spectra of pure Cu metal differed from that of Zn. The acoustic emission of pure-metal copper and zinc under impact was investigated at room temperature. The waveforms and the frequency spectra were detected. A wideband lead zirconate-titanate (PZT) transducer of 0.5 MHz central frequency was used to detect the AE signals with a lubricant of SAE 40 as a couplant. The AE waveforms were recorded on magnetic tape and were examined by the spectrum analyzer as the tape was played back. The AE frequency response of copper shown in Fig. 1(a) dropped significantly from 30 dB at 10 kHz to 5 dB at 150 kHz. The AE signals of zinc showed a different spectrum; see Fig. 1(b). The spectra for the pure copper and zinc are quite distinct. The results showed that different metals have different AE spectra. These metals could be recognized by watching their AE signals. The relative behaviors of the family of the Cu–Zn alloys were thus very interesting.

I. EXPERIMENT

Elongated Cu–Zn specimens were prepared by the casting method for the one-dimensional propagation of AE signals. The purities of the starting materials of copper and zinc were 99.92% and 99.995%, respectively. The samples for the γ phase of Cu–Zn were very difficult to prepare because of the low boiling temperature of zinc. The ingots of Cu–Zn in the proper molar ratios (9:1, 7:3, 6.5:3.5, 6.3:3.7, 6:4, 5.5:4.5, 5:5, and 4.5:5.5) were homogenized at 833 K for 6 h
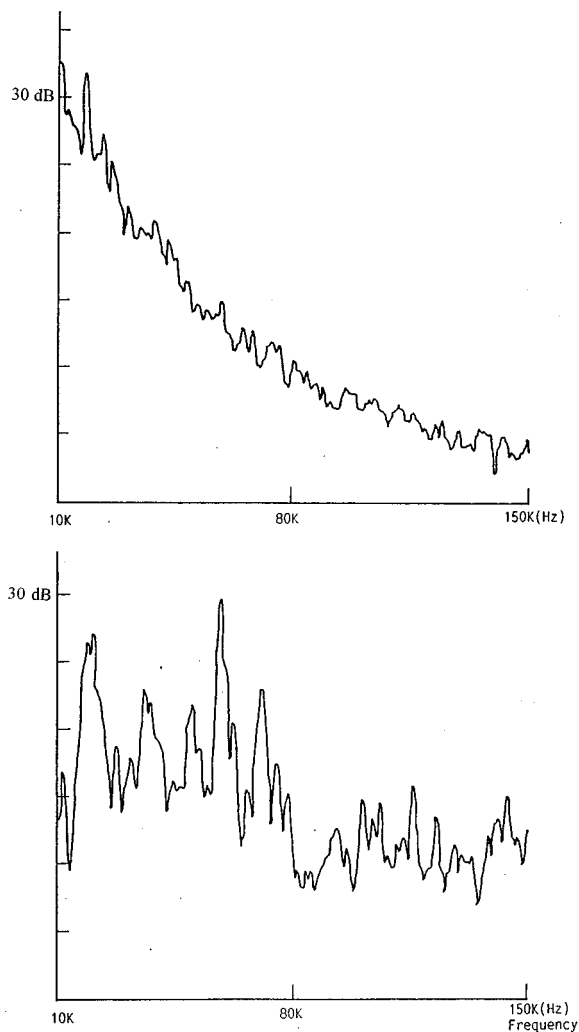
FIG. 1. Spectrum of AE signals in (a) Cu; (b) Zn metal.

to eliminate segregation, x-ray tested for defects, and treated by the hot extrusion method to form an elongated cylindrical shape. The lengths of the specimens were 100.0 (4), 70.0 (4), and 50.0 (5) cm, the mean diameter being 6.2 (1) mm as listed in Table I. The slenderness was defined as the ratio of specimen length per radius. Samples were annealed at 573 K for 1 h. The two ends of the specimens were polished as the

TABLE I. Cu composition and sizes for the Cu–Zn alloys.

Specimen	Cu wt.%	Length (cm)	Mean diameter (mm)	Slenderness
AL	90	100.0	6.25	320
BL	70	100.0	6.25	320
CL	65	100.0	6.25	320
CS		50.0	6.25	160
DL	63	100.0	6.25	320
DM		70.0	6.25	224
EL	60	100.0	6.08	329
EM		70.0	6.08	230
FM	55	70.0	6.25	224
FS		50.0	5.69	161
GL	50	100.0	6.2	320
HL	45	100.0	6.25	320
HS		50.0	6.22	161

mirror for the Michelson interferometer. The polishing process used 320, 400, 600, 800, and 1200 sandpapers and 0.3- and 0.05-μm Al_2O_3 powders.

The relative percentage of the constituents of Cu–Zn alloys was determined using the acoustic-impulse spectroscopy. A modification to the AI technique was made by substituting the usual accelerometer pickup with a Michelson optical interferometer. A specimen of the alloy fashioned in the shape of a bar was impacted at one end. The AE signals were detected and recorded in real time on the magnetic tape shown in Fig. 2. In this study, a pendulum was used to generate the idealized δ impulse of 22.27 dyn.s. The Michelson–Morley interferometer was used as a transducer to produce a signal proportional to the displacement of the end of the bar. Since the pressure of a light beam was very low, the loading on the specimen was negligible. The transmission/reflection ratio of the beam splitter was 2:7. While performing the experiments, AE signals were recorded simultaneously on the audio channel of the videotape recorder for subsequent playback, during which process a Fourier analysis of the signal was produced. The first 5-ms AE burst was analyzed by the spectrum analyzer shown in Fig. 2. It was found that the AE waveforms of the Cu–Zn alloys differed from those of the pure copper and zinc metals.

The handmade photodiode preamplifier shown in Fig. 2 transferred current to voltage. The output voltage of the preamplifier was provided by the N-channel-field-effect transistor (FET). There was an impedance-matching network between the preamplifier and the tape recorder. An LF356 operation amplifier was used to match the I/O impedances of the circuits. While the magnetic tape was playing, the videotape recorder was set to be ''still'' as shown in Fig. 2(b), as the signal of interest appeared on the monitor screen. This section of AE signal appeared at 60-Hz repetition frequency and was fed to a gated amplifier. A single AE burst was selected by the gated amplifier with various delay and gate-width functions. The obtained spectrum was repeatable, while the gate width was fixed. The gate bandwidth was from 1 to 20 kHz. The voltage gain for the amplifier shown in Fig. 2 was 26 dB. The trigger level of the counter was adjusted to be above the noise level, and the AE rate was counted.

II. CONCLUSION

When a single pulse propagated in the elongated Cu–Zn specimen, it partly reflected and partly transmitted, forming a series of signals. Impulse acoustic emission occurs at low frequencies since the input impulse was small in order to achieve the purpose of the elastic strains. The annealing effect of the sample preparation also improved the solid mesostructure. Figure 3 shows the frequency response for the initial 5-ms AE signals in $Cu_{0.9}Zn_{0.1}$. The attenuation of the high frequencies was larger than that of the low frequencies of the echo. Only the resonance frequencies remain after the multireflections. Figure 4 shows the resonance spectrum in $Cu_{0.9}Zn_{0.1}$ 0.6 s after the initial impulse. The gate time of 5 ms was fixed for all specimens. The cause of the resonances being seen in the spectra is the length of the sample bar. The spontaneous sound pulse initially carried the material infor-
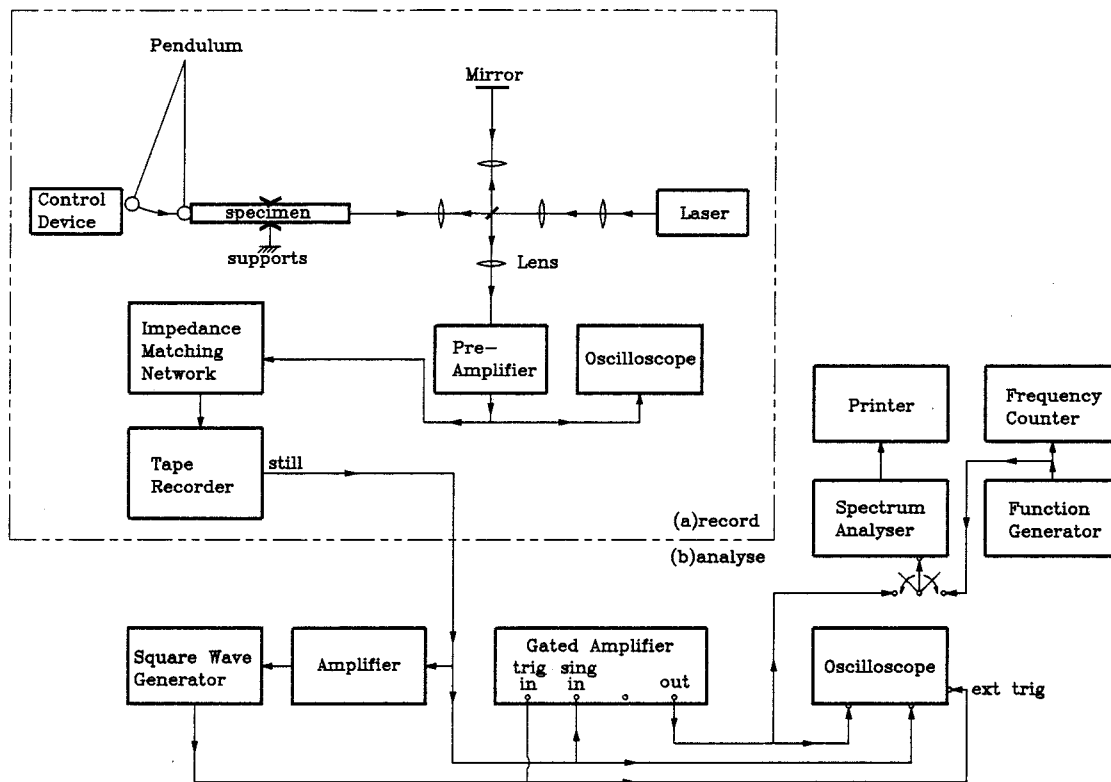
FIG. 2. Design of the impulse spectrum analysis. (a) Setup of record, (b) analyze devices.

mation, but the shape of the samples determined the resonance frequency at the end of the signals. We thus focus on the first 5 ms of AE burst for the purpose of materials composition.

Figures 5 and 6 show the frequency spectra in $Cu_{0.65}Zn_{0.35}$ with sample lengths 100.0 (4) and 50.0 (5) cm, respectively. The bandwidth varies as the length of the specimen changes. This also occurs in $Cu_{0.63}Zn_{0.37}$, $Cu_{0.6}Zn_{0.4}$, $Cu_{0.55}Zn_{0.45}$, and $Cu_{0.45}Zn_{0.55}$. The outer profile of each obtained frequency spectrum was fitted by a Gaussian function. All calculations utilized the MATHEMATICA[9] installed on a PC. The bandwidth was defined as the frequency width at the half amplitude of the outer profile.

In theory, the duration or the strength of the impulse decreases as the bandwidth of the frequency spectrum in-

creases. The wider the spectrum, the more material information is available. The mass and length of the pendulum was 1.9715 (4) g and 30.75 (5) cm, respectively. The maximum impulse was 27.85 dyn.s. The frequency responses in $Cu_{0.5}Zn_{0.5}$ for the different impulses were investigated, using 18.93, 22.27, 25.62, and 27.85 dyn.s, respectively. The bandwidth is inversely proporational to the strength of the impulse.

The initial 5-ms frequency spectra in $Cu_{0.9}Zn_{0.1}$, $Cu_{0.7}Zn_{0.3}$, $Cu_{0.65}Zn_{0.35}$, $Cu_{0.63}Zn_{0.37}$, $Cu_{0.6}Zn_{0.4}$, $Cu_{0.5}Zn_{0.5}$, and $Cu_{0.45}Zn_{0.55}$ were analyzed at a fixed length of 100.0 (4) cm. Their profiles for various compositions were similar.
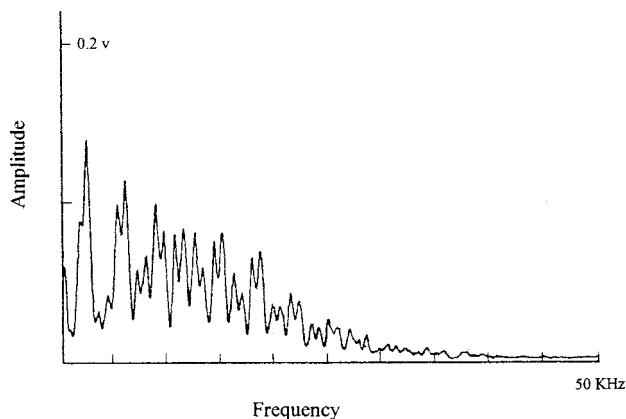
FIG. 3. The frequency spectrum in $Cu_{0.9}Zn_{0.1}$. Gated time 5 ms. Impulse 22.27 dyn.s.
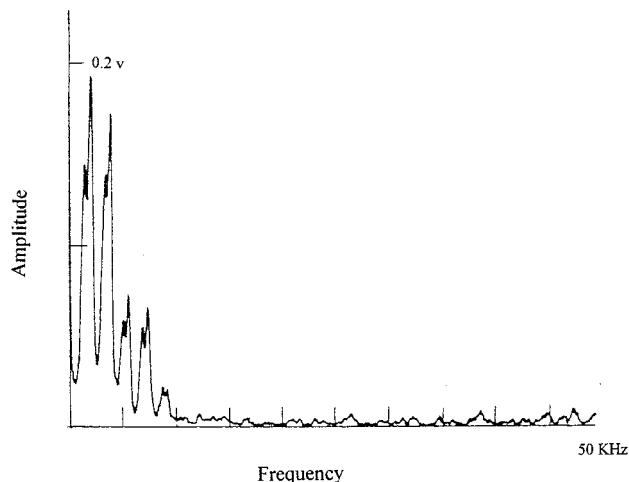
FIG. 4. The attenuation in $Cu_{0.9}Zn_{0.1}$ for signals of 0.6 s after the initial impulse. Gated time 5 ms. Impulse 22.27 dyn.s.
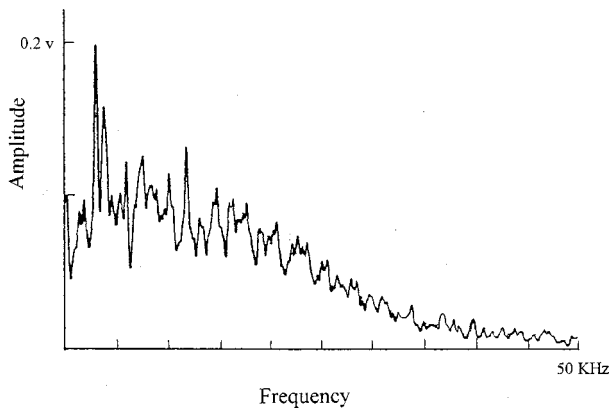
FIG. 5. Effect of specimen length; the frequency spectrum in $Cu_{0.65}Zn_{0.35}$. Gated time 5 ms. Impulse 22.27 dyn.s. Length 100.0 (4) cm.

The Cu–Zn composition is proportional to the bandwidth of the received signal shown in Fig. 7. This linear relationship is proper for the α and β phases of Cu–Zn alloys. In summary, the empirical formula from our measurements for the Cu composition in the Cu–Zn alloy is:

$$\sigma = k(C_0 - C) + \sigma_0,$$

where σ is the bandwidth (kHz), and C is the Cu percentage in the family of the Cu–Zn alloys. The characteristic constants C_0 and σ_0, which appear at the critical point of α and
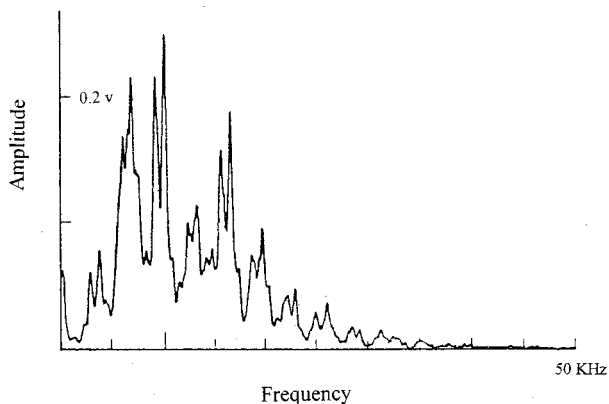
FIG. 6. Effect of specimen length; the frequency spectrum in $Cu_{0.65}Zn_{0.35}$. Gated time 5 ms. Impulse 22.27 dyn.s. Length 50.0 (5) cm.
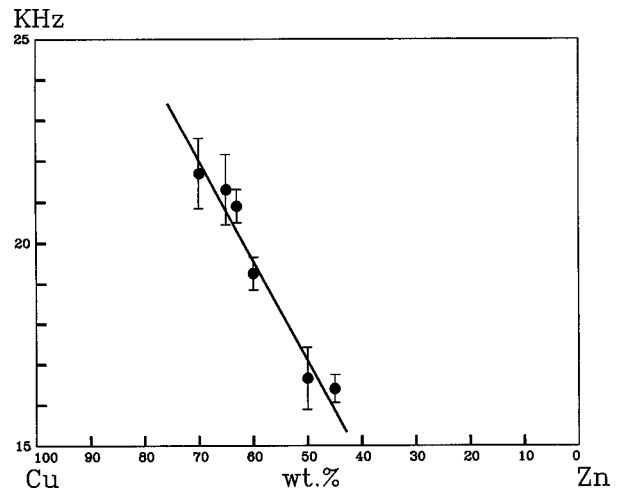
FIG. 7. The linear relationship of bandwidth vs Cu percentage in the Cu–Zn alloys.

γ phases[10] for the family of the Cu–Zn alloys, were 58% and 15 kHz, respectively, derived from Fig. 7. The experimental constant k was 0.263 kHz.

ACKNOWLEDGMENT

[1] R. Schroeer, R. Rowand, and H. Kamm, Mater. Eval. **28**(11), 237 (1970).
[2] D. C. Zimmerman and M. Kaouk, Trans. ASME, J. Vib. Acoust. **116**, 222 (1994).
[3] A. Dimorogonas, *Vibration for Engineers* (Prentice-Hall, Englewood Cliffs, NJ, 1996), 2nd ed., p. 231.
[4] D. Ensminger, *Ultrasonics* (Marcel Dekker, New York, 1973), p. 243.
[5] J. C. Spanner, *Acoustic Emission Techniques and Applications* (Prentice-Hall, Englewood Cliffs, NJ, 1974), p. 12.
[6] J. Kaiser, Ph.D. thesis, Techniqsche Hochschule, Munich, Germany, 1950.
[7] E. Esmail and I. Grabec, Phase Transit. **9**, 281 (1987).
[8] P. C. Lin, C. K. Sun, and C. S. Jan, *Proceedings of the 2nd ROC–ROK Joint Workshop on Fracture of Materials* (National Tsing Hua University, Hsinchu, 1986), p. 127.
[9] S. Wolfram, *Mathematica* (Addison-Wesley, Palo Alto, CA, 1991), 2nd ed.
[10] C. Kittel, *Introduction to Solid State Physics* (Wiley, New York, 1986), 5th ed., p. 553.

Hypothesis testing for geoacoustic environmental models using likelihood ratio

Christoph F. Mecklenbräuker[a)]
Ruhr-University of Bochum, D-44780 Bochum, Germany

Peter Gerstoft[b)]
Marine Physical Laboratory, Scripps Institution of Oceanography, University of California at San Diego, La Jolla, California 92093-0704

Johann F. Böhme[c)] and Pei-Jung Chung[c)]
Signal Theory Group, Department of Electrical Engineering, Ruhr-University of Bochum, D-44780 Bochum, Germany

A generalized likelihood ratio test is developed for testing acoustic environmental models with an application to parameter inversion using an acoustic propagation code. The signal-to-noise ratio in acoustic measurements proves to limit the details on geoacoustic environments that can be determined by matched field processing methods. A hypothesis test serves in Monte Carlo simulations as a tool to determine minimal signal levels for the bottom parameter inversion. The term ''hierarchy of models'' is used for denoting a sequence of models in which each particular model contains all previous ones. For determining the model order and its parameters, a combined parameter estimation and multiple sequential test is proposed. Given the observed data, how many parameters should be included in the model? The last question is important for the order selection in hierarchies of models with an increasing number of parameters. Multiple sequential hypotheses testing provides a procedure to determine the model order in a statistically justified way. Monte Carlo simulations show the behavior of the test for selecting a model order as a function of the signal-to-noise (SNR) ratio. The test is applied to broadband data measured using a vertical array near the island of Elba in the Mediterranean Sea and compared with Akaike's Information Criterion. © *1999 Acoustical Society of America.* [S0001-4966(99)03502-X]

PACS numbers: 43.60.Pt, 43.30.Pc [JCB]

INTRODUCTION

Previous literature on geoacoustic inversion focused primarily on the parameter estimation problem.[1–4] The *structure* of the acoustic propagation model (i.e., its parametrization) was assumed to be known *a priori*. Which parameters are relevant and should be included into the model as *unknowns* is usually decided on intuitive physical grounds—independently of the observed experimental data. However, both background noise and fluctuations in the quantities severely limit the *observable details* of an acoustic environment.

Various approaches to structural model identification are available in the signal processing literature.[5–7] Ljung[7] gives a good discussion of the subject. Most problems considered so far assume that the true model structure (although unknown in detail) is embedded in a hierarchy. This hierarchy is constructed from model structures of increasing complexity. Good examples of such model structures are the familiar autoregressive moving average (ARMA) models.

There seems no general optimum way to *build* such a hierarchy for geoacoustic environmental models, since the acoustic parameters (e.g., sound speed and attenuation profiles) do not have a natural *order*: Obviously, there is no specific first, second, third,..., parameter. As a consequence, building such a hierarchy is subjective and the acoustician stays responsible for the design according to specific needs. However, indications of the ''relative importance'' of individual parameters can be numerically obtained.

In this paper we deal with statistical hypothesis tests for acoustic environments based on observed data and a replica on a vertical array of sensors. It is an extension of the work in Refs. 8 and 9. The replica is generated using environmental model parameters (sound speed profile, attenuations, and densities) and an acoustic propagation model. The array output is modeled as a superposition of a stationary noise process and the signal of interest. Both the parameter estimation[10] and testing are performed by analysis of data in the frequency domain using a finite Fourier transform.

The purpose of this hypothesis testing is to verify estimated parameters of environmental models that were obtained previously by the inversion of observed data.[11] The inversion was based on data from a calibrated vertical array and carried out using information at multiple frequencies from a single broadband source. A range-dependent adiabatic normal mode code[12] was used as the forward model. The global optimization was implemented by a directed Monte Carlo search based on genetic algorithms (GA) and

[a)]Present address: Siemens AG, A-1101 Vienna, Austria. Electronic mail: christoph.mecklenbraeuker@siemens.at
[b)]Electronic mail: gerstoft@mpl.ucsd.edu
[c)]Electronic mail: {boehme,pjc}@sth.ruhr-uni-bochum.de

the Bartlett objective function.[10] The inversion included the estimation of all important forward model parameters, which can be divided into geometric, geoacoustic, and ocean sound-speed variables. From analyzing the *a posteriori* parameter distributions of the GA, it is known that not all parameters can be equally well estimated.[10]

In order not to bias the test, a different dataset is used for testing and estimation, but the datasets are based on the same acquisition. The Fourier-transformed data is split in two subsets for estimation and testing in a comb-like fashion. In this way, the whole frequency range is available to both stages of processing—adjacent frequency bins are merely spaced farther apart.

Global search necessitates a huge number of forward solutions to be computed, vastly limiting the number of frequencies used in the estimation procedure. The test can verify an obtained model against a set of alternatives by incorporating data from more frequencies than were used to estimate the associated environmental parameters. A set of alternative environmental models is readily available from the inversion itself and given by the final populations of the GA.

The definition of objective functions for environmental parameter estimation, and the choice of test statistics in hypothesis testing using multifrequency data is still under discussion.[13,14] Exploiting the asymptotic Gaussianity of data in the frequency domain allows defining approximate likelihood functions, which can be maximized for the parameter estimation, and can be used for hypothesis tests based on likelihood ratios.[13,14] The proposed likelihood ratio test (LRT) is based on multifrequency data and exploits the asymptotic Gaussianity of short-time Fourier-transformed measurement data.

This test is related to a solution to the detection problem in passive sonar, seismics, and radar applications using a multiple sequential F test that is based on a frequency–domain regression.[15–17] The estimated signal-to-noise ratio (SNR) for the observed data in the frequency domain turns out to be the basic quantity from which the LRT is constructed. This is very appealing from a physical point of view. In this paper, we define the SNR in the frequency domain via the quotient of eigenvalues of the spectral density matrix (SDM) of the sensor outputs. In Sec. II D we give a more detailed discussion of these quotients in signal space.

The LRT compares the geometric means over the frequency of the estimated noise spectral levels under the hypothesis and alternatives. In the case of only one single source, this is related to the sum of Bartlett powers in dB.

Monte Carlo simulations are performed for a numerical analysis of the proposed algorithm. The behavior of the combined inversion and hypotheses testing is computed over the SNR.

Finally, the test is applied to broadband data measured using a vertical array near the island of Elba in the Mediterranean Sea.[11] It is assumed that optimum parameter estimates for a given environmental model have already been found by using a global optimization approach.[10]
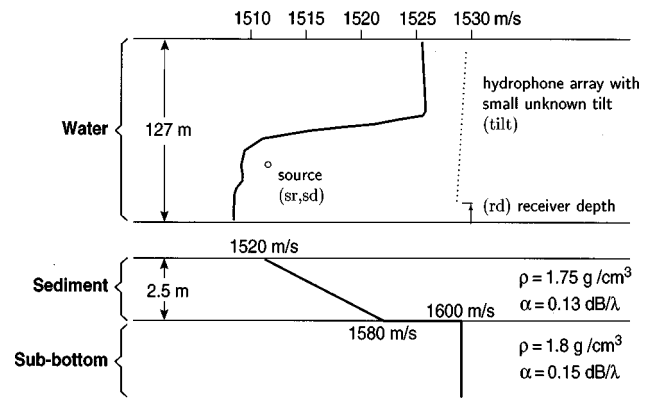
FIG. 1. Range-independent baseline model for acoustic propagation in the shallow ocean north of Elba island; see Ref. 19 for further details.

I. PROPAGATION AND DATA MODEL

We consider a single wide-band source and the usual linear model in frequency domain for the output of an array of N sensors with spatially uncorrelated additive noise,

$$\mathbf{x}(\omega) = \mathbf{d}(\omega;\mathbf{m})s(\omega) + \mathbf{u}(\omega). \tag{1}$$

In this paper, vectors are denoted by lowercase boldface, matrices in uppercase boldface, and * is the Hermitian transpose operation. Let $\mathbf{x}$ be the Fourier transform of the output of the vertical sensor array. Correspondingly the source signal is denoted by s and the noise by $\mathbf{u}$. The transfer function $\mathbf{d}(\omega;\mathbf{m}) \in \mathbb{C}^N$ is calculated by the SNAP forward model code, which calculates the Green's function G for the ocean acoustic frequency–domain wave equation.[12,18]

The source/receivers geometry and geoacoustic environment for the baseline model are shown in Fig. 1 for a range independent environment and in Fig. 2 for a range dependent environment. The source signal s and the transfer function $\mathbf{d}(\omega;\mathbf{m})$ are assumed to be deterministic. The additive noise in time domain is stochastic, stationary, and zero mean.

The data $\mathbf{x}(\omega)$ at the receiving array are asymptotically complex normal distributed with mean $\mathbf{d}(\omega;\mathbf{m})s(\omega)$ and covariance $\mathbf{C}_u(\omega) = \nu(\omega)\mathbf{I}$, where $\nu(\omega) > 0$ denotes the power spectral density of the noise. The vector-valued transfer function $\mathbf{d}(\omega;\mathbf{m})$ depends nonlinearly on the environmental parameters, which are summarized in a vector $\mathbf{m}$. In this paper, the dimension of $\mathbf{m}$ may vary with the structure of the model. The *true model* corresponding to the data is characterized by the r-dimensional parameter vector $\mathbf{m}^\bullet$.

We use the word "model" for the geoacoustic parameters of an ocean acoustic wave guide with given structure. Let us denote the set of all models by $\mathcal{M}$. The set of all replica vectors $\mathbf{d}(\omega;\mathbf{m})$ that can be calculated by SNAP for all models is denoted by $\mathcal{D}$. The models are indexed by the parameter vector $\mathbf{m}$, which is an element of the associated parameter set $\mathcal{M} \subset \mathbb{R}^r$. We assume $\mathbf{m}^\bullet \in \mathcal{M}$. The *mapping* between the parameter set $\mathcal{M}$ and the replicas $\mathcal{D}$ is termed a *model structure*. In Sec. III the sets $\mathcal{M}$ and $\mathcal{D}$ will be given a hierarchical buildup.

II. LIKELIHOOD RATIO TEST

Considering the model (1) at a discrete set of frequencies ω_j ($j=1,...,J$), it can be shown that the log-likelihood function is given by

$$\mathcal{L}(\mathbf{m}) = -\frac{1}{J} \sum_{j=1}^{J} \log(1 - B(\omega_j;\mathbf{m})), \tag{2a}$$

$$B(\omega;\mathbf{m}) = \frac{\mathbf{d}^*(\omega;\mathbf{m})\hat{\mathbf{C}}_x(\omega)\mathbf{d}(\omega;\mathbf{m})}{|\mathbf{d}(\omega;\mathbf{m})|^2 \operatorname{tr} \hat{\mathbf{C}}_x(\omega)}, \tag{2b}$$

where $\hat{\mathbf{C}}_x(\omega)$ denotes a nonparametric estimate of the spectral density matrix (SDM) of the data.[20] We use the sample mean

$$\hat{\mathbf{C}}_x(\omega) = \frac{1}{KL} \sum_{k=0}^{K-1} \sum_{l=0}^{L-1} \mathbf{x}_{k,l}(\omega)\mathbf{x}_{k,l}^*(\omega) \tag{3}$$

of KL Fourier-transformed data snapshots $\mathbf{x}_{k,l}(\omega)$. The observed data $\mathbf{x}(t)$ in time domain $t=0,1,...,KT-1$ is divided into K snapshots of duration T each. These are Fourier transformed using L orthogonal windows $\nu_t^{(l)}$ depending on snapshot duration T and selected analysis bandwidth W. Here, we used discrete prolate spheroidal sequences as data tapers.[21–23,14] The bandwidth of resolution $0<W<\frac{1}{2}$ is selected such that (3) is nonsingular. The number L of data tapers in (3) is essentially equal to the time–bandwidth product: $L=\lfloor 2WT\text{-}1 \rfloor$, where $\lfloor x \rfloor$ is the largest integer smaller than or equal to x. The Fourier-transformed snapshots are calculated for $k=0,...,K-1$ and $l=0,...,L-1$ by

$$\mathbf{x}_{k,l}(\omega) = \sum_{l=0}^{T-1} \nu_t^{(l)}\mathbf{x}(t+kT)e^{-j\omega t}.$$

The maximum-likelihood (ML) estimate for the parameter vector $\mathbf{m}$ of $\mathcal{M}$ is defined as

$$\hat{\mathbf{m}} = \arg \max_{\mathbf{m} \in \mathcal{M}} \mathcal{L}(\mathbf{m}). \tag{4}$$

Note, that the log-likelihood function can be easily interpreted as the *averaging of the Bartlett power over frequency bins in dB*. This approach of averaging in log units was empirically found to have optimal side lobe suppression.[24]

After estimates have been obtained in this way, the resulting models can be validated using hypotheses tests. We start with an introductory example for which the likelihood ratio test is known to be optimal in Sec. II A. However, this simple setting does not apply here. Proceeding to Sec. II B, we formulate the test problem that is appropriate for validation. It turns out that a straightforward implementation of the LRT is not feasible and a possible solution is presented in Sec. II C.

A. Simple hypothesis and alternative

We test which one of two models $\mathcal{M}_0=\{\mathbf{m}_0\}$, $\mathcal{M}_1 = \{\mathbf{m}_1\}$ has generated the measurement data $\mathbf{x}(\omega)$. In this test problem, the hypothesis and alternative are both of the *simple type*, i.e., they do not contain unknown parameters. The Neyman–Pearson Lemma applies, dictating that the most powerful test is based on the likelihood ratio.[7] The

hypothesis H_0 states ''$\mathcal{M}_0$ is true'' and the alternative H_1 reads ''$\mathcal{M}_1$ is true.'' The LRT of H_0 against H_1 constructs the test statistic $T=\mathcal{L}(\mathbf{m}_0)-\mathcal{L}(\mathbf{m}_1)$ and compares its value with a critical value t_α, which depends on the chosen level α of the test.

B. Validating a specified model against a set of alternatives

A more interesting setting is to validate a particular selected model against a set of competing models with the same parametrization, deciding whether $\mathbf{m}_0 \in \mathcal{M}_0=\{\mathbf{m}^\bullet\}$ or $\mathbf{m}_0 \in \mathcal{M}_1 = \mathcal{M}\backslash\mathcal{M}_0$. The model $\mathcal{M}_0$ should be compared with all competing models inside the alternative $\mathcal{M}_1$, which contains all models except for $\mathbf{m}_0$. The test uses the quantity $t(\mathbf{x}) = \mathcal{L}(\mathbf{m}_0) - \max_{\mathbf{m}_1 \in \mathcal{M}_1} L(\mathbf{m}_1)$. We are dealing with a *composite* alternative, and, therefore, optimality of the LRT cannot be guaranteed. In terms of the Bartlett Power, the test statistic is written as

$$t(\mathbf{x}) = \min_{\mathbf{m}_1 \in \mathcal{M}_1} \frac{1}{J} \sum_{j=1}^{J} \log \frac{1 - B(\omega_j;\mathbf{m}_1)}{1 - B(\omega_j;\mathbf{m}_0)}. \tag{5}$$

The LRT now compares this quantity with a predetermined threshold value t_α that depends on the level α of the test and the distribution of the test statistic (5).

In general, there exists a set $\mathcal{K}_\alpha \subset \mathcal{M}_1$ of parameter vectors for which H_0 is rejected. This α-critical region can be viewed as a confidence region for $\mathbf{m}$: parameter vectors $\mathbf{m} \in \mathcal{K}_\alpha$ cannot be rejected against H_0. By sampling $\mathcal{M}_1$ and repeating the test for each individual $\mathbf{m} \in \mathcal{M}_1$, numerical approximations to $\mathcal{K}_\alpha$ are obtained.

Unfortunately, this direct approach is not feasible, due to the incomplete knowledge about the distribution of the test statistic. The fraction inside (5) is the ratio of two χ^2-distributed random variables, but they are not independent. This problem arises because we are testing a particular $\mathbf{m}_0 \in \mathbb{R}^r$ against all alternatives with the same parametrization: they are of the same order r.

C. Sequential LRT using three steps

The difficulties described in the previous section disappear when we test a *smaller* against a *bigger* model.[7] They are avoided by testing the models in a three step sequential procedure. We will use the following hypotheses H_i and alternatives A_i ($i=1,2,3$):

H_1: no signal in the data, A_1: $\mathbf{d}_0 \in \mathcal{D}_0$ or $\mathbf{d}_1 \in \mathcal{D}_1$ generated the data,

H_2: replica vector $\mathbf{d}_0 \in \mathcal{D}_0$ generated the data,

A_2: the data cannot be adequately modeled by $\mathbf{d}_0$,

H_3: replica vector $\mathbf{d}_1 \in \mathcal{D}_1$ generated the data,

A_3: the data cannot be adequately modeled by $\mathbf{d}_1$.

We have omitted the dependency on ω in notation for all quantities, $\mathbf{d}_0 = \mathbf{d}(\omega;\mathbf{m}_0)$, and $\mathbf{d}_1 = \mathbf{d}(\omega;\mathbf{m}_1)$.

Some comment is necessary on A_1: physically, we know that it is not possible for two *differing* geoacoustic environments to be correct at the same time. So in A_1, the logical ''or'' can be substituted by an ''exclusive or'' opera-
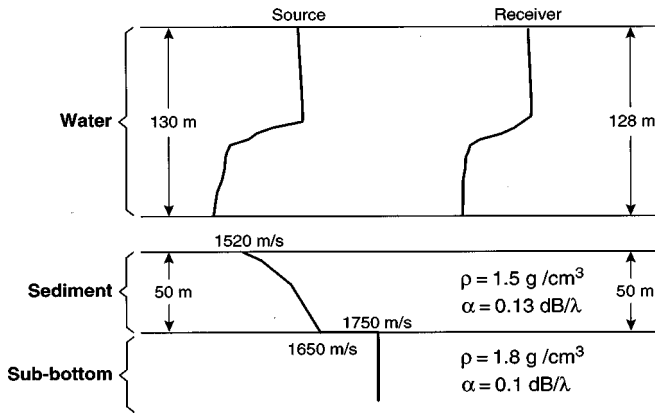
FIG. 2. Range-dependent geoacoustic baseline model with differing properties at the source and receiver locations.

tion. For the algorithm, however, it is more suitable to implement the ''inclusive or'' which is easier to formulate and makes no logical difference in this case.

In mathematical terms, the above H_i, A_i are formulated as

H_1: $\mathbf{x} = \mathbf{u}$,

A_1: $\mathbf{x} = (\mathbf{d}_0 \quad \mathbf{d}_1)\begin{pmatrix} s_0 \\ s_1 \end{pmatrix} + \mathbf{u}$,   with $|s_0|^2 + |s_1|^2 \neq 0$;

H_2: $\mathbf{x} = \mathbf{d}_0 s_0 + \mathbf{u}$,   with arbitrary $s_0 \neq 0$

A_2: $\mathbf{x} = (\mathbf{d}_0 \quad \mathbf{d}_1)\begin{pmatrix} s_0 \\ s_1 \end{pmatrix} + \mathbf{u}$,   with $s_1 \neq 0$ and $s_0 \neq 0$;

H_3: $\mathbf{x} = \mathbf{d}_1 s_1 + \mathbf{u}$,   with arbitrary $s_1 \neq 0$

A_3: $\mathbf{x} = (\mathbf{d}_0 \quad \mathbf{d}_1)\begin{pmatrix} s_0 \\ s_1 \end{pmatrix} + \mathbf{u}$,   with $s_0 \neq 0$ and $s_1 \neq 0$.

Step 1: First, we test H_1 against the alternative A_1, and if the hypothesis is rejected, we conclude that *the data contain a signal, and at least one of the models will be correct*; we proceed with Step 2. If the hypothesis is accepted the test stops at this point. In this case, we have an identifiability problem due to lack of signal power.

Step 2: We test the hypothesis H_2 with arbitrary $s_0 \neq 0$ against the alternative A_2. If the hypothesis is accepted, we conclude that H_2 *is true* and the test stops here. If, on the other hand, H_2 is rejected, we go to Step 3.

Step 3: This is a cross-check: we test the hypothesis H_3 with arbitrary $s_1 \neq 0$ against the alternative A_3.

In each step, the test statistics $t_1(\mathbf{x})$, $t_2(\mathbf{x})$, and $t_3(\mathbf{x})$ can be put into the form

$$t_i(\mathbf{x}) = -\frac{1}{J} \sum_{j=1}^{J} \log\left(1 + \frac{n_1}{n_2} V_i(\omega_j)\right), \tag{6}$$

with

$$V_i(\omega) = \frac{n_2}{n_1} \frac{\mathrm{tr}[(\mathbf{P}_3(\omega) - \mathbf{P}_{i-1}(\omega))\hat{\mathbf{C}}_x(\omega)]}{\mathrm{tr}[(\mathbf{I} - \mathbf{P}_3(\omega))\hat{\mathbf{C}}_x(\omega)]}, \tag{7}$$

FIG. 3. An interpretation of the test statistic and spectral density matrix eigenvalues.

where the projection matrices $\mathbf{P}_{i-1}(\omega)$ ($i = 1,2,3$) are associated with the signal subspaces under H_i in each step of the test; see Sec. 1 of the Appendix.

$\mathbf{P}_0(\omega) = \mathbf{0}$,

$\mathbf{P}_1(\omega) = \mathbf{d}_0 \mathbf{d}_0^* / |\mathbf{d}_0|^2$,

$\mathbf{P}_2(\omega) = \mathbf{d}_1 \mathbf{d}_1^* / |\mathbf{d}_1|^2$, $\tag{8}$

$\mathbf{P}_3(\omega) = \mathbf{Q}\mathbf{Q}^*$,   where $\mathbf{Q} = \mathrm{orth}(\mathbf{d}_0, \mathbf{d}_1)$.

The integers n_1, $n_2 \in \mathbb{N}$ are explained in Sec. II E. The projection matrix $\mathbf{P}_3$ is associated with the alternatives: it has rank two. The signal space under the alternatives is spanned by both $\mathbf{d}_0$ and $\mathbf{d}_1$. If the geoacoustic model is identifiable, then it is asserted that the vectors $\mathbf{d}_0$ and $\mathbf{d}_1$ are linearly independent. Matrix $\mathbf{Q}$ contains two columns being a unitary basis of the two-dimensional space spanned by $\mathbf{d}_0$ and $\mathbf{d}_1$.

This test strategy ensures that the difference of the projection matrices in the denominator of (6) is a projection operator that is orthogonal to $\mathbf{I} - \mathbf{P}_3$. This makes $V_i(\omega)$ an F_{n_1, n_2}-distributed random variable.

D. Interpretation in signal space

The test statistics can be easily interpreted in the signal/noise space analogy. The following discussion is for *Step 2* of the test, but the reasoning for the third step is completely equivalent. Figure 3 describes graphically what eigenvalues of the spectral density $\mathbf{C}_x$ are grouped together in the nominator and denominator of the F variable (7) if the hypothesis H_2 is true. In this discussion, we replace $\hat{\mathbf{C}}_x(\omega_j)$ in (6) by its expectation $\mathbf{C}_x(\omega_j)$ to make the analogy more clear. The frequency dependence of the quantities will be suppressed in notation for convenience.

In the equation described in Fig. 3, $\mathbf{U}$ denotes the unitary eigenvector matrix of $\mathbf{C}_x$. The dominant eigenvalue (EV) corresponding to the signal eigenvector $\mathbf{d}_0$ is denoted by λ_1. The noise EVs are given by $\lambda_2, \ldots, \lambda_N$. The projection matrix $\mathbf{P}_3$ projects onto a two-dimensional subspace of $\mathbb{C}^N$. The dominant eigenvector of $\mathbf{C}_x$ and one of the noise eigenvectors are a basis of this subspace. By resorting the eigenvectors in $\mathbf{U}$, we can always achieve that $\mathbf{P}_3$ is associated with the first two eigenvectors—and thus with λ_1, λ_2 in the following sense:

$$\mathrm{tr}[\mathbf{P}_3 \mathbf{C}_x] = \lambda_1 + \lambda_2 = |\mathbf{d}_0|^2 |s|^2 + 2\nu.$$

On the other hand, $\mathbf{P}_1$ is associated with the dominant signal EV λ_1 alone,

$$\text{tr}[\mathbf{P}_1\mathbf{C}_x] = \lambda_1 = |\mathbf{d}_0|^2 |s|^2 + \nu.$$

And the projection matrix of the difference projector $\mathbf{P}_3 - \mathbf{P}_1$ is associated with the single noise EV λ_2 only. The nominator in (6) is associated with all the other noise EVs,

$$\text{tr}[(\mathbf{I}-\mathbf{P}_3)\mathbf{C}_x] = \lambda_3 + \cdots + \lambda_N = (N-2)\nu.$$

Thus, we see that the signal power is canceled out of the F variable (7) if the hypothesis H_1 is true:

$$\frac{n_1}{n_2}V_2 \approx \frac{\text{tr}[(\mathbf{P}_3-\mathbf{P}_1)\mathbf{C}_x]}{\text{tr}[(\mathbf{I}-\mathbf{P}_3)\mathbf{C}_x]} = \frac{1}{N-2}.$$

In this way, the test statistic becomes a pivot, i.e., independent of the unknown parameters.[25] Somewhat loosely stated, the test statistic compares one selected noise EV to the arithmetic mean of all the other noise EV. If this ratio exceeds some predetermined threshold, we conclude that the selected replica vector $\mathbf{d}_0$ is not the only dominant eigenvector of $\mathbf{C}_x$, and the hypothesis H_2 is rejected. If the alternative A_2 is true, V_2 depends on $|s|^2/\nu$.

In the nonasymptotic case, V_i in (7) can be interpreted as the increase of the signal-to-noise ratio, if the model is enlarged by the alternative A_i.

E. Degrees of freedom

The degrees of freedom (DOF) n_1, n_2 of the F_{n_1,n_2}-distributed random variable are given by[13]

in *Step 1*: $n_1 = 4KL$, $n_2 = KL(2N-4)$,

in *Steps 2 and 3*: $n_1 = 2KL$, $n_2 = KL(2N-4)$,

if $\mathbf{m}_1$ is *not* estimated from the same data where the test statistic is based upon. The factor KL stems from Eq. (3). This was ensured by using a different and larger set of frequency bins ω_j for the test than for the inversion.

The ratio $n_1/n_2 = 1/(N-2)$ is equal to the ratio of the signal- and noise-subspace dimensions. Asymptotically, i.e., for a large observation time, $V_i(\omega_j)$ and $V_i(\omega_k)$ are independent if $\omega_j \neq \omega_k$.

We must be more careful in the case when $\mathbf{m}_1$ is itself dependent on the data. This is the case if $\mathbf{m}_1$ is *estimated* from the measurement data. In this case, the DOF are given by the more complicated formulas:

in *Step 1*, $n_1 = KL(r_1 + r_2 + 4)$,

$$n_2 = KL(2N - (r_1 + r_2 + 4));$$

in *Steps 2 and 3*, $n_1 = KL(r_1 + r_2 + 2)$,

$$n_2 = KL(2N - (r_1 + r_2 + 4)),$$

where r_1, r_2 denote the number of environmental parameters (i.e., the dimension of $\mathbf{m}_1, \mathbf{m}_2$).[13] This can be circumvented easily by splitting the data into two disjoint sets for the purpose of estimation and test. We can either straightforwardly split in the time domain or exploit asymptotic independence in the frequency domain for adjacent frequency bins. In the first case, weak effects of nonstationarity in the background

noise could lead to trouble. In the latter case, we recommend an interleaved scheme: a comb-like separation of estimator and test frequencies. If such an approach is feasible then the DOF do not depend on r_1 or r_2.

Alternatively, the DOF might be obtained from the Fischer Information Matrix of the unknown parameters $\mathbf{m}$. The "nonlinear DOF" r_p are strongly related to the numerical rank of the Fischer Information Matrix.[26]

F. Calculation of thresholds

The test statistics from (6) are easily interpreted as the arithmetic mean of a sample of independent identically distributed random variables $T_j = \log(1 + (n_1/n_2)V_i(\omega_j))$ whose probability density and cumulants can be evaluated in closed form (see Sec. 2 of the Appendix), e.g., for mean and variance, we obtain

$$\mu_T = \Psi\left(\frac{n_1+n_2}{2}\right) - \Psi\left(\frac{n_2}{2}\right) \approx \log\left(1 + \frac{n_1}{n_2}\right),$$

$$\sigma_T^2 = \Psi'\left(\frac{n_2}{2}\right) - \Psi'\left(\frac{n_1+n_2}{2}\right) \approx \frac{2n_1}{n_2(n_1+n_2)}. \tag{9}$$

Here, $\Psi(x) = d\log\Gamma(x)/dx$ and $\Psi'(x) = d\Psi(x)/dx$ are polygamma functions.[27] The α-critical value t_α can be derived from a normal approximation for the distribution $F_T(t)$ of (6) for a large number of frequencies J using the inverse error function[27]

$$t_\alpha = \mu_T + \frac{\sigma_T\sqrt{2}}{\sqrt{J}}\,\text{erf}^{-1}(2\alpha-1). \tag{10}$$

A more accurate value for t_α can be obtained via the Cornish–Fisher expansion of the inverse cumulative distribution function of the test statistic[28] or bootstrapping.[25] Experimentally, it was shown that the performance of the test does not improve using these more elaborate approximations.

III. MODEL STRUCTURE IDENTIFICATION

The replica-vector set $\mathcal{D}$ is now given an additional hierarchical buildup. We define an increasing sequence $\mathcal{D}_1, \mathcal{D}_2, \ldots,$ of subsets, such that
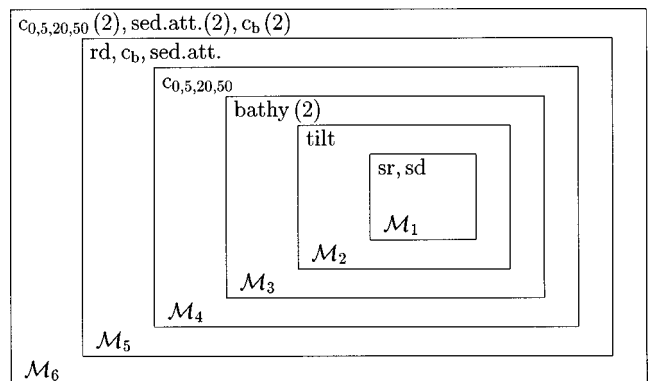
FIG. 4. The box-like structure for geoacoustic models $\mathcal{M}_1, \ldots, \mathcal{M}_6$ used for the inversion of real data. The meaning of the parameter name abbreviations is given in Table I.

1742   J. Acoust. Soc. Am., Vol. 105, No. 3, March 1999

Mecklenbräuker *et al.*: Hypothesis testing   1742

TABLE I. The models used for the inversion (Ref. 9) of real data. BP is Bartlett power in dB from (13); the maximum is zero. r is the number of parameters over which optimization was performed. The notation (2) denotes that a value of this parameter was estimated for both the source and receiver range. Inversion parameters: source range, source depth, bathymetry, array tilt, velocity profile, receiver depth of deepest hydrophone in array, bulk velocity in sediment, sediment attenuation.

Model	r	BP	Inversion parameters $\mathbf{m}$
$\mathcal{M}_1$	2	−0.41	sr, sd
$\mathcal{M}_2$	4	−0.28	sr, sd, bathy.(2)
$\mathcal{M}_3$	5	−0.25	sr, sd, bathy.(2), tilt
$\mathcal{M}_4$	9	−0.23	sr, sd, bathy.(2), tilt, $c_{0,5,20,50}$
$\mathcal{M}_5$	12	−0.23	sr, sd, bathy.(2), tilt, $c_{0,5,20,50}$, rd, c_b, sed. att.
$\mathcal{M}_6$	18	−0.22	sr, sd, bathy.(2), tilt, rd, $c_{0,5,20,50}$ (2), sed. att. (2), c_b (2)

FIG. 5. The standardized test statistic $t_{2,m}$ for each stage in the model hierarchy as applied to the real data. The horizontal index m denotes the test of hypothesis $H_{2,m} = \mathcal{M}_{p-1}$ against the alternative $A_{2,m} = \mathcal{M}_{p-1}$ or $\mathcal{M}_p$. For details see Table I. The dashed horizontal line shows the threshold value t_α for a false-alarm rate of $\alpha = 5\%$.

$$\mathcal{D}_1 \subset \mathcal{D}_2 \subset \cdots \subset \mathcal{D}_p \subset \cdots \subset \mathcal{D} \subset \mathbb{C}^N.$$

The model subsets $\mathcal{D}_p$ are associated with parameter sets $\mathcal{M}_p$ because each replica vector $\mathbf{d}(\cdot; \mathbf{m}_p) \in \mathcal{D}_p$ is indexed by a parameter vector $\mathbf{m}_p \in \mathcal{M}_p \subset \mathbb{R}^{r_p}$. The dimension $r_p \in \mathbb{N}$ of the parameter set $\mathcal{M}_p$ increases monotonically with p.

For two arbitrary models, we say ''model structure $\mathcal{M}_p$ is included in $\mathcal{M}_q$'' iff $\mathcal{D}_p \subset \mathcal{D}_q$. We write $\mathcal{M}_p < \mathcal{M}_q$. We can think of the *smaller* model structure $\mathcal{M}_p$ being generated from $\mathcal{M}_q$ by *freezing* some elements of $\mathbf{m}_2$ to constant nominal values of a *baseline model*.

As a specific example, consider Fig. 4. The ''Russiandoll''-like figure gives an intuitive visualization of the problem. The meaning of the parameter name abbreviations is given in Table I. Model $\mathcal{M}_1$ only includes the two source coordinates (*sr,sd*) as unknown parameters; all other physical quantities are given from the reference model, Fig. 1. The next model additionally includes the tilt of the receiving (nominally vertical) array (tilt is defined as horizontal displacement between the bottom and top hydrophone in the array). Model $\mathcal{M}_3$ is enlarged to include two parameters for bathymetry: the ocean depth at the source and receiver location.

The order of the parameters $\mathbf{m}_p = (m_1, \ldots, m_p) \in \mathcal{M}_p$ in the pth model structure $\mathcal{M}_p$ seems to be completely arbitrary at first. However, the acoustician has an intuitive idea about the ''relative importance'' of the individual parameters. In this way, the question arises as to how to design the hierarchy.

The rigorous approach consists in fixing one parameter of the highest-order model $\mathcal{M}_P$ to the nominal value of the baseline model. After this has been done for all parameters in turn, the very set of $P-1$ parameters is selected, which gives the *least degradation of the maximum-likelihood value*. This procedure is repeated for $\mathcal{M}_{P-1}, \mathcal{M}_{P-2}, \ldots$, and so on. This approach is computationally prohibitive for a practical numbers of inversion parameters.

The experienced acoustician can get help from two sources: first, he can calculate the Fischer information matrix for the parameters at their *nominal values*: this gives an indication of variances in the single parameter estimates and their mutual correlations. This could be called the *local* approach and should be repeated for several model vectors. Finally, the *a posteriori* distributions of Genetic Algorithms[10,14] also indicate spreading of the estimates: this is a practical *global* approach for hierarchy construction.

TABLE II. Models used for simulation (Ref. 28). r is the number of parameters over which optimization was performed. Parameters: source range, source depth, bathymetry, array tilt. Unspecified parameters are given in Fig. 1. Model $\mathcal{M}$ generated the simulated datasets.

Model	r	Inversion parameters $\mathbf{m}$	Search ranges	Fixed values
$\mathcal{M}_1$	2	sr, sd	5500 m < sr < 5700 m 75 m < sd < 85 m	tilt = 0 m bathy = 127 m
$\mathcal{M}_2$	3	sr, sd, tilt	5500 m < sr < 5700 m 75 m < sd < 85 m −3 m < tilt < 3 m	bathy = 127 m
$\mathcal{M}_3$	4	sr, sd, tilt, bathy	5500 m < sr < 5700 m −3 m < tilt < 3 m 125 m < bathy < 133 m	···
$\mathcal{M}$	···	···	···	sr = 5600 m, sd = 80 m tilt = 0.3 m, bathy = 130.5 m

A. Identification algorithm using LRT

We can now formulate Algorithm 1 for the structure identification problem. It returns the estimated model order $\hat{p}$ and the corresponding parameter $\hat{\mathbf{m}}_p$. We need hypotheses and alternatives analogous to Sec. II B for each model order m: they are denoted by $H_{i,m}$, $A_{i,m}$, respectively. In particu-lar, $\mathbf{d}_0 \leftarrow \mathbf{d}(\cdot;\hat{\mathbf{m}}_p)$ and $\mathbf{d}_1 \leftarrow \mathbf{d}(\cdot;\hat{\mathbf{m}}_{p+1})$ are substituted in Eq. (8). The algorithm starts with Step 1 for $\mathcal{M}_1$: this decides whether there is a significant input signal. This step is only needed once, whereas Steps 2 and 3 are repeated for all model orders.

Algorithm 1: model identification using a LRT.

$\hat{\mathbf{m}}_1 := \arg\max_{\mathbf{m}_1 \in \mathcal{M}_1} \mathcal{L}(\mathbf{m}_1)$

if $H_{1,1}$ cannot be rejected against $A_{1,1}$ then
 stop   "*identifiability problem: we don't know what p is*"
main loop:
for $p := 1,2,...,$do
 $\hat{\mathbf{m}}_{p+1} := \arg\max_{\mathbf{m}_{p+1} \in \mathcal{M}_{p+1}} \mathcal{L}(\mathbf{m}_{p+1})$
 if $H_{2,p}$ cannot be rejected against $A_{2,p}$ then
 $\hat{p} := p$, stop "*this is a conservative selection*"
 else
  if $H_{3,p}$ cannot be rejected against $A_{3,p}$ then
   $\hat{p} := p+1$, stop
  else
   $\hat{p} \geq p+1$, continue *with the loop over p*
end *of* for *loop*
output $\hat{p}, \hat{\mathbf{m}}_p$

B. Akaike's information criterion

Alternatively, we can adopt Akaike's Information Crite-rion (AIC) approach to the order selection problem for acoustic models; cf. Ref. 7. In the present application, the AIC selects the model order $\hat{m} \in \mathbb{N}$, which minimizes the criterion:

$$\text{AIC}[m] = -\mathcal{L}(\hat{\mathbf{m}}_p) + \frac{r_p}{N}. \tag{11}$$

From this simple form of $\text{AIC}[m]$, we can directly calculate the required increase in likelihood to equalize the cost of additional parameters. The AIC prefers $\mathcal{M}_{p+1}$ over $\mathcal{M}_p$ iff

$$\mathcal{L}(\hat{\mathbf{m}}_{p+1}) - \mathcal{L}(\hat{\mathbf{m}}_p) > \frac{1}{N}(r_{p+1} - r_p). \tag{12}$$

IV. EXAMPLES

The examples are all based on the environment from the North Elba sea trial;[19] see Figs. 1 and 2. In Sec. IV A the examples are based on synthetic data and in Secs. IV B and IV C on real data.

The experimental data were collected near the Island of Elba in the Mediterranean Sea during a sea trial in October 1993.[11,4] A vertical array of $N = 48$ sensors approximately spanning the whole water column of 128-m ocean depth was used. The signal source was located at a range of 5600 m and at depth 80 m below the surface. The transmitted signal was centered at 170 Hz and modulated with a pseudorandom noise sequence giving a total bandwidth of approximately 20 Hz. A record of one minute (6×10^4 samples at a sampling frequency of 1 kHz) of time samples was used. The SDM $\hat{\mathbf{C}}_x(\omega)$ was estimated from $K = 15$ nonoverlapping windowed Fourier-transformed snapshots of 4-s duration each. The 4000 samples per snapshot were zero padded to enable a FFT of length 2^{12}. $L = 4$ data windows with bandwidth pa-rameter $W = 6.25 \times 10^{-4}$ were used in (3), making $KL = 60$. Adjacent frequency bins are separated by $\Delta f = \frac{125}{512}$ Hz ≈ 0.244 Hz.

A. Simulation of sequential test

First the algorithm is used to determine the correct model order as a function of the SNR. Simulated datasets are generated as follows: The SNAP code calculates the replica vector for the range-independent environment $\mathcal{M}$ given in Table II. Uncorrelated Gaussian noise is added to the replica for obtaining a desired SNR. For each SNR, we conduct 50 independent random experiments: each experiment is carried out with a new choice of signal and corrupted by noise that is independent of the other realizations. The data were gener-ated by a selected model in the largest model structure con-sidered and corrupted by additive noise at a prescribed SNR. In each experiment, we calculated the ML estimates and ap-plied the proposed algorithm for the first model structures by global optimization of (2a) using a genetic algorithm, analo-gous to Ref. 10. For each SNR, this is repeated 50 times in order to make a statistical interpretation of the result. For each model order and SNR, 22 500 forward models were calculated during optimization.

The nonoptimized parameters in each model $\mathcal{M}_p$ are given fixed values from the baseline model, Fig. 1. The base-line model is different from the *true* model, although its pa-rameters are close guesses to the true values based on geo-logical archives. If the fixed parameters were *true* it is clear that we would always favor a low-order model.

Monte Carlo estimates for the probabilities of the test
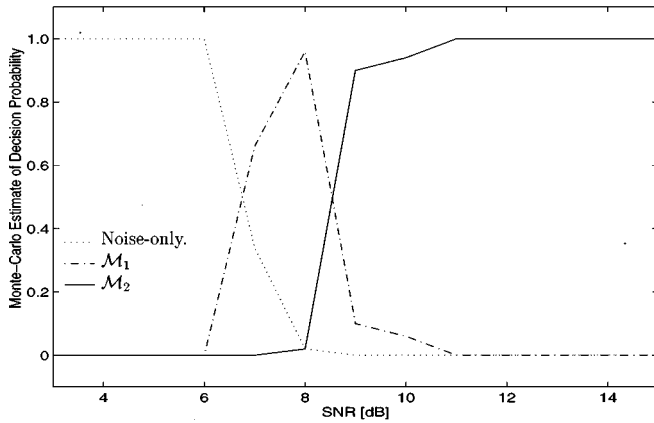
FIG. 6. The simulation of LRT $\mathcal{M}_1$ against $\mathcal{M}_2$ for various SNR levels.

FIG. 8. The AIC simulation result based on 100 Monte Carlo runs.

decisions as a function of the SNR are given in Figs. 6 and 7. Typical threshold effects can be clearly observed in the figures: at a characteristic SNR value, the test decides with high probability in favor of the correct model order. In specific intervals of SNR, *downgraded* models are preferred to a full model containing all parameters. Each downgraded lower-order model has its own range in the SNR in which it is dominant, indicating identification problems for higher-order models at the corresponding SNR levels. Thus, in Fig. 6 for a SNR lower than 6 dB, there is not enough signal in the data to determine even the $\mathcal{M}_1$ model, and above 10 dB there is enough information to determine at least the $\mathcal{M}_2$ model. Around 8 dB, the model structure $\mathcal{M}_1$ is best. In Fig. 7 we also include the model $\mathcal{M}_3$. It is seen that above 10-dB model $\mathcal{M}_3$ is favored, and $\mathcal{M}_2$ is only favored in a narrow region around 9 dB.

The corresponding results for the AIC criterion (12) are shown in Fig. 8. If the improvement in the maximum likelihood between $\mathcal{M}_p$ and $\mathcal{M}_{p+1}$ exceeds $1/N = \frac{1}{48} \approx 2.083 \times 10^{-2}$ per additional parameter, $\mathcal{M}_{p+1}$ is preferred. It is seen that this approach is not as conservative as the LRT, but AIC does not guarantee a false-alarm rate α. We accept model $\mathcal{M}_3$ down to a level of 6 dB and for a low SNR we accept model $\mathcal{M}_2$.

B. Application to North Elba data

For a set of six range-dependent ocean acoustic models,[11] the environmental parameters were estimated by a globally convergent stochastic algorithm using a frequency-domain measurement data at three distinct frequencies (167.72, 169.19, and 172.61 Hz). The search range used for each parameter is indicated in Table III. This rather slim broadband approach was selected for computational reasons, due to the large number of forward models that had to be calculated during the optimization: 20 000 forward models are calculated for each model order. In a second step, the obtained results were validated by the LRT using measurement data at the much broader frequency range 159.91–179.93 Hz, incorporating the measurement at $42 - 3 = 39$ distinct frequency bins. From the selected frequencies $\omega_j/2\pi = \Delta f(2j + 653)$, for $j = 1,...,42$, we discarded the three frequency bins mentioned before that were used for parameter inversion. The SNR in the data varies between about 33 dB at the center frequency and 22 dB at the ends of the range—which is quite high.

The models build a hierarchy of increasing complexity and model $\mathcal{M}_p$ contains $\mathcal{M}_{p-1}$ as a special case; see Table I,

FIG. 7. The simulation of multiple sequential LRT for the first three models.

TABLE III. GA inversion model with parameter search bounds. Each parameter was discretized into 128 values.

Model parameter	Lower bound	Upper bound
Geometric		
Source range (m)	5300	5900
Source depth (m)	72	82
Array tilt (m)	−3	3
Receiver depth (m)	110	115
Bathymetry-src (m)	127	134
Bathymetry-rcv (m)	127	134
Sediment		
Sound speed, c_0 (m/s)	1510	1560
Sound speed, δ_1 (m/s)	0	100
Sound speed, δ_2 (m/s)	0	100
Sound speed, δ_3 (m/s)	0	100
Attenuation (dB/λ)	0	0.4
Bottom		
Sound speed, δ_4 (m/s)	0	200
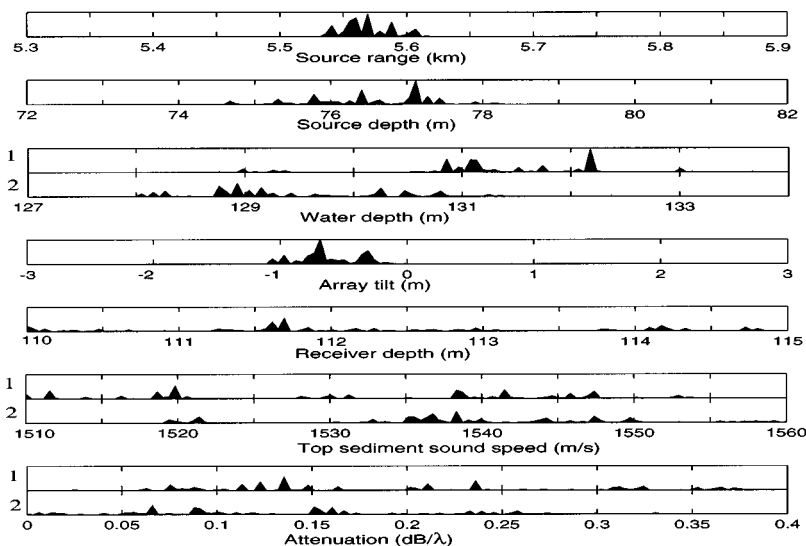
FIG. 9. The *a posteriori* distribution for the most important parameters for model $\mathcal{M}_6$ using the combined band. 1 and 2 refers to the source and receiver environments, respectively.

where also the Bartlett Power (in dB) for the best estimated models are shown;

$$\mathrm{BP}_p = 10\log_{10}\sum_j \left[1 - B(\omega_j;\hat{\mathbf{m}}_p)\right],$$

$$\text{with } j \in \{687, 693, 707\}. \tag{13}$$

Using Eq. (6) with $H_{2,m}$ as a hypothesis and $A_{2,m}$ as an alternative, the test statistics in Fig. 5 are computed. We cannot adopt both model structures $\mathcal{M}_p$ and $\mathcal{M}_{p+1}$ at the same time, *if they differ in their parameters*. This is what the test decides. If the test statistic $t_2(\mathbf{x})$ is smaller than the α-critical value (shown as a solid horizontal line), then $\mathcal{M}_p$ is rejected. The α-critical value for the test was found from the normal approximation given by Eq. (10). Figure 5 shows the result of a sequential test for identifying the correct model structure. The calculated LRT test statistics $t_{2,m}$ for the model hierarchy $\mathcal{M}_1 < \cdots < \mathcal{M}_6$ are shown together with the threshold (dashed horizontal line) for $\alpha = 5\%$.

C. Confidence regions and *posteriori* distributions

During the GA optimization, all obtained samples of the search space are stored and used to produce *a posteriori* probability distributions for the parameters. For a system of r parameters, the result is an r-dimensional space. This is difficult to display and therefore only marginal probability distributions are shown. The samples are ordered according to their energy, and the probability distribution is scaled using a Boltzmann distribution.[10] The *a posteriori* distributions are useful for evaluating the convergence of the inverse solution and uniqueness of the solution. While it does not give the model order it clearly indicates which parameters are important for the inversion; see also the comments in Sec. III.

An example of this is shown for the North Elba case.[11] For the $\mathcal{M}_6$ model the *a posteriori* distributions for the more important parameters are illustrated in Fig. 9. It is seen that, except for the receiver depth, the geometric parameters were well determined. That is, all distributions were compact over the search interval and had well-defined single peaks. The model $\mathcal{M}_3$ contains all geometric parameters, except for the

receiver depth. By interpretation of the *a posteriori* distributions from $\mathcal{M}_6$, we obtain an indication on the order of the parameters that should be incorporated into $\mathcal{M}_p$ for $p > 3$.

In general, it would be expected that the source and receiver depths are about equally important. The source depth is much more important here because it is placed in the thermocline. Further, the search interval for the receiver depth is half of the search interval for the source depth.

V. CONCLUSIONS

Hypothesis testing is a powerful tool as part of an acoustic inversion procedure. For a given model structure (set of parameters to estimate), the estimated values of parameters found by the optimization can be statistically justified. This is in clear contrast to the usual procedure, where we just arbitrarily select a set of parameters and then optimize the parameter values.

A multiple sequential LRT was applied to the model identification problem and shown suitable for the validation of estimated parameters. Auxiliary hypotheses and alternatives were needed to circumvent problems due to otherwise incomplete knowledge of the test statistics. In each step of the proposed sequential test, the computed LRT test statistic can be interpreted in terms of the estimated incremental SNR if the corresponding hypothesis is true. In the single frequency case, all cumulants of the test statistics are given analytically. In the broadband case, the distribution of the test statistics can be closely approximated by a Gaussian distribution.

The examples illustrate several uses of hypothesis testing. Before the test, an inversion algorithm should have determined the parameter estimates. This is usually done for a set of different model structures. A multiple sequential LRT can then be used to estimate the correct model structure, i.e., how many free parameters should be used in an inversion. It is illustrated that the *a posteriori* distributions obtained from the inversion can be used to order the set of parameters. This helps in designing the structure hierarchy.

How many parameters can be estimated for a given model structure depends on the SNR. The higher the SNR,

the more parameters we can afford to fit. Conversely, for poor SNR, it is best to focus on just the most important parameters. Otherwise, the higher-order parameters are just fitted to the noise (thus increasing the variance of the estimate).

By varying the SNR in Monte Carlo simulations, we can determine a minimum required SNR at the receiver array during a sea trial that will be needed to invert a given set of geoacoustic parameters. This was implemented using both hypothesis testing and Akaike's Information Criterion (AIC). From the simulations, it is observed that the LRT at a false-alarm rate of 5% gives similar results to the AIC, but is slightly more conservative.

Finally, we conclude with some remarks concerning the practical case where the signal space is not strictly rank one. We must distinguish two possible causes for signals with rank higher than one: First, the source might vibrate with higher degrees of freedom, e.g., multipole radiation.[29] A log-likelihood function can be formulated for this case also. Thus, this does not, in principle, present a problem to the LRT. Although the details of the presented algorithm will change. Second, the signal might decorrelate due to random environmental effects, losing coherence between the source and receivers. This case is more difficult. A log-likelihood function is not known to the authors in this case and, consequently, no LRT can be formulated.

APPENDIX

1. Derivation of the likelihood ratios, Eq. (6)

The log likelihoods for the hypotheses H_1, H_2, H_3 and the alternatives are given by

$$\mathcal{L}_i = -\frac{1}{J} \sum_{j=1}^{J} \log \operatorname{tr}[(\mathbf{I} - \mathbf{P}_{i-1}(\omega_j))\hat{\mathbf{C}}_x(\omega_j)].$$

The hypotheses are formulated by $i=1,2,3$ and the alternatives by $i=4$. For the cases $i=2,3$, this reduces to (2a) up to an irrelevant additive constant; cf. Ref. 13. The LRT calculates differences of these log-likelihood functions. To be more specific: to test H_i against A_i, we need to construct

$$t_i(\mathbf{x}) \overset{\text{Def}}{:=} \mathcal{L}_4 - \mathcal{L}_i$$

$$= \frac{1}{J} \sum_{j=1}^{J} \log \frac{\operatorname{tr}[(\mathbf{I} - \mathbf{P}_{i-1}(\omega_j))\hat{\mathbf{C}}_x(\omega_j)]}{\operatorname{tr}[(\mathbf{I} - \mathbf{P}_3(\omega_j))\hat{\mathbf{C}}_x(\omega_j)]} \quad (i = 1,2,3).$$
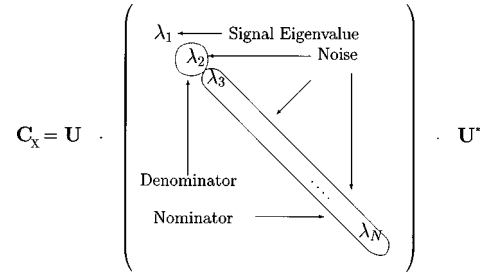
Inserting $\mathbf{P}_3(\omega_j) - \mathbf{P}_3(\omega_j)$ into the denominator yields (6).

2. Proof of Eq. (9)

Let $T = \log(1 + (n_1/n_2)F)$ be a random variable, where F is F_{n_1,n_2} distributed. Observe that the related random variable $Z = 1/[1 + (n_1/n_2)F]$ is beta distributed with parameters $p = n_2/2$ and $q = n_1/2$; cf. Ref. 30. Knowing this, we can express the moment-generating function

$$M_T(s) \overset{\text{Def}}{:=} \mathsf{E}[e^{Ts}] = \mathsf{E}[e^{-(\log Z)s}] = \mathsf{E}[Z^{-s}] = \frac{B(p-s,q)}{B(p,q)},$$

by means of the beta function. Using the identity $B(x,y) = \Gamma(x)\Gamma(y)/\Gamma(x+y)$, the cumulants of T can be expressed by polygamma functions,

$$\kappa_r \overset{\text{Def}}{:=} \frac{d^r}{ds^r} \log M_T(s) \bigg|_{s=0}$$

$$= (-1)^r[\Psi^{(r-1)}(p) - \Psi^{(r-1)}(p+q)].$$

They are defined as derivatives of the log-gamma function:

$$\Psi^{(r)}(x) \overset{\text{Def}}{:=} (d^r/dx^r)\log\Gamma(x);$$ see Refs. 25 and 24 for further details and approximations. The mean and variance μ_T, σ_T^2 in (9) are given by κ_1, κ_2, respectively. If both DOF n_1, n_2 are *even*, this reduces to the finite sum

$$\kappa_r = \sum_{k=0}^{n_1/2-1} \frac{1}{(k+n_2/2)^r}.$$

[1] M. J. Hinich, "Maximum-likelihood estimation of the position of a radiating source in a waveguide," J. Acoust. Soc. Am. **66**, 480–483 (1979).

[2] A. B. Baggeroer, W. A. Kuperman, and P. N. Mikahalevsky, "An overview on matched field methods in ocean acoustics," IEEE J. Ocean Eng. **18**, 401–424 (1993).

[3] A. Tolstoy, *Matched Field Processing for Underwater Acoustics* (World Scientific, Singapore, 1993).

[4] J. L. Krolik, "The performance of matched-field beamformers with Mediterranean vertical array data," IEEE Trans. Signal Process. **44**, 2605–2611 (1996).

[5] H. Akaike, "A new look at the statistical model identification," IEEE Trans. Autom. Control. **AC-19**, 716–723 (1974).

[6] J. Rissanen, "A universal prior for integers and estimation by minimum description length," Ann. Stat. **11**, 416–431 (1983).

[7] L. Ljung, *System Identification, Theory for the User*, Information and System Sciences Series (Prentice–Hall, Englewood Cliffs, 1987).

[8] C. F. Mecklenbräuker and P. Gerstoft, "Hypothesis testing for acoustic environmental models using likelihood ratio," in 3rd *European Conference on Underwater Acoustics*, edited by J. Papadakis (Crete U.P., Crete, 1996), pp. 465–470.

[9] C. F. Mecklenbräuker, P. Gerstoft, P. J. Chung, and J. F. Böhme, "Generalized likelihood ratio test for selecting a geo-acoustic environmental model," IEEE Proc. ICASSP-97, 1997, Vol. I, pp. 463–466.

[10] P. Gerstoft, "Inversion of seismoacoustic data using genetic algorithms and *a posteriori* distributions," J. Acoust. Soc. Am. **95**, 770–782 (1994).

[11] P. Gerstoft and D. F. Gingras, "Parameter estimation using multifrequency range dependent acoustic data in shallow water," J. Acoust. Soc. Am. **99**, 2839–2850 (1996).

[12] F. B. Jensen and M. C. Ferla, "SNAP: The SACLANTCEN normal-mode acoustic propagation model," SACLANT Undersea Research Centre, SM-121, La Spezia, Italy, 1979.

[13] J. F. Böhme, "Statistical array signal processing of measured sonar and seismic data," Proc. SPIE 2563 Advanced Signal Processing Algorithms (San Diego), July 1995.

[14] P. Gerstoft and C. F. Mecklenbräuker, "Ocean acoustic inversion with estimation of a posteriori probability distributions," J. Acoust. Soc. Am. **104**, 808–819 (1998).

1747   J. Acoust. Soc. Am., Vol. 105, No. 3, March 1999

Mecklenbräuker *et al.*: Hypothesis testing   1747

[15] D. Maiwald and J. F. Böhme, ''Multiple testing for seismic data using bootstrap,'' IEEE Proc. ICASSP-94, 1994, Vol. 6, pp. 89–92.

[16] H. Messer, ''The potential performance gain in using spectral information in passive detection/localization of wideband sources,'' IEEE Trans. Signal Process. **43**, 2964–2974 (1995).

[17] A. Ephraty, J. Tabrikian, and H. Messer, ''Robust source detection in shallow water based on application of a test for spatial stationarity,'' IEEE Trans. Signal Process. (submitted).

[18] F. B. Jensen, W. A. Kuperman, M. B. Porter, and H. Schmidt, *Computational Ocean Acoustics* (AIP Press, Woodbury, 1994).

[19] D. F. Gingras and P. Gerstoft, ''Inversion for geometric and geoacoustic parameters in shallow water: experimental results,'' J. Acoust. Soc. Am. **97**, 3589–3598 (1995).

[20] C. F. Mecklenbräuker, D. Maiwald, and J. F. Böhme, ''F-test in matched field processing: Identifying multimode propagation,'' IEEE Proc. ICASSP-95, 1997, Vol. **5**, pp. 3123–3126.

[21] D. Slepian, ''Prolate spheroidal wave functions, Fourier analysis, and uncertainty—Part V: The discrete case,'' Bell Syst. Tech. J. **57**, 1371–1429 (1978).

[22] D. J. Thomson, ''Jackknifing multiple-window spectra,'' Proc. IEEE ICASSP-94, 1994, Vol. 6, pp. 73–76.

[23] D. B. Percival and A. T. Walden, *Spectral Analysis for Physical Applications, Multitaper and Conventional Univariate Techniques* (Cambridge U.P., Cambridge, 1993).

[24] A. B. Baggeroer, W. A. Kupermann, and H. Schmidt, ''Matched field processing: Source localization in correlated noise as an optimum parameter estimation problem,'' J. Acoust. Soc. Am. **93**, 2798–2808 (1993).

[25] P. Hall, *The Bootstrap and Edgeworth Expansion* (Springer-Verlag, New York, 1992).

[26] A. B. Baggeroer and H. Schmidt, ''Parameter estimation theory bounds and the accuracy of full field inversions,'' in *Full Field Inversion Methods in Ocean and Seismo-Acoustics*, edited by O. Diachok, A. Caiti, P. Gerstoft, and H. Schmidt (Kluwer Academic, Dordrecht, 1995), pp. 79–84.

[27] M. Abramowitz and I. Stegun, *Handbook of Mathematical Functions* (Dover, New York, 1972), 9th ed.

[28] P-J. Chung, ''Identifikation von geo-akustischen Ausbreitungsmodellen im Flachwasser mittels maximum-likelihood-quotiententests,'' Diplomarbeit, Ruhr-Universität Bochum, August 1996.

[29] C. F. Mecklenbräuker, A. Waldhorst, P. Gerstoft, and G. Haralabus, ''Matched field processing using multipole expansion,'' in *4th European Conference on Underwater Acoustics*, edited by A. Alippi and G. B. Cannelli, CNR-IDAC, 1998, pp. 15–20.

[30] N. L. Johnson and S. Kotz, *Continuous Univariate Distributions—2*, Applied Probability and Statistics (Wiley, New York, 1970).

Prediction of conductive hearing loss based on acoustic ear-canal response using a multivariate clinical decision theory

Pawel Piskorski, Douglas H. Keefe, Jeffrey L. Simmons, and Michael P. Gorga
Boys Town National Research Hospital, 555 North 30th Street, Omaha, Nebraska 68131

This study evaluated the accuracy of acoustic response tests in predicting conductive hearing loss in 161 ears of subjects from the age of 2 to 10 yr, using as a ''gold standard'' the air–bone gap to classify ears as normal or impaired. The acoustic tests included tympanometric peak-compensated static admittance magnitude (SA) and tympanometric gradient at 226 Hz, and admittance-reflectance (YR) measurements from 0.5 to 8 kHz. The performance of individual, frequency-specific, YR test variables as predictors was assessed. By applying logistic regression (LR) and discriminant analysis (DA) techniques to the multivariate YR response, two univariate functions were calculated as the linear combinations of YR variables across frequency that best separated normal and impaired ears. The tympanometric and YR tests were also combined in a multivariate manner to test whether predictive efficacy improved when 226-Hz tympanometry was added to the predictor set. Conductive hearing loss was predicted based on air–bone gap thresholds at 0.5 and 2 kHz, and on a maximum air–bone gap at any octave frequency from 0.5 to 4 kHz. Each air–bone gap threshold ranged from 5 to 30 dB in 5-dB steps. Areas under the relative operating characteristic curve for DA and LR were larger than for reflectance at 2 kHz, SA and Gr. For constant hit rates of 80% and 90%, both DA and LR scores had lower false-alarm rates than tympanometric tests–LR achieved a false-alarm rate of 6% for a sensitivity of 90%. In general, LR outperformed DA as the multivariate technique of choice. In predicting an impairment at 0.5 kHz, the reflectance scores at 0.5 kHz were less accurate predictors than reflectance at 2 and 4 kHz. This supports the hypothesis that the 2–4-kHz range is a particularly sensitive indicator of middle-ear status, in agreement with the spectral composition of the output predictor from the multivariate analyses. When tympanometric and YR tests were combined, the resulting predictor performed slightly better or the same as the predictor calculated from the use of the YR test alone. The main conclusion is that these multivariate acoustic tests of the middle ear, which are analyzed using a clinical decision theory, are effective predictors of conductive hearing loss. © *1999 Acoustical Society of America.* [S0001-4966(99)04202-2]

PACS numbers: 43.64.Ha [BLM]

INTRODUCTION

The primary acoustic-immittance response used in assessment of the clinical status of the middle ear (ME) has been the 226-Hz tympanogram. Such a tympanogram includes measurements of peak-compensated static admittance magnitude (SA), tympanometric peak pressure (TPP), and tympanometric gradient (Gr) or width. Low values of static admittance or gradient tend to be associated with the presence of middle-ear effusion (MEE) (e.g., Roush *et al.*, 1995).

Typically, the presence of MEE is predicted based on a single tympanometric response. Since even a single-frequency tympanogram has several test variables, (e.g., compensated admittance and gradient), it is possible that the use of more than one test variable might improve the ability to detect the presence of MEE. Logistic regression (LR) and discriminant analysis (DA) are two multivariate statistical techniques that are capable of classifying cases into discrete categories. Studies have used DA to detect MEE using four tympanometric variables and the acoustic reflex (Nozza *et al.*, 1992a; Nozza *et al.*, 1992b). However, no improvement in test performance was found for the DA over the univariate analysis insofar as the tympanometric gradient discriminated between normal and diseased states as well as

the DA. LR has been used to predict the presence of MEE based upon a multivariate combination of tympanometric and otoscopic variables (Nozza *et al.*, 1994). Combining acoustic admittance with otoscopist's findings did not result in an improvement in sensitivity and specificity compared to when only admittance measures were used, but did improve the specificity relative to that using the otoscopist's findings alone.

An alternative view of middle-ear status in adults and children has focused on the use of acoustic-immittance measurements at ambient ear-canal pressure, but across a wide frequency range. These are termed admittance-reflectance (YR) tests in this report. Keefe *et al.* (1993) measured impedance, admittance, and (pressure) reflectance responses from 125 to 10 700 Hz in adults and infants of age 1–24 months in a group of normal-hearing subjects, and found systematic changes over development. Irrespective of these development differences, reflectance was a minimum in the frequency range for which hearing sensitivity is best (i.e., 2–4 kHz) in all subject groups. These observations led them to hypothesize that the 2- to 4-kHz range might be useful for clinical tests of middle-ear status, because that is the frequency range for which the normal middle ear is most effi-

cient at absorbing sound energy. This hypothesis differs from standard clinical practice, which is based upon measurements at frequencies for which the middle ear is not an efficient absorber of energy (i.e., 226 Hz). A number of other studies have used wideband, ambient-pressure, acoustic tests to characterize the adult middle ear, with particular emphasis on reflectance tests (Stinson et al., 1982; Hudde, 1983; Stinson, 1990; Voss and Allen, 1994). These studies emphasize the utility of reflectance in controlling for probe position in the ear canal, and the reflectance responses measured for normal ears in similar frequency ranges across various studies are broadly consistent.

Standard tympanometry measures an acoustical immittance as a function of ear-canal pressure, typically at a single frequency, whereas the YR tests measure acoustical immittance as a function of frequency at a single ear-canal pressure, typically at ambient pressure conditions. Multifrequency admittance tympanometry can be regarded as a synthesis of these two approaches, because a response is obtained over a range of both frequency (up to 2 kHz) and ear-canal pressure. Multifrequency tympanometry has been used to predict the presence of otitis media (OM) in children (Margolis et al., 1994), with a gold standard based on findings at surgery. The results yielded higher sensitivity to mechanical disturbances related to past occurrences of OM than that based upon 226-Hz tympanometry. Predictive studies using multifrequency tympanometry have relied on the knowledge of an expert to evaluate and classify the acoustic responses.

The difficulty of defining a normal versus impaired ear is an inherent problem for research on the middle ear. Classification of middle ears into normal-ear or impaired-ear categories is problematical because there are many different kinds of impairments. In any decision theory analysis, a *gold standard* must first be adopted so that the efficacy of the predictor can be compared with it. In most research to date, the gold standard has been based upon a single class of impairments, with the alternative being described as a normal response.

In previous tympanometric studies, there have been a number of different test criteria (gold standards) used to indicate the presence of MEE. Test performance in a study using DA achieved a sensitivity of 90% and a specificity of 86% based on findings at surgery following myringotomy for a sample of 111 ears with a history of chronic or recurrent otitis media; however, this sample was obviously biased toward ears with significant middle-ear dysfunction (Nozza et al., 1992b). Nozza et al. (1994) studied a larger population ($n=249$) using acoustic predictors of MEE that included univariate and multivariate analyses of peak-compensated static admittance, tympanometric width (TW), acoustic reflex, and otoscopic findings. LR was used as the technique for the multivariate analyses. The optimal values of sensitivity and specificity were obtained for peak-compensated admittance and otoscopy with sensitivity and specificity values at 81% and 85%, respectively. When otoscopy was used as the gold standard for identification of MEE, the test performances of tympanometric variables were approximately the same with the best univariate performance obtained using

TW. The diagnoses from otoscopy and from surgery disagreed in 21% of the ears. A possible factor underlying this disagreement is that ears qualified for surgery may have had a higher *a priori* probability for the presence of MEE. Nevertheless, different results were observed depending on the choice of the gold standard.

A different approach to defining a gold standard is to focus on the presence or absence of a conductive hearing loss rather than the presence or absence of a middle-ear pathology. Tympanometry has rarely been used to predict conductive hearing loss, but one study found a sensitivity of 93% and specificity of 76% when a 25-dB air-conduction threshold was used as a gold standard to classify an impaired ear (Dempster and MacKenzie, 1991). In general, however, little is known about the relationships between acoustic ear-canal responses and conductive hearing loss.

It is worthwhile contrasting this situation for conductive hearing loss with the extensive literature concerning the use of acoustic ear-canal responses (evoked otoacoustic emissions) to predict cochlear hearing loss using clinical decision theory. In a transient-evoked otoacoustic emission (TEOAE) study aimed at identifying cochlear hearing loss, Prieve et al. (1993) varied the audiometric threshold serving as the criterion separating normal and impaired ears at any octave frequency, and found that a 20-dB HL threshold was optimal. Consequent use of relative operating characteristic (ROC) analysis on single and multiple TEOAE measures via discriminant analysis resulted in areas under the ROC curve of 0.93–0.96 in the 2- to 4-kHz range. In a distortion product otoacoustic emission (DPOAE) study aimed at identifying cochlear hearing loss, Gorga et al. (1993) again varied audiometric threshold and found that a threshold gold standard of 20-dB HL was optimal. Although test performance was near chance levels in identification of cochlear impairment at 0.5 kHz, excellent predictive accuracy was achieved at higher frequencies. The use of acoustic responses to predict cochlear hearing loss is well established in these and many other studies.

In contrast to the difficulties of defining a gold standard for each middle-ear pathology, the presence or absence of a conductive hearing loss is operationally well defined as the gap between the air-conduction and bone-conduction thresholds. The success of acoustical ear-canal tests in predicting cochlear hearing loss suggests that it might be worthwhile to examine whether acoustical immittance tests can also predict a conductive hearing loss. As for the reasons why we focus on the conductive hearing loss, as opposed to a ME pathology in general, there are at least two major factors. We can improve screening reliability in ears at risk of conductive hearing loss, which is the second most common cause of the pediatric visit, by finding a more accurate measure that can discriminate between normal and impaired ears. Using reflectance measures in tandem with an OAE test may help differentiate cochlear from conductive impairments. For practical reasons, in essence, we are using a functional measure of middle-ear energy transfer (i.e., the air–bone gap) in much the same way as auditory thresholds are used as a gold standard for OAE tests of cochlear function. The focus on

the prediction of a conductive hearing loss is the aim of the research described in this report.

One possible limitation of this approach is that the errors associated with measuring bone-conduction thresholds are probably higher than those associated with measuring air-conduction thresholds (see sec. III). That is, the gold standard may be flawed. The likely outcome of this type of error would be an observed reduction in the test efficacy of any predictor, but the comparison of a number of acoustic predictors should remain valid.

Another difference between the assessment of cochlear and conductive hearing loss is that cochlear hearing loss is defined at each test frequency typically using as a predictor some EOAE response at the same test frequency. In contrast, conductive hearing loss is often defined as present or absent based upon the air-bone gap at any or all frequencies, but using as a predictor only the 226-Hz tympanogram. We propose a number of different gold standards for conductive hearing loss, either based upon a criterion value of the air-bone gap at a single test frequency (0.5 or 2 kHz), or based upon a criterion value of the maximum air-bone gap across all test frequencies. We have used both tympanometric and YR responses as acoustic predictors. In the latter case, the analyses are inherently multivariate, resulting in the combination of responses across frequencies.

I. METHODS

A. Subjects

The test group consisted of a typical clinical population of children with symptoms of otitis media in addition to a baseline population of normal, asymptomatic children. The study was based on data from a subject group ranging in age from 2 to 10 yr (92 subjects, 174 ears). We had respectively 10, 100, and 54 ears in our final group of 164 grouped into ranges of 2–3 years old, 4–6 years old, and 7–10 years old. Subjects were drawn from a group of children who were seen through the Boys Town National Research Hospital ENT clinic or whose parents responded to verbal solicitation for participation in a research project. In order to be included in the study the following measurements had to be successfully obtained for each child for at least one ear: air-conduction thresholds for at least 0.5 and 2 kHz, bone-conduction thresholds for at least 0.5 kHz for the same ear, a tympanogram, and an admittance-reflectance (YR) measurement.

B. Clinical measurements

Audiometric thresholds, acoustic immittance, and admittance-reflectance (YR) measurements were all obtained during the same test session. Otologic data were not available in this study. Audiometric threshold evaluation was performed by a clinical audiologist using either conditioned play audiometry (CPA), in 104 out of 164 cases, or conventional audiometric techniques (CONV), in 58 out of 164 cases, depending on the developmental level of each subject. Pure-tone air-conduction (AC) and bone-conduction (BC) thresholds were obtained at 0.5 kHz, 2 kHz and, if possible, at 1 and 4 kHz, with a standard diagnostic audiometer

(Grason-Stadler, GSI-16) linked to insert or dynamic earphones (Etymotic ER-3A or Telephonic TDH-50P).

Bone-conduction thresholds were measured using masked or unmasked condition. Our subjects were drawn from the population seen in an audiology clinic where an air–bone gap equal to or less than 10 dB is considered within normal limits. When the unmasked air–bone gap exceeded 10 dB in a given subject, effective masking levels of narrow-band noise were applied to the nontest ear during bone-conduction testing to ensure against participation of that ear in the determination of threshold. Potential subjects with unmasked air–bone gaps greater than 10 dB who could not be tested successfully using masking were not included in the study. The ratio of masked versus unmasked bone conduction varied from one frequency to another, i.e., at 500 Hz we obtained 53 unmasked and 108 masked BC thresholds, while at 2000 Hz we had 90 unmasked and 52 masked BC thresholds.

These data were acquired for the subject within a double-walled, sound-attenuating Industrial Acoustic Company chamber. For subjects in discomfort, often related to middle-ear symptoms, it was sometimes not possible to obtain threshold data at all frequencies.

Tympanometry was performed in the audiology clinic using a standard 226-Hz immittance device (Grason-Stadler, GSI-33 Middle Ear Analyzer). For numerical purposes,[1] the relative gradient rather than tympanometric width was used to record tympanometric gradient (Gr), defined as follows. The fractional height of a single-peaked tympanogram is the vertical distance between the peak and the point where the compliance pattern is 100 daPA wide. The total height of the compliance pattern is the vertical distance between the peak and the tail as measured from the starting pressure point. The relative gradient is the dimensionless ratio of the fractional height to the total height, so that a flat tympanogram has a relative gradient equal to zero.

Examples of audiometric data obtained from a normal ear and an impaired ear classified as having a conductive hearing loss are shown in Fig. 1. The top panel shows the air-conduction (AC) thresholds and the bone-conduction (BC) thresholds, while the bottom panel shows the air–bone gap, calculated as the difference (in decibels) between the AC and BC thresholds. The BC thresholds, indicative of cochlear sensitivity, are similar in both subjects, while the AC thresholds, indicative of transmission through the middle-ear pathway to the cochlea, increased in the impaired ear. The maximum air–bone gap in the impaired ear occurred at 1 kHz, and had a value of 40 dB relative to the normal air–bone gap of 0 dB for an average healthy ear. The only exception in the normal ear occurred at 250 Hz, where a 5-dB air–bone gap was observed. Even though such a small air–bone gap would not be considered clinically significant, all responses at 250 Hz were not included in further analyses, because of an increased sensitivity to error due to inadequate earphone fit at low frequencies.

C. Admittance-reflectance (YR) measurements

The methodology for measuring input admittance and energy reflectance has been described previously in detail
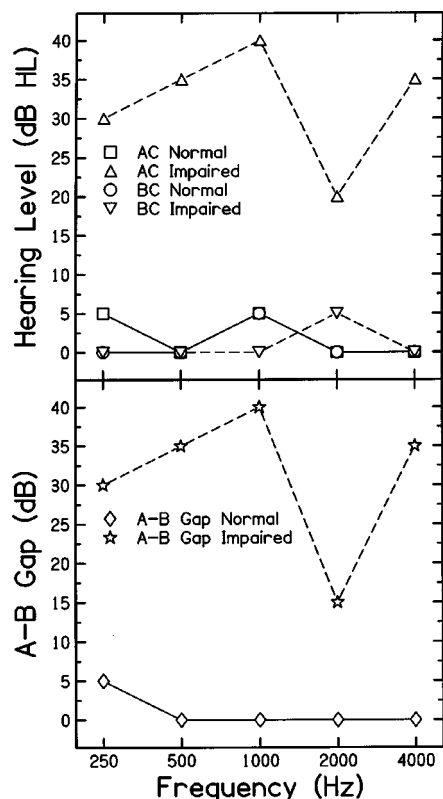
FIG. 1. The top panel illustrates the air-conduction thresholds and bone-conduction thresholds for a typical normal ear (solid lines) and impaired ear (dashed lines). The bottom panel illustrates the corresponding air–bone gaps in decibels.

(Keefe *et al.*, 1992). Briefly, the input signals were produced by a sound source and the responses were measured by a pair of microphones, with all transducers housed in an Etymotic ER-10C probe assembly. A calibration procedure was conducted using a broadband chirp stimulus (250–10 700 Hz) in five calibration tubes of different lengths, each closed at its opposite end. This calibration provided the Thevenin pressure and Thevenin impedance associated with the probe and measurement system by fitting the measured pressure responses in the tube set to the modeled impedance functions. The model was based upon a cylindrical-tube geometry, including an ideal closed end. After calibration on each day, the probe was inserted into the ear to be tested, and data were acquired using the same broadband chirp stimulus. Given the Thevenin parameters from calibration, the acoustic admittance at the tip of the probe assembly was calculated using the measured pressure response. The energy reflectance was calculated in terms of the measured admittance using the cross-sectional area of the calibration tubes, which all had the same area. This is a modification of the earlier methodology, which used the cross-sectional area inferred from the measurement of the acoustic resistance (the real part of the inverse of the acoustic admittance). Two sets of calibration tubes were available based on the size of a foam ear tip (''child'' or ''adult'') most suitable for each subject. This ear tip was then used in the calibration procedure with one or the other of the tube sets approximating the diameter of the ear into which the selected ear tip would comfortably fit. The

YR test is most accurate when the ear canal area is within 20% of the actual calibration tube area (Keefe *et al.*, 1993).

The complex acoustic admittance is expressed in terms of its real part, the conductance (G), and its imaginary part, the susceptance (B) by

$$Y(f) = G(f) + jB(f), \tag{1}$$

where j is the unit imaginary number corresponding to a time dependence t on all variables of $e^{j2\pi ft}$ at frequency f. The frequency dependence of the conductance level controls the difference between sound-pressure level (SPL) in the ear canal and power level absorbed in the ear, because the power $\Pi(f)$ absorbed by the middle ear is expressed by

$$\Pi(f) = \tfrac{1}{2}G(f)|p(f)|^2, \tag{2}$$

where $|p(f)|^2$ is the squared magnitude of pressure at frequency f. The equivalent volume V is defined in terms of the susceptance by

$$V(f) = \rho c^2 \frac{B(f)}{2\pi f}, \tag{3}$$

where ρ is the density of air, and c is the phase velocity of sound. Finally, the energy reflectance $|R(f)|^2$ is defined in terms of the admittance Y by

$$|R(f)|^2 = \left| \frac{1 - Z_c Y(f)}{1 + Z_c Y(f)} \right|^2, \tag{4}$$

where the characteristic impedance Z_c of a cylindrical tube of area S, similar to the ear-canal area, is $Z_c = \rho c/S$. The energy reflectance represents the ratio of the reflected to incident energy. Its value is relatively insensitive to differences in probe location (assuming negligible losses in the ear canal and the adequacy of a cylindrical-tube model for transmission in the ear canal).

The conductance, equivalent volume, and reflectance are the three YR variables chosen to represent the acoustic response of each ear. Because any pair of these variables can be used to calculate the remaining variable, there is a redundancy implicit in this representation. However, some pairs of variables may be better predictors than other pairs. This redundancy was retained to test which combination of YR variables has the greatest predictive efficacy. All YR variables were initially stored as 1/12-octave averaged responses, but further averaging over each third octave or octave was applied to reduce the number of YR variables that were input to subsequent statistical analyses.

Figure 2 presents examples of reflectance data for the same pair of normal and impaired ears as in Fig. 1. From top to bottom, the conductance (G), energy reflectance ($|R|^2$), and equivalent volume (V) are plotted as a function of frequency. The energy reflectance is much higher in the mid-frequency region (1–4 kHz) for the impaired ear than for the normal ear, and the equivalent volume at frequencies below 2 kHz is smaller for the impaired ear than for the normal ear. The resonance just above 4 kHz, which appears in the conductance and equivalent volume as well as the reflectance, has a higher quality factor for the impaired ear. Thus, the YR responses in this pair of ears are clearly discernible.
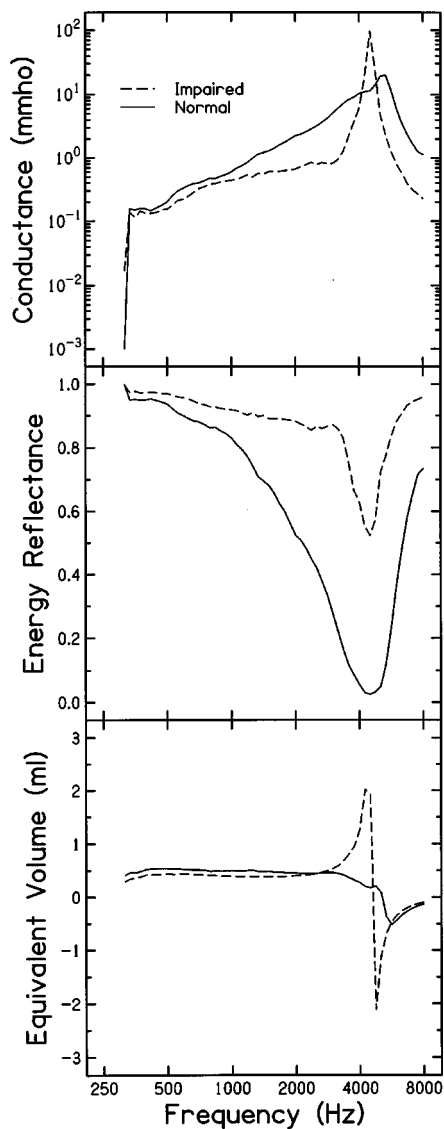
FIG. 2. For a normal (solid line) and impaired (dashed line) ear, the YR responses plotted are: (a) The conductance in mmho versus frequency (the mho is a name for the CGS unit of acoustic admittance, and 1 mmho=0.001 mho); (b) energy reflectance versus frequency; (c) equivalent volume versus frequency.

D. Criteria for inclusion in study

The auditory status of subjects included in the study ranged from normal to moderate conductive hearing loss. Based on the audiological evaluation, all subjects with sensorineural and mixed losses, or with perforated tympanic membranes and patent tubes, were excluded from subsequent analyses.

In order to assure the hermetic seal of the probe in the ear canal, the YR data sets were evaluated for non-negative equivalent volume measurements, after averaging the response over frequencies from 250 to 1000 Hz. This criterion is based on the fact that the ears of subjects in this age range are compliance dominated at low frequencies (implicit in the results of Keefe *et al.*, 1993). Thus, if the equivalent volume were negative at low frequencies, this would indicate a leak in the placement of the probe assembly within the ear canal. Such a low-frequency leak forms a low-impedance acoustic

pathway in parallel with the ear-canal pathway, and its mass-like inertance at low frequencies dominates the calculated equivalent volume. This inclusion criterion identified 3 of 164 YR responses as invalid, corresponding to a data rejection rate of less than 2%. Upon excluding these 3 cases, there were a total of 161 ears used in the main set of analyses.

E. Clinical decision theory

Clinical decision theory is useful in comparing the efficacies of alternative diagnostic tests that discriminate diseased from normal cases (Swets and Pickett, 1982; Swets, 1988). In past hearing-research studies using ROC analyses, clinical decision theory has been limited to discrimination between two states or outcomes based on the use of a single input test result.

Without loss of generality, we can assume that the higher value of the test result indicates the absence of an abnormality. The true status of a case can be established based on a so-called "gold standard." For test results which are binary, the accuracy is defined by a pair of parameters—sensitivity or hit rate, and specificity or correct rejection rate. Sensitivity is defined as the probability that the test result is positive given that the ear is impaired, and specificity is defined as the probability that the test result is negative given that the ear is normal. There are two other probabilities in this 2-by-2 decision matrix: the false-alarm rate, which is the probability that the test result is positive given that the ear is normal, and the miss rate, which is the probability that the test result is negative given that the ear is impaired.

The sensitivity and specificity values are subject to variation on two independent dimensions: (1) the test's capacity to discriminate an impaired from a normal state, and (2) the decision criterion, or gold standard, that is adopted for declaring a test result to be positive (Swets and Pickett, 1982). In typical practice, the decision criterion is varied over the full range of values with a pair of sensitivity and specificity values measured for each choice of decision criterion. The estimate of the area under the ROC curve quantifies the performance of any particular diagnostic test in a bias-free manner, and can range from 0.5 for a test with no diagnostic ability up to a value of 1.0 for a test with perfect diagnostic ability.

The area under the ROC curve can be calculated non-parametrically without having to generate the ROC curve (Bamber, 1975; Hanley and McNeil, 1982) with the area estimate slightly below that of a maximum likelihood estimate. We used the Wilcoxon–Mann–Whitney (WMW) statistic to estimate area under ROC curves, which employs a trapezoidal rule for integrating the area under the curve. It is biased below the true theoretical value of the ROC area (Song, 1997).[2]

Alternatively, it is sometimes useful to adopt a particular decision criterion, particularly when there is *a priori* knowledge of how the test might be used. It may be useful to investigate the performance of various diagnostic tests relative to a fixed, high value of sensitivity if the test is designed to correctly identify most of the impaired ears as impaired. The specificity of each test would be calculated at this fixed

sensitivity, and the test with the highest specificity would be the ''best'' at this reference sensitivity.

In comparing test performance for prediction of a conductive hearing loss, we examined both the area under the ROC curve and the specificities at fixed sensitivities.

F. Multivariate analyses

This section describes the generalization of clinical decision theory to the case of multivariate inputs. The tympanogram has two independent variables if peak-compensated static admittance and gradient are used, whereas the 1/12-octave-averaged YR response has tens of variables, so that a multivariate approach must be followed. The general idea is to combine the multiple variables into a single output variable that is, in some sense, optimal for predicting conductive hearing loss. In fact, it is straightforward to combine the tympanometric and YR variables together so as to generate a univariate output variable that includes both the frequency dependence and the static-pressure dependence of acoustic ear-canal response. Once such a univariate output variable is obtained, it can be utilized as input to clinical decision theory. This methodology is general and may be applicable to the evaluation of the performance of other clinical tests, whether using acoustic and/or some other types of inputs.

Two such multivariate techniques that produce an ''optimal'' univariate output are discriminant analysis (DA) and logistic regression (LR) (Kleinbaum et al., 1988). They have in common the property that their outputs are a combination of the multivariate input variables weighted by coefficients that are calculated within the analysis.

DA calculates a linear (or, more generally, polynomial) discriminant function (DF), based on a set of input variables, which has the highest power of separating cases into one of two predefined groups. DA defines the optimal combination of input variables by jointly maximizing the separation of the means of the normal and impaired populations, and minimizing the within-group variances.

The binomial logistic regression model transforms a set of continuously distributed outcomes into a probability space in which results are coded as zeros or ones with an appropriate probability via the logit transformation (Hosmer and Lemeshow, 1989). Each regressor (variable) in the LR has a coefficient which measures its contribution to variations in its corresponding input variable, and each such coefficient is calculated based upon the data using a maximum likelihood method.

The univariate linear discriminant function and the maximum likelihood estimate of the LR coefficient are usually quite close in predictive efficacy when the independent variable is approximately normally distributed within each of the outcome groups, i.e., 0 or 1 (Hosmer and Lemeshow, 1989). LR is generally considered by biostatisticians to be preferable to DA for predicting the presence or absence of an impairment based on a multivariable input (Kleinbaum et al., 1988). The assumptions on which each statistic is based are slightly different and are less restrictive for LR. The standard forms of these multivariate predictors may have merit when all statistical assumptions are fully satisfied, but they do not

TABLE I. Distribution of subjects.

| AB gap (dB) | 500 Hz | | 2000 Hz | | 500–4000 Hz | |
	Normal	Impaired	Normal	Impaired	Normal	Impaired
5	38	120	87	53	32	129
10	70	88	105	35	64	97
15	96	62	117	23	89	72
20	116	42	125	15	108	53
25	127	31	133	7	117	44
30	132	26	134	6	126	35
No. of subjects	Total=158		Total=140		Total=161	

provide a bias-free interpretation as does clinical decision theory, nor are they necessarily the best choice when the statistical assumptions are not satisfied.

Rather than adopting one or the other of the techniques, we have chosen the more practical approach of comparing their actual test performance using clinical decision theory. The discriminant function (DF) is the univariate output from DA that optimally separates normal and impaired ears, while the logit function (LOGIT) is the corresponding univariate output from LR. As such, the clinical decision theory analyses proposed in the previous sections are carried out after the multivariate analyses. This approach results in a bias-free comparison of univariate and multivariate techniques.

Three classes of models have been investigated based upon a gold standard derived from a criterion value of the air–bone gap. Conductive hearing loss is predicted based upon: (i) various univariate inputs including single tympanometric variables and single YR variables; (ii) multivariate inputs consisting of all YR variables (conductance, equivalent volume, and reflectance) averaged over each octave (or third octave) from 0.5 to 8 kHz; (iii) multivariate inputs consisting of all YR variables and two tympanometric variables (SA and Gr). The reason for excluding the 250-Hz octave of YR responses was that these responses were more sensitive to small calibration errors than higher-frequency responses. Preliminary analyses using tympanometric peak pressure showed that its predictive efficacy was much poorer than SA and GR; hence, it was not included in the main analyses.

As summarized in Table I, separate analyses were conducted using gold standards based upon the air–bone gap at 0.5 kHz (158 subjects with complete data records), the air–bone gap at 2 kHz (140 subjects with complete data records), and the maximum air–bone gap at any octave frequency tested in the range from 0.5 to 4 kHz (161 subjects with data for at least one octave-test frequency). The gold standard associated with each particular threshold value of an air–bone gap was varied over a range from 5 to 30 dB in 5-dB steps. For the purposes of data analyses, a threshold value of 5 dB means that an air–bone gap of 5 dB or less was associated with a normal ear, while an air–bone gap of 10 dB or more was associated with an impaired ear.

II. RESULTS

A. Univariate analysis

The first set of results compares the performance of peak-compensated static admittance magnitude (SA) with

1754   J. Acoust. Soc. Am., Vol. 105, No. 3, March 1999

Piskorski et al.: Prediction of conductive hearing loss   1754
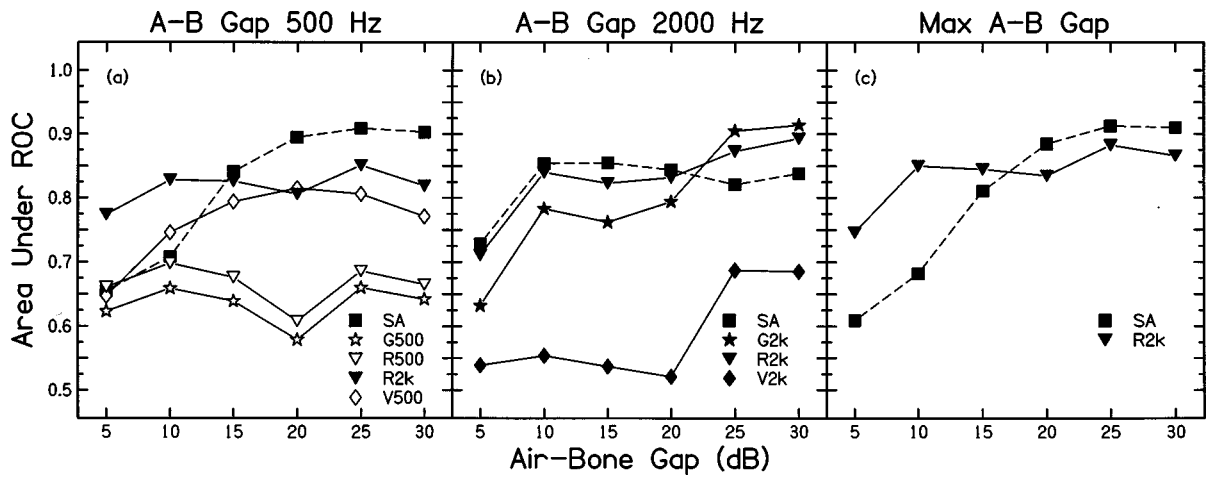
FIG. 3. Areas under the ROC curve evaluated using air–bone gap criteria from 5 to 30 dB as gold standards: (a) air–bone gap at 500 Hz, (b) air–bone gap at 2000 Hz, (c) maximum air–bone gap from 500 to 4000 Hz. The performances of individual YR and tympanometric variables are plotted.

particular individual YR response variables in predicting a conductive hearing loss. For the gold standards based upon the presence of conductive hearing loss at a single frequency (0.5 or 2 kHz), the YR responses at corresponding frequencies were used in comparisons. For the gold standard based upon the maximum air–bone gap at any frequency, the YR response at 2 kHz was used in comparisons. In addition, the YR response at 2 kHz was compared in its ability to predict a conductive hearing loss at 0.5 kHz. This is because reflectance in the frequency range 2–4 kHz has been proposed as a potentially sensitive indicator of middle-ear status (as discussed in the Introduction).

Figure 3 shows the areas under the ROC curve for air–bone gap criteria varying from 5 to 30 dB at 0.5 kHz, 2 kHz, and the maximum air–bone gap at any octave frequency from 0.5 up to 4 kHz. At each air–bone gap criterion, slightly different numbers of ears were tested due to differences in the ability to obtain behavioral measures (air and bone conduction). In predicting air–bone gap at 0.5 kHz, we used complete records of 158 ears, while for 2 kHz, data were available from 140 ears. The maximum air–bone gap criterion naturally contained the highest number of complete records (161 ears), because it was based on all of the air–bone gap data obtained from 0.5 up to 4 kHz for each subject's ear. Of particular interest are the air–bone gap thresholds corresponding to the prediction of a mild conductive loss, because this assesses test performance in classifying a conductive loss that is meaningful clinically. The gold standards for these are the air–bone gaps of 15 and 20 dB. Thus the corresponding air–bone gaps for a mild conductive loss are 20 and 25 dB, respectively.

Although the tympanometric predictor (SA) was measured at 226 Hz (the filled square symbol), its ability to predict conductive loss at higher frequencies is superior in most comparisons to that of individual YR variables. For predicting a conductive hearing loss at 0.5 kHz, the reflectance at 2 kHz (R2k, the filled inverted triangle) is a better predictor than reflectance, conductance, or equivalent volume at 0.5 kHz (all open symbols). This shows that the YR responses at the frequency of hearing loss are not necessarily better predictors than the YR responses at other frequencies. For pre-

dicting a conductive hearing loss at 2 kHz, the SA and R2k are the best univariate predictors, attaining areas under the ROC curve in the range of 0.85, while the conductance at 2 kHz has slightly lower areas, near 0.78. The equivalent volume at 2 kHz is a poor predictor of conductive hearing loss at 2 kHz, while the equivalent volume at 0.5 kHz performed much better in predicting hearing loss at 0.5 kHz. For predicting the maximum conductive hearing loss across all test frequencies, tympanometry and reflectance at 2 kHz perform at about the same level for conductive impairments ranging from 15 to 30 dB.

B. Univariate versus multivariate analysis: Areas under the ROC curve

The next set of results compares the performance of the multivariate tests and the univariate tympanometric tests. Figure 4 shows the performance in predicting conductive hearing loss of two multivariate discriminant functions (DF, DF+) two multivariate logistic regressions (Logit, Logit+), the tympanometric gradient (Gr), and tympanometric peak-compensated static admittance (SA). The layout of Fig. 4 parallels that of Fig. 3, and the SA curves on each panel are identical in both figures in order to establish a baseline for comparison. The DF and LR analyses take as inputs the octave-averaged YR responses of reflectance, equivalent volume, and conductance at each of five frequencies (0.5, 1, 2, 4, and 8 kHz), corresponding to 15 input variables. The DF+ and LR+ analyses take as inputs the same 15 YR variables listed above as well as the two tympanometric variables, SA and Gr. Thus the comparison of DF+ and DF tests assesses the multivariate performance of discriminant analysis under two conditions: when the tympanometric measurement is included with the YR measurement, and when only the YR measurement is used. Similarly, the comparison of LR+ and LR assesses the multivariate performance of logistic regression under the same two conditions. The DF+ and LR+ tests have the property that they are based on an acoustic assessment of the middle-ear response as a function of both frequency and ear-canal pressure. In each case, it is important to note that the frequency and static-pressure variations
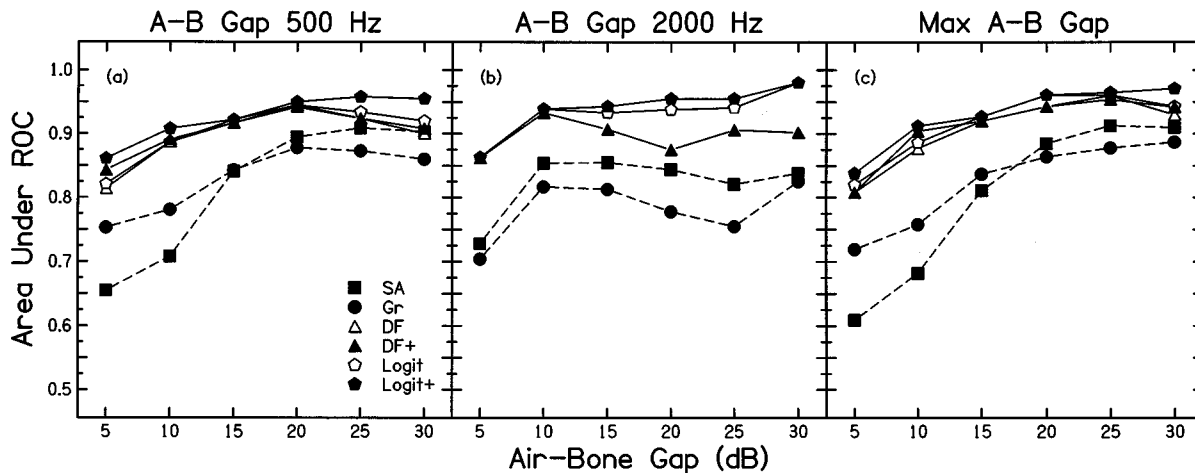
FIG. 4. Areas under the ROC curve evaluated using air–bone gap criteria from 5 to 30 dB as gold standards: (a) air–bone gap at 500 Hz, (b) air–bone gap at 2000 Hz, (c) maximum air–bone gap from 500 to 4000 Hz. The performance of multivariate outputs (DF, Logit, DF+, Logit+) is compared to that of tympanometric variables (Gr and SA). The SA variable plot is redrawn from Fig. 3 to facilitate comparisons.

are not measured simultaneously, and the YR and tympanometric measurements use a different probe assembly.

In contrast to the relatively weak predictive power of the single-variable reflectance measures (Fig. 3), the multivariate combinations of these variables (DF, DF+, Logit, Logit+) outperform both univariate tympanometric tests (Fig. 4). For air–bone gaps of 15 and 20 dB, the areas under the ROC curve using multivariate approaches are as high as 0.92–0.95 for predicting a conductive hearing loss at 0.5 kHz, 0.94–0.96 for predicting hearing loss at 2 kHz, and 0.93–0.96 for predicting a maximum hearing loss in the range from 0.5 to 4 kHz. The multivariate areas under the ROC curve always are larger than the tympanometric areas across all gold standards. It is interesting to note that tympanometric peak-compensated static admittance and tympanometric gradient have roughly similar predictive efficacy at 0.5 kHz and at predicting a maximum hearing loss across frequency, at least for air–bone gaps of 15 dB or greater. However, the gradient does not perform as well in predicting hearing loss at 2 kHz. The logistic regressions always outperform discriminant analyses (Logit versus DF, or Logit+ versus DF+), although the differences may not always be significant.

The inclusion of tympanometric information with the YR variables in the multivariate predictor (filled triangles and diamonds) always either increases test performance slightly or has no effect (to within ±0.005 in the calculated areas under the ROC curve) compared to the YR variables alone (open triangles and diamonds). At 0.5 kHz (the left-hand panel), and for the maximum hearing loss across frequency (the right-hand panel), including the tympanometric variables did not improve test performance for gold standards of 15 and 20 dB. For these cases, the filled symbols precisely overlap the open symbols, thus obscuring the latter. This means that the multivariate stepwise procedure eliminated the tympanometric variables, thereby producing identical outputs. In the case of predicting a mild conductive hearing loss at 2 kHz, the inclusion of the tympanometric variables slightly improved test performance for LR, but again had no effect for DA at any air–bone gap.

C. Univariate versus multivariate analysis: Cumulative distributions

Cumulative distributions of normal and impaired populations can be used as an alternative way of comparing test performance. Cumulative distributions of tympanometric variables (Gr and SA) and the multivariate logistic function (LF) are shown in Fig. 5. These distributions are based on a gold standard corresponding to a 20-dB maximum air–bone gap across the 0.5- to 4-kHz frequency range for a normal ear, and a 25 dB or greater gap for an impaired ear. Figure 5(d) shows separate probability distributions of normal and
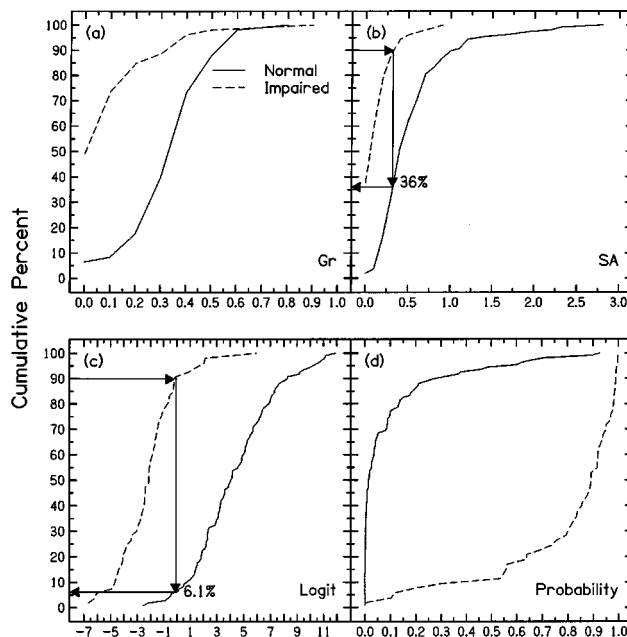
FIG. 5. Cumulative distribution for normal and impaired ears generated using single tympanometric variables are compared with those generated using the multivariate output variables: (a) Gr, (b) SA, (c) Logit, and (d) the probability of impairment distribution for normal and impaired (separate) ears based on the Logit function in (c). The graphical constructions in (b) and (c) illustrate a calculation scheme for the false-alarm rate corresponding to a 90% hit rate (sensitivity).

impaired ears after the logistic transformation into a probability of impairment. For example, the 90% fixed sensitivity point on panel 5(c) corresponds to the 10% cumulative distribution point of impaired ears on panel 5(d). The probability of impairment at this point on the logistic distribution is 0.38. If the calculated LF for any given subject exceeds 0.38 probability of impairment, the ear is classified as impaired, and otherwise normal. A similar analysis for the 80% fixed sensitivity point on panel 5(c) corresponds to a probability of impairment of 0.64. Thus, there is a correspondence between the probability that a given ear is impaired, and the resulting test sensitivity. If the midpoint (Logit=0) of the logistic function is chosen for which the probability of impairment is 0.50, then the corresponding test sensitivity is 89% and specificity is 95%.

Greater separations between normal (the solid line) and impaired (the dashed line) distributions in Fig. 5 denote better discriminations between healthy and impaired ears. A flat tympanogram (SA=0) is indicative of an impaired ear, but many normal ears also have low values of SA. Thus, the distributions are not well separated. The same problem is present in the tympanometric gradient distributions, although there is better separation than for the SA distributions. The cumulative distribution for the Logit function shows greater separation between the normal and impaired ears.

D. Univariate versus multivariate analysis: Specificity at fixed sensitivity

Direct comparisons of these cumulative distributions are not as informative as a comparison of test performance at a fixed value of sensitivity or specificity. While this corresponds to a particular choice of observer bias from the perspective of ROC theory, such a choice may be appropriate for assessing test performance in a desired clinical mode of application.

By selecting a fixed sensitivity from the impaired distribution, it is possible to determine the false-alarm rate (equal to one minus specificity) from the normal distribution by means of the orthogonal projection onto the normal distribution (see the arrow diagram). These operations are illustrated in Fig. 5 for the SA and Logit panels, which show that SA attains a false-alarm rate of 36%, while the Logit function achieves a false-alarm rate of 6%, for a fixed sensitivity of 90%. This procedure makes it possible to construct plots of the specificity for the predictive tests at a fixed value of sensitivity.

Focusing on gold standards of 15- and 20-dB air–bone gaps (i.e., mild conductive loss), the specificity values at fixed sensitivities of 80% (open symbols) and 90% (filled symbols) are plotted at 0.5 kHz (Fig. 6), 2 kHz (Fig. 7), and a maximum conductive hearing loss in the range from 0.5 up to 4 kHz (Fig. 8) for both the tympanometric and multivariate approaches. Because the ROC curves were monotonic, the specificity at 80% sensitivity always exceeded specificity at 90% sensitivity; that is, there is a trade-off between sensitivity and specificity such that higher sensitivity always resulted in lower specificity. The comparison of the tympanometric variables showed that Gr outperformed SA at the 80% fixed sensitivity, but that Gr usually underperformed
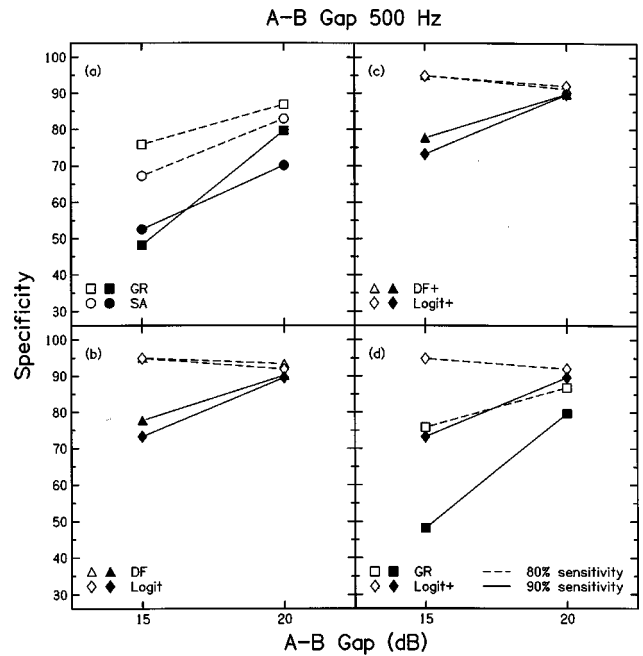
FIG. 6. Specificities of tympanometric and multivariate variables are compared at fixed sensitivities of 80% and 90% for air–bone gap criteria of 15 and 20 dB at 500 Hz: (a) Gr and SA, (b) DF and Logit, (c) DF+ and Logit+, (d) Gr and Logit+.

SA at the 90% fixed sensitivity [panels (a) in all three figures]. The differences in specificities were as large as 25%. The Logit functions tended to have equal or higher specificities than the discriminant functions [panels (b) and (c) of Figs. 6, 7, and 8], except for the case of predicting hearing loss at 0.5 kHz with a 90% fixed sensitivity, for which the discriminant functions yielded better results.

The single best predictor overall was Logit+, and it al-
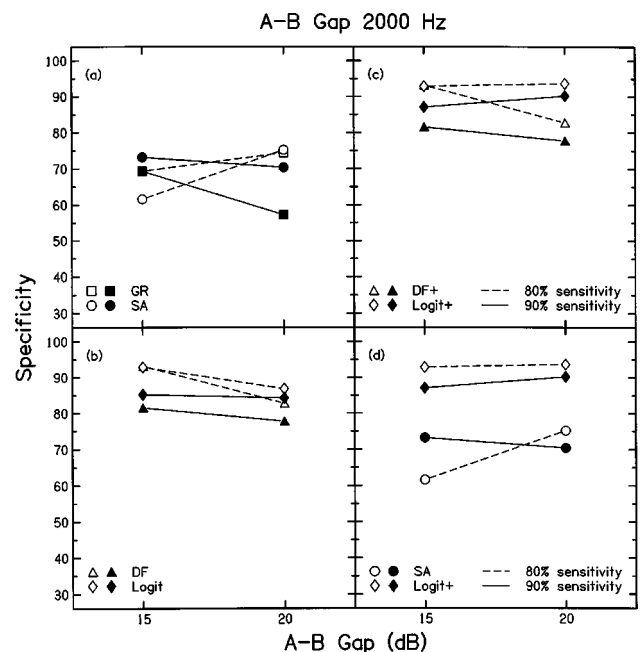
FIG. 7. Specificities of tympanometric and multivariate variables are compared at fixed sensitivities of 80% and 90% for air–bone gap criteria of 15 and 20 dB at 2000 Hz: (a) Gr and SA, (b) DF and Logit, (c) DF+ and Logit+, (d) SA and Logit+.
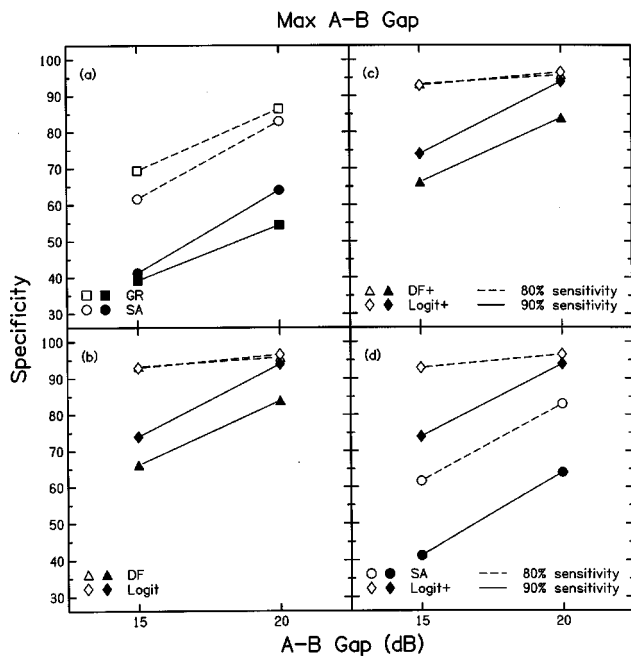
FIG. 8. Specificities of tympanometric and multivariate variables are compared at fixed sensitivities of 80% and 90% for a maximum air–bone gap of 15 and 20 dB at any octave frequency between 500 and 4000 Hz: (a) Gr and SA, (b) DF and Logit, (c) DF+ and Logit+, (d) SA and Logit+.

ways outperformed the tympanometric variables, which is illustrated in the comparisons shown in panels (d) of Figs. 6, 7, and 8. At a fixed sensitivity of 80%, the specificities for the Logit+ predictors varied from 93% to 97% for conductive hearing losses exceeding 15 or 20 dB, whereas the specificities for the tympanometric predictors varied from 62% to 87%. At a fixed sensitivity of 90%, the specificities for the Logit+ predictors varied from 73% to 94%, whereas the specificities for the tympanometric predictors varied from 39% to 80%. Averaging across the two fixed sensitivities, the specificities of all tests were higher using the air–bone gap criterion of 20 dB than for the criterion of 15 dB.

Restricting attention to the logistic regression outputs for a criterion value of 20 dB, the specificity of the Logit at the 80% fixed sensitivity ranged from 87% to 97%, depending on the choice of gold standard for conductive hearing loss (0.5 kHz, 2 kHz, or maximum loss between 0.5 and 4 kHz), while the specificity at the 90% fixed sensitivity ranged from 84% to 94%. The specificity of the Logit+ at the 80% fixed sensitivity ranged from 92% to 97% depending on the gold standard, and the Logit+ specificity at the 90% fixed sensitivity ranged from 90% to 94%. Thus, it is possible to achieve high specificity and high sensitivity in detecting the presence of a conductive hearing loss using a multivariate clinical decision theory.

E. Multivariate diagnostics

Figure 9 illustrates the underlying details associated with discriminant analysis and logistic regression. In the DA method,[3] the relative importance of each variable in the multivariate linear combination is expressed in terms of an F ratio. F-ratio values for DA and squared t-ratio values[4] for LR directly indicate the discriminant power of each single variable within the solution set. In the example in Fig. 9, the reflectance at 2 kHz (R2k) is the most significant variable in the DF+ (because it has the highest F ratio), and in the Logit+ (because it has the highest squared t ratio).

Discriminant function and logistic regression classification coefficients are plotted in the bottom panels of Fig. 9. Each set of coefficients is the solution of the discriminant analysis [Fig. 9(b)] or logistic regression [Fig. 9(d)] optimization. In this example, the input to the multivariate analysis consisted of 15 YR and 2 tympanometric variables. The DA solution set included only 5 variables (reflectance at 2 and 4 kHz, equivalent volume at 0.5 and 4 kHz, and the 226-Hz peak-compensated static admittance magnitude) sorted according to their respective F ratios in decreasing order of relative importance in the DF classification function. The LR solution set included 7 variables, of which 5 are the same variables chosen in the DF. The additional variables were the reflectance at 1 kHz (R1k) and the conductance at 0.5 kHz (G500).

The DF and LF linear combinations take the following forms for this example:

$$DF = 2.93 - 4.62(R2k) - 1.49(SA)$$
$$- 2.18(R4k) + 2.23(V500) + 1.04(V4k), \tag{5}$$

and

$$Logit = 0.09 - 9.98(R2k) - 2.74(SA) - 4.14(R4k)$$
$$+ 4.92(V500) + 1.75(V4k) + 5.45(R1k)$$
$$+ 1.24(G500). \tag{6}$$

The DF and Logit scores were generated such that they tended to be positive for normal hearing subjects and negative for subjects with conductive hearing loss. The DF coefficients were adjusted so that the overall mean of the corresponding scores was 0 and the pooled within-group variance was 1. The signs of the DF and Logit coefficients in Eqs. (5) and (6) are consistent with the observation that impaired ears tend to have higher reflectance and lower equivalent volume than normal ears, in agreement with the individual results in Fig. 2. The functional dependence of SA (both in LR and DA) is ambiguous (see Fig. 10 for more details), insofar as its sign in both equations is opposite from its role as a univariate predictor. This is probably due to partial correlations between SA and other variables in the predictor set. The inclusion of SA only slightly improves test performance. In addition, the reflectance at 1 kHz (R1k) enters the equations as inversely correlated with the reflectance variables at other frequencies, despite the fact that it is positively correlated with them in independent tests. This is also most likely caused by partial correlations between predictor input variables which produce an under- or overcompensation in the DF or Logit variables.

The scatter-plot matrix in Fig. 10 summarizes important relationships between variables, including correlations between multivariate outputs (DF, PROBI) and univariate (SA, R2k) variables, and the gold standard criterion (MAXABG) used to classify responses as normal or impaired. The series of plots along the main diagonal of the matrix present the
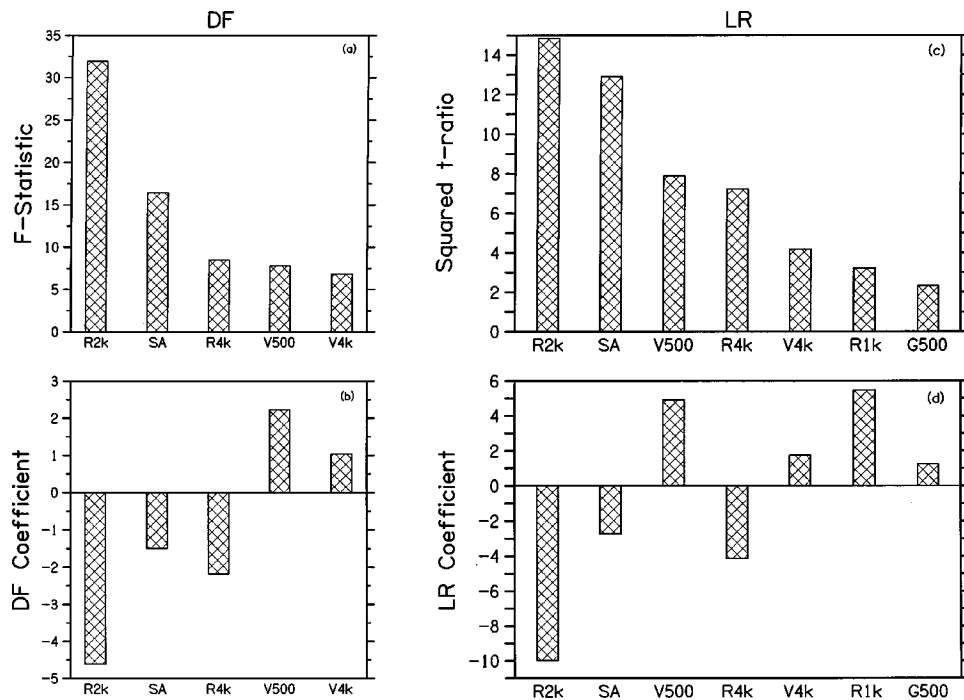
FIG. 9. *F*-statistic scores (a) and DF coefficient estimates (b) for a particular example of discriminant analysis. Squared *t*-ratio scores (c) and LR coefficient estimates (d) for the same data set but analyzed using logistic regression. Any variables not illustrated were not present in the multivariate predictors.

distributions for normal (open circles) and impaired (filled circles) ears of, from top to bottom, multivariate discriminant function score (DF), probability of impairment (PROBI) based on the logistic regression scores, peak-compensated static admittance magnitude (SA), energy reflectance at 2 kHz (R2k), and maximum air–bone gap of 15 dB used as the gold standard in this case. The top two multivariate outputs (DF, PROBI) feature excellent separation between normal and impaired cases. The pair of DF distributions each approximates a normal distribution with similar variances. Thus, their properties satisfy the underlying assumptions of the DA model. The probability that an ear is impaired (PROBI) for the normal and impaired distributions approximates a binomial distribution, again as expected from the underlying assumptions of logistic regression. The qualitative structure of the overlap regions associated with the DA and the LR is different, although their predictive efficacies are similar. The distributions of the univariate predictors, SA and R2k, have a greater degree of overlap, which parallels the cumulative distribution results in Fig. 5.

The series of ten plots below the main diagonal show pairwise relationships between variables by plotting each ear response and displaying linear regression lines and confidence ellipses ($p = 0.683$) for normal and impaired ears. As before, the least overlap and most stable patterns (monotonicity between normal and impaired distributions) are achieved in the multivariate methods. The bottom row of plots, labeled on the bottom left by MAXABG, show the relationships between the maximum air–bone gap distributions (between 0.5 and 4 kHz) for the normal and impaired ears as a function of the DF, the probability of impairment (PROBI), the SA, and the 2-kHz reflectance (R2k). The division between normal and impaired ears in these four panels

is a horizontal line of demarcation separating the normal ears (open circles) from the impaired ears (filled circles). The ideal predictor would have a vertical line of demarcation separating impaired ears from normal ears, that is, if MAX-ABG were perfectly predicted by DF in the first panel, all the impaired responses would be in the upper-left-hand quadrant and all the normal responses would be in the lower-right-hand quadrant. Impaired ears have low DF scores and high PROBI values in this representation, and show an adequate approximation to this ideal. The DF scores do tend to reside in the upper left-hand quadrant for impaired ears and in the lower right-hand quadrant for normal ears, as do the two corresponding confidence ellipses. Comparing the confidence ellipses in the PROBI with R2k panels, it is obvious that there is significantly greater overlap in the R2k distributions, because the confidence ellipses tend to lie directly above one another. An interesting and possibly problematic, case arises in the third plot on the bottom row, which shows the dependence of MAXABG on SA. Similar SA scores have both high and low values of air–bone gap making SA a poor predictor variable. Additionally, the linear relationships for the normal and impaired populations are quite different (positive versus negative slope), which adversely affects SA properties in the multivariate combination [see Fig. 9(d)], and may explain its negative coefficient which associates lower values of SA as being indicative of no impairment.

The remaining six scatter plots between pairs of the DF, PROBI, SA, and R2k variables illustrate their internal correlations. Perhaps the most interesting is the panel in row 2 labeled by PROBI and column 1 labeled by DF. This is a scatter plot showing the correlation between the DA and LR outputs. To first approximation, the tendency for all points to lie near a downward sloping line is indicative of a high cor-
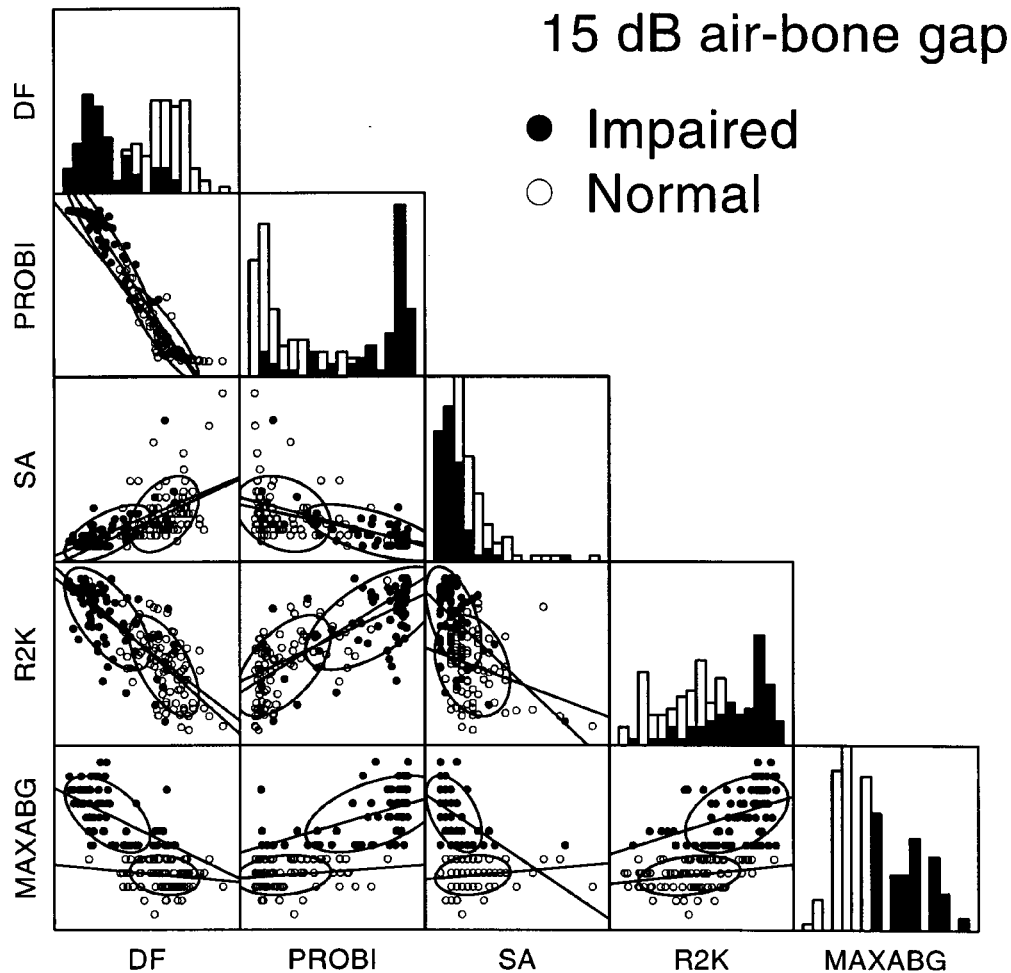
FIG. 10. Scatter plot matrix (SPLOM) based on the maximum air–bone gap score (MAXABG) at octave frequencies from 500 to 4000 Hz, multivariate output predictors (DF and PROBI, which is the LR probability of impairment), individual variables SA from tympanometry, and R2k from reflectance. Symbols coded as either open circles (normal ears) or filled circles (impaired cars) represent scores for which MAXABG was either ≤15 dB, or >15 dB, respectively. The row variables from top to bottom, and column variables from left to right, are DF, PROBI SA, R2K, and MAXABG. The lower half of the SPLOM is shown including diagonal elements. Along the diagonal are histograms of the corresponding variables, e.g., the bottom histogram shows the classification of normal and impaired ears based on the gold standard MAXABG. The bottom row of the matrix shows the distributions of MAXABG as functions of DF, PROBI, SA, and R2K. Each scatter plot also includes separate linear regression lines and confidence ellipses for normal and impaired ears. Each confidence ellipse is centered on its distribution mean, the standard deviations of each of the pair of variables determine its major axes, the covariance between the pair of variables determines its orientation, and the size of the ellipse is scaled by the 0.683 probability, which encompasses the central part of the distribution out to ±1 standard deviation, to the extent that normal and impaired ears are normally distributed.

relation such that high values of PROBI are associated with low values of DF. Most impaired ears lie in the upper-left quadrant and most normal ears lie in the lower-right quadrant. However, the confidence ellipse for impaired ears contains a few normal cases, and the confidence ellipse for normal ears contains a few impaired cases. This indicates cases which are likely to be classified differently by the two multivariate methods.

III. DISCUSSION

A. Acoustic prediction of conductive hearing loss

In contrast to most studies evaluating middle-ear assessment techniques, which have tended to concentrate on predicting a middle-ear pathology, our approach has been to focus on the acoustic prediction of a conductive hearing loss. The rationale for devising a test to predict a conductive hear-

ing loss is based on the following: (1) the subject population was representative of the most prevalent form of middle-ear dysfunction, for which it is important to know whether a conductive hearing loss exists, (2) the ability to predict a conductive hearing loss would have significance for neonatal screening programs, in which audiograms cannot be obtained, (3) the widespread use of otoacoustic emission tests to predict the presence of cochlear hearing loss may be improved if used in conjunction with a test to predict the presence of conductive hearing loss.

The commonly used tympanometric tests, peak-compensated static admittance magnitude and gradient, do have predictive power in assessing a conductive hearing loss, but they have the drawback that a high sensitivity is obtained only by accepting a low specificity. This means that tympanometry may be used to classify impaired ears as impaired, but at the cost of classifying a substantial fraction of normal

ears as impaired. Tympanometric peak pressure (TPP) was not found to be an accurate predictor of conductive hearing loss. Results using TPP were not reported due to its chance level performance in preliminary tests. The lack of significance for TPP parallels previous results (Margolis *et al.*, 1994).

The YR responses, which are straightforward to measure in infants and adults (Keefe *et al.*, 1993), have greater predictive power than 226-Hz tympanometry in assessing a conductive hearing loss when evaluated in a multivariate framework. It is possible to achieve both high sensitivity and high specificity with a YR test. For example, when the YR test was used to predict whether the maximum conductive hearing loss at any octave frequency in the range from 0.5 to 4 kHz exceeded 20 dB, a specificity of 94% was achieved at a sensitivity of 90%. The subject population included a typical clinical population of children with symptoms of otitis media as well as asymptomatic children in the same 2–10 year age range. The YR test was successful in predicting a conductive hearing loss in children at risk for otitis media, the second most common reason (after the common cold) for a physician visit. The YR and tympanometric tests were also compared using clinical decision theory and cumulative distributions, and, regardless of which analysis approach was adopted, the YR test always outperformed tympanometry.

Calculating test performance in terms of sensitivity and specificity is a simple and powerful technique when applied directly to results from ROC analysis obtained with single test variables, and it can be generalized to a multivariate combination of variables with optimum discrimination properties. These measures are independent of disease prevalence (Turner and Nielsen, 1984) and, thus, can be applied to any clinical test.

Two classes of multivariate techniques, logistic regression and discriminant analysis, were compared in assessing the performance of the YR test. Across all test conditions, the LR and DA performed similarly. This is encouraging insofar as it supports the hypothesis that the multivariate techniques are robust predictors; even when a methodologically different multivariate technique was used, the outcomes were similar. However, logistic regression did perform slightly better than discriminant analysis, and we conclude that it is the more promising multivariate approach. This result confirms theoretical arguments favoring the use of logistic regression that were cited in the Introduction.

When the YR and 226-Hz tympanometric responses were combined as multivariate inputs and compared to the multivariate function of the YR responses alone, the addition of the tympanometric responses sometimes increased the predictive accuracy, although the magnitudes of the shifts were not large. This supports the view that the YR test may be useful as a clinical audiologic tool in test conditions for which static pressurization is a disadvantage. For example, static pressurization cannot be used in testing neonates, and it may cause discomfort in some older children. Nevertheless, the fact that the addition of a 226-Hz tympanogram to the YR score did produce a slight advantage under some conditions is evidence that a more comprehensive acoustic test, which varies both frequency and ear-canal pressure, may be desirable for diagnostic applications.

Multifrequency tympanometry is one example of this type of test. However, previous research on multifrequency tympanometry has relied on visual classification of tympanograms by experts, rather than a multivariate, statistical approach as used in this report. As remarked earlier, the frequency content of the YR inputs selected for the multivariate predictors is consistent with the hypothesis that the 2- to 4-kHz range is a particularly sensitive indicator of middle-ear status. However, multifrequency tympanometry is somewhat limited in this regard, in that the upper frequency limit is approximately 2.4 kHz. A recently developed technique of reflectance tympanometry (Keefe and Levi, 1996) enables acoustic tests of the middle ear, in which ear-canal pressure is varied over the normal tympanometric range and frequency is varied up to 10 kHz (Margolis *et al.*, 1998). Such a test may provide more complete information on middle-ear response than the YR test and 226-Hz tympanogram used in the present study, but no predictive studies using reflectance tympanometry have been reported.

B. Multivariate analyses using 1/3-octave YR responses

Because the YR response is obtained over a broad frequency range, the question arises whether an octave-based YR response is adequate to describe the middle-ear characteristics that are important to the prediction of hearing loss. In an effort to evaluate this question, we investigated the performance of a multivariate test using 1/3-octave measurements of admittance and reflectance. This tripled the number of YR variables from 15 to 45. Such an increase in the number of input variables has the potential disadvantage of producing a less robust predictor,[5] but more detail is captured in each ear's acoustic response.

When 1/3-octave YR responses were provided as inputs to the multivariate clinical decision approach, the estimate of the area under the ROC curve using logistic regression was higher than that obtained using discriminant analysis, and both were larger than the tympanometric areas under the ROC curves. Direct comparisons between the octave and the 1/3-octave tests across all test conditions showed for DA that the 1/3-octave tests had better performance than the octave tests in 50% of cases, and for LR that the 1/3-octave tests had better performance than the octave tests in 58% of cases. We conclude that there was little or no benefit in using a larger set of variables.

C. Factors influencing the gold standard

The air–bone gap represents the difference between sensitivity thresholds measured via air conduction and bone conduction. A discussion of factors that might influence the accuracy of these measurements is, therefore, warranted. First is the issue of whether or not behavioral threshold is a valid measurement of the boundary between auditory sensation and no sensation. According to the signal-detection theory of Green and Swets (1974), a behavioral response may be affected by both sensitivity to a stimulus and re-

sponse proclivity, and that the concept of a clear-cut threshold is unsupported. Indeed, Wilber (1991) suggests that any physical, mental, or emotional factors which affect the examinee may affect the ability to respond to pure-tone stimuli. Thus, if the examinee is frightened, distrustful, uninterested in either the stimulus or the task set forth by the tester, fatigued, or physically ill, threshold measurement may not be as accurate as expected. In light of the subject population of this study, it is possible that these factors were present at some times. Because this study was oriented toward routine usage in an audiology clinic, the techniques used to measure threshold were consistent with current clinical practice, and their rigor is less than that typically used in psychoacoustic research.

There is also a question of inherent problems related to accurate clinical assessment of bone-conduction threshold (Dirks, 1994). For instance, a reliable method to specify vibrational output of the bone-conduction testing system on individual patients is currently lacking. Next is the fact that bone-conduction sensitivity measures are not independent of the state of the middle ear. The list of middle-ear lesions having some impact on bone-conduction thresholds includes otitis media (Huizing, 1960), which was the condition of interest in the current study. Another issue involves placement or location of the bone vibrator. In assessing our subjects, we utilized mastoid placement. It has been suggested that there is poorer reliability with this type of placement as opposed to frontal bone placement and that variations in location of the bone oscillator on the mastoid can result in a threshold difference of 10 dB or more (Dirks, 1994; Wilber, 1991). However, other studies have reported reliability differences between mastoid and frontal bone placement that did not show great practical advantage (Dirks, 1964; Studebaker, 1962).

Another issue is how central masking might affect bone-conduction threshold. Central masking refers to a shift or worsening in the threshold in the test ear due to the presence of masking in the nontest ear. Dirks (1964) reported that bone-conduction thresholds were 4–5 dB worse for mastoid placement following the introduction of masking. Studebaker (1962) showed shifts for bone conduction as high as 7–12 dB at 2 kHz when the nontest ear was masked. On the other hand, Zwislocki (1953) reported that the central masking effect did not exceed 5 dB. Based on these concerns it appears that bone-conduction thresholds have some practical limitations and should be used realistically rather than as representations of pure assessment of the ''cochlear reserve.'' This does not negate the fact that bone-conduction results can be used to estimate the magnitude of conductive hearing loss. A reliability study was outside the scope of the research described in this report.

D. Perspectives for future research

One potential limitation of multivariate approaches is that the output predictor function, e.g., the DF and Logit function, is defined based upon the same subject population for which the predictor's test performance is to be assessed. It may be that the output function is idiosyncratic to, and a better predictor on, this subject population than on any other subject population. That is, the multivariate test may not generalize with sufficient accuracy to other subject populations. Such a problem might occur due to significant correlations in YR variables across frequency. An effective way of handling this problem is to develop the multivariate predictor on one set of subjects, and then evaluate the accuracy of the predictor on another set of subjects. It is recommended that the training and test sets have equal numbers of subjects. Such an approach provides a test of the generalizability of the predictor. A predictor is robust if there is only a small decrement in test efficacy in the test set compared to the training set. However, the numbers of subjects in our tests (140–161), although reasonably large compared to other tests of middle-ear status, were not large enough to divide into a pair of equal-sized training and test sets. It remains for future research to test the robustness of this class of multivariate predictors of conductive hearing loss.

Nevertheless, we did observe that the multivariate test performances were similar for DA and LR. Because those are unrelated methods of constructing multivariate predictors, their similar test performance suggests that the multivariate predictors were robust. These considerations provide a cogent reason to prefer the octave-band YR test over the 1/3-octave-band YR test, because a fewer number of input variables would be expected to lead to a more stable and robust predictor. Future research needs to identify the optimum analysis bandwidth and choice of YR variables, assuming that such an optimum exists, for a test of conductive hearing loss. There is scope for improving the multivariate analyses. Stepwise procedures were used to add or remove individual input variables from the DA and LR solutions, based upon a gold standard defined at each threshold value of the air–bone gap. An alternative approach is to specify the inputs to be included in the multivariate analysis, thereby removing the automated stepwise decision rules.

The relatively high performance in identification of a conductive hearing loss based upon measurements of the air–bone gap is even more compelling given the uncertainty inherent to the bone-conduction threshold measurement. Any improvement in the accuracy of measuring bone-conduction thresholds should further improve the performance of predicting conductive hearing losses.

The test population was by no means chosen to cover all possible middle-ear pathologies that might be related to conductive hearing loss. More research is needed to understand the relationships between more sophisticated acoustic tests of middle-ear status analyzed using a multivariate clinical decision theory, and the presence or absence of conductive hearing loss in subject populations with different types of middle-ear pathologies.

An extension of the present study would be to investigate, using a multivariate clinical decision theory, the efficacy of reflectance tympanometry in predicting a conductive hearing loss. Such a test would measure the middle-ear response over a broad range of frequencies using a tympanometric range of static pressures in the ear canal. Another application with potential clinical utility would involve a combination of tests to predict the presence of conductive hearing loss as well as cochlear hearing loss, e.g., the com-

bination of a YR test with an otoacoustic emissions test. The technique of multivariate clinical decision theory appears well suited to combining not only acoustic variables, but also any other variables, hypothesized to be clinically useful in assessing middle-ear status.

IV. CONCLUSIONS

Clinical decision theory has been applied to the prediction of a conductive hearing loss in a subject population including patients at risk for otitis media. A multivariate analysis of admittance-reflectance responses yielded an output that successfully predicted the presence of conductive hearing losses with areas under the ROC curve as large as 0.97.

When the multivariate test performance was assessed at fixed sensitivity of 90%, the specificity was as high as 94%. We conclude that admittance-reflectance tests are well suited to predicting the presence of conductive hearing loss in clinical populations, and the inclusion of a 226-Hz tympanogram may slightly improve overall test performance.

[1]Both the relative gradient and tympanometric width characterize the shape of tympanogram. The relative gradient form (ratio form) is more convenient for statistical analyses, i.e., the relative gradient is zero for a flat tympanogram, while the tympanometric width (TW) is undefined. One can think of a simple transformation between two representations as follows: $Gr=1/(1+TW)$, which, in the limit as $TW \to \infty$, converges to zero. Statistical analysis can handle Gr much better than TW for these obvious reasons.

[2]The uncertainty [standard error (SE)] of the ROC area estimators can be calculated using two methods: (i) a nonparametric method (Hanley and McNeil, 1982), and (ii) an upper-bound estimate of the variance of the Mann–Whitney U statistic (Bamber, 1975). However, if the aim is to compare the performance of alternative diagnostic tests using data input from the same group of subjects, the standard errors must be calculated taking into account the correlations between the input data sets (Swets and Pickett, 1982; Hanley and McNeil, 1983).

[3]A default value of F to remove $(F=4)$ was used in the process of backward (for octave averaged data) or forward (for 1/3-octave averaged data) stepwise elimination in the DA. This F to remove is defined as a threshold such that if the F statistic for a given variable was less than the F-to-remove value, then the variable was removed from the model. For example, all F-statistic values in Fig. 9 exceed this default value of 4. This choice of default value tended to overly restrict the number of variables permitted to enter the output function (DF or Logit), but it ensured a parsimonious representation of the multivariate predictor. Based on the number of degrees of freedom in our analysis $(n=160)$, the lowest admissible F ratio that would achieve the statistical significance at $(p=0.05)$ is $F=2.27$. An order of magnitude higher significance level $(p \leq 0.005)$ corresponds to an F ratio of 3.50. The least significant variable in the solution set had an F ratio equal to 6.82, which corresponds with the significance level of $p=1.67 \times 10^{-5}$, all other variables being more significant.

[4]Classical testing in statistics is based on three fundamental tests: the Wald, Likelihood Ratio, and Score (Lagrange Multiplier) tests. Properties of the tests are based on asymptotic theory and the tests give identical results in the limit of large sample size. Most statisticians favor the likelihood ratio test due to its higher reliability in small samples and because it is a fundamental measure on which model fitting is based (Steinberg and Colla, 1991). The ratio of logistic regression coefficient to its standard error is

represented as a t ratio, which is a guide to the significance of an individual parameter. The chi-square p value is reported for each coefficient. The Wald test is the best known inferential procedure in applied statistics. It is obtained by first estimating a model and next imposing a linear constraint on the estimated parameters. The statistic is based on the constraint and the appropriate elements of the covariance matrix of the parameter vector. A test of whether a single parameter is zero is conducted in a Wald test by dividing the squared coefficient by its variance and referring the result to a chi-squared distribution on one degree of freedom. Thus each t ratio is itself the square root of a simple Wald test. For a binary model, the Wald statistic and its significance levels (chi squared) are equivalent to the t ratios and p values given with the parameter estimates.

[5]One initial problem in the 1/3-octave analysis was that the stepwise-backwards technique that had been used in the LR and DA analyses with the octave data could not be used with the commercial statistics software (SYSTAT, version 7.0), due to numerical instabilities. This problem was solved by using a stepwise-forwards technique, for which the software operated properly. The statistical literature on stepwise techniques in multivariate analysis is outside the scope of this report so that a brief description will suffice. A stepwise-backwards model begins with all the input variables in the model, and, in each step, excludes the least significant variable until all the variables remaining are significant, at which step the final solution is obtained (the DF or the Logit function). A stepwise-forwards model begins with no input variables in the model, and, in each step, includes the most significant variable until there are no more significant variables to add. Another level of complexity is that variables can re-enter the model after having been excluded on a previous step, or variables can leave the model after having been included on a previous step. The two approaches usually do not converge to the same solution, and there is no guarantee that either of the approaches is optimal. The statistics literature describes other approaches to choose the input variables, including the brute force approach of testing each possible combination of inputs and choosing the model that performs best. Even so, the more fundamental problem of the generalizability of the model must be assessed.

Bamber, D. (**1975**). ''The area above the ordinal dominance graph and the area below the receiver operating characteristic graph,'' J. Math. Psychol. **12**, 387–415.

Dempster, J. H., and MacKenzie, K. (**1991**). ''Tympanometry in the detection of hearing impairments associated with otitis media with effusion,'' Clin. Otolaryngol. **16**, 157–159.

Dirks, D. (**1964**). ''Factor related to bone conduction reliability,'' Arch. Otolaryngol. **79**, 551–558.

Dirks, D. (**1994**). ''Bone-conduction threshold testing,'' in *The Handbook of Clinical Audiology*, edited by J. Katz (Williams and Wilkins, Baltimore), 4th ed., pp. 132–136.

Gorga, M. P., Neely, S. T., Bergman, B., Beauchaine, K. L., Kaminski, J. R., Peters, J., and Jesteadt, W. (**1993**). ''Otoacoustic emissions from normal-hearing and hearing-impaired subjects: Distortion product responses,'' J. Acoust. Soc. Am. **93**, 2050–2060.

Green, D. M., and Swets, J. A. (**1974**). *Signal Detection Theory and Psychophysics* (Krieger, New York).

Hanley, J. A., and McNeil, B. J. (**1982**). ''The meaning and use of the area under a receiver operating characteristic (ROC) curve,'' Radiology **143**, 29–36.

Hanley, J. A., and McNeil, B. J. (**1983**). ''A method of comparing the areas under receiver operating characteristic curves derived from the same cases,'' Radiology **148**, 839–843.

Hosmer, and Lemeshow (**1989**). *Applied Logistic Regression* (Wiley, New York).

Hudde, H. (**1983**). ''Measurement of the eardrum impedance of human ears,'' J. Acoust. Soc. Am. **73**, 242–247.

Huizing, E. H. (**1960**). ''Bone conduction: The influence of middle ear,'' Acta Oto-Laryngol. Suppl. **51**, 1–99.

Keefe, D. H., and Levi, E. (**1996**). ''Maturation of the middle and external ears: Acoustic power-based responses and reflectance tympanometry,'' Ear Hear. **17**, 361–373.

Keefe, D. H., Ling, R., and Bulen, J. C. (**1992**). ''Method to measure acoustic impedance and reflection coefficient,'' J. Acoust. Soc. Am. **91**, 470–485.

Keefe, D. H., Bulen, J. C., Hoberg-Arehart, K., and Burns, E. M. (**1993**). ''Ear-canal impedance and reflection coefficient in human infants and adults,'' J. Acoust. Soc. Am. **94**, 2617–2638.

Kleinbaum, D. G., Kupper, L. L., and Muller, K. E. (**1988**). *Applied Regression Analysis and Other Multivariate Methods* (PWS-Kent, Boston), 2nd ed.

Margolis, R. H., Hunter, L. L., and Giebink, G. S. (**1994**). ''Tympanometric evaluation of middle ear function in children with otitis media,'' Ann. Otol. Rhinol. Laryngol. **103**, 34–38.

Margolis, R. H., Saly, G., and Keefe, D. H. (**1998**). ''Wideband reflectance tympanometry in normal adults,'' J. Acoust. Soc. Am. (submitted).

Nozza, R. J., Bluestone, C. D., and Kardatzke, D. (**1992a**). ''Sensitivity, specificity, and predictive value of immittance measures in the identification of middle ear effusion,'' in *Screening Children for Auditory Function* (Bill Wilkerson Center Press, Nashville), Chap. 22, pp. 315–329.

Nozza, R. J., Bluestone, C. D., Kardatzke, D., and Bachman, R. (**1992b**). ''Towards the validation of aural acoustic immittance measures for diagnosis of middle ear effusion in children,'' Ear Hear. **13**, 442–453.

Nozza, R. J., Bluestone, C. D., Kardatzke, D., and Bachman, R. (**1994**). ''Identification of middle ear effusion by aural acoustic admittance and otoscopy,'' Ear Hear. **15**, 310–323.

Prieve, B. A., Gorga, M. P., Schmidt, A., Neely, S. T., Peters, J., and Jesteadt, W. (**1993**). ''Analysis of transient-evoked otoacoustic emissions in normal-hearing and hearing-impaired ears,'' J. Acoust. Soc. Am. **93**, 3308–3319.

Roush, J., Bryant, K., Mundy, M., Zeisel, S., and Roberts, J. (**1995**). ''Developmental changes in static admittance and tympanometric width in infants and toddlers,'' J. Am. Acad. Audiol **6**, 334–338.

Song, H. H. (**1997**). ''Analysis of correlated ROC areas in diagnostic testing,'' Biometrics **53**, 370–382.

Steinberg, D., and Colla, P. (**1991**). ''Logistic Regression—A Supplementary Module For SYSTAT and SYGRAPH,'' SYSTAT, Inc.

Stinson, M. R. (**1990**). ''Revision of estimates of acoustic energy reflectance at the human eardrum,'' J. Acoust. Soc. Am. **88**, 1773–1778.

Stinson, M. R., Shaw, E. A. G., and Lawton, B. W. (**1982**). ''Estimation of acoustical energy reflectance at the eardrum from measurements of pressure distribution in the human ear canal,'' J. Acoust. Soc. Am. **72**, 766–773.

Studebaker, G. A. (**1962**). ''Placement of vibrator in bone conduction testing,'' J. Speech Hear. Disorders, **5**, 321–331.

Swets, J. A., and Pickett, R. M. (**1982**). *Evaluation of Diagnostic Systems: Methods from Signal Detection Theory* (Academic, New York).

Swets, J. A. (**1988**). ''Measuring the accuracy of diagnostic systems,'' Science **240**, 1285–1293.

Turner, R. G., and Nielsen, D. W. (**1984**). ''Application of clinical decision analysis to audiological tests,'' Ear Hear. **5**, 125–133.

Voss, S. E., and Allen, J. B. (**1994**). ''Measurement of acoustic impedance and reflectance in the human ear canal,'' J. Acoust. Soc. Am. **95**, 372–384.

Wilber, L. A. (**1991**). ''Pure-tone audiometry: Air and bone conduction,'' in *Hearing Assessment*, 2nd ed., edited by W. Rintelmann (Allyn and Bacon, Baltimore).

Zwislocki, J. (**1953**). ''Acoustic attenuation between the ears,'' J. Acoust. Soc. Am. **25**, 752–759.

Strategies used to detect auditory signals in small sets of random maskers

Beverly A. Wright[a]
Audiology and Hearing Sciences Program and Institute for Neuroscience, Northwestern University,
2299 North Campus Drive, Evanston, Illinois 60208-3550

Kourosh Saberi[b]
Division of Biology, Caltech, Pasadena, California 91125

Detection performance for a masked auditory signal of fixed frequency can be substantially degraded if there is uncertainty about the frequency content of the masker. A quasimolecular psychophysical approach was used to examine response strategies in masker-uncertainty conditions, and to investigate the influence of uncertainty when the number of different masker samples was limited to ten or fewer. The task of the four listeners was to detect a 1000-Hz signal that was presented simultaneously with one of ten ten-tone masker samples. The masker sample was either fixed throughout a block of two-interval forced-choice trials or was randomized across or within trials. The primary results showed that: (1) When the signal level was low and the masker sample differed between the two intervals of a trial, most listeners based their responses more on the presence of specific masker samples than on the signal. (2) The detrimental effect of masker uncertainty was clearly evident when only four maskers were randomly presented, and grew as the size of the masker set was increased from two to ten. (3) The slopes of psychometric functions measured with the same masker samples differed among the fixed and two random-masker conditions. (4) There were large differences in the influence of masker uncertainty across masker samples and listeners. These data demonstrate the great susceptibility of human listeners to the influence of masker uncertainty and the ability of quasimolecular investigations to reveal important aspects of behavior in uncertainty condition. © *1999 Acoustical Society of America.*
[S0001-4966(99)03303-2]

INTRODUCTION

This paper concerns how the ability to detect a known auditory signal amidst additional masking sounds is degraded when there is uncertainty as to which masking sounds are to be presented. In most laboratory experiments in hearing, the listener has little or no trial-to-trial uncertainty about the general characteristics of the stimulus. There is, however, considerable uncertainty inherent in normal listening situations, and uncertainty about the characteristics of the signal or masker makes an auditory signal more difficult to detect. The influence of signal uncertainty is generally small, increasing signal thresholds by 3–6 dB when the masker is either fixed or relatively stable and the signal frequency (e.g., Green, 1961; Veniar, 1958a,b), duration (Dai and Wright, 1995), or starting time (Egan *et al.*, 1961) is randomly varied across trials. In contrast, when different masker samples are randomly presented, a signal of fixed frequency can be much harder to detect than would be predicted on the basis of the frequency selectivity of the peripheral auditory system (e.g., Neff and Green, 1987; Watson and Kelly, 1981). For example, maskers consisting of ten tones with frequencies randomly selected on each observation interval can produce as much as 20 dB more masking of a fixed-frequency tone than

a broadband noise of equal power (e.g., Neff and Green, 1987). Signal detection is most difficult when there is uncertainty about both the signal and the masker (e.g., Spiegel and Green, 1982). In the most extreme case, a signal that is itself randomly varied in frequency and temporal position within a sequence of randomly selected masker frequencies can be as much as 65 dB more difficult to detect than a signal presented at a fixed frequency and temporal position within a fixed sequence of masking tones (Watson, 1987). The experiments reported here focus on the influence of masker uncertainty, but the approach differs from that used in most earlier studies.

Previous investigations have typically reported the detection threshold for a signal in a masker-uncertainty condition as a single value that was based on the responses across a block of trials in which a large number of different masker samples were presented. Green (1964) used the term ''molar psychophysics'' to describe this class of experiment because the resulting threshold estimate represents an average of the responses over many heterogeneous trials, obscuring the performance on individual trials.

We have instead examined masker uncertainty using what Green (1964) termed a ''quasimolecular'' approach. With this method, signal threshold is determined by the series of responses over multiple presentations of the same masker sample. Unlike the molar technique, this approach yields many threshold values from each block of trials in an

[a]Electronic mail: b-wright@nwu.edu
[b]Electronic mail: kourosh@etho.caltech.edu

uncertainty condition, one for each different masker sample presented. The resulting values thus represent an average of the responses over many homogeneous, rather than heterogeneous, trials.

Using a quasimolecular approach, the following basic question can be addressed: Is it harder to detect a known signal that is masked by a particular masker X when that masker is randomly intermixed with other maskers than when only masker X is presented? The answer is obtained by comparing two measurements: (1) signal threshold in a fixed-masker condition in which only masker X is presented, and (2) signal threshold in a random-masker condition estimated from the responses obtained on *only those trials* in which masker X is presented. A higher threshold in the random than the fixed condition indicates that uncertainty about which masker is to be presented makes the signal more difficult to detect in masker X. To our knowledge, only Pfafflin (1968) and Wright and McFadden (1990) have examined masker uncertainty using this technique. Others who used the quasimolecular approach to study the masking produced by sets of randomly presented reproducible noises did not report performance in the fixed condition (Green, 1964; Gilkey, 1985). Pursuing similar issues with molar psychophysics, Watson and his colleagues (Watson and Kelly, 1981; Spiegel and Watson, 1981; Watson, 1987) reported performance in both fixed and random-masker conditions.

The task of the listeners in the two present experiments was to detect a tonal signal of a fixed and known frequency that was presented simultaneously with one of ten multi-tonal masker samples. The masker sample was either fixed throughout a block of two-interval forced-choice trials or was randomized across or within trials. The two experiments differed only in the method used to determine the masked threshold of the signal. The results address the following five aspects of the influence of masker uncertainty.

Masker bias: Previous quasimolecular investigations have shown that listeners treat particular masker samples as being more likely to contain the signal when different samples are presented on the two observation intervals of a trial (e.g., Green, 1964; Pfafflin and Mathews, 1966; Wright and McFadden, 1990). Given such a masker bias, measured performance is artificially good when the signal is presented in the favored sample, because then the bias leads to the correct choice of the signal interval even at very low signal levels. Performance is spuriously poor, however, when the signal is presented in the unfavored sample, because then the bias leads to the choice of the nonsignal interval containing the favored masker. Many molar investigations of masker uncertainty have used large numbers of masker samples to try to minimize this problem. Here we further document the existence of masker bias and describe a method by which separate measurements can be made both of this bias and of the sensitivity to the presence of the signal.

Psychometric functions: Molar psychophysical data indicate that psychometric functions measured with random multi-tonal maskers have shallower slopes than those measured with broadband noise (Kidd *et al.*, 1995a, 1998; Neff and Callaghan, 1987) or than those predicted for an ideal observer (Lutfi, 1994). Shallow psychometric slopes have

also been reported for individual masker samples presented in random-masker conditions (Neff and Callaghan, 1987). Little, however, is known of the relationship between the slope of psychometric functions in fixed- and random-masker conditions. In apparently the only investigation of this issue, Watson and Kelly (1981) tentatively concluded from a molar analysis that the slope of the psychometric function did not change significantly as the amount of uncertainty was varied from minimal to very high. Here we show that the slopes of psychometric functions measured with the same masker sample differ systematically among fixed-masker and two types of random-masker conditions.

Size of the masker set: In most previous studies of masker uncertainty, a different masker sample was presented on every trial or observation interval in random-masker conditions (e.g., Lutfi, 1994; Neff and Callaghan, 1988; Watson *et al.*, 1976). In the remaining experiments a small, but constant, number of samples were used (e.g., Pfafflin, 1968). There has been no systematic investigation of how the influence of masker uncertainty is affected by the number of possible masker samples to be presented. Here we report that the mean detrimental effects of two types of masker uncertainty grow approximately in parallel as the size of the masker set increases from two to ten.

Sample-specific influence of masker uncertainty: The aim of many experiments using molar psychophysics has been to determine the conditions under which masker uncertainty is most disruptive. Those studies have manipulated such variables as the number and frequency distribution of the tones in each masker sample (Lutfi, 1994; Neff and Callaghan, 1988; Neff *et al.*, 1993; Watson *et al.*, 1976), the repetition pattern of the masker (Kidd *et al.*, 1994, 1995b), and the presentation mode (monotic or dichotic; Kidd *et al.*, 1994; Neff, 1995). There is, however, a scarcity of information on the influence of uncertainty for specific masker samples belonging to the same general category. Only Pfafflin (1968) has reported the influence of uncertainty on the detection of a tonal signal in a set of 12 frozen noises. Her results show relatively small overall effects of uncertainty probably because her noise maskers all sounded quite similar. Nevertheless, some of her masker samples were more affected by uncertainty than others. Here we report marked and consistent differences in the influence of uncertainty across different masker samples.

Individual differences: Individual listeners tested using molar psychophysics show marked threshold differences in random-masker conditions (Leek, 1987; Neff and Dethlefs, 1995). These differences are not paralleled in the performance of the same listeners on the detection of tones in quiet or in measures of peripheral filter width made with notched noise, suggesting that the threshold variations in random-masker conditions are due to the introduction of uncertainty (Neff and Dethlefs, 1995). Here we report large individual differences in performance in both random- and fixed-masker conditions, and show that listeners' reactions to masker uncertainty are not necessarily revealed solely by their performances in random-masker conditions.

I. EXPERIMENT 1: ADAPTIVE TRACKING

A. Method

1. Listeners

Four listeners (two female, JF and WD) ranging in age from 19 to 23 years were paid for their participation. All had hearing within 15 dB of normal between 125 and 8000 Hz as determined by a Bekesy tracking procedure and had previous experience in other psychoacoustic tasks.

2. Stimuli

The signal was a 1000-Hz tone and the masker was one of up to ten different ten-tone complexes. The signal and masker were gated together for a total of 200 ms using a cosine-squared rise/fall time of 16.8 ms. The frequencies of the ten tones in each of the ten masker samples were chosen at random from a uniform distribution ranging from 200–5000 Hz, excluding the region from 800–1200 Hz around the signal. Also, to guarantee that the tones in each 200-ms sample were orthogonal, no two masking components in a given sample were allowed to be closer than 5 Hz (1/duration). The phases of the masking tones were randomly selected from a uniform distribution ranging from 0 to 359 degrees. Once chosen, the frequencies and phases of the ten tones in each of the ten masker samples were fixed throughout the entire experiment. The signal was always presented in zero phase. Table I lists the frequencies and phases comprising each of the masker samples (A–J). The individual masking tones were each presented at 50 dB SPL, producing an overall level of 60 dB SPL. Similar stimulus parameters produced substantial masking in previous experiments on masker uncertainty (Neff and Green, 1987; Neff and Callaghan, 1988; Neff et al., 1993).

The signal and masker were digitally generated in the time domain at a sampling rate of 20 000 Hz using a digital-signal-processing board (TDT AP2). They were delivered separately through two 16-bit digital-to-analog converters (TDT DA1) followed by separate 10-kHz low-pass filters (TDT FLT3, 60 dB attenuation at 11.5 kHz), separate programmable attenuators (TDT PA4), and a single sound mixer (TDT SM3). The listeners were seated in a sound-treated room and listened monaurally through the left earpiece of Sennheiser HD450 headphones.

3. Procedure

The procedure was two-interval forced-choice with feedback. The two observation intervals of a single trial were marked by lights, and were separated by 300 ms. The signal level was adjusted adaptively using the three-down/one-up rule of Levitt (1971) which tracks the 79% correct point on the psychometric function. The step size was 8 dB through the first reversal, 4 dB through the next three reversals, and 2 dB thereafter. The adaptive track was terminated after 60 trials. The first four reversals were discarded, and threshold was calculated as the mean of the remaining reversals. Two conditions employed multiple independent adaptive tracks, as described below. Six to ten blocks of trials were collected from each listener in each condition.

TABLE I. The frequencies (Hz) and phases (degrees) of the ten components in each of the ten masker samples (A–J). The signal was always a 1000-Hz tone presented at zero phase.

	Frequency (Hz)	Phase (deg)		Frequency (Hz)	Phase (deg)
A	1692	157.2	B	443	296.4
	1717	108.9		1573	26.0
	2530	25.2		1626	290.7
	2687	66.4		2343	134.0
	2737	325.9		2394	218.5
	2873	165.0		2494	73.9
	3023	308.5		2696	151.3
	3748	336.6		3539	117.1
	4104	197.1		3674	107.8
	4329	219.1		4202	79.7
C	458	299.2	D	352	179.3
	514	2.6		364	165.7
	2320	66.4		1317	324.2
	2445	327.2		2293	213.8
	2584	120.8		2334	283.1
	2666	253.1		2454	217.4
	2692	258.1		2714	104.7
	3665	269.5		3815	230.3
	3905	294.9		4334	158.1
	4891	31.0		4891	6.8
E	2156	338.1	F	550	124.6
	2536	105.4		631	59.6
	2663	131.6		663	278.4
	2849	336.8		1925	334.4
	3066	206.3		2201	277.7
	3133	284.7		3439	117.9
	3321	159.2		3609	0.0
	3546	321.8		3651	243.0
	3906	25.1		3789	197.9
	4689	181.6		4420	8.7
G	255	357.1	H	355	293.5
	434	171.0		1887	198.6
	797	245.3		1980	237.9
	2009	55.9		2382	185.9
	2399	226.8		2957	179.4
	3246	57.8		2967	249.9
	3397	236.9		3218	117.2
	3828	100.5		3375	126.8
	4015	167.4		3445	345.8
	4202	126.5		4304	307.5
I	709	53.2	J	208	275.3
	1227	208.7		308	217.6
	1436	214.6		1268	27.2
	1478	161.5		1293	150.0
	1556	178.5		1343	142.4
	2027	111.6		2167	267.2
	2514	162.3		2350	255.1
	3119	355.4		3031	109.3
	4005	193.7		3641	214.8
	4661	31.6		4678	304.0

4. Conditions

There were three listening conditions. In the *fixed condition*, the same masker sample was presented on every observation interval throughout an entire block of 60 trials. The ten different masker samples were presented in random order across blocks.

In the *random-by-trial condition*, the same masker
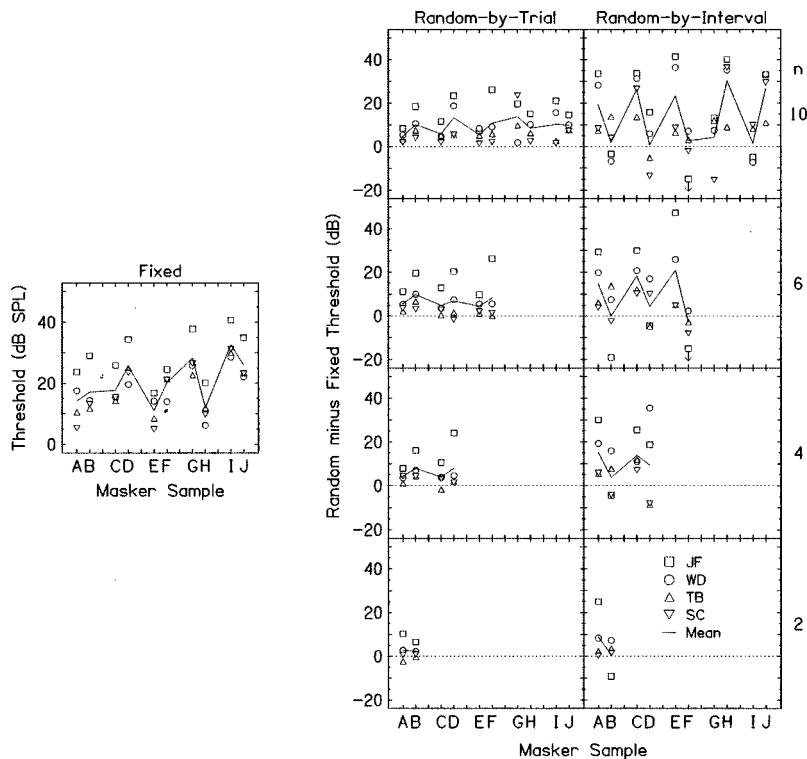
FIG. 1. Individual (symbols) and mean (lines) adaptive results of the four listeners for the ten masker samples (A–J). The floating panel shows the signal thresholds for each masker sample in the fixed condition. The remaining panels show the threshold differences for each masker sample between the random-by-trial and fixed conditions (left column) and between the random-by-interval and fixed conditions (right column) for the four masker-set sizes (rows).

sample was presented on both observation intervals of a single trial, but the particular masker sample was chosen quasi-randomly across trials from n possibilities, where n equalled 2, 4, 6, or 10 in different blocks of trials. The particular samples used when $n < 10$ were chosen arbitrarily but always included the same samples as in the tests using fewer samples. The same sets of maskers were used throughout the experiment. Performance for each masker sample was monitored with a separate adaptive track. Thus there were n interleaved tracks in each test. To obtain the 60 responses necessary to complete the track for each masker sample, the particular sample was chosen at random, without replacement, from a pool of 60 instances of each of the n samples. Thus there were $60n$ trials in each block. Breaks were provided after every 60 trials within a block to make the experimental session as similar to that in the fixed condition as possible.

Finally, in the *random-by-interval condition*, different masker samples were presented on the two observation intervals of a trial, and the particular masker samples were chosen quasi-randomly across trials from n possibilities ($n = 2, 4, 6$, or 10). To simultaneously measure performance for each masker sample and monitor the influence of the masker sample in the nonsignal interval on the response pattern, the masker samples were presented in fixed pairs (A and B, C and D, E and F, G and H, I and J). The pairings were made arbitrarily and were maintained throughout the experiment. Both members of a sample pair were always presented within the same trial, but the order of their presentation within the trial was random. A separate adaptive track monitored performance for each masker sample, yielding n interleaved tracks. Data in the random-by-interval condition were collected in the same manner as in the random-by-trial condition.

The initial signal levels were 25, 35, and 45 dB SPL in the fixed, random-by-trial, and random-by-interval conditions, respectively. Example trials were provided at the beginning of each block. In those trials the signal level was 15 dB higher than the initial signal level used in the actual trials. Each listener was generally tested on all three conditions, presented in random order, during each 2-h listening session.

B. Results and discussion

Figure 1 presents the individual (symbols) and mean (lines) results of the four listeners for the ten masker samples (A–J). Plotted in the floating panel are the signal thresholds in the fixed condition. The remaining panels show the threshold differences between the fixed and each of the two random conditions (columns) for the four masker-set sizes (rows). The mean threshold differences between the random-by-trial and fixed condition were consistently positive (left column), indicating that uncertainty about which sample was to be presented on a trial made the signal harder to detect. In contrast, the threshold differences between the random-by-interval and fixed condition fluctuated markedly (right column). When the set size was ten, the difference was around 30 dB for one sample and near 0 dB for the other sample of each masker pair. Every listener had at least one negative difference score, indicating a lower threshold in the random-by-interval than the fixed condition. It seems unlikely that this oscillating pattern of difference scores resulted from peculiarities in the influence of uncertainty on particular masker samples. A more plausible scenario is that the listeners treated one masker sample of a pair in the random-by-interval condition as being more likely to contain the signal. This possibility is explored in the second experiment.

```
                    stimulus
              (1)   (2)      (3)   (4)
              x'y   yx'      y'x   xy'
RESPONSE   1  28    65       77    31
           2  62    25       13    59    ----
              --    --       --    --
              90    90       90    90  | 360
```

```
                    stimulus
              (1) + (3)      (2) + (4)
              sig in int 1   sig in int 2
RESPONSE   1   105           96
           2   75            84     ----
              ---           ---
              180           180   | 360
                    d's = 0.11
```

```
                    stimulus
              (1) + (4)      (2) + (3)
              x in int 1     x in int 2
RESPONSE   1   59            142
           2   121           38     ----
              ---           ---
              180           180   | 360
                    d'm = −0.86
```

FIG. 2. *Top*: A representative stimulus-response matrix from a single fixed pair of masker samples in the random-by-interval condition. *Middle*: The submatrix used to derive the listener's sensitivity to the signal, d'_s, independent of any bias toward or against the masker sample. *Bottom*: The submatrix used to derive the listener's preference to select an interval based on the presence of a particular masker sample, d'_m, independent of the presence of the signal. A negative d' resulting from this calculation merely indicated that the listener favored masker sample *y* rather than masker sample *x*. All values of d'_m are reported as positive values. See text for details on all three matrices.

II. EXPERIMENT 2: CONSTANT STIMULI

A. Introduction

Experiment 2 introduces a technique for simultaneously measuring both signal detectability and masker bias in the random-by-interval condition. This technique employs the method of constant stimuli, from which information about the slopes of the psychometric functions in fixed- and random-masker conditions may be obtained. Furthermore, the signal thresholds derived in this experiment are free of the influence of masker bias. This allows the evaluation of the contributions of the size of the masker set, of the particular masker sample, and of the individual listener to the magnitudes of both the random-by-trial and random-by-interval uncertainty effects.

B. Method

The listeners, stimuli, and conditions were the same as in experiment 1. The differences between the two experiments were that, here, (1) the signal level was fixed throughout a block of trials rather than being adjusted adaptively, and (2) both the observation interval in which the signal was presented and the masker sample that contained the signal were recorded with the response on each trial. Using this method, it was possible to estimate both the listener's sensitivity to the signal and the extent to which the listener was biased toward intervals containing particular masker samples.

The top of Fig. 2 illustrates a representative stimulus-response matrix from a single fixed pair of masker samples in the random-by-interval condition. The stimuli are listed along the top of the matrix as $\langle x'y \rangle$, $\langle yx' \rangle$, $\langle y'x \rangle$, and $\langle xy' \rangle$, where the letter indicates the particular masker sample, the letter sequence indicates the presentation order between the two observation intervals, and the prime indicates the signal interval. The responses are listed along the side of the matrix as $\langle 1 \rangle$ for "signal in the first interval" or $\langle 2 \rangle$ for "signal in the second interval."

To determine the listener's sensitivity to the signal in a particular masker sample independent of bias toward or against that sample, the responses were pooled over columns in which the signal was presented in the same observation interval. Thus the responses were added across the $x'y$ and $y'x$ [columns (1) and (3)], and across the yx' and xy' [columns (2) and (4)] stimulus patterns. This pooling resulted in the two-by-two matrix shown at the middle of Fig. 2. The index of detectability for the signal (d'_s) was calculated using this new matrix by taking the total proportion of correct responses [in the example, $(105+84)/360 = 0.53$] and looking up the d' value corresponding to that proportion correct in a forced-choice table (Green and Swets, 1964; Swets, 1964).

Similarly, to determine the listener's preference to select an interval based on the presence of a particular masker sample, independent of the presence of the signal, the responses were combined over columns in which a particular masker sample (chosen arbitrarily as sample *x*) was presented in the same observation interval. Thus, the responses were added across the $x'y$ and xy' [columns (1) and (4)], and across the yx' and $y'x$ [columns (2) and (3)] stimulus patterns. This yielded another two-by-two matrix, shown at the bottom of Fig. 2, from which the masker bias (d'_m) was calculated. In some cases, a negative d' resulted from this calculation. That merely indicated that the listener favored masker sample *y*, rather than masker sample *x*. All values of d'_m are reported as positive values.

For the random-by-interval condition, each stimulus pattern $(x'y, yx', y'x, xy')$ was presented a total of 180 times. To obtain measures of d'_s and d'_m that were based on different data sets, the data for each pattern were divided into two sets of 90 trials each. The 360 responses (4 patterns×90 trials) from the even-numbered blocks formed one set and those from the odd-numbered blocks formed the other. Each set, such as the one in Fig. 2, was used to calculate both d'_s and d'_m. Thus d'_s obtained from the even-numbered trials could be compared to d'_m obtained from the odd-numbered trials, and the reverse. Note that Fig. 2 shows the data from only one of the two sets of responses; a complete figure for one masker pair (*x* and *y*) would include three parallel matrices containing the other data set. When there were ten masker samples, five such pairs of matrices were produced.

For the random-by-trial and fixed conditions, the two possible stimulus patterns $(x'x$ and $xx')$ were each presented a total of 180 times. Thus d'_s was calculated from a total of 360 trials. No measure of d'_m was necessary or possible.
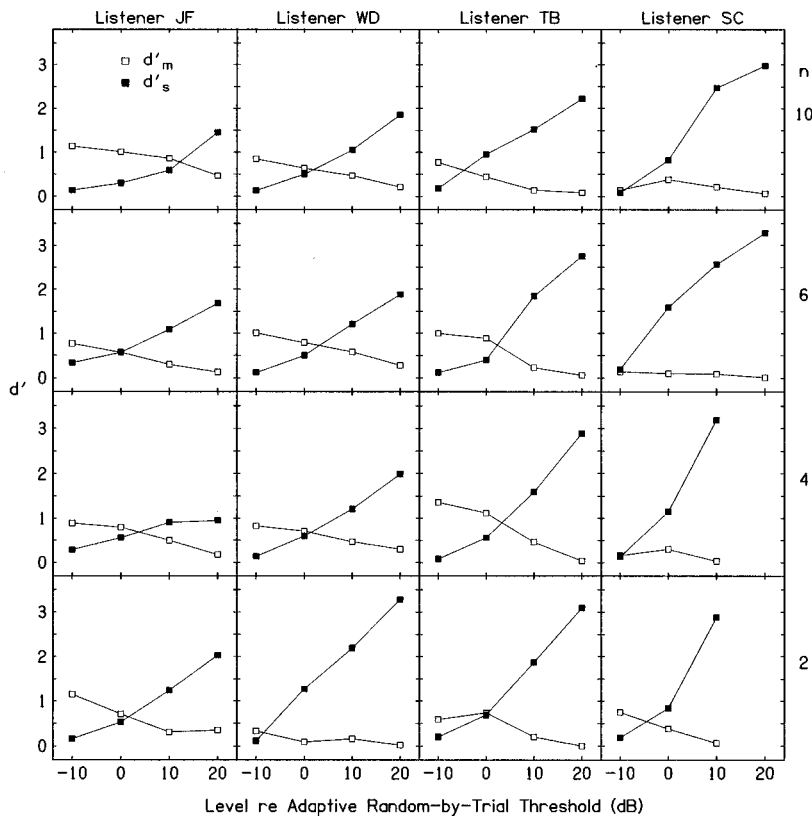
FIG. 3. Individual psychometric functions (columns) for d'_s (filled squares) and d'_m (open squares) averaged across the sample pairs tested for each set size (rows). The abscissa shows the signal level relative to the adaptively measured random-by-trial threshold.

For the two random conditions, the signal was presented at four different levels denoted -10, 0, $+10$, and $+20$ dB. For the fixed condition, the signal levels were chosen specifically for each listener, but typically included the values 0, -5, -10, and -20 dB. These levels are all expressed relative to the signal level at threshold obtained for each listener, number of masker samples, and particular sample in the random-by-trial condition in experiment 1. The signal levels were defined relative to the adaptive random-by-trial thresholds so that the levels used would produce a reasonable range of d' values for each masker sample in each condition, despite the large differences in the amounts of masking produced by each masker individually. Breaks were provided after every 60 trials. Data were collected in three-block sets in each condition in the order: (1) random-by-interval, (2) random-by-trial, (3) random-by-interval, (4) fixed. The second phase of data collection in the random-by-interval condition was added when it was realized that more trials were needed to have independent estimates of d'_s and d'_m.

C. Results and discussion

1. Masker bias

The d' values measured in the random-by-interval condition are plotted in Fig. 3 for each listener (columns) and each masker-set size (rows). The even- and odd-numbered trials produced similar estimates of d'_s, and of d'_m, and therefore were averaged, yielding one estimate of d'_s and one of d'_m at each signal level for each pair of masker samples. Each panel shows the values of d'_s and d'_m averaged over the sample pairs tested for each set size.[1] For example, each point in the top row of panels represents the mean of five estimates of d', one estimate for each of the five pairs of

masker samples, and each point in the bottom row represents one estimate of d' from the single pair of masker samples tested.

For all listeners, as expected, d'_s (filled squares) increased from near 0 to above 1 as the signal level was increased from -10 to $+20$ dB. In contrast, for three of the four listeners (all but SC), d'_m (open squares) frequently decreased from around 1 to 0 as the signal level was increased over the same range. Thus, at low signal levels, the majority of listeners made their responses based more on the presence of a particular masker sample than on the presence of the signal. Individual listeners consistently favored the same sample of a pair regardless of the masker-set size, but the favored sample often differed across listeners. When only one sample of the masker pair had masking components lower than the signal frequency, listeners JF, WD, and TB all favored that sample (B over A, F over E), but those same three listeners differed in their preferences for the remaining samples. The magnitude of d'_m at the signal level of -10 dB did not differ systematically across the masker pairs. For listener SC, d'_m was essentially constant at about 0 at all signal levels, indicating that his responses were influenced almost entirely by the presence of the signal.

In 77% of the cases where there was a bias (24 of 31 instances), threshold in the fixed condition was higher for the favored than for the unfavored masker sample. Likewise, in 78% of the cases where the adaptive random-by-interval threshold was lower than the adaptive random-by-trial or fixed threshold (25 of 32 instances in Fig. 1), threshold in the fixed condition was higher for that masker sample than for the other sample in the pair. Thus listeners tended to favor the more effective masker when they had difficulty hearing
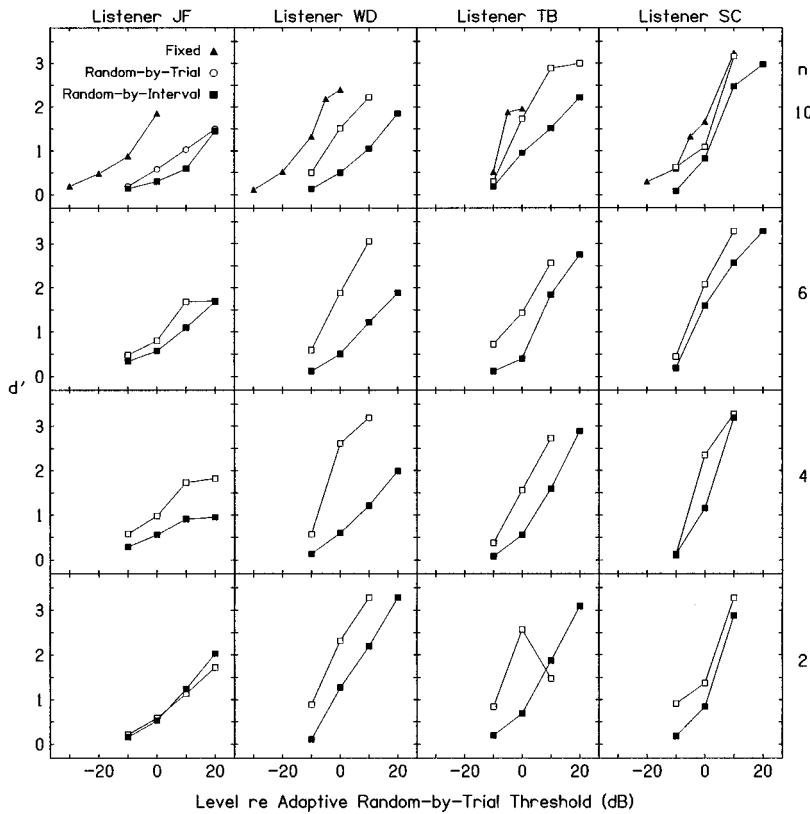
FIG. 4. As in Fig. 3, but for d'_s in the fixed (filled triangles), random-by-trial (open circles), and random-by-interval (filled squares) conditions.

the signal. Threshold in fixed conditions is traditionally thought to be proportional to the amount of masker energy contained in the peripheral auditory filter centered on the signal frequency. Perhaps the listeners who were susceptible to masker bias tended to favor the maskers with the higher fixed thresholds, because those maskers, with their extra energy near the signal frequency, sounded more like they contained the signal. It is possible that the three listeners who showed masker bias made their judgments on such a timbral aspect of the stimulus, while the remaining unbiased listener focused on the signal frequency. This interpretation is in accord with the reports of Neff and her colleagues that individual listeners adopt either holistic or analytic listening strategies when faced with masker uncertainty (Neff *et al.*, 1993; Neff and Dethlefs, 1995).

These masker-bias results show that when the detection task is difficult due to uncertainty, listeners essentially change the task. Here, rather than responding randomly when the signal was difficult to detect, listeners instead responded systematically to particular masker samples. While that result might be attributed to the signal-like qualities of some masker samples, there are data showing response bias even when the randomized variable had no signal-like characteristics. For example, Lee (1994) asked listeners to indicate which of two observation intervals contained the higher rate of sinusoidal amplitude modulation of a tonal carrier. When she randomly presented two different carrier frequencies on the two intervals of a trial, one of her two listeners consistently selected as signal the interval with the higher-frequency carrier. We also have preliminary results from listeners who were asked to detect the longer of two temporal intervals each marked by two brief tones. When we ran-

domly marked the temporal intervals by low-frequency tones in one observation interval and high-frequency tones in the other, listeners responded systematically to the tone frequency rather than to the longer temporal interval. Particular tonal frequencies do not inherently sound more signal-like when the signal is a higher modulation rate or longer temporal interval. Thus listeners appear to adopt the task of imposing order on the randomized variable when the assigned task becomes difficult.

2. Psychometric functions

Figure 4 is plotted in the same manner as Fig. 3, but shows the mean psychometric functions for d'_s for the fixed (filled triangles; top row only), random-by-trial (open circles), and random-by-interval (filled squares) conditions.[1] To derive the signal levels that corresponded to 79% correct detections from each of the psychometric functions that went into the mean functions in Fig. 4, the data for each function (d'_s versus signal level in dB) were fitted with a least-squares straight line from which the slope and intercept of the function was determined. Inspection of individual functions showed that a linear fit was acceptable for estimating the relative steepness of the functions.

Table II lists the mean slopes of the psychometric functions in the three conditions calculated across the masker samples in each masker set. Results are shown for the individual listeners and their mean. The slope of the psychometric functions was generally steepest in the random-by-trial condition, intermediate in the fixed condition, and shallowest in the random-by-interval condition. The mean psychometric slope was (1) steeper in the random-by-trial than the random-

TABLE II. Mean slopes of the psychometric functions in the three conditions calculated across all of the masker samples (n) in each masker set. The individual listener means, and the grand mean and $\pm$ one standard error of the mean, are listed.

		Condition		
n	Listener	Fixed	Random-by-trial	Random-by-interval
	JF	0.048	0.053	0.042
	WD	0.062	0.086	0.057
10	TB	0.146	0.101	0.067
	SC	0.109	0.141	0.108
	Mean	0.091	0.095	0.069
	se	(0.004)	(0.004)	(0.004)
	JF	0.050	0.045	0.045
	WD	0.062	0.131	0.060
6	TB	0.148	0.092	0.093
	SC	0.115	0.165	0.117
	Mean	0.094	0.108	0.079
	se	(0.006)	(0.006)	(0.003)
	JF	0.048	0.045	0.043
	WD	0.068	0.131	0.062
4	TB	0.155	0.118	0.095
	SC	0.117	0.177	0.153
	Mean	0.097	0.117	0.088
	se	(0.008)	(0.004)	(0.002)
	JF	0.048	0.050	0.063
	WD	0.068	0.156	0.104
2	TB	0.129	0.090	0.099
	SC	0.095	0.119	0.135
	Mean	0.085	0.104	0.100
	se	(0.006)	(0.000)	(0.000)

by-interval condition for every set size, and in 11 of the 16 individual cases, (2) steeper in the random-by-trial than the fixed condition for every set size and for 10 of the 16 individual cases, and (3) steeper in the fixed than the random-by-interval condition for all but the set size of 2, and in 11 of the 16 individual cases. Using molar psychophysics, Neff and Callaghan (1987) measured the slopes of psychometric functions in d'/dB units with stimuli and conditions similar to those tested here. The mean slopes of their four listeners were in the same general range as the present report at 0.088 in the random-by-trial condition (termed ''fixed'' by them) and 0.095 in the random-by-interval condition (termed ''random'' by them). Two of their four listeners had steeper slopes in the random-by-trial than the random-by-interval condition. They did not report results for the fixed condition. Differences in the psychometric slope across conditions are usually thought to indicate that different internal nonlinear transformations of the stimulus scale occur either at peripheral or central sites in each condition (Egan, 1965; Laming, 1986; Saberi and Green, 1997). Such nonlinearities may be modeled as a power-law transformation of the stimulus scale. On a logarithmic scale, the exponent becomes the constant of proportionality, i.e., the slope. Laming has described psychometric slopes from one to eight for visual and auditory tasks (see also Egan, 1965; Dai, 1995; Saberi and Green, 1997).

The actual signal SPL estimated to yield 79% correct detections was calculated by determining the relative signal level that corresponded to a d'_s of 1.15 (79% correct) from

the fitted functions and then adding that value to the appropriate random-by-trial threshold measured adaptively. This was a straightforward process for the fixed and random-by-trial conditions, for which there were separate adaptive thresholds for each masker sample. For the random-by-interval condition, however, the calculation of the actual signal SPL was complicated by the fact that each pair of masker samples produced only one d'_s psychometric function. The actual signal SPL used in that condition was calculated by adding the single 79% correct value from the d'_s function separately to each of the two adaptive threshold values of the two maskers in the pair. This calculation assumes that the signal threshold in each of the maskers in a pair would have been increased by the same amount due to random-by-interval uncertainty had it been possible to measure each one independently.[2] It is doubtful that this assumption is strictly true. However, the results obtained with it are orderly and seem more reasonable than the adaptive measurements of the influence of random-by-interval uncertainty shown in Fig. 1, for which no correction for bias was applied.

Figure 5 is plotted in the same manner as Fig. 1, but shows the results obtained from the actual signal SPLs for 79% correct detections derived from the d'_s psychometric functions.[1] These results are free of the influence of masker bias. In contrast to the mean difference scores calculated from the adaptive thresholds shown in Fig. 1, the mean differences between the random-by-interval and fixed condition (right column) were consistently larger than those between the random-by-trial and fixed condition (left column). Thus uncertainty about which masker was to be presented impaired performance, and the magnitude of that impairment was greater in the random-by-interval than the random-by-trial condition.

3. Size of the masker set

Figure 6 shows the mean effect of random-by-trial (open squares) and random-by-interval (filled squares) uncertainty as a function of the number of different masker samples presented in each test. Each point represents the mean difference score calculated across all of the samples tested for each set size in Fig. 5.[1] Thus the left-most points are based on difference scores from two samples and the right-most points from ten samples. The error bars indicate $\pm$ one standard error of the mean. Note that because the psychometric slopes sometimes differed among the fixed and random conditions (Table II), the calculated magnitudes of the uncertainty effects depends on the percent-correct level chosen for examination.

Two aspects of these data deserve notice. First, performance was clearly degraded with only two samples for random-by-interval uncertainty, and four samples for random-by-trial uncertainty. The demonstration of clear effects of uncertainty with only a few masker samples shows that listeners are very susceptible to the influence of masker uncertainty, and presumably to other forms of uncertainty as well. This susceptibility provides additional support for the idea that everyday situations are better represented by conditions with than without uncertainty. It also shows the feasibility of quasimolecular investigations of the stimulus characteristics that lead to large or small uncertainty effects.

1772   J. Acoust. Soc. Am., Vol. 105, No. 3, March 1999

B. A. Wright and K. Saberi: Random maskers   1772
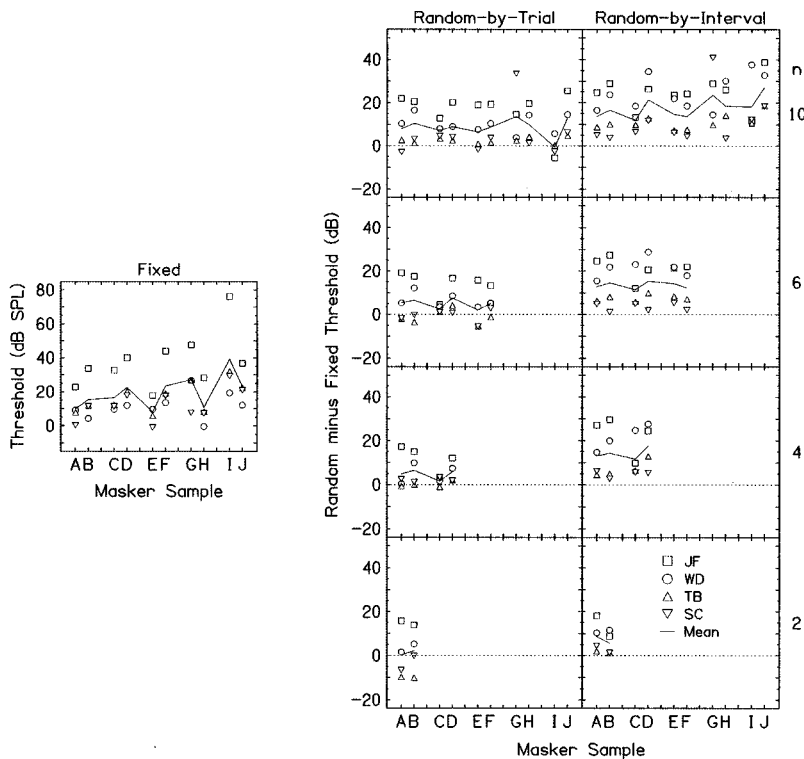
FIG. 5. Parallel to Fig. 1, but the values were derived from the d_s' psychometric functions, thereby removing the influence of masker bias from the threshold estimates in the random-by-interval condition. Note that the ordinate range in the floating panel is greater than in Fig. 1.

Second, the mean detrimental influence of random-by-trial uncertainty grew by about 7 dB, and that of random-by-interval uncertainty by about 11 dB, as the size of the masker set was increased from two to ten. The difference in the rate of growth between the two types of uncertainty was due almost exclusively to performance with a set size of two. For set sizes of four and greater, random-by-interval uncertainty was consistently about 9 dB greater than random-by-trial uncertainty. For both types of uncertainty, the mean growth reached a plateau for set sizes of four and six, but increased again for the set size of ten. The magnitude and form of this growth should be interpreted with caution, because only samples A and B were tested with the smallest set size. When only those samples were included in the analysis, both types of uncertainty grew by about 8 dB, with the same pattern as for the whole data set, as the set size was increased

from two to ten. Though based on a limited set of masker samples, the roughly parallel increase in the two types of uncertainty with set size suggests that listeners may use the same detection strategy less successfully, or less efficiently, in the random-by-interval than the random-by-trial condition.

For comparison, the mean adaptive estimates of random-by-trial uncertainty were on average 1 dB larger than the constant-stimuli estimates. For set sizes of two, four, six, and ten, the adaptive values were 3, 6, 7, and 9 dB, and the constant-stimuli values 1, 5, 5, and 9 dB. The mean adaptive estimates of random-by-interval uncertainty were on average 4 dB smaller than the constant-stimuli estimates. For set sizes of two, four, six, and ten, the adaptive values were 5, 10, 8, and 13 dB, and the constant-stimuli values 7, 14, 13, and 18 dB. To the extent that the mean of quasimolecular adaptive estimates corresponds to molar measurements in other experiments, the present results indicate that molar and molecular estimates are similar for random-by-trial uncertainty, but that molar analyses may underestimate the influence of random-by-interval uncertainty.

4. Sample-specific influence of masker uncertainty

The influence of uncertainty differed among the masker samples. As shown in Fig. 5, when the set size was ten, the mean influence of random-by-trial uncertainty ranged from -1 dB (sample I) to 14 dB (sample G) and the mean influence of random-by-interval uncertainty ranged from 12 dB (sample C) to 27 dB (sample J). The mean magnitude of the uncertainty effect for each masker sample showed a Spearman rank correlation of $r_s = 0.65$ ($p < 0.05$) between the two types of uncertainty. Thus the effects of the two types of uncertainty tended to be both large, or both small, for the same masker samples.

FIG. 6. The mean effect of random-by-trial (open squares) and random-by-interval (filled squares) uncertainty as a function of the number of different masker samples presented in each test. Each point represents the mean difference score calculated across all of the samples tested for each set size in Fig. 5. The error bars indicate ± one standard error of the mean.

There were significant Spearman rank correlations between the mean magnitude of the random-by-interval uncertainty effect and the frequency difference between the nearest masker components below and above the signal frequency ($r_s = 0.65$, $p < 0.05$, two-tailed test), and between the adaptive measure of random-by-trial uncertainty and that same frequency difference ($r_s = 0.64$, $p < 0.05$):[3] The smaller the frequency difference, the greater the uncertainty effect. Both random-by-interval ($r_s = 0.55$, $p < 0.10$) and adaptive random-by-trial ($r_s = 0.81$, $p < 0.05$) uncertainty were also significantly correlated with the frequency distance to the masking component nearest to the signal frequency (but not with the frequency distance to the nearest component exclusively above or below the signal frequency): The closer the nearest component, the greater the uncertainty effect. Other reports have also associated masking components close to the signal frequency with the production of uncertainty effects (Neff and Callaghan, 1987; Lutfi and Doherty, 1994). One interpretation of these relationships is that listeners use a narrow attentional filter matched to a single peripheral filter in the fixed condition, but use a wider attentional filter whose output represents the sum of the outputs of multiple separate peripheral filters in the random conditions (Lutfi, 1993; Neff *et al.*, 1993). The increase in the bandwidth of the attentional filter would lead to an increase in signal threshold. As observed, this threshold increase would be greatest when the frequency separation of the masking components closest to the signal frequency was small.

5. Individual differences

Finally, there were systematic differences in the performance patterns across individual listeners. For example, listener JF, who had the largest uncertainty effect in 70% of the cases in Fig. 5 (squares), also showed the highest threshold in every fixed condition in Fig. 5 (squares), the shallowest mean psychometric function in every case (Table II), and the most masker bias (her average d'_m across set sizes at -10 dB from Fig. 3 was 0.99, compared to 0.76 for WD, 0.93 for TB, and 0.30 for SC). In contrast, listener SC, who had or tied for the smallest uncertainty effect in 59% of the cases in Fig. 5 (inverted triangles), also showed the steepest mean psychometric functions in 58% of all the cases and 88% of the random cases in Table II, and the least masker bias (right column of Fig. 3).

Using molar psychophysics, Neff and her colleagues have reported remarkably large threshold differences across listeners in random-masker conditions (Neff *et al.*, 1993; Neff and Dethlefs, 1995). Using quasimolecular psychophysics, the present listeners show similarly marked threshold differences in the random-masker conditions, but also show large threshold differences in the fixed condition (see floating panels in Figs. 1 and 5). The threshold differences in the fixed condition are important because with the quasimolecular approach the uncertainty effect is measured by subtracting threshold in the fixed- from that in the random-masker condition. This analysis reveals that the actual uncertainty effect is sometimes different from that apparently indicated by the threshold in the random-masker condition. For example, listener WD, who had the largest or second largest uncertainty effect in 89% of the cases in Fig. 5 (circles) had the lowest threshold in 70% of the fixed conditions (Fig. 5; circles). Therefore, her actual thresholds in the random-masker conditions (fixed threshold plus the difference threshold plotted in Fig. 5) were much lower, on average by 26 dB, than those of listener JF. The actual thresholds of WD in the random-masker conditions thus give the mistaken impression that she was not influenced much by uncertainty.

III. SUMMARY

A quasimolecular psychophysical approach was used to investigate how uncertainty about the frequency content of a ten-tone masker sample affected the ability to detect a 1000-Hz signal. The masker sample was either fixed throughout a block of two-interval forced-choice trials (fixed condition) or was randomized across (random-by-trial condition) or within (random-by-interval condition) trials. The results showed the following.

(1) *Masker bias:* When the signal level was low and different masker samples were presented on the two observation intervals of a trial, listeners often based their responses more on the presence of a particular masker sample than on the presence of the signal (Fig. 3). Signal threshold in the fixed condition was higher in the favored than than the unfavored sample in the majority of cases. Adaptively measured signal thresholds in the random-by-interval condition were clearly skewed by this bias (Fig. 1). A method was described by which masker bias can be identified and separated from sensitivity to the signal (Fig. 2).

(2) *Psychometric functions:* Psychometric functions measured with the same masker sample were generally steepest in the random-by-trial condition, intermediate in the fixed condition, and shallowest in the random-by-interval condition (Fig. 4, Table II).

(3) *Size of the masker set:* Performance was clearly degraded with only two masker samples for random-by-interval uncertainty and four samples for random-by-trial uncertainty. As the size of the masker set was increased from two to ten, the mean magnitude of the effect of both types of uncertainty grew in parallel by an average of 9 dB (Fig. 6).

(4) *Sample-specific influence of masker uncertainty:* The magnitudes of both types of uncertainty effects varied by 15 dB across individual masker samples. Signal detection was most affected by both types of masker uncertainty in samples that had frequency components close to the signal frequency.

(5) *Individual differences:* There were systematic differences in the performance patterns across individual listeners. The two listeners who were the most and least affected by both types of masker uncertainty also showed, respectively, the shallowest and steepest psychometric functions, and the most and least masker bias. Threshold in the random-masker conditions did not reliably reflect which listeners were most influenced by uncertainty.

[1]The data of listener JF in the random-by-interval condition for masker samples E and F collected with a set size of six are omitted from the mean values reported for her in Figs. 3 and 4. That is because the psychometric function fitted to her data for those samples did not yield a signal level for 79% correct detections that was between -100 and $+100$ dB. To include her data in the grand means in Figs. 5 and 6 and Table II, the average difference across samples between the magnitudes of her random-by-interval uncertainty effects (Figs. 5 and 6) and her psychometric slopes (Table II) when $n=10$ and $n=6$ was calculated. That value was then subtracted from her uncertainty effect for samples E and F when $n=10$ and used as the estimate of her performance for those samples when $n=6$.

[2]A single-interval method would not necessarily solve this problem. At first glance it may appear that the hit rate in a single-interval task could be considered the sensitivity to the signal and the false-alarm rate the masker bias. However, sensitivity to the signal (d'_s) in a single-interval task is calculated from both the hit and false-alarm rates. Furthermore, it would be difficult to determine the proportion of hits made due to the presence of the signal versus those made due to a bias toward the masker, or the proportion of false alarms made due to the tendency to say ''signal'' versus those made due to a bias toward the masker.

[3]For masker samples A and E that had no components below the signal frequency, the frequency difference was calculated as the frequency of the nearest component above the signal frequency (minus zero).

Dai, H. (**1995**). ''On measuring psychometric functions: A comparison of the constant-stimulus and adaptive up-down methods,'' J. Acoust. Soc. Am. **98**, 3135–3139.

Dai, H., and Wright, B. A. (**1995**). ''Detecting signals of unexpected or uncertain durations,'' J. Acoust. Soc. Am. **98**, 798–806.

Egan, J. P. (**1965**). ''Masking-level differences as a function of interaural disparities in intensity of signal and of noise,'' J. Acoust. Soc. Am. **38**, 1043–1049.

Egan, J. P., Greenberg, G. Z., and Schulman, A. I. (**1961**). ''Interval of time uncertainty in auditory detection,'' J. Acoust. Soc. Am. **33**, 771–778.

Gilkey, R. H., Robinson, D. E., and Hanna, T. E. (**1985**). ''Effects of masker waveform and signal-to-masker phase relation on diotic and dichotic masking by reproducible noise,'' J. Acoust. Soc. Am. **78**, 1207–1219.

Green, D. M. (**1961**). ''Detection of auditory sinusoids of uncertain frequency,'' J. Acoust. Soc. Am. **33**, 897–903.

Green, D. M. (**1964**). ''Consistency of auditory detection judgements,'' Psychol. Rev. **71**, 392–407.

Green, D. M., and Swets, J. A. (**1964**). *Signal Detection Theory and Psychophysics* (Wiley, New York).

Kidd, G. Jr., Mason, C. R., and Rohtla, T. L. (**1995a**). ''Binaural advantage for sound pattern identification,'' J. Acoust. Soc. Am. **98**, 1977–1986.

Kidd, G. Jr., Mason, C. R., and Dai, H. (**1995b**). ''Discriminating coherence in spectro-temporal patterns,'' J. Acoust. Soc. Am. **97**, 3782–3790.

Kidd, G. Jr., Mason, C. R., Rohtla, T. L., and Deliwali, P. S. (**1998**). ''Release from masking due to spatial separation of sources in the identification of nonspeech auditory patterns,'' J. Acoust. Soc. Am. **104**, 422–431.

Kidd, G. Jr., Mason, C. R., Deliwala, P. S., Woods, W. S., and Colburn, H. S. (**1994**). ''Reducing informational masking by sound segregation,'' J. Acoust. Soc. Am. **95**, 3475–3480.

Laming, D. (**1986**). *Sensory Analysis* (Academic, London).

Lee, J. (**1994**). ''Amplitude modulation rate discrimination with sinusoidal carriers,'' J. Acoust. Soc. Am. **96**, 2140–2147.

Leek, M. R. (**1987**). ''Directed attention in complex sound perception,'' in *Auditory Processing of Complex Sounds*, edited by W. A. Yost and C. S. Watson (Erlbaum, Hillsdale, NJ), pp. 278–288.

Levitt, H. (**1971**). ''Transformed up-down methods in psychoacoustics,'' J. Acoust. Soc. Am. **49**, 467–477.

Lutfi, R. A. (**1993**). ''A model of auditory pattern analysis based on component-relative-entropy,'' J. Acoust. Soc. Am. **94**, 748–758.

Lutfi, R. A. (**1994**). ''Discrimination of random, time-varying spectra with statistical constraints,'' J. Acoust. Soc. Am. **95**, 1490–1500.

Lutfi, R. A., and Doherty, K. A. (**1994**). ''Effect of component-relative-entropy on the discrimination of simultaneous tone complexes,'' J. Acoust. Soc. Am. **96**, 3443–3450.

Neff, D. L. (**1995**). ''Signal properties that reduce masking by simultaneous, random-frequency maskers,'' J. Acoust. Soc. Am. **98**, 1909–1920.

Neff, D. L., and Callaghan, B. P. (**1987**). ''Psychometric functions for multicomponent maskers with spectral uncertainty,'' J. Acoust. Soc. Am. **81**, S53 (A).

Neff, D. L., and Callaghan, B. P. (**1988**). ''Effective properties of multicomponent simultaneous maskers under conditions of uncertainty,'' J. Acoust. Soc. Am. **83**, 1833–1838.

Neff, D. L., and Dethlefs, T. M. (**1995**). ''Individual differences in simultaneous masking with random-frequency, multicomponent maskers,'' J. Acoust. Soc. Am. **98**, 125–134.

Neff, D. L., and Green, D. M. (**1987**). ''Masking produced by spectral uncertainty with multicomponent maskers,'' Percept. Psychophys. **41**, 408–415.

Neff, D. L., Dethlefs, D. L., and Jesteadt, W. (**1993**). ''Informational masking for multicomponent maskers with spectral gaps,'' J. Acoust. Soc. Am. **94**, 3112–3126.

Pfafflin, S. M. (**1968**). ''Detection of auditory signal in restricted sets of reproducible noise,'' J. Acoust. Soc. Am. **43**, 487–490.

Pfafflin, S. M., and Mathews, M. V. (**1966**). ''Detection of auditory signals in reproducible noise,'' J. Acoust. Soc. Am. **39**, 340–345.

Saberi, K., and Green, D. M. (**1997**). ''Evaluation of maximum-likelihood estimators in nonintensive auditory psychophysics,'' Percept. Psychophys. **59**, 867–876.

Spiegel, M. F., and Watson, C. S. (**1981**). ''Factors in the discrimination of tonal patterns. III. Frequency discrimination with components of well-learned patterns,'' J. Acoust. Soc. Am. **69**, 223–230.

Spiegel, M. F., and Green, D. M. (**1982**). ''Signal and masker uncertainty with noise maskers of varying duration, bandwidth, and center frequency,'' J. Acoust. Soc. Am. **71**, 1204–1210.

Swets, J. A. (**1964**). *Signal Detection and Recognition by Human Observers* (Wiley, New York), pp. 682–683.

Veniar, F. A. (**1958a**). ''Signal detection as a function of frequency ensemble. I,'' J. Acoust. Soc. Am. **30**, 1020–1024.

Veniar, F. A. (**1958b**). ''Signal detection as a function of frequency ensemble. II,'' J. Acoust. Soc. Am. **30**, 1075–1078.

Watson, C. S. (**1987**). ''Uncertainty, informational masking, and the capacity of immediate auditory memory,'' in *Auditory Processing of Complex Sounds*, edited by W. A. Yost and C. S. Watson (Erlbaum, Hillsdale, NJ), pp. 267–277.

Watson, C. S., and Kelly, W. J. (**1981**). ''The role of stimulus uncertainty in the discrimination of auditory patterns,'' in *Auditory and Visual Pattern Recognition*, edited by D. J. Getty and J. H. Howard (Erlbaum, Hillsdale, NJ), pp. 37–59.

Watson, C. S., Wroton, H. W., Kelly, W. J., and Benbassat, C. A. (**1976**). ''Factors in the discrimination of tonal patterns. I. Component frequency, temporal position, and silent intervals,'' J. Acoust. Soc. Am. **57**, 1175–1185.

Wright, B. A., and McFadden, D. (**1990**). ''Uncertainty about the correlation among temporal envelopes in two comodulation tasks,'' J. Acoust. Soc. Am. **88**, 1339–1350.

The effects of signal duration on NoSo and NoSπ thresholds at 500 Hz and 4 kHz

Leslie R. Bernstein and Constantine Trahiotis
Surgical Research Center, Department of Surgery (Otolaryngology) and Center for Neurological Sciences, University of Connecticut Health Center, Farmington, Connecticut 06030

A two-interval, two-alternative temporal forced-choice procedure was used to measure NoSo and NoSπ masked thresholds with 500-Hz and 4-kHz tonal signals. The duration of the signal was either 10, 20, 40, or 320 ms. The maskers were 200-Hz-wide bands of Gaussian noise centered at the frequency of the signal and presented continuously. Decreasing the duration of the 500-Hz tonal signal resulted in a modest *increase* (1.5 dB or so) in the masking-level difference (MLD) measured between NoSo and NoSπ conditions. In contrast, decreasing the duration of the 4-kHz tonal signal resulted in a substantial *decrease* (4.5 dB or so) in the MLD. Comparisons of the data with thresholds predicted from analyses based on ''windows of temporal integration'' provided quantitatively acceptable accounts of the data. The data obtained in the NoSπ condition at 4 kHz, which are novel and were of primary interest, were well-accounted for in a statistical sense. However, there were small, but systematic, discrepancies between the predictions and the data. Those discrepancies, although small in magnitude, suggest that binaural temporal integration at high frequencies, where the envelopes of the stimuli convey the information, may be inherently different from both monaural temporal integration and binaural temporal integration at low frequencies. © *1999 Acoustical Society of America.* [S0001-4966(99)05203-0]

PACS numbers: 43.66.Dc, 43.66.Pn [DWG]

INTRODUCTION

In 1958, Blodgett *et al.* reported thresholds for detection of a 500-Hz tonal signal, masked by continuous broadband noise, as a function of the duration of the signal. The design of their study allowed them to determine whether differential changes in performance occur between stimulus conditions in which detection is mediated by binaural cues (e.g., NoSπ, NπSo) and stimulus conditions in which detection is mediated by monaural cues (e.g., NoSo, NmSm). Their principal finding was that reducing the duration of the signal below 15–20 ms or so produced slightly larger increases in threshold for the ''monaural'' conditions than for the ''binaural'' conditions. Green (1966) obtained a similar result using a broadband masker and a signal frequency of 250 Hz in that the MLD was larger for a 10-ms-long signal than for a 100-ms-long signal. Both Blodgett *et al.* and Green noted that the larger MLDs obtained at the shorter durations of the signal are consistent with the assumption that the ''critical band'' that is operative for binaural conditions is somewhat broader than that which is operative for monaural conditions. This interpretation was, no doubt, related to the fact that their stimuli were gated on and off with rise/decay times of only 0.5 ms. For such stimuli of very short duration, relatively less signal energy would be lost as a result of spectral ''splatter'' in the binaural conditions if the critical band were broader. As a consequence, the binaural ''temporal integration'' functions would be slightly more ''shallow'' as compared to their monaural counterparts.

Data obtained more recently by Kohlrausch (1986, 1990), who employed signal frequencies between 300 and 800 Hz, essentially replicated Blodgett *et al.*'s empirical findings and showed virtually the same differential effects of duration discussed above. Kohlrausch minimized spectral splatter by imposing 5-ms, linear rise/decay ramps on his shortest stimuli, which had a duration of 20 ms. Therefore, we interpret Kohlrausch's data as indicating that Blodgett *et al.*'s findings may not have been the result of differing spectral resolution across monaural and binaural processing. Rather, the observed differences may reflect differing temporal properties, rather than differing spectral properties, of the monaural and binaural systems (see Kohlrausch, 1990; Langhans and Kohlrausch, 1992).

We were especially interested in conducting similar experiments utilizing high-frequency signals in the NoSπ configuration. A comparison of such data collected at low and high frequencies would indicate whether temporal integration in binaural conditions differs for spectral regions where the salient binaural information is mediated by the *envelope* (for high signal frequencies) or by the full waveform including the fine structure (for low signal frequencies). In order to address these issues, we conducted an experiment in which we measured NoSo and NoSπ detection thresholds, as a function of the duration of the signal, for either low-frequency (500 Hz) or high-frequency (4 kHz) tonal signals masked by continuous narrow bands of Gaussian noise. In order to avoid spectral splatter, our gated signals and continuous maskers were identically filtered. When the frequency of the signal was 500 Hz, we were able to replicate Blodgett *et al.*'s (1958) and Kohlrausch's (1990) general findings. However, when the frequency of the signal was 4 kHz, we obtained *steeper* temporal integration functions in NoSπ as compared to NoSo conditions. This is the *opposite* of what was observed for these two conditions at 500 Hz. This interaction, between the effects of signal frequency and

monaural versus binaural processing, suggests that differences in temporal integration data obtained in NoSo vs NoSπ stimulus conditions cannot be explained by appealing to any single factor or mechanism.

I. EXPERIMENT

A. Procedure

We measured NoSo and NoSπ detection thresholds for 500-Hz or 4-kHz tones masked by 200-Hz-wide bands of Gaussian noise centered at the frequency of the signal. The noise maskers were generated by digitally filtering broadband Gaussian noise (TDT AP2) through a 480-tap finite impulse response (FIR) filter (TDT PD1) of the desired center frequency and bandwidth. This resulted in bands of noise having rejection rates in excess of 1700 dB/oct. The maskers were presented continuously at an overall level of 70 dB SPL. The tonal signals were also generated digitally, rectangularly gated, and passed through the same 200-Hz-wide FIR filter used to generate the maskers. This resulted in tonal signals which had 5-ms rise–decay ramps and equivalent rectangular durations of 10, 20, 40, and 320 ms.

A bandwidth of 200 Hz was chosen for the filter, through which all stimuli passed, because that bandwidth was (1) wide enough to pass all of the energy associated with our shortest duration (10 ms) signal, (2) narrow enough to yield a substantial MLD for a tonal signal having a frequency of 4 kHz, and (3) not much larger than the processing or critical bandwidth at 500 Hz. Our intent for including the third constraint was to guard against appreciable ''internal'' losses of signal energy stemming from the greater splatter of signal energy that would have occurred had a larger filtering bandwidth been employed (recall that the masker and signal were passed through the same bandpass filter). When the data are presented, it will be shown that this condition was fulfilled.

The stimuli were presented in a two-interval, two-alternative temporal forced-choice procedure. Each trial consisted of a 500-ms warning interval and two observation intervals. A visual display on a computer monitor marked each interval, began 20 ms prior to when the signal could occur, and remained on for the duration of the signal in that block of trials. Observation intervals were separated by 450 ms. The tonal signal was presented with equal *a priori* probability in either the first or second interval. Correct-answer feedback was provided via the computer monitor for approximately 400 ms after the listener responded.

For each listener, four- to seven-point psychometric functions were measured for each combination of signal frequency, interaural configuration, and duration. Values of signal-to-noise ratio (S/N) were chosen to ''bracket'' a d' value of 0.76 (approximately equal to 71% correct). A minimum of two 80-trial blocks was run for each value of S/N. Values of d' obtained for each S/N were averaged to yield a ''final'' psychometric function representing performance for that particular condition and listener. Psychometric functions were fit using the functional form $\log d' = \log m + k \log (S/N)$ to provide an estimate of threshold ($d' = 0.76$).

Testing began with the NoSπ condition at 4 kHz. One of the four signal durations (10, 20, 40, or 320 ms) was chosen at random and, for that signal duration, one 80-trial block was completed for each of the four to seven values of S/N to be used to construct the psychometric function. The values of S/N were also chosen in random order. After one 80-trial block was completed at each S/N, a second 80-trial block was completed at each S/N using a new random order. This process was repeated with another signal duration until all four durations had been tested in this manner. This same process was carried out for the NoSo condition at 4 kHz, followed by the NoSo and NoSπ conditions at 500 Hz, respectively. Finally, for two of the listeners, all four conditions were visited in reverse order yielding 320 trials (80 $\times 4$) per point for each psychometric function measured. The third listener was unable to participate in this further testing, and his psychometric functions were based on 160 trials per point. On rare occasions, it was necessary to test additional values of S/N when it became apparent that the final psychometric function would not bracket a d' of 0.76.

Stimuli were presented via TDH-39 earphones to three young adults with no evidence or history of hearing loss. During the experiments, the listeners were seated within single-walled IAC sound-attenuating booths. All listeners received extensive practice prior to the collection of data.

B. Results and discussion

Figure 1 displays the mean detection thresholds obtained as a function of signal duration, averaged across the three listeners. The error bars represent ± 1 standard error of the mean. The thresholds obtained in the NoSo and NoSπ conditions for the 500-Hz and 4-kHz signals are plotted in panels (a) and (b), respectively. The dashed, dotted, and solid lines represent predicted thresholds and will be discussed later. The inset in each panel displays the masking-level difference (MLD) obtained as a function of the duration of the signal. As expected, the thresholds obtained with the 500-Hz signal [panel (a)] increased as the duration of the signal was decreased from 320 to 10 ms. Linear regression analyses indicated that the slope of the line relating S/N at threshold to signal duration was -9.6 dB/decade for the NoSo condition, and -8.5 dB/decade for the NoSπ condition. As indicated in the inset, this difference in slope resulted in about a 1.5-dB *increase* in the MLD when the signal duration was reduced from 320 to 10 ms.

These findings, *considered only in terms of the overall change in the MLD* that occurred as the duration of the signal was decreased, are similar to those reported by Blodgett *et al.* (1958). However, the *patterning* of our data differs from the patterning of the data obtained in these earlier studies. Those investigators, who employed a broadband masker, obtained increases in the MLD only when the duration of the signal was less than 15–20 ms or so. The increases in the MLD they observed were the result of a relative ''steepening'' of the slope relating threshold to signal duration for the NoSo configuration, in comparison to the slope relating
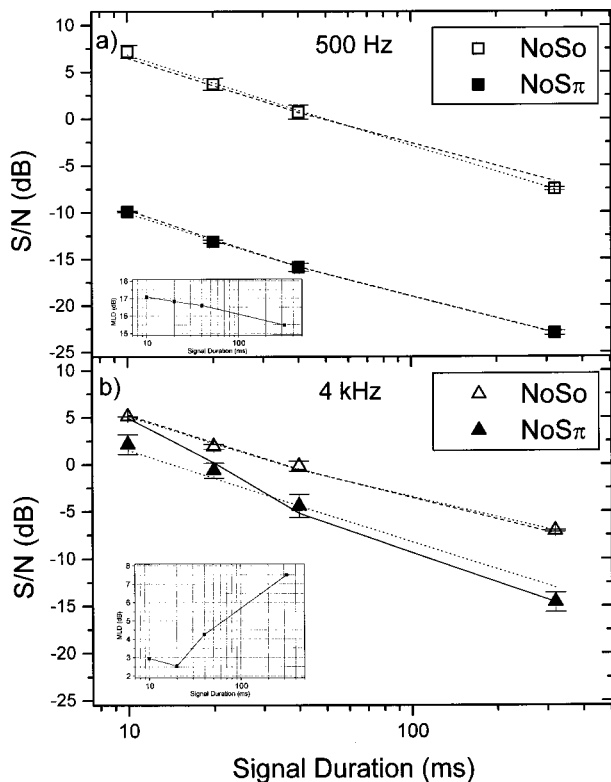
FIG. 1. Threshold S/N (in dB) as a function of the duration of the signal. Open and closed symbols represent data obtained with the NoSo and NoSπ configurations, respectively, for the 500-Hz [panel (a)] and 4-kHz [panel (b)] tonal signals. The data points represent the average across the three listeners. Error bars represent ±1 standard error of the mean. The inset within each panel displays the masking-level difference (MLD) obtained as a function of the duration of the signal. The dashed, dotted, and solid lines represent predicted thresholds derived from the analyses described in the text.

threshold to signal duration for the NoSπ configuration. In contrast, our data indicate that the MLD increased at an essentially constant rate as the duration of the signal was decreased.

The essentially linear increase in the MLD we observed as the duration of the signal was decreased does not appear to be amenable to explanations based on loss of signal energy resulting from spectral splatter in the NoSo condition. This is because the MLD increased even when the duration of the signal was decreased from 320 to 40 ms. In order for there to have been any appreciable loss of signal energy (which was confined to a 200-Hz band centered at 500 Hz), the width of the monaural critical band would have to be less than 25 Hz (the reciprocal of the 40-ms duration of the signal). Clearly, this is not the case.

This is not to say that spectral splatter could not have affected the MLD obtained with our 10-ms signal. For that duration, loss of energy resulting from spectral splatter would occur if the monaural critical band at 500 Hz were appreciably smaller than 100 Hz. Then, consistent with Blodgett *et al.*'s (1958) argument, the MLD would be expected to increase if the *binaural* critical band were larger than 100 Hz. However, some recent investigations (e.g., Kohlrausch, 1988; Kollmeier and Holube, 1992; van der Heijden and Trahiotis, 1998; Holube *et al.*, 1998) indicate

that the width of the critical band that is operative at 500 Hz for *both* monaural and binaural processing conditions is about 80 to 150 Hz wide. The data in panel (a) indicate no local relative increase in NoSo thresholds for the shortest signal durations. Therefore, they are consistent with the notion that there is but one size of underlying critical bandwidth mediating the processing of stimuli presented in NoSo and NoSπ conditions. Thus, rather than the differential effects of duration being mediated in an indirect fashion by spectral factors, our data appear to be consistent with there being differences in *temporal* processing, *per se*. This conclusion echoes arguments made recently by Kohlrausch (1990), who also emphasized the essential equivalence of monaural and binaural critical bandwidths while discussing data concerning binaural temporal integration.

Perhaps the differences between Blodgett *et al.*'s (1958) data and ours are somehow related to the fact that they employed a broadband masking noise whereas we (1) employed a narrow-band masking noise, and (2) gated the signal through the same filter used to produce the masker. Independent of the differences in the bandwidth of the stimuli in the two investigations, it seems worthwhile to note that off-frequency listening was *not* a factor in either experiment. This is so because (1) Blodgett *et al.*'s use of a broadband masker would only have resulted in poorer signal-to-noise ratios in off-frequency "channels," and (2) the spectra of our signals were limited to the nominal bandwidth of our maskers. These two experiments, therefore, are distinct from and should be carefully differentiated from related experiments reported by Wightman (1971). Wightman employed stimuli which were explicitly chosen to evaluate the interplay of spectral splatter and off-frequency listening under monaural- and binaural-processing conditions.

The data obtained at 4 kHz [panel (b)] are quite different from those obtained at 500 Hz. While both NoSo and NoSπ thresholds increased as the duration of the signal was decreased, linear regression analyses indicated that the slope of the line relating S/N at threshold to signal duration was −7.9 dB/decade for the NoSo condition, and −11.3 dB/decade for the NoSπ condition. Consequently, as shown by the inset, the MLD *decreased* by about 4.5 dB as the signal duration was reduced from 320 to 20 ms. Overall, the striking feature of the data in Fig. 1 is that *decreasing* the duration of the signal results in *increases* in the MLD at 500 Hz and *decreases* in the MLD at 4 kHz.

Figure 2 displays the data from Fig. 1 "normalized" by plotting the thresholds obtained in NoSo conditions (open symbols) and NoSπ conditions (closed symbols) *re* the thresholds obtained with a signal duration of 320 ms in that same condition. This manner of plotting the data makes it apparent that (1) thresholds in the NoSo condition increase more *slowly* with decreases in duration of the signal for 4-kHz tones than for 500-Hz tones, and (2) thresholds in the NoSπ condition increase more *quickly* with decreases in duration of the signal for 4-kHz tones than for 500-Hz tones. As a consequence, the differential changes in the magnitudes of the MLDs that occur as the duration of the signals is decreased for 500-Hz vs 4-kHz tones appear to result from factors affecting *both* monaural and binaural processing.
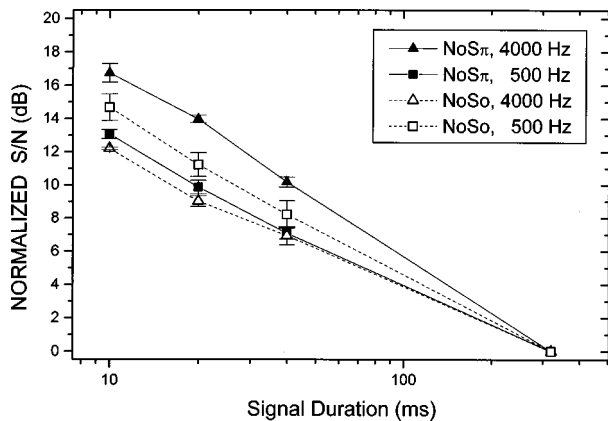
FIG. 2. ''Normalized'' threshold as a function of the duration of the signal. The thresholds obtained in the NoSo conditions (open symbols) and NoSπ conditions (closed symbols) are plotted re the thresholds obtained with a signal duration of 320 ms in that same condition.

II. GENERAL DISCUSSION

A. Analyses of the data

1. NoSo thresholds: Integration of power

Our finding that NoSo thresholds for 4-kHz tonal signals increased at a slower rate as the duration of the signal was decreased, as compared to their counterparts at 500 Hz, is consistent with other studies concerned with temporal integration when monaural cues mediate performance (e.g., Plomp and Bouman, 1959; Watson and Gengel, 1969). In fact, our NoSo thresholds at each frequency are well fit by the form of the function suggested by Plomp and Bouman

$$y = -10 \log_{10}(1 - e^{-t/\tau}),$$

where t is the duration of the signal, τ is the ''time constant'' and y (in dB) is the *increase* in threshold relative to a signal of infinite duration.

In order to fit our NoSo data, we used the average value of the time constants found by Plomp and Bouman at 500 Hz (330 ms) and 4 kHz (250 ms), respectively. In addition, in accordance with their findings, we assumed that 2000 ms represented an effectively ''infinite'' duration for the integration of auditory information. Finally, we found the appropriate offset in dB that minimized the least-squared error. The fitted functions are shown in panel (a) of Fig. 1 by the dashed lines connecting the open squares (NoSo thresholds at 500 Hz) and in panel (b) of Fig. 1 by the dashed lines connecting the open triangles (NoSo thresholds at 4 kHz). More than 99% of the variance in our NoSo data was accounted for by the predicted values.

We also compared our data to those published recently by Oxenham (1998). He measured monaural thresholds for detection of a 6-kHz tonal signal temporally centered within a 500-ms masker, as a function of the duration of the signal and the bandwidth of the masker. Plotting our data together with Oxenham's revealed that our thresholds paralleled those he obtained for masker bandwidths of 300, 600, and 1200 Hz. Our data do not display the ''flattening'' of the function relating threshold to signal duration that Oxenham observed when he employed masking bandwidths of 120 Hz or less. For those small bandwidths, Oxenham suggested that the de-

tection of short signals could be mediated by changes in the ''modulation spectrum'' produced by the addition of the signal to the noise. Therefore, to the extent that the slope relating threshold to signal duration is diagnostic, our data, like the data obtained by Oxenham for his larger bandwidths, do not appear to require consideration of the modulation spectrum for their interpretation. Thus, overall, it appears that the patterning of the data obtained under NoSo conditions conforms well to that observed by others in prior studies. Consequently, those data provide a valid reference for estimating the masking-level difference at 500 Hz and 4 kHz.

2. NoSπ thresholds: A trading relation between $\Delta\rho$ and duration

We now turn our attention to the data obtained in the NoSπ conditions, which are of primary interest. In order to interpret those data, we began by assuming that the thresholds obtained in this study at 500 Hz reflected a ''trading'' relation between the duration of the Sπ signal and the amount of decorrelation ($\Delta\rho$) of the diotic masking noise required at threshold. That type of reciprocal relation between duration and $\Delta\rho$ was found recently by Bernstein and Trahiotis (1997), who measured correlation discrimination and NoSπ detection. The earlier study differed from the present one in that both signals and maskers were gated and were of equal duration save for short masker ''fringes'' at the onset and the offset of the stimuli. An important consequence of employing gated signals and maskers of essentially equal duration, while varying the duration of the stimuli, is that signal-to-noise ratio is virtually unaffected by the length of any ''window of integration'' presumed to be involved in the processing of the stimuli. Put differently, for the stimuli in the earlier study, regardless of the length of window of integration, signal-to-noise ratio would not vary with duration.

Our first analysis of the NoSπ data obtained in the present study with a *continuous* masker was predicated on the assumption that changes in threshold result from a trading relation between $\Delta\rho$ and duration (rather than from any ''window-related'' changes in signal-to-noise ratio). Specifically, we employed the form of the function suggested by Plomp and Bouman (1959) to relate $\Delta\rho$ to the duration of the signal. This type of analysis is tantamount to assuming that the listeners based their decisions exclusively on information available during the presentation of the signal. A second, independent analysis of the current data that does include window-related effects will be presented later.

In order to account for the NoSπ thresholds obtained at 500 Hz, we first transformed them to measures of $\Delta\rho$ using the equation $\Delta\rho = 1 - [(1 - S/N)/(1 + S/N)]$ (see Durlach *et al.*, 1986), where ρ refers to the normalized correlation of the NoSπ *waveform*. Then, we fit the data employing the Plomp and Bouman equation while using $10 \log \Delta\rho$ as the dependent variable. The time constant associated with this fit was 273 ms. Transformations of the fits to the data back to S/N (in dB) are plotted in Fig. 1 as the dashed line connecting the solid squares. The use of $\Delta\rho$ as the underlying dependent variable yields an excellent fit to

the data, and accounts for more than 99% of their variation with duration.

Accounting for the NoSπ thresholds at 4 kHz turned out to be a much more complicated (and illuminating) endeavor. In order to fit the data in a manner parallel to that employed at 500 Hz, thresholds, in S/N, were again transformed to values of $\Delta\rho$. Now, however, $\Delta\rho$ reflected changes in the normalized correlation of the *envelope* of the NoSπ waveform (van de Par and Kohlrausch, 1995; Bernstein and Trahiotis, 1996a). This proved to be problematic. As can be seen from the data in panel (b) of Fig. 1, the S/N required to reach threshold in the 4-kHz, NoSπ condition was near or above 0 dB for signal durations of 20 and 10 ms, respectively. This outcome appears to be incompatible with our basic assumption (used successfully to account for 500-Hz thresholds) that detection thresholds reflect a ''trading relation'' between $\Delta\rho$ and the duration of the signal. The incompatibility stems from the fact that, for a tonal signal in Gaussian noise, the envelope-based $\Delta\rho$ is a *nonmonotonic* function of S/N and $\Delta\rho$ is *maximal* for S/N in the vicinity of 0 dB (van de Par and Kohlrausch, 1995; Bernstein and Trahiotis, 1996a). In addition, $\Delta\rho$ decreases monotonically and, essentially, symmetrically with either increases or decreases of S/N about that point. Because this is so, the increases in S/N above 0 dB that were required as the duration of the signal was decreased from 20 to 10 ms are not interpretable as increases in $\Delta\rho$. Therefore, given the actual S/N values required to reach threshold as a function of duration, the assumption that the listeners base their decisions solely on changes of interaural correlation of the envelope that are inversely related to duration is untenable.

One interpretation of this outcome is that the listeners could have based their decisions, at least in part, on some cue other than $\Delta\rho$. In fact, after noting that the NoSπ thresholds obtained with the 10- and 20-ms-long signals at 4 kHz were only 2 dB or so below their NoSo counterparts, we realized that the listeners' performance in the NoSπ condition may have been mediated by a *combination* of monaural and binaural cues. In order to test this hypothesis, we computed the S/N required to reach threshold, at each signal duration, under the assumption that the d' values representing detectability under monaural (d'_{mon}) and binaural (d'_{bin}) conditions combined independently to yield ''d'_{comb}'' (i.e., $d'_{comb} = \sqrt{d'^2_{mon} + d'^2_{bin}}$) values associated with the thresholds that we actually measured.

For a particular duration of the signal, an iterative process was begun by choosing a starting value of S/N. The next step was to find the value of d'_{mon} corresponding to that starting value of S/N. This was accomplished by simply interpolating along a psychometric function fitted to the NoSo data from all three listeners at that duration. To illustrate the procedure, let us assume the duration of the signal to be 20 ms and the value of S/N to be 0.2 dB, the actual threshold S/N predicted from the procedure. By using this value, no further iterations are necessary. The value of d'_{mon} corresponding to this S/N, obtained from the psychometric function, was 0.49.

In order to obtain d'_{bin} let us assume that the 7.5-dB MLD obtained at a duration of 320 ms means that the NoSπ thresholds for that duration reflect, essentially, the use of only binaural cues. Next, the *obtained* threshold S/N at this duration (-14.6) is transformed to its corresponding *envelope-based* $\Delta\rho$, which is 0.032. Then, beginning with this value of $\Delta\rho$, we use temporal integration functions of the form specified by Plomp and Bouman (1959) in order to estimate the values of $\Delta\rho$ that would be required to reach threshold at the shorter signal durations *if only binaural cues were operative*. For this example, we use a time constant of 450 ms in the Plomp and Bouman equation because that value, when used in the manner being described, yields the best overall fit to the NoSπ detection thresholds as a function of duration.

From the temporal integration function, we find that the $\Delta\rho$ required to reach threshold (71% correct, $d' = 0.76$) for the 20-ms-long Sπ signal serving as our exemplar is 0.38. Consequently, our analysis reveals that if only binaural cues were operative, a $\Delta\rho$ of 0.38 would correspond to $d' = 0.76$.

Next, the *actual* envelope-based $\Delta\rho$ produced by our exemplar S/N of 0.2 dB, which is 0.27, is used, along with the *predicted* $\Delta\rho$ and the slope of the psychometric function relating d' to $\Delta\rho$, in order to derive the d'_{bin} that corresponds to a $\Delta\rho$ of 0.27. The slope of the psychometric function used is the slope of the empirical psychometric function relating d' to S/N ($\Delta\rho$) at a duration of 320 ms. That is, we assume that the slopes of the psychometric functions relating d' to $\Delta\rho$, but not their intercepts, are independent of duration. That assumption is made in lieu of knowledge concerning whether and to what degree NoSπ thresholds for short-duration stimuli are ''contaminated'' by the listeners' use of monaural cues, which is precisely the goal of the analysis. We find that d'_{bin}, for our example, is 0.58. Finally, using this value of d'_{bin} and the value of d'_{mon} (0.49), which was discussed above, we compute d'_{comb} (i.e., $\sqrt{d'^2_{mon} + d'^2_{bin}}$) to be 0.76, the value of d' corresponding to threshold performance in our experiment. No further iteration is necessary because, for purposes of this explanation, we used the value of predicted S/N that we knew yields our targeted level of performance ($d' = 0.76$).

Using the illustrated approach iteratively for data obtained at each duration, it was possible to estimate the degree to which actual performance depended upon binaural cues, monaural cues, or their combination. It is important to understand that the predicted thresholds were derived principally from relations within the empirical data. The only ''free parameter'' utilized was the Plomp and Bouman-derived time constant used to define the ''binaural'' temporal integration function. Thus, the Plomp and Bouman-derived time constant was used as a means toward an end, and the value of the time constant, *per se*, was not paramount.

The solid line in panel (b) of Fig. 1 represents thresholds predicted using the combination-of-cues procedure described above. The value of the time constant utilized was 450 ms. Predictions made using time constants differing by a factor of two or so resulted in predicted thresholds differing by only about 1 dB. Therefore, the predictions are quite robust.

The predicted thresholds are close to those obtained (solid triangles) and account for more than 94% of the variability in the data. Nevertheless, the fact that the obtained

threshold is almost 3 dB *below* the predicted threshold at a signal duration of 10 ms, in our judgment, is important and casts doubt on the adequacy of the underlying assumptions.[1]

In an effort to improve the fit to the NoSπ thresholds at 4 kHz, we explored several modifications of the manner by which predictions were made. They included (1) relaxing the assumption that d'_{mon} and d'_{bin} add independently by making predictions while varying their angle of vectorial addition, (2) recomputing values of $\Delta\rho$ after subjecting the stimuli to half-wave, square-law rectification and low-pass filtering (Bernstein and Trahiotis, 1996b), and (3) recomputing values of $\Delta\rho$ after adding interaurally uncorrelated noise which served to change the shape of the function relating S/N to $\Delta\rho$. None of these modifications removed the overestimation of NoSπ thresholds for the 10-ms-long signal. Therefore, at this time, we are unable to account satisfactorily for the data obtained at 4 kHz in the NoSπ condition under the general assumptions that (1) listeners base their decisions on $\Delta\rho$ computed during the presentation of the signal, (2) there exists a "trading relation" between $\Delta\rho$ and the duration of the signal, and (3) performance is mediated by a combination of binaural and monaural cues.[2]

3. NoSo and NoSπ thresholds: A fixed-duration temporal window

A second, independent analysis of the data was undertaken in an attempt to provide a better account of the data. The purpose of this analysis was to determine whether all of the thresholds could be accounted for by assuming that the listeners process the stimuli while utilizing a temporal window of suitable and *fixed* duration. Under this assumption, the increases in threshold that occur as the duration of the signal is decreased stem from inherent decreases in signal-to-noise ratio that result from integrating masker power before and after the presentation of the signal.[3]

Our strategy was to determine how well the data could be fit without utilizing complicated functions having several parameters. Thus, we attempted to account for the data with a double-sided, symmetric, exponential temporal window. We found that more than 99% of the variance in the data obtained in the NoSo conditions was accounted for by an exponential window a having a time constant of 494 ms for the thresholds obtained at 500 Hz, and by an exponential window having a time constant of 103 ms for the NoSo thresholds obtained at 4 kHz. Those predicted thresholds are represented in Fig. 1 by the dotted lines connecting the open squares [panel (a)] and the dotted lines connecting the open triangles [panel (b)], respectively. Note that the predictions of NoSo thresholds from this analysis coincide almost exactly with the predictions obtained in the first analysis.

We found that more than 99% of the variance in the NoSπ thresholds at 500 Hz could be accounted for by an exponential window having a time constant of 143 ms. The predicted thresholds are represented by the dotted line connecting the closed squares [panel (a)]. Once more, the predicted thresholds from this analysis coincide almost exactly with the predicted thresholds obtained in the first analysis.

By far the most interesting, and perhaps the most important, aspect of this analysis became apparent when we attempted to account for the NoSπ thresholds obtained at 4 kHz with our approach using a fixed-duration temporal window. We found that 98% of the variance in the data could be accounted for by a temporal window having a time constant of 700 ms. The predictions are shown by the dotted line, which statistically and visually provides an adequate account of the data (closed triangles).

Once again, however, we feel compelled to question the validity of the fitted function. The indication that there is a problem is that the slope of the line representing the fitted function is *slightly more shallow* than the slope of −11.3 dB/decade that characterizes the best-fit straight line through the data. In fact, *no* reasonable window applied to changes in signal-to-noise ratio and having a finite time constant could yield predictions having a slope steeper than −10 dB/decade (i.e., we exclude windows constructed such that some part of the temporal portion of the stimulus containing the signal is weighted to a lesser extent than the portion which contains only the masker). Therefore, despite the fact that a statistically acceptable fit was attained for the NoSπ thresholds at 4 kHz, we are not yet willing to accept the notion that rises in threshold with decreases in signal duration can be explained on the basis of decreases in the effective signal-to-noise ratio within a finite window. We prefer to defer judgment until more high-frequency, binaural temporal integration data become available through experiments conducted by us and others using a variety of stimulus conditions.

One other issue deserves consideration. We believe, on logical grounds, that the listeners' decisions were not based on a combination of monaural and binaural cues at the output of the fixed temporal windows assumed in our second analysis. If such a combination of monaural and binaural cues were used, then one would expect the slope of the best-fit line connecting the NoSπ thresholds at 4 kHz to be *shallower than* −10 dB/decade. That expectation follows from the fact that a slope of −10 dB/decade describes performance under the assumption that a constant amount of the binaural cue (within our analysis, effective signal-to-noise ratio) mediates performance at each duration. Now, if the listener were to use monaural cues at the shortest durations where the levels of the signals at threshold could support monaural detection, then thresholds should be *lower* than those expected on the basis of only binaural information. As a result, the slope of the best-fit line connecting the data points under those assumptions would be shallower than −10 dB/decade. As noted above, the slope of the best-fit line through the data is −11.3 dB/oct. Therefore, we believe that the data cannot be explained by the listeners' use of a combination of monaural and binaural cues in conjunction with an underlying fixed-duration temporal window.

In conclusion, it appears that temporal processing for binaural detection must be accounted for differently for high-frequency and low-frequency stimuli. These differences in temporal processing should be distinguished from differences in temporal processing for monaural and binaural detection as discussed by Kohlrausch (1986, 1990) and as observed in this study.

B. Other considerations

At this time, it is unclear whether, or to what extent, the frequency-related differences we found in binaural detection are a result of different aspects of the waveform that convey the binaural information at low and high frequencies. They could also result from differences in processing within (central) mechanisms that mediate binaural interaction at low and high frequencies or, perhaps, from other temporal-processing phenomena, such as ''binaural sluggishness.'' Of course, all three types of possibilities are not mutually exclusive.

Binaural sluggishness is commonly accounted for in terms of temporal windows whose time constants appear to be dependent upon the particular binaural cue being processed (interaural temporal disparities or interaural intensitive disparities) and/or the spectral locus of the stimuli (e.g., Grantham and Wightman, 1978, 1979; Grantham, 1984; Stern and Bachorski, 1983; Bernstein and Trahiotis, 1992). In fact, we believe that the temporal-integration windows we have assumed in the analysis of the NoSπ data obtained in this experiment are conceptually indistinguishable from the binaural temporal windows derived in experiments using maskers having interaural parameters that changed dynamically (e.g., Kollmeier and Gilkey, 1990; Holube et al., 1998; Culling and Summerfield, 1998). In order to understand this, note that the addition of an Sπ signal to a diotic masker produces changes in the interaural parameters of the compound stimulus. Those changes are the binaural ''cues'' that mediate detection. Now, as the duration of the signal is decreased such that it becomes less than the nominal duration of the window itself, the magnitude of the binaural cues at the output of the temporal window must also decrease. Consequently, the temporal windows assumed to be operating across the diverse tasks of interest appear to be functionally and conceptually equivalent.

Our suspicion is that differences in the magnitudes of the binaural ''time constants'' measured across the various tasks may reflect the influence of uncontrolled ''confounding'' factors that preclude direct measurement of the putative temporal window that describes the temporal resolution of the binaural system. Essentially the same view was recently discussed by Holube et al. (1998) in the context of experiments designed to measure auditory-filter bandwidths and time constants in monaural- and binaural-listening conditions. Those authors raised the possibility that measures of the ability of the binaural system to integrate information across time could be inextricably influenced by binaural sluggishness, per se, as well as by the spectral/temporal properties of the stimuli themselves. These important theoretical issues do not detract from the principal finding in this experiment that the integration of auditory information across time depends upon both the center frequency of the stimuli and whether monaural cues or binaural cues are being processed.

[1]Our colleague, Dr. Marcel van der Heijden, raised the question of whether the inability to account adequately for the threshold with a signal duration of 10 ms might be the result of there being an insufficient number of degrees of freedom within the envelope of the 10-ms-long, 200-Hz-wide stimulus to permit a meaningful estimate of the value of the normalized interaural correlation. A number of additional analyses revealed that the bandwidth-time product of the envelope yielded a sufficient number of degrees of freedom for that stimulus.

[2]We also considered whether we could derive a ''purely binaural'' temporal integration function for our purposes from data obtained by Nuetzel and Hafter (1976) and by McFadden and Moffit (1977). They measured listeners' ability to discriminate interaural temporal disparities (ITDs) for high-frequency signals, as a function of duration. Data obtained in both of those studies indicated that thresholds declined when duration was increased from 50 to 500 ms. We decided that using data from those two studies to derive a temporal integration function to be used to fit our data was probably not a valid exercise. That conclusion was based on (1) the large range of interindividual differences observed in those studies, and (2) the questionable validity of casting their lateralization/ITD-discrimination data in terms of $\Delta\rho$, the dependent variable required for our analysis. It is tempting to infer that the fact that there are no references to studies of the MLD as a function of duration (including the classic study of Blodgett et al., 1958) in the reports of Nuetzel and Hafter and McFadden and Moffit indicates that those authors also viewed their lateralization/ITD-discrimination data as not being comparable to the earlier MLD detection data.

[3]It is important to understand that this type of model cannot be applied to our earlier study employing pulsed signals and maskers. The reason is that the duration of the masking noise in the former study was only very slightly longer than the duration of the signal. One would also have to postulate the presence of a continuously present, additive, internal noise having a magnitude approximating the magnitude of the external noise. That, to us unrealistic, level of internal noise is required in order to account for the -3 dB per doubling nature of the decline in threshold with duration. Furthermore, neither set of mechanisms assumed to operate in our two, independent analyses could account for what have been termed ''forward/backward masker fringe effects'' on the MLD (McFadden, 1966; Robinson and Trahiotis, 1972; Trahiotis et al., 1972; Kohlrausch, 1986), wherein NoSπ thresholds decrease as the duration of the (especially forward) masker fringe is increased.

Bernstein, L. R., and Trahiotis, C. (**1992**). ''Detection of antiphasic sinusoids added to the envelopes of high-frequency bands of noise,'' Hearing Res. **62**, 157–165.

Bernstein, L. R., and Trahiotis, C. (**1996a**). ''On the use of the normalized correlation as an index of interaural envelope correlation,'' J. Acoust. Soc. Am. **100**, 1754–1763.

Bernstein, L. R., and Trahiotis, C. (**1996b**). ''The normalized correlation: Accounting for binaural detection across center frequency,'' J. Acoust. Soc. Am. **100**, 3774–3784.

Bernstein, L. R., and Trahiotis, C. (**1997**). ''The effects of randomizing values of interaural disparities on binaural detection and on discrimination of interaural correlation,'' J. Acoust. Soc. Am. **102**, 1113–1120.

Blodgett, H. C., Jeffress, L. A., and Taylor, R. W. (**1958**). ''Relation of masked threshold to signal-duration for various interaural phase-combinations,'' Am. J. Psychol. **71**, 283–290.

Culling, J. F., and Summerfield, Q. (**1998**). ''Measurements of the binaural temporal window using a detection task,'' J. Acoust. Soc. Am. **103**, 3540–3553.

Durlach, N. I., Gabriel, K. J., Colburn, H. S., and Trahiotis, C. (**1986**). ''Interaural correlation discrimination: II. Relation to binaural unmasking,'' J. Acoust. Soc. Am. **79**, 1548–1557.

Grantham, D. W. (**1984**). ''Discrimination of dynamic interaural intensity differences,'' J. Acoust. Soc. Am. **76**, 71–76.

Grantham, D. W., and Wightman, F. L. (**1978**). ''Detectability of varying interaural temporal differences,'' J. Acoust. Soc. Am. **63**, 511–523.

Grantham, D. W., and Wightman, F. L. (**1979**). ''Detectability of a pulsed

tone in the presence of a masker with time-varying interaural correlation,'' J. Acoust. Soc. Am. **65**, 1509–1517.

Green, D. M. (**1966**). ''Interaural phase effects in the masking of signals of different durations,'' J. Acoust. Soc. Am. **39**, 720–724.

van der Heijden, M., and Trahiotis, C. (**1998**). ''Binaural detection as a function of interaural correlation and bandwidth of masking noise: Implications for estimates of spectral resolution,'' J. Acoust. Soc. Am. **103**, 1609–1614.

Holube, I., Kinkel, M., and Kollmeier, B. (**1998**). ''Binaural and monaural auditory filter bandwidths and time constants in probe tone detection experiments,'' J. Acoust. Soc. Am. **104**, 2412–2425.

Kohlrausch, A. (**1986**). ''The influence of signal duration, signal frequency and masker duration on binaural masking level differences,'' Hearing Res. **23**, 267–273.

Kohlrausch, A. (**1988**). ''Auditory filter shape derived from binaural masking experiments,'' J. Acoust. Soc. Am. **84**, 573–583.

Kohlrausch, A. (**1990**). ''Binaural masking experiments using noise maskers with frequency-dependent interaural phase differences. I. Influence of signal and masker duration,'' J. Acoust. Soc. Am. **88**, 1737–1748.

Kollmeier, B., and Gilkey, R. H. (**1990**). ''Binaural forward and backward masking: Evidence for sluggishness in binaural detection,'' J. Acoust. Soc. Am. **87**, 1709–1719.

Kollmeier, B., and Holube, I. (**1992**). ''Auditory filter bandwidths in binaural and monaural listening conditions,'' J. Acoust. Soc. Am. **92**, 1889–1901.

Langhans, A., and Kohlrausch, A. (**1992**). ''Spectral integration of broadband signals in diotic and dichotic masking experiments,'' J. Acoust. Soc. Am. **91**, 317–326.

McFadden, D. M. (**1966**). ''Masking-level differences with continuous and with burst masking noise,'' J. Acoust. Soc. Am. **40**, 1414–1419.

McFadden, D., and Moffitt, C. M. (**1977**). ''Acoustic integration for lateralization at high frequencies,'' J. Acoust. Soc. Am. **61**, 1604–1608.

Nuetzel, J. M., and Hafter, E. R. (**1976**). ''Lateralization of complex waveforms: Effects of fine-structure, amplitude, and duration,'' J. Acoust. Soc. Am. **60**, 1339–1346.

Oxenham, A. J. (**1998**). ''Temporal integration at 6 kHz as a function of masker bandwidth,'' J. Acoust. Soc. Am. **103**, 1033–1042.

van de Par, S., and Kohlrausch, A. (**1995**). ''Analytical expressions for the envelope correlation of certain narrow-band stimuli,'' J. Acoust. Soc. Am. **98**, 3157–3169.

Plomp, R., and Bouman, M. A. (**1959**). ''Relation between hearing threshold and duration for pure tones,'' J. Acoust. Soc. Am. **31**, 749–758.

Robinson, D. E., and Trahiotis, C. (**1972**). ''Effects of signal duration and masker duration on detectability under diotic and dichotic listening conditions,'' Percept. Psychophys. **12**, 333–334.

Stern, R. M., and Bachorski, S. J. (**1983**). ''Dynamic cues in binaural perception,'' in *Hearing—Physiological Bases and Psychophysics*, edited by R. Klinke and R. Hartmann (Springer, New York).

Trahiotis, C., Dolan, T. R., and Miller, T. E. (**1972**). ''Effect of 'backward' masker fringe on the detectability of pulsed diotic and dichotic tonal signals,'' Percept. Psychophys. **12**, 335–338.

Watson, C. S., and Gengel, R. W. (**1969**). ''Signal duration and signal frequency in relation to auditory sensitivity,'' J. Acoust. Soc. Am. **46**, 989–997.

Wightman, F. L. (**1971**). ''Detection of binaural tones as a function of masker bandwidth,'' J. Acoust. Soc. Am. **50**, 623–636.

A signal detection analysis of auditory-frequency discrimination in the rat

Sanjiv K. Talwar and George L. Gerstein
Department of Neuroscience, A-304 Richards Building, University of Pennsylvania, Philadelphia, Pennsylvania 19104

The frequency-discrimination behavior of rats in a simple go/no-go task was analyzed using the theory of signal detection. Discrimination acuity was studied and the receiver operating characteristic (ROC) was generated in subjects by varying the reinforcement schedule and signal probability. The detectability indices d', A', and sensitivity index (SI) and response-bias indices B'' and responsivity index (RI) were used to describe behavior. A' gave the most suitable psychometric functions while RI best described response-bias behavior. Weber ratios were 6.25%±0.23% at 5 kHz in three subjects. The best method to obtain the ROC was to vary the probability with which subjects were reinforced. The ROC in two subjects demonstrated classical forms; in another subject, the function was asymmetric to the extent that detectability was not independent of response bias. Subjects altered their decision criterion in reporting a signal from trial to trial depending on previous trial events. On any given trial, subjects made a decision in one of several "decision states." Variables that influenced decision states included previous reinforcement and timeouts. The data indicate that timeouts may not be a useful feature in go/no-go tasks. The identification of multiple-decision states within a single behavioral session is a convenient method to generate the ROC without expressly manipulating experimental conditions. © *1999 Acoustical Society of America.* [S0001-4966(99)01802-0]

INTRODUCTION

Since the late 1950s and early 1960s, the theory of signal detection (SDT, Green and Swets, 1966) has won an important place in the psychological literature. During this period, SDT has successfully been used to model the process of decision making in psychoacoustic studies in human beings. In general, SDT techniques that have been used in humans have, in comparison to the methods of classical psychophysics, more adequately described the performance of subjects in auditory psychophysical tasks. The theory itself has broad application; it is not only concerned with sensory and perceptual processes, but also with recall and recognition memory and discrimination learning (Swets, 1996).

Judging from the literature though, the applicability of SDT to animal behavior has been very unevenly explored. Researchers in memory have adapted the theory to good effect in animal models (see Banks, 1970; White *et al.*, 1996); so also have experimenters in psychopharmacology (e.g., Katz, 1988; Sahgal, 1987). Surprisingly, however, SDT is seldom invoked in studies which should be considered as a natural application of the theory: the study of animal sensory-discrimination ability, especially those involving the auditory system. For instance, investigators have continued to use the methods of classical threshold theory in preference to SDT for investigating auditory-discrimination acuity, despite the evidence that has been adduced to demonstrate its inadequacy (Swets, 1996). One important reason for this is that standard SDT techniques are time consuming and difficult to apply in animal psychophysics (Long, 1994; Burdick, 1979). Nonetheless, a few discrimination acuity studies in animal subjects have been done using SDT methodology, and their authors have been unanimous in their recognition

of the potential usefulness of the method (Blough, 1967; Clopton, 1972; Hack, 1963; Marston, 1996; Terman, 1970).

The present study seeks to examine further the applicability of signal-detection analysis to animal auditory-discrimination behavior. Specifically, it seeks to characterize the frequency-discrimination behavior of the white rat, and to study some procedural variables that effect it, using signal-detection methods and a simple yes–no operant procedure that is easy to implement.

A. The theory of signal detection

Discrimination studies usually require subjects to distinguish between two stimuli S+ and S− that typically differ on only one stimulus dimension—for example, tones of different frequencies. In such experiments, in a given stimulus presentation or trial, any one of four responses is possible: "yes" to S+ (hit); "yes" to S− (false alarm); and their behavioral complements: "no" to S+ (miss); "no" to S− (correct rejection). SDT essentially seeks to model the decision processes behind making such discriminations and is based on statistical decision theory developed in the 1950s (Peterson *et al.*, 1954; Green and Swets, 1966). Briefly, SDT suggests that the presentation of a stimulus causes a sensory state which has a Gaussian distribution; two similar stimuli (S+ and S−) have overlapping distributions (of equal variance) whose means are separated by an amount proportional to the "detectability" of the S+ (signal) from the S−. Due to the overlap of sensory states caused by the two stimuli, a subject can sometimes be unsure if a stimulus is S+ or S−. SDT theorizes that a subject discriminating S+ from S− does so by basing decisions on a (subjective) response crite-

rion that can depend on experimental conditions; sensations exceeding this criterion are reported as S+ and those below, as S−. According to this model, even though the signal remains unchanged, different data points ($[x,y]$=[false-alarm probability, hit probability]) can be obtained across experimental sessions if the location of the observer's response criterion is made to vary. When hit probabilities are plotted against false-alarm probabilities, these data describe a characteristic curve (the receiver operating characteristic, or ROC) whose form is dictated by the underlying distribution (see Fig. 4 for example ROCs). The ROC thus represents an isosensivity condition with all points on the curve representing the same signal detectability without regard to the particular conditions under which observations are made. The specific location of a point on an ROC is taken as the ''response bias'' and reflects the location of the response criterion. Signals of different strengths produce different ROCs that are parameterized by its detectability.

If the ROCs predicted by SDT provide a reasonably good fit to experimental data, we can say that the model is consistent with discrimination behavior. An easy way to evaluate this fit is to plot hit- and false-alarm probabilities on probability scales (i.e., on coordinate scales that linearly space the corresponding normal deviates, or z score). Theoretical ROC curves become straight lines of unit slope when plotted on such scales. Data that are not linear cannot be in accord with the normal distribution assumption, while a non-unit slope implies unequal variance; such data can more easily be explained by assuming other underlying distributions instead of the Gaussian distribution hypothesized by classical SDT. Experimentally, the ROC may be obtained by attempting to sufficiently alter the response bias of an observer across experimental sessions. Several factors can influence response bias: these include the cost vs benefit of a decision and the relative frequency with which the S+ occurs. Internal factors such as motivation and innate drive to make a particular response can play a confounding role, especially in animal subjects, for which it can be difficult to control. Although the theoretical ROC may be an idealization of real-world discrimination behavior, the data, at least in humans, do show many of its characteristics and have been obtained in many situations (see Swets, 1996); the data usually plot linear on double probability scales, although the equal-variance assumption is often not supported. In animals, the business of obtaining complete ROC curves by manipulating response bias seems to be much more difficult, although ROC curves have been obtained in the pigeon, monkey, goldfish, and rat as well (Blough, 1967; Clopton, 1972; Hack, 1963; Marston, 1996).

The fact that both signal sensitivity and response bias are separately reflected in ROC curves provides a means to measure signal detectability uncontaminated by experimental conditions. Over the last few decades, a number of behavioral indices have been suggested that provide an indication of the detectability of a stimulus as well as the degree of response bias (see Swets, 1996). The original measure of detectability proposed was the parametric index d', which represents the distance between the means of the Gaussian S+ and S− distribution in standard-deviation units. The cor-

responding bias measure, β, is the ratio of the ordinates of the two distributions at the point of the subject's (hypothesized) decision criterion. These values can be calculated from a table of normal distributions (Green and Swets, 1966). However, empirical data do not support some of the more restrictive assumptions regarding the nature of the underlying distributions behind the ROC; thus, it may sometimes be preferable to use nonparametric indices to measure behavior. Such indices are based on the geometry of the ROC and are available in mathematical form; for example, a commonly used measure of detectability is the index A', which represents the area under the ROC (Pollack and Norman, 1964; Grier, 1971). A similar detectability measure is the ''sensitivity index'' (SI) (Frey and Colliver, 1973). Corresponding measures for response bias are B'' (Hodos, 1970; Grier, 1971) and the ''responsivity index'' (RI) (Frey and Colliver, 1973). It should be noted that all behavioral indices are derivable from the hit- and false-alarm probabilities of a single experimental session because, in fact, they assume the existence of the ROC in all subjects. It follows that the knowledge of the complete ROC is not essential for measuring detectability, although it is of benefit if specific underlying distributions need to be modeled or if knowledge of the best-fitted function is desired.

Discrimination studies using SDT in animal subjects usually employ discrete yes–no trial operant procedures in which a subject is required to decide which of two alternatives is presented [a rating procedure has been used in pigeons and a variant of the yes–no method in rats (Blough, 1967; Marston, 1996)]. An ideal yes–no procedure might incorporate a ''two lever'' paradigm in which responses to S+ and S− are different, with a response on one lever taken as yes while a response on the other lever is taken as no. In this paradigm, the consequences of responses can be made equal: hits and correct rejections are both rewarded, while misses and false alarms are punished. Since responses to S+ and S− are the same, and their consequences symmetrical, this paradigm might help to minimize response bias. The procedure seems to provide good stimulus control and it may be relatively easy to manipulate response bias to obtain the ROC—as has been done, for example, in monkeys (Clopton, 1972). Unfortunately, however, this sort of task requires long training times (Burdick, 1979). A simpler paradigm is one that incorporates a go/no-go structure in which subjects learn to make a ''go'' response to S+ and withhold response to S−. Usually, only the go response to S+ is rewarded while a false alarm is punished with a timeout; a miss or a correct rejection has no consequences. In this report, we employed this straightforward task to deem its effectiveness for a signal-detection study of frequency-discrimination behavior in the rat.

I. METHOD

A. Subjects

Eight female albino wistar rats (subjects RN14–RN16; RN21–RN25) obtained from Charles River Co. served in the study. At the start of training, subjects RN21 to RN25 were experimentally naive young adults each 250–300 g in

weight, while subjects RN14/15/16 had been previously trained in a modified go/no-go procedure for the study of frequency-difference limens (Talwar and Gerstein, 1998). The rats were housed in pairs, in Plexiglas cages (20 $\times$10$\times$10 in.), and were maintained in a 12-h artificial-light cycle with behavioral data being gathered during the dark cycle. Subjects had free access to food but water access was restricted. Water rewards were available in the operant chamber. At the end of the day, subjects had ten min free access to water to make up any acute water deficits. Subjects were trained/tested daily. Under this regimen, our rats maintained 80%–90% of their *ad libitum* weight. The care and use of animals in this study conformed to the NIH Guide for Care and Use of Laboratory Animals (revised 1987).

B. Apparatus

The operant chamber was a sound-transparent cage suspended from the ceiling of a double-walled anechoic, sound-attenuated room (IAC, Bronx, NY). The walls of the operant cage (12$\times$10$\times$10 in.) were constructed with slim metal bars (1/16-in.) with a 1/2-in. wire-mesh floor and ceiling (wire diameter 1/32 in.). At the center of one wall of the cage, 4 in. above the floor, was affixed a nosing hole with a photoelectric sensor. Below the nosing hole, a metal spout and small trough delivered water reinforcement; a solenoid valve controlled its delivery. Sound stimuli were presented from a loudspeaker placed above the nosing hole making an angle of 60 deg with the cage floor. On the left wall, at its center, a lever was affixed 2 in. from the floor.

All behavioral events were supervised by a PC interfaced to the acoustical and behavioral manipulanda through an appropriate I-O card (National Instruments, lab PC+) and behavioral interface (Coulbourn, universal environment interface). Timing, amplitude, and frequency of auditory stimuli were under software control. Continuous sine waves from a voltage variable system (VVS model 404, <1% THD) oscillator were shaped to have a rise and fall time of 5 ms. The frequency of the generated pure tones were monitored by a Hewlett Packard electronic counter (#5512 A), fed into a Crown D-75 power amplifier, an attenuator, and then into the loudspeaker (Realistic #40-1377). All sound stimuli were delivered at the sound-pressure level 50 dB *re*: 0.0002 dynes/cm^2.

C. Calibration

Test-cage sound calibration was carried out with a 1/4-in. Bruel & Kjaer condenser microphone using a 1-kHz, 94-dB sound-pressure level pistonphone (B&K) pure-tone source signal as a reference sound source. The loudspeaker's frequency response was flat between 5 to 40 kHz, with the range of intensities remaining within $\pm$4 dB when tested at the sound-pressure level 50 dB. Sound-pressure levels were measured at four different positions around the region of the observing lever and nosing hole, with sound amplification set to deliver tones at the sound-pressure level 50 dB when measured at the observing lever. The range of dB differences at 5

kHz remained less than $\pm$2 dB within this region. To make certain that no intensity cues adulterated the frequency-discrimination task, small increments in frequencies were made around 5 kHz with the microphone positioned at the observing lever. These frequency increments contained increases of 1% to 20% from 5 kHz. No significant intensity difference with any small incremental change of frequency was detected—the observed 1-dB maximum change that we detected was well below intensity-difference limens reported for the albino rat (around 2–4 dB; Hack, 1971; Syka *et al.*, 1996). No standing waves were detected in the test cage, and the area of the cage within which the rat moved approximated a free field. These calibrations were repeated often over the experimental period.

D. Psychophysical procedure: Testing

Subjects pressed an observing lever and were presented with a pair of pure tones. Tone duration was 1 s and tone interval was 100 ms. A single trial consisted either of tones of matching frequency (the S−) or nonmatching frequency (S+). Both S− tones were presented at test frequency, while the second tone in S+ contained an increment in frequency (Δf) from the test frequency. (In this report, all frequency increments are expressed in % difference from the test frequency. A ''signal'' refers to a change in frequency, i.e., S+.) The data we report here are from subjects tested at 5 kHz. Subjects were trained to make a nosing response to S+ and withhold responses to S−. A hit was a response to S+ within 2 s after the start of the second tone and was reinforced with 0.1-ml water. A false alarm was a response to S− within the same time interval; this was punished by inactivating the lever for 8–12 s. A miss of S+ or a correct rejection of S− had no consequences and the next trial could be immediately activated. Any response that occurred before 0.2 s after the start of the second tone was aborted: the same trial was then repeated on the next lever activation. Subjects under stimulus control had near-zero abort rates.

Testing was organized in blocks of trials (sessions). A light within the nosing hole indicated the start, and end, of a session. Sessions were suitably spaced apart in time during the day so that subjects were not satiated before working through five to eight sessions. Our experiments were mainly concerned with three procedural variables—signal strength, signal probability, and reinforcement schedule—all of which remained constant within a session but were sometimes systematically altered across sessions. Specifically, the variables that we altered were: (i) the comparison frequency Δf; (ii) the *a priori* probability of S+ on a given trial, $P[\text{S}+]$: (iii) the probability of a reward given that the subject scored a hit, $p[r|h]$. The details of these alterations are made explicit below along with each experiment that we performed. Within a session, trials were presented in (pseudo) random computer-generated sequence. The number of trials in a session varied according to the aim of the experiment. The initial trials in a session (usually 20) were ''warm-up'' trials to enable subjects to get accustomed to the prevailing experimental parameters.

E. Training

Naive subjects were shaped to ''poke'' into the nosing hole to obtain a water reward in the first session. After this, the conditioned stimulus was introduced which consisted of pure tones of alternating frequencies 5 and 10 kHz ($\Delta f = 100\%$). Tone duration was 1 s and tone interval 100 ms, delivered at the sound-pressure level 50 dB. The stimulus came on randomly after 10–20 s of silence and continued until a nosing response terminated the signal; this response was reinforced. Responses in the stimulus interval were punished by resetting the time interval before the next presentation. Within two to three sessions, the nosing response came under stimulus control. At this stage, the subjects experienced in frequency discrimination joined the training schedule. An observing lever was introduced into the cage, which subjects learned to press to start a trial. Thereafter, training sessions were identical to test sessions except that S− trials were repeated (correction trials) when false alarms occurred. During training, all sessions consisted of 100 trials presented at random with $P[S+]=0.5$ and $p[r|h]=1$. Training at $\Delta f=100\%$ continued until the detectability measure A' (see Sec. I F) was greater than 0.95. The experienced subjects achieved this performance level within a week; the naive subjects took around 2–3 weeks to achieve this performance level. Thereafter, the Δf was reduced in steps. Rarely— following extended sessions at difficult Δf's—the number of aborted trials increased in a session; this signified loss of stimulus control. When this happened, the subject was immediately retrained at an easy task ($\Delta f=20\%$) with correction trials and usually recovered within a session. While subjects learned the basic task within a week, performance was seen to improve over the long term, a phenomenon that seems to be common in frequency discrimination (Talwar and Gerstein, 1998). Subjects were considered fully trained when A' values at $\Delta f=4\%$ did not show (visual) improvement over seven sessions. Total training time for naive subjects was around 5 weeks, often with multiple sessions within a day. Even so, for the purpose of obtaining ROC curves, this training time was somewhat insufficient since the frequency of outliers was relatively high. The data we report in experiments 1 and 2 (below) of this study were obtained from subjects who were each trained for a total of at least 2–3 months. After this time, behavior was more stable although outliers were still encountered occasionally (around one every 10–12 sessions).

F. Analysis of behavior

Events on every trial were recorded and hit rates and false-alarm rates were calculated for all sessions. The hit rate (defined as the conditional probability of a go response given an S+ trial) was the ratio: number of hits in a session/ number of S+ trials in a session. Similarly, the false-alarm rate, or the conditional probability of a go response given S−, was the ratio: number of false alarms in a session/ number of S− trials in a session. When sessions contained correction trials, data from these trials were not considered (Jenkins, 1965). Similarly, data from the warm-up trials at the start of every session were also not considered.

To analyze performance, we used the parametric detectability index d' (Green and Swets, 1966) and the nonparametric detectability indices A' (Grier, 1971; Pollack and Norman, 1964) and SI (Frey and Colliver, 1973). To measure response bias, we considered the nonparametric response bias indices B'' (Grier, 1971; Hodos, 1970) and RI (Frey and Colliver, 1973). The computation formulas for the relevant indices, where $h=$ hit rate and $f=$ false-alarm rate, are

$$d'=z(f)-z(h),$$

where $z(.)$ is the z score or the normal deviate,

$$(1)$$

$$A'=1/2+[(h-f)(1+h-f)]/[4h(1-f)], \quad (2)$$

$$B''=[h(1-h)-f(1-f)]/[h(1-h)+f(1-f)], \quad (3)$$

$$\mathrm{SI}=[h-f]/[2(h+f)-(h+f)^2], \quad (4)$$

$$\mathrm{RI}=[h+f-1]/[1-(h-f)^2]. \quad (5)$$

Detectability (d', A', and SI) and response bias (B'' and RI) were calculated from the hit- and false-alarm rates of relevant sessions. Frequency-discrimination acuity was investigated based on the detectability of each Δf signal (see experiment 1). To obtain the ROC, experimental conditions were varied across sessions with constant Δf. Hit rates were plotted against false-alarm rates so that each session produced one data point; these data were then fit by the average detectability of the data. Specifically, the predicted isosensitivity curve from the average $d'(A'/\mathrm{SI})$ measure of the data was calculated by solving the $d'(A'/\mathrm{SI})$ equation [Eqs. (1), (2), (3)] for h and plotting the function in the f interval [0 1] (see experiment 2).

II. EXPERIMENT

A. Experiment 1: Frequency discrimination acuity

1. Procedure

We investigated frequency-discrimination ability in subjects RN14/15/16. The subjects were tested at 5 kHz and their performance specifically evaluated at Δf signals of 20%, 15%, 10%, 8%, 6%, 4%, 2%, and 1% (their performance at $\Delta f=100\%$ was already known by the end of the training period). We defined sessions with $\Delta f \geqslant 8\%$ as ''easy'' sessions. Sessions with Δf's $<8\%$ were considered ''difficult.'' The day began with a randomly chosen easy session with 30 warm-up trials. Thereafter, random difficult sessions alternated with easy sessions with 20 warm-up trials in each session. Each session consisted of 100 trials under the conditions $P[S+]=0.5$ and $p[r|h]=0.5$. A relatively low $p[r|h]$ was used so that subjects would work longer. Occasionally, some sessions at $\Delta f=0\%$ (three sessions in each subject) were also run, to rule out guessing strategies or the presence of cues. Performance was at chance; thus, if the pseudorandom trial-sequence structure we used provided clues about the probability of the next trial being S+, our subjects did not seem to take any advantage of them (cf. Jenkins, 1965; Terman, 1970). After a suitable amount of data were collected from the three subjects, we examined the

performance of RN14 and RN15 in sessions in which the *a priori* probability of S+ on a trial was lowered to $P[S+]=0.2$. In these sessions, 20 S+ trials were randomly interspersed among 80 S− trials.

For each hit/false-alarm rate pair, we calculated values for the three detectability indices d', A', and SI. Psychometric functions were obtained by plotting detectability against frequency difference. We attempted to determine the empirical utility of d', A', and SI as detectability measures in frequency discrimination. To do this, the data underwent a routine analysis of variance and F ratios were calculated for each detectability measure. For our purpose, the most satisfactory measure would minimize within-group (error) variance and hence maximize the corresponding F ratios. Specifically, F ratios were calculated from detectability measures at all Δf's excluding $\Delta f = 1\%$. This was because the rats' performance at $\Delta f = 1\%$ was often at chance level, i.e., A' around 0.5. We found that the different indices differentially stabilized variances at different performance levels; taking into account chance performance could give a misleading impression of the relative strength of the indices when judged by F ratios.

2. Results

In the Appendix, we have entered the raw data from six sessions in all three subjects RN14/15/16 from $\Delta f = 100\%$ to 1%, at 5 kHz. The specific experimental conditions under which they were obtained are also listed. From these data we report the subjects' frequency-discrimination performance.

Figure 1 presents the psychometric functions based on the detectability index A' in all subjects. The left half of the figure [graphs 1(a)–(c)] shows the psychometric functions of subjects under the signal-probability condition $P[S+] = 0.5$. Figure 1(d) and (e) show the functions obtained when subjects RN14/15 worked in the condition $P[S+] = 0.2$. Signal strength, on the abscissa, is depicted using a linear scale (performance at $\Delta f = 100\%$ and $\Delta f = 0\%$ is not shown). As can be seen in the figure, the psychometric functions take the general form of the classical ogive (on a log scale they plot linear). While the functions across the two signal-probability conditions generally follow the same curve, in individual subjects the difference is clear: the data were generally less variable in the low signal-probability condition $P[S+] = 0.2$; consequently, the functions are smoother. To underline this, we note an example statistic: in both subjects RN 14/15, mean A' values at $\Delta f = 6\%$ had a coefficient of variability (standard deviation/mean) less than 0.06 with $P[S+] = 0.5$ and less than 0.04 in sessions with $P[S+] = 0.2$.

The data from our subjects showed that signal detectability—as measured by A'—remained constant (>0.95) for all frequency differences from $\Delta f = 100\%$ to $\Delta f = 20\%$. As the psychometric functions in Fig. 1 depict, as Δf was made less than 20%, detectability decreased gradually; in general, we found close to chance-level performance at $\Delta f = 1\%$ ($A' = 0.5$) even in the best-performing subject. However, at $\Delta f = 2\%$, frequency-discrimination performance was usually greater than chance in all subjects, indicating that rats can sometimes detect this weak signal at 5 kHz. In Table I we list the F ratios obtained from all the
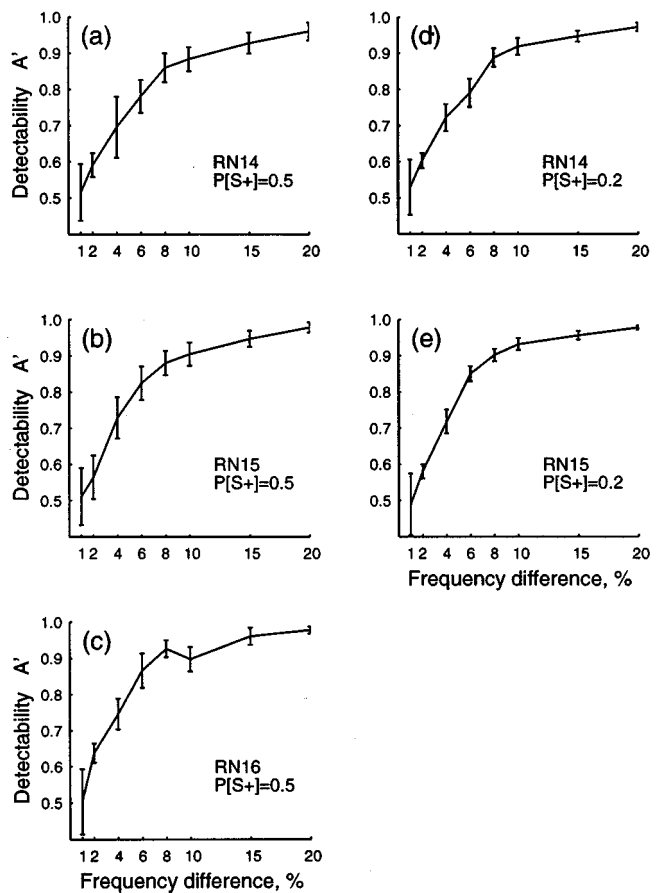
FIG. 1. Detectability A' as a function of frequency difference in subjects RN14/15/16. (a)–(c) Show performance of subjects when *a priori* signal probability ($P[S+]$) was 0.5, while (d) and (e) show performance of RN14/15 with $P[S+]=0.2$. Subjects were tested at 5 kHz and each data point is the mean of six test sessions. Bars represent s.d.

psychometric functions in the three subjects using d', A', and SI. From the table it can be seen that, among the three indices, the index A' generally gave the largest F ratios—although the difference compared to SI was little. In comparison, however, the index d' consistently produced the lowest F ratios. This relationship by F ratios is reflected in the geometrical form of the psychometric functions based on the different indices. For example, in Fig. 2(a) and (b), we plot a psychometric function based on SI and d' instead of A'. The data used to generate the functions in Fig. 2 are the same as that used for Fig. 1(e) i.e., subject RN15 when $P[S+]=0.2$). A visual comparison of the form of the functions based on the three different indices can thus be made. We defined the ''best'' frequency-discrimination function as

TABLE I. F ratios for the psychometric functions measured in subjects RN14/15/16 in different signal probability, $P[S+]$, conditions. The underlying raw hit/false-alarm-rate data is available in Table AI.

Subject/condition	A'	SI	d'
RN14; $P[S+]=0.2$	178.5	156.5	36.5
RN14; $P[S+]=0.5$	59.74	49.87	25.68
RN15; $P[S+]=0.2$	373.3	287.5	48.5
RN15; $P[S+]=0.5$	83.91	84.17	41.84
RN16; $P[S+]=0.5$	101.7	97.84	44.81
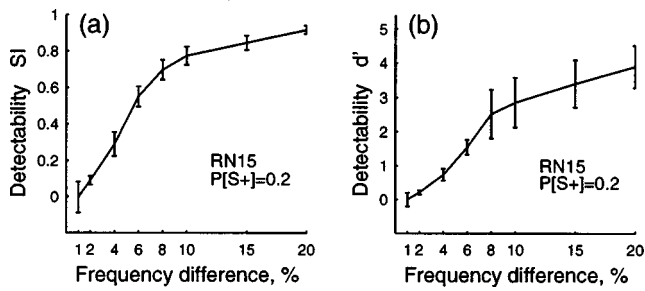
FIG. 2. Psychometric functions using the indices SI and d' instead of A' in the subject RN15 in the condition of $P[S+]=0.2$. For comparison, Fig. 1(e) shows the same data using the index A'.

FIG. 3. Effect on response bias with decreasing signal strength. (a) Plot of the progression of hit- and false-alarm rates in subjects RN14/15 as frequency difference is decreased from 100% to 1%. Each data point represents 600 trials. (b) Plot of the response bias as measured by RI and B'' as a function of frequency difference in subject RN14.

the function that took the form of the classical ogive in that it was well rounded and had a steep tangent around threshold-frequency changes (4% to 8%). Based on these geometric criteria, we found that the detectability measure A' generally delivered the best functions. The functions using SI were similar to those using A', although they tended to be a little less rounded and steep around threshold. In contrast, the functions fathered by d' were much flatter, and around threshold-frequency changes the slopes were shallow (although the slopes at large Δf's were correspondingly greater). A factor related to the different forms of the psychometric function is the differential effects on data variability at different signal strengths by each index. The data generally showed that A' was the most variable at $\Delta f \leqslant 6\%$ (or signal detectability less than $A'=0.8$). At small Δf's (1% and 2%), where the detectability of the signal was near chance level ($A'=0.5$; SI=0), the index SI stabilized the data to a greater extent than A' (the standard-deviation bars in Fig. 2 at small Δf show this effect). The index d' had similar effects relative to A': for Δf's $\leqslant 8\%$ (or signals that registered as $d'<2$) the index d' greatly stabilized data, while for larger Δf's the variability was correspondingly increased.

The psychometric functions in Figs. 1 and 2 can be used to measure frequency difference thresholds or limens (DL) in the rat. By convention, the frequency DL of classical psychophysics is based on hit rates of 0.5. At the same time, however, for the frequency DL to be a meaningful measure across studies, false-alarm rates are required to be low. For example, a false-alarm rate of around 0.05 is usually considered satisfactory. This threshold performance level ($h=0.5$; $f=0.05$) corresponds to a signal detectability of $A'\cong0.85$ [from Eq. (2)]. To measure frequency DLs based on A' measures, we used the psychometric function of subjects RN14/15 with $P[S+]=0.2$ and subject RN16 with $P[S+]=0.5$ as data. The frequency differences corresponding to $A'=0.85$ in these functions were 6.5%, 6.2%, and 6.05%, respectively. Thus, the frequency DL, as Weber ratios (difference limen/test frequency) for white rats, on the basis of these data, is 6.25% $\pm0.23\%$ at 5 kHz.

Although the psychometric functions in Figs. 1 and 2 give an idea of the manner in which signal detectability decreases with decreasing-frequency difference, they do not give any idea of the way in which bias may be affected. The effect of decreasing-frequency difference on both detectabil-

ity and bias can be demonstrated in a hit-rate versus alarm-rate plot shown in Fig. 3(a). In the figure, we show data obtained from subjects RN14 and RN15; each data point represents 600 trials under the conditions $P[S+]=0.5$ and $P[r|h]=0.5$. At $\Delta f=100\%$, the points start out in the top-left quadrant of the graph and make their way toward the main diagonal with decreasing-frequency difference. The negative diagonal can be taken as being indicative of neutral, or zero, response bias towards a go response when the subject is unsure about the status of a signal. Points that tend to drift to the top-right corner are indicative of a bias toward making a go response. Under the particular experimental parameters in which the data were obtained, data points always remained above the negative diagonal in the unit square defined by hit rate and false-alarm rate; as the task became harder, the data points tended to move further away from the negative diagonal. If we define response bias in this manner—i.e., the bias demonstrated by a subject toward making a go response under ambiguous signal conditions—it is clear, then, that subjects were biased toward making the go response at all signal strengths and that this tendency increased, to some extent, as the signal got weaker.

In Fig. 3(b) we examine the suitability of the response-bias measures B'' and RI to express the above idea of response bias. The data are from subject RN14. Both indices (B'' and RI) are plotted against decreasing-frequency differences. The response-bias index (RI) shows that response bias

increases as frequency difference becomes smaller; this appropriately quantifies the idea, obtained from Fig. 2(a), of increased response bias on the part of a subject as the discrimination task becomes harder. Response bias as measured by the index B'' also indicates that subjects demonstrate a relatively high response bias at large frequency differences. However, the index B'' suggests that response bias actually *decreases* as frequency differences become smaller [in Fig. 3(b), the right hand B'' scale is inverted because more negative values for B'' represent a greater bias toward making a go response]. This is not in accord with the idea of response bias conveyed by Fig. 2(a). Thus, for our purpose, we found that the index RI is better suited than B'' to express response bias.

B. Experiment 2: Generating ROC curves

1. Procedure

In the three subjects RN21, RN22, and RN23, we attempted to generate complete ROC curves by varying experimental conditions. We focused on independently manipulating the two variables $P[r|h]$ (the probability of reinforcing a hit), and $P[S+]$ (the *a priori* probability of S+ on a trial) using two different experimental procedures:

(i) The reinforcement schedule was varied by systematically changing the value of $p[r|h]$ while $P[S+]$ remained fixed at 0.5 in sessions of 100 trials. Δf remained constant across sessions until sufficient data were obtained to make a firm statement about the form of the ROC at that signal strength. The performance of RN21 was investigated at Δf's of 10%, 6%, and 4%; RN22 and RN23 had sessions at Δf's of 10% and 6%. $P[r|h]$ was varied in the range 0 to 1 taking on values of 0, 0.1, 0.2, 0.5, and 1. We defined $P[r|h] \geq 0.5$ as high-reinforcement sessions and $P[r|h] < 0.5$ as low-reinforcement sessions. The first session of the day had high reinforcement; in subsequent sessions the density of reinforcements alternated between high and low. Occasionally, two to three sessions were run consecutively in which $P[r|h]$ was low.

(ii) Subjects RN22 and RN23 were then shifted to sessions across which we varied $P[S+]$. Subjects RN22 was tested at Δf's of 10% and 6% while RN23 was tested at $\Delta f = 10\%$. In these sessions all hits were reinforced, i.e., $P[r|h] = 1$. $P[S+]$ took on values of 0.5, 0.2, and 0.1. The total number of trials varied with $P[S+]$. When $P[S+]$ was 0.5, each session had 50 S+ and 50 S− trials. When $P[S+]$ was 0.2, 50 S+ trials and 250 S− trials were presented within a session. When $P[S+]$ was as low as 0.1, however, we presented only 25 S+ trials vs 250 S− trials within a session. Initially, $P[S+]$ was varied randomly across sessions within a day. Thereafter, $P[S+]$ was held constant for all sessions in a day and was changed across days.

The data from the above procedures were plotted in the ROC plane defined by hit- and false-alarm rates. For any
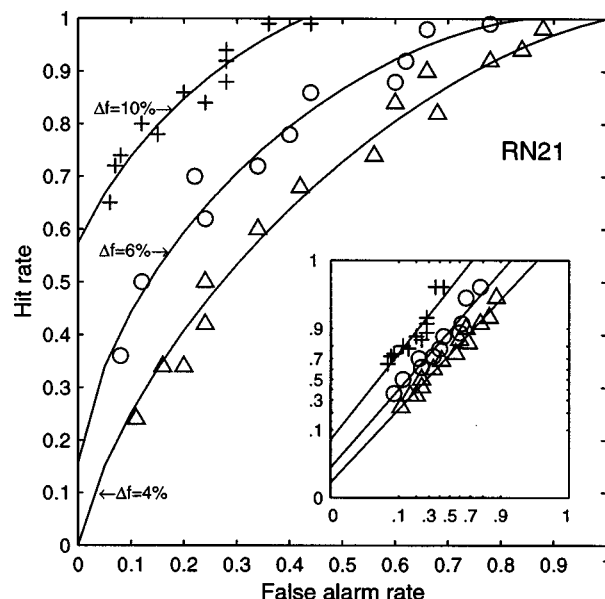
FIG. 4. ROC functions in subject RN21 generated by varying the probability of reinforcement of a hit. The data are fitted by the index A'. The subject was tested at 5 kHz with frequency differences of 10%, 6%, and 4%. Each data point is based on 100 trials. The inset shows the same data plotted in binormal coordinates.

given experimental manipulation, we fitted the data points with one of the three sensitivity measures A', SI, or d' depending on which index gave the best fit (although we generally found that there was not much difference between them). For all data points obtained for a given frequency difference, the average sensitivity measure was calculated and the isosensitivity curve predicted by this average measure was superimposed on the data (see Sec. I F). Statistical goodness of fit was not expressly evaluated; rather we relied on a visual inspection of the data to estimate it.

2. Results

We found that varying the reinforcement schedule ($P[r|h]$) was more effective than varying the likelihood of a signal ($P[S+]$) for generating ROC curves. In Fig. 4 we plot hit rates vs false-alarm rates obtained in subject RN21 when $P[r|h]$ was varied in [0 1] and across Δf's of 4%, 6%, and 10%. As the figure shows, the ROCs described by the locus of the data points at each Δf are close to the classical form described in the literature (Green and Swets, 1966). The data are reasonably symmetrical around the negative diagonal; they are fit by the curve predicted by mean A' values of data points at each Δf. The ROCs at each Δf are distinct and are parameterized by signal strength. Visual inspection shows that mean A' provides a good fit to the data at all Δf's, the index SI also appeared to be as suitable as A'. The index d' provided a good fit at Δf's of 6% and 8%; at $\Delta f = 10\%$, however, it did not fit the data quite as well as A' or SI. (ROCs predicted by mean d' are slightly more upwardly convex than the curves of A'. The curves of SI are intermediate between those of d' and A'; in the context of data noise, if the data are symmetrical, these differences may not matter practically) The inset of Fig. 4 shows the data from RN21 plotted in binormal coordinates. Statistically, a linear

fit to the data is justified (coefficient of linear correlation, p < 0.01) at all Δf's. The slope of the ROC at $\Delta f = 6\%$ is 1.08; at $\Delta f = 8\%$, 1.15; and at $\Delta f = 10\%$, 1.3.

In general, response bias in a session was proportional to the associated $P[r|h]$ reinforcement condition. Response bias was maximum when $p[r|h] = 1$. The data points from these sessions formed the extreme upper part of the ROC curve—that is, hit rates were maximized at the expense of false alarms. Sessions with $P[r|h] = 0.5$, however, only had a marginal effect in reducing response bias; in general subjects continued to respond relatively liberally. Switching from $P[r|h] = 1.0$ to $P[r|h] \leq 0.2$ usually would result in a relatively large shift in response bias, and subjects would respond more conservatively in that data points usually occupied the lower-central regions of the curve. Nonetheless, many sessions, even at $P[r|h] = 0.1$, gave data that extended into the upper reaches of the ROC. We found that the best way to reliably obtain sufficient data points on the extreme-lower part of the curve was to add sessions in extinction, i.e., sessions in which subjects were never rewarded ($P[r|h] = 0$).

In Fig. 5(a) we show the ROC plots obtained in subject RN22 at Δf's of 6% and 10%. The characteristics are similar to the ROCs obtained in RN21, although the data are somewhat noisier. These data were equally well fit by all three indices, A', SI, and d'. In the figure, we used the index SI to fit the data. When plotted in binormal coordinates, as is done in the inset of the figure, the data maps onto straight lines; the slope at $\Delta f = 6\%$ is 1.26 while the slope at $\Delta f = 10\%$ is 1.39.

In contrast to the classical form of the ROC in subjects RN21 and RN22, the data we obtained from RN23 were nowhere as symmetrical. In Fig. 5(b) we show data obtained from RN23 at $\Delta f = 6\%$. A large number of data points were obtained to conclusively make a statement about the form of the function. As can be inferred from the spread of data points in the figure, the best-fit curve for these data is a curve that is grossly asymmetrical, with the bend in the curve occurring after the negative diagonal is crossed. Superimposed on the data points in Fig. 5(b) is the curve predicted by the mean d' values of the data; the fit provided by d' was the closest approximation to a satisfactory fit. A' gave the worst fit, while the index SI provided a fit intermediate to the curves of mean d' and A'. Clearly, for these data, none of the indices were suitable. It is apparent from the figure that signal detectability was greater when the subject responded liberally (high-response bias) than when the subject responded conservatively (low-response bias). This means that signal detectability in this subject—as measured by d', A', or SI—was *not* completely independent of response bias. Nevertheless, as we show in the inset of the figure, the z transforms of the points can still be justifiably fit by a straight line, although the slopes were high in comparison with the other subjects (slope=1.66). The data at $\Delta f = 10\%$ in this subject was also as asymmetrical, but is not shown in Fig. 5(b) because of several overlapping data points. The z transform of these data also gave a straight line (slope 1.81). Despite the exaggerated slopes in subject RN23, then, the characteristic of increasing slope with increasing frequency
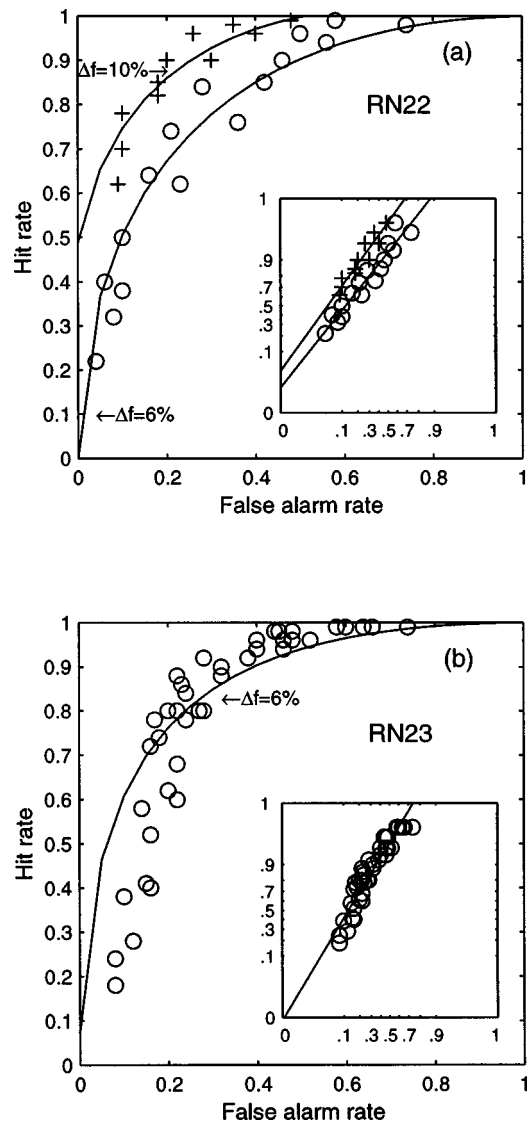
FIG. 5. ROCs in subjects RN22/23 obtained by varying reinforcement schedules. Data from RN22 [(a)] are from sessions at frequency differences of 6% and 10%; data from RN23 [(b)] are from sessions with 6% frequency difference. The data from RN22 are fitted by SI, while d' is used to fit data from RN23. The insets show the same data plotted in binormal coordinates. Subjects were tested at 5 kHz. Each data point represents 100 trials.

difference was maintained across all subjects.

We had less success in obtaining complete ROC curves when we varied the likelihood that S+ would appear on a given trial ($P[S+]$). An example, from subject RN22, is shown in Fig. 6. As can be seen, the data only describes partial curves; mean d' gave the best fit. Within this partial data range, response bias was generally proportional to $P[S+]$ values. We found that a $P[S+]$ of 0.5 was more than enough to guarantee high responsivity. However, it proved difficult to manipulate the subjects' response bias so that they would report conservatively enough to provide data points on the lower leg of the curve. Lowering $P[S+]$ to 0.2 and 0.1 often decreased response bias to a fair extent, but the effect was not always consistent. The inconsistency may be related to the levels of thirst motivation in the subjects during a particular session; this could have had a confounding effect on $P[S+]$. For example, a thirsty subject tended to
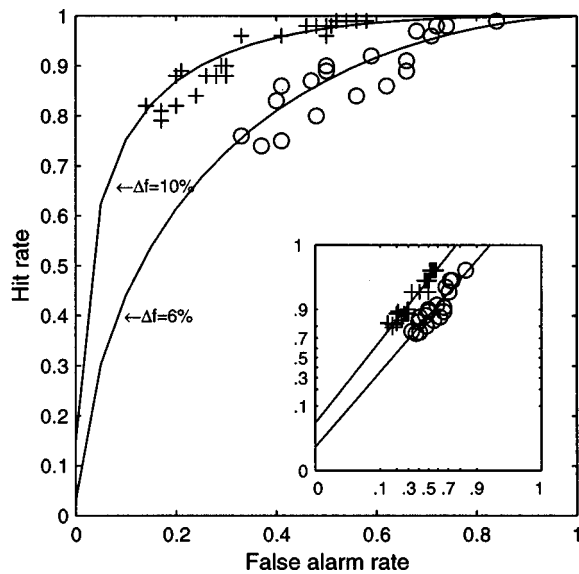
FIG. 6. The ROC generated in subject RN22 by varying the *a priori* signal probability of S+ from 0.5 to 0.1. The subject was tested at 5 kHz with frequency differences of 6% and 10%. Each data point represents at least 100 trials.

display high responsivity even during low $P[S+]$. The same subject at other times would respond more conservatively in the presence of the same low $P[S+]$. Nonetheless, we point out that we never obtained data that mirrored a sufficiently conservative response bias, even when subjects did not appear to be that thirsty (sometimes they stopped working). We also attempted to control for levels of motivation by varying $P[S+]$ across a time frame of days, instead of changing them at random within daily sessions. This did not make a difference and we concluded that the effect of varying $P[S+]$ was not strong enough to alter response bias sufficiently. In the inset of Fig. 6, the data are plotted on normal coordinates. As can be seen, the slopes of the ROC lines, once again, increase with increasing signal detectability (specifically, slope at 6% $\Delta f = 1.16$, at 10% $\Delta f = 1.26$).

C. Experiment 3: Analyzing the effects of reinforcement

Our results showed that reinforcement schedules can have a strong effect on a rat's response strategy in frequency discrimination. Therefore, we next examined the local effects of reinforcement on the rat's behavior within a session. Our aim was to derive an explanation for the efficacy of reinforcement schedules in generating the ROC. As a first step, we examined a subject's behavior on a given trial and tried to relate it to the presence (or absence) of reinforcement on the previous trial. For example, on a previous trial a subject may have been reinforced if it responded in the presence of S+, i.e., a hit. On the present trial, a subject can then be hypothesized to be making a decision in a ''state'' of previous reinforcement. Other possibilities on the previous trial are a miss, false alarm, or correct rejection. These represent a current state of previous nonreinforcement. We can, hence, list the possible events on any given current trial as: S+ given previous reinforcement (S+|rf); S− given previous reinforcement (S−|rf); S+ given previous nonreinforcement
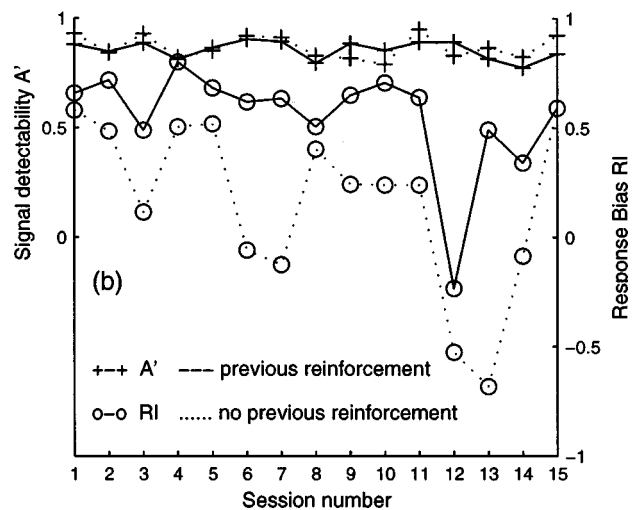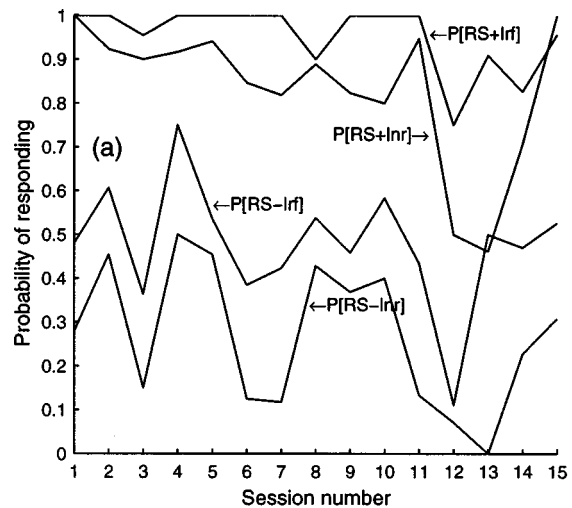
FIG. 7. The upper half (a) shows the probability of responding to S+ and S− in the two decisions states of antecedent reinforcement (rf) and absence of reinforcement (nr). Data are from subject RN22 across 15 sessions with at least 100 trials per session. The lower half (b) graphs signal detectability as well as response bias in the two decision states using the indices A' and RI, respectively.

(S+|nr); S− given previous nonreinforcement (S−|nr). We computed the probability of a go response under each of these conditions; that is, we evaluated the two pairs, $P[RS+|rf]$ and $P[RS−|rf]$; $P[RS+|nr]$ and $P[RS−|nr]$, where R indicates the go response. It is easily seen that these quantities represent the hit- and false-alarm rates under two different hypothesized decision states that the subjects may be considered to be operating under: the presence or absence of previous reinforcement.

We illustrate by means of Fig. 7(a), which represents an arbitrary strip of data from 15 sessions ($\Delta f = 10\%$) in a subject (RN22) in which all hits were rewarded ($P[r|h] = 1$). The probability of a go response in the above four different conditions is plotted against the sessions from which they were taken. As Fig. 7(a) shows, the probability of a go response to S+ (or hit rates) following a previous reinforcement was higher than when following no previous reinforce-

ment; that is, $P[\text{RS}+|\text{rf}] > P[\text{RS}+|\text{nr}]$. Similarly, the probability of a go response to S− (or false-alarm rates) were much higher when previous trials were reinforced than when they were not, that is $P[\text{RS}-|\text{rf}] \gg P[\text{RS}-|\text{nr}]$. The difference in false-alarm rates between the two states was statistically significant (t test, $p < 0.01$). Since hit and false-alarm probabilities were clearly different across the two hypothesized decision states linked to previous reinforcement history, the question arose whether signal detectability was different across them. Figure 7(b) plots the sequence of detectability (A') and response bias (RI) values for the case of antecedent reinforcement and nonreinforcement for the data shown in Fig. 7(a) There was no significant difference between A' values in the two states, as can be inferred from the figure; there was, however, a considerable difference in the response bias as measured by RI Response bias was clearly higher on trials following previous reinforcement than on trials following previous nonreinforcement (due either to previous miss, false alarm, or correct rejection). We examined a total of 20 such data strips across subjects at random. Fourteen of them showed a clear difference in response bias between the two states. At the same time, only two of these data strips showed that A' was, along with response bias, also different between the two states ($p < 0.01$). [This was probably due to the ceiling effect on $P[\text{RS}+|\text{rf}]$; this can be seen in Fig. 7(a).] On the basis of these data, we concluded that high-response-bias states were associated with previous reinforcement, while low-response-bias states were associated with previous nonreinforcement. Signal detectability, on the other hand, was independent of previous events.

The above result seemed to suggest that previous reinforcement history directly influenced decision behavior across trials. To identify possible confounding events, we looked at data from sessions in which only some hits were rewarded. In these data, several hypothetical decision states were defined based on the events of the previous trial. These states were: (i) previous hit with reinforcement (rf+), (ii) previous hit without reinforcement (rf−), (iii) previous false alarm (fa), (iv) previous correct rejection (rj), (v) previous miss (ms). Under the hypothesis that these five decision states exist within the paradigm, we calculated hit rates and false-alarm rates for each of them. Thus, we isolated five pairs of hit- and false-alarm rates corresponding to the five decision states under which they were obtained: $P[\text{RS}+|\text{rf}+]$ and $P[\text{RS}-|\text{rf}+]$; $P[\text{RS}+|\text{rf}-]$ and $P[\text{RS}-|\text{rf}-]$; $P[\text{RS}+|\text{fa}]$ and $P[\text{RS}-|\text{fa}]$; $P[\text{RS}+|\text{rj}]$ and $P[\text{RS}-|\text{rj}]$; $P[\text{RS}+|\text{ms}]$ and $P[\text{RS}-|\text{ms}]$. If reinforcement played a strong role in modifying local behavior, we reasoned that this would be specifically reflected in the differences in response bias between the states of previous hit with reinforcement and previous hit with nonreinforcement. Confounding factors, if present, would show in response-bias differences relative to the other three states that were also associated with nonreinforcement (false alarm, correct rejection, miss). Data for this analysis were sessions with $P[r|h] = 0.5$ and $P[\text{S}+] = 0.5$ (fixed $P[\text{S}+]$ to control for possible effects of varying signal probabilities). Sessions were pooled together by subject and by Δf's to make several data files. For a satisfactory analysis, we required that each
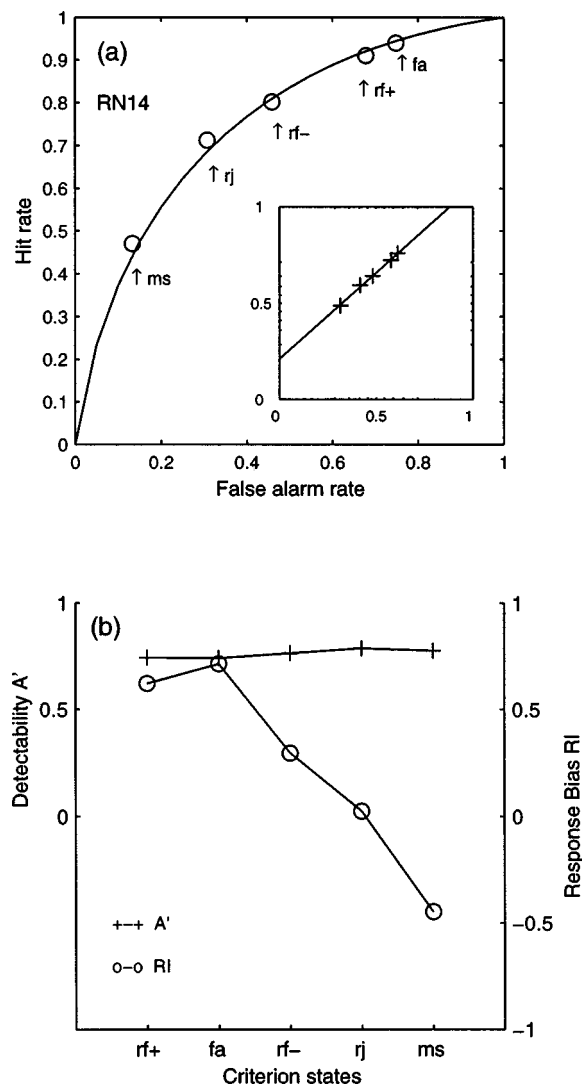
FIG. 8. (a) Plot of the hit rates against false-alarm rates in the five defined decision states: hit with reinforcement (rf+), hit without reinforcement (rf−), false alarms (fa), correct rejection (rj), and miss (ms). Subject was RN14 with session $P[r|h]$ and $P[\text{S}+]$ both at 0.5. The data points are fitted by mean SI to give the ROC of the subject. The inset of the figure plots the points in binormal coordinates. (b) Plot of the signal detectability (A') and response bias (RI) in the five different decision states. Subject was tested at 5 kHz at $\Delta f = 6\%$.

of the above five points (hit/false-alarm rate pairs) isolated from the data represented at least 100 trials. Since the least number of trials was usually associated with a previous miss, the number of misses essentially dictated which data files were available for analysis. A total of 14 data files from subjects RN 14/15/16/24/25 fit these criteria, the smallest of which had a total of 1400 trials. These files represented sessions during the training period of subjects after the task was learned, but performance at small Δf's had not yet peaked.

Our findings were fairly consistent across all subjects and were somewhat unexpected. To show the results, we use, as an example, the data file from subject RN14 with $\Delta f = 6\%$ and which consisted of 1500 trials. Figure 8(a) is a plot of the five data points (hit rate vs false-alarm rates) obtained by assuming the existence of five decision states. As can be seen, the five points are well-spread out and describe a smooth curve that is symmetrical—a classical ROC

plot. The data is fitted with a curve predicted by mean SI of the data points (SI fit these data best, although the difference from d'/A' is marginal). Mean detectability in terms of A' of these data points was nearly identical to the detectability calculated from the overall hit/false-alarm rate in the entire data ($A' = 0.76$). In the inset of Fig. 8(a) we plot the data points in binormal coordinates; a straight line is fitted with slope 0.89. In Fig. 8(b), we compare signal detectability (A') and response bias (RI) in the five hypothesized states. As can be seen, detectability remained constant across the five decision states while response bias was very different. Response bias was high after a previously reinforced hit (rf+) and was significantly lower following a hit that was not reinforced (rf−). This fact indicates that reinforcement played a strong role in altering decision behavior across trials. Surprisingly, however, response bias following a false alarm (fa) was much higher than the response bias following a nonreinforced hit; in fact, in this subject, response bias following a false alarm was even greater than response bias after reinforced hits. This finding is unexpected, since both false alarms and nonreinforced hits were, by definition, unrewarded. We concluded that, while nonreinforcement of a response can lower response bias on the next trial, some factor(s) in false-alarm trials override the effect of nonreinforcement. Figure 8(b) further shows that the subject responded relatively conservatively following a previous correct rejection, while the most conservative response strategy was following a previous miss. The five data points that define the ROC in Fig. 8(a) correspond to these different response bias or decision states. From these data, we concluded that certain response-bias levels on current trials are, at the least, correlated with specific events on previous trials.

In Fig. 9 we show ROCs obtained in subjects RN15/16/24 using the same analysis (data from RN15/24 is fitted with mean d', RN16 with mean A'). The insets of the figures show detectability as well as response bias across the five decision states. The slopes on double-probability plots of the data from RN15/16/24 are 1.23, 1.13, and 1.22, respectively. Although they were some minor variations across the data from different subjects—mainly related to the exact spread of data points over the ROC—within a particular individual, decision behavior was highly similar across all Δf's. Table II shows the response bias (RI) values across decision states in each data file we analyzed; RI values are listed by subject and Δf. A (one-way) analysis of variance of these data showed that response bias was significantly different between the five decision states ($F = 80.13$, $p < 0.001$). Figure 10 sums the differences in responses bias across all decision states in all data files. As the figure indicates—and what was borne out by statistical t tests ($p < 0.001$)—three significantly different response-bias states could be clearly identified over the entire data set (in the case of subject RN14, all five states were significantly different). In general, subjects responded most liberally in the state of previous reinforced hit and previous false alarm; i.e., they made decisions reflecting high-response bias. They responded relatively conservatively in the states of previous nonreinforced
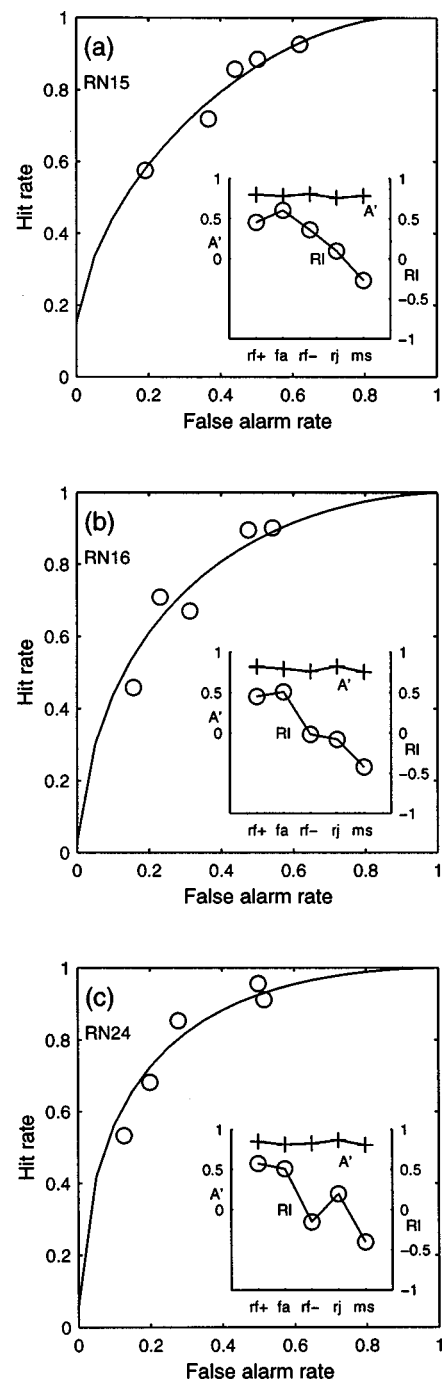
FIG. 9. Response bias in the five decision states in subjects RN15/16/24. As in Fig. 8, hit rates were plotted against false-alarm rates in the different decision states to give the ROC in all three subjects. Data in (a) are fitted with A', while (b) and (c) are fitted with d'. The insets of the figure show signal detectability (A') and response bias (RI) in the five different decision states. Subjects RN15/16/24 were tested at 5 kHz at frequency differences of 6%, 8%, and 10%, respectively.

hit and correct rejection (although previous correct rejection tended to be lower). The most conservative response strategy or lowest response bias was recorded in trials that followed a miss. Thus, by sorting data based on decision states reflecting different response-bias levels, a sufficient spread of data points (Figs. 8 and 9) were available to plot a complete ROC curve from within a single body of data without the need for deliberate manipulation of experimental conditions.

TABLE II. Measurements of response bias (RI) across five possible decision or criterion states identified within a session. rf+=previous reinforced hit; fa=previous false alarm; rf−=previous nonreinforced hit; rj=previous correct rejection; ms=previous miss.

Subject/Δf	rf+	fa	rf−	rj	ms
RN14;$\Delta f = 4$	0.530	0.510	0.095	0.005	−0.281
RN14;$\Delta f = 6$	0.622	0.715	0.296	0.024	−0.447
RN14;$\Delta f = 8$	0.589	0.530	0.036	−0.148	−0.525
RN14;$\Delta f = 10$	0.603	0.571	−0.011	−0.082	−0.157
RN15;$\Delta f = 4$	0.441	0.507	0.395	0.030	0.013
RN15;$\Delta f = 6$	0.454	0.603	0.360	0.097	−0.274
RN15;$\Delta f = 8$	0.560	0.467	−0.217	0.155	−0.513
RN16;$\Delta f = 6$	0.595	0.662	0.148	0.111	−0.046
RN18;$\Delta f = 8$	0.451	0.509	−0.019	−0.080	−0.423
RN16;$\Delta f = 10$	0.597	0.640	0.215	0.108	−0.021
RN25;$\Delta f = 20$	0.495	0.508	0.010	0.078	−0.139
RN24;$\Delta f = 10$	0.577	0.507	−0.154	0.188	−0.406
RN25;$\Delta f = 20$	0.536	0.537	0.311	0.124	−0.096
RN25;$\Delta f = 12$	0.565	0.543	0.217	0.083	0.133

III. DISCUSSION

In this study, we carried out an SDT analysis of frequency discrimination in the white rat using a simple go/no-go paradigm. Specifically, we investigated frequency acuity, the form of the ROC, and analyzed the effects of reinforcement on behavior. The main advantage of SDT for discrimination-acuity studies like auditory-frequency discrimination is that it provides independent indices for signal detectability as well as response bias. A less pragmatic, although crucial benefit of the theory, is that it provides a testable hypothetical framework within which animal cognition can be suitably investigated. While a few investigators (see the Introduction) have previously urged larger application of SDT to animal-discrimination behavior, it is clear, at least judging from the amount of discrimination-acuity studies that use threshold measures instead of SDT, that the technique is underutilized.
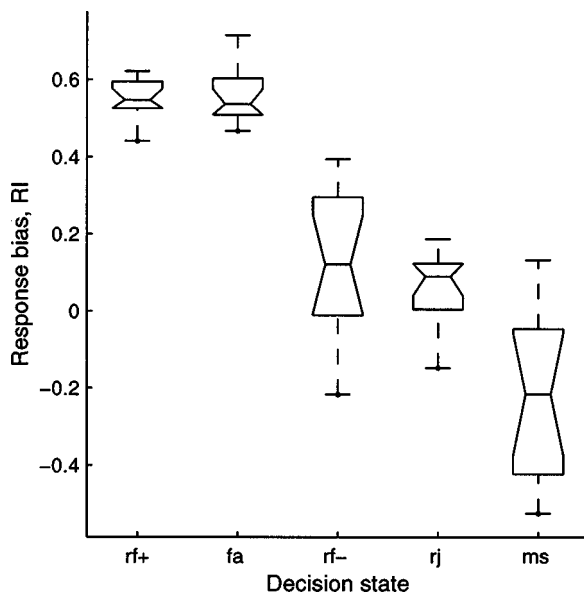
FIG. 10. Response bias (RI) across the five decision states rf+, fa, rf−, rj, and ms, over all data in five subjects. The notches at the sides of the boxes in the plot represent the 95%-confidence interval of the mean. The horizontal lines within the boxes signify the median while the ''whiskers'' of the boxes represent the range of the data.

The point is often made that the use of signal-detection methods for investigating discrimination acuity in animals is inconvenient and time consuming (Long, 1994). This is true when we consider relatively sophisticated procedures like 2-lever paradigms which are routinely employed in studies in psychopharmacology and memory. In acuity studies like frequency discrimination that involve small differences in the quality of a stimulus, the use of such procedures are likely to result in very long training times (see Burdick, 1979). However, our study suggests that even a simple, easily learned, yes–no procedure may be able to sustain a detailed SDT study. With the use of this procedure, we were able to obtain reasonably well-defined ROCs in three subjects by manipulating the rats' external environment, as well as several ROCs by a method that identified different response-bias states within sessions. Thus, our study showed that the SDT model is consistent with frequency-discrimination behavior in the rat.

A. Signal detectability

To measure frequency-discrimination performance, we considered the parametric index d' (Green and Swets, 1966) and the nonparametric detectability indices A' and SI (Grier, 1971; Frey and Colliver, 1973). An analysis of variance of the data showed that the F ratios for the A' measure were slightly greater than those for SI and considerably larger than those for d'. The use of A' led to smooth psychometric functions that expressed the typical characteristics of an ogive. These functions were very similar to intensity-discrimination functions in rats also obtained using signal-detection methods (Terman, 1970). The functions by SI were almost as good as those of A', while d' generally led to less-rounded functions. For our purpose, then, A' best expressed the functional relationship between signal detectability and signal strength. It may be difficult to generalize from this, especially given the fact that the data is from a limited number of subjects and the study was not specifically designed to compare the usefulness of detectability measures. However, we point out that Frey and Colliver (1973) also reached a similar conclusion using data obtained from discrimination studies in other species.

The index A' showed that subjects performed nearly perfectly for all frequency differences larger than 20%. For differences less than 20%, detectability decreased gradually. The A' measure indicated that the rat's auditory system can resolve frequency differences as small as 2%, since performance at this level was usually greater than chance. At all frequency differences, A' proved to be a stable and accurate measure of frequency discrimination with coefficients of variation less than 0.06. Stability was further improved when the probability of S+ on a trial was decreased; in addition, discrimination seemed to be a little better. This finding is odd; a possible explanation, though, is the ''ceiling'' effect for A', which can corrupt data when hit rates are close to 1: when false-alarm rates are relatively high, the hit rates are bound by the ceiling and a worse detectability measure might result. In the standard conditions of our experiment, we fixed $P[r|h]$ at 0.5 to reduce this effect (also for the more prag-

matic reason of increasing the number of trials in a day). Nevertheless, with $P[S+]=0.5$, hit rates were still sometimes close to 1. Lowering signal probability to $P[S+]=0.2$ decreased this tendency and could account for the improved stability (as well as the slight improvement).

Although SDT has invalidated the theoretical concept of the difference limen (DL) as a measure of discrimination acuity, the frequency DL may still be useful as an empirical measure: a large database of frequency DLs already exists which serves to place any new animal study in context. In this regard SDT provides a useful method to measure frequency DLs based on a threshold definition of $A'=0.85$; this performance level is equivalent to the conventional threshold in classical psychophysics: viz, hit rates of 0.5 (and false-alarm rates of 0.05 since low false-alarm rates are necessary for the DL to be a meaningful measure). Another factor that makes $A=0.85$ a suitable definition of threshold is that the indices d', A', and SI differentially stabilized data at different signal strengths. The variability in A', for example, was considerably reduced for detectabilities larger than $A'=0.8$. This seems to be in general agreement with the ''sweet point'' for threshold measurements in humans in two-alternative, forced-choice procedures since A' is equivalent to %-correct response in the 2AFC procedure (Green, 1990; Swets, 1996). By this threshold definition, then, we measured a frequency DL of 6.25%±0.23% at 5 kHz in the white rat; these measurements are in the same range as that measured by Syka *et al.* (1996) using conventional threshold methods and the same go/no-go paradigm in hooded rats. The advantage of using signal-detection methods in frequency DL measurements is one of convenience and accuracy; it eliminates the need to keep false-alarm rates to a minimum, a factor that is not always easy to ensure. Moreover, the use of signal-detection methods sets the investigator free from the need to maintain strict experimental constancy across sessions to ensure data stability.

B. Response bias

In a discrimination task, response bias is best interpreted as the tendency of a subject to make a particular response under ambiguous signal conditions; thus, it reflects the subjects' decision strategy. The indices that we studied to measure the degree of response bias were the nonparametric measures B'' and RI (Hodos, 1970; Grier, 1971; Frey and Colliver, 1973). Of these, RI was the more satisfactory measure. The go/no-go procedure that we used was asymmetrical in that only one physical response was required and the consequences of a response was not equal. Under these conditions, it was not surprising to find that rats exhibited a relatively strong response bias toward a go response whenever signal status was doubtful—at least under the standard experimental conditions that we defined. Both B'' and RI showed that in easy discrimination tasks, subjects are biased towards making a go response. Presumably, the decision to make a go response under ambiguous signal conditions is not tempered by the cost vs benefit of the situation. As frequency differences become smaller, and the task becomes harder, the index RI shows that the general level of responsivity increases, i.e., subjects become more biased to making a go

response. Nevertheless, the amount of this increase is not as much as might be expected given the nature of the paradigm. Some auditory studies, despite the use of two-lever tasks, have found in rats a similar amount of bias developing with decreasing signal strength (Irwin and Terman, 1970; Terman, 1970). The index B'', on the other hand, did not support a conclusion that is in accord with a ''common sense'' idea of response bias. This is a consequence of the fact that at low-signal sensitivity (i.e., when hit rate=false-alarm rate), B'' is incapable of differentiating between very conservative and very liberal response criterion (see Suboski, 1967; Frey and Colliver, 1973).

C. ROC curves in frequency discrimination

The index A', being equivalent to area under the ROC curve, rests on the assumption that, in fact, such an empirical function exists. Moreover, for A' to be invariant across experimental conditions, the ROC must, at least, remain within certain bounds (Pollack and Norman, 1964). In this study, to generate empirical ROC curves, we varied experimental conditions by changing the probability of reinforcement as well as the *a priori* probability of the signal. Since rats generally show a high-response bias, obtaining data points reflecting liberal response strategies was easy; the chief requirement in generating complete ROC curves was to manipulate response bias so that data points would reflect sufficiently conservative decision strategies. In signal-detection terms, we manipulated the decision criterion of subjects to alter their response bias from liberal to conservative.

The most effective method to manipulate response bias was to alter the reinforcement probability of a hit. This method was more effective than simply lowering the relative frequency at which S+ was presented. By altering the frequency with which S+ appeared, we were not able to obtain complete ROC curves; even at very low S+ signal probability subjects did not respond conservatively enough to give data points on the lower half of the curve. The range of the data points we obtained was similar to that obtained by Hack (1963) in rats using a similar method. Generally, subjects decreased their response bias at low-signal probabilities; even so, subject motivation seemed to play a role in this and the effect was not always reliable. In contrast to this method, however, altering the reinforcement schedule had a stronger effect in decreasing overall responsivity. Subjects tended to be more conservative in reporting S+ if they happened not to be often rewarded for it. In general, for reward probabilities greater than around 0.5, responsivity remained high. When the probability of reward decreased to 0.1–0.2, responsivity declined. Nonetheless, the only way to achieve data points that reflected a sufficiently conservative response strategy and produced data points on the lower extremity of the ROC curve was to include behavioral sessions in which subjects were never rewarded. In learning terms, this represents behavior in extinction. By this manipulation we were able to obtain the complete ROC curve.

The form of the ROC in two of our subjects, RN21 and RN22, was an upwardly convex function generally symmetrical about the negative diagonal. In the literature this form is classical. Of course, many functions can be fit

through a limited number of data points; here we tried to provide enough to make a stronger statement about the form. In general, all three indices d', A', and SI provided adequate fits for the data obtained from these subjects; sufficiently so that they served as suitable sensitivity indices across all experimental conditions and frequency differences. Given the similarity in the forms of the functions predicted by the three indices, and taking into account the inherent noise in the data, it is difficult to make a clear overall choice of one over the other; there were instances in the study when one of the indices, in turn, provided a slightly better fit than the others. In contrast to the functions obtained in subjects RN21/22, the ROC in subject RN23 was grossly asymmetrical; the bend in the curve was skewed toward the top-right corner of the ROC plot. The mean A' (or mean $d'/$SI for that matter) of the data consistently underestimated signal detectability when response bias was high and overestimated it when it was low. In other words, when the subject responded very conservatively, its performance was not as good as when it responded liberally; detectability, thus, was not completely independent of response bias. For this subject, then, all three indices d', A', and SI failed to be good measures of detectability. It is sometimes easy to lose sight of the fact that detectability indices directly measure the *behavior* of an animal and not the sensory ability of the auditory system. The assumption we work under is that the behavior of an animal in operant tasks is the direct expression *solely* of sensory ability. If we assume that sensitivity is, in fact, independent of response bias, the data from subject RN23 suggests—to the extent that the commonly used SDT indices are appropriate detectability measures—that there may sometimes exist a gap between the sensory capability of the rat and its actual behavior, at least in a go/no-go task within the confines of a laboratory. Another behavioral interpretation of these data, however, is that the go/no-go task may sometimes provide less than ideal stimulus control when the probability of reinforcement is low. Alternatively, there remains the possibility that this skewed ROC is a legitimate expression of sensory ability in this subject—in which case, different indices are needed to measure detectability.

In many cases, it may be beneficial to assume certain underlying S+ and S− distributions (other than Gaussian) that predict the ROC forms actually observed experimentally. From these assumptions it may be possible to develop parametric measures for signal detectability; after all, such measures are more powerful than nonparametric ones. For symmetric ROC data, it is appropriate to model the underlying S+ and S− distributions as Gaussian distributions with equal variance. Such a model predicts straight lines of unity slope on probability scales. Equal variances for the S+ and S− distribution is reflected on probability scales as a family of parallel lines (Green and Swets, 1966). An appropriate index in this case is the parametric measure d', which indicates the distance between the hypothesized S+ and S− distributions. Our data, when plotted in binormal coordinates, invariably satisfied statistical requirements for a straight-line fit. However, the curves we obtained did not result in parallel lines of unity slope. As frequency difference increased, the ROC lines, in addition to shifting upward, also tended to increase in slope. This feature, common to all of our subjects, seems to be unusual for frequency discrimination in rats, since data from other signal detection studies often seem to demonstrate slopes that decreased with signal strength (Swets, 1996). In subjects RN21/22 at small frequency differences (4% to 6%), the lines demonstrated slopes around unity; at larger frequency differences the slopes remained less than 1.5. In these subjects, at least at threshold-frequency differences, d' by itself can be considered a suitable parametric index and the equal-variance Gaussian model is valid for frequency discrimination. A model that can account for the increase in slopes with signal strength is one that assumes two Gaussian distributions with the variance of the S+ distribution *decreasing* as its mean increases. It might be beneficial to apply such methods to ROC forms that are as asymmetrical as the data from RN23. If necessary, other distributions (e.g., gamma and exponential distributions) can also be assumed to develop the appropriate indices (e.g., Clopton, 1972; Swets, 1996). In summary, our observations of frequency-discrimination behavior in rats suggest that the detectability index that best fits the form of the ROC functions may need to be chosen on the basis of individual subjects.

D. Decision making in frequency discrimination

The ROCs we generated were obtained by long-term systematic manipulation of experimental conditions. As such, despite the use of an easily learned go/no-go procedure, the experiment was laborious. A long training period was required to reduce outliers for obtaining good ROCs Further, our results indicate that different methods of altering response bias may not be not equally effective in animal subjects.

In this study, we developed a convenient method to obtain complete and relatively clean ROCs which involved a straightforward analysis of a single body of data. The experimental requirements for the method are simply that animal subjects are trained in go/no-go sessions in which only some hits are rewarded—without the necessity of systematically altering conditions, and without the need for extended training. The method is based on the observation that reinforcement schedules are effective in manipulating response bias in animal subjects [similar observations have been made for pigeons in discrimination tasks (Nevin, 1965, 1967)]. We found that a subject whose response was reinforced on a given trial was more likely to respond to the next trial (under ambiguous signal conditions) than if it had previously experienced an absence of reinforcement. In other words, rats demonstrated higher-response bias on trials immediately following previous reinforcement than on trials following previous nonreinforcement. However, the condition of nonreinforcement is associated with the events nonreinforced hits, false alarms, correct rejections, and misses. To filter out possible confounding variables, we classified trials according to each event on previous trials. A signal-detection analysis of these data showed that past events of reinforced hits, unreinforced hits, false alarms, correct rejections, and misses, were all associated with relatively different response-bias levels on current trials. Signal detectability, on the other hand, was

independent of past-event history. Thus, rats can be said to operate in several different decision states linked to previous-event history; the response-bias levels of these decision states span the range from liberal to conservative. Given a sufficient number of trials within the data, and by sorting trials on the basis of past events, a sufficient spread of five data points is obtained which makes it possible to completely define the ROC of a subject. The curves we obtained by this method shared all the characteristics of ROCs otherwise obtained by the more traditional methods we employed; they were symmetrical and were very well fitted by the mean A' (d', SI) value of the data points. The detectability of the signal by mean A' (d', SI) was identical to the detectability otherwise calculated from the entire data file from which the data points were isolated. Since SDT interprets a shift in response bias as a shift in the decision criterion of a subject, the implication of these data is that the rat's decision criterion can shift rapidly across trials in a frequency-discrimination task. The overall response bias that is calculated, from the hit- and false-alarm rates in a behavioral session, merely represents the ''average'' response bias a subject demonstrates across all trials.

In general, across all subjects, we found that the five decision states we defined reflect at least three significantly different response-bias (RB) levels: a high-RB state associated with previous reinforced hit and previous false alarm; a lower-RB state associated with previous nonreinforced hit and correct rejection; a lowest-RB state associated with previous miss. Naturally, the fact that these associations exist does not, by itself, imply a causal relationship between specific events and subsequent decision strategies in frequency discrimination. However, the fact that RB following nonreinforced hits was significantly lower than RB following reinforced hits indicates that the relationship between nonreinforced response and subsequent low RB is one of cause–effect rather than mere correlation. Nevertheless, it is clear that other factors exist that confound this effect. This is apparent from the fact that while our subjects responded very liberally on trials following false-alarm responses, they were significantly less likely to respond following nonreinforced correct responses. From the rats' point of view there is, *a priori*, no difference between the two trials: in both conditions the rat is not rewarded for a response to what it believes is a signal (behavioral theory makes the necessary assumption that a trained subject only responds to a ''likely'' signal). It is worth noting, therefore, that, as far as the rat is concerned, false-alarm trials differ from nonreinforced-hit trials only in the fact that a timeous period follows a false-alarm response. A reasonable conclusion, then, is that the presence of a timeout period following a response diminished the likelihood that a rat would withhold the next response to an ambiguous signal. The implication of this is clear: timeouts—at least in the way they were used in this study—are of questionable use in go/no-go paradigms. In procedures that seek to limit liberal responding, they may, in fact, be contraindicated. More generally, on the basis of our data, it seems that timeouts *do not* serve to punish responses in the absence of the S+ (the very reason for their use in psychophysical experiments); if anything, they reinforce the

rats' normal inclinations (we note that during timeouts, our rats appeared to wait out the period; sometimes they pressed the observation lever in anticipation). It is possible that the lowering of RB following nonreinforced hits is a short-term phenomenon and that response bias reverts to its ''normal'' high levels (shared by reinforced hits) during the timeout period. The high RB levels associated with previous false alarms explains the difficulty we experienced in obtaining sufficiently conservative response strategies in the go/no-go task. This was especially seen in the experiments in which signal probability, $P[S+]$, was varied. Sessions with low $P[S+]$, by definition, had many more S− trials and, consequently, more false alarms; this may have offset an otherwise bias-lowering effect that low $P[S+]$ may have had. Further, all hits were reinforced in the varying $P[S+]$ experiments so that there were no nonreinforced hits to help in lowering response bias. From the foregoing observations, the prediction is that the rat will show more conservative response strategies in go/no-go procedures in which timeouts are not incorporated. This may be advantageous. With suitable combinations of procedural variables like reinforcement schedule, signal probability, and (probably) timeouts, it is possible that the simple go/no-go procedure can be made more effective in animal psychoacoustics.

It is more difficult to account for the fact that while RB was not significantly different between the states of previous nonreinforced hit or a correct rejection (although correct rejection tended to be lower), the response bias following previous miss was significantly lower. Correct rejection and miss both represent the same behavioral event in that a subject makes a decision that S− was presented and withholds response; consequences are the same for either event. This finding, however, can be accounted for if we note that a previous miss is not necessarily in a causal relationship with low RB on current trials. In the process of making several discriminations, a ''miss,'' by definition, most often occurs when RB—for whatever reason—is the lowest. Thus, a previous miss and subsequent low RB are simply associated by nature of their temporal proximity while the rat happens to be in a temporarily low RB state. The factors underlying this low-RB state need to be further identified; at present this behavior seems complex. In summary, we might model the normal decision strategy of the rat in frequency discrimination as reflecting a high response-bias state; occasionally, as a consequence of unrewarded hits, the response bias is temporarily reduced. Timeouts, if present, serve to obscure the temporary reductions in response bias. Other factors may be superimposed on these fluctuations of response bias causing trends, so that sometimes misses as well as correct rejections occur normally.

IV. CONCLUSIONS

The straightforward go/no-go task we used to investigate frequency discrimination in the rat was an adequate vehicle-for a signal-detection study of behavior. The frequency-difference limen we measured using SDT methods was 6.25% in three subjects; this value is around the same that has previously been measured in rats for the same paradigm. Rats demonstrated a relatively strong bias toward making a

go response in ambiguous signal conditions; nonetheless, this tendency can be manipulated by altering experimental conditions. For the data we gathered, the index A' was, by and large, the most suitable measure of frequency-discrimination acuity. Response bias, on the other hand, was effectively tracked by the index RI. ROC curves were generated by varying reinforcement schedules and signal probability; the manipulation of reinforcement schedules proved to be a stronger influence on the rats' behavior. For data points in the ROC plane, there was little to choose between the indices d', A', and SI while fitting ROC functions. When the ROC data were plotted in binormal coordinates, straight lines were obtained whose slopes increased with increasing signal strengths. Despite this common ROC feature, the data indicate that ROC forms are not consistent between subjects. In one subject (out of three), none of the detectability indices we tested proved adequate across experimental conditions.

By classifying trials on the basis of previous trial history of events, we found that while the decision criterion our rats adopted to report a signal varied widely from trial to trial, signal detectability remained unaffected. On any given trial, the rat could be said to be operating in one of several differ-

ent decision states. A given decision state can be predicted by events on past trials. Previous reinforcement history and, possibly, timeouts are among factors that influence decision behavior. The finding of multiple decision states within a session provided a means to generate the ROC from the data of a single session. For animal subjects, the identification of multiple decision or criterion states in which they may operate represents a significant advantage for convenience and methodology in obtaining ROC functions. Further, the signal-detection analysis that we applied to analyze the local effect of reinforcement may be potentially useful for other behavioral studies; the more general method could be useful as a tool to investigate the behavioral effects of any procedural variable.

APPENDIX

Below in Table AI is listed the raw data from six sessions in subjects RN 14/15/16 after a period of at least 2 months of frequency-discrimination training. Subjects were tested at 5 kHz.

TABLE AI. Hit rates (h) and false-alarm rates (f) in three subjects under different signal-probability conditions.

Subject/ condition	$\Delta f = 100\%$		$\Delta f = 20\%$		$\Delta f = 15\%$		$\Delta f = 10\%$		$\Delta f = 8\%$		$\Delta f = 6\%$		$\Delta f = 4\%$		$\Delta f = 2\%$		$\Delta f = 1\%$	
	h	f	h	f	h	f	h	f	h	f	h	f	h	f	h	f	h	f
RN14	1.00	0.08	1.00	0.13	0.90	0.05	0.90	0.21	0.90	0.17	0.80	0.50	0.75	0.50	0.70	0.59	0.60	0.58
$P[S+]=0.2$	0.95	0.03	0.95	0.12	0.95	0.12	0.85	0.06	0.80	0.21	0.95	0.62	0.80	0.59	0.60	0.49	0.65	0.67
	1.00	0.06	1.00	0.05	1.00	0.13	1.00	0.21	0.85	0.29	0.80	0.40	0.65	0.32	0.60	0.52	0.55	0.50
	0.95	0.08	1.00	0.11	0.90	0.14	0.95	0.28	1.00	0.35	0.95	0.75	0.70	0.41	0.70	0.61	0.55	0.48
	1.00	0.09	0.95	0.05	1.00	0.27	0.80	0.17	0.85	0.28	0.85	0.32	0.85	0.50	0.70	0.55	0.55	0.59
	1.00	0.02	1.00	0.07	0.90	0.12	1.00	0.33	0.95	0.34	0.95	0.63	0.90	0.77	0.90	0.84	0.70	0.60
RN14	0.98	0.12	0.96	0.10	0.98	0.30	0.94	0.32	0.98	0.42	1.00	0.88	0.92	0.82	0.84	0.76	0.62	0.70
$P[S+]=0.5$	0.98	0.10	0.98	0.14	0.98	0.14	1.00	0.50	0.92	0.52	0.96	0.74	1.00	0.92	0.86	0.76	0.76	0.70
	1.00	0.12	1.00	0.30	1.00	0.18	0.92	0.28	0.94	0.22	0.96	0.74	0.94	0.66	0.94	0.90	0.76	0.74
	0.96	0.14	1.00	0.02	0.86	0.08	0.94	0.52	0.88	0.40	0.78	0.52	0.72	0.38	0.72	0.64	0.92	0.90
	1.00	0.06	1.00	0.24	0.96	0.26	0.98	0.24	0.82	0.34	1.00	0.84	0.92	0.86	0.88	0.86	0.88	0.82
	1.00	0.02	0.98	0.06	0.90	0.30	0.84	0.24	1.00	0.52	0.76	0.20	0.82	0.76	0.76	0.70	0.74	0.78
RN15	1.00	0.02	1.00	0.04	0.95	0.08	1.00	0.26	0.95	0.32	0.80	0.25	0.70	0.42	0.90	0.86	0.80	0.86
$P[S+]=0.2$	0.95	0.03	1.00	0.10	1.00	0.15	0.95	0.25	0.95	0.30	0.95	0.44	0.75	0.54	0.70	0.65	0.70	0.67
	1.00	0.07	0.95	0.05	1.00	0.19	0.85	0.10	1.00	0.33	0.85	0.36	0.90	0.59	0.85	0.80	0.80	0.83
	1.00	0.05	0.95	0.03	1.00	0.13	0.95	0.27	1.00	0.36	0.90	0.29	0.70	0.45	0.65	0.54	0.60	0.65
	1.00	0.01	1.00	0.09	0.90	0.06	1.00	0.19	0.90	0.33	0.85	0.36	0.85	0.60	0.85	0.78	0.70	0.68
	1.00	0.06	0.95	0.06	0.95	0.19	0.95	0.14	0.95	0.26	0.80	0.31	0.80	0.59	0.70	0.64	0.80	0.70
RN15	0.98	0.02	0.92	0.10	0.94	0.18	1.00	0.50	1.00	0.72	0.92	0.52	0.86	0.74	0.86	0.84	0.66	0.72
$P[S+]=0.5$	1.00	0.04	1.00	0.06	1.00	0.24	0.92	0.10	0.88	0.26	0.76	0.12	0.84	0.64	0.68	0.56	0.88	0.86
	0.98	0.06	1.00	0.04	0.96	0.04	0.96	0.24	0.96	0.38	1.00	0.80	1.00	0.86	0.82	0.78	0.76	0.64
	0.98	0.08	0.96	0.04	0.96	0.18	0.88	0.30	0.94	0.24	0.76	0.30	0.94	0.60	0.62	0.60	0.62	0.60
	1.00	0.02	0.96	0.04	1.00	0.32	0.94	0.22	0.94	0.28	0.98	0.50	0.74	0.46	0.84	0.70	0.70	0.66
	1.00	0.04	0.98	0.04	0.92	0.04	1.00	0.46	1.00	0.52	0.84	0.52	0.80	0.56	0.74	0.74	0.82	0.86
RN16	1.00	0.04	1.00	0.10	1.00	0.30	0.86	0.28	0.88	0.10	0.98	0.20	0.88	0.56	0.64	0.48	0.66	0.76
$P[S+]=0.5$	1.00	0.10	0.98	0.08	1.00	0.04	1.00	0.50	0.98	0.32	0.92	0.34	0.86	0.66	0.88	0.72	0.64	0.70
	0.98	0.04	0.98	0.02	0.90	0.04	0.86	0.24	0.94	0.08	0.78	0.26	0.92	0.76	0.90	0.82	0.78	0.72
	0.98	0.06	0.96	0.10	0.98	0.06	0.94	0.38	1.00	0.26	0.94	0.42	0.78	0.50	0.74	0.60	0.62	0.56
	0.98	0.02	0.98	0.02	0.92	0.12	0.96	0.18	0.92	0.28	0.98	0.72	0.68	0.22	0.76	0.64	0.62	0.58
	1.00	0.04	0.98	0.08	0.98	0.12	0.96	0.18	0.98	0.30	0.80	0.20	0.92	0.70	0.84	0.76	0.72	0.66

Banks, W. P. (**1970**). ''Signal detection theory and human memory,'' Psychol. Bull. **74**(2), 81–99.

Blough, D. S. (**1967**). ''Stimulus generalization as signal detection in pigeons,'' Science **158**, 940–941.

Burdick, C. K. (**1979**). ''The effect of behavioral paradigm on auditory discrimination learning: A literature review,'' J. Aud. Res **19**, 59–82.

Clopton, B. M. (**1972**). ''Detection of increments in noise intensity by monkeys,'' J. Exp. Analysis Behav. **17**, 473–481.

Frey, P. W., and Colliver, J. A. (**1973**). ''Sensitivity and responsivity measures for discrimination learning,'' Learning Motivat. **4**, 327–342.

Green, D. M., and Swets, J. A. (**1996**). *Signal Detection Theory and Psychophysics* (Wiley, New York).

Green, D. M. (**1990**). ''Stimulus selection in adaptive psychophysical procedures,'' J. Acoust. Soc. Am. **87**, 2662–2674.

Grier, J. B. (**1971**). ''Nonparametric indexes for sensitivity and bias: computing formulas,'' Psychol. Bull. **75**(6), 424–429.

Hack, M. H. (**1963**). ''Signal detection in the rat,'' Science **139**, 758–759.

Hack, M. H. (**1971**). ''Auditory intensity discrimination in the rat,'' J. Comp. Physiol. Psychol. **74**, 315–318.

Hodos, W. (**1970**). ''Nonparametric index of response bias for use in detection and recognition experiments,'' Psychol. Bull. **74**(5), 351–354.

Irwin, R. J., and Terman, M. (**1970**). ''Detection of brief tones in noise by rats,'' J. Exp. Analysis Behav. **13**, 135–143.

Jenkins, H. M. (**1965**). ''Measurement of stimulus control during discriminative operant conditioning,'' Psychol. Bull. **64**(5), 365–376.

Katz, J. L. (**1988**). ''Effects of drugs on stimulus control of behavior. I. Independent assessment of effects on response rates and stimulus control,'' J. Pharmacol. Exp. Therapeut. **223**(3), 617–623.

Long, G. R. (**1994**). ''Psychoacoustics,'' in *Comparative Hearing: Mammals*, edited by R. R. Fay and A. N. Popper (Springer, New York), pp. 18–56.

Marston, H. M. (**1996**). ''Analysis of cognitive function in animals, the value of SDT,'' Cognit. Brain Res. **3**, 269–277.

Nevin, J. A. (**1965**). ''Decision theory in studies of discrimination in animals,'' Science **150**, 1057.

Nevin, J. A. (**1967**). ''Effects of reinforcement scheduling on simultaneous discrimination performance,'' J. Exp. Analysis Behav. **10**, 251–260.

Peterson, W. W., Birdsall, T. G., and Fox, W. C. (**1954**). ''The theory of signal detectability,'' Transcripts of the IRE Professional Group on Information Theory, p. 171.

Pollack, L., and Norman, D. A. (**1964**). ''A non-parametric analysis of recognition experiments,'' Psychonomet. Sci. **1**, 125–126.

Sahgal, A. (**1987**). ''Contrasting effects of vasopressin, desglycinamide-vasopressin and amphetamine on a delayed matching to position task in rats,'' Psychopharmacology **93**, 243–249.

Suboski, M. D. (**1967**). ''The analysis of classical discrimination experiments,'' Psychol. Bull. **68**, 235–242.

Swets, J. A. (**1996**). *Signal Detection Theory and ROC Analysis in Psychology and Diagnostics: Collected Papers* (Erlbaum, Hillsdale, NJ).

Syka, J., Rybalko, N., Brozek, G., and Jilek, M. (**1996**). ''Auditory frequency and intensity discrimination in pigmented rats,'' Hearing Res. **100**, 107–113.

Talwar, S. K., and Gerstein, G. L. (**1998**). ''Auditory frequency discrimination in the white rat,'' Hearing Res. **126**, 135–150.

Terman, M. (**1970**). ''Discrimination of auditory intensities by rats,'' J. Exp. Analysis Behav. **13**, 145–160.

White, K. G., Ruske, A. C., and Colombo, M. (**1996**). ''Memory procedures, performance and processes in pigeons,'' Cognit. Brain Res. **3**, 309–317.

Importance of temporal-envelope cues in consonant recognition

René van der Horst,[a] A. Rens Leeuw, and Wouter A. Dreschler
Clinical and Experimental Audiology, D2, University of Amsterdam, Meibergdreef 9, 1105 AZ Amsterdam, The Netherlands

The role of different modulation frequencies in the speech envelope were studied by means of the manipulation of vowel–consonant–vowel (VCV) syllables. The envelope of the signal was extracted from the speech and the fine-structure was replaced by speech-shaped noise. The temporal envelopes in every critical band of the speech signal were notch filtered in order to assess the relative importance of different modulation frequency regions between 0 and 20 Hz. For this purpose notch filters around three center frequencies (8, 12, and 16 Hz) with three different notch widths (4-, 8-, and 12-Hz wide) were used. These stimuli were used in a consonant-recognition task in which ten normal-hearing subjects participated, and their results were analyzed in terms of recognition scores. More qualitative information was obtained with a multidimensional scaling method (INDSCAL) and sequential information analysis (SINFA). Consonant recognition is very robust for the removal of certain modulation frequency areas. Only when a wide notch around 8 Hz is applied does the speech signal become heavily degraded. As expected, the voicing information is lost, while there are different effects on plosiveness and nasality. Even the smallest filtering has a substantial effect on the transfer of the plosiveness feature, while on the other hand, filtering out only the low-modulation frequencies has a substantial effect on the transfer of nasality cues. © *1999 Acoustical Society of America.* [S0001-4966(99)00302-1]

PACS numbers: 43.66.Mk, 43.71.Es [JWH]

INTRODUCTION

Speech intelligibility can be related to the temporal envelope of the acoustical speech signal (Houtgast and Steeneken, 1985). When analyzing the temporal domain of a speech signal, Rosen (1992) classified the temporal structure of speech into three categories of speech cues: envelope cues, periodicity cues, and temporal fine-structural cues. This classification is based on the time-scale of the dominant temporal structure in each category. Envelope cues consist of the frequencies 2 to 50 Hz, and are able to transmit the following phonetic and prosodic information: segment duration, rise–fall time (which can convey consonantal manner information), the presence or absence of voicing, syllabification, and stress.

Periodicity cues—containing the frequencies from 50 to 500 Hz—signal the strength and frequency of vocal fold vibrations, and therefore can convey phonetic information about consonant voicing and manner, as well as prosodic information about intonation and stress.

Temporal fine-structure. The periodicity of the temporal fine-structure ranges from 600 Hz to 10 kHz, and conveys information about the spectral distribution of energy of the speech signal. These cues are essentially the same as the spectral envelope structure, which cues consonant place and vowel quality.

A. Information contained in the speech envelope

Van Tasell *et al.* (1987) found that consonants can be recognized to some extent by the wideband speech envelope alone. In these experiments, they used noise signals modulated with the temporal envelope of the wideband speech signal to be certain that the only phonetic information transferred is that contained in the speech temporal envelope. In this way, a score of 22-percent-transferred information was reached when the bandwidth of the temporal envelope was reduced to contain only the modulation frequencies up to 20 Hz. The transferred information in the 200-Hz and 2000-Hz conditions was 29% and 35%, respectively.

Another approach was followed by Drullman *et al.* (1994). They first filtered the speech signal in frequency bands, and kept the original speech carrier. The frequency bands had a width of a quarter of an octave, half an octave, or one octave. They reduced the information in each temporal envelope by low-pass filtering, and modulated the carrier of each original speech band with this filtered envelope, in order to leave the temporal fine-structure intact. In this way, they were able to assess the relative importance of the fast and slow envelope variations. It was concluded that the envelope modulations above 16 Hz could be filtered out without reducing the speech intelligibility. But if all temporal variations were filtered out, the speech reception fell to a score of about 20 percent for consonant recognition. So, cues other than temporal envelope can account for about only 20% of a speech intelligibility score.

An important observation of this study was that the frequency width of the processing bands had an influence on intelligibility. For frequency bands wider than a quarter of an octave, higher scores were measured, and it was argued that subjects were able to resolve spectral information within each processing band and use that in the speech-recognition task. The envelope of a wideband signal is the sum of multiple narrow-band envelopes (i.e., the envelopes in every critical band). The auditory system can make use of multiple

---

envelopes within such a wideband signal. Therefore, filtering out the envelope modulations of a wideband signal does not guarantee that the narrow-band envelopes are filtered in the same way.

Shannon et al. (1995) combined aspects of the stimuli of Van Tasell et al. (1987) and Drullman et al. (1994). They used noise as the carrier, but extracted the envelope from the speech signal in one to four processing bands. The number of processing bands was an experimental variable. Consonant recognition increased from about 50% when using only one processing band, to 90 percent when using four bands. When envelope fluctuations were low-pass filtered at 16 Hz, which differed significantly from the other conditions (low-pass filtered at 50, 160, and 500 Hz), the consonant-recognition scores started at somewhat less than 40 percent for one processing band and increased to about 80% with four processing bands.

To summarize, when reviewing the conditions as used by Van Tasell et al. (1987), one can conclude that the envelope signal not only contained the envelope cues as defined by Rosen (1992), but also the periodicity cues (200-Hz condition) and even the cues of the spectral fine-structure (2000-Hz condition). Only the 20-Hz condition contained the envelope cues alone; this condition shows the relative importance of envelope information as extracted from a wideband speech signal. But this method uses a wideband envelope, and one cannot guarantee that any manipulation applied on this wideband envelope is equally applied on the envelopes in every critical band. With the method of Drullman et al. (1994) the envelopes were down-sampled to 244 Hz, so the bandwidths of the envelopes could be up to 122 Hz, this affects the envelopes extracted from filter bands wider than 244 Hz. It ensures that the envelope signals contain almost only the envelope cues. But Drullman et al. (1994) left the spectral fine-structure of the speech signal intact; thus, their stimuli contained temporal fine-structural cues as well as temporal envelope cues. Shannon et al. (1995) used noise as the carrier, so the spectral fine-structure of the speech signal was lost, but the processing bands were very broad in comparison with the critical bandwidth. They extracted the envelopes by half-wave rectification and low-pass filtering with 16, 50, 160, and 500 Hz as cut-off frequencies. So, in the 160- and 500-Hz conditions, the periodicity cues were still present.

Therefore, we designed a new experiment in which the influence of *only* the narrow-band temporal envelopes on the recognition of consonants was measured.

B. Temporal envelope manipulation

In order to degrade the temporal information in every critical band, the speech signal was transformed into a temporal–spectral envelope representation. Therefore, the stimuli were passed through a filter bank consisting of band-pass filters with bandwidths equal to the critical bandwidth of the human auditory system (Glasberg and Moore, 1990).

From each band of the speech signal, the temporal envelope was derived by means of a Hilbert transformation. Our hypothesis is that the temporal envelope in every critical

TABLE I. Center-frequencies and equivalent rectangular bandwidths of the band filters used.

F_c	BW	F_c	BW
150	41	1306	166
193	46	1480	184
241	51	1674	205
294	56	1890	229
354	63	2131	255
420	70	2399	284
494	78	2697	315
576	87	3030	352
667	97	3400	392
769	108	3812	436
882	120	4271	486
1008	134	4782	541
1149	149	5352	602

band represents the way the auditory system analyzes the envelope information of speech sounds.

In this spectral–temporal representation, the temporal information was degraded by filtering each envelope. In order to remove all fine-spectral information from the stimulus, the resulting envelope was modulated on narrow-band noises, so all information about the speech carrier has been lost. These narrow-band noises were created by using a noise with a long-term spectrum equal to speech and feeding this signal through the aforementioned filter bank. The different processing bands were summed to compose the final stimulus.

In this way, we hope to assess the importance of the narrow-band temporal envelopes alone on the intelligibility of a speech signal, and assess the relative importance of different modulation frequencies of this narrow-band temporal envelope.

I. METHOD

A. Signal processing scheme

1. Analysis and synthesis

The following were the signal-processing steps used to construct the stimuli:

Filter bank. The speech signal was split up in the frequency domain in 26 different frequency bands, center-frequencies ranging from 150 to 5350 Hz. The filters were triangular shaped, their center-frequencies and bandwidths are described in Table I. The filters were implemented as time-aligned, linear-phase, finite impulse response filters.

Envelope detector. An envelope detector was implemented by means of the Hilbert transformation, using the analytic signal. Because the filtered speech signal is a real, causal, and band limited signal [$F_i(t)$ in Fig. 1], the Hilbert transform can be used to find the appropriate imaginary part [$X_i(t)$ in Fig. 1] of the analytic signal.

The signal $S_i(t)$ is thought of as an analytic signal

$$S_i(t) = R_i(t) + jX_i(t), \tag{1}$$

$$R_i(t) = F_i(t), \tag{2}$$

$$X_i(t) = \mathcal{H}\{R_i(t)\}, \tag{3}$$

where $\mathcal{H}\{\cdot\}$ denotes the Hilbert transform.

1802   J. Acoust. Soc. Am., Vol. 105, No. 3, March 1999

van der Horst et al.: Importance of temporal-envelope cues   1802
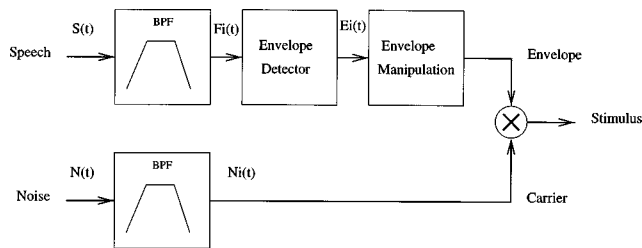
FIG. 1. Signal scheme of the digital-signal processing per frequency band for the creation of the stimuli.

TABLE II. Center-frequencies and notch widths of the envelope filters used.

nr	F_c	BW	Condition
0	⋯	0	reference (R)
1	8	4	low–narrow (LN)
2	8	8	low–medium (LM)
3	8	12	low–wide (LW)
4	12	4	center–narrow (CN)
5	12	8	center–medium (CM)
6	12	12	center–wide (CW)
7	16	4	high–narrow (HN)
8	16	8	high–medium (HM)
9	16	12	high–wide (HW)

The magnitude of the complex signal, at any given moment, can be seen as a measure of the instantaneous envelope, and the angle as a measure of the instantaneous frequency of the speech signal. Thus, when using the Hilbert transform ($\mathcal{H}$), the envelope signal [$E_i(t)$ in Fig. 1] would be

$$E_i(t) = |F_i(t) + j\mathcal{H}\{F_i(t)\}|, \qquad (4)$$

where $F_i(t)$ denotes the filtered-speech band.

Modulation and summation. The manipulated envelopes were multiplied with narrow-band noise carriers [$N_i(t)$ in Fig. 1], which were obtained by filtering a wideband noise with a long-term spectrum equal to speech [$N(t)$], with the same filter bank as described above. The different frequency bands were summed to become the stimulus signal.

2. Manipulation of temporal information

The envelope signals were manipulated (filtered) to contain only certain modulation frequencies. When the envelope is low-pass filtered, one removes the transients in the envelope contour. When the envelope is high-pass filtered, one removes the global or coarse envelope variations.

In our study, the envelope is notch-band filtered in order to suppress the temporal-envelope information in a band of modulation frequencies.

Manipulations of the carrier also took place. Just as in the experiments from Van Tasell *et al.* (1987) and Shannon *et al.* (1995), the information contained in the spectral fine-structure of the signal was reduced by replacing the speech carrier with noise. In this manner, one can be sure that the subject is unable to use the information contained in the temporal fine-structure, which is the same as the instantaneous spectral envelope, and can only make use of the information as it occurs in the temporal envelope.

B. Experimental design

An experimental variable was the amount of temporal-envelope information contained in the stimulus. There were ten different experimental conditions of band-rejection filtering:

(i) no filtering as the control condition to assess the influence of the signal processing on the consonant recognition, and also be able to relate the data with the experiments of Drullman *et al.* (1994), Van Tasell *et al.* (1987), and Shannon *et al.* (1995).

(ii) nine conditions of envelope notch filtering, around three different center frequencies and with three different notch widths. The center-frequencies used were

8, 12, and 16 Hz; the notch widths were 4-, 8-, and 12-Hz wide. (See Table II.)

In this way, one can assess the relative importance of the different sources of speech information under testing, i.e., temporal-envelope information and spectral fine-structural information.

As an example of the signals, the envelope representation of the VCV syllable /aba/ is plotted in Fig. 2(a). This set of envelopes represents the speech signals as they were extracted from the original speech recording. These envelopes were used to construct the stimulus in the reference condition. As an example of notch filtering, the narrow-band envelopes from the LW condition are plotted in Fig. 2(b). These envelopes were used to construct the stimuli by modulating a set of narrow-band noises. The resulting waveforms of the /aba/ stimulus in the reference- and the LW condition are plotted in Fig. 2(c) and (d), respectively.

C. Procedure

Vowel–consonant–vowel syllables (VCV) were used to measure consonant recognition. The stimuli consisted of 18 Dutch consonants in three different vowel contexts (/a/, /i/, /u/), resulting in a list of 54 different VCV stimuli. The consonants used were five plosives: (/b/, /d/, /p/, /t/, /k/), 6 fricatives: (/f/, /x/, /s/, /ʃ/, /v/, /z/), 2 nasals: (/m/, /n/), three semivowels: (/l/, /w/), and (/l/, /n/, /h/).

The speech material was a female voice recorded on digital audio tape (DAT). One token of each VCV word was sampled with a computer at 16-kHz sampling frequency in order to be manipulated. The stimuli were created off-line according to the signal-processing scheme described in the above section. The stimuli were equalized to have an equal rms level, converted to a 16-bit format, and stored on hard disk.

These stimuli were presented to the subjects monaurally via an audiometer Interacoustics AC5 and a TDH39P headphone at a level of 70 dB SP. On the computer display, 18 buttons were presented with all possible consonant responses labeled. The subject ''pressed'' the response buttons with a mouse. Consonant recognition was measured by counting the number of correctly identified consonants in an 18-alternative, forced-choice procedure.

Every subject was first made comfortable with the experimental task and the possible response categories by be-
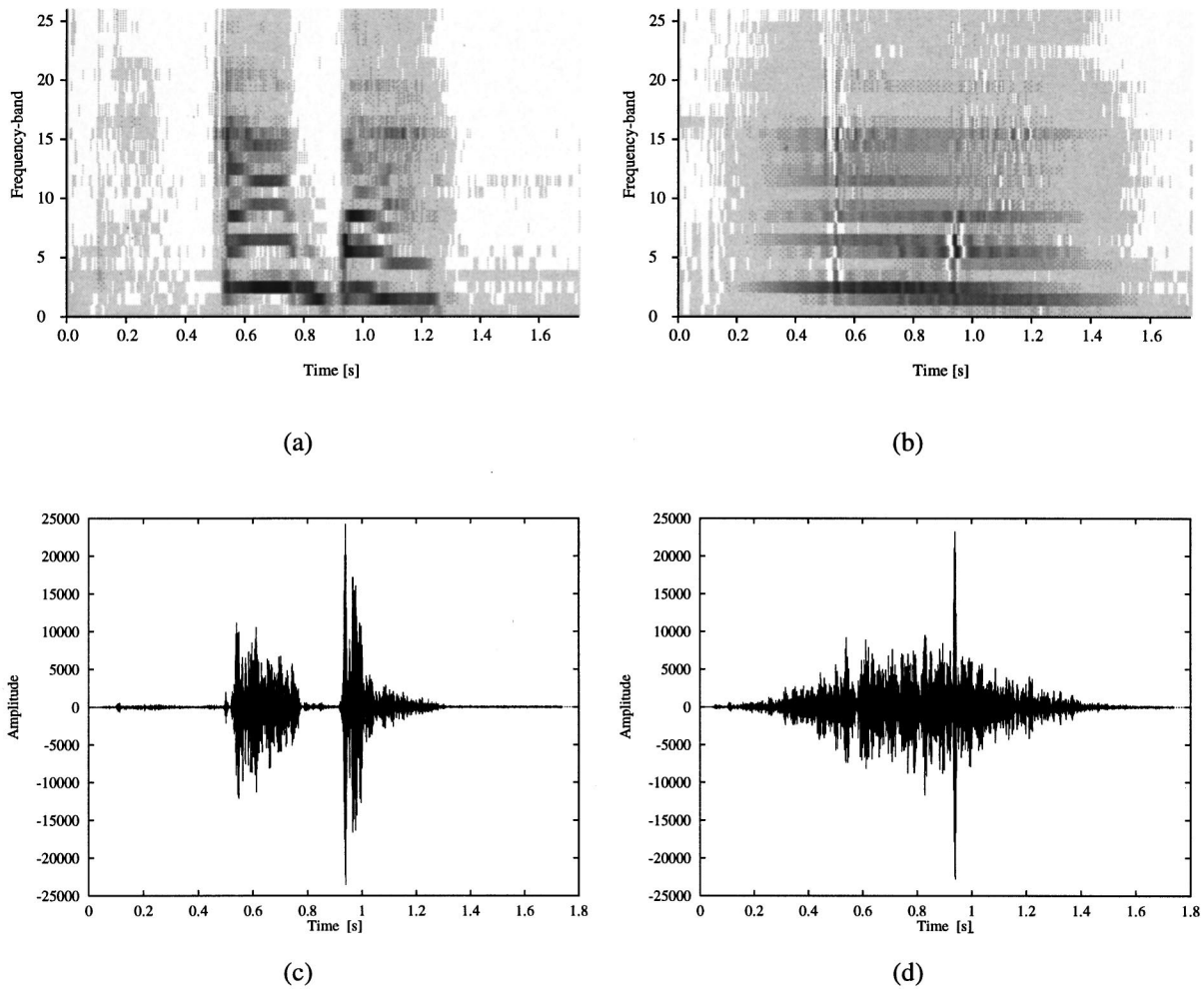
FIG. 2. Envelope representations of the stimulus /aba/ in the reference condition (a) and the LW condition (b). These are plotted similar to spectrograms: larger amplitude is depicted as darker gray. These envelope sets were used to modulate the narrow-band noises; the waveforms of the resulting stimuli are plotted in (c) and (d), respectively.

ing presented two lists of stimuli of the reference condition in a random order, with feedback of the presented consonant when the subject responded incorrectly. To avoid order effects of the conditions, every subject was presented a different sequence of conditions according to a digram-balanced Latin square (Wagenaar, 1969). In every experimental condition, two lists (108 stimuli) were presented to the subject in a random order. In the measurements, only correct/incorrect feedback was returned by means of green/red light on the computer display.

D. Subjects

Ten subjects with hearing thresholds better than 20 dB HL for frequencies from 125 Hz to 8 kHz were tested in a soundproof booth. The subjects were between 18 and 40 years old, and were paid. Three of the subjects had some experience with psychophysical experiments.

II. RESULTS

A. Number of correct consonant identifications

The proportions of correct responses in test and retest for all subjects are plotted in Fig. 3 as a function of the notch

width of the envelope filtering and with the center-frequency of the notch as a parameter. The influence of the signal processing can be seen in the result of the reference condition; the average of all subjects in this condition is 71%. The results of all other conditions are lower than the reference condition. Furthermore, the following trends can be seen:

(i) higher center frequencies of the notch give a higher score.

(ii) wider notch widths result in either no effect (high- and middle-center frequencies) or a large detrimental effect (low center frequencies) on the score.

An analysis of variance on the scores using the three factors of subjects, conditions, and test/retest gives the levels of statistical significance as depicted in Table III. It reveals that the subjects' scores were significantly different, the conditions gave significantly different results, and there was a significant learning effect between test and retest. Also, the interaction between subjects and conditions is significant. This means that different subjects had significantly different scoring patterns over the conditions. Furthermore, the interaction between subjects and repetitions is significant. So, different subjects had significantly different learning effects.
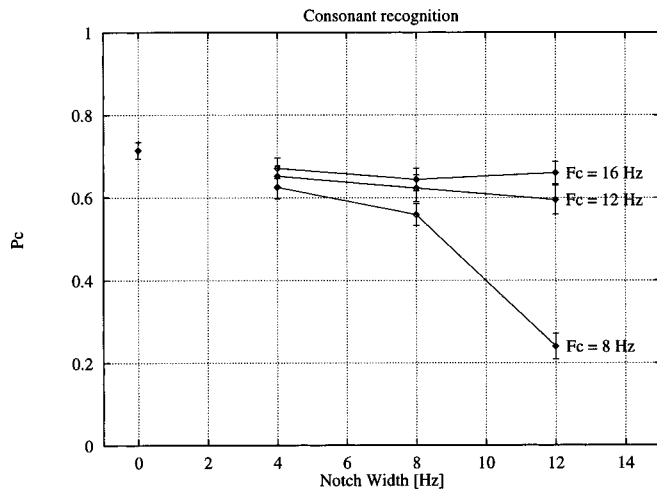
FIG. 3. Results of the consonant-intelligibility test as a function of the notch-width of the envelope filtering. The center frequency of the notch filtering is a parameter. Results for all subjects ($N=10$) and test and retest are averaged. Standard error of the mean is plotted as an error bar.

TABLE IV. One-tailed probabilities from the Wilcoxon signed-rank test performed on all pairs of conditions. Only significant values are displayed ($P<0.01$). For clarity, larger P values are substituted with a dot ($\cdot$). The conditions are labeled with the abbreviations as used in Table II.

	LN	LM	LW	CN	CM	CW	HN	HM	HW
R	0.001	0.001	0.001	0.005	0.001	0.001	0.005	0.006	$\cdot$
LN		$\cdot$	0.001	$\cdot$	$\cdot$	$\cdot$	0.003	$\cdot$	$\cdot$
LM			0.001	0.001	$\cdot$	$\cdot$	0.001	0.001	0.001
LW				0.001	0.001	0.001	0.001	0.001	0.001
CN					$\cdot$	$\cdot$	$\cdot$	$\cdot$	$\cdot$
CM						$\cdot$	0.005	$\cdot$	$\cdot$
CW							0.002	$\cdot$	0.005
HN								$\cdot$	$\cdot$
HM									$\cdot$

The interaction between conditions and test/retest is not significant.

The Wilcoxon signed-rank test was performed on all pairs of conditions in order to assess the significance of the differences between the conditions. All p values significant on a 0.01 level are tabulated in Table IV. Condition R, the reference condition, scores significantly higher than all other conditions except condition HW. Condition LM scores significantly lower than the high center-frequency conditions HN, HM, HW, and the condition CN, but not differently from conditions CM and CW. Condition LW scores significantly lower than all other conditions.

When looking per center frequency, one can see that there is no significant effect of a larger notch width around the high- and middle center frequencies (conditions HN, HM, HW, and conditions CN, CM, CW, respectively). For the low center frequency, there is only the aforementioned condition LW that differs from conditions LN and LM. Between conditions LN and LM there is no significant difference. When looking per notch width, one can see that the conditions with the widest notch widths (LW, CW, and HW) all differ significantly among themselves. But for the other notch widths, there is only a significant difference between the scores from the high- and the low center frequencies (conditions LN vs HN and conditions LM vs HM, respectively).

TABLE III. Analysis of variance on the scores. Dimensions in the design are subjects, conditions, and repetition. The highest interaction is taken as an error estimate.

Design	F_{prob}
subjects	$p<0.001$
conditions	$p<0.001$
subjects$\times$conditions	$p<0.001$
repetitions	$p<0.001$
subjects$\times$repetitions	$p<0.005$
conditions$\times$repetitions	$p=0.29$

B. Confusion between consonants

Confusion matrices were analyzed by means of multidimensional scaling and sequential information analysis.

1. Multidimensional scaling

The asymmetric confusion matrices had to be converted to symmetric similarity matrices in order to be analyzed by INDSCA (Carroll and Chang, 1970). This was accomplished by means of a procedure suggested by Houtgast and used by Klein *et al.* (1970). In this procedure, the cells of the similarity matrix, $s(i,j)$, are calculated not only from the four confusion elements $c(i,j)$, $c(j,i)$, $c(i,i)$, and $c(j,j)$, but from the total correspondence between the response distributions for the stimuli i and j. Mathematically

$$s(i,j)=s(j,i)=\frac{1}{2}*\left(\sum_{k=1}^{n} (c(i,k)+c(j,k)) - \sum_{k=1}^{n} |c(i,k)-c(j,k)| \right), \quad (5)$$

in which the dissimilarity of the response distributions, $\Sigma_{k=1}^{n}|c(i,k)-c(j,k)|$, is subtracted from the total number of valid responses on the stimuli i and j, $\Sigma_{k=1}^{n}(c(i,k)+c(j,k))$.

The results of INDSCAL analysis in two dimensions are plotted in Fig. 4.

In the stimulus space, the first perceptual dimension is always positive for the plosive phonemes, and always negative for the fricative phonemes. The nasals and semivowels are somewhat in-between. So, the first dimension seems to make a separation between ''plosiveness'' and ''fricativeness'' of the phonemes. Looking at the second perceptual dimension, one can see the nasals and semivowels having a positive value, and the fricatives having a negative value with the /s/ phoneme at the extreme. The plosives have both positive (/b/, /p/) and negative values (/d/, /t/) for their second dimension. Therefore, it seems that the second dimension is related to the amount of low-frequency energy in the phoneme, because nasals and plosives like /b/ and /p/ are known to have a large amount of low-frequency energy, especially when compared with /s/ and /ʃ/, which consist of almost only high-frequency energy.
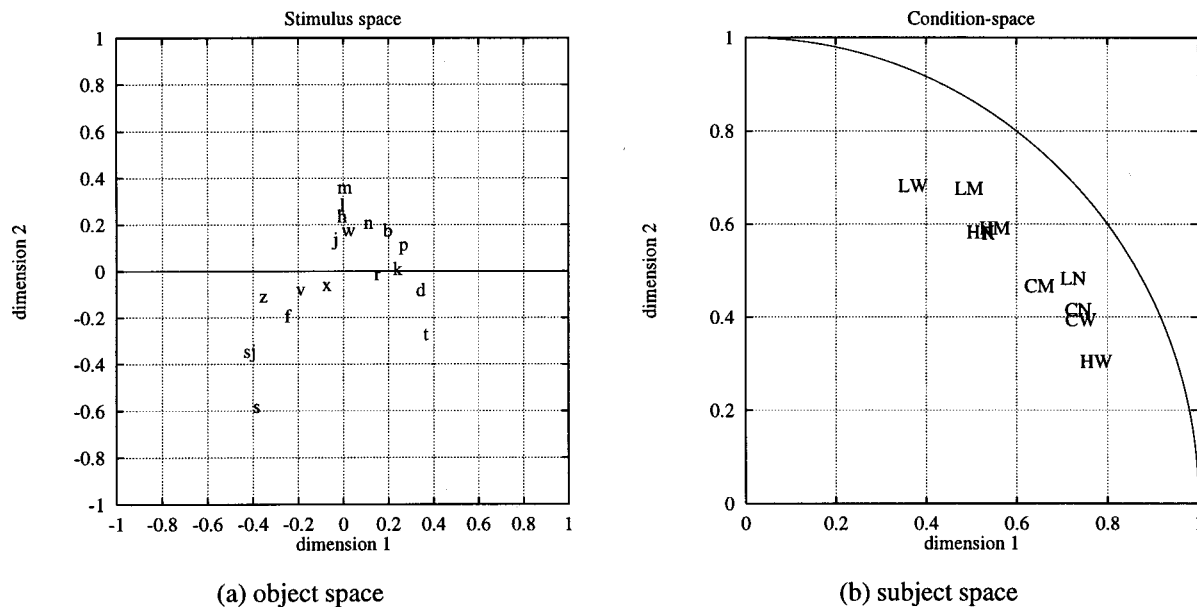
FIG. 4. The object and subject space of the INDSCAL analysis in two dimensions, related to the position of the stimuli and the weighting of perceptual information across conditions, respectively. ''sj'' is used as a symbol for the phoneme /ʃ/.

In the so-called subject space, each experimental condition is plotted according to the weight of the perceptual dimensions defined in the stimulus space. So, it can be regarded as a ''condition space.'' The quarter of a circle represents points for which 100% of the variance is explained. Obviously this is not the case, but for each condition, about 78% to 87% of the variance can be explained in two dimensions, even for the most difficult condition [LW in Fig. 4(b)]. For the reference condition R, both dimensions appear to be about equally important. The same is true for the conditions HN and HM [see Fig. 4(b)]. These conditions are characterized by the fact that all modulation frequencies up to at least 12 Hz are present. When the middle frequencies (8–12 Hz) are filtered out (conditions LN, CN, CM, CW, and HW), the weighting of the first dimension increases at the expense of the weighting of the second dimension. Thus, the ability to discriminate on the basis of the second perceptual dimension is reduced. So, filtering out modulation frequencies between 8–12 Hz blurs the distinction between high-frequency energy phonemes and low-frequency energy phonemes. If the lowest modulation frequencies (below 6 Hz) are filtered out (LM and LW), the opposite effect appears: The weighting of the second dimension increases at the expense of the weighting of the first dimension. Thus, the ability to discriminate on the basis of the first perceptual dimension is reduced. So, filtering out modulation frequencies below 6 Hz blurs the distinction between plosiveness cues and fricativeness cues.

2. Sequential information analysis

Sequential information analysis (Wang and Bilger, 1973) was applied for each experimental condition to assess the amount of information transfer from stimulus to response for a set of the most relevant phonetic features. In these analyses,[1] the sequence in which the information transmis-

sion per phonetic feature is analyzed influences the outcome. In eight out of ten conditions, the order of analysis as applied by the program was frication, plosiveness, place, nasality, and voicing. For reasons of comparison between experimental conditions, the order of analysis in the other two conditions was forced to be the same.

The total amount of transferred information is plotted in Fig. 5(a), and the information-transfer function for the phonetic features are plotted in the Fig. 5(b)–(f), respectively. The maximum amount of transferred information for 18 equally often presented stimuli is 4.17.

In general, the patterns in the total transferred information and the information transfer for the phonetic features are very similar to the pattern found for a simple tally of consonants correctly identified (Fig. 3), that is,

(i)   the reference condition has the highest value,
(ii)   the values for the high- and middle center frequencies do not differ much from this value and,
(iii)   are also not much dependent on the notch width
(iv)   only the values for the low center frequencies are strongly dependent on the notch width, and
(v)   only the LW (low center frequency, wide notch width) condition differs strongly from the other values.

There are a few deviations from this general pattern:

(i)   the values for the transfer of the voicing feature are all very low (<0.2), which follows directly from the removal of the periodicity cues,
(ii)   for plosiveness, there is a large difference between the reference condition and the high- and middle center frequency conditions,
(iii)   for nasality, there is a large difference between all low center-frequency conditions and the high- and middle center frequency conditions,
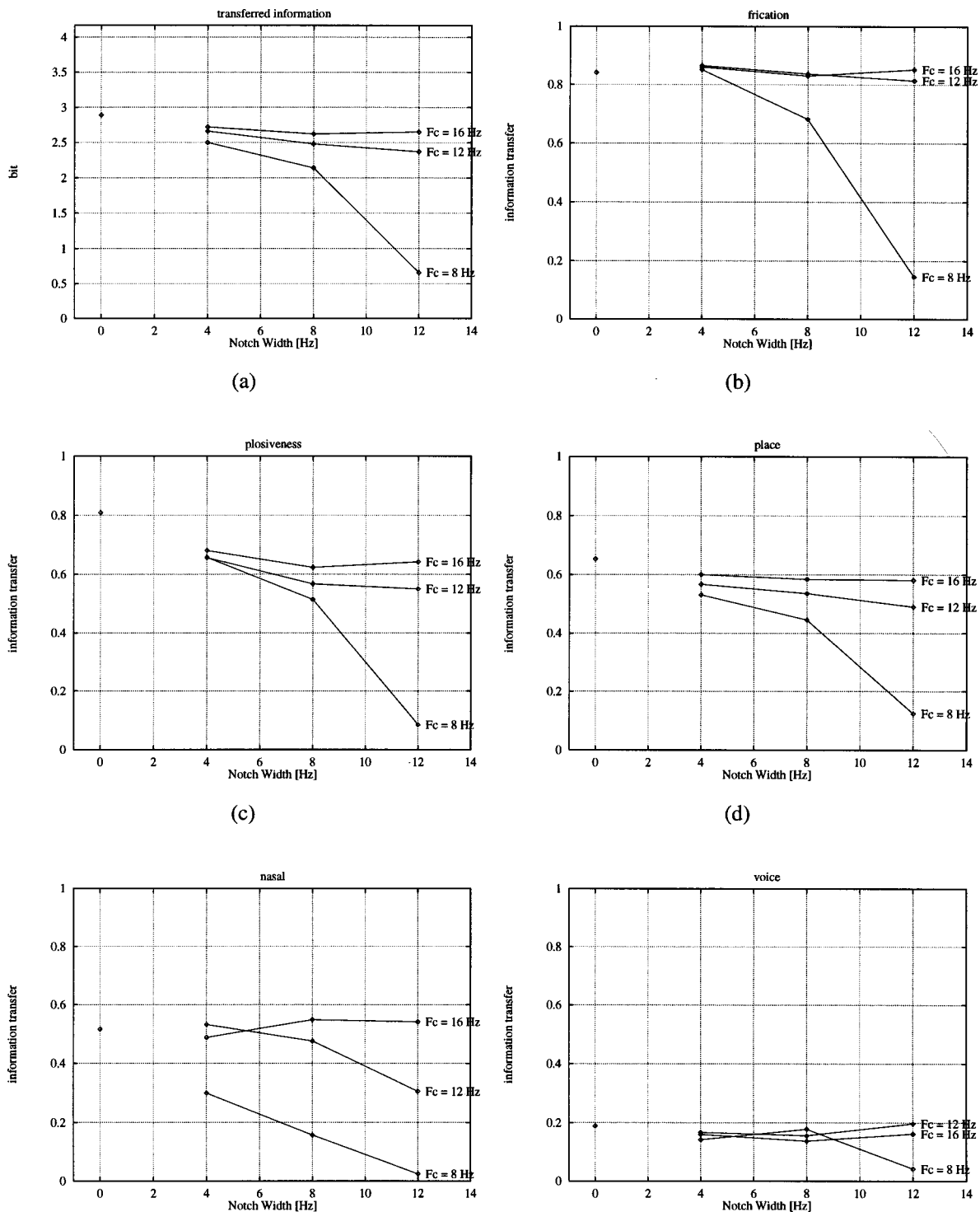
FIG. 5. Results from the SINFA analysis plotted against the notch-width and with the center frequency as parameter. In (a), the total amount of transferred information is displayed. Information-transfer functions for the features frication, plosiveness, place, nasality, and voicing are plotted in (b)–(f), respectively.

(iv) for nasality, the middle center frequency conditions seem as dependent on notch width as the low center frequency conditions.

In order to assess the influence of replacing the speech carrier by noise on the individual phonetic features, the unconditional measures of information transfer were calculated for each of the features. In this way, the influence of the signal processing on the information transfer of each pho-

netic feature can be assessed independently. When looking at the amount of information transfer for the reference conditions in Table V, it can be seen that this particular analysis–resynthesis method has a different impact on the transfer of the different phonetic features. While the frication and plosive cues are almost completely transferred (0.84 and 0.83, respectively), just two-thirds (0.64) of the place cues and only half (0.49) of the nasality cues get through, and more

TABLE V. Amount of information transfer for each phonetic feature in the reference condition, assessed independently.

Feature	Information transfer
frication	0.841
plosive	0.833
place	0.641
nasality	0.488
voicing	0.387

FIG. 7. Results of the consonant-intelligibility test as a function of the lower edge-frequency of the notch of the envelope filtering expressed as the $-\log 2(f_l)$. Results for all subjects ($N=10$) and test and retest are averaged. Standard error of the mean is plotted as an error bar.

than 60% of the voicing information gets lost in the processing.

III. DISCUSSION

The goal of these experiments was to assess the relative importance of different regions of modulation frequencies for consonant recognition in speech signals containing only narrow-band envelope cues. Therefore, the speech signal was transformed in such a representation that it was possible to filter out different modulation frequencies in the region between 2 and 20 Hz. As can be seen in Fig. 3, the recognition of consonants is very robust for filtering of the narrow-band envelopes, and only large notch filtering around 8 Hz (condition LW) gives a substantial degradation of the score.

The results from Fig. 3 seem to suggest that a notch of a certain width is more detrimental to the score when it is around a lower center frequency; therefore, the results were also plotted with a logarithmic scale of notch width in Fig. 6.

When plotted in this way, it seems that the scores are directly dependent on the notch width expressed in octaves.

The lengths of the speech sounds were in the range of 0.5–0.7 s. Therefore, when filtering very low-modulation frequencies, one tends to smear the signal beyond its own length, resulting in a substantial lengthening of the signal and a gradual fading in and out of the signal [see also Fig. 2(b)]. So, the envelope cues gets ''blurred'' and the stimuli are hardly perceived as VCV syllables. This blurring is inherent to the filtering of very low frequencies but can also be considered an artifact of the signal processing.

The amount of smearing is directly related to the lower edge of the notch, and therefore the recognition scores were also plotted against this value (see Fig. 7). This plot is very similar to Fig. 6, and consequently does not give a better understanding of the results with respect to the underlying processes responsible for this degradation.

The relative amount of information transmitted in the reference condition is 0.69. This is three times as much as the relative amount of transmitted information as reported by Van Tasell *et al.* (1987) in their 20-Hz condition. This difference can only be explained by the fact that in this experiment, 26 narrow-band envelopes were used as the carriers of the information, thus conveying dynamic spectral-shape information.

The amount of medial consonant recognition as reported by Drullman *et al.* (1994) was around 90% in their reference condition and about 85% in their 16-Hz low-pass condition. In our experiment, only 71% of the consonants were correctly recognized by the subjects. This difference can only be accounted for by the lack of periodicity- and temporal fine-structure cues that were removed from the stimuli in this experiment.

The consonant-recognition scores in the experiment of Shannon *et al.* (1995) were almost 90 percent in the condition with four processing bands. In our experiment there were more processing bands, and thus more information. But the extra envelopes did not add more usable information for the subjects; it even degraded the recognition scores in comparison with the results from Shannon *et al.* (1995). The largest difference between the outcome of Shannon *et al.* (1995) and our results is in the information received on voicing. They found that temporal information in only two processing bands can transfer 90% of the voicing cues. In our experiment, only 39% of the voicing cues were transferred in our reference condition.

One aim of this experiment was to assess the importance of different modulation frequencies, but due to the choice of

FIG. 6. Results of the consonant-intelligibility test as a function of the notch-width of the envelope filtering expressed as octaves. Results for all subjects ($N=10$) and test and retest are averaged. Standard error of the mean is plotted as an error bar.

filtering out modulations and, therefore, the inherent smearing in the low–wide condition, one cannot conclude decisively whether the low scores in that condition are caused by the large importance of the low-modulation frequencies or by this smearing effect.

Figure 6 suggests that the width of the notch, and therefore the amount of envelope information that is filtered out, can serve as an explanation for the results. On the other hand, Fig. 7 suggests that the lower edge frequency of the notch, and therefore the amount of smearing, is responsible for the degradation of the recognition scores. Because the trends in these figures are very similar, one cannot favor one explanation over the other based on this experimental data.

IV. CONCLUSIONS

(1) Consonant recognition seems very robust for notch filtering the narrow-band envelope representation.

(2) Only large notch filtering (condition low-wide) gives a substantial degradation of consonant recognition.

(3) The perception of the modulations in speech sounds is better described with a logarithmic frequency scale of modulation rate than with a linear scale.

(4) There are two explanations that describe the experimental results equally well. On the one hand, the amount of the modulation spectrum still present in the stimuli is directly proportional with the scores. This can be concluded from the fact that the amount of remaining modulation spectrum is inversely proportional to the width of the notch as expressed in octaves. On the other hand, the amount of temporal smearing is inversely proportional with the score. This follows from the fact that the temporal smearing is inversely proportional to the lowest edge-frequency of the notch filter.

(5) More information in the form of more narrow-band envelopes does not result in higher scores.

(6) The use of a high number of processing bands, as used in this study, has a detrimental effect on the transfer of voicing cues.

[1]The sequential information analysis was carried out with the computer program FEATURE INFORMATION XFER (FIX) from M. Johnson, Dept. of Phonetics and Linguistics, University College, London.

Carroll, J. D., and Chang, J. J . (**1970**). ''Analysis of individual differences in multidimensional scaling via an *n*-way generalization of the 'eckart-young' decomposition,'' Psychometrica **35**, 283–319.

Drullman, R., Festen, J. M., and Plomp, R. (**1994**). ''Effects of temporal envelope smearing on speech reception,'' J. Acoust. Soc. Am. **95**, 1053–1064.

Glasberg, B. R., and Moore, B. C. J. (**1990**). ''Derivation of auditory filter shapes from notched-noise data,'' Hearing Res. **47**, 103–138.

Houtgast, T., and Steeneken, H. J. M. (**1985**). ''A review of the mtf concept in room acoustics and its use for estimating speech intelligibility in auditoria,'' J. Acoust. Soc. Am. **77**, 1069–1077.

Klein, W., Plomp, R., and Pols, L. C. W. (**1970**). ''Vowel spectra, vowel spaces and vowel identification,'' J. Acoust. Soc. Am. **48**, 999–1009.

Rosen, S. (**1992**). ''Temporal information in speech: acoustic, auditory and linguistic aspects,'' Philos. Trans. R. Soc. London, Ser. B **336**, 367–373.

Shannon, R., Zeng, F.-G., Kamath, V., Wygonski, J., and Ekelid, M. (**1995**). ''Speech recognition with primarily temporal cues,'' Science **270**, 303–304.

Van Tasell, D. J., Soli, S. D., Kirby, V. M., and Widin, G. P. (**1987**). ''Speech waveform envelope cues for consonant recognition,'' J. Acoust. Soc. Am. **82**, 1152–1161.

Wagenaar, W. A. (**1969**). ''Note on the construction of digram-balanced latin squares,'' Psychol. Bull. **72**, 384–386.

Wang, M. D., and Bilger, R. C. (**1973**). ''Consonant confusions in noise: a study of perceptual features,'' J. Acoust. Soc. Am. **54**, 1248–1266.

Sound localization in noise in normal-hearing listeners[a]

Christian Lorenzi,[b] Stuart Gatehouse, and Catherine Lever

MRC, Institute of Hearing Research (Scottish Section), Royal Glasgow Infirmary, Queen Elizabeth Building,
16 Alexandra Parade, Glasgow G31 2ER, Scotland, United Kingdom

The ability to localize a click train in the frontal–horizontal plane was measured in quiet and in the presence of a white-noise masker. The experiment tested the effects of signal frequency, signal-to-noise ratio (S/N), and masker location. Clicks were low-pass filtered at 11 kHz in the broadband condition, low-pass filtered at 1.6 kHz in the low-pass condition, and bandpass filtered between 1.6 and 11 kHz in the high-pass condition. The masker was presented at either −90, 0, or +90 deg azimuth. Six signal-to-noise ratios were used, ranging from −9 to +18 dB. Results obtained with four normal-hearing listeners show that (1) for all masker locations and filtering conditions, localization accuracy remains unaffected by noise until 0–6 dB S/N and decreases at more adverse signal-to-noise ratios, (2) for all filtering conditions and at low signal-to-noise ratios, the effect of noise is greater when noise is presented at ±90 deg azimuth than at 0 deg azimuth, (3) the effect of noise is similar for all filtering conditions when noise is presented at 0 deg azimuth, and (4) when noise is presented at ±90 deg azimuth, the effect of noise is similar for the broadband and high-pass conditions, but greater for the low-pass condition. These results suggest that the low- and high-frequency cues used to localize sounds are equally affected when noise is presented at 0 deg azimuth. However, low-frequency cues are less resistant to noise than high-frequency cues when noise is presented at ±90 deg azimuth. When both low- and high-frequency cues are available, listeners base their decision on the cues providing the most accurate estimation of the direction of the sound source (high-frequency cues). Parallel measures of click detectability suggest that the poorer localization accuracy observed when noise is at ±90 deg azimuth may be caused by a reduction in the detectability of the signal at the ear ipsilateral to the noise. © *1999 Acoustical Society of America.* [S0001-4966(99)00303-3]

PACS numbers: 43.66.Qp, 43.66.Pn [DWG]

INTRODUCTION

The ability to judge the direction of a sound source has been studied both under headphones (lateralization studies) and in the free field (localization studies). The effect of noise on the ability to lateralize sound sources has been frequently examined (e.g., Houtgast and Plomp, 1968; Robinson and Egan, 1974; Yost, 1975; Cohen, 1981; Gaskell and Henning, 1981; Ito *et al.*, 1982; Stern *et al.*, 1983). In contrast, there has been little research on the localization of sound sources in noise (Jacobsen, 1976; Abel and Hay, 1996; Good and Gilkey, 1996), and so it remains unclear whether the processes used by listeners to localize sound sources in quiet are also used to localize sound sources in noisy environments (a more typical situation).

The ability to localize a sound is dependent on three acoustic cues: Interaural time differences (ITD) at low frequencies, interaural level differences (ILD) and spectral cues at high frequencies. Timing information carried by the envelopes of high-frequency stimuli can also be used by the binaural system to localize a sound source. Following the "duplex" theory originally developed by Lord Rayleigh (1907), Kistler and Wightman (1992) argued that in listeners with normal hearing, localization judgments in the frontal–horizontal plane are primarily based on an analysis of ITD and ILD cues. They also showed that, in the horizontal plane, low-frequency ITDs are the dominant cues for localization of broadband sounds, while ILDs and spectral shape are the dominant cues for localizing high-frequency sounds.

In the context of the duplex theory, it is generally assumed that a listener's consistency or resolution in localizing sound sources is related to the ability to detect small changes in interaural differences (Mills, 1958, 1960). Measurements of just noticeable differences (jnd's) in the presence of interfering noise have been reported for temporal fine structure ITD cues (e.g., Houtgast and Plomp, 1968; Cohen, 1981; Ito *et al.*, 1982; Stern *et al.*, 1983) and for ILD cues (Stern *et al.*, 1983). These studies showed that when noise is presented diotically, both ITD and ILD jnd's exhibit similar dependencies on signal-to-noise ratio, with ITD and ILD jnd's becoming larger as signal-to-noise ratio decreases. Moreover, both ITD and ILD jnd's are worse when the noise is interaurally out of phase than when it is presented diotically. In other words, the interaural condition which favors signal detection [or largest masking-level difference (MLD), Hirsh (1948)] results in poor lateralization (e.g., Cohen, 1981; Stern *et al.*, 1983). Other investigations indicated that the mechanism sensitive to interaural-envelope time differences is significantly more susceptible to noise than the mechanism sensitive to ITDs in the fine structure of the signals (Yost, 1975; Gaskell and Henning, 1981). Moreover, it

has been argued that ITDs in the envelopes of high-frequency sounds do not contribute significantly to localization performance (Middlebrooks and Green, 1990). This suggests that envelope cues are not likely to play a role in sound localization in noise, and that the dominant cues used for localizing sounds, i.e., fine structure ITD cues and ILD and spectral shape cues, are equally affected by an interfering noise. The degree to which these results can be generalized to free-field situations is, however, necessarily limited as lateralization studies do not take into account the effects of (i) head and pinna diffraction, and (ii) head movements. The results above were based on ITD and ILD jnd's measured for baseline ITD and ILD of 0. These data do not, therefore, provide any information about the extent to which the processing of each cue would be affected by noise as the sound source moves to the spatial periphery.

The effects of signal-to-noise ratio, masker location and signal sensation level on localization performance in the free field were extensively studied by Good and Gilkey (1996) and Good et al. (1997). In a series of experiments, they measured the ability to localize a broadband click train in the frontal–horizontal plane, in quiet and in the presence of an interfering broadband noise. Head movements of listeners were restricted. Their results showed that localization judgments performed when the noise is presented straight ahead (at 0 deg azimuth) are more accurate than those performed when the noise is to the left or to the right (at −90 and +90 deg azimuth, respectively). When noise is presented straight ahead, localization accuracy decreases nearly monotonically as the signal-to-noise ratio is lowered. However, localization accuracy is not greatly affected by the noise until the signal-to-noise ratio drops to the detection threshold (here, detection threshold is measured for the case when the signal and the noise are presented from the same speaker directly in front of the listener). Their results also showed that judgments are shifted towards the masker location when the signal-to-noise ratio is lowered. In another series of experiments, Good et al. (1997) measured the ability to detect the click-train signal in quiet and in the presence of noise. They used these free-field detection data to determine the sets of conditions in the localization experiments where the signals were at approximately equal sensation levels. This allowed them to compare localization accuracy at different spatial locations without the confounding effects of changes in detectability. Their results showed that, in most conditions, localization accuracy increases with the signal sensation level (ranging from −4 to +8 dB SL). However, reasonably good localization accuracy was observed for signals in the frontal hemisphere which were only a few decibels above detection threshold.

The effect of signal frequency on localization accuracy in the free field was investigated by Jacobsen (1976), Perrott (1984), and Abel and Hay (1996). Jacobsen (1976) used a discrimination task which assessed the just-noticeable shift in the position of a sound source: i.e., the minimum audible angle (MAA). Measurements of the horizontal-plane MAA were reported for a sinusoidal signal masked by a broadband noise and presented at 0 deg azimuth. This study showed that, as long as the level of the signal is 10–15 dB above its

masked threshold, the MAA is no greater than when there is no masking noise (<3 deg). However, when the signal is presented at a low sensation level (3 dB), the MAA increases to over 6 deg when the signal frequency is 3 kHz, but remains at about 3 deg when the signal frequency is 0.5 kHz. Perrott (1984) measured the smallest detectable angular separation between two temporally overlapping tones of different frequencies presented to two different loudspeakers in the frontal–horizontal plane. His results indicate that spatial acuity deteriorates when a target sound and a masking sound are presented simultaneously and when they are close in frequency. In a similar manner to Good and Gilkey (1996), Abel and Hay (1996) used a source-identification task in which the ability to localize a narrow band of noise centered at 0.5 or 4 kHz was measured in the presence of a continuous white noise producing a homogeneous sound field. The signals and the masking noise were played at 80 and 65 dB SPL, respectively, and the experiment was conducted in a semireverberant room. Head movements of listeners were restricted. The ability to localize the 0.5-kHz signal was affected by the noise masker, especially for frontal and sides conditions. In comparison, the ability to localize the 4-kHz signal was not affected by the noise masker.

Although lateralization studies have shown that fine structure ITD and ILD cues are equally resistant to noise when stimuli are presented under headphones (e.g., Stern et al., 1983), the extent to which these results can be generalized to free-field situations remains unclear. The results of the localization studies performed by Jacobsen (1976) and Abel and Hay (1996) suggest that ITD and ILD and spectral shape cues are not equally affected by the presence of noise. However, the results of these studies are apparently contradictory, with greater disruption for high frequencies in Jacobsen (1976) and the converse (greater effects for low frequencies) in Abel and Hay (1996).

This discrepancy may be due to differences in the experimental paradigms used by these authors; a discrimination paradigm on the one hand, and an identification paradigm on the other. Further investigation of the processes underlying sound localization in noise is therefore warranted. The present study aims to assess the relative susceptibility to noise of low-frequency ITD cues and high-frequency ILD and spectral cues in the free field using the sound-source identification paradigm described by Good and Gilkey (1996). In a first set of experiments, we measured the ability of normal-hearing listeners to localize a click-train signal in the frontal–horizontal plane, in quiet and in noise. The click-train signal was subjected to selective filtering which forced listeners to localize the click train using predominantly low-frequency ITD cues or high-frequency ILD and spectral cues. In each condition, the effects of signal-to-noise ratio and masker location on localization performance were tested. A second set of experiments investigated the relation between localization performance and the detectability of the signal as a function of signal azimuth and masker location.

I. METHOD

A. Listeners

Three male listeners (CH, PA, and TO) and one female listener (CA) participated in the experiment. Listeners ranged in age from 23 to 33 years. They had no reported hearing impairments, and measured hearing-threshold levels not exceeding 15 dB at any of the frequencies of 0.25, 0.5, 1, 2, 4, and 8 kHz.

B. Apparatus and stimuli

Sound-localization ability was assessed by means of a 1.25-m-radius hemisphere placed in a sound-treated chamber (3 m long, 3 m wide, 2 m high). Eleven speakers were mounted on the inner surface of the hemisphere, at 0 deg elevation along the horizontal plane. Speakers were 18 deg apart in each plane at azimuths ranging from −90 to +90 deg. The surface of the hemisphere was covered with foam so as to attenuate reflections. Speakers were full range (150 Hz–20 kHz). All SPLs were measured at the listener's head position. The loudspeakers were RS type 433-309 with flat frequency response (+1 dB) between 0.15–20 kHz. The gain of each speaker was balanced so that levels emanating from each speaker were within 1.5 dB SPL for frequencies 100 Hz to 1 kHz. Listeners sat in the (theoretical) center of the full sphere, 1.25 m from each speaker, facing the speaker at 0 deg azimuth and 0 deg elevation. The speakers were visible and numbered. A personal computer and software controlled signal presentation. Listeners responded using a response box with a matrix of buttons configured like the speaker matrix. Listeners were informed that the experiment investigated only localization ability in the frontal–horizontal plane. Because of this instruction, listeners never volunteered that the signal came from behind.

The signal and masker were similar to those used by Good and Gilkey (1996). They were generated digitally at a sampling rate of 44.1 kHz. The signal was a train of 23-μs pulses, which were repeated at a rate of 100 Hz. The pulse train had a duration of 300 ms and was shaped with 25-ms cosine onset and offset ramps. The pulse train was low-pass filtered digitally at 11 kHz in the ''broadband'' condition, low-pass filtered at 1.6 kHz in the ''low-pass'' condition, and bandpass filtered between 1.6 and 11 kHz in the ''high-pass'' condition. All the rejection slopes were 96 dB per octave. The resulting pulse train was attenuated digitally and presented through one channel of a 16-bit digital-to-analog converter at a sampling rate of 44.1 kHz. The overall level of the signal was fixed to 70 dB SPL (rms).

The masker was a 900-ms white noise shaped with 25-ms cosine onset and offset ramps. It was low-pass filtered digitally at 14 kHz (96 dB per octave rejection slope). Twenty different samples of filtered noise were generated and a random one was chosen for each trial. The masker was attenuated digitally and presented through a separate channel of the 16-bit digital-to-analog converter used to play the signal. Six noise levels were used: 52, 58, 64, 70, 76, and 79 dB SPL. The signal-to-noise ratio thus ranged from −9 to +18 dB. The masker was presented at either −90, 0, or +90 deg azimuth. The signal and masker were switched to the appro-

priate speakers. The switching hardware also added signal and masker when they were spatially coincident. The signal was temporally centered within the masker.

As the speakers were mounted on a rigid structure and the room environment was not anechoic, there exists the possibility that the acoustic properties of the room and experimental rig combination might disrupt the ILD, spectral shape, and ITD cues that are required for sound-source identification in the frontal–horizontal plane. Therefore, a series of experiments was performed using KEMAR recordings to assess the extent to which that might have occurred. White noise, broadband click trains, low-pass click trains, and high-pass click trains were presented from each loudspeaker in turn and recorded on a DAT device from the two Zwislocki couplers on the KEMAR manikin. To investigate ILD cues, the difference between the spectra at the two couplers was computed in 1/3-octave bands as a function of frequency and compared to the averaged data of Shaw (1975). The results showed agreement to within ±3 dB for all speaker angles between ±90 deg. Assessment of ITD cues proceeded in two stages. Initially, the reverberation time [T_{60}] for each stimulus and for each speaker angle was derived. These ranged from 0.16 to 0.26 s and exhibited no dependence on frequency or angular orientation. However, reverberation times provide an incomplete representation of the extent to which ITD cues might be preserved. The recordings were therefore bandpass filtered at discrete frequencies and a cross correlogram as a function of frequency computed. From each cross correlogram, the maximum value of the function was identified and the ITD which provided that maximum was recorded. Comparison was then made with the data of Kuhn (1977), who provided values for ITD as a function of frequency and angular orientation. Our recordings align with those of Kuhn (1977) to within 0.09 ms and the values of our peak cross-correlation range from 0.72 to 0.79 for angles of ±90 deg compared to 0.81 to 0.86 for 0 deg azimuth. Thus, the ITD and ILD cues which can be used for localization in the frontal–horizontal plane are sufficiently preserved in our experimental situation. Although these measures address the ''steady-state'' situations and hence are relevant to the noise signal, they do not completely characterize the transient click stimulus used as the target. Measures of the reverberant echoes to a single token of the click show that, in the time period 5–20 ms after such a stimulus, these echoes were at least 18 dB reduced from the original for the wideband, low-pass, and high-pass clicks. Thus, for the signal-to-noise ratios employed in the experiment and the values for which listeners' errors become material, the extraneous cues which might have led to a percept of a stimulus orientation outside the frontal–horizontal plane (elevation or front/rear confusion) were not likely to be audible. No such percept was reported by listeners.

C. Procedure

1. Localization

Listeners were asked which of the 11 numbered speakers was the most likely source of the target sound presented

1812   J. Acoust. Soc. Am., Vol. 105, No. 3, March 1999

Lorenzi *et al.*: Localization in noise: Normal-hearing listeners   1812
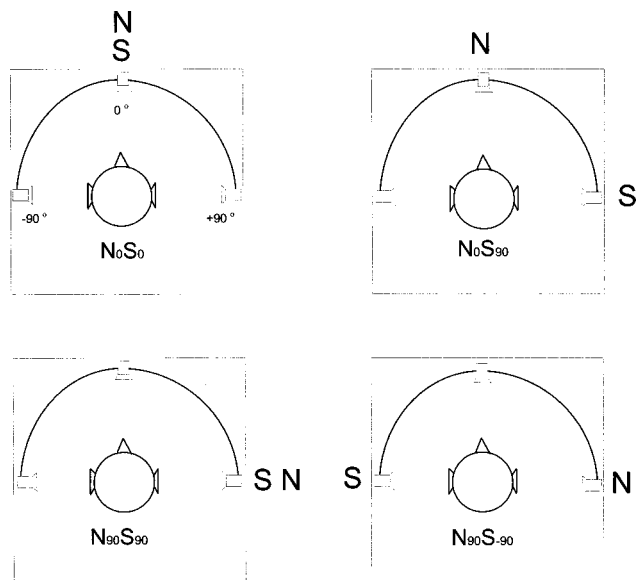
FIG. 1. Azimuths of the signal (S) and noise (N) used in the detection experiments. Four conditions were tested (referred to as N_0S_0, N_0S_{90}, $N_{90}S_{90}$, and $N_{90}S_{-90}$): Noise was presented at 0 deg azimuth (top panels) or at +90 deg azimuth (bottom panels); signal and noise were either spatially coincident (left panels) or maximally separated (right panels).

in each experimental trial. They were asked to look straight ahead and to hold their heads and eyes steady during a stimulus presentation.

An experimental session consisted of three separate listening sessions, one for each of the three masker locations (−90, 0, or +90 deg azimuth). A listening session comprised 40 experimental runs. Within a run, there were 77 trials, one presentation of the 11 speakers at each of the seven noise levels (including the ''in quiet'' condition) in random order. Within a run, successive target sounds were varied at random through ±1 dB from the nominal level to minimize any (residual) absolute level cues associated with a particular speaker which might be used for source identification. The intertrial interval was fixed at 1.5 s. No feedback was given during the run. To eliminate the effects of training, the order of experimental sessions was randomized between listeners. In addition, ten training runs were provided at the beginning of each experimental session.

2. Detection

In a second set of experiments, the audibility of the signal was assessed by measuring the sensitivity (d') of each listener using a blocked procedure for four combinations of the signal (S) and the masking noise (N) locations, referred to as N_0S_0, N_0S_{90}, $N_{90}S_{90}$, and $N_{90}S_{-90}$. Figure 1 illustrates these four experimental conditions: The masking noise was either presented straight ahead (top panels) or at the side (bottom panels), and signal and masker were either spatially coincident (left panels) or maximally separated (right panels). The detection measurements utilized the stimuli (click trains and masking noises) and the signal-to-noise ratios used in the localization measurements. This is likely to be more informative than a single measure of detection threshold. In each condition and for each listener, we measured five-point psychometric functions, using a single interval yes/no task,

based on 50 trials per point. The gated noise masker was present in each trial. The signal was present in 50% of the trials. The silent interval between trials was 1.5 s. The five most adverse signal-to-noise ratios used in the localization experiments were involved in the detection experiment. Listeners received no training or feedback during this experiment.

D. Data analysis

Various statistics have been used to quantify localization performance (see also Hartmann, 1983; Good and Gilkey, 1996):

(1) The root-mean-square (rms) error, D, which corresponds to the rms average of the difference between the azimuth of the source and the listener's response. The run rms error ($\bar{D}$) corresponds to the rms average across speakers of the rms error for each speaker. D and $\bar{D}$ are used to quantify a listener's accuracy in localizing sound sources. In the present experiment, $\bar{D}$ should vary between 0 (perfect localization) and 80.4 deg (random guessing).
(2) The signed error, E, which corresponds to the average deviation of the listener's responses from his/her mean response. The run signed error ($\bar{E}$) corresponds to the signed error E averaged across speakers. E and $\bar{E}$ take into account the sign of this deviation, and therefore indicate any systematic response biases to the left (negative error) or right (positive error). In the present experiment, $\bar{E}$ is equal to 0 deg both in the case of perfect localization and random guessing.
(3) The response standard deviation, s, which indicates the variability of listeners' responses. $\bar{s}$ corresponds to the response standard deviation, s, averaged across speakers. s and $\bar{s}$ are considered as measures of localization consistency. In the present experiment, $\bar{s}$ should vary between 0 (perfect localization) and 57.5 deg (random guessing).
(4) The proportion of variance accounted for by the best-fitting linear relation between the perceived angles and the actual source angles, r^2, which also indicates the variability of listeners' responses. r^2 can be considered primarily as a measure of localization consistency, though with a potential contribution from localization accuracy. In the present experiment, r^2 will vary between 0 (random guessing) and 1 (perfect localization). It should be noted that r^2 could be unity in circumstances where localization is not perfect. This would occur, for example, if all responses fell along a straight line (as in Fig. 2) with slope less than or greater than 1, that is, if a subject's perception and response of azimuth were compressed or expanded.

When a listener is asked to localize a given source in the presence of an interfering one, his responses may be biased towards or away from the location of the interfering source (a ''pulling'' or ''pushing'' effect as described by Butler and Nauton, 1964). The $\bar{D}$ and $\bar{s}$ statistics should be sensitive to
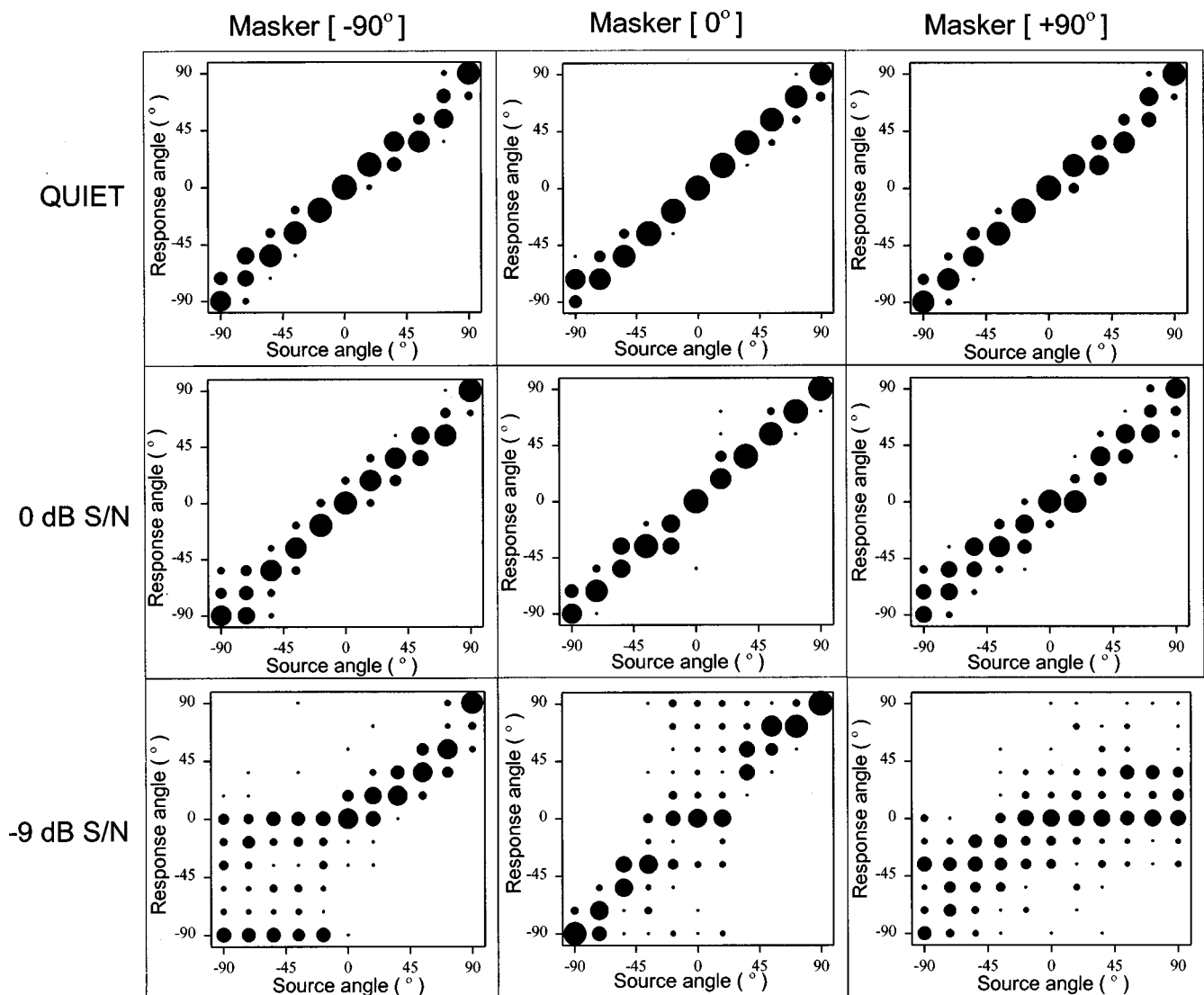
FIG. 2. Localization data for one listener (CH) at three signal-to-noise ratios [in quiet (top panels), at 0 dB S/N (middle panels), and at −9 dB S/N (bottom panels)], and three masker locations: −90 deg azimuth (left panels), 0 deg azimuth (middle panels), and +90 deg azimuth (right panels), using broadband clicks. In each panel, the response angle is plotted as a function of the actual source angle. The area of each symbol on the scatter plot represents the number of responses made at that angle for any given signal location.

such systematic response bias in the pattern of responses. The magnitude and direction of the effects will depend on the type and extent of the biases involved. For example, at an adverse S/N ratio a listener may indicate the same azimuth for almost all trials (see Fig. 3 for an example), and thus simple interpretation of $\bar{s}$ might confuse the circumstances leading to high consistency. In the present experiment, the run signed error $\bar{E}$, supposed to describe these response biases, will not distinguish between the absence of response bias, the presence of a bias to 0 deg azimuth and a bias to −90 and +90 deg azimuth, since the signed error will be 0 deg in each case. This statistic is therefore not suited to quantify response biases such as pushing or pulling effects. As with $\bar{D}$ and $\bar{s}$, values of r^2 are influenced by the variability in the listener's responses. As pointed out by Good and Gilkey (1996), this statistic is however less sensitive to systematic bias in the pattern of responses than $\bar{D}$ because localization performance is described by the best-fitting line.

In the data analysis, we decided to use the $\bar{D}$ statistic as the primary measure of overall localization accuracy, and the r^2 statistic for confirmatory purposes. It should be kept in mind that the $\bar{D}$ statistic includes the contribution of systematic response bias, while the r^2 statistic does so to a lesser extent (Good and Gilkey, 1996). Any effects which might be evident in *both* the $\bar{D}$ and r^2 statistics are therefore unlikely to be simple consequences of the response biases that individual listeners might have adopted.

II. RESULTS AND DISCUSSION

A. Localization data

1. Broadband condition

Figure 2 shows a selection of the results obtained in the broadband condition for one normal-hearing listener (CH). In each panel, the response angle is plotted as a function of the signal angle, for one of three signal-to-noise ratios (in

1814   J. Acoust. Soc. Am., Vol. 105, No. 3, March 1999

Lorenzi *et al.*: Localization in noise: Normal-hearing listeners   1814
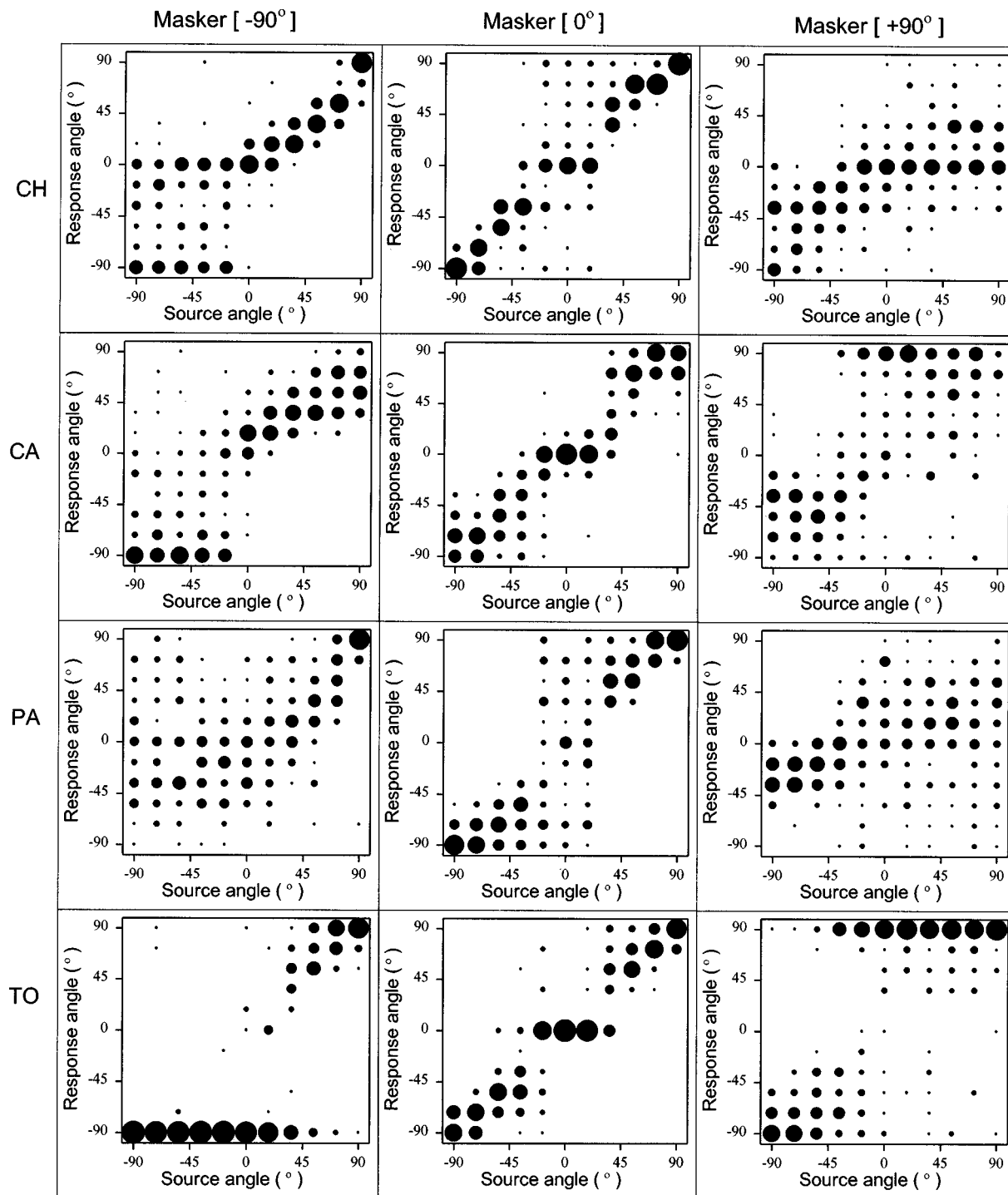
FIG. 3. Localization data for each listener and for the three masker locations: -90 deg azimuth (left panels), 0 deg azimuth (middle panels), and $+90$ deg azimuth (right panels). The data were obtained with broadband clicks at the most adverse signal-to-noise ratio (-9 dB). Other details are as in Fig. 2.

quiet, and 0 and -9 dB S/N), and for one of the three masker locations (-90, 0, and $+90$ deg azimuth). The three top panels therefore represent three replications of the same condition (obtained in different runs). The area of each symbol on the scatter plot represents the number of responses made at that angle for any given signal location. Each vertical column then sums to 40 repeated measures. Ideal performance would be represented by all points lying on the major diagonal. For the two higher signal-to-noise ratios and for the three masker locations, all points fall close to the major di-

agonal of each panel. This suggests that localization performance is not greatly affected by noise when the signal level is greater than the masker level. At -9 dB S/N, the points diverge from the major diagonal, indicating that localization performance worsens when the signal level is lower than the masker level. Inspection of Fig. 2 shows this to occur especially in the region of the masker. The three bottom panels at -9 dB S/N show a variation in response pattern as a function of masker location. In particular, the response patterns for masker at $+90$ and -90 deg azimuth differ from those at 0

Masker [-90°]   Masker [0°]   Masker [+90°]
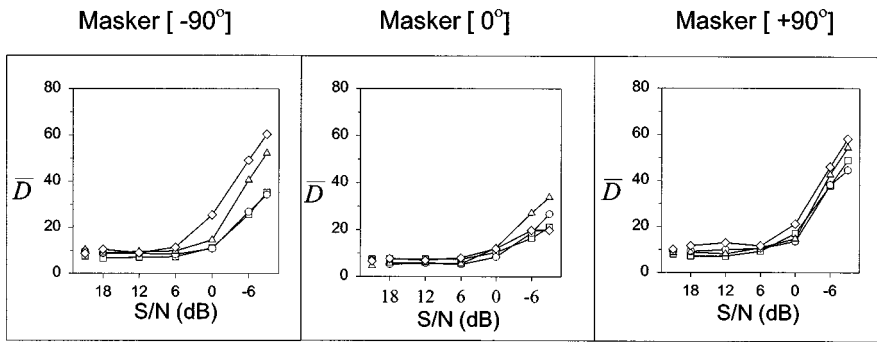
FIG. 4. Values of $\bar{D}$ (rms error) are plotted as a function of signal-to-noise ratio for each listener and for the three masker locations. The data were obtained with broadband clicks. The unconnected symbols correspond to the in quiet condition. Unfilled circles: CH; squares: CA; triangles: PA; diamonds: TO.

deg azimuth. In addition, the response pattern at −90 deg azimuth is not a mirror image of the pattern at +90 deg azimuth. Thus, we observe different forms of bias in the listener's responses.

Figure 3 shows similar representations for the responses of the four listeners, for the three masker locations, at a single (adverse) signal-to-noise ratio. These scatter plots reveal in more detail the presence of response biases:

(1) When noise is presented straight ahead, responses at 0 deg azimuth dominate for two listeners (CA and TO). Listener PA shows the converse pattern of responses, i.e., responses are symmetrically distributed near −90 and +90 deg azimuth. The pattern of responses of listener CH seems intermediate between those of listeners CA and TO and listener PA.

(2) When noise is presented at the sides of the listeners, responses around 0 deg azimuth dominate in two listeners (CH and PA) and responses at azimuths close to that of the masker dominate for the other two listeners (CA and TO).

Thus, substantial response biases occur for the three masker locations tested here, and the direction of these biases vary between listeners. A pulling effect similar to that reported by Butler and Naunton (1964) and Good and Gilkey (1996) is observed in two out of the four listeners (CA and TO), and a pushing effect is observed in the third (PA) and perhaps the fourth (CH) listener. Thus, response biases are a potential issue and might contaminate any single metric.

Figures 4 and 5 show $\bar{D}$ and r^2 as a function of signal-to-noise ratio for each masker location, respectively. In each panel, each curve corresponds to the data of an individual listener, and the unconnected symbol corresponds to the in quiet condition. Above 0–6 dB S/N, localization accuracy and consistency remain unaffected by noise, independent of

the location of noise. Below 0–6 dB S/N, localization accuracy and consistency decrease monotonically and reach a lower level when noise is at the sides of the listener ($34.23 \deg \leqslant \bar{D} \leqslant 60.47 \deg$; $0.15 \leqslant r^2 \leqslant 0.66$) than straight ahead ($\bar{D} \leqslant 33.9°$; $r^2 \geqslant 0.77$). Figure 4 reveals some between-listeners variability. Localization performance decreases similarly in two out of the four listeners (PA and TO) when noise is at −90 or +90 deg azimuth. Localization judgments remain, however, more accurate and more consistent in the other two listeners (CH and CA) when noise is at −90 deg azimuth.

2. Low-pass and high-pass conditions

When the signal has a broad amplitude spectrum, both ITD and ILD and spectral shape cues are available to the listener. Localization accuracy was measured with the low-pass- and high-pass-filtered versions of the broadband click train, in order to determine the extent to which low-frequency or high-frequency cues are affected by noise. The low-pass signal contained only frequencies below 1.6 kHz, so that ITD cues were the dominant cues for localizing this sound. Conversely, the high-pass signal contained only frequencies above 1.6 kHz, so that ILD and spectral shape cues were the dominant cues for localizing this sound. Localization performance was measured for only two masker locations: 0 deg azimuth and +90 deg azimuth, as no systematic difference was observed in the broadband-filtering condition when noise was on the right side or the left side. Figures 6 and 7 show $\bar{D}$ and r^2 as a function of signal-to-noise ratio for each listener, for the two masker locations (0 and +90 deg azimuth) and for low-pass-, high-pass-, and broadband-filtered clicks. First, all panels of Figs. 6 and 7 indicate that localization proficiency in quiet is similar in the low-pass, high-pass, and broadband conditions. Thus, there are suffi-

Masker [-90°]   Masker [0°]   Masker [+90°]
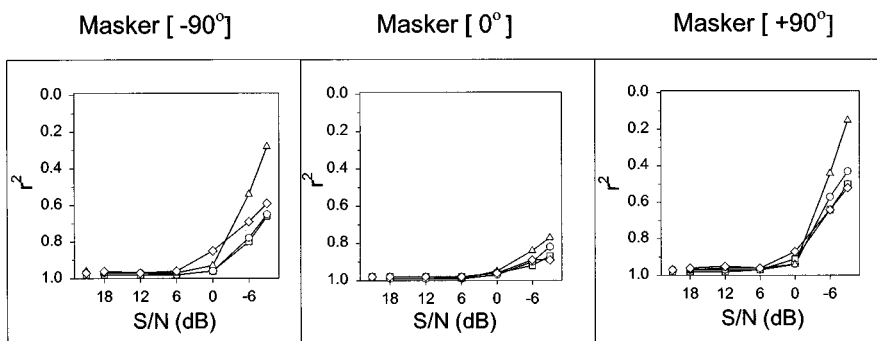
FIG. 5. Values of r^2 are plotted as a function of signal-to-noise ratio for each listener and for the three masker locations: −90 deg azimuth (left panels), 0 deg azimuth (middle panels), and +90 deg azimuth (right panels). The data were obtained with broadband clicks. Other details are as in Fig. 4.
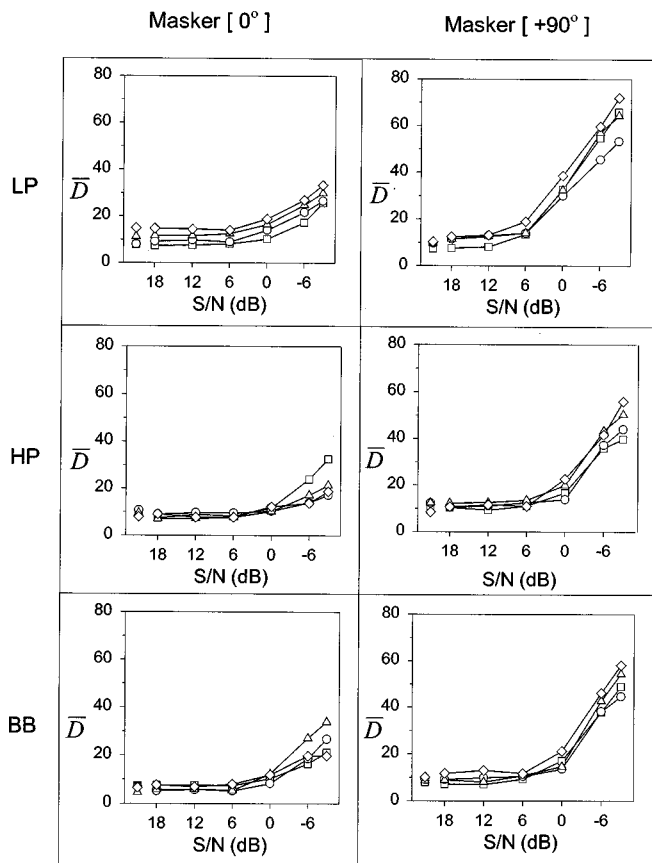
FIG. 6. Values of $\bar{D}$ are plotted as a function of signal-to-noise ratio for each listener and for two masker locations: 0 deg azimuth (left panels) and +90 deg azimuth (right panels). Data were obtained with low-pass (LP, top panels), high-pass (HP, middle panels), and broadband (BB, bottom panels) filtered clicks. Other details are as in Fig. 4.

cient cues for localization for both high-frequency stimuli (predominantly ILD and spectral shape cues) and low-frequency stimuli (predominantly ITD cues). Figures 4 through 7 provide a visual representation of the effects of noise on localization accuracy and consistency. The common patterns in Figs. 4 and 5 and in Figs. 6 and 7 strongly suggest that these effects are largely unconnected with patterns of response bias. Therefore, the $\bar{D}$ representations in Figs. 4 and 6 are appropriate for further study.

As a method of further quantifying the effects in the 12 panels of Figs. 4 and 6, the rms errors were aggregated across signal-to-noise ratios in addition to speaker angle. The resultant values are thus themselves rms errors and are listed in Table I. Together, Table I and Figs. 4 and 6 show that: (1) overall, there are no systematic differences in localization accuracy for the broadband condition between masker locations of -90 and $+90$ deg azimuth, (2) for all filtering conditions, localization accuracy is poorer when noise is at ± 90 deg azimuth compared to 0 deg azimuth. Part of this is due to the masker exerting its influence at lower signal-to-noise ratios, in the former case, (3) localization accuracy is similar for the broadband and highpass conditions for masker location at $+90$ deg azimuth. For the low-pass condition, localization accuracy is degraded. These results suggest that ITD and ILD and spectral shape cues are similarly affected by noise when the latter is presented straight ahead, but ILD and
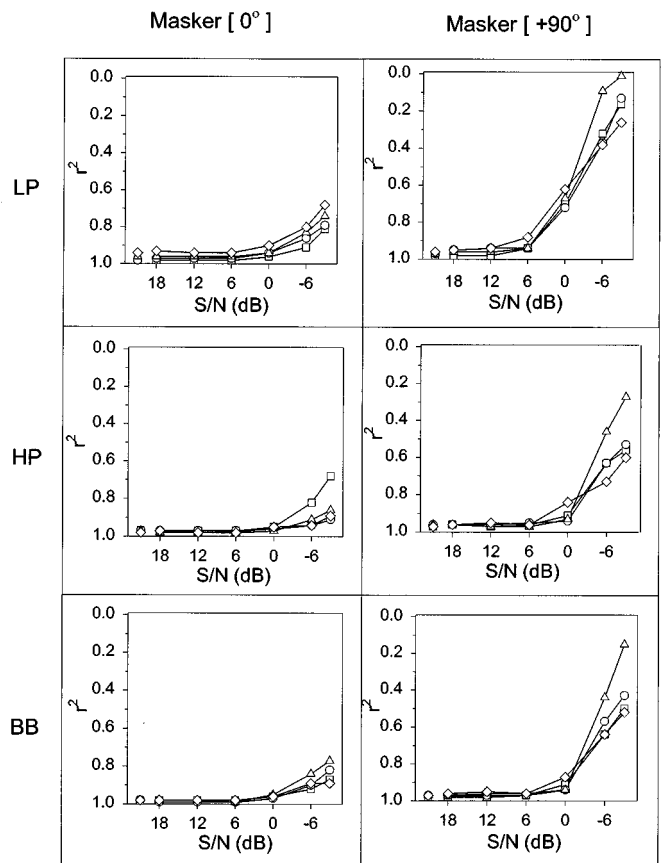
FIG. 7. Values of r^2 are plotted as a function of signal-to-noise ratio for each listener. Other details are as in Fig. 6.

spectral shape cues appear to be more resistant to noise when the latter is presented at the sides of the listener. When both cues are available, listeners seem to base their decision on the best cue available; that is, ILD and spectral shape cues.

B. Detection data

Because of MLD and head-shadow effects, the detectability of the clicks is not constant across azimuths but increases with the spatial separation between clicks and noise (e.g., Good *et al.*, 1997). It is therefore important to estimate the extent to which detection and localization performance are related, in order to clarify whether the current localization data reflect the performance of binaural localization mechanisms or the performance in detecting a masked signal. To address the issue of audibility, the sensitivity (d') to the presence of the broadband, low-pass-, and high-pass-filtered clicks was measured as a function of signal-to-noise ratio in the four experimental conditions illustrated in Fig. 1, using a blocked procedure. A limited number of both signal and nonsignal trials ($n=50$) was used. To compute a value for d' in the case of perfect performance (50/50), hit rate was artificially adjusted to 49/50, and zero identification (0/50) adjusted to 1/50. This process results in a ceiling value of $d'=3.5$.

The psychometric functions of the four listeners are presented in Fig. 8. Overall, psychometric functions are very similar in the broadband, low-pass, and high-pass conditions. In each row of Fig. 8, the second and fourth panels show

TABLE I. Values of the rms error aggregated across signal-to-noise ratios (in addition to source angles) for the three filtering conditions, and for the different masker locations.

| Filtering | BB | | | LP | | HP | |
Noise azimuth	−90 deg	0 deg	+90 deg	0 deg	+90 deg	0 deg	+90 deg
Listeners							
CA	14.33	11.13	19.34	12.07	34.94	14.57	19.06
CH	15.32	14.23	19.29	14.07	25.29	11.5	20.25
PA	20.8	13.56	21.18	16.93	28.83	11.5	23.53
TO	24.95	11.56	24.57	19.65	32.2	11.09	23.13

that, for three out of the four listeners (CA, CH, and TO), detection performance of the click train is near perfect when the spatial separation between clicks and noise is maximum. The detection performance of the fourth listener (PA) is also very good until 0 dB S/N, but drops at the most adverse signal-to-noise ratio. In each row of Fig. 8, the first and third panels show that, for all listeners, detection performance decreases when clicks and noise are spatially coincident: d' ranges between 2 and 4 when signal-to-noise ratio is greater than 0 dB, but drops to chance level at the most adverse signal-to-noise ratios.

In three out of the four listeners (CA, CH, and TO), the psychometric functions obtained when noise is presented straight ahead are very similar to those obtained when noise is presented at the sides. This result would tend to suggest that the decrease in localization accuracy observed when noise is presented at the sides is not attributable to a reduction in the detectability of the clicks. Also, the signal-to-noise ratios used in the current experiment generally lead to similar detection performance in the low-pass and high-pass conditions. This suggests that the poorer localization accuracy observed in the low-pass condition is not caused by worse audibility of the low-frequency clicks. However, a comparison of localization and detection data obtained when noise is presented at the sides reveals that the listener who generally shows the worst localization accuracy (listener PA) also shows the worst detection performance. Therefore, the overall audibility of the signal is likely to have affected the accuracy of localization judgments.

The detection data that we have gathered so far rely on
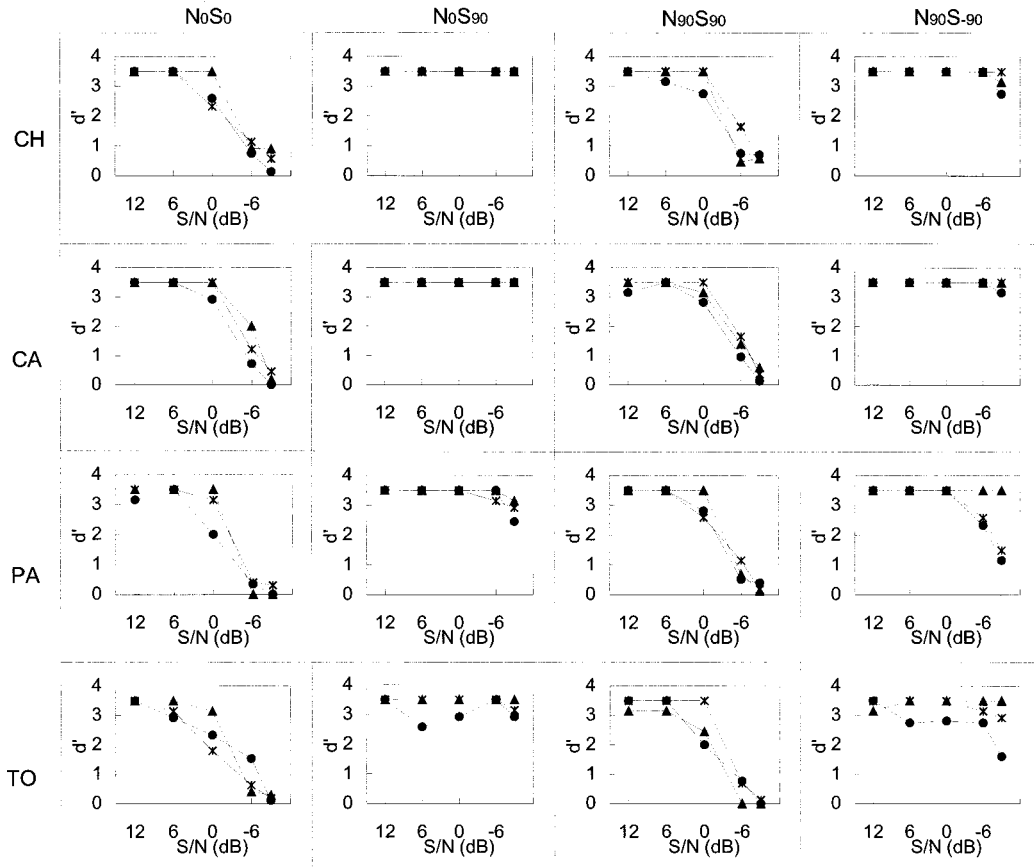
FIG. 8. Psychometric functions for each listener, showing binaural detection performance (d') as a function of signal-to-noise ratio. Each row presents the data for a given listener. Each column presents the data obtained in one of the four experimental conditions illustrated in Fig. 1 (referred to as N_0S_0, N_0S_{90}, $N_{90}S_{90}$, and $N_{90}S_{-90}$). Each panel shows the data obtained in the broadband (BB, stars), low-pass (LP, circles), and high-pass (HP, triangles) conditions.
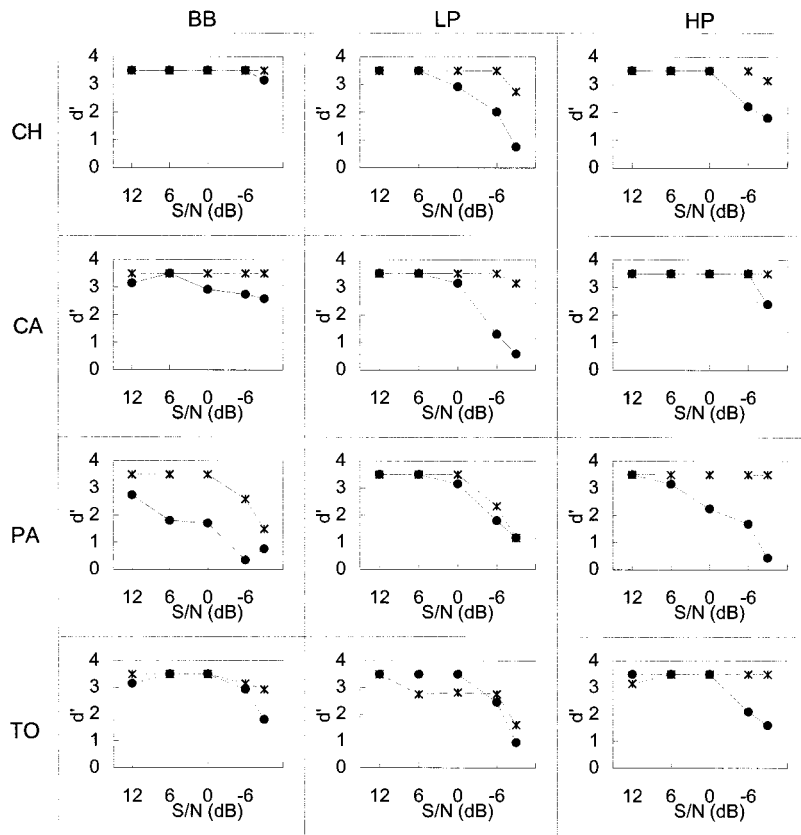
FIG. 9. Psychometric functions for each listener, showing binaural-detection performance (stars) and monaural-detection performance (circles) as a function of signal-to-noise ratio, in the $N_{90}S_{-90}$ condition. In the monaural condition, the left ear of the listener was plugged with an earmold. Each row presents the data for a given listener. The data were obtained in the broadband (BB, left panels), low-pass (LP, middle panels), and high-pass (HP, right panels) conditions.

the detection of the clicks at *either* ear of the listener. However, the ability to localize sounds in the frontal–horizontal plane is mainly based on binaural processes, and hence on detection at *both* ears. It could be argued that the decrease in localization accuracy observed when noise is presented at the sides of the listener may have been caused in part by a reduction in the audibility of the clicks at the ear ipsilateral to the noise. As a consequence, listeners may have operated monaurally at the most adverse signal-to-noise ratios, and would not have had access to normal interaural cues. To address this issue, psychometric functions for the monaural detection of the clicks were measured in the fourth condition illustrated in Fig. 1; that is, when signal and noise are at −90 and +90 deg azimuth, respectively (condition $N_{90}S_{-90}$). The left ear of each listener (i.e., the ear contralateral to the noise) was plugged by an earmold performing a 30-dB attenuation at 0.25, 0.5, 1, 2, 4, and 8 kHz. Figure 9 presents the individual data obtained in the broadband, low-pass, and high-pass conditions, plotted along with the corresponding data obtained with unoccluded ears. Figure 9 shows that plugging the ear contralateral to the noise generally degrades the detection performance. Therefore, these results indicate that the ear ipsilateral to the noise becomes gradually unable to detect the click train as signal-to-noise ratio is lowered. This supports the assumption that listeners do not access normal interaural cues at the most adverse signal-to-noise ratios when noise is presented at the sides of the listener. Although these data explain the worse localization performance observed when noise is presented at the sides rather than straight ahead, they do not explain why ITD cues are more affected by noise than ILD and spectral shape cues when noise is presented at the sides.

III. CONCLUSIONS

We measured the ability of normal-hearing listeners to localize a click-train signal in the frontal–horizontal plane, in quiet and in noise. Although this addresses a restricted set of issues concerning localization abilities, it does represent a systematic investigation of the ways in which and the extent to which use of low-frequency ITD cues and high-frequency ILD and spectral cues might be compromised in the presence of interfering noise. The results confirm and extend previous results from Good and colleagues (Good and Gilkey, 1996; Good *et al.*, 1997):

(1) The ability of normal-hearing listeners to localize a broadband sound in noise is very robust until very low signal-to-noise ratios. Below a given signal-to-noise ratio, localization performance degrades, and the rate of this degradation depends on the masker location. When the noise masker is presented straight ahead, localization performance worsens gradually, but when the noise is at the sides, localization performance degrades rapidly.

(2) Our data show that different listeners adopt different response patterns (biases) at the more adverse signal-to-noise ratios. The response patterns vary (a) within an individual listener as a function of masker location, and (b) as a function of source angle for a particular masker location, within a particular listener. Our data exhibit forms of bias in addition to the pulling effect described

by Butler and Nauton (1964) and Good and Gilkey (1996).

In addition, our results show that both low-frequency ITD and high-frequency ILD and spectral cues provide an accurate estimate of the direction of the sound source in quiet and when an interfering noise is presented straight ahead. However, our results suggest that low-frequency ITD cues are less resistant to noise than high-frequency ILD and spectral cues when the noise is presented at the sides of the listener. Moreover, the accuracy of localization judgments was found to be similar in the broadband and high-pass conditions. This result suggest that, when more than one cue is available (as in the broadband condition), listeners base their decision on the cue(s) providing the most accurate estimate of the direction of the sound source; that is, the high-frequency ILD and spectral cues when noise is at the sides. This result contrasts with the results obtained in quiet conditions by Wightman and Kistler (1992), who showed that listeners' responses are governed by the low-frequency ITD cues when the sound source is broadband. It therefore appears that the dominance of ITD cues observed in quiet does not apply to noisy conditions. However, it is important to emphasize here that it is an oversimplification to adopt such a classic ''duplex theory'' approach, and interpret the current results in terms of low-frequency ITD cues and high-frequency ILD cues. The head and the pinnae are known to produce complex direction-dependent spectral effects at each ear, leading to a complex ILD function of frequency. Monaural spectral cues may also be involved in horizontal-plane localization, especially when other binaural cues are disturbed.

Measurements of signal detectability show that the relation between detection performance and localization accuracy is not straightforward. In certain cases, both covary, which suggests that the audibility of the sound source constrains the ability to report its direction. The current experiment showed that monaural detection is affected by the masker location, detection being worse at the ear ipsilateral to the masker when the latter is presented at the sides of the listener. The resulting degradation in interaural cues is assumed to have caused the degradation in localization accuracy observed when noise is at the sides. However, these detection data do not explain why low-frequency ITD cues are less resistant to noise than high-frequency ILD and spectral cues when the noise is presented at the sides of the listener. A potential explanation involves the hypothesis that localization based on low-frequency ITDs requires detection in each ear, while localization based on high-frequency ILDs might be achieved on the basis of absolute level rather than ILD. Such hypothesis, however, requires further experimental investigation.

ACKNOWLEDGMENTS

Abel, S. M., and Hay, V. H. (**1996**). ''Sound localization. The interaction of aging, hearing loss and hearing protection,'' Scand. Audiol. **25**, 3–12.

Butler, R. A., and Naunton, R. F. (**1964**). ''Role of stimulus frequency and duration in the phenomenon of localization shift,'' J. Acoust. Soc. Am. **36**, 917–922.

Cohen, M. F. (**1981**). ''Interaural time discrimination in noise,'' J. Acoust. Soc. Am. **70**, 1289–1293.

Gaskell, H., and Henning, B. (**1981**). ''The effect of noise on time-intensity trading in lateralization,'' Hearing Res. **4**, 161–174.

Good, M., and Gilkey, R. H. (**1996**). ''Sound localization in noise: The effect of signal-to-noise ratio,'' J. Acoust. Soc. Am. **99**, 1108–1117.

Good, M., Gilkey, R. H., and Ball, J. M. (**1997**). ''The relation between detection in noise and localization in noise in the free field,'' in *Binaural and Spatial Hearing in Real and Virtual Environments*, edited by R. H. Gilkey and T. R. Anderson (Erlbaum, Hillsdale, NJ), pp. 349–376.

Hartmann, W. M. (**1983**). ''Localization in rooms,'' J. Acoust. Soc. Am. **74**, 1380–1391.

Hirsh, I. J. (**1948**). ''The influence of interaural phase on interaural summation and inhibition,'' J. Acoust. Soc. Am. **20**, 536–544.

Houtgast, T., and Plomp, R. (**1968**). ''Lateralization threshold of a signal in noise,'' J. Acoust. Soc. Am. **44**, 807–812.

Ito, Y., Colburn, S., and Thompson, C. L. (**1982**). ''Masked discrimination of interaural time delays with narrow-band signal,'' J. Acoust. Soc. Am. **72**, 1821–1826.

Jacobsen, T. (**1976**). ''Localization in noise,'' (Technical Report No. 10). (Technical University of Denmark Acoustics Laboratory, Denmark).

Kistler, D. J., and Wightman, F. L. (**1992**). ''A model of head-related transfer functions based on principal components analysis and minimum-phase reconstruction,'' J. Acoust. Soc. Am. **91**, 1637–1647.

Kuhn, G. F. (**1977**). ''Model for the interaural time differences in the azimuthal plane,'' J. Acoust. Soc. Am. **62**, 157–167.

Lorenzi, C., Gatehouse, S., and Lever, C. (**1997**). ''Sound localization in noise in normal-hearing listeners,'' J. Acoust. Soc. Am. **101**, 3104(A).

Middlebrooks, J. C., and Green, D. M. (**1990**). ''Directional dependence of interaural envelope delays,'' J. Acoust. Soc. Am. **87**, 2149–2162.

Mills, A. W. (**1958**). ''On the minimum audible angle,'' J. Acoust. Soc. Am. **30**, 237–246.

Mills, A. W. (**1960**). ''Lateralization of high-frequency tones,'' J. Acoust. Soc. Am. **32**, 132–134.

Perrott, D. R. (**1984**). ''Concurrent minimum audible angle: A re-examination of the concept of auditory spatial acuity,'' J. Acoust. Soc. Am. **75**, 1201–1206.

Rayleigh, Lord (**1907**). ''On our perception of sound direction,'' Philos. Mag. **13**, 214–232.

Robinson, D. E., and Egan, J. P. (**1974**). ''Lateralization of an auditory signal in correlated noise and in uncorrelated noise as a function of signal frequency,'' Percept. Psychophys. **15**, 281–284.

Shaw, E. A. G. (**1975**). ''Transformation of sound pressure level from the free field to the eardrum in the horizontal plane,'' J. Acoust. Soc. Am. **56**, 1848–1861.

Stern, R. M., Slocum, J. E., and Phillips, M. S. (**1983**). ''Interaural time and amplitude discrimination in noise,'' J. Acoust. Soc. Am. **73**, 1714–1722.

Wightman, F. L., and Kistler, D. (**1992**). ''The dominant role of low-frequency interaural time differences in sound localization,'' J. Acoust. Soc. Am. **91**, 1648–1661.

Yost, W. A. (**1975**). ''Comments on 'lateralization and the binaural masking-level difference' [G. B. Henning, J. Acoust. Soc. Am. **55**, 1259–1263 (1974)],'' J. Acoust. Soc. Am. **57**, 1214–1215.

Nonsense-syllable recognition in noise using monaural and binaural listening strategies

Michael D. Arsenault and Jerry L. Punch
Department of Audiology and Speech Sciences, Michigan State University, East Lansing, Michigan 48824

Using a binaurally equipped KEMAR manikin, syllables of the CUNY Nonsense Syllable Test were recorded in sound field at 0-degree azimuth against a background of cafeteria noise at 270-degrees azimuth, at several signal-to-noise (S/N) ratios. The combination of inputs recorded at each ear was delivered to ten normal-hearing (NH) and eight sensorineurally hearing-impaired (HI) listeners through insert earphones to produce five experimental listening conditions: (1) binaural head shadow (HS), in which ear presentation was analogous to the original stimulus recording, (2) binaural favorable (BF), in which the noise-shadowed (right-ear) recording was presented to both ears, (3) monaural favorable (MF), in which the noise-shadowed recording was presented only to the right ear, (4) monaural unfavorable (MU), in which the noise-unshadowed (left ear) recording was presented only to the left ear, and (5) simulated monaural aided (SMA), in which the noise-shadowed recording was presented to the right ear and the noise-unshadowed recording—attenuated by 20 dB relative to the HS condition—was presented to the left ear. All main effects (subject type, listening condition, and S/N ratio) were statistically significant. Normal listeners showed 3.3- and 3.2-dB advantages, respectively, due to head-shadow and binaural squelch, over hearing-impaired listeners. Some hearing-impaired listeners performed better under the SMA or BF conditions than under the HS condition. Potential digital signal processing strategies designed to optimize speech understanding under binaurally aided listening conditions are discussed. © *1999 Acoustical Society of America.* [S0001-4966(99)02103-7]

PACS numbers: 43.66.Sr, 43.66.Rq, 43.66.Dc [RHD]

INTRODUCTION

Binaural hearing, as opposed to monaural hearing, would appear to be a listener's most important means for communicating effectively in noisy environments. The superiority of binaural over monaural hearing in adverse listening conditions is well documented for normal-hearing individuals. Pollack and Pickett (1958), describing the now well-known *cocktail party effect*, concluded that ''...large gains in word intelligibility above a background of speech babble may be obtained with stereophonic listening as compared with nonstereophonic listening'' (p. 133). Additional studies have demonstrated the potential advantages of binaural listening in noisy acoustic environments for both normal-hearing and hearing-impaired listeners (for example, see Dirks and Wilson, 1969a, b). Nonetheless, hearing-impaired individuals regard diminished understanding of speech in the presence of competing background noise as their most common communication problem. In general, research strongly supports the advantage of binaural hearing aid fittings for hearing-impaired listeners in relatively quiet environments (Byrne, 1981; Schreurs and Olsen, 1985), but largely fails to demonstrate the superiority of binaural hearing, or binaural amplification, in noisy environments (Dirks and Carhart, 1962; Grimes *et al.*, 1981; Mueller *et al.*, 1981; Nabelek and Mason, 1981; Schreurs and Olsen, 1985; Festen and Plomp, 1986; Levitt *et al.*, 1987; Peissig and Kollmeier, 1997).

Two factors potentially contributing to a binaural advantage in speech intelligibility are binaural-squelch and head-shadow effects (HSEs). Binaural squelch is the overall general improvement in hearing against a noise background demonstrated when the second of two ears is added to that of the ear exposed to the more favorable monaural listening condition (Byrne, 1981). Head-shadow effects generally refer to the diffraction of sound to the ear on the opposite side of the head, due to the interposition of the head between the source and the ear receiving the shadowed sound. The HSEs produce interaural level differences (ILDs) and interaural time differences (ITDs) (Kuhn, 1987), typically resulting in a reduction in sound intensity on the opposite side of the head that may exceed 15 dB at frequencies above 1 kHz (Abbagnaro *et al.*, 1975; Byrne, 1981). Depending on the orientation of the head with respect to primary and secondary signal sources, head-shadow effects can potentially facilitate or impede speech perception, whether listening is monaural or binaural. The potential advantage of HSEs in binaural listening, with respect to enhanced speech detection and/or recognition, derives from the interaural differences in timing and level produced by the spatial separation of the primary speech signal from noise and reverberated signals (Byrne, 1981). A major effect, again depending on spatial separation and head orientation, is to alter the relative S/N ratios at the two ears. Carhart (1965) reported HSEs as high as 13 dB for speech stimuli. Recent summaries of the speech intelligibility performance of normal-hearing and hearing-impaired listeners, respectively, can be found in Ericson and McKinley (1997) and Koehnke and Besing (1997).

Given the continuing research attention to applications of signal processing for the hearing impaired (Nabelek and Mason, 1981; Durlach and Pang, 1986; Brey *et al.*, 1987; Levitt, 1987; Levitt *et al.*, 1987; Schwander and Levitt,

1987; Kollmeier and Peissig, 1990; Nilsson *et al.*, 1993; Kimberley *et al.*, 1994), the potential to implement digital signal processing (DSP) strategies to enhance speech intelligibility in adverse listening conditions remains promising for this population. In this study, we investigated the contributions of monaural and interaural cues that lead to relative improvements in speech recognition performance in noisy environments. Toward this end, we studied nonsense-syllable recognition under a variety of monaural and binaural listening conditions in which binaural squelch and HSEs influenced speech intelligibility in normal-hearing and hearing-impaired listeners. This research was motivated by our desire to determine whether selected patterns of routing signals interaurally, as might be achieved with DSP algorithms in binaural hearing aids, result in improved speech intelligibility in noise.

The importance of the contribution of HSEs to aided binaural hearing in adverse conditions was addressed in a series of experiments by Bronkhorst and Plomp (1988, 1989, 1992). The stimuli used for these studies, Danish sentences, incorporated binaural cues generated from diffractions of sound caused by the head and from HSEs. In particular, the effects of head-induced ITDs and ILDs generated by a KE-MAR manikin in an anechoic room were explored for normal-hearing and hearing-impaired listeners, while controlling for the potentially confounding effect of type of background noise. Binaural intelligibility level differences (BILDs), changes in the S/N ratio producing a given intelligibility percentage, were computed with reference to a free-field condition with the talker and noise at 0-degree azimuth. With the speaker in front (0-degree azimuth) and the noise source at a 90-degree azimuth, the mean gain due to binaural hearing and head shadow was 9.4 dB. In that situation, the mean gain from binaural hearing over monaural hearing was 2.5 to 3 dB, similar to the results of Carhart (1965). Bronkhorst and Plomp (1988, 1989), however, when comparing a simulated binaural hearing aid arrangement with a simulated monaural hearing aid (a 20-dB attenuation of one ear relative to a reference condition), reported a mean gain of only 0.2 to 0.5 dB for a 90-degree-azimuth noise source. These values were based on the results for the best monaural conditions (i.e., with the ear ipsilateral to the noise source either plugged or with the level at that ear attenuated).

Nilsson *et al.* (1993) and Nilsson and Soli (1994) replicated Bronkhorst and Plomp's (1988) normative study utilizing American English sentences and found similar results. Findings from these combined studies suggest that symmetrically hearing-impaired individuals utilize ITD cues as well as normal-hearing individuals, while ILD cues produce variable results that depend on the high-frequency hearing loss of hearing-impaired listeners. In addition, these studies suggest that a monaural hearing aid fitting may be appropriate in certain situations when interaural level disparities are deleterious to binaural listening. The findings of Bronkhorst and Plomp (1988, 1989) and Nilsson *et al.* (1993) may explain why binaural amplification has not been conclusively demonstrated as superior to monaural amplification in optimizing speech recognition in the presence of noise.

Abbagnaro *et al.* (1975) reported that the greatest ITD

between ears in a free-field environment was generated when one of the ears was oriented at 90-degrees azimuth to the signal. The measured delay (at 90 degrees) was greatest for the low frequencies (0.8 ms at 0.2 kHz), with the magnitude of time delay being frequency dependent up to 1 kHz. Thus, to maximize the ILD and ITD cues afforded from a binaural listening condition, a listener in a poor acoustic environment is likely to understand speech better if the talker is positioned in front and the adverse noise to one side. In this situation the binaural system would be allowed to use the time disparities of 0.6–0.8 ms in the lower frequencies and would be afforded additional help from an increased S/N ratio in the higher frequencies in the shadowed ear. The overall binaural gain in separating speech from noise by moving the noise from a frontal position (0 degree) to a lateral position (90 or 270 degrees) should be some value derived from combination of the ILD and ITD cues. Bronkhorst and Plomp (1989) point out that positioning in which the talker is located in front of the listener and the noise source is to one side allows for a more natural listening arrangement. By introducing time delays in the noise, and providing a more favorable S/N ratio to at least one ear by maintaining the speaker in front, head shadow may lead to a positive binaural experience.

Carhart *et al.* (1967) studied, in normal listeners, the effects of interaural time delays and phase disparities on the intelligibility of spondee and monosyllabic words. They used continuous and modulated white noise, as well as connected speech (single talker), as background competition. In the antiphasic condition, they observed masking level differences (MLDs) of 7 dB for spondees and 4 dB for monosyllabic word recognition. The MLDs associated with varying the interaural timing increased in size as the time delay, for either speech or noise, was increased from 0.1 to 0.8 ms. The MLDs never exceeded those for antiphasic listening and were typically smaller. The investigators suggested that MLDs for speech stimuli are governed by the MLDs within the frequency range necessary for recognizing that particular speech stimulus and that they are task dependent. Dirks and Wilson (1969a) demonstrated that phase shifts induced in either speech or noise by the introduction of interaural time differences (ITDs) during binaural listening tasks produce measurable MLDs in hearing-impaired listeners.

Kollmeier and Peissig (1990) attempted to improve speech intelligibility for spatially separated speech and noise by use of a DSP algorithm that increased the binaural dissimilarities generated by HSEs. Their results, however, did not suggest a clear binaural advantage in adverse listening conditions for hearing-impaired or normal-hearing listeners, for either processed or unprocessed speech. They suggested that individual assessment for ITD and binaural (versus monaural) intelligibility advantage may be useful in predicting benefit from binaural amplification for the hearing impaired.

In this study, we determined, at several S/N ratios, the relative contributions of the shadowed and unshadowed ears to nonsense-syllable recognition under selected conditions simulating monaural and binaural amplification. For the original binaural recordings, the source of nonsense syllables was located at 0-degree azimuth, and cafeteria noise was located at 270-degrees azimuth. The combined signals, as

recorded via a KEMAR manikin (Burkhard and Sachs, 1975) were delivered to the listeners through insert earphones. The ILDs and ITDs of the original recordings were preserved in some of the playback conditions, but not in others. Measurements were made in groups of both normal-hearing and hearing-impaired listeners.

Nonsense syllables from the CUNY Nonsense Syllable Test, or NST (Resnick *et al.*, 1975), were used as stimuli. This closed-response test was designed to be sensitive to the kinds of consonant confusion errors made by hearing-impaired listeners and has been demonstrated to be reliable and to exhibit negligible learning effects from repeated administrations (Dubno and Dirks, 1982; Levitt *et al.*, 1987). The NST materials were selected for this investigation because the relative dependency of recognition of these materials on their high-frequency content suggested that they might provide the most sensitive measure of any differences among the various experimental strategies attributable to head-shadow effects.

Three research questions were framed in recognition of the potential that DSP programming might incorporate one or more of the investigated strategies in hearing aids for use by hearing-impaired listeners to improve speech intelligibility in noise:

(1) Does signal processing designed to eliminate presentation of the signal to the ear receiving a relatively unfavorable S/N ratio result in a monaural listening advantage when compared to binaural presentation?
(2) Does a special binaural condition in which routing the combined signal at the noise-shadowed ear to the contralateral unshadowed ear offer an advantage over either binaural presentation of recorded head-shadow effects (shadowed and unshadowed stimuli) or monaural presentation of the noise-shadowed ear?
(3) Does a listening condition simulating monaural amplification at the shadowed ear, and an open opposite ear, produce improved intelligibility performance over that achieved in a condition simulating aided monaural listening at the shadowed ear, and an occluded opposite ear?

I. METHODS

A. Subjects

Ten listeners with pure tone thresholds ≤20 dB HL at all audiometric frequencies between 0.25 and 6 kHz comprised a normal-hearing (NH) group of subjects. A group of eight hearing-impaired (HI) listeners exhibiting various degrees of sensorineural hearing loss was recruited from a clinical population whose speech recognition scores in quiet were symmetrical, within 16%, in the two ears. Prior to participation in the study, these hearing-impaired subjects underwent a routine audiometric evaluation consisting of air- and bone-conduction pure tone audiometry, speech recognition threshold (SRT) assessment, speech recognition performance assessment in quite (36 dB SL *re*: SRT), and tympanometry. Mean hearing thresholds of these subjects, with standard deviations, are displayed in Table I. Results reveal a

TABLE I. Audiometric results for hearing-impaired listeners ($n=8$), showing mean air-conduction thresholds and standard deviations, in dB hearing level, by ear.

Ear	Frequency in kHz							
	0.25	0.5	1	1.5	2	3	4	6
Right: Th	28.1	31.2	38.1	43.1	43.7	47.5	46.9	41.9
s.d.	17.9	18.7	21.2	17.3	17.9	18.1	20.2	16.5
Left: Th	45.0	30.0	39.4	41.9	45.0	47.5	48.1	40.6
s.d.	15.3	17.7	20.9	16.9	15.3	12.2	15.6	20.8

mean mild-to-moderate, bilaterally symmetrical, hearing impairment between 0.5 and 6 kHz. For individual hearing-impaired subjects, pure tone audiometric thresholds in the two ears were within 10 dB of each other at each of the octave frequencies 500–4000 Hz, and SRTs were within 5 dB interaurally.

B. Stimuli

The CUNY-NST (Resnick *et al.*, 1975) was chosen for this study, for reasons stated above. The test is comprised of six random forms of seven subsets of eight to ten consonant–vowel (CV) or VC syllables. Subsets differ across vowel context, consonant class, and consonant position. Each test item is embedded in the carrier phrase ''You will mark (*syllable*), please.'' Each form is comprised of 55 test items with one repeated item in each subset, for a total of 62 stimuli. The second occurrence of the repeated item was omitted for scoring purposes. A digital audio tape (DAT) recording of the original CUNY-NST was used consisting of nonsense syllables recorded by a male talker on one channel and cafeteria noise on the other. The competing noise has been described by Resnick *et al.* (1975) as ''...cafeteria noise from which the extreme transients had been removed.'' The noise was gated to coincide with the presentation of individual carrier phrases that included the stimulus items.

C. Stimulus recordings

Stimulus recordings were made in a conventional, double-walled, audiometric sound room located in the Hearing Research Laboratory at Michigan State University. All stimuli were recorded using a KEMAR manikin fitted with average adult pinna replicas and a DB-100 Zwislocki coupler for each ear. Settings of a special preamplifier (Etymotic Research) ensured that sound-field effects (i.e., body baffle, concha, and ear canal resonance) were incorporated into the recordings. KEMAR was placed 1.35 m from a Sentry 100A loudspeaker at 0-degree azimuth, serving as the speech signal source. An additional loudspeaker placed 1.35 m to the left of KEMAR (at 270-degrees azimuth) provided the competing cafeteria noise. These speakers were calibrated using a pink-noise input prior to recording and found to be similar and relatively flat (±3 dB) from 0.125–14 kHz. Stimulus materials were delivered from a DAT unit (Panasonic SV 3900), amplified (Crown D150 A), and led to the loudspeakers. The recordings were made by passing the electrical signals from microphone preamplifiers connected to the Zwis-
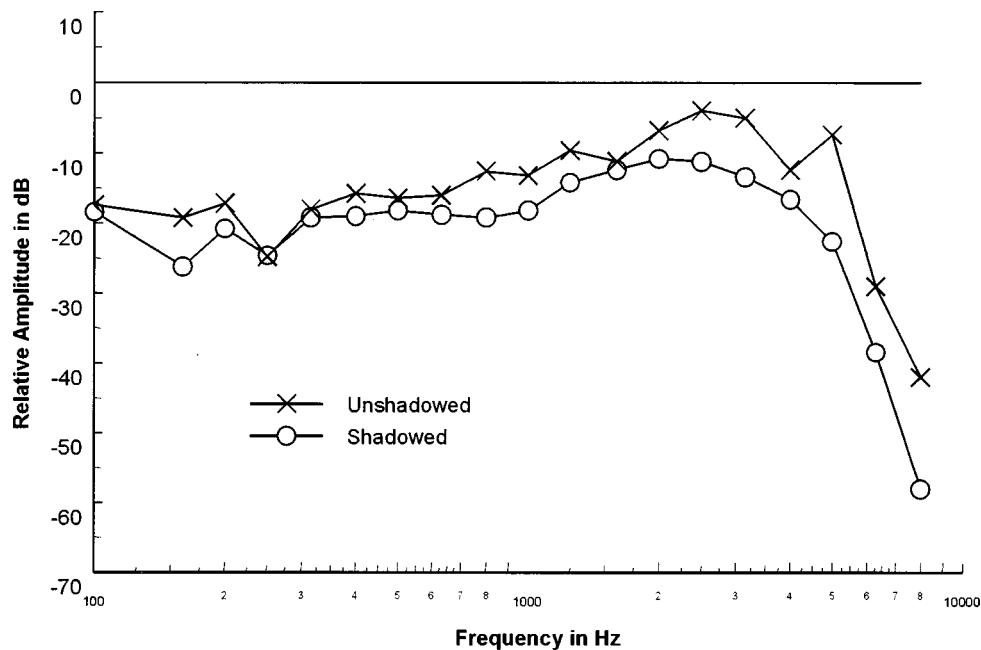
FIG. 1. Pink-noise spectra as measured in sound field at KEMAR's noise-unshadowed and shadowed ears (left and right ears, respectively), with the source on the left side (270-degrees azimuth). One-third octave band measurements were made using an overall C-weighted source sound-pressure level of 85 dB.

locki couplers to separate channels of a two-channel DAT recorder (Sony DTC-75ES). The combined speech and noise stimulus waveforms recorded separately at the left and right ears will be referred to in this article as channels 1 and 2, respectively. During the recording process, KEMAR's position was fixed so that the speech signal was maintained at a constant level for both ears (i.e., C-weighted sound level of 65 dB, at 0-degree azimuth), while the output level of the cafeteria noise was adjusted to achieve the desired S/N ratios at KEMAR's left ear. Reference values for designating the recording levels of speech and noise stimuli were established by comparing the level of pink noise produced in the Zwislocki coupler of KEMAR's left ear (channel 1) with 65-dB, C-weighted, pink noise at a free-field microphone position to be occupied by the center of KEMAR's head.

Each of the six randomized forms of the NST was recorded at −8, −4, 0, 4, and 8 S/N ratios, specified relative to KEMAR's left ear, for a total of 30 lists. This range of S/N ratios was chosen to incorporate S/N subsets that would be unlikely to produce floor or ceiling performance effects in either of our groups of normal-hearing or hearing-impaired listeners.

Figure 1 depicts the one-third octave, long-term average, levels of pink noise measured at both the shadowed (right) and unshadowed (left) ears of KEMAR, with the signal source at 270-degrees azimuth. This comparison allowed us to quantify relative head-shadow effects. These fast Fourier transform (FFT) tracings demonstrated differences between shadowed and unshadowed ears as great as 6–8 dB between 1–4 kHz, and 10–16 dB above 4 kHz. This outcome is in general agreement with data from Nilsson *et al.* (1995) and Duda (1997).

All interaural level and time differences were preserved in the KEMAR recordings. This approach was different from that of Bronkhorst and Plomp (1988), who used an audiometer to mix the recorded speech and noise signals from each ear during test administration. For the purpose of this project and throughout this paper, the terms ILD and ITD are used only to refer to those interaural cues present in the noise. As the speech source was placed directly in the front of KEMAR, no ILD or ITD differences between KEMAR's ears could be expected for the nonsense syllables.

D. Data collection

During data collection, combined speech and noise signals from the two respective channels of the DAT recordings, each representing a specific ear of KEMAR, were delivered to a pair of insert earphones (Etymotic Research ER-3A) by a clinical audiometer (Madsen OB822) calibrated to ANSI specifications (ANSI S3.6, 1989). Right and left earphones were alternated for successive subjects, in each subject group, to control for transducer effects. Under conditions requiring the original recording configuration to be preserved, channels 1 and 2 of the DAT recordings were respectively presented to the left (unshadowed, more-negative S/N) and right (shadowed, more-positive S/N) ears. Presentation level was set by equating a known level of taped pink noise to that of frequent VU peaks in the speech stimuli, while measuring the output from the insert earphones in a 2-cc coupler. Speech sound-pressure level in the unshadowed ear was 70 dB for normal-hearing listeners and at the individually determined MCLs (most comfortable levels) for the hearing-impaired listeners. The UCLs (uncomfortable loudness levels) were measured in the unshadowed ear for the hearing-impaired subjects to ensure that playback levels did not exceed their loudness tolerance limits; the sound-

TABLE II. Summary of five experimental listening conditions, showing signal channels directed to respective ears, via insert earphone, during data collection.

Experimental condition	Label	Left ear	Right ear
Binaural head shadow	HS	Unshadowed (Ch 1)	Shadowed (Ch 2)
Binaural favorable	BF	Shadowed (Ch 2)	Shadowed (Ch 2)
Monaural favorable	MF	No signal	Shadowed (Ch 2)
Monaural unfavorable	MU	Unshadowed (Ch 1)	No signal
Simulated monaural aided	SMA	Unshadowed (Ch 1), attenuated 20 dB *re*: HS	Shadowed (Ch 2)

pressure levels of UCLs ranged between 95 and 105 dB. The MCLs and UCLs were established in conjunction with the simple up–down procedure of Levitt (1970) and the instructions suggested by Morgan *et al.* (1974), using a special recording of the cafeteria noise at KEMAR's unshadowed ear.

To minimize the likelihood of ceiling effects in the NH subjects and floor effects in the HI subjects, only the three poorest of the five recorded S/N ratios (−8, −4, and 0 dB) were administered to the NH listeners, and only the three best S/N ratios (0, 4, and 8 dB) were administered to the HI listeners. A total of 15 lists were administered to each subject (5 listening conditions ×3 S/N ratios). Presentation of lists and S/N ratios was counterbalanced with respect to the various listening conditions, using a Latin-square design. All data collection was performed in an audiometric sound suite located in Central Michigan University's Speech and Hearing Clinic.

The five experimental conditions in which intelligibility performance on the NST was measured are summarized in Table II. They were as follows:

(1) Head shadow (HS): Binaural (dichotic) condition with presentation of (noise-unshadowed) channel 1 to the left ear and (noise-shadowed) channel 2 to the right ear, as in the original recording. In this condition, binaural cues and the monaurally improved S/N ratio were preserved.
(2) Binaural favorable (BF): Binaural (diotic) condition with simultaneous presentation of channel 2 (the stimulus at the more favorable S/N ratio) to both ears.
(3) Monaural favorable (MF): Monaural condition with presentation of channel 2 alone to the right ear. Only the stimulus recorded at the ear contralateral to the noise was presented to the right ear. This stimulus condition was identical to BF except that it was presented monaurally.
(4) Monaural unfavorable (MU): Monaural condition with presentation of channel 1 alone to the left ear. Only the stimulus recorded at the ear ipsilateral to the noise was presented to the left ear.
(5) Simulated monaural aided (SMA): Binaural (dichotic) presentation of channels 1 and 2, as in the original recording (condition 1), with the signal on the poor (noise-unshadowed) side attenuated by 20 dB.

The SMA condition was similar to the free-field, 20-dB ipsi-attenuation condition described by Bronkhorst and Plomp (1989). It was included to evaluate the relative effects of a dichotic, hearing aid-simulated condition and a true monaural condition—condition 3—as a follow-up to the work of Bronkhorst and Plomp (1988, 1989). As pointed out by Festen and Plomp (1986), previous studies of speech perception in noise have attempted to compare binaural listening to monaural listening with the nontest ear occluded. With monaural hearing aid fittings, the nonfitted ear is typically unoccluded, allowing for some degree of binaural listening in a symmetrically impaired listener. Thus, the inclusion of conditions 3 and 5 allowed a direct, realistic comparison of true monaural hearing (MF) with a simulated monaural aided situation in which the aid is worn on the shadowed ear (SMA).

Recalling our three research questions, question 1 can be addressed by comparing MF with HS; question 2, by comparing BF with HS, and BF with MF; and question 3, by comparing SMA with MF.

II. RESULTS AND DISCUSSION

An arcsin transformation, as described by Thornton and Raffin (1978), was performed on the raw scores for purposes of statistical analysis. Mean NST performance and standard errors of the mean for each listening condition, S/N ratio, and subject group are summarized in Fig. 2. The across-group 8-dB S/N ratio offset described above is indicated by parenthesized S/N values in the figure's abscissa.

As anticipated, no floor or ceiling effects were observed overall in the data for either subject group, at any S/N ratio. Mean percentage scores on the NST ranged from 40.7% (HI/MU) to 87.1% (NH/HS). Also, as might be expected, standard errors for the HI group were generally higher than those for the NH group across all conditions and S/N ratios.

Linear regression was performed on the psychometric functions for the various listening conditions to derive performance-intensity (PI) functions, based on the three S/N ratios relevant to each subject group. For the NH group, the PI functions ranged from 1.4%–2.2%/dB across all conditions, and for the HI group, from 2.1%–2.5%/dB. To compare across selected pairs of conditions, the lateral shifts between these mean functions, in dB, were calculated. Table III displays the calculated mean S/N ratio shifts between the compared conditions, which are shown as algebraic relationships in the first column.

Contrasting the MF to MU conditions revealed an 8.9-dB mean improvement in S/N ratio for the NH group, and a 5.6-dB improvement for the HI group. Thus, normal listeners showed a 3.3 (8.9 minus 5.6) dB S/N ratio advantage over hearing-impaired listeners, due to HSEs. This 3.3-dB differential in S/N ratio represents a notable reduction in syllable recognition for the HI listeners. They were less able than the NH listeners to utilize fully the head-shadow (ILD) cues associated with the S/N ratio differences. This finding is presumably due to the inability of the hearing-impaired subjects to hear the acoustic cues for phonemic identification, and is consistent with the findings of
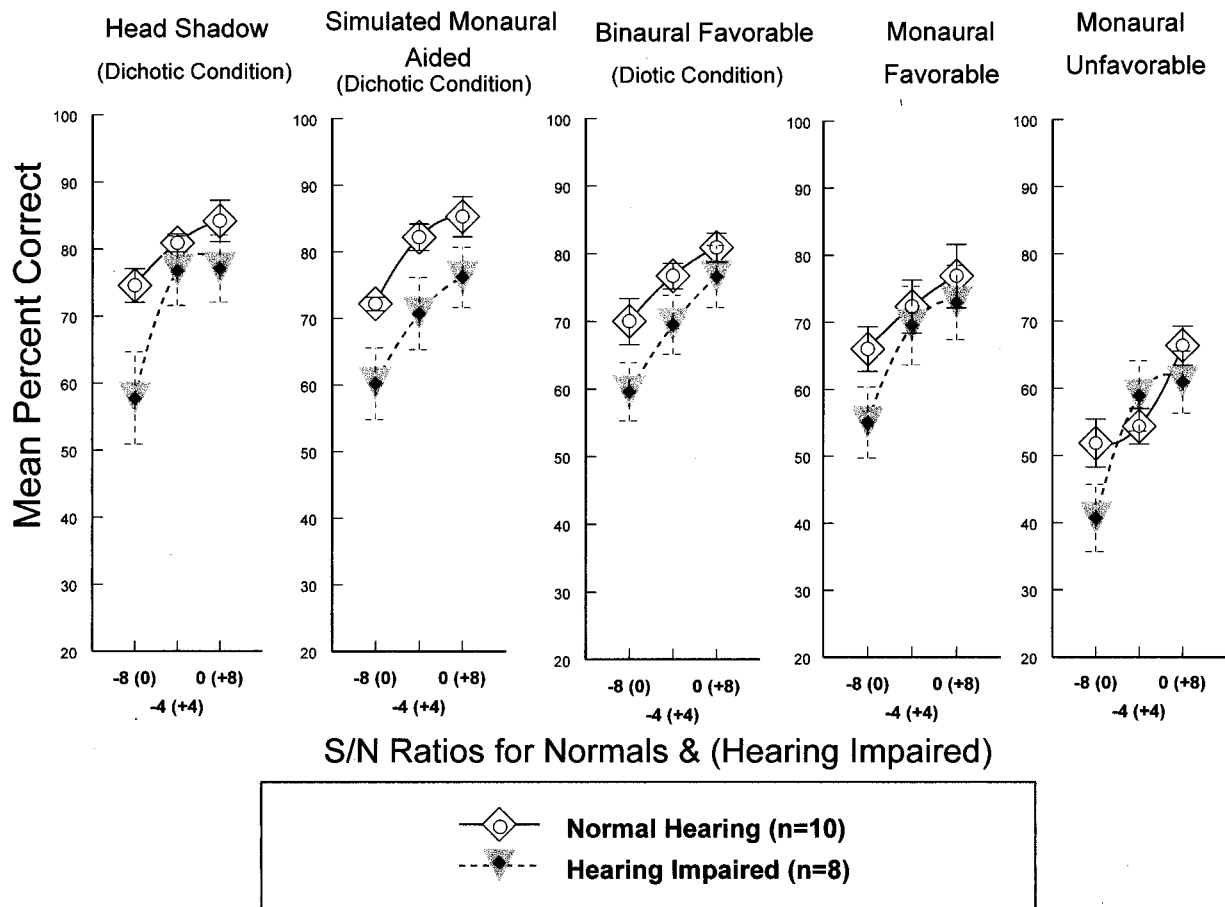
FIG. 2. Group mean performance, for normal-hearing ($n=10$) and hearing-impaired ($n=8$) subjects, on the Nonsense Syllable Test for all experimental conditions and S/N ratios. Note the use of an 8-dB offset between groups, as described in the text.

Bronkhorst and Plomp (1988) and Nilsson and colleagues (1993, 1994).

Comparing the HS condition to the MF condition provides an index of binaural squelch (Byrne, 1981; Carhart, 1965). Regression slopes and intercepts of the performance-intensity (PI) functions for HS and MF conditions revealed mean 4.9- and 1.7-dB S/N ratio shifts toward better performance under the HS condition for the normal-hearing and hearing-impaired groups, respectively. The difference of 3.2 dB agrees closely with the data of Bronkhorst and Plomp (1989), who reported a 2.7-dB disparity in BILDs under the analogous conditions for hearing-impaired listeners. Clearly, these results indicate a relative inability of hearing-impaired listeners to take advantage of binaural-squelch effects. They

TABLE III. Mean shifts in performance-intensity functions between selected conditions, expressed as S/N ratios, in dB.

Conditions compared	Normal hearing	Hearing impaired
MF–MU	8.9	5.6
HS–MU	12.3	7.0
HS–MF	4.9	1.7
HS–BF	2.3	0.3
BF–MF	2.6	1.4
SMA–MF	4.9	1.6

also provide a generally negative answer to our first research question.

The differences for the HS versus MU conditions demonstrate 12.3- and 7.0-dB shifts in S/N ratio for the normal-hearing and hearing-impaired groups, respectively. This comparison reveals the advantage of binaural cues (HS) over monaural listening when speech and noise are heard only at the ear ipsilateral to the masker. The sizeable difference of 12.3 dB for normal-hearing listeners is close to the 13 dB reported by Carhart (1965) and Carhart et al. (1967).

It should be noted that the performance difference of 7.4 dB between HS and MU (12.3 dB) and HS and MF (4.9 dB) for the NH listeners is fairly close to the 8.9-dB difference between MF and MU, and the analogous value for HI listeners, 5.3 dB, is close to the 5.6-dB difference between MF and MU. This comparison of direct and indirect measures of MF with MU reveals an internal consistency in our data.

Comparison of the dichotic HS condition with the diotic BF condition revealed a 2.3-dB advantage of HS over BF for the NH group, and a meager 0.3-dB advantage of HS over BF for the HI group. This finding, which relates to our second research question, suggests that normal listeners benefited from the full array of binaural cues available to them in the HS condition, while hearing-impaired listeners did not. Despite the poor S/N ratio present at the left (noise-unshadowed) ear, routing the stimulus having the better S/N

TABLE IV. ANOVA results, showing all main effects to be significant at the 0.001 level, with no significant interactions.

Variable	df	F
Subject type (ST)	1	22.30[a]
Listening condition (LC)	4	24.61[a]
S/N ratio (SNR)	2	35.41[a]
ST by LC	4	0.71
ST by SNR	2	2.73
LC by SNR	8	0.15

[a]$p < 0.001$.

ratio to the noise-unshadowed ear did not improve recognition performance for either subject group. The HI listeners as a group, therefore, did not benefit from special binaural processing in which the combined stimulus at the noise-shadowed ear was also routed diotically to the contralateral unshadowed ear. They did benefit slightly, however, under this special diotic condition when compared to listening monaurally in the noise-shadowed ear (BF–MF). For this latter comparison, NH listeners benefited to a greater extent (2.6 dB, as opposed to 1.4 dB for the HI group). Note that this outcome is pertinent to group performance; this point will be discussed later with respect to a further analysis.

Performance under the SMA condition was considerably better than under MF for NH listeners (4.9 dB), and somewhat better (1.6 dB) for HI listeners. Recall that the SMA condition was included to simulate a monaurally aided condition in which the unaided ear remains open. These results suggest that experimenters attempting to compare binaural with monaural amplification (in listeners with symmetrical hearing thresholds) should leave the unaided ear unoccluded in the monaural condition. To do otherwise may produce misleading predictions with regard to real-world performance. Results also suggest that allowing some amplification to occur at the noise-unshadowed ear (SMA) leads to improved performance over that occurring in monaural listening at the noise-shadowed ear (MF). Reduced gain at the noise-unshadowed ear (SMA), however, was no more beneficial over MF than when fully audible cues were available at both ears (HS), given that the outcomes were essentially identical for the HS–MF and SMA–MF comparisons.

The calculated S/N ratio shifts between MF and the three binaural conditions HS, BF, and SMA (Table III) demonstrate that the HS and SMA conditions yielded the best listening performance overall (a 4.9-dB shift in both cases), with the BF strategy trailing (with a 2.6-dB shift) for the NH group. For the HI group, mean performance was 1.4–1.7 dB better under each of the binaural conditions than under the best monaural condition.

A three-factor multilevel (one between–two within) analysis of variance (ANOVA) was used on the transformed scores to evaluate the main effects of subject type, listening condition, and S/N ratio. Table IV displays the results. All main effects were significant at the 0.001 level. There were no significant interaction effects. A Student Newman–Keuls post hoc analysis revealed results to be significantly different overall at each S/N ratio (with means ranging from 1.81 rad for the worst to 2.14 rad for the best S/N ratio), and the monaural conditions to be significantly different at each S/N

ratio. A contrast model of the ANOVA was performed to test for linearity of the PI functions as the S/N ratio was changed. The linear model of S/N ratio ($F = 70.57$) was significant at the 0.001 level, as compared to the quadratic model ($F = 3.18$). This finding suggests that the subjects' performance improved in a linear fashion with increasing S/N ratio, as expected.

Post hoc analysis of the different listening conditions revealed the HS and SMA conditions to be different from MF, and the HS, SMA, BF, and MF conditions each to be different from MU ($p < 0.05$). The only binaural condition not significantly different from MF was BF. As shown in Table III, BF yielded mean improvements of 2.6 dB and 1.4 dB (shifts in S/N ratio) over MF for NH and HI groups, respectively. This finding agrees within 1.2 dB of the data of Bronkhorst and Plomp (1989). Recall that the BF condition routed the signal in the noise-shadowed, or favored, ear to both ears simultaneously, thus offering listeners no interaural time or level disparities. The other two binaural conditions (HS and SMA), dichotic in nature, offered some additional spatial cues that were utilized by the listeners. The fact that HS and SMA showed similar advantages over MF, for either NH or HI listeners, may be explained by the findings of Bronkhorst and Plomp (1989). Specifically, they found that attenuating the signal with the poorer S/N ratio by 20 dB did not significantly interfere with the binaural unmasking effects of ITD cues, while enhancing the unmasking related to ILD. Our findings, along with theirs, suggest that when the (open) unaided ear is being exposed to a competing noise level that is high with respect to that in the aided ear, binaural amplification may still be slightly more beneficial than monaural amplification. Although Bronkhorst and Plomp utilized an adaptive SRT technique, it is reasonable to assume that listeners in our study used the same binaural unmasking cues as in their study for consonant recognition during the SMA condition.

To evaluate performance across the different conditions, a model of ranked performance was created. An assumption

TABLE V. Rank-order of NST performance for the five listening conditions, with overall percentage of occurrences in parentheses, collapsed across three S/N ratios (Table Va: normal-hearing subjects; Table Vb: hearing-impaired subjects).

	Rank				
	Worst				Best
Condition	1	2	3	4	5
(a) NH					
MU	22 (73.3)	6 (20.0)	2 (6.7)	0 (0.0)	0 (0.0)
MF	3 (10.0)	11 (36.7)	8 (26.7)	5 (16.7)	3 (10.0)
BF	4 (13.3)	6 (20.0)	6 (20.0)	9 (30.0)	5 (16.7)
SMA	0 (0.0)	3 (10.0)	6 (20.0)	8 (26.7)	13 (43.3)
HS	1 (3.3)	4 (13.3)	8 (26.7)	8 (26.7)	9 (30.0)
(b) HI					
MU	18 (75.0)	4 (16.7)	2 (8.3)	0 (0.0)	0 (0.0)
MF	3 (12.5)	8 (33.3)	3 (12.5)	9 (37.5)	1 (4.2)
BF	2 (8.3)	4 (16.7)	7 (29.9)	5 (20.8)	6 (25.0)
SMA	0 (0.0)	5 (20.8)	8 (33.3)	4 (16.7)	7 (29.2)
HS	1 (4.2)	3 (12.5)	4 (16.7)	6 (25.0)	10 (41.7)

was made that the categorical variables could be ranked in such a way that the conditions could represent a linear progression from the worst listening condition to the best. The order of the listening conditions along the condition axis was based on the S/N ratio shifts observed in the NH group. The order of these conditions, from worst (1) to best performance (5), was as follows: MU, MF, BF, SMA, and HS. The raw performance scores were then ranked among those five conditions within each S/N ratio and totaled by ranks per condition across all S/N ratios for each subject group. Table Va and b show the cross-tabulated results for NH and HI groups, respectively. The numbers represent the cumulative occurrences in which subjects' performance ranked at the given values for the listed conditions. Values are totaled across all subjects within a particular group and across the three S/N ratios. A Spearman correlation for ranked data was significant for both groups at the 0.01 level ($r = -0.590$ and -0.575 for NH and HI groups, respectively). The negative correlations are consistent with the fact that the monaural listening conditions were ranked the lowest of all the conditions within a single S/N ratio. A Cochran–Mantel–Haenszel test for nonzero correlation between the two groups was significant at the 0.001 level ($\chi^2 = 51.867$). This suggests that hearing-impaired and normal-hearing listeners performed in a similar manner across all listening conditions, and further substantiates the similar rank orders for the two subject groups.

Percentages of time that specific rankings occurred for the various listening conditions are shown in parentheses in Table V. For our purposes, we will focus only on the last column and on the proportions of time the binaural conditions BF, SMA, and HS were ranked as best-performing across the three S/N ratios in each subject group. For the NH group, performance on the SMA condition ranked best 43.3% of the time, while performance on HS ranked best 30% of the time, and BF performance ranked best only 16.7% of the time. The finding that normal listeners performed best in the SMA condition more often than in the HS condition is consistent with the conclusion of Bronkhorst and Plomp (1989) that attenuating the poorer, unshadowed ear will ''hardly affect binaural unmasking due to ITD and that it will increase the gain due to ILD in certain situations...'' (p. 1382). Thus, the SMA condition may have increased the binaural unmasking for the normal-hearing group. On an intuitive level, it is not surprising that a reduction in the amplitude of high-level noise reaching the noise-unshadowed ear should result in improved intelligibility, even though the speech signal at that ear was also attenuated.

In contrast, for the HI group, performance in the HS condition ranked as best most frequently (41.7% of the time), followed by SMA (29.2%) and BF (25%). This difference in ranking patterns between subject groups may reflect a relative lack of audibility of the signal in the higher frequencies, as well as the dependence of audibility on ITD cues, for these hearing-impaired listeners. In other words, while the signal at the shadowed ear was not manipulated in the SMA condition to enhance its audibility, attenuating the signal at the unshadowed ear (in that same condition) may have de-

tracted from the binaural unmasking cues due to their reduced audibility. The overall rankings, in combination with the data reported in Tables III and IV, suggest that hearing-impaired listeners rely, as a listening strategy, on interaural cues mediated largely by head shadow, despite their inability to take full advantage of them. Normal-hearing listeners are able to utilize the available ILD cues to maximize their performance. One major practical utilization of the SMA listening strategy for them, apparently, is the ability to use a finger to plug the canal of an acoustically disadvantaged ear in appropriate communicative situations.

III. CONCLUSIONS

This research was aimed at evaluating various monaural and binaural listening strategies in the presence of noise, with a view toward the potential application of DSP schemes that might improve aided speech understanding by hearing-impaired listeners. Three of the five experimental conditions were binaural listening conditions—one diotic and two dichotic—designed to take maximum advantage of head-shadow and other interaural cues.

As previous research has shown, hearing-impaired subjects, in contrast to normal-hearing subjects, are unable to take full advantage of the acoustical environment with respect to head-shadow cues (MF–MU) and binaural-squelch effects (HS–MF). We observed mean detriments of 3.3 and 3.2 dB in these respective comparisons for hearing-impaired subjects, when contrasted to normal-hearing subjects.

Our mean results suggest that, when compared to performance under the monaural favorable condition, both the normal-hearing and hearing-impaired groups performed better when interaural cues were available, either in the HS or SMA condition. Results of the ranked-performance analysis suggest that the exaggerated ILD cues present in the SMA condition led to more occasions in which SMA was responsible for at least slightly improved intelligibility performance among normal-hearing, but not among hearing-impaired, listeners. Hearing-impaired listeners perform about equally well—or equally poorly—under each of these binaural conditions, and in some instances show improved performance when utilizing unadulterated head-shadow effects (i.e., HS, a binaural dichotic condition readily achieved with conventional binaural amplification). Thus, Bronkhorst and Plomp's (1989) suggestion that a monaural aided condition might enhance binaural unmasking in the hearing impaired, due to exaggerated ILD cues, may not be generally applicable to this population.

Maximum performance, as suggested by the hearing-impaired group's mean performance across the binaural conditions of Table V, may well have been affected by S/N ratio. For example, while listening in conditions with better S/N ratios, hearing-impaired listeners may do equally well with any binaural strategy, including the SMA condition in our study. Under worsening S/N ratios, some hearing-impaired listeners may perform better with true binaural amplification, while others may benefit from SMA or BF processing strategies. Under the worst acoustic conditions, at least some listeners may do better with monaural amplification. We observed intelligibility performance in our hearing-

impaired subjects that resulted in ranking the SMA condition best about 29% of the time (and best or second-best about 46% of the time). Performance of these subjects, as revealed by the ranked-performance analysis, was strikingly similar for the SMA and BF conditions. This latter finding suggests that there are times when either monaural amplification or diotically delivered stimuli could lead to improved speech intelligibility in individual hearing-impaired listeners.

Unfortunately, the small number of hearing-impaired subjects (8) does not permit a further analysis of the effect of S/N ratio on the relative performance of individual listeners. Nonetheless, our overall findings shed some light on the potential for using DSP strategies in conjunction with binaural hearing aids to improve the intelligibility of speech in noise for hearing-impaired listeners. Although some of these strategies can be accomplished manually—albeit inconveniently—by wearers of binaural hearing aids, adaptive DSP adjustments seem promising as realistic solutions in light of the rapidly changing nature of both DSP technology and everyday listening environments. With appropriate attention to signal-monitoring and signal-routing capabilities, the ability to switch listening strategies adaptively in various acoustical environments might be accomplished rather handily with DSP technology.

This research allows us to suggest several general directions that might be pursued to increase speech recognition substantially in noisy environments for hearing-impaired listeners. One of the most obvious potential uses of DSP-based binaural amplification is that it could act as a digital switch. If the S/N ratio in a given ear exceeds a specified differential value from the S/N ratio in the opposite ear, based on an amount measured or predicted to yield better performance with monaural amplification in a particular listening situation, the DSP circuit might switch off entirely the output to the ear at which S/N is relatively poor. Another possibility might involve a reduction in amplifier gain at the ear exposed to a relatively unfavorable S/N ratio. A third option might allow for rerouting the combined signal exhibiting the better S/N ratio to both ears. It would presumably be important in these cases to maintain frequency shaping and compression of the signal and, in the case of (dichotic) binaural listening, other operations essential for preserving or enhancing ITD and ILD cues. Implementation of these processing strategies would likely require use of an algorithm, or algorithms, that can effectively monitor the S/N ratios existing in the two ear canals of a binaurally aided listener.

The audibility of the signal was not varied for individual listeners in this study. A next step might be to repeat this research utilizing a wearable digital processor capable of amplification that controls for audibility in a manner that allows one to determine if some of the missing binaural advantage in hearing-impaired listeners can be recouped by manipulating signal audibility. Incorporating a time delay that would restore normal ITDs in the BF condition might also be worthy of investigation. Such studies should include relatively large numbers of hearing-impaired subjects.

Abbagnaro, L. A., Bauer, B. B., and Torick, E. L. (**1975**). ''Measurements of diffraction and interaural delay of a progressive sound wave caused by the human head,'' J. Acoust. Soc. Am. **53**, 693–700.

American National Standards Institute (**1989**). ANSI S3.6-1989, ''American National Standard Specification for Audiometers'' (ANSI, New York).

Brey, R. H., Robinette, M. S., Chabries, D. M., and Christiansen, R. W. (**1987**). ''Improvement in speech intelligibility in noise employing an adaptive filter with normal and hearing-impaired subjects,'' J. Rehab. Res. Dev. **24**, 75–86.

Bronkhorst, A. W., and Plomp, R. (**1988**). ''The effect of head-induced interaural time and level differences on speech intelligibility in noise,'' J. Acoust. Soc. Am. **83**, 1508–1516.

Bronkhorst, A. W., and Plomp, R. (**1989**). ''Binaural speech intelligibility in noise for hearing-impaired listeners,'' J. Acoust. Soc. Am. **86**, 1374–1383.

Bronkhorst, A. W., and Plomp, R. (**1992**). ''Effect of multiple speechlike maskers on binaural speech recognition in normal and impaired hearing,'' J. Acoust. Soc. Am. **92**, 3132–3139.

Burkhard, M. D., and Sachs, R. M. (**1975**). ''Anthropometric manikin for acoustic research,'' J. Acoust. Soc. Am. **58**, 214–222.

Byrne, D. (**1981**). ''Clinical issues and options in binaural hearing aid fitting,'' Ear Hear. **2**, 187–193.

Carhart, R. (**1965**). ''Monaural and binaural discrimination against competing sentences,'' Intern. Audiol. **4**, 5–10.

Carhart, R., Tillman, T., and Johnson, K. (**1967**). ''Release of masking for speech through interaural time delay,'' J. Acoust. Soc. Am. **42**, 124–138.

Dirks, D., and Carhart, R. (**1962**). ''A survey of reactions from users of binaural and monaural hearing aids,'' J. Speech Hear. Disord. **27**, 311–321.

Dirks, D. D., and Wilson, R. H. (**1969a**). ''The effect of spatially separated sound sources on speech intelligibility,'' J. Speech Hear. Res. **12**, 5–38.

Dirks, D. D., and Wilson, R. A. (**1969b**). ''Binaural hearing of speech for aided and unaided conditions,'' J. Speech Hear. Res. **12**, 650–664.

Dubno, J. R., and Dirks, D. D. (**1982**). ''Evaluation of hearing-impaired listeners using a nonsense-syllable test,'' J. Speech Hear. Res. **25**, 135–141.

Duda, R. O. (**1997**). ''Elevation dependence of the interaural transfer function,'' in *Binaural and Spatial Hearing in Real and Virtual Environments*, edited by R. H. Gilkey and T. R. Anderson (Erlbaum, Hillsdale, NJ).

Durlach, N. I., and Pang, X. D. (**1986**). ''Interaural magnification,'' J. Acoust. Soc. Am. **80**, 1849–1850.

Ericson, M. A., and McKinley, R. L. (**1997**). ''The intelligibility of multiple talkers separated spatially in noise,'' in *Binaural and Spatial Hearing in Real and Virtual Environments*, edited by R. H. Gilkey and T. R. Anderson (Erlbaum, Hillsdale, NJ).

Festen, J. M., and Plomp, R. (**1986**). ''Speech-reception threshold in noise with one and two hearing aids,'' J. Acoust. Soc. Am. **79**, 465–471.

Grimes, A. M., Mueller, H. G., and Malley, J. D. (**1981**). ''Examination of binaural amplification in children,'' Ear Hear. **2**, 208–210.

Kimberley, B. P., Dymond, R., and Gamer, A. (**1994**). ''Bilateral digital hearing aids for binaural hearing,'' ENT J. **73**, 176–179.

Koehnke, J., and Besing, J. (**1997**). ''Binaural performance in listeners with impaired hearing: aided and unaided results,'' in *Binaural and Spatial Hearing in Real and Virtual Environments*, edited by R. H. Gilkey and T. R. Anderson (Erlbaum, Hillsdale, NJ).

Kollmeier, B., and Peissig, J. (**1990**). ''Speech intelligibility enhancement by interaural magnification,'' Acta Oto-Laryngol. Suppl. **469**, 215–223.

Kuhn, G. F. (**1987**). ''Physical acoustics and measurements pertaining to directional hearing,'' in *Directional Hearing*, edited by W. A. Yost and G. Gourevitch (Springer-Verlag, New York).

Levitt, H. (**1970**). ''Transformed up-down methods in psychoacoustics,'' J. Acoust. Soc. Am. **49**, 467–477.

Levitt, H. (**1987**). ''Digital hearing aids: A tutorial review,'' J. Rehab. Res. Dev. **24**, 7–20.

Levitt, H., Sullivan, J. A., Neuman, A. C., and Rubin-Spitz, J. A. (**1987**). ''Experiments with a programmable master hearing aid,'' J. Rehab. Res. Dev. **24**, 29–54.

Morgan, D. E., Wilson, R. H., and Dirks, D. D. (**1974**). ''Loudness discomfort level: Selected methods and stimuli,'' J. Acoust. Soc. Am. **56**, 577–581.

Mueller, H. G., Grimes, A. M., and Jerome, J. J. (**1981**). ''Performance-intensity functions as a predictor for binaural amplification,'' Ear Hear. **2**, 211–214.

Nabelek, A. K., and Mason, D. (**1981**). ''Effect of noise and reverberation on binaural and monaural word identification by subjects with various audiograms,'' J. Speech Hear. Res. **24**, 375–383.

Nilsson, M. J., Jayaraman, S., and Soli, S. D. (**1993**). ''The separate contribution of head-shadow and binaural interactions to directional hearing in noise,'' J. Acoust. Soc. Am. **94**, 1888(A).

Nilsson, M. J., and Soli, S. (**1994**). ''The separate contribution of interaural time and level differences and headshadow to directional hearing in normal and hearing-impaired listeners,'' Paper presented at the 6th annual meeting of the Am. Acad. Audiol., Richmond, VA.

Nilsson, M., Soli, S., and Sumida, A. (**1995**). Development of norms and percent intelligibility functions for HINT, in *Research Communication* (House Ear Institute, Los Angeles, CA).

Peissig, J., and Kollmeier, B. (**1997**). ''Directivity of binaural noise reduction in spatial multiple noise-source arrangements for normal and impaired listeners,'' J. Acoust. Soc. Am. **101**, 1660–1670.

Pollack, I., and Pickett, J. M. (**1958**). ''Stereophonic listening and speech intelligibility against voice babble,'' J. Acoust. Soc. Am. **30**, 131–133.

Resnick, S. B., Dubno, J. R., Hoffnung, S., and Levitt, H. (**1975**). ''Phoneme errors on a nonsense syllable test,'' J. Acoust. Soc. Am. Suppl. 1 **58**, S114.

Schreurs, K. K., and Olsen, W. O. (**1985**). ''Comparison of monaural and binaural hearing aid use on a trial period basis,'' Ear Hear. **6**, 198–202.

Schwander, T., and Levitt, H. (**1987**). ''Effect of two-microphone noise reduction on speech recognition by normal-hearing listeners,'' J. Rehab. Res. Dev. **24**, 87–92.

Thornton, A. R., and Raffin, M. J. (**1978**). ''Speech-discrimination scores modeled as a binomial variable,'' J. Speech Hear. Res. **21**, 507–518.

Level discrimination of single tones in a multitone complex by normal-hearing and hearing-impaired listeners

Karen A. Doherty
Communication Sciences and Disorders, Syracuse University, Syracuse, New York 13244

Robert A. Lutfi
Department of Communicative Disorders, University of Wisconsin, Madison, Wisconsin 53706

A conditional-on-a-single-stimulus (COSS) analysis procedure [B. G. Berg, J. Acoust. Soc. Am. **86**, 1743–1746 (1989)] was used to estimate how well normal-hearing and hearing-impaired listeners selectively attend to individual spectral components of a broadband signal in a level discrimination task. On each trial, two multitone complexes consisting of six octave frequencies from 250 to 8000 Hz were presented to listeners. The levels of the individual tones were chosen independently and at random on each presentation. The target tone was selected, within a block of trials, as the 250-, 1000-, or 4000-Hz component. On each trial, listeners were asked to indicate which of the two complex sounds contained the higher level target. As a group, normal-hearing listeners exhibited greater selectivity than hearing-impaired listeners to the 250-Hz target, while hearing-impaired listeners showed greater selectivity than normal-hearing listeners to the 4000-Hz target, which is in the region of their hearing loss. Both groups of listeners displayed large variability in their ability to selectively weight the 1000-Hz target. Trial-by-trial analysis showed a decrease in weighting efficiency with increasing frequency for normal-hearing listeners, but a relatively constant weighting efficiency across frequency for hearing-impaired listeners. Interestingly, hearing-impaired listeners selectively weighted the 4000-Hz target, which was in the region of their hearing loss, more efficiently than did the normal-hearing listeners. © *1999 Acoustical Society of America.* [S0001-4966(99)00203-9]

PACS numbers: 43.66.Sr [JWH]

INTRODUCTION

Everyday listening often requires a person to attend selectively to individual spectral prominences in a complex sound. A COSS analysis (conditional-on-a-single-stimulus) procedure has been used in several studies (Berg, 1989; Lutfi, 1989; Berg and Green, 1990, 1991; Lutfi, 1992; Dai and Berg, 1992; Doherty, 1994; Doherty and Turner, 1996) to estimate how well normal-hearing listeners can attend to the individual spectral components of complex sounds in various discrimination tasks. However, application of COSS analysis to the hearing-impaired population has been limited. In the present study, COSS analysis is used to investigate how hearing-impaired listeners selectively attend to individual spectral components of a complex signal in a simple level-discrimination task. The study is a companion to an earlier study by Doherty and Lutfi (1996), which required listeners to combine or integrate information from multiple spectral components. In that study, the complex consisted of the six octave frequencies from 250 to 8000 Hz. On each trial, listeners were asked to identify which of two multitone complexes had a higher overall intensity. The signal was a level increment placed on all six tones in the complex. In that study, listeners were not required to selectively attend to individual spectral components inasmuch as all tones provided relevant information for the task. In general, the pattern of weights given to individual components was reliable within and across listening sessions for both normal-hearing and hearing-impaired listeners. Moreover, individual differences observed in the weighting functions of normal-hearing listeners contrasted with the similarity of the hearing-impaired listeners' weighting functions. Indeed, all but one of the 14 hearing-impaired listeners in that study placed greatest weight on a spectral component in the region of their hearing loss.

Results from the Doherty and Lutfi (1996) study have implications for how hearing-impaired listeners might perform on a selective-listening task. For example, because the hearing-impaired listeners tend to place greatest weight on frequencies in the region of their hearing loss, they might perform best on a selective-listening task when the target tone is in a region of hearing loss. For the same reason, if the target tone is in a region of normal-hearing sensitivity, hearing-impaired listeners might have difficulty ignoring the information from the nontarget components present in the region of their hearing loss. Such a hypothesis assumes, of course, that hearing-impaired listeners have a rather rigid listening strategy and are not capable of adjusting their weights to accommodate different listening tasks.

Several studies have used COSS weights to evaluate selective listening of normal-hearing listeners (Lutfi, 1992; Berg and Green, 1991; Stellmack, Willihnganz, Wightman, and Lutfi, 1997). Lutfi (1992), for example, designated one tone in a sequence of tones as the target and all other tones in the sequence as the context. The temporal position of the target was varied across blocks of trials so that it was either at the beginning (first tone), middle (sixth tone), or end (tenth tone) of the sequence. The target component was the

only component in the complex that provided relevant information about the task, so the ideal listening strategy was to weight only the target component. Lutfi reported that the pattern of weights was similar for both frequency- and intensity-discrimination tasks. Although weights were not ideal, the target tone typically received the greatest weight regardless of its position in the sequence. In addition, there was a tendency for listeners to give the last tone in the sequence a relatively higher weight regardless of the target position. Interestingly, some listeners placed negative weights on tones immediately preceding and following the target. Lutfi (1992) suggests that these listeners might have performed the task using a within-stimulus comparison listening strategy, similar to profile analysis (Green, 1983).

Berg and Green (1991) assessed normal-hearing listeners' ability to selectively attend to target components in a profile listening task. In a profile-analysis task, overall stimulus level is roved so that listeners are compelled to detect a change in the overall shape of the complex spectrum, rather than simply a change in level of any single component. In such a task, the appropriate listening strategy is to make simultaneous, within-stimulus comparisons between the level of the signal component and the level of the nonsignal components. In Berg and Green (1991), the signal spectrum was the same as the standard spectrum except the shape of the signal spectrum was altered by increasing the amplitude of a single component (i.e., target tone). The target tone was either a 280-, 1000-, or 3620-Hz tone. Thus, the listeners had to selectively identify the signal component in order to compare it to the nonsignal components. When the target was 1000 Hz (i.e., middle component) the weights were near optimal. However, weights were nonoptimal when the target was at a lower or higher frequency than 1000 Hz. A display of these listeners' thresholds as a function of signal frequency resulted in a bowl-shaped function.

The purpose of the present study was to use COSS analysis to assess how well normal-hearing and hearing-impaired listeners selectively attend to or weight a target tone embedded in a broadband signal. The study is similar to Doherty and Lutfi's (1996), except that in the present study, only one of the six components in the complex has been selected as the target tone. Also, the present study includes a much larger number of listeners to allow for a more accurate assessment of individual differences in listening strategies.

TABLE I. Hearing-impaired listeners' thresholds (dB HL).

Sub/TE	Age/Sex	Frequency (kHz)							
		0.25	0.50	1.0	2.0	3.0	4.0	6.0	8.0
mlb/r	73/F	25	25	25	25	30	45		50
jnr/r	39/M	15	10	15	30		35		45
hil/r	75/F	20	25	20	25		35	50	65
rmp/l	48/M	30	25	35	50		55		55
gce/f	55/M	20	20	35	45		60		55
arj/l	68/M	5	20	35	45		55		65
wet/r	54/F	15	20	35	35		35		45
emw/l	57/M	10	10	15	20	25	45	65	65
fae/l	60/M	15	10	5	20	50	55		60
mjb/r	38/F	20	15	15	15	30	55		60
maw/l	49/F	5	0	0	15	30	50		45
ras/l	48/M	25	20	25	30	50	55	45	25
avg/r	32/M	5	0	0	0	10	50	10	20
aml/r	33/F	30	20	10	5	15	40	55	65
pal/r	47/F	15	15	35	50	25	25		20

I. GENERAL METHOD

A. Subjects

A group of 15 hearing-impaired listeners, eight males and seven females, between 32 and 75 years of age, were paid to participate in this study. All listeners had a bilateral sensorineural hearing loss. The degree of their loss varied (Table I), but all had pure-tone thresholds of 65 dB HL (ANSI, 1989) or less from 250–8000 Hz. Thresholds at interoctave frequencies were tested whenever the difference between thresholds at adjacent frequencies was 20 dB or greater (ASHA, 1978). Thresholds in the listeners' right and left ears differed by less than 10 dB at all test frequencies. Fifteen normal-hearing listeners, three males and 12 females, between 21 and 40 years of age, were paid to participate in this study. Normal-hearing listeners' pure-tone air-conduction thresholds were ≤15 dB HL (ANSI, 1989) from 250–8000 Hz in both ears. Both groups of listeners demonstrated acoustic-immittance measures within the 90%-normal range for compensated static acoustic admittance (ASHA, 1990).

B. Stimuli

Stimuli were multitone complexes that consisted of octave frequencies from 250–8000 Hz. Each tone was 50 ms in duration with 2-ms, cosine-squared, rise–fall times. The
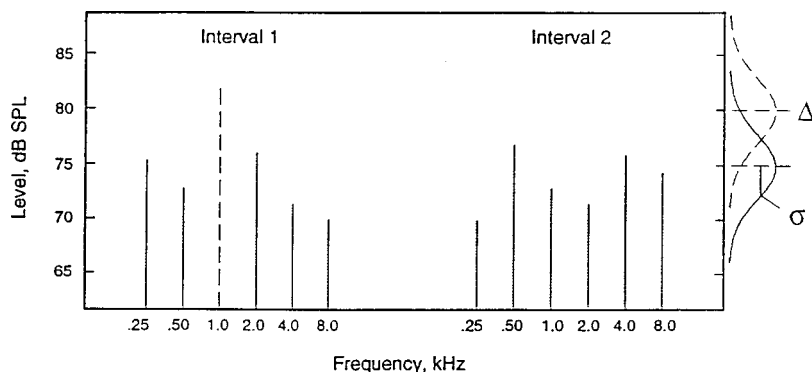
FIG. 1. Example of a single trial on a selective-listening task. The target is a level increment placed on the 1-kHz tone of the complex in interval one.
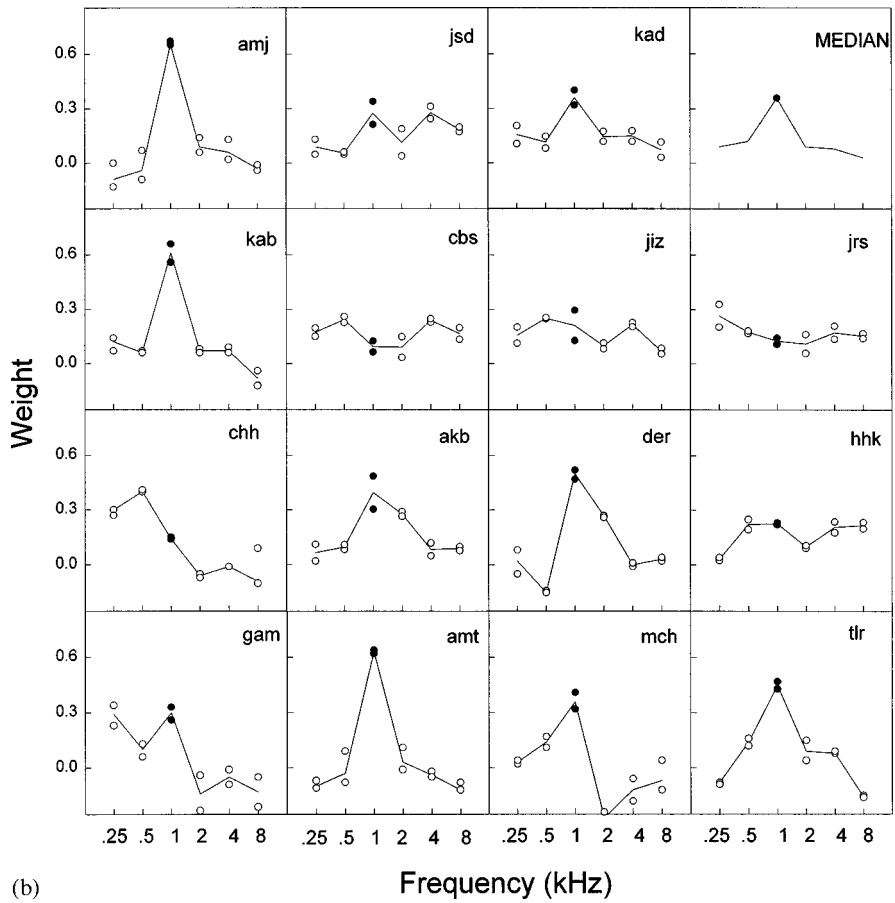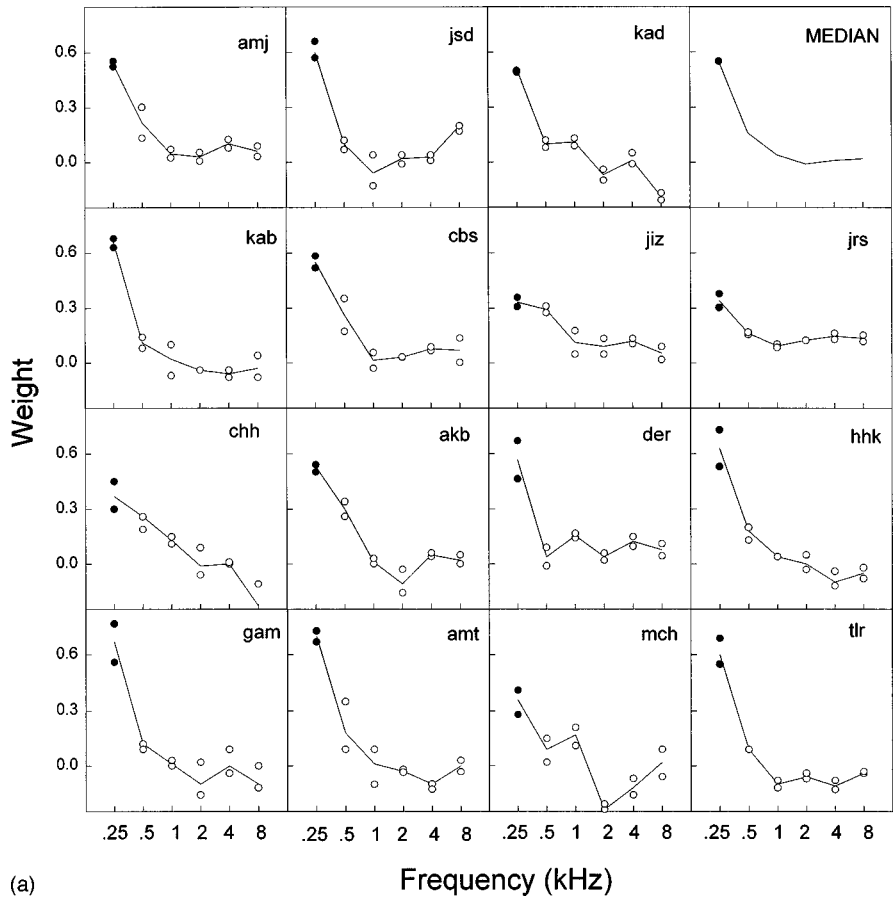
FIG. 2. Independent estimates (circles) of average weights (solid lines) for 15 normal-hearing listeners on the 250- [panel (a)], 1000- [panel (b)], and 4000-Hz [panel (c)] target conditions. Filled circles represent independent estimates of the target weight. The median of the 15 normal-hearing listeners' weights is shown in the upper right-hand panel of each figure.

FIG. 2. (*Continued.*)

(c)

Frequency (kHz)
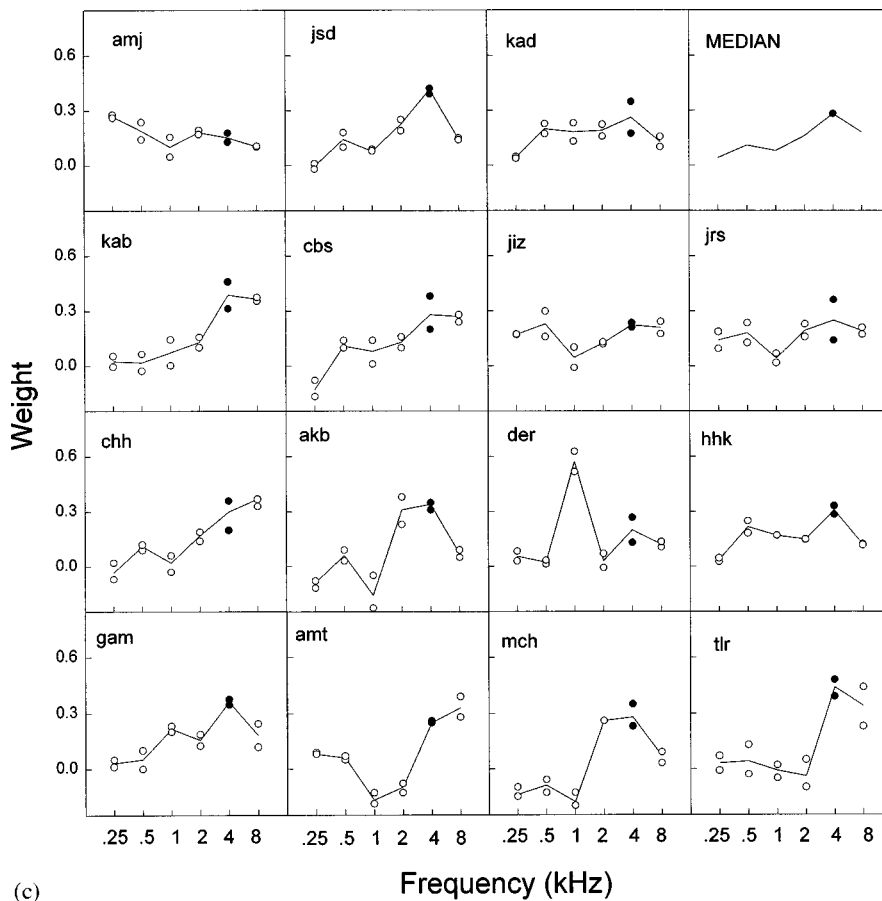
level of each tone was selected at random from one of two normal distributions of levels in dB, one for the target and the other for the nontarget components. The standard deviation of both distributions was fixed at 5 dB for the normal-hearing listeners and 3 dB for the hearing-impaired listeners. The mean of the target distribution was 65 and 80 dB SPL for normal-hearing and hearing-impaired listeners, respectively. The mean of the nontarget distribution was systematically adjusted to yield a performance level close to a d' of one (Green and Swets, 1966). Three different target-tone conditions were assessed. Across blocks of trials, the target was presented at either 250, 1000, or 4000 Hz.

Stimuli were generated digitally with an IBM PC AT and played through a 16-bit, digital-to-analog converter (DAC) at a sampling rate of 20 kHz. The output of the DAC was low-pass filtered at 10 kHz at 120 dB/octave to attenuate aliased components. Note that the average level of the lowest-frequency aliased component at 12 000 Hz is 65 $-32=33$ dB SPL. At this level, the aliased component at 12 000 Hz would have been inaudible for the hearing-impaired listeners, but might have been just barely audible on some trials for the normal-hearing listeners.

C. Procedure

Each listener was seated in an IAC sound-attenuation chamber and presented computer-generated stimuli monaurally over an HD-520 Sennheiser earphone. The Sennheiser earphone was calibrated using a binaural loudness-balancing procedure with a TDH-49 earphone (ANSI, 1973).

A fixed, two-interval, forced-choice (2IFC) procedure was used. On each trial, subjects were presented with two multitone complexes. For one of these complexes, the level of the target was selected at random from the target distribution of levels. The levels of all the other tones were selected independently and at random from the nontarget distribution of levels (see Fig. 1). A 500-ms silent interval separated the two signals. There was an equal probability that the level of the target tone would be selected from the target distribution in either the first or the second interval. Subjects were asked to indicate which of the two sounds they perceived to have the louder target tone. Before a new target tone was tested, 100 trials of the target tone alone were presented to listeners in order to familiarize them with its pitch. The order in which target tones were presented was counterbalanced across listeners.

Responses were collected via a keyboard and visual feedback was presented on a CRT after each response. With a few exceptions, a total of 1000 trials was collected for each subject on each condition. Less than 1000 trials were collected for the following subjects: RAS on the 1000-Hz target condition (400 trials); MJB on the 4000-Hz condition (600 trials), and AMT on the 250-Hz condition (500 trials). For another subject (AML), 2000 trials were collected on the 250-Hz condition in order to obtain a more reliable estimate of weights. Therefore, of the 90 weighting functions obtained in this study, only four were not computed from 1000 trials. The 1000 trials were collected in approximately 1 h.
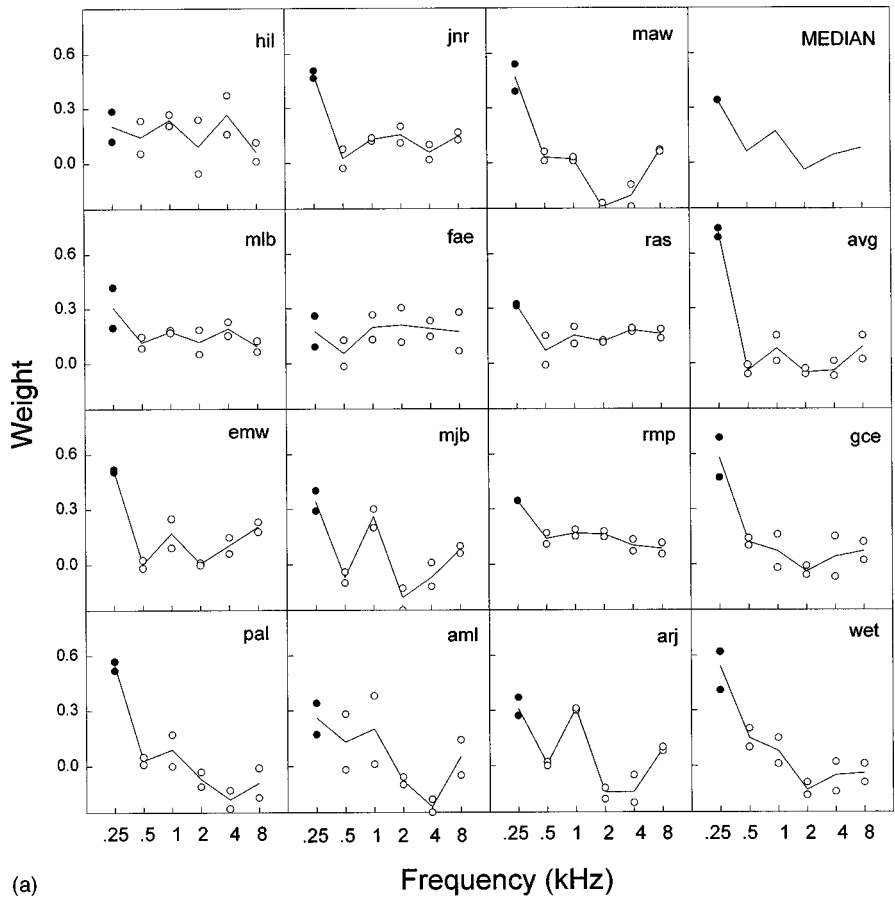
FIG. 3. Independent estimates (circles) of average weights (solid lines) for 15 hearing-impaired listeners on the 250- [panel (a)], 1000- [panel (b)], and 4000-Hz [panel (c)] target conditions. Filled circles represent independent estimates of the target weight. The median of the 15 hearing-impaired listeners' weights is shown in the upper right-hand panel of each figure.

FIG. 3. (*Continued.*)

(c)   Frequency (kHz)
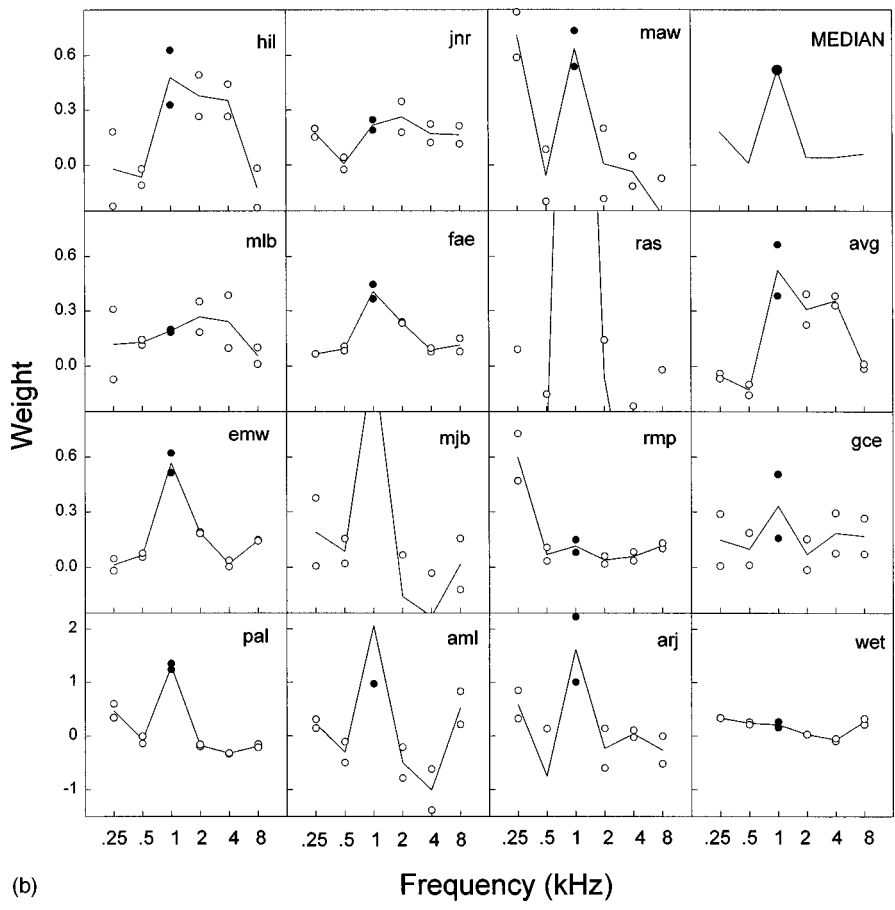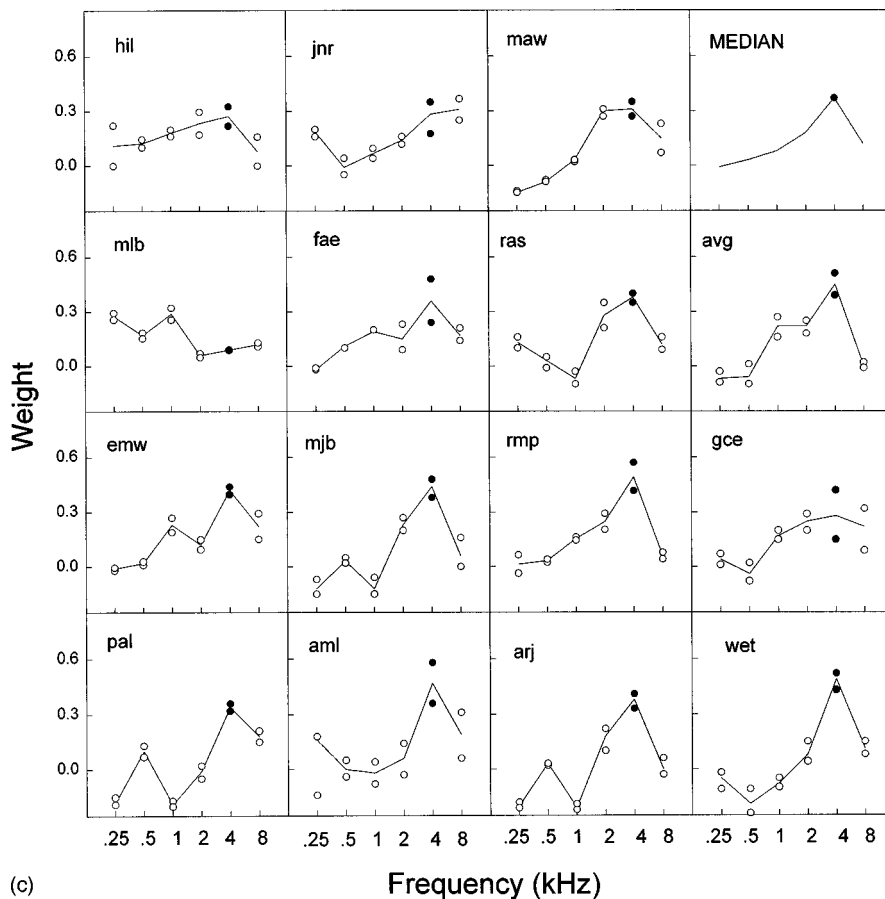
No more than one target tone was tested on the same day. Subjects were permitted to take breaks between blocks of trials as they felt the need.

Weights were normalized such that the sum of the absolute weights equaled unity (i.e., $|x_1|+|x_2|+|x_3|+,...,|x_6|=y$; $x_1/y=a_1$, $x_2/y=a_2,...,x_6/y=a_6$; $\Sigma|a_i|=1$).

II. ANALYSIS

A. Weighting analysis

Estimates of the weights were obtained using the COSS analysis method described by Berg (1989). The weights for each tone were estimated from the slopes of the COSS functions for each tone. Each COSS function relates the probability of a second-interval response across trials to the level difference of a given tone between intervals. These conditional-response probabilities were obtained from the records of the trial-by-trial data. Two COSS functions were obtained to estimate the average weight for each tone in the complex. The first estimate was obtained from the set of trials for which subjects correctly responded to the second interval, and the second was obtained from the set of trials for which subjects incorrectly responded to the second interval. A least-squares fitting procedure was used to fit the COSS data with a cumulative Gaussian function. A COSS function with a relatively steep slope indicates the tone has a greater influence or weight on a listener's decision, whereas a relatively shallow slope indicates the tone contributed little to the listener's overall decision on the task. The weights were normalized for ease of making comparisons across subjects and to demonstrate the relative weight each individual component had on the listener's decision on the task.

B. Efficiency measures

A measure of a listener's overall performance efficiency (η_{obt}) was determined by comparing the listener's obtained performance to that of a theoretical ideal listener's performance on the same task, one that maximizes percent correct. The overall performance efficiency, η_{obt}, can be considered a product of two separate performance efficiencies: that given by how closely the listener's weighting strategy approaches the ideal weighting strategy (η_{wgt}), and that representing the efficiency of all other processing not related to these weights (η_{noise}). These other processing factors would include, for instance, any degradation in the sensory representation of the stimulus that might be due to a hearing loss. Measures of listening efficiencies were determined by first computing $\eta_{wgt}=(d'_{wgt}/d'_{ideal})^2$, which is obtained by comparing the listener's weights to the ideal listener's weight for a given listening task. The value d'_{wgt} corresponds to the performance level that would have been achieved using the listener's weighting function as the single determinant of performance. Then, any additional loss in overall performance efficiency that cannot be accounted for by η_{wgt} is attributed to η_{noise}. The relationship between all three efficiency measures as described by Berg (1990) is

$$\eta_{\text{obt}} = \eta_{\text{wgt}} \times \eta_{\text{noise}},$$

or equivalently,

$$(d'_{\text{obt}}/d'_{\text{ideal}})^2 = (d'_{\text{wgt}}/d'_{\text{ideal}})^2 \times (d'_{\text{obt}}/d'_{\text{wgt}})^2.$$

III. RESULTS

A. Spectral weighting functions

Weighting functions for normal-hearing listeners are shown in Fig. 2(a)–(c) for the 250-, 1000-, and 4000-Hz target tones, respectively. Only in the 250-Hz condition did all 15 listeners give the target tone the greatest weight. Of the 15 normal-hearing listeners, six (AKB, TLR, KAB, MCH, KAD, and GAM) gave greatest weight to the target tone in all three target conditions. Weighting functions for two normal-hearing listeners (JIZ and JRS) were fairly flat for all three target conditions, although they did give the 250-Hz target a slightly higher weight than the nontarget tones. As a group, the normal-hearing listeners varied how they weighted the 1000- and 4000-Hz target tones.

Weighting functions for the hearing-impaired listeners are shown in Fig. 3(a)–(c) for the 250-, 1000-, and 4000-Hz target tones, respectively. It should be noted that age effects are not apparent among the impaired listeners, which indicates that the age difference probably is not important. Of the 15 hearing-impaired listeners, only FAE and HIL did not weight the 250-Hz target tone the greatest. The pattern of weights obtained for the hearing-impaired listeners varied for the 1000-Hz target-tone condition. In the 4000-Hz target condition, hearing-impaired listeners gave greatest weight to the target tone more often than normal-hearing listeners. Median weights were similar for both groups of listeners on all target conditions (see upper right-hand panel in Figs. 2 and 3), which obscure important individual differences.

Statistical comparisons were made between normal-hearing and hearing-impaired listeners' average weights of each of the six components in each of the target conditions (Fig. 4). Of the 18 comparisons (3 target listening conditions×6 components in each condition), only five were significantly different between the two groups of listeners. Of the three target tones, only the 250-Hz target was weighted significantly ($t = 2.455$, $df = 28$, $p < 0.05$) different by the two groups. That is, the normal-hearing listeners weighted the 250-Hz target tone greater than hearing-impaired listeners. In all three target conditions, normal-hearing listeners weighted the 500-Hz component significantly greater than hearing-impaired listeners (0.25-kHz condition: $t = 3.74$, $df = 28$, $p < 0.001$; 1-kHz condition: $t = 2.44$, $df = 28$, $p < 0.05$; 4-kHz condition: $t = 3.21$, $df = 28$, $p < 0.01$). Last, in the 250-Hz target condition, hearing-impaired listeners weighted the 1000-Hz component significantly ($t = -3.53$, $df = 28$, $p < 0.001$) greater than normal-hearing listeners.

B. Component preference

A single weighting function consists of six weights that correspond to each of the six components in the complex stimulus, one of which is the target component. The three
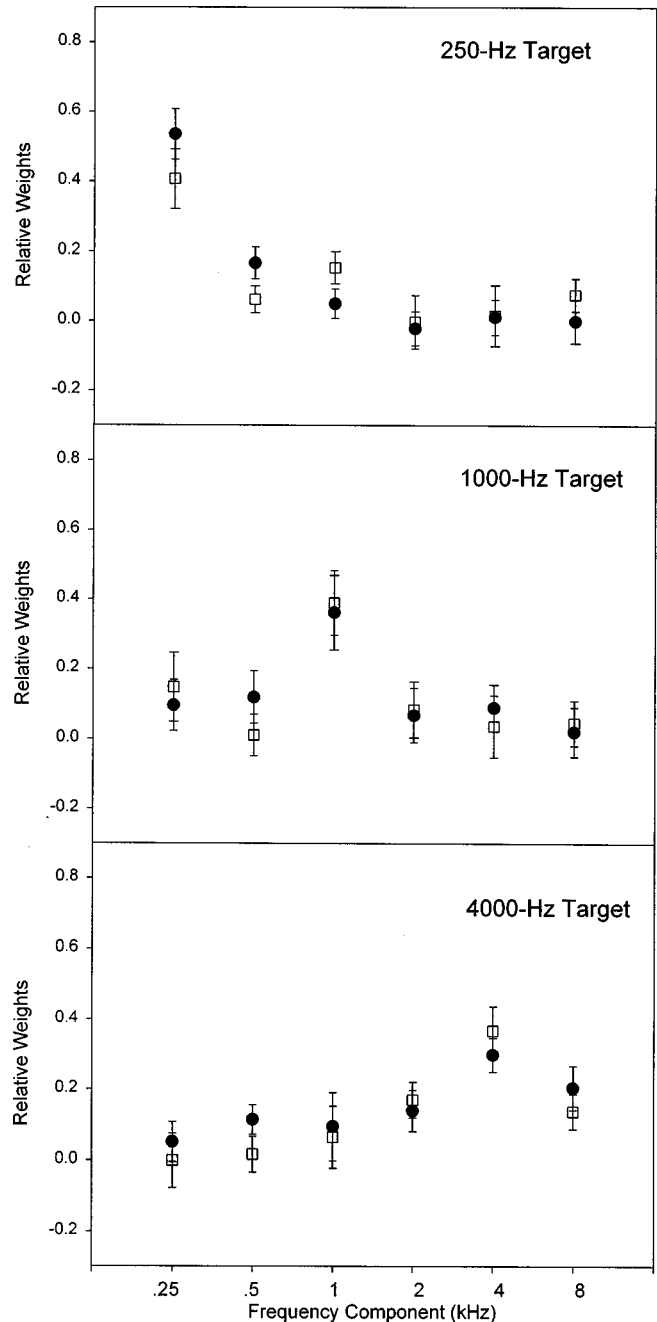
FIG. 4. In the upper, middle, and bottom panels, mean weights and 95%-confidence intervals are shown for normal-hearing (filled circles) and hearing-impaired listeners (unfilled squares) on the 250-, 1000-, and 4000-Hz target conditions, respectively.

panels in Fig. 5 represent the listeners' preference to weight a given component the greatest in each of the target conditions. Each bar represents the number of listeners who gave greatest weight to a specific frequency component. For example, in the 250-Hz condition, shown in the top panel of Fig. 5, all normal-hearing listeners and most hearing-impaired listeners weighted the 250-Hz tone the greatest. In the 1000-Hz condition, there were large differences in the listeners' preference to weight one component over another. In the 4-kHz condition, more hearing-impaired than normal-hearing listeners weighted the target tone the greatest. A few normal-hearing listeners actually weighted the lower-frequency components the greatest.
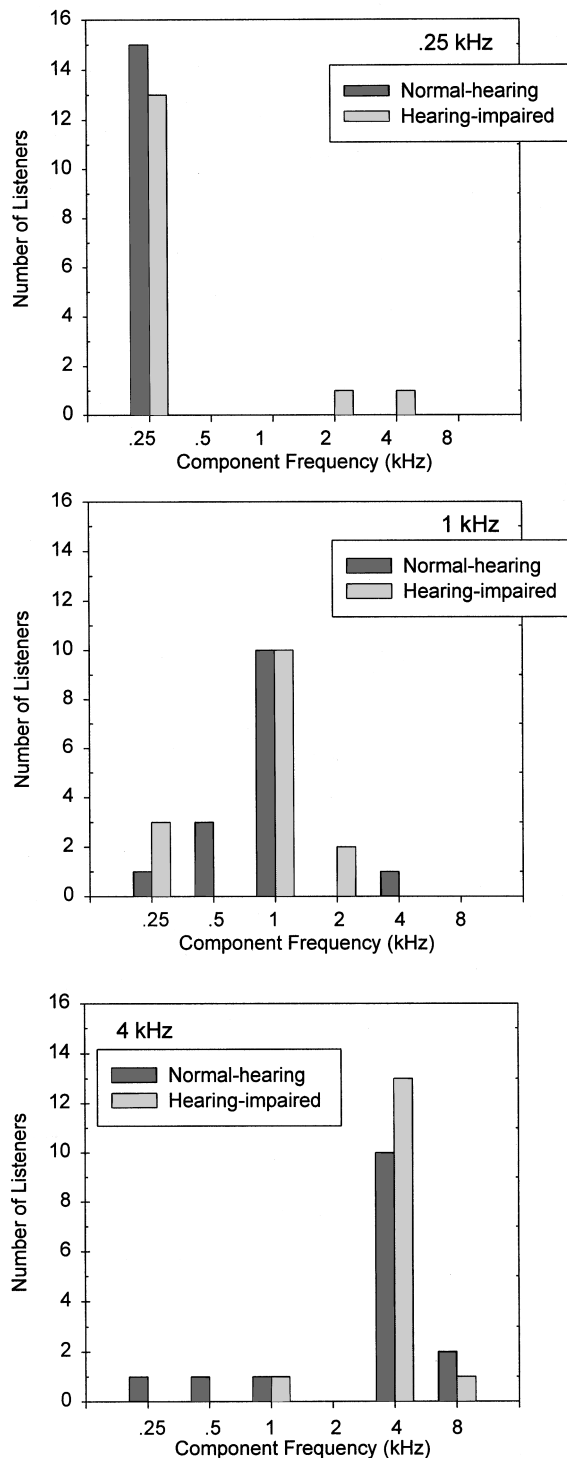
FIG. 5. The top, middle, and bottom bar panels correspond to the 250-, 1000-, and 4000-Hz target conditions, respectively. Dark and shaded bars indicate the number of normal-hearing and hearing-impaired listeners, respectively, who gave maximum weight to that frequency component.

C. Efficiency measures

Average weighting-efficiency (η_{wgt}) and noise-efficiency (η_{noise}) measures for both groups of listeners on the three target conditions are shown in the upper and lower panels of Fig. 6, respectively. A highly efficient system is characterized by high efficiencies for both weighting and noise. A univariate analysis of variance revealed that normal-
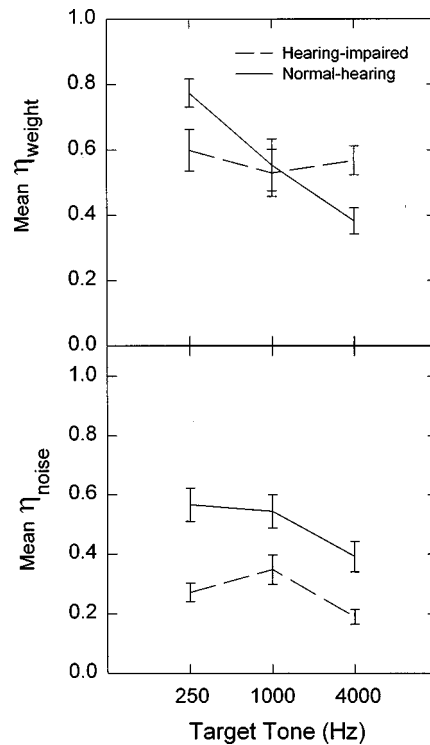
FIG. 6. Mean weighting efficiency (top panel) and noise efficiency (bottom panel) measures for normal-hearing (solid line) and hearing-impaired (broken line) listeners as a function of target frequency. Error bars indicate the standard error of the mean.

hearing listeners' noise-efficiency (η_{noise}) measures were significantly ($p < 0.01$) higher than the hearing-impaired listeners on all three target conditions. Weighting-efficiency measures (η_{wgt}) differed significantly ($p < 0.01$) between the normal-hearing and hearing-impaired listeners only for the 4000-Hz target condition, which was when the weighting efficiencies were higher for the hearing-impaired listeners.

Interestingly, normal-hearing listeners' weighting-efficiency measures decreased as the frequency of the target increased, but hearing-impaired listeners' weighting efficiencies remained roughly constant. Noise-efficiency measures remained fairly consistent across target frequencies for both groups of listeners, but were generally higher for the normal-hearing listeners.

D. Comparisons across listening tasks

A comparison of listeners' efficiency measures on the selective-listening task in the present study and the Doherty and Lutfi (1996) study, where listeners were asked to combine information from all six components in the stimulus, are shown in the three panels in Fig. 7. These data represent the subset of normal-hearing listeners who participated in both studies. The line joining the unfilled and filled symbols in these figures represents the change in efficiency, for individual listeners, across the two listening tasks. Except for the 250-Hz target frequency, the lines tend to be steeper than 45 deg, which indicates that the reduced efficiency observed in the selective-listening condition was mostly due to a change in the listeners' ability to attend (η_{wgt}) to the information, rather than from other unspecified factors (η_{noise}). This pro-
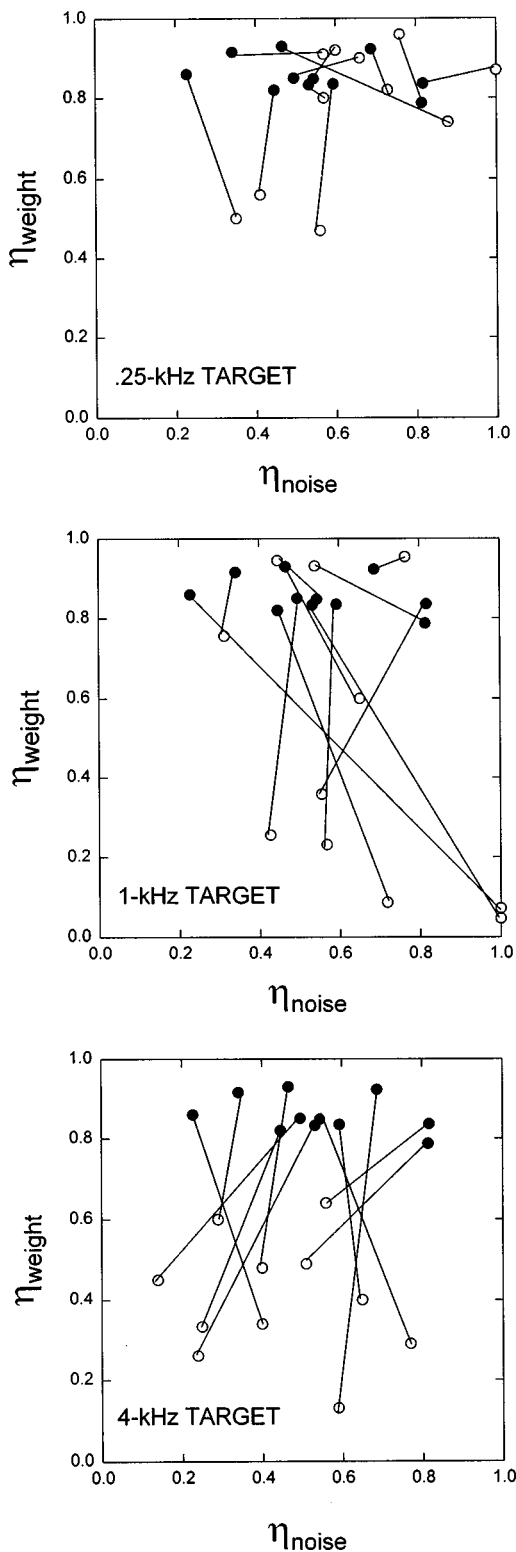
FIG. 7. A comparison of 11 normal-hearing listeners' efficiency measures across two different listening tasks. The upper, middle, and bottom panels show the 250-, 1000-, and 4000-Hz selective-listening task (unfilled circles) compared with a listening task requiring listeners to integrate information across spectral components (filled circles). Efficiency measures for each listener across conditions is connected by a line.

vides evidence that inefficient weights have a greater effect on a listener's performance when the demands of the listening task require listeners to attend to a single component of the complex than when they are required to integrate information across components.

IV. DISCUSSION

In the present study, COSS analysis was used to estimate the weighting strategies of normal-hearing and hearing-impaired listeners when discriminating the level of a single target tone (250, 1000, or 4000 Hz) embedded in a multitone complex. Large individual differences were observed for both groups of listeners in the 1000-Hz target condition. In the 250-Hz target condition, more normal-hearing than hearing-impaired listeners weighted the target greatest, but more hearing-impaired than normal-hearing listeners weighted the 4000-Hz target greatest. Each listener's overall performance in the present study was assessed in terms of two types of efficiency measures: a weighting efficiency (η_{wgt}), which accounted for how well listeners weighted the spectral information, and a noise efficiency (η_{noise}), which accounted for all other factors that might have limited the listeners' overall performance on the task. Recall that high weighting-efficiency measures indicate an efficient weighting strategy, and high noise-efficiency measures indicate that few factors other than listening strategy influenced performance. In the limit for the ideal observer, both weighting- and noise efficiency are unity. The hearing-impaired listeners' noise-efficiency measures were significantly lower than the normal-hearing listeners for all three target frequencies, but their weighting-efficiency measures were significantly higher for the 4000-Hz target, which is in the region of their hearing loss. This is consistent with Doherty and Lutfi's (1996) finding that hearing-impaired listeners also tend to weight the spectral information in the region of their hearing loss greatest even when all spectral components provide equal information for the task. This might suggest that hearing-impaired listeners learn to be more attentive to the information in the region of their hearing loss in order to compensate to some extent for their hearing loss. However, three of five listeners who had a hearing loss equal to or greater than 30 dB at 1000 Hz did not weight the 1000-Hz target greatest. In fact, two of them obtained the lowest weighting-efficiency measure of all the hearing-impaired listeners on this condition.

One important conclusion of the Doherty and Lutfi (1996) study was that inefficient weighting strategies did not greatly affect listeners' overall performance on their listening task. It was suggested this might have to do with the type of attentional demands that were required of the listeners. The efficiency measures obtained for 11 normal-hearing listeners in the Doherty and Lutfi (1996) study were compared with the efficiency measures obtained from the same listeners in the present selective-listening study. The comparison showed that inefficient weights had a greater impact on performance in the selective-listening task. This is not too surprising, given that in the earlier Doherty and Lutfi study, all six tones in the complex were designated target tones and therefore all contributed information for the task. As a result, if listeners inefficiently weighted one of the target tones, they could still benefit from the information provided by the other five target tones. In the present selective-listening study, however, only one of the six tones provided relevant information and therefore, if a listener were to fail to give greatest weight to the target tone, it would greatly affect their performance on the

task. This finding provides evidence in support of Doherty and Lutfi's (1996) hypothesis that inefficient weights have a greater influence on overall performance when the listening task requires listeners to selectively attend to individual spectral components.

Differences in the hearing-impaired listeners' performance on the selective-listening task were primarily related to differences in their weighting strategies. As expected, listeners who weighted the target tone greatest and nontarget tones least obtained the highest overall-performance scores on the task. Thus, improving a hearing-impaired listener's weighting strategy would likely improve their overall performance in such selective-listening tasks. The degree of improvement, however, would still be limited by factors that contribute to their low noise efficiency. That is, a listener with both a low weighting- and noise-efficiency measure might receive some benefit by improving their weighting strategy, but their performance would still be largely limited by their low noise efficiency.

There are some possible clinical applications for obtaining weighting functions in hearing-impaired listeners. For example, hearing-impaired listeners who give undue weight to spectral information in the region of their hearing loss may not benefit from traditional amplification of this information. In some cases, it might even adversely affect how the listener processes the entire sound.

ACKNOWLEDGMENTS

ANSI (**1973**). ANSI S3.7-1973, ''American National Standard Method for Coupler Calibration of Earphones'' (American National Standards Institute, New York).

ANSI (**1989**). ANSI S3.6-1989, ''Specifications for Audiometers'' (American National Standards Institute, New York).

American Speech-Language-Hearing Association (**1990**). ''Guidelines for screening for hearing impairments and middle ear disorders,'' ASHA **32**(2), 17–24.

American Speech-Language-Hearing Association (**1978**). ''Guidelines for manual pure-tone audiometry,'' ASHA **20**, 297–301.

Berg, B. G. (**1989**). ''Analysis of weights in multiple observation tasks,'' J. Acoust. Soc. Am. **86**, 1743–1746.

Berg, B. G. (**1990**). ''Observer efficiency and weights in a multiple observation task,'' J. Acoust. Soc. Am. **88**, 149–158.

Berg, B. G., and Green, D. M. (**1990**). ''Spectral weights in profile listening,'' J. Acoust. Soc. Am. **86**, 758–766.

Berg, B. G., and Green, D. M. (**1991**). ''Spectral weights and the profile bowl,'' Q. J. Exp. Psychol. **43A**, 449–458.

Dai, H., and Berg, B. G. (**1992**). ''Spectral and temporal weights in spectral shape discrimination,'' J. Acoust. Soc. Am. **92**, 1346–1355.

Doherty, K. A. (**1994**). ''Spectral weights measured in listeners with sensorineural hearing loss,'' Doctoral dissertation, University of Wisconsin-Madison, Madison, WI.

Doherty, K. A., and Lutfi, R. A. (**1996**). ''Spectral weights for overall level discrimination in listeners with sensorineural hearing loss,'' J. Acoust. Soc. Am. **99**, 1053–1058.

Doherty, K. A., and Turner, C. W. (**1996**). ''Use of a correlational method to estimate a listener's weighting function for speech,'' J. Acoust. Soc. Am. **100**, 3769–3773.

Green, D. M. (**1983**). ''Profile analysis: A different view of auditory intensity discrimination,'' Am. Psychol. **38**(2), 133–142.

Green, D. M., and Swets, J. A. (**1966**). *Signal Detection Theory and Psychophysics* (Wiley, New York).

Lutfi, R. A. (**1989**). ''Informational processing of complex sound. Intensity discrimination,'' J. Acoust. Soc. Am. **86**, 934–944.

Lutfi, R. A. (**1992**). ''Informational processing of complex sound. III: Interference,'' J. Acoust. Soc. Am. **91**, 3391–3401.

Stellmack, M. A., Willihnganz, M. S., Wightman, F. L., and Lutfi, R. A. (**1997**). ''Spectral weights in level discrimination by preschool children: analytical listening conditions,'' J. Acoust. Soc. Am. **101**, 2811–2821.

Gap detection by early-deafened cochlear-implant subjects

P. A. Busby and G. M. Clark

Department of Otolaryngology, University of Melbourne, Parkville, 3052, Victoria, Australia

Two studies investigating gap-detection thresholds were conducted with cochlear-implant subjects whose onset of profound hearing loss was very early in life. The Cochlear Limited multiple-electrode prosthesis was used. The first study investigated the effects of pulse rate (200, 500, and 1000 pulses/s) and stimulus duration (500 and 1000 ms) on gap thresholds in 15 subjects. Average gap thresholds were 1.8 to 32.1 ms. There was essentially no effect of pulse rate and for almost all subjects, no effect of stimulus duration. For two subjects, performance was poorer for the 1000-ms stimulus duration. The second study investigated the relationships between gap thresholds, subject variables, and speech-perception scores. Data from the first study were combined with those from previous studies [Busby *et al.*, Audiology **31**, 95–111 (1992); Tong *et al.*, J. Acoust. Soc. Am. **84**, 951–962 (1988)], providing data from 27 subjects. A significant negative correlation was found between age at onset of deafness and gap thresholds and most variability in gap thresholds was for the congenitally deaf subjects. Significant negative correlations were found between gap thresholds and word scores for open-set Bamford–Kowal–Bench (BKB) sentences in the auditory–visual condition and lipreading enhancement scores for the same test. © *1999 Acoustical Society of America.* [S0001-4966(99)03703-0]

PACS numbers: 43.66.Ts, 43.66.Mk, 43.71.Ky [JWH]

INTRODUCTION

Gap detection is a frequently used measure of auditory temporal resolution. Recent studies have shown that the gap-detection thresholds of postlinguistically deaf adults using electric stimulation (Moore and Glasberg, 1988; Preece and Tyler, 1989; Shannon, 1989) are generally similar to those found for normally hearing subjects using acoustic stimulation (Fitzgibbons and Gordon-Salant, 1987; Fitzgibbons and Wightman, 1982; Florentine and Buus, 1984; Hall and Grose, 1997; Penner, 1977), and are in the range of 2–10 ms for both subject groups. Gap-detection thresholds for both electric and acoustic stimulation in general become poorer with decreasing sensation level, ranging from 30 to 100 ms for electric and acoustic stimulation near absolute-hearing thresholds (Fitzgibbons and Gordon-Salant, 1987; Florentine and Buus, 1984; Hall and Grose, 1977; Moore and Glasberg, 1988; Penner, 1977; Preece and Tyler, 1989; Shannon, 1989). These similarities suggest that differences in the peripheral neural excitation patterns produced by electric and acoustic stimulation, such as greater synchronization for electric stimulation (Javel, 1990), are not major factors influencing this measure of auditory temporal resolution.

We have also measured gap-detection thresholds in early-deafened cochlear-implant subjects using the Cochlear Limited prosthesis (Busby *et al.*, 1992; Tong *et al.*, 1988), for whom the onset of profound deafness was typically at birth or a very early age. These subjects have been profoundly deaf for most of their life, and most if not all of their auditory experience has been via electric stimulation. They are, therefore, an important subject group for evaluation, as their performance may indicate the consequences of both auditory deprivation from early childhood and electric stimulation as the primary means of auditory experience. In our studies, gap thresholds were 5 ms or less for eight of the 12

early-deafened subjects tested and were, therefore, within the range reported for postlinguistically deaf adults. For the other four early-deafened subjects, gap thresholds were considerably larger and ranged from 14 to 95 ms. These four subjects were implanted at an older age, above 20 years of age, than the other eight subjects, between 5 and 16 years of age, suggesting that age at implantation and/or the duration of auditory deprivation prior to implantation may be factors influencing gap detection. There are other factors which may be related to these variations in gap thresholds, such as the duration of normal auditory function prior to the onset of profound deafness and postoperative experience with electric stimulation, but it was not possible to further examine these relationships because of the small number of subjects evaluated.

These differences between early-deafened subjects, and between early-deafened and postlinguistically deaf subjects, could be related to physiological and morphological differences in the neural structure of the auditory pathway caused by the absence or limited duration of auditory experience since birth, consistent with experimental animal studies which have shown that auditory deprivation results in incomplete maturation and/or degeneration within the auditory system (Harrison *et al.*, 1991; Moore, 1990; Saada *et al.*, 1966; Seldon *et al.*, 1996; Webster and Webster, 1977). Additional changes in auditory function may have also arisen as the consequence of postoperative experience with electric stimulation, consistent with experimental animal studies which have shown that changes within the auditory pathway can be induced in both juvenile and adult animals. Chronic electric stimulation in the neonatally deafened cat has been shown to result in enhanced phase locking of inferior colliculus units (Snyder *et al.*, 1995), and an expansion in the representation of the site of stimulation at the inferior colliculus (Snyder

et al., 1990). Similarly, marked changes in the spatial representation of the tonotopic cochlear map at the primary auditory cortex have been produced by unilateral partial cochlear lesions in the normally hearing adult cat (Rajan *et al.*, 1993).

The first objective of this study was to determine whether gap-detection thresholds from early-deafened subjects vary for different pulse rates (200, 500, and 1000 pulses/s) and stimulus durations (500 and 1000 ms). In our previous studies described above, gap-detection thresholds were only measured using 1000 pulses/s at a stimulus duration of 1000 ms. The second objective was to determine the relationships between gap-detection thresholds, subject variables related to auditory deprivation and experience, and measures of speech-perception performance. The multiple-electrode cochlear implant manufactured by Cochlear Limited was used.

With respect to pulse rate, it is possible that poorer gap-detection thresholds could arise at low pulse rates because the pulsatile stimuli may produce percepts which are less smooth than those produced by a high rate of stimulation. This is because the time interval between individual pulses is longer at low rates, leading to an increased roughness of the signal and greater stimulus uncertainty in the processing of small temporal gaps. Alternatively, gap-detection thresholds could be poorer at high rates of stimulation because the coding of fine temporal characteristics of the signal may be compromised as the interpulse time interval approaches the refractory period of auditory-nerve fibers, resulting in the poorer transmission of a temporal gap. For instance, Javel (1990) showed a decrease in the synchronization of discharge probabilities of auditory-nerve fibers as the pulse-rate period approached the refractory period. It has also been shown that the demyelinization of auditory-nerve fibers, which can arise from pathological changes associated with a long duration of profound deafness, will lead to an increase in the refractory period (Shepherd and Javel, 1997) and this may result in the poor transmission of the temporal gap at high rates of stimulation.

With respect to stimulus duration, poorer gap-detection thresholds may be found for the longer duration because of adaptation effects produced by continual stimulation of the same group of residual auditory-nerve fibers prior to the onset of the gap period. It has been suggested in acoustic studies with normally hearing subjects that the rate of adaptation after the onset of stimulation and recovery from adaptation may be factors related to the poorer gap-detection thresholds recorded for infants and children as compared to those for adults (Trehub *et al.*, 1995). It is possible, therefore, that gap-detection thresholds could vary with different pulse rate and stimulus duration conditions. Furthermore, data collection from early-deafened subjects would provide important information about temporal resolution using electric stimulation where there is a likelihood of less-than-optimal auditory functioning.

There have been only a few reports documenting the effects of pulse rate on gap-detection thresholds using pulsatile stimulation. Dobie and Dillier (1985) presented data from two adult subjects, one deafened in the first year of life from meningitis, for the pulse rates 80 to 1000 pulses/s. Gap

thresholds were less than 5 ms for both subjects, although there was a tendency for higher thresholds at lower pulse rates, 4.5 and 5 ms at 80 pulses/s, and 2 and 1.8 ms at 1000 pulses/s. Note that as far as sinusoidal electric stimulation is concerned, previous studies with postlinguistically deaf subjects have suggested that sinusoidal frequency has a minimal effect on gap-detection thresholds. Preece and Tyler (1989) showed in three subjects that there was no effect of frequency, from 63 to 4000 Hz, on gap thresholds over a wide range of loudness levels, except at very low sensation levels where gap-detection thresholds decreased as sinusoidal frequency increased. Shannon (1989) also showed that gap-detection thresholds were similar for sinusoidal (1000 Hz) and pulsatile (1000 pulses/s) electric stimuli presented at a comfortable listening level in the one subject tested.

In addition, measures of gap detection at different pulse rates would be particularly relevant to the speech-processing strategies of the Cochlear Limited prosthesis, as low rates of stimulation have typically been used. In the case of the older MPEAK strategy, the pulse rate is equal to estimates of the acoustic fundamental frequency for voiced sounds (approximately 100 to 300 pulses/s) while for unvoiced sounds, a pseudorandom pulse rate between 200 and 300 pulses/s is used (Skinner *et al.*, 1991). For the newer SPEAK strategy, the pulse rate is determined by the number of stimulated electrodes and is typically 250 pulses/s when six electrodes are stimulated (Skinner *et al.*, 1994).

The second objective of this study was to determine the relationships between gap-detection thresholds for early-deafened subjects, subject variables related to the amount of auditory deprivation and experience, and measures of speech-perception performance. Data collected in this study were combined with those from our previous studies (Busby *et al.*, 1992; Tong *et al.*, 1988) to provide group data for 27 early-deafened subjects. The subject variables examined included those related to the period of auditory deprivation (age at onset of deafness, duration of deafness, and age at implantation) and those related to experience with electrically evoked hearing sensations (duration of implant use). It is possible that gap-detection thresholds may be poorer as a result of long-term auditory deprivation and/or may improve with postoperative experience. The importance of these subject variables to the speech-perception performance of implanted children has also been investigated in several studies (cf. Proceedings of the NIH Consensus Statement, 1995). For instance, Fryauf-Bertschy *et al.* (1997) showed that open-set word-recognition scores were higher in children implanted before 5 years of age, full-time users of the implant had higher scores on almost all measures, and that children required several years of experience with the implant before significant scores on open-set words were obtained.

As far as the relationship between gap detection and speech perception is concerned, it has been suggested that gap thresholds of less than about 40 ms should be sufficient to perceive speech information coded by temporal gaps (Bosman and Smoorenburg, 1997; Muchnik *et al.*, 1994; Tyler *et al.*, 1989). This information would include cues for the identification of consonants, as well as gaps marking syllable and word boundaries. Several studies using single-and

TABLE I. Summary of subject histories.

Subject	Age at confirmation of profound–total hearing loss (months)	Cause of deafness	Age at implantation (years)	Age at testing (years)	Duration of implant use (years)
S1	10	cytomegalovirus	7.8	11.8	4.1
S2	24	meningitis	3.5	9.3	5.9
S3	6	rubella	6.6	11.4	4.8
S4	18	Usher's syndrome	20.0	20.9	0.9
S5	6	Usher's syndrome	14.8	21.2	6.4
S6	47	meningitis	5.2	10.4	5.2
S7	15	congenital, unknown	11.6	13.9	2.2
S8	12	congenital, unknown	13.5	14.6	1.0
S9	11	congenital, unknown	6.6	11.0	4.4
S10	12	congenital, unknown	10.4	11.6	1.2
S11	39	meningitis	4.8	9.8	5.1
S12	16	cytomegalovirus	4.6	11.4	6.8
S13	24	Klippel–Feil and Mondini syndromes	8.6	11.8	3.2
S14	15	rubella	5.2	10.3	5.1
S15	12	congenital, unknown	17.5	21.5	4.0

multiple-electrode stimulation in postlinguistically deaf adults have shown significant negative correlations between gap-detection thresholds and scores for speech-perception tests, indicating that subjects with higher gap thresholds had lower speech-perception scores (Cazals *et al.*, 1991; Gantz *et al.*, 1993; Hochmair-Desoyer *et al.*, 1985; Muchnik *et al.*, 1994; Tyler *et al.*, 1989). Similar negative correlations between gap-detection thresholds and speech-perception scores have also been recorded for hearing-impaired adults (Tyler *et al.*, 1982) and children (Dreschler and Plomp, 1985) using acoustic stimulation. In addition, Bosman and Smoorenburg (1997) showed that gap-detection thresholds negatively correlated with the lipreading enhancement scores, the difference between scores for the auditory–visual and vision-alone conditions, for sentence perception by profoundly hearing-impaired listeners. It may be the case that those subjects with better gap thresholds are better able to effectively perceive syllable and word boundaries in the sentence materials.

I. EFFECTS OF PULSE RATE AND STIMULUS DURATION

A. Method

1. Subjects and electric-stimulation hardware

The histories of the 15 early-deafened subjects are summarized in Table I. The average age of the subjects at the time of diagnosis of the profound–total sensorineural hearing loss was 17.8 months (s.d.=11.6 months), with a range of 6 to 47 months. Three subjects were deafened as a result of meningitis; at 24, 47, and 39 months of age for S2, S6, and S11, respectively. The other subjects were congenitally deaf from a variety of etiologies. All subjects were fitted with high-gain hearing aids at the time of diagnosis. The subjects were implanted with the Cochlear Limited prosthesis of 22 electrodes (Clark *et al.*, 1987) and the average age of the subjects at the time of implantation was 9.4 years (s.d.=5.1 years), with a range of 3.5 to 20 years. The electrode array was fully inserted into the scala tympani for most subjects. In some cases, some electrodes were not used in the speech-processing strategies as they were external to the scala tympani or stimulation produced unpleasant sensations. The average age of the subjects at the time of testing was 13.4 years (s.d.=4.3 years), with a range of 9.3 to 21.5 years, and the average duration of implant use at the time of testing was 4.0 years (s.d.=1.9 years), with a range of 0.9 to 6.8 years.

The residual auditory-nerve fibers were stimulated using biphasic current pulses with a pulse duration of 200 μs/phase. The Cochlear Limited prosthesis can deliver electric current between 15 and 1500 μA, which is converted to a scale of 239 levels with approximately a 2.5% increase in current for each level (Skinner *et al.*, 1991), although there are some minor variations across individual prostheses. In this report, electric-stimulation levels are described using these current levels. Bipolar stimulation was used for all subjects. For most subjects, except S1, S3, and S13, the two electrodes of the bipolar pair were separated by one electrode, which corresponds to "BP+1" in the Cochlear Limited clinical procedures. For S1, S3, and S13, the two electrodes were separated by two electrodes, corresponding to "BP+2" in the clinical procedures. The term "electrode" describes the basal member of the bipolar pair. Stimulation was on electrode 14 for all subjects, where electrodes are numbered 22–1 in an apical–basal direction. This electrode was selected so that these data could be combined with our previous data (Busby *et al.*, 1992; Tong *et al.*, 1988) which were collected using stimulation on electrode 14.

2. Procedure

Gap-detection thresholds were measured separately for two stimulus durations, 500 and 1000 ms, and for three pulse rates, 200, 500, and 1000 pulses/s. The reference stimulus was either 1000 or 500 ms in duration and contained no gap. The comparison stimulus had the same duration and pulse rate, but contained a gap of variable duration located 500 and 250 ms after the onset of the stimulus, for the 1000- and
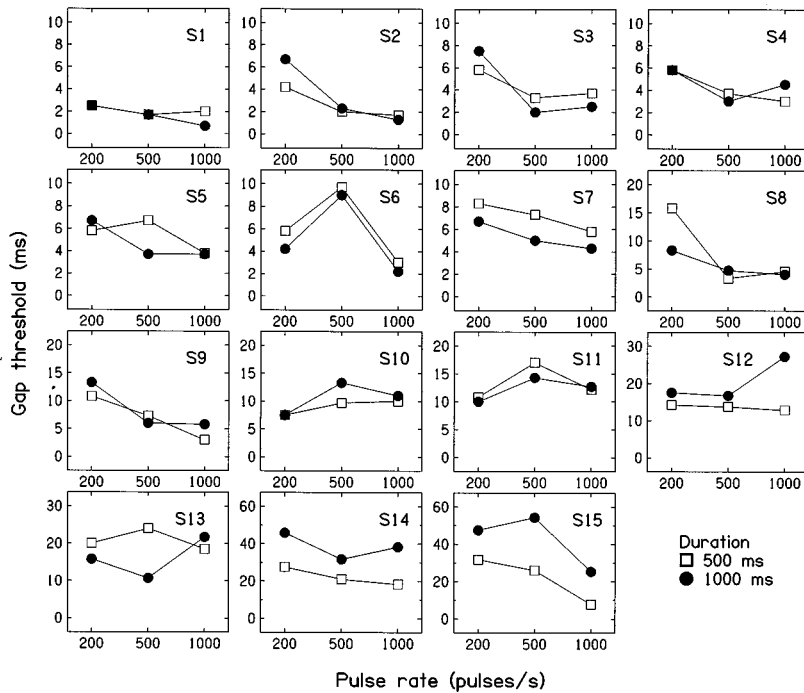
FIG. 1. Gap-detection thresholds as a function of pulse rate and stimulus duration for 15 early-deafened subjects.

500-ms stimulus durations, respectively (Busby *et al.*, 1992; Tong *et al.*, 1988). The current levels for the reference and comparison stimuli were the same and were adjusted to a comfortable listening level using an ascending–descending technique. Current was increased until stimulation became too loud or uncomfortable; it was then decreased to the maximum comfortable listening level. Note that as gap-detection thresholds are sensitive to the loudness of the stimuli (Shannon, 1989), at least for stimuli presented at loudness levels of less than 7 on a category scale of 1 (threshold) to 10 (comfortable listening level), particular attention was given to this adjustment procedure. Separate measures were made at each pulse rate and stimulus duration.

An adaptive three-interval forced-choice procedure was used to obtain the gap-detection thresholds. Each trial consisted of three intervals separated by 500 ms. Two of the intervals were the reference stimulus and one was the comparison stimulus, and the interval with the comparison was randomly selected in each trial. Each interval was cued by a number (1–3) graphically displayed on a computer screen. The subject selected the number corresponding to the comparison in each trial using a verbal response or computer mouse. Visual feedback was provided after each trial. A two-down, one-up adaptive procedure which converged on the 70.7%-correct point (Levitt, 1971) was used to obtain the gap-detection threshold. The comparison was chosen to be clearly different from the reference at the beginning of the adaptive procedure. The step-size of change to the duration of the gap was one pulse for the last six reversals, which corresponded to 5, 2, and 1 ms for 200, 500, and 1000 pulses/s, respectively. Each run was terminated after ten reversals and the average of the last six was taken as the result.

Subjects were typically seen once per week at their school for 30–40 min per session. Training was provided prior to data collection, although most subjects found the

task very easy and gave consistent gap thresholds across conditions with a minimal amount of training. A single data point was then taken for each condition. These gap thresholds were compared with those obtained during training to determine whether performance had changed. Also examined were the gap thresholds for the last six reversals to determine whether there was marked variation during data collection. Typically, the standard deviations of the last six reversals were in the range 0.5 to 2 pulses, with a tendency of larger standard deviations for subjects with poorer thresholds. The largest s.d. was recorded for S13, 4.7 pulses (9.4 ms) at 500 pulses/s for a stimulus duration of 500 ms. In addition, all subjects were experienced with psychophysical testing procedures as they had been tested using the same procedures but with other sets of stimuli, such as different electrodes.

B. Results

Figure 1 shows the gap-detection thresholds for the 15 subjects separately as functions of stimulus duration and pulse rate. The ordering of subjects is from the smallest to largest average gap threshold. Note that the vertical scale increases for subjects S8 to S15 to accommodate the larger thresholds for these subjects. The gap-detection thresholds averaged across pulse rates and stimulus durations ranged from 1.8 to 12.8 ms for S1 to S11, which is similar to the range found for postlinguistically deaf adults. Average thresholds were higher for S12 to S15 and ranged from 17.0 to 32.1 ms. To determine whether thresholds differed significantly across subjects, the data were analyzed using a one-way analysis of variance. *Post hoc* analysis of the means using the Tukey test was used to determine which subjects contributed to the significant effects. A significant difference between subjects was recorded [$F(14,75) = 15.97$, $p < 0.001$]. Mean gap thresholds for S14 and S15 were

higher than those for S1–S13, thresholds for S13 were higher than those for S1–S7, and thresholds for S12 were higher than those for S1–S5.

For most subjects, there were no significant effects of pulse rate or stimulus duration on gap-detection thresholds with the exception of two and three subjects, respectively. The data for each subject were separately analyzed using a two-way analysis of variance to determine whether thresholds varied for the three pulse rates or two stimulus durations. *Post hoc* analyses of the means using the Tukey test were used to determine which pulse rates contributed to the significant effects. Small but significant differences between pulse rates were recorded for S6 $[F(2,2)=192.45, \ p=0.005]$ and S7 $[F(2,2)=31.7, \ p=0.031]$. For S6, thresholds for each pulse rate were different from each other and were ordered 1000, 200, and 500 pulses/s, from lowest to highest, and the mean difference in thresholds between 1000 and 500 pulses/s was 6.75 ms. For S7, thresholds for 1000 pulses/s were less than those for 200 pulses/s, and the mean difference in thresholds was 2.45 ms. Also for S7, a very small but significant difference was recorded for stimulus duration $[F(1,2)=51.16, \ p=0.019]$ and thresholds were higher for the 500-ms stimulus duration than for the 1000-ms stimulus duration, with a mean difference of 1.8 ms. It is likely that these differences in gap thresholds across pulse rates and stimulus durations for these two subjects are not of importance, as the gap thresholds were less than 10 ms and were within the range of those from postlinguistically deaf adults. In addition, it is possible that these small differences were due to within-subject variability in gap detection, as only one data point was taken at each pulse rate and stimulus duration. The standard deviations of the gap thresholds across pulse rates and stimulus durations for S6 and S7, 3.1 and 1.5 ms, respectively, were similar to those for S1 to S13, which ranged from 0.7 (S1) to 5.3 ms (S12). The s.d.'s for S14 and S15, 10.4 and 16.8 ms, respectively, were much larger than those for the other subjects. Considerably larger differences in gap thresholds between the two stimulus durations were also recorded for S14 $[F(1,2)=32.64, \ p=0.029]$ and S15 $[F(1,2)=27.52, \ p=0.034]$. Thresholds were higher for the 1000-ms stimulus duration than for the 500-ms stimulus duration, with a mean difference of 16.3 and 20.3 ms for S14 and S15, respectively.

II. ANALYSIS OF GROUP DATA

A. Method

Gap-detection data for the 1000 pulses/s signal at 1000-ms stimulus duration from the current study were combined with data from our previous studies collected using the same stimulus characteristics (Busby *et al.*, 1992; Tong *et al.*, 1988), providing group data for 27 early-deafened subjects. These data were collected using electrode 14, and in the Spectra speech-processing strategy of the Cochlear Limited prosthesis, the acoustic-frequency bandwidth allocated to this electrode is 1350–1550 Hz for BP+1 stimulation and 1150–1350 Hz for BP+2 stimulation. In previous studies

TABLE II. Summary of etiologies for the 27 subjects.

Cause of deafness	Number of subjects
Meningitis	10
Congenital, unknown	7
Usher's syndrome	5
Rubella	2
Cytomegalovirus	2
Klippel–Feil and Mondini syndromes	1

with postlinguistically deaf adults, there has not been any evidence of marked variation in gap thresholds for different electrodes on the array (Shannon, 1989).

Examined were the relationships between gap-detection thresholds, subject variables related to auditory deprivation and experience, and measures of speech-perception performance. It is possible that gap-detection thresholds may be poorer as a result of long-term auditory deprivation and/or may improve with postoperative experience. For speech perception, gap detection may be an important variable influencing performance when a limited amount of speech information is provided, as is the case for cochlear implants. Note that in our first study, there was essentially no effect of pulse rate on gap-detection thresholds. Thus, it was considered reasonable to examine the relationships between gap thresholds at 1000 pulses/s and speech-perception performance with speech-processing strategies which use pulse rates in the range from 100 to 300 pulses/s (Skinner *et al.*, 1991, 1994). The following data were obtained from the clinic histories: age at onset of profound deafness, etiology of deafness (summarized in Table II), duration of deafness prior to implantation, age at implantation, and duration of implant use. Also calculated was the total time period of auditory stimulation (age at onset of deafness plus duration of implant use) to determine whether total auditory experience (acoustic and electric) was a variable influencing gap-detection thresholds. Note that for the congenitally deaf subjects, the total time period of auditory stimulation was equal to the duration of implant use, and duration of deafness prior to implantation was equal to age at implantation. In addition, age at the time of testing was included as a variable to determine whether differences in gap-detection thresholds across subjects were influenced by any cognitive or task-dependent factors related to chronological age.

For measures of speech-perception performance, however, clinical data were not available for all subjects on all tests which have been used in clinic assessments. The speech-perception data reported here were collected on average within 0.35 years (s.d.=0.39 years) of the gap-detection thresholds. Selected were data from two closed-set monosyllabic word tests presented in the audition-alone condition: the picture vocabulary test (Plant, 1984), which consists of 12 words presented using a 12-alternative, forced-choice paradigm ($n=21$), and the NU-CHIPS test (Elliott and Katz, 1980), which consists of 50 words presented using a four-alternative, forced-choice paradigm ($n=14$). In the picture vocabulary test, high scores could be obtained by primarily using vowel cues. The NU-CHIPS test predominately measures consonant perception, as the test is designed so that
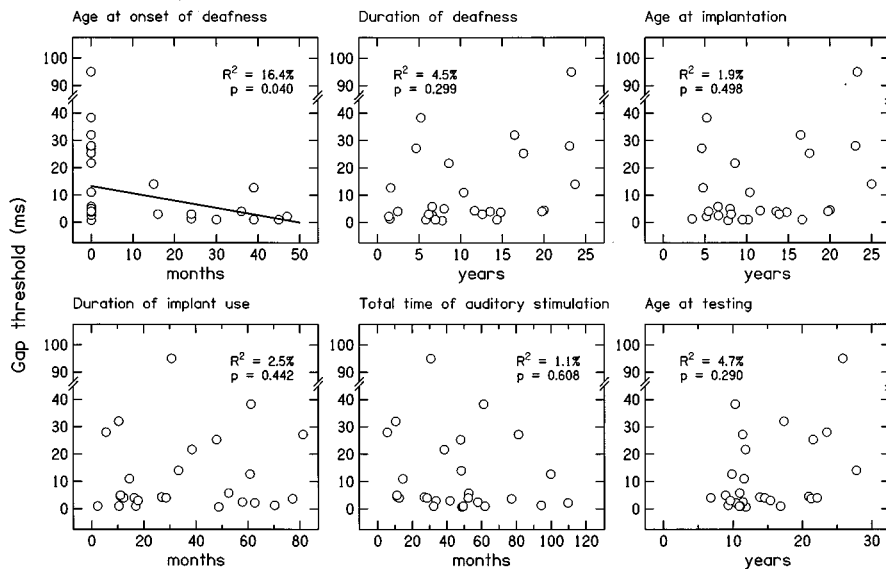
FIG. 2. Gap-detection thresholds as functions of six subject variables. Provided in each graph are the correlation coefficient and level of significance. A linear regression line has been fitted in the one case of a significant correlation.

manner, place, and voicing cues must be used to achieve high scores. Also selected were word scores for the BKB open-set sentence test (Bench and Bamford, 1979), presented in the audition-alone ($n=14$), vision-alone ($n=19$), and combined auditory–visual ($n=21$) conditions. Finally, the lipreading enhancement scores ($n=19$) were calculated from the word scores for BKB sentences using

$$\text{Lipreading enhancement} = (AV-V)/(100-V), \qquad (1)$$

where V and AV were the scores for the vision-alone and auditory–visual conditions, respectively, providing the percent score of the possible improvement over the vision-alone score (Tyler *et al.*, 1992).

The correlations between gap-detection thresholds, subject variables, and speech-perception scores were calculated using the Pearson product moment coefficient of correlation, and are expressed using the coefficient of determination (R^2) to indicate the proportion of variance for which it accounted. In some of these analyses, however, it was necessary to exclude data from one subject because of the very high gap-detection threshold. This subject was PRE2 from the Tong *et al.* (1988) study, where the gap-detection threshold (95 ms) was considerably larger than those for the other subjects (0.7 to 38 ms). The fit of the linear-correlation model to the data was assessed using the pure error and lack of fit tests (Minitab, Inc., 1998). In all cases, there was no evidence of a lack of fit [$p>0.1$].

We also compared the mean performance of the congenitally and meningitically deaf subjects using *t*-tests to determine whether there was any difference between the two subject groups. This would indicate whether auditory experience prior to the onset of profound deafness during early childhood resulted in better gap-detection thresholds and speech-perception scores.

B. Results

Figure 2 shows the gap-detection thresholds as functions of each of the six subject variables investigated. Also provided in each graph are the correlation coefficients and cor-

responding levels of significance. A significant negative correlation, shown by the linear regression line, was recorded between age at onset of deafness and gap-detection threshold [$R^2=16.4\%$, $p=0.040$], indicating that subjects who became deaf at a later age had lower gap thresholds. Also, gap thresholds were significantly smaller for the meningitically deaf subjects [$t(20)=2.63$, $p=0.016$], consistent with the results of the correlation analysis. Note that age at onset of deafness also correlated with three of the other subject variables. Significant negative correlations were recorded with duration of deafness [$R^2=24.3\%$, $p=0.009$] and age at testing [$R^2=14.6\%$, $p=0.049$], indicating that subjects who became deaf at a younger age had been deaf for a longer period of time at the time of data collection and were tested at an older age than those subjects who became deaf at an older age. A significant positive correlation was recorded between age at onset of deafness and the total time of auditory stimulation [$R^2=28.6\%$, $p=0.004$], indicating that those subjects who became deaf at an older age had a greater amount of total auditory stimulation at the time of data collection than those subjects who became deaf at a younger age. The lack of a significant correlation between gap-detection thresholds and age at testing [$R^2=1.9\%$, $p=0.498$], indicating that these two measures were not linearly related, suggests that any cognitive or task-related factors related to chronological age may not have influenced the performance of this group of subjects. A significant difference between the meningitically and congenitally deaf subject groups was recorded for total time of auditory stimulation [$t(16)=2.43$, $p=0.027$], which was likely due to the contribution of normal hearing in early childhood for the meningitically deaf subjects. There were no significant differences between the two subject groups for duration of deafness [$t(16)=1.88$, $p=0.079$], age at implantation [$t(18)=1.99$, $p=0.330$], duration of implant use [$t(18)=0.55$, $p=0.590$], and age at testing [$t(17)=1.31$, $p=0.210$].

However, it was clear that most of the variability in gap-detection thresholds was found for the congenitally deaf subjects, as shown by the spread of data for subjects with a
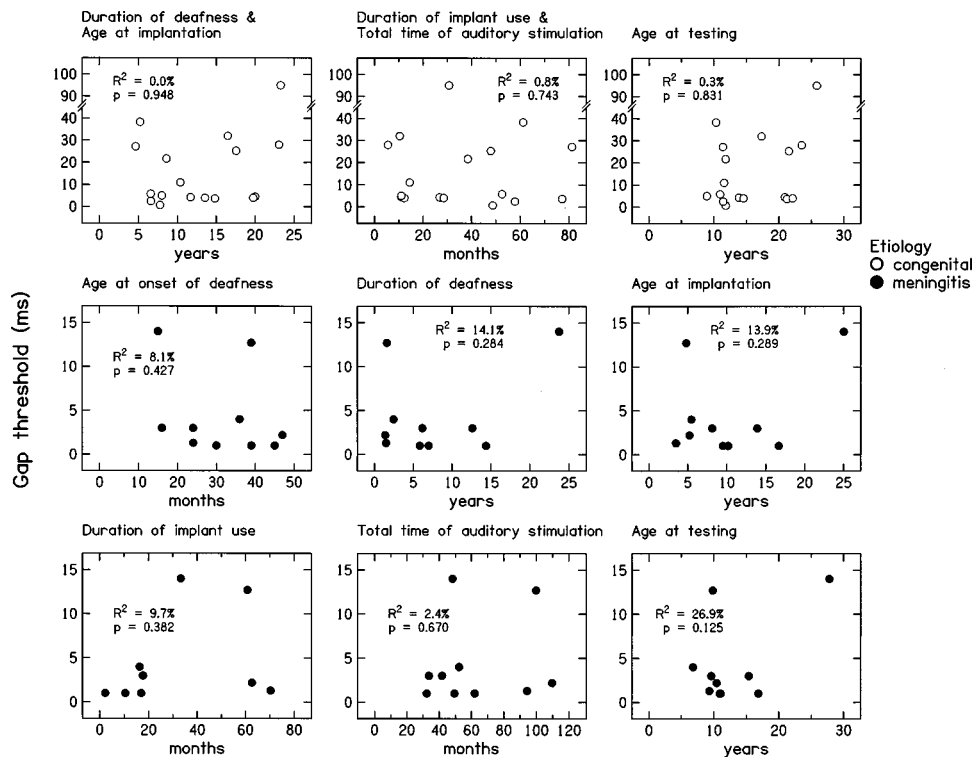
FIG. 3. Gap-detection thresholds of subjects as functions of subject variables divided on the basis of a congenital hearing loss (upper three graphs) or a hearing loss from meningitis (lower six graphs). Provided in each graph are the correlation coefficient and level of significance.

0-month age at onset of deafness (first graph in Fig. 2). Figure 3 shows the same set of data as in Fig. 2 divided according to whether the subjects had a congenital hearing loss ($n=17$), first row of three graphs, or a hearing loss as a result of meningitis ($n=10$), second and third row of graphs. No correlations were significantly above chance. In the case of the congenitally deaf subjects, this result indicated that between-subject variability in gap-detection thresholds was not correlated with the duration of auditory deprivation prior to implantation (age at implantation) and/or postoperative experience with the electrically evoked hearing sensations (duration of implant use). There were no obvious relationships between gap thresholds and etiology, which was not surprising given that the etiology was unknown for almost half of these congenitally deaf subjects (Table II). Even where there was a known etiology, such as Usher's syndrome ($n=5$), both small and large gap-detection thresholds were recorded (3.7, 4.0, 4.5, 28.0, and 32.0 ms). It was also clear that, with the exception of two subjects, gap-detection thresholds for the meningitically deaf subjects were less than 5 ms. The two subjects with the poorer thresholds (13 and 14 ms) were not similar with respect to any of the subject variables examined. These generally good gap-detection thresholds for the meningitically deaf subjects contrast with those for the congenitally deaf subjects, where thresholds were above 21 ms for 41% of subjects. For the other 59% of congenitally deaf subjects, thresholds were less than 11 ms. However, the lack of a significant correlation between age at onset of deafness and gap-detection thresholds for the meningitically deaf subjects (Fig. 3) suggests that the significant correlation between these two factors in the analysis of data from all subjects (Fig. 2) needs to be interpreted with caution. Finally, these findings may suggest that the lack of both normal hearing at birth and auditory stimulation in early

childhood, as was the case for the congenitally deaf subjects, increases the likelihood of poorer gap-detection thresholds.

Figure 4 shows the speech-perception scores for the different tests as a function of gap-detection thresholds. Significant negative correlations, shown by the linear regression lines, were found between gap-detection thresholds and word scores for BKB sentences in the auditory–visual condition [$R^2=18.8\%$, $p=0.049$], indicating that subjects with smaller gap-detection thresholds had higher word scores, and the lipreading enhancement scores for BKB sentences [$R^2=21.6\%$, $p=0.048$], indicating that subjects with smaller gap thresholds had a greater improvement in auditory–visual perception over vision-alone performance. No other correlations between gap-detection thresholds and speech-perception scores were significant.

With respect to differences between the meningitically and congenitally deaf subject groups, scores were higher for the meningitically deaf subjects for BKB sentences in the alone [$t(3)=3.29$, $p=0.046$], and auditory–visual [$t(15)=2.21$, $p=0.043$] conditions. However, this finding for the audition-alone condition needs to be interpreted with caution, as there were only three meningitically deaf subjects. No significant differences between the two subject groups were recorded for the picture vocabulary [$t(7)=0.34$, $p=0.750$], NU-CHIPS [$t(6)=0.19$, $p=0.860$], BKB sentences in the vision-alone condition [$t(13)=0.18, p=0.860$], and the lipreading enhancement [$t(10)=1.46$, $p=0.170$] scores.

The auditory–visual BKB word scores and the lipreading enhancement scores also correlated with other variables. Table III shows the correlations between word scores for BKB sentences in the three conditions, the lipreading enhancement scores, and the subject variables investigated in this study. For the auditory–visual BKB scores, significant
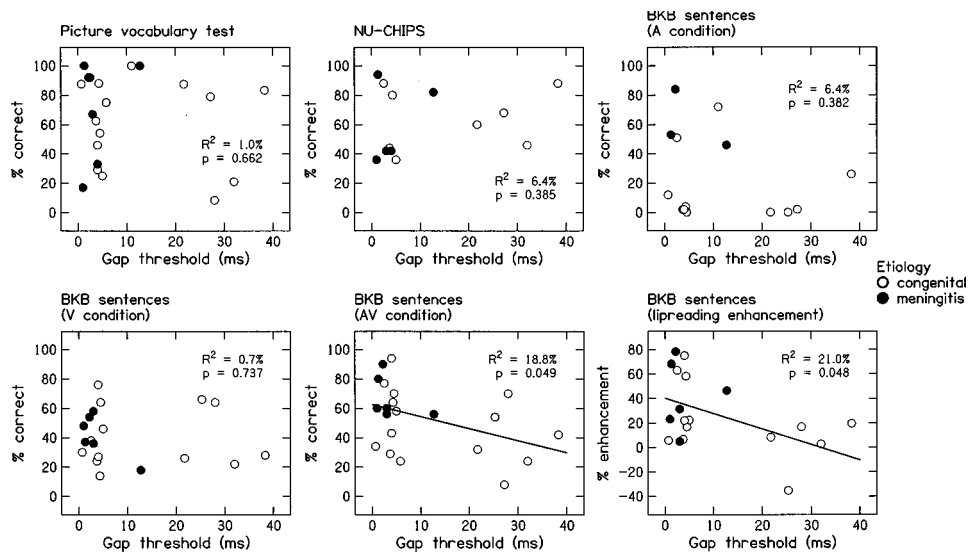
FIG. 4. Speech-perception scores as functions of gap-detection thresholds. Filled symbols show the meningitically deaf subjects and unfilled symbols show the congenitally deaf subjects. Provided in each graph are the correlation coefficient and level of significance. A linear regression line has been fitted in the two cases of a significant correlation.

positive correlations were recorded with the lipreading enhancement scores [$R^2 = 51.5\%$, $p = 0.001$] and the vision-alone condition scores [$R^2 = 38.6\%$, $p = 0.005$]. For the lipreading enhancement scores, a significant positive correlation was recorded with the audition-alone condition scores [$R^2 = 38.8\%$, $p = 0.030$]. These correlations suggest that scores in the auditory–visual condition were related to vision-alone performance, and that the ability to improve on vision-alone perception for the auditory–visual condition, the lipreading enhancement score, was related to performance in the audition-alone condition.

The BKB scores in the auditory–visual condition did not correlate with any of the six subject variables investigated in

TABLE III. Correlation coefficients, and significance levels, between word scores for BKB sentences and subject variables. The (+) and (−) indicate significant positive and negative correlations, respectively.

Speech score and subject variable	BKB sentences (auditory–visual condition)	Lipreading enhancement scores
BKB sentences (auditory–visual condition)	⋯ ⋯	$R^2 = 51.5\%$ (+) $p = 0.001$
BKB sentences (audition-alone condition)	$R^2 = 26.4\%$ $p = 0.072$	$R^2 = 38.8\%$ (+) $p = 0.030$
BKB sentences (vision-alone condition)	$R^2 = 38.6\%$ (+) $p = 0.005$	$R^2 = 0.0\%$ $p = 0.936$
Age at onset of deafness	$R^2 = 15.6\%$ $p = 0.076$	$R^2 = 16.7\%$ $p = 0.082$
Duration of deafness	$R^2 = 0.0\%$ $p = 0.935$	$R^2 = 26.8\%$ (−) $p = 0.023$
Age at implantation	$R^2 = 0.4\%$ $p = 0.774$	$R^2 = 24.3\%$ (−) $p = 0.032$
Duration of implant use	$R^2 = 8.0\%$ $p = 0.213$	$R^2 = 3.3\%$ $p = 0.459$
Total time of auditory stimulation	$R^2 = 0.1\%$ $p = 0.900$	$R^2 = 12.1\%$ $p = 0.144$
Age at testing	$R^2 = 0.2\%$ $p = 0.856$	$R^2 = 24.9\%$ (−) $p = 0.029$

our study (Table III). To determine the contributions of the two variables which significantly correlated with these auditory–visual scores, the vision-alone scores and the gap-detection thresholds, a multiple linear regression model was fitted to the data

$$\text{AV score} = 37.3 + 0.645 \text{ (V score)} - 0.591 \text{ (gap)}, \quad (2)$$

where AV and V correspond to the auditory–visual and vision-alone conditions, respectively. The model accounted for just over half the variance [$R^2 = 51.2\%$, $p = 0.003$]. Examination of the conditional contributions of each predictor variable showed that the vision-alone score accounted for 38.6% of the total variance as the first predictor, and the gap-detection thresholds accounted for an additional 12.6% of the total variance as the second predictor. The regression coefficient for the vision-alone score was significantly different from zero [$t = 3.38$, $p = 0.004$], but this was not the case for the gap-detection threshold coefficient [$t = -2.04$, $p = 0.059$]. Note that the nonsignificant coefficient for gap detection does not necessarily indicate that this variable did not contribute to the regression model. The correlation coefficient adjusted for degrees of freedom, $R^2(\text{adj})$, can be used to compare models with different numbers of predictor variables. The inclusion of gap detection in the two-predictor model resulted in a better fit than a single-predictor model using the vision-alone score: $R^2(\text{adj}) = 35.0\%$ for the vision-alone model and $R^2(\text{adj}) = 45.2\%$ for the vision-alone and gap-detection model.

The lipreading enhancement scores were negatively correlated with three of the six subject variables investigated (Table III): duration of deafness [$R^2 = 26.8\%$, $p = 0.023$], indicating that enhancement scores were lower for subjects with a longer duration of deafness, age at implantation [$R^2 = 24.3\%$, $p = 0.032$], indicating that scores were lower for subjects implanted at an older age, and age at testing [$R^2 = 24.9\%$, $p = 0.029$], indicating that scores were lower for subjects tested at an older age. Note that these three subject variables were highly correlated with each other [$R^2 \geqslant 87.2\%$, $p < 0.001$], indicating that subjects with a longer duration of deafness were implanted at a later age and were tested at an older age. In addition, significant negative cor-

relations $[R^2 \geq 30.5\%, p < 0.040]$ were found between these three subject variables and the audition-alone BKB word scores. This multicollinearity between these speech scores and subject variables placed limitations on the use of multiple linear regression to further analyze the lipreading enhancement scores. Nevertheless, two multiple linear regression models were fitted to the data in order to examine the contribution of the gap-detection thresholds. Duration of deafness was selected as the single variable to represent the three subject variables which correlated with the lipreading enhancement score, as it had the highest correlation. The first model was

Enhancement score$=30.6+0.669$ (A score)-1.19 (gap),
$$\tag{3}$$

where A indicates the audition-alone condition. The model accounted for over half the variance $[R^2 = 54.3\%, p = 0.029]$. The audition-alone score accounted for 38.8% of the total variance as the first predictor, and the gap-detection threshold accounted for an additional 15.5% of the total variance as the second predictor. The regression coefficient for the audition-alone score was significantly different from zero $[t = 2.32, p = 0.046]$, but this was not the case for the gap-detection threshold coefficient $[t = -1.75, p = 0.115]$. Note that the inclusion of gap thresholds in the two-predictor model leads to a better fit than a single-predictor model using the audition-alone score: $R^2(\text{adj}) = 32.7\%$ for the audition-alone model and $R^2(\text{adj}) = 44.2\%$ for the audition-alone and gap-threshold model. The second model was:

Enhancement score$=57.4-1.92$ (duration deaf)-0.850 (gap).
$$\tag{4}$$

However, it was clear that this model was inappropriate because the regression coefficients for both predictors were not significantly different from zero; duration of deafness $[t = -2.10, p = 0.052]$ and gap-detection thresholds $[t = -1.71, p = 0.107]$, indicative of multicollinearity between variables. Of the two models, therefore, the more appropriate fit for our data was obtained with the model combining the audition-alone scores and gap-detection thresholds.

III. DISCUSSION

The main findings from our first study were that there was essentially no influence of pulse rate on the gap-detection thresholds of early-deafened cochlear-implant subjects, and with the exception of two subjects, there was also no influence of stimulus duration (Fig. 1). For pulse rate, this finding suggests that any stimulus uncertainty that may have arisen from the longer pulse periods when using lower pulse rates was not a factor influencing performance. In the two cases where a small but significant effect of pulse rate was found, performance was best for the 1000 pulses/s stimuli. While this would be consistent with the hypothesis that signal uncertainty could lead to poorer gap-detection thresholds, the size of the difference in gap thresholds across pulse rates was very small (less than 6 ms), all gap thresholds were less than 10 ms for these two subjects, and the range in gap thresholds across pulse rates and stimulus durations was

similar to that found for most subjects. Thus, it is unlikely that these differences were of any importance. It should also be noted that there may have been a bias toward larger gap thresholds at the lower pulse rates because the smallest gap which could be presented, and the step-size of the adaptive procedure, was a single pulse: 5 ms at 200 pulses/s compared to 1 ms at 1000 pulses/s. An alternative hypothesis was that gap thresholds could have been poorer at higher pulse rates because there may have been a reduction in neural-discharge synchronization as the pulse period approached the refractory period of auditory-nerve fibers (Javel, 1990), leading to a poorer representation of the temporal structure of the stimuli. It was also possible that neural synchronization may have been additionally compromised in our early-deafened subjects because of the degenerative effects of long-term sound deprivation from an early age (Shephered and Javel, 1997). However, our findings indicated that this measure of temporal resolution in early-deafened subjects was not influenced by these factors. Furthermore, as pulse rate did not appear to influence gap-detection thresholds, at least for rates up to 1000 pulses/s, the transmission of speech information coded by temporal gaps is likely to be available to implant subjects using speech-processing strategies which stimulate at different rates: 250 pulses/s for the SPEAK strategy of the Cochlear Limited device when stimulating six electrodes (Skinner *et al.*, 1994) and 883 pulses/s for the continuous interleaved sampling (CIS) strategy of the Clarion device when stimulating eight electrodes with a 75-μs/phase pulse duration (Tyler *et al.*, 1996).

The effect of stimulus duration was quite marked for the two subjects, S14 and S15, whose overall level of performance was also considerably poorer than that of the other subjects (Fig. 1). For these two subjects, it is possible that the poorer gap thresholds at 1000 ms were due to adaptation effects with the longer stimulus duration. Both the rate and extent of adaptation after the onset of stimulation and recovery from adaptation during the gap period would be important factors. It has been suggested that these adaptation effects could be more apparent in younger subjects than in adults (Trehub *et al.*, 1995), suggesting that auditory experience and/or developmental factors may influence temporal resolution. However, S14 was implanted at a much younger age than S15, and S14 was also younger than S15 at the time of testing (Table I). Thus, the variables which identify these two subjects are not clear from our study. It may also be the case that auditory attention was reduced at the longer stimulus duration, leading to elevated gap thresholds. In further studies, it would be useful to measure gap thresholds over a series of different durations of the initial segment to determine whether the rate and extent of adaptation influences gap-detection thresholds in subjects with limited auditory experience.

Some of these adaptation effects may also be similar to those found for tone decay, although the stimulus duration is typically longer in the case of tone decay. For instance, Brimacombe and Eisenberg (1984) recorded tone decay for electric stimulation in three out of 17 subjects implanted with a single-channel prosthesis. These three subjects had less auditory experience than the other subjects because they had

become deaf at an earlier age, had been deaf for a longer period of time, and had less postoperative experience. Experimental animal studies have also shown instances of a rapid reduction in the neural spike activity from poststimulus-time histograms for continuous electric stimulation (Javel, 1990; Shepherd and Javel, 1997), which may be due to demyelinization of auditory-nerve fibers. It may be the case that for the two subjects in our study with the poorest performance (S14 and S15), there was considerable neural damage and/or degeneration of the auditory pathway, resulting in generally poor gap-detection thresholds and a sensitivity to stimulus duration.

It may be possible to further investigate the effects of degenerative processes on gap detection by examining the relationships between gap thresholds, and the absolute-hearing thresholds and dynamic ranges of hearing. For instance, gap-detection thresholds may vary for different electrodes along the array in subjects with considerable variations in absolute-hearing thresholds and dynamic ranges across these electrodes. It has been shown that hearing thresholds are generally higher and the size of the dynamic range is larger in the experimental animal with marked pathological changes arising from long-term profound deafness (Shepherd and Javel, 1997).

The analysis of the group data from 27 early-deafened subjects in our second study showed that gap-detection thresholds negatively correlated with age at onset of deafness, and that most of the variability in gap thresholds was found for the congenitally deaf subjects (Fig. 2). This finding may suggest that the likelihood of poorer gap thresholds is greater for congenitally deaf subjects than for the meningitically deaf subjects. However, variability in gap thresholds for the congenitally deaf subjects did not appear to be linearly related to the duration of auditory deprivation prior to implantation, and postoperative experience with electric stimulation (Fig. 3). Limiting factors in our study were sample size ($n = 17$) and the multiple correlations between variables. Thus, while the variables influencing gap detection in early-deafened subjects have yet to be fully identified, it appears that severe disruption to normal auditory development within the period prior to or soon after birth is an important factor.

For the meningitically deaf subjects, less variability in gap thresholds was found and 80% of thresholds were less than 5 ms (Fig. 3). There were also no correlations with any of the subject variables investigated for this group of subjects. This suggests that gap-detection thresholds were probably close to normal prior to the onset of profound deafness for these meningitically deaf subjects, and that the period of auditory deprivation prior to implantation did not result in any consistent deterioration in gap thresholds across subjects. For instance, gap thresholds of 1 and 3 ms were recorded for two subjects who were implanted 12 and 14 years after meningitis. It also appears that any postmeningitic damage to the cochlea and peripheral neural structures, such as new bone formation and a marked reduction of the number of spiral ganglion cells (Nadol, 1997), did not appear to be a factor influencing this measure of temporal resolution. Higher thresholds were found in two cases, 13 and 14 ms

(Fig. 3), and while there was no similarity across variables for these two subjects, it is possible that duration of deafness could have been a relevant factor for one subject, as the duration of profound deafness was 24 years after meningitis at 15 months of age.

It is interesting to note that for both the congenitally and meningitically deaf subjects, the results suggested that the duration of both auditory deprivation and auditory experience after implantation may not be important factors influencing gap detection (Fig. 3). Experimental animal studies have also shown that the temporal resolution properties of inferior colliculus neurones are not markedly influenced by auditory deprivation after neonatal deafening (Snyder et al., 1995). In addition, chronic electric stimulation appeared to enhance the temporal processing properties of these inferior colliculus neurones. While our results did not show any clear influence of auditory experience on gap thresholds, it has been suggested that the efficiency in which the central auditory system extracts the fine temporal features of the signal may be influenced by age-related developmental factors (Hall and Grose, 1994) and, therefore, possibly by auditory experience.

Our results differ from those reported by Tyler et al. (1989), who showed that gap-detection thresholds negatively correlated with duration of deafness in postlinguistically deaf adult implant subjects using a range of different implant prostheses. However, gap thresholds were measured by presenting acoustic stimuli via the speech processors worn by these subjects; thus, the gap thresholds were influenced by both the transmission capabilities of the speech-processing hardware and the temporal resolution skills of the subjects. In addition, there were marked differences between the two subject groups. In our study, the onset of deafness was very early in life, while the onset of deafness was predominantly in adulthood in the Tyler et al. (1989) study. In further studies with early-deafened subjects, it would be useful to obtain data from a larger group of subjects to increase the sample size, and to also monitor any postoperative changes in performance over time in these subjects. It is possible that subjects at different chronological ages may show different patterns of results over time, such as improvements in gap thresholds in younger, but not older, subjects. This would indicate whether there were periods of sensitivity to electrically evoked changes in auditory function in early-deafened subjects.

Significant negative correlations between gap-detection thresholds and speech-perception scores were recorded for BKB sentences in the auditory–visual condition and the lipreading enhancement scores for the same test (Fig. 4). No correlations between gap thresholds and scores for closed and open-set speech tests in the audition-alone condition were significant. These two significant correlations suggest that the ability to detect temporal gaps in the electrically coded speech signal assists in auditory–visual perception, possibly by marking word and syllable boundaries. However, the auditory–visual BKB scores and the lipreading enhancement scores also correlated with scores for the vision-alone and audition-alone conditions, respectively, and with several subject variables in the case of the lipreading enhancement

scores (Table III). For BKB sentences in the auditory–visual condition, it was reasonable to suggest that gap-detection thresholds contributed to subject performance. However, the contribution of gap thresholds to the lipreading enhancement scores was less clear as the multiple regression models did not provide highly satisfactory fits to the data. The role of gap detection in auditory–visual perception has also been found for profoundly hearing-impaired listeners using acoustic stimulation, where gap thresholds negatively correlated with the lipreading enhancement scores for sentences (Bosman and Smoorenburg, 1997).

The lack of any significant correlations between gap thresholds and scores for speech tests in the audition-alone condition in our study (Fig. 4) differs from several studies showing significant correlations between these two measures for acoustic stimulation in hearing-impaired listeners (Dreschler and Plomp, 1985; Tyler *et al.*, 1982) and in cochlear-implant subjects (Tyler *et al.*, 1989). In our study, it is possible that the lack of correlations between these measures was because most of the gap thresholds in the correlation analyses with speech-perception measures were less than 30 ms, and gap thresholds on the order of 30–40 ms are probably sufficient to perceive speech information coded by temporal gaps (Bosman and Smoorenburg, 1997; Muchnik *et al.*, 1994; Tyler *et al.*, 1989). Also, gap-detection thresholds were obtained for a single electrode in our study. While studies with postlinguistically deaf adults have indicated that gap thresholds do not appear to vary along the array, it is possible that gap thresholds could be elevated at locations with very poor nerve survival. Thus, it would be important to measure gap thresholds for electrodes along the array where there is some evidence of marked variation in neural survival, as shown by variations in hearing thresholds and the size of the dynamic range (Shepherd and Javel, 1997). Another possibility is that the contribution of temporal gaps to speech perception may be much less than that from other electric parameters, and the performance of subjects predominantly reflects the processing of these other sources of speech information, such as spectral information which is coded by stimulation on the different electrodes. Unfortunately, speech tests were not administered to some subjects with poor gap thresholds because of the clinical impression that performance would be poor and that subjects would be discouraged by test difficulty. For example, only 51% of subjects were assessed using the more difficult BKB sentences in the audition-alone condition compared to 78% of subjects for the easier auditory–visual condition. In further studies, it would be important to ensure that speech-perception data were collected from all subjects without discouraging them from participating in clinic and research studies. To achieve this, however, more appropriate tests may need to be developed which can be administered to those subjects who clinically receive limited benefit from their implant prostheses, and are at an age where cooperation could be rather problematic.

ACKNOWLEDGMENTS

Bench, R. J., and Bamford, J., editors (**1979**). *Speech-Hearing Tests and the Spoken Language of Hearing-Impaired Children* (Academic, London).

Bosman, A. J., and Smoorenburg, G. F. (**1997**). ''Speechreading supplemented with auditorily presented speech elements in the profoundly hearing impaired,'' Audiology **36**, 29–45.

Brimacombe, J. A., and Eisenberg, L. S. (**1984**). ''Tone decay in subjects with the single-channel cochlear implant,'' Audiology **23**, 321–332.

Busby, P. A., Tong, Y. C., and Clark, G. M. (**1992**). ''Psychophysical studies using a multiple-electrode cochlear implant in patients who were deafened early in life,'' Audiology **31**, 95–111.

Cazals, Y., Pelizzone, M., Kasper, A., and Montandon, P. (**1991**). ''Indication of a relation between speech perception and temporal resolution for cochlear implantees,'' Ann. Otol. Rhinol. Laryngol. **100**, 893–895.

Clark, G. M., Blamey, P. J., Busby, P. A., Dowell, R. C., Franz, B. K., Musgrave, G. N., Nienhuys, T. G., Pyman, B. C., Roberts, S. A., Tong, Y. C., Webb, R. L., Kuzma, J. A., Money, D. K., Patrick, J. F., and Seligman, P. M. (**1987**). ''A multiple-electrode intracochlear implant for children,'' Arch. Otolaryngol. **113**, 825–828.

Dobie, R. A., and Dillier, N.. (**1985**). ''Some aspects of temporal coding for single-channel electrical stimulation of the cochlea,'' Hearing Res. **18**, 41–55.

Dreschler, W. A., and Plomp, R. (**1985**). ''Relations between psychophysical data and speech perception for hearing-impaired subjects. II,'' J. Acoust. Soc. Am. **78**, 1261–1270.

Elliott, L. L., and Katz, D. R. (**1980**). *Northwestern University Children's Perception of Speech (NU-CHIPS)* (Auditec, St. Louis, MO).

Fitzgibbons, P. J., and Gordon-Salant, S. (**1987**). ''Temporal gap resolution in listeners with high-frequency sensorineural hearing loss,'' J. Acoust. Soc. Am. **81**, 133–137.

Fitzgibbons, P. J., and Wightman, F. L. (**1982**). ''Gap detection in normal and hearing-impaired listeners,'' J. Acoust. Soc. Am. **72**, 761–765.

Florentine, M., and Buus, S. (**1984**). ''Temporal gap detection in sensorineural and simulated hearing impairments,'' J. Speech Hear. Res. **27**, 449–455.

Fryauf-Bertschy, H., Tyler, R. S., Kelsay, D. M. R., Gantz, B. J., and Woodworth, G. G. (**1997**). ''Cochlear implant use by prelingually deafened children: the influences of age at implant and length of device use,'' J. Speech Lang. Hear. Res. **40**, 183–199.

Gantz, B. J., Woodworth, G. G., Abbas, P. J., Knutson, J. F., and Tyler, R. S. (**1993**). ''Multivariate predictors of audiological success with multichannel cochlear implants,'' Ann. Otol. Rhinol. Laryngol. **102**, 909–916.

Hall, J. W., and Grose, J. H. (**1994**). ''Development of temporal resolution in children as measured by the temporal modulation transfer function,'' J. Acoust. Soc. Am. **96**, 150–154.

Hall, J. W., and Grose, J. H. (**1997**). ''The relation between gap detection, loudness, and loudness growth in noise-masked normal-hearing listeners,'' J. Acoust. Soc. Am. **101**, 1044–1049.

Harrison, R. V., Nagasawa, A., Smith, D. W., Stanton, S., and Mount, R. J. (**1991**). ''Reorganization of auditory cortex after neonatal high frequency cochlear hearing loss,'' Hearing Res. **54**, 11–19.

Hochmair-Desoyer, I. J., Hochmair, E. S., and Stiglbrunner, H. K. (**1985**). ''Psychoacoustic temporal processing and speech understanding in cochlear implant patients,'' in *Cochlear Implants*, edited by R. A. Schindler and M. M. Merzenich (Raven, New York), pp. 291–304.

Javel, E. (**1990**). ''Acoustic and electrical encoding of temporal information,'' in *Cochlear Implants: Models of the Electrically Stimulated Ear*, edited by J. F. Miller and F. A. Spelman (Springer-Verlag, New York), pp. 247–295.

Levitt, H. (**1971**). ''Transformed up–down methods in psychoacoustics,'' J. Acoust. Soc. Am. **49**, 467–476.

Minitab, Inc. (**1998**). MINITAB STATISTICAL PACKAGE, Version 12.1 for Windows (State College, PA)

Moore, B. C. J., and Glasberg, B. R. (**1988**). ''Gap detection with sinusoids and noise in normal, impaired, and electrically stimulated ears,'' J. Acoust. Soc. Am. **83**, 1093–1101.

Moore, D. R. (**1990**). ''Auditory brainstem of the ferret: bilateral cochlear lesions in infancy do not effect the number of neurones projecting from the cochlear nucleus to the inferior colliculus,'' Dev. Brain Res. **54**, 125–130.

Muchnik, C., Taitelbaum, R., Tene, S., and Hildesheimer, M. (**1994**). ''Auditory temporal resolution and open speech recognition in cochlear implant recipients,'' Scand. Audiol. **23**, 105–109.

Nadol, J. B. (**1997**). ''Patterns of neural degeneration in the human cochlea and auditory nerve: implications for cochlear implantation,'' Otolaryngol.-Head Neck Surg. **117**, 220–228.

Penner, M. J. (**1977**). ''Detection of temporal gaps in noise as a measure of the decay of auditory sensation,'' J. Acoust. Soc. Am. **61**, 552–557.

Plant, G. (**1984**). ''A diagnostic speech test for severely and profoundly hearing-impaired children,'' Aust. J. Audiol. **6**, 1–9.

Preece, J. P., and Tyler, R. S. (**1989**). ''Temporal-gap detection by cochlear prosthesis users,'' J. Speech Hear. Res. **32**, 849–856.

Proceedings of the NIH Consensus Development Conference on Cochlear Implants in Adults and Children (National Institutes of Health, Bethesda, Maryland, 1995).

Rajan, R., Irvine, D. R. F., Wise, L. Z., and Heil, P. (**1993**). ''Effect of unilateral partial cochlear lesions in adult cats on the representation of lesioned and unlesioned cochleas in primary auditory cortex,'' J. Comp. Neurol. **338**, 17–49.

Saada, A. A., Niparko, J. K., and Ryugo, D. K. (**1966**). ''Morphological changes in the cochlear nucleus of congenitally deaf white cats,'' Brain Res. **736**, 315–328.

Seldon, H. L., Kawano, A., and Clark, G. M. (**1996**). ''Does age at cochlear implantation affect the distribution of 2-deoxyglucose label in cat inferior colliculus?'' Hearing Res. **95**, 108–119.

Shannon, R. V. (**1989**). ''Detection of gaps in sinusoids and pulse trains by patients with cochlear implants,'' J. Acoust. Soc. Am. **85**, 2587–2592.

Shepherd, R. K., and Javel, E. (**1997**). ''Electrical stimulation of the auditory nerve. I. Correlation of physiological responses with cochlear status,'' Hearing Res. **108**, 112–144.

Skinner, M. W., Clark, G. M., Whitford, L. A., Seligman, P. M., Staller, S. J., Shipp, D. B., Shallop, J. K., Everingham, C., Menapace, C. M., Arndt, P. L., Antogenelli, T., Brimacombe, J. A., Pijl, S., Daniels, P., George, C. R., McDermott, H. J., and Beiter, A. L. (**1994**). ''Evaluation of a new spectral peak coding strategy for the Nucleus 22 channel cochlear implant system,'' Am. J. Otolaryngol. **15 (Suppl. 2)**, 15–27.

Skinner, M. W., Holden, L. K., Holden, T. A., Dowell, R. C., Seligman, P. M., Brimacombe, J. A., and Beiter, A. L. (**1991**). ''Performance of post-linguistically deaf adults with the wearable speech processor (WSP III) and mini speech processor (MSP) of the Nucleus multi-electrode cochlear implant,'' Ear Hearing **12**, 3–22.

Snyder, R., Leake, P., Rebscher, S., and Beitel, R. (**1995**). ''Temporal resolution of neurons in cat inferior colliculus to intracochlear electrical stimulation: effects of neonatal deafening and chronic stimulation,'' J. Neurophysiol. **73**, 449–467.

Snyder, R. L., Rebscher, S. J., Cao, K., Leake, P. A., and Kelly, K. (**1990**). ''Chronic intracochlear electrical stimulation in the neonatally deafened cat. I. Expansion of central representation,'' Hearing Res. **50**, 7–34.

Tong, Y. C., Busby, P. A., and Clark, G. M. (**1988**). ''Perceptual studies on cochlear implant patients with early onset of profound hearing impairment prior to normal development of auditory, speech, and language skills,'' J. Acoust. Soc. Am. **84**, 951–962.

Trehub, S. E., Schneider, B. A., and Henderson, J. L. (**1995**). ''Gap detection in infants, children, and adults,'' J. Acoust. Soc. Am. **98**, 2532–2541.

Tyler, R. S., Gantz, B. J., Woodworth, G. G., Parkinson, A. J., Lowder, M. W., and Schum, L. K. (**1996**). ''Initial independent results with the Clarion cochlear implant,'' Ear Hearing **17**, 528–536.

Tyler, R. S., Moore, B. C. J., and Kuk, F. K. (**1989**). ''Performance of some of the better cochlear-implant patients,'' J. Speech Hear. Res. **32**, 887–911.

Tyler, R. S., Opie, J. M., Fryauf-Bertschy, H., and Gantz, B. J. (**1992**). ''Future directions for cochlear implants,'' J. Speech-Lang. Pathol. Audiol. **16**, 151–164.

Tyler, R. S., Summerfield, Q., Wood, E. J., and Fernandes, M. A. (**1982**). ''Psychoacoustic and phonetic temporal processing in normal and hearing-impaired listeners,'' J. Acoust. Soc. Am. **72**, 740–752.

Webster, D. B., and Webster, M. (**1977**). ''Neonatal sound deprivation affects brain stem auditory nuclei,'' Arch. Otolaryngol. **103**, 392–396.

Temporal mechanisms underlying recovery from forward masking in multielectrode-implant listeners

Monita Chatterjee[a)]

Department of Auditory Implants and Perception, House Ear Institute, 2100 West Third Street, Los Angeles, California 90057

This paper describes a detailed study of recovery from forward masking in six users of the Nucleus-22 cochlear implant with a range of performance in speech-recognition tests. Recovery from a 300-ms-long pulse train presented at 1000 pps was found to be fastest in the poorer performers. The shape of the recovery function was found to be most strongly influenced by masker duration, suggesting that temporal integration plays a prominent role in recovery from forward masking. The recovery functions are reasonably well described by a sum of two exponentially decaying processes. Their relative weights depend on the amount of temporal integration occurring during the masker, and show strong intersubject variability. Nonmonotonicities sometimes observed in the recovery functions may be accounted for by considering the influence of neural adaptation. © *1999 Acoustical Society of America.* [S0001-4966(99)00403-8]

PACS numbers: 43.66.Ts, 43.66.Mk, 43.66.Dc, 43.66.Ba [DWG]

INTRODUCTION

In the relative absence of detailed spectral information, time-domain analysis is likely to play an important role in electrically stimulated auditory perception. This paper addresses two aspects of temporal processing: (a) recovery from forward masking, and (b) temporal integration, and attempts to relate subjects' performance in speech-perception tasks to their psychophysical capabilities.

A. Recovery from forward masking

Psychophysical studies have revealed that the auditory system recovers exponentially from prior stimulation, with a time constant that varies with masker level, duration, and frequency (e.g., Jesteadt *et al.*, 1982; Carlyon, 1988). Models based on physiological studies of single-fiber responses to acoustic stimuli have suggested a close relationship between the processes of adaptation and recovery (Smith, 1977; Harris and Dallos, 1979; Eggermont, 1985). It is widely accepted that the site of the adaptation observed in auditory neurons is at the inner-hair cell–auditory nerve synapse (Smith and Brachman, 1982; Westerman and Smith, 1984). At the single neuron level, the decrement in response due to adaptation can be described as the sum of at least two decaying exponentials and a constant. The two exponentials have different time constants, and are known as the rapid and short-term components of adaptation. It has been suggested (Eggermont, 1985) that the rapid component of perstimulus adaptation is identical to the decrement in response caused by refractoriness at the nerve membrane.

In electrical stimulation of the auditory system, the inner-hair cell–auditory nerve synapse is bypassed. However, a rapid decrement in response, similar to rapid adaptation, can be observed at high stimulation rates (Javel, 1990;

Dynes and Delgutte, 1992), leading some researchers to speculate that adaptation in the auditory nerve may not originate solely in the synapse with the inner-hair cell (Killian *et al.*, 1990).

Relatively few detailed studies of recovery from forward masking have been performed in electrical stimulation of the auditory system. Using long trains of pulses as maskers, Shannon (1990) found that, when the different intensity transformations were accounted for, the temporal course of recovery was similar in electric and acoustic stimulation, and proposed that recovery from forward masking is determined by retrocochlear processes. This idea is supported by Shannon and Otto's (1990) finding that forward masking follows similar time courses in patients with cochlear and brainstem implants. On the other hand, physiological studies of forward masking in the electrically stimulated auditory nerve suggest close relationships between psychophysical and physiological forward masking (Killian *et al.*, 1990). In a two-pulse masking paradigm, Brown *et al.* (1996) found that psychophysical forward-masked thresholds recovered at rates that were very similar to intracochlear physiological measurements with the same stimuli in the same subjects, for short delays between the masker pulse and the probe pulse. These results suggest that for very brief maskers and short probe delays, psychophysical recovery from forward masking can be directly tied to the recovery of primary auditory neurons. When longer forward maskers are used (as in Shannon's study), retrocochlear mechanisms are likely to play a role.

In a previous study of forward-masked patterns in cochlear-implant users (Chatterjee and Shannon, in press), we found that recovery from forward masking showed both subject and parameter dependence. In the present study, we measured the behavior of these recovery functions in greater detail, as a function of masker level, duration, and the masker–probe separation. The experiments described in this paper were performed with a pool of six subjects with vary-

TABLE I. Scores obtained by each subject in the CUNY sentence test and the NU6 word test, along with other potentially pertinent information.

Subject	Gender	Age (years)	CUNY Sentence test, sound only	NU6 words	Etiology of deafness	Duration of profound deafness on implanted side (years)	Duration of implant use (years)
N4	M	40	99.02%	70%	Trauma	5	5
N9	F	55	100%	60%	Hereditary	17	7
N7	M	55	99.02%	48%	Unknown	8	2
N15	F	77	75.49%	40%	Cochlear otosclerosis	2	1
N3	M	56	79.4%	24%	Unknown	11	7
N14	M	63	47.05%	18%	Unknown	2	1

ing levels of speech recognition, with the aim of identifying fundamental differences in temporal processing between good and poor performers.

B. Temporal integration

The impact of a forward masker, and the recovery from it, are likely to depend on the amount of temporal integration occurring throughout its duration. Temporal integration is a fundamental property of sensory systems, found at all levels of processing, from the relatively rapid integration of excitatory potentials at the sensory-nerve membrane to the slower integration of stimulus energy by the entire system, as measured in psychophysical experiments. Models of the auditory system typically include a short-term temporal integrator which performs a ''smoothing'' function, with a time constant less than 10 ms and a ''central'' integrator with a time constant of approximately 200 ms (Zwislocki, 1960). Although it is intuitively appealing to consider temporal inte-

gration at threshold to be due to the summation of neural potentials, as suggested by Zwislocki, mechanisms underlying psychophysically observed ''temporal integration'' are not well understood (Viemeister and Wakefield, 1991). The concept of a fixed temporal integrator may not apply to most realistic auditory situations. For instance, van den Brink and Houtgast (1990) have shown that the auditory system integrates energy over time most efficiently for signals that are approximately as wide as a critical band. Spectral energy, however, is most efficiently integrated for brief stimuli occupying a temporal ''window'' of about 30 ms. In addition, the nonlinear amplitude transformation of the auditory system may have a strong influence on the time constant of temporal integration (Penner, 1978; Buus et al., 1997; Oxenham et al., 1997). When considering temporal integration in cochlear-implant listeners, who possess a very steep loudness function, this factor may be very important.

The present study includes two measures of temporal
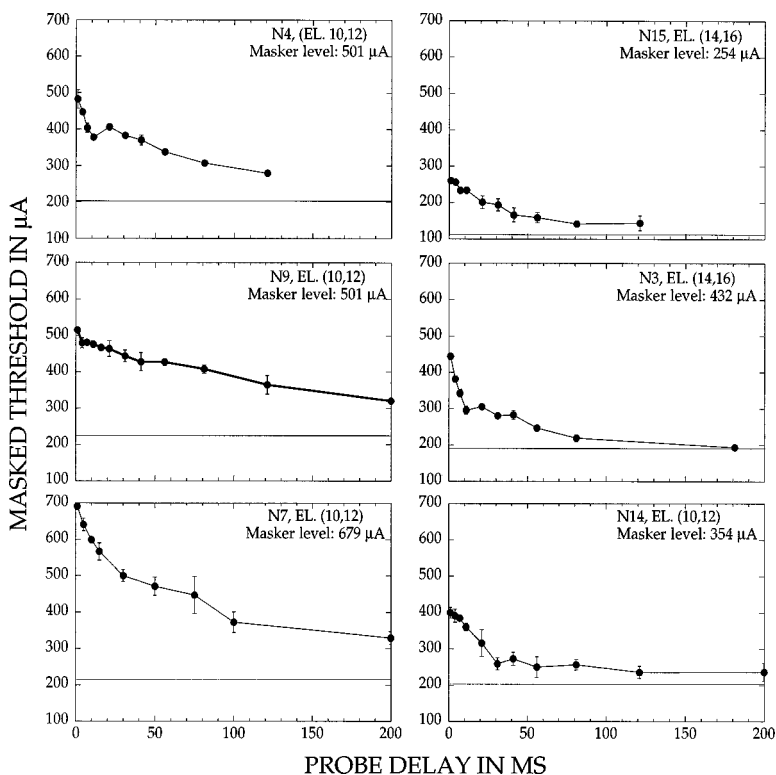
FIG. 1. Masked threshold in μA as a function of probe delay in ms. Results from six subjects. Masker: 300 ms, 1000 pps, comfortable loudness. Probe: 20 ms, 1000 pps. Solid horizontal line in each panel shows quiet threshold for the probe. The electrode pair stimulated and the masker level are indicated in each panel.
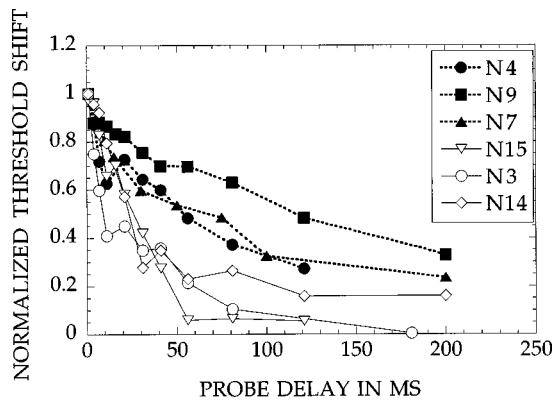
FIG. 2. Results of Fig. 1 replotted as the ratio of masked-threshold shift (masked threshold–quiet threshold) at each probe delay to the maximum shift. Intermittent lines: good performers. Solid lines: poor performers.

integration in cochlear-implant listeners: (a) the traditional threshold-duration function, and (b) the change in forward-masked threshold of a probe as a function of masker duration, for a fixed delay between masker and signal.

I. METHODS

Subjects were six postlingually deafened adult users of the Nucleus-22 cochlear-implant system. Three of the subjects perform well with the device. They are able to regularly use the telephone, and score above 95% correct on the CUNY sentence test without the aid of lipreading. The remaining three subjects are poor performers. They score less than 80% correct on the same sentence test, and are unable to communicate freely over the telephone. The good performers and one of the poor performers are highly trained, having participated in many experiments of a similar nature over the past year. The remaining subjects were given at least 6 h of training before data collection began. Table I shows the scores obtained by these subjects on the CUNY sentence test and the NU6 word test without the aid of lipreading.

Stimuli were delivered to the subjects using a custom interface (Shannon *et al.*, 1990). Stimuli were software generated. Both masker and probe were trains of biphasic pulses, 200 μs/phase, presented at 1000 pulses/s (no ramps were used, as spectral splatter is not a concern in the deaf cochlea). Levels were computed from the manufacturer's calibration table for each individual patient. The delay between masker offset and probe onset (probe delay) was changed from 1 to 200 ms. All stimuli were presented in the bipolar-plus-one (BP+1) mode of stimulation. Electrode pairs are specified as a pair (X,Y) where X indicates the electrode that receives the anodic pulse first. Thresholds were measured using a two-interval, forced-choice (2IFC), 3 down, 1 up paradigm. Using this method, the probe level converges at a level that produces 79.4%-correct responses (Levitt, 1971). The mean of the last eight reversals (of a maximum of 13 reversals or 60 trials) was calculated as the masked threshold. Stimuli were presented in two intervals. The intervals were accompanied by visual markers on the computer monitor. The subject heard the masker in both intervals. Randomly, the probe was present in only one of them. The subject indicated which interval contained the probe by pressing

the appropriate mouse button. Visual feedback was provided. Threshold shift was measured as (masked threshold–quiet threshold). An average of 2–4 repetitions was taken for each data point.

II. RESULTS

A. Recovery from forward masking

1. Measurements made at comfortable level: Masker and probe on the same electrode pair

Figure 1 shows recovery functions (masked threshold in microamperes versus probe delay in ms) measured at a level judged to be within the comfortable range of each of the six cochlear-implant listeners. The masker level in each case is indicated in microamperes. As subjects N3, N14, and N15 had narrower dynamic ranges (steeper loudness-growth functions), ''comfortable loudness'' in their case was reached at lower current levels than for the other subjects. The masker was a 300-ms-long train of 200-μs/phase pulses, presented at 1000 pulses/s. The probe was 20-ms long, and was identical to the masker in all other respects. In each case, the masker and probe were presented to the same electrode pair. Quiet
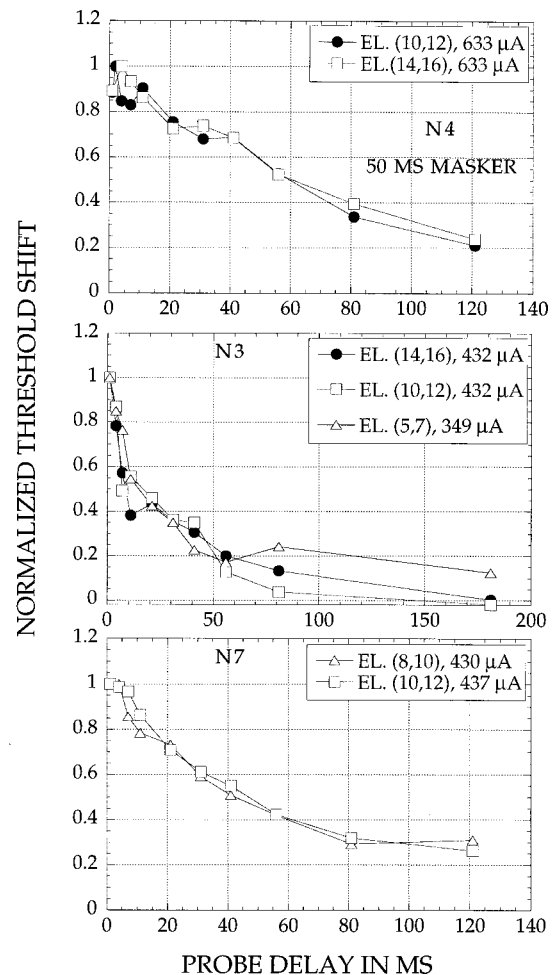
FIG. 3. Effect of changing masker–probe location on the shape of the recovery function. Masker and probe were presented to the same electrode pair in each case. Top panel: Subject N4, masker 50-ms long. Middle and bottom panels: Subjects N3 and N7, masker 300-ms long. The electrode pair stimulated and the level of the masker are indicated in each case. Note that electrodes are numbered (1 to 22) from base to apex. The filled circles are replotted from Fig. 2.
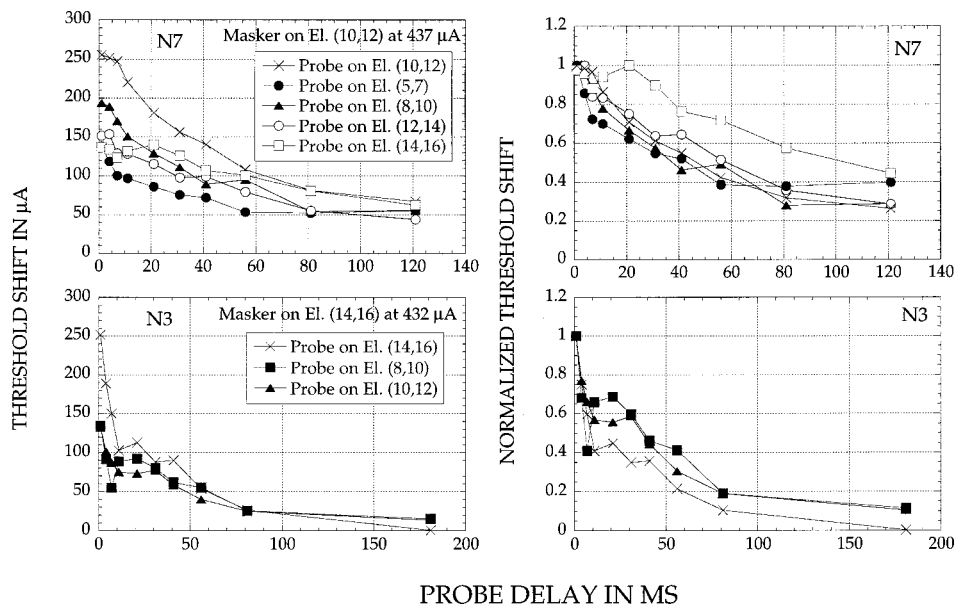
FIG. 4. Effect of changing masker–probe separation. Results from two subjects. Top: Results from subject N7. Recovery functions are shown for varying probe-electrode pairs as the masker-electrode pair is kept constant (10,12). Bottom: Results from subject N3. Masker-electrode pair is fixed at (14,16) while probe pair varies. Left-hand panels in each case show the raw-threshold shifts; right-hand panels show the normalized-threshold shift in each case. Open symbols indicate probe-electrode pairs basal to the masker, closed symbols indicate probe-electrode pairs apical to the masker. Crosses indicate probe-electrode pair=masker-electrode pair.

threshold for the probe is indicated by the horizontal solid line below each function. In order to facilitate across-subject comparison, Fig. 2 plots the same data in the form of normalized-threshold shifts (the ratio of masked-threshold shift to the maximum shift). Two features of the results are noteworthy. First, the implant listeners span a wide range of recovery functions. Second, the three poorer performers (open symbols, solid lines in Fig. 2) show the fastest recovery from the 300-ms masker, and form a distinct cluster near the lower left-hand quadrant.

With regard to the shapes of the individual functions, two components are generally evident: (a) a rapidly recovering component which dominates within the first few ms after masker offset, and (b) a slowly recovering component which dominates at probe delays of 30 ms and longer. For instance, in the case of subject N9, the slow component is clearly the more dominant of the two, whereas in subject N3, the early rapid component is more heavily weighted. In some cases, a plateau or nonmonotonicity is present in the region of transition between the two limbs of the recovery function.

The intersubject differences noted above may have been due to the fact that the recovery functions shown in Figs. 1 and 2 were obtained with stimuli presented to different electrode pairs and at different absolute-current levels for each subject. In order to examine this possibility, the effects of changing the electrode location, as well as masker level, were examined.

2. Measurements made at comfortable level: Effect of cochlear location

Figure 3 shows recovery functions obtained at different cochlear locations in three subjects. In each case, the masker is presented at a level within the comfortable range, and levels are chosen that evoke similar masked thresholds at the shortest probe delay. Masker and probe were presented to the same electrode pair in each case. Because stimulation at different electrode pairs sometimes results in different thresholds and dynamic ranges, the functions are normalized to the maximum-threshold shift in each case (note that the solid

points are replotted from Fig. 2). The consistent rate of recovery observed within the limited range of locations studied suggests that cochlear location is not a primary determinant of the recovery function.

3. Measurements made at comfortable level: Masker and probe on different electrode pairs

Figure 4 shows examples of recovery functions obtained using the same paradigm, with the exception that the probe is presented to different electrode pairs while the masker is always presented to a fixed electrode pair. Moving the probe to an electrode pair different from the masker sometimes results in a pronounced nonmonotonicity in the recovery function. There are two possible explanations for this:

(A) Increasing the physical distance between the masker and probe decreases their spatial interaction, hence reducing the masked threshold. The change in the shape of the recovery function could be due to a simple level dependence, likely to be peripheral in origin.

(B) Increasing the physical distance changes the nature of the temporal interaction between the two channels or neural pathways excited by the masker and the probe, respectively. This could also change the shape of the recovery function. Such a change in the interaction is more complex than a simple level dependence, and could be retrocochlear in origin.

In order to distinguish between the two possibilities, we measured the effect of masker level on the recovery function, when masker and probe were presented to the same electrode pairs. If possibility (A) is correct, then we should find a similar dependence on masker level when the masker and probe are presented to the same electrode pair.

4. Effects of masker level

Figure 5 shows examples of recovery functions obtained at different masker levels for five subjects. The left-hand panels show the raw masked thresholds in μA, while the right-hand panels show the normalized-threshold shifts. In
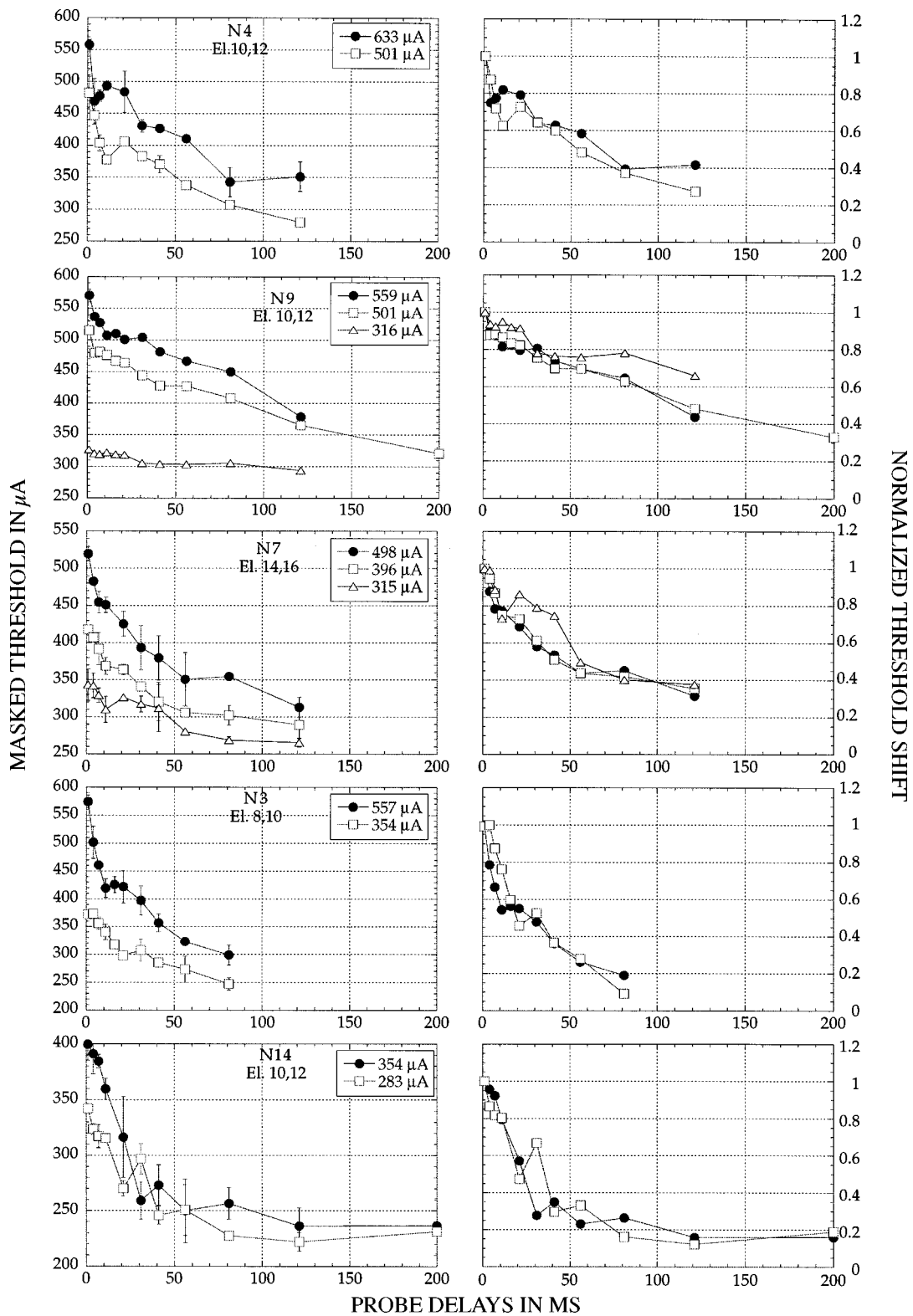
FIG. 5. Effect of changing masker level. Masker- and probe-electrode pairs (indicated in each left-hand panel) are fixed in each case. Left-hand panels: masked threshold as a function of probe delay. The parameter is masker level (ranging from very soft to medium loud). Right-hand panels show the data from the left-hand panel for each subject, normalized to the maximum-threshold shift.

general, the functions do not show large changes with masker level, except for a tendency toward slower recovery at very soft levels. In order to directly address the question raised in the previous section, we compared the shape of recovery from a masker placed on the same electrode pair as the probe (8,10 in N3 and 14,16 in N7), with recovery from

a masker placed on a distant electrode pair (14,16 in N3 and 10,12 in N7) in subjects N3 and N7. These measurements were made for masker levels at which the threshold shifts at the shortest probe delays were very close. Results are shown in Fig. 6. It is apparent that in the case of N3, the nonmonotonicity is more pronounced when the masker and probe are
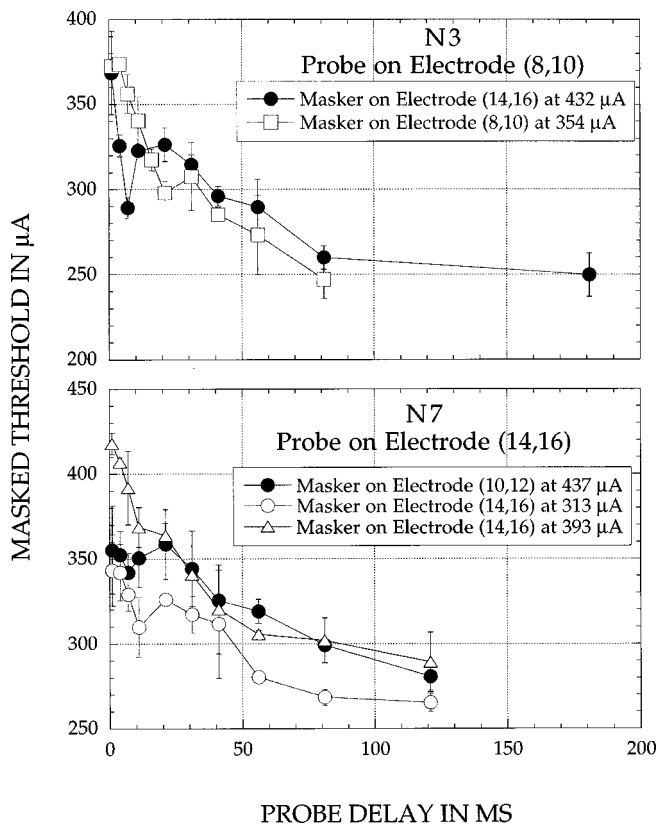
FIG. 6. Results from subjects N3 (top) and N7 (bottom). Open circles in each case show recovery functions obtained when masker and probe are presented to the same electrode pair. Filled symbols show recovery functions for the same probe, when the masker is presented to a different electrode pair. The masker levels were selected so that they produced the same amount of masking at the shortest probe delay (1 ms).

on different electrode pairs, even though the amount of masking at short-probe delays is the same. In the case of subject N7, the nonmonotonicity appears both when the masker is on the same electrode pair as the probe, and when the masker is on a different electrode pair. However, the shapes of the functions are again quite different in the two cases. This experiment shows that possibility (B) does contribute to some degree when the masker and probe are presented to different "channels."

5. Effects of masker duration

The impact of a forward masker is likely to be dependent on both its level and its duration. The previous experiments have shown that when masker and probe are presented to the same electrode pair, changing the level of the masker results in a multiplicative shift of the recovery function. If changing the duration of the masker results in a similar multiplicative shift, we might conclude that duration and level of the masker have equivalent impact. Figure 7 shows examples of recovery functions obtained in six subjects at different masker durations, keeping all other parameters fixed. With the exception of N3 and N15 (both poorer performers), most subjects showed some difference in masking between a 300-ms and a 50-ms masker. In subjects N9 and N7, the rapid-recovery component becomes more dominant as masker duration decreases. In N9, the subject with the slowest recovery, the change with masker duration is most dramatic. In most subjects, the impact of masker duration was minimal at the shortest probe delay. It is apparent from these
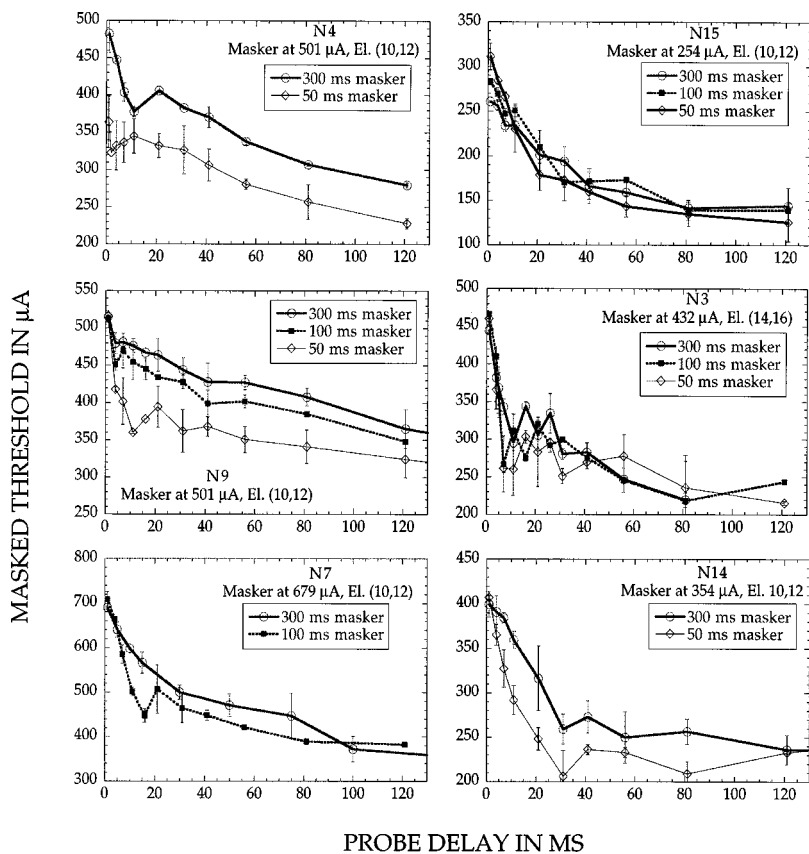
FIG. 7. Effect of masker duration. Masker and probe presented to the same electrode pair and at a comfortable loudness in each case (indicated in each panel).
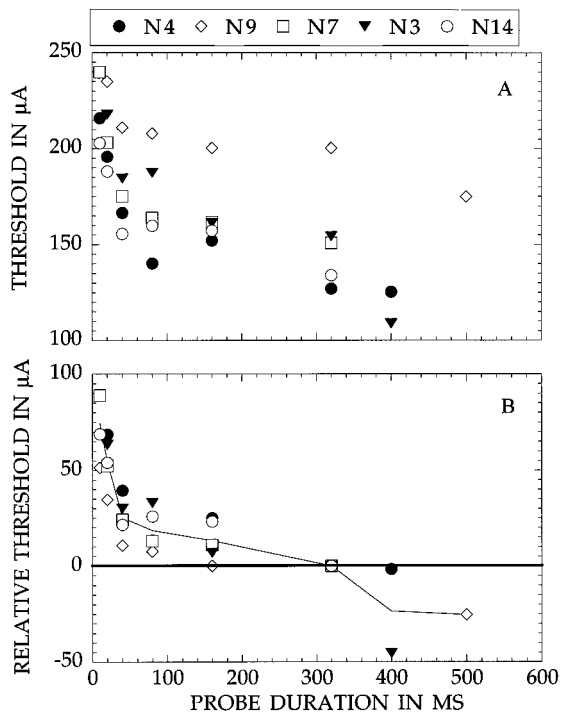
FIG. 8. (a) Quiet threshold as a function of probe duration for five subjects. (b) The same data replotted as (quiet threshold−threshold of 320-ms probe). Solid line shows the mean computed across subjects.

FIG. 9. Masked threshold as a function of masker duration. Probe delay is fixed at 10 ms for N4, N9, N7, N3, and N14. Probe delay is fixed at 11 ms for N15. The parameter is masker level. The vertical axes are identical in all panels.

results that changes in the duration and the level of the masker have different effects on the shape of the recovery function.

The results of the experiments described so far suggest that the observed intersubject differences in the recovery functions (Figs. 1 and 2) are not influenced by changes in the cochlear location of the masker, or the level of the masker. On the other hand, these intersubject differences appear to be amplified in the presence of long-duration maskers. As masker duration is shortened, recovery follows a faster time course in the better performers, converging with the faster recovery observed in the poorer performers.

B. Temporal integration

The results of experiment II A 5 above suggest that temporal integration as reflected in the effect of masker duration has less impact on the recovery function in some subjects relative to others. It may be that the intersubject variability in the recovery functions observed in experiment II A 5 (Fig. 7) is related to differences in temporal integration of the masker. Experiment B is directed at measuring temporal integration at threshold, and comparing results with the suprathreshold forward-masking measure. Subjects N4, N9, N7, N3, and N14 participated in this experiment.

1. Temporal integration at threshold

Quiet thresholds were measured using the same two-interval two-alternative forced-choice procedure used for masked thresholds. Figure 8 shows thresholds in microamps plotted against probe duration (ms) for one electrode pair in each subject tested. It is apparent that the functions are similar in their shape. A large part of the integration occurs within the first 50 ms.

2. Suprathreshold temporal integration functions

Forward-masked thresholds were measured as a function of masker duration, for a fixed probe delay. Compared to the threshold-duration function (Fig. 8), the suprathreshold effect of temporal integration shows stronger subject dependence. In Fig. 9, we plot the masked thresholds as a function of masker duration in subjects N4, N9, N7, N3, and N14, for a fixed probe delay of 10 ms. For consistency, we have included pertinent data for N15 (who did not participate in the temporal integration experiments) for a fixed probe delay of 11 ms (data obtained from Fig. 7). The high-masked threshold for the lowest masker duration in subject N7's data may be a result of something similar to the "confusion effect" (Neff, 1986), where the probe appears to be an extension of the masker, and the masker+probe interval is indistinguishable from the masker-only interval. Setting this issue aside, it is apparent that although subjects N9, N7, and N4 are all good performers, temporal integration of the masker has differential impacts on masked threshold. The functions are also level dependent. The three poorer performers show little or no temporal integration for masker durations above 50 ms; in some cases, their functions are even nonmonotonic.

From experiment B, we conclude the following:

(a) at threshold, temporal-integration functions are remarkably similar across subjects, regardless of their performance in speech-related tasks, and

(b) above threshold, the shape of the temporal-integration functions can show strong dependence on level, as well as more intersubject variability.

All subjects showed some temporal integration within
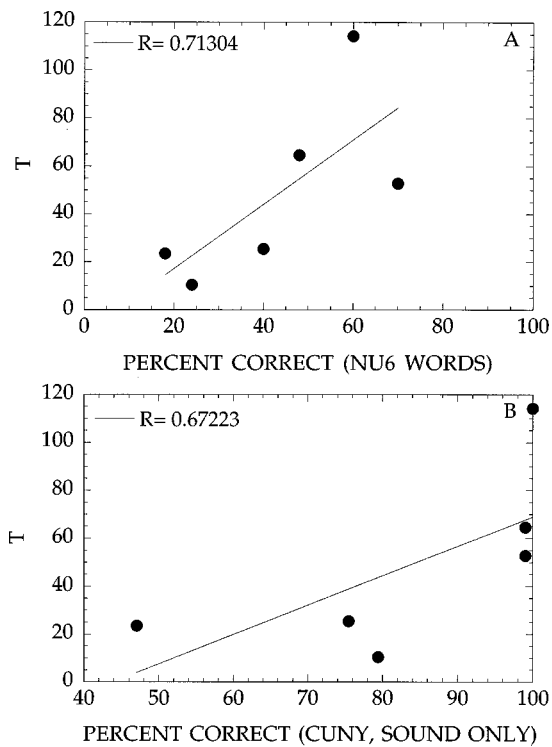
FIG. 10. Relationship between rate of recovery and scores in speech-recognition tests. The vertical axis represents the probe delay T required for the masked-threshold shift to reach half of its value at the shortest probe delay (1 ms), derived from Fig. 2. The horizontal axis represents the scores in the CUNY sentence test (upper panel) and the NU6 word test (lower panel). Each point represents data from one subject. The solid line represents the least-squares fit to the data. R = correlation coefficient.

the first 50 ms. For durations greater than 50 ms, the amount of temporal integration depends on masker level and upon the individual subject.

III. DISCUSSION

The primary result of this study proves that subjects with poorer speech-recognition scores recover fastest from prior stimulation. Figure 10(a) and (b) are scatter plots to demonstrate this relationship. The vertical axis represents the probe delay at which the masked-threshold shift reaches half of its maximum, calculated from the data shown in Fig. 2. The horizontal axes show the percentage of CUNY sentences and NU6 words correctly identified by each subject, from Table I. The solid line represents a linear curve fit to the data (R indicates the correlation coefficient). It is important to note the inadvisability of making strong inferences from the present data set, given the small size of the subject pool used in this study. Overall, the result is counterintuitive. It is difficult to understand why a slowly recovering system performs better with a dynamic stimulus such as speech. On the other hand, the relationship of the psychophysical measures reported here to speech performance may be only indirect. At present, we can offer no speculation as to what the true relationship might be.

Data published by Brown *et al.* (1990) appear to contradict this result. In a two-pulse experimental paradigm, they found that the time constant of recovery of the electrically evoked action potential (EAP) is negatively correlated with
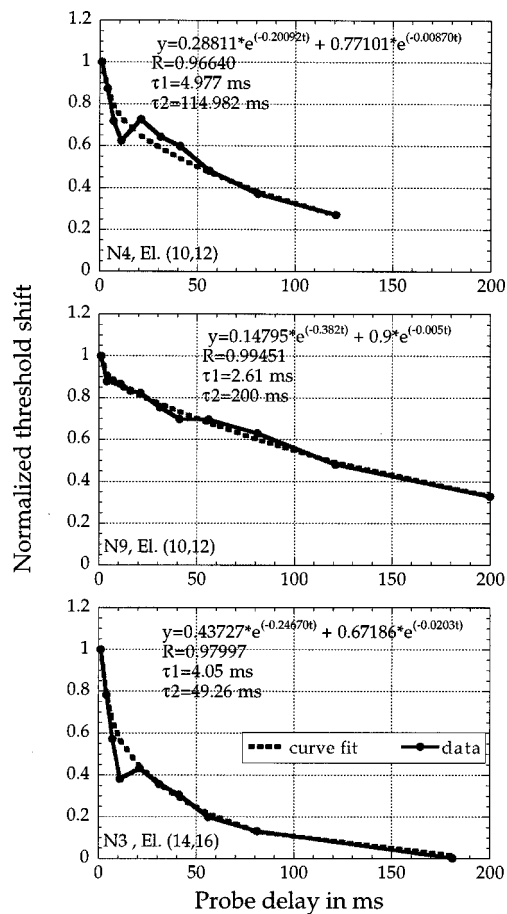
FIG. 11. Examples of curve fits (intermittent lines) to the data from Fig. 2 (three subjects) using the sum-of-two-exponentials equation. R represents the correlation of the curve fit to the data.

the subject's speech recognition; the faster the recovery, the better the speech performance. One explanation for the discrepancy between the two sets of data must lie in the impact of temporal integration. For the long-duration maskers used here, temporal integration would play a significant role relative to the one-pulse masker used by Brown *et al.* in their study.

A. Mechanisms underlying the recovery process

In general, the data presented here can be described as follows:

(1) Recovery functions appear to have two components, a rapid and a slow component.
(2) Differences between subjects for a given condition, and between conditions for a given subject, can be described as differences in the relative weights of the two components.
(3) Under certain conditions, nonmonotonicities or plateaus appear in the region of transition between these components (10–20-ms probe delay). As the nonmonotonicity is not always evident, for the present we will consider it a secondary phenomenon.

Figure 11 shows examples of recovery functions and curve fits for subjects N3, N4, and N9. The equation used for the curve fit and the time constants of the rapid and slow

components are indicated in each case. The curve fit was performed assuming an equation of the form

$$y = A_1 e^{(-t/\tau_1)} + A_2 e^{(-t/\tau_2)}, \tag{1}$$

where the first and second term represent the rapid and slowly recovering components with time constants τ_1 and τ_2, respectively. A_1 and A_2 are constants. Making the assumption that the slow component dominates at long probe delays, the last three or four points in the recovery function were fit by an exponential. This exponential function was then subtracted from the original data. Assuming that the rapid component dominates at short probe delays, the first few points of the remainder were fit by a second exponential function. The sum of the two exponentials represents the curve fits shown in these figures. The fit appears to be satisfactory (R = correlation coefficient).

In good performers, masker duration has a strong impact on the relative weights of these two components. At very short masker durations, the rapid component appears to dominate, while at longer masker durations, the slow component plays a larger role.

In poorer performers, the amount of temporal integration is least for masker durations above 50 ms. Consistent with this result, poorer performers show the fastest recovery for the longer duration masker. Their recovery functions are also the least dependent on masker duration. From these observations, we infer that

(a)   the two components of the recovery functions represent two separate mechanisms, and
(b)   temporal integration influences the slow component of recovery more than the rapid component.

We speculate that two processes are involved: (a) an early rapid recovery, and (b) a second, slower recovery process preceded by a slow temporal-integration mechanism. In this framework, the shorter the masker duration, the lesser the temporal integration, the less the contribution of the second mechanism, and the faster the recovery from masking. Subjects with lesser temporal integration will show a more rapid recovery than subjects with more temporal integration. In the two-exponential model, the influence of temporal integration will be reflected in the ratio of A_2/A_1 in Eq. (1). Thus, we can propose a process described by the equation

$$y = A_1 [e^{(-t/\tau_1)} + f(D) e^{(-t/\tau_2)}], \tag{2}$$

where D represents the masker duration. The function $f(D)(=A_2/A_1)$ corresponds to the contribution of temporal integration and increases monotonically with masker duration. At small D, $f(D)$ is ~0, and the process is dominated by the first term.

The data suggest that the rapid portion of the recovery function is common to all subjects. The slower portion, and the associated slow temporal integration, are present to different degrees in the different subjects, being more dominant in the good performers and less in the poor performers. Below, we explore two possibilities to account for the two mechanisms of recovery.

One possibility is that there is an early, periphery-driven process, associated with rapid temporal integration, followed by a slower, central process, associated with slow temporal integration. Some results of Brown *et al.* (1996) are relevant here. In a two-pulse experiment, they measured recovery in users of the Ineraid implant, both physiologically and psychophysically. They found that the psychophysical recovery appeared to be proportional to the physiological EAP recovery for probe-pulse delays within the first 10 ms, but assumed a slower recovering-time course at longer probe delays. These results strongly support the idea of an early, rapidly recovering, periphery-dominated mechanism, followed by a slower recovering central mechanism.

In psychophysical experiments in cats stimulated electrically via electrodes in the cochlear nucleus or inferior colliculus, Gerken *et al.* (1991) found reduced temporal integration after deafness induced by noise exposure. They concluded that long-term temporal integration by the auditory system must occur at a retrocochlear stage.

1. Can adaptation account for the nonmonotonicity?

The sum-of-two-exponentials model does not account for the plateaus or nonmonotonicities observed in the data. Chimento and Schreiner (1991) have found evidence for nonmonotonic trends arising from the interactions between adaptation and recovery in single-unit neurons in cats. It is possible that adaptation to the probe tone interacts with recovery from the masker (Eggermont, 1985) to produce the plateaus and/or nonmonotonicities we have observed here. It is known, for instance, that at short probe delays, the neural response to the probe is not only depressed, but also shows decreased adaptation. As the probe delay increases, both the overall neural response and the onset transient show recovery (Smith, 1977; Harris and Dallos, 1979). Thus, the *amount of adaptation* in the response to the probe recovers with increasing time separation between the masker and the probe.

In the following, we borrow from the findings described above to try and account for the nonmonotonicities observed in the data. It is possible that the phenomena underlying the psychophysical results are not determined at the auditory nerve. Whatever the level of processing at which these phenomena arise, we speculate that they exhibit similar recovery and adaptation properties. If we assume that the total neural response (onset and steady state) is important for detecting the probe, we can account for the nonmonotonicities in the data as follows: The recovery from masking and the adaptation during the response work in opposite directions, the former decreasing the total response to the probe and the latter increasing it. Let us assume that the net threshold shift is determined by a function of the form

$$y = \{A_1 e^{(-t/\tau_1)} + A_2 e^{(-t/\tau_2)}\}(1 - e^{(-t/\tau_3)}), \tag{3}$$

where the term within the second parenthesis represents the effect of recovering adaptation. We assume that the *amount of adaptation* recovers as $(1 - e^{(-t/\tau_3)})$, where τ_3 is a constant. Thus, the terms within the first parenthesis represent the decrease in threshold shift (increase in neural response) due to recovery, and the term within the second parenthesis represents the increase in threshold shift due to the adaptation of the response.
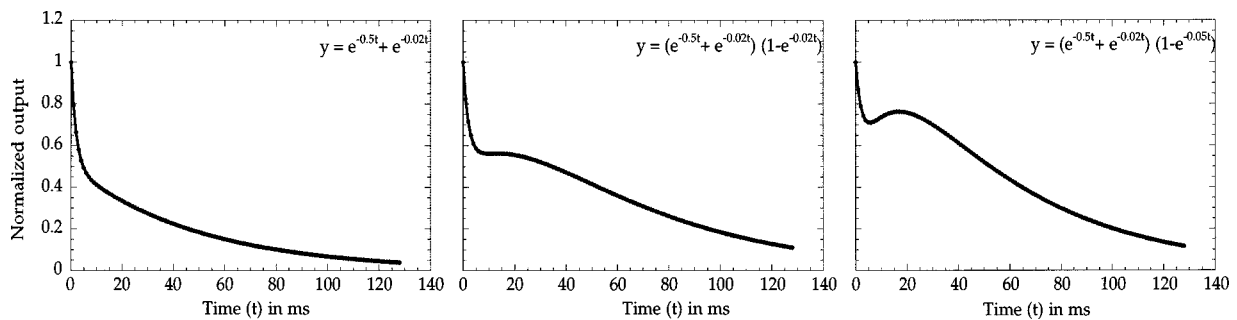
FIG. 12. Examples of functions obtained using a sum of two exponentials to describe the recovery, and a second term to describe the effect of adaptation.

Figure 12 shows the result of this manipulation assuming $A_1 = A_2 = 1.00$, $\tau_1 = 2$ ms, $\tau_2 = 50$ ms, and three different values of τ_3: infinity (i.e., no adaptation to the probe, left-hand panel), 50 ms (middle panel), and 20 ms (right-hand panel). It is evident that this equation can explain the majority of qualitative trends observed in the results. Given the absence of evidence supporting our speculations, we have not attempted to precisely fit the data with this equation.

2. Mechanisms of temporal integration

The results of the temporal-integration experiments suggest that at threshold, a considerable part of temporal integration is accomplished within the first 100 ms of the stimulus duration, in a way that is surprisingly similar across subjects. Above threshold, however, the situation is more complex—the temporal-integration functions obtained across subjects (Fig. 9) show two major trends. One is similar to the threshold measure, in that most of the integration is accomplished within the first 100 ms of the stimulus. This function is dominant in poorer performers and found in the good performers at low levels. The second trend is present in two of the three good performers only, and shows a slower integration at higher levels, persisting up to 200 ms or more.

We speculate that the rapidly integrating function represents a periphery-dominated mechanism, present near threshold and similar across subjects. At higher stimulus levels, other, higher-order processes are set in motion and intersubject differences may become more obvious.

IV. CONCLUSION

We conclude that the time constant of recovery from forward masking is a potential indicator of the subjects' speech-recognition performance. Our experiments suggest that recovery from forward masking in electrical stimulation involves multiple mechanisms. It appears that at least two processes describe the recovery function: (a) a rapidly recovering process, and (b) a slower recovering process. The relative weights of the two processes depend on the amount of temporal integration occurring during the masker and show large intersubject variability. Nonmonotonicities observed in the data can be accounted for by considering the influence of neural adaptation.

Brown, C. J., Abbas, P. J., and Gantz, B. (**1990**). ''Electrically evoked whole-nerve action potentials: data from human cochlear implant users,'' J. Acoust. Soc. Am. **88**, 1385–1391.

Brown, C. J., Abbas, P. J., Borland, J., and Bertschy, M. R. (**1996**). ''Electrically evoked whole nerve action potentials in Ineraid cochlear implant users: responses to different stimulating electrode configurations and comparison to psychophysical responses,'' J. Speech Hear. Res. **39**, 453–467.

Buus, S., Florentine, M., and Poulsen, T. (**1997**). ''Temporal integration of loudness, loudness discrimination, and the form of the loudness function,'' J. Acoust. Soc. Am. **101**, 669–680.

Carlyon, R. P. (**1988**). ''The development and decline of forward masking,'' Hearing Res. **32**, 65–80.

Chatterjee, M., and Shannon, R. V. (**1998**). ''Forward masked excitation patterns in multielectrode electrical stimulation,'' J. Acoust. Soc. Am. **103**, Pt. 1, 2565–2571.

Chimento, T. C., and Schreiner, C. E. (**1991**). ''Adaptation and recovery from adaptation in single fiber responses of the cat auditory nerve,'' J. Acoust. Soc. Am. **90**, 263–273.

Dynes, S. B. C., and Delgutte, B. (**1992**). ''Phase-locking of auditory-nerve discharges to sinusoidal electric stimulation of the cochlea,'' Hearing Res. **58**, 79–90.

Eggermont, J. J. (**1985**). ''Peripheral auditory adaptation and fatigue: a model oriented view,'' Hearing Res. **18**, 57–71.

Gerken, G. M., Solecki, J. M., and Boettcher, F. A. (**1991**). ''Temporal integration of electrical stimulation of auditory nuclei in normal-hearing and hearing-impaired cat,'' Hearing Res. **53**, 101–112.

Harris, D. M., and Dallos, P. (**1979**). ''Forward masking of auditory nerve fiber responses,'' J. Neurophysiol. **42**(4), 1083–1107.

Javel, E. (**1990**). ''Acoustic and electrical encoding of temporal information,'' in *Models of the Electrically Stimulated Cochlea*, edited by J. M. Miller and F. A. Spelman (Springer, New York).

Jesteadt, W., Bacon, S. P., and Lehman, J. R. (**1982**). ''Forward masking as a function of frequency, masker level, and signal delay,'' J. Acoust. Soc. Am. **71**, 950–962.

Killian, M. J. P., Klis, S. F. L., and Smoorenburg, G. F. (**1994**). ''Adaptation in the compound action potential response of the guinea pig VIIIth nerve to electrical stimulation,'' Hearing Res. **81**, 66–82.

Levitt, H. (**1971**). ''Transformed up-down methods in psychoacoustics,'' J. Acoust. Soc. Am. **49**, 467.

Neff, D. L. (**1986**). ''Confusion effects with sinusoidal and narrow-band noise forward maskers,'' J. Acoust. Soc. Am. **79**, 1519–1529.

Oxenham, A. J., Moore, C. J., and Vickers, D. A. (**1997**). ''Short-term temporal integration: evidence for the influence of peripheral compression,'' J. Acoust. Soc. Am. **101**, 3676–3687.

Penner, M. J. (**1978**). ''A power law transformation resulting in a class of short-term integrators that produce time-intensity trades for noise bursts,'' J. Acoust. Soc. Am. **63**, 195–201.

Schmiedt, R. A., Mills, J. H., and Boettcher, F. A. (**1996**). ''Age-related loss of activity of auditory-nerve fibers,'' J. Neurophysiol. **76**(4), 2799–2803.

Shannon, R. V. (**1990**). ''Forward masking in patients with cochlear implants,'' J. Acoust. Soc. Am. **88**, 741–744.

Shannon, R. V. (**1990**). ''A model of temporal integration and forward masking for electrical stimulation of the auditory nerve,'' in: *Models of the Electrically Stimulated Cochlea*, edited by J. M. Miller and F. A. Spelman (Springer, New York).

Shannon, R. V., and Otto, S. R. (**1990**). ''Psychophysical measures from electrical stimulation of the human cochlear nucleus,'' Hearing Res. **47**(1–2), 159–168.

Shannon, R. V., Adams, D. D., Ferrel, R. L., Palumbo, R. L., and Grandgenett, M. (**1990**). ''A computer interface for psychophysical and speech research with the Nucleus cochlear implant,'' J. Acoust. Soc. Am. **87**, 905–907.

Smith, R. L. (**1977**). ''Short-term adaptation in single auditory nerve fibers: some poststimulatory effects,'' J. Neurophysiol. **40**(5), 1098–1112.

Smith, R. L., and Brachman, M. L. (**1982**). ''Adaptation in auditory-nerve fibers: a revised model,'' Biol. Cybern. **44**(2), 107–120.

van den Brink, W. A., and Houtgast, T. (**1990**). ''Spectro-temporal integration in signal detection,'' J. Acoust. Soc. Am. **88**, 1703–11.

Viemeister, N. F., and Wakefield, G. H. (**1991**). ''Temporal integration and multiple looks,'' J. Acoust. Soc. Am. **90**, 858–865.

Westerman, L. A., and Smith, R. L. (**1984**). ''Rapid and short-term adaptation in auditory nerve responses,'' Hearing Res. **15**(3), 249–260.

Zeng, F.-G., and Shannon, R. V. (**1995**). ''Possible origins of the non-monotonic intensity discrimination function in forward masking,'' Hearing Res. **82**(2), 216–224.

Zwislocki, J. J. (**1960**). ''Theory of temporal auditory summation,'' J. Acoust. Soc. Am. **32**, 1046–1060.

Interarticulator programming in VCV sequences: Lip and tongue movements

Anders Löfqvist[a] and Vincent L. Gracco

Haskins Laboratories, 270 Crown Street, New Haven, Connecticut 06511

This study examined the temporal phasing of tongue and lip movements in vowel–consonant–vowel sequences where the consonant is a bilabial stop consonant /p, b/ and the vowels one of /i, a, u/; only asymmetrical vowel contexts were included in the analysis. Four subjects participated. Articulatory movements were recorded using a magnetometer system. The onset of the tongue movement from the first to the second vowel almost always occurred before the oral closure. Most of the tongue movement trajectory from the first to the second vowel took place during the oral closure for the stop. For all subjects, the onset of the tongue movement occurred earlier with respect to the onset of the lip closing movement as the tongue movement trajectory increased. The influence of consonant voicing and vowel context on interarticulator timing and tongue movement kinematics varied across subjects. Overall, the results are compatible with the hypothesis that there is a temporal window before the oral closure for the stop during which the tongue movement can start. A very early onset of the tongue movement relative to the stop closure together with an extensive movement before the closure would most likely produce an extra vowel sound before the closure. © *1999 Acoustical Society of America.* [S0001-4966(99)00503-2]

PACS numbers: 43.70.Aj, 43.70.Bk [WS]

INTRODUCTION

Interarticulator programming, i.e., the temporal and spatial coordination of different articulators during speech, has been the focus of much work in speech motor control. One example of this line of research is the coordination of oral and laryngeal articulatory events in the production of voiceless consonants (e.g., Gracco and Löfqvist, 1994; Löfqvist, 1980; Löfqvist and Yoshioka, 1981; Löfqvist and Yoshioka, 1984). In the production of these sounds, a glottal abduction/adduction gesture occurs while a closure or constriction is made in the oral cavity. Variations in the temporal programming of the oral and laryngeal gestures are used to produce contrasts of voicing and aspiration (e.g., Löfqvist, 1995). The phasing of the oral and laryngeal articulations is also important for the management of air pressure and air flow (e.g., Koenig *et al.*, 1995; Löfqvist *et al.*, 1995; Löfqvist and McGowan, 1992; McGowan *et al.*, 1995). Here, an increase in oral air pressure is made to drive the noise source. Another example of interarticulator programming that has received particular attention is the control of velar movements in the production of nasal consonants (e.g., Bell-Berti and Krakow, 1991; Clumeck, 1976; Kollia *et al.*, 1995; Krakow, 1989). Also in this case, the timing of the velar movements relative to other oral articulators is important for producing the correct sound sequence. The timing patterns between the velar and other articulatory movements appear to vary across languages, in particular with respect to the presence or absence of nasal vowels in a language.

This paper presents a study of another case of interarticulator programming, i.e., the timing of lip and tongue movements in sequences with a vowel, a bilabial stop consonant, and a vowel. In producing such a sequence, a speaker has to do two or three tasks: move the tongue between the positions for the first and second vowels; close and open the lips for the stop consonant; if the stop is voiceless, open and close the glottis. Here, the focus is on the temporal coordination of the two first tasks. In addition, the kinematics of the tongue movement between the two vowels is evaluated.

Although there are acoustic studies of such VCV sequences (e.g., Öhman, 1966; Magen, 1997) that have examined the anticipatory coarticulation from the second vowel to the first, only a few published studies appear to have addressed the timing of lip and tongue movements using records of articulator motion. Houde (1968), in an x-ray study of one subject, noted that there was a tendency ''for the lip to begin its vertical transition to closure before the tongue points begin their transitions from their initial target positions to the next target position'' (Houde, 1968, p. 61). He also added, however, that the evidence was meager and that it was hard to establish the time at which a transition began. Gay (1977), also using x rays and two subjects, made a much stronger and precise statement: ''The movement of the tongue body from the first to the second vowel does not begin until after closure for the intervocalic consonant is completed'' (Gay, 1977, p. 187). However, an earlier study of Gay (1974) appears to suggest that the tongue movement does in fact start before the oral closure (see Fig. 6 in Gay, 1974). Lubker *et al.* (1977) examined the hypothesis that there was a fixed relationship between the onsets of the tongue movement and the rounding of the lips for a vowel. Using x ray, they studied one subject and concluded that their notion of synchronous programming between the tongue and the lips was not supported by the data.

Alfonso and Baer (1982) combined x ray, electromyography, and acoustic/perceptual analyses to study tongue

[a]Electronic mail: lofqvist@haskins.yale.edu

movements in the sequence /əpVp/ produced by a single subject, where the vowel (V) was one of several American English vowels. Since they were making frame-by-frame measurements of the x-ray films, they measured the horizontal and vertical movements separately. Their results suggested that the horizontal and vertical movements of the tongue dorsum start at different times during the sequence (see Figs. 10 and 11 in Alfonso and Baer, 1982). The vertical tongue movement trajectories for the different vowels began to diverge after the oral closure for the first stop consonant, while the horizontal trajectories diverged during the first schwa vowel /ə/. The perceptual results also showed that listeners could identify the upcoming vowel from the schwa vowel. Of interest to note in their results is that the magnitude of the horizontal tongue dorsum movement was much larger than the vertical movement for this subject. Thus, the timing difference may be related to the movement magnitude.

The purpose of this study was thus to examine the timing of lip and tongue movements using a larger number of subjects, a more varied speech material, and a state-of-the-art movement transduction system. In addition, tongue movement kinematics is evaluated as a function of consonant voicing and vowel context. Since we have recently conducted a detailed study of lip and jaw kinematics in bilabial stop consonant production (Löfqvist and Gracco, 1997), the kinematics of lip and jaw movements is not specifically addressed here.

The timing of the lip and tongue movements in the present study can appropriately be discussed within the theoretical framework of anticipatory coarticulation. The production of a bilabial stop consonant does not in itself require any tongue movements, although they may occur as a result of jaw movements made for the closure and release of the stop consonant. Thus, the tongue movement can, in principle, start anywhere before, or during, the stop closure. Studies of anticipatory coarticulation have been particularly concerned with how long in advance of an upcoming segment its acoustic and/or articulatory properties can be anticipated. For example, several studies of the anticipatory coarticulation of lip rounding have been made. Some of these studies (e.g., Benguerel and Cowan, 1974; Lubker, 1981; Sussman and Westbury, 1981) suggested that the onset of lip rounding started earlier as the number of consonants before the rounded vowel increased, supporting what has been called a look-ahead model of coarticulation. Other studies (e.g., Bell-Berti and Harris, 1979, 1981, 1982) showed that the onset of lip rounding was constrained to start within a relatively fixed temporal window, supporting what has come to be known as a frame mode of coarticulation. Later, some of the early studies were questioned since they had failed to use the proper control conditions of placing the consonants between unrounded vowels. When such control conditions are included, the extent of anticipatory lip rounding appears to be limited. In addition, recent studies (e.g., Perkell and Matthies, 1992) have suggested that both an unconstrained look-ahead model and a constrained frame model of anticipatory labial coarticulation are untenable and should be replaced by hybrid models. In a hybrid model, the onset of the lip rounding gesture for a vowel follows the look-ahead

model, while the maximum acceleration of the rounding movement obeys a frame model. Since there is considerable variability between subjects in their patterns of coarticulation, Abry and Lallouache (1995) propose that anticipatory labial coarticulation should be modeled separately for each subject. Earlier work on anticipatory coarticulation of lip rounding tended to focus only on factors of motor control. More recent work also suggests that perceptual factors may well play a role in limiting the degree of coarticulation to maintain the integrity of the speech signal.

It is not entirely clear what such models of anticipatory coarticulation predict for the onset of the tongue movement from the first to the second vowel in a VCV sequence with a labial stop consonant. One methodological problem is that it is not easy to define a boundary between the two vowels based on acoustic or articulatory records. Studies of anticipatory coarticulation usually use an acoustically defined landmark, such as the onset of a vowel, as a base for the measurements. In an articulatory sense, such a point is arbitrary, since the tongue movement for the vowel starts before such an acoustically defined point. In addition, the tongue movement between the two vowels in a VpV sequence is continuous. One might argue that the onset of the tongue movement should be constrained in the sense that the speaker avoids to start it so much in advance of the stop consonant that an ''extra'' vowel is produced and perceived. A perceptual study by Carré *et al.* (1996), using an acoustic model of the vocal tract, showed this to happen when the movement to the second vowel started very much in advance of the bilabial stop closure. Based on this hypothesis, one might further hypothesize that in those instances where the tongue movement onset occurs well in advance of the lip closure for the stop consonant, the magnitude of the tongue movement should be small, so as not to introduce an extra segment. To test this hypothesis, the present study examined the relationship between the interval from the onset of the tongue movement from the first to the second vowel to oral closure for the stop and the magnitude of the tongue movement from its onset to the stop closure. If this hypothesis were correct, we would expect a negative correlation between these two variables, i.e., a tongue movement starting well before the stop closure should show a small displacement before the oral closure. Another hypothesis would relate the onset of the tongue movement from the first to the second vowel to the magnitude of the tongue movement trajectory itself. Based on this hypothesis, one might expect a positive correlation between the interval from tongue movement onset to lip closing onset and the size of the tongue movement trajectory between the two vowels.

To examine these specific hypotheses and other factors influencing the tongue movement trajectory, measurements were made of the onset of the tongue movement from the first to the second vowel relative to the onset of the lip closing movement for the stop consonant and also relative to the acoustically defined oral closure for the stop. The magnitude of the tongue movement trajectory was also measured to see if it was related to the timing of the tongue and lip movement. In addition, the duration of the tongue movement trajectory was measured to examine the relationship between

movement amplitude and duration. Finally, a calculation was made of the percentage of the tongue movement from the first to the second vowel that occurred during different intervals of the VCV sequence, such as during the first vowel, during the stop closure, and during the second vowel.

I. METHOD

A. Subjects

Two female (LK, DR) and two male subjects (VG, AL) participated. All subjects had normal speech and hearing and no history of speech or hearing disorders. Three of the subjects (LK, DR, VG) are native speakers of American English. Subjects LK and DR grew up in the midwest, while subject VG grew up in Florida; they all currently live in the northeast. Speaker AL is a native speaker of Swedish who is also fluent in English. Subjects VG and AL are the two authors.

B. Linguistic material

The linguistic material consisted of V_1CV_2 sequences, where the first and second vowels (V_1 and V_2) were always one of /i, a, u/, and the consonant (C) one of /p, b/. The sequences were placed in the carrier phrase ''Say ... again'' with sentential stress occurring on the second vowel (V_2) of the sequence. Ten repetitions of each sequence were recorded. Only the sequences with asymmetric vowel contexts were included in the analysis, since it is virtually impossible to define movement onsets and offsets in sequences with symmetrical vowel contexts due to the small and inconsistent amount of tongue movement.

C. Procedure

The movements of the lips, the jaw, and the tongue were recorded using a three-transmitter magnetometer system (Perkell *et al.* 1992). Receivers were placed on the upper and lower lips, on the lower incisors, and on four positions on the tongue. The tongue receivers will be referred to as tongue tip, tongue blade, tongue body, and tongue rear. The lip receivers were placed below and above the vermilion border of the upper and lower lip, respectively, with a vertical separation of approximately 1 cm when the lips were in a closed position. For the tongue, the first receiver was placed as far back as the subject could tolerate, and the second one close to the tongue tip; next, an attempt was made to space the other two receivers evenly between the first and the second. Two additional receivers placed on the nose and the upper incisors were used for the correction of head movements. The receivers on the lips, the incisors, and the nose were attached using Iso-Dent (Ellman International). For the tongue receivers, Ketac-Bond (ESPE) was used. Care was taken during each receiver placement to ensure that it was positioned at the midline with its long axis perpendicular to the sagittal plane. Two receivers attached to a plate were used to record the occlusal plane by having the subject bite on the plate during recording. All data were subsequently corrected for head movements and rotated to bring the oc-

clusal plane into coincidence with the *x* axis. This rotation was performed to obtain a uniform coordinate system for all subjects (cf. Westbury, 1994).

The articulatory movement signals (induced voltages from the receiver coils) were sampled at 625 Hz after low-pass filtering at 200 Hz. The resolution for all signals was 12 bits. After voltage-to-distance conversion, the movement signals were low-pass filtered using a 25-point triangular window with a 3-dB cutoff at 17 Hz; this was done forwards and backwards to maintain phase. To obtain instantaneous velocity, the first derivative of the position signals was calculated using a three-point central difference algorithm. The velocity signals were smoothed using the same triangular window. A measure of lip opening was obtained by subtracting the vertical position of the lower lip receiver from that of the upper lip receiver. All the signal processing was made using the Haskins Analysis Display and Experiment System (HADES) (Rubin and Löfqvist, 1996). The acoustic signal was preemphasized, low-pass filtered at 9.5 kHz, and sampled at 20 kHz.

To define the onset of the closing movement of the lips for the stop consonant, the second derivative of the derived lip opening signal was used. Using a zero crossing in the first derivative of the lip opening signal was difficult when the first vowel was /u/ that included lip rounding. Here, the rounding gesture made the lip opening change continuously and a zero crossing would not appear in the first derivative at a point in time close to the oral closure. Thus, the onset of the lip closure for the stop consonant was defined as the minimum in the second derivative of the lip opening signal prior to the oral closure, cf. Fig. 1. This point was defined algorithmically. Figure 1 presents the acoustic, lip opening, and tongue body signals for one production of the sequence ''api'' by subject VG. Since the interpretation of a second derivative is not always straightforward, the lip opening signal and its first derivative are also included in Fig. 1. We should add that the actual lip opening is at zero throughout the oral closure. The change in the lip opening signal during the closure is due to the fact that it represents the vertical distance between the receivers on the upper and lower lips, and these receivers move during the closure (cf. Löfqvist and Gracco, 1997; Westbury and Hashi, 1997). The tongue body receiver was used for analyzing tongue kinematics. Its tangential velocity $[v = \sqrt{(\dot{x}^2 + \dot{y}^2)}]$ was calculated. Tongue movement onsets and offsets were identified algorithmically from the tangential velocity signal as minima during the first and second vowels. Their identification is also shown in Fig. 1. We should note that at these points in time, the horizontal and vertical velocity of the tongue is not necessarily zero. The magnitude of the tongue movement trajectory from vowel to vowel was obtained by summing the Euclidean distances between successive samples from movement onset to offset. In addition, the Euclidean distance between the tongue body receiver at movement onset and offset was also measured and used to assess the extent to which the movement trajectory was a straight line or a curved path. This was done by calculating the ratio between the tongue movement measured as a trajectory and as a straight line. A ratio of 1 indicates that the movement trajectory follows a straight line
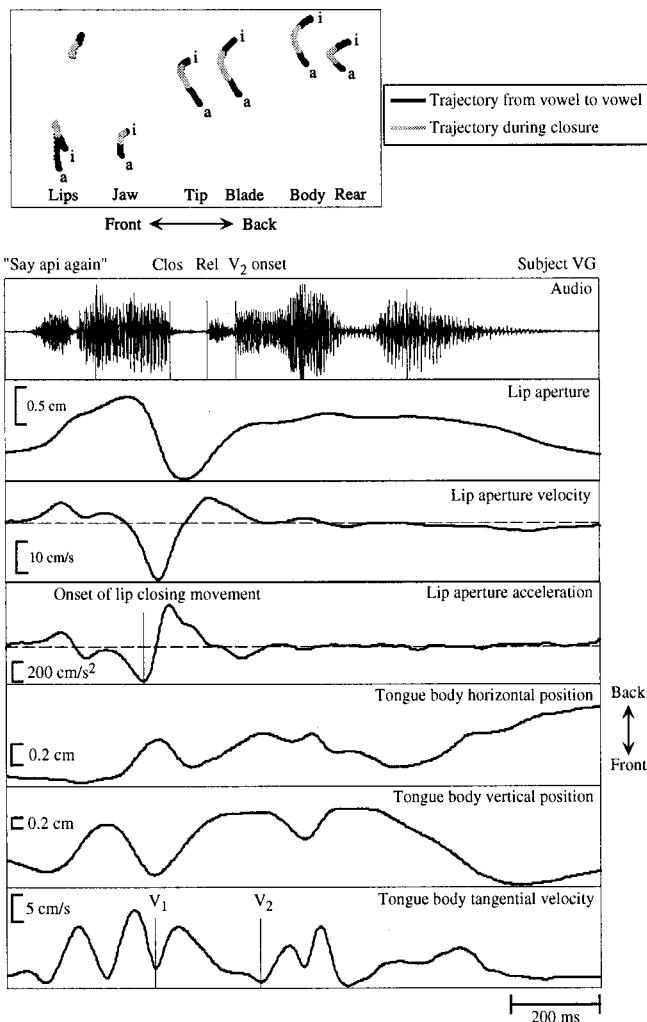
FIG. 1. Acoustic and movement signals recorded during the production of the utterance ''Say api again'' by subject VG. In addition to the derived lip aperture signal, its first and second derivatives are shown. The labels in the audio signal correspond to the onset and release of the oral closure for the consonant, and the onset of the second vowel in /api/. The label in the lip aperture acceleration signal marks the onset of the lip closing movement for the consonant. The labels in the tangential velocity signal of the tongue body identify the onset and offset of the tongue movement from the first to the second vowel in /api/. The top panel shows the receiver trajectories from the first to the second vowel and also the part of the trajectory made during the oral closure for the consonant.

path while a ratio greater than 1 shows that the trajectory is a curved path.

The onset and release of the oral closure were identified in waveform and spectrogram displays of the acoustic signal. The onset of the closure was identified by the decrease in the amplitude of the acoustic waveform, and by the disappearance of spectral energy at higher frequencies. The release was identified by its burst. The onset of regular glottal vibrations for the second vowel was also marked. Measurements of closure duration and of voice onset time were made. All the labeling was made by the first author. Analyses of variance and t-tests were used to assess the influence of vowel context and consonant voicing on timing and movement parameters. A p value of ≤ 0.05 was adopted as significant.

The kinematic signals represent the movements of receivers placed at the midline of the lips, the jaw, and the tongue. When presenting the results, we will use the terms ''tongue body receiver'' and ''tongue body'' interchangeably, while acknowledging that we are only examining the movements of a single point. Thus, we make no claims about asymmetrical movements of the left and right sides of the lips, or the tongue. The tongue and lower lip signals contain the contribution of the jaw. These are the appropriate movements to examine when the focus of the analysis is on the lower lip and the tongue as end effectors. It is reasonable to assume that a speaker has joint control of different articulators during speech production to produce the desired results.

II. RESULTS

Figure 2 shows receiver movement trajectories from the first to the second vowel for all subjects and sequences with a voiced stop /b/. The whole trajectory from vowel to vowel is shown as well as the part of the trajectory that occurred during the oral closure for the consonant. The letters at the onset/offset of each trajectory identify the positions for the respective vowels. A tracing of the outline of the hard palate is also shown for identification purposes. Since this outline was obtained by having the subject move the tongue tip receiver from the alveolar ridge and as far backwards as possible, these tracings do not necessarily give the true outline of the palate in the posterior region. In these figures, a few facts should be noted. The tongue receivers can move in both straight-line and curved paths. An analysis of the shape of the trajectories for the tongue body receiver was made by calculating the ratio between the movement amplitudes measured as the actual path length and as the Euclidean distance between the receiver positions at movement onset and offset. For all subjects, this ratio tended to be highest for the sequences with /i/ and /u/ as the two vowels, with values of 1.2 or higher. Only in one case, the sequence /abi/ for subject LK, did the tongue body receiver move in a straight line. The trajectory for a pair of VCV sequences with the same vowels but in different positions, such as /abi/ and /iba/, do not show paths that are mirror images of each other. This is due, in part, to the fact that the context for the first and second vowels differ due to the carrier phrase used, and also to the stress pattern. The trajectories of the four tongue receivers show both similarities and differences. For example, subject LK shows very similar trajectories for the tongue tip, tongue blade, and tongue body receivers, but a different pattern for the tongue rear receiver. In particular, for the sequence /ibu/ of her productions, the tongue rear receiver is moving backward while the other three tongue receivers are moving backward and downward. Similarly, in the sequence /ubi/ the rear tongue receiver is moving backward and up while the other tongue receivers are moving forward and up. Similar differences can also be found in the productions of subject DR. On the other hand, subject AL shows more of a similarity in the trajectories of the tongue receivers.

The first analysis focused on the onset of the tongue body movement from the first to the second vowel relative to the oral closure for the stop consonants. The results are shown in Fig. 3. This figure plots frequency distributions of the interval between the onset of the tongue body movement and the acoustically defined oral closure, collapsed across

consonant voicing and vowel contexts ($n = 120$). The data have been grouped into 25-ms bins. It is evident from these results that they do not agree with the findings of Gay (1977). Only in 7% of the productions for subject LK did the tongue movement start after the oral closure for the consonant. For the remaining three subjects, the tongue movement always started before the closure. The interval between the tongue movement onset and the oral closure ranged up to 175 ms for subjects LK and DR, whereas it was more narrowly distributed for the two remaining subjects, VG and AL. A separate t-test for each subject showed that stop con-

sonant voicing had no reliable influence on the interval between the onset of the tongue movement and the lip closure (pooled across vowel contexts) for subjects LK, VG, and AL ($t_{118} = -0.17$, -1.78, and -1.42, respectively). Voicing had a reliable effect for DR ($t_{118} = -3.87$), but the difference was only 7 ms. An analysis of variance performed for each subject showed that the quality of the first vowel had a reliable influence on the interval between the onset of the tongue movement and the oral closure ($F_{2,114} = 15.69$, 26.84, 123.89, 303.70, for subjects LK, DR, VG, and AL, with corresponding η^2 values of 0.19, 0.32, 0.66, and 0.83). However, the
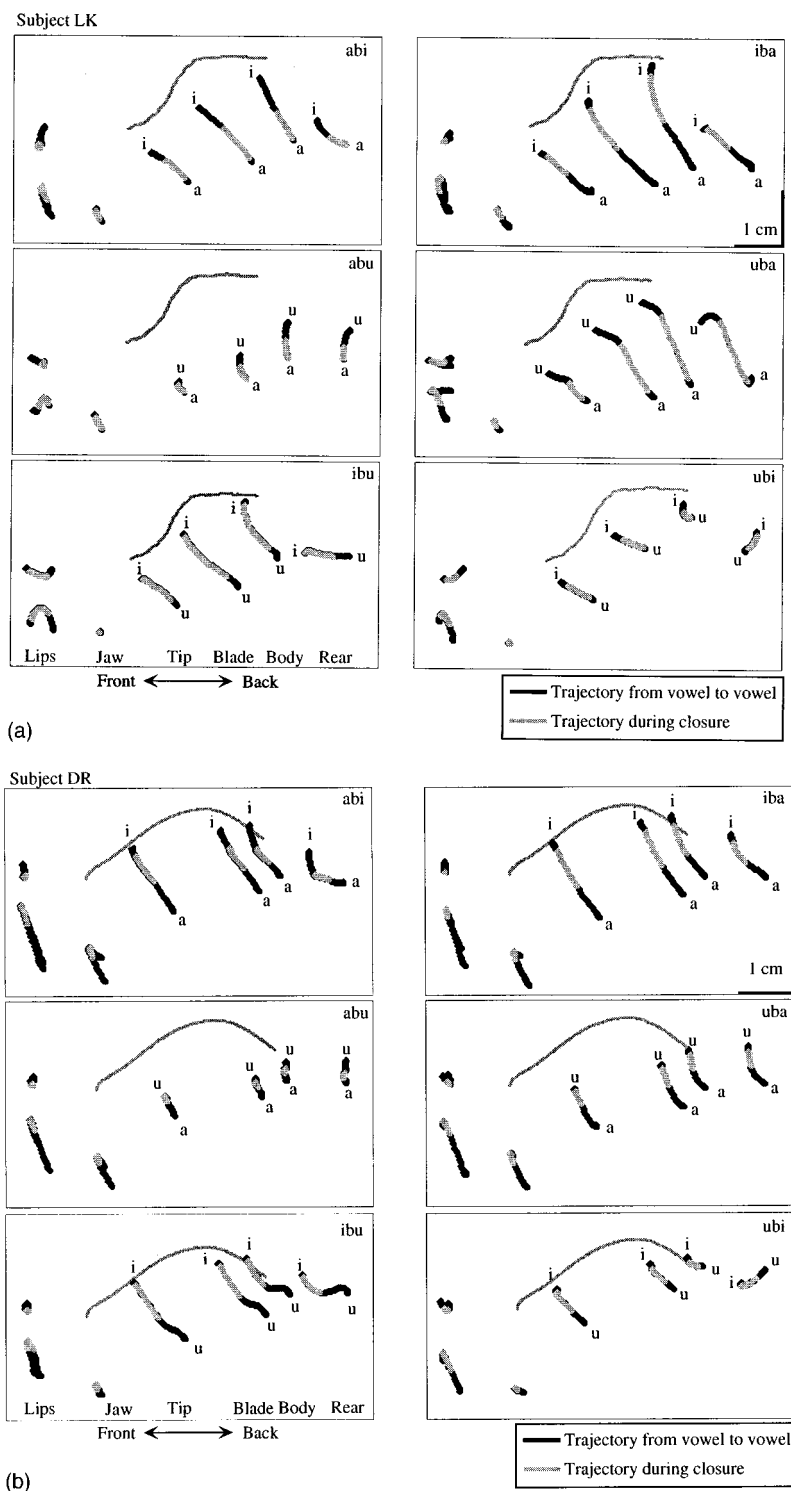
FIG. 2. (a) Plots of receiver trajectories during single productions of sequences with a voiced bilabial stop /b/ and asymmetric vowel contexts for subject LK. The trajectory from the first to the second vowel is shown and also the part of the trajectory that occurred during the oral closure for the consonant. (b) Plots of receiver trajectories during single productions of sequences with a voiced bilabial stop /b/ and asymmetric vowel contexts for subject DR. The trajectory from the first to the second vowel is shown and also the part of the trajectory that occurred during the oral closure for the consonant. (c) Plots of receiver trajectories during single productions of sequences with a voiced bilabial stop /b/ and asymmetric vowel contexts for subject VG. The trajectory from the first to the second vowel is shown and also the part of the trajectory that occurred during the oral closure for the consonant. (d) Plots of receiver trajectories during single productions of sequences with a voiced bilabial stop /b/ and asymmetric vowel contexts for subject AL. The trajectory from the first to the second vowel is shown and also the part of the trajectory that occurred during the oral closure for the consonant.

Subject VG

abi | iba
abu | uba
ibu | ubi

Lips Jaw Tip Blade Body Rear
Front ◄————► Back

—— Trajectory from vowel to vowel
····· Trajectory during closure

(c)

Subject AL

abi | iba
abu | uba
ibu | ubi

Lips Tip Blade Body Rear
Front ◄————► Back

—— Trajectory from vowel to vowel
····· Trajectory during closure
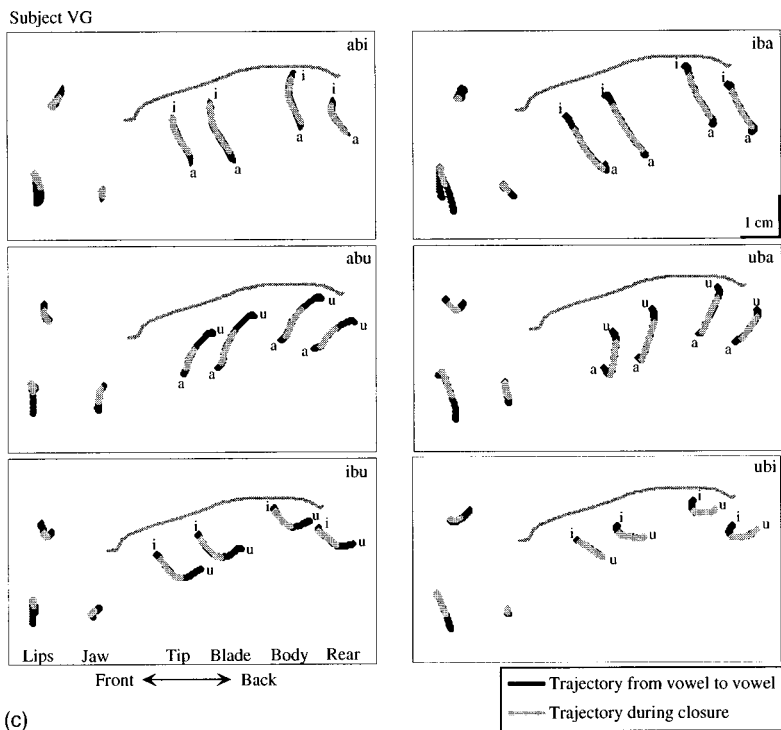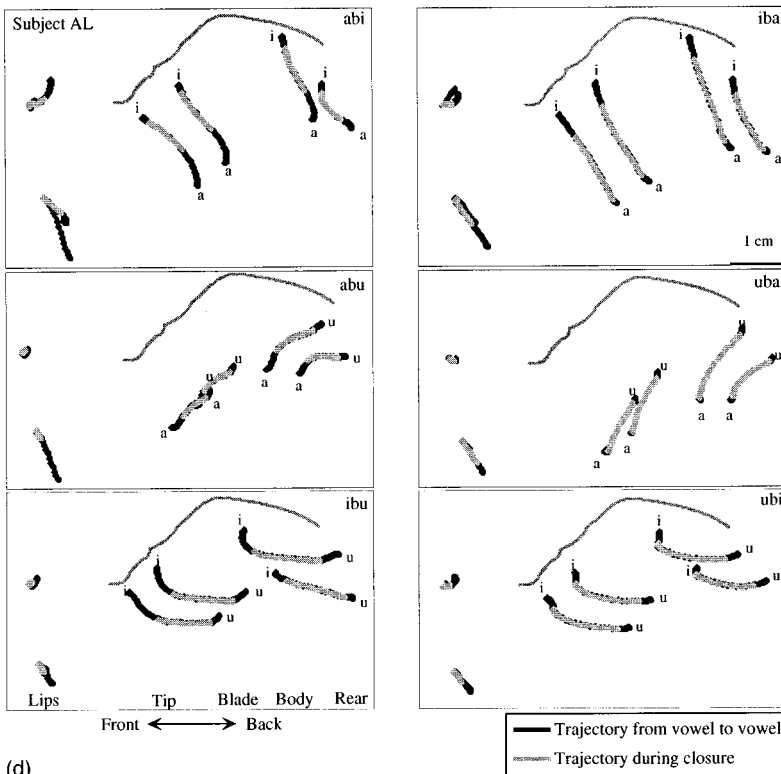
(d)

FIG. 2. (*Continued.*)

pattern varied between subjects. For subjects DR, VG, and AL, the interval decreased in the order /i/>/a/>/u/; the average values in ms were 95, 75, and 70 for DR, 65, 40, and 25 for VG, and 95, 70, and 45 for AL. For subject LK, this interval was always shortest when the first vowel was /a/, 15 ms compared to 60 and 70 ms for /i/ and /u/.

The next analysis examined the phasing between the onset of the tongue body movement and the onset of the lip closing movement. The results are summarized in Fig. 4 for all subjects and sequences. A first thing to note in this figure is that subject DR always started the tongue movement before the lip movement. For the other three subjects, the pattern varies, although they all show the tongue movement leading when the first vowel is /i/. For subjects VG and AL, the lip movement tended to lead in the other vowel contexts. The same thing was true for subject LK, except that in the sequences /upa/ and /uba/ the tongue movement started approximately 100 ms before the lip movement. With the exception of these two sequences for subject LK, the interval between the tongue and lip movement onsets was less than
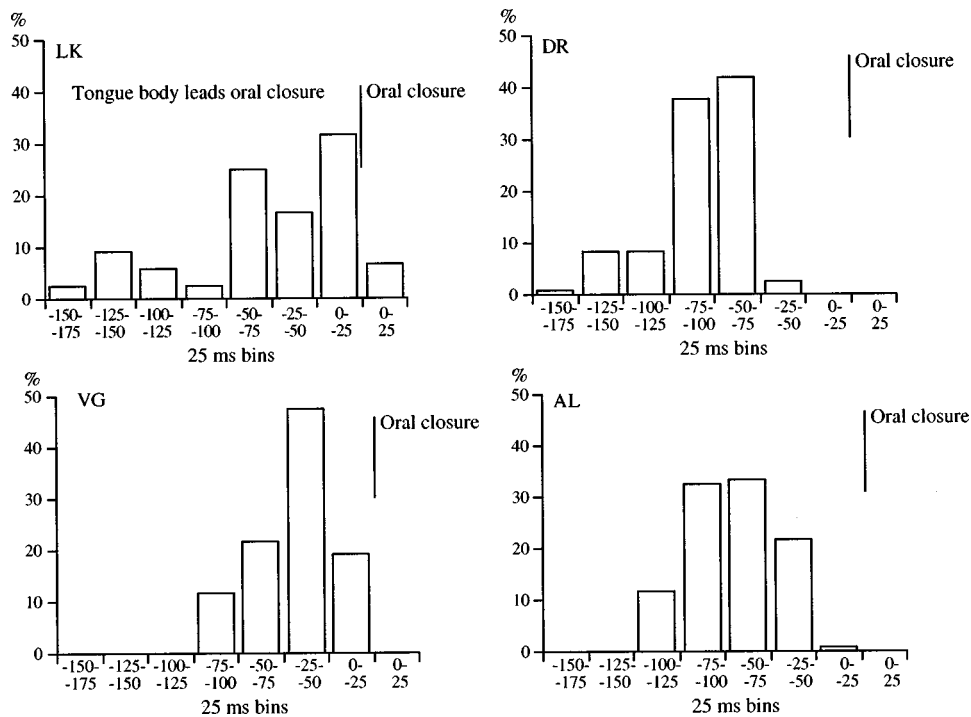
FIG. 3. Frequency distributions of the interval between the onset of the tongue movement from the first to the second vowel and the oral closure for the consonant. The bin size is 25 ms.

50 ms for all subjects and sequences. A t-test for each subject's productions showed that stop consonant voicing had no reliable effect on the interval between tongue and lip movement onsets for subjects LK, VG, and AL ($t_{118}=0.67$, -1.55, and -1.16). For subject DR, there was a very small but reliable difference of 10 ms due to voicing ($t_{118}=-2.53$).

The magnitude of the tongue movement trajectory between the first and second vowels is shown in Fig. 5. Overall, the magnitude was larger for subject AL than for the other subjects. For DR and VG, the trajectory was usually less than 1.5 cm. There was no reliable influence of consonant voicing on the trajectory for subjects LK, DR, and VG ($t_{118}=0.47$, 0.25, 1.15). Subject AL always had a longer trajectory when the consonant was voiced ($t_{118}=-4.18$). The average difference was 0.3 cm. The effect of vowel context did not appear to be consistent between subjects. The only apparent pattern was that subjects LK, DR, and VG showed small trajectories for the sequences /upi/ and /ubi/.

There is, however, another influence of vowel context on the magnitude of the tongue movement that is evident in Fig. 5. Mirror vowel sequences do not show the same magnitude of the tongue movement. For example, it is always the case that the tongue movement is larger in the sequences /ipa, iba/ than in the sequences /api, abi/. Similarly, the magnitude is larger in the sequences /ipu, ibu/ than in /upi, ubi/. Finally, the magnitude is larger for /upa, uba/ than for /apu, abu/ for subjects LK and DR. The reason for these differences can be found in Fig. 6. This figure plots the tongue body receiver positions for the three vowels /i, u, a/ when they occur as the first and second vowel in the VCV sequence. The measurements were made at the minimum tangential velocity shown in Fig. 1. Two findings emerge in this figure. First, the filled symbols (circles and triangles) for the sequences with /a/ and /u/ as the first vowel are higher and
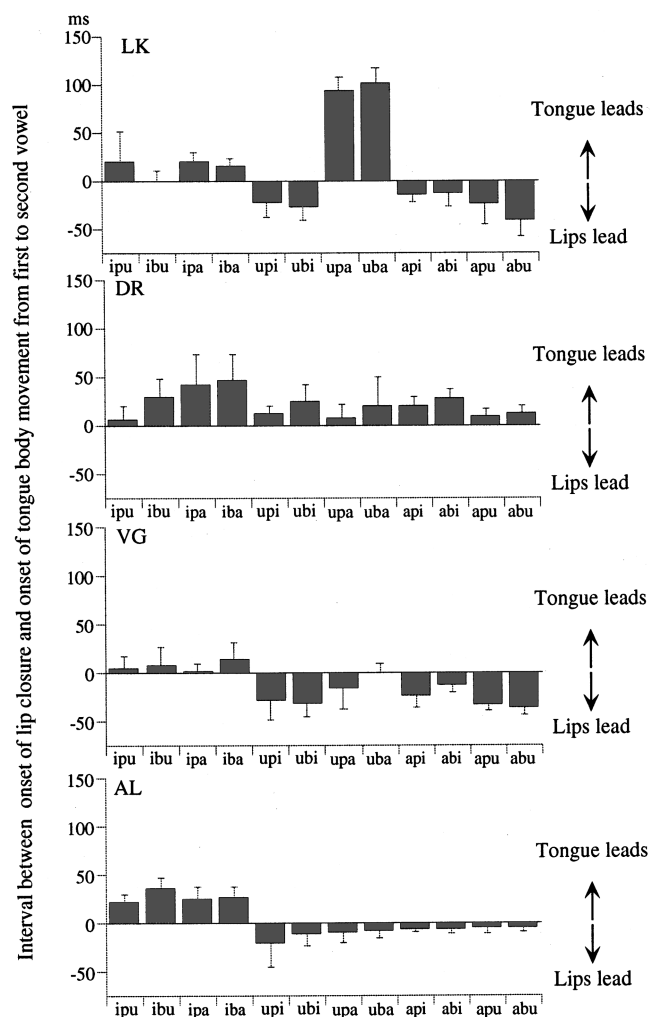
FIG. 4. The interval between the onset of the tongue movement from the first to the second vowel and the onset of the lip closing movement for the consonant. Means and standard deviations are shown.

Tongue body movement trajectory from first to second vowel
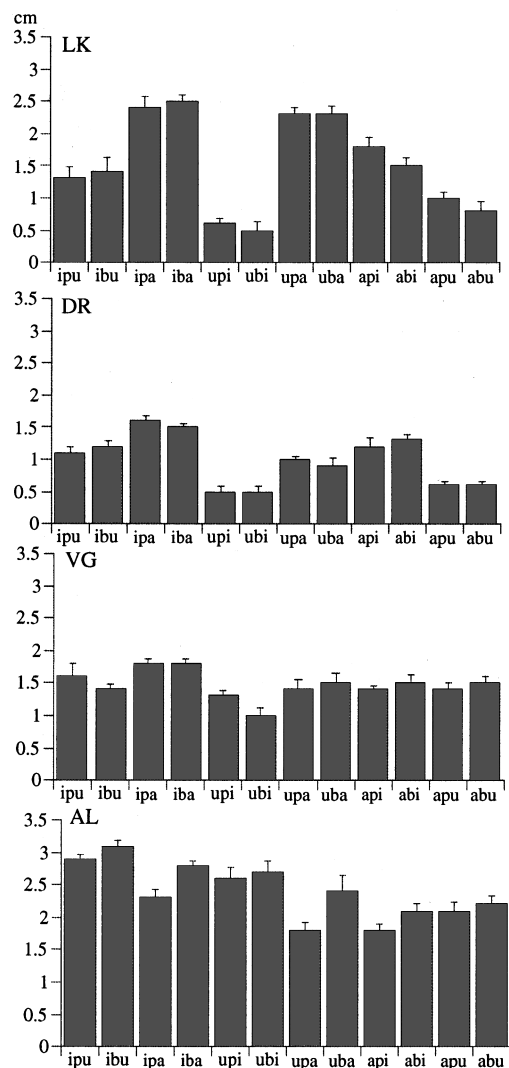
FIG. 5. The magnitude of the tongue movement trajectory from the first to the second vowel. Means and standard deviations are shown.

more forward in the plots than the unfilled symbols for the same vowels when they occur as the second vowel. Second, there is much less difference in the tongue body position for the vowel /i/ when it is the first or the second vowel in the sequence. Thus, if we compare the sequences /ipa, iba/ with the sequences /api, abi/, we see that the position of the tongue body for the vowel /a/ is lower and further back in /ipa, iba/ than it is in /api, abi/, see the unfilled and filled triangles. The same is true for the sequences /ipu, ibu/ and /upi, ubi/, where the tongue body position for the vowel /u/ is different when it occurs as the second and first vowels (see the unfilled and filled circles). Thus, the tongue body position for /a/ and /u/ differs when these vowels occur as the first and second vowel of the sequence. However, the filled and unfilled squares associated with the vowel /i/ occurring as the first and second vowel overlap for subjects VG and AL, and show a relatively small difference for subjects LK and DR. The variations in tongue body position for the vowels /a, u/ account for the difference in the magnitude of the tongue movement in sequences with mirror vowels. The movement trajectories shown in Fig. 2 also show similar

differences in the tongue body position for the same vowel when it is the first and the second vowel in the sequence.

We next turn to the relationship between the phasing of lip and tongue movements and the duration and magnitude of the tongue movement trajectory. One hypothesis proposed in the Introduction is that the tongue movement from the first to the second vowel starts earlier relative to the onset of the lip closing movement as the magnitude of the tongue movement trajectory increases. The relevant results are presented in Fig. 7 showing scatter plots of the interval between the onsets of the lip closing movement and the tongue body movement versus the tongue body movement trajectory. Overall there is a positive correlation between the onset and the magnitude of the tongue movement. That is, the onset of the tongue movement tended to start earlier relative to the lips when the tongue body movement is large. The correlation coefficients for all productions, pooled across vowel contexts and consonant voicing ($n = 120$), were 0.69, 0.43, 0.53, and 0.50 for subjects LK, DR, VG, and AL, respectively. In contrast, there was no significant correlation between the onset of the tongue movement in relation to the onset of the lip closing movement and the duration of the oral closure for any subject.

If the tongue movement starts well in advance of the lip closing movement, and hence well in advance of the oral closure for the consonant, an extra vowel segment might be perceived. One might thus hypothesize that in those cases where the tongue movement started well before the oral closure, the movement up to the oral closure would be rather small, so as not to cause any perceptual effects. That is, one would expect a negative correlation between the onset of the tongue movement relative to the oral closure and the magnitude of the tongue movement displacement from its onset to the oral closure. Such a negative correlation was only found for one subject, VG, however, and it was not significant ($r = -0.15$). For the other three subjects, the correlations were positive but small ($r = 0.1$ (ns), 0.38, and 0.27, for LK, DR, and AL, respectively).

Two of the subjects, LK and DR, showed a positive correlation between the tongue movement trajectory and its duration, with $r = 0.81$ and 0.73. For the two other subjects, these correlation coefficients were very low, -0.10 (ns) and 0.29 for VG and AL, respectively. These results are shown in Fig. 8. The duration of the tongue movement did not correlate with the duration of the oral closure for subjects LK and DR. For subject VG, there was positive correlation of 0.41, whereas for subject AL there was a reliable negative correlation of -0.2

The final analysis of tongue–lip phasing focused on how much of the tongue movement occurred during four different parts of the VCV sequence. These parts were (1) from the onset of the tongue movement to the oral closure for the stop; (2) during the oral closure; (3) between the stop release and the onset of the second vowel; and (4) during the second vowel. For each of these parts, the tongue movement was calculated as a percentage of the total movement trajectory. The results are shown in Fig. 9. This figure shows the cumulative percentage of the tongue movement during the four parts of the sequence, shown in their order of occurrence
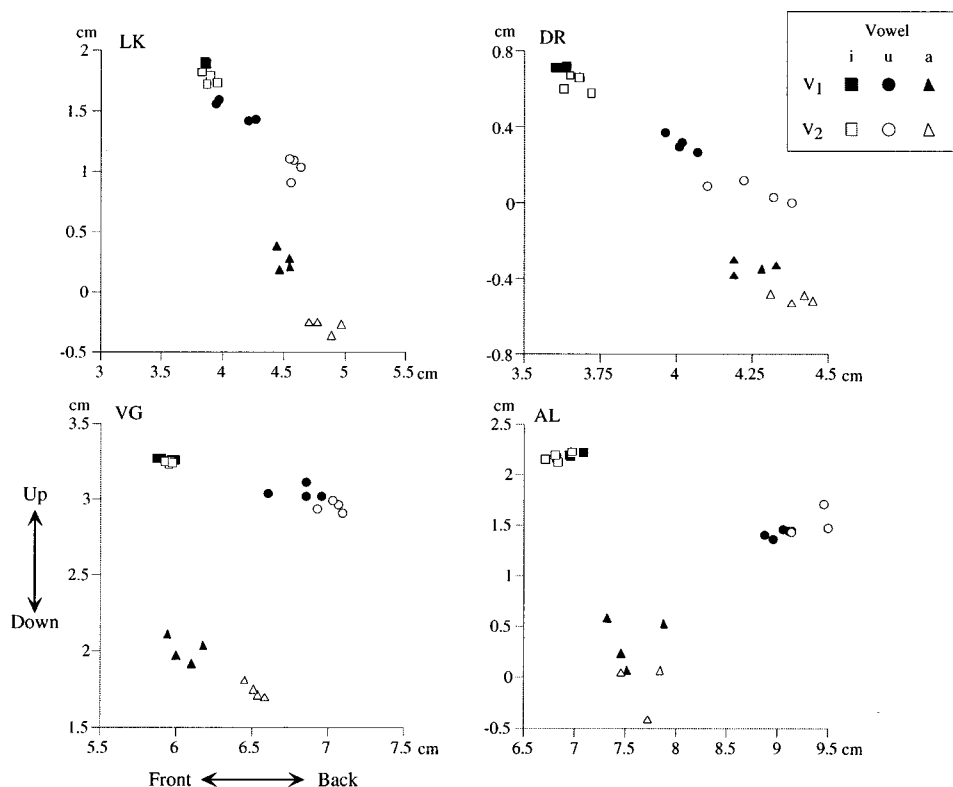
FIG. 6. Plot of the average tongue body positions for the three different vowels when they occur as the first (filled symbols) or second (unfilled symbols) vowel in the VCV sequence.

from bottom to top in the figure. That is, the relative movement from the onset of the tongue movement to the oral closure for the stop is shown at the bottom. Overall, the black portion of each bar is the largest. This indicates that most of the tongue movement took place during the oral closure for the stop. For subjects LK, VG, and AL 55%, 60%, and 57% of the total trajectory took place during the

closure; for subject DR, the corresponding value was 35%.

As might be expected, consonant voicing had a very robust effect on the relative tongue movement trajectory between the release of the consonant and the onset of the vowel. It was much larger for the voiceless stops: 18%–50% vs 5%–12% for LK, 24%–45% vs 4%–9% for DR, 12%–29% vs 3%–13% for VG, and 10%–21% vs 4%–7% for AL.
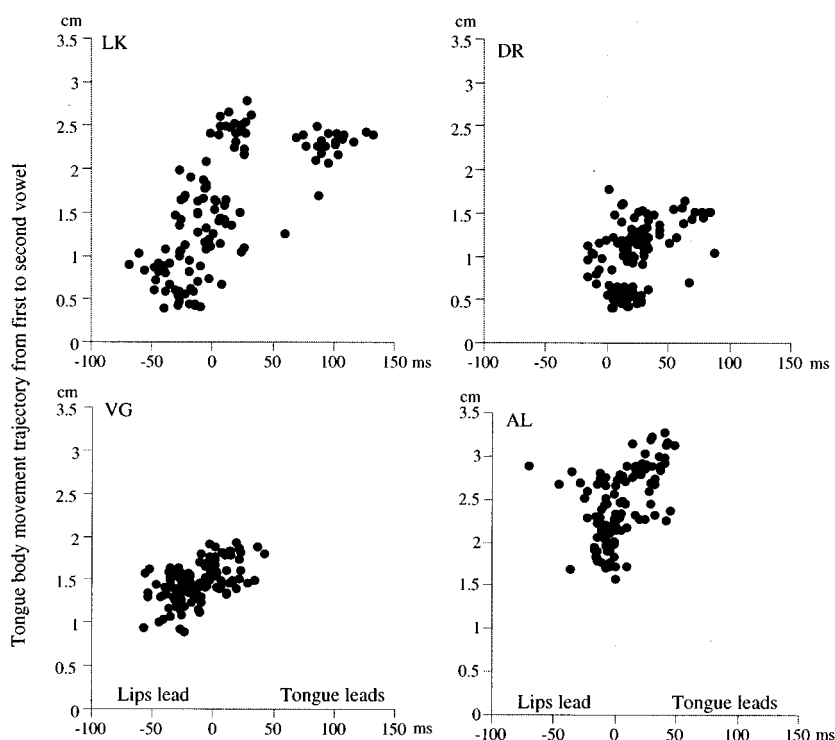
FIG. 7. Plot of the interval between the onsets of the tongue body and lip closing movements versus the magnitude of the tongue movement trajectory from the first to the second vowel.
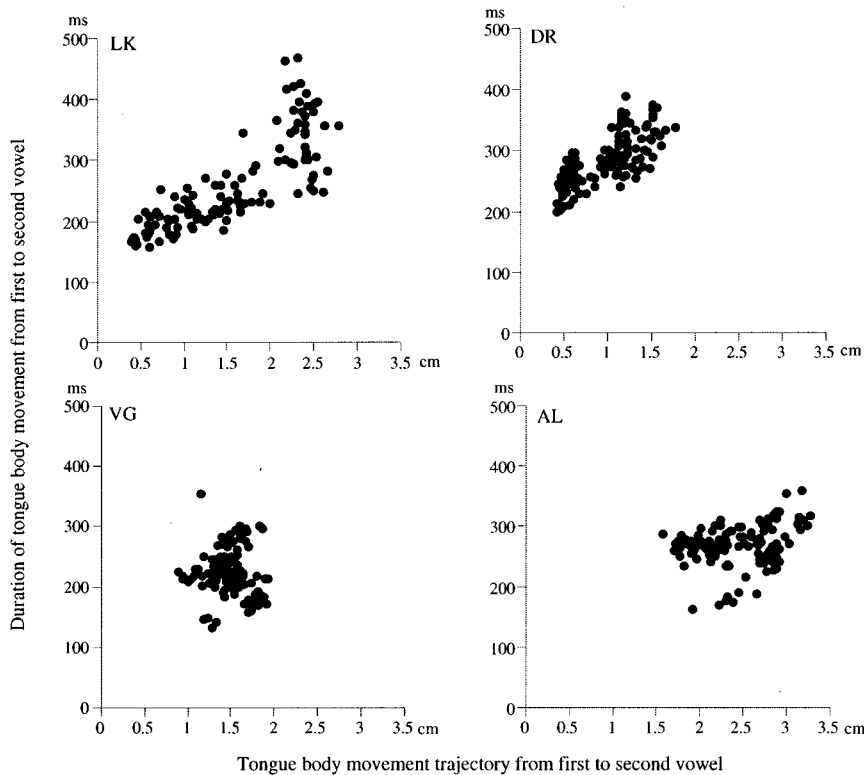
FIG. 8. Plot of the magnitude and duration of the tongue movement trajectory from the first to the second vowel.

This was related to the difference in voice onset time between voiced and voiceless stops, which was also significant for all subject. However, the duration of the oral closure did not differ as a function of consonant voicing for any subject. Figure 9 also suggests that the relative tongue movement during the first vowel up to the oral closure tends to be larger for voiced than for voiceless stops. A test performed for each subject showed this difference to be reliable for subjects LK, DR, and VG (t_{118}= 13.5, 8.63, and 31.4), but not for subject AL (t_{118}=0.69). The values for the voiced and voiceless contexts were 27% vs 5%, 35% vs 14%, and 16% vs 10% for subjects LK, DR, and VG, while for subject AL the value was the same, 9%, for both contexts. Apart from these general influences of stop consonant voicing, there was no consistent pattern across speakers for vowel context.

Finally, the tongue body position and velocity at the onset of the movement and at the oral closure for the stop was examined for the influence of the upcoming vowel. As can be expected, this influence increased between the first and the second point in time. Although the effect of the second vowel was in many cases reliable at both points in time, an examination of the η^2 values showed them to increase from the first to the second point. This was particularly the case for the velocities, since at the instant of oral closure the tongue was moving in different directions depending on the identity of the second vowel. It proved difficult to assess possible differences in the timing of the horizontal and vertical component of the tongue body movement, however. The reason was that in many cases the tongue body was moving very slowly, which made the identification of zero crossings for movement onset unreliable. In those instances where it was possible to reliably identify the movement onset, the interval between the onset of the vertical and horizontal movement of the tongue body was 50 ms or less, with no clear pattern of one component consistently leading the other.

III. DISCUSSION

The present results show that the tongue movement from the first to the second vowel in a sequence of vowel-bilabial stop-vowel most often started before oral closure for the stop consonant. In only a small percentage of the productions of one subject (LK) did the tongue movement start after the consonant closure (Fig. 3). This is contrary to the results presented by Gay (1977). Subjects differed in the details of their patterns of lip–tongue phasing. For two of the subjects, LK and DR, the tongue movement could start up to 175 ms before the closure for the consonant. The timing of the tongue movement with respect to the closing movement of the lips for the consonant also differed between subjects. One subject, DR, always started the tongue movement before the onset of the lip movement, irrespective of the nature of the first and second vowels (Fig. 4). For the other three subjects, the pattern of lip–tongue phasing varied. For example, all three of them, LK, VG, and AL, always had the tongue movement leading the lip movement when the first vowel was /i/. In the remaining sequences, subjects VG and AL always showed the lips leading the tongue, whereas subject LK had the tongue leading the lips in the sequences where the first vowel was /u/ and the second vowel was /a/. Generally, the interval between the tongue and lip movement onsets was 50 ms or less. Taken together these results suggest that there is a temporal window during which the tongue movement from the first to the second vowel can start. However, the size and location of this window is different for
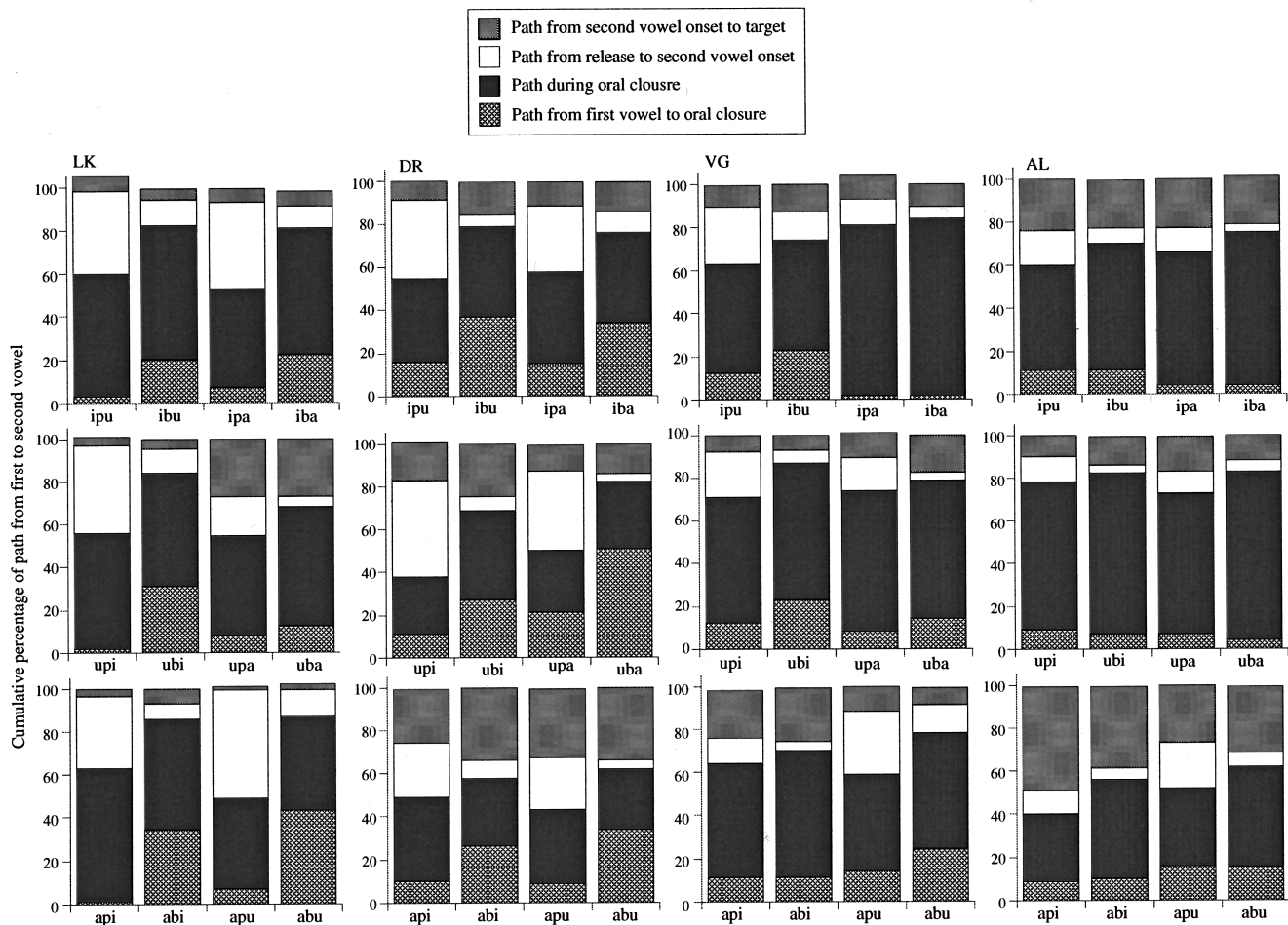
FIG. 9. The cumulative percentage of the tongue movement trajectory during four parts of the vowel–consonant–vowel sequence, shown in their order of occurrence from bottom to top: (1) from the onset of the tongue movement to the oral closure for the stop; (2) during the oral closure; (3) between the stop release and the onset of the second vowel; and (4) during the second vowel.

different subjects. In this respect, the present results are compatible with the proposal by Abry and Lallouache (1995) that anticipatory coarticulation should be modeled as a continuous variable that has to be adjusted for individual subjects.

It is thus apparent from the present results that speakers differ in their patterns of interarticulator programing. For example, one would draw a quite different conclusion about the phasing of the lip and tongue movements if one only studied the results for subject DR in Fig. 4, since she always had the tongue movement leading the lip movement. Similarly, by only focusing on the subset of the linguistic material where the first vowel was /i/, one would arrive at a different conclusion than if all the vowel contexts were examined.

In spite of this variability between subjects, there were several common patterns. The results shown in Fig. 5 indicate that the tongue movement trajectory was larger in the sequences /ipa, iba/ than in /api, abi/. Differences in the tongue body movement onset and offset positions for the same vowel occurring in the first or second position can account for these differences, as shown in Fig. 6. It would appear that the stress pattern of the word is mostly responsible for this difference. The tongue body positions are most different for the vowels /a, u/ when they occur as the first and second vowel in the VCV sequence but very small, or nonexistent, for the vowel /i/. Most likely, the increased duration

of the second vowel due to the stress pattern can explain the differential variability in tongue position for /a, u/ compared to /i/. In addition, the high front tongue position for the diphthong /ai/ in the carrier sentence might contribute to the small difference in tongue body position for the vowel /i/.

For all of the subjects, there was a clear tendency for the onset of the tongue movement to occur earlier with respect to the onset of the lip closing movement as the tongue movement trajectory increased (see Fig. 7). This is similar to the finding of Alfonso and Baer (1982) for the vertical and horizontal components of the tongue dorsum movement. As explained above, it proved difficult in the present experiment to consistently identify movement onsets from zero crossings in the horizontal and vertical velocity signals of the tongue body. When a movement onset could be identified, the interval between the onset of the vertical and horizontal component was 50 ms or less.

Although the onset of the tongue body movement is free to vary within certain limits, one might argue that the onset of the lip closing movement would be more constrained. This was indeed the case. Obviously, the onset of the lip closing movement must precede the oral closure and it never occurred more than 100 ms before the acoustically defined oral closure. An examination of the relationship between the onsets of the lip closing movement and the tongue movement

relative to the oral closure, pooled across consonant voicing and vowel contexts, showed that they tended to covary for three of the subjects, DR, VG, and AL ($r = 0.47$, 0.25, and 0.44), but not for subject LK ($r = 0.01$, ns). If the tongue movement starts well before the oral closure, one might expect that the speech could be compromised, because an ''extra'' vowel might be perceived. Similarly, an extensive tongue movement following the release of the stop could result in an ''extra'' vowel after the consonant. A perceptual study by Carré *et al.* (1996), using an acoustic model of the vocal tract, showed this to be the case. Possibly, the finding in the present study that most of the tongue movement trajectory took place during the stop closure is related to avoiding such effects. On the other hand, the specific hypothesis that the amount of tongue movement during the first vowel should be small when the movement started well before the stop closure was not supported by the data. For three of the subjects, the relative magnitude of the tongue movement during the first vowel was larger when the consonant was voiced than when it was unvoiced. This may be related to the commonly observed longer acoustic vowel duration before voiced consonants. Interestingly, subject AL did not show any such difference. Possibly, the reason the three native speakers of American English showed such an effect of consonant voicing is that such voicing conditioned differences of vowel duration appear to be larger in American English than in most other languages (e.g., Chen, 1970). We should add further that, in instances where anticipatory tongue movements have been observed to span large temporal intervals (e.g., Magen, 1997), the intervening vowels have been the schwa which may not have a clear articulatory specification.

In summary, the present study has shown that the timing of lip and tongue movements in the production of VCV sequences with a bilabial stop consonant is influenced by the magnitude of the tongue movement trajectory. Overall, the results are compatible with the hypothesis that there is a temporal window before the oral closure for the stop during which the tongue movement can start. The results are also generally compatible with the idea that extensive tongue movements before and after the stop closure are avoided so as not to create perceptual effects. Thus, more than 50% of the tongue movement trajectory between the two vowels occurred during the stop closure. The measurement techniques developed for this study will also be useful in the future to address the influences of other variables on the programing of lip and tongue movements, such as stress and prosodic boundaries.

ACKNOWLEDGMENTS

Abry, C., and Lallouache, T. (**1995**). ''Le MEM: un modèle d'anticipation paramétrable par locuteur, Données sur l'arrondisement en français,'' Bull. Comm. Parlée **3**, 85–99.

Alfonso, P., and Baer, T. (**1982**). ''Dynamics of vowel articulation,'' Language and Speech **25**, 151–173.

Bell-Berti, F., and Harris, K. S. (**1979**). ''Anticipatory coarticulation: Some implications from a study of lip rounding,'' J. Acoust. Soc. Am. **65**, 1268–1270.

Bell-Berti, F., and Harris, K. S. (**1981**). ''A temporal model of speech production,'' Phonetica **38**, 9–20.

Bell-Berti, F., and Harris, K. S. (**1982**). ''Temporal patterns of coarticulation: Lip rounding,'' J. Acoust. Soc. Am. **71**, 449–454.

Bell-Berti, F., and Krakow, R. A. (**1991**). ''Anticipatory velar lowering: A coproduction account,'' J. Acoust. Soc. Am. **90**, 112–123.

Benguerel, A. P., and Cowan, H. A. (**1974**). ''Coarticulation of upper lip protrusion in French,'' Phonetica **30**, 41–55.

Carré, R., Chennoukh, S., Jospa, P., and Maeda, S. (**1996**). ''The ears are not sensitive to certain coarticulatory variations: Results from VCV synthesis/perceptual experiments,'' in *1st ESCA ETRW on Speech Production Modeling and 4h Speech Production Seminar*, Autrans, pp. 13–16.

Chen, M. (**1970**). ''Vowel length variation as a function of the voicing of the consonant environment,'' Phonetica **22**, 129–159.

Clumeck, H. A. (**1976**). ''Patterns of soft palate movement in six languages,'' J. Phonetics **4**, 337–351.

Gay, T. J. (**1974**). ''A cinefluorographic study of vowel production,'' J. Phon. **2**, 255–266.

Gay, T. J. (**1977**). ''Articulatory movements in VCV sequences,'' J. Acoust. Soc. Am. **62**, 183–193.

Gracco, V. L., and Löfqvist, A. (**1994**). ''Speech motor coordination and control: Evidence from lip, jaw, and laryngeal movements,'' J. Neurosci. **14**, 6585–6597.

Houde, R. (**1968**). *A study of tongue body motion during selected consonant sounds*, Speech Communications Research Laboratory, Santa Barbara, SCRL Monograph 2.

Koenig, L. K., Löfqvist, A., Gracco, V. L., and McGowan, R. S. (**1995**). ''Articulatory activity and aerodynamic variation during voiceless consonant production,'' J. Acoust. Soc. Am. **97**, 3401.

Kollia, H. B., Gracco, V. L., and Harris, K. S. (**1995**). ''Articulatory organization of mandibular, labial, and velar movements during speech,'' J. Acoust. Soc. Am. **98**, 1313–1324.

Krakow, R. A. (**1989**). ''The articulatory organization of syllables: A kinematic analysis of labial and velar gestures,'' Unpublished doctoral dissertation, Yale University.

Löfqvist, A. (**1980**). ''Interarticulator programming in stop production,'' J. Phon. **8**, 475–490.

Löfqvist, A. (**1995**). ''Laryngeal mechanisms and interarticulator timing in voiceless consonant production,'' in *Producing Speech: Contemporary Issues. For Katherine Safford Harris*, edited by F. Bell-Berti and L. Raphael (AIP Press, Woodbury, NY), pp. 99–116.

Löfqvist, A., and Gracco, V. L. (**1997**). ''Lip and jaw kinematics in bilabial stop consonant production,'' J. Speech Hear. Lang. Res. **40**, 877–893.

Löfqvist, A., and McGowan, R. S. (**1992**). ''Influence of consonantal environment on voice source aerodynamics,'' J. Phon. **20**, 93–110.

Löfqvist, A., and Yoshioka, H. (**1981**). ''Interarticulator programming in obstruent production,'' Phonetica **38**, 21–34.

Löfqvist, A., and Yoshioka, H. (**1984**). ''Intrasegmental timing: Laryngeal-oral coordination in voiceless consonant production,'' Speech Commun. **3**, 279–289.

Löfqvist, A., Koenig, L. L., and McGowan, R. S. (**1995**). ''Vocal tract aerodynamics in /aCa/ utterances: Measurements,'' Speech Commun. **16**, 49–56.

Lubker, J., McAllister, R., and Lindblom, B. (**1977**). ''On the notion of interarticulator programming,'' J. Phon. **5**, 213–226.

Lubker, J. F. (**1981**). ''Temporal aspects of speech production: Anticipatory labial coarticulation,'' Phonetica **38**, 51–65.

Magen, H. (**1997**). ''The extent of vowel-to-vowel coarticulation in English,'' J. Phon. **25**, 187–205.

McGowan, R. S., Koenig, L. L., and Löfqvist, A. (**1995**). ''Vocal tract aerodynamics in /aCa/ utterances: Simulations,'' Speech Commun. **16**, 67–88.

Öhman, S. (**1966**). ''Coarticulation in VCV utterances: Spectrographic measurements,'' J. Acoust. Soc. Am. **39**, 151–168.

Perkell, J., and Matthies, M. (**1992**). ''Temporal measures of anticipatory labial coarticulation for the vowel /u/: Within- and cross-subject variability,'' J. Acoust. Soc. Am. **91**, 2911–2925.

Perkell, J., Cohen, M., Svirsky, M., Matthies, M., Garabiéta, I., and Jackson, M. (**1992**). ''Electromagnetic midsagittal articulometer (EMMA) systems

for transducing speech articulatory movements,'' J. Acoust. Soc. Am. **92**, 3078–3096.

Rubin, P. E. R., and Löfqvist, A. (**1996**). ''HADES (Haskins Analysis Display and Experiment System),'' Haskins Labs. Status Rep. Speech Res. (available at www.haskins.yale.edu/HASKINS/SR/sr.html).

Sussman, H. M., and Westbury, J. R. (**1981**). ''The effects of antagonistic gestures on temporal and amplitude parameters of anticipatory labial coarticulation,'' J. Speech Hear. Res. **24**, 16–24.

Westbury, J. (**1994**). ''On coordinate systems and the representation of articulatory movements,'' J. Acoust. Soc. Am. **95**, 2271–2273.

Westbury, J., and Hashi, M. (**1997**). ''Lip-pellet positions during vowels and labial consonants,'' J. Phon. **25**, 405–419.

Pitch accent in spoken-word recognition in Japanese

Anne Cutler[a)]
Max-Planck-Institute for Psycholinguistics, P.O. Box 310, 6500 AH Nijmegen, The Netherlands

Takashi Otake[b)]
Faculty of Foreign Languages, Dokkyo University, 1-1 Gakuen-cho Soka, Saitama 340, Japan

Three experiments addressed the question of whether pitch-accent information may be exploited in the process of recognizing spoken words in Tokyo Japanese. In a two-choice classification task, listeners judged from which of two words, differing in accentual structure, isolated syllables had been extracted (e.g., *ka* from *baka* HL or *gaka* LH); most judgments were correct, and listeners' decisions were correlated with the fundamental frequency characteristics of the syllables. In a gating experiment, listeners heard initial fragments of words and guessed what the words were; their guesses overwhelmingly had the same initial accent structure as the gated word even when only the beginning CV of the stimulus (e.g., *na-* from *nagasa* HLL or *nagashi* LHH) was presented. In addition, listeners were more confident in guesses with the same initial accent structure as the stimulus than in guesses with different accent. In a lexical decision experiment, responses to spoken words (e.g., *ame* HL) were speeded by previous presentation of the same word (e.g., *ame* HL) but not by previous presentation of a word differing only in accent (e.g., *ame* LH). Together these findings provide strong evidence that accentual information constrains the activation and selection of candidates for spoken-word recognition. © *1999 Acoustical Society of America.*
[S0001-4966(99)03003-9]

PACS numbers: 43.71.Es, 43.71.Hw [WS]

INTRODUCTION

A Japanese word spoken in isolation has a characteristic prosodic pattern: its pitch-accent pattern. In Tokyo Japanese, words can be accented or unaccented. In accented words, one mora of the word is marked as carrying accent and is assigned the accent label high (H). If the marked mora is the first in the word, subsequent morae will be labeled low (L): the pattern will therefore be HL for a two-mora word, HLL for a three-mora word, and so on. If the marked mora is the second or a later mora in the word, the first mora will be low, all other morae between the first and the accented mora will be high, and all morae after the accented mora will be low. Thus *Toyota* is a three-mora word (*to-yo-ta*) in which the first mora is accented: HLL; *Mitsubishi* has four morae (*mi-tsu-bi-shi*) with accent falling on the second mora: LHLL. In unaccented words the first mora is labeled L and all subsequent morae are labeled H; the pattern LHH can therefore describe both an unaccented word and an accented word with accent on the final mora. Unaccented words are refered to as type 0; type 1 words have accent on the first mora, type 2 on the second, and so on. Thus HLL is type 1; LHLL is type 2, and LHH is type 3 or 0.

In fact, the pitch accent system of Japanese is yet more complex than the above description suggests, and there is a large and lively literature on the question of how best to capture its regularities (e.g., Haraguchi, 1977, 1988; McCawley, 1977; Pierrehumbert and Beckman, 1988; Sugito, 1982). Particular controversies concern, for instance, the be-havior of accent in words beginning with a long vowel. However, none of the research reported in the present paper used these controversial cases, and the chief characteristic of the Tokyo Japanese accent system which is important for our study is unaffected by the phonological disputes. Words differ in pitch accent, and at least in CVCV-initial words the system described above implies that the first two morae cannot both be assigned the same pitch accent label. There are only two possible ways to label the initial two morae of such a word: HL- or LH-. Our research addresses the role of this word-initial accent distinction in the recognition of Tokyo Japanese.

Any distinction in word-initial position is potentially informative for our understanding of how human listeners recognize spoken words. Human word recognition is a highly efficient process. Relevant information about segment identity is exploited as soon as it becomes available, and it may become available as much as a whole syllable in advance (Martin and Bunnell, 1981, 1982). Coarticulatory information can lead to earlier identification of upcoming segments (Lahiri and Marslen-Wilson, 1991), and mismatching coarticulatory information can hamper recognition (Whalen, 1984, 1991; Marslen-Wilson and Warren, 1994; McQueen *et al.*, in press). We ask in this paper whether pitch-accent information in the initial portions of Japanese words can also be used in recognition as soon as it becomes available.

Psycholinguists usually conceive of the process by which spoken words are recognized as consisting of separable subparts. In the initial stage candidate words are activated by information in the signal; this process of activation is usually held to be bottom-up and not open to influence from higher levels of processing (Norris, 1994; Marslen-

---

[a)]Electronic mail: anne.cutler@mpi.nl
[b)]Electronic mail: otake@dokkyo.ac.jp

Wilson, 1987; but see McClelland and Elman, 1986). Activated word candidates then compete for recognition and a winning candidate emerges at this later competitive stage. Thus the input may activate many candidate words which are not actually present in the signal, and these will compete with and potentially slow the recognition of the actually spoken word (McQueen *et al.*, 1994); the more efficient the exploitation of different sources of information in the signal, therefore, the fewer such spurious competitors will be activated.

To be sure, listeners sometimes do not exploit potentially relevant information, particularly in the earliest stages of word recognition. The initial activation of word candidates in English does not appear to draw on stress information, for instance; word pairs which are distinguished by stress where this does not involve a vowel-quality difference, e.g., *FORbear* and *forBEAR*, are both initially activated irrespective of which one was spoken (Cutler, 1986). Since most stress differences in English in fact do involve vowel-quality differences—in the case of pairs such as *SUBject* and *subJECT*, or *REfuse* and *reFUSE*—it is apparently efficient enough for such vowel differences to be exploited in initial activation, enabling *SUBject* to be distinguished from *subJECT* in much the same way as *batter* from *better*, or *marine* from *maroon*, without additional exploitation of the suprasegmental cues which distinguish *FORbear* from *forBEAR*. Fewer than 20 minimal pairs in English are distinguished solely by suprasegmental structure, so that the failure to incorporate into the initial activation process any means of distinguishing them results in only a trivial increase in the already extensive number of homophonic word pairs in English (e.g., *match, angle, career*). Thus stress information may fail to be exploited in word recognition in English because it does not produce a significant and reliable effect on the number of activated candidate words.

In the present study we consider the question of whether initial pitch accent patterns play a role in the recognition of spoken words in Tokyo Japanese. The general efficiency of the word-recognition process, and all the evidence of early use of relevant information in the signal to constrain activation of candidate words, lead to the supposition that distinctive pitch-accent information in the initial portions of words may be exploited by listeners. And yet, it has been claimed that pitch accent is unimportant for recognition of Japanese utterances. Thus Shibata (1961, p. 19) writes: ''The reason why the dialectal differences [in accent] are so great, I believe, is that accent plays no very important role in communication;'' and Vance (1987, p. 107) maintains: ''There is little doubt that the functional load of accent distinctions in standard Japanese is very low... accent is probably the most difficult aspect of standard pronunciation for non-standard speakers to master, but incorrect accent patterns very seldom cause any confusion for listeners.''

One reason why this may be true is that pitch accent in Japanese certainly provides information other than that relevant to word recognition. One of the most salient characteristics of the pitch accent system is that it is dialectally variable. The two major dialect groups of Japan, Tokyo Japanese and Osaka Japanese, differ noticeably in pitch accent patterns. Thus pitch accent patterns constitute a major cue to a speaker's dialectal background, and listeners will be accustomed to exploiting pitch accent to gain such information about speakers. Pitch accent could, in consequence, be less important for word recognition due to the fact that it is usefully providing another sort of information. [''The primary importance of accent patterns is social rather than linguistic. Incorrect patterns mark a speaker as a nonnative of the Tokyo area'' (Vance, 1987, p. 107).] Note that Scott and Cutler (1984) showed that perceptual exploitation of a phonetic effect as a correlate of syntactic structure was not manifested by listeners for whom that same phonetic effect was a marker of sociolect.

Further, because pitch accent differences are signalled by $F0$, the information which they provide may only relatively slowly become available, so that activation of words may occur without reference to pitch accent information; Cutler and Chen (1997) showed that some tonal distinctions in Cantonese were perceptually available later than the segmental information distinguishing the vowels of the same syllable. A study by Walsh Dickey (1996) indeed suggests that pitch-accent processing is slow. In her experiment Japanese listeners were asked to make same–different judgments on pairs of CVCV words or nonwords; when members of a pair differed, it could be either on one of the four phonetic segments or in pitch accent. ''Different'' judgments were significantly slower for pairs differing in pitch accent than for pairs which differed segmentally, irrespective of the position of the segmental difference. Walsh Dickey argued that perception of the pitch accent could not be accurately determined until the second syllable since it could best be achieved by comparison of the two syllables. Note that Cutler and Chen's (1997) study of the perception of Cantonese tone also included a same–different judgment experiment, and also found that pairs differing in tone were judged more slowly than pairs differing in any segment.

However, the claim that pitch-accent information is not important to listeners in spoken-word recognition has hardly been put to direct experimental test. Nishinuma (1994; Nishinuma *et al.*, 1996) studied the classification of pitch-accent patterns by nonnative adult learners of Japanese; this task, like Walsh Dickey's (1996) same–different method, does not actually require word recognition. Otake *et al.* (1993) varied initial accent pattern in experiments in which listeners detected CV targets; responses to initial targets were equally rapid and accurate whether the word began with a HL- (e.g., *monaka*) or LH- (e.g., *kinori*) accent pattern, but, again, this tells us only that neither initial pattern causes listeners perceptual difficulty. In an earlier study we observed that Japanese listeners find cross-spliced words with a correct segmental sequence but an impossible accent pattern (one which could not occur in the language) hard to process (Otake *et al.*, 1996). The only study we could find which directly addressed the role of pitch accent in word recognition was by Minematsu and Hirose (1995). In two of the three experiments they report, native listeners were presented with misaccented speech. Misaccented words in isolation proved harder to recognize than their correctly accented counterparts; however, misaccenting had less effect in context than

in isolation. Their other study used the gating task, in which words are presented in successively larger fragments. Minematsu and Hirose do not state the actual stimuli used in this experiment, only that they were four-mora words with accent types 0, 1, and 2. They found that HL- words were recognized on the basis of less information than LH- words. As the four-mora vocabulary contains only about 7.5% HL-words (NHK, 1985), this result suggests that listeners were effectively using accent to rule out candidate words: HL-portions rule out more competitors than LH- portions do.

Experiment 2 below also uses the gating task, but in a way specifically designed to assess the contribution of pitch accent in spoken-word recognition. Experiment 3 addresses the same issue via another standard psycholinguistic lexical-processing task: lexical decision. Before describing those experiments, however, we report an initial study in which we investigated the domain of available accentual information. Cutler (1986) argued that English stress, where it involves no segmental correlate in vowel quality, can hardly be computed without comparison across syllables—thus English listeners can only tell whether the syllable *for-* comes from *FORbear* or *forBEAR* when they hear the word's second syllable and compare the relative stress levels of the two syllables. Walsh Dickey (1996), as described above, made exactly the same claim about the perception of pitch-accent patterns. If such cross-syllable comparison is indeed necessary, it could reduce the relative usefulness of pitch accent in constraining lexical activation. In experiment 1, therefore, we used a two-choice classification procedure to ask: Does a single CV syllable extracted from either syllable of a bimoraic/bisyllabic word contain sufficient accentual information to enable the accent pattern of the whole word to be accurately identified by listeners?

I. EXPERIMENT 1

A. Materials

Thirty-two words were chosen, all with the segmental structure CVCV (where V was always short), and each containing the mora/syllable *ka*. Half of the words had initial accent (HL), half did not (LH); in this and in the later experiments, accent assignment was checked against the Tokyo Japanese reference data given by Sugito (1995). For each pattern, in half of the words the syllable *ka* was word-initial, in half word-final. Each word was paired with another word with the contrasting accent pattern, such that the two members of a pair contained the same phonemic segment adjacent to the *ka* (e.g., *kage/kagi; baka/gaka*). The full set of words was: HL: *baka, buka, deka, huka, kika, naka, waka, yoka, kage, kagu, kako, kaku, kame, kare, kasa, kazu*; LH: *gaka, yuka, geka, nuka^, shika, haka^, taka, hoka, kagi^, kago, kake^, kaki, kami^, kara^, kase^, kaze*. The LH words marked with ^ have final accent, the others are unaccented.

All words were recorded by three female speakers of Tokyo Japanese, who were naive as to the purpose of the experiment. The 96 resulting productions were digitized, using the ESPS speech editing system with WAVES+, and the *ka* syllables were extracted from each production. These 96 *ka* tokens were recorded, in random order, onto digital audio

tape. Note that vowel-final short syllables produced in isolation are typically closed with a glottal stop, and this was the case in all 48 *ka*-final tokens; this glottal stop was included in the tokens on the tape.

The following nine acoustic measures were computed, using ESPS, for each syllable: minimum fundamental frequency ($F0$); maximum $F0$; $F0$ range; mean $F0$; standard deviation of $F0$; total syllable duration; vowel duration; mean rms amplitude; and standard deviation of rms amplitude. The $F0$ and amplitude measures were computed across the voiced portions of the signal only; aspiration following the /k/, and creak, if any, preceding the glottal stop, were not included in these measures, nor in the vowel duration measure.

B. Subjects

Twenty-four undergraduates of Dokkyo University participated in the experiment. All were native speakers of Japanese, from the Kanto area (Tokyo and environs, but excluding Ibaraki and Tochigi prefectures where dialectal differences from Tokyo Japanese can be observed in accent patterns). They received a small payment for participating.

C. Procedure

Subjects were tested individually or in pairs. They heard the tape containing the *ka* tokens from a JVC Victor DAT player over Audio-Technical ATH-A9 headphones, and were required to choose for each token between two words from which it might have come (e.g., *kage* HL versus *kagi* LH; *baka* HL versus *gaka* LH). These choices were written on the response sheet, in both kanji and hiragana orthography, and the subjects circled their choice for each token. Note that subjects were never asked to decide whether a syllable was word-initial or word-final; each choice was between two initial syllables (one H, one L) or between two final syllables (one H, one L). The choice was, further, always between the two members of a phonetically matched pair, minimizing the possibility that coarticulatory information adjacent to the *ka* boundary could provide clues to identify the source word. Each pair occurred on the response sheet six times (corresponding to the two source words spoken by each of the three speakers), and it was given three times in each possible order, with neither source word nor speaker keeping the same order.

D. Results

1. Perceptual judgments

The overall correct response rate was high (74%). Responses were more accurate for H (87%) than L syllables (61%; $F1[1,23]=72.75$, $p<0.001$; $F2[1,84]=97.63$, $p<0.001$), and for initial (80%) than final syllables (68%; $F1[1,23]=23.92$, $p<0.001$; $F2[1,84]=18.41$, $p<0.001$). There was no significant difference in response rate to final H syllables which were accented (80% correct) versus unaccented (85%).

There was, however, a significant effect of speaker, with speaker 1 receiving lower correct-identification scores (64%) than speakers 2 and 3 (78%, 79%; $F1[2,46]=17.51$, p

TABLE I. Mean values on eight acoustic measures (note: the ninth measure referred to in the text, $F0$ range, is the minimum-maximum $F0$ difference), and mean percent correct responses, for H versus L *ka* syllables in initial versus final position, for each speaker (S1, S2, S3).

	Minimum $F0$ (Hz)	Maximum $F0$ (Hz)	Mean $F0$ (Hz)	s. d. $F0$ (Hz)	Mean rms amplitude	s.d. rms amplitude	Total duration (s)	Vowel duration (s)	Percent correct responses
Initial syllables									
H									
S1	270	288	282	5.9	1326	274	1.34	0.83	96.4
S2	223	248	237	7.8	1004	283	1.29	0.87	83.9
S3	233	262	254	9.7	931	218	1.26	0.76	90.6
Mean	242	266	258	7.8	1087	258	1.30	0.82	90.3
L									
S1	200	231	215	8.4	1000	298	1.57	1.00	47.9
S2	176	209	188	10.5	694	169	1.31	0.76	80.2
S3	164	195	181	10.9	647	193	1.47	0.75	79.2
Mean	180	212	195	10.0	780	220	1.45	0.84	69.1
Final syllables									
H									
S1	221	254	239	9.0	1214	373	1.36	0.98	82.8
S2	184	212	193	8.0	882	143	1.34	0.88	86.5
S3	186	216	200	7.8	716	229	1.84	1.41	82.8
Mean	197	227	211	8.3	937	248	1.51	1.09	84.0
L									
S1	183	257	210	22.6	1003	353	1.31	0.84	30.2
S2	138	189	162	18.2	799	234	1.11	0.62	64.1
S3	159	241	187	24.0	569	312	1.88	1.52	63.0
Mean	160	229	186	21.6	790	299	1.43	0.99	52.4

<0.001; $F2[2,84]=13.02$, $p<0.001$). An analysis of the results excluding speaker 1 revealed that both the main effect of H/L (H 86%, L 72%) and the main effect of position (initial 84%, final 74%) remained statistically significant across the productions of speakers 2 and 3 ($F1[1,23]=18.24$, $p<0.001$, $F2[1,56]=20.01$, $p<0.001$ for H/L, $F1[1,23]=11.83$, $p<0.005$, $F2[1,56]=8.57$, $p<0.005$, for position).

Fifteen of the 96 items received scores below chance; all were L syllables mistakenly judged by the majority of subjects as H. Eleven of those were spoken by speaker 1. Of the fifteen items, eight had scores significantly below chance (9/24 or less); six of these (*ka* from *kago, baka, naka, buka, deka, yoka*) were spoken by speaker 1, and five of these were final L syllables. Thus this speaker (who, as shown below, had a notably high voice) systematically failed to produce clearly final-L syllables (not one of her eight final-L items was identified with accuracy significantly above chance). The other low-scoring items were from *kami, kasa, kaze, kase, kika* (speaker 1), *naka, deka, yoka* (speaker 2), and *yoka* (speaker 3).

Subjects scored less well in the first quartile of the experiment (66% correct) than in the following quartiles (76%, 75%, 79%); an analysis of variance showed a significant effect of quartile ($F1[3,59]=10.07$, $p<0.001$) and *t*-tests showed performance in the first quartile to be significantly worse than in each of the later quartiles, which did not significantly differ.

2. Acoustic analyses

Table I shows the mean value on each of the nine measures, separately for the four syllable types, for each speaker and averaged across speakers. Analyses of variance across the tokens were computed for each measure. The main focus of interest here is where acoustic differences between H and L syllables are to be observed, since the listeners' task in this experiment was in effect the H/L categorization.

Pitch: The five measures which we made of the pitch characteristics of the syllables revealed a simple and consistent pattern. The minimum, maximum, and mean $F0$ values for the syllables tended to pattern together: if one of these measures showed a significant difference between H syllables and L syllables, so did the others. Likewise, the two remaining measures, $F0$ range and standard deviation of $F0$ (both of which provide crude estimates of the amount of pitch movement across a syllable), also pattern together, and separately from the other set.

The minimum, maximum, and (therefore also the) mean $F0$ were all significantly higher in H syllables than in L syllables ($F0$ min: $F[1,28]=259.33$, $p<0.001$; $F0$ max: $F[1,28]=56.43$, $p<0.001$; $F0$ mean: $F[1,28]=310.78$, $p<0.001$), and were also significantly higher in initial than in final syllables ($F0$ min: $F[1,28]=107.75$, $p<0.001$; $F0$ max: $F[1,28]=9.08$, $p<0.01$; $F0$ mean: $F[1,28]=126.45$, $p<0.001$). On each measure there was also a significant interaction between H/L and position, whereby the H/L difference was greater in initial than in final syllables ($F0$ min: $F[1,28]=16.28$, $p<0.001$; $F0$ max: $F[1,28]$

$=64.34$, $p<0.001$; $F0$ mean: $F[1,28]=58.92$, $p<0.001$).

All three of these measures also showed a significant effect of speaker ($F0$ min: $F[2,56]=79.23$, $p<0.001$; $F0$ max: $F[2,56]=48.53$, $p<0.001$; $F0$ mean: $F[2,56]=104.49$, $p<0.001$). The source of this effect was that speaker 1 had a significantly higher voice, approximately 35 Hz higher on each $F0$ measure, than the other two. An analysis of the results for only the syllables of speakers 2 and 3 showed that all the main effects and interactions remained significant as reported above (for H/L: $F0$ min: $F[1,28]=121.39$, $p<0.001$; $F0$ max: $F[1,28]=22.34$, $p<0.001$; $F0$mean: $F[1,28]=128.6$, $p<0.001$; for position: ($F0$ min: $F[1,28]=54.15$, $p<0.001$; $F0$ max: $F[1,28]=6.57$, $p<0.02$; $F0$ mean: $F[1,28]=66.41$, $p<0.001$; for the interaction: ($F0$ min: $F[1,28]=6.35$, $p<0.02$; $F0$ max: $F[1,28]=24.33$, $p<0.001$; $F0$ mean: $F[1,28]=27.23$, $p<0.001$).

Both the $F0$ range and the standard deviation of $F0$ were significantly greater for L than for H syllables ($F0$ range: $F[1,28]=52.12$, $p<0.001$; $F0$sd: $F[1,28]=59.61$, $p<0.001$), and significantly greater in final than in initial syllables ($F0$ range: $F[1,28]=43.82$, $p<0.001$; $F0$sd: $F[1,28]=36.37$, $p<0.001$). The interaction was also significant (greater H/L differences in final than in initial syllables; $F0$ range: $F[1,28]=22.99$, $p<0.001$; $F0$sd: $F[1,28]=30.58$, $p<0.001$). On neither of these two measures was there a significant effect of speaker.

Duration: Neither durational measure showed significant H/L differences. Final syllables were longer than initial (overall: $F2[1,28]=4.9$, $p<0.05$; vowel: $F2[1,28]=29.8$, $p<0.001$).

Amplitude: H syllables had significantly greater mean amplitude than L syllables ($F[1,28]=10.85$, $p<0.005$). There was no difference between initial and final syllables, or interaction between H/L and syllable position. The standard deviation of amplitude showed no main effect of either variable. However, there was again an effect of speaker on both amplitude measures (mean: $F[2,56]=64.61$, $p<0.001$; s.d.: $F[2,56]=31.92$, $p<0.001$), and again, this was due to deviance of the productions of speaker 1, who spoke significantly louder than the others.

3. Correlations

To obtain a uniform measure of listeners' performances, the responses were converted to percentage H judgments, that is, the percentage of correct responses for syllables which actually were H, and the percentage of error responses for those which actually were L. Correlation coefficients were then computed across mean H responses per item and the acoustic measures obtained for each item.

Over all 96 tokens, there were significant positive correlations between H responses and four of the nine acoustic measures: subjects were more likely to decide that a syllable was H when it had high minimum $F0$ ($r[95]=0.66$, $p<0.001$), high maximum $F0$ ($r[95]=0.52$, $p<0.001$), high mean $F0$ ($r[95]=0.67$, $p<0.001$), and high mean amplitude ($r[95]=0.38$, $p<0.001$). There were significant negative correlations with two other measures: subjects were

more likely to decide that a syllable was H when it had low $F0$ range ($r[95]=-0.32$, $p<0.002$) and low $F0$ standard deviation ($r[95]=-0.38$, $p<0.001$). These correlations suggest that high absolute $F0$ and high amplitude signaled a H syllable; pitch movement signaled a L syllable.

Responses to initial syllables showed the same pattern of relationship to $F0$ and amplitude as displayed in the overall correlations ($F0$ min: $r[47]=0.86$, $p<0.001$; $F0$ max: $r[47]=0.89$, $p<0.001$; $F0$ mean: $r[47]=0.91$, $p<0.001$; $F0$ range: $r[47]=-0.30$, $p<0.04$; $F0$ sd: $r[47]=-0.29$, $p<0.05$; rms-mean: $r[47]=0.50$, $p<0.001$), while only four of the six significant correlations in the overall analysis were significant for final syllables ($F0$ min: $r[47]=0.66$, $p<0.001$; $F0$ mean: $r[47]=0.52$, $p<0.001$; $F0$ range: $r[47]=-0.55$, $p<0.001$; $F0$ sd: $r[47]=-0.66$, $p<0.001$). The pattern of correlation was furthermore not the same for each speaker. Responses to all three speakers' productions correlated in the same way with the $F0$ measures, but only the responses to the productions of speaker 2 showed a statistically significant relationship to amplitude.

Nor was the pattern the same for H versus L syllables separately. The likelihood of H responses to syllables which actually were H correlated only with the maximum and the mean $F0$, and only relatively weakly: $F0$ max: $r[47]=0.29$, $p<0.05$; $F0$ mean: $r[47]=0.32$, $p<0.05$. In contrast, the likelihood of H responses to syllables which actually were L correlated with minimum $F0$ ($r[47]=0.37$, $p<0.01$), with maximum $F0$ ($r[47]=0.43$, $p<0.002$) and with mean $F0$ ($r[47]=0.44$, $p<0.002$), plus a marginal correlation with mean amplitude ($r[47]=0.25$, $p<0.09$).

E. Discussion

It is clear that Japanese listeners can determine with a high degree of success from which of two accentually different bisyllabic words a single syllable has been extracted. Overall, there was a higher percentage of correct responses for H than for L syllables, and there were somewhat lower correlations of responses to H syllables with acoustic factors; these two aspects of the results may reflect a bias towards treating the single syllables as monomoraic isolates marked H [note that of Japanese monomoraic words, 70% have type 1 accent (NHK, 1985)].

We expected that listeners' judgments would principally be based on $F0$ values, and the pattern of correlations is certainly consistent with such an interpretation: syllables with high absolute $F0$ were judged H, syllables with $F0$ movement were judged L. Listeners can also make some use of the amplitude. Durational factors seem to play little role in signaling whether a syllable is H or L.

However, not all speakers are equally successful at conveying the H/L difference. Our speaker 1 produced these two syllable types in a less differentiated way than speakers 2 and 3, and correspondingly she received a lower mean percentage of correct responses from the listeners. Recall also that scores were lower at the beginning of the experiment than at the end, i.e., listeners seemed to have been learning the task. It could be that part of this involved learning about the characteristics of the particular speakers' voices. Speaker 1 spoke with a higher-pitched voice than the other two speakers did,
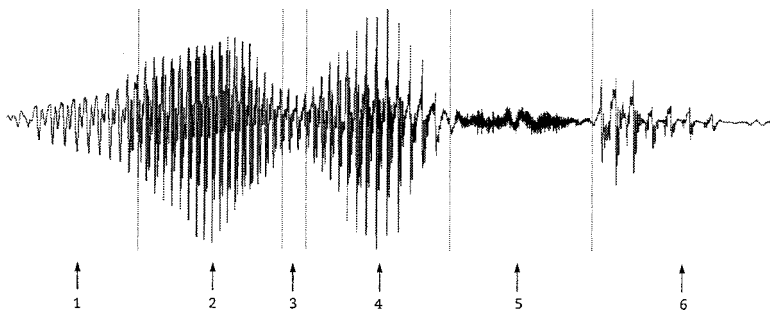
FIG. 1. How the gating fragments were prepared in experiment 2, illustrated on the word *nagasa*. The boundaries of the six phonetic segments were marked, then a marker was placed at the midpoint of each segment. Fragment 1 included the carrier plus the word up to the midpoint 1, fragment 2 the carrier plus the word up to the midpoint 2, and so on. ''Fragment'' 7 consisted of the carrier plus the entire word.

and this too, may have influenced the success with which her productions were judged; the response rates may have been more uniform had all speakers had comparable $F0$. Certainly the inconsistency among speakers which we observed suggests that listeners cannot rely on clear information being immediately available from all speakers.

Perhaps the most interesting aspect of the present results, however, is that cues to the H/L distinction are better conveyed in initial than in final syllables. The acoustic measures showed greater H/L differentiation in initial than in final syllables; the overall percentage correct was higher for initial than for final syllables; and the correlations between responses and acoustic factors were stronger in initial than in final syllables. This suggests that pitch accent information may already be available to listeners in just the position where it would be of most use to them in distinguishing spoken words. The question of whether listeners are, in fact, able to exploit the available cues to this purpose is addressed in experiment 2 via a gating task, in which we can examine the lexical hypotheses which listeners entertain when they are presented with fragmentary information about the initial portions of a word.

II. EXPERIMENT 2

A. Materials

Twenty-four pairs of Japanese words were selected. Within each pair, the two words began with the same initial bimoraic CVCV sequence, again with V always short, but differed in segmental structure from the fifth segment (third mora) on. The accent pattern of the two words also differed; in one word the initial CVCV sequence was HL, in the other LH. In this way we made sure that the initial segmental information alone could not determine listeners' word guesses. Thus *nagasa* and *nagashi* formed a pair; both begin *naga-*; the accent pattern of *nagasa* is HLL, while *nagashi* is LHHˆ. There were 22 pairs with three morae, and 2 with four morae; no words contained moraic nasals, geminate consonants, or long vowels. The complete set of pairs (in HL-/LH- order) was: *bakufu/bakuchi, hanabi/hanawa, hokubu/hokuro, kamotsu/kamome, karafuru/karamatsu, karasu/karada, karuteru/karudera, kasegi/kasetsu, kokugi/ kokugo, maguchi/maguro, moguri/mogura, mokuba/mokuji, nagasa/nagashi, namida/namiki, nimotsu/nimono, nomichi/ nomiya, sashizu/sashiki, sekiri/sekiyu, tachiba/tachiki, tomato/tomari, wakaba/wakate, wakame/wakare, warabi/ waraji, yomichi/yomise*. All but four LH- words (*nagashi* LHHˆ, *nomiya* LHL, *karudera* LHHHˆ, *wakare* LHHˆ) were unaccented.

A further 24 words were selected to serve as practice and warmup items. Some of these fillers contained moraic nasals, geminate consonants, or long vowels. Twelve were three-mora words (eight LHH, four HLL), and twelve four-mora (six LHHH, four HLLL, two LHHL).

All words were recorded by a male native speaker of Tokyo Japanese, in a short carrier phrase *Sore wa...* (''It is...''). The speaker avoided fully devoicing potentially devoiced vowels in the first two morae of the words, so that $F0$ measures could be undertaken. A gated version of each word was made, in which the word was presented in increasingly large fragments. The carrier phrase was always included [as preceding context greatly facilitates recognition of the segmental identity of very short fragments of Japanese speech (Kuwabara, 1982)], and the word fragments incremented by phoneme transitions. To achieve this, the segments of each word were labeled such that the portion of the signal carrying information about each phoneme was demarcated as closely as could be ascertained; this was achieved by a combination of visual inspection of the waveform and auditory judgment. A marker was then placed at, as near as could be determined, the midpoint of each such demarcated region. Each additional fragment then added a portion of the word up to the next marker. (Most cuts were made on a zero crossing; otherwise, the offset of the signal of a fragment was ramped to avoid abrupt amplitude changes which might lead to the perception of illusory clicks. The ramping was achieved by multiplying the fragment's final frame with a mask consisting of a linear ramp from 1.0 to 0.0.) Thus the word *nagasa* was presented in seven fragments; fragment 1 contained the carrier plus transition into the initial phoneme, fragment 2 continued into the first vowel, fragment 3 into the second consonant, fragment 4 into the second vowel, fragment 5 into the third consonant, fragment 6 into the third vowel, and fragment 7 contained the whole word. The advantage of this procedure, over a procedure in which successive fragments are incremented by a constant temporal interval, is that each fragment is guaranteed to contain more relevant phonetic information than the preceding fragment, and that the (perceptually informative) transitions from one segment to the next are minimally disrupted. Figure 1 illustrates the gating procedure.

Two experimental tapes were made, each containing all filler words and one member of each experimental pair. Ac-

cent pattern was counterbalanced across tapes; each tape contained 12 HL- and 12 LH- experimental words, and the members of any pair occurred at the same position on both tapes.

B. Subjects

Thirty-six undergraduate members of Dokkyo University participated in the experiment, in return for a small payment. All were native speakers of Tokyo Japanese from the Tokyo metropolitan area or Kanegawa, Saitama, or Chiba prefecture. None had taken part in experiment 1. Eighteen participants heard each experimental tape.

C. Procedure

The listeners were tested individually or in groups of two to five. The words were again presented over headphones from a DAT player; the tape was stopped after presentation of each fragment to allow time for the listener to record a guess as to the word's identity, along with a confidence rating for that guess. The guesses were written on a response form in normal Japanese orthography, and the confidence ratings were recorded by circling a number on a scale of 1 to 5, with 1 representing no confidence and 5 representing complete certainty.

An important determinant of guessing responses in a task such as this is word frequency, or familiarity. Thus we wished to compare the relative familiarity of the actual target words and the words guessed by the listeners. However, we could find no published frequency norms for Japanese containing all the relevant words. Accordingly we collected relative familiarity judgments for all guessed words and targets from a separate group of 45 subjects, none of whom had participated in the listening tasks. These subjects judged for 1033 pairs of items (1033 separate word guesses collected in the experiment below, with in each case the actual word that was being presented when the guess was produced) which member of the pair was the more familiar word to them. The average ratings computed across subjects for each item pair allowed us to make the requisite comparisons.

When the gating task is used to study the word recognition process, three dependent variables may be evaluated (Grosjean, 1996): the point at which the spoken word is definitively recognized, the confidence ratings assigned to correct guesses as a function of amount of information available, and the nature of the candidate words proposed at each point in the stimulus presentation. In the present study, the recognition of the spoken word was not the focus of interest; the first of these dependent variables was therefore not relevant. Instead, we used the task to assess listeners' recognition of accent pattern; in particular, we wished to know whether listeners made effective use of the accentual cues available in the initial bimoraic portion of each stimulus pair (such as *naga-* in *nagasa* HLL and *nagashi* LHH), a portion which was segmentally matched but accentually different. This question is most directly addressed by analyzing the candidate word guesses produced by listeners at fragments 1, 2, 3, and 4, and in particular by comparing the accent pattern of these candidate words for target words beginning HL- and
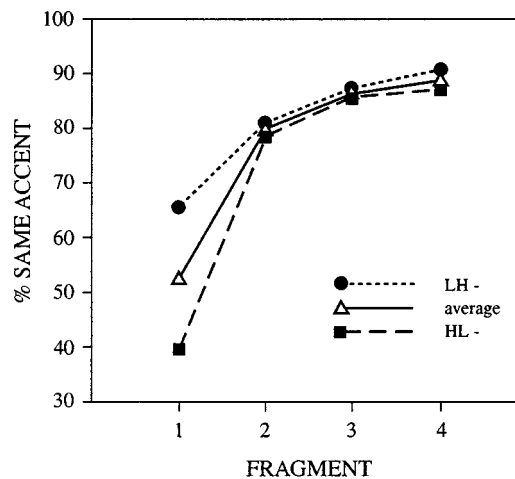
FIG. 2. Experiment 2: Proportion of guessed words with same initial accent pattern as the spoken word.

LH-. From fragment 5 onwards, segmental information could distinguish the members of the word pairs; for the first four fragments, however, the only distinguishing information was accentual.

Acoustic analyses of the initial bimoraic portions were carried out in the same manner as in experiment 1, in order to explore what cues listeners would use to guide their word guesses (in particular, should there prove to be considerable interitem variability in the proportion of accentually correct word guesses).

The confidence ratings of accentually correct versus incorrect guesses were also compared, as well as the rated familiarity of accentually correct versus incorrect guesses in comparison to the target word.

D. Results

1. Accent recognition

The word guesses were scored by hand and the accent pattern of each guess ascertained. Since the initial bimoraic (segmentally ambiguous) portion was the crucial focus of interest, only the corresponding initial portion of the accent pattern of each guess was considered. In effect, this resulted in a two-way classification of alternative ''initial accent patterns:'' type 1 (HL-) versus all other (LH-, including types 0, 2, and 3) patterns. Thus for *nagashi* LHH^, guesses such as *nagai* LHL and *namae* LHH (unaccented) were scored as accentually correct. Figure 2 shows the proportion of guesses which had the same initial accent pattern as the spoken word, for each of the first four fragments, separately for HL- and LH- words, and averaged across these.

At fragment 1, which contained information only about the initial consonant of the word, 52.66% of guessed words had a correct initial accent pattern. This number was not significantly different from chance, which is 50% for this two-way classification ($z = 1.53$, $p > 0.05$). It can be seen that in fact LH- words produce more guesses with the correct accent pattern than HL- words at this point. This is presumably the expected lexical type frequency effect: the vocabulary contains approximately 60% LH- to 40% HL- words (NHK, 1985).

At fragment 2, which contained information as to the initial CV mora, 79.63% of guessed words had a correct initial accent pattern, and this was significantly higher than would be predicted by chance ($z = 17.38$, $p < 0.001$). It is thus obviously the case that as soon as any vocalic information was available, subjects were able to use it to extract accent information. Note that virtually never were the word guesses which subjects produced on the basis of such minimal information actually correct; but they did manifest the correct initial accent pattern. Thus the 18 listeners given *nagasa* HLL guessed for the second fragment (*na*-) 16 different words, all different from *nagasa*: *nabe nagashi naifu naito naka nakai nama namida nanzan napukin Nara Narita Naruse NASA nasu Natoo*. The initial accent pattern of 14 of these guesses is HL-; only two (*nagashi nakai*) begin LH-. It is clear from this list that segmental information was well perceived; indeed, for fragment 2, for example, 94.09% of guesses began with the correct consonant and 98.27% had the correct vowel, both types of segmental information being significantly better represented in the guessed words than the accentual information ($t[47] = 5.31$ for consonants, 8.65 for vowels, both $p < 0.001$).

The proportion of guessed words with correct accent pattern continued to show further small increments across fragments 3 and 4: 86.57% and 88.88% correct, respectively. The arrival of distinctive segmental information in fragment 5 considerably narrowed the range of subjects' guesses, and nearly all words were recognised by all listeners by the sixth fragment. Note that some pairs, e.g., *karuteru karudera*, involved more fragments than in Fig. 1.

2. Acoustic analyses and correlations

The analysis of the $F0$ characteristics of the initial bimoraic portions of the words showed, as in experiment 1, a significant difference between H and L syllables. The H syllables in word-initial position had a mean $F0$ of 190.7 Hz with a standard deviation of 15.1 Hz, while L word-initial syllables had a mean $F0$ of 116.3 Hz with a standard deviation of 6.8 Hz (recall that the speaker in this case was a male). The average minimum, maximum, and range measures were also significantly higher for H than L syllables ($F0$ min: $t[46] = 7.79$, $p < 0.001$; $F0$ max: $t[46] = 24.43$, $p < 0.001$; $F0$ range: $t[46] = 3.3$, $p < 0.002$; $F0$ mean: $t[46] = 18.53$, $p < 0.001$; $F0$ sd: $t[46] = 3.89$, $p < 0.001$).

There was, however, no significant correlation between acoustic measures and the accent patterns of guesses at fragment 2, at which these differences in the first syllable are first available. This probably reflects the fact that the proportion of responses with correct accent pattern was already so high that there was no scope for interitem variation through which effects of the acoustic information could be observed. One correlation with the fragment 3 responses reached our criterion (0.05) of statistical significance: for words beginning LH-, the greater the standard deviation of $F0$ across syllable 1, the higher the proportion of responses with LH-accent patterns ($r[23] = 0.44$, $p < 0.04$). This is in line with the results of experiment 1 in which pitch movement was associated with L judgments to isolated syllables.
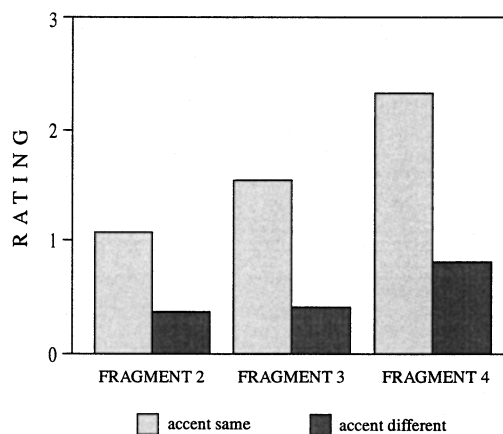
FIG. 3. Experiment 2: Confidence ratings for incorrect word guesses with same initial accent pattern as spoken word versus differing pattern.

3. Confidence ratings

Figure 3 shows listeners' confidence ratings for incorrect word guesses at fragments 2, 3, and 4. Although listeners were well aware that these fragments do not suffice to discriminate words, so that their confidence in their guesses was in general very low, they were nevertheless significantly more confident in guesses with the same initial accent pattern as the spoken word (mean rating 1.67) than in guesses with different accent (mean 0.5; $t[95] = 7.71$, $p < 0.001$).

4. Familiarity

The relative familiarity judgments for the guessed words and targets were analyzed. Here 63% of guesses were rated higher in familiarity than their targets. However, the strength of this familiarity effect was not significantly different for words which had the same initial accent pattern as their targets (61.5% more familiar) than for words which had different accent than their targets (65% more familiar).

E. Discussion

Experiment 2 has shown that even partial presentation of the first vowel of a word is sufficient for listeners to ascertain the initial accent pattern of a spoken Japanese word in nonconstraining context, and to use this information to restrict the word candidates which they consider possible continuations of this fragment.

In our third experiment we use a response-time measure to address the question of whether activation of word candidates in spoken-word recognition is constrained by pitch-accent information. The task which we use is auditory lexical decision (Goldinger, 1996), in which listeners' response time to decide whether a spoken string is a real word is measured. In this task, repeated presentation of a word leads to accelerated responses on the second presentation (''repetition priming''). As described in the introduction, minimal stress pairs in English (*FORbear–forBEAR*) are both activated when either one is heard. Minimal pitch-accent pairs in Japanese also exist, such as *ame* which with HL accent means ''rain'' and with LH accent ''candy.'' If either form activates both lexical representations, as in English, then presentation of one member of a pair (e.g., *ame* HL) should produce

repetition priming for a subsequent presentation of the other member (e.g., *ame* LH). However, if pitch-accent information fully constrains lexical activation, repetition priming should be affected only by the same word, not by its minimal pair. Experiment 3 tested this issue.

III. EXPERIMENT 3

A. Materials

Twenty-four minimal accent-pairs of bimoraic bisyllabic words were chosen. The complete set was: *ame, chiri, kaki, kiji, michi, mushi, sake, shiro, washi; aka, asa, ashi, hashi, ichi, ima, ishi, kame, kami, kata, mesu, seki, sumi, toshi, umi.* One member of each accent pair was initially accented (HL), while the other was either LH unaccented (the first 9 pairs in the list) or LH accented on the second mora (the remaining-15 pairs).

One hundred other words were chosen to serve as control and filler words. Twenty-four of these were bimoraic/bisyllabic and were used as control words; the remaining words could be two, three, or four morae in length, and some contained long vowels, moraic nasals, or geminate consonants. One hundred and eight nonwords were also constructed; these were constructed to resemble the filler words in phonological structure.

All words and nonwords were recorded by a female native speaker of Tokyo Japanese, and digitized. Six running orders (tapes) were constructed; each contained all filler words and all nonwords, in the same order. For each accent-pair, one member served as target on three tapes and the other on the other three tapes; each tape contained 12 HL and 12 LH experimental target words. Each set of three tapes on which a given target word occurred differed in the nature of the prime word which preceded the target; on one tape the prime was (a different token of) the same word as the target (e.g., *ame* HL was preceded by *ame* HL), on another tape it was the accent pair (e.g., *ame* HL was preceded by *ame* LH), and on the third tape it was the control word (e.g., *ame* HL was preceded by *eki* HL). The nature of the prime was counterbalanced across tapes for each experimental word accent pattern. The prime preceded the target immediately or with one, two, or three intervening items; this factor was also counterbalanced with the other variables. Each running order was copied to DAT tape and timing marks were placed at the onset of each item.

B. Subjects

Ninety undergraduate members of Dokkyo University participated in the experiment, some for course credit and some for a small payment. Again, all were native speakers of Tokyo Japanese from the Tokyo metropolitan area or Kanegawa, Saitama, or Chiba prefecture, and none had participated in experiments 1 or 2. Fifteen subjects heard each of the six running orders.

C. Procedure

Subjects were tested individually or in pairs. The stimuli were presented over headphones from a DAT recorder as

TABLE II. Experiment 3: Mean response times (ms) to decide that target is a word, as a function of preceding presentation of same word, accent pair, or control word.

	Prime type		
	Same word	Accent pair	Control
HL words	751	795	781
LH words	761	821	781
Mean	756	808	781

before. Subjects were seated in front of two response keys in a quiet room. They were instructed to decide for each item as quickly as possible whether or not it was a real word of Japanese, and to press the YES response key to signify a positive decision, the NO response key for a negative decision. Only YES responses were recorded. Timing and data collection were controlled by a Toshiba computer running the NESU experimental control software.

D. Results and discussion

The response times were subjected to separate analyses of variance with subjects and with items as random factors. Missing responses were replaced by the mean for the relevant subject in the relevant condition. Miss rates were not analyzed because the proportion of missed data was very low (4.5% of the total including responses which were lost due to equipment malfunction as well as failures to respond and erroneous decisions). The mean RTs across items and subjects are presented in Table II.

The statistical analyses revealed a main effect of prime type ($F1[2,168]=14.78$, $p<0.001$; $F2[2,46]=10.04$, $p<0.001$). *Post hoc* analyses showed that decisions to target words when the target had been preceded by itself as prime were significantly faster than when it had been preceded by a control word ($t1[89]=2.27$, $p<0.03$; $t2[47]=2.25$, $p<0.03$) or when it had been preceded by its accent pair ($t1[89]=4.56$, $p<0.001$; $t2[47]=3.71$, $p<0.001$); the difference between the accent-pair prime condition and the control condition was significant across subjects but not across items.

There was no significant effect of the lag between prime and target, and no significant effect of the target word's pitch-accent pattern, nor did either of these factors interact with the prime-type-effect. There was also no significant effect of the tapes variable, which was included in the analysis by subjects. An additional unequal-*N* analysis across items compared the HL/LH-accented pairs with the HL/LH- unaccented pairs; this accent-type factor had no effect itself and did not interact with any other factor, including prime type.

The experiment thus revealed no facilitation of lexical-decision responses as a result of prior presentation of a word's minimal accent pair. Only prior presentation of the word itself produced repetition priming. This result indicates that HL/LH minimal accent pairs do not facilitate recognition of one another's lexical representations, which in turn suggests that pitch accent information constrains lexical activation.

IV. GENERAL DISCUSSION

Results from three experiments have clearly demonstrated that the pitch-accent information available in spoken Tokyo Japanese words can be, and is, exploited by listeners in the process of word recognition. In experiment 1 listeners were easily able to assign a syllable to one of two word choices on the basis of accentual structure. In experiment 2, listeners used accentual information to guide their guesses of completions of partial word fragments, and they were more confident in guesses with the same accentual structure as the word from which the fragment actually came in than in guesses with different accentual structure. In experiment 3, repetition priming for a spoken word was exercised by its own representation but not by that of its minimal accent pair. Accent information constrains the activation and selection of word candidates in the process of spoken-language recognition by human listeners.

This contradicts the suggestion, referred to in the Introduction, that Japanese pitch accent has little importance for word recognition, and instead confirms the suggestion, based on the earlier findings of Minematsu and Hirose (1995), that listeners actively use this information. It also demonstrates that the recognition of Japanese words is sensitive to nonsegmental information in a way that the recognition of English words apparently is not. As described in the introduction, lexical stress in English appears to play no role in word activation (Cutler, 1986). However, recent results demonstrating that lexical processing is constrained by stress in a language otherwise closely similar to English, namely Dutch (Koster and Cutler, 1997; van Donselaar and Cutler, 1997), suggest that the situation of English is rather unusual [probably because of the very strong correlation of English stress with vowel quality (see Cutler *et al.*, 1997)]. Thus Japanese is allied with many other languages in that word activation can draw on nonsegmental information. The correlations between listener performance and the various $F0$ measures which we report above in experiment 1 suggest that it is the suprasegmental factors of pitch level and pitch movement that listeners are drawing on to derive accentual constraints on word identity. The results of experiment 2 show that this information is exploited very early: short CV syllables, truncated midway through the vowel, provide sufficient cues to the distinction between words beginning HL- versus LH-. This is consistent with research on the perception of tone in Norwegian and in Chinese showing similarly that suprasegmental information can be exploited even in very short speech fragments. Thus Efremova *et al.* (1963) found that Norwegian listeners needed only part of a syllable to distinguish, in a forced-choice task, between two forms of the same verb differing in tonic accent (signaled in Norwegian via fundamental frequency variation). Similarly, Tseng (1990) found that tones on isolated Mandarin Chinese vowels could be correctly identified in fragments comprising only the initial 25% of the vowels; and even though the Cantonese listeners in Cutler and Chen's (1997) experiment responded more rapidly to segmental distinctions than to tonal distinctions, they still made use of the tonal information as early as it became available. In experiment 2, likewise, word-initial segmental structure was perceived even

more accurately than accentual structure, but a very short fragment of speech still provided significant information about accent.

As we pointed out in the Introduction, little research has previously addressed the role of Japanese accent in the process of word recognition. Walsh Dickey's (1996) study used a same–different judgment task, and thus did not actually require lexical processing. Hirose *et al.* (1993) report, as well as the pilot version of work reported by Minematsu and Hirose (1995), a gating experiment in which synthesized versions of four-mora real words and nonwords with various accent patterns were presented to listeners; the smallest fragment included the boundary of the third and fourth morae, and the fragments increased in duration outwards from that point. The listeners in their experiment were not asked to name the words, however; they were required to identify the accentual pattern (and were able to do so, usually without needing to hear the entire word). Similarly, Nishinuma's (1994; Nishinuma *et al.*, 1996) experiments with non-native listeners required explicit identification of the accent pattern. In our experiments, however, the listeners never suggested that they were aware that our research was centered on the role of accentual information. All the tasks which we used involved decisions about words, and the participants in our experiments simply engaged, as instructed, in lexical processing. Insofar as our study can be compared directly with that of Minematsu and Hirose (1995), our results are in accord with theirs; their finding that words in isolation were significantly harder to identify when misaccented also suggests that accentual patterns constrain word activation.

The experimental materials in our study were deliberately confined to simple cases in which the manifestations of pitch accent could be easily observed. In experiment 1 we used only words with the structure CVCV in which all vowels were short; the overlapping parts of the experimental pairs in experiment 2 again had just this structure; and the minimal pairs of experiment 3 were either CVCV or VCV, once more with only short vowels. None of our experimental items contained nasal morae, geminates, or long vowels; in future work it will clearly be interesting to extend our investigations to these other phonological structures. In our experiments we also avoided as far as possible the occurrence of devoiced syllables, in which the manifestation of accent has been the subject of considerable attention (see e.g., Maekawa, 1990). Note, however, that by examining only the clear cases we have nevertheless produced a finding which can generalize to the majority of Japanese utterances. Of all the possible Japanese morae (defined in terms of separate IPA transcriptions) 60% in fact have the structure CV; Otake (1990) computed that CV morae accounted for over 70% of mora tokens in actual speech samples.

Limits on the generality of our findings may arise, of course, from other factors. As mentioned in the Introduction, accent patterns vary across dialect. Some dialects, in fact (especially those spoken in the northern part of Japan, such as the Ibaraki and Tochigi provinces), do not manifest accent variation. Speakers of these dialects would thus presumably not behave exactly as the listeners in the present study. Whether speakers of nonaccentual dialects would display

sensitivity to accentual information in recognizing words in Tokyo Japanese and other accentual dialects is as yet an open question. In the present study we were careful to confine our materials, and the dialects spoken by our listeners, to one variety: Tokyo Japanese. We see no reason in principle why our results should not generalize to other accentual varieties, however.

A substantial minority of (especially) longer words [about 10% (Shibata, 1961)] can have more than one possible accent pattern (although a given speaker will tend to use only one of them, just as a speaker of English may choose between stress patterns as in *CONtroversy* versus *conTROversy*). Such factors could, again, reduce the value of accentual information for lexical access, making it (like, in fact, most information in the speech signal) not fully deterministic, but probabilistic in nature.

Additional reservations which must be maintained pending further investigations include the practical usefulness of accentual information in natural continuous-speech contexts. For instance, preceding context can cause assimilation of accent patterns, as when the accent of the initial mora of *kodomo* LHH ''child'' can be raised from L to H in *kono kodomo* LH HHH ''this child'' (Hattori, 1960). Pitch accent patterns of words can also interact with following speech context. In particular, the distinction between final-accented and unaccented words becomes realised in context, in that the two accent types exercise differing effects on a following phonologically weak element such as a particle: an accented final mora will force L accent on the following element but an unaccented final mora will not. This final-accented versus unaccented distinction plays a central role in the challenge which Pierrehumbert and Beckman's (1988) autosegmental/ metrical account of the pitch-accent system poses to earlier views. Pierrehumbert and Beckman support their model with extensive phonetic data, and there is phonetic evidence (e.g., Maekawa, 1990, 1995; Kubozono, 1993; Warner, 1997) supporting their analysis [but see Vance (1995) for phonetic support for the alternative view].

Our findings, however, crucially concern word-initial accent effects, and although there is disagreement on how these should be described—as successions of different markings (HL versus LH) or as different associations of tones (L%-HL-L versus L%-H-HL)—there is no controversy as to the existence of pitch-accent differences in the initial portions of Japanese words. Moreover, the robustness of the pitch-accent effects which we have observed in a variety of word processing tasks does not suggest exploitation of accentual information to be a resource with only very limited application in language recognition.

One as yet unanswered question concerns the fine detail of our general demonstration that listeners are able to exploit pitch-accent patterns in word recognition. We have in the present experiments addressed only the crudest distinction which it is possible to draw on the basis of initial pitch-accent patterns: a division between type 1 accent [accent on the first mora, comprising about 40% of lexical types (NHK, 1985)] and all other accent types (the remaining 60% of lexical types). The present results do not shed light on the question of whether listeners can continue to narrow their word-

recognition choices on the basis of later-arising distinctions (LHH versus LHL; LHHH versus LHHL, etc.). Our supposition based in part on the conclusions drawn from research on other languages, e.g., the use of stress information in lexical processing in English versus Dutch, would be that pitch-accent information will be used to the extent that it exercises a useful degree of constraint on the population of potential word candidates. The crude bipartite division which is made possible by exploitation of the initial HL- versus LH- distinction is obviously a highly effective means of cohort reduction, but we suspect that the added value of later-arising distinctions may be very much less. Whether listeners can usefully distinguish final-accented versus unaccented words is also an empirical issue which remains to be addressed; Sugito (1998) argues that speakers do distinguish these accentual structures even in isolation, but our results, concerning as they do exclusively the initial portions of words, do not answer the question of whether listeners can exploit this distinction. (For instance, would minimal pairs with these two accent patterns prime one another's representations? Consider *hashi*, one of our minimal pairs in experiment 3. We compared *hashi* HL ''chopsticks'' with *hashi* LH ''bridge;'' but there is also *hashi* LH unaccented ''edge.'' The results of experiment 3 suggest that *hashi* HL and *hashi* LH, do not activate one another's representations. But is this also true of *hashi* LH, and *hashi* LH unaccented?)

Machine recognition of spoken Japanese, as recent research (Hirose, 1997; Hirose and Iwano, 1997) has established, can be rendered more efficient by explicit analysis of $F0$ contours and comparison of the result with stored information on the accentual patterns of words. This is exactly as would be expected, given that, as our series of experiments has shown, human listeners engaging in the processing of spoken words find it effective to do the same.

ACKNOWLEDGMENTS

Cutler, A. (**1986**). ''Forbear is a homophone: lexical prosody does not constrain lexical access,'' Language and Speech **29**, 201–220.

Cutler, A., and Chen, H.-C. (**1997**). ''Lexical tone in Cantonese spoken-word processing,'' Percept. Psychophys. **59**, 165–179.

Cutler, A., Dahan, D., and van Donselaar, W. (**1997**). ''Prosody in the comprehension of spoken language: A literature review,'' Language and Speech **40**, 141–201.

Efremova, I. B., Fintoft, K., and Ormestad, H. (**1963**). ''Intelligibility of tonic accents,'' Phonetica **10**, 203–212.

Goldinger, S. (**1996**). ''Auditory lexical decision,'' Language and Cognitive Processes **11**, 559–567.

Grosjean, F. (**1996**). ''Gating,'' Language and Cognitive Processes **11**, 597–604.

Haraguchi, S. (**1977**). *The Tone Pattern of Japanese: An Autosegmental Theory of Tonology* (Kaitakusha, Tokyo).

Haraguchi, S. (**1988**). ''Pitch accent and intonation in Japanese,'' in *Autosegmental Studies on Pitch Accent*, edited by H. van der Hulst and N. Smith (Foris, Dordrecht), pp. 123–150.

Hattori, S. (**1960**). ''On'inron kara mita nihongo no akusento (Japanese accent from the point of view of phonology),'' in *Gengogaku no Hoohoo*, by S. Hattori (Iwanami, Tokyo), pp. 240–272.

Hirose, K. (**1997**). ''Disambiguating recognition results by prosodic features,'' in *Computing Prosody*, edited by Y. Sagisaka, N. Campbell, and N. Higuchi (Springer, Heidelberg), pp. 327–342.

Hirose, K., and Iwano, K. (**1997**). ''A method of representing fundamental frequency contours of Japanese using statistical models of moraic transition,'' in Proceedings of EUROSPEECH 97, Rhodes, pp. 311–314.

Hirose, K., Minematsu, N., and Ito, M. (**1993**). ''Experimental study on the role of prosodic features in the human process of spoken word perception,'' in Proceedings of the ESCA Workshop on Prosody, pp. 200–203.

Koster, M., and Cutler, A. (**1997**). ''Segmental and suprasegmental contributions to spoken-word recognition in Dutch,'' in Proceedings of EUROSPEECH 97, Rhodes, pp. 2167–2170.

Kubozono, H. (**1993**). *The Organization of Japanese Prosody* (Kurosio, Tokyo).

Kuwabara, H. (**1982**). ''Perception of CV-syllables isolated from Japanese connected speech,'' Language and Speech **25**, 175–183.

Lahiri, A., and Marslen-Wilson, W. D. (**1991**). ''The mental representation of lexical form: A phonological approach to the recognition lexicon,'' Cognition **38**, 245–294.

Maekawa, K. (**1990**). ''Production and perception of the accent in the consecutively devoiced syllables in Tokyo Japanese,'' in Proceedings of the First International Conference on Spoken Language Processing, Kobe, Vol. 1, pp. 517–520.

Maekawa, K. (**1995**). ''Is there 'dephrasing' of the accentual phrase in Japanese?'' in *Papers from the Linguistics Laboratory* (Working Papers in Linguistics, Ohio State University), Vol. 44, pp. 146–165.

Marslen-Wilson, W. D. (**1987**). ''Parallel processing in spoken word recognition,'' Cognition **25**, 17–102.

Marslen-Wilson, W., and Warren, P. (**1994**). ''Levels of perceptual representation and process in lexical access: words, phonemes, and features,'' Psychol. Rev. **101**, 653–675.

Martin, J. G., and Bunnell, H. T. (**1981**). ''Perception of anticipatory coarticulation effects,'' J. Acoust. Soc. Am. **69**, 559–567.

Martin, J. G., and Bunnell, H. T. (**1982**). ''Perception of anticipatory coarticulation effects in vowel-stop consonant-vowel sequences,'' J. Exp. Psychol. Hum. Percept. Perf. **8**, 473–488.

McCawley, J. (**1977**). ''Accent in Japanese,'' in *Studies in Stress and Accent*, edited by L. Hyman (Univ. of Southern California, Los Angeles), pp. 261–302.

McClelland, J. L., and Elman, J. L. (**1986**). ''The TRACE model of speech perception,'' Cogn. Psychol. **18**, 1–86.

McQueen, J. M., Norris, D. G., and Cutler, A. (**1994**). ''Competition in spoken word recognition: Spotting words in other words,'' J. Exp. Psychol. Learn. Mem. Cog. **20**, 621–638.

McQueen, J. M., Norris, D. G., and Cutler, A. (**in press**). ''Lexical influence in phonetic decision-making: Evidence from subcategorical mismatches,'' J. Exp. Psychol. Hum. Percept. Perf.

Minematsu, N., and Hirose, K. (**1995**). ''Role of prosodic features in the human process of perceiving spoken words and sentences in Japanese,'' J. Acoust. Soc. Jpn. **16**, 311–320.

NHK (Nihon Hoosoo Kyookai) (**1985**). Nihongo Hatsuon Akusento Jiten (NHK's Dictionary of Japanese Accent and Pronunciation) (NHK, Tokyo).

Nishinuma, Y. (**1994**). ''How do the French perceive tonal accent in Japanese? Experimental evidence,'' in Proceedings of the Third International Conference on Spoken Language Processing, Yokohama, pp. 1739–1742.

Nishinuma, Y., Arai, M., and Ayusawa, T. (**1996**). ''Perception of tonal accent by Americans learning Japanese,'' in Proceedings of the Fourth International Conference on Spoken Language Processing, Philadelphia, Vol. 1, pp. 646–649.

Norris, D. G. (**1994**). ''Shortlist: A connectionist model of continuous speech recognition,'' Cognition **52**, 189–234.

Otake, T. (**1990**). ''Rhythmic structure of Japanese and syllable structure,'' IEICE Technical Report **89**, 55–61.

Otake, T., Hatano, G., Cutler, A., and Mehler, J. (**1993**). ''Mora or syllable? Speech segmentation in Japanese,'' Journal of Memory and Language **32**, 358–378.

Otake, T., Yoneyama, K., Cutler, A., and van der Lugt, A. (**1996**). ''The representation of Japanese moraic nasals,'' J. Acoust. Soc. Am. **100**, 3831–3842.

Pierrehumbert, J. B., and Beckman, M. E. (**1988**). *Japanese Tone Structure* (MIT, Cambridge, MA).

Scott, D. R., and Cutler, A. (**1984**). ''Segmental phonology and the perception of syntactic structure,'' Journal of Verbal Learning and Verbal Behavior **23**, 450–466.

Shibata, T. (**1961**). ''Nihongo no akusento'' (Japanese accent) Gengo Seikatsu **117**, 14–20.

Sugito, M. (**1982**). *Nihongo Akusento no Kenkyuu* (Studies on Japanese accent) (Sanseido, Tokyo).

Sugito, M. (**1995**). *Osaka-Tokyo Akusento Onsei Jiten* (Osaka-Tokyo Accent Pronunciation Dictionary), CD-ROM (Maruzen, Tokyo).

Sugito, M. (**1998**). ''Hana to hana no seisei to chikaku'' (Production and perception of *hana* and *hana*), in *Hana to Hana: Nihongo Onsei no Kenkyuu* (Hana and Hana: Studies on Japanese Speech) (Izumishoin, Osaka).

Tseng, C.-Y. (**1990**). *An Acoustic Phonetic Study on Tones in Mandarin Chinese* (Academia Sinica, Taipei).

van Donselaar, W., and Cutler, A. (**1997**). ''Exploitation of stress information in spoken-word recognition in Dutch,'' J. Acoust. Soc. Am. **102**, 3136(A).

Vance, T. J. (**1987**). *An Introduction to Japanese Phonology* (State Univ. of New York, Albany).

Vance, T. J. (**1995**). ''Final accent vs. no accent: Utterance-final neutralization in Tokyo Japanese,'' Journal of Phonetics **23**, 487–499.

Walsh Dickey, L. (**1996**). ''Limiting-domains in lexical access: Processing of lexical prosody,'' in *Linguistics in the Laboratory*, edited by M. Dickey and S. Tunstall, University of Massachusetts Occasional Papers in Linguistics (Univ. of Massachusetts, Amherst), Vol. 19, pp. 133–155.

Warner, N. (**1997**). ''Japanese final-accented and unaccented phrases,'' Journal of Phonetics **25**, 43–60.

Whalen, D. H. (**1984**). ''Subcategorical mismatches slow phonetic judgments,'' Percept. Psychophys. **35**, 49–64.

Whalen, D. H. (**1991**). ''Subcategorical phonetic mismatches and lexical access,'' Percept. Psychophys. **50**, 351–360.

Recognition of spectrally degraded and frequency-shifted vowels in acoustic and electric hearing

Qian-Jie Fu[a] and Robert V. Shannon

Department of Auditory Implants and Perception, House Ear Institute, 2100 West Third Street, Los Angeles, California 90057

The present study measured the recognition of spectrally degraded and frequency-shifted vowels in both acoustic and electric hearing. Vowel stimuli were passed through 4, 8, or 16 bandpass filters and the temporal envelopes from each filter band were extracted by half-wave rectification and low-pass filtering. The temporal envelopes were used to modulate noise bands which were shifted in frequency relative to the corresponding analysis filters. This manipulation not only degraded the spectral information by discarding within-band spectral detail, but also shifted the tonotopic representation of spectral envelope information. Results from five normal-hearing subjects showed that vowel recognition was sensitive to both spectral resolution and frequency shifting. The effect of a frequency shift did not interact with spectral resolution, suggesting that spectral resolution and spectral shifting are orthogonal in terms of intelligibility. High vowel recognition scores were observed for as few as four bands. Regardless of the number of bands, no significant performance drop was observed for tonotopic shifts equivalent to 3 mm along the basilar membrane, that is, for frequency shifts of 40%–60%. Similar results were obtained from five cochlear implant listeners, when electrode locations were fixed and the spectral location of the analysis filters was shifted. Changes in recognition performance in electrical and acoustic hearing were similar in terms of the relative location of electrodes rather than the absolute location of electrodes, indicating that cochlear implant users may at least partly accommodate to the new patterns of speech sounds after long-time exposure to their normal speech processor. © *1999 Acoustical Society of America.*
[S0001-4966(99)00603-7]

INTRODUCTION

The auditory periphery processes incoming sounds and presents a complex temporal-spectral pattern of neural information to the brain. Central pattern recognition mechanisms are trained during childhood to recognize and distinguish speech patterns in the listener's native language. The central pattern recognition mechanisms must accommodate to differences in talker gender, speaking rate, competing noise, changes in the listening environment, etc. However, in conditions of reduced spectral resolution, as experienced by hearing impaired and cochlear implant listeners, it is still unknown how pattern recognition is affected by alterations in the temporal-spectral pattern of information. The present study is aimed at understanding the possible interaction between spectral resolution and spectral shifting.

The channel vocoder has been used for almost 60 years to study the effect of spectral resolution on speech recognition (Dudley, 1939). Generally, channel vocoders estimate speech parameters from temporal frames of speech (speech analysis), encode and transmit the parameters to the receiver on a frame-by-frame basis, and reconstruct the speech signal (speech synthesis) at the receiver. In the analysis stage, the channel vocoder employs a bank of bandpass filters to estimate the slowly time-varying spectral magnitudes in each band (envelope). The envelope in each band is extracted by

half-wave rectification and low-pass filtering, Hilbert transforms, or other methods. In the classic vocoder an estimate of voicing and voice pitch are included in this stage. In the synthesis stage, the envelopes are multiplied by the voiced or unvoiced signal sources and the resulting signals are passed through corresponding bandpass filters. The outputs of the bandpass filters are summed to form the output synthesized speech signal. Typically, 16–20 bandpass filters are used to cover the audio band 0–4 kHz. However, the amount of spectral information preserved in the processed speech can be systematically manipulated by changing or limiting the number of spectral bands. A simplified extension of this approach, the noise-band vocoder, uses multiple noise-band carriers to represent the speech envelope signals from broad spectral bands without implementing the voicing detector and pitch estimator (Hill *et al.*, 1968; Villchur, 1977; Shannon *et al.*, 1995). Another type of simplified vocoder uses sinusoidal carriers. Recent studies have shown no significant difference in speech recognition performance between noise-band and sinusoidal carriers (Dorman *et al.*, 1997a; Fu, 1997). The noise-band vocoder was used to process speech sounds with varying amounts of spectral resolution in the present study.

The relation between speech performance and spectral resolution has been extensively investigated (e.g., Boothroyd *et al.*, 1996; Dubno and Dorman, 1987; Dubno and Schaefer, 1995; Hill *et al.*, 1968; ter Keurs *et al.*, 1992, 1993). Hill *et al.* (1968) measured speech recognition as a function of

---
[a]Electronic mail: qfu@hei.org

the number of bands with a sinusoidal vocoder. They found that both vowel and consonant recognition increased rapidly as the number of bands was increased from 3 to 6, then slowly improved from 6 to 12 bands. Zollner (1979) found that word recognition increased from 21% in a 2-band condition to 94% in a 6-band condition, and up to 98% in an 11-band condition. He concluded that only six frequency bands of information were sufficient to obtain near perfect speech performance. Shannon *et al.* (1995) investigated speech recognition as a function of the number of bands using the noise-band vocoder method. They found high levels of phoneme, word, and sentence recognition even with as few as four bands of spectral information. Dorman *et al.* (1997a) measured recognition of multi-talker vowels as a function of the number of bands. They found that the vowel score continued to increase significantly up to 9 bands. Fu (1997) further investigated the effect of frequency divisions, total frequency range, as well as sinusoidal and noise-band carriers, and found results similar to the previous studies. Overall, the results from these studies indicate that a high level of speech recognition is possible with 4–6 bands of spectral information.

The sinusoidal vocoder and noise-band vocoder have proven to be powerful tools for quantifying the effect of reducing spectral information on speech performance. These two methods have also been used to simulate the listening situation in cochlear implants. One multiband, vocoderlike processor that has been successfully used in several implant systems is the continuous interleaved sampling (CIS) strategy. The CIS strategy divides speech into several frequency bands and the temporal envelope is extracted from each band (Wilson *et al.*, 1991). The extracted temporal envelope from each band is used to modulate the current level of a biphasic pulse train, which stimulates one monopolar electrode (relative to a remote ground) or a bipolar electrode pair within the cochlea. Pulses shaped by temporal envelopes extracted from low-frequency bands are sent to stimulation sites in the apical region of cochlea. Temporal envelopes extracted from high-frequency bands are sent to stimulation sites in the basal region of cochlea. If the spectral information can be fully utilized, implanted listeners should have speech performance comparable to normal-hearing subjects listening to an equivalent processor (Fishman *et al.*, 1997; Dorman *et al.*, 1989) because temporal processing is essentially normal and unimpaired in implant subjects (Shannon, 1992, 1993). Recent studies on speech performance in cochlear implants showed that a high level of speech recognition is possible in cochlear implant listeners with as few as four stimulated electrode pairs (Fishman *et al.*, 1997). The best performance in implanted subjects was comparable to performance in normal-hearing subjects with the same number of channels. However, considerable variability was observed in the performance of implant listeners. One potential source of this variability is the proximity of the stimulating electrodes to functional auditory nerve fibers. The speech information delivered to each electrode is not necessarily matched to the tonotopic location of electrodes based on the cochlear place-to-frequency map (Greenwood, 1990). A mismatch between analysis filters and electrode locations may have the effect of

frequency compression or expansion without altering the temporal properties of the signal.

Considerable research has demonstrated that speech recognition, particularly vowel recognition, is reduced significantly by frequency compression or expansion. Daniloff *et al.* (1968) investigated the effect of various degrees of frequency compression, with and without time restoration, on vowel intelligibility. They found that over a limited range of frequency compression, vowel phonemic quality was relatively unaffected by proportionate shifting of fundamental frequency and formant structure. However, beyond a frequency compression ratio of about 50%, intelligibility declined sharply. Nagafuchi (1976) measured the intelligibility of frequency-shifted speech in normal-hearing adults and children. The results showed that vowel recognition decreased rapidly with increasing frequency expansion or compression. Performance was reduced to half for frequency shifts beyond 50% frequency compression or 200% expansion. Similar results have been reported by several other researchers (Beasley *et al.*, 1976; Wallace and Koury, 1981). These results all showed that vowel recognition performance decreased dramatically when the frequency shift exceeded 40%–60%. Dorman *et al.* (1997b) measured speech recognition with a five-band sinusoid vocoder in conditions in which the carrier bands were shifted up to 5 mm (about a 1-oct shift) basally from the analysis bands. This shift simulated speech processing in cochlear implants, in that the implant electrodes are located more basally than the frequency of the information they convey. Speech recognition performance dropped off dramatically (10%/mm) as the carrier bands were shifted basally, particularly for vowels.

The above results indicate that speech recognition, especially for vowels, is highly sensitive to frequency shifting. Performance is reduced significantly as a result of frequency compression or expansion exceeding 40%–60%. However, most of these studies have applied frequency shifting to complete speech signals; little is known about the effect of frequency shifting when only coarse spectral information is available. One intuitive assumption is that speech signals with greater spectral resolution are less affected by spectral alterations. Experiment 1 investigated the effects of spectral shifting on vowel recognition in five normal-hearing listeners. Medial vowel stimuli were represented by 4, 8, or 16 modulated noise bands, generated using the noise-band vocoder technique. The noise carrier bands were progressively shifted apically or basally from the tonotopic frequency allocation of the analysis bands.

In electrical stimulation, spectral information is delivered to electrodes in different tonotopic locations. Speech recognition may be impaired if the electrodes are delivering spectral information that is not matched to the tonotopic locations of the electrodes. It seems reasonable to hypothesize that the best performance would be obtained if the assigned frequency allocation of analysis filter bands matched the normal acoustic characteristic frequency of electrode locations within the cochlea (tonotopic-matching hypothesis). The mapping of characteristic frequency to electrode location in this case is referred to as the *normal acoustic map* (Greenwood, 1990). However, most cochlear implants assign a

standard default set of frequency bands to electrodes. This default mapping may match the correct spectral information to the correct tonotopic location in some implant listeners but not in others. Implant speech recognition is highly variable across listeners, perhaps because of a frequency-location mismatch across subjects. Even in those cases in which a frequency-location mismatch occurs initially, the listeners may adjust to the altered tonotopic distribution of spectral information over time (accommodation hypothesis). In this case the frequency assigned to a given electrode versus the electrode location is referred to as the *adapted electrical map*.

Experiment 2 measured vowel recognition in five cochlear implant listeners using electrode location shifts corresponding to the acoustic frequency shifts in experiment 1. The electrode insertion depths of these five implant patients varied over 7 mm. The recognition patterns as a function of frequency allocations might indicate which hypothesis is applicable to cochlear implant users.

I. EXPERIMENT 1: ACOUSTIC STIMULATION

Experiment 1 measured the effect of spectral shifting in normal-hearing listeners. Spectral resolution was varied by varying the number of bands in a noise-band vocoder. The analysis and carrier bands were shifted either together or relative to each other. Speech pattern recognition was measured with multi-talker vowels.

A. Methods

1. Subjects

Five subjects with normal hearing participated in this experiment. All had thresholds better than 15 dB HL at audiometric test frequencies from 250 to 8000 Hz. The subjects ranged in age from 25 to 35 years and were all native speakers of American English.

2. Stimuli and procedure

Vowel recognition was measured in a 12-alternative identification paradigm, including 10 monophthongs and 2 diphthongs, presented in an /h/-vowel-/d/ context (heed, hawed, head, who'd, hid, hood, hud, had, heard, hoed, hod, hayed). The tokens for these closed-set tests were digitized natural productions from five men, five women, and five children, drawn from the speech samples collected by Hillenbrand *et al.* (1994). On each trial a stimulus token was chosen randomly, without replacement, from the 180 tokens (12 vowels, 15 talkers). Following presentation of each token, the subject responded by pressing 1 of 12 buttons, each marked with one of the possible responses. No feedback was provided, and subjects were instructed to guess if they were not sure, although they were cautioned not to provide the same response for each guess. Results reflect a single run (180 tokens) for each condition for acoustic listeners.

Subjects were well familiarized with the test materials in their unprocessed form and with the test procedure from prior experiments. However, no familiarization with the processed speech sounds was provided. The subjects started the

formal test without any training. Conditions were presented in random order within each subject and were counterbalanced across subjects.

All test materials were stored on computer disk and were output via custom software to a 16-bit D/A converter (TDT DD1) at a 16-kHz sampling rate. Speech sounds were presented in a randomized test sequence using a Tucker-Davis-Technologies (TDT) AP2 array processor in a host PC connected via an optical interface. All signals were presented at 70 dB (A-weighted scale) diotically through Sennheiser HDA200 headphones to the subjects who were seated in a double-walled sound-attenuating booth (IAC).

3. Signal processing

The acoustic processors that generated the spectrally degraded and spectrally shifted speech stimuli were constructed as follows. The original speech was first preemphasized to spectrally flatten the signal using a first-order Butterworth high-pass filter with a cutoff frequency of 1200 Hz, and then band-pass filtered into 4, 8, or 16 frequency bands using eighth-order Butterworth bandpass filters (-96 dB per octave). The corner frequencies and bandwidths of the frequency bands were dependent on the simulated tonotopic locations and the number of bands. The simulated tonotopic locations of frequency bands were determined by the following equation:

$$P(i) = P_0 - \text{BW}*i, \quad i = 0,1,...,N, \tag{1}$$

where P_0 is the most apical location for a given frequency allocation in mm (from the base), BW is the tonotopic bandwidth of each band in mm, and N is the number of bands. The tonotopic bandwidth (BW) of each band was 3.75 mm for the 4-band processor, 1.875 mm for the 8-band processor, and 0.9375 mm for the 16-band processor. The corner frequencies of bands were determined by the following equation, from Greenwood (1990):

$$F(i) = 165.4*(10^{(35.0-P(i))*0.06} - 0.88). \tag{2}$$

Note that Eq. (2) refers to a 35-mm-long cochlea and that actual lengths can vary by several mm. The allocated frequencies for given tonotopic locations will vary based on the actual lengths. This variation may shift the location of the peak performance, but the recognition patterns as a function of frequency allocation will remain the same. Combining Eqs. (1) and (2), all corner frequencies of bands could be determined for a given number of bands and a given analysis frequency range. The attenuation at the crossover point of adjacent filter bands was -3 dB. The most apical location, P_0, was varied from 21.25 to 28.00 mm from the base for the 4-, 8- and 16-band processors. A total of ten different frequency allocations were generated between these endpoints. Experimental conditions are shown schematically in Fig. 1. Table I lists the 17 corner frequencies of each frequency range for the 16-band processor. The nine corner frequencies for the 8-band processor, and the five corner frequencies for the 4-band processor can also be obtained from Table I by reading only every other value for the 8-band processor or only every fourth value for the 4-band processor.
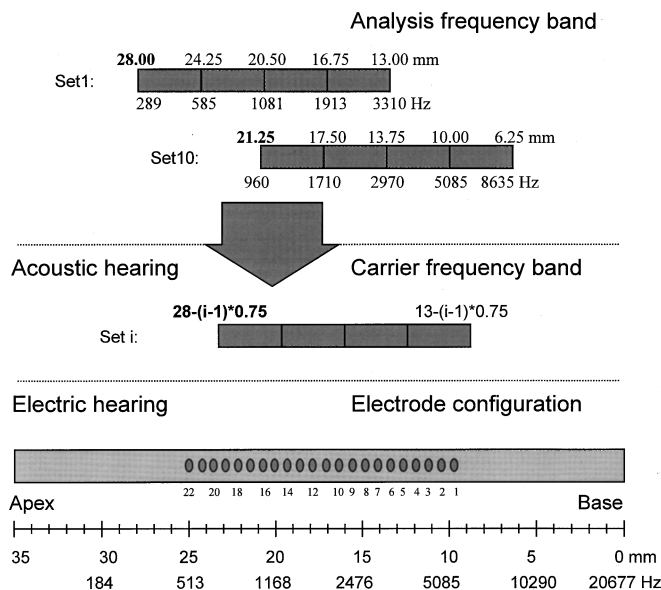
FIG. 1. Schematic representation of the relative tonotopic locations of analysis and carrier bands for the four band condition. The overall frequency range was the same for the 8- and 16-band conditions. The tonotopic location and frequency range of the electrodes in a fully inserted cochlear implant is indicated in the lower section.

The temporal envelope in each band was extracted by half-wave rectification and low-pass filtering (eight-order Butterworth: -48 dB/oct) with a 160-Hz cutoff frequency. The envelope of each band was used to modulate a wideband noise, which was then spectrally limited by a bandpass filter (defined as the carrier band). The formulas [Eqs. (1) and (2)] were exactly the same for the carrier bands but the most apical location, P_0, was not necessarily the same for the analysis and carrier bands, resulting in a possible tonotopic shift. The outputs from all bands were then summed. All combinations of analysis filter bands and carrier filter bands for different conditions are listed in Table II. Condition 1 simulates a cochlear implant with differing electrode inser-

tion depths and frequency allocations matched to the actual tonotopic locations of the electrodes. Condition 2 simulates a cochlear implant with differing electrode insertion depths with a fixed frequency allocation. Condition 3 simulates a cochlear implant with relatively shallow insertion depth with different frequency allocations. Condition 4 simulates a cochlear implant with near full insertion depth with different frequency allocations.

B. Results

In the first condition the analysis and carrier bands were the same, and the tonotopic frequency allocations of both shifted together. Figure 2 shows vowel recognition in five normal-hearing subjects as a function of the most apical cochlear location of the frequency allocation, for 4-, 8-, and 16-band processors. Results showed that vowel recognition was only mildly affected by frequency allocation as long as the analysis and carrier bands were matched. For the condition $P_0 = 21.25$ mm the lowest corner frequency was 960 Hz, which means that all spectral information below 960 Hz was eliminated. Yet, even with this large loss of low-frequency information, vowel recognition dropped only 20% from the best performance. This result is consistent with an earlier finding indicating the dominant influence of the second formant in speech intelligibility (Thomas, 1968). A two-way, repeated-measures analysis of variance (ANOVA) showed a significant effect of the number of bands $[F(2,18) = 410.51, p < 0.001]$ as well as a significant effect of frequency allocation $[F(9,18) = 50.31, p < 0.001]$, but no interaction between the number of bands and frequency allocation $[F(18,120) = 0.71, p = 0.80]$. As the most apical location was shifted basally, post hoc Tukey HSD tests indicated that vowel score began to decrease significantly when the most apical edge was 24.25, 23.50, and 22.75 mm (the corresponding frequencies are 585, 665, and 753 Hz) for 4-band processors, 8-band processors, and 16-band processors, respectively.

TABLE I. The corner frequencies of ten frequency allocations for a 16-band processor. The corner frequencies for an eight-band processor and a four-band processor can also be obtained based on the table.

Corner frequency	The most apical edge of frequency allocation (mm from the base)									
	28.00	27.25	26.50	25.75	25.00	24.25	23.50	22.75	22.00	21.25
1	289	337	390	448	513	585	665	753	851	960
2	350	404	464	530	604	686	777	877	989	1113
3	418	480	548	624	708	801	904	1019	1146	1287
4	496	566	644	730	826	932	1049	1180	1324	1485
5	585	665	753	851	960	1081	1214	1363	1528	1710
6	686	777	877	989	1113	1250	1402	1572	1759	1967
7	801	904	1019	1146	1287	1443	1617	1809	2022	2259
8	932	1049	1180	1324	1485	1663	1860	2079	2322	2592
9	1081	1214	1363	1528	1710	1913	2138	2387	2663	2970
10	1250	1402	1572	1759	1967	2198	2453	2737	3052	3401
11	1443	1617	1809	2022	2259	2522	2813	3136	3494	3891
12	1663	1860	2079	2322	2592	2890	3222	3589	3997	4449
13	1913	2138	2387	2663	2970	3310	3687	4106	4570	5085
14	2198	2453	2737	3052	3401	3788	4217	4694	5222	5808
15	2522	2813	3136	3494	3891	4332	4821	5363	5964	6631
16	2890	3222	3589	3997	4449	4951	5508	6125	6809	7569
17	3310	3687	4106	4570	5085	5656	6289	6992	7771	8635

TABLE II. The most apical edges of frequency allocations used in analysis and carrier filter bands for four experimental conditions.

Conditions		The most apical edge of frequency allocation (mm from the base)									
		1	2	3	4	5	6	7	8	9	10
1	Analysis	28.00	27.25	26.50	25.75	25.00	24.25	23.50	22.75	22.00	21.25
	Carrier	28.00	27.25	26.50	25.75	25.00	24.25	23.50	22.75	22.00	21.25
2	Analysis	27.25	27.25	27.25	27.25	27.25	27.25	27.25	27.25	27.25	27.25
	Carrier	28.00	27.25	26.50	25.75	25.00	24.25	23.50	22.75	22.00	21.25
3	Analysis	28.00	27.25	26.50	25.75	25.00	24.25	23.50	22.75	22.00	21.25
	Carrier	22.00	22.00	22.00	22.00	22.00	22.00	22.00	22.00	22.00	22.00
4	Analysis	28.00	27.25	26.50	25.75	25.00	24.25	23.50	22.75	22.00	21.25
	Carrier	25.00	25.00	25.00	25.00	25.00	25.00	25.00	25.00	25.00	25.00

In cochlear implants the speech information delivered to each electrode location does not necessarily match the acoustic information that would be represented at that location in a normal cochlea. To evaluate the effect of a mismatch between the delivered information and the tonotopic location, we independently varied analysis and carrier bands in normal-hearing listeners. First we fixed the analysis bands and varied the carrier bands, a manipulation analogous to fixing the speech analysis filters in a cochlear implant and moving the electrode. Figure 3 shows vowel recognition as a function of the most apical edge of the carrier frequency allocation when the most apical edge of the analysis frequency allocation was fixed at $P_0 = 27.25$ mm (337 Hz). Panel (a) shows the original data and panel (b) shows the same data normalized to the matched condition ($P_0 = 27.25$ mm). An ANOVA on the normalized data showed no significant interaction between the number of bands and frequency allocation [$F(18,120) = 1.38$, $p = 0.15$] but a significant effect of frequency allocation [$F(9,18) = 226.97$, $p < 0.001$]. As the carrier bands were shifted basally, post hoc Tukey HSD tests indicated that the vowel recognition score dropped significantly when the most apical edge of the carrier bands was moved to 24.25 mm (585 Hz) or more basally for all processors.

In the next condition we fixed the carrier band and varied the estimated tonotopic location of the analysis bands. This manipulation is analogous to fixing the electrode location in a cochlear implant and varying the frequency allocation of analysis filter bands. Figure 4(a) shows vowel recognition as a function of the most apical edge of the analysis bands when the most apical edge of the carrier bands was fixed at $P_0 = 22.00$ mm (851 Hz). Figure 4(b) shows vowel recognition functions from Fig. 4(a) normalized to the matched condition ($P_0 = 22.00$ mm: 851 Hz). A two-way ANOVA on the normalized data showed no significant interaction between the number of bands and frequency allocations [$F(18,120) = 1.35$, $p = 0.17$] but a significant effect of frequency allocation [$F(9,18) = 88.71$, $p < 0.001$]. Post hoc Tukey HSD tests indicated that the performance dropped significantly when the apical edges of the analysis filter bands were moved to 25.75 mm (448 Hz) or more apically.

To enable a direct comparison with data from cochlear implants in experiment 2, we fixed the carrier bands at two tonotopic locations, one shifted 3 mm from the other. Figure 5 shows vowel recognition as a function of the most apical edge of the analysis bands for the two 4-band carrier conditions. The most apical edge of the carrier bands was fixed at either 25.00 mm (513 Hz) or 22.00 mm (851 Hz) while the most apical edge of the analysis bands was shifted from 28.00 to 21.25 mm in steps of 0.75 mm. A one-way ANOVA showed a significant effect of frequency allocation for the apical carrier set [$F(9,40) = 145.34$, $p < 0.001$] as well as for the basal carrier set [$F(9,40) = 28.16$, $p < 0.001$]. The best performance was observed when the analysis and carrier bands were matched in frequency, or when the analysis bands were slightly more apical. Normalized vowel recognition decreased as much as 20%/mm as the analysis bands were shifted relative to the carrier bands.

To evaluate the role of talker gender on the tolerance for spectral shifting, we fixed the analysis bands at $P_0 = 27.25$ mm (337 Hz) and shifted the carrier bands from 32.50 to 21.25 mm in 0.75-mm steps. Figure 6(a) shows vowel recognition scores normalized to the matched condition as a function of the difference in cochlear location between analysis and carrier bands for a 16-band processor.
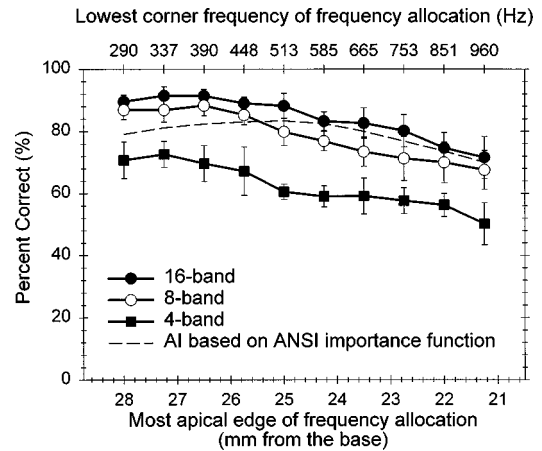
FIG. 2. Vowel recognition scores as a function of the most apical edge of the analysis and carrier bands for the 4-, 8-, and 16-band processor in five normal-bearing subjects. The analysis filter bands and carrier filter bands were matched in each condition. The dashed line in the upper panel indicates the AI prediction for the present conditions using the ANSI weighting function for monosyllables. Error bars indicate ± one standard deviation.
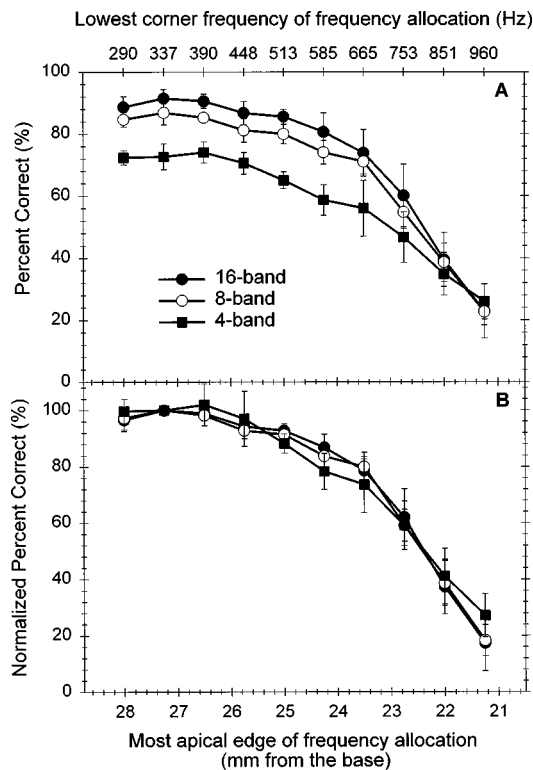
FIG. 3. Vowel recognition scores as a function of the most apical edge of the carrier filter bands for the 4-, 8-, and 16-band processors. The most apical edge of the analysis filter bands was fixed at 27.25 mm from the base (337 Hz) and the carrier bands were shifted over a 6.75-mm range (from $P_0 = 289–960$ Hz). Error bars indicate $\pm$ one standard deviation. Lower panel: results normalized to the matched condition ($P_0 = 27.25$ mm).
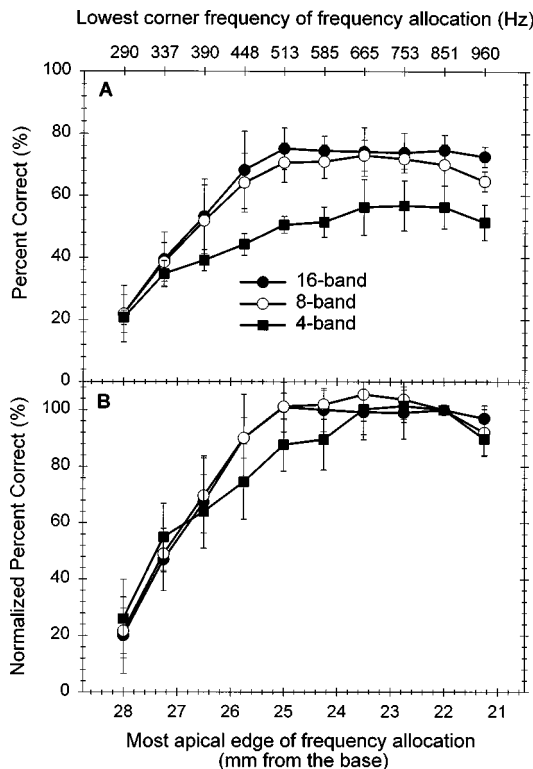
FIG. 4. Vowel recognition scores as a function of the most apical edge of the analysis filter bands for the 4-, 8-, and 16-band processors. The most apical edge of the carrier filter bands was fixed at 22.00 mm (851 Hz). Error bars indicate $\pm$ one standard deviation. Lower panel: results normalized to the matched condition ($P_0 = 22.00$ mm).
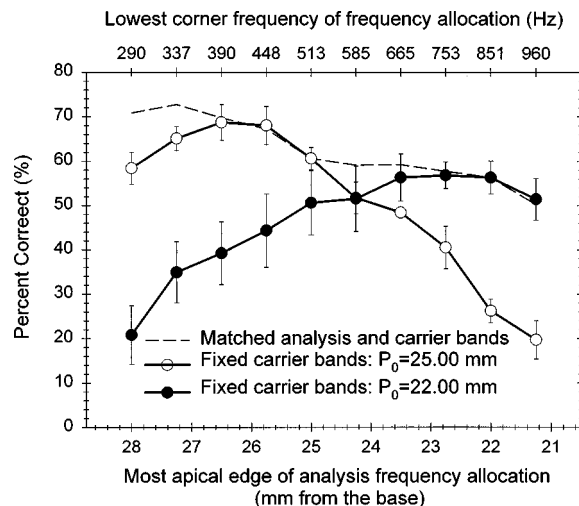
FIG. 5. Vowel recognition scores as a function of the most apical edge of the tonotopically shifted frequency allocation sets for the 4-, 8-, and 16-band processors. The most apical edge of the carrier filter bands was fixed at 25.00 mm (513 Hz: open symbols) or 22.00 mm (851 Hz: filled symbols). Error bars indicate $\pm$ one standard deviation.

The zero point on the x axis represents the condition where the analysis band and carrier band are matched. Negative shifts indicate conditions where the carrier bands were more basal than the analysis bands, resulting in frequency raising. Positive shifts represent conditions where the carrier bands
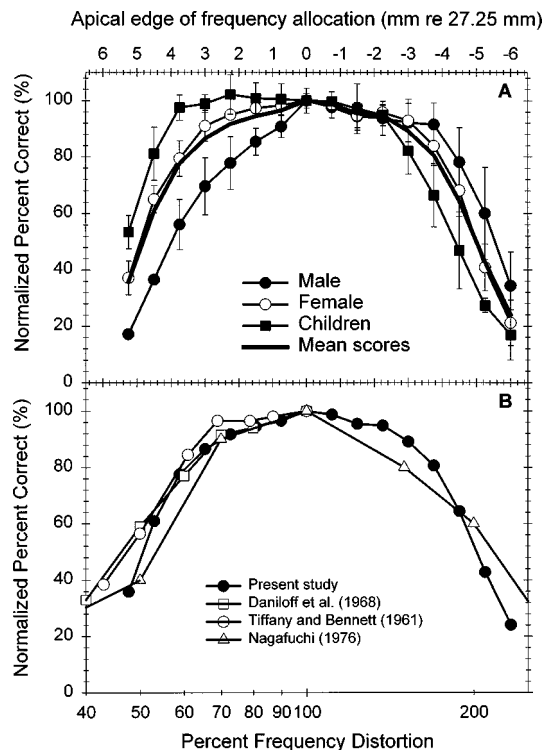
FIG. 6. Vowel recognition scores as a function of the difference in the apical edge of the analysis and carrier frequency allocation sets for men, women, and children talkers with 16-band processors. The most apical edge of the analysis filter bands was fixed at 27.25 mm from the base (337 Hz). The most apical edge of the carrier filter bands was varied from 32.50 mm (88 Hz) to 21.25 mm (960 Hz). The thick solid line presents the average function for all talkers. Error bars indicate $\pm$ one standard deviation. Lower panel: comparison of present results for 16-band processors with earlier studies of frequency compression and expansion with whole speech.

were more apical than the analysis bands, resulting in frequency lowering. The filled circles show vowel scores for male talkers. *Post hoc* Tukey HSD tests showed that vowel scores dropped significantly when the carrier bands were shifted apically 0.75 mm compared to the analysis frequency allocations (lowering). However, *post hoc* Tukey HSD tests showed no significant performance drop for up to a 3.75-mm basal shift (raising) for male talkers. The open circles show vowel scores for female talkers. *Post hoc* Tukey HSD tests showed no performance drop between +3.00 and −3.00 mm compared to the matched condition. Similarly, no performance drop was observed between +2.25 and −3.75 mm for child talkers (filled squares).

C. Discussion

The results of the present experiments demonstrate the effect of spectral resolution and spectral shifting on vowel recognition. Spectral resolution was altered by reducing the spectral information to 4, 8, or 16 bands using a noise-band vocoder. Spectral shifting was accomplished by shifting the noise carrier bands relative to the analysis bands or vice versa. When the analysis and carrier bands were matched in frequency location and frequency range, vowel recognition was relatively unaffected by tonotopic location (Fig. 2). Independent of the spectral shift, vowel recognition scores improved markedly when the number of bands was increased from 4 to 8, and showed a further small improvement when the number of bands was further increased to 16, consistent with previously reported results (Dorman *et al.*, 1997a; Fu, 1997).

1. Effects of spectral region

Vowel recognition was only mildly affected by changes in the spectral region as long as the carrier bands and analysis bands were matched, i.e., when the speech envelope information was delivered to the appropriate tonotopic place. When the most apical edges of both analysis and carrier bands were shifted basally from 28.00 to 21.25 mm, the corresponding frequency regions were shifted from 289–3310 Hz to 960–8635 Hz, as listed in Table I. Vowel scores for 16-band processors started to drop significantly when the most apical location was 22.75 mm (frequency range of 753–6992 Hz). This reduction in speech recognition can be predicted from traditional articulation index (AI) theory. As the frequency region was shifted to a more basal location, more low-frequency speech information was lost. As the most apical edge was shifted from 28.00 to 23.50 mm, the frequency region changed basally from 289–3310 Hz to 665–6289 Hz. With these midfrequency regions, either the loss of low-frequency speech information was roughly compensated by the gain of high-frequency speech information or the contribution of these lost low frequency cues was relatively small, resulting in a similar AI value and similar speech performance. However, once the highest frequency in the region was above 6300 Hz, corresponding to a frequency region with the most apical edge at 22.75 mm, the extra speech information from high-frequency regions above 6300 Hz did not contribute much additional information. Therefore, the loss of low-frequency information was not offset by

a gain in high frequency information, resulting in a decrease in AI value. Predictions from AI theory (based on the ANSI standard frequency weighting function for monosyllables) are shown as a dashed line in Fig. 2. The AI predictions match the present data well for frequency allocations with the most apical edge at 25.75 mm or more basal. The ANSI monosyllable weighting (ANSI, 1969) is likely to be more high-frequency biased than a function appropriate for vowels and may underestimate the contribution of lower bands to vowel identification. This may explain the poorer fit for the most apical locations seen in Fig. 2. In general, as long as the analysis and carrier bands are matched, performance as a function of tonotopic location can be predicted by AI theory. As the spectral resolution (number of bands) was decreased, a similar function was obtained, but at a lower overall performance level.

2. Effects of spectral resolution

One might expect that speech signals with higher spectral resolution would be less affected by spectral alterations. Thus, the lack of interaction between frequency shifting and spectral resolution in experiment 1 was surprising. In all conditions, the pattern of results was similar for 4, 8, or 16 bands. In addition, the normalized pattern of results for all three levels of spectral resolution was similar to previous studies that used whole speech with full spectral resolution. This suggests that the relative decrement in performance due to spectral region or spectral shifting is independent of the spectral resolution. Although vowel recognition was significantly affected by the number of bands (4, 8, or 16) and by frequency region, there was no interaction between the number of bands and shifts in the tonotopic range. This suggests that the performance drop as a function of tonotopic band location was due to the loss of useful spectral information and that this loss could not be restored by increasing the spectral resolution (number of bands).

3. Effects of spectral mismatch

Two manipulations were used to explore speech pattern recognition as a function of the spectral mismatch between the analysis and carrier band. In one case the tonotopic location of the carrier bands was systematically changed while the spectral range of the analysis bands was fixed. In this approach, the spectral distribution of speech information was held constant while the tonotopic location to which speech information was presented was shifted along the cochlea. In the other case the spectral range of the analysis bands was varied while the tonotopic location of the carrier bands was fixed. While the general pattern of results was similar for the two manipulations, there were still some differences, as described in the following sections.

a. Varying frequency allocations of the carrier band. Figures 3 and 6 show the effect of a shift in cochlear location of the tonotopic pattern. Here the analysis bands were fixed at a frequency allocation that produced good performance ($P_0 = 27.25$ mm) when the analysis and carrier bands were matched (see Fig. 2). Vowel scores decreased as the carrier bands were shifted apically or basally, illustrating the detri-

mental effect of spectral mismatching in either direction. In this case, the analysis bands were the same in every condition, so the entire effect was due to the shift in the tonotopic location to which the information was delivered. The results indicate that vowel recognition was robust to tonotopic shifts either apically or basally of up to 3 mm, which corresponds to a frequency lowering/raising ratio of about 60%. Vowel scores dropped significantly when spectral information was shifted by more than 4 mm, which corresponds to a lowering/raising factor of about 80%.

The present results are remarkably similar to those of studies (Tiffany and Bennett, 1961; Daniloff *et al.*, 1968; Shriner *et al.*, 1969; Nagafuchi, 1976) in which the whole speech signal was frequency compressed or expanded. Daniloff *et al.* (1968) found that vowel intelligibility decreased rapidly when frequency was compressed by more than 70%. Nagafuchi (1976) demonstrated a significant reduction in the recognition of Japanese monosyllables with frequency compression or expansion of more than about 80%. Figure 6(b) compares the present results with those of earlier studies. The close correspondence between the present results, obtained with reduced spectral resolution, and previous results with whole speech, combined with the lack of interaction between spectral resolution and spectral shift in the present experiments, further demonstrates that the reduction in vowel recognition observed under conditions of tonotopic alteration is independent of spectral resolution. This result suggests that spectral resolution and spectral alteration have independent effects on speech recognition.

b. Varying frequency allocations of the analysis band. Fixing the carrier band and varying the analysis band not only changes the degree of spectral mismatch between analysis bands and carrier bands, but also varies the spectral distribution of speech information determined by the analysis filter bands. In this case, the performance is determined by both the speech information transmitted by the analysis filter bands and the degree of spectral mismatch instead of the degree of spectral mismatch alone. For the frequency allocations in the present study, analysis bands that are located more apically will have more bands assigned to the low-frequency regions, which may be advantageous for vowel recognition (see Fig. 2). The greater spectral information transmitted by the analysis filter bands may offset the detrimental effect of the spectral mismatch with the carrier frequency allocation and may produce best performance not when the analysis and carrier bands are matched, but rather at a compromise location where the analysis frequency division is optimal and the analysis-carrier mismatch is not too large. This tradeoff is apparent in Fig. 5, which shows that the best performance was not obtained when the analysis and carrier bands were perfectly matched, but when the analysis bands were shifted 0.75–1.5 mm apically relative to the carrier bands.

4. Effects of talker gender

One interesting aspect of the results in Fig. 6 is the effect of talker gender. Listeners can tolerate a larger basal shift in male talkers than in females or children, and can tolerate a larger apical shift in females and children than in

males. This result suggests that the frequency range over which listeners can tolerate tonotopic alteration is absolute. Since male talkers are already on the low-frequency edge of this range, listeners cannot tolerate much frequency lowering for male voices. Conversely, children's voices are already on the high-frequency edge of this range, so listeners cannot tolerate much frequency raising of children's voices. To compare the present gender effect with that of previous studies we compare the frequency lowering thresholds, i.e., the frequency lowering ratio at which the recognition score fell to 50% of its performance in the matched condition. In Tiffany and Bennett's experiment (1961) the lowering threshold was about 53% for male talkers and 40% for female talkers. Daniloff *et al.* (1968) reported a similar 52% lowering threshold for a male talker and 45% for a female talker. Frequency lowering thresholds in the present results were 54% for males, 46% for females, and 43% for children. Thus, all these studies demonstrated a similar gender effect.

II. EXPERIMENT 2: ELECTRIC STIMULATION

Cochlear implants deliver a signal with degraded spectral information (4–20 channels) to locations evenly distributed along the scala tympani. In most cases the electrode locations are in the basal and middle turns, covering an equivalent frequency region of 513–6000 Hz. Aligning the analysis frequencies with each electrode pair becomes a problem, because the exact tonotopic location of each electrode is not known. Even if the exact tonotopic location of each electrode could be determined, we would still not know which neurons were stimulated by each electrode. Due to the etiology of the individual patient, the neural population stimulated by each electrode may not be located immediately adjacent to the electrode. Commercial devices select a frequency allocation that strikes a balance between the low-frequency range of speech information and the higher frequency tonotopic location of the electrodes. This frequency mapping may lead to speech envelope information being presented to a tonotopic location that would acoustically receive higher-frequency information. Experiment 2 evaluates the effect of such a mismatch between analysis filter frequencies and electrode locations in implant listeners. Vowel recognition was measured using two electrode configuration sets, which had the same stimulation mode and spacing, but one set was located 3 mm basal to the other. For each of these electrode sets, vowel recognition was measured as a function of the frequency range of the analysis filters.

A. Methods

1. Subjects

The subjects in the second experiment were five postlingually deafened adults with the Nucleus-22 cochlear implant and at least 6 months experience utilizing the SPEAK speech processing strategy. The subjects ranged in age from 39 to 71 years and were all native speakers of American English. All subjects had 20 active electrodes available for use. Table III contains relevant information for the five subjects, including their most recent scores on the CUNY sentence test, presented without lip reading in the sound field.

TABLE III. Subject information for five Nucleus-22 cochlear implant listeners who participated in the present study. Frequency table refers to the frequency allocation used by the listener in their everyday processor. Frequency table 7 has a frequency range of 120–8658 Hz while frequency table 9 has a range of 150–10 823 Hz. Frequency table 9 is intended to be an approximate tonotopic map to the electrode locations for a full electrode insertion. Insertion depth is reported as the number of stiffening rings outside the round window from the surgical report. A full insertion would be 0 rings out.

Subject	Age	Gender	Cause of deafness	Duration of use (years)	Insertion depth (rings out)	Frequency table	Score (CUNY)	Score (vowel)
N3	55	M	Trauma	6	3	7	79.4%	58.1%
N4	39	M	Trauma	4	4	9	99.0%	74.2%
N7	54	M	Unknown	4	0	9	99.0%	65.6%
N9	55	F	Hereditary	7	4	9	100.0%	71.3%
N17	71	F	Trauma	1	10	7	85.3%	52.5%

2. Stimuli and procedure

The same vowel stimuli were used as in experiment 1. All stimuli were preprocessed with the signal processing methods described below, and presented at comfortable listening levels through a custom implant interface (Shannon *et al.*, 1990) instead of the headphone used for the acoustic experiments. Results reflect two runs (360 tokens) for each condition for each implant listener.

3. Signal processing

Vowel recognition performance was measured as a function of tonotopically shifted frequency allocations using a custom four-channel CIS processing strategy (Wilson *et al.*, 1991) instead of the SPEAK processing strategy (McDermott *et al.*, 1992). The implementation of these customized speech processing strategies in Nucleus-22 cochlear implant users was accomplished as follows. The signal was first pre-emphasized using a first-order Butterworth high-pass filter with a cutoff frequency of 1200 Hz to whiten the spectrum, and then band-pass filtered into four broad frequency bands using eighth-order Butterworth filters. The corner frequencies of the frequency bands were determined by Eqs. (1) and (2). The most apical location, P_0, was systematically changed from 28.00 to 21.25 mm in steps of 0.75 mm, resulting in ten different frequency allocations (Fig. 1). The envelope of the signal in each band was extracted by half-wave rectification and low-pass filtering (eighth-order Butterworth) with a 160-Hz cutoff frequency. The acoustic amplitude (A) was transformed into the electric amplitude (E) by a power-law function with an exponent of 0.2 ($E = A^{0.2}$; Fu and Shannon, 1998). Then this transformed electric amplitude was used to modulate the amplitude of a 500 pulse/s biphasic pulse train. Each pulse had a 100-μs phase duration. The stimulation order of the four channels was 1-3-2-4 for four electrode pairs. Two four-electrode sets were used in the present study. All sets used BP+1 electrode mode, and the spacing between stimulated electrode pairs was five electrodes (3.75 mm). The apical set consisted of the four electrode pairs (20,22), (15,17), (10,12), and (5,7). The basal set consisted of electrode pairs (16,18), (11,13), (6,8), and (1,3).

B. Results

Figure 7 shows vowel recognition as a function of the most apical cochlear edge of tonotopically-shifted analysis

filter bands in five cochlear implant listeners. Panel (a) shows the recognition scores from individual cochlear implant subjects and panel (b) shows the mean scores from these five subjects for both apical and basal electrode locations compared to the acoustic results from Fig. 5. The filled symbols in Fig. 7(a) show the individual recognition scores as a function of the analysis filter locations when the speech information extracted from four analysis bands was delivered to four apical electrode pairs. Open symbols represent data from the basal electrode locations. Figure 7(b) shows the mean scores from the five implant subjects as a function of the tonotopic location of the analysis frequency bands with the apical electrode set (filled circles) and the basal electrode set (open circles). An ANOVA showed a significant effect of
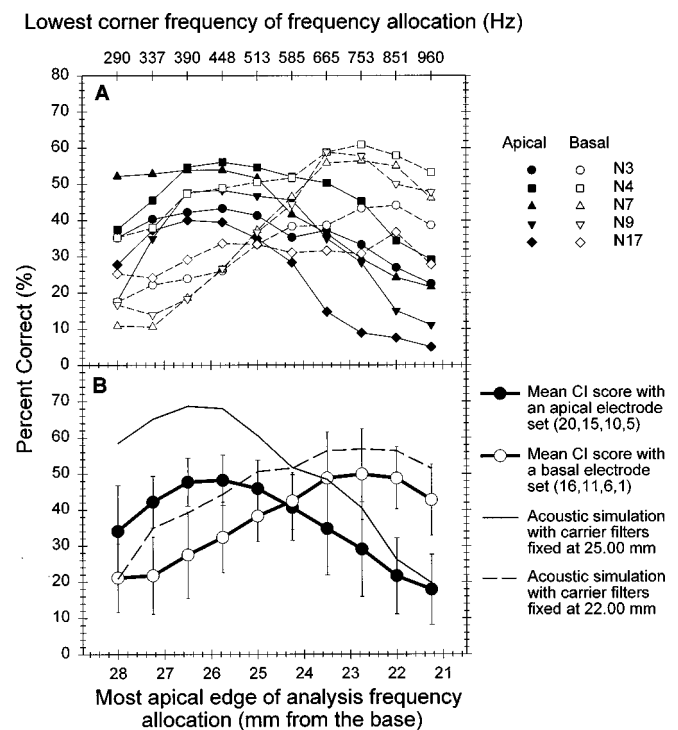
FIG. 7. Vowel recognition scores as a function of the most apical edge of the analysis filters for two different electrode configurations. Top panel presents individual results from five Nucleus-22 cochlear implant listeners. Lower panel presents average implant results compared to results from similar conditions in normal-hearing listeners from Fig. 5. Error bars indicate ± one standard deviation.

TABLE IV. The center frequencies of ten frequency allocations for the four-band processor.

	The most apical edge of frequency allocation (mm from the base)									
	28.00	27.25	26.50	25.75	25.00	24.25	23.50	22.75	22.00	21.25
Band 1	411	473	542	618	702	795	898	1013	1140	1281
Band 2	795	898	1013	1140	1281	1438	1611	1804	2017	2254
Band 3	1438	1611	1804	2017	2254	2516	2808	3131	3489	3886
Band 4	2516	2808	3131	3489	3886	4327	4816	5358	5959	6626

frequency allocation for the apical electrode set [$F(9,40)=4.84$, $p<0.001$] as well as for the basal electrode set [$F(9,40)=5.84$, $p<0.001$]. *Post hoc* Tukey HSD tests indicated that the score was significantly lower when the most apical edge of the frequency allocation was 22.75 mm or more basal for the apical set, and when the most apical edge of the frequency allocation was 25.75 mm or more apical for the basal set. Although the absolute level of performance was better for normal hearing than implant listeners, the overall pattern of results was similar. Normalized scores for the two groups of listeners were not significantly different for the apical set [$F(9,80)=0.74$, $p=0.67$] or basal set [$F(9,80)=0.76$, $p=0.65$]. Note that normal hearing subjects have different peak levels for the apical and basal set, whereas the peaks for the implant listeners are the same.

C. Discussion

For both apical and basal sets of electrodes, the functions in Fig. 7 show a maximum performance for analysis bands in a limited spectral region, indicating that vowel recognition in implant listeners was a strong function of the frequency allocation of analysis bands.

One interesting observation is that the pattern of vowel recognition as a function of the analysis frequency location is remarkably similar between electric and acoustic hearing [Fig. 7(B)]. It is difficult to know exactly the tonotopic location of the electrodes in an individual implant patient, but, in general, the electrodes are located more basally than the speech information that is delivered. If the best performance was still determined by the normal acoustic map, then we would expect the implant functions to peak at 25.00 mm or more basally. Only one of the implant subjects had a full electrode insertion, which would place the most apical electrode at approximately 25.00 mm from the base. Subject N17 has ten rings out, which means that her most apical electrode is roughly 18.00 mm from the base. Yet in these two subjects and in the other three (who had intermediate electrode locations) the functions had a peak when the apical edge of the analysis filters was 26.00 mm from the base. Although there was some individual variation in the functions, none showed a peak for the apical electrode set that was more basal than 26.00 mm (from the base). Since the electrode insertion depths of these five patients varied over 7 mm, it is unlikely that the peak in the function is determined by the normal acoustic map.

The frequency allocations in the present study are based on the Greenwood (1990) formula, so that they are somewhat different from the allocations in the clinical frequency tables used in the Nucleus-22 processor. However, further analysis shows that best performance occurred at the closest match to the frequency allocation in their clinical processor, with which they had at least 6 months of experience. For example, for the apical electrode set, the center frequencies of the 4-bands in the clinical speech processor for electrodes (20, 15, 10, 5) were 229, 1246, 2500, and 5307 Hz for clinical frequency set 9, and were 183, 997, 2000, and 4245 Hz for clinical frequency set 7. Table IV shows the center frequencies of the 4-band frequency allocations used in the present study, which did not exactly match the distributions in either set 7 or 9. However, if we assume that the most important frequency region for speech recognition to be 1000–3000 Hz, the best matched frequency allocations were $P_0 = 25.75 - 24.25$ mm for the apical electrode set, and $P_0 = 23.50 - 22.00$ mm for the basal electrode set. The data of the present study show that the best performance was obtained for these frequency allocations in both cases. Another interesting observation is that the peak difference between normal-hearing subjects and implant listeners was much smaller for the basal set than for the apical set. The clinical frequencies assigned to the electrodes in the basal set were virtually logarithmically spaced, but the apical set had a mixed spacing for the clinical assigned frequencies. The logarithmic frequency spacing among the electrodes in the basal set was closer to that of analysis filter bands used in the present study, indicating that better speech performance could be obtained if the frequencies of the analysis filter bands were close to the clinical assigned frequencies. All these results suggest that implant patients have adapted to an electrical tonotopic pattern different from the normal acoustic tonotopic pattern. The best matching frequencies are more likely determined by the adapted electrical map (accommodation hypothesis) than by the normal acoustic map (tonotopic-matching hypothesis).

One important question regarding accommodation is whether the asymptotic level of performance would equal the performance of the unaltered stimulus. Posen *et al.* (1993) found that, even after considerable training with spectrally altered stimuli, speech performance was not completely restored to the original level for stimuli without alteration. Results of the present study show that the functions in implant listeners have a lower peak level of performance than those in acoustic listeners, even though the overall shape of the functions was quite similar. It is likely that the difference in peak performance was caused by a partial accommodation to the spectral mismatch between the analysis bands and tonotopic location of the stimulated electrodes. The duration and degree of accommodation to such as mismatch is as yet unknown. Rosen *et al.* (1997) observed a rapid accommodation

of normal-hearing subjects listening to frequency-shifted speech with a 4-band noise vocoder. They found that speech recognition performance was near chance when the carrier noise bands were shifted by 6.46 mm relative to the analysis bands. After only 3 h of training, performance with a single talker increased to about half of that observed with the original unshifted 4-band processor. However, Rabinowitz and Eddington (1995) reported that speech performance was still worse than a one-channel condition when speech information was delivered in a reverse tonotopic distribution (low-frequency speech information was delivered to basal electrodes and visa versa) even after the patient had used the experimental processor for 3 days. These results indicate that the performance level of the altered stimulus and accommodation periods may depend strongly on the degree of spectral mismatch of the altered stimulus.

A severe spectral mismatch may result in a lower asymptotic level of performance as well as a longer accommodation period. One might expect that assigning the frequencies of analysis bands based on the normal acoustic map in the initial fitting of a cochlear implant speech processor may solve this problem. It is probably true that the frequency allocations based on the normal acoustic map require virtually no or very short accommodation periods. However, such an allocation for implants with shallower insertion depths may result in a loss of important low-frequency speech information, which cannot be restored by accommodation (Fig. 2). In that case, a frequency allocation with better spectral resolution might provide better performance even though there is some spectral mismatch between analysis and carrier bands (Fig. 5, open circles). The present results indicate that a tradeoff between spectral resolution (accommodation hypothesis) and spectral mismatch (tonotopic-matching hypothesis) should be considered carefully in the initial fitting of a cochlear implant speech processor.

III. SUMMARY AND CONCLUSIONS

Four conclusions are summarized based on the results in the acoustic stimulation study and the last conclusion is made based on the results in the electric stimulation study.

(1) Vowel recognition was only mildly affected by shifting the entire frequency range 6.75 mm along the cochlea, as long as spectral and tonotopic locations were matched. The decline in performance at more basal locations could be explained by AI theory.
(2) Best performance was obtained when the analysis bands and carrier bands were matched in tonotopic position and extent. Performance declined steeply as the tonotopic location of either carrier bands or analysis bands were shifted relative to each other by more than 3 mm.
(3) Spectral resolution, as represented by the number of noise carrier bands in a noise-band vocoder, had a separate and independent affect on speech recognition from both spectral range and spectral mismatch. Greater spectral resolution did not provide additional robustness against the deleterious effects of tonotopic shifting and mismatching.

(4) The effect of spectral shifting was clearly dependent on talker gender, with male voices tolerating more basal shift and children's voices tolerating more apical shift. This suggests that the frequency range over which listeners can tolerate tonotopic shifting is fixed.
(5) The implant subjects have accommodated to the tonotopic patterns provided by their clinical implant processor and have the same sensitivity to spectral shifting as normal-hearing listeners.

ANSI (**1969**). ANSI S3.5-1969. ''American National Standard Methods for the Calculation of the Articulation Index'' (American National Standards Institute, New York).

Beasley, D. S., Mosher, N. L., and Orchik, D. J. (**1976**). ''Use of frequency-shifted/time-compressed speech with hearing impaired children,'' Audiology **15**, 395–406.

Boothroyd, A., Mulhearn, B., Gong, J., and Ostroff, J. (**1996**). ''Effects of spectral smearing on phoneme and word recognition,'' J. Acoust. Soc. Am. **100**, 1807–1818.

Daniloff, R. G., Shiner, T. H., and Zemlin, W. R. (**1968**). ''Intelligibility of vowels altered in duration and frequency,'' J. Acoust. Soc. Am. **44**, 700–707.

Dorman, M. F., Dankowski, K., McCandless, G., and Smith, L. M. (**1989**). ''Consonant recognition as a function of the number of channels of stimulation by patients who use the Symbion cochlear implant,'' Ear Hearing **10**, 288–291.

Dorman, M. F., Loizou, P. C., and Rainey, D. (**1997a**). ''Speech understanding as a function of the number of channels of stimulation for processors using sine-wave and noise-band outputs,'' J. Acoust. Soc. Am. **102**, 2403–2411.

Dorman, M. F., Loizou, P. C., and Rainey, D. (**1997b**). ''Simulating the effect of cochlear-implant electrode insertion-depth on speech understanding,'' J. Acoust. Soc. Am. **102**, 2993–2996.

Dubno, J. R., and Dorman, M. F. (**1987**). ''Effects of spectral flattening on vowel identification,'' J. Acoust. Soc. Am. **82**, 1503–1511.

Dubno, J. R., and Schaefer, A. B. (**1995**). ''Frequency selectivity and consonant recognition for hearing-impaired and normal-hearing listeners with equivalent masked thresholds,'' J. Acoust. Soc. Am. **97**, 1165–1174.

Dudley, H. (**1939**). *The Vocoder*, Bell Labs Record **17**, pp. 122–126.

Fishman, K., Shannon, R. V., and Slattery, W. H. (**1997**). ''Speech recognition as a function of the number of electrodes used in the SPEAK cochlear implant speech processor,'' J. Speech Hear. Res. **40**, 1201–1215.

Fu, Q.-J. (**1997**). ''Speech perception in acoustic and electric hearing,'' Ph.D. dissertation, University of Southern California—Los Angeles.

Fu, Q.-J., and Shannon, R. V. (**1998**). ''Effects of amplitude nonlinearity on speech recognition by cochlear implant users and normal-hearing listeners,'' J. Acoust. Soc. Am. **104**, 2570–2577.

Greenwood, D. D. (**1990**). ''A cochlear frequency-position function for several species—29 years later,'' J. Acoust. Soc. Am. **87**, 2592–2605.

Hill, F. J., McRae, L. P., and McClellan, R. P. (**1968**). ''Speech recognition as a function of channel capacity in a discrete set of channels,'' J. Acoust. Soc. Am. **44**, 13–18.

Hillenbrand, J., Getty, L., Clark, M., and Wheeler, K. (**1994**). ''Acoustic characteristics of American English vowels,'' J. Acoust. Soc. Am. **97**, 3099–3111.

McDermott, H. J., McKay, C. M., and Vandali, A. E. (**1992**). ''A new portable sound processor for the University of Melbourne/Nucleus Limited Multichannel cochlear implant,'' J. Acoust. Soc. Am. **91**, 3367–3371.

Nagafuchi, M. (**1976**). ''Intelligibility of distorted speech sounds shifted in frequency and time in normal children,'' Audiology **15**, 326–337.

Posen, M. P., Reed, C. M., and Braida, L. D. (**1993**). ''Intelligibility of frequency-lowered speech produced by a channel vocoder,'' J. Rehabil. Res. Dev. **30**, 26–38.

Rabinowitz, W. M., and Eddington, D. (**1995**). ''Effects of Channel-to-Electrode Mappings on Speech Reception with the Ineraid Cochlear Implant,'' Ear Hear. **16**, 450–458.

Rosen, S., Faulkner, A., and Wilkinson, L. (**1997**). ''Perceptual adaptation by normal listeners to upward shifts of spectral information in speech and its relevance for users of cochlear implants,'' in *Speech, Hearing, and Language: Work in Progress* (Phonetics and Linguistics, University College, London), Vol. 10.

Shannon, R. V. (**1992**). ''Temporal modulation transfer functions in patients with cochlear implants,'' J. Acoust. Soc. Am. **91**, 1974–1982.

Shannon, R. V. (**1993**). ''Psychophysics of electrical stimulation,'' in *Cochlear Implants: Audiological Foundations*, edited by R. S. Tyler (Singular, San Diego), pp. 357–388.

Shannon, R. V., Adams, D. D., Ferrel, R. L., Palumbo, R. L., and Grantgenett, M. (**1990**). ''A computer interface for psychophysical and speech research with the Nucleus cochlear implant,'' J. Acoust. Soc. Am. **87**, 905–907.

Shannon, R. V., Zeng, F-G., Kamath, V., Wygonski, J., and Ekelid, M.

(**1995**). ''Speech recognition with primarily temporal cues,'' Science **270**, 303–304.

Shriner, T. H., Beasley, D. S., and Zemlin, W. R. (**1969**). ''The effects of frequency division on speech identification in children,'' J. Speech Hear. Res. **12**, 402–412.

ter Keurs, M., Festen, J. M., and Plomp, R. (**1992**). ''Effect of spectral envelope smearing on speech reception. I,'' J. Acoust. Soc. Am. **91**, 2872–2880.

ter Keurs, M., Festen, J. M., and Plomp, R. (**1993**). ''Effect of spectral envelope smearing on speech reception. II,'' J. Acoust. Soc. Am. **93**, 1547–1552.

Thomas, I. B. (**1968**). ''The influence of first and second formants on the intelligibility of clipped speech,'' J. Audio. Eng. Soc. **16**, 182–185.

Tiffany, W. R., and Bennett, D. A. (**1961**). ''Intelligibility of slow-played speech,'' J. Speech Hear. Res. **4**, 248–258.

Villchur, E. (**1977**). ''Electronic models to simulate the effect of sensory distortions on speech perception by the deaf,'' J. Acoust. Soc. Am. **62**, 665–674.

Wallace, W., and Koury, G. (**1981**). ''Transfer effects from listening to frequency-controlled and frequency-shifted accelerated speech,'' J. Speech Hear. Res. **24**, 185–191.

Wilson, B. S., Finley, C. C., Lawson, D. T., Wolford, R. D., Eddington, D. K., and Rabinowitz, W. M. (**1991**). ''New levels of speech recognition with cochlear implants,'' Nature (London) **352**, 236–238.

Zollner, V. M. (**1979**). ''Intelligibility of the Speech of a Simple Vocoder,'' Acustica **43**, 271–272.

Segmental and syllabic representations in the perception of speech by young infants

Peter D. Eimas[a]

Department of Cognitive and Linguistic Sciences, Brown University, Box 1978, Providence, Rhode Island 02912

In a series of four experiments, the ability of 3- to 4-month-old infants to form categorical representations to syllable-initial consonants in monosyllabic stimuli (experiments 1 and 2) and to initial and final syllables in bisyllabic stimuli (experiments 3 and 4, respectively) was investigated. Experiment 1 yielded no evidence of categorical representations for the initial consonant. However, the results indicated that the four or six stimuli presented during the initial phase of familiarization had been remembered. The results of experiment 2, which employed a less stringent familiarization criterion, replicated the findings of experiment 1, although there was some evidence for categorization for infants whose familiarization performance more closely matched the weaker criterion. In experiment 3, there was strong evidence for a categorical representation of the initial syllable of bisyllabic stimuli for infants experiencing six familiar stimuli. In experiment 4, there was less robust evidence of categorization of the final syllable of bisyllabic stimuli, but again only when six familiar stimuli were experienced. The results were discussed in terms of the earliest representation of speech being syllables that could be modified by the rhythmic nature of the infant's native language. © *1999 Acoustical Society of America.* [S0001-4966(99)01203-5]

PACS numbers: 43.71.Ft [WS]

INTRODUCTION

A characteristic of spoken language is its very nearly continuous nature. Moreover, when discontinuities occur in the form of short periods of silence and abrupt changes in the nature of the acoustic energy, these discontinuities tend to bear no consistent relation to our percepts, be they words or prelexical units (e.g., phonetic segments and syllables). In addition, the speech signal is marked by a lack of invariant spectral and temporal information for the identification of specific phonetic contrasts (Liberman *et al.*, 1967; but see Stevens and Blumstein, 1981) and to a lesser extent their syllabic combinations, thereby making explanation of the processes of word acquisition and recognition as yet difficult to describe.

Nevertheless, conventional wisdom holds that a direct relation between the acoustics of speech and words (see, for example, Klatt, 1979, 1989) is impractical. Presumably, the variation in the production of words both between and within speakers would create an indefinite number of mappings between the signal and the mental instantiation of words. Consequently, processing hypotheses have centered on the constraint that the speech stream is initially segmented into smaller, prelexical representational units that serve as the basis for lexical acquisition and access, despite the nearly continuous nature of speech and the absence of invariant cues for sublexical segmentations (e.g., Pisoni and Luce, 1987; Mehler, 1981; Jusczyk, 1996, 1997).

Phonemes and syllables are the most frequently proposed units. Phonemes provide the smaller inventory of units, and given the small number of phonemes in any language, the acquisition and recognition of words by means of a phoneme-by-phoneme procedure would be relatively efficient. However, the lack of invariance arising from the effects of coarticulation, among other contextual factors, makes the physical realization and representation of the phoneme problematic (Liberman *et al.*, 1967) and consequently not easily segmented and identified. The repertoire of syllables in any language is considerably larger, especially in languages with complex syllabic structures such as English. Nevertheless, coarticulatory effects would be less a problem in that coarticulatory effects across segments within syllables are (or can be) informative. Of course, coarticulatory effects across syllables remain a problem. In addition, it is also true that if lexical searches begin at any identified phoneme or any identified syllable, greater cognitive economy will be achieved if the search begins with syllabic structures, as the ratio of successful to unsuccessful searches will be considerable higher with syllabic-initiated searches (Cutler and Norris, 1988).

Recent research has sought to provide evidence regarding the representational forms, typically phonemic segments or syllables, which prelinguistic infants use to represent speech in order to further our understanding of lexical acquisition and later lexical access. The first study to directly investigate a possible role of syllables as processing units in infant speech perception was that of Bertoncini and Mehler (1981). They found that 4-day-old infants discriminated the reversal of the initial and final consonants of patterns with three synthetic segments only when the consonants were the syllable-initial and syllable-final consonants of a consonant–vowel–consonant (CVC) syllable which is a legal syllabic structure and not when the same consonants began and ended a CCC utterance, which is not a legitimate syllable. More-

over, reversal of the first and third consonants in a VCCCV structure, which has a permissible bisyllabic configuration, were likewise discriminated. The authors concluded that "We interpret our results as favoring a view according to which the syllable is the natural unit of segmentation and processing" (p. 247)—a view that Mehler and his colleagues have been instrumental in developing since the early 1980's (Mehler, 1981; Mehler *et al.*, 1981; Mehler, Segui, and Frauenfelder, 1981; Bertoncini *et al.*, 1995).

Bijeljac-Babic, Bertoncini, and Mehler (1993) have provided further evidence that the syllable is the unit of processing and the basis for the representation of speech by infants. They showed that 4-day-old infants, born into French-speaking homes, distinguished a list composed of bisyllabic utterances from one composed of trisyllabic utterances. This occurred even when the natural difference in duration between utterances of two, as opposed to three, syllables was reduced by means of algorithms that compress and expand natural speech, while maintaining their intelligibility. Moreover, infants from the same population did not discriminate two-syllable utterances that had either four or six phonemes, despite the fact that the difference in duration between these utterances was nearly the same as that between the two- and three-syllable utterances.

A number of experiments on the formation of categorical representations for speech by Jusczyk and his colleagues (Bertoncini *et al.*, 1988; Jusczyk and Derrah, 1987; Jusczyk, Kennedy, and Jusczyk, 1995; Jusczyk *et al.*, 1990) have likewise produced evidence that in its entirety supports a syllabic form of representation of speech by young infants, either 4 days or 2 months of age. In addition, the findings indicate that by 2 months of age the encoding of CV syllables to which the infant had been familiarized was highly detailed.

In a typical experiment (Bertoncini *et al.*, 1988; Jusczyk and Derrah, 1987), an infant is presented with a series of monosyllabic stimuli during the first, familiarization phase that has a common phonetic segment, either the consonant [b] with varying vowels ([bi] as in bee, [bo] as in bowl, [bɚ] as in berg, and [ba] as in body) or the vowel [i] with varying consonants ([bi], [si], [li], and [mi]). Based on studies of categorization in the visual domain (see Quinn and Eimas, 1986, 1996, for reviews), the expectation is that if a categorical representation was formed at the level of the segment and was sufficiently salient, then evidence of discrimination would only be available if a novel CV test stimulus differed with respect to the initial common consonant in the former case, and with respect to the final common vowel in the latter case. Differences in the previously variable segment, whether the vowel or consonant, would be unnoticed or not sufficiently attended to in order to cause dishabituation. This was *not* the case with 2-month-old infants. After familiarization with the series of [bV] syllables, infants discriminated about equally the addition of the syllable [bu] to the familiar stimuli which had a novel vowel along with the common consonant and which should not have been discriminated had categorization occurred, the syllable [da], which consisted of a novel consonant and a familiar vowel, and the syllable [du], which had a novel consonant and a novel vowel and like [da] should have been discriminated. After familiariza-

tion with syllables with a common vowel and differing initial consonants, discrimination occurred to all test stimuli whether they differed from the familiar stimuli in the consonant alone ([di]) or the vowel alone ([ma]) as well as in both the consonant and vowel ([da] and [dɪ]). Categorization, as defined, had not occurred in either case, but rather it would appear that each CV had been represented, and consequently any segmental change was sufficient to cause dishabituation. It is important to note that during the test trials, the familiar and novel stimuli were both presented.

After familiarization with the common consonant, the 4-day-old infants, like the 2-month-olds, showed discrimination of a novel vowel, whether paired with a familiar or novel consonant, [bu] or [du], respectively. However, they did not discriminate [da], which had a novel consonant, but importantly did not have a novel vowel. In addition, all of the test stimuli were discriminated after familiarization with stimuli having the common vowel [i], except [di], the stimulus with only a novel consonant. The findings with stimuli with a common vowel are thus in accord with a categorical representation based on vocalic segments (cf. Mehler *et al.*, 1996). Nevertheless, the neonate data as a whole were taken by the authors to support syllabic representations in which the consonants were represented with sparse, if any, detail. As a consequence, distinctions would not be made between the novel and familiar consonants, such as [b] and [d], and discrimination would be governed by the novelty of the salient vowel. With regard to the older infants, each familiar CV syllabic sequence appeared to be quite specifically represented and thus any new sequence, whether novel with respect to the vowel, consonant, or both, would be detected, as was the case. Of course, the fact that infants did not evidence categorization of the common consonant or vowel does not necessarily indicate that these segments and their common nature were not part of the representation of speech. Under other, as yet unknown conditions, evidence of their abstraction and categorization might well be obtained.

Based on these data demonstrating a lack of evidence from young infants for categorical representations at the segmental level, it might be argued that infants below 6 months of age are unable to form categories based on the common elements of speech, an argument that is weakened in that a form of categorization exists in infants this age as defined by categorical perception (Eimas, 1997; Jusczyk, 1996, 1997). In addition, that this is not the case is attested to by the findings of Jusczyk *et al.* (1995) that likewise add strong support for a syllabic unit of representation in infancy that, as will be argued later together with the present findings, is the initial or default representation of speech. In their first experiment, 2–3-month-old infants were familiarized with four bisyllabic utterances that had a common stressed first syllable, [ba]: [ba.zi], [ba.lo], [ba.mɪt], and [ba.dɛs]. (The period marks the syllabic boundary.) On attaining the criterion for familiarization, a syllable was added to the original familiar stimuli such that the test phase included the new stimulus plus the familiar stimuli. The novel stimulus differed from the familiar stimuli (a) in the final unstressed syllable (as did all the test stimuli), but had the same initial syllable ([ba.nʌl]), (b) in a single feature in the initial conso-

nant of the first syllable ([pa.mʌl]), (c) by two features in the initial consonant of the first syllable ([ka.fʌl] or [na.bʌl]), with the latter stimulus interestingly containing both of the familiar segments from the first syllable, although no longer as a complete syllable or part of a single syllable, and (d) in the vowel of the familiar first syllable ([bæ.vɚn]). Infants detected the presence of the novel stimulus in all situations except condition (a), where the initial syllable was familiar—evidence in accord with the view that a categorical representation was formed based on a detailed representation of the initial CV syllable, and not the vowel alone [see, particularly, test condition (b)]. Moreover, this representation must have encoded the presence of the second syllable, but merely as being present without featural, segmental, or wholistic syllabic details. Otherwise, the test stimulus [ba.nʌl] in condition (a) would have been considered novel.

Given the importance of the manner in which speech is represented both during the initial acquisition of words and their later recognition, further evidence related to the categorization and representation of speech by young infants with a somewhat different experimental procedure was sought. A familiarization-preference testing procedure was used that, in different forms, has been successful in demonstrating quite specific categorical representations of natural kinds and artifacts in young infants in the visual domain (for reviews of this literature, see Quinn and Eimas, 1986, 1996). In the first two experiments, infants were familiarized with a number of monosyllabic speech patterns with one common and at least one variable segment across the patterns (for example, CV syllables with the common initial segment [b] and a different vowel in all syllables, as well as a final consonant in some syllables). In other words, all of the test stimuli had a novel coda. On attaining the familiarization criterion, two novel syllables are presented successively, one in which the familiar consonant is paired with a novel coda (novel vowel and novel or familiar final consonant if present), and the other in which a novel initial consonant is paired with the same novel coda. Given that the common initial consonant had been recognized as being the same in all instances and represented as a category based on the initial segment, and given the young infant's strong preference for novelty, then discrimination should only occur for the test stimulus with the novel initial consonant. This procedure is more sensitive in experiments on the formation of categories in infants than that used by Jusczyk and his colleagues in that the familiar stimuli are not presented during the test trials. Thus, it is more difficult in the present procedure to compare the novel stimuli with the familiar stimuli—memory is required and it is not unreasonable to assume that memory for a common segmental element that was always presented would be stronger than that for the relatively many individual syllables that had been presented less frequently. Hence, the assumption was that if segmental categories were formed, the present procedure would be more likely to evidence their existence.

In experiments 3 and 4, almost exactly the same procedure was used with the single exception that infants were tested with bisyllabic utterances with either a common initial syllable (experiment 3) or a common final syllable (experiment 4). In this manner, it was possible to compare the in-fant's ability to represent the basic units of speech, segments, and syllables, and to infer the initial, more salient representational unit of speech and its relation to the representation of speech by adult listeners.

I. EXPERIMENT 1

In this experiment, 3- to 4-month-old infants were familiarized with either four or six monosyllabic patterns, each of which had the same initial consonant, [b] or [d]. The use of four or six familiar stimuli was undertaken to further test earlier findings that evidence for categorization is more likely to be obtained when the demands on memory are greater—that is, when there were six familiar stimuli (Bomba and Siqueland, 1983). On reaching the criterion for familiarization, they were then presented with two novel patterns, one, for example, with a novel vowel paired with the familiar consonant and the other with the same novel vowel but paired with a novel consonant, the previously unheard initial consonant [b] or [d]. As noted, the expectation based on previous research in speech and vision is that if a categorical representation for the familiar segment was formed and sufficiently robust, infants should show greater responsivity to the pattern with the novel consonantal segment than to the pattern with the familiar consonant, the novel variation in the vowel being ignored. Indeed, the level of responsivity to the test stimulus with the familiar initial consonant should approximate what it had been at the end of familiarization, given only categorical representations for the initial consonant.

A. Method

1. Participants

The listeners were 64 infants, 3–4 months of age ($M = 3.33$ months; s.d.$= 0.48$ months) and to the best of our knowledge, all came from monolingual English-speaking home environments. There were 24 females and 40 males. An additional 32 infants failed to complete the experiment for the following reasons: seven were fussy, 18 failed to look long enough and thus were not sufficiently exposed to the familiarizing sounds, and seven did not attain the familiarization criterion within 15 min. The vast majority of infants in this and the other studies to be reported was Caucasian and from middle- and upper-middle-class homes situated in the greater Providence, RI area. The infants in all experiments were recruited by obtaining permission of their mothers to participate shortly after their birth at Women and Infants Hospital of Rhode Island. Parents were paid a small honorarium for their participation.

2. Stimuli

The stimuli were 18 syllables, produced by a male speaker of North American English with list intonation, most of which were words for adults but, of course, not for infants. Nine of the stimuli began with [b] and nine with [d]. They were as follows: bead, deed, bid, did, bed, dead, bad, dad, bay, day, boo, due, bot, dot, boat, dote, birt, and dirt.[1] The vowels widely sampled the acoustic space containing American English vowels. The stimuli were recorded onto a DAT

recorder by a male speaker of American English. They were then sampled at 20 kHz and stored on the disk of a Gateway 2000 computer. The stimuli were then edited and stored in 18 individual files, one for each stimulus. From each set of nine stimuli that was assigned to 32 infants, 16 of the infants received four or six stimuli that were randomly selected to serve as the familiar stimuli. The selection procedure was repeated eight times. Thus, each group of four or six randomly selected stimuli was assigned to two infants in order that the stimuli and their arrangement would be identical during familiarization, while the test-trial stimuli differed only with respect to whether the infants heard the novel or familiar initial consonant on the first or second test trial. To create the test-trial stimuli for each pair of infants who would receive the same familiar stimuli, two unfamiliar stimuli with the same novel coda were randomly selected eight times, one with the familiar initial consonant and one with a novel initial consonant.

The six to-be-familiar stimuli were arranged into six different randomly ordered files, each containing all six stimuli separated by 200 ms of silence. The two test-trial stimuli were each arranged into two files of six identical stimuli, with each stimulus again separated by 200 ms of silence. Thus, the familiar and novel stimuli were presented in an identical manner.

For the 32 infants who received only four stimuli during familiarization, the selection and arrangement of the four to-be-familiar and two test stimuli were as described for infants receiving six stimuli, with the sole exception that each of the files contained only four stimuli. In summary, each pair of infants received a random selection of the stimuli during familiarization, either four or six stimuli, as well as a random selection of two of the remaining stimuli for presentation during the test trials, one with a familiar initial consonant and one with a novel initial consonant. Both test stimuli had the same novel vowel and familiar or novel final consonant, if present.

3. Apparatus

The stimuli were presented to the infant by means of programs developed by John Mertus at Brown University as part of the BLISS system and were heard over a mini Advent speaker. The overall-intensity level (measured at the infant's head) was approximately 78 dB(A) SPL.

The speaker was located approximately 65 cm from the infant's head and directly above a picture of a woman's face that was well lighted and situated on a black panel directly below the Advent speaker. The picture, which was 15.4 ×14.7 cm, was located approximately 61 cm from the infant's eyes and subtended angles of 14 deg 3′ vertically and 13 deg 30′ horizontally. Just below the woman's jaw was a hole in the black panel, through which a permanently mounted TV camera recorded the entire face of the baby. The baby's facial image was displayed on a monitor located in a separate room. The experimenter in the room with the monitor viewed the baby and pressed a button on a response panel whenever the picture of the woman was centered on the infant's corneas. Pressing the button initiated presenta-

tion of the speech stimuli and releasing it stopped presentation when the stimulus file with the four or six stimuli being presented ended.

4. Procedure

As noted, a familiarization-preference procedure was used (cf. Best, McRoberts, and Sithole, 1988; Miller and Eimas, 1996). Each infant was positioned in a reclining infant's seat in a dimly lighted, sound-attenuated room facing the lighted picture of the woman's face and the speaker. After the infant was comfortably settled by the first experimenter, the experiment began. The first experimenter, who was seated to the side of the infant, listened to recorded music over earphones to mask the speech stimuli being presented. The second experimenter, who was naive with respect to the experimental condition, observed the infant's face on the monitor in a separate room and presented the stimuli when the infant was appropriately focused on the woman's face. When the button was pressed and the speech presented, the entire file of four or six randomly ordered stimuli was presented. The second experimenter released the button whenever the infant looked away from the picture, which stopped stimulus presentation when the stimulus file was completed. The second experimenter could, by turning her head briefly, observe a second monitor that displayed the trial number of the familiarization or test-trial period and thus would know when to terminate the experiment. Interexperimenter reliability for this procedure across a variety of dependent measures has been found to be quite high in our laboratory, being between 0.84 and 0.96 (Eimas and Miller, 1992).

A trial was defined as the observation of the picture by an infant for at least 4 s, followed by a continuous period of looking away from the picture for a period of at least 1 s. If the infant looked away from the picture for less than 1 s during a trial, the clock recording total observation time for that trial stopped, and then continued when the infant resumed looking at the picture. The familiarization period lasted for at least six trials and ended when the mean looking time for the final three trials was 50% of that for the first three trials. The six files were presented in a fixed order across the first six trials, and the order was repeated if there were more than six trials of familiarization. This insured that the individual familiar stimuli, whether there were four or six stimuli, were presented in the six different random orders, and given the duration of the stimuli, the silence between stimuli, the minimal duration of a trial, and the familiarization criterion, each stimulus was heard at least 12 times. In summary, half the infants were randomly assigned to each familiarization condition (six versus four stimuli), and half the number of these infants was familiarized with a random selection of stimuli with the initial consonant [b] and half with the initial consonant [d].

On completion of the familiarization phase, the test-trial period was immediately initiated. There were six trials; three presented the novel stimulus with the familiar initial consonant, and three the novel stimulus with the novel initial consonant. The order in which the two novel test stimuli were

1904   J. Acoust. Soc. Am., Vol. 105, No. 3, March 1999

Peter D. Eimas: Segmental and syllabic categories   1904

TABLE I. Mean fixation times (s) and standard deviations as a function of the number of familiarization stimuli and experiments.

| Familiar stimuli | Familiarization trials | | | | Test-trial difference scores[a] | | | |
| | First three | | Last three | | Familiar | | Novel | |
	M	s.d.	M	s.d.	M	s.d.	M	s.d.
	Experiment 1							
4	21.58	12.50	8.49	4.73	2.83	6.34	3.45	7.54
6	23.17	9.80	8.13	3.34	3.65	5.16	3.42	5.59
	Experiment 2							
4	23.65	15.14	10.40	4.92	2.33	6.28	4.01	7.79
6	23.35	16.85	10.15	6.49	2.35	6.65	2.30	4.82
	Experiment 3							
4	24.58	9.16	8.43	3.25	5.26	6.49	5.73	7.95
6	33.72	20.30	11.26	5.33	1.54	6.61	3.85	6.44
	Experiment 4							
4	33.78	25.34	9.44	4.96	2.29	6.30	1.91	5.13
6	33.81	18.99	10.57	5.28	0.98	6.03	2.59	7.91

[a]Mean looking-time differences when the test-trial consonant or syllable was the same or different from that heard during the familiarization trials.

presented alternated across the six trials, with each stimulus beginning the test-trial series for half of the infants.

B. Results and discussion

1. Familiarization

Table I shows the mean looking times for the first three and final three trials of familiarization as a function of the number of stimuli experienced during familiarization. The results have been averaged across the two initial consonants ([b] and [d]) inasmuch as the initial consonant never produced a reliable or even near-reliable main effect or interaction during either phase of the series of experiments. An analysis of variance of the familiarization data, performed separately on the data from each of the familiarization conditions,[2] initial consonant ([b] vs [d]) by trials (first three vs last three), showed that the trials effect was reliable [$F(1,30) > 74.49$, $p < 0.001$, in each analysis]. There was a reliable decrement in looking times across trials, which is not surprising given the nature of the familiarization phase. All other F values were less than 1.00.

2. Test phase

Difference scores were computed by subtracting the mean looking times averaged across the last three trials of familiarization from the mean looking times for the three test trials when the initial test-trial consonant was familiar; that is, the same as that heard during familiarization, and when it was novel or different. Fixation times on any particular test trial greater than 60 s (which were at least 3 s.d.'s above the mean of a given condition) were eliminated and replaced by the mean of that particular condition and trial. There was one such score in experiment 1, and it occurred when the familiar and test-trial initial consonants were the same. The mean difference scores are shown in Table I. The concern of the present experiments is whether categorization occurred. To reiterate, the criteria for categorization are a mean difference

score not reliably greater than chance (zero in this case) when the initial consonants were familiar and a difference score greater than chance when the initial consonants were novel, as well as a significant difference between the two difference scores.[3] Given these criteria, categorization did not occur when the number of familiarization exemplars was four or six. In both conditions, the two difference scores were greater than expected by chance [$t(31) > 2.83$, $p < 0.01$, for all tests] and the two scores in each familiarization condition did not differ [$t(31) < 1.0$, $p > 0.10$, in each case].

The data do, however, support the contention that the infants encoded and represented the four or six familiar syllables for at least the duration of the experiment, and treated each test-trial syllable as novel, whether only the coda had been changed or whether the initial consonant and the coda were both changed. If this is indeed the case, it would indicate that the syllables had been represented with a considerable amount of specificity with respect to both the initial consonant and the following vowel (cf. Jusczyk et al., 1995).

II. EXPERIMENT 2

At issue at this point was whether some simple experimental manipulation would function to enhance the probability of finding evidence for categorization of the initial consonantal segment. One such variable might well be the duration of the familiarization period. Given a shorter period of familiarization with the consequence that each exemplar is experienced less frequently, it is possible that it will become difficult or even impossible to encode and remember all of the familiar exemplars. In addition and more importantly, infants will be relatively more likely to strongly encode and remember those characteristics that are common to each pattern, and hence provide evidence for a categorical representation based on the initial consonant (cf. Bomba and Siqueland, 1983). In the next experiment, the frequency with which the infants experienced each exemplar was (presumably) decreased by making the criterion for familiarization more lenient, now being 75% of the looking time during the first 3 min rather than 50%.

A. Method

1. Participants

There were 64 infants, 29 females and 35 males, 3 to 4 months of age ($M = 3.24$ months; s.d. $= 0.41$ months). An additional 16 infants failed to complete the experiment, 11 because they were excessively fussy, and five because they did not look sufficiently long at the picture to become familiar with the sounds, or failed to meet the criterion for familiarization. The infants were from the same population of infants as that described in experiment 1.

2. Stimuli and apparatus

The stimuli, their manner of arrangement, and the apparatus were identical to those of experiment 1.

3. Procedure

In all respects, with but one exception, the procedural details were the same as those employed in experiment 1. The one exception was the criterion for familiarization, which was changed from 50% to 75% of the mean looking time for the first three familiarization trials during the final three familiarization trials. This manipulation was partially successful. The mean number of familiarization trials in experiment 2 was less than in experiment 1, but the difference was marginally reliable only when there were six stimuli [6.23 vs 7.63 trials; $t(62) = 1.96$, $p < 0.05$, one-tailed]. With four familiar stimuli, the difference was 7.31 vs 6.25 trials [$t(62) < 1.00$, $p > 0.10$].

B. Results and discussion

1. Familiarization

Table I shows the mean looking times for the first three and final three trials of familiarization as a function of the number of familiar stimuli. Analysis of variance of the familiarization data, initial consonant ([b] vs [d]) by trials (first three versus last three), revealed significant effects for trials [$F(1,30) > 42.55$, $p < 0.001$, in each familiarization condition], there being a reliable decrement in looking times across trials as expected, given the manner in which the familiarization phase was conducted. All other F values for main effects and interactions were less than 1.00.

2. Test phase

Difference scores were computed for individual infants as described in experiment 1. There were three looking times greater than 60 s that were replaced by the mean scores for the condition and trial from which they were removed; two of the scores occurred when the familiar and test-trial initial consonants were different and one occurred when they were the same. The mean difference scores are shown in Table I. Inspection of Table I shows that the looking times in all four conditions again showed recovery—that is, an increase over the mean times for the last three trials of familiarization. Moreover, in all four conditions the difference scores were reliably greater than chance: [$t(31) > 2.50$, $p < 0.025$ in each instance]. In addition, there was no difference between the difference scores for familiar and novel initial consonants when the number of familiar exemplars was either four or six syllables [$t(31) < 1.00$, $p > 0.10$, in each case]. These measures thus provided no evidence for categorization.

It would appear then that reducing the infants' exposure to the familiar stimuli did not produce evidence for a categorical representation. However, a closer inspection of the data shows that this conclusion needs to be somewhat tempered. What is true is that the criterion for familiarization in this experiment, while set at 75%, was considerably surpassed. In actuality, the mean looking time on the final three trials was 44% of the mean looking time on the first three trials, a higher percentage than that of experiment 1, which was 37%, but one that is still considerably below that of the 75% criterion that was sought. Nevertheless, there were 32 infants who produced looking times on the last three trials of familiarization that were higher than 50%, being on average

62%, and took fewer trials to attain the familiarization criterion than the infants of experiment 1, 6.63 vs 7.47 [$t(94) = 1.84$, $0.05 < p < 0.10$], and interestingly these infants showed some evidence for categorization. There was a reliable difference [$t(31) = 2.24$, $p < 0.05$] between test trials with familiar and novel consonants (2.13 vs 3.82 s). However, both difference scores were greater than chance [$t(31) = 2.35$, $p < 0.05$ and $t(31) = 3.34$, $p < 0.001$, respectively], which is not in accord with the test-trial performance being governed solely by categorical representations. Moreover, given the results to be presented showing the formation of categorical representations for syllables in experiments 3 and 4, these consonantal categorical representations may well not be the initial representation of speech, but rather ones that are derived from *a priori* syllabic representation, or at the very least, less salient than syllabic representations.

III. EXPERIMENT 3

Experiment 3 was undertaken to determine whether infants would form a categorical representation for the initial syllables of bisyllabic utterances. The stimulus patterns began with [ba] or [da]. Each infant was familiarized with a random selection of four or six bisyllabic patterns, and on attaining the criterion for familiarization was presented with two new stimulus patterns, one in which both syllables were novel and one in which only the final syllable was novel, the initial syllable having been experienced during familiarization. The novel second syllable was the same for both test-trial stimuli. As described earlier, categorization of the initial syllable would be evidenced if infants showed above-chance responding to the pattern with a novel initial syllable and near-chance responding to the pattern with the familiar initial stimulus, as well as a reliable difference in responding to the two patterns.

A. Method

1. Participants

The listeners were 64 infants, 3–4 months of age ($M = 3.35$ months; s.d. $= 0.38$ months). There were 26 females and 38 males. Fifty additional infants failed to complete the experiment for the following reasons: 32 were fussy, 14 failed to look long enough and thus were not sufficiently exposed to the familiarizing sounds, one fell asleep, and three did not attain the familiarization criterion within 15 min.

2. Stimuli and apparatus

The stimuli were 18 naturally produced bisyllabic utterances by the same male speaker of American English who produced the stimuli for experiments 1 and 2. Nine of the stimuli began with [ba] and nine with [da]. They were as follows: ba.pea, da.pea, ba.tad, da.tad, ba.mid, da.mid, ba.said, da.said, ba.nay, da.nay, ba.zoo, da.zoo, ba.woe, da.woe, ba.gir, da.gir, ba.cog, and da.cog (the period represents the syllabic boundary). The stimuli were produced with list intonation and with the attempt to produce weak stress on the first syllable. Weak stress was sought so as not to make the constant syllable too distinctive relative to the constant

consonant of the first two experiments. The mean peak F_0 was 101 Hz for the initial syllable and 103.9 Hz for the second syllable. The lowest F_0 was 85 and 83.6 Hz in the first and second syllables, respectively. The peak amplitude, taken at approximately the midpoint of the vowel, differed by less than 0.3 dB across syllables. The F_0 and amplitude differences were not statistically reliable. Finally, the mean duration of the initial and final syllables was 216.1 and 437 ms, respectively ($p < 0.01$). This large difference was probably due to many factors, including the naturally longer final syllables and the particular consonants and vowels that made up the variable second syllable. It would thus appear that the two syllables were fairly close in terms of stress, although the initial syllable was perceived as weakly stressed by naive adult listeners in an informal test, despite its short duration.

Four or six stimuli were randomly selected for each infant for the familiarization period, and two of the remaining stimuli, one beginning with [da] and one with [ba] and each with the same final syllable, were randomly selected for the test phase. The stimuli were arranged in exactly the same manner as in experiments 1 and 2, thereby ensuring that each familiar stimulus was heard at least 12 times, given the duration of a stimulus file. The apparatus was the same as that described in experiment 1.

3. Procedure

The procedural details were identical to those used in the first experiment.

B. Results and discussion

1. Familiarization

Table I shows the mean looking times for the first three and last three trials of familiarization.[4] An analysis of variance of the individual looking times for each familiarization condition, initial syllable ([ba] vs [da]) by trials (first three versus last three), revealed significant effects for trials [$F(1,30) > 51.50$, $p < 0.001$, in each familiarization condition], there being a reliable decrement in looking times across trials. All other F values for main effects and interactions failed to attain significance [$F(1,30) < 1.40$, $p > 0.10$, in all tests].

2. Test phase

Individual difference scores were computed as described above and displayed in Table I. There were five looking times that were greater than 60 s, three of which occurred on test trials with the novel initial syllable and two on trials with the familiar initial syllable. Infants familiarized with four bisyllabic patterns showed no evidence of categorization. The difference scores on test trials with the familiar and novel initial syllables did not differ from each other [$t(31) < 1.00$, $p > 0.10$], and both were significantly greater than chance [$t(31) > 4.08$, $p < 0.001$, in each instance].

However, for those infants familiarized with six bisyllabic patterns there was statistically reliable evidence for categorization. When the test-trial pattern contained the familiar initial syllables, the difference score (1.54 s) did not differ

from chance [$t(31) = 1.32$, $p > 0.10$], whereas when the initial syllables were novel, the difference score (3.85 s) did differ from chance [$t(31) = 3.38$, $p < 0.001$] and the two difference scores were statistically different [$t(31) = 2.23$, $p < 0.05$].

In sum, it would appear that categorization of a syllabic structure was in fact evidenced, but only when the number of familiar exemplars was relatively large.[5] This is not a new finding, at least in the visual domain. For example, Bomba and Siqueland (1983; also see Quinn, 1987) obtained no evidence for categorization of geometric forms with six variants of the forms, but did find strong evidence for categorization when the number of familiar exemplars was increased to 12. Finally, given the fact that after familiarization with four exemplars, both difference scores were significantly greater than chance, it would appear that the infants had encoded (represented) each of the familiar patterns, with the consequence that any test-trial pattern differing in both syllables or only the second syllable was considered novel and in being novel attracted attention. The final experiment sought evidence for the categorization of the final syllable in bisyllabic patterns, primarily in order to add generality to the findings of experiment 3. The stimulus patterns were like those used in experiment 3 in that the initial and final syllables were interchanged, thereby creating a constant final syllable during familiarization.

IV. EXPERIMENT 4

A. Method

1. Participants

The infants were 64 infants, 3–4 months of age ($M = 3.51$ months; s.d.$= 0.43$ months). There were 27 females and 37 males. Thirty-nine additional infants failed to complete the experiment for the following reasons: 21 were fussy, six failed to look long enough and thus were not sufficiently exposed to the familiarizing sounds, three fell asleep and nine did not attain the familiarization criterion within 15 min.

2. Stimuli and apparatus

The stimuli were 18 bisyllabic utterances, again produced by the same male speaker of American English with list intonation and (attempted) weak stress on the second, common syllable. The mean peak F_0 values were 106.33 and 99.94 Hz and the lowest F_0 values were 83 and 78.6 Hz for the first and second syllables, respectively. Both differences were not statistically significant. The mean peak amplitude of the unstressed syllable was 2.14 dB greater than that of the stressed syllable, and this difference was significant [$t(34) = 3.91$, $p < 0.01$]. Finally, the mean duration of the initial syllable was 351.3 ms and 372.6 ms for the second syllable, a nonsignificant difference. It would thus appear that the first variable syllable was somewhat more stressed than the second constant syllable, although this was not apparent to adult listeners, perhaps because of the repetition of the constant second syllable. Nine of the stimuli ended with the syllable [ba] and nine with [da]. They were as follows: pea.ba, pea.da, tad.ba, tad.da, mid.ba, mid.da, said.ba,

said.da, nay.ba, nay.da, zoo.ba, zoo.da, woe.ba, woe.da, gir.ba, gir.da, cog.ba, and cog.da. The stimuli were produced, arranged, and selected for individual infants as in experiment 3. The apparatus was the same as that described in experiment 1.

3. Procedure

The procedural details were identical to those used in the first and third experiments.

B. Results and discussion

1. Familiarization

Table I provides the mean looking times for the first three and last three trials of familiarization for both familiarization conditions. Analysis of variance of the individual looking times, initial syllable ([ba] vs [da]) by trials (first three versus last three), revealed as expected reliable effects for trials [$F(1,30) > 35.83$, $p < 0.001$, in both familiarization conditions], the looking times on the last three trials reliably declining. All other F values for main effects and interactions failed to attain significance [$F(1,30) < 2.0$, $p > 0.10$].

2. Test phase

Individual difference scores were computed as described above and displayed in Table I. There were four looking times greater than 60 s, two on trials with the novel final syllables and two on trials with the familiar final syllable. Infants familiarized with four bisyllabic patterns again showed no evidence of categorization. The difference scores on test trials with the familiar and novel initial syllables did not differ from each other [$t(31) < 1.33$, $p > 0.10$] and both were significantly greater than chance [$t(31) > 2.06$, $p < 0.05$, in each instance].

However, for those infants familiarized with six bisyllabic patterns containing a common final syllable, there was evidence for categorization, although it was not as compelling as when the familiar patterns contained a common initial syllable. When the test-trial pattern contained the familiar final syllable, the difference score (0.98 s) did not differ from chance [$t(31) = 0.92$, $p > 0.10$], whereas when the final syllable was novel, the difference score (2.59 s) was marginally different from chance [$t(31) = 1.86$, $0.05 < p < 0.10$]. The two difference scores were likewise only marginally different from each other [$t(31) = 1.71$, $0.05 < p < 0.10$]. Of interest is the basis for this difference in the evidence for categorization as a function of position of the common syllable when there were six familiar bisyllablic stimuli. It is possible that the common syllabic information was physically more distinctive or salient in experiment 3 than experiment 4, especially given the greater intensity of the variable initial syllable in experiment 4. However, there are data that argue against this explanation. First, analyses of the stimuli showed that the common syllable was, in fact, longer on average by 156 ms when it occurred in syllable final position (experiment 4) than when it formed the initial syllable (experiment 3) [$t(1,34) = 12.27$, $p < 0.001$]. Thus, the perceptual prominence of the common syllable in experiment 3 can be considered to be less than that of experiment 4. Nevertheless, the increased duration of the common syllable in experiment 4 was carried by the vocalic information, and its longer duration might have masked the initial consonant more in experiment 4 than in experiment 3, thereby making the common syllable less distinctive when it appeared in final position. Second, the variable syllable, which might have masked the common syllable or attracted attention, was actually longer by 86 ms in experiment 3 than in experiment 4 [$t(1,34) = 4.92$, $p < 0.001$]. And finally, there was no reliable difference across experiments in the range of F_0 within a syllable (approximately 16 to 24 Hz) for either the common or variable syllables across experiments [$t(34) < 1.10$, $p > 0.10$, in each case]. Thus, there is only moderate evidence that the reason for the difference between experiments can be attributed to the acoustic signal, *per se*. If this is indeed true, one can speculate that the difference is related to the nature of the infant's processing system; for example, the manner in which attention is allocated. This processing difference may reflect the beginnings of attentional development to a language-specific effect (English in this case), namely, that the prosodic pattern of bisyllabic utterances in English is predominantly that of a strong syllable followed by a weak syllable (Cutler and Carter, 1987), and this effect develops as infants increasingly experience more of their native language. This conjecture is substantiated by the fact that infants by 9 months of age are reliably sensitive to this characteristic of English as evidenced by greater responsivity to strong–weak than to weak–strong bisyllabic English words (Jusczyk, Cutler, and Redanz, 1993). Interestingly, this difference may also be related to the findings with adult listeners that word-initial information often plays an especially important role in word recognition (e.g., Marslen-Wilson and Welch, 1978; Marslen-Wilson, 1987).

In sum, the results following familiarization with four different bisyllabic patterns were consistent with that of experiment 3 in that there was evidence that each of the bisyllabic patterns had been encoded, but no evidence that the common quality of the final syllable had been recognized and encoded. When there were six familiar stimuli, however, the pattern of results indicated that there was again evidence for categorization, but it was by no means as robust as that which had been obtained with a common initial syllable. Moreover, analyses of the stimuli did not provide strong reasons for weaker categorization of the final syllable in bisyllabic utterances based on the acoustic characteristics of the stimuli.

V. GENERAL DISCUSSION

The present series of experiments adds support to the contention that the speech stream is initially segmented by infants into syllabic structures, as first put forth by Mehler (1981) and Bertoncini and Mehler (1981), or at the least that the syllabic representations are initially the more robust. Experiment 1 failed to reveal evidence for categorical representations based on segmental units—the initial consonant of CV or CVC utterances. However, both test stimuli, whether they included a novel or familiar initial consonant plus a novel coda, showed reliable evidence of recovery in looking time compared with the final levels of familiarization—a

finding supporting the contention that the infants had encoded and remembered the list of familiar monosyllabic stimuli. In experiment 2, which replicated experiment 1 but with a less stringent criterion for familiarization, there was weak evidence for categorization, but only for those subjects who more closely approximated the familiarization criterion and thus had less exposure to the familiar stimuli. They showed a nearly significant preference for the novel consonant. However, they also showed reliable increments in response times to test-trial stimuli with novel and familiar initial consonants—a finding not in accord with performance being governed solely by a categorical representation for the initial consonant. It would appear that under some circumstances, as yet not well defined, infants 3 and 4 months of age can begin to demonstrate evidence of categorical representations based on segmental units. However, it remains to be determined if these segmental representations, whether formed directly from the speech signal or derived from syllabic representations, are difficult to demonstrate because they are simply beginning to develop and consequently are relatively weak and thus less prominent, but will be more strongly evidenced later in infancy.

The final two experiments provided strong evidence for categorization of the common initial syllable of bisyllabic stimuli (experiment 3) and weaker evidence for the categorization of the final syllable (experiment 4), but in each instance only when there were six as opposed to four familiar stimuli. In these successful cases, there was significant or near-significant recovery and preference for the test-trial stimulus with a novel initial or final syllable, and the recovery for the stimulus with the familiar syllable was not significantly different from chance. There would thus appear to be reasonable support for the contention of Mehler (1981) and Bertoncini and Mehler (1981) that the syllable is the natural unit of speech processing in the very young infant. Indeed, if the CV-like representations of infants included information about vowel duration and intensity, and were functional at the start of language processing, sufficient information would be available for infants to discriminate between languages with different rhythmicities (Mehler *et al.*, 1996), whether either language is familiar or not (Nazzi, 1996), and permit discovering other efficient means for segmenting and representing speech if necessary. Moreover, with this view of the initial representation of speech, it is possible, or so it will be argued below, to accommodate the data from both infants and adults concerning the representation of speech and the early influence of phonologically based characteristics of the parental language on the representation of speech.

Given that this is indeed the manner in which the infant initially attempts to segment speech, this processing constraint that is seemingly an inherent part of our speech-processing system need not be the final form of the segmentation process, nor need it be the only way in which we segment the stream of speech. Early experience with phonologically different languages and the resulting acoustic–phonetic differences in the speech signal may result in different processing strategies by adult listeners. Whereas monolingual speakers of French, which is a syllable-timed language, segment speech into syllabic representations that

are presumably used for lexical access and recognition (Cutler *et al.*, 1986; Pallier *et al.*, 1993), a study with bilingual French and British-English speakers (Cutler *et al.*, 1992) showed that listeners whose dominant language was French showed clear evidence of syllabification, but only for French materials and not for British-English materials. Listeners whose dominant language was British English, a stress-timed language that is also marked by ambisyllabicity, showed no evidence of syllabification for English or French materials, as was true for monolingual speakers of British English (Cutler *et al.*, 1986). To accommodate these results, Cutler *et al.* (1992) argued that different segmentation strategies fall into two classes: restricted because they depend on language-specific phonological processes (and their acoustic–phonetic consequences) for development, and unrestricted because they are available to all language users, most likely even after having acquired a restricted strategy. They further proposed that a syllabic-segmentation procedure is restricted, whereas a segmentally based strategy presumably employed by English listeners and French-dominant listeners when processing British English is general and universally available, which is to say simply that it is part of the biology of language. Moreover, Cutler *et al.* (1992) have argued that the acquired restricted syllabic-segmentation procedure is optional. It can be ''switched off'' when its use may prove to be inefficient. This is, they contended, what presumably occurred when French-dominant bilinguals were processing British-English materials: after long exposure to British English, they learned that a syllabic segmentation is, with sufficient frequency, inefficient. Monolingual French speakers, in not having the long exposure to English, have not learned to inhibit a syllabic-segmentation strategy with English words, and thus attempt to syllabify English, and do so relatively efficiently. A second restricted strategy requiring experience is evidenced by native Japanese speakers, whose language has a periodicity based on morae, the subsyllabic prelexical structures of Japanese (Otake *et al.*, 1993).

Although this view of general and restricted strategies is consistent with the data from adult listeners described above, it does not accommodate the findings with infants. Moreover, other findings with adult listeners exist that are not easily reconciled with this view. However, they are compatible with the evidence from infant listeners and support the idea that the early default (natural or unrestricted) representational system is based on syllables (e.g., Mehler, 1981; Bertoncini and Mehler, 1981; Bertoncini *et al.*, 1988; Jusczyk *et al.*, 1995). The evidence from adult listeners comes from a series of studies using a syllable-matching paradigm (Mehler *et al.*, 1981) with two dialects of English [Australian (Bradley, Sánchez-Casas, and Garcia-Albea, 1993) and North American (Allopenna, 1996)] and with Dutch (Zwitserlood *et al.*, 1993). These languages, despite being marked by ambisyllabicity, hypothesized by researchers (e.g., Cutler *et al.*, 1986) to be a causal factor for British English speakers' failure to use a syllabic-segmentation procedure, all showed evidence that can be interpreted as favoring a syllabic-segmentation strategy. Further evidence of a syllabic-segmentation strategy in North-American English comes from an attentional induction procedure (Finney, Pro-

topapas, and Eimas, 1996; Pitt, Smith, and Klein, 1998).

Granted that there are unrestricted and restricted strategies (Cutler *et al.*, 1986, 1992) and given the infant and adult data in their entirety, it is at least arguable that the syllabic-segmentation strategy is the unrestricted strategy; that is, the general or biologically given natural strategy (see Eimas, 1997, for a more complete discussion of this view and the relevant data). Other strategies, e.g., a segmentation strategy based on phonetic segments or morae, are restricted, which is to say acquired by experience with the native language. This unrestricted syllable-segmentation strategy is, if reinforced by the native language, retained as the basis for the segmentation and representation of lexical items during the initial stages of word learning and the later on-line processing of speech by mature listeners. On the other hand, given a native language such as Japanese and (quite possibly) British English, the unrestricted syllabic representational units can be (and most likely are) rapidly replaced to permit the use of morae or segments.

Furthermore, in bilinguals for example, one of the restricted strategies can be added to the use of the syllabic-segmentation strategy to permit combinations of strategies for the initial acquisition of words and their later recognition by more mature users of human languages, as would appear to be the case for French-dominant bilinguals processing British English. That is, for these listeners, an unrestricted syllabic-segmentation strategy would be used with French, whereas the restricted segmentally based strategy would be used with British English. In other words, the unrestricted syllabic-segmentation strategy, if used with one language acquired during infancy, need not necessarily be used with all languages acquired at the same time. Something analogous may be seen in the process of language development in infants whose native language is North-American English (and quite possibly British English). As was shown in experiment 2, segmental categories (representations) did appear, albeit weakly, under some conditions, and there is evidence that infants about 6 months of age are able to form equivalence classes based on consonants, in this case a number of fricatives (Kuhl, 1980). It thus might be that native speakers of English, like the bilinguals described above, possess two processing strategies, one unrestricted and one restricted, with the latter developing gradually with experience with the native language. Be that as it may, a most important function of the initial unrestricted strategy is that it provides the infant with a means for acquiring and representing words or a standard for finding a more efficient or an additional strategy for this task, which in turn makes possible the acquisition of other forms of linguistic knowledge, e.g., syntax, that are necessary for full competence in a human language.

ACKNOWLEDGMENTS

[1]Four of the nine stimuli beginning with [b] and with [d] in experiments 1 and 2 had the final consonant [d], and three the final consonant [t]. This was done in order to begin to explore, albeit unsystematically, whether listeners who heard a varying number of familiar stimuli with the same or different initial and final consonants performed differently, or performed differently when the novel test stimulus had the same or different novel initial and final consonants. There was no apparent effect of the final consonant.

[2]Each of the familiarization conditions was analyzed separately as if it was a separate experiment, given the strong possibility that if categorization were to occur, it would be evident only in the condition with six familiarization stimuli (cf. Bomba and Siqueland, 1983). Moreover, if this were the case, it would be unlikely to obtain a significant interaction between the number of familiar stimuli and the measure of categorization given the inherent variability of data of this nature and the relatively small increments in the recovery scores on average when they occur (see, for example, Miller and Eimas, 1996).

[3]There is another measure of categorization commonly used in the visual domain, the novel preference score (e.g., Quinn and Eimas, 1996). It is computed for each infant by taking the total looking time to the test stimulus from the novel category and dividing it by the sum of the looking times to both test-trial stimuli and converting the ratio to a percentage. Categorization is taken to occur if the mean preference for the novel-category stimulus over the stimulus from the familiar category is significantly greater than 50%. This score is not independent of the measures of categorization used in the present experiments, and thus it is not surprising that when it was computed for each familiarization condition in the four experiments, it did not alter the conclusions in any instance.

[4]After familiarization with six stimuli, the mean looking time and variance on the first three trials were higher than usual. They were the result of consistently longer looking times by four of the 16 infants, for reasons that are not apparent.

[5]In a replication of the experiment on the categorization of the initial syllable when four familiar stimuli were heard, the findings were well matched by those from the earlier study. First, there was a reliable decrement in looking times during familiarization $[F(1,30)=85.31, p<0.001]$, and second and more importantly, both difference scores, that with a familiar and that with a novel initial syllable, showed reliable increments in looking times $[M=2.43$ s; s.d.$=4.37$; $t(31)=3.14$, $p<0.001$ and $M=3.70$ s; s.d. $=5.77$; $t(31)=3.63$, $p<0.001$, respectively]. In addition, the difference between the two test-trial difference scores was not significant $[t(31)=1.32, p>0.10]$. Thus, there was no evidence for categorization, although there was again evidence that the individual familiar patterns had been remembered.

Allopenna, P. (**1996**). ''A re-examination of the syllable's role in the on-line segmentation of English,'' unpublished doctoral dissertation, Brown University, Providence, RI.

Bertoncini, J., and Mehler, J. (**1981**). ''Syllables as units in infant speech perception,'' Infant Beh. Devel. **4**, 247–260.

Bertoncini, J., Bijeljac-Babic, R., Jusczyk, P. W., Kennedy, L. J., and Mehler, J. (**1988**). ''An investigation of young infants' perceptual representations of speech sounds,'' J. Exp. Psychol.: General **117**, 21–33.

Bertoncini, J., Floccia, C., Nazzi, T., and Mehler, J. (**1995**). ''Morae and syllables: Rhythmical basis of speech perception representations in neonates,'' Lang. Speech **38**, 311–330.

Best, C. T., McRoberts, G. W., and Sithole, N. M. (**1988**). ''Examination of perceptual reorganization for nonnative speech contrasts: Zulu click discrimination by English-speaking adults and infants,'' J. Exp. Psychol.: Hum. Percept. Perform. **14**, 345–360.

Bijeljac-Babic, R., Bertoncini, J., and Mehler, J. (**1993**). ''How do 4-day-old infants categorize multisyllabic utterances?'' Devel. Psychol. **29**, 711–721.

Bomba, P. C., and Siqueland, E. R. (**1983**). ''The nature and structure of infant form categories,'' J. Exp. Child Psychol. **35**, 294–328.

Bradley, D. C., Sánchez-Casas, R. M., and Garcia-Albea, J. E. (**1993**). ''The status of the syllable in the perception of Spanish and English,'' Lang. Cog. Proc. **8**, 197–233.

Cutler, A., and Carter, D. M. (**1987**). ''The predominance of strong initial syllables in the English vocabulary,'' Comput. Speech Lang. **2**, 133–142.

Cutler, A., and Norris, D. (**1988**). ''The role of strong syllables in segmentation for lexical access,'' J. Exp. Psychol.: Hum. Percept. Perform. **14**, 113–121.

Cutler, A., Mehler, J., Norris, D., and Segui, J. (**1986**). ''The syllable's

differing role in the segmentation of French and English,'' J. Mem. Lang. **25**, 385–400.

Cutler, A., Mehler, J., Norris, D., and Segui, J. (**1992**). ''The monolingual nature of speech segmentation by bilinguals,'' Cogn. Psychol. **24**, 381–410.

Eimas, P. D. (**1997**). ''Infant speech perception: Processing characteristics, representational units, and the learning of words,'' in *Perceptual Learning: The Psychology of Learning and Motivation*, edited by R. L. Goldstone, D. L. Medin, and P. G. Schyns (Academic, New York), Vol. 36, pp. 127–169.

Eimas, P. D., and Miller, J. L. (**1992**). ''Organization in the perception of speech by young infants,'' Psychol. Sci. **3**, 340–345.

Finney, S., Protopapas, A., and Eimas, P. D. (**1996**). ''Attentional allocation to syllables in American English,'' J. Mem. Lang. **35**, 893–909.

Jusczyk, P. W. (**1996**). ''Language acquisition: Speech sounds and the beginning of phonology,'' in *Handbook of Perception and Cognition: Speech Language and Communication*, edited by J. L. Miller and P. D. Eimas (Academic, San Diego), 2nd ed., pp. 263–301.

Jusczyk, P. W. (**1997**). *The Discovery of Spoken Language* (MIT, Cambridge, MA).

Jusczyk, P. W., Cutler, A., and Redanz, N. (**1993**). ''Preference for the dominant stress patterns of English words,'' Child Dev. **64**, 675–687.

Jusczyk, P. W., and Derrah, C. (**1987**). ''Representation of speech sounds by young infants,'' Devel. Psychol. **23**, 648–654.

Jusczyk, P. W., Kennedy, L. J., and Jusczyk, A. M. (**1995**). ''Young infants retention of information about syllables,'' Infant Beh. Dev. **18**, 27–42.

Jusczyk, P. W., Bertoncini, J., Bijeljac-Babic, R., Kennedy, L. J., and Mehler, J. (**1990**). ''The role of attention in speech perception by young infants,'' Cogn. Dev. **5**, 265–286.

Jusczyk, P. W., Jusczyk, A. M., Kennedy, L. J., Schomberg, T., and Koenig, N. (**1995**). ''Young infants' retention of information about bisyllabic utterances,'' J. Exp. Psychol.: Hum. Percept. Perform. **21**, 822–836.

Klatt, D. H. (**1979**). ''Speech perception: a model of acoustic-phonetic analysis and lexical access,'' J. Phon. **7**, 279–312.

Klatt, D. H. (**1989**). ''Review of selected models of speech perception,'' in *Lexical Representation and Process*, edited by W. Marslen-Wilson (MIT, Cambridge, MA), pp. 169–226.

Kuhl, P. K. (**1980**). ''Perceptual constancy for speech-sound categories in early infancy,'' in *Child Phonology: Vol. 2, Perception*, edited by G. H. Yeni-Komshian, J. F. Kavanagh, and C. F. Ferguson (Academic, New York), pp. 41–66.

Liberman, A. M., Cooper, F. S., Shankweiler, D. P., and Studdert-Kennedy, M. (**1967**). ''Perception of the speech code,'' Psychol. Rev. **74**, 431–461.

Marslen-Wilson, W. (**1987**). ''Functional parallelism in spoken word-recognition,'' Cognition **25**, 71–102.

Marslen-Wilson, W., and Welch, A. (**1978**). ''Processing interactions and lexical access during word recognition in continuous speech,'' Cogn. Psychol. **10**, 29–63.

Mehler, J. (**1981**). ''The role of syllables in speech processing: Infant and adult data,'' Philos. Trans. R. Soc. London, Ser. B **295**, 333–352.

Mehler, J., Segui, J., and Frauenfelder, U. (**1981**). ''The role of the syllable in language acquisition and perception,'' in *The Cognitive Representation of Speech*, edited by T. F. Myers, J. Laver, and J. Anderson (North-Holland, Amsterdam), pp. 295–305.

Mehler, J., Dommergues, J. Y., Frauenfelder, U., and Segui, J. (**1981**). ''The syllable's role in speech segmentation,'' J. Verb. Learn. Verb. Behav. **20**, 298–305.

Mehler, J., Dupoux, E., Nazzi, T., and Deheane-Lambertz, G. (**1996**). ''Coping with linguistic diversity: The infant's viewpoint,'' in *Signal to Syntax: Bootstrapping from Speech to Grammar in Early Acquisition*, edited by J. L. Morgan and K. Demuth (Erlbaum, Mahwah, NJ), pp. 101–116.

Miller, J. L., and Eimas, P. D. (**1996**). ''Internal structure of voicing categories in early infancy,'' Percept. Psychophys. **58**, 1157–1167.

Nazzi, T. (**1996**). ''Pole of prosody in the discrimination of foreign languages by newborns.'' Poster presented at the XXVIIIth Stanford Child Language Research Forum, Stanford University, April, 1996.

Otake, T., Hatano, G., Cutler, A., and Mehler, J. (**1993**). ''Mora or syllable? Speech segmentation in Japanese,'' J. Mem. Lang. **32**, 258–278.

Pallier, C., Sebastián-Gallés, N., Felguera, T., Christophe, A., and Mehler, J. (**1993**). ''Attentional allocation within the syllabic structure of spoken words,'' J. Mem. Lang. **32**, 373–389.

Pisoni, D. B., and Luce, P. A. (**1987**). ''Acoustic–phonetic representations in word recognition,'' Cognition **25**, 21–52.

Pitt, M. A., Smith, K. L., and Klein, J. M. (**1998**). ''Syllabic effects in word processing: Evidence from the structural induction paradigm,'' J. Exp. Psychol.: Hum. Percept. Perform. **24**, 1596–1611.

Quinn, P. C. (**1987**). ''The categorical representation of visual pattern information by young infants,'' Cognition **27**, 145–179.

Quinn, P. C., and Eimas, P. D. (**1986**). ''On categorization in early infancy,'' Merrill–Palmer Quart. **32**, 331–363.

Quinn, P. C., and Eimas, P. D. (**1996**). ''Perceptual organization and categorization in young infants,'' in *Advances in Infancy Research*, edited by C. Rovee Collier and L. P. Lipsitt (Ablex, Norwood, NJ), Vol. 10, pp. 1–36.

Stevens, K. K., and Blumstein, S. (**1981**). ''The search for invariant acoustic correlates of phonetic features,'' in *Perspectives on the Study of Speech*, edited by P. D. Eimas and J. L. Miller (Erlbaum, Hillsdale, NJ), pp. 1–38.

Zwitserlood, P., Schriefers, H., Lahiri, A., and von Donselaar, W. (**1993**). ''The role of syllables in the perception of spoken Dutch,'' J. Exp. Psychol.: Learn. Mem. Cogn. **19**, 260–271.

Model-based approach to envelope and positive instantaneous frequency estimation of signals with speech applications

Ramdas Kumaresan and Ashwin Rao
Department of Electrical Engineering, University of Rhode Island, Kingston, Rhode Island 02881

An analytic signal $s(t)$ is modeled over a T second duration by a pole-zero model by considering its periodic extensions. This type of representation is analogous to that used in discrete-time systems theory, where the periodic frequency response of a system is characterized by a finite number of poles and zeros in the z-plane. Except, in this case, the poles and zeros are located in the complex-time plane. Using this signal model, expressions are derived for the envelope, phase, and the instantaneous frequency of the signal $s(t)$. In the special case of an analytic signal having poles and zeros in reciprocal complex conjugate locations about the unit circle in the complex-time plane, it is shown that their instantaneous frequency (IF) is always positive. This result paves the way for representing signals by positive envelopes and positive IF (PIF). An algorithm is proposed for decomposing an analytic signal into two analytic signals, one completely characterized by its envelope and the other having a positive IF. This algorithm is new and does not have a counterpart in the cepstral literature. It consists of two steps. In the first step, the envelope of the signal is approximated to desired accuracy using a minimum-phase approximation by using the dual of the autocorrelation method of linear prediction, well known in spectral analysis. The criterion that is optimized is a waveform flatness measure as opposed to the spectral flatness measure used in spectral analysis. This method is called linear prediction in spectral domain (LPSD). The resulting residual error signal is an all-phase or phase-only analytic signal. In the second step, the derivative of the error signal, which is the PIF, is computed. The two steps together provide a unique AM-FM or minimum-phase/all-phase decomposition of a signal. This method is then applied to synthetic signals and filtered speech signals. © *1999 Acoustical Society of America.*
[S0001-4966(99)01003-6]

PACS numbers: 43.72.Ar [JLH]

INTRODUCTION

Many natural and man-made signals of interest are time-varying or nonstationary in nature, i.e., their frequency content or spectrum changes with time. Examples include speech signals, animal calls, biological/biomedical signals such as cardiac rhythms, etc. Techniques for characterizing such signals are of great importance in applications involving such signals. A collection of short-time Fourier spectra known as spectrogram is a common tool for analyzing such time-varying signals. Unfortunately, the spectrogram suffers from the need to compromise time and frequency resolution, i.e., a large time window is required to resolve closely spaced frequencies. To overcome this problem, a number of so-called time-frequency distributions or representations have been developed.[1,2] The time-frequency analysis tools are very useful in visualizing the time and frequency behavior of simple signals like a chirp. However, when the signals are complex, as in the case of speech, it is hard to interpret time-frequency representations because of the interactions between components in the signal. The time-frequency analysis methods also create a practical problem. They result in enormous 2D data sets. Although sometimes these 2D data sets can be viewed by humans to sort out the important features of interest, it is hard to program a machine to reliably extract such features. Hence it has been difficult to apply these methods to automatic signal classification problems.

In the area of speech processing, the above problem is circumvented by directly extracting features from short segments of a speech signal. Such algorithms are based on short-term spectral analysis in the form of linear prediction (which captures the spectral envelope of a signal with a few parameters),[3,4] cepstral analysis,[5] and Mel-cepstrum.[6] Using these procedures, spectral templates or feature vectors are computed and used in applications like machine recognition/verification. However, these methods are vulnerable to interference and channel degradations as encountered in telephone speech. Signals are also often analyzed over short-time intervals, using specific signal models, such as sum of sinusoidal or damped sinusoidal signals or phase-modulated sinusoidal signals. If such models are appropriate for the data at hand, then significant advantages can be gained. In this paper a model-based approach is proposed for representing signals by their envelope and instantaneous frequency which is guaranteed to be positive.

A. Envelope and instantaneous frequency of signals

Many of the above-mentioned methods represent a signal by characterizing its power as a function of time and frequency. Are there other alternatives? Clearly, a signal's phase and envelope carry information about how various components of the signal are related to each other. Hence, is it possible to characterize a signal by its phase and envelope

modulations? In his 1946 paper, among other important ideas, Gabor approached this question by defining the so-called analytic signal or pre-envelope.[7,8] Recall that if $s_r(t)$ is a real signal, then the corresponding analytic signal is $s(t) = s_r(t) + j\hat{s}_r(t)$, where $\hat{s}_r(t)$ is the Hilbert transform[9] of $s_r(t)$. The Fourier transform of $s(t)$, $S(\omega)$, is nonzero only for $\omega > 0$. The envelope of $s_r(t)$ is then defined as $|s(t)|$ and its instantaneous frequency (IF) is denoted by the first derivative of $s(t)$'s phase function scaled by $1/2\pi$. An analytic signal is valuable because it permits an unambiguous characterization of a real signal in terms of its envelope and IF.[10] Characterizing a signal by envelope and IF is also commonly referred to as AM-FM modeling of signals.[11–14]

Engineers and scientists are most familiar with IF in the context of frequency-modulated signals as in a FM radio. But what about the IF of an arbitrary signal? For an arbitrary signal, the IF is typically an erratic function whose range may extend from negative to positive infinity.[10] For example, for a signal consisting of two complex sine waves, i.e., $s(t) = a_1 e^{j\omega_1 t} + a_2 e^{j\omega_2 t}$, the IF could lie anywhere in the range of $(-\infty, \infty)$ depending on the relative sizes of a_1 and a_2. The general impression among researchers is that the IF function is unusable unless it is sufficiently smoothed.[15] Some incompletely resolved questions regarding IF include: how do we interpret the envelope and IF of naturally occurring (not man-made) signals like speech? How are phase or IF and envelope related to each other? Is IF more important than envelope? When is a signal's IF a smooth function? Under what conditions is a signal's IF guaranteed to be positive, and so on. Further, one of the factors that has discouraged researchers[15,16] in using phase and envelope to represent a signal is the following: for example, if bandpass filtered speech is decomposed into envelope and IF, then the resulting modulations, rather ironically, have bandwidths that are typically much greater compared to that of the original band-limited signal.

In addition to Gabor, Dugundji, and others,[7,8,17–22] significant contributions to understanding analytic signals were made nearly 30 years ago by Voelcker.[23,24] Voelcker proposed a methodical way to understanding the IF and log-envelope of signals which may help answer some of the questions raised above. Unfortunately, Voelcker's work never became popular because it was somewhat hard to read. He proposed that complex-valued signals (and hence analytic signals) be modeled as polynomials or a ratio of polynomials in the complex variable t (time), just like a given system or frequency response may be modeled by a ratio of polynomials in the s-domain (continuous-time systems) or the z-domain (discrete-time systems). He called it "product representation of signals." Once we realize that signals may be represented by a polynomial or a ratio of polynomials with complex coefficients, then a myriad of ideas that have been developed in systems literature can be applied to this so-called product representation of signals. In this paper we extend Voelcker's work by applying some of the well-known ideas from the theory of linear prediction[25] to his signal model.

A motivation for representing signals by envelope and IF comes from our desire to understand and model the signal processing function performed by the auditory periphery, particularly the cochlea. The cochlea is known[26] to decompose acoustic stimuli into frequency components along the length of the basilar membrane. This phenomenon is called tonotopic decomposition. Further, it is also known that the nerve fibers emanating from a high-frequency location in the cochlea "phase-lock" to the envelope of the stimulus around that frequency, i.e., convey information about the envelope modulations in the signal.[27] Thus, to a first-order approximation, it is often argued that the tonotopic location/place along the length of the basilar membrane conveys the IF or frequency information about the signal, and the rate of nerve fiber activity around that location conveys the envelope information. Hence analytical signal models that explicitly characterize the envelope and phase variations of a complex stimulus on a short-time basis may eventually help in understanding the cochlear function.

B. Organization of the paper

In Sec. I we consider complex-valued periodic signals and express them as a product of so-called elementary signals à la Voelcker. This type of representation is analogous to that used in discrete-time systems theory, where the periodic frequency response of a system is characterized by a finite number of poles and zeros, except in our case the poles and zeros are located in a complex-time plane. Using this signal model, we derive expressions for the envelope, phase, and the instantaneous frequency. In the special case of an analytic signal having poles and zeros in reciprocal complex conjugate locations about the unit circle in the complex-time plane, it is shown in Sec. II that their instantaneous frequency (IF) is always positive. This result paves the way for representing signals by positive envelopes and positive IF (PIF) as desired in literature associated with time-frequency distributions.[10,14] In Sec. III we propose a new algorithm which consists of two steps to achieve a unique decomposition of an analytic signal into two analytic signals, one completely described by its envelope and the other having a positive IF. This type of decomposition is different from those known in the cepstral literature.[5] In the first step, the envelope of the signal is approximated to desired accuracy using a minimum-phase approximation by using the dual of the autocorrelation method of linear prediction[25] well known in spectral analysis. The criterion that is optimized is a waveform flatness measure as opposed to the spectral flatness measure used in the spectral domain. We call our method, linear prediction in spectral domain (LPSD). The resulting residual error signal is an all-phase or phase-only analytic signal. In the second step, the derivative of the error signal is approximated. The two steps together provide a unique AM-FM or minimum-phase/all-phase decomposition of a signal. This method is then applied to synthetic signals and filtered speech signals.

I. ENVELOPE AND IF IN TERMS OF A SIGNAL MODEL

Consider a periodic analytic signal $s(t)$, with period T seconds. Let $\Omega = 2\pi/T$ denote its fundamental angular fre-

quency. If $s(t)$ has finite bandwidth, it may be described by the following model for a sufficiently large M, over an interval of T seconds:

$$s(t) = e^{j\omega_t t} \sum_{k=0}^{M} a_k e^{jk\Omega t}. \tag{1}$$

$e^{j\omega_t t}$ represents a frequency translation. In other words, $\omega_t \geq 0$ is the nominal carrier frequency of the signal. a_k are the complex amplitudes of the sinusoids $e^{jk\Omega t}$; $a_0 \neq 0$ and $a_M \neq 0$. By analytic continuation we may regard $e^{j\Omega t}$ as a complex variable (à la the complex variable Z). That is, t, the time variable, is regarded as complex-valued. Note that in Eq. (1) the Mth degree polynomial in $e^{j\Omega t}$ represents the complex envelope of the signal $s(t)$. We may factor this polynomial into its $M(=P+Q)$ factors and rewrite $s(t)$ as

$$s(t) = a_0 e^{j\omega_t t} \underbrace{\prod_{i=1}^{P} (1 - p_i e^{j\Omega t})}_{s_{\text{MinP}}(t)} \underbrace{\prod_{i=1}^{Q} (1 - q_i e^{j\Omega t})}_{s_{\text{MaxP}}(t)}; \tag{2}$$

$p_1, p_2, \ldots, p_P$, and $q_1, q_2, \ldots, q_Q$ denote the polynomial's roots; $p_i = |p_i| e^{j\theta_i}$, $q_i = |q_i| e^{j\phi_i}$. p_i denote roots inside the unit circle in the complex plane, q_i are outside the unit circle. Currently we assume that there are no roots on the circle. That is $|p_i| < 1$ and $|q_i| > 1$. Each factor of the form $(1 - p_i e^{j\Omega t})$ in the above is called an ''elementary signal.''[23] The p_i and q_i are referred to as zeros of the signal $s(t)$. The above expressions, representing a band-limited periodic signal, may be recognized as the counterpart of the frequency response of a finite impulse response (FIR) filter in discrete-time systems theory.[28] More generally, if $s(t)$ consists of an infinite number of spectral lines [i.e., its Fourier transform, $S(\omega) = \sum_{k=0}^{\infty} a_k \delta(\omega - k\Omega)$], then we can represent $s(t)$ over T seconds to desired accuracy using a sufficient number of poles and zeros as follows:

$$s(t) = a_0 e^{j\omega_0 t} \underbrace{\frac{\prod_{i=1}^{P}(1 - p_i e^{j\Omega t})}{\prod_{i=1}^{U}(1 - u_i e^{j\Omega t})}}_{s_{\text{MinP}}(t)} \underbrace{\prod_{i=1}^{Q} (1 - q_i e^{j\Omega t})}_{s_{\text{MaxP}}(t)}. \tag{3}$$

p_i and q_i correspond to zeros inside and outside the unit circle, respectively. u_i correspond to the signal's poles. Since the spectrum of the signal is assumed to have only positive frequencies, poles are restricted to be inside the unit circle. Again this representation is analogous to causal, stable IIR filters in discrete-time systems literature. Even more generally, if the spectrum of $s(t)$ is two-sided then we may model $s(t)$ using poles and zeros inside and outside the unit circle. $e^{j\omega_t t}$, the arbitrary frequency translation, is analogous to an arbitrary time shift in the impulse response in the case of a discrete-time filter. In summary, we model complex-valued periodic signals using an all-zero or a pole-zero signal model as in Eqs. (2) and (3), respectively. This type of signal modeling goes back to the work of Cauchy and Hadamard and is related to the theory of entire functions.[29,30] Voelcker called this way of modeling signals as ''product representation of

signals.'' We shall primarily work with the all-zero models since they are easier to use.

The factors corresponding to the zeros inside the unit circle, $\prod_{i=1}^{P}(1 - p_i e^{j\Omega t})$, constitute the minimum-phase (MinP) signal. Similarly, the factors corresponding to the zeros outside the circle, $\prod_{i=1}^{Q}(1 - q_i e^{j\Omega t})$, constitute the maximum-phase (MaxP) signal. These are the direct counterparts of the frequency responses of the well-known minimum- and maximum-phase FIR filters in discrete-time systems theory;[5] just as in systems theory (see Sec. 10.3 in Ref. 5) the phase of the MinP signal is the Hilbert transform of its log-envelope. That is, the MinP signal may be expressed in the form $e^{\alpha(t) + j\hat{\alpha}(t)}$. See Appendix A for details. $\hat{\alpha}(t)$ is the Hilbert transform of $\alpha(t)$. Similarly, since a maximum-phase (MaxP) signal has zeros outside the unit circle, it may be expressed as $e^{\beta(t) - j\hat{\beta}(t)}$. Thus, envelope or phase alone is sufficient to essentially characterize a MinP or a MaxP signal. [Along the same lines, an all-phase (AllP) analytic signal (the analog of an all-pass filter) would be of the form $e^{j\gamma(t)}$.] Thus $s(t)$ may be expressed as

$$s(t) = A_c e^{j\omega_c t} \underbrace{e^{\alpha(t) + j\hat{\alpha}(t)}}_{\text{MinP}} \underbrace{e^{\beta(t) - j\hat{\beta}(t)}}_{\text{MaxP}}, \tag{4}$$

where the ''hat'' stands for Hilbert transform. ω_c is $Q\Omega$ (contributed by the linear phase term from the MaxP signal) plus the arbitrary frequency translation, ω_t, shown in Eq. (2). A_c is $a_0 \prod_{i=1}^{Q}(-q_i)$. See Appendix A for details. The expressions for $\alpha(t)$ and $\beta(t)$ are derived in Appendix A.

$$\alpha(t) = \sum_{k=1}^{\infty} \sum_{i=1}^{P} -\frac{|p_i|^k}{k} \cos(k\Omega t + k\theta_i)$$

and

$$\beta(t) = \sum_{k=1}^{\infty} \sum_{i=1}^{Q} -\frac{1/|q_i|^k}{k} \cos(kQt + k\phi_i). \tag{5}$$

Closed-form expressions can be obtained for $\dot{\alpha}(t)$ and $\dot{\hat{\beta}}(t)$.[23,31] The ''dot'' stands for the time-derivative operation. Note that the envelope of $s(t)$ is $A_c e^{\alpha(t) + \beta(t)}$ and the IF is $\omega_c + \dot{\hat{\alpha}}(t) - \dot{\hat{\beta}}(t)$. A detailed description of properties of envelope and IF of signals described by Eq. (2) can be found in Ref. 31. We briefly summarize the main points here. The envelope, log-envelope, and phase (or IF) of $s(t)$ are not band-limited quantities. It can be shown that if $s(t)$ is band-limited then $|s(t)|^2$ and $d\angle s(t)/dt|s(t)|^2$ are band-limited. Further, it can also be shown that no ''information'' is lost by filtering the log-envelope and IF of a band-limited $s(t)$, using a lowpass filter with bandwidth equal to that of the signal $s(t)$. That is, in principle, it is possible to essentially reconstruct the signal $s(t)$ given ideally filtered versions of log-envelope and IF of $s(t)$. The counterpart of this property in the systems domain is the property of complex cepstrum (see Ch. 12 in Ref. 5). That is, even though the complex cepstrum of a finite-length discrete-time sequence is infinite in length, only a finite number of samples of the complex cepstrum is needed to recover the original sequence.

Using the above product representation model, in addition to being able to obtain explicit expressions for the log-envelope and IF, it is also easy to gain intuitive understanding of the relationship between phase and envelope of signals based on familiar results in systems theory. Just like the unit circle in the (discrete-time) z plane corresponds to the interval between zero frequency and the sampling frequency,[5] the unit circle in the complex-time plane corresponds to the interval of T seconds. If a periodic signal is such that a zero of the signal, p_i or q_i, is close to the unit circle, then significant phase changes will occur in the temporal neighborhood of this zero, which will be reflected in the IF values. Specifically, a zero close to the unit circle will result in a large spike in the IF. In fact, if a zero happens to fall on the circle, the envelope goes to zero (at a time instant determined by the zero's location) and the IF at that time instant is undefined (à la group delay of systems). Thus if we want to use IF and log-envelope as information-bearing attributes of a signal, then it is necessary to "tame" these quantities by shaping the signal spectrum. That is, we must preprocess the signal such that the zeros, p_i and q_i, stay away from the unit circle. This preprocessing then becomes part and parcel of the signal representation.

A. Extension to nonstationary signals

The model in Eq. (2) describes a stationary and periodic signal. Of course, most signals of interest are not stationary and certainly not periodic. Hence, as in the case of short-time spectral analysis/spectrogram, we may consider a short T-second segment of a nonstationary signal and imagine that it is periodically extended in order to apply the model in Eq. (2). Then, successive overlapping T-second segments of a signal may be described as in Eq. (2), possibly with slowly drifting parameters (p_i and q_i) and the associated envelope and IF they represent. Thus although the model described in this section is strictly valid for a periodic signal, we intend to apply it to nonstationary signals by viewing the signal through a sliding T-second window. In fact there is no reason to fix the window length to T seconds. The window length may be a function of the nominal center frequency of the signal $s(t)$ as its characteristics change. Next, we use the above model to define a signal whose IF is positive.

II. POSITIVE INSTANTANEOUS FREQUENCY (PIF) OF A SIGNAL

Recall that an analytic signal is said to be minimum-phase (MinP) if its log-envelope ($\ln|s(t)|$) and its phase angle are related by Hilbert transform. An analytic signal is said to be maximum-phase (MaxP) if its log-envelope is the negative of the Hilbert transform of its phase angle. An important property of these signals is that their logarithm is also an analytic signal. Another important aspect is that either envelope or phase of these signals is essentially sufficient information to characterize these signals. An analytic signal is said to be all-phase (AllP) if its envelope, $|s(t)|$, is constant. That is, AllP is a pure phase signal with one-sided spectrum. Now we shall discuss signals whose IF is always positive.

A. General case

Let $s(t)$ be any analytic signal with spectrum confined to the positive side of the frequency axis,

$$s(t) = a(t)e^{j\phi(t)}. \tag{6}$$

Let $a(t) > 0$. The IF of $s(t)$ is $\dot{\phi}(t)/2\pi$. The IF could lie anywhere in the interval of $(-\infty, \infty)$ depending on the makeup of $s(t)$. Let us rewrite $s(t)$ as

$$s(t) = e^{\ln a(t) + j\phi(t)}. \tag{7}$$

Adding and subtracting in the exponent the term[31] $j\,\widehat{\ln a}(t)$, ("hat" stands for Hilbert transform), we get after rearranging,

$$s(t) = \underbrace{e^{\ln a(t) + j\,\widehat{\ln a}(t)}}_{\text{MinP}}\underbrace{e^{j(\phi(t) - \widehat{\ln a}(t))}}_{\text{AllP}}. \tag{8}$$

The above is analogous to the unique decomposition of the frequency response of a linear, causal, continuous-time system into its minimum-phase and all-pass parts.[9] Observe that in the above the first term on the right is a MinP analytic signal. If we multiply both sides of the above by $e^{-\ln a(t) - j\,\widehat{\ln a}(t)}$ (which is also MinP with spectrum confined to positive frequencies), since the spectrum of $s(t)$ is already confined to positive frequencies only, it follows that the spectrum of $e^{j(\phi(t) - \widehat{\ln a}(t))}$ is nonzero only for positive frequencies. Hence $e^{j(\phi(t) - \widehat{\ln a}(t))}$ must be an AllP analytic signal. The AllP signal is also called a Blaschke function in analytic function theory,[32,33] and may be written as a product of all-phase "sections," i.e., as $\Pi_i(t - z_i)/(t - z_i^*)$. It can be shown that the AllP signal has not only a one-sided spectrum but has the remarkable property that its IF is a positive definite function.[23,32] Based on this property we have defined a function $\psi(t)$, called the positive IF (PIF),[34] of any analytic signal $s(t)$ as follows:

$$\psi(t) = \text{PIF of } s(t) = \frac{d(\phi(t) - \widehat{\ln a}(t))}{dt}. \tag{9}$$

In words, we define an analytic signal's PIF as the derivative of that part of its phase which is left over after removing the contribution due to the signal's log-envelope (specifically the Hilbert transform of its log-envelope) from the original phase. The main point is that any analytic signal can be characterized by two positive functions: a positive envelope function (the magnitude of the MinP part) and a positive IF function (of its AllP part) rather than by its usual IF [phase-derivative, $\dot{\phi}(t)$]. This is an important observation that we repeatedly exploit.

B. Periodic case

Although the above decomposition is valid for any analytic signal, as mentioned before, in practice one has to work with a finite, T-second, segment of a possibly nonstationary signal, $s(t)$. Hence, we may invoke the (periodic extension) model we have used in Eq. (1). We shall repeat Eqs. (2) and (4) here for convenience.

$$s(t) = a_0 e^{j\omega_t t} \prod_{i=1}^{P} (1 - p_i e^{j\Omega t}) \prod_{i=1}^{Q} (1 - q_i e^{j\Omega t}) \qquad (10)$$

$$= A_c e^{j\omega_c t} \underbrace{e^{\alpha(t) + j\hat{\alpha}(t)}}_{\text{MinP}} \underbrace{e^{\beta(t) - j\hat{\beta}(t)}}_{\text{MaxP}}. \qquad (11)$$

Note that the zeros, q_i, and p_i are assumed to be outside and inside the unit-circle, respectively. We shall reflect the q_i to inside the circle (as $1/q_i^*$) and cancel them using poles. Then we group all the zeros inside the unit circle to form a different MinP signal and the zeros outside the circle and the poles that are their reflections inside the unit circle to form the all-phase or AllP part of the signal. That is,

$$s(t) = a_0 e^{j\omega_t t} \underbrace{\prod_{i=1}^{P} (1 - p_i e^{j\Omega t}) \prod_{i=1}^{Q} \left(1 - \frac{1}{q_i^*} e^{j\Omega t}\right)}_{\text{MinP}}$$

$$\times \underbrace{\frac{\prod_{i=1}^{Q}(1 - q_i e^{j\Omega t})}{\prod_{i=1}^{Q}(1 - (1/q_i^*)e^{j\Omega t})}}_{\text{AllP}}. \qquad (12)$$

Equivalently, multiplying and dividing Eq. (11) by $e^{j2\hat{\beta}(t)}$ and collecting terms we get

$$s(t) = \underbrace{A_c e^{\alpha(t) + \beta(t) + j(\hat{\alpha}(t) + \hat{\beta}(t))}}_{\text{MinP}} \underbrace{e^{j(\omega_c t - 2\hat{\beta}(t))}}_{\text{AllP}}. \qquad (13)$$

This grouping of signals is, of course, analogous to well-known decomposition of a linear discrete-time system into minimum-phase and all-pass systems (see Sec. 5.6 in Ref. 5). Analogous to the fact that the group delay of the all-pass filters is always positive (Sec. 5.5 in Ref. 5), the IF of AllP part will always be positive (even if ω_t, the frequency translation, is zero). See Appendix B for a derivation of the IF of an AllP signal. Thus the PIF, $\psi(t)$, of $s(t)$ is a positive function and is as follows:

$$\psi(t) = \omega_c - 2\dot{\hat{\beta}}(t). \qquad (14)$$

The expression for $\hat{\beta}(t)$ is the same as that of $\beta(t)$ in Eq. (5) with cosine replaced with sine. Of course, we could also group the zeros outside the unit circle together to form a MaxP-AllP decomposition. That is, we could also rewrite Eq. (12) as a MaxP/AllP product as follows:

$$s(t) = A_c e^{\alpha(t) + \beta(t) - j(\hat{\alpha}(t) + \hat{\beta}(t))} e^{j(\omega_c t + 2\hat{\alpha}(t))}. \qquad (15)$$

In this case the IF corresponding to the AllP part will be always negative (assuming the frequency translation ω_t is zero) and may be called negative IF (NIF). If we can separate the MinP and the AllP components of the signal $s(t)$, the
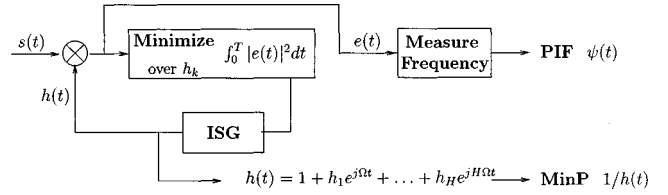
FIG. 1. LPSD algorithm; $1/h(t)$ corresponds to the MinP part of the signal $s(t)$. $\psi(t)$ corresponds to the IF of the AllP part of the signal $s(t)$.

MinP part conveys the AM information, i.e., $e^{\alpha(t) + \beta(t)}$ [or equivalently, its logarithm $\alpha(t) + \beta(t)$] around the carrier ω_c and the AllP part conveys the PIF information, $\psi(t)$.

The next question is: given $s(t)$ over a T-second interval, how do we compute the PIF of the signal or equivalently separate the MinP and AllP components? There are at least three not so elegant ways to separate the MinP and AllP components. First, one could find the Fourier coefficients of $s(t)$, then root the polynomial formed using the Fourier coefficients, i.e., find p_i and q_i, and then group them as in Eq. (12) to separate the components. Alternatively, one could compute the log-envelope of $s(t)$ (i.e., $\ln|s(t)|$), compute its Hilbert transform, and subtract it from the phase of $s(t)$ [as in Eq. (8)]. Third, we can use the block diagram in Fig. 12.7 (p. 784) of Oppenheim and Schafer[5] by replacing their $X(e^{j\omega})$ by $s(t)$. In this case one computes the logarithm of $s(t)$ and keeps the causal part of its spectrum (i.e., spectrum corresponding to the positive frequencies) as the MinP part. The AllP part is obtained by dividing $s(t)$ by the MinP part as in Ref. 5. However, there is a new and elegant way of achieving this decomposition which we describe next.[34] Remarkably, it does not require explicit computation of the logarithm or the Hilbert transform or rooting of a polynomial. We also called this method a generalized AM-FM demodulator since the outputs of the algorithm are the envelope and PIF.

III. ALGORITHM FOR DECOMPOSING AN ANALYTIC SIGNAL INTO ENVELOPE AND PIF

Although in the previous section we have pointed to the fact that any analytic signal can be written as a product as in Eq. (13), the question is how do we separate these multiplied components? In this section we describe a remarkably simple algorithm to separate the MinP and AllP components. This is shown in Fig. 1. It consists of two parts. In the first part, which consists of a multiplier or modulator, an inverse signal generator (ISG), and an error minimization block, a model fitting procedure is used to flatten the envelope of the signal $s(t)$.

This is achieved by minimizing the energy of an error signal $e(t)(=h(t)s(t))$. The energy of $e(t)$ is defined as follows:

$$\int_0^T |e(t)|^2 dt = \int_0^T |s(t)h(t)|^2 dt. \qquad (16)$$

$h(t)$ is a signal generated by the ISG using the formula $h(t) = 1 + \sum_{k=1}^{H} h_k e^{jk\Omega t} \cdot \Omega = 2\pi/T$. In other words, the ISG

generates a low-pass periodic signal. The error energy is minimized by choosing the coefficients, h_k. The reader who is familiar with model-based spectral analysis will immediately recognize the analogy between this method and the "autocorrelation method" of linear prediction.[4,25] In the autocorrelation method, a discrete-time FIR filter, called an inverse filter or prediction-error filter, with frequency response $H(e^{j\omega})$ (with first coefficient held at unity), is used to flatten the envelope of a spectrun $X(e^{j\omega})$ of a sequence $x(n)$ by minimizing the error $\int_0^{2\pi}|X(e^{j\omega})H(e^{j\omega})|^2 d\omega$. This is an exact analog of Eq. (16). Analogous to the autocorrelation method, the error in Eq. (16) is a measure of the flatness of the envelope of $e(t)$. Also, minimizing the error in Eq. (16) amounts to performing linear prediction on the Fourier coefficients of the signal $s(t)$ and hence we called it linear prediction in spectral domain or LPSD in earlier work.[34] The signal $h(t)$ may be called the "inverse signal" analogous to the inverse filter.

Similar to the MinP property of the prediction-error filter used in linear prediction,[25] minimizing $\int_0^T |e(t)|^2 dt$ results in a $h(t)$ that is a MinP signal (having all its signal zeros inside the unit circle). This is true even if the envelope of $s(t)$ goes to zero at some points between 0 and T seconds, i.e., even if some p_i or q_i fall on the unit circle. The significance of this MinP property is that, as we already know, $h(t)$'s log-envelope and phase are Hilbert transforms. Because the error minimization is performed to flatten $s(t)$'s envelope, if the value of H is chosen sufficiently large, then $h(t)$ will be given by

$$h(t) \approx e^{-(\alpha(t)+\beta(t))}e^{-j(\hat{\alpha}(t)+\hat{\beta}(t))}. \tag{17}$$

Thus, $1/h(t)$ is the desired approximation to $s(t)$'s MinP component and hence the name "inverse signal" for $h(t)$. Consequently, the error signal $e(t)$ will be $e(t) \approx A_c e^{j(\omega_c t - 2\hat{\beta}(t))}$, and hence is an approximation to the AllP component of $s(t)$. In the second part, denoted in Fig. 1 as "measure frequency," the PIF is computed as $\dot{e}(t)/|e(t)|$ or $d\angle e(t)/dt$. The next section describes the algorithm used to minimize the error $\int_0^T |e(t)|^2 dt$.

A. LPSD algorithm using signal samples

In this section we present the details of the LPSD algorithm for computing the MinP and AllP approximations given the samples of the signal $s(t)$. The algorithm amounts to performing linear prediction on the discrete Fourier transform (DFT) values of the signal samples. Let $s[n]$ ($n = 0,1,...,K$), given by Eq. (1), denote samples of the given signal; $K = N-1$. Let $\Omega = 2\pi/N$ be the assumed fundamental frequency. By replacing $h(t)$ and $e(t)$ by their respective sampled versions, we have

$$e[n] = s[n]h[n] = s[n] + \sum_{k=1}^{H} h_k s[n]e^{jk\Omega n}, \tag{18}$$

which can be further expressed in matrix notation as

$$\begin{pmatrix} s[0] \\ s[1] \\ \vdots \\ s[K] \end{pmatrix} + \begin{pmatrix} s[0] & s[0] & \cdots & s[0] \\ e^{j\Omega}s[1] & e^{j2\Omega}s[1] & \cdots & e^{jH\Omega}s[1] \\ \vdots & \vdots & \ddots & \vdots \\ e^{jK\Omega}s[K] & e^{j2K\Omega}s[K] & \cdots & e^{jKH\Omega}s[K] \end{pmatrix}$$

$$\times \begin{pmatrix} h_1 \\ h_2 \\ \vdots \\ h_H \end{pmatrix} = \begin{pmatrix} e[0] \\ e[1] \\ \vdots \\ e[K] \end{pmatrix}. \tag{19}$$

If we let $\mathbf{s}$, $\mathbf{H}$, $\mathbf{h}$, and $\mathbf{e}$ denote the vectors/matrices from left to right in Eq. (19), then the solution vector, $\mathbf{h}$, that minimizes $\mathbf{e}^T\mathbf{e} = \Sigma_{n=0}^{N-1}|e[n]|^2$, in Eq. (19), is given by

$$\tilde{\mathbf{h}} = -(\mathbf{H}^T\mathbf{H})^{-1}\mathbf{H}^T\mathbf{s}. \tag{20}$$

Here T stands for conjugate-transpose and $(\ )^{-1}$ denotes matrix inverse operation. The matrix, $\mathbf{H}$, can be further decomposed into a product $\mathbf{H} = \mathbf{S}_{N \times N}\mathbf{X}_{N \times H}$:

$$\mathbf{H} = \begin{pmatrix} s[0] & 0 & \cdots & \cdots & 0 \\ 0 & s[1] & 0 & \cdots & 0 \\ \vdots & \vdots & \ddots & \vdots & \vdots \\ 0 & 0 & \cdots & 0 & s[K] \end{pmatrix}_{N \times N}$$

$$\times \begin{pmatrix} 1 & 1 & \cdots & 1 \\ e^{j\Omega} & e^{j2\Omega} & \cdots & e^{jH\Omega} \\ \vdots & \vdots & \ddots & \vdots \\ e^{jK\Omega} & e^{j2K\Omega} & \cdots & e^{jHK\Omega} \end{pmatrix}_{N \times H}. \tag{21}$$

In Eq. (21), observe that $\mathbf{S}$ is a diagonal matrix consisting of signal samples while $\mathbf{X}$ is essentially the DFT matrix. Using this decomposition, the solution vector, $\tilde{\mathbf{h}}$, given by Eq. (20), can be rewritten as

$$\tilde{\mathbf{h}} = -(\mathbf{X}^T\mathbf{S}^T\mathbf{S}\mathbf{X})^{-1}\mathbf{X}^T\mathbf{S}^T\mathbf{s}. \tag{22}$$

Clearly, the solution depends only on the magnitude of $s[n]$. $h[n]$ can then be reconstructed by substituting elements of the vector $\tilde{\mathbf{h}}$ in $h[n] = 1 + \Sigma_{k=1}^{H} h_k e^{jk\Omega n} \cdot s_{\text{MinP}}[n]$ can then be computed as $1/h[n]$; the log-envelope and phase of $s_{\text{MinP}}[n]$ correspond to $\alpha[n]+\beta[n]$ and $\hat{\alpha}[n]+\hat{\beta}[n]$, respectively. The positive frequency, $\omega_c - 2\dot{\hat{\beta}}[n]$, can be found as the IF of the error signal, $e[n]$, using any standard IF estimator such as the phase difference between neighboring samples.[35] Instead, as mentioned earlier, we may also apply the LPSD algorithm again to $\dot{e}[n]$ [because the envelope of the first derivative of $e(t)$ is $\psi(t)$, which is the PIF]. We call this step the second-stage LPSD.

The LPSD algorithm attempts to flatten the envelope of the signal $s(t)$ by using an adaptive amplitude demodulator. This process not only eliminates the AM but also automatically removes from the phase of $s(t)$ a quantity equal to the Hilbert transform of the log-envelope of $s(t)$. This is what

causes the IF of $e(t)$ to be positive. Instead, if we simply "clip" $s(t)$, i.e., obtain $s(t)/|s(t)|$, then its phase derivative, the traditional IF, will not always be positive. Second, the MinP property of $h(t)$ guarantees that the envelope approximation $1/|h(t)|$ will never equal zero. Further, MinP signals will have their energy concentrated over a relatively small region in the spectral domain analogous to a MinP filter which has its impulse response peaking close to origin. It is also possible to use the LPSD algorithm to achieve a MinP-MaxP (instead of MinP-AllP) decomposition of $s(t)$. Separation of these components may also be viewed as deconvolution of their spectra in the frequency domain. Third, an important advantage of the LPSD algorithm is that it achieves the separation of the MinP and AllP components without explicitly rooting a polynomial or computing the logarithm or Hilbert transform of the signal $s(t)$.

B. Simulation results

We now provide results of applying the LPSD procedure to decompose synthetic signals. It will be followed by an example of a speech signal.

1. Synthetic signals

A signal $s(t)$ consisting of nine [$M=8$ in Eq. (1)] harmonically related complex exponentials with frequencies 0, 200 Hz,..., up to 1.6 kHz, with amplitudes 1, 3.37, 3.42, 9.45, 15.76, 5.4, 5.4, 3.72, and 1.5, respectively, and whose respective phases (in radians) were 0, -0.3, -1.3, -3.1, 2.8, 2.7, -1.3, -0.9, and -0.6, was synthesized. $s(t)$ corresponds to a mixed phase signal consisting of four zeros inside and four zeros outside the unit circle. The signal is periodic with 5-msec periods (200-Hz fundamental frequency) and has a carrier frequency of 800 Hz (corresponding to its MaxP component's translation $Q\Omega$, $\omega_c = 2\pi \times 800$ and $\omega_t = 0$). The signal was sampled at 16 kHz. In Fig. 2(a) we have displayed the signal's zeros while in Fig. 2(b) we have plotted its magnitude spectrum.

The signal samples were fed to the LPSD algorithm described in the previous subsection. The coefficients of the inverse signal $h(t)$ were computed using Eq. (20). Once the coefficients of $h(t)$ are computed, then $h(t)$ (actually its samples) is synthesized. For the case of 60 coefficients [i.e., $H=60$ in Eq. (19)], the estimated log-envelope given by $1/|h(t)|$ is shown (solid line) in Fig. 3(a). Actually, two periods (10 msec) of the log-envelope are shown. Also shown is the true envelope (dashed line) given by $\ln|s(t)|$. They perfectly match and hence the dashed line is not visible. The magnitude of the error signal $e(t)$ is shown in the dashed-dotted line in Fig. 3(a), and is close to unity, indicating that the error signal $e(t)$ is indeed AllP. In Fig. 3(b) we have plotted the signal's raw IF [obtained by differencing the phase angles of adjacent samples of the signal $s(t)$]. Note that the raw IF goes negative (dashed line). On the other hand, the PIF (i.e., $\omega_c - 2\dot{\beta}[n]$) computed by differencing the phases of the neighboring samples of the error signal $e(t)$, stays positive, as it should. The PIF can also be obtained by using the LPSD algorithm on $\dot{e}(t)$; we call this second-stage LPSD. The PIF obtained by differencing the phase-angles of neighboring samples of $e(t)$ or by using the
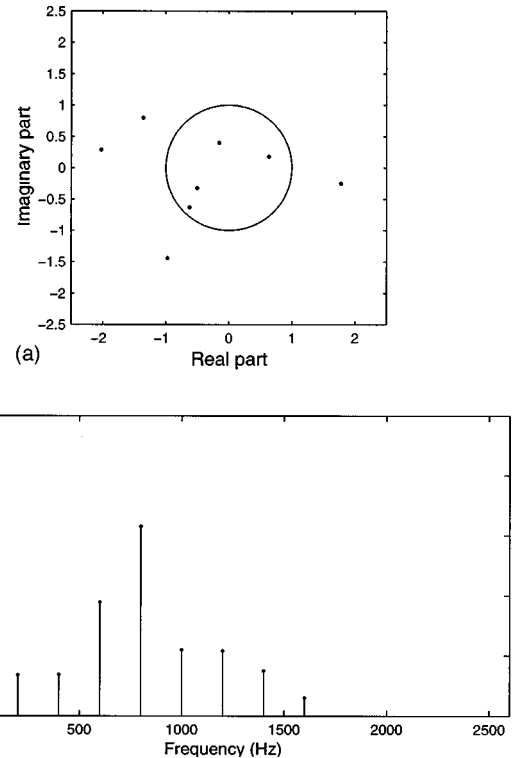
FIG. 2. The eight zeros of the synthetic signal $s(t)$ are shown in (a); its magnitude spectrum is plotted in (b). The signal (sampled at 16 kHz) has a 200-Hz fundamental frequency and a carrier frequency of 800 kHz.

second-stage LPSD gave essentially the same results. Also plotted in Fig. 3(b) is the true PIF (dashed-dotted line, again not visible). The true PIF was obtained, for the purpose of comparison, by using the roots of the polynomial in Eq. (1) and synthesizing the AllP signal given in Eq. (12) and determining its IF. ω_c was estimated as the mean of PIF and $\dot{\hat{\beta}}[n]$ was separated by subtracting ω_c's estimate from the PIF. Further, $\dot{\hat{\alpha}}[n]$ was computed by subtracting the estimate of $\dot{\hat{\beta}}[n]$ from the MinP signal's ($1/h(t)$'s) IF; the solid line in Fig. 3(c) corresponds to the separated $\dot{\hat{\alpha}}[n]$; it matches with the true one (obtained using the signal's roots) shown as a dashed-dotted line. In Fig. 3(d) we have displayed the real part of the signal reconstructed using the separated MinP and MaxP components using a solid line; the dashed-dotted line corresponds to two periods of the real part of the original signal $s(t)$; they match exactly.

Figure 3(e) corresponds to the estimated PIF (solid line) when $H=20$ in first stage and $H=15$ in second-stage LPSD. Clearly, a higher model order [the results of which are shown in Fig. 3(b)] results in a better approximation. The effect of varying a signal's duration and changing model order is shown in Fig. 3(f): we have plotted $-10 \log$ (error) as a function of the signal length and model order; "error" denotes sum of squared error between the true PIF and the estimated one. First, not surprisingly, the approximation gets better as model order increases. Second, as T approaches the true period (80 samples) of the signal, the approximation improves. However, as T further increases, the assumed fundamental frequency, Ω, decreases and hence LPSD requires a much higher order for a better approximation.
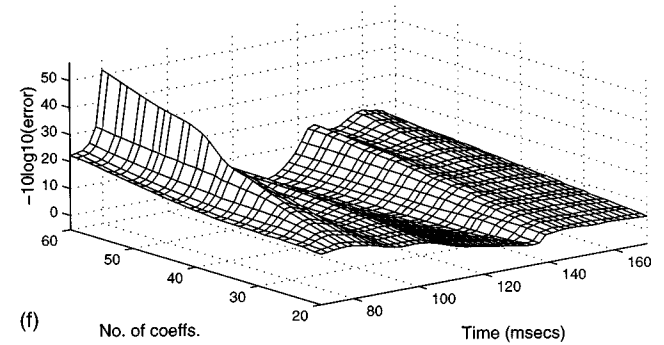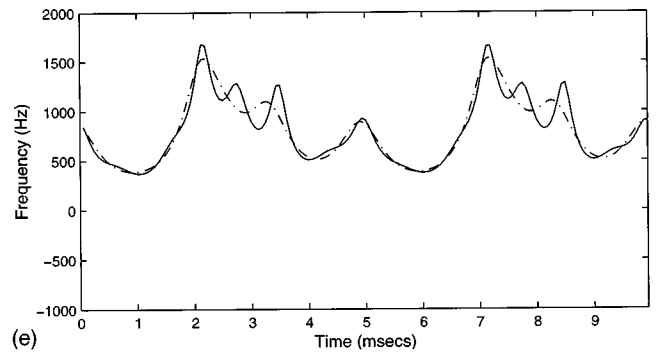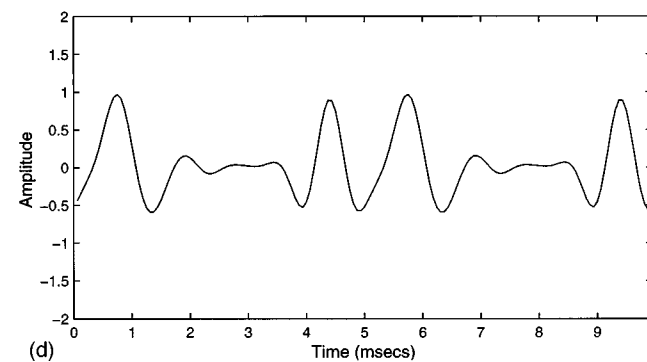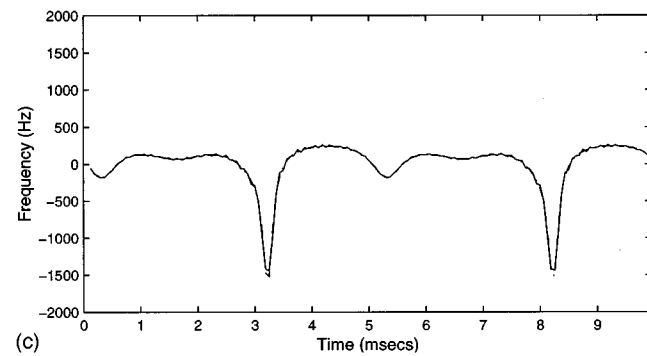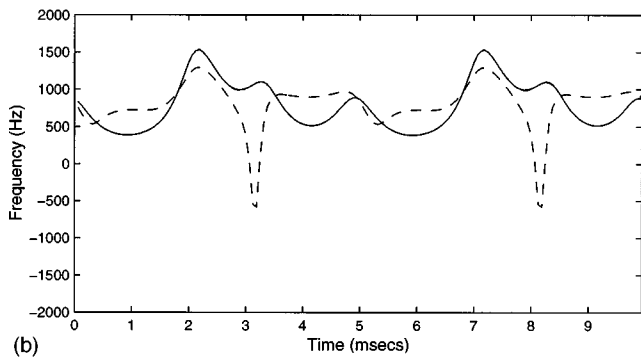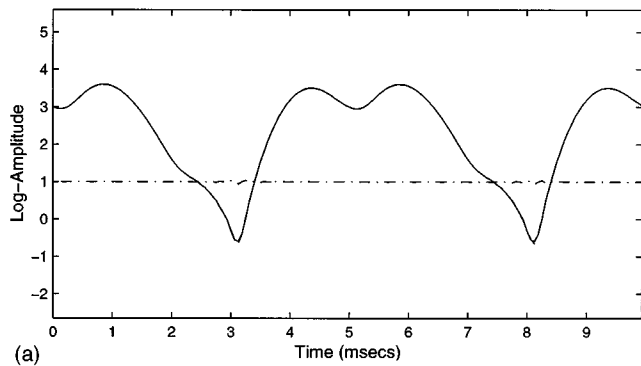
FIG. 3. The separated log-envelope using LPSD (60 coefficients) is shown (solid line) in (a); the true one is shown as dashed line; the magnitude of the error signal $e(n)$ is shown as dashed-dotted line. In (b) we plot the signal's raw IF (dashed) which goes negative; the solid line refers to estimate of PIF ($H=15$ in second stage); the true PIF is also displayed (dashed-dotted). First stage estimate of $\hat{\alpha}[n]$ is shown as solid line in (c) along with true $\hat{\alpha}[n]$ plotted as dashed-dotted line. The real part of the reconstructed signal using the separated components is plotted in (d) (using solid line) along with the real part of the original signal $s(t)$ (dashed-dotted line); they match exactly. The PIF when 20 coefficients were used in LPSD's first stage and 15 in the second is plotted in (e). The effect of increasing a signal's duration and increasing model order is shown in (f). We plot $-\log_{10}$ (error) as a function of the signal length (in samples) and model order; error denotes sum of squared error between true PIF and estimated one. Time is shown in samples.

The above example had no roots with unit magnitude. To test LPSD on signals with some zeros on the unit circle, magnitude of one of the zeros of the signal used in a previous example was set to unity. We used $H=40$ in LPSD's first stage and $H=10$ in the second one. The results are displayed in Fig. 4(a) and (b). In Fig. 4(a) we plot the log envelopes; sharp dips in the signal's log magnitude (dashed line) are due to the on-circle zero. Observe that the approximation (solid line) tends to exclude this zero. Further observe that the magnitude of the error signal $e(t)$ is unity, but

for the time corresponding to location of on-circle zero (dashed-dotted line). In Fig. 4(b) we show the approximated PIF using a solid line along with the true $\omega_c - 2\dot{\hat{\beta}}[n]$ (dashed line). Clearly, the PIF approximates the spikes due to on-circle zeros in addition to closely matching the IF due to zeros off the unit circle. To summarize thus far, given a signal $s(t)$, its various components (MinP/MaxP/AllP), which are actually multiplied components, can be separated using simple linear techniques without resorting to logarith-
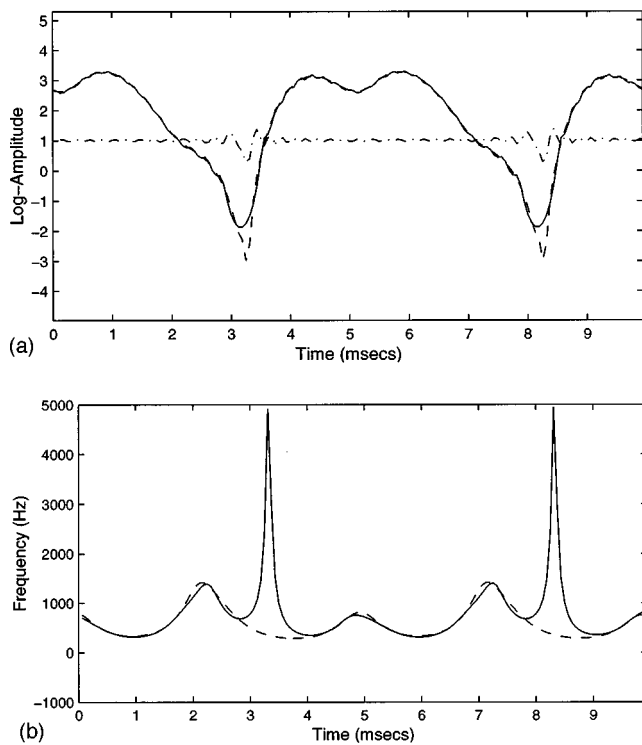
FIG. 4. We consider a signal with a zero of unity magnitude. Its log envelope is shown in (a) as a dashed line; dips correspond to location of the on-circle zero. We used $H=40$ in LPSD's first stage and $H=10$ in the second one. The estimated log envelope and PIF are plotted (solid lines) in (a) and (b), respectively; original functions are shown using dashed line; dashed-dotted line in (a) denotes error's magnitude.

mic processing or rooting algorithms. We now give an example using speech signals.

2. Speech signal

In this section we give results of processing clean voiced speech, obtained from the TIMIT database, in the sentence *train/dr3/fcke0/si1111.wav* which corresponded to the utterance "How do we define it?" Figure 5(a) shows the results for a segment, whereas Fig. 5(b) shows the results for the entire sentence. The signal (sampled at 16 kHz) was preemphasized using a high-pass filter (with transfer function $1-0.98z^{-1}$) and its analytic version was computed using the fast Fourier transform (FFT) based Hilbert transformer in Matlab. We then chose 14.56 ms of the signal (samples 6851:7084) that was part of the phoneme /iy/. This signal was then bandpass filtered using three bandpass filters (BPFs) which were part of "Lyon's Passive Long Wave Cochlear Model" proposed by Lyon.[36] The bandpass filters (BPFs) were manually chosen such that their center frequencies were roughly centered around the formant locations. In Fig. 5(a) we have shown the magnitude spectrum of the preemphasized speech signal (solid line) along with the normalized magnitude responses of the three BPFs (dotted lines). The signals at these BPFs' output were inputs to our LPSD algorithm. The bandwidths (B_c) for BPFs centered at $\approx$500 Hz, 2.25 kHz, and 5 kHz were approximately 120, 340, and 900 Hz, respectively. These bandwidths roughly correspond to the critical bandwidths of the auditory filters at the given center frequencies. Recall that LPSD assumes a fundamental
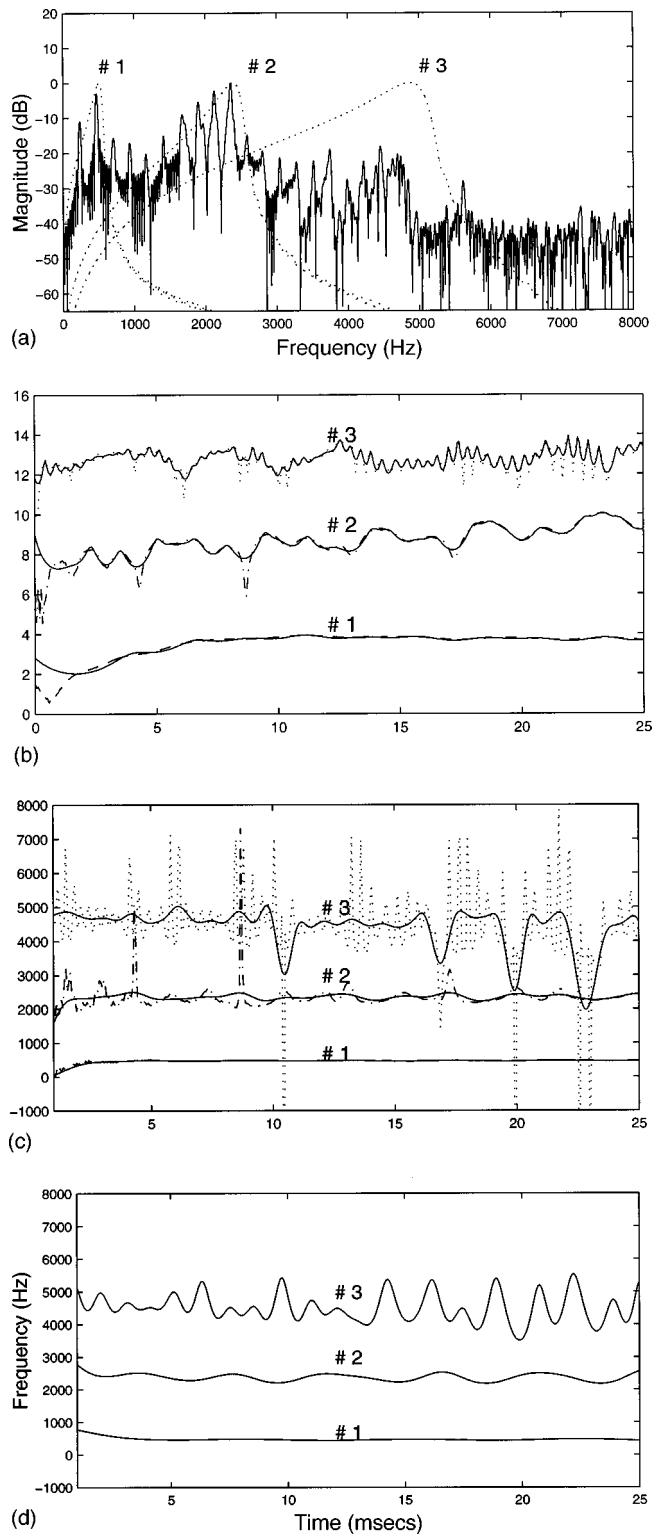
FIG. 5. The spectrum of a preemphasized voiced speech segment is displayed in (a). The signal was filtered using 3 BPFs [magnitude responses shown in (a) as dotted lines] which correspond to Lyon's auditory filters. LPSD parameters were selected based on BPFs' bandwidths. The estimated log envelopes are shown (not to scale) in (b) as solid lines along with the signals' true log envelopes shown as dashed, dashed-dotted, and dotted lines for BPFs 1, 2, and 3, respectively. The raw IFs for signals filtered by BPFs #1, #2, and #3 are displayed in (c) as dashed, dashed-dotted, and dotted lines respectively, along with corresponding lowpass filtered (with order 50 and cutoffs 120, 340, and 900 Hz) IFs shown as solid lines. In (d) we plot the PIFs estimated using LPSD with $H=4$, 11, and 28, respectively.
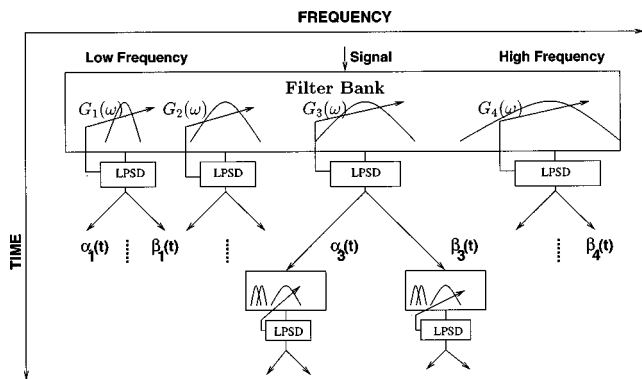
FIG. 6. We envision a ''tonotopic signal analyzer'' as a general purpose processor that decomposes an input signal (on the time-frequency plane) around regions of dominant spectral energies into carrier frequencies, log amplitudes, and MinP-AllP (or MinP-MaxP) modulations [$\alpha_k(t)$ and $\beta_k(t)$]. These modulations are further broken down into their respective center frequencies, and so on. The result is a treelike break-up of the signal wherein higher nodes of the tree correspond to more significant temporal-spectral events in the signal.

frequency, Ω, of $2\pi/N$; this corresponds to 32 Hz for the present example. Having specified a certain bandwidth for envelope approximation, one can compute the algorithm's model order as $H = 2\pi B_c/\Omega$. Based on these calculations, we chose LPSD model orders, H, to be 12, 33, and 84, corresponding to three times the critical bandwidths for first-stage envelope approximation. The values of H were set to 4, 11, and 28 for approximating the PIFs in second-stage processing. One may also keep H fixed and vary the processing interval for each BPF proportional to $1/B_c$. Our goal was not to parsimoniously describe the signal but to demonstrate that the carrier frequency and the modulations carry sufficient information to describe the signal. The estimated log envelopes are shown in Fig. 5(b) as solid lines (not to scale) along with the signal's Hilbert envelopes for each of the three filters (dashed, dashed-dotted, and dotted for BPFs 1, 2, and 3, respectively). The raw IFs (obtained by phase-differencing) for signals filtered by the three BPFs are displayed in Fig. 5(c) as dashed, dashed-dotted, and dotted lines, respectively, along with corresponding lowpass filtered (with order 50 and cutoffs 120, 340, and 900 Hz) IFs shown as solid lines. The PIFs resulting from second-stage processing are depicted in Fig. 5(d).

Based on earlier discussions we can see that the sharp spikes in raw log-envelopes and most of the spikes in raw IFs (especially for signals at output of BPFs 2 and 3) are due to signal zeros very close to the unit circle; the latter may be caused by neighboring peaks in the signal's spectral envelope (or neighboring formants). Further, the raw IFs also go negative at times. In general, the raw log-envelopes and IFs are highly fluctuating quantities. Clearly, the LPSD may be viewed as a technique to compute a signal's envelope's logarithm. The IF approximated by LPSD has two distinct advantages over techniques that merely filter the raw IF. First, in the absence of on-circle zeros, it is always positive. Second, it approximates the typically impulsive IF better (due to the all-pole model assumption) as opposed to lowpass filtered IF.

When a composite signal consists of many spectral regions of interest which are time-varying, as in speech, the
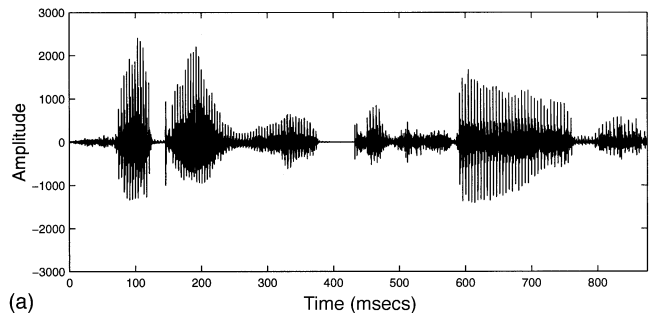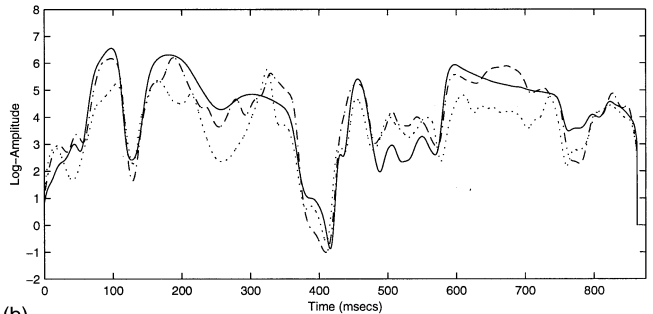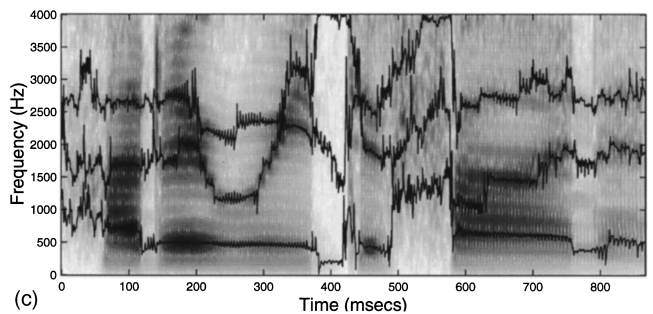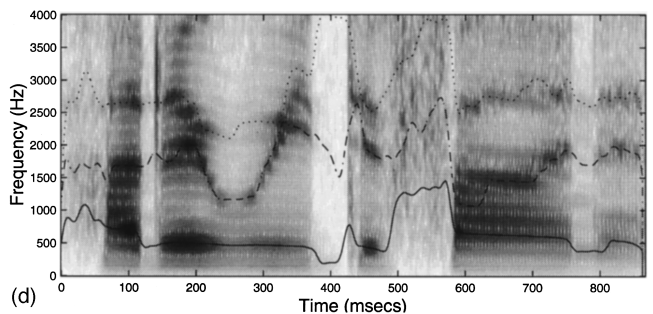
FIG. 7. (a) The speech signal for the sentence ''How do we define it?'' is plotted; this segment was obtained from the TIMIT database (TIMIT/train/dr3/fcke0/si1111.wav). (b) We have displayed the estimated average log-envelopes as solid, dashed-dotted, and dotted lines at the output of the three time-varying filters. The details of the time-varying bandpass filters (BPFs) are given in Ref. 31. (c) We have superimposed on the spectrogram the estimated PIFs of the components at the output of the time-varying BPFs. (d) The averages of the PIFs are shown. They tend to follow the trajectories of the first three formants.

signal must be decomposed by a bank of time-varying filters which may then be followed by envelope and PIF decomposition described here. The bank of filters must be data adaptive and should form part of the speech signal representation. A block diagram depicting this basic idea is shown in Fig. 6. We have made some progress in implementing this block diagram,[31] but due to space limitations the details are not presented here. Figure 7(a), (b), (c), and (d) show the results

of processing the entire sentence ''How do we define it?'' using this decomposition. We may call this approach ''Tonotopic Signal Analysis (TSA),'' since the procedure not only attempts to track the formant center frequencies but also provides the details of modulations (the α and β) about those frequencies. Reference 31 provides several such speech processing examples.

IV. DISCUSSION

In this paper our main accomplishment is the decomposition of an analytic signal into two analytic signals using a simple (LPSD) algorithm. Decomposition of analytic functions of a complex variable has been studied in systems theory and filter design since the days of Henrik Bode[37] in the 1930s. However, much of that work dealt with frequency responses, i.e., frequency is viewed as a complex variable s (continuous-time systems) or z (discrete-time systems). Cepstrum-related research[5] may be viewed as an extension of this work. Voelcker's contribution, which extends Gabor's work,[7] is that he recognized that analytic functions could be used for studying the relationships between phase and envelope of signals by treating time as a complex variable. To our knowledge, Voelcker did not attempt to decompose signals into MinP and MaxP or AllP components. The MinP/MaxP/AllP decomposition was, perhaps, first done by Oppenheim and colleagues (see Ch. 12 in Ref. 5, and references therein). However, their decomposition was achieved by rooting a polynomial or computing logarithm/log-derivative in the z-transform or frequency domain. In contrast, the significance of our result is that the MinP-AllP or MinP-MaxP decomposition is achieved using an elegant adaptive demodulator without rooting, Hilbert transformation, or phase unwrapping, directly from the given signal $s(t)$. A similar procedure can be developed for the frequency domain as well. The primary difference between our approach and the cepstrum analysis is that we explore the signal's logarithm in the time domain which yields a physically acceptable quantity like the positive instantaneous frequency. This helps us in characterizing the IF of signals which consist of many components such as a speech formant. The average PIF (i.e., the carrier frequency) indicates the place-location of a signal's spectral concentration.

Unfortunately, in this paper, we still need to form the analytic signal before the proposed decomposition can be achieved. That is, since in practice only real-valued signals are available for processing, one has to compute its Hilbert transform. In more recent work[38] we have proposed an algorithm which avoids computation of the analytic signal. It is possible to obtain the envelope and PIF directly from the real signal under certain restrictions.

APPENDIX A: MINIMUM AND MAXIMUM PHASE SIGNALS

An elementary signal,[23] $e(t)$, is defined as

$$e(t) = 1 - pe^{j\Omega t}, \tag{A1}$$

where $p = |p|e^{j\theta}$. If $|p| < 1$ then $e(t)$ is called a MinP signal, since no other signal with the same envelope has a smaller phase angle. Observe that $|e(t)| > 0$. Taking the natural logarithm of both sides and using the series expansion, $\ln(1-y) = \sum_{k=1}^{\infty}(-y^k/k)$, we get

$$\ln(1 - pe^{j\Omega t}) = \sum_{k=1}^{\infty} \frac{-p^k e^{-jk\Omega t}}{k}. \tag{A2}$$

After exponentiating both sides, we get the following identity:

$$1 - pe^{j\Omega t} = \exp\left(\sum_{k=1}^{\infty} \frac{-|p|^k}{k} \cos(k\Omega t + k\theta) \right.$$
$$\left. + j\sum_{k=1}^{\infty} \frac{-|p|^k}{k} \sin(k\Omega t + k\theta) \right). \tag{A3}$$

From the above expression we note that for an elementary MinP signal, $e(t)$, the logarithm of its envelope and its phase angle are related through the Hilbert transform. Similarly, for an elementary MaxP signal $(1 - qe^{j\Omega t})$ where $q = |q|e^{j\phi}$, $|q| > 1$, we get the following identity:

$$1 - qe^{j\Omega t} = (-qe^{j\Omega t})\exp\left(\sum_{k=1}^{\infty} \frac{-|1/q|^k}{k} \cos(k\Omega t + k\phi) \right.$$
$$\left. - j\sum_{k=1}^{\infty} \frac{-|1/q|^k}{k} \sin(k\Omega t + k\phi) \right). \tag{A4}$$

The key difference between Eqs. (A3) and (A4) is the change in the sign of the phase function.

Using the above identities in Eq. (2) yields

$$s_{\text{MinP}}(t) = e^{\alpha(t) + j\hat{\alpha}(t)} \tag{A5}$$

and

$$s_{\text{MaxP}}(t) = A_0 e^{\beta(t) + j(\omega_0 t - \hat{\beta}(t))}, \tag{A6}$$

where

$$\alpha(t) = \sum_{k=1}^{\infty} \sum_{i=1}^{P} -\frac{|p_i|^k}{k} \cos(k\Omega t + k\theta_i) \tag{A7}$$

and

$$\beta(t) = \sum_{k=1}^{\infty} \sum_{i=1}^{Q} -\frac{1/|q_i|^k}{k} \cos(k\Omega t + k\phi_i). \tag{A8}$$

Thus $s(t)$ as described in Eq. (2) can be compactly represented as

$$s(t) = A_c e^{j\omega_c t} e^{\alpha(t) + j\hat{\alpha}(t)} e^{\beta(t) - j\hat{\beta}(t)}, \tag{A9}$$

where A_c corresponds to the overall amplitude of the signal and ω_c denotes its ''carrier'' frequency. ω_c is equal to $Q\Omega$ plus any arbitrary frequency translation that the signal $s(t)$ may have been subjected to. The log-envelope and phase of

$s(t)$ are expressed in terms of $\alpha(t)$ and $\beta(t)$ as

$$\ln|s(t)| = \alpha(t) + \beta(t) + \ln A_c \qquad (A10)$$

and

$$\angle s(t) = \omega_c t + \hat{\alpha}(t) - \hat{\beta}(t), \qquad (A11)$$

respectively. The above expressions can be a useful pedagogical tool in explaining phase-envelope relationships in the signal as well as systems domains. For instance, the well-known results in Ref. 39, where one attempts to reconstruct a signal from either phase or magnitude information, may easily be explained using the above expressions. For example, if a pair of roots of $s(t)$ occurs in complex conjugate reciprocal locations, i.e., $p_i = 1/q_i^*$, then the ith term in the summation in Eqs. (A7) and (5) are identical and hence vanish from the expression for phase in Eq. (A11). Hence, in this case, phase does not uniquely specify the signal $s(t)$. This is essentially theorem 1 in Ref. 39, which is stated in the systems domain. Similarly if $p_i = -1/q_i^*$, then from Eq. (A10) we see that magnitude alone is not sufficient to specify a signal $s(t)$. In general, both phase and envelope are required to represent $s(t)$.

The instantaneous frequency (IF) of $s(t)$ is the derivative of the phase of $s(t)$ and is simply $\omega_c + \dot{\hat{\alpha}}(t) - \dot{\hat{\beta}}(t)$ (where the dot stands for the first derivative), i.e., it consists of a dc (corresponding to carrier frequency) and a sum of IFs of $s(t)$'s MinP and MaxP components. Thus we have

$$\frac{d\angle s(t)}{dt} = \omega_c - \Omega \left[\sum_{k=1}^{\infty} \left(\sum_{i=1}^{P} |p_i|^k \cos(k\Omega t + k\theta_i) \right.\right.$$
$$\left.\left. - \sum_{i=1}^{Q} |1/q_i|^k \cos(k\Omega t + k\phi_i) \right) \right]. \qquad (A12)$$

Clearly, the spectrum of $s(t)$'s IF [given by Eq. (A12)] contains an infinite number of harmonic components (Ω being the fundamental frequency). A closed-form expression for IF is obtained by summing Eq. (A12) as

$$d\angle s(t)/dt$$
$$= \omega_c - \Omega \left[\sum_{i=1}^{P} \frac{|p_i|(\cos(\Omega t + \theta_i) - |p_i|)}{1 - 2|p_1|\cos(\Omega t + \theta_i) + |p_1|^2} \right.$$
$$\left. - \sum_{i=1}^{Q} \frac{|1/q_i|(\cos(\Omega t + \phi_i) - |1/q_i|)}{1 - 2|(1/q_i)|\cos(\Omega t + \phi_i) + |(1/q_i)|^2} \right]. \qquad (A13)$$

The above reveals that $s(t)$'s IF tends to $\pm\infty$ whenever one or more of its zeros tend to lie on the unit circle (see Ref. 31 for details). All these results were known to Voelcker.

APPENDIX B: SIGNALS WITH POSITIVE INSTANTANEOUS FREQUENCY

Consider a signal, $z(t)$, which is a ratio of two signals as follows:

$$z(t) = \frac{1 - qe^{j\Omega t}}{1 - (1/q^*)e^{j\Omega t}}; \qquad (B1)$$

"*" denotes complex conjugation, $q = |q|e^{j\phi}$, and $|q| > 1$. Rearranging the numerator we have

$$z(t) = -qe^{j\Omega t} \frac{1 - (1/q)e^{-j\Omega t}}{1 - (1/q^*)e^{j\Omega t}}. \qquad (B2)$$

Simplifying the above equation, we find that $z(t)$'s envelope is a constant (equal to $|q|$) for all time, t, and that its phase angle is

$$\angle z(t) = \Omega t + \pi + \phi + 2\sum_{k=1}^{\infty} \frac{|1/q|^k}{k} \sin(k\Omega t + k\phi). \qquad (B3)$$

Taking the first derivative of $\angle z(t)$, its IF can be expressed as

$$\frac{d\angle z(t)}{dt} = \Omega \left(1 + 2\sum_{k=1}^{\infty} \left|\frac{1}{q}\right|^k \cos(k\Omega t + k\phi) \right). \qquad (B4)$$

Since the right side of Eq. (B4) is $\Omega(1 - |1/q|^2)|1 - (1/q^*)e^{j\Omega t}|^{-2}$ and is analogous to a "power spectrum," $z(t)$'s IF is always positive. We may generalize this result to the case of a signal consisting of a product of rational signals as in Eq. (B2), i.e., $z(t)$ of form

$$z(t) = \prod_{i=1}^{L} \frac{1 - q_i e^{j\Omega t}}{1 - (1/q_i^*)e^{j\Omega t}}. \qquad (B5)$$

Since the phase angle contribution due to each of the L terms in the above equation adds up, the corresponding IF is

$$\frac{d\angle z(t)}{dt} = \Omega \sum_{i=1}^{L} \left(1 + 2\sum_{k=1}^{\infty} \left|\frac{1}{q_i}\right|^k \cos(k\Omega t + k\phi_i) \right). \qquad (B6)$$

Since each of the L terms in the above summation is positive, we claim that the final IF given by Eq. (B6) is positive. These results are analogous to the results well known in discrete time all-pass (AP) systems, where the equivalent of IF is the group delay;[40] our derivation is slightly different than the one given in Oppenheim and Schafer.[5]

[1] L. Cohen, "Time-frequency distributions—A review," Proc. IEEE **77**, 941–981 (1989).

[2] F. Hlawatsch and G. F. Boudreaux-Bartels, "Linear and quadratic time-frequency signal representations," IEEE ASSP Magazine **9**, 21–67 (April 1992).

[3] B. S. Atal and S. L. Hanauer, "Speech analysis and synthesis by linear prediction of the speech wave," J. Acoust. Soc. Am. **50**, 637–655 (1971).

[4] J. I. Makhoul, "Linear prediction: A tutorial review," Proc. IEEE **63**, 561–580 (1975).

[5] A. V. Oppenheim and R. W. Schafer, *Discrete-Time Signal Processing* (Prentice-Hall, Englewood Cliffs, NJ, 1989).

[6] S. Davis and P. Mermelstein, "Comparison of parametric representations for monosyllabic word recognition in continuously spoken sentences," IEEE Trans. Acoust., Speech, Signal Process. **4**, 357–366 (1980).

[7] D. Gabor, "Theory of communication," Proc. IEE **93**, 429–457 (1946).

[8] J. Dugundji, "Envelopes and preenvelopes of real waveforms," IRE Trans. Inf. Theory **4**, 53–57 (1958).

[9] A. Papoulis, *The Fourier Integral and its Applications* (McGraw-Hill, New York, 1962).

[10] L. Cohen, *Time-Frequency Analysis* (Prentice-Hall, Englewood Cliffs, NJ, 1995).

[11] P. Maragos, T. F. Quatieri, and J. F. Kaiser, "Energy separation in signal modulations with applications to speech," IEEE Trans. Signal Process. **41**, 3024–3051 (1993).

[12] F. Casacuberta and E. Vidal, "A nonstationary model for the analysis of

transient speech signals,'' IEEE Trans. Acoust., Speech, Signal Process. **35**, 226–228 (1987).

[13] T. F. Quatieri, T. E. Hanna, and G. C. O'Leary, ''Am-fm separation using auditory motivated filters,'' IEEE Trans. Speech Audio Process. **5**, 465–480 (1997).

[14] P. J. Loughlin and B. Tacer, ''On the amplitude- and frequency-modulation decomposition of signals,'' J. Acoust. Soc. Am. **100**(3), 1594–1601 (1996).

[15] J. L. Flanagan, ''Parametric coding of speech spectra,'' J. Acoust. Soc. Am. **68**, 412–419 (1980).

[16] A. V. Oppenheim, R. W. Schafer, and T. G. Stockham, ''Nonlinear filtering of multiplied and convolved signals,'' Proc. IEEE **56**, 1264–1291 (1968).

[17] L. Mandel, ''Interpretation of instantaneous frequencies,'' Am. J. Phys. **42**, 840–846 (1974).

[18] E. Bedrosian, ''The analytic signal representation of modulated waveforms,'' Proc. IRE **50**, 2071–2076 (1962).

[19] J. Shekel, ''Instantaneous frequency,'' Proc. IRE **41**, 548–548 (1953).

[20] D. Vakman, ''On the analytic signal, the Teager-Kaiser energy algorithm, and other methods for defining amplitude and frequency,'' IEEE Trans. Signal Process. **44**, 791–797 (1996).

[21] M. Poletti, ''The homomorphic analytic signal,'' IEEE Trans. Signal Process. **45**, 1943–1953 (1997).

[22] B. Picinbono, ''On instantaneous amplitude and phase of signals,'' IEEE Trans. Signal Process. **45**, 552–560 (1997).

[23] H. B. Voelcker, ''Towards a unified theory of modulation part I: Phase-envelope relationships,'' Proc. IEEE **54**, 340–354 (1966).

[24] H. B. Voelcker, ''Towards a unified theory of modulation part II: Phase-envelope relationships,'' Proc. IEEE **54**(5), 735–755 (1966).

[25] S. M. Kay, *Modern Spectral Estimation: Theory and Application* (Prentice-Hall, Englewood Cliffs, NJ, 1987).

[26] *Auditory Computation*, edited by H. L. Hawkins, T. A. McMullen, A. N. Popper, and R. R. Fay (Springer-Verlag, New York, 1996).

[27] S. Khanna and M. C. Teich, ''Spectral characteristics of the responses of primary auditory-nerve fibers to frequency modulated signals,'' Hearing Res. **39**, 143–158 (1989).

[28] L. B. Jackson, *Signals, Systems, and Transforms* (Addison-Wesley, Reading, MA, 1991).

[29] *Entire Functions*, edited by R. P. Boas (Academic, New York, 1954).

[30] A. G. Requicha, ''Contributions to a zero based theory of band limited signals,'' Ph.D. thesis, University of Rochester, Rochester, NY, 1970.

[31] A. Rao, ''Signal analysis using product expansions inspired by the auditory periphery,'' Ph.D. thesis, University of Rhode Island, Kingston, RI, June 1997.

[32] R. Nevanlinna, *Analytic Functions* (Springer-Verlag, Berlin, 1970).

[33] W. Rudin, *Real and Complex Analysis* (McGraw-Hill, New York, 1987).

[34] R. Kumaresan and A. Rao, ''An algorithm for decomposing an analytic signal into AM and positive FM components,'' in *Proceedings of the IEEE International Conference on Acoustics, Speech and Signal Processing*, Seattle, WA, May 1998, pp. III:1561–1564.

[35] S. M. Kay, ''A fast and accurate single frequency estimator,'' IEEE Trans. Speech Audio Process. **37**, 1987–1990 (1989).

[36] M. Slaney, ''Auditory toolbox,'' Tech. Rep. 45, Apple Computer, Inc., 1994.

[37] *Network Analysis and Feedback Amplifier Design*, edited by H. W. Bode (Van Nostrand, Princeton, 1945).

[38] R. Kumaresan, ''An inverse signal approach to computing the envelope of a real valued signal,'' IEEE Signal Process. Lett. **October**, 256–259 (1998).

[39] M. H. Hayes, J. S. Lim, and A. V. Oppenheim, ''Signal reconstruction from phase or magnitude,'' IEEE Trans. Speech Audio Process. **28**, 672–680 (1980).

[40] E. A. Robinson, *Time Series Analysis and Applications* (Goose Pond, Houston, 1981).

Fractal dimensions of speech sounds: Computation and application to automatic speech recognition[a)]

Petros Maragos[b)]
*Department of Electrical and Computer Engineering, National Technical University of Athens,
Zografou 15773, Athens, Greece*

Alexandros Potamianos[c)]
AT&T Labs, 180 Park Avenue, Post Office Box 971, Florham Park, New Jersey 07932-0971

The dynamics of airflow during speech production may often result in some small or large degree of turbulence. In this paper, the geometry of speech turbulence as reflected in the fragmentation of the time signal is quantified by using fractal models. An efficient algorithm for estimating the short-time fractal dimension of speech signals based on multiscale morphological filtering is described, and its potential for speech segmentation and phonetic classification discussed. Also reported are experimental results on using the short-time fractal dimension of speech signals at multiple scales as additional features in an automatic speech-recognition system using hidden Markov models, which provide a modest improvement in speech-recognition performance. © *1999 Acoustical Society of America.* [S0001-4966(99)02403-0]

PACS numbers: 43.72.Ar, 43.72.Ne [JLH]

INTRODUCTION

The dynamics of speech airflow might create small or large degrees of turbulence during production of speech sounds by the human vocal-tract system. Static airflow and acoustic characteristics of turbulent speech, e.g., fricative and stop sounds or sounds with aspiration, have been studied by several researchers; references and related discussion can be found in Fant (1970), Flanagan (1972), and Stevens (1971). While the majority of work in this area has mainly associated turbulence in speech with consonants, it is also possible to have vowels uttered with some (speaker-dependent) amount of aspiration which adds some small degree of turbulence to them. To produce natural-sounding synthetic speech, it was judged necessary to simulate an aspiration noise source in speech-synthesis systems (Klatt, 1987).

Most approaches modeling speech turbulence at the speech-waveform level have focused on the random nature of the corresponding signal component. Another important aspect of speech sounds that contain frication or aspiration is the high degree of geometrical complexity and fragmentation of their time waveforms; due to lack of a better approach, this has been left unmodeled and treated in the past as noise. In this paper, we use the theory of fractals (Mandelbrot, 1982) to model the geometrical complexity of speech waveforms via their fractal dimension, which quantifies the degree of signal fragmentation. In Sec. I, we provide some motivation and justification from the field of speech aerodynamics for using fractal dimension to quantify the degree of turbulence in speech signals. In Sec. II, a simple and efficient algorithm is described for measuring the fractal dimension. The algorithm is based on multiscale nonlinear operators of morphological filtering that iteratively expand and contract the signal's graph (Maragos, 1994; Serra, 1982). Some of our contributions include the measurement and study of the fractal dimension of speech signals in a short-time (phoneme-based) and multiscale framework, which we believe is necessary since speech signals are nonstationary and their fragmentation may vary across different time scales. In this area, we extend the preliminary experiments in Maragos (1991) by providing measurements averaged over large numbers of phonemic instances from the TIMIT and ISOLET databases. Another contribution is to the field of speech recognition: the multiscale fractal dimensions of short-time speech segments are used as additional features in an automatic speech-recognition system based on hidden Markov models (HMMs). As discussed in Sec. III, the fractal features can offer a modest improvement to the performance of HMM-based speech recognizers.

I. SPEECH AERODYNAMICS AND FRACTALS

Conservation of momentum in the airflow during speech production yields the Navier–Stokes governing equation (Tritton, 1988)

$$\rho\left(\frac{\partial \mathbf{u}}{\partial t} + \mathbf{u} \cdot \nabla \mathbf{u}\right) = -\nabla p + \mu \nabla^2 \mathbf{u}, \tag{1}$$

where ρ is the air density, p is the air pressure, $\mathbf{u}$ is the (vector) air-particle velocity, and μ is the (assumed constant) air-viscosity coefficient. It is assumed that flow compressibility is negligible [valid since in speech flow (Mach numbers)$^2 \ll 1$], and hence $\nabla \cdot \mathbf{u} = 0$. An important parameter characterizing the type of flow is the Reynolds number $\mathrm{Re} = \rho U L / \mu$, where U is a velocity scale for $\mathbf{u}$ and L is a

typical length scale, e.g., the tract diameter. For the air we have very low μ, and hence high Re. This causes the inertia forces [in the left-hand side of Eq. (1)] per unit volume to have a much larger order of magnitude than the viscous forces $\mu\nabla^2\mathbf{u}$. While μ is low and may not play an important role for the speech airflow through the interior of the vocal tract, it is essential for the formation of boundary layers along the tract boundaries and for the creation of vortices. A *vortex* is a region of similar (or constant) vorticity $\boldsymbol{\omega}$, where $\boldsymbol{\omega}=\nabla\times\mathbf{u}$. Vortices in the airflow have been experimentally found above the glottis by Teager and Teager (1990) and Thomas (1986), and theoretically predicted by Kaiser (1983), Teager and Teager (1990), and McGowan (1988), using simple geometries. There are several mechanisms for the creation of vortices: (1) velocity gradients in boundary layers, (2) separation of flow, which can easily happen at cavity inlets due to adverse pressure gradients [see Kaiser (1983), and Teager and Teager (1990) for experimental evidence of separated flow during speech production], and (3) curved geometry of tract boundaries, where due to the dominant inertia forces the flow follows the curvature and develops rotational components. After a vortex has been created, it can propagate downstream as governed by the vorticity equation (Tritton, 1988)

$$\frac{\partial\boldsymbol{\omega}}{\partial t}+\mathbf{u}\cdot\nabla\boldsymbol{\omega}=\boldsymbol{\omega}\cdot\nabla\mathbf{u}+\nu\nabla^2\boldsymbol{\omega}, \quad \nu=\mu/\rho. \quad (2)$$

The term $\boldsymbol{\omega}\cdot\nabla\mathbf{u}$ causes vortex twisting and stretching, whereas $\nu\nabla^2\boldsymbol{\omega}$ produces diffusion of vorticity. As Re increases (e.g., in fricative sounds or during loud speech), all these phenomena may lead to instabilities and eventually result in *turbulent flow*, which is a ''state of continuous instability'' (Tritton, 1988) characterized by broad-spectrum rapidly varying (in space and time) velocity and vorticity. The transition to turbulence during speech production may occur for lower Re closer to the glottis because there is an air jet flowing out from the vocal cords, and for jets, turbulence starts at a much lower Re than for flows attached to walls (as is the case downstream in the vocal tract).

Modern theories that attempt to explain turbulence (Tritton, 1988) predict the existence of eddies (vortices with a characteristic size λ) at multiple scales. According to the energy-cascade theory, energy produced by eddies with large size λ (of the order of the boundary-layer thickness) is transferred hierarchically to the small-size eddies, which actually dissipate this energy due to viscosity. A related result is the Kolmogorov law

$$E(k,r)\propto r^{2/3}k^{-5/3}, \quad (3)$$

where $k=2\pi/\lambda$ is the wave number in a finite nonzero range, r is the energy-dissipation rate, and $E(k,r)$ is the velocity wave number spectrum, i.e., Fourier transform of spatial correlations. This multiscale structure of turbulence can in some cases be quantified by *fractals*. Mandelbrot (1982) and others have conjectured that several geometrical aspects of turbulence (e.g., shapes of turbulent spots, boundaries of some vortex types found in turbulent flows, shape of particle paths) are fractal in nature. We may also attempt to understand aspects of turbulence as cases of chaos. Specifically,

chaotic dynamical systems converge to attractors whose sets in phase space or related time-series signals can be modeled by fractals; references can be found in the survey by Peitgen *et al.* (1992). There are several mechanisms in high-Re speech flows that can be viewed as routes to chaos; e.g., vortices twist, stretch, and fold (due to the bounded-tract geometry) (Tritton, 1988; Mandelbrot, 1982). This process of twisting, stretching, and folding has been found in low-order nonlinear dynamical systems to give rise to chaos and fractal attractors.

All the above theoretical considerations and experimental evidence, and the fact that the speech signal is produced by a nonlinear dynamical system that often generates small or large degrees of turbulence, motivated our study of its fractal aspects. In this paper, we use fractals as a mathematical and computational vehicle to analyze various degrees of turbulence in speech signals. One of the main quantitative ideas that we focus on is the fractal dimension of speech signals, because it can quantify their graph's roughness (fragmentation). Because the relationship between turbulence and its fractal geometry or the fractal dimension of the resulting signals is currently not well understood, in this paper we conceptually equate the amount of turbulence in a speech sound with its fractal dimension. Although this may be a somewhat simplistic analogy, we have found the short-time fractal dimension of speech to be a feature useful for speech-sound classification into phonetic classes, segmentation, and recognition.

II. FRACTAL DIMENSIONS OF SPEECH

A. Preliminaries on fractal dimensions

Let the continuous real-valued function $S(t)$, $0\leqslant t\leqslant T$, represent a short-time speech signal and let the compact planar set

$$\mathcal{F}=\{(t,S(t))\in\mathbb{R}^2:0\leqslant t\leqslant T\}, \quad (4)$$

represent its *graph*. Mandelbrot (1982) defines the *fractal dimension* of $\mathcal{F}$ as equal to its Hausdorff dimension D_H; in general, $1\leqslant D_H\leqslant 2$. The signal S is called *fractal* if its graph is a fractal set, i.e., if D_H strictly exceeds 1 (=the topological dimension of $\mathcal{F}$). Next, we discuss two other dimensions closely related to D_H.

Minkowski–Bouligand dimension D_M: This is conceptually based on Minkowski's idea of finding the length of (possibly irregular) curves $\mathcal{F}$: Dilate $\mathcal{F}$ with disks of radius ε by forming the union of these disks centered at all points of $\mathcal{F}$ and thus create a ''Minkowski cover.'' Find the area $A(\varepsilon)$ of the dilated set, and set its multiscale length equal to $\lim_{\varepsilon\to 0}L(\varepsilon)$, where $L(\varepsilon)=A(\varepsilon)/2\varepsilon$. Then, D_M is the constant D in the power law $L(\varepsilon)\propto\varepsilon^{1-D}$ as $\varepsilon\to 0$, which $L(\varepsilon)$ obeys if $\mathcal{F}$ is fractal.

Box-Counting dimension D_B: Partition the plane with a grid of squares of side ε and count the number $N(\varepsilon)$ of squares that intersect the curve. Then, the box dimension is obtained by replacing the Minkowski cover area with the box cover area, i.e., it is equal to $D_B=\lim_{\varepsilon\to 0}\log[N(\varepsilon)]/\log(1/\varepsilon)$.

In general, $1 \leqslant D_H \leqslant D_M = D_B \leqslant 2$. In this work, we focus only on D_M, which we shall henceforth call the ''fractal dimension'' D because: (i) It is closely related to D_H and hence able to quantify the fractal aspects of a signal. (ii) It coincides with D_H in many cases of practical interest. (iii) It is much easier to compute than D_H. (iv) It will be applied to sampled signals where most approaches can yield only approximate results. (v) D_M can be more robustly estimated than D_B, which suffers from uncertainties due to the grid translation or its spacing ε relative to the signal's amplitude. Note that $D_B = D_M$ in the continuous-time case, but they correspond to two different algorithms (with different performances) for sampled signals.

B. Morphological covering algorithm

As shown by Maragos and Sun (1993), and Maragos (1994), D will not change if we replace the disks in the Minkowski cover of $\mathcal{F}$ with other compact planar shapes B. Thus, if $\varepsilon B = \{\varepsilon b : b \in B\}$ is an ε-scaled shape B, we can obtain multiscale multishape-area distributions

$$A_B(\varepsilon) = \text{area}(\mathcal{F} \oplus \varepsilon B) \qquad (5)$$

where $\mathcal{F} \oplus \varepsilon B$ is the set resulting from the morphological set dilation of $\mathcal{F}$ by εB:

$$\mathcal{F} \oplus \varepsilon B = \{z + \varepsilon b \in \mathbb{R}^2 : z \in \mathcal{F}, \ b \in B\}. \qquad (6)$$

The infinitesimal order of the multiscale-area function yields the fractal dimension of $\mathcal{F}$, i.e.,

$$D = 2 - \lim_{\varepsilon \to 0} \frac{\log[A_B(\varepsilon)]}{\log(\varepsilon)}. \qquad (7)$$

Assuming now that $A_B(\varepsilon) \propto \varepsilon^{2-D}$ as $\varepsilon \to 0$ yields that

$$\log[A_B(\varepsilon)] = (2 - D)\log(\varepsilon) + \text{constant}, \quad \text{as } \varepsilon \to 0. \quad (8)$$

Thus, in practice, D can be estimated by least-squares fitting a straight line to and measuring the slope of the plot of the data $\log[A_B(\varepsilon)]$ vs $\log(\varepsilon)$.

Implementing the set dilation $\mathcal{F} \oplus \varepsilon B$ involves representing the signal graph $\mathcal{F}$ as a binary-image signal and dilating this binary image. However, this two-dimensional processing of a one-dimensional signal $S(t)$ on the one hand is unnecessary, and on the other hand increases the requirements in storage space and the time complexity for implementing the covering method. Thus, for purposes of computational efficiency, it is desirable to obtain the area $A_B(\varepsilon)$ by using *one-dimensional operations* on $S(t)$. Toward this goal, let us consider first the morphological dilation $\oplus$ and erosion $\ominus$ of the signal $S(t)$ by a real-valued function $G(t)$ defined as

$$(S \oplus G)(t) = \sup_x \{S(x) + G(t-x)\},$$

$$(S \ominus G)(t) = \inf_x \{S(x) - G(x-t)\}.$$

These signal dilations and erosions are one-dimensional nonlinear signal operators whose computational structure is similar to a convolution and correlation, respectively. Then (Maragos and Sun, 1993; Maragos, 1994), if we select as B

any compact single-connected and symmetric planar set, and if we define

$$G_\varepsilon(t) = \sup\{y \in \mathbb{R} : (t, y) \in \varepsilon B\} \qquad (9)$$

as the function (structuring element) whose graph is the top boundary of εB, we obtain

$$A_B(\varepsilon) = \int_0^T [(S \oplus G_\varepsilon)(t) - (S \ominus G_\varepsilon)(t)]dt + O(\varepsilon^2),$$

$$(10)$$

where $S \oplus G_\varepsilon$ and $S \ominus G_\varepsilon$ are the dilation and erosion, respectively, of S by G at scale ε. Thus, instead of creating the cover of a one-dimensional signal by dilating its graph in the plane by a set B (which means two-dimensional processing), $S(t)$ can be transformed via an erosion and a dilation by functions G_ε. These dilations and erosions create an area strip as a layer either covering or being peeled off from the graph of the speech signal at various scales. We refer to this whole approach as the *morphological covering method*.

Discrete covering method: To adapt our previous discussion to the case of a discrete-time finite-length speech signal $S[n]$, $n = 0,1,...,N$, we use covers at discrete scales $\varepsilon = 1,2,...$, and B becomes a finite set of pixels in the discrete plane. If we restrict the discrete set B to be convex and of radius $= 1$, then the corresponding function $G[n]$ (at scale $\varepsilon = 1$) is restricted to have a centered three-sample support and only two possible shapes: a *triangle*, defined by $G_t[-1] = G_t[1] = 0$ and $G_t[0] = h \geqslant 0$, or a *rectangle*, defined by $G_r[-1] = G_r[0] = G_r[1] = h \geqslant 0$. The height h is allowed to vary and match the amplitude range of the signal S. The main result in the discrete case is the following scale-recursive algorithm (Maragos, 1994):

$$S \oplus G[n] = \max_{-1 \leqslant k \leqslant 1} \{S[n+k] + G[k]\}, \quad \varepsilon = 1$$

$$S \ominus G[n] = \min_{-1 \leqslant k \leqslant 1} \{S[n+k] - G[k]\},$$

$$S \oplus G_{\varepsilon+1} = (S \oplus G_\varepsilon) \oplus G, \quad \varepsilon \geqslant 2 \qquad (11)$$

$$S \ominus G_{\varepsilon+1} = (S \ominus G_\varepsilon) \ominus G,$$

where $\varepsilon = 1,2,3,...,\varepsilon_{\max}$. For $n = 0, N$, the local max/min operations take place only over the available samples. Next, we compute the areas $A_B[\varepsilon]$ by replacing the $\int_0^T$ in (10) with summation $\Sigma_{n=0}^N$. Finally, we fit a straight line using least-squares to the plot of $(\log A_B[\varepsilon], \log \varepsilon)$. The slope of this line is an estimate of $2 - D$ and gives us the fractal dimension of S. For real-world signals with some fractal structure, the assumption of a constant D at all scales ε may not be true. Hence, instead of a global dimension, we estimate the *multiscale fractal dimension* MFD$[\varepsilon]$, which for each ε is equal to the slope of a line segment fitted via least-squares to the log–log plot of (8) over a short moving window $\{\varepsilon, \varepsilon + 1,...,\varepsilon + w\}$ of w scales, where in practice w ranges from 3 to 10. Throughout this paper, we have used $w = 10$.

The height $h = G[0]$ of the structuring function G is important because it controls the finesse or coarseness of the multiscale-area measurements. A good practical rule is to set h less than or equal to the signal's dynamic range divided by the number of its samples. We experimentally observed that
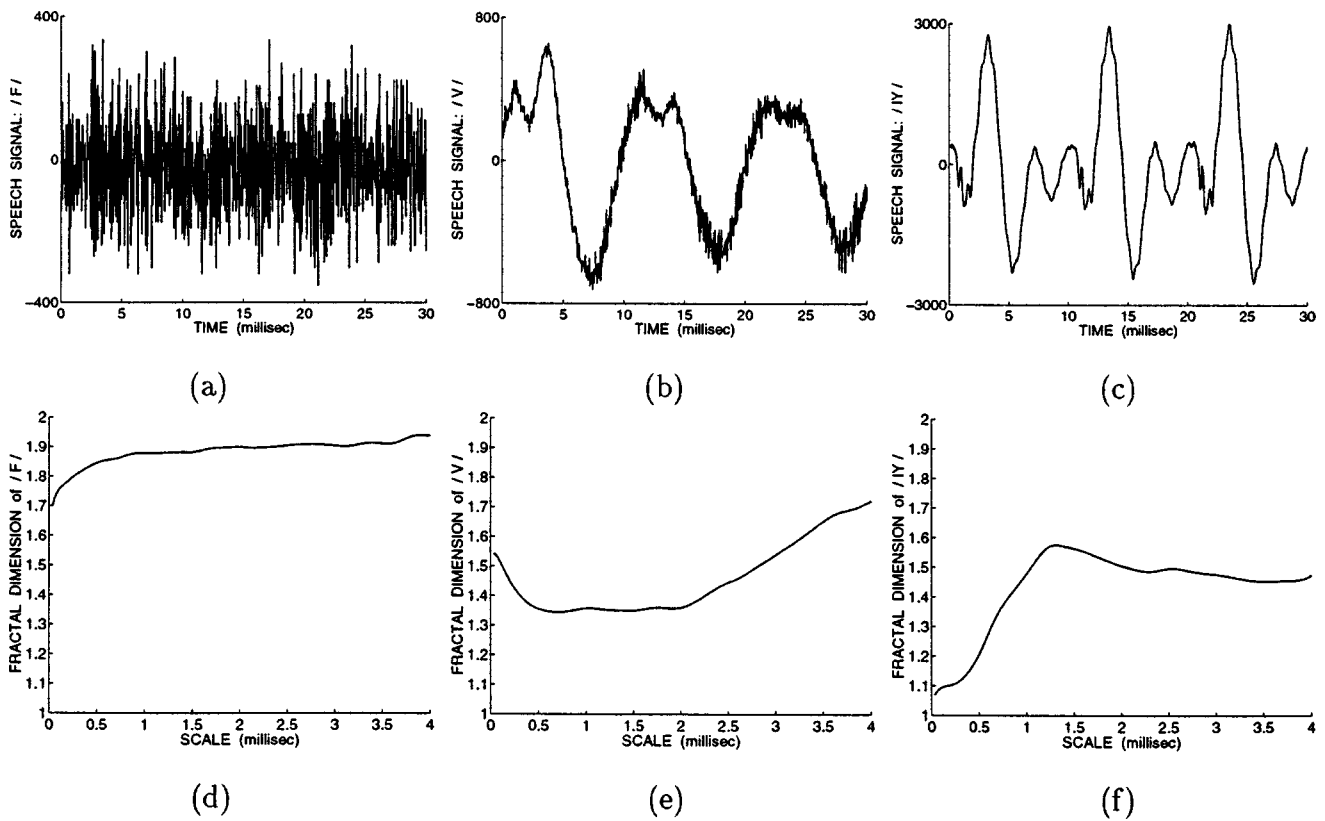
FIG. 1. Top row shows waveforms from speech sounds sampled at 30 kHz. Bottom row shows their multiscale fractal dimensions estimated over moving windows of 10 scales.

this rule performs very similarly to the case $h = 0$. When $h = 0$, i.e., when the function G becomes a flat function corresponding to B being a horizontal segment, Dubuc *et al.* (1989) have shown that the fractal dimension can still be computed from the above covering method (for continuous-time signals). This case has two advantages: the erosions/dilations can be performed faster, and the algorithm yields local fractal dimensions that are invariant to any affine transformation $S(t) \mapsto aS(t) + b$ of the amplitude range ($a > 0$). Therefore, we henceforth select $h = 0$.

Applying the morphological covering method on a *sampled* signal incurs a discretization error in the estimated fractal dimension. Namely, the graph of the sampled signal has lost some of the degree of fragmentation inherent in the graph of the continuous-time signal or presents a distorted view of the geometry of the continuous-time graph due to a small number of available samples and/or a small number of available scales. Thus, the error depends on the sampling frequency and the essential bandwidth (i.e., the frequency range containing most of the area under the square amplitude spectrum of the signal). Analytic formulas for the error currently do not exist, but experimenting with special cases could be instructive. We have applied the above discrete flat covering algorithm to the particular case of a sampled sine and measured the error between the estimated fractal dimension (at scale $\varepsilon = 1$) versus the theoretically correct value of 1. By analyzing sampled sine signals over a fixed finite-time interval, we experimentally observed that for a fixed sampling frequency, increasing the frequency of the sine increases the dimension error. Further, for a fixed frequency of

the sine, increasing the sampling frequency decreases the error. We conjecture that this error depends on the oversampling ratio, i.e., the ratio of the sampling frequency divided by the sine frequency. As indicative values from this (experimentally found) error law, with $w = 5$, to obtain an estimated dimension $\leqslant 1.1$ (i.e., an error $\leqslant 10\%$) we need an oversampling ratio of at least 20:1, whereas an estimated dimension $\leqslant 1.01$ (i.e., an error $\leqslant 1\%$) requires an oversampling ratio of at least 70:1. At present, we have no such guidelines for more general signals, but increasing the sampling frequency decreases the error.

C. Experiments on measuring fractal dimension of speech signals

Figure 1 shows 30-ms segments of an unvoiced fricative, a voiced fricative, and a vowel speech sound extracted from words spoken by a male speaker and sampled at 30 kHz ($N = 900$), together with their corresponding profiles of MFD[ε] for scales $\varepsilon = 1,...,120$. This range of ε corresponds to time scales from 1/30 to 4 ms. The reason for using a higher than usual sampling rate is to approximate as closely as possible the geometrical roughness of the continuous-time speech signal and decrease the discretization error in the estimated fractal dimension. However, similar results have been observed at lower sampling rates (10 and 16 kHz) and are reported in the following sections. We have conducted many experiments similar to the ones shown in Fig. 1, from which we conclude the following: (1) Unvoiced fricatives (/f/, /th/, /s/), affricates, stops (during their turbulent phase),

and some voiced fricatives like /z/ have a high fractal dimension $\in [1.6, 1.9]$ at all time scales (mostly constant at scales >1 ms), consistent with the turbulence phenomena present during their production. (2) Vowels at small scales (<0.1 ms) have a small fractal dimension $\in [1, 1.3]$. This is consistent with the absence or small degree of turbulence (e.g., for loud or breathy speech) during their production. However, at scales >2–3 ms, i.e., at scales of the same order as the distance between the major consecutive peaks in the speech waveform, their fractal dimension increases appreciably. Here, we observe a phenomenon similar to the previously mentioned increase of the estimated fractal dimension of a fixed-time segment of a sine when the sampling frequency remains constant and the sine frequency increases. (3) Some voiced fricatives like /v/ and /th/ have a mixed behavior. If they do not contain a fully developed turbulence state, their fractal dimension is medium-to-high [1.3, 1.6] at scales <0.1 ms, increases at large scales >5 ms (for the same reasons as for vowels), and may decrease for intermediate scales. Overall, their dimension is high (>1.6), although often somewhat lower than the dimension of their unvoiced counterparts. Thus, we have found that the short-time fractal dimension D (computed over ~10–30-ms frames and evaluated at a scale <0.1 ms) can roughly distinguish three classes of speech sounds: (i) vowels (small D), (ii) low-turbulence voiced fricatives, e.g., /v/, /th/ (medium D), and (iii) unvoiced fricatives, high-turbulence voiced fricatives, stops, and affricates (large D). Thus, the fractal dimension consistently quantifies the well-known fact that the geometrical fragmentation of the waveforms of these three speech classes increases in the same order. However, for loud speech (where the air velocity and Re increase, and hence turbulence occurs more often) or for breathy voice (especially for female speakers), the fractal dimension of several speech sounds, e.g., vowels, may significantly increase. In general, the fractal-dimension estimates may be affected by several factors including (a) the time scale, (b) the specific discrete algorithm (usually most algorithms for sampled signals underestimate the true fractal dimension since some signal's roughness has been lost during sampling), and (c) the speaking style. Therefore, we do not assign any particular importance to the absolute estimates but only to their average ranges for classes of speech sounds and to their relative differences.

We also used D estimated at a single small time scale, i.e., MFD$[\varepsilon = 1]$, as a short-time feature for purposes of speech segmentation and for signaling important events along the speech signal. Figure 2 shows the waveform of the word ''soothing'' and its short-time fractal dimension, average zero-crossing rate, and mean-square amplitude as functions of time. While the fractal dimension D behaves similarly with zero crossings, it has several advantages: For example, it can segment and distinguish between a vowel and a voiced fricative, whereas the zero crossings usually fail because the rapid fluctuations of the voiced fricative may not appear as fluctuations around zero amplitude, which would increase the zero-crossing rate but as a graph fragmentation which increases D. We have also observed cases where D could detect voiced stops but the zero crossings could not.
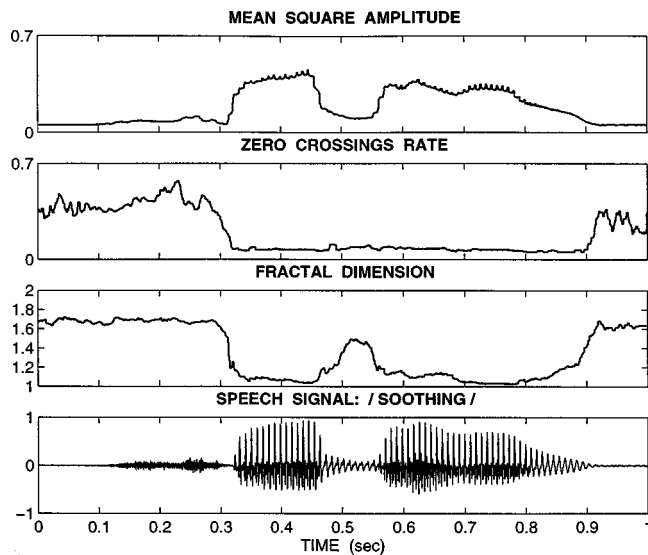
FIG. 2. Speech waveform of the word ''soothing'' sampled at 10 kHz and short-time speech measurements (fractal dimension at scale $\varepsilon = 1$, normalized zero-crossings rate, and normalized mean-square amplitude) over a 10-ms window, computed every 1 ms and postsmoothed by a 3-point median filter.

Related to the Kolmogorov 5/3-law, [Eq. (3)] is the fact that the variance between particle velocities at two spatial locations P and $P + \Delta P$ varies $\propto (\Delta P)^{2/3}$. These distributions have identical form to the case of fractional Brownian motion (Mandelbrot, 1982) whose variances scale with time differences T as T^{2H}, $0 < H < 1$, the frequency spectra vary $\propto 1/f^{2H+1}$, and time signals are fractal with dimension $D = 2 - H$. Thus, putting $H = 1/3$ leads to $D = 5/3$ for speech turbulence. Of course, Kolmogorov's law refers to wave number (not frequency) spectra, and we dealt with pressure (not velocity) signals from the speech flow. Thus, we should be cautious on how we interpret this result for speech. However, it is interesting to note that in our experiments with fricative sounds, we observed D (for time scales <0.1 ms) in the range [1.65, 1.7] or often exactly 5/3 = 1.67. In previous work, Pickover and Khorasani (1986) reported global fractal dimensions of $D = 1.66$ for speech signals. However, they made no connection to the 5/3 law. Further, they used much longer time scales, i.e., 10 ms to 2 s, and a different algorithm for computing fractal dimension. Thus, their work referred to time scales above the phoneme level, whereas our work is clearly below the phoneme time scale.

D. Experiments averaged over multiple phonemic instances

In Fig. 3, the short-time fractal dimension D is shown computed over scales from 1/16 to 4 ms, using a 20-ms analysis window. For each phoneme, the mean and standard deviation (shown as error bars) of the MFD is computed from 200 instances (100 from male and 100 from female speakers) of each phoneme in the TIMIT database. These experiments reinforce the claims made in the previous section that the short-time fractal dimension D in small scales can help discriminate among broad phonemic classes. Note that the standard deviation of the MFD distribution is typi-
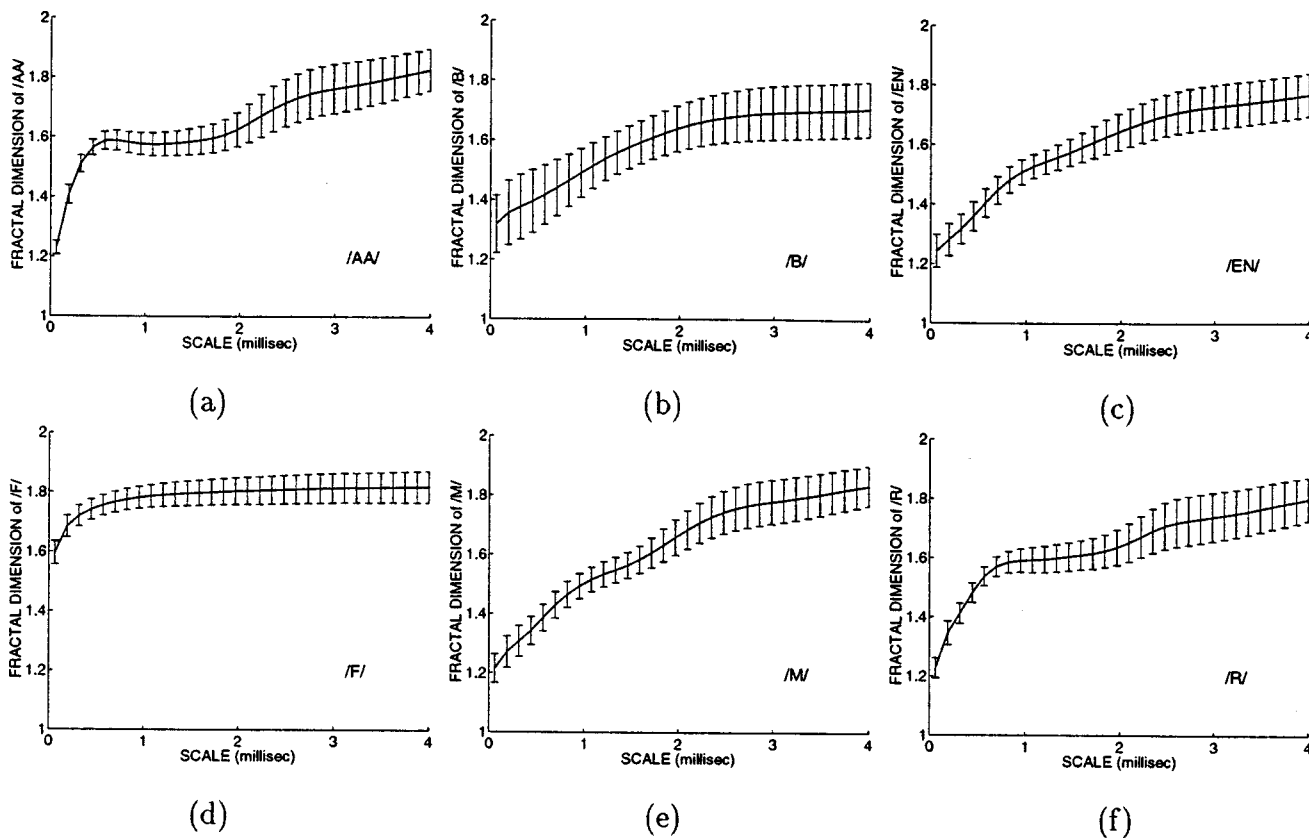
FIG. 3. Mean and standard deviation (error bars) of the multiscale fractal dimension distribution for the phonemes /aa/, /b/, /en/, /f/, /m/, /r/ calculated from the TIMIT database (20-ms analysis window, updated every 10 ms).

cally smaller for D computed over smaller time scales (<1 ms), with the exception of the phoneme /b/. Further, the differences among the average fractal dimensions are larger for smaller (<1 ms) time scales.

In Fig. 4(a), we compare the multiscale fractal dimension for the unvoiced fricative /sh/, the corresponding voiced fricative /zh/, and the vowel /uh/, averaged over 200 phonemic instances obtained from the TIMIT database. Clearly, the small- and medium-scale fractal dimension measurement is smaller for voiced than for unvoiced sounds. The MFD is very small for vowels.

Plosives are a highly confusable set of phonemes. Multiscale fractal dimension is able to discriminate between voiced and unvoiced plosives produced with identical vocal-tract configuration (thus having very similar short-time spectral envelopes), i.e., /p/ and /b/, /t/ and /d/, etc. For example, in Fig. 4(b) we show the MFD for the voiced–unvoiced plosive pair /d/ and /t/ averaged over 200 occurrences. Again,

the MFD is smaller for the voiced /d/ than for the unvoiced /t/. The discriminative power of the fractal dimension for fricatives and plosives, where traditional spectral features are inadequate, could be a valuable asset for speech recognition, as discussed next.

III. APPLICATION TO AUTOMATIC SPEECH RECOGNITION

It has been demonstrated that the multiscale fractal dimension can potentially be used to discriminate among phonetic classes. Here, we attempt to incorporate the fractal dimension in a hidden Markov model (HMM)-based speech recognizer; mixtures of Gaussian distributions are used to model the observation probabilities for each HMM state.

To successfully incorporate a feature in a pattern classifier, the new features must contain (if possible) only information *relevant* to the discrimination task, i.e., not be redun-
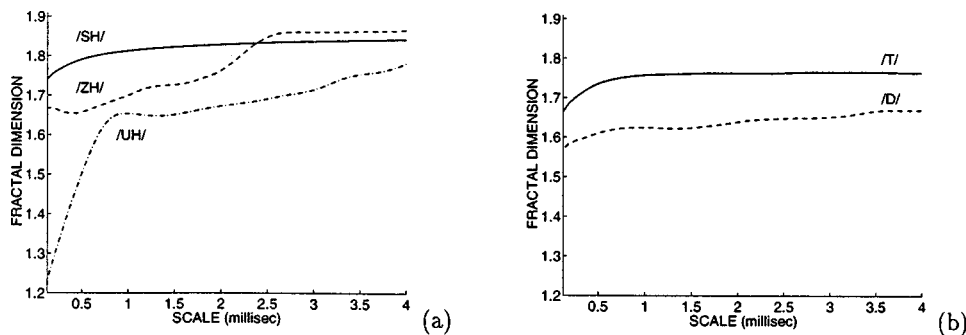
FIG. 4. Multiscale fractal dimension: (a) phonemes /sh/, /zh/, /uh/ and (b) phonemes /t/, /d/; averaged over 200 phonemic instances from the TIMIT database (20-ms analysis window, updated every 10 ms).

TABLE I. Word percent correct for the *E*-set recognition task using 5-mixture Gaussians per HMM state.

$\{A,C_1,...,C_{12},\Delta A,\Delta C_1,...,\Delta C_{12}\}$	$\{A,C_1,...,C_{12},\Delta A,\Delta C_1,...,\Delta C_{12}\}$ $+$ $\{D_1,\Delta D_1\}$	$\{A,C_1,...,C_{12},\Delta A,\Delta C_1,...,\Delta C_{12}\}$ $+$ $\{D_1,D_{11},\Delta D_1,\Delta D_6,\Delta D_{11},\Delta D_{16}\}$
81.2%	83.5%	84.5%

dant or irrelevant. The fractal dimension of a speech signal is defined in this paper to be a two-dimensional (2-D) distribution in time and scale. The main issue is how to represent this 2-D distribution so that it fits in the HMM framework. The feature vectors used in speech recognition are typically computed over a 20–30-ms window and are updated every 5–10 ms. Fractal dimension is a feature with high temporal resolution; thus, it might be advantageous to avoid oversmoothing. An 8-ms averaging window (updated every 10 ms)[1] was arbitrarily chosen, and is being used to compute the fractal features in the remainder of this paper. The ''standard'' speech-recognition features (i.e., cepstrum and mean-square amplitude) are computed using a 20-ms window.

The second issue to be resolved is the dimensionality of the fractal-feature vector. Smaller dimensionality presents a computational advantage, but comes with a performance tradeoff if relevant information is lost during the dimensionality reduction process. It is clear from Figs. 3 and 4 that the fractal dimensions of adjacent scales are highly correlated. Further, the fractal dimension of large scales (>1.5 ms) provide little information relevant to the discrimination task at hand. Various empirical procedures exist for decorrelating a feature vector. In this paper, we chose the simplistic approach of sparsely sampling the low end of fractal scales (<1 ms).

The feature vector augmented with fractal features as described above was applied to the speech-recognition task of the highly confusable *e*-set consisting of the following spoken letters: b, c, d, g, p, t, v, and z. The *e*-subset of the ISOLET database consists of 2700 word occurrences sampled at 16 kHz (Cole *et al.*, 1990). The HMM-based HTK recognition package was used for all experiments (Young, 1995). A hold-one-out (''round-robin'') procedure was used during training so that all 2700 words were available for testing. As a result, the statistical significance of recognition performance comparisons was five times higher than in Singer and Lippmann (1992).

The standard-feature set consisted of the mean-square amplitude (usually called ''energy''[2]) A, the first twelve cepstrum coefficients $C_1,...,C_{12}$ computed from a mel filter-bank (Davis and Mermelstein, 1992) and their first time derivatives ΔA and $\Delta C_1,...,\Delta C_{12}$. The standard feature vector was augmented by the fractal dimension of scale one $D_1 = \text{MFD}[1]$ and its first time derivative ΔD_1. Scale one corresponds to a time scale of 1/16 ms. The fractal features are assumed to be independent of the standard features and to belong in separate probability ''streams.''[3] Five-state left–right hidden Markov models were used in these experiments. As shown in Table I, combining the standard and the fractal features gives a modest 12% reduction in the word-error rate over using the standard features alone. Further improvement is achieved when the higher-scale fractal dimensions (scales 6, 11, and 16, corresponding to time scales of 0.38, 0.69, and 1 ms) are used in addition to D_1 as shown in the third column of Table I; this yields an error reduction of 18%. Further augmentation of the fractal-feature vector has not shown experimentally any performance improvement. Henceforth, we refer to the feature vector consisting of $\{D_1,D_{11},\Delta D_1,\Delta D_6,\Delta D_{11},\Delta D_{16}\}$ as the ''fractal''-feature vector.

Next, we attempted to improve overall performance by augmentation of our feature set with the second time derivatives of the energy and cepstrum features $\{\Delta\Delta A,\Delta\Delta C_1,...,\Delta\Delta C_{12}\}$ and by doubling the complexity of the HMM models, i.e., using ten instead of five Gaussian distributions per mixture per state. As shown in Table II, as the complexity of the models and/or the dimensionality of the standard features increases, the improvement in performance achieved by using the fractal features becomes marginal. Note that similar recognition performance (about 10%–15% word-error rate) was reported for the ISOLET database in Singer and Lippmann (1992).

Preliminary experiments on general phoneme-recognition tasks have shown similar performance improvements when the standard-feature vector was augmented with fractal features. Overall, fractal features can provide modest improvement to recognition performance with a small increase in the dimensionality of the feature vector.

IV. CONCLUSIONS

In this paper, motivated by considerations based on the dynamics of the speech airflow, we have conjectured that short-time speech sounds contain various degrees of turbu-

TABLE II. Word percent correct for the *E*-set recognition task.

Models	Features $\{A,C,\Delta A,\Delta C,\Delta\Delta A,\Delta\Delta C\}$	$\{A,C,\Delta A,\Delta C,\Delta\Delta A,\Delta\Delta C\}$ $+$ $\{D,\Delta D\}$
5-mixture Gaussians	85.6%	86.3%
10-mixture Gaussians	88.6%	88.9%

lence at multiple time scales below the phoneme time scale. To quantify these various degrees of turbulence, we have proposed the use of the multiscale fractal dimension (MFD), measured via an efficient signal-processing algorithm based on simple morphological dilation/erosion operators. Several experimental observations have been made by measuring the MFD of short-time speech sounds and demonstrating its potential for classification into certain broad phonetic classes and for speech segmentation.

Motivated by the novel information that the MFD can extract from the speech waveforms, we investigated the application of MFD as a fractal-feature vector to the problem of HMM-based automatic speech recognition. By augmenting the standard-feature vector (containing short-time spectral information) used in current speech-recognition systems with elements of the MFD vector, we have experimentally observed an improvement in performance, i.e., a modest reduction in the error of certain word-recognition tasks over standard-speech databases.

For future research, there are certain issues relating to the design of the classifier and the augmentation of the feature vector with fractal features that deserve further investigation. Such issues include the dimensionality of the fractal-feature vector and the time scales of the fractal dimension used as features during recognition. The choice of the duration of the short-time analysis frame and alternative ways of incorporating the fractal-feature vector in the HMM framework should also be considered more carefully. Additional performance improvements may be achieved with a more careful choice of these parameters. Further, despite the novelty of the information represented by the MFD vector, the improvement in performance that we observed when combining spectral and fractal features turned out to be relatively modest for HMM models with high complexity. This relatively small improvement in performance could be due to a correlation between the standard fractal features and the multiscale fractal dimension. Specifically, preliminary experiments lead us to pose a question whether the fractal dimension is correlated with the high-frequency part of the spectrum. Thus, a formal study might be useful to investigate the existence and degree of any possible correlation between spectral features and multiscale fractal dimension.

ACKNOWLEDGMENTS

[1]We chose to update all features every 10 ms because it is unclear how to incorporate features sampled with different frequencies in the HMM framework.

[2]We prefer the term ''mean-square amplitude'' over the term ''energy'' because, as Kaiser (1990) has discussed, the energy in an oscillatory signal is more appropriate to be related to the physical energy of the source producing this signal. Such an energy is proportional both to the oscillation amplitude squared and the frequency squared and can be measured via the Teager–Kaiser energy operator.

[3]All stream weights are assumed to be unity.

Cole, R., Muthusamy, Y., and Fanty, M. (**1990**). ''The ISOLET Spoken Letter Database,'' Tech. Rep. CSE 90-004, Oregon Graduate Institute of Science and Technology, Portland, Oregon.

Davis, S., and Mermelstein, P. (**1992**). ''Comparison of Parametric Representations for Monosyllabic Word Recognition in Continuously Spoken Sentences,'' IEEE Trans. Acoust., Speech, Signal Process. **28**, 357–366.

Dubuc, B., Quiniou, J. F., Roques-Carmes, C., Tricot, C., and Zucker, S. W. (**1989**). ''Evaluating the Fractal Dimension of Profiles,'' Phys. Rev. A **39**, 1500–1512.

Fant, G. (**1970**). *Acoustic Theory of Speech Production* (Mouton, Hague).

Flanagan, J. L. (**1972**). *Speech Analysis, Synthesis, and Perception* (Springer-Verlag, New York).

Kaiser, J. F. (**1983**). ''Some Observations on Vocal Tract Operation from a Fluid Flow Point of View,'' in *Vocal Fold Physiology: Biomechanics, Acoustics, and Phonatory Control*, edited by I. R. Titze and R. C. Scherer (The Denver Center for the Performing Arts, Denver, CO), pp. 358–386.

Kaiser, J. F. (**1990**). ''On a Simple Algorithm to Calculate the 'Energy' of a Signal,'' in *Proceedings of the IEEE International Conference on Acoustics, Speech, and Signal Processing*, Albuquerque, New Mexico, pp. 381–384.

Klatt, D. H. (**1987**). ''Review of Text-To-Speech Conversion for English,'' J. Acoust. Soc. Am. **82**, 737–793.

Mandelbrot, B. B. (**1982**). *The Fractal Geometry of Nature* (Freeman, New York).

Maragos, P. (**1991**). ''Fractal Aspects of Speech Signals: Dimension and Interpolation,'' in *Proceedings of the IEEE International Conference on Acoustics, Speech, and Signal Processing*, Toronto, Canada (IEEE, New York), pp. 417–420.

Maragos, P. (**1994**). ''Fractal Signal Analysis Using Mathematical Morphology,'' in *Advances in Electronics and Electron Physics*, Vol. 88, edited by P. Hawkes and B. Kazan (Academic, New York).

Maragos, P., and Sun, F. K. (**1993**). ''Measuring the Fractal Dimension of Signals: Morphological Covers and Iterative Optimization,'' IEEE Trans. Signal Process. **41**, 108–121.

McGowan, R. S. (**1988**). ''An Aeroacoustics Approach to Phonation,'' J. Acoust. Soc. Am. **83**, 696–704.

Peitgen, O., Jürgens, H., and Saupe, D. (**1992**). *Chaos and Fractals* (Springer-Verlag, New York).

Pickover, C. A., and Khorasani, A. (**1986**). ''Fractal Characterization of Speech Waveform Graphs,'' Comput. Graph. **10**, 51–61.

Serra, J. (**1982**). *Image Analysis and Mathematical Morphology* (Academic, New York).

Singer, E., and Lippmann, R. P. (**1992**). ''A Speech Recognizer Using Radial Basis Function Neural Networks in an HMM Framework,'' in *Proceedings of the IEEE International Conference on Acoustics, Speech, and Signal Processing,* San Francisco, California, pp. 629–632.

Stevens, K. N. (**1971**). ''Airflow and Turbulence Noise for Fricative and Stop Consonants: Static Considerations,'' J. Acoust. Soc. Am. **50**, no. 4 (2), 1180–1192.

Teager, H. M., and Teager, S. M. (**1990**). ''Evidence for Nonlinear Sound Production Mechanisms in the Vocal Tract,'' in *Speech Production and Speech Modeling*, edited by W. J. Hardcastle and A. Marchal, NATO Advanced Study Institute Series D, Vol. 55, Bonas, France, July 1989 (Kluwer Academic, Boston), pp. 241–261.

Thomas, T. J. (**1986**). ''A Finite Element Model of Fluid Flow in the Vocal Tract,'' Comput. Speech Lang. **1**, 131–151.

Tritton, D. J. (**1988**). *Physical Fluid Dynamics* (Oxford U.P., New York).

Young, S. (**1995**). *The HTK Book* (Cambridge Research Lab: Entropics, Cambridge, England).

Computer identification of musical instruments using pattern recognition with cepstral coefficients as features

Judith C. Brown[a)]

Physics Department, Wellesley College, Wellesley, Massachusetts 02181 and Media Lab, Massachusetts Institute of Technology, Cambridge, Massachusetts 02139

Cepstral coefficients based on a constant Q transform have been calculated for 28 short (1–2 s) oboe sounds and 52 short saxophone sounds. These were used as features in a pattern analysis to determine for each of these sounds comprising the test set whether it belongs to the oboe or to the sax class. The training set consisted of longer sounds of 1 min or more for each of the instruments. A k-means algorithm was used to calculate clusters for the training data, and Gaussian probability density functions were formed from the mean and variance of each of the clusters. Each member of the test set was then analyzed to determine the probability that it belonged to each of the two classes; and a Bayes decision rule was invoked to assign it to one of the classes. Results have been extremely good and are compared to a human perception experiment identifying a subset of these same sounds. © *1999 Acoustical Society of America.* [S0001-4966(99)00703-1]

PACS numbers: 43.75.Cd [WJS]

INTRODUCTION

The perception of timbre by humans has been widely studied over the past four decades with the elusive goal of correlating the results of perceptual experiments with a small number of acoustical properties of the sounds studied. Many of the studies have used perceived proximity ratings as a measure of similarity of sounds followed by analysis using multidimensional scaling (MDS) techniques, while others have modified the acoustic signal and then done perception experiments to determine whether the altered signal could be distinguished from the original. There have been a wide range of results identifying various spectral and temporal properties and assigning weights to their saliency.

As is often the case in research in musical acoustics, the first work was reported in Helmholtz' (1885/1954) monumental work. He postulated that timbre perception depended on the spectral shape resulting from real-time frequency analysis on the basilar membrane. This is called his ''harmonic structure'' theory.

Saldano and Corso (1964) did experiments to distinguish between Helmholtz' theory and the formant theory of musical quality according to which there is a strengthening of partials in certain regions due to resonances of the musical instrument. Their spectral results were equivocal, but they demonstrated the importance of onset patterns for timbre recognition. Experiments by Risset and Mathews (1969) pointed out the importance of the time-varying properties of the onset in trumpet sounds.

Clark *et al.* (1964) found timbre to be determined by the attack transient, by modulation during the steady state, and to some degree by one or more formants. In an interesting study to determine the relative effects of spectral and temporal properties on timbre, Strong and Clark (1967a, b) interchanged spectral and temporal envelopes on sounds by a number of wind instruments and found that the results depended on the instrument.

In an early MDS study supporting the importance of spectral properties, Plomp (1970) found a 0.86 correlation between a three-dimensional perceptual space and a three-dimensional physical space derived from differences in SPL outputs of a $\frac{1}{3}$-octave band filter. Later experiments by Plomp (1976) supported the formant theory of musical instruments. Wedin and Goude (1972), in another MDS study, found three principal factors, all derived from the long term average spectrum.

In a series of widely cited papers, Grey (1977, 1978), Grey and Gordon (1978) and Grey and Moorer (1977), were able to use MDS to correlate experimental results with three acoustical properties, both spectral and temporal. Similar results were reported later by Krumhansl (1989) and McAdams and others (1995).

Charbonneau (1981) reduced the information in the acoustic signal and concluded that humans perceive the time variations of groups of partials rather than individual ones.

Kendall (1986) found that steady-state-alone conditions were matched as well as using the entire unaltered signal and concluded that ''the perceptual importance of transients in defining the characteristic sounds of instruments has been overstated.''

The preceding resume is admittedly sketchy and slanted toward information about the frequency domain as that is more pertinent to the present study. Two recent articles do an excellent job of reviewing the entire timbre perception literature (McAdams, 1993; Hajda *et al.*, 1997).

There has been little work attempting computer ''perception'' of timbre, or musical instrument identification, particularly when compared to the large volume of research by the speech community on automatic speaker/speech recognition. This emphasis is understandable in view of the enormous range of practical applications of the latter, for example, the identification of a speaker calling a bank to

---

[a)]Electronic mail: brown@media.mit.edu

conduct a transaction and the enormous field of communications applications.

The literature on automatic identification of musical instruments consists for the most part of reports in conference proceedings. Kaminskyj and others (1995, 1996) reported preliminary calculations using temporal features. De Poli and Tonella (1993) used a neural net calculation to classify sounds with a procedure similar to Grey's and based on his parameters. Cosi and others (1994) used features based on an auditory model followed by a neural net to classify instrument tones and reported successful classification.

Langmead (1995a,b) used auditory-based features and found that a temporal factor, which he called spectral onset asynchrony, was the most effective in creating timbre categories. Kostek and Wieczorkowska (1997) reported on an examination of various sound parameters, initially from the frequency domain but with temporal features added, with the as yet unachieved goal of separating musical instrument sounds.

With rare exceptions the timbre perception studies as well as the computer identification work has used a single example of each instrument. The current study, reported by Brown (1997, 1998a, b, c), does not compute a distance measure between single examples of a number of classes of instruments, but rather determines whether a statistically significant number of instruments from two different classes can be grouped correctly. It is more similar in method and goal to speaker/speech studies than to previous timbre studies.

This study is motivated by a long-time interest in the properties of musical signals which give rise to human percepts, and the objective measurement of these properties by computer. While a calculation of this type cannot answer the question of whether humans are using the same information in their decisions, it can, nevertheless, provide a solid scientific conclusion as to whether there is sufficient information present in the chosen properties of the waveform for a correct decision.

There are also a number of practical applications to this problem as formulated. One is in the field of audio indexing (Wilcox, 1994), the goal of which is the automatic identification of the segments in an audio stream. A successful solution to this problem would eliminate the necessity of sequential monitoring by a human. Another application is the long-studied automatic transcription problem (Moorer, 1975), which has as goal the conversion of an audio stream into a written score. Finally, and potentially most important, the explosion of internet sites has made automatic recognition methods of great importance in classifying and reducing the sheer volume of material to be searched on the internet.

The current study was inspired by one of the most successful methods of automatic speaker identification (Reynolds and Rose, 1995 and references therein), which involved the use of a Gaussian mixture model with cepstral coefficients as features. It can be argued that sound production by a musical instrument is analogous to quasi-steady vowel production by a singer in which the shape of the vocal tract determines the spectrum (Strong, 1998). This seems the appropriate description for the case of instruments, such as

strings and natural horns, where the spectrum is largely determined by a resonator of fixed shape. The vowel analog may be less obvious in the case of instruments, such as the woodwinds of this study, where the dimensions of the resonator change to produce different notes.

Independent of analog chosen, a set of features used successfully for speech/vowel/speaker identification are the cepstral coefficients which have been used in this study. The method of analysis to be described does not take into account the temporal evolution of the spectral features as is done with hidden Markov models in speech identification, but rather treats all data frames independently, as done with speaker identification.

In choosing instruments for this study it was desirable to have similar (or at least overlapping) frequency ranges, a similar excitation mechanism, and similar resonators. The oboe and the saxophone met these criteria because they are both conical bore, reed instruments with overlapping frequency ranges, and in the case of the soprano sax, the frequency range is almost identical. They have similar attacks and decays, and a scientist/woodwind musician (Coleman, 1997) reported that the soprano sax and oboe can be difficult to distinguish when playing music of a similar style. Preliminary experiments with human subjects supported this observation. Since humans are thought to be the ultimate receivers, these seemed to be an extremely challenging pair of instruments to study for an initial test of this method as applied to musical instruments.

I. METHOD OF PATTERN RECOGNITION

A. Introduction

The goal of a pattern recognition calculation is to classify a group of patterns called the test set into two or more classes. This is done by calculating features for the test set and comparing them to the same features for known examples of the classes called the training set; i.e., the computer ''learns'' what the values of the features are for an example of each of the known classes. These are then used as a basis for comparison to the unknown sounds.

This process is analogous to that followed by human subjects in classifying sounds. Humans build up mental representations of sounds made by different sources. Then, when asked to classify a new, unknown sound, they compare it to each of these mental representations to make a decision. See, for example, Galotti (1994) or any other introductory text on cognitive psychology.

For computer identification, an unknown sound can be segmented into shorter ''frames'' and a feature vector calculated for each of these frames. If the feature vector is of dimension M, then each frame contributes a point in an M-dimensional space. The classifier must then adopt a distance measure for determining whether the given points are closer to those of class A or B (in the case of two classes) and, based on this, make a likelihood decision, i.e., make the decision that minimizes the probability of error.

B. Feature selection: Cepstral coefficients

In any pattern recognition problem the most crucial step is the choice of features since this determines whether the

classes can be differentiated. In this work the musical instrument was modeled as a resonator with a periodic excitation, with the sound produced analyzed in the same manner as in the speaker identification work previously mentioned. In speech analysis the glottal impulses are treated as a periodic excitation followed by a filter, which is the vocal tract or resonator (Rabiner and Schafer, 1978). The musical analog for reed woodwind instruments is the pressure-controlled opening and closing of the reed(s) delivering puffs of air into a cylindrical or conical bore resonator.

A set of features which has been particularly successful in characterizing the vocal tract resonances which identify individual speakers, speech, or vowels are the cepstral coefficients. See Rabiner and Schafer (1978) and Rabiner and Juang (1993) for a discussion of the use of cepstra for speech applications. The cepstrum is the Fourier transform of the log magnitude spectrum (Oppenheim and Schafer, 1975); it involves two transforms which makes it computationally more intensive than FFT-based calculations. These features will be applied to musical instruments to determine whether they offer instrument specific information sufficient to differentiate the instruments producing the sounds.

For musical signals the information in a constant Q transform is more useful than that of a linear FFT as the frequencies can be chosen to map directly on to the notes of the musical scale (Brown, 1991). The cochlea of the ear, except at the low-frequency end, is usually modeled by a third octave filter bank which has a ratio of adjacent center frequencies of $2^{1/3}$ or 1.26. In this implementation, the signal input was divided into 23-ms frames and a FFT was calculated. A constant Q transform equivalent to a third octave filter bank was calculated from these Fourier coefficients using the method described by Brown and Puckette (1992) with Hamming windowed kernels. Although the previous description was for $\frac{1}{12}$- or $\frac{1}{24}$-octave filters, it is equally applicable for any desired filter bandwidth.

The transformation from constant Q coefficients to cepstral coefficients was carried out using Eq. 10.1 from O'Shaughnessy (1987),

$$c[n] = \sum_{k=1}^{M} \log(X^{cq}[k])\cos\left(n\left(k-\frac{1}{2}\right)\frac{\pi}{M}\right),\qquad(1)$$

for $n=1,2,...,N$.

Here $X^{cq}[k]$ is the kth constant Q coefficient, $M=18$, and $N=18$ to give 18 cepstral coefficients.

In this implementation the constant Q coefficients were roughly equivalent to a third octave filter bank with 18 coefficients and center frequencies from 100 to 5439 Hz. They were transformed to 18 cepstral coefficients using Eq. (1) above. The lower limit of 100 Hz was chosen to match that of the lowest note of the tenor sax and a frequency ratio of 1.265 was chosen to give an upper frequency below the Nyquist for a sampling rate of 11 025 Hz.

C. Method of clusters

Rather than comparing all points in an unknown sound to all points in the training set, Popat and Picard (1997) have used the method of clustering (Therrien, 1989) to summarize the training data for each class. The method of clustering involves grouping points calculated from the 23-ms frames of the known, or ''training'' sound, into so-called clusters. Thus each class can be characterized by a number of clusters. After determining the parameters for the clusters, an arbitrary probability density for each class can be modeled as a sum of weighted Gaussians, called a Gaussian mixture model. The probability that each point of the unknown sound belongs to that class can then be calculated.

The optimum number of clusters can be determined either by software or by heuristics. Once the number of clusters is decided, the cluster ''centers'' for the training set are determined by choosing a distance measure between the training samples and the cluster centers. A common method, called the K-means algorithm, minimizes the Euclidian distances between the sample features and the cluster centers by an iterative procedure. It can be shown that the mean of the feature values of the samples assigned to a given cluster will minimize this distance. Thus the kth cluster can be characterized by a mean $\boldsymbol{\mu}_k$ and a standard deviation $\boldsymbol{\sigma}_k$. For the case of a single cluster, the training data are represented by the mean and standard deviation of the totality of feature values for this sound. The mathematics of this process is described in the section on calculations.

II. EXPERIMENTAL SETUP

A. Sound database and processing

In order for a study of this type to be statistically valid, it should include examples by many different instruments of the same class. This means doing in-house recordings of mostly amateurs with instruments which are probably not examples of the highest quality available, or of taking performances by professionals from recordings. There is also the choice of whether to take excerpts from real performances or to study isolated notes or sequences of notes. For example, the McGill set of CDs is available for studies of single notes usually by a single instrument.

All of these studies are of interest, but it was decided that the most general and challenging study, the one which was most similar to speaker/speech problems as well as having greater relevance to the other applications mentioned in the Introduction, would involve the study of excerpts from real performances by experts. This meant taking these excerpts from recordings and gave the widest variety of sounds from each of these instruments as could possibly be found.

All of the sound samples in this study were excerpted either from the Wellesley College Music Library collection of compact disks, audio cassettes, and records or from the personal collection of Jay Panetta, a member of the Music Department faculty. These were listened to and segments of solo oboe and sax were excerpted for the experiment. The excerpts were of solos by the instruments in order to insure that the features calculated belonged to the instrument class to be identified. Each of the excerpts involved a number of different notes, the intention being to capture a random selection on the recording as would be appropriate for an audio indexing problem.

It was particularly difficult to get examples of solo sax

music, and there remains a small amount of background (low intensity contribution from other instruments in the ensemble) music in a few of these sax sounds. There are soprano, alto, and tenor saxophone sounds included in the study. Ideally it would have been preferable to include only soprano sax sounds, but there would not have been a large enough number of sounds for good statistics. In practice this was of less concern since the subjects in the expert group reported below were unable to identify the type of sax reliably and the documentation on the recording often did not include information about the type of sax in the performance.

For the calculation of features, the sounds were downsampled from a 44 100-Hz sampling rate to 11 025 Hz since an upper range of 5500 Hz was thought to be sufficient to characterize the sounds, and this speeded up the calculations. The resampling software is part of Dan Ellis' dspB software (Ellis, 1992). It consists of a Hanning-windowed ideal sinc interpolator in a polyphase rational-intermediate-frequency implementation, where both the window length and the sampling-frequency ratio are chosen to allow arbitrary accuracy in aliasing rejection and output sampling rate. A 256-point Fourier transform was taken with a hop size of 128 points giving 23-ms segments with frames overlapping by 11.5 ms. Frames with average amplitude less than 600 (for 16-bit samples) were dropped.

B. Training set

As is customary in pattern recognition problems, the system must be trained on examples of each of the classes. An oboe sound and a sax sound of approximately 1-min duration representing each of the instrument classes were chosen for the training set. Alternatively, a number of shorter sounds by different instruments of each class might also have been used, but it was thought to be of interest to determine whether the system could be trained on a single instrument.

There were two such long oboe sounds from different instruments and four long sax sounds also from different instruments. The calculations were carried out with each of the two oboe sounds paired with each of the four sax sounds (eight combinations with a single representative of each class in any one calculation) to determine the effect of choice of training sounds. The best results were obtained with a 61-s (5254 frames) excerpt from a performance of Peter Christ playing Persichetti's ''Parable for Solo Oboe'' and a 53-s (4565 frames) tenor saxophone excerpt of Archie Shepp from the CD ''Yasmina/Poem for Malcolm.'' The average over the entire time interval of the 18 constant Q coefficients for these two sounds can be found in Figs. 1 and 2. These spectra are quite distinctive. The oboe has a formant at around 1300 Hz in agreement with the literature (Strong and Plitnik, 1977) which attributes oboe formants at around 1000 and 3000 Hz to the mechanical properties of the reeds (Fransson, 1967). Rossing (1990) summarizes these results. The energy in the first three coefficients in this figure is somewhat perplexing, as the corresponding frequencies are below the normal range of the oboe. The recording is taken from a record, so possibly there is turntable noise, or there might be subharmonics for some of the notes which occur. In

FIG. 1. Constant Q coefficients (—) and standard deviations (···) for Persichetti's ''Parable for Solo Oboe'' averaged over 61 s. Frequencies vary from 100 Hz to 5.43 kHz by third octaves.

any case the magnitudes of these coefficients are well below the peak energy of this spectrum.

The saxophone spectrum has a broad peak at around 500–600 Hz, well below this. Cepstral coefficients calculated from these constant Q coefficients using Eq. (1) are shown in Figs. 3 and 4. These are the mean values of these coefficients averaged over the entire sound. Notes from $A\sharp_2$ to G_5 were included in the sound from Figs. 2 and 4. The mean note was $G\sharp_3$ with a standard deviation of eight semitones. Notes from B_3 to G_6 were included for the oboe (Figs. 1 and 3) with a mean of $C\sharp_5$ and a standard deviation of eight semitones as well.

For comparison to the spectra of Figs. 1 and 2, recordings of soprano, alto, and tenor saxophones and an oboe playing the same chromatic scale from C_4 to B_4 were taken from the University of Iowa Electronic Music Studios Web Site (http://theremin.music.uiowa.edu/). This octave was chosen because it is in a range accessible to each of these
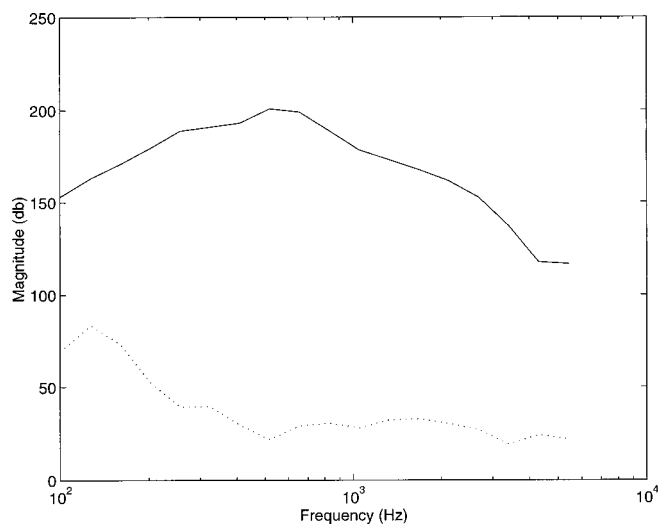
FIG. 2. Constant Q coefficients (—) and standard deviations (···) for ''Yasmina/Poem for Malcolm'' for saxophone averaged over 53 s. Frequencies vary from 100 Hz to 5.43 kHz by third octaves.
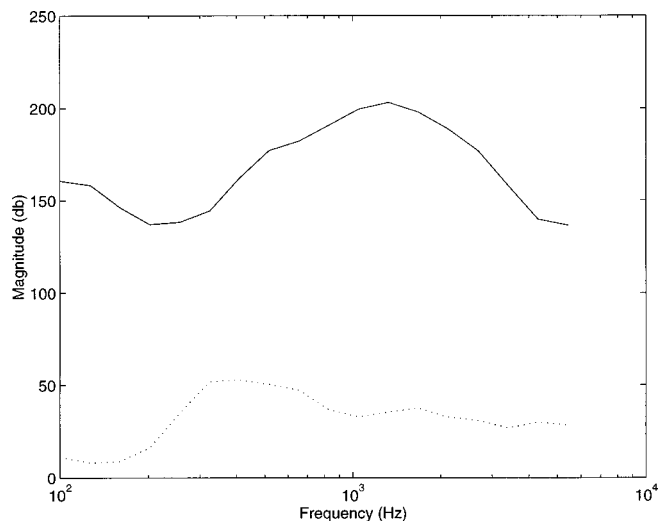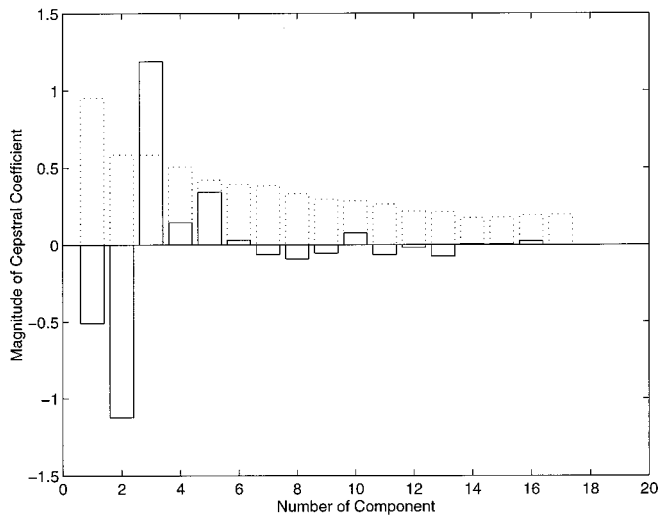
FIG. 3. Cepstral coefficients (−) and standard deviations (···) for Persichetti's "Parable for Solo Oboe" averaged over 61 s.
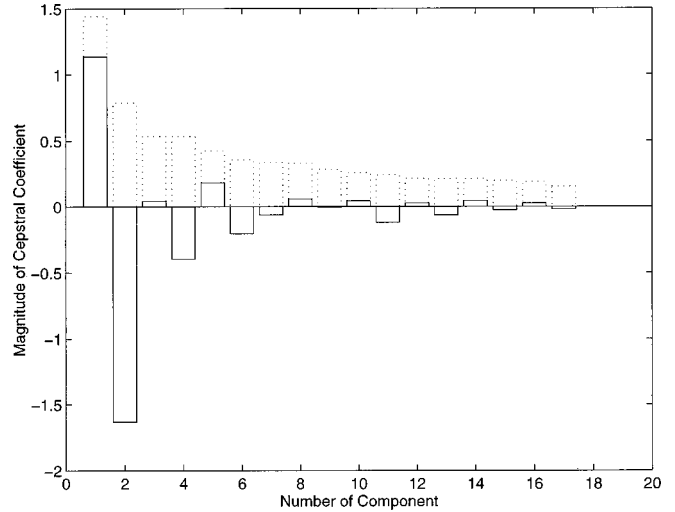
FIG. 4. Cepstral coefficients (−) and standard deviations (···) for "Yasmina/Poem for Malcolm" for saxophone averaged over 53 s.

instruments, and it is possible to compare spectra with the same notes being played. See Fig. 5 for their average constant Q spectra. The resolution of this transform was the same as that of the previous two figures, but a sampling rate of 32 000 Hz rather than 11 025 Hz was chosen to show the behavior of the higher frequency components. The oboe shows a resonance peak at 1400 Hz similar to that of Fig. 1; the soprano sax has a smaller peak roughly centered at 800 Hz and the alto and tenor spectra peak at around 400 Hz though the tenor has a second smaller peak at slightly over 1000 Hz. All of the sounds dropped off from their maximum values by around 50 dB or more at 5000 Hz showing that little information was lost by resampling at 11 025 for the calculations.

Finally, examples of the variation of the cepstral coefficients with note can be found in Figs. 6 and 7. The low-quefrency values are similar for the notes of a given instru-

ment class, and it is these which give the most important information on the resonator.

C. Test set

Initially a set of 31 sax sounds was included in the study. Excluding two long sounds, these were of average length 2.0 s and standard deviation 0.8 s, and the perception experiment with the expert group was carried out on these sounds. Later, with the help of Jay Panetta, more solo sax sounds were added to the study since it was felt that some of the sounds in the initial group were less "clean" than was desirable. All of these sounds were included in the machine identification calculations. This latter group of 21 sounds was longer with a mean of 7.8 s and s.d. of 2.4 s.

There were 28 oboe sounds included in the study with average length 2.5 s and standard deviation 2.1 s. One of the
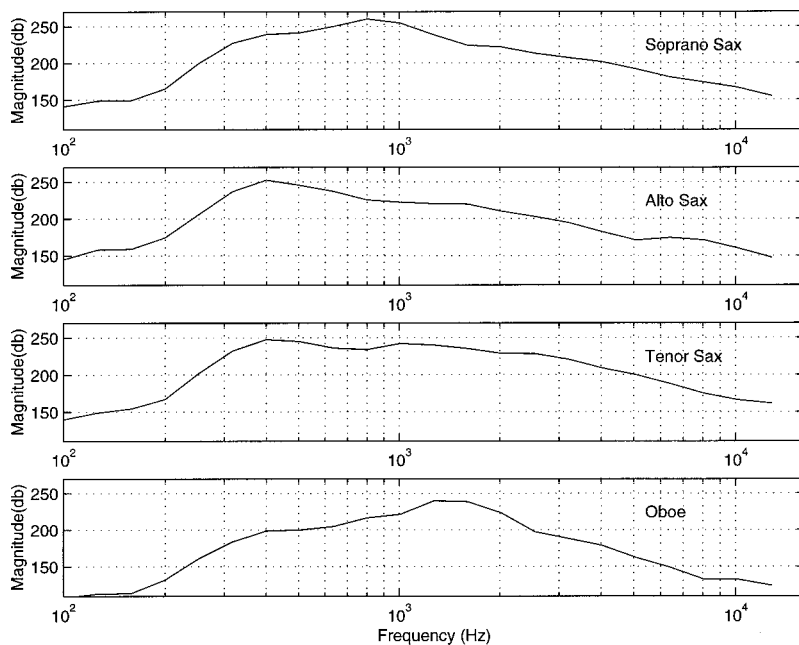
FIG. 5. Average constant Q spectra of soprano, alto, and tenor saxophones and an oboe playing a two octave chromatic scale from C_4 to B_4.
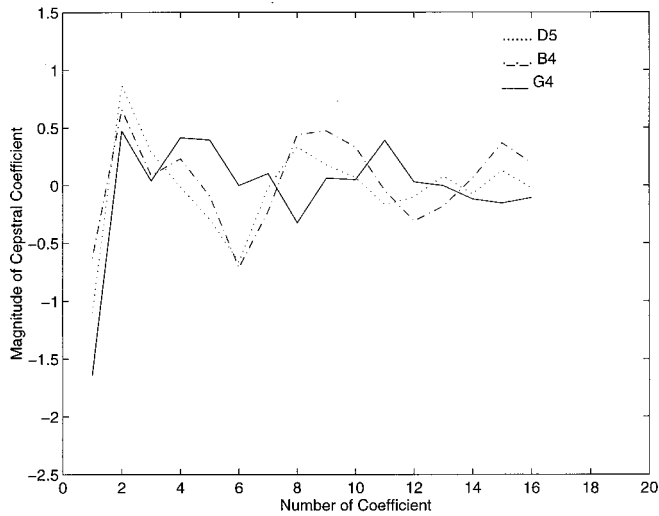
FIG. 6. Example of cepstral coefficients for three notes for oboe excerpted from Mozart's ''Concerto for Oboe and Orchestra in C'' K314 played by Niesemann.

sounds was inadvertently omitted from the perception experiment by experts reported in Table I, but is included in the computer identification experiment.

III. CALCULATIONS

A. Background

A K-means algorithm written by Kris Popat was used in all calculations to determine the cluster means and variances. The number of clusters was an input parameter allowing the results to be checked for optimum performance.

In order to classify the unknown sounds into two classes A and B (oboe and sax in this case), calculations were made of the probability densities that the points defined by the feature vectors of an unknown U belonged to each of the classes. These were then compared to find the greater probability density. For example, given N 23-ms segments of an unknown sound U, then for each of these segments, a feature
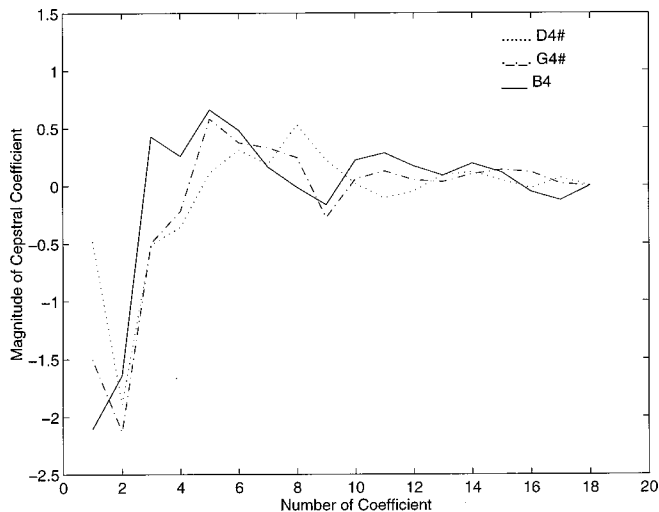
FIG. 7. Example of cepstral coefficients for three notes for soprano sax from a CD of demonstration sounds.

TABLE I. Summary of results on human and computer instrument identification. Each column gives the average fractional error for each experiment (average per person errors divided by the number of sounds presented). Listening conditions are described in the section on human perception results.

	Controlled env	Auditorium	Computer
Oboe	4/27=0.15	2.7/16=0.17	1/28=0.04
Sax	2.5/31=0.08	2/17=0.12	5/52=0.10

vector $\mathbf{x}^i$ with components $x_1^i, x_2^i, \ldots, x_{18}^i$ was calculated, where the components were the cepstral coefficients for the ith segment and $i = 1, \ldots, N$.

Then the probability density of measuring feature vector $\mathbf{x}^i$ for cluster k of class Ω if U is a member of class Ω is:

$$p(\mathbf{x}^i | \Omega_k) = \frac{1}{\sqrt{2\pi\sigma_{\Omega_k}^2}} \exp - (\mathbf{x}^i - \boldsymbol{\mu}_{\Omega_k})^2 / 2\sigma_{\Omega_k}^2. \tag{2}$$

Using a Gaussian mixture model (Reynolds and Rose, 1995) to model the probability density function best describing the training data, and summing over all clusters, then the total probability density that feature vector $\mathbf{x}^i$ is measured if U belongs to class Ω is

$$p(\mathbf{x}^i | \Omega) = \sum_{k=1}^{K} p_k p(\mathbf{x}^i | \Omega_k), \tag{3}$$

where p_k is the probability of occurrence of the kth cluster. It is equal to the number of vectors in the training set assigned to this cluster divided by the total number of vectors in the training set.

The total probability density that all of the N feature vectors measured for unknown U belong to class Ω is given by the product of the individual probability densities:

$$p(\mathbf{X} | \Omega) = p(\mathbf{x}^1 \cdots \mathbf{x}^N | \Omega) = \prod_{i=1}^{N} p(\mathbf{x}^i | \Omega), \tag{4}$$

where $\mathbf{X} = \{\mathbf{x}^1 \cdots \mathbf{x}^N\}$ is defined as the set of all feature vectors measured for unknown sound U. This assumes statistical independence of the feature vectors. While this simplifying assumption is not strictly valid here, it is a widely accepted technique in the speech community and has been experimentally shown to be effective in calculations (Rabiner and Huang, 1993).

Equation (4) is the probability density of measuring the set of feature vectors $\mathbf{X}$ for unknown U if U belongs to class Ω. The quantity of interest for the Bayes decision rule is the *a posteria* probability that a measurement of $\mathbf{X}$ means it is more probable that U is a member of class Ω than another class. Letting $\Omega^{(m)}$ where $m = 1, 2, \ldots, M$ represent the M classes, then the desired *a posteria* probability is:

$$\hat{\Omega} = \arg \max \Pr(\Omega^{(m)} | \mathbf{X}),$$

where $1 \leq m \leq M$ and $\hat{\Omega}$ is the class which maximizes this probability.

From Bayes' rule,

$$\hat{\Omega} = \arg\max \frac{p(\mathbf{X}|\Omega^{(m)})\Pr(\Omega^{(m)})}{\Pr(\mathbf{X})}. \tag{5}$$

The probability of measuring the set of features $\mathbf{X}$ is

$$\Pr(\mathbf{X}) = \sum_{i=1}^{M} p(\mathbf{X}|\Omega^{(m)})\Pr(\Omega^{(m)}) \tag{6}$$

and is the same for all classes. Similarly, if the classes are equally probable, $\Pr(\Omega^{(m)}) = 1/M$ independent of the class. This is the case with equal numbers of test sounds, but it is true as well if there is no *a priori* reason for one class's being more probable. Although in the present experiment the numbers of members of the classes in the test set was known, the goal of the experiment is to be able to distinguish between instruments in a situation where there is no information as to the composition of the test set. It would run counter to this purpose to make an assumption about a particular test set which would not be valid for the general case.

Dropping functions which do not vary with class,

$$\hat{\Omega} = \arg\max p(\mathbf{X}|\Omega^{(m)}).$$

For $1 \leq m \leq M$, and this is the probability density in Eq. (4).

With two classes $\Omega^{(1)}$ and $\Omega^{(2)}$, then if

$$p(\mathbf{X}|\Omega^{(1)}) > p(\mathbf{X}|\Omega^{(2)}),$$

the unknown U is assigned to class $\Omega^{(1)}$, and otherwise to class $\Omega^{(2)}$. This is called a likelihood ratio test. It is a decision rule which minimizes the probability of error and is thus an optimal decision rule. Equivalently, this can be stated as the log likelihood ratio:

$$\log(p(\mathbf{X}|\Omega^{(1)})) - \log(p(\mathbf{X}|\Omega^{(2)})) > 0, \tag{7}$$

which is the function graphed in the results section. This function was chosen for reasons of convention and ease of interpretation, since it is easy visually to pick out the positive cases.

B. Results

1. Human perception

a. Controlled listening experiment. The first experiment on human instrument identification used seven expert listeners as subjects. These were people who had had extensive listening and/or performing experience with these instruments. Twenty-seven oboe samples and 31 sax samples were presented, and the subjects were asked to classify them as either oboe or sax. If they were classified as sax, the subjects were also asked to identify the kind of sax. There was imperfect agreement among subjects in this secondary classification, and these experiments were not pursued.

The samples were presented in a controlled listening environment, with the subjects either listening over speakers in a soundproof recording studio or over headphones in a quiet room. The subjects could listen to a given sound as often as they wished before making a choice. The experiment was forced choice, so the subjects guessed if they were otherwise unable to make a decision.

The results are presented in Table I. The subjects made an average of 4 errors per person for an average error of 15% for the oboe and an average of 2.5 errors for the sax for an average error of 8%.

b. Auditorium experiment. Another test with quite different listening conditions was carried out in an auditorium using as subjects the 32-member audience at a talk on musical perception. These subjects had varied musical backgrounds ranging from members of the Wellesley College Music Department to people with no formal musical training, but all had an interest in music or perception since they had chosen to attend the lecture. The sound system in the room was excellent as it was designed for a musical acoustics course rather than for a typical auditorium. The subjects were presented with roughly half the sounds that had been heard by the previous group. Each sound was followed by 4 s of silence with a forced choice of oboe or sax. The total number of sounds was reduced compared to the expert listener group as it was felt that a 3-min test was sufficiently taxing for the patience of this captive group.

The results are shown in the third column of Table I. They essentially duplicated the 15% error rate for the previous group for the oboe, and had a slightly higher 12% error rate for the sax sounds.

2. Machine identification

Figure 8 summarizes the results on machine identification using the optimum choice of training sounds (indicated in Figs. 1–4) and number of clusters, which were three for the oboe and one for the sax. It is a plot of the log probability that each sound fits the Gaussian describing the correct class minus the log probability for the other class from Eq. (7). The upper curve is for the oboe sounds and the lower curve for the sax sounds. The x axis is numbered by sound sample. For both curves the positive values represent correct choices by the computer and the negative values are misses. There are five errors for the sax and one for the oboe, although it could be argued that one of the sax errors was sufficiently close to zero to be called no decision. The average number of errors varying all possible training sounds and varying the number of clusters from one to three was 15.9% total with a standard deviation of 6.8%.

IV. DISCUSSION AND CONCLUSIONS

Overall results are summarized in Table I comparing the average fractional error (average per person number of errors over the number of sounds evaluated) for each instrument with those of the computer. The computer has a lower error rate than the humans for the oboe samples and an error rate roughly the same for the sax samples. This success for the computer occurred despite the advantage of context which some of the human subjects commented upon as an important indicator for them, i.e., the humans assumed, usually correctly, that jazz sounds were played by a saxophone. The computer based its decision on feature values and was, of course, unable to distinguish jazz from classical styles.

The similarity of the success rates of human and machine identification is interesting for two reasons. First, it
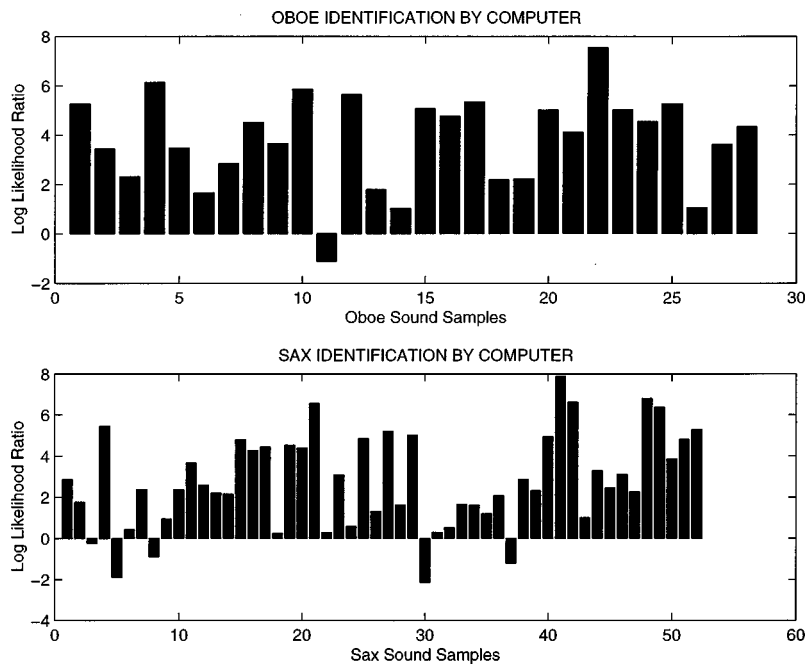
FIG. 8. Log likelihood ratio for oboe and sax sounds plotted against sound sample number. The calculations were done with three clusters for the oboe and one cluster for the sax.

should be recalled that humans have trained for many years on many different pieces of sax and oboe music; whereas the computer has only approximately a minute of one particular saxophone performance and one particular oboe performance to analyze and ''learn'' the oboe and sax features. Second, the success of the machine with this method is somewhat surprising since it is based totally on spectral information, whereas it is generally thought that human instrument identification is based on temporal as well as spectral cues.

The study of musical sounds using cepstral coefficients as features holds promise in a number of areas. As computations on properties of instruments by the study of the sounds they produce, they give new and complementary information, adding to knowledge from impedance and other passive methods. New knowledge of instrument properties can also lead to new information about human perception, as spectral cues are certainly of great importance to humans in their decision processes.

Finally, just as no number of experiments can fully validate a scientific theory, while a single counterexample can refute it, a computer identification experiment cannot prove what cues are actually used in human perception but rather demonstrate whether sufficient information for identification is present in the features studied. Thus, this study cannot assess the relative importance of spectral and temporal information used by humans for instrument identification, but it can indeed affirm that there is sufficient information in features derived from spectral properties to distinguish between these two instruments.

ACKNOWLEDGMENTS

Brown, J. C. (**1991**). ''Calculation of a constant Q spectral transform,'' J. Acoust. Soc. Am. **89**, 425–434.

Brown, J. C. (**1997**). ''Cluster-based probability model for musical instrument identification,'' J. Acoust. Soc. Am. **101**, 3167A.

Brown, J. C. (**1998a**). ''Computer Identification of Wind Instruments using Cepstral Coefficients,'' in *Proceedings of the 16th International Congress on Acoustics and 135th Meeting of the Acoustical Society of America*, Seattle, Washington, pp. 1889–1890.

Brown, J. C. (**1998b**). ''Computer identification of wind instruments using cepstral coefficients,'' J. Acoust. Soc. Am. **103**, 2967 (abstract).

Brown, J. C. (**1998c**). ''Musical Instrument Identification using Autocorrelation Coefficients,'' in *Proceedings International Symposium on Musical Acoustics 1998*, Leavenworth, Washington.

Brown, J. C., and Puckette, M. S. (**1992**). ''An efficient algorithm for the calculation of a constant Q transform,'' J. Acoust. Soc. Am. **92**, 2698–2701.

Charbonneau, G. R. (**1981**). ''Timbre and the perceptual effects of three types of data reduction,'' Comput. Music J. **5**, 10–19.

Clark, M., Robertson, P., and Luce, D. A. (**1964**). ''A preliminary experiment on the perceptual basis for musical instrument families,'' J. Audio Eng. Soc. **12**, 199–203.

Coleman, W. F. (**1997**). Private communication.

Cosi, P., De Poli, G., and Lauzzana, G. (**1994**). ''Timbre classification by NN and auditory modeling,'' in *Proceedings of the International Conference on Artificial Neural Networks*, pp. 925–928.

De Poli, G., and Tonella, P. (**1993**). ''Self-organizing neural networks and Grey's timbre space,'' ICMC Proceedings, pp. 441–444.

Ellis, D. P. W. (**1992**). ''A Perceptual Representation of Audio,'' MS thesis, Department of Electrical Engineering and Computer Science, Massachusetts Institute of Technology.

Fransson, F. (**1967**). ''The Source Spectrum of Double-Reed Woodwind Instruments,'' Report STL-APSR 1, 25 Royal Institute of Technology, Stockholm.

Galotti, K. M. (**1994**). *Cognitive Psychology In and Out of the Laboratory* (Brooks/Cole, Belmont, CA).

Grey, J. M. (**1977**). ''Multidimensional perceptual scaling of musical timbres,'' J. Acoust. Soc. Am. **61**, 1270–1277.

Grey, J. M. (**1978**). ''Timbre discrimination in musical patterns,'' J. Acoust. Soc. Am. **64**, 467–472.

Grey, J. M., and Gordon, J. W. (**1978**). ''Perceptual effects of spectral modifications on musical timbres,'' J. Acoust. Soc. Am. **63**, 1493–1500.

Grey, J. M., and Moorer, J. A. (**1977**). ''Perceptual evaluations of synthesized musical instrument tones,'' J. Acoust. Soc. Am. **62**, 454–462.

Hajda, J. M., Kendall, R. A., Carterette, E. C., and Harshberger, M. L. (**1997**). ''Methodological issues in timbre research,'' in *Perception and Cognition of Music*, edited by I. Deliege and J. Sloboda (Psychology Press, East Essex, UK), pp. 253–307.

Helmholtz, H. L. F. (**1885/1954**). *On the Sensations of Tone* (Dover, New York).

Kaminskyj, I., and Materka, A. (**1995**). ''Automatic Source Identification of Monophonic Musical Instrument Sounds,'' IEEE Int. Conf. on Neural Networks **1**, 189–194.

Kaminskyj, I., and Voumard, P. (**1996**). ''Enhanced Automatic Source Identification of Monophonic Musical Instrument Sounds,'' in *Proceedings of the 1996 Australian New Zealand Conference on Intelligent Information Systems*, pp. 76–79.

Kendall, R. A. (**1986**). ''The role of acoustic signal partitions in listener categorization of musical phrases,'' Music Perception **4**, 185–214.

Kostek, B., and Wieczorkowska, A. (**1997**). ''Parametric Representation of Musical Sounds,'' Arch. Acoust. **22**, 3–26.

Krumhansl, C. L. (**1989**). ''Why is musical timbre so hard to understand?'' in *Structure and Perception of Electroacoustic Sound and Music*, edited by S. Nielzen and O. Olsson, Excerpta Medica 846 (Elsevier, Amsterdam), pp. 43–53.

Langmead, C. J. (**1995a**). ''Sound Analysis, Comparison and Modification Based on a Perceptual Model of Timbre,'' ICMC **1995**, 475–478.

Langmead, C. J. (**1995b**). ''A theoretical model of timbre perception based on morphological representations of time-varying spectra,'' Master's Thesis, Dartmouth College.

McAdams, S., and Bigand, E. (**1993**). ''Recognition of Auditory Sound Sources and Events,'' in *Thinking in Sound: The Cognitive Psychology of Human Audition* (Oxford U.P., Oxford).

McAdams, S., Winsberg, S., Donnadieu, S., De Soete, G., and Krimphoff, J. (**1995**). ''Perceptual scaling of synthesized musical timbres: Common dimensions, specificities, and latent subject classes,'' Psychological Research **58**, 177–192.

Moorer, J. A. (**1975**). ''On the Segmentation and Analysis of Continuous Musical Sound by Digital Computer,'' Ph.D. dissertation, Stanford Department of Music Report No. STAN-M3.

O'Shaughnessy, D. (**1987**). *Speech Communication: Human and Machine* (Addison–Wesley, Reading, MA).

Oppenheim, A. V., and Schafer, R. W. (**1975**). *Digital Signal Processing* (Prentice–Hall, Englewood Cliffs, NJ).

Plomp, R. (**1970**). ''Timbre as a multidimensional attribute of complex tones,'' in *Frequency Analysis and Periodicity Detection in Hearing*, edited by R. Plomp and G. F. Smoorenburg (Sijthoff, Leiden), pp. 397–414.

Plomp, R. (**1976**). *Aspects of Tone Sensation* (Academic, London).

Popat, K., and Picard, R. W. (**1997**). ''Cluster-Based Probability Model and Its Application to Image and Texture Processing,'' IEEE Trans. Image Process. **6**, 268–284.

Rabiner, L. R., and Huang, B.-H. (**1993**). *Fundamentals of Speech Recognition* (Prentice-Hall, Englewood Cliffs, NJ).

Rabiner, L. R., and Schafer, R. W. (**1978**). *Digital Processing of Speech Signals* (Prentice-Hall International, London).

Reynolds, D. A., and Rose, R. C. (**1995**). ''Robust text-independent speaker identification using Gaussian mixture speaker models,'' IEEE Trans. Speech Audio Process. **3**, 72–83.

Risset, J. C., and Mathews, M. V. (**1969**). ''Analysis of musical-instrument tones,'' Phys. Today **22**, 23–30.

Rossing, T. D. (**1990**). *The Science of Sound* (Addison-Wesley, Reading, MA).

Saldanha, E. L., and Corso, J. F. (**1964**). ''Timbre cues and the identification of musical instruments,'' J. Acoust. Soc. Am. **36**, 2021–2026.

Strong, W. (**1998**). Private communication.

Strong, W., and Clark, M. (**1967a**). ''Synthesis of wind-instrument tones,'' J. Acoust. Soc. Am. **41**, 39–52.

Strong, W., and Clark, M. (**1967b**). ''Perturbations of synthetic orchestral wind-instrument tones,'' J. Acoust. Soc. Am. **41**, 277–285.

Strong, W. J., and Plitnik, G. R. (**1977**). *Music, Speech, and High Fidelity* (Brigham Young Univ., Provo, UT).

Therrien, C. W. (**1989**). *Decision Estimation and Classification* (Wiley, New York).

Wedin, L., and Goude, G. (**1972**). ''Dimensional analysis of the perception of instrument timbres,'' Scandinavian Journal of Psychology **18**, 228–240.

Wilcox, L., Kimber, D., and Chen, F. (**1994**). ''Audio indexing using speaker identification,'' ISTL Technical Report No. ISTL-QCA-1994-05-04.

Vibrational patterns and frequency responses of the free plates and box of a violin obtained by finite element analysis

J. Bretos[a] and C. Santamaría

Departamento de Fisica Aplicada II, Universidad del Pais Vasco, Apdo. 644-48080 Bilbao, Spain

J. Alonso Moral

Conservatorio Superior de Música de Bilbao ''Juan Crisóstomo de Arriaga,'' Bilbao, Spain

By means of the finite-element method, a study of the vibrational behavior of the violin has been developed in two parts. In the first part, the analysis concerns the free violin plates and their tuning process, which has been accurately described by this numerical tool. In the second part, the whole violin box—except for the neck—has been modeled and its first ten eigenmodes have been calculated. In both parts, the calculated vibrational patterns and frequency responses have been compared with experimental measurements of other researchers. © *1999 Acoustical Society of America.* [S0001-4966(99)02503-5]

PACS numbers: 43.75.De [WJS]

INTRODUCTION

The violin is one of the most studied instruments in musical acoustics.[1] This is, in part, because the violin has enjoyed a very important role as a solo instrument, or as part of an ensemble, from the Baroque period to the present day. From a scientific point of view, its wonderful sounds involve a great number of interesting acoustical problems,[2] many of them related to the complex shape of its beautiful body.

A cursory examination of the violin reveals that the plates are of complex shape. The violin maker focuses great attention on their carving, but not only to achieve their beautiful outline; a suitable tuning of the top- and back-free plates is desirable to get good results when they are assembled in the whole instrument.[3] Hutchins is the pioneer in the description of suitable tuning in physical terms,[4–6] following the observations of F. Savart in the last century.[1] Thus, the traditional carving of the violin plates developed by luthiers adjusts the frequencies, input admittances, quality factors, and vibrational patterns of certain natural eigenmodes (#1, #2, and #5) empirically. The last one (#5) is called the ring mode because of the shape of its nodal lines.

There are many factors which affect the vibrational behavior of these complicated violin components, such as the geometrical design: arching and distribution of thicknesses; elastic parameters and density of wood; the anisotropy and inhomogeneity of the materials. Hence, numerical calculations can be useful to estimate the influence of each of these individual parameters. Finite-element modeling has been used by many researchers with good results. Rodgers has studied many aspects which have important influences on the tuning of violin plates, from the elastic properties of wood[7] to the distribution of thicknesses.[8,9] Richardson *et al.* have made comparisons between numerical and experimental vibrational patterns as well,[10] and a general feature of all these works is that they reproduce the conclusions stated by the experimental observations of Hutchins and other researchers.[11]

The modeling of the whole body of the violin is necessarily much more complicated. Nevertheless, some researchers have successfully obtained interesting results using finite-element techniques.[12] However, experimental observations of eigenmodes of the violin body,[13,14] reveal that its vibrational patterns are very complicated. Therefore, an accurate numerical calculation of these normal modes needs very sophisticated modeling. Moreover, it is highly desirable to establish relationships between the vibrational behavior of the free plates and the assembled violin structure, and this would seem to be amenable to numerical analysis.[3,15] A clear description of the relationships would explain the efforts of the luthiers to tune the violin plates properly before closing the box.

The primary objective of the present work is to determine the above relationships. Hence, the most important aim of the work has been the simultaneous finite-element analyses of free violin plates and the violin box, including all its components except for the neck. Regarding the free violin plates, an improvement of the meshes for finite-element analysis has been implemented with a precise modeling of the geometrical details of the violin plates following a Stradivarius pattern.[16] Thus, an accurate analysis of the tuning process of these components has been achieved for selected types of wood. Moreover, a study of the vibrational effects of certain parts, like the bass bar of the top plate, has been developed as well. Regarding the whole violin box, as stated before, a numerical analysis of the violin box with well-tuned plates has been completed, and the vibrational patterns of the whole structure have been compared with those related to the free plates.

I. FINITE-ELEMENT MODEL

Finite-element model for the violin box has been carried out using ABAQUS software, available in a vectorial supercomputer CONVEX (C-3820).[17] Figure 1 shows the defined

---

[a]Author to whom correspondence should be addressed.
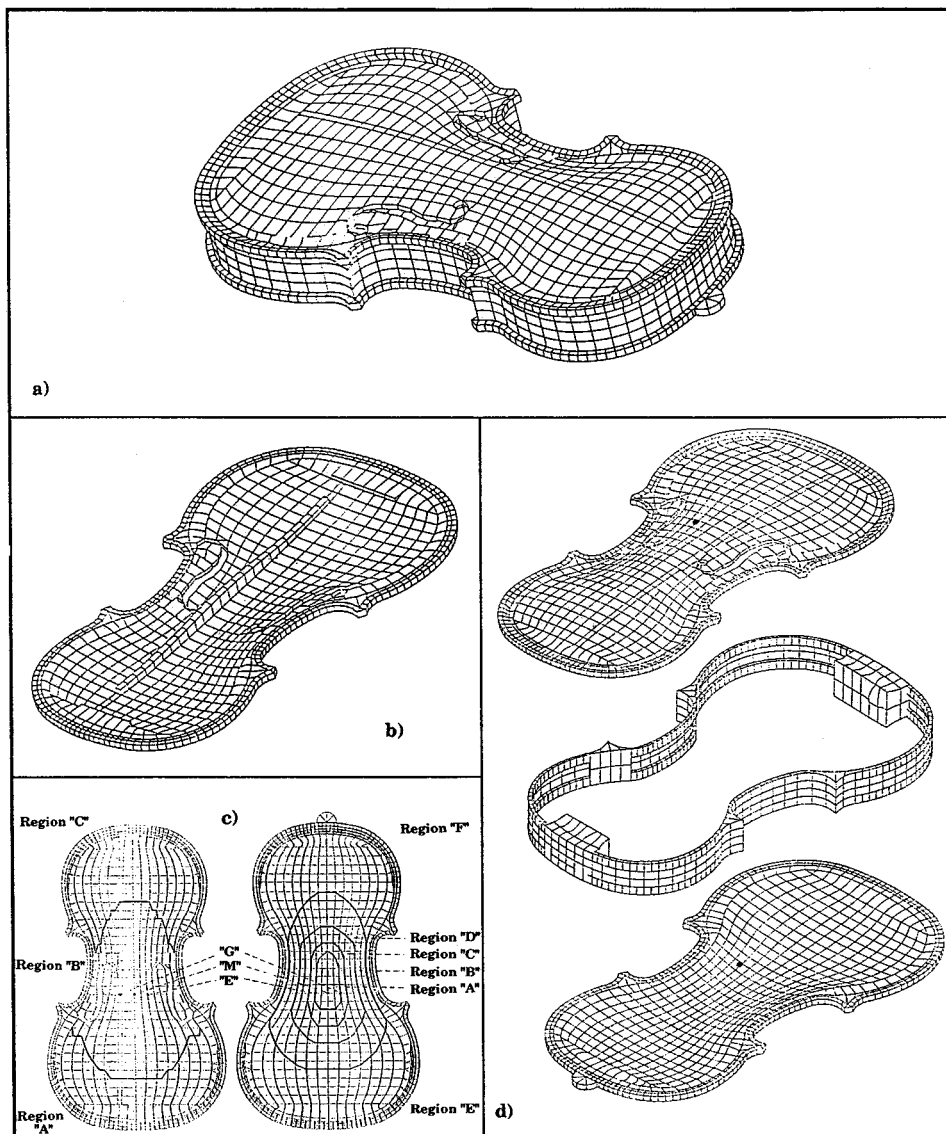
FIG. 1. Meshes defined for the finite-element modeling of a violin box. (a) Mesh for the whole structure of the violin; (b) Detail of the inner face of the top plate with the addition of the bass bar; (c) Outer faces of the back and top plate. Regions A, B, C, D, and E mean zones with different thickness. G, M, and E are points where the frequency response was calculated. (d) The violin divided in its plates and joining system composed of ribs, lining strips, end blocks, and corner blocks. (Dot shows the location of the sound-post.)

mesh in two different frames: the first one for the whole structure and the second one divided in parts corresponding to each part of the violin box.

The meshes for the violin plates consist of 7200 nodes for 900 three-dimensional elements. The geometrical outline for the outside surfaces were taken from a model developed by Ake Ekwall.[18] The distribution of thicknesses is that suggested by Hutchins, these being the most suitable for these components.[5] These distributions can be checked as well in Fig. 1, as the meshes have been divided into several regions which blend smoothly into each other. Each of them will have a different thickness in the carving process. The top plate is divided into three parts with an ovoidal area for the central region. The back plate features a concentric distribution of regions with a different thickness distribution. Finally, the shape of the *f*-holes and the bass bar (whose location and design is indicated in Fig. 1) comes from a plan corresponding to a Stradivarius model dated 1720.[16]

As far as the complete violin box is concerned, great attention has been focused on an accurate description of the whole joining system: ribs, lining strips, end and corner blocks, as shown in Fig. 1. The sound-post is also included.

For this reason, the complete mesh was composed of nearly 17 000 nodes for 2500 three-dimensional elements (shell type for the ribs and solid type for the rest of the box).

Concerning the mechanical properties, the elastical parameters and density were chosen to correspond to typical values for types of wood regarded as the most appropriate for violin components.[19,20] These varieties are spruce (commonly *picea excelsa*) for the top plate and sound-post and maple (commonly *acer platanoides*) for the back plate and other parts of the instruments (ribs, blocks, ...). The values for their mechanical parameters used in this work are shown in Table I.

Using the results for the eigenfrequencies, ABAQUS can also calculate the frequency response of the system to a certain excitation. In this case, this excitation was defined as a force of constant amplitude over a frequency range of 0 to 12 kHz with all its frequency components uncorrelated. In the program it is called a random excitation, and its corresponding response is labeled as a random response. Input data for the material damping are required for the calculation of random responses. This is why values for the Q-factor (or other equivalent parameters) of each eigenmode must be intro-

TABLE I. Values for the elastic parameters and density of the types of wood used in violin components. (ρ: density; E_1: Young modulus; G_{ij}: shear modulus; ν_{ij}: Poisson ratio; $i = 1$: direction along the grain of wood; $i = 2,3$: directions across the grain of wood.)

	ρ (Kgm^{-3})	E_1 (GPa)	$E_2 = E_3$ (GPa)	$G_{12} = G_{13}$ (GPa)	G_{23} (GPa)	$\nu_{12} = \nu_{13}$	ν_{23}
Spruce[a]	420	15.13	1.20	0.70	0.059	0.3	0.03
Maple[b]	610	14.30	2.00	1.27	0.620	0.3	0.03

[a]Top plate, sound-post.
[b]Black plate, ribs, end and corner blocks, lining strips.

duced in the model. Hence, an average value of 50 has been taken from the experimental data of Alonso Moral and Jansson,[13]

II. NUMERICAL RESULTS FOR FREE VIOLIN PLATES

The finite-element method was used to extract eigenvalues and to calculate random responses for top and back plates in several steps of their building process. In regard to the random responses, they were calculated at three points on the plates, as shown in Fig. 1. The three points were located on the top plate just in the line where the bridge is supported in the completed violin. Point ''G'' is under the ''bass foot'' of the bridge nearest to the G_3-string ($G_3 = 198$ Hz). Point ''E'' is at a similar location but under the ''treble foot'' of the bridge near the E_5-string ($E_5 = 660$ Hz). Finally, point ''M'' is located in the middle between these latter points. Similar points were chosen for the back plate, even though there is no bridge present.

The building processes used in both plates were chosen so as to obtain the desired vibrational patterns for eigenmodes #1, #2, and #5 as proposed by Hutchins.[5,6] Moreover, harmonic relationships between their frequencies have been achieved as well: i.e., octave (1:2) between eigenmodes #2 and #5 of the back plate and double octaves (1:2:4) among eigenmodes #1, #2, and #5 of the top plate.

As stated before, the outer-surface contours for the back and the top plates were taken from Ake Ekwall.[18] That is why arching distribution was fixed, and the simulated building process consisted only of a choice for the thickness distribution beginning from initial values similar to those proposed by Hutchins.[6] The carving process and the final thickness distribution will obviously depend on the material properties defined in the numerical analysis. Thus, this part of the work describes a numerical analysis of the tuning of a violin plate for a particular type of wood following Hutchins' ideas to achieve the mode shapes and frequency relationships proposed by the same researcher.

The carving process in both top and back plates has been divided into several steps in order to observe the influence of decreasing the thickness in certain parts of the plates on the vibrational patterns and eigenfrequencies. The most important results are summarized in the following paragraphs.

A. Back plates

The carving process begins with an initial distribution of constant thickness (5 mm) for the whole plate. The second step makes the plate thinner to achieve a concentrical distribution of thicknesses characterized by the following values:

region ''A'': 5 mm, region ''B'': 4.5 mm; region ''C'': 4.0 mm; region ''D'': 3.5 mm; region ''E'': 3.0 mm, and region ''F'': 2.5 mm. The third step involves a decrease in thickness of 0.5 mm for the latter distribution. In this step, eigenmodes #1, #2, and #5 already have their characteristic vibrational patterns. Finally, a refinement was required to achieve an exact octave relationship between the frequencies of #2 and #5. This last step leads to a final distribution which decreases the thicknesses of regions A, B, and C to 3.4 mm. This gives the final distributions: region A: 3.4 mm; region B: 3.4 mm; region C: 3.4 mm; region D: 3.0 mm; region E: 2.5 mm, and region F: 2.0 mm.

In Fig. 2, the calculated vibrational patterns and frequencies of the first eight natural eigenmodes are presented. The most remarkable results are those related to the eigenmodes #1, #2, and #5: the torsional pattern for #1, the bending pattern for #2, and the annular pattern for #5, commonly known as the ring mode. These vibrational patterns are compared in Fig. 2 with others obtained experimentally by Richardson et al.[10] The agreement is good not only for the vibrational patterns but also for the natural frequencies, despite the inevitable differences of shape and mechanical properties of wood between the modeled violin plates and the real ones.

The calculated random responses provide interesting information about the vibrational effects of the carving process, as can be seen in Fig. 3. This figure shows the random responses calculated at point M in the first and last steps of the carving process of the violin back plate. A first characteristic of these spectra is that they do not show clear antiresonances, but it can be easily understood if the algorithm used is considered. Effectively, the number of frequency values between two consecutive eigenfrequencies needs to be specified in ABAQUS, so that the program may calculate the response of the whole system to each of these intermediate frequencies. In our case, as the model of the whole violin box includes a large number of nodes and elements, the number of intermediate frequencies was reduced in order to minimize the time spent using the computer. Thus, the resonance peaks are defined clearly while the antiresonances lack precision. Regarding the acoustical information provided by these spectra, the most remarkable feature is the growth of input admittance at this point M for the ring mode (#5). This prominent resonance maximum for #5 is characteristic in well-tuned violin back plates.[21]

B. Top plates

Because the violin top plate has a bass bar glued to the inner face, the carving process was divided into two parts.

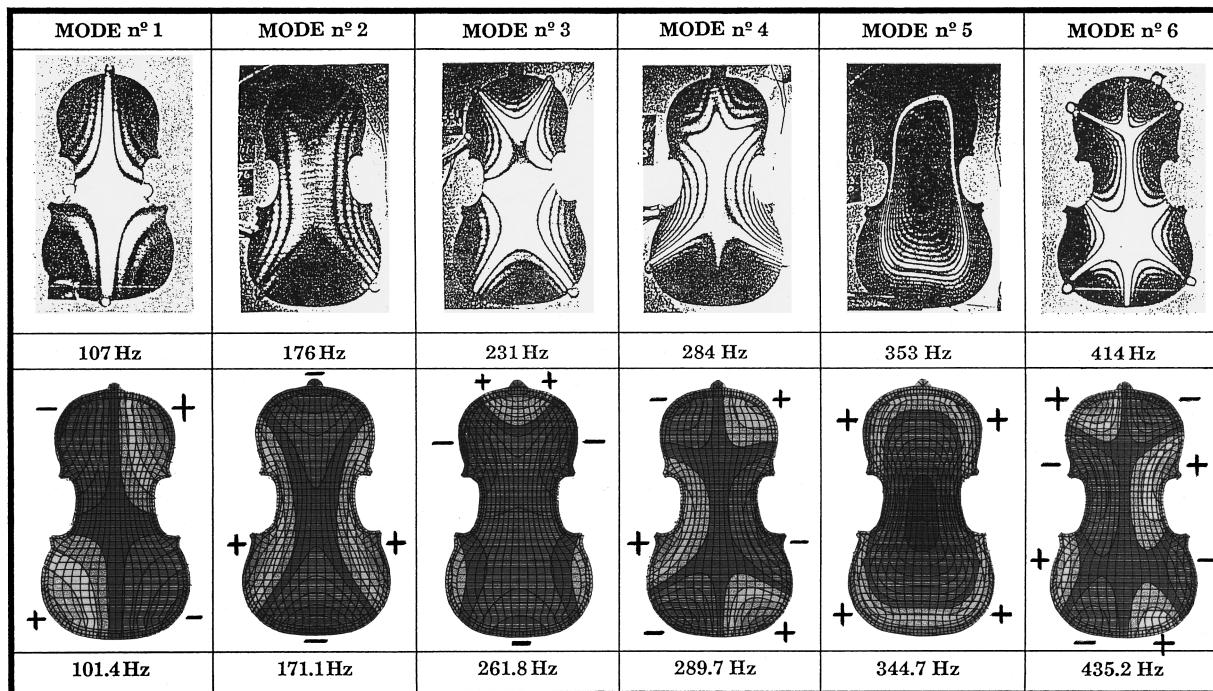| MODE nº 1	MODE nº 2	MODE nº 3	MODE nº 4	MODE nº 5	MODE nº 6
107 Hz	176 Hz	231 Hz	284 Hz	353 Hz	414 Hz
101.4 Hz	171.1 Hz	261.8 Hz	289.7 Hz	344.7 Hz	435.2 Hz

FIG. 2. Comparison between vibrational patterns and natural frequencies of a violin back plate calculated by finite-element analysis and the experimental results measured by Richardson et al.[10] (+ and − represent antiphase movement of the structure).

The first stage is similar to that described for the back plate, and consists of achieving a suitable distribution of thickness. Initially this is defined by a constant thickness of 4 mm for the whole plate. The second step gives different thicknesses for regions A, B, and C (Fig. 1): 3.5 mm for region A; 4.0 mm for region B, and 3.0 mm for region C. The third step decreases the thicknesses by 1 mm for regions A and B, and 0.8 mm for region C. In the second stage the bass bar is added, first as a rectangular bar, which is then progressively thinned to achieve the desired vibrational patterns for eigenmodes #1, #2, and #5 and their characteristic harmonic relationships between frequencies (1:2:4).

The calculated frequencies and vibrational patterns for the first eight natural eigenmodes of a violin top plate are presented in Fig. 4. As in the case of the back plates, these numerical results are compared with experimental measurements from Richardson et al.[10] and the same comments about the good agreement (between vibrational patterns or natural frequencies) can be made.

The results for the random responses are presented in the four spectra of Fig. 5. Case (a) shows the random response calculated at point G in the stage just before the addition of the bass bar. In this step, mode #5 features its characteristic ring-shaped nodal line; moreover, the relationships 1:2:4 between the frequencies of modes #1, #2, and #5 are achieved as well. Hence, the top plate is tuned well, but this situation is destroyed when the bass bar is first added, as can be seen in case (b). In this latter case, the random response is calculated when the bass bar is added but without being carved following its typical geometrical outline (Fig. 1). Mode #5 lacks its prominent resonance maximum because its vibrational pattern has been disturbed. However, when the bass bar is carved appropriately, the first vibrational behavior is

re-established but translated to a higher frequency range. This can be seen in case (c), where the random response belongs to the final step of the carving process. Mode #5 again has the highest level of input admittance, as in case (a), although its frequency has increased more than 10%. Thus, the carving and the location of the bass bar allow it to raise the frequency of mode #5 with a small addition of mass. As in the case of the back plate, high natural frequencies in top plates with minimum weight are useful to achieve brilliant violin sounds. Moreover, the ring-mode frequency of 346.2 Hz is similar to that calculated for the back plate. Finally, case (d) shows the random response in the same step but calculated at point E. The differences between cases (c) and (d) demonstrate the asymmetric vibrational pattern of the top plate, which is caused by the addition of the bass bar. Thus, the ring mode #5 has a greater value of input admittance in point E, that is, in the region where the E_5-string is supported on the bridge in the whole violin. A comparison between spectrum (d) and the frequency response measured by Richardson et al.[10] shows the good agreement between the resonance peaks of those experimental results and the calculations presented in this work.

III. NUMERICAL RESULTS FOR THE ASSEMBLED VIOLIN BOX

The tuned free violin plates were the basis for the assembled instrument. Thus, the modeling of the whole violin box included the top and back plates in the final step of their carving process. Thus, their natural modes #1, #2, and #5 had appropriate vibrational patterns and frequencies corresponding to octave relationships (1:2 between modes #2 and #5 of the back plate with a value of 344.7 Hz for the fre-
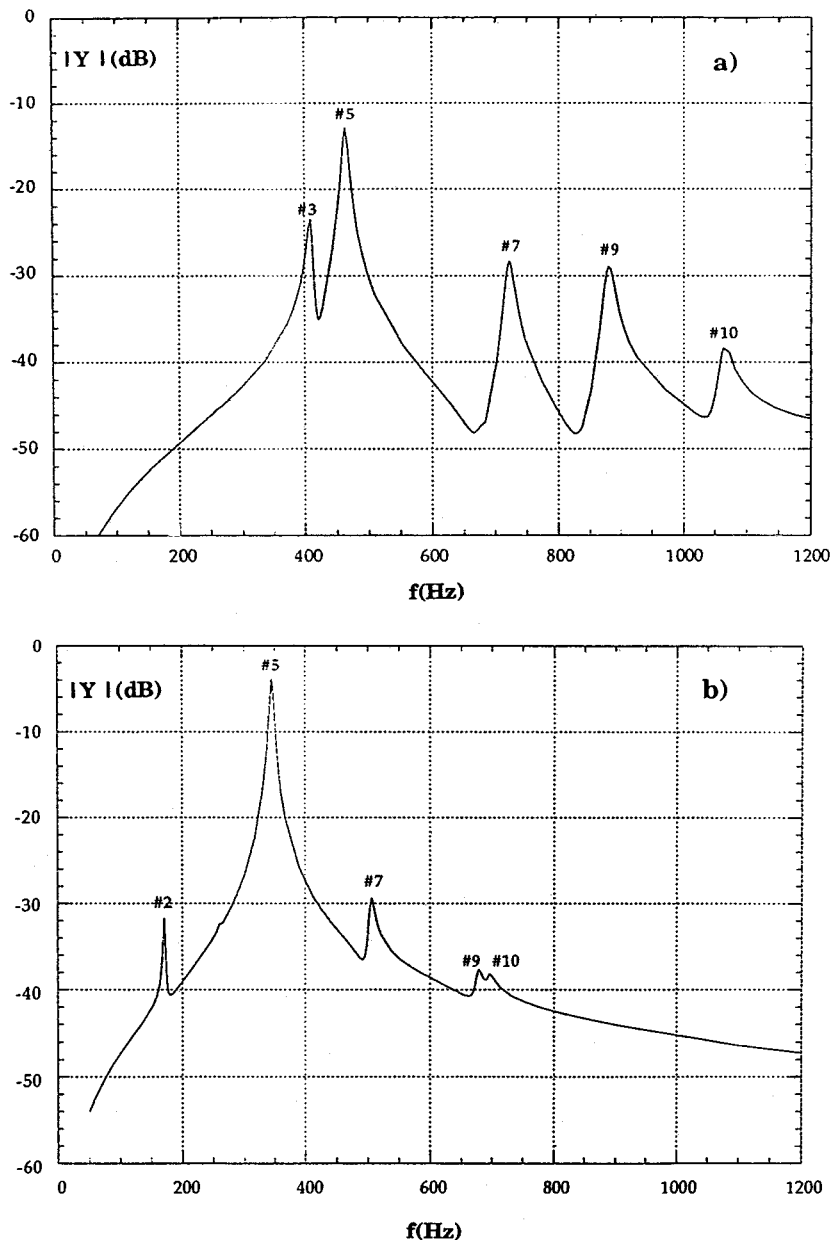
FIG. 3. Frequency responses of a violin back plate calculated numerically for a random excitation applied at point M. (a) First step of the carving process (back plate with a constant thickness of 5 mm). (b) Last step of the carving process (mode #5 tuned at 344.7 Hz and octave relationship—1:2—between modes #2 and #5).

quency of #5, and 1:2:4 between modes #1, #2, and #5 of the top plate with a value of 346.2 Hz for its ring mode).

The first ten natural eigenmodes and random responses were calculated for the complete violin box (except for the neck). Figure 6 shows a selection of the calculated vibrational patterns. These vibrational patterns show motion of the the top and back separately. The same color in both plates indicates an in-phase movement (displacements in the same direction); blue and red colors mean antiphase movement. In the following paragraphs, the most remarkable results will be described.

Mode #1 exhibits torsional vibrational behavior in the top and back plates. Moreover, both plates vibrate in phase and in a similar way to their second natural torsional eigenmode. These natural eigenmodes are similar in character to the third and fourth modes in the free top plate (Fig. 4) and back plate (Fig. 2), respectively. This eigenmode has been labeled as the second mode of corpus (C_2) by other researchers.[13]

Modes #2 and #3 (Fig. 6) have vibrational patterns with a strong similarity. Both of them involve in-phase bending of the top and back plates, but in a different direction. In the case of #2, the bending is along the grain in the top plate and across the grain in the back plate. In mode #3, the situation is reversed. In experimental analysis of the whole violin box (including the neck), the eigenmode #2 has been labeled as the first mode of top plate (T_1) and eigenmode #3 as the third mode of corpus (C_3).[13] However, the present calculations agree better with the experimental results of Marshall,[14] where these eigenmodes are called bending corpus eigenmodes. These modes are significant because the frequencies and input admittances of these eigenmodes are closely related to violin quality.[22] Moreover, the vibrational feature of mode C_3 in high-quality violins has been recently studied in depth.[23]

Mode #4 can be classified as a corpus mode as well because the plates move in phase. This mode has not been detected in many experimental works.[24] However, the situa-
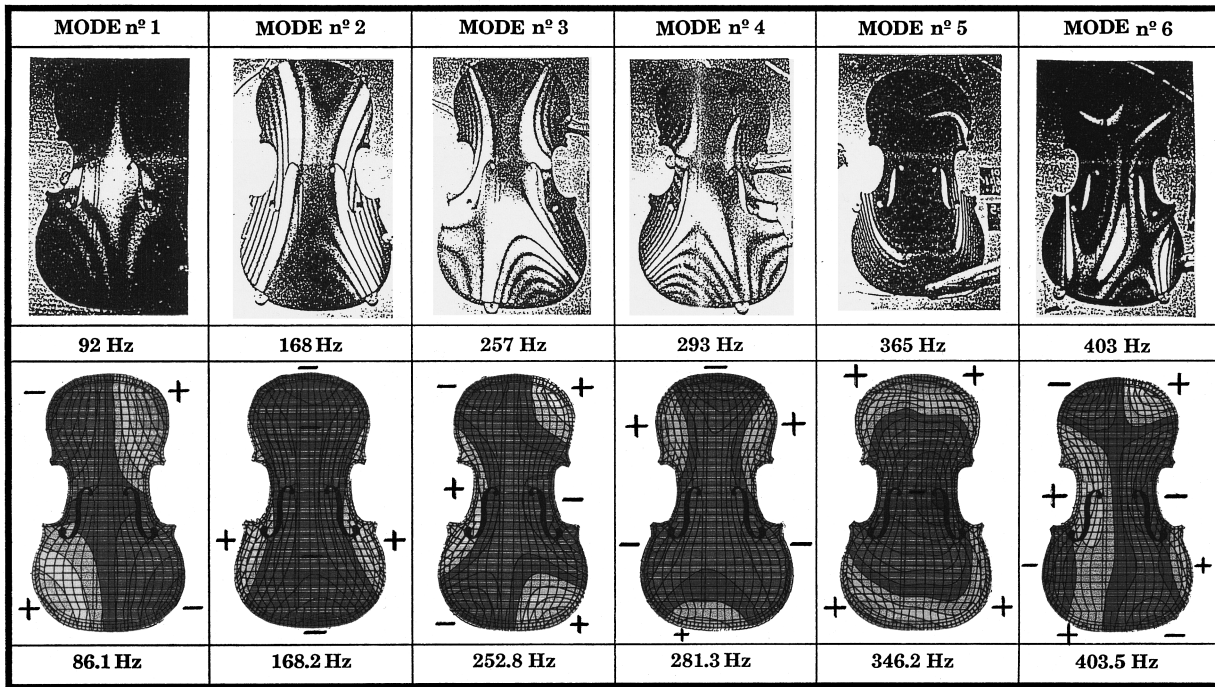
FIG. 4. Comparison between vibrational patterns and natural frequencies of a violin top plate calculated by finite-element analysis and experimental results measured by Richardson *et al.* [10] (+ and − represent antiphase movement of the structure).
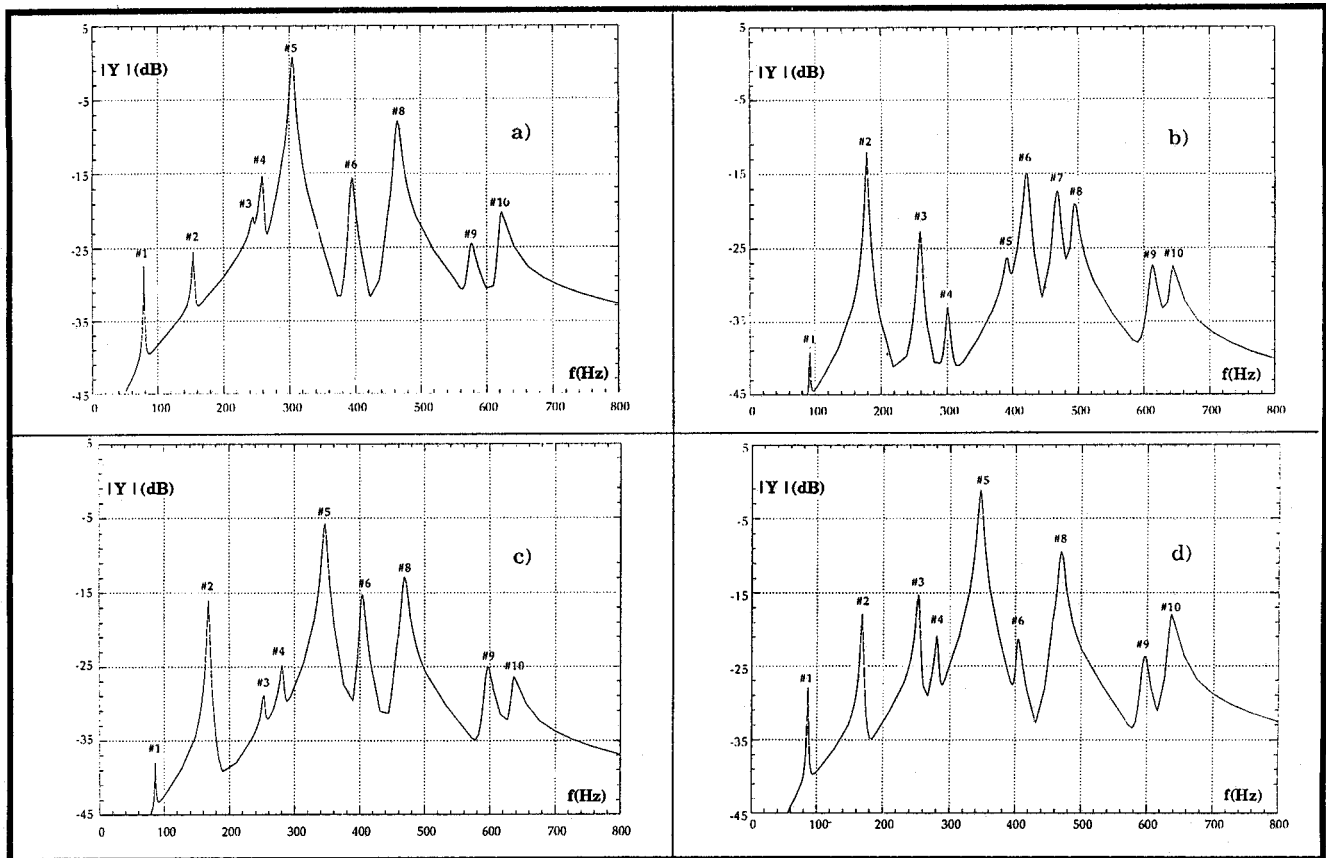
FIG. 5. Frequency responses of a violin top plate calculated numerically. (a) Step of the carving process before the addition of the bass bar (random excitation applied at point G). (b) Step of the carving process just after the addition of the bass bar (random excitation applied at point G). (c) Final step of the carving process of the top plate (mode #5 tuned at 346.2 Hz and octave relationships—1:2:4—among modes #1, #2, and #5) (random excitation applied at point G). (d) Final step of the carving process of the top plate (random excitation applied at point E).
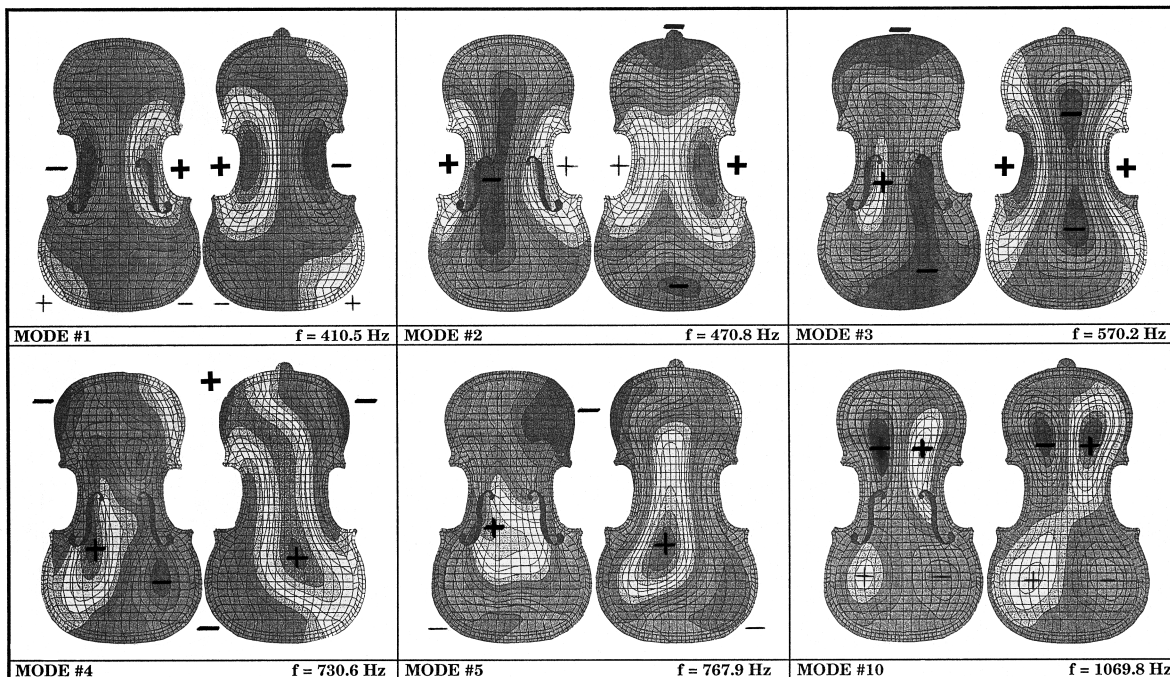
FIG. 6. Vibrational patterns and frequencies corresponding to the natural modes #1, #2, #3, #4, #5, and #10 of a violin box calculated by finite-element analysis. [Same symbol (+ or −) in top and back plate represents displacement in the same direction. + and − represent antiphase movement of the structure.]

tion is rather different with mode #5 [case (d) of Fig. 6]. It features a characteristic ring-shaped nodal line in both plates, especially in the back plate. Thus, the in-phase movement of the top and back plates resembles the vibrational pattern of their #5 natural eigenmode (or ring mode). This eigenmode can be clearly indentified with the fourth eigenmode of corpus labeled C_4 by other researchers.[13] This eigenmode seems to be very important in the musical quality of the violin.[22]

Figure 6 also shows an example of the vibrational patterns of higher eigenmodes (mode #10). Such modes belong to the type called plate eigenmodes[13] and are characterized by nodal regions near the ribs.

Table II offers a comparison between calculated frequencies and those obtained experimentally by other researchers. The agreement is good, taking into account the differences between the measured violins and the modeling of this work such as the differences in the mechanical properties of the wood, in the geometrical design of the instru-

ments, the air coupling, and the presence of the neck. As suggested before, many of the eigenmodes of the wooden structure seem to be important for the musical quality of the violin.[22] However, certain modes involving coupling between the wooden structure and the air cavity should also be analyzed if full information is desired for instrument makers' purposes. One of the most important modes is that called A0 by Alonso Moral and Jansson[13] which consists of the coupling structure with the air cavity acting as a Helmholtz resonator. Its frequency is a little below the range of the corpus modes calculated in this work, and has an important role among the low-frequency resonances. Finally, the so-called A1 cavity mode should be mentioned as well (first eigenmode of the enclosed air cavity as an air column). Its frequency is near 500 Hz, close to the T1 eigenmode, and certain work has demonstrated its effects on the tone quality of the violin.[25]

Random responses for the complete body have been cal-

TABLE II. Calculated values for the natural frequencies of a violin box compared with experimental measurements from other researchers.

Mode	Calculated frequencies (Hz)	Measured frequencies (Hz)			
		J. Alonso & E. Jansson Ref. 13	K. D. Marshall Ref. 14	R. T. Miller Ref. 24	
				a	b
#1	410.5	363 ± 38 (#C_2)	410.5	415/430	⋯
#2	470.8	448 ± 27 (#T_1)	466.1	470/484	430/438
#3	570.2	533 ± 45 (#C_3)	574.1	590/575	524
#4	730.6	⋯	⋯	700/720	⋯
#5	767.9	688 ± 85 (#C_4)	656.1	⋯	620

[a]Violin corresponding to Klotz school (c. 1780).
[b]Violin made by Theo Miller (1988).
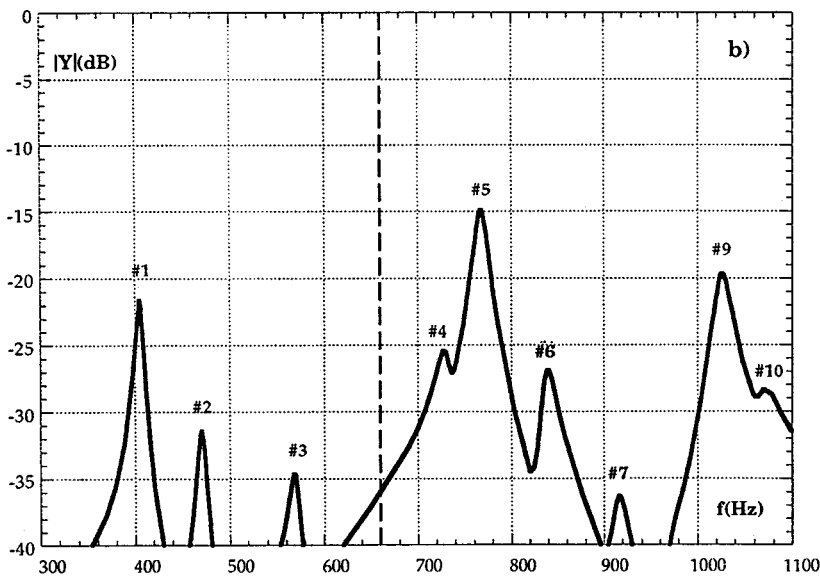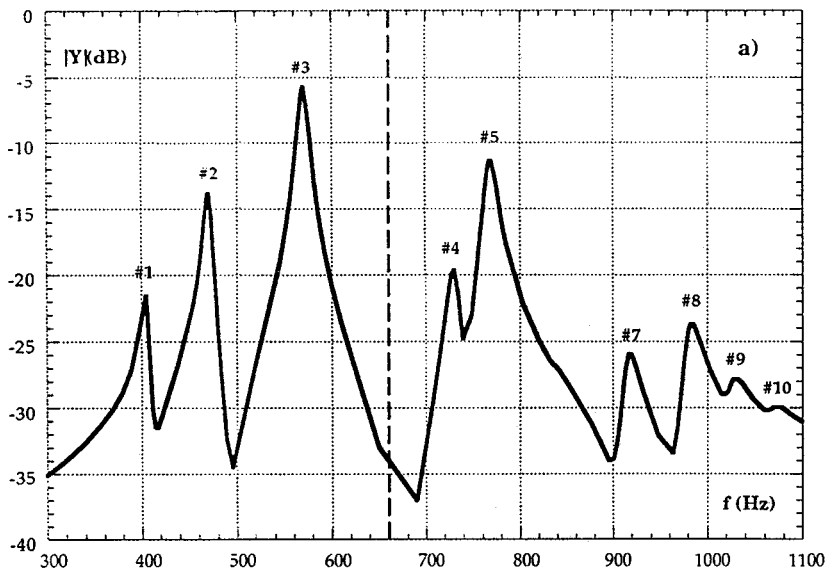
FIG. 7. Frequency responses of a violin box determined from finite-element analysis. (a) Random excitation applied in point G of top plate. (b) Random excitation applied in point E of top plate.

culated with the force applied at points G, M, and E of the top plate. These points have been described in the discussion on the top plate. Figure 7(a) shows the random response from application at point G. Figure 7(b) shows the same for point E. Noteworthy is the difference in response between the two, illustrating the asymmetry of the vibration response of the violin box, caused mainly by the sound-post and, to a lesser degree, by the bass bar glued to the top plate. The asymmetry is most easily observed by comparing the higher level of input admittance of the lowest eigenmodes in Fig. 7(a) with that shown in Fig. 7(b). The vertical dashed line is located at the fundamental frequency of the open E_5-string. In Fig. 7(b), only eigenmodes with a frequency higher than 660 Hz show strong responses.

A final comment can be made for the high level of input admittance corresponding to eigenmode #3 [or C_3 (Ref.13)]. Recent investigations have shown that a prominent resonance peak between 500 and 600 Hz is present in high-

quality violins.[23] Thus, the numerical calculations presented in this work seem to properly describe the vibrational behavior of a good instrument.

IV. CONCLUSIONS

As regards the free violin plates, the main conclusions are related to the analysis of their tuning method. In both plates, an accurate description of how the carving process adjusts the vibrational patterns and frequency relationships of modes #1, #2, and #5 has been developed. Moreover, it has been observed in the back plates that a suitable distribution of thicknesses allows the maker to obtain a particular value of frequency for the ring mode with the least total mass. In the case of the top plate, a special role is played by the bass bar. It allows the top plate to be tuned at a higher frequency with the addition of less mass when the bass bar is properly located and shaped.

Regarding the whole violin box, the most important aim has been the accurate modeling of all its components with special attention to accurate modeling of the instrument's shape. Thus, accurate results have been calculated for the vibrational patterns. There is good agreement with results experimentally measured by other researchers. Many of the eigenmodes which seem to be important in the quality of the violin have been analyzed numerically.

[1] C. M. Hutchins, "A history of violin research," J. Acoust. Soc. Am. **73**, 1421–1440 (1983).

[2] M. E. McIntyre and J. Woodhouse, "The acoustics of stringed musical instruments," Inter. Sci. Rev. **3**(2), 157–173 (1978).

[3] J. Alonso Moral and C. M. Hutchins, "From properties of free top plates of free back plates and of ribs to properties of assembled violins." Report STL-QPSR 1/1984, pp. 1–29. Speech Transmission Laboratory, Royal Institute of Technology (KTH), Stockholm (1984).

[4] C. M. Hutchins, K. A. Stetson, and P. A. Taylor, "Clarification of free plate tap tones by holographic interferometry. The acoustics of violin plates," J. Catgut Acoust. Soc. **16**, 15–23 (1971).

[5] C. M. Hutchins, "The acoustics of violin plates," Sci. Am. **245**(4), 170–186 (1981).

[6] C. M. Hutchins, "Plate tuning for violin makers," Catgut Acoust. Soc. NL **39**, 25–32 (1983).

[7] O. E. Rodgers, "The effects of the elements of wood stiffness on violin plate vibration," J. Catgut Acoust. Soc. **1**(1) (Ser. II), 2–8 (1988).

[8] O. E. Rodgers, "Influence of local thickness changes on violin plate frequencies," Catgut Acoust. Soc. J. **1**(5) (Ser. II), 13–16 (1990).

[9] O. E. Rodgers, "Influence of local thickness changes on violin top plate frequencies," Catgut Acoust. Soc. J. **1**(7) (Ser. II), 6–10 (1991).

[10] B. E. Richardson, G. W. Roberts, and G. P. Walker, "Numerical modelling of two violin plates," J. Catgut Acoust. Soc. **47**, 12–16 (1987).

[11] N. E. Molin, L. E. Lindgren, and E. V. Jansson, "Parameters of violin plates and their influence on plate modes," J. Acoust. Soc. Am. **83**, 281–291 (1988).

[12] A. Isaksson, H. O. Saldner, and N. E. Molin, "Influence of enclosed air on vibrational modes of a shell structure," J. Sound Vib. **187**, 451–466 (1995).

[13] J. Alonso Moral and E. V. Jansson, "Eigenmodes, input admittance and the function of the violin," Acustica **50**, 329–337 (1982).

[14] K. D. Marshall, "Modal analysis of a violin," J. Acoust. Soc. Am. **77**, 695–709 (1985).

[15] M. Schleske, "Eigenmodes of vibration in the working process of a violin," Catgut Acoust. Soc. J. **3**(1) (Ser. II) (May), 2–8 (1996).

[16] S. Sacconi, *I Segreti di Stradivarii* (Libreria del Convegno, Cremona, 1979).

[17] J. Bretos, C. Santamaria, and J. Alonso Moral, "Finite element analysis and experimental measurements of natural eigenmodes and random responses of wooden bars used in musical instruments," Appl. Acoust. **56**(3), 141–156 (1999).

[18] Å. Ekwall, "Undersökning av 17 fiolvälvningsbeskrivning samt vidare utveckling," Slöjd och ton. **50**, 152 (1980).

[19] M. A. Hutchins, "Physical measurements on sampling of European spruce and maple for violin top and back plates," Catgut Acoust. Soc. NL **40**, 28–30 (1983).

[20] D. W. Haines, "On musical instrument wood," J. Catgut Acoust. Soc. **31**, 23–32 (1979).

[21] J. Alonso Moral and C. M. Hutchins, "Input admittance and vibration patterns of free violin plates," Report STL-QPSR 2–3/1982, pp. 60–75. Speech Transmission Laboratory, Royal Institute of Technology (KTH), Stockholm (1983).

[22] J. Alonso Moral and E. V. Jansson, "Input admittance, eigenmodes and quality of violins," Report STL-QPSR 2–3/1982, pp. 60–75. Speech Transmission Laboratory, Royal Institute of Technology (KTH), Stockholm (1982).

[23] E. V. Jansson, B. K. Niewczyk, and L. Fryden, "On body resonance C_3 and violin construction," Catgut Acoust. Soc. J. **3**(3) (Ser. II) (1997).

[24] R. T. Miller, "Visualizing complete violin modes," Catgut Acoust. Soc. J. **2**(2) (Ser. II), 1–5 (1992).

[25] C. M. Hutchins, "A study of the cavity resonances of a violin and their effects on its tone and playing qualities," J. Acoust. Soc. Am. **87**, 392–397 (1990).

Time-domain simulation of acoustical waveguides with arbitrarily spaced discontinuities

A. Barjau
*Department of Mechanical Engineering, Polytechnical University of Catalunya,
Diagonal 647, 08028 Barcelona, Spain*

D. H. Keefe
Boys Town National Research Hospital, 555 North 30th Street, Omaha, Nebraska 68131

S. Cardona
*Department of Mechanical Engineering, Polytechnical University of Catalunya,
Diagonal 647, 08028 Barcelona, Spain*

The multiconvolution algorithm [Martínez *et al.*, J. Acoust. Soc. Am. **84**, 1620–1627 (1988)] to calculate the impulse response or reflection function of a musical instrument air column has proved to be useful, but it has the limitation that the spacing between discontinuites is constrained to be some multiple of $c\Delta t$ (for phase velocity c and time step Δt). This paper presents an improved method, the continuous-time interpolated multiconvolution (CTIM), where such a limitation has been removed. The response of an air column, modeled as an arbitrary one-dimensional acoustic waveguide constructed using cylindrical or conical bore segments with viscothermal damping and tone-hole discontinuities, is obtained through continuous-time convolutions between analytical reflection and transmission functions and discrete-time pressure signals. The arbitrary spacing between discontinuites is accounted for by interpolation of the discrete-time pressure signals. Many musical instrument air columns possess tone holes that are opened or closed so that tones of different pitches are produced. A time-domain calculation is presented of the acoustic responses of tone-hole discontinuities that may be open or closed. The resulting reflection and transmission functions are well suited for use in the CTIM. © *1999 Acoustical Society of America.*
[S0001-4966(99)01502-7]

PACS numbers: 43.75.Pq [WJS]

INTRODUCTION

The simulation of the acoustical behavior of wind instruments requires the dynamical description of the main two parts of such systems, the bore and the driver, and their mutual interaction. As the driver is essentially a nonlinear system, it is always described in the time domain through a differential equation. For that reason, even if the bore behaves, under playing conditions, approximately as a linear system, so that its description can be made either in time domain or in frequency domain, it is a time-domain response [usually its input impulse response $h(t)$] that is used when studying the bore-to-driver feedback.

There are mainly two techniques to calculate $h(t)$: either as the inverse Fourier transform (FT) of the corresponding frequency response [the input impedance $Z(\omega)$] or directly in the time domain. The first technique implies all the inconveniences associated with numerical FTs. To overcome these difficulties, Martínez *et al.* (1988a) proposed a direct method in the time domain through a numerical multiconvolution process which has proven to be useful. However, that algorithm has a limitation: the time step Δt used in the calculation has to be small enough so that each of the spacings between discontinuities along the bore (changes in diameter, in taper, open and closed tone holes etc.) is an exact multiple of $c\Delta t$ (where c is the phase velocity of sound in air neglecting dissipation). Smith (1992) worked with a similar idea to

simulate wave propagation in strings. There is a brief discussion of a band-limited interpolation method to treat the case where Δt is not an exact multiple of $c\Delta t$, but there is no discussion of how this method is generalized to model wave propagation in conical waveguides with discontinuities representing tone holes.[1] These limitations are serious for application to musical wind instruments, because, on the one hand, the discontinuities are not uniformly placed and adjacent pairs of discontinuities may be separated by distances less than $c\Delta t$ (for typical digital audio sample rates), and, on the other hand, it is well known that certain numerical instabilities arise in modeling conical spans that do not arise in modeling cylindrical spans.

In this report, a time-domain method is presented to overcome this difficulty. The continuous-time interpolated multiconvolution (CTIM) uses continuous-time convolutions between analytical reflection and transmission functions associated with the bore discontinuities and discrete-time pressure signals. The arbitrary spacing between discontinuites is accounted for in the CTIM method by interpolation of the discrete-time pressure signals. Results concerning CTIM have been presented in a preliminary form (Barjau *et al.*, 1992).

An acoustic waveguide is composed of smooth sections of tubing wherein sound propagates, to first approximation, as a unidimensional wave. Any localized portion of the

waveguide that produces a reflected wave is represented as a node in the waveguide and is termed a discontinuity. Such discontinuities include abrupt changes between smooth sections of tubing, as, for example, in the joining of a conical bore to a cylindrical bore. Many acoustic waveguides can be specified in terms of a set of cylindrical-bore and conical-bore sections that are concatenated together, which can vary in terms of the bore diameter or bore taper. Multiconvolution depends on a time-domain description of the acoustic response within each section of smoothly varying air column, and so on a time-domain representation of the reflection and transmission of sound energy at each discontinuity. Any change in bore diameter or bore taper forms one class of discontinuities. Another class of discontinuities arises when a finite section of tubing is joined to the main bore at a particular location. Tone holes on woodwind musical instruments are an important example of this class of discontinuities. Such a tone hole is usually represented by a cylindrical-bore segment that is joined at one end to the main bore, and is open or closed at its opposite end (a so-called undercut tone hole may be represented by a concatenation of conical-bore to a cylindrical-bore section).

The time-domain acoustic response at a general bore discontinuity involving a change in diameter and/or taper is well understood by calculations explicitly performed in the time domain (Agulló *et al.*, 1992). Using a Fourier transform method (FT), the acoustic response at a tone hole open or closed has been calculated (Martínez *et al.*, 1988a). We have found it useful to calculate the acoustic response of the open or closed tone hole directly in the time domain, but in a manner that parallels the approximations that are well understood from the frequency-domain experiments. The Appendix consists of a detailed discussion of the time-domain calculations of tone-hole discontinuities in a form that is directly applicable to the CTIM algorithm. The results are tabulated in Table I with coefficients that are calculated or cited from the existing literature later in this report.

The basic problem we address is that one sample period Δt is associated with a spatial propagation distance $\Delta x = c\Delta t$, and that this distance is large compared to the spacing of some discontinuities in wind instrument air columns and other acoustic waveguides of interest. The solution is to relinquish the spatial discretization of the acoustic waveguide into sections of length Δx. Instead, the waveguide is represented as a set of circuit nodes, one at each discontinuity, that are connected by arbitrary lengths of smooth bore sections. The response at each node is calculated in discrete time at the sample rate, but the spatial transfer function between each adjacent pair of nodes is a continuous function of location along the waveguide and discretized in time. Results obtained using CTIM are compared to those obtained using the Martínez *et al.* multiconvolution.

I. THE MULTICONVOLUTION ALGORITHM OF MARTÍNEZ *et al.*

In a multiconvolution method, the bore output to a given input signal is obtained by adding the reflections reaching the input section and coming from the discontinuities found along the bore. This process, which follows the real process

taking place in the bore, is described in Fig. 1. The input signal is split into a transmitted (T_1) and a reflected (R_1) wave at the taper discontinuity, the transmitted wave is split again when it reaches the tone hole into a transmitted (T_2) and a reflected (R_2) wave, and so on. Each asterisk (*) in Fig. 1 denotes the convolution operation with the succeeding transmission or reflection function, and an additional convolution operation is added at each new discontinuity traced by the temporal ordering of the arrows in the figure. Such a method of calculation calls for the knowledge of all the elementary reflection and transmission functions associated with all the possible elementary discontinuities. These are different, in general, for the inward and outward propagating waves.

There are two important points that deserve some attention. On one hand, it is clear that the number of waves increases very quickly with time, and so it is inefficient to follow the time evolution of each wave. This can be overcome by adding up all inward waves and all outward waves at each node and at each time step, and working with just two propagating waves.

On the other hand, some elementary reflection functions contain growing exponentials (whenever the propagating wave sees a taper decrease) (Agulló *et al.*, 1992). In such a case, the convolution product at such a node is unbounded and hence numerically unstable. The use of a recursive algorithm solves this problem (Martínez *et al.*, 1988a):

$$y(t) = h(t) * x(t), \quad \text{with } h(t) = a e^{bt}, \tag{1}$$

$$y(t+\Delta t) = y(t) e^{b\Delta t} + a e^{b\Delta t} \int_0^{\Delta t} e^{-b\tau} x(t+\tau)\, d\tau, \tag{2}$$

for the case of an impulse response $h(t)$ with an initial amplitude ''a'' and exponential growth rate ''b.'' Equation (2) shows that the output at some later time $y(t+\Delta t)$ can be calculated in terms of the output at a former time $y(t)$ and a convolution over the time interval from 0 to Δt.

The use of Eq. (2) is also advisable for any convolutions involving exponential kernels (Barjau *et al.*, 1990), as it requires shorter time histories of $x(t)$ (and so less computer memory) and fewer operations than the standard convolution defined in Eq. (1)

The viscothermal losses and time delay between nodes are represented through the propagation functions $\sigma^\pm(t - L/c)$ which relate the inward and outward pressure waves (p^+ and p^-, respectively) at one end of a uniform span (between consecutive discontinuities) of length L (see Fig. 2) with the inward and outward pressure waves, respectively, at the other end by means of a convolution integral:

$$p^\pm(L,t) = p^\pm(0,t) * \sigma^\pm(t-L/c)$$

$$= \int_{-\infty}^t p^\pm(0,t-\tau)\sigma^\pm(\tau-L/c)\, d\tau. \tag{3}$$

In Martínez *et al.* algorithm, these functions are taken to be the approximate ones proposed by Cardona for the case of a conical-bore geometry, which generalizes the more familiar

TABLE I. Coefficients **a** and **b** associated with the usual bore discontinuities.
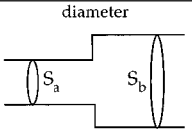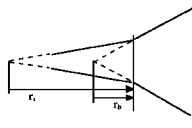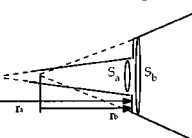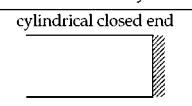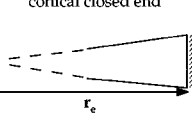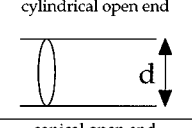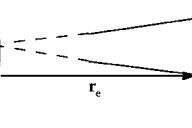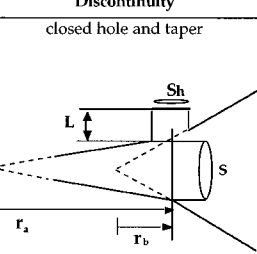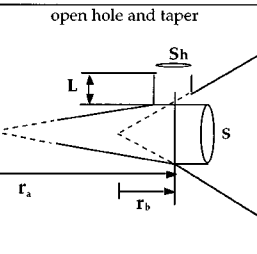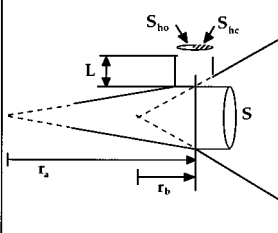
Discontinuity	a_0	$\{a_1\quad a_2\quad a_{31}\quad a_{32}\}$	$\{b_1\quad b_2\quad b_3\}$
diameter	$a_0 = \dfrac{B-1}{B+1}$ with $B = \dfrac{S_a}{S_b}$	$\{0\quad 0\quad 0\quad 0\}$	$\{0\quad 0\quad 0\}$
taper	$a_0 = 0$	$\{v\quad 0\quad 0\quad 0\}$ with $v = -\dfrac{c}{2}\left(\dfrac{1}{r_b} - \dfrac{1}{r_a}\right)$	$\{v\quad 0\quad 0\}$
diameter and taper	$a_0 = 1$	$\left\{v\dfrac{2B}{B+1}\quad 0\quad 0\quad 0\right\}$ with $B = \dfrac{S_a}{S_b}$, $v = -\dfrac{c}{B+1}\left(\dfrac{B}{r_b} - \dfrac{1}{r_a}\right)$	$\{v\quad 0\quad 0\}$

Discontinuity	a_0	$\{a_1\quad a_2\quad a_{31}\quad a_{32}\}$	$\{b_1\quad b_2\quad b_3\}$
cylindrical closed end	$a_0 = 1$	$\{0\quad 0\quad 0\quad 0\}$	$\{0\quad 0\quad 0\}$
conical closed end	$a_0 = 1$	$\{2v\quad 0\quad 0\quad 0\}$ with $v = \dfrac{c}{r_e}$	$\{v\quad 0\quad 0\}$
cylindrical open end	$a_0 = 0$	$\{0\quad 0\quad 0\quad -a^2\}$ with $a^2 = \dfrac{Ke}{d}$, $K = 267{,}5\ \mathrm{m/s}$	$\{0\quad 0\quad -a\}$
conical open end	$a_0 = 0$	$\{0\quad 0\quad 0\quad -b^2\}$ with $b = a - \dfrac{c}{2r_e}$	$\{0\quad 0\quad -b\}$

Discontinuity	a_0	$\{a_1\quad a_2\quad a_{31}\quad a_{32}\}$	$\{b_1\quad b_2\quad b_3\}$
closed hole and taper	$a_0 = -1$	$\left\{\dfrac{v_+}{\Delta}\quad -\dfrac{v_-}{\Delta}\quad 0\quad 0\right\}$ with $\Delta = \sqrt{1 - L_c\dfrac{S_h}{S}\left(\dfrac{1}{r_b} - \dfrac{1}{r_a}\right)}$ $v_\pm = \dfrac{c}{L_c}\dfrac{S}{S_h}(-1 \pm \Delta)$	$\{v_+\quad v_-\quad 0\}$
open hole and taper	$a_0 = 0$	$\{v\quad 0\quad 0\quad 0\}$ with $v = -\dfrac{c}{2L_o}\dfrac{S_h}{S} - \dfrac{c}{2}\left(\dfrac{1}{r_b} - \dfrac{1}{r_a}\right)$	$\{v\quad 0\quad 0\}$

TABLE I. (*Continued.*)

Discontinuity	a_0	$\{a_1 \quad a_2 \quad a_{31} \quad a_{32}\}$	$\{b_1 \quad b_2 \quad b_3\}$
partially open hole	$a_0 = -1$	$\left\{\dfrac{v_+}{\Delta} \quad -\dfrac{v_-}{\Delta} \quad 0 \quad 0\right\}$ $\Delta = \sqrt{1 - L_c \dfrac{S_h}{S}\left(\dfrac{1}{r_b} - \dfrac{1}{r_a}\right) - \dfrac{S_{hc}}{S}\dfrac{S_{ho}}{S}\dfrac{L_c}{L_o}}$ $v_\pm = \dfrac{c}{L_c}\dfrac{S}{S_h}(-1 \pm \Delta)$	$\{v_+ \quad v_- \quad 0\}$
anechoic hole	$a_0 = 0$	$\dfrac{c}{L_i}\left\{\dfrac{v_+(1-\beta)+v_t}{v_+ - v_-} \quad -\dfrac{v_-(1-\beta)+v_t}{v_+ - v_-} \quad 0 \quad 0\right\}$ with $v_\pm = \dfrac{c}{2L_i}\left(\beta \pm \sqrt{\beta^2 - 4\dfrac{L_i}{c}v_t}\right)$, $\beta = 1 + \dfrac{S_h}{2S} + \dfrac{L_i}{c}v_t$, $v_t = \dfrac{c}{2}\left(\dfrac{1}{r_b} - \dfrac{1}{r_a}\right)$.	$\{-v_+ \quad -v_- \quad 0\}$

cylindrical-bore result (Cardona, 1980; Martínez *et al.*, 1988a):

$$\sigma^\pm(t-L/c) = B^\pm \varepsilon(t-L/c)$$

$$\times \frac{\xi}{2\sqrt{\pi}(t-L/c)^{3/2}} e^{-\xi^2/4(t-L/c)}, \tag{4}$$

where $B^- = r_2/r_1$ and $B^+ = r_1/r_2$, such that r_1 and r_2 are the distances from the full cone apex to the input and the output section of the conical span, respectively, and $L = |r_2 - r_1|$ (Fig. 2). Function $\varepsilon(t)$ is the Heaviside step function. The damping coefficient ξ is the same as that used by Nederveen (1969), appropriate to the limit of small viscothermal damping:

$$\xi = \sqrt{2}\zeta_0 \frac{L}{c^{3/2}D_m}.$$
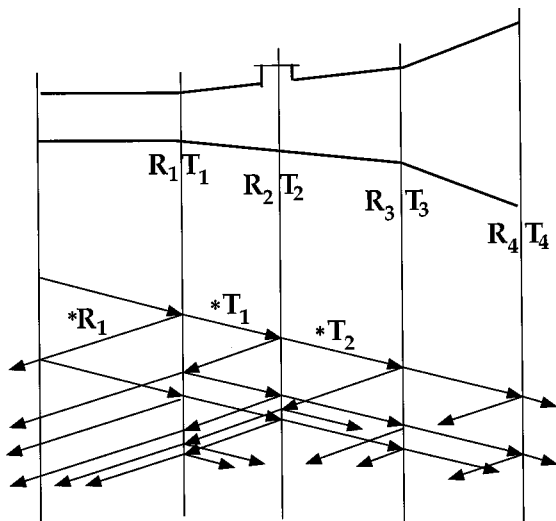
FIG. 1. Multiconvolution process.

Here D_m is the conical span mean diameter (that is, the arithmetical mean between D_1 and D_2), and ζ_0 depends upon the air density ρ, the shear viscosity η, the air thermal conductivity κ, the specific heat at constant pressure C_p, and the ratio γ between the specific heats at constant pressure and constant volume:

$$\zeta_0 = \sqrt{2}c\left\{\sqrt{\frac{\eta}{\rho c}} + (\gamma-1)\sqrt{\frac{\kappa}{\rho c C_p}}\right\}.$$

In Eq. (3), the time delay (L/c) associated with the propagation along the span is included in the propagation function. However, it is perfectly possible to consider the delay in the pressure wave:

$$p^\pm(L,t) = p^\pm(0, t-L/c) * \sigma^\pm(t).$$

This is actually how the algorithms of Martínez *et al.* and Smith work: the delay is taken into account through a shift register containing the values of pressure at uniformly spaced positions, and the damping is added only at the end of each span, at the same time as convolutions with the corresponding reflection and transmission functions associated with each discontinuity are performed.

$\dashv\!\!\wedge\!\!\wedge\!\!\wedge\!\!\vdash\rightarrow$ p_-, outward wave
$\leftarrow\!\dashv\!\!\wedge\!\!\wedge\!\!\wedge\!\!\vdash$ p_+, inward wave
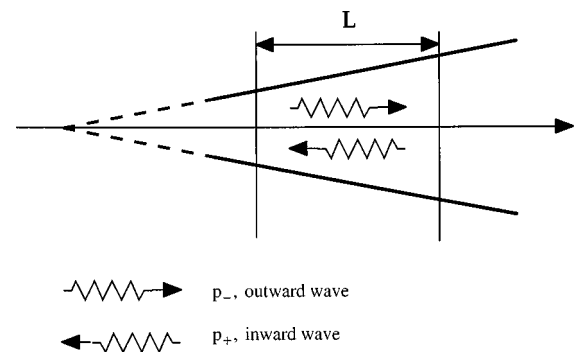
FIG. 2. Inward and outward propagating waves.
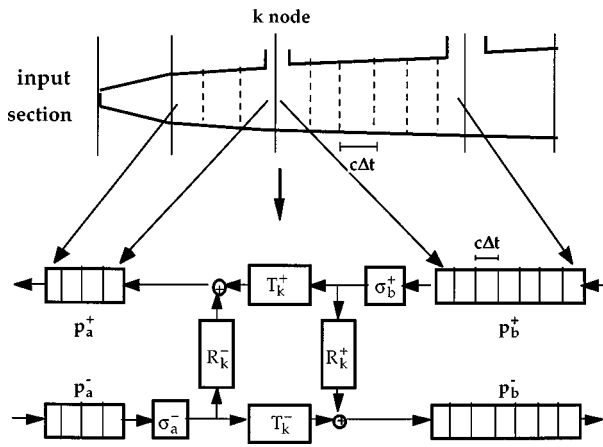
FIG. 3. Martínez multiconvolution algorithm.

This process is schematized in Fig. 3, for which the kth node discontinuity is represented by a scattering junction with four time-domain response functions: the outward-wave reflectance R_k^- and transmittance T_k^-, and the inward-wave reflectance R_k^+ and transmittance T_k^+. Only two of these functions are generally needed, because the transmittances are related to the reflectances via the Dirac delta distribution $\delta(t)$ by $T_k^-(t) = \delta(t) + R_k^-(t)$, and $T_k^+(t) = \delta(t) + R_k^+(t)$. The reflectances are simply proportional to one another for many interesting discontinuities, in which case there is only a single convolution to calculate for each of the inward and outward functions at each node. The left column of Table I lists the possible discontinuities for which a corresponding time-domain representation has been calculated.

The use of these shift registers implies a limitation on these algorithms: the time step used in the calculation has to be small enough so that the spacing between discontinuities is an integer multiple of $c\Delta t$. This constraint usually leads to sampling frequencies higher than audio rates, or else inaccuracies in modeling the waveguide structure.

II. CTIM: CONTINUOUS TIME-INTERPOLATED MULTICONVOLUTION

In the continuous time-interpolated multiconvolution (CTIM) method, the delay introduced by the spans between discontinuities is included in the propagation functions $\sigma^{\pm}(t - L/c)$. No shift registers are used, and the pressure values are only calculated at the right and left sides of each discontinuity. At every time step, four convolutions associated with the propagation functions and the reflection and transmission functions are performed.

This process is schematized in Fig. 4. The outward pressure $p_l^-(k,t)$ impinging on the kth discontinuity from the left is partially transmitted and partially reflected. Its partially transmitted component contributes to the outward pressure $p_r^-(k,t)$ on the opposite (right) side of the discontinuity. Its partially reflected component contributes to the inward pressure $p_l^+(k,t)$ on the same (left) side of the discontinuity. The inward pressure $p_r^+(k,t)$ impinging on the kth discontinuity from the right similarly contributes a transmitted component to $p_l^+(k,t)$ on the left side and a reflected component to $p_r^-(k,t)$ on the right side of the discontinuity.
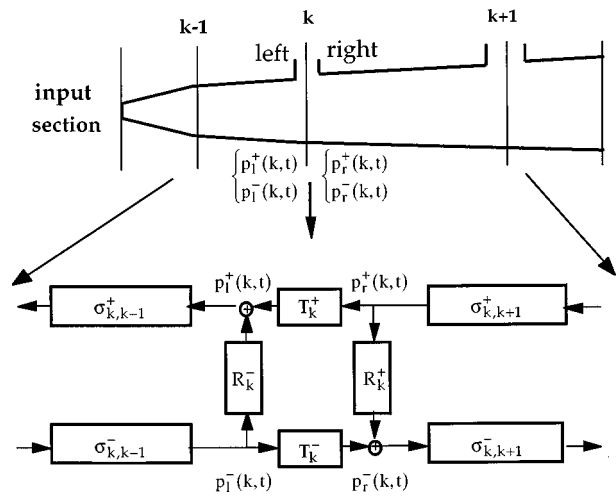
FIG. 4. The CTIM method scheme.

A. Convolutions with $R(t)$ and $T(t)$

For the particular case of a woodwind bore, the reflection and transmission functions [denoted generally by $F(t)$] associated with each discontinuity are always of the form (Martínez et al., 1988b)

$$F(t) = a_0 \delta(t) + a_1 e^{b_1 t} + a_2 e^{b_2 t} + a_{31} e^{b_3 t} + a_{32} t e^{b_3 t}$$

$$\equiv a_0 \delta(t) + \{a\}^T \{f(t)\}, \tag{5}$$

with

$$\{f(t)\}^T = \{e^{b_1 t} \quad e^{b_2 t} \quad e^{b_3 t} \quad t e^{b_3 t}\}$$

and

$$\{a\}^T = \{a_1 \quad a_2 \quad a_{31} \quad a_{32}\}.$$

The acoustic response function at a discontinuity is specified by b_1, b_2, b_3 and $\{a\}$, such that $\{a\}^T$ is the transpose of $\{a\}$.

The convolution between these functions $F(t)$ and the pressure signal will then contain a part proportional to that pressure plus a second part which allows a recursive computation:

$$p_F(t) = F(t) * p(t) = a_0 p(t) + \{a\}^T \{z(t)\},$$

$$\{z(t)\} = \{f(t)\} * p(t). \tag{6}$$

The recursion algorithm for $\{z(t)\}$ can be derived from that for $\{f(t)\}$:

$$\{f(t+\Delta t)\} = \begin{bmatrix} e^{b_1 \Delta t} & 0 & 0 & 0 \\ 0 & e^{b_2 \Delta t} & 0 & 0 \\ 0 & 0 & e^{b_3 \Delta t} & 0 \\ 0 & 0 & e^{b_3 \Delta t} \Delta t & e^{b_3 \Delta t} \end{bmatrix} \{f(t)\}$$

$$\equiv [\Theta]\{f(t)\},$$

such that $[\Theta]$ denotes the 4×4 matrix. Substitution into Eq. (6) gives

$$\{z(t+\Delta t)\} = \int_0^{t+\Delta t} \{f(t+\Delta t-\tau)\}p(\tau)\,d\tau$$

$$= [\Theta]\{z(t)\} + [\Theta]\int_t^{t+\Delta t}\{f(t-\tau)\}p(\tau)\,d\tau$$

$$= [\Theta]\{z(t)\} + [\Theta]\int_0^{\Delta t}\{f(-\tau)\}p(t+\tau)\,d\tau. \quad (7)$$

The integral in Eq. (7) can be calculated analytically assuming a polynomial approach for $p(t+\tau)$ in the interval $[0,\Delta t]$. For typical audio sample periods Δt, a linear approach is sufficient, and in that case

$$p(t+\tau) = \{(1-\tau/\Delta t) \quad \tau/\Delta t\}\begin{Bmatrix} p(t) \\ p(t+\Delta t) \end{Bmatrix}.$$

This interpolation is applied within the integrand for $p(t)$, and so is not equivalent to an interpolation between two discrete samples $z(t)$ and $z(t+\Delta t)$. While a simple linear interpolation in the discrete-time sequence would lead to significant errors, the linear interpolation within the integrand preserves the accuracy of the convolution with the short-time response of the system. This technique has been successfully used by Barjau *et al.* (1990) and Martínez *et al.* (1988a).

Substitution of this linear approach into Eq. (7) leads to

$$\{z(t+\Delta t)\} = [\Theta]\{z(t)\} + [\Theta][\tilde{\Theta}]\begin{Bmatrix} p(t) \\ p(t+\Delta t) \end{Bmatrix}$$

with

$$[\tilde{\Theta}] = \frac{1}{\Delta t}\begin{bmatrix} \frac{1}{b_1^2}\{(b_1\Delta t-1)+e^{-b_1\Delta t}\} & \frac{1}{b_1^2}\{1-(1+b_1\Delta t)e^{-b_1\Delta t}\} \\ \frac{1}{b_2^2}\{(b_2\Delta t-1)+e^{-b_2\Delta t}\} & \frac{1}{b_2^2}\{1-(1+b_2\Delta t)e^{-b_2\Delta t}\} \\ \frac{1}{b_3^2}\{(b_3\Delta t-1)+e^{-b_3\Delta t}\} & \frac{1}{b_3^2}\{1-(1+b_3\Delta t)e^{-b_3\Delta t}\} \\ \frac{2}{b_3^3}\left\{\left(1-\frac{b_3\Delta t}{2}\right)-\left(1+\frac{b_3\Delta t}{2}\right)e^{-b_3\Delta t}\right\} & \frac{2}{b_3^3}\left\{1-\left[1+b_3\Delta t+\frac{1}{2}(b_3\Delta t)^2\right]e^{-b_3\Delta t}\right\} \end{bmatrix}.$$

The final algorithm to calculate $p_F(t+\Delta t)$ is then

$$p_F(t+\Delta t) = a_0 p(t+\Delta t) + \{a\}^T\{z(t+\Delta t)\},$$

$$\{z(t+\Delta t)\} = [\Theta]\{z(t)\} + [A]\begin{Bmatrix} p(t) \\ p(t+\Delta t) \end{Bmatrix}, \quad (8)$$

with $[A] = [\Theta][\tilde{\Theta}]$.

If a Nth-order polynomial is chosen for $p(t+\tau)$ in $[0,\Delta t]$, the recursion for $\{z(t+\Delta t)\}$ contains $(N+1)$ pressure values: $\{p(t-(N-1)\Delta t) \quad \cdots \quad p(t) \quad p(t+\Delta t)\}^T$, and the $[\tilde{\Theta}]$ matrix is more complicated.

For each kind of discontinuity, all the values in $\{a\}^T$, $[\Theta]$, and $[A]$ are calculated once and stored before starting the simulation. Thus, the computation becomes extremely fast. Moreover, only a few pressure values have to be stored at the discontinuities, so that computer memory requirements are modest.

To calculate the inward pressure wave at the left-hand side of discontinuity k (in Fig. 4), the convolutions are

$$p_l^+(k,t) = T_k^+(t)*p_r^+(k,t) + R_k^-(t)*p_l^-(k,t). \quad (9a)$$

For the outward pressure wave at the right-hand side of the same discontinuity, the calculation is

$$p_r^-(k,t) = T_k^-(t)*p_l^-(k,t) + R_k^+(t)*p_r^+(k,t). \quad (9b)$$

Actually, it is not always necessary to perform four convolutions [as Eqs. (9a) and (9b) suggest] at each discontinuity. As pointed out before, whenever the pressure is continuous across the junction, the reflectances $R^\pm(t)$ and the transmittances $T^\pm(t)$ are related through a Dirac distribution $\delta(t)$, and so only two convolutions are required. Furthermore, the number of convolutions can be reduced to one when both sides of the node are cylindrical, as in that case $R^+(t) = R^-(t) = R(t)$. This type of simplification has been discussed by Välimäki *et al.* (1993).

As all convolutions in Eqs. (9a) and (9b) are of the recursive type, if a linear approach is used for the pressure, only the current and previous values of $p_l^-(k,t)$ and $p_r^+(k,t)$ are required.

For the usual discontinuities found in woodwinds and for a linear approach for $p(t+\tau)$, the values of $\{a\}$ and $\{b\}$
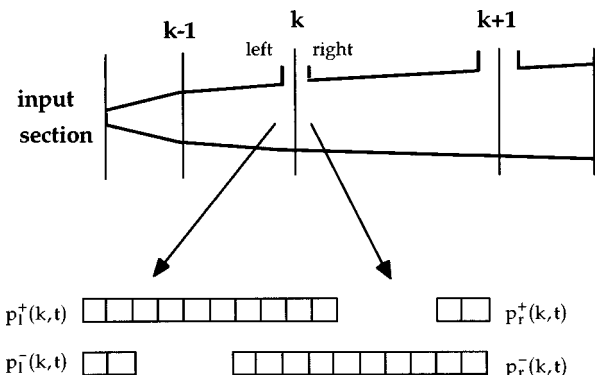
FIG. 5. Required pressure values at the left- and the right-hand sides of a discontinuity.
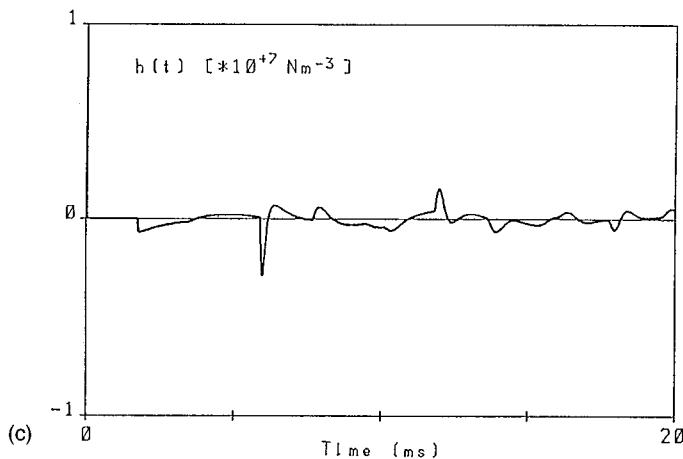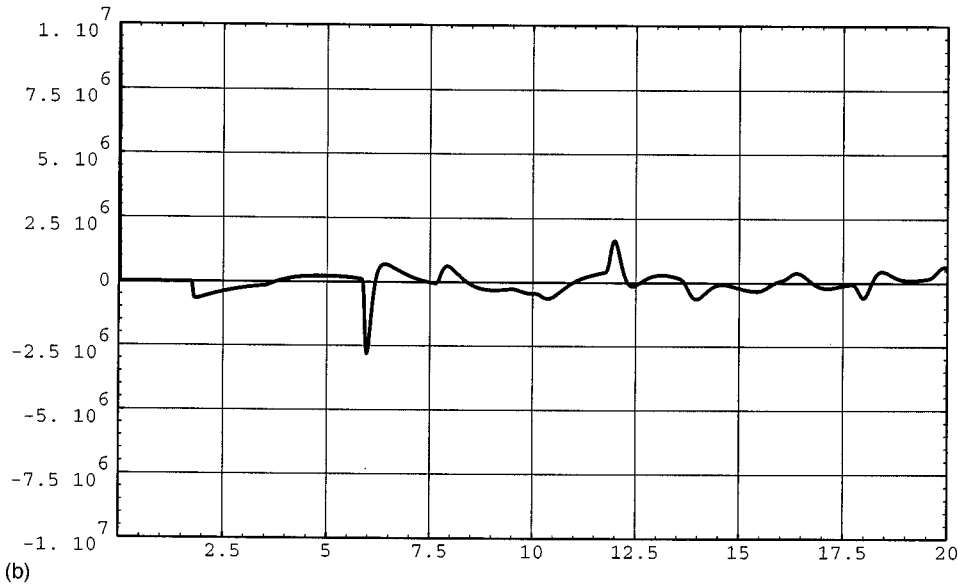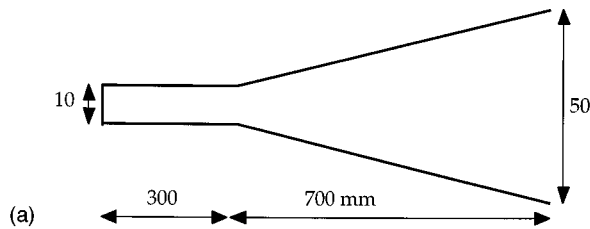
FIG. 6. Geometry (a) of a bore and impulse response $h(t)$ at its entrance section obtained (b) through CTIM and (c) through the multiconvolution algorithm of Martínez *et al.*

defined in Eq. (5) for the case $F(t) = R^-(t)$ (reflection function) are presented in Table I.

B. Convolution with the propagation functions

The convolution with the propagation functions is not of the recursive type, and thus longer pressure records are required.

When calculating the inward and outward waves at discontinuities $(k-1)$ and $(k+1)$, respectively, from $p_l^+(k,t)$ and $p_r^-(k,t)$, the following convolutions are needed:

$$p_l^-(k+1,t) = p_r^-(k,t) * \sigma_{k,k+1}^-(t - L_{k,k+1}/c),$$

$$p_r^+(k-1,t) = p_l^+(k,t) * \sigma_{k,k-1}^+(t - L_{k,k-1}/c),$$

(10)

where $L_{k,k-1}$ and $L_{k,k+1}$ are the distances between discontinuities $k,k-1$ and $k,k+1$ respectively. Though Eqs. (10) may suggest that there are two different propagation functions for each span (the outward one and the inward one), actually these functions are either equal, if the span is a cylindrical one, or proportional through the factors $B_\pm$ defined in Eq. (4) if it is a conical one:

$$\sigma_{k,k-1}^+(t) = \sigma_{k-1,k}^-(t) \quad \text{for the cylindrical span,}$$

$$\sigma_{k,k-1}^+(t) = (B_+/B_-)\sigma_{k-1,k}^-(t) \quad \text{for the conical span.}$$

It is clear then that longer time histories of $p_r^-(k,t)$ and $p_l^+(k,t)$ need to be known over durations for which the propagation function responses are non-negligible. This non-symmetrical storage of pressure values at both sides of each
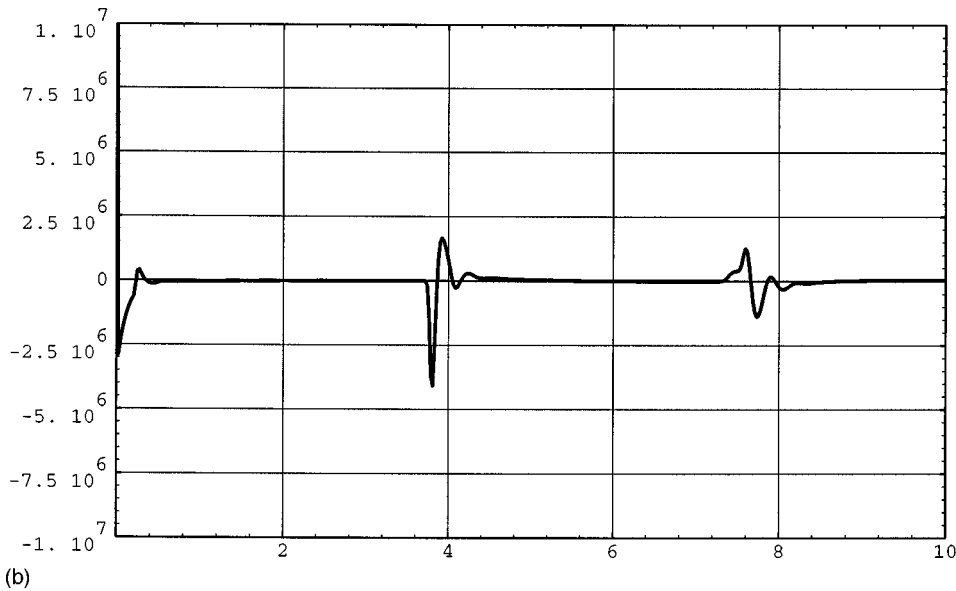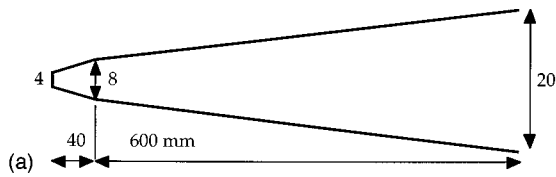
FIG. 7. Geometry (a) of a bore and impulse response $h(t)$ at its entrance section obtained (b) through CTIM and (c) through the multiconvolution algorithm of Martínez *et al.*
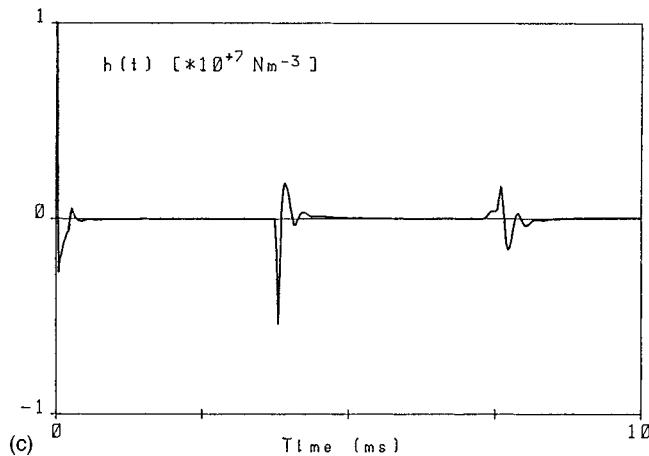
discontinuity is represented in Fig. 5 by a longer list of samples stored for p_r^- and p_l^+ as contrasted with the two samples stored for p_l^- and p_r^+.

There is a particularly interesting point concerning these convolutions in Eq. (10). As the calculation is a numerical one, the time t will be some multiple of the sample period, $t = n\Delta t$. Defining the propagation delay from node k to $k+1$ to be $T_{k,k+1} \equiv L_{k,k+1}/c$ and that from node $k-1$ to k to be $T_{k,k-1} \equiv L_{k,k-1}/c$, and taking into account that $\sigma_{k,k+1}^-(t - T_{k,k+1}) = 0$ if $t < T_{k,k+1}$, and that $\sigma_{k,k-1}^+(t - T_k) = 0$ if $t < T_{k,k-1}$, the convolutions in Eq. (10) can be written as

$$p_l^-(k+1, n\Delta t) = \int_{T_{k,k+1}}^{n\Delta t} p_r^-(k, n\Delta t - \tau)$$
$$\times \sigma_{k,k+1}^-(\tau - T_{k,k+1}) \, d\tau, \qquad (11a)$$

$$p_r^+(k-1, n\Delta t) = \int_{T_{k,k-1}}^{n\Delta t} p_l^+(k, n\Delta t - \tau)$$
$$\times \sigma_{k,k-1}^+(\tau - T_{k,k-1}) \, d\tau, \qquad (11b)$$

and so the whole time histories of $p_r^-(k,t)$ and $p_l^+(k,t)$ in the time intervals $[0, n\Delta t - T_{k,k+1}]$ and $[0, n\Delta t - T_{k,k-1}]$, respectively, would seem to be needed. This is not the case in applications to musical instrument air columns for which the propagation functions between nodes are of short duration, thus limiting the range of integration times.

In order to maintain a causal response, the convolutions at each node need to be carried out in a causal order. The outward pressures $P_l^-(k,t)$ at each of the nodes are calculated from Eq. (11a) from left to right along the waveguide, beginning at the input end of the waveguide and ending at the output end of the waveguide (the bell of a musical instru-
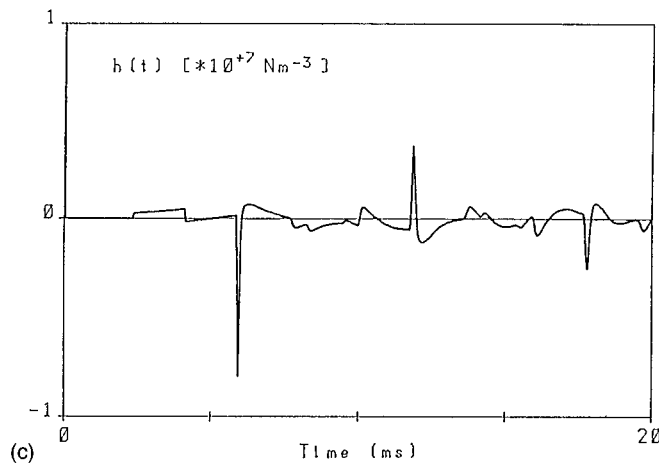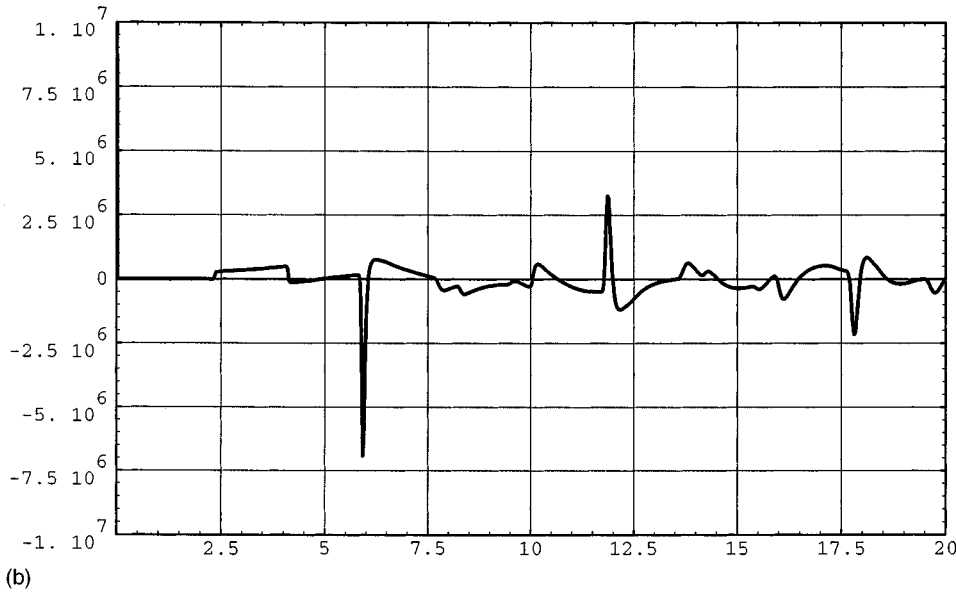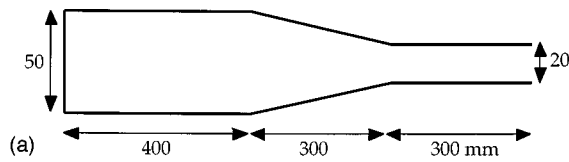
FIG. 8. Geometry (a) of a bore and impulse response $h(t)$ at its entrance section obtained (b) through CTIM and (c) through the multiconvolution algorithm of Martínez *et al.*

ment). The inward pressures $p_r^+(k,t)$ at each of the nodes are calculated from Eq. (11b) from right to left along the waveguide, beginning at the output and of the waveguide and ending at the input end.

III. RESULTS WITH CTIM

Several tubes have been calculated by means of CTIM, and the results have been compared to those obtained through the multiconvolution of Martínez *et al.*

Figures 6(a), 7(a), and 8(a) show the geometries of three bores, the last two showing discontinuities whose associated reflection functions contain growing exponentials (Agulló, 1992). For the case in Fig. 6(a), the algorithm of Martínez *et al.* (which requires that the spacing between discontinuities is a multiple of $c\Delta t$) would have implied the use of a minimum of 21 nodes (or points of calculation in the pressure registers). In that case, the associated time resolution would have been of $\Delta t \approx 1$ ms. To reach a $\Delta t \approx (1/44.1)$ ms

(which is the time step used in CTIM), it would have been necessary to refine the spatial resolution and go up to 924 nodes. With CTIM, only three nodes are strictly necessary.

For the tube in Fig. 7(a), CTIM also uses 3 nodes instead of 1452 required to attain $\Delta t \approx (1/44.1)$ ms in the multiconvolution of Martínez, and for the tube in Fig. 8(a), the nodes reduction is from 484 to 4 in CTIM. The capacity requirements are then greatly reduced.

Figures 6(b), 7(b), and 8(b) show the corresponding results with CTIM, and Figs. 6(c), 7(c), and 8(c) those obtained by Martínez (1988b). It is clear that no accuracy has been lost with CTIM compared to the Martínez multiconvolution, a result which is consistent with our theoretical formulation.

IV. CONCLUSIONS

The CTIM algorithm makes possible an exact time-domain simulation of the response of an acoustical wave-

guide with discontinuities that are at arbitrary locations on the waveguide, subject only to the approximations of linear acoustics, small viscothermal wall loss, and a sufficiently high sample rate. The CTIM algorithm removes the restriction that discontinuities be located at spatial distances that are multiples of $c\Delta t$, and this property of CTIM has been confirmed by numerical analysis. For the case of musical instrument air columns constructed by joining a set of cylindrical-bore or conical-bore segments, the CTIM enables simulations of the process of sound transmission purely in the time domain. As such, CTIM is well suited to computational modeling of wind instruments, and is a basis for digital sound synthesis via physical modeling.

A unified time-domain description of the acoustic response of tone holes has been obtained. For both open and closed tone holes, the time-domain responses include details of tone-hole models that are useful for applications to musical instruments. The model of an anechoically terminated tone hole is relevant to CTIM algorithms in which the tone hole is modeled as a subsidiary waveguide with multiconvolution nodes at either end of the waveguide.

APPENDIX: ACOUSTICAL REPRESENTATION OF TONE-HOLE DISCONTINUITIES IN THE TIME DOMAIN

1. Introduction

This appendix describes the calculation of the reflection and transmission functions of tone-hole discontinuities based upon the use of a time-domain approach adapted from Agulló *et al.* (1992). Attention is restricted to the case that only a single propagating mode exists in the main air column and the tone hole, which sets upper limits on the maximum diameters of the air column and tone hole for a given signal bandwidth. These upper limits are not a concern in applications of this theory to musical wind instruments. The reflection and transmission functions calculated in this Appendix are used in the CTIM procedure as further set forth in Table I.

Two approaches are considered. The first one models the tone hole as a lumped acoustic element. This approach is valid when the tone-hole length is sufficiently short that there is no need to take account of the time delay for propagation down to the end of the tone hole and back. The second approach models the tone hole as a subsidiary waveguide, and it is useful whenever the hole length is sufficiently large.

In the first case, the corresponding reflectances are global functions which describe the behavior of the whole side branch. For an open hole, this behavior is approximately that of a pure inertance, while for a closed one, it approximately corresponds to a pure compliance. These behaviors are mathematically expressed through the following expressions relating acoustical pressure and velocity at the hole entrance section:

$$\frac{dp_h(t)}{dt} = \frac{\rho c^2}{L_c} v_h(t) \quad \text{(closed hole)}, \tag{A1}$$

$$p_h(t) = \rho L_o \frac{dv_h(t)}{dt} \quad \text{(open hole)}, \tag{A2}$$

where the effective tone-hole length L_c is the ratio of the enclosed volume of the tone hole to its surface area, and L_o is the sum of the hole length plus the radiative equivalent length.

In the second case, the transmission and reflection functions are local ones, and so independent of the particular end condition of the hole (or side branch). The hole is thus considered as an anechoic branch, and the reflections taking place at its end have to be calculated in a similar way to that of a simple waveguide. If the hole is a cylindrical one, this anechoic condition is mathematically expressed as

$$p_h(t) = \rho c v_h(t). \tag{A3}$$

In the previous equations, the localized disturbances in the three-dimensional acoustic field under the tone hole are not taken into account. A better model results when introducing them through two inertance corrections: (1) a positive junction inertance between the main waveguide and the tone hole, which accounts for a localized flow disturbance in the neighborhood of the junction, and (2) a negative inertance, which takes into account the stretching of the streamlines into the inner junction of the tone hole, and thus a local reduction of the kinetic energy density within the main waveguide. The junction inertance is represented as an inner equivalent length L_i, and the open-hole and closed-hole expressions relating acoustical pressure and velocity generalize to

$$\frac{dp_h(t)}{dt} = \frac{\rho c^2}{L_c} v_h(t) + \rho L_i \frac{dv_h(t)}{dt} \quad \text{(closed hole)}, \tag{A4}$$

$$p_h(t) = \rho L_o \frac{dv_h(t)}{dt} + \rho L_i \frac{dv_h(t)}{dt} \quad \text{(open hole)}. \tag{A5}$$

It is obvious that the junction inertance contribution for the open hole can be included by redefining L_o as $L_o + L_i$, and this modification is assumed in the following. Adding the junction inertance for the anechoic tone hole generalizes Eq. (A3) to the following form:

$$p_h(t) = \rho c v_h(t) + \rho L_i \frac{dv_h(t)}{dt}. \tag{A6}$$

The negative inertance may be included in a generalized tone-hole model, but it is simpler to include it as a modification of the existing model. As a first effect, the negative inertance produces a slight reduction in the length of each of the main waveguide sections on either side of the tone hole with no significant loss of accuracy (for musical wind instrument geometries). This length reduction differs slightly as whether the tone hole is closed, open, or anechoic, but it is a straightforward adjustment of each of the main waveguide lengths in each case. As a second effect, the presence of the negative inertance slightly reduces L_i in Eqs. (A4)–(A6) for the closed, open, and anechoic tone holes, respectively. We assume that this adjustment has been carried out for each of the main waveguide sections. The detailed description of the theory and experiments underlying the evaluation of these inertances can be found in [Nederveen (1963), Keefe (1982a, b, 1990) and Dubos (1998)].
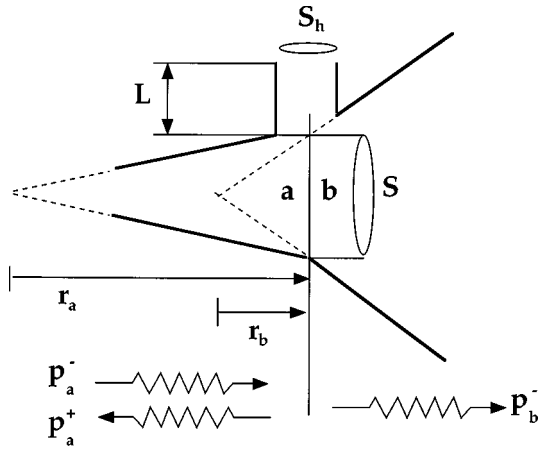
FIG. A1. The geometry for a single tone hole of area S_h located at the junction of a left conical span ''a'' and right conical span ''b.'' The conical spans have the same area S at the tone-hole location but arbitrary tapers. The origin of conical span ''a'' is located a distance r_a from the tone hole and that for conical span ''b'' is located a distance r_h away. Each of these distances may be positive or negative in value corresponding to an conical-span origin to the left or right of the tone hole. An incoming wave p_a^- to the tone-hole discontinuity results in a partially reflected wave p_a^+ and partially transmitted wave p_b^-.

2. The tone hole as a localized waveguide discontinuity

A single tone hole of cylindrical cross-sectional area S_h and height L is joined to an air column composed of conical or cylindrical segments, such that the coordinate r measures distance along the air column. The most general condition is such that the conical span just to the left (towards the input end of the waveguide with variables identified by superscript ''a'') and the conical span just to the right (towards the output end of the waveguide with variables identified by superscript ''b'') of the tone hole have different conical tapers but the same bore diameter at the mid-point location of the tone hole, as indicated in Fig. A1. The distance from the hypothetical apex of conical span ''a'' to the tone hole is $r_a = r_a^0$, and the corresponding distance for conical span ''b'' is $r_b = r_b^0$. From now on, r_a^0 and r_b^0 will be called simply r_a and r_b.

Assuming that pressure waves are spherical at both sides of the hole, the pressure and linear velocity waves at sides ''a'' and ''b'' of the discontinuity can be obtained from the velocity potential $\phi(r,t)$ satisfying the wave equation in spherical coordinates:

$$\frac{1}{c^2}\frac{\partial^2 \phi(r,t)}{\partial t^2} - \frac{2}{r}\frac{\partial \phi(r,t)}{\partial r} - \frac{\partial^2 \phi(r,t)}{\partial r^2} = 0,$$

(A7)

$$p(r,t) = \frac{\partial \phi(r,t)}{\partial t}, \quad v(r,t) = -\frac{1}{\rho}\frac{\partial \phi(r,t)}{\partial r},$$

where ρ is the air density and ''r'' is the longitudinal coordinate along the bore (see Fig. A1), measured in a conical-bore span from its virtual apex.

The general solution for the velocity potential $\phi(r,t)$ relative to a reference location r_0 is

$$\phi(r,t) = \frac{1}{r}[\psi^+(t+(r-r_0)/c) + \psi^-(t-(r-r_0)/c)]$$

$$\equiv \frac{1}{r}[\psi^+(\tau^+) + \psi^-(\tau^-)],$$

(A8)

where $\tau^\pm = t \pm (r-r_0)/c$, and ψ^+ and ψ^- are reduced potential functions corresponding to leftward and rightward waves traveling in the conical span.

In order to determine the particular form of these propagation functions, it is necessary to assume the particular initial and boundary conditions associated with the specific problem to be solved. In the present case, the air column is considered to be at rest for $t<0$, and a pressure impulse of unit strength is assumed to reach the duct section where the hole is located from the left-hand side (span ''a'') at $t=0$.

When calculating the elementary reflection or transmission functions associated to a discontinuity, the duct at either side is assumed to behave as an anechoic termination (Agulló et al., 1988). For the case of the tone hole in Fig. A1, this implies that only a rightward wave is present in span ''b'' at the rhs of the discontinuity, corresponding to the transmitted wave in the main waveguide, while both rightward (inicident) and leftward (reflected) waves will be present in span ''a'' at the lhs of the hole. These boundary conditions together with the initial conditions given in the previous paragraph are expressed mathematically as follows:

$$\phi_{\mathrm{lhs}}(r_a,t) \equiv \phi_a(t) = \frac{1}{r_a}[\psi_a^+(\tau^+) + \psi_a^-(\tau^-)]_{r=r_a}$$

$$= \frac{1}{r_a}[\psi_a^+(t) + \psi_a^-(t)],$$

(A9)

$$\phi_{\mathrm{rhs}}(r_b,t) \equiv \phi_b(t) = \frac{1}{r_b}[\psi_b^-(\tau^-)]_{r=r_b} = \frac{1}{r_b}\psi_b^-(t).$$

$$\phi_{a,b}(r,t) = 0 \quad \text{for } t<0 \quad \text{and } \forall r,$$

(A10)

$$\frac{1}{r}\left[\frac{\partial \psi_a^-(r,t)}{\partial t}\right]_{r_a} = q\,\delta(t).$$

From the last equation, it follows that $\psi_a^-(r,t) = r_a q \varepsilon(t)$, where $\varepsilon(t)$ is the Heaviside step function.

The continuity of flow equation is expressed by

$$Sv_a(t) = Sv_b(t) + S_h v_h(t).$$

(A11)

If the negative inertance corrections are included into slightly reduced main waveguides sections on either side of the tone hole, the pressure can be considered uniform over the hole section S_h and equal to the pressure value at both sides of the discontinuity:

$$p_a(t) = p_b(t) = p_h(t).$$

(A12)

These last two equations can be rewritten using Eq. (A9) as

$$\frac{1}{r_a}\frac{d\psi_a^+(t)}{dt}+q\,\delta(t)=\frac{1}{r_b}\frac{d\psi_b^-(t)}{dt}=p_h(t),$$

$$\frac{1}{r_a}\left[-\frac{d\psi_a^+(t)}{dt}+\frac{c}{r_a}\psi_a^+(t)\right]+q\,\delta(t)+\frac{c}{r_a}\varepsilon(t)$$

$$=\frac{1}{r_b}\left[\frac{d\psi_b^-(t)}{dt}+\frac{c}{r_b}\psi_b^-(t)\right]+\frac{S_h}{S}\rho c v_h(t).$$

(A13)

Because the incident pressure signal in span ''a'' is taken to be an impulse, the reflected pressure signal back into span ''a'' is the reflection function $R_h(t)$ and the transmitted pressure signal into span ''b'' is the transmission function T_h. These are mathematically expressed by

$$R_h(t)=\frac{1}{q}p_a^+(t)=\frac{1}{q}\frac{1}{r_a}\frac{d\psi_a^+(t)}{dt},$$

$$T_h(t)=\frac{1}{q}p_b^-(t)=\frac{1}{q}\frac{1}{r_b}\frac{d\psi_b^-(t)}{dt}.$$

(A14)

The first condition in Eq. (A13) takes the form

$$R_h(t)=-\delta(t)+T_h(t).$$

(A15)

This equation is integrated with the result

$$\frac{1}{r_a}\psi_a^+(t)=-\varepsilon(t)+\frac{1}{r_b}\psi_b^-(t).$$

(A16)

Eliminating $\psi_a^+(t)$ and its derivative from the remaining pair of conditions in Eq. (A13) leads to

$$\frac{1}{2}\rho c A_h v_h(t)+\frac{1}{r_b}\frac{d\psi_b^-(t)}{dt}+v_t\frac{1}{r_b}\psi_b^-(t)=q\,\delta(t),\quad(A17)$$

where the taper attenuation factor v_t and the area ratio A_h are

$$v_t=\frac{c}{2}\left(\frac{1}{r_b}-\frac{1}{r_a}\right),\quad A_h=\frac{S_h}{S}.$$

(A18)

The taper attenuation factor differs from zero only when there is a discontinuity in conical taper directly at the location of the tone hole, which includes the case of a transition from cylindrical to conical span.

a. Open hole

If the hole is open, Eqs. (A2) and (A17) can be combined to give a first-order differential equation for $\psi_b^-(t)$:

$$\frac{1}{r_b}\frac{d\psi_b^-(t)}{dt}+(v_o+v_t)\frac{1}{r_b}\psi_b^-(t)=q\,\delta(t),$$

(A19)

where the open-hole attenuation factor v_o is

$$v_o=\frac{c}{2}\frac{A_h}{L_o}.$$

(A20)

The length L_o includes the effect of the inner junction inertance.

The reflection and transmission functions are

$$R_h(t)=-(v_o+v_t)e^{-(v_o+v_t)t}\varepsilon(t),$$

$$T_h(t)=\delta(t)-(v_o+v_t)e^{-(v_o+v_t)t}\varepsilon(t).$$

(A21)

It is rare for a tone hole to be exactly placed at a discontinuity in taper, so that the following expressions are more typically used:

$$R_h(t)=-v_o e^{-v_o t}\varepsilon(t),\quad T_h(t)=\delta(t)-v_o e^{-v_o t}\varepsilon(t).$$

(A22)

b. Closed hole

Neglecting the inner junction inertance correction and combining Eq. (A1) with Eq. (A17) results in a second-order differential equation:

$$\frac{1}{v_c}\frac{1}{r_b}\frac{d^2\psi_b^-(t)}{dt^2}+\frac{1}{r_b}\frac{d\psi_b^-(t)}{dt}+v_t\frac{1}{r_b}\psi_b^-(t)=q\,\delta(t),\quad(A23)$$

where the closed-hole attenuation coefficient is

$$v_c=\frac{2c}{A_h L_c}.$$

(A24)

The eigenvalues of the homogeneous equation are

$$v_\pm=\frac{v_c}{2}(-1\pm\Delta)\quad\text{with}\quad\Delta=\sqrt{1-(4v_t/v_c)}.\quad(A25)$$

The potential $\psi_b^-(t)$ is a superposition of exponential functions, and its time derivative yields the transmission function

$$T_h(t)=\frac{1}{qr_b}\frac{d\psi_b^-(t)}{dt}=\frac{1}{\Delta}(v_+ e^{v_+ t}-v_- e^{v_- t})\varepsilon(t).\quad(A26)$$

In the absence of taper discontinuity at the tone-hole location, the eigenvalues simplify to

$$v_+=0,\quad v_-=-v_c,$$

and the transmission function becomes

$$T_h(t)=v_c e^{-v_c t}\varepsilon(t).$$

(A27)

The reflection function in both cases is obtained from

$$R_h(t)=T_h(t)-\delta(t).$$

For the closed tone hole, it is important to include the negative inertance in the adjustment of the lengths of the main waveguide sections on either side, because the effects are significant for musical wind instruments. For closed holes with a sufficiently short length L_c, the term involving the inner junction inertance in Eq. (A4) is not significant and can be neglected.

c. Anechoic tone hole

As the closed hole length increases, the time delay for round-trip wave propagation within the tone hole becomes sufficiently long that the lumped-element model of the tone hole is no longer appropriate. This means that the anechoic tone hole model should be adopted, and the inner junction inertance should be retained in this model via Eq. (A6).

Combining this equation with the junction conditions in Eqs. (A11) and (A12) results in the following system of equations:

1962   J. Acoust. Soc. Am., Vol. 105, No. 3, March 1999

Barjau *et al.*: Simulation of acoustical waveguides   1962

$$\frac{1}{r_b}\frac{d\psi_b^-(t)}{dt} = \rho c v_h(t) + \rho L_i \frac{dv_h(t)}{dt},$$

$$\frac{1}{r_b}\frac{d\psi_b^-(t)}{dt} + \frac{\nu_t}{r_b}\psi_b^-(t) + \frac{1}{2}A_h\rho c v_h(t) = q\,\delta(t). \tag{A28}$$

These equations can be rewritten in matrix form as

$$\begin{bmatrix} \rho L_i & -1 \\ 0 & 1 \end{bmatrix}\begin{Bmatrix} \dfrac{dx(t)}{dt} \\ \dfrac{dy(t)}{dt} \end{Bmatrix} + \begin{bmatrix} \rho c & 0 \\ \rho c\,\dfrac{A_h}{2} & \nu_t \end{bmatrix}\begin{Bmatrix} x(t) \\ y(t) \end{Bmatrix} = \begin{Bmatrix} 0 \\ q\,\delta(t) \end{Bmatrix}, \tag{A29}$$

or

$$\begin{Bmatrix} \dfrac{dx(t)}{dt} \\ \dfrac{dy(t)}{dt} \end{Bmatrix} + \begin{bmatrix} \dfrac{c}{L_i}\left(1+\dfrac{A_h}{2}\right) & \dfrac{\nu_t}{\rho L_i} \\ \rho c\,\dfrac{A_h}{2} & \nu_t \end{bmatrix}\begin{Bmatrix} x(t) \\ y(t) \end{Bmatrix} = \begin{Bmatrix} \dfrac{q}{\rho L_i}\,\delta(t) \\ q\,\delta(t) \end{Bmatrix}, \tag{A30}$$

where we have defined $y(t)=(1/r_b)(d\psi_b^-(t)/dt)$ and $x(t)=v_h(t)$ in order to simplify the notation.

These equations can be decoupled through a diagonalization process of the matrix appearing in Eq. (A30) (which will be called $[D]$). The new variables satisfy the homogeneous matrix equation:

$$\begin{Bmatrix} \dfrac{du(t)}{dt} \\ \dfrac{dz(t)}{dt} \end{Bmatrix} + \begin{bmatrix} \nu_+ & 0 \\ 0 & \nu_- \end{bmatrix}\begin{Bmatrix} u(t) \\ z(t) \end{Bmatrix} = \begin{Bmatrix} 0 \\ 0 \end{Bmatrix}, \tag{A31}$$

where ν_+, ν_- are the eigenvalues of $[D]$:

$$\nu_\pm = \frac{c}{2L_i}(\beta\pm\Delta) \quad \text{with} \quad \beta = 1 + \frac{A_h}{2} + \nu_t\frac{L_i}{c},$$

$$\Delta = \sqrt{\beta^2 - 4\frac{L_i}{c}\nu_t}.$$

The old variables are related to the new ones through the matrix

$$\begin{Bmatrix} x(t) \\ y(t) \end{Bmatrix} = \begin{bmatrix} \dfrac{2}{\rho c A_h}(\nu_+ - \nu_t) & \dfrac{2}{\rho c A_h}(\nu_- - \nu_t) \\ 1 & 1 \end{bmatrix}\begin{Bmatrix} u(t) \\ z(t) \end{Bmatrix}$$

$$\equiv [S]\begin{Bmatrix} u(t) \\ z(t) \end{Bmatrix}. \tag{A32}$$

The solution of Eq. (A31) is straightforward:

$$\begin{Bmatrix} u(t) \\ z(t) \end{Bmatrix} = \begin{Bmatrix} u(0)e^{-\nu_+ t}\varepsilon(t) \\ z(0)e^{-\nu_- t}\varepsilon(t) \end{Bmatrix}, \tag{A33}$$

and the initial values $u(0)$, $z(0)$ are determined by imposing the initial conditions in Eq. (A30):

$$[S]\begin{Bmatrix} -\nu_+ u(0)\varepsilon(t)+u(0)\,\delta(t) \\ -\nu_- z(0)\varepsilon(t)+z(0)\,\delta(t) \end{Bmatrix} + [D][S]\begin{Bmatrix} u(0)\varepsilon(t) \\ z(0)\varepsilon(t) \end{Bmatrix}$$

$$= \begin{Bmatrix} \dfrac{q}{\rho L_i}\,\delta(t) \\ q\,\delta(t) \end{Bmatrix}.$$

The transmission function $T_h(t)=(1/q)(dy(t)/dt)$ and the reflection function $R_h(t)$ are then

$$T_h(t) = \delta(t) + \frac{(c/L_i)}{\nu_+ - \nu_-}[(\nu_+(1-\beta)+\nu_t)e^{-\nu_+ t}$$

$$- (\nu_-(1-\beta)+\nu_t)e^{-\nu_- t}]\varepsilon(t),$$

$$R_h(t) = \frac{(c/L_i)}{\nu_+ - \nu_-}[(\nu_+(1-\beta)+\nu_t)e^{-\nu_+ t}$$

$$- (\nu_-(1-\beta)+\nu_t)e^{-\nu_- t}]\varepsilon(t).$$

If there is no taper discontinuity at the location of the anechoic tone hole ($\nu_t=0$), then these functions simplify to

$$T_h(t) = \delta(t) + \frac{c}{L_i}(1-\beta)e^{-c\beta t/L_i}\varepsilon(t),$$

$$R_h(t) = \frac{c}{L_i}(1-\beta)e^{-c\beta t/L_i}\varepsilon(t),$$

and, in the limit that the junction inertance is neglected ($L_i=0$), these relations become

$$T_h(t) = \frac{1}{\beta}\,\delta(t), \quad R_h(t) = \frac{1-\beta}{\beta}\,\delta(t).$$

If there is a taper discontinuity but the junction inertance is neglected, Eqs. (A28) reduce to a first-order differential one:

$$\left(1+\frac{A_h}{2}\right)\frac{dy(t)}{dt} + \nu_t y(t) = \beta\frac{dy(t)}{dt} + \nu_t y(t) = q\,\delta(t), \tag{A34}$$

and the transmission function is

$$T_h(t) = \frac{1}{q}\frac{dy(t)}{dt} = \frac{1}{\beta}\,\delta(t) - \frac{\nu_t}{\beta^2}e^{-(\nu_t/\beta)t}\varepsilon(t). \tag{A35}$$

[1] In recently presented work, van Walstijn and Smith (1998) state that a digital waveguide composed of a set of conical-bore segments can be modeled using a truncated infinite impulse response (TIIR) approach in which numerical instabilities are avoided. The feasibility and accuracy of the TIIR approach in this application have yet to be assessed.

Agulló, J., Barjau, A., and Martínez, J. (**1988**). ''Alternatives to the impulse response $h(t)$ to describe the acoustical behavior of conical ducts,'' J. Acoust. Soc. Am. **84**, 1606–1612.

Agulló, J., Barjau, A., and Martínez, J. (**1992**). ''On the time-domain description of conical bores,'' J. Acoust. Soc. Am. **91**, 1089–1105.

Barjau, A., Cardona, S., and Keefe, D. (**1992**) ''Multiconvolution in waveguides with arbitrarily spaced discontinuities,'' J. Acoust. Soc. Am. **91**, 2374(A).

Barjau, A., Cardona, S., and Jordi, L. (**1990**). ''Fast simulation of the internal pressure in a double-reed woodwind,'' *Colloque international sur les modèles physiques dans l'analyse, la production et la création sonore* (Maison des Sciences de l'Homme, Paris), Vol. 13, pp. 159–178.

Cardona, S. (**1980**). ''Contribució a l'estudi de l'acústica de la tenora, Ph.D. thesis, Universitat Politècnica de Catalunya, Barcelona, Spain.

1963 J. Acoust. Soc. Am., Vol. 105, No. 3, March 1999

Barjau *et al.*: Simulation of acoustical waveguides 1963

Dubos, V., Kergomard, J., Khettabi, A., Dalmont, J.-P., Keefe, D. H., and Nederveen, C. J. (**1998**). ''Theory of sound propagation in a duct with a branched tube using modal decomposition,'' Acta Acustica (in press).

Keefe, D. H. (**1982a**). ''Experiments on the single woodwind tone hole,'' J. Acoust. Soc. Am. **72**, 688–699.

Keefe, D. H. (**1982b**). ''Theory of the single woodwind tone hole,'' J. Acoust. Soc. Am. **72**, 676–687. Erratum, *ibid.* **73**, 694 (1983).

Keefe, D. H. (**1990**). ''Woodwind air column models,'' J. Acoust. Soc. Am. **88**, 35–51.

Martínez, J., Agulló, J., and Cardona, S. (**1988a**). ''Conical bores. Part II: Multiconvolution,'' J. Acoust. Soc. Am. **84**, 1620–1627.

Martínez, J., and Agulló, J. (**1988b**). ''Conical bores. Part I: Reflection functions associated with discontinuities,'' J. Acoust. Soc. Am. **84**, 1613–1619.

Nederveen, C. (**1969**). ''Acoustical aspects of woodwind instruments,'' Ph.D. thesis, Frits Knut, Amsterdam, Chap. 3.

Nederveen, C., and van Wulfften, D. W. (**1963**). ''Resonance frequency of a gas in a tube with a short closed side-tube,'' Acustica **13**, 65–70.

Smith, J. (**1992**). ''Physical modeling using digital waveguides,'' Comput. Music J. **16**(4), 74–91.

Välimäki, V., Karjalainen, M., and Laakso, T. I. (**1993**). ''Modeling of woodwind bores with finger holes,'' in *Proceedings of the International Computer Music Conference*, Tokyo, Japan.

van Walstijn, M., and Smith, J. O. (**1998**). ''Use of truncated infinite impulse response (TIIR) filters in implementing efficient digital waveguide models of flared horns and piecewise conical bores with unstable one-pole filter elements,'' in *Proceedings International Symposium on Musical Acoustics 1998*, edited by D. Keefe, T. Rossing, and C. Schmid (Acoustical Society of America and Catgut Acoustical Society, New York).

Effects of subglottal pressure variation on professional baritone singers' voice sources

Johan Sundberg
KTH Voice Research Centre, Speech Music Hearing, SE-10044 Stockholm, Sweden

Maria Andersson
Logopedmottagningen, Karlstad, Sweden

Clara Hultqvist
Logopedmottagningen, Västerås, Sweden

Five professional operatic baritone singers' voice-source characteristics were analyzed by means of inverse filtering of the flow signal as captured by a flow mask. The subjects sang a long sustained diminuendo, from loudest to softest, three times on the vowels [a:] and [æ:] at fundamental frequencies representing 25%, 50%, and 75% of their total pitch range as measured in semitones. During the diminuendos, they repeatedly inserted the consonant [p] so that associated subglottal pressures could be estimated from the oral pressure during the p-occlusions. Pooling the three takes of each condition, ten subglottal pressures, equidistantly spaced between highest and lowest, were selected for analysis. Sound-pressure levels (SPL), peak-to-peak glottal airflow, maximum flow declination rate, closed quotient, glottal dc flow, and the level difference between the two lowest partials of the source spectrum (H1–H2) were determined. All parameters except the glottal dc flow showed a systematic variation with subglottal pressure or the fractional excess pressure over threshold. The results are given in terms of equations representing the average across subjects for the relation between subglottal pressure and each of the mentioned voice-source parameters. © *1999 Acoustical Society of America.* [S0001-4966(99)06303-1]

INTRODUCTION

Important contributions to the personal voice characteristics derive from the glottal voice source (Childers and Lee, 1991). This signal can be readily analyzed by inverse filtering of the flow signal during voice production. Along with voice fundamental frequency and mode of phonation, vocal loudness is a factor of major influence on the glottal voice source. The question we pose in this paper is, what are the effects on the voice source of vocal-loudness variation?

In previous research (Holmberg *et al.*, 1994; Sulter, 1996; Sulter and Wit, 1996), the effects of vocal-loudness variation on the voice source has been analyzed in untrained voices by contrasting soft, mid, and loud phonation. However, in such voices, increases of loudness are typically accompanied not only by pitch increases (Gramming *et al.*, 1998) but also, presumably, by changes of other voice-source parameters. This makes it difficult to tease out the effect of loudness variation. Professional singers, on the other hand, can be assumed to have developed a more independent variation of glottal parameters. For example, increases of loudness are not allowed to be accompanied by increases of fundamental frequency in singing. We therefore selected professional male singers for our study, the purpose of which was to describe the dependence of voice-source parameters on subglottal pressure.

I. METHOD

Five professional baritone singers, age range 29–65 years, participated as subjects. They all earn their livelihood from singing only. They sang a diminuendo at constant pitch, continuously repeating the syllables [pa:] and [pæ:] on three fundamental frequencies located at 25%, 50%, and 75% of their professional pitch range as measured in semitones. Three renderings of each condition were recorded.

The experimental setup is shown in Fig. 1. Airflow was picked up by means of a Rothenberg-type flow mask (Rothenberg, 1973). Subglottal pressure P_s was estimated from the oral pressure during the [p]-occlusion. This pressure was captured by a pressure transducer (Glottal Enterprises) attached to a thin plastic tube which the subject held in the corner of his mouth. This method has been found to yield reasonably accurate estimations of P_s (see, e.g., Hertegård *et al.*, 1995). The flow and pressure signals were recorded on separate tracks on a multichannel TEAC PCM recorder together with an audio signal picked up by a B&K condenser microphone 30 cm in front of the subject's mouth. Calibration signals of flow, pressure, and sound level were all recorded on the same tape; airflow obtained from a pressure tank attached to the flow mask via a flow meter, pressure by means of a water manometer and sound level by recording vowel sounds with SPL values determined from a sound-level meter that was held next to the recording microphone.

II. ANALYSIS

SPL was measured by B&K sound-level recorder (2307) analysis of the audio track. Subglottal pressures were recorded on a strip chart recorder. For each vowel and pitch condition, ten subglottal pressures, equidistantly spaced be-
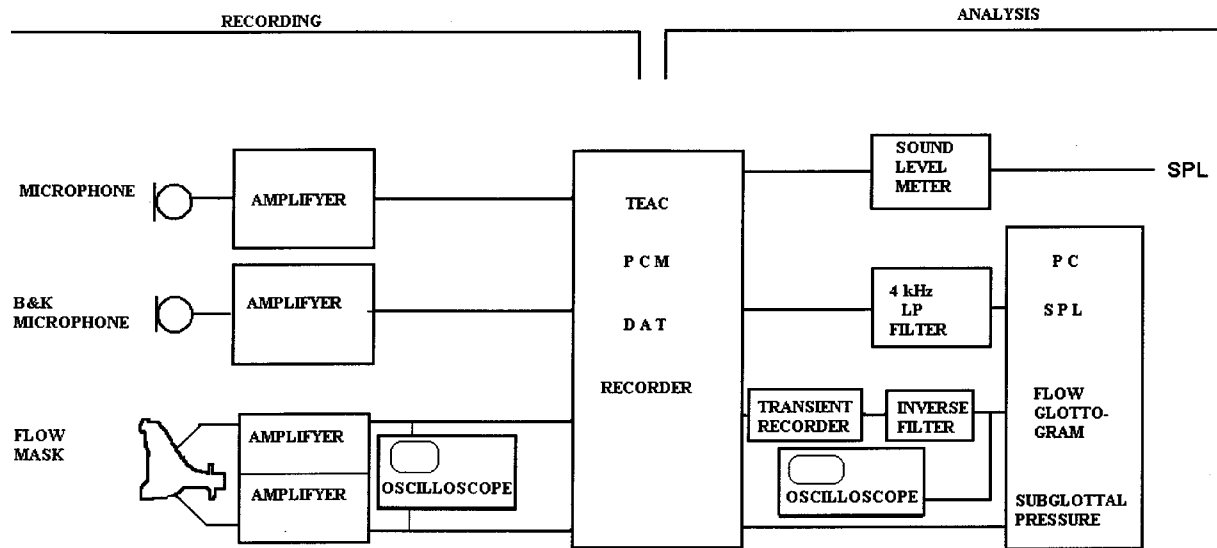
FIG. 1. The experimental setup used for the recording and the analysis. In cases where the flow signal overloaded the amplifier of the inverse-filter unit, flow glottograms were derived by inverse filtering the B&K signal.

tween the extreme values, were selected from the three renderings. The syllables following these pressure signals were then submitted to inverse-filtering analysis. This filtering was realized by a Glottal Enterprises MSIF-2 device, the output of which was recorded on computer files using the SWELL signal-editing program. A closed phase, void of ripple at the frequencies of the two lowest formants, was used as the criterion for tuning the two filters, although in many cases of loud singing, a ripple corresponding to the ''singer's formant'' could not be eliminated. Mostly, the same filter settings could be used for the entire sequence of syllables. On a second track of the same computer files, the pressure signal was recorded. The SWELL program calculated the time derivative of the flow glottogram. Figure 2 shows a typical example of a resulting computer file.

From the files containing the flow glottograms, mid vowel sections were selected and the following measures were determined: (1) the ac flow, the peak-to-peak amplitude of the flow; (2) the dc flow, the mean flow during the closed phase; (3) the closed quotient, the ratio duration of closed phase/period time; (4) the maximum of the flow declination rate (MFDR), i.e., the negative peak amplitude of the flow derivative, Fig. 3. In addition, (6) the level difference between 1st and 2nd harmonics of the source spectrum (H1–H2) was determined by fast Fourier transform (FFT) analysis of the flow glottogram waveform.

For some subjects, the flow microphone overloaded the amplifier for the loudest productions. For one of these subjects, a B&K condenser microphone was used to pick up the audio signal, which was then inverse filtered using a com-
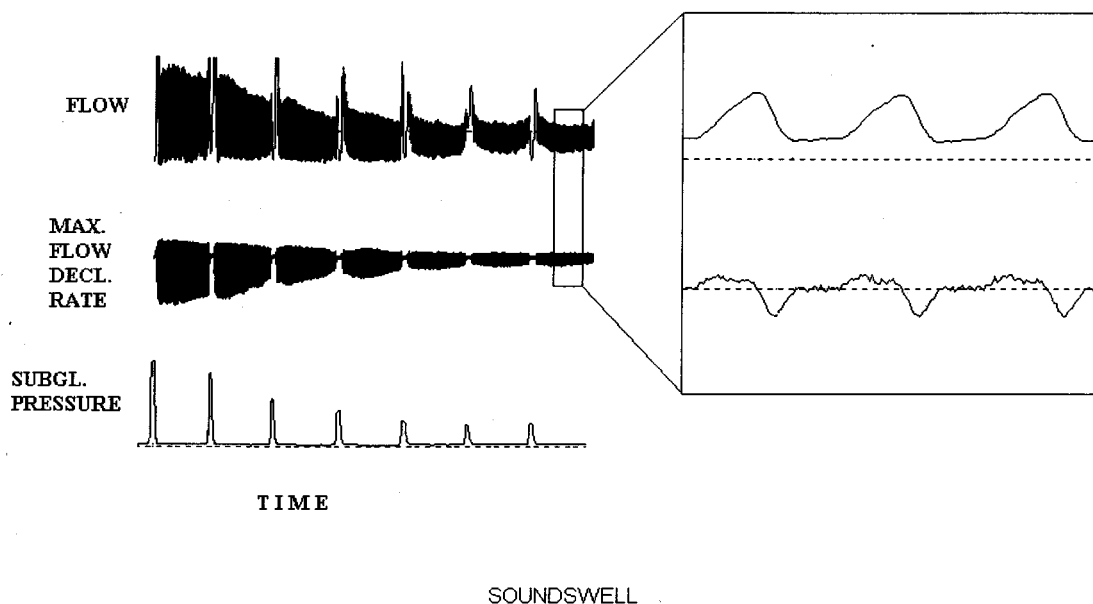
FIG. 2. Typical example of a computer file showing the inverse-filtered flow, its derivative, and the associated subglottal pressures recorded when the singer sang a diminuendo while repeating the syllable [pV:]. The panel to the right shows a close-up of the flow and differentiated flow signals.
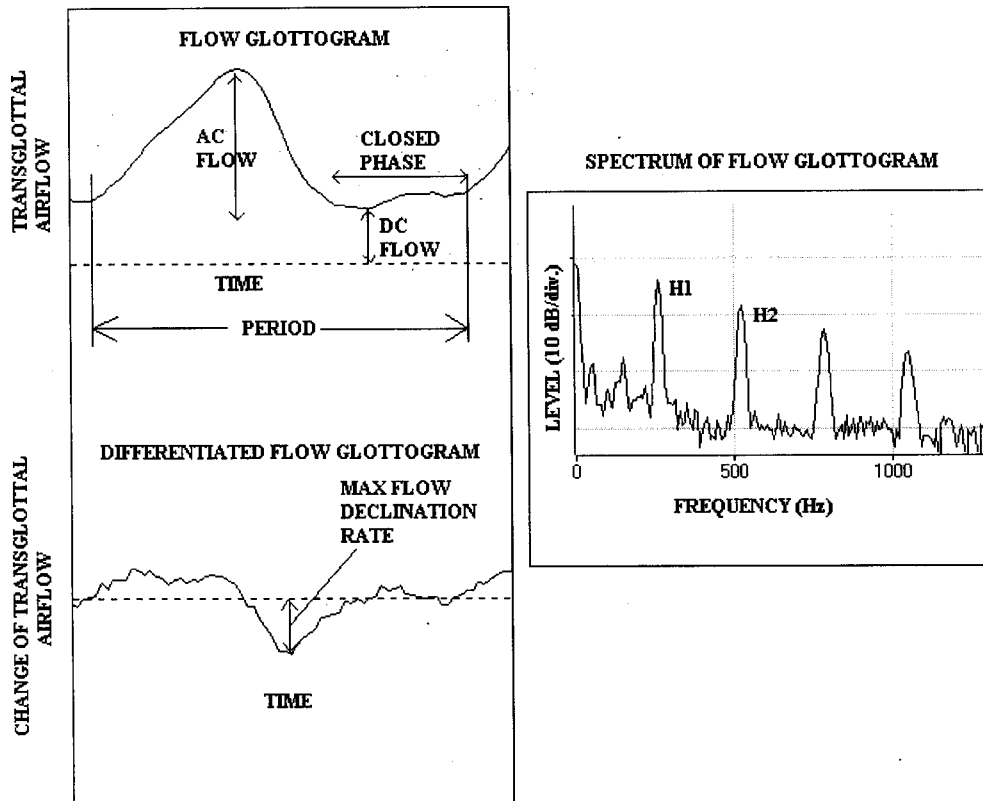
FIG. 3. Illustration of the measures secured from the flow glottograms.

puter program. Comparisons with results of inverse filtering of the same overloaded flow signals showed that the overloading did not appreciably affect the flow glottograms. For one subject, mask leakage reduced the number of useful glottograms.

III. RESULTS

In the experiment, each subject repeated each condition three times. The same subglottal pressures often occurred in more than one of these repeats. To estimate the reproducibility of the data obtained, two or three glottograms that were produced with the same subglottal pressures in different takes were compared for at least three different subglottal pressures for each subject. Pooling data for all subjects, these values were compared in scatter plots, one for each parameter. A quantitative measure of the agreement was obtained in terms of the equations for the best linear fit (linear correlation). Ideally, the slope value should be 1 and the constant 0. Table I shows the values obtained for this correlation.

Replicability was poorest for the dc flow, thus suggesting that glottal leakage was not varied systematically by the singers. For the other parameters, the slope of the trendline varied between 1.08 and 0.93. The constant varied between 0.49 and -1.33 for H1 and H2, respectively, and considerably less for the other parameters. These results indicate that, except for the dc flow, the data obtained from the inverse filtering were reliable, and that for each subject the flow glottograms produced at a given P_s were similar.

SPL is closely related to P_s (Schutte, 1980) and to the log of the MFDR (Fant, 1979; Gauffin and Sundberg, 1989). SPL is also dependent on $F0$ and $F1$, but these effects were

small, as $F1$ was more than one octave above $F0$ and also similar in both vowels analyzed. Therefore, in examining the relations between SPL, P_s, and MFDR, the data for both vowels and for the three pitches were pooled.

The subjects varied vocal loudness over a wide range. The ratio between the highest and lowest subglottal pressures used for the same fundamental frequency varied between 6.6 and 16.0 for the subjects and the SPL at 0.3 m between about 60 and 95 dB.

According to Titze (1992), flow-glottogram parameters are strongly correlated to the fractional excess pressure over threshold $(P_s - P_{Thr})/P_{Thr}$, where P_s is the subglottal pressure and P_{Thr} is the phonation-threshold pressure. This pressure was determined as the lowest pressure that produced phonation. $(P_s - P_{Thr})/P_{Thr}$ showed a strong correlation with

TABLE I. Reliability of flow glottogram measures shown in terms of the slope, constant, and correlation coefficient r for the overall best linear fit of pairs of values, three for each singer. The pairs were selected from two different takes pertaining to the same $F0$ and subglottal pressures.

Parameter	Equation		
	Slope	Constant	r
Subglottal pressure	1.0081	−0.0161	1.00
Period time	0.9415	0.0003	0.99
ac flow	1.0764	−0.0323	0.97
MFDR	1.0692	−0.0042	0.98
Closed phase	0.9339	0.0000	0.93
H1	1.0141	0.4902	0.94
H2	1.0652	−1.3351	0.95
dc flow	0.8437	0.0114	0.78

FIG. 4. Typical example of the correlation between $(P_s - P_{Thr})/P_{Thr}$ and SPL of the vowels [a:] and [æ:] as sung by subject 5 at three different pitches. The data for the best linear fit are shown in the upper-left corner.

FIG. 5. Typical example of the correlation between $(P_s - P_{Thr})/P_{Thr}$ and MFDR for the vowels [a:] and [æ:] as sung by subject 2 at a low, middle, and high pitch (squares, circles, and triangles).

SPL as illustrated by the typical example in Fig. 4. Correlation data for the singers and pitches are listed in Table II. For two of the subjects, the best linear fit differed clearly between $F0$. On the other hand, their SPL values showed a similar relation with subglottal pressure, regardless of $F0$. This indicates that difficulties to determine an accurate value for P_{Thr} caused this scatter. The mean correlation coefficient across all subjects and pitches was 0.948 (s.d. 0.046). The relation could be quantitatively described as

$$\text{SPL} @ 0.3 \text{ m} = C_1^* \ln[(P_s - P_{Thr})/P_s] + C_2, \quad (1)$$

where the mean of $C_1 = 9.71$ (s.d. 1.8) and the mean of $C_2 = 71.2$ (s.d. 7.9). A doubling of P_s caused a mean increase of 9.9 dB SPL (s.d. 1 dB) and a doubling of $(P_s - P_{Thr})/P_{Thr}$ yielded an SPL increase of 6.4 dB.

$(P_s - P_{Thr})/P_{Thr}$ correlated strongly also with MFDR. Figure 5 offers a typical example of this relationship. Corre-

lation data for the various singers and pitches are listed in Table II. The mean correlation coefficient was 0.907 (s.d. 0.039). The relation could be expressed as

$$\text{MFDR} = C_1^*(P_s - P_{Thr})/P_{Thr} + C_2. \quad (2)$$

The mean slope $C_1 = 215$ (s.d. 49), and the mean intercept $C_2 = 156$ (s.d. 101).

The peak-to-peak amplitude of the glottogram increased linearly with $(P_s - P_{Thr})/P_{Thr}$. Figure 6 shows a typical example, and correlation data for the various singers and pitches are listed in Table II. The mean correlation coefficient was 0.907 (s.d. 0.019). The relation could be quantitatively described as

$$\text{ac} = C_1^*(P_s - P_{Thr})/P_{Thr} + C_2, \quad (3)$$

where the mean of the slope $C_1 = 0.10$ (s.d. 0.03) and the mean of the intercept $C_2 = 0.14$ (s.d. 0.08).

TABLE II. Constants [slope, intercept Icpt, correlation coefficient r; for the closed quotient Q_{closed}, see Eq. (4)] describing the relation between the $(P_s - P_{Thr})/P_{Thr}$ and the indicated voice-source parameters.

Singer	$F0$	SPL@ 0.3 m			MFDR			Peak-to-peak amplitude			Q_{closed}		
		Slope	Icpt	r	Slope	Icpt	r	Slope	Icpt	r	A	α	B
1	139	6.30	73.3	0.952	234	362	0.926	0.09	0.24	0.878	0.6	1.5	−0.511
1	196	8.40	73.7	0.969	276	155	0.942	0.08	0.16	0.909	0.55	1.7	−0.598
1	276	9.34	73.5	0.986	244	182	0.917	0.06	0.14	0.923	0.5	1.2	−0.693
2	139	8.61	78.0	0.917	233	247	0.894	0.14	0.15	0.899	0.5	1.4	−0.693
2	196	10.07	75.4	0.991	224	79	0.875	0.13	0.15	0.895	0.4	0.8	−0.916
2	278	7.88	82.0	0.961	237	173	0.893	0.13	0.02	0.890	0.5	0.6	−0.693
3	139	9.35	62.4	0.972	102	133	0.838	0.06	0.26	0.905	0.5	0.5	−0.693
3	196	10.27	66.0	0.971	176	49	0.862	0.09	0.18	0.913	0.5	0.8	−0.693
3	278	10.04	74.9	0.926	170	254	0.881	0.08	0.23	0.882	0.55	0.4	−0.598
4	139	13.66	50.2	0.981	197	63	0.98	0.06	0.14	0.983	0.47	0.3	−0.755
4	196	11.39	66.3	0.968	385	134	0.971	0.10	0.12	0.984	0.55	0.5	−0.598
4	278	9.51	78.1	0.993	37	6	0.887	0.16	0.41	0.877	0.4	0.7	−0.916
5	139	9.09	72.8	0.927	255	40	0.926	0.14	0.09	0.931	0.55	0.8	−0.598
5	196	9.03	75.0	0.887	252	14	0.918	0.14	0.06	0.937	0.5	0.8	−0.693
5	278	12.65	66.4	0.924	175	179	0.89	0.06	0.01	0.926	0.6	0.4	−0.511
mv		9.71	71.2	0.918	215	156	0.897	0.10	0.14	0.907	0.51	0.83	−0.68
s.d.		1.82	7.9	0.058	49	101	0.03	0.03	0.08	0.019	0.059	0.431	0.12
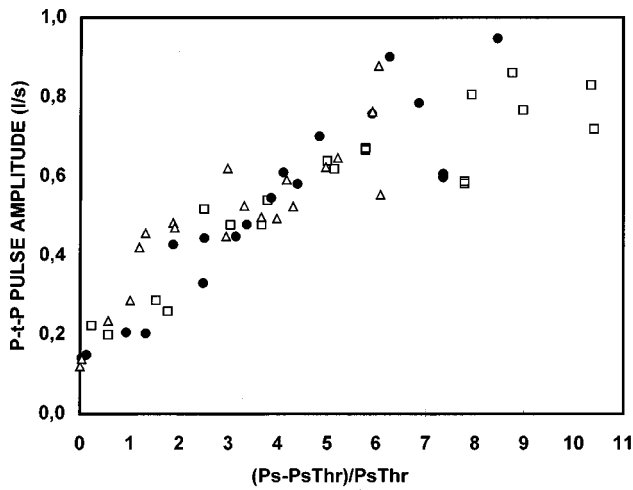
FIG. 6. Typical example of the correlation between $(P_s - P_{Thr})/P_{Thr}$ and the peak-to-peak amplitude of the glottogram for the vowels [a:] and [æ:] as sung by subject 3 at a low, middle, and high pitch (squares, circles, and triangles).

The closed quotient increased with P_s up to a limit close to 50% of the period time, as illustrated by the typical example in Fig. 7. The relation could be approximated by

$$Q_{closed} = A - e^{(-\alpha*(P_s - P_{Thr})/P_{Thr}) + B}. \tag{4}$$

As Q_{closed} tended to be zero at phonation threshold pressure P_{Thr}, $B = \ln(A)$ in Eq. (4). The values of α and A varied depending on subject, see Table II. Averages across subjects and pitches were for the constant A, 0.51 (s.d. 0.59), for α, 0.83 (s.d. 431), and for B, −0.68 (s.d. 0.120). The agreement between the values calculated with the expression above, using constants averaged for each pitch and subject, was assessed by eta^2, defined as

$$1 - SS_{resid}/SS_{mean}, \tag{5}$$

where SS_{resid} is the sum of the squared differences between observed and calculated values of Q_{closed}, and SS_{mean} is the sum of the squared differences between observed and averaged differences between calculated and observed values of Q_{closed}. The eta^2 was computed for each subject and pitch. The average across pitches and singers amounted to 0.953 (s.d. 0.0467).

The closed quotient correlated with H1−H2, the mean correlation coefficient being −0.879, s.d. 0.066. Using the mean across subjects, vowels, and pitches, the best linear fit could be described as

$$H1 - H2 = 21.5 - 31.1 * Q_{closed}. \tag{6}$$

The standard deviations for the slope and the constant were 11.5 and 4.8, respectively. Thus, by and large, the level difference between partials 1 and 2 of the source spectrum decreased linearly with increasing closed quotient Q_{cl}. For increasing pressure, H1−H2 asymptotically approached 5 dB, approximately.

Glottal leakage showed an inconsistent variation with P_s for all subjects.

Summarizing, the effects of P_s were reasonably similar in all subjects and systematic for all parameters except glottal leakage. With decreasing subglottal pressure, ac flow and
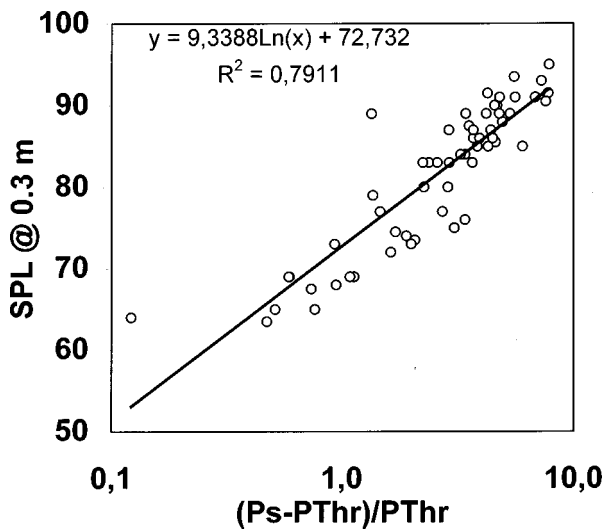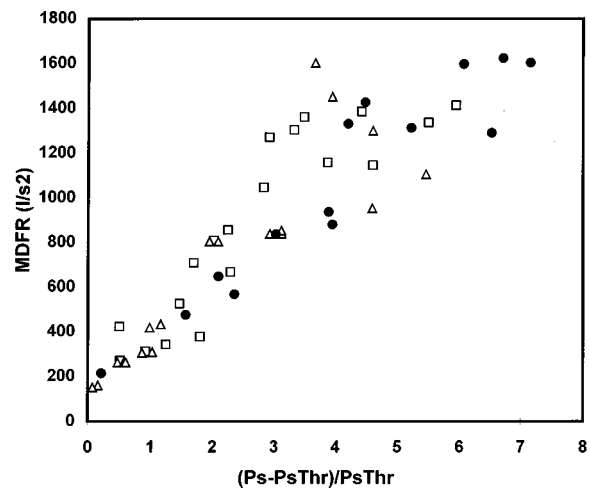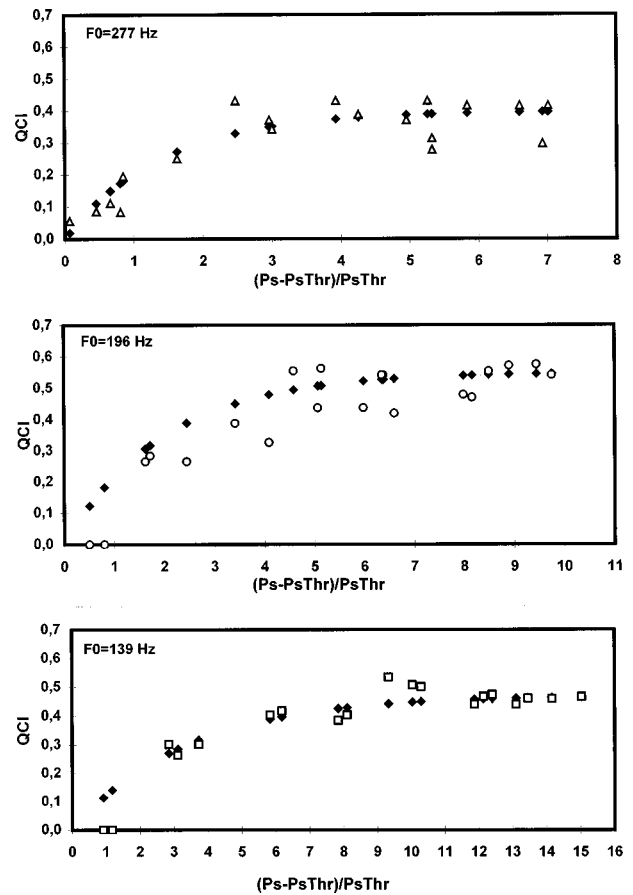

FIG. 7. Typical example of the correlation between $(P_s - P_{Thr})/P_{Thr}$ and the closed quotient for the vowels [a:] and [æ:] as sung by subject 4 at a low, middle, and high pitch (lower, middle and top panels). Closed diamonds represent the best fits.

MFDR decreased continuously, while H1−H2 and Q_{closed} showed a strong negative correlation and approached an asymptote of about 5 dB and 0.5, respectively.

IV. DISCUSSION

These results are encouraging in the sense that highly systematic relations were found between P_s and various flow-glottogram parameters. Probably an important condition for our results was that the subjects were professional singers, as such subjects are likely to develop a particularly systematic control over phonation. Thus, our results are not necessarily representative of untrained voices.

On the other hand, if singers know how to change one single voice-control parameter at a time, our findings may be quite elucidating regarding theory of phonation. Moreover, the range of variation of P_s was considerably greater than those observed earlier in investigations of untrained subjects' voice-source characteristics; a wide dynamics helps reveal the effects of vocal loudness on the voice source. This suggests that, for some purposes, it may be more helpful to study the voice source in singers than in untrained subjects.

Recently, the voice-source characteristics of country singers have been investigated (Sundberg *et al.*, 1997). Under conditions of loud singing and speaking at high fundamental frequencies, values of Q_{closed} as high as 0.7 were

sometimes found. A perceptual test suggested that phonation was perceived as ''pressed'' under these conditions. Our professional operatic baritone singers tended to reach maximum values of Q_{closed} in the vicinity of 0.5, thus supporting the assumption that pressed phonation is avoided in this type of singing.

Our findings can be compared with those obtained by Titze (1992) for professional tenor singers, and by Sulter and Wit for male adult trained voices (Sulter and Wit, 1996). At comparable subglottal pressure, Titze's and Sulter and Wit's data on MFDR were higher than those observed in our baritone subjects. Titze found that the peak flow amplitude was proportional to $0.3*(P_s - P_{\text{Thr}})/P_{\text{Thr}}$, while for our subjects, the relation could be approximated as $ac = 0.1*(P_s - P_{\text{Thr}})/P_{\text{Thr}} + 0.14$. His approximation of the closed quotient was $Q_{\text{closed}} = 0.6(P_{\text{Thr}}/P_s) - 0.6$. This is in good agreement with our data at the lowest $F0$, but gives greater values than those observed for our singers, for low pressures at high $F0$. These differences may possibly be related to a difference in vocal-fold morphology between these tenors and baritones. Our data for ac, Q_{closed}, and SPL are similar to those reported by Sulter and Wit.

It is also interesting to compare our data with those derived from the Liljencrants Fant (LF) model (Fant *et al.*, 1985), which describes the glottal voice-source waveform in mathematical terms and predicts the associated acoustic effects as well as its dependence on subglottal pressure. We found that for our singer subjects, SPL increased by an average of 10 dB per doubling of subglottal pressure. This is in good agreement with the value of 9 dB predicted theoretically (Fant, 1982) and also with measurements reported earlier (e.g., Schutte, 1980). For the relation between H1–H2 and the open quotient Q_{op}, the LF model predicts

$$\text{H1–H2} = 0.27*e^{(5.5*Q_{\text{op}})} \tag{7}$$

(Fant, 1997). However, the data underlying this relation can also be approximated by a linear function

$$\text{H1–H2} = 21.2 - 31.4*Q_{\text{closed}} \tag{8}$$

(Fant, personal communication), which is only marginally different from our values. This indicates that, in this respect, our data are in good agreement with the LF model. The MFDR, the negative peak amplitude of the differentiated flow glottogram, is almost identical with the parameter E_e of the LF model. However, the moment of the excitation of the vocal tract, which corresponds to the moment when the second derivative of the flow signal reaches its negative peak, is sometimes slightly delayed as compared to the moment at which the first derivative reaches its negative peak. For a male speaker, Fant *et al.* (1996) found that E_e was proportional to $P_s^{1.1}$ which is very close to the linear relation we found for MFDR and P_s According to theory, E_e is closely tied to both P_s and SPL; for a more accurate quantification of vocal loudness, it should be advantageous to use the second derivative E_e rather than MFDR in future investigations.

Our results were derived from sequences in which the subjects gradually decreased vocal loudness. There seems to be no reason to doubt that the results are also valid for increases of vocal loudness.

V. CONCLUSIONS

By using professional baritone singers, detailed information on the effects of variation of P_s on the glottal voice source were obtained, since such subjects are able to vary the voice source systematically over a wide pressure range. The effects of P_s were reasonably similar among subjects and systematic for all parameters except glottal leakage. The effects can be approximated by a set of equations [Eqs. (1)–(4) and (6)] showing that SPL is a linear function of pressure, and the maximum flow declination rate and the peak-to-peak flow amplitude are linear functions of the fractional excess pressure over the phonation-threshold pressure. The closed quotient, asymptotically approaching 0.5 with increasing pressure, was related to this normalized excess pressure by means of a power function, while the level difference between the two lowest source spectrum partials, asymptotically approaching 5 dB with increasing pressure, was linearly related to the closed quotient.

ACKNOWLEDGMENTS

Childers, D. G., and Lee, C. K. (**1991**). ''Vocal quality factors: Analysis, synthesis perception,'' J. Acoust. Soc. Am. **90**, 2394–2410.

Fant, G. (**1979**). ''Glottal source and waveform analysis,'' Speech Transmission Laboratory Quarterly Progress and Status Report KTH, Stockholm (STL-QPSR) 1/1979, pp. 85–107.

Fant, G. (**1982**). ''Preliminaries to analysis of the human voice source,'' STL-QPSR 4/1982, pp. 1–27.

Fant, G. (**1997**). ''The voice source in connected speech,'' Speech Commun. **22**, 125–139.

Fant, G. (Personal communication, 1998).

Fant, G., Liljencrants, J., and Qiguang, L. (**1985**). ''A four-parameter model of glottal flow,'' STL-QPSR 4/1985, pp. 1–13.

Fant, G. and Kruckenberg, A. (**1996**). ''Voice source properties of the speech code,'' STL-QPSR 4/1996, pp. 45–56.

Gauffin, J., and Sundberg, J. (**1989**). ''Spectral correlates of glottal voice source waveform characteristics,'' J. Speech Hear. Res. **32**, 556–565.

Gramming, P., Sundberg, J., Ternström, S., Leanderson, R., and Perkins, W. (**1988**). ''Relationships between changes in voice pitch and loudness,'' J. Voice **2**, 118–126.

Hertegård, S., Gauffin, J., and Lindestad, P. Å. (**1995**). ''A comparison of subglottal and intraoral pressure measurements during phonation,'' J. Voice **9**, 149–155.

Holmberg, E., Hillman, R., Perkell, J., and Gress, C. (**1994**). ''Relationships between intraspeaker variation in aerodynamic measures of voice production and variation in SPL across repeated recordings,'' J. Speech Hear. Res. **37**, 484–495.

Rothenberg (**1973**). ''A new inverse-filtering technique for deriving the glottal airflow waveform during voicing,'' J. Acoust. Soc. Am. **53**, 1632–1645.

Schutte, H. (**1980**). ''The Efficiency of Voice Production,'' Dissertation, University Hospital, Groningen.

Sulter, A. M. (**1996**). ''Variations of Voice Quality Features and Aspects of Voice Training in Males and Females,'' Dissertation, Groningen University.

Sulter, A. M., and Wit, H. P. (**1996**). ''Glottal volume velocity waveform characteristics in subjects with and without vocal training, related to gender, sound intensity, fundamental frequency and age,'' J. Acoust. Soc. Am. **100**, 3360–3373.

Sundberg, J., Cleveland, T., Stone, E., and Iwarsson, J. (**1997**). ''Voice source characteristics in six premiere country singers,'' STL-QPSR 1/1997, pp. 105–117.

Titze, I. (**1992**). ''Phonation threshold pressure: a missing link in glottal aerodynamics,'' J. Acoust. Soc. Am. **91**, 2926–2935.

A microcosm of musical expression: II. Quantitative analysis of pianists' dynamics in the initial measures of Chopin's Etude in E major

Bruno H. Repp[a)]

Haskins Laboratories, 270 Crown Street, New Haven, Connecticut 06511-6695

Patterns of expressive dynamics were measured in bars 1–5 of 115 commercially recorded performances of Chopin's Etude in E major, op. 10, No. 3. The grand average pattern (or dynamic profile) was representative of many performances and highly similar to the average dynamic profile of a group of advanced student performances, which suggests a widely shared central norm of expressive dynamics. The individual dynamic profiles were subjected to principal components analysis, which yielded five Varimax-rotated components, each representing a different, nonstandard dynamic profile associated with a small subset of performances. Most performances had dynamic patterns resembling a mixture of several components, and no clustering of performances into distinct groups was apparent. Some weak relationships of dynamic profiles with sociocultural variables were found, most notably a tendency of female pianists to exhibit a greater dynamic range in the melody. Within the melody, there were no significant relationships between expressive timing [Repp, J. Acoust. Soc. Am. **104**, 1085–1100 (1998)] and expressive dynamics. These two important dimensions seem to be controlled independently at this local level and thus offer the artist many degrees of freedom in giving a melody expressive shape. © *1999 Acoustical Society of America.* [S0001-4966(99)00803-6]

INTRODUCTION

In a previous article, Repp (1998a) reported a detailed quantitative analysis of pianists' expressive timing (the pattern of inter-onset interval durations between successive tones) in bars 1–5 of 115 commercially recorded performances of Chopin's Etude in E major, op. 10, No. 3. Although the grand average timing pattern was representative of many performances, principal components analysis of the data suggested at least four independent strategies of deviating from this central norm. Each individual pianist's timing pattern could be approximated by a weighted combination of these four strategies. A wide variety of combinations was represented in the sample, and no two individual patterns were exactly the same. In addition, there was a wide range of basic tempi and of degrees of tempo modulation. There were no strong relationships between any of these variables and sociocultural characteristics of the artists, although some weak trends were observed.

Timing is only one aspect of musical expression, though a very important one. It also happens to be the one that is easiest to measure in acoustically recorded performances. Another extremely important aspect of expression on the piano is dynamics—the relative intensities of successive and simultaneous tones. Although musical-instrument-digital-interface (MIDI) recordings give easy access to this information in the form of key-press velocities that are highly correlated with the sound levels of tones, expressive dynamics has received much less attention than expressive timing in performance research (but see Shaffer, 1981; Gabrielsson,

1987; Todd, 1992; Repp, 1996a). In particular, very little is known objectively about individual differences in expressive dynamics, even though informal listening suggests that such differences do exist in performances of the same music by great artists, preserved in acoustic recordings.

One methodological problem in measuring the expressive dynamics of acoustic recordings is that it is extremely difficult to estimate accurately the relative intensities of several simultaneous complex tones, even when their fundamental frequencies are known. Their harmonics are interleaved and often coincident, unpredictable phase relationships affect the amplitude at any given frequency, and the amplitude of the lowest harmonic (the fundamental frequency) is only roughly proportional to a tone's overall amplitude (Repp, 1993). At present, there seems to be no signal processing algorithm that can perform this task. Therefore, analyses of expressive dynamics in acoustically recorded performances (such as Gabrielsson, 1987, and the present study) are currently restricted to measuring the overall amplitudes of successive tone clusters—the ''horizontal'' dynamics. Information about ''vertical'' dynamics (the relative intensities of simultaneous tones, constituting the sonic texture) remains unavailable.

It is possible to ignore the fact that most successive acoustic events in music are composed of several individual tones and to regard total sound energy as the perceptually most relevant measure of horizontal dynamics (as does Todd, 1992, 1994). This may be sufficient for perception of rhythm. However, human listeners perceptually segregate music into individual voices if the compositional structure provides a basis for doing so. In homophonic music, as used in the present study, one voice (the melody, usually in the

[a)]Electronic mail: repp@haskins.yale.edu

highest pitch register) is more important than the others (the accompaniment) and is usually played with greater intensity. The listener's attention is drawn to the melody, and therefore the expressively most relevant measure of horizontal dynamics would seem to be the intensities of the melody tones (cf. Palmer, 1996a). From this perspective, measurements of overall intensity are but an approximation to the desired measure of horizontal dynamics. They seem to provide a sufficiently informative approximation, however, and will have to do until more sophisticated signal processing algorithms are developed.

This article presents the results of detailed analyses of the horizontal dynamic patterns measured in the 115 recordings of the Chopin Etude excerpt, with special attention to individual differences. The analyses were largely analogous to those of expressive timing presented in Repp (1998a). The main question was whether, and how many, fundamentally different patterns of dynamic shaping can be distinguished in this large sample of performances, and how these patterns are related to the musical structure. A secondary question was whether the identified patterns have any relationship to sociocultural differences among the artists.

Towards the end of the article, possible relationships between expressive timing and dynamics are examined. This is an extremely important issue about which very little is known at present. Todd (1992) has pointed out a tendency for dynamics to increase along with tempo and thus to be inversely related to expressive timing (measured in terms of inter-onset intervals). This is only a global tendency, however, that is often violated. Over longer musical passages, a significant correlation is usually obtained because the large-scale phrase structure constrains both timing and dynamics (Todd, 1992; Palmer, 1996a; Repp, 1996a). However, it is not clear whether a similar relationship holds at the most detailed level of expressive variation within a phrase, which is the subject of the present study (see also Palmer, 1996a). Also, given that substantial individual differences exist in both timing and (as the present data will show) dynamics, the question arises whether these individual differences covary. Repp (1996a) addressed this issue previously in performances of Schumann's ''Träumerei'' by ten advanced student pianists who did not show very large individual differences in either timing or dynamics. He did find a weak but significant relationship between the residual patterns (deviations from the average pattern) of timing and dynamics, such that some pianists tended to play more softly than average when they played slower than average at any given moment in the music. In the present sample of distinguished recording artists, much larger individual differences were expected, which provided an opportunity to reexamine the relationship of timing and dynamics.

I. METHOD

A. The music

A simplified score of the musical excerpt is shown on top of Fig. 1.[1] The music is divided into several horizontal strands or voices. The melody is in the soprano voice and includes both short (sixteenth) and longer notes. The accompanying alto voice has sixteenth notes throughout. Some additional filler notes in the right-hand part (which may be considered as forming a ''mezzo-soprano'' voice) and the lower voices (tenor and bass) in the left-hand part also have an accompanying function. The melody is clearly the most important voice and is generally also played with greater intensity than the other voices. When melody tones are sustained, the alto (bars 1–3) and mezzo-soprano/alto (bar 4) voices come to the fore and are more important than the lower voices. Following Repp (in press), the 38 alternating soprano and alto or mezzo-soprano notes forming the ''top line'' of the musical texture will be referred to as *primary notes* (or primary tones, when played). There is one primary note in every sixteenth-note metrical position of the music (for simplicity, the initial eighth-note upbeat will be treated here as if it were another sixteenth note), and it is defined to be always the highest note in its position. (Thus, in bar 4, positions 6–8, the mezzo-soprano notes are the primary notes.) Only four primary notes are not accompanied by lower note onsets: the initial upbeat and the alto notes in the seventh metrical position of bars 1, 2, and 3. These alto notes, however, are accompanied by sustained notes in both higher and lower voices. Since piano tones decay over time (see Martin, 1947; Repp, 1997c), these sustained tones have lost some of their energy when a primary alto note is played.

B. Measurement and analysis procedures

It was assumed that the perceptually most relevant horizontal dynamic pattern is that of the primary tones. It reflects the dynamic shaping of the melody as well as the dynamic contrast between melody and accompaniment. However, since the relative intensities of the primary tones could not be measured directly, the question arose to what extent the pattern of overall intensities resembled that of the primary tones alone. Clearly, additional tones accompanying a primary tone will raise the overall intensity, and the extent of that increase is likely to depend on the number and relative intensity of these additional tones. The acoustic complexity of piano tones and of their temporal relationships in expressive performance makes it difficult, however, to predict these effects mathematically. Therefore, some preliminary measurements and analyses were performed on synthesized performances, to get some indication of the extent to which the overall dynamic profile parallels the dynamic profile of the primary tones. These results are described in Appendix A.

A total of 117 recordings of the Chopin excerpt were procured. (For a detailed description, see Repp, 1998a.) Most of them (102) were obtained on a digital audio tape onto which they had been copied from compact discs and long-playing records. (Two of these copies turned out to be duplicates of others, but they were included in all analyses.) Although there was considerable variation in the recorded sound level, no distortion was noticed when listening to the tape. The remaining 15 recordings were available from a previous study (Repp, 1997a), saved as digitized sound files. Using SOUNDEDIT16 software, all recordings were input as analog signals to a Macintosh Quadra 660AV computer, sampled at a rate of 20.055 kHz, and stored as separate files in 16-bit format. (Some of the 15 recordings digitized earlier

were in 8-bit format.) Each waveform was subsequently scaled multiplicatively to maximum peak amplitude using the ''normalize'' function of SOUNDEDIT16. Measurements of tone (chord) onset times had already been performed (Repp, 1998a) and served to guide the amplitude analysis.

Using SIGNALYZE software, the root-mean-square amplitude envelope of each digitized waveform was computed with a rectangular integration window of 30 ms, and subsequently an automatic peak-picking routine was employed to determine the peak amplitude following each note (chord) onset. The amplitudes were then converted into peak sound levels (PSLs) in decibels (dB). These measurements obviously did not achieve the precision and validity of the previous timing measurements (Repp, 1998a). Interactions among simultaneous tones and multiple sources of distortion (surface noise, recording techniques, room acoustics) made the data rather noisy. Nevertheless, they were believed to be sufficiently informative about the pianists' dynamic strategies to justify the following analyses.

Each performance yielded a series of 38 PSL values (cf. the score in Fig. 1) that constituted its *dynamic profile*. These data were subjected to various correlational analyses, including principal components analysis with Varimax rotation. A brief introduction to this technique may be found in Repp (1998a). Twenty-three of the 38 PSLs derived from positions in which there were note onsets in the soprano voice. Separate analyses were conducted on these *melodic dynamic profiles*, in order to separate melodic dynamic variation from the usually large dynamic difference between melody and accompaniment.

II. RESULTS AND DISCUSSION

A. Three aspects of expressive dynamics

Like expressive timing, expressive dynamics has three largely independent aspects. The first of these is the *basic dynamic level*, which can be measured by computing the average PSL of a whole passage and which corresponds to dynamic markings in the score (such as *piano* or *forte*) that apply across a number of bars. In the present analyses, however, the average PSL was meaningless because it depended on several uncontrolled factors that varied between performances, including the original recording level, the recording level in the transfer from the original medium to digital tape, the input level to the computer, and the subsequent normalization to maximum amplitude. Although human listeners may be able to recover information about the dynamic level of the original performance from the spectral content of piano tones, no spectral or perceptual analyses were attempted in the present study. All absolute dB values in the figures displayed in this article are meaningless.

The second aspect of expressive dynamics is its *variability* or *range*, which is most conveniently measured by the standard deviation of the PSLs or a multiple thereof. This measure is meaningful in the present context, even though it represents a conflation of the pianist's dynamic range in performance and the dynamic range of the recording. Old recordings in particular may exhibit a restricted dynamic range, even though the original performance may have had a

wide range. High surface noise from old recordings may also reduce the measured dynamic variability by masking soft tones.

The third aspect is the pattern of PSL values that constitutes the *dynamic profile*. This was the aspect of primary interest in this study, and it was the only aspect that entered the correlational statistics because they entailed a conversion of the data into standard scores having a mean of zero and a standard deviation of one. Therefore, the findings on dynamic variability will be discussed first.

B. Dynamic variability and range

Although the difference between the largest and smallest PSL values in a performance would be the most direct measure of its dynamic range, the standard deviation (s.d.) provides a more robust index. The absolute dynamic range may be taken to be approximately four times the s.d. (i.e., the width of a 95% confidence interval around the mean PSL). The performance with the widest dynamic range was that by Cherkassky (s.d.=6.8 dB, a range of about 27 dB), followed by Kyriakou (6.5 dB), and Duchâble (5.9 dB). The performances with the narrowest dynamic range were those by W. Haas, Malcuzinsky, and Horowitz-1972 (all s.d.'s=2.4 dB, a range of about 10 dB).

In the present musical excerpt, the overall dynamic variability reflects in part the difference in average dynamic level between melody and accompaniment, that is, the difference between the 23 positions in the music in which there is a melody note onset in the soprano voice and the 15 positions in which there is not. Indeed, the difference between the average PSLs of melody and accompaniment (ΔMA) was highly correlated with the s.d. ($r=0.78$, $p<0.001$). The largest ΔMA was shown by Cherkassky (10.6 dB), followed by Kentner (9.3 dB) and Hesse-Bukowska (8.6 dB). The smallest difference was exhibited by Horowitz-1972 (0.7 dB), followed by Slenczynska-1975 (1.7 dB) and Bingham (1.8 dB).

However, there was also significant dynamic variation within the melody (and, to a lesser extent, within the accompaniment). Therefore, the standard deviation of the PSLs was also computed for the melody positions separately (ms.d.). The widest melodic dynamic range was shown by Kyriakou (ms.d.=6.6 dB, a range of about 26 dB), followed by Duchâble (6.1 dB) and Ciani (5.7 dB). The narrowest melodic ranges were exhibited by W. Haas (ms.d.=2.0 dB, a range of about 8 dB), Malcuzinsky (2.1 dB), and Horowitz-1972 (2.1 dB). There was a high correlation between the overall and melodic dynamic ranges ($r=0.80$, $p<0.001$), and the multiple correlation of the overall s.d. with both ms.d. and ΔMA was 0.97. However, the correlation between the latter two variables was only 0.31 ($p<0.01$). The dynamic variability thus is best characterized by these two semi-independent measures, which are listed for all performances in Appendix B.

C. The grand average dynamic profile

A grand average dynamic profile was obtained by averaging the dynamic profiles of all 117 performances. This
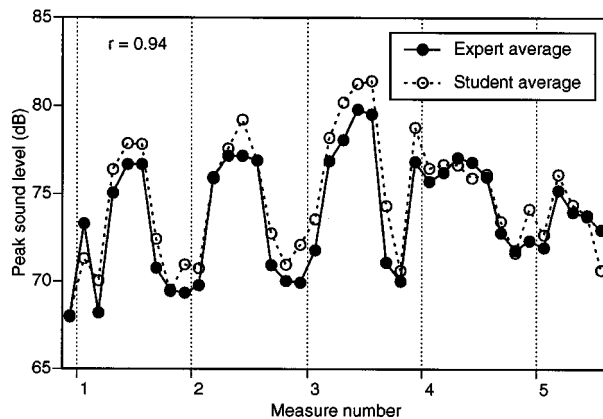
FIG. 1. Grand average dynamic profile of all 117 performances ("expert average"), compared with the grand average profile of multiple performances by 18 advanced students and amateurs ("student average"). A crude score of the music is shown for guidance.

profile is practically identical with the first unrotated principal component (UPC-I) of the data set, except that the latter is computed over standardized dynamic profiles and is expressed likewise in terms of standard scores. The grand average profile ("expert average") is shown in Fig. 1 together with the measured dynamic profile of a synthetic performance on a digital piano, representing the average dynamics of multiple performances of the Chopin excerpt by 18 student and amateur pianists ("student average," see Appendix A). The two profiles have been aligned so that the first data points coincide. They are extremely similar ($r = 0.94$, $p < 0.001$). One of the few systematic differences is a lower PSL for the students than for the experts in the final position; it is explained by the fact that the students played the excerpt with a final chord, as shown in the crude score above the figure, whereas the experts followed the original score in which the sixteenth-note motion continues in the alto voice. The high similarity of the two average profiles extends an observation made previously about expressive timing to the realm of expressive dynamics, namely that the central tendencies of (advanced) student and expert performances reflect a common performance norm (Repp, 1995b, 1997a, 1997b). With regard to timing, expert performances are distinguished from student and amateur performances by their larger deviations from the common standard, that is, by their often greater individuality. Although a detailed comparison with student performances was not part of the present study, the question about the diversity of dynamic profiles in expert performances was of prime interest.

The grand average profile shows very clearly the difference between melody (peaks) and accompaniment (troughs). The only melody tone that, on average, is as soft as the accompaniment is the initial eighth-note upbeat. The accompaniment stays at a fairly constant dynamic level in bars 1–3 but increases somewhat in intensity in bar 4, which is prob-

ably due to the doubling of the accompaniment tones in the right hand (mezzo-soprano plus alto voice). The melody starts out softly, though with a clear dynamic accent on the initial downbeat, and stays at a fairly constant level, about 7 dB above the accompaniment, in bars 1, 2, and 4. The melodic peak in bar 3 (position 5) is marked by a *crescendo* and a dynamic peak which, however, is already reached on the preceding note (position 4). A *decrescendo* occurs in bar 5.

In at least one previous study, a moderate correlation between melodic pitch and intensity has been observed (Repp, 1996a). When this correlation is computed across all primary notes in the present excerpt, it is highly significant ($r = 0.82$, $p < 0.001$). However, it must be attributed in part to the dynamic contrast between melody and accompaniment rather than to relative pitch height as such. Within the melody, the correlation is smaller but still substantial ($r = 0.67$, $p < 0.001$). Although this provides statistical support for a relationship between pitch and dynamics, it does not prove a direct causal connection ("the higher the louder"). For example, the general fact that both the melodic pitch contour and the expressive dynamic contour tend to be arched within a phrase may account for the correlation. Closer inspection of the dynamic profile shows a number of local dissociations: For example, in bar 1, intensity (PSL) increases from the first to the second melody tone (positions 1 and 3) even though pitch decreases by a semitone; in bar 3, intensity stays the same between the third and fourth melody tones (positions 4 and 5) even though pitch increases by five semitones; and in bar 4, positions 2 and 3, intensity increases slightly even though pitch decreases by five semitones. Clearly, it would be rash to consider dynamic variation a consequence of pitch variation; at most, pitch is only one of several factors influencing expressive dynamics.

One factor that normally would be expected to affect dynamics is metrical structure. In this very slow music, however, no metrical accents are evident. Such accents would be expected to occur in the first and fifth positions of each bar, but the PSLs in these positions do not differ from those in neighboring positions within the melody or accompaniment. This confirms what musical intuition suggests, namely that the dynamic variation in this piece has only two main functions: to separate the melody from the accompaniment and to give the melody expressive shape. The distinction between these two functions underlies the following analyses of the melody with and without accompaniment.

The grand average dynamic profile is not just a statistical artifact: There are many individual performances whose dynamic profiles are very similar to it. In the principal components analysis (PCA) on the complete dynamic profiles (38 data points), the first unrotated principal component (UPC-I, which is equivalent to the grand average) accounted for 61% of the variance in the data. In the PCA on the melodic dynamic profiles (23 data points), the first unrotated component (mUPC-I) accounted for 48% of the variance. Ninety-six of the 117 performances showed correlations above 0.7 with the UPC-I profile, and 65 showed correlations above 0.7 with the mUPC-I profile. Figure 2(a) and (b) illustrates the individual profiles with the highest respective loadings (correlations). The performances by Kentner and Licad
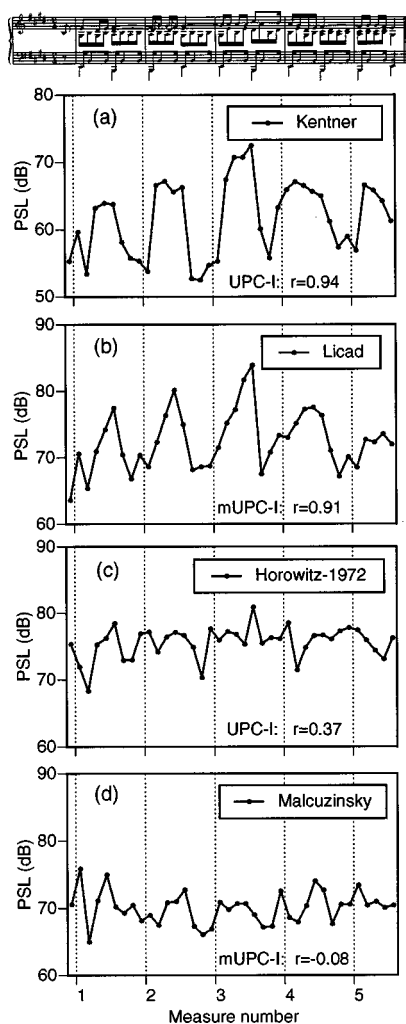
FIG. 2. The performances with (a) the most typical dynamic profile, (b) the most typical melodic dynamic profile, (c) the most atypical dynamic profile, and (d) the most atypical melodic dynamic profile. The relevant PC loadings are shown.

may be considered the ones with the most typical complete and melodic dynamic profiles, respectively. Figure 2(c) and (d) shows the individual profiles with the lowest respective correlations. Horowitz-1972 and Malcuzinsky thus have the least typical dynamic profiles, both of which exhibit very little differentiation between melody and accompaniment. The correlation of Malcuzinsky's melodic profile with mUPC-I is exceptionally low (-0.08); the next-lowest correlation is 0.33. The UPC-I and mUPC-I loadings are moderately correlated ($r = 0.66$, $p < 0.001$) and may be regarded as indices of typicality. The UPC-I loadings of all performances are listed in Appendix B.

D. Rotated principal components

Although the first principal component (PC) in each PCA accounted for a large percentage of the variance, additional PCs made significant contributions. The traditional criteria for accepting PCs as significant are a discontinuity in the successive percentages of variance accounted for and/or an eigenvalue greater than one (which means that the PC accounts for more than $100/n$% of the variance, where n is the number of variables). Neither criterion applied in the

present case because no discontinuities were apparent and because the number of data points ($m = 38$ or 23) was smaller than the number of variables ($n = 117$) and thereby imposed an upper limit on the number of independent PCs. Therefore, the eigenvalue criterion was set at n/m in each analysis; in other words, a PC had to account for more than $100/m$% of the variance to be accepted as significant. By this criterion, five PCs were considered significant in each analysis. Together, they accounted for 77% of the variance of the complete profiles and for 75% of the variance of the melodic profiles.

No attempt was made to immediately interpret these additional PCs, each of which accounted for only a small amount of variance. Instead, a Varimax rotation was performed, which distributed the total variance accounted for among the PCs and maximized their range of correlations with the individual profiles. Each rotated PC represents a standardized dynamic profile that is uncorrelated with the other PCs and can be interpreted as a strategy of dynamic shaping. The rotated PCs will be referred to as PC-I through PC-V in the complete profile analysis, and mPC-I through mPC-V in the melodic profile analysis. The five rotated PCs of the complete analysis are related to those of the melodic analysis, but they are not completely congruent. Their numbering follows the output of the statistical program used (SYSTAT) and does not reflect the amount of variance each PC accounts for.

In the complete analysis, PC-I accounts for 17% of the variance. The corresponding melodic profile is mPC-IV, which accounts for 13% of the variance in the melodic profiles. They are in reasonable agreement, as can be seen in Fig. 3(a), and will be referred to collectively as the ''type I'' profile. The PC-I pattern is characterized by *crescendi* during all melodic gestures, particularly from the initial upbeat to the first downbeat and during the following three-note gesture in bar 1, which leads to an early dynamic peak. The melodic peak in bar 3 is deemphasized relative to the other melodic gestures. A second dynamic peak occurs in bar 4, and there is a small final *crescendo* in bar 5. The accompaniment is generally much softer than the melody, except in the second half of bar 4 where it reaches almost the same level. The mPC-IV pattern differs from the PC-I pattern in that it shows a more pronounced *crescendo* towards the melodic peak in bar 3, but a deemphasis of the gesture-final long notes in bars 1 and 4. No individual profile shows a very high correlation with these patterns. The most representative performances, by Timofeyeva and Richter, respectively, are shown in Fig. 3(b) and (c). Other pianists with relatively high loadings are Haase, Malcuzinsky [see Fig. 2(d)], Koyama, and Vásáry.

Figure 4(a) shows the type II profile, which is defined by two highly correlated PC patterns, PC-II and mPC-V, each of which accounts for 13% of the variance in its respective PCA. The type II profile shows a consistent differentiation of melody and accompaniment and a marked *decrescendo* through bars 4 and 5. Melodic gestures show relatively little dynamic variation, and in particular no *crescendi* (unlike the type I profile). The performance most representative of both PC-II and mPC-V profiles is that by Perlemuter, shown in

FIG. 3. (a) The type I profile (PC-I) and the corresponding melodic profile (mPC-IV), and the performances with the highest loadings on (b) PC-I and (c) mPC-IV.

FIG. 5. (a) The type III profile (PC-III) and the corresponding melodic profile (mPC-III), and the performances with the highest loadings on (b) PC-III and (c) mPC-III.

Fig. 4(b). Its melodic gestures are remarkably uninflected. Others with high loadings include Koczalski, Cherkassky, and Goldenweiser.

Figure 5 shows the type III pattern, defined by the moderately correlated PC-III and mPC-III profiles, which account for 13% and 12% of the variance, respectively. It is charac-

FIG. 4. (a) The type II profile (PC-II) and the corresponding melodic profile (mPC-V), and (b) the performance with the highest loadings on both PC-II and mPC-V.

terized by a relative lack of differentiation between melody and accompaniment throughout, and by a pronounced dynamic arch that reaches its emphatic peak on the highest melody note. The performance most representative of PC-III, Slenczynska-1956 [Fig. 5(b)], exhibits the dynamic arch but does not show the accent on the melodic peak and maintains a better distinction between melody and accompaniment than the PC-III pattern. The performance of Ashkenazy-1974 [Fig. 5(c)], which has the highest loading by far on mPC-III, does exhibit a lack of differentiation and does show the peak accent but exhibits a less pronounced arch. Other performances that load fairly highly on PC-III include Slenczynska-1975, Bingham, and Donohoe.

In the complete profile analysis, PC-IV accounts for the largest percentage of the variance (20%). The same is true for its analog in the melodic analysis, mPC-II (21%). The two patterns are in close agreement, as can be seen in Fig. 6(a), and will be referred to as type IV. This profile is characterized by a very soft beginning in bar 1 but a clear distinction between melody and accompaniment in the following bars. The melodic gestures in bars 3, 4, and 5, however, show an abrupt drop in energy (an effect referred to as *subito piano* in musical parlance) on or before the final long note, which is played as softly as the accompaniment. This is especially noteworthy for the melodic peak in bar 3 which is conspicuously deemphasized, in contrast to the type I and III profiles. The parallel between the soft-spoken three-note melodic gesture in bar 1 and the sudden attenuation of its recur-
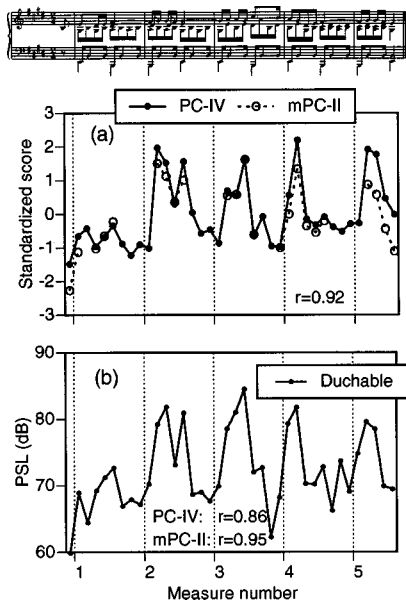
FIG. 6. (a) The type IV profile (PC-IV) and the corresponding melodic profile (mPC-II), and (b) the performance with the highest loadings on both PC-IV and mPC-II.

rence in the second half of the melodic gesture in bar 4 should also be noted. The performance most representative of this interesting strategy, both in its complete and purely melodic versions, is the one by Duchâble, shown in Fig. 6(b). Other performances with high loadings are those by Aide, Hesse-Bukowska, Coop, and Levant.
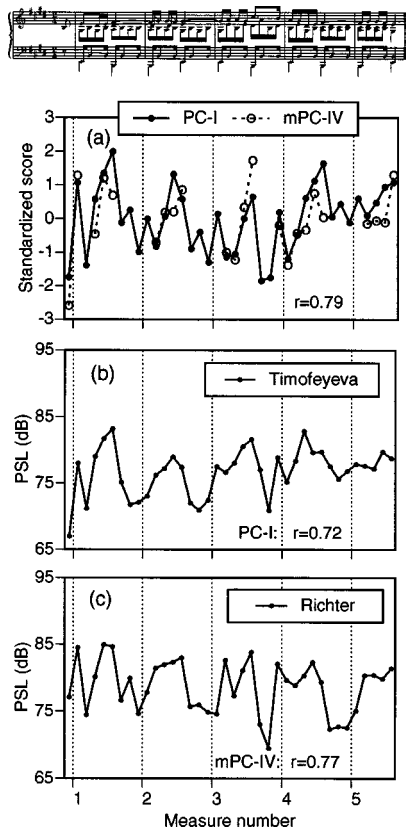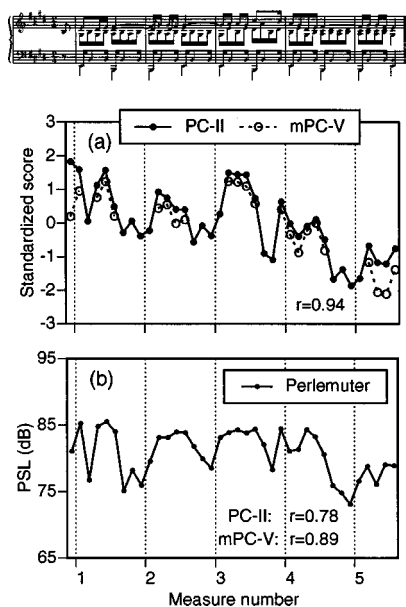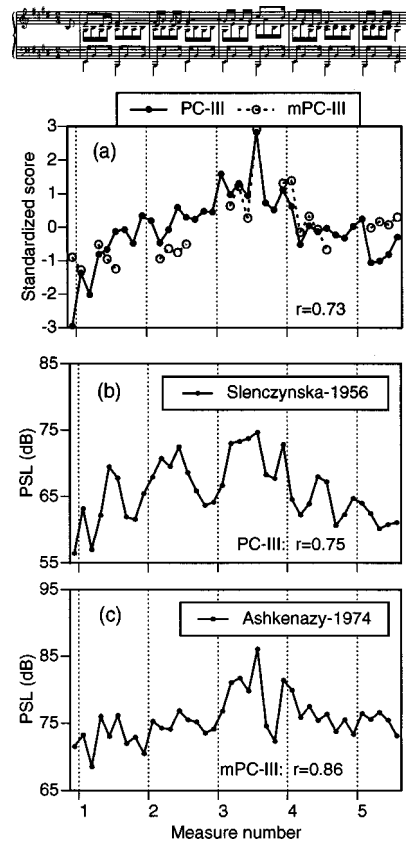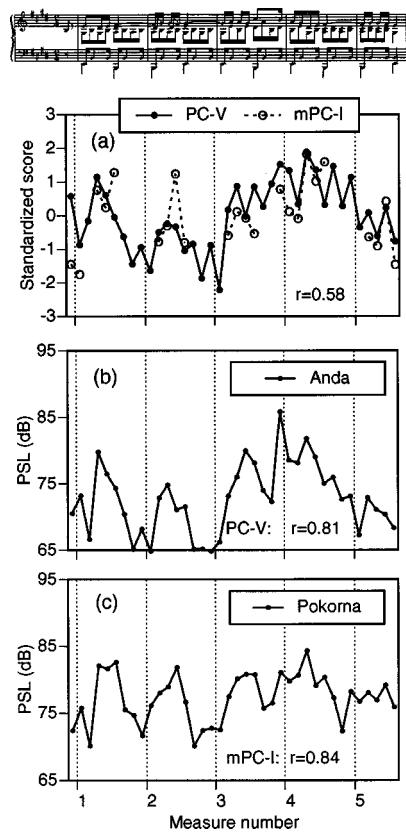

FIG. 7. (a) The type V profile (PC-V) and the corresponding melodic profile (mPC-I), and the performances with the highest loadings on (b) PC-V and (c) mPC-I.

Finally, the type V strategy is illustrated in Fig. 7. Figure 7(a) shows the two defining PC patterns, PC-V and mPC-I, which are only moderately similar. They account for 14% and 15% of the variance in the respective PCAs. PC-V is characterized by a strong initial upbeat, a deemphasis of bar 2, a high dynamic level in bars 3 and 4 with little differentiation of melody and accompaniment, and a final *decrescendo*. The mPC-I pattern deviates in certain details, such as the emphasis on the third note in the four-note melodic gesture of bar 2. The individual performances most representative of these patterns, by Anda and Pokorna, respectively, are shown in Fig. 7(b) and (c). Anda has the highest PC-V loading by far; others with moderately high loadings are Cortot-1942 and Lortie. The mPC-I loadings tend to be higher and include performances by Badura-Skoda and Egorov-1979, among others.

Performances such as those illustrated in the preceding five figures, which load primarily on one of the five PCs, are in the minority. Most performances have modest loadings on two or more of the PCs, which implies that their dynamic profiles can be described as a linear combination of several types. Figures 8 and 9 illustrate four such ''hybrid'' profiles, derived from the complete PC profiles. Figure 8 shows several linear combinations of PC profiles in which equal weights are given to the different profiles. (The PC profiles were added and then converted back into z-scores, which is equivalent to averaging them.) Figure 9 shows corresponding performance profiles that have approximately equal loadings on several PCs. Thus, Cortot-1933 [Fig. 9(a)] has a type I-V profile [$r = 0.74$ with the profile in Fig. 8(a)], Liberace [Fig. 9(b)] has a type II-V profile [$r = 0.76$ with the profile in Fig. 8(b)], M. Haas [Fig. 9(c)] has a type III-IV-V profile [$r = 0.94$ with the profile in Fig. 8(c)], and Egorov-1978 [Fig. 9(d)] represents a mixture of all five types, though he is leaning towards type IV [$r = 0.81$ with the profile in Fig. 8(d)]. It should be noted that the linear combination of all five PCs in Fig. 8(d) is almost identical with the grand average profile (Fig. 1). This follows from the fact that the PCA decomposed the variation among individual profiles into five mutually uncorrelated patterns that account for roughly equal amounts of variance. In terms of these diverse profile types, the most common profile shape (the grand average) seems the most complex, though from another perspective it is the simplest one (viz., the norm). The strategies represented by the rotated PCs are different ways of deviating from the central norm or prototype. The more such ways are adopted simultaneously, the less the net deviation will be.

The pianists' loadings on the different PCs tend to show small negative intercorrelations (computed across all 117 performances), due to the fact that a high loading on one PC implies lower loadings on the others. Some pairs of PCs (I–II, I–III, II–V) exhibit higher negative correlations of their loadings (around −0.3) than other pairs, suggesting that they do not mix as readily as others. However, two-dimensional plots of the PC loadings revealed no clusters or gaps in the distributions, just as in the analysis of the timing data (Repp, 1998a). This suggests that individual performances are fairly uniformly distributed in the multidimen-
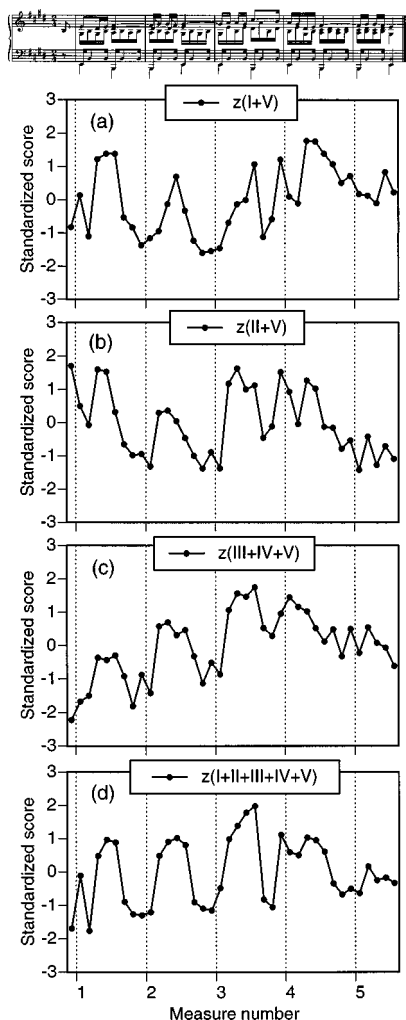
FIG. 8. Four equally weighted combinations of complete PC profiles: (a) PC-I+PC-V, (b) PC-II+PC-V, (c) PC-III+PC-IV+PC-V, and (d) all five PCs.

FIG. 9. Performances that best exemplify the combinations shown in Fig. 8.

sional space defined by the PC coordinates. The PC loadings of all performances may be found in Appendix B.

E. Similarity among performances

The intercorrelations among all performance profiles were computed, both for complete and melodic profiles. Each matrix contained 117*116/2=6786 correlations. As expected, two correlations stood out in each matrix—the ones between the two pairs of recordings revealed to be duplicates in the timing analysis (Repp, 1998a). The two versions of Zarankin, which derived from different CDs (one was misattributed to a pianist named van der Voss), were perfectly correlated. The two versions of Aide (copied twice from the same recording by mistake) correlated 0.990 (0.981 for the melody only). These correlations were much higher than the next-highest correlations, which proves beyond any doubt that these pairs of performances were in fact identical. The imperfect correlations for Aide must have been due to some kind of small measurement error.

The highest correlation between the complete dynamic profiles of two different performances was 0.929 (Kahn and Kentner). This is about as similar as dynamic profiles of

different artists get. Figure 10(a) shows them superimposed. [Kentner's profile is also shown in Fig. 2(a).] Both are examples of typical profiles that correlate highly with the grand average profile and load on several rotated PCs. The highest correlation between the melodic profiles of different performances was 0.924 (Slenczynska-1975 and Renard), as shown in Fig. 10(b). They are both type III profiles [cf. Fig. 5(a)]. There were only four negative correlations among the complete profiles, the lowest of which was −0.109 (Slenczynska-1975 and Malcuzinsky). The contrast between Slenczynska's highly arched profile and Malcuzinsky's flat profile may be gauged by comparing Figs. 10(b) and 2(d). Negative correlations were more frequent among the melodic profiles and reached a minimum of −0.508 (Haase and Crown). Figure 10(c) shows that Haase makes strong *crescendi* during melodic gestures and especially in bar 5 (a type I profile), whereas Crown tends to deemphasize melodic peaks and makes a *decrescendo* at the end (a type II profile).

Seven pianists were represented by two different performances each, recorded many years apart except in the case of Egorov, whose two recordings are separated by only one year. However, none of these artists showed exceptionally high correlations between his or her two dynamic profiles. The highest correlations were shown by Cziffra (0.867 com-

1979   J. Acoust. Soc. Am., Vol. 105, No. 3, March 1999

Bruno H. Repp: Musical expression: Dynamics   1979
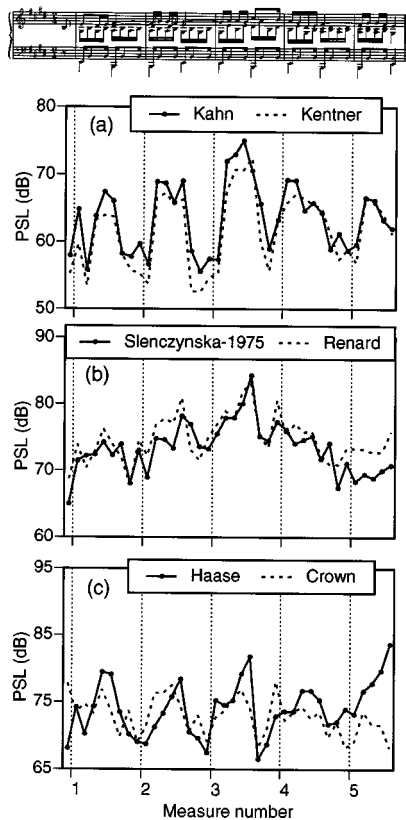
FIG. 10. The two most similar performances in terms of (a) complete dynamic profiles and (b) melodic dynamic profiles; also, (c) the two most dissimilar performances in terms of complete profiles.

plete, 0.758 melodic), Slenczynska (0.728 complete, 0.834 melodic), and Cortot (0.777 complete, 0.680 melodic). Arrau, Ashkenazy, and Egorov showed only moderate correlations, the last a very low melodic correlation. The lowest consistency was exhibited by Horowitz (0.270 complete, 0.224 melodic). Thus there was little evidence for the maintenance of an individual dynamic profile across many years, or even across one year in the case of Egorov. In general, little is known about pianists' consistency in this respect, though an individual dynamic profile can certainly be replicated in repeated takes on the same day (Repp, 1996a).

F. Sociocultural variables

As described in Repp (1998a), information about five sociocultural variables was available: artists' gender, nationality (i.e., country of birth, without regard to educational history), birth date, recording date, and age at the time of recording (which was negatively correlated with birth date but unrelated to recording date). Except for gender, the data were somewhat incomplete but sufficient for a preliminary investigation. The dependent variables were the two indices of dynamic range (ms.d., the standard deviation of the melodic PSLs, and ΔMA, the difference between the average PSLs of melody and accompaniment), the two typicality indices (UPC-I and mUPC-I loadings), and the rotated PC loadings in the PCAs on the complete and melodic profiles.

Recording dates were unrelated to measures of dynamic range (which suggests, surprisingly, that old recordings were not of more limited dynamic range than new CDs) but mar-

ginally related to typicality: The correlation with mUPC-I loadings reached significance ($r = 0.25$, $p < 0.05$); that with UPC-I loadings did not. Thus, there was a slight tendency for more recent recordings to exhibit a more typical melodic dynamic profile, which is consistent with the frequent claim of music critics that performances are less individual now than many years ago. Recording date showed some more substantial correlations with dynamic strategies. In particular, it was negatively correlated with the type II pattern ($r = -0.40$, $p < 0.001$, with PC-II loadings; $r = -0.33$, $p < 0.001$, with mPC-V loadings). This pattern, which is characterized by a relatively uninflected melody and a marked drop in dynamic level towards the end of the phrase (see Fig. 4), is thus more frequently encountered in older recordings. Weaker, positive correlations of recording date with the type I pattern ($r = 0.23$, $p < 0.05$, with PC-I loadings; $r = 0.32$, $p < 0.01$, with mPC-IV loadings) and with the type V pattern ($r = 0.25$, $p < 0.05$, with PC-V loadings; $r = 0.31$, $p < 0.01$, with mPC-I loadings) indicated that these strategies are encountered more often in recent recordings.

Artists' birth dates, like recording dates, showed a slight positive correlation with mUPC-I ($r = 0.22$, $p < 0.05$), a negative correlation with type II ($r = -0.33$, $p < 0.001$, with PC-II loadings; $r = -0.31$, $p < 0.01$, with mPC-V loadings), and a marginal positive correlation with type I ($r = 0.22$, $p < 0.05$, with PC-I loadings), but a stronger positive correlation with type V ($r = 0.31$, $p < 0.01$, with PC-V loadings; $r = 0.45$, $p < 0.001$, with mPC-I loadings). Thus, a melodic profile that gives special emphasis to bar 4 but deemphasizes bar 2 (type V) is favored more by younger generations of pianists.

Age at the time of recording was related weakly to two melodic dynamic strategies: positively to type II ($r = 0.24$, $p < 0.05$, with mPC-V loadings) and negatively to type V ($r = -0.26$, $p < 0.01$, with mPC-I loadings). These correlations have the opposite sign of those for birth date, which reflects the negative correlation between birth date and age at the time of recording. Thus, the type II pattern is more associated with older artists, the type V pattern more with younger artists.

Effects of nationality were difficult to assess because of the many countries represented. As in the earlier timing analysis, the analysis was restricted to three well-represented nationalities with strong traditions of Chopin performance: French, Polish, and Russian. However, one-way analyses of variance (ANOVAs) revealed no significant effects of this independent variable on any of the dependent variables.

Gender was similarly analyzed in one-way ANOVAs, but making use of the complete sample. One significant difference emerged: Female pianists exhibited a significantly greater dynamic range in the melody [$F(1,113) = 7.1$, $p < 0.01$]. The average ms.d. was 3.9 dB for women as compared to 3.4 dB for men. This greater dynamic inflection may indicate a more liberal display of emotion by female than by male artists. A second effect fell just short of significance: Women exhibited somewhat higher average mUPC-I loadings (0.729) than men (0.658) [$F(1,113) = 3.66$, $p < 0.06$], which means that the female pianists in the sample tended to

produce somewhat more typical or conventional melodic dynamic patterns than did the male pianists.

G. Relationships with expressive timing

Todd (1992) has described a tendency for dynamics to covary with timing, which may be summarized as ''the faster, the louder'' (or vice versa). If timing is measured in terms of IOI duration, this implies a negative correlation. While there are numerous exceptions to this rule, it may be considered as a default or ''unmarked'' case whose violation is ''marked'' and thereby conveys special expressive effects. It is not clear, however, whether this reasoning can be applied at the local level considered here.

To begin with, the grand average timing profile (Repp, 1998a, Fig. 4) was compared with the grand average dynamic profile (Fig. 1). Their overall correlation was positive ($r = 0.44$, $p < 0.01$), contrary to Todd's rule.[2] The reason for this is that the accompaniment during sustained melody notes is generally played both faster and softer than the melody. A more meaningful correlation, therefore, is that for the melody notes only. It was negative but failed to reach significance ($r = -0.33$). Moreover, it dropped to -0.05 when the very long IOI and the corresponding PSL of the first downbeat were omitted. Thus, there was not really any relation between typical timing and typical dynamics within the melody. The same was true within the accompaniment ($r = 0.08$). There was no evidence for any nonlinear relationship either.

Next, the correlations between the grand average timing profile and the melodic dynamic PC patterns were examined. There was a sizeable positive correlation with mPC-IV ($r = 0.64$, $p < 0.001$), the dynamic type I pattern. It will be recalled that the type I profile is characterized by *crescendi* within melodic gestures, and these *crescendi* correspond to the *ritardandi* that typically occur as well. Intuitively, however, type I does not seem ''marked,'' even though it violates Todd's rule. The *subito piano* strategy of type IV seems much more deserving of that epithet.

Next, the correlations between the grand average melodic dynamic profile and the four timing PC profiles were computed. The only significant correlation was with timing PC-III ($r = -0.48$, $p < 0.05$), which is characterized by an exceptionally long first (initial downbeat) IOI. With that IOI omitted, the correlation withered.

Finally, the $4 \times 5 = 20$ correlations between the PC profiles for melodic timing and the PC profiles for melodic dynamics were examined. The only sizeable correlation was between the PC-I for timing and the dynamic mPC-IV ($r = 0.67$, $p < 0.001$). This relationship is essentially the same as the one between the grand average timing profile and mPC-IV, for the PC-I for timing is similar to the grand average timing profile.

Even though there were no relationships between major timing strategies and dynamic strategies, some interdependence of the two expressive parameters at the individual level seemed possible. Therefore, the correlations between melodic timing and dynamics were computed for all 115 individual performances. Only 18 correlations reached significance ($|r| > 0.43$, $p < 0.05$), and all but one were negative. The highest negative correlations were shown by Fou Ts'ong ($r = -0.74$, $p < 0.001$) and Karolyi ($r = -0.67$, $p < 0.001$), whereas the only significant positive correlation was exhibited by Malcuzinsky ($r = 0.57$, $p < 0.01$). It may be recalled that Malcuzinsky has the most atypical melodic dynamic profile [Fig. 2(d)]. While it is possible that timing and dynamics were functionally linked for these 18 artists, it seems just as likely that they pursued independent strategies that just happened to show some correspondence. Moreover, the initial downbeat probably accounted for the negativity of most correlations (see above).

To examine whether there was any relationship between the relative typicality of individual timing profiles and dynamic profiles, the correlation between the respective UPC-I loadings was computed across all performances. It was zero. Next, possible associations of the PC patterns for timing and dynamics were investigated by computing the $4 \times 5 = 20$ cross correlations between the respective PC loadings. While some of these correlations reached significance due to the large degrees of freedom, they were too small ($r < 0.3$) to have any explanatory value.

A final possibility examined was that the degrees of timing modulation and of dynamic modulation might be associated with each other, regardless of the pattern exhibited. However, the relevant correlations were nonsignificant.

In summary, then, these analyses suggest that expressive timing and expressive dynamics are independently controlled at the within-phrase level of detail considered here. The possibility remains that there are even more local dependencies than were considered in these analyses, such as within melodic gestures. However, this would be difficult to prove, given the small number of data points.

III. GENERAL DISCUSSION

This is the first study of individual differences in expressive dynamics in a large sample of expert performances. Individual patterns of expressive dynamics proved to be at least as diverse as individual patterns of expressive timing. For timing, four ''strategies'' had been identified, one of which concerned only the initial downbeat IOI (Repp, 1998a). For dynamics, there were five strategies that affected the dynamic shaping throughout the phrase. Moreover, for timing there was a dominant strategy (PC-I) which resembled the grand average timing profile, whereas for dynamics none of the five strategies was particularly prevalent or similar to the grand average profile. In a sense, therefore, expressive dynamics offers more opportunities for the exhibition of individuality than does expressive timing, at least in the musical excerpt studied. However, because timing tends more towards a central norm and because there are fewer categorically distinct options of deviating from this norm, individuality in timing may be more conspicuous when it occurs.

The central norm is identified with the grand average profile. This seems to be as valid for dynamics as it is for timing. For both expressive dimensions, the majority of performances shows a moderate to high degree of similarity with the grand average profile. This profile is a statistical summary of all the individual variation, and as such it re-

veals the *potentialities* of timing or dynamics. An appropriate metaphor may be to regard a musical passage as a flexible ribbon varying continuously in thickness or stiffness, due to its internal structure. Points of high flexibility are those where the music is less cohesive and invites the performer to ''stretch'' or ''bend'' it. A typical (mainstream, conventional, textbook) performance tries to realize all these potentialities simultaneously, as would a sophisticated computer algorithm (yet to be devised) that generates expressive variation deterministically from a complete structural representation. An individual (original, creative, unconventional) performance deviates from the normative pattern, following one or more of several possible expressive strategies. Such strategies necessarily highlight some aspects of the musical structure while deemphasizing others, but it is far from clear that this is the artist's purpose in expressive performance. Some strategies create contrast between notationally similar structures by giving them different temporal or dynamic shapes.

Dynamic strategies seem less constrained by the musical structure than timing strategies. Timing within a rhythmic group usually has to exhibit continuity and smoothness, or else the listener will perceive momentary hesitations and accelerations that are aesthetically undesirable. This restricts timing to basic acceleration–deceleration shapes (Todd, 1992). Expressive dynamics does not seem to be restricted in this way. Besides smooth *crescendi* and *decrescendi*, a variety of other accent patterns is possible, both in conformity with and against the underlying metrical grid. Whereas timing imparts a particular movement to a musical gesture, gives it coherence, and separates it from other gestures, dynamics give it a particular ''flavor'' or character. Short of wild exaggeration of accents or contrasts, dynamic patterns do not seem to sound deviant or irregular as easily as do timing patterns. These observations are rather speculative, however, and need further investigation.

Many performers blend different strategies into novel combinations. While this may seem especially creative, it is an interesting paradox that, the more strategies are combined, the more the resulting pattern resembles the grand average profile. The central norm is the combination of all possible strategies of deviating from it; it is synthetic. A truly original performance follows a single deviant strategy; in this sense it is analytic.[3] There is another paradox here, however, in that the PCs—the result of a Varimax rotation—were determined automatically in order to maximize the number of performances with high loadings. As a result, for every truly original performance (i.e., one loading highly on a single PC) there are several other performances that are original in more or less the same way. Where, then, does true originality lie? The PCs could have been rotated to a different configuration, one that does not satisfy the Varimax criterion but accounts for just as much variance in the data. Would the PCs of any such rotation be associated with *uniquely* individual performances? This seems unlikely in view of the relatively uniform distribution of the PC loadings in the two-dimensional spaces spanned by pairs of PCs. It seems likely that any rotated PC would be associated with small groups of performances. Thus, originality can only be

equated with nontypicality, i.e., distance from the central prototype, not with uniqueness or with a distinct region in the space of possibilities. Of course, the large number of degrees of freedom available in expression makes any individual performance effectively unique, but there are always other performances that are similar to it in one way or another. In other words, the territory of expressive possibilities has been well explored by artists, and while there are many uninhabited regions, they probably will remain so because they are inhospitable to both performers and listeners.

As was already pointed out in the earlier article on timing (Repp, 1998a), the psychological status of the expressive strategies remains unclear. At this point, they are merely descriptive coordinates that make it possible to talk about the differences among 115 performances without having to describe each of these performances. It does not seem to be the case that different expressive strategies reflect different structural interpretations of the music, at least not in a categorical sense; nor do ''pure'' strategies seem to be more pure in any cognitive sense than ''mixed'' strategies. While structural interpretation draws on a limited set of categorically distinct possibilities, expressive shaping draws on a circumscribed but continuous and therefore effectively unlimited range of possibilities. The musical excerpt studied here does not really contain any structural ambiguities, at least not any that performers feel compelled to resolve, and therefore the performance analyses do not provide any evidence of categorically different structural interpretations. Rather, as already argued in Repp (1998a), they reveal continuous individual variability within constraints set by a single structural frame.

The apparent independence of timing and dynamics in the Chopin excerpt studied here may seem surprising. An interdependence between these two expressive dimensions may well be found in other kinds of music that have a more pronounced rhythmic structure (e.g., various dance forms). The present negative result may be due to the slow, almost arhythmic nature of the music, which offers maximal freedom in expressive shaping and was selected for that reason. Certainly, the independence of timing and dynamics increases the performer's degrees of freedom tremendously. Then there are additional factors that were not even considered here because they are too difficult to analyze objectively in acoustic recordings (such as ''touch,'' articulation, and pedaling). And it should not be forgotten that timing and dynamics each have three independent aspects: basic tempo and dynamic level, timing modulation and dynamic modulation, and timing pattern and dynamic pattern. Basic tempo and dynamic level primarily set the emotional tone of a performance: calm versus excited and gentle versus forceful, respectively. Degree of modulation defines a nonspecific dimension ranging from understatement to exaggeration. Patterns give shape and character. Expressive timing patterns are forms of movement; they govern the variable rate at which the musical sound structure unfolds. Dynamic patterns are part of the sound structure itself. They are a part of what is unfolding, whereas timing governs *how* this unfolding is taking place.

It is sometimes thought that music does not have any

expressive dynamics, because the intensities at which individual notes are to be played are not specified in the score—they are ''added'' by the performer. However, this is a serious misconception. Music in which all notes are of equal intensity does not sound right, especially when distinctions among voices are to be made. It is not the music represented in the score but a distortion of it. Therefore, music must always have *some* expressive dynamics, just as it must have *some* expressive timing (unless the music is specifically intended to be performed without expression). Elsewhere, the author has argued that a typical timing pattern is the most appropriate default timing pattern for a piece of music (Repp, 1995b, 1997a). This argument may now be extended to the typical dynamic pattern.[4] A performance possessing both of these patterns (plus appropriate articulation, pedaling, etc.) will be a perfectly acceptable realization of the score, and may in fact be considered as being the best approximation to what the score represents. Individual performances may deviate from these normative expressive patterns, but they do not ''deviate from the score.''

The present research also extends to dynamics a finding obtained repeatedly for timing (Repp, 1995b, 1997a, 1997b): The grand average profile of a group of advanced student pianists and amateurs is extremely similar to that of a large sample of expert recording artists. This suggests that the same norm of expressive shaping underlies performances at different levels of expertise. However, expert pianists' performances are much more diverse in timing than student performances, which tend to stay close to the norm. Without any doubt, this is also true for dynamics, even though no detailed analysis of individual differences in students' dynamic profiles has yet been conducted for the Chopin excerpt. Repp (1996a) commented on the narrow range of variation of student pianists' dynamic profiles in Schumann's ''Träumerei.'' This relative conservatism of student pianists is not at all surprising and may have a number of reasons, among them relative inexperience, lesser creativity compared to famous artists, and the increasing homogenization of classical music performance due to the influence of recordings and the competition circuit.

In this article and its predecessor (Repp, 1998a), evaluative comments have been studiously avoided; the analyses have been purely descriptive and objective. Yet, the reader may have been wondering about the relation of all this expressive diversity to the perceived quality of the performances. This topic will be addressed in the third and final installment in this series of papers (Repp, in preparation).

APPENDIX A: PRELIMINARY ACOUSTIC MEASUREMENTS

To investigate how the overall intensities of piano sonorities depend on the relative intensities of their component tones, acoustic measurements were performed on two performances whose individual tone intensities were known.

1. Method

In the course of several previous studies, 18 advanced student and amateur pianists had played the Chopin Etude excerpt repeatedly (three or ten times) on a Roland RD-250s digital piano and had been recorded in MIDI format. These MIDI data were imported into a spreadsheet program, and the key-press velocities of individual notes were averaged across each pianist's repeated performances and then across all pianists. These grand average velocities, assumed to represent a typical dynamic pattern for the music, were combined with MIDI instructions specifying constant sixteenth-note inter-onset intervals of 500 ms as well as synchronous note onsets and offsets (following the score literally), without pedal.[5] This performance was played under computer control on the digital piano. It will be referred to as the SA (student average) performance.

A second performance was played on the digital piano by a skilled young pianist (H.S.) and recorded in MIDI format. It differed from the computer-generated performance in that it was expressively timed and included both pedaling and small asynchronies among nominally simultaneous note onsets. In particular, the melody notes tended to precede the notes in the other voices, especially those played by the same (right) hand, as is commonly found in expressive performance (Palmer, 1996b; Repp, 1996b). This will be referred to as the HS performance.

Two reduced versions were created from the MIDI instructions for each of these two performances. In one, the MIDI velocities of all secondary notes were set to zero, so that only the primary notes remained. In the other, the primary notes were moreover shortened to 100-ms duration and, in the HS performance, the pedal instructions were deleted. This eliminated all acoustic overlaps among successive primary tones caused by sustained melody tones, decay of immediately preceding damped tones (see Repp, 1995a), and pedaling.

All six versions were played back under computer control on the digital piano, were recorded electronically onto digital audio tape, and then were resampled by a Macintosh Quadra 660AV computer at a rate of 22.055 kHz. Using SIGNALYZE software, the root-mean-square amplitude envelopes of the digitized waveforms were computed with a sliding rectangular integration window of 30 ms, and subsequently an automatic peak-picking routine was employed to determine the peak amplitude following each note onset. These peak amplitudes were then converted into peak sound levels (PSLs) in decibels (dB).

2. Results and discussion

Figure A1 compares the dynamic profiles for the full performances with the versions containing primary notes
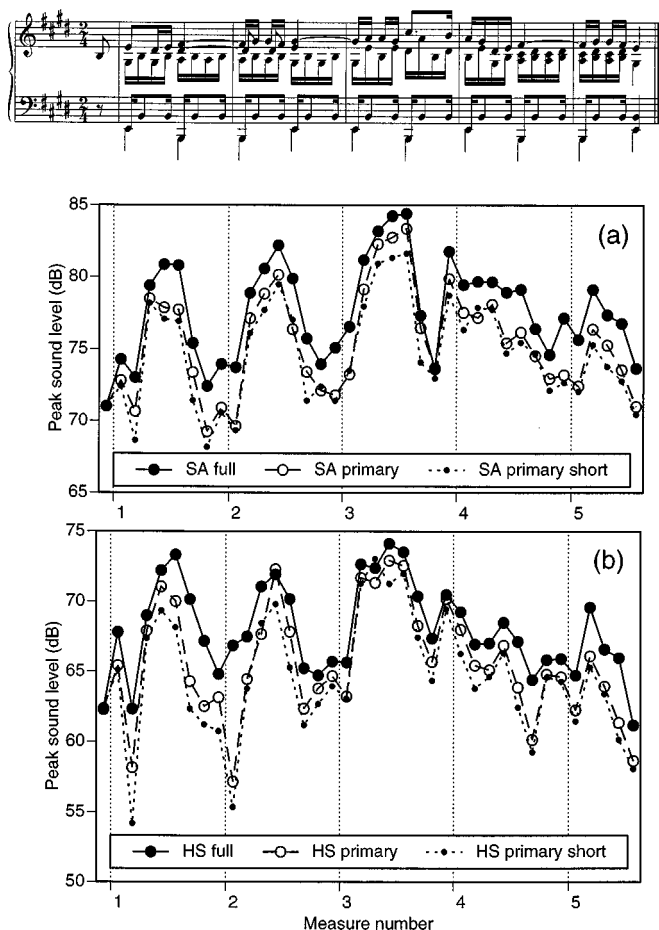
FIG. A1. Measured peak sound levels of three versions of (a) the computer-generated SA performance and (b) the human HS performance. The three versions are: full (all notes), primary notes only, and short (truncated) primary notes.

FIG. A2. Measured peak sound levels as a function of the MIDI velocity of the primary notes for the three versions of (a) the SA performance and (b) the HS performance.

only. (The difference in average absolute sound level between the SA and HS performances is meaningless.) The PSLs of the initial upbeat are identical in the three versions of each performance because it was not accompanied by any other tone. As expected, the PSL values for the full performance are generally higher than those for the primary tones only, due to the contribution of the secondary (lower-pitched) tones and the sustained melody tones. The PSL values for the primary tones in turn are somewhat higher than those of the short primary tones, reflecting the contribution of the overlaps of successive tones. In the case of the SA performances [Fig. A1(a)], the dynamic profiles of the three versions are highly similar: The full and primary profiles correlate 0.96, and the primary and primary-short profiles correlate 0.98. Even if only the 23 melody-note positions are considered, the correlations are still of the same magnitude. For the HS performances [Fig. A1(b)], the correlation between the full and primary profiles is not quite as high ($r = 0.89$), whereas that between the primary and primary-short profiles is 0.97. If only the melody notes are considered, the corresponding correlations are 0.95 and 0.97, respectively. It can be seen in Fig. A1(b) that the major discrepancies between primary and full PSLs occur during the accompaniment passages, where the primary notes are relatively soft.

This correlational evidence suggests that the overall dy-namic profile is quite representative of the dynamic profile of the primary notes, especially of the melody notes. The analysis went one step further by investigating whether the overall PSLs could be predicted from the known MIDI (key-press) velocities of the individual notes. Figure A2 shows the measured PSLs as a function of the MIDI velocities of the primary notes. Quadratic functions have been fitted to the data points. For the primary and primary-short versions, these functions are very similar to the function obtained in a previous study, where PSL measurements were averaged across many different pitches on the same digital piano (Repp, 1993; see Repp, 1997c, Fig. 1). Deviations of individual data points from the function may reflect imperfect calibration of different pitches on the electronic instrument and/or measurement error of some kind. The function for the full SA performance is also similar, even though many additional notes contributed to the overall PSLs. Only the function for the full HS performance is different and reflects larger contributions of the additional notes when the MIDI velocity of the primary note is low than when it is high.

Linear regression analyses were subsequently conducted, with the full performance PSLs as the dependent variable and the MIDI velocities of the individual notes as the independent variables. The velocities of the primary notes constituted the first independent variable, and the velocities of additional mezzo, alto, tenor, and bass notes yielded four additional independent variables that were padded with zeroes in positions where there were no note onsets.

A standard regression analysis on the SA full performance data accounted for 93% of the variance ($R = 0.97$). Naturally, the largest contribution was made by the primary-note velocities, which alone accounted for 89% of the variance, but small additional contributions were made by the secondary notes in each voice. In a subsequent stepwise re-
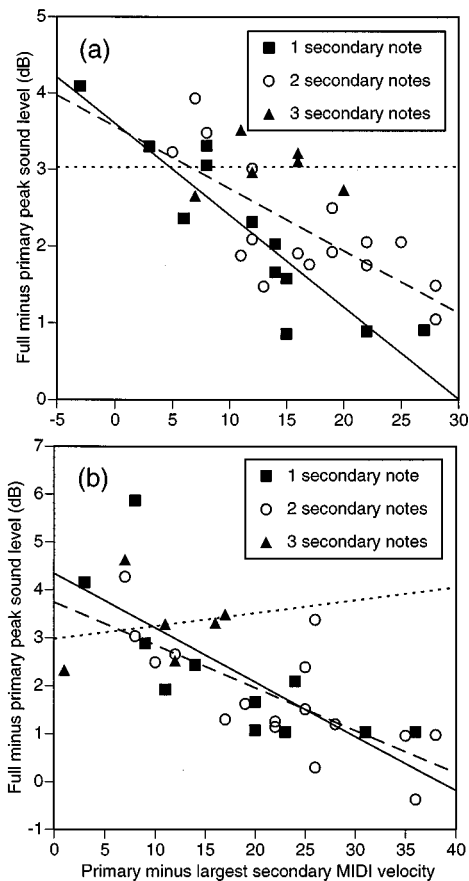
FIG. A3. The increase in peak sound level due to secondary notes as a function of the velocity difference between the primary note and the loudest secondary note, and of the number of secondary notes, for (a) the SA performances and (b) the HS performances.

gression analysis, however, only the contribution of secondary alto notes reached significance.

A standard regression analysis on the HS full performance data accounted for 85% of the variance ($R = 0.92$). The primary-note velocities alone accounted for 78% of the variance. In a stepwise regression analysis, the contributions of secondary mezzo, tenor, and bass notes reached significance, but, in contrast to the SA performance results, secondary alto notes made no contribution at all. This may have been due to a tendency of secondary alto notes onsets to lag behind primary melody note onsets. The variance not accounted for must be attributed to varying asynchronies and tone overlaps. No attempt was made to enter these additional variables into a regression analysis, though they would have to be included in a complete predictive model.

Figure A3 illustrates graphically the contribution of secondary notes. The difference between the full and primary PSLs (i.e., the increase in PSL due to secondary notes) is shown as a function of the MIDI velocity difference between the primary note and the most prominent secondary note in the same position, regardless of voice. The solid regression line represents positions in the music where there was only a single secondary note. Clearly, this extra tone contributed to the overall PSL in proportion to its intensity relative to the primary tone.[6] The dashed regression line represents positions in which there were two secondary notes accompanying a primary note. The additional contribution of the second (softer) secondary note is reflected in the difference between the solid and dashed regression lines; such a difference is evident only for the SA performances [Fig. A3(a)]. The dotted regression line represents the five positions in the music where there were three secondary notes; here there is no longer any relationship between the relative velocity of the strongest of them and the PSL increase, but some contribution of the third secondary note is suggested, at least for the SA performances.

Regression analyses were conducted with the independent variables recoded as the velocities of primary, second, third, and fourth notes, ordered according to velocity magnitude and regardless of voice. The standard regression equations accounted for the same amounts of variance as previously. In stepwise regression analyses, primary, second, and third notes made significant contributions in the SA performances; primary, second, and fourth notes in the HS performances.

The y-axis intercepts of the regression lines in Fig. A3 indicate that addition of an equally intense tone of lower pitch to a primary tone results in an increase of about 4 dB in overall PSL. If peak amplitudes were strictly additive, the expected increase would be 6 dB. Palmer and Brown (1991) have presented data showing that the peak amplitudes of two simultaneous piano tones of different pitch are nearly additive: The combined amplitude increased by 81% to 96%, which translates into 5.2 to 5.8 dB. The smaller increases observed here may be due to smoothing by the 30-ms temporal window used in determining the PSLs. The similar y-axis intercepts of the regression lines for the AS and HS performances suggest that onset asynchronies in the HS performances were not responsible.

APPENDIX B: PERFORMANCE STATISTICS

ms.d. = standard deviation of melodic PSLs (dB).
ΔMA = difference between average PSLs of melody and accompaniment (dB).
UPC-I = loadings on first unrotated PC for the complete profile (index of typicality)
PC-I through PC-V = loadings on rotated PCs for the complete profile

Pianist	ms.d.	ΔMA	UPC-I	PC-I	PC-II	PC-III	PC-IV	PC-V
Aide	3.1	4.6	0.810	0.201	0.264	0.137	0.806	0.298
Aide 2	2.9	4.9	0.797	0.161	0.325	0.083	0.800	0.314
Anda	4.3	6.6	0.740	0.210	0.290	0.177	0.204	0.811
Anievas	3.6	5.7	0.743	0.118	0.249	0.289	0.650	0.301
Arrau 1930	3.9	6.2	0.837	0.142	0.457	0.506	0.529	0.251

Pianist	ms.d.	ΔMA	UPC-I	PC-I	PC-II	PC-III	PC-IV	PC-V
Arrau 1956	4.5	4.6	0.798	0.458	0.153	0.379	0.669	0.038
Ashkenazy 1959	3.4	5.5	0.787	0.227	0.368	0.254	0.521	0.366
Ashkenazy 1974	3.4	3.2	0.721	0.168	0.262	0.692	0.237	0.324
Backhaus	3.1	6.0	0.857	0.552	0.353	0.315	0.442	0.230
Badura-Skoda	3.3	5.4	0.738	0.565	0.024	0.081	0.319	0.608
Berezovsky	3.7	4.1	0.811	0.570	0.047	0.461	0.268	0.466
Bingham	3.9	1.8	0.672	0.503	0.071	0.734	0.172	0.061
Binns	3.0	3.4	0.695	0.524	0.260	0.375	0.179	0.238
Biret	2.9	2.6	0.762	0.253	−0.111	0.460	0.485	0.575
Brailowsky	3.8	5.8	0.737	0.251	0.648	0.350	0.337	0.107
Browning	2.4	2.7	0.792	0.522	0.407	0.555	0.130	0.228
Cherkassky	5.4	10.6	0.850	0.299	0.679	0.340	0.216	0.447
Ciani	5.7	7.1	0.809	0.240	0.371	0.578	0.413	0.235
Ciccolini	3.4	6.0	0.802	0.654	0.158	0.140	0.376	0.414
Cliburn	3.8	3.6	0.769	0.544	0.081	0.417	0.492	0.129
Coop	4.5	7.2	0.835	0.233	0.142	0.261	0.752	0.388
Cortot 1933	3.0	6.2	0.874	0.506	0.383	0.252	0.291	0.538
Cortot 1942	3.8	4.9	0.799	0.291	0.367	0.367	0.141	0.693
Costa	4.1	7.7	0.806	0.310	0.582	0.312	0.203	0.464
Crown	2.3	3.5	0.513	0.148	0.760	−0.089	0.199	0.170
Cziffra 1954	2.9	6.3	0.903	0.480	0.189	0.339	0.504	0.466
Cziffra 1981	3.7	6.5	0.841	0.497	0.052	0.182	0.674	0.364
Darré	5.3	6.6	0.663	−0.004	0.600	0.195	0.298	0.449
Donohoe	4.1	2.8	0.676	0.055	0.493	0.725	0.240	0.095
Drzewiecki	4.5	5.2	0.828	0.232	0.102	0.586	0.483	0.442
Duchâble	6.1	5.8	0.687	0.122	0.169	0.277	0.858	−0.008
Egorov 1978	2.8	4.0	0.818	0.357	0.300	0.328	0.493	0.326
Egorov 1979	2.4	5.8	0.802	0.604	0.267	0.079	0.320	0.493
Ellegaard	4.3	6.0	0.733	0.016	0.519	0.240	0.638	0.201
Entremont	3.0	2.5	0.602	0.555	0.263	0.346	0.072	0.146
Farrell	3.0	5.1	0.720	0.620	0.201	−0.001	0.417	0.298
Fou Ts'ong	5.0	6.5	0.836	0.201	0.082	0.481	0.599	0.465
François	3.6	4.6	0.799	0.295	0.528	0.431	0.414	0.144
Goldenweiser	3.5	8.2	0.770	0.151	0.679	0.180	0.308	0.458
Goldsand	3.2	6.4	0.844	0.610	0.398	0.232	0.507	0.092
Goodman	2.5	6.0	0.791	0.252	0.396	0.160	0.526	0.403
Haas, M.	5.0	5.5	0.819	0.053	0.146	0.556	0.529	0.546
Haas, W.	2.0	2.8	0.711	0.439	0.333	0.228	0.097	0.540
Haase	3.5	5.4	0.705	0.712	0.151	0.167	0.326	0.169
Harasiewicz	3.6	6.4	0.861	0.313	0.336	0.246	0.408	0.622
Hesse-Bukowska	4.5	8.6	0.883	0.422	0.266	0.227	0.775	0.182
Hobson	2.5	4.2	0.782	0.589	0.309	0.146	0.167	0.551
Horowitz 1951	3.6	3.2	0.554	0.334	0.464	0.158	0.076	0.259
Horowitz 1972	2.1	0.7	0.370	0.174	−0.028	0.537	−0.065	0.283
Iturbi	2.9	5.9	0.784	0.269	0.684	0.178	0.558	0.049
Janis	2.5	4.8	0.755	0.217	0.536	0.193	0.492	0.242
Johannesen	3.3	6.6	0.873	0.428	0.245	0.319	0.569	0.342
Joyce	3.9	5.5	0.725	0.368	0.374	0.177	0.447	0.226
Kahn	3.8	8.2	0.884	0.170	0.464	0.291	0.667	0.352
Karolyi	3.9	4.2	0.779	−0.005	0.475	0.488	0.374	0.470
Katz	3.7	5.3	0.826	0.219	0.548	0.403	0.522	0.164
Kentner	3.6	9.3	0.936	0.324	0.342	0.280	0.624	0.481
Kersenbaum	2.9	5.5	0.862	0.454	0.479	0.209	0.359	0.433
Kilényi	2.9	3.4	0.778	0.409	0.307	0.623	0.241	0.211
Koczalski	3.8	2.9	0.401	0.012	0.776	0.243	0.099	−0.137
Koyama	4.4	4.9	0.801	0.591	0.035	0.439	0.388	0.302
Kyriakou	6.6	7.1	0.887	0.259	0.186	0.551	0.598	0.361
Larrocha	4.0	6.1	0.805	0.459	0.499	0.192	0.399	0.242
Levant	4.7	8.2	0.838	0.364	0.303	0.165	0.682	0.278
Liberace	2.5	4.8	0.658	0.321	0.529	−0.034	0.153	0.539

Pianist	ms.d.	ΔMA	UPC-I	PC-I	PC-II	PC-III	PC-IV	PC-V
Licad	4.2	6.0	0.912	0.471	0.319	0.527	0.418	0.313
Lopes	3.1	5.2	0.859	0.408	0.298	0.292	0.472	0.426
Lortat	3.2	3.1	0.664	0.643	0.249	0.311	0.245	0.025
Lortie	2.8	3.5	0.758	0.350	0.022	0.407	0.277	0.645
Magaloff	2.8	5.6	0.904	0.345	0.313	0.391	0.642	0.284
Magin	3.8	6.5	0.834	0.511	0.056	0.258	0.392	0.608
Malcuzinsky	2.1	2.3	0.433	0.672	0.294	−0.090	−0.037	0.134
Mamikonian	2.5	4.7	0.873	0.491	0.221	0.269	0.530	0.389
Manz	5.4	4.0	0.743	0.404	0.100	0.449	0.167	0.574
Murdoch	3.0	4.6	0.849	0.389	0.581	0.427	0.321	0.226
Niedzielski	3.0	2.9	0.500	0.001	0.047	0.228	0.345	0.482
Novaes	5.2	7.0	0.900	0.347	0.260	0.405	0.668	0.277
Paderewski	2.9	2.7	0.696	0.201	0.321	0.444	0.598	−0.044
Pennario	3.0	7.4	0.866	0.350	0.480	0.053	0.688	0.291
Penneys	3.2	6.9	0.816	0.517	0.282	−0.035	0.483	0.509
Perahia	4.5	2.3	0.727	0.167	0.134	0.678	0.325	0.361
Perlemuter	2.5	4.6	0.649	0.220	0.784	0.255	0.141	0.141
Pokorna	2.7	5.1	0.829	0.505	0.240	0.223	0.290	0.594
Pollini	2.8	6.2	0.915	0.428	0.229	0.347	0.511	0.498
Ranki	3.4	2.7	0.749	0.631	0.114	0.510	0.195	0.238
Renard	3.4	3.4	0.759	0.105	0.395	0.667	0.416	0.159
Richter	2.2	6.6	0.699	0.590	0.620	−0.002	0.306	0.037
Saperton	4.2	5.0	0.718	0.271	0.417	0.227	0.407	0.278
Sasaki	3.6	6.9	0.865	0.581	0.158	0.173	0.397	0.584
Sauer	3.3	6.7	0.854	0.291	0.290	0.194	0.661	0.406
Schein	2.7	6.8	0.867	0.236	0.375	0.159	0.632	0.488
Shebonova	2.6	5.6	0.876	0.447	0.468	0.236	0.312	0.517
Simon	3.3	4.0	0.792	0.216	0.367	0.323	0.392	0.488
Skavronsky	3.8	3.3	0.699	0.416	0.064	0.511	0.131	0.481
Slenczynska '56	5.2	2.8	0.657	0.095	0.414	0.754	0.197	0.107
Slenczynska '75	4.2	1.7	0.592	−0.101	0.355	0.741	0.218	0.209
Slobodyanik	4.2	6.3	0.896	0.391	0.250	0.379	0.408	0.575
Smith	3.3	4.8	0.801	0.594	0.238	0.255	0.147	0.582
Sofronitzky	4.1	5.8	0.853	0.225	0.288	0.390	0.616	0.353
Solomon	3.1	4.8	0.688	0.514	0.138	0.015	0.661	0.081
Székely	4.5	6.9	0.842	0.607	0.123	0.235	0.423	0.442
Timofeyeva	3.2	4.3	0.820	0.716	0.104	0.308	0.301	0.375
Uninsky	3.0	6.7	0.731	0.236	0.661	0.019	0.546	0.144
Varsi	3.5	5.4	0.870	0.308	0.132	0.387	0.615	0.449
Vásáry	2.9	4.9	0.724	0.645	0.234	0.090	0.355	0.243
Vered	3.2	5.0	0.831	0.391	0.255	0.424	0.340	0.462
Virsaladze	3.4	8.2	0.848	0.467	0.297	0.259	0.490	0.347
Volondat	2.3	6.0	0.832	0.502	0.368	0.122	0.612	0.181
Weissenberg	2.9	3.8	0.774	0.498	0.101	0.423	0.373	0.313
Wild	3.9	6.8	0.826	0.482	0.450	0.146	0.450	0.291
Woodward	4.3	2.8	0.711	0.277	−0.040	0.703	0.458	0.174
Woytowicz	2.9	4.8	0.751	0.463	0.548	0.495	0.224	0.005
Yamazaki	2.9	5.6	0.875	0.410	0.319	0.307	0.406	0.509
Yokoyama	3.5	4.0	0.702	0.647	0.013	0.211	0.190	0.486
Zarankin	3.9	6.6	0.871	0.490	0.459	0.275	0.572	0.111
Zarankin 2	3.9	6.7	0.872	0.490	0.461	0.273	0.572	0.112
Zayas	3.9	6.8	0.854	0.487	0.366	0.258	0.302	0.509

[1]Slurs and expression marks are omitted in this computer-generated score, and the second half of bar 5, which was not included in the measurements, has been condensed into a chord to save space. See Repp (1998a, Fig. 1) for an original score of the music.

[2]All timing–dynamics correlations were computed between the IOI durations and the PSLs of the tones *initiating* (and filling) the IOIs. The initial upbeat and the final, very long IOI were not included, so that there were only 35 data points.

[3]Although, in theory, an especially creative artist could go beyond the strategies identified here and choose a completely novel pattern, one that might map onto a ''nonsignificant'' PC profile in the PCA, such patterns are more likely to be perceived as abnormal and do not seem to occur in the present sample.

[4]Although the statistical support is similar, the argument is weaker for dynamics than for timing because the typical timing pattern is backed up by strong perceptual results (Repp, 1992, 1998b) which have not been dupli-

cated for dynamics so far (Repp, 1995c). The typical timing pattern seems to be ''demanded'' by the musical structure in a way that the typical (melodic) dynamic pattern is not.

[5] Although the author generally insists on the terminological distinction between *note* (a printed symbol) and *tone* (an acoustic signal), in the context of MIDI applications it is customary to refer to actions on the keyboard as *notes*. MIDI notes have onsets, offsets, and velocities; tones have onsets, poorly defined offsets (because of decay), and peak intensities; printed notes have none of these, only nominal values.

[6] One data point has been omitted from Fig. A3(b) because it seemed anomalous. In position 2-1 of the music [see Fig. A1(b)], a very soft primary alto note was accompanied by a louder bass note; the velocity difference was −13, but the PSL difference was almost 10 dB, which is well above the solid regression line in Fig. A3(b).

Gabrielsson, A. (**1987**). ''Once again: The theme from Mozart's Piano Sonata in A major (K.331),'' in *Action and Perception in Rhythm and Music*, edited by A. Gabrielsson (Royal Swedish Academy of Music Publication No. 55, Stockholm), pp. 81–103.

Martin, D. W. (**1947**). ''Decay rates of piano tones,'' J. Acoust. Soc. Am. **13**, 535–541.

Palmer, C. (**1996a**). ''Anatomy of a performance: Sources of musical expression,'' Music Percept. **13**, 433–453.

Palmer, C. (**1996b**). ''On the assignment of structure in music performance,'' Music Percept. **14**, 23–56.

Palmer, C., and Brown, J. C. (**1991**). ''Investigations in the amplitude of sounded piano tones,'' J. Acoust. Soc. Am. **90**, 60–66.

Repp, B. H. (**1992**). ''Probing the cognitive representation of musical time: Structural constraints on the perception of timing perturbations,'' Cognition **44**, 241–281.

Repp, B. H. (**1993**). ''Some empirical observations on sound level properties of recorded piano tones,'' J. Acoust. Soc. Am. **93**, 1136–1144.

Repp, B. H. (**1995a**). ''Acoustics, perception, and production of *legato* articulation on a digital piano,'' J. Acoust. Soc. Am. **97**, 3862–3874.

Repp, B. H. (**1995b**). ''Expressive timing in Schumann's 'Träumerei:' An analysis of performances by graduate student pianists,'' J. Acoust. Soc. Am. **98**, 2413–2427.

Repp, B. H. (**1995c**). ''Detectability of duration and intensity increments in melody tones: A partial connection between music perception and performance,'' Percept. Psychophys. **57**, 1217–1232.

Repp, B. H. (**1996a**). ''The dynamics of expressive piano performance: Schumann's 'Träumerei' revisited,'' J. Acoust. Soc. Am. **100**, 641–650.

Repp, B. H. (**1996b**). ''Patterns of note onset asynchronies in expressive piano performance,'' J. Acoust. Soc. Am. **100**, 3917–3932.

Repp, B. H. (**1997a**). ''The aesthetic quality of a quantitatively average music performance: Two preliminary experiments,'' Music Percept. **14**, 419–444.

Repp, B. H. (**1997b**). ''Expressive timing in a Debussy Prelude: A comparison of student and expert pianists,'' Musicae Scientiae **1**, 257–268.

Repp, B. H. (**1997c**). ''Acoustics, perception, and production of legato articulation on a computer-controlled grand piano,'' J. Acoust. Soc. Am. **102**, 1878–1890.

Repp, B. H. (**1998a**). ''A microcosm of musical expression: I. Quantitative analysis of pianists' timing in the initial measures of Chopin's Etude in E major,'' J. Acoust. Soc. Am. **104**, 1085–1100.

Repp, B. H. (**1998b**). ''Variations on a theme by Chopin: Relations between perception and production of deviations from isochrony in music,'' J. Exp. Psychol. **24**, 791–811.

Repp, B. H. (**in press**). ''Control of expressive and metronomic timing in pianists,'' J. Motor Behav.

Repp, B. H. (**in preparation**). ''A microcosm of musical expression: III. Aesthetic evaluation of pianists' expression in the initial measures of Chopin's Etude in E major.''

Shaffer, L. H. (**1981**). ''Performances of Chopin, Bach, and Bartók: Studies in motor programming,'' Cogn. Psychol. **13**, 326–376.

Todd, N. P. McA. (**1992**). ''The dynamics of dynamics: A model of musical expression,'' J. Acoust. Soc. Am. **91**, 3540–3550.

Todd, N. P. McA. (**1994**). ''The auditory ''primal sketch:'' A multiscale model of rhythmic grouping,'' J. New Music Res. **23**, 25–70.

Scattering properties of encapsulated gas bubbles at high ultrasound pressures

Peter J. A. Frinking[a)]
Thoraxcentre, Erasmus University Rotterdam, 3000 DR Rotterdam, The Netherlands

Nico de Jong
Thoraxcentre, Erasmus University Rotterdam, 3000 DR Rotterdam, The Netherlands and Interuniversity Cardiology Institute Netherlands (ICIN), 3501 DG Utrecht, The Netherlands

E. Ignacio Céspedes
Thoraxcentre, Erasmus University Rotterdam, 3000 DR Rotterdam, The Netherlands and Endosonics Corporation, Rancho Cordavo, California 95670

Encapsulated types of contrast agents possess a specific acoustical signature. When the applied acoustic pressure exceeds a specific threshold, the scattering level increases abruptly for a short time. A ''dualistic'' character of the encapsulated gas bubbles explains this signature, observed for Quantison™ (air bubbles encapsulated by a shell of human albumin). For acoustic pressures below a threshold, the bubbles act as encapsulated gas bubbles and are stable linear or nonlinear scatterers, depending on the applied acoustic pressure. For acoustic pressures above the threshold, the bubbles rupture and release the contained gas, subsequently acting as free-gas bubbles. The effect is transient and lasts until the released free-gas bubbles are dissolved in the surrounding liquid. This explanation was investigated experimentally and evaluated by theoretical models. A 15–20-dB increase in scattering, the appearance of higher harmonics, and a finite duration of the effect could be measured and agreed with corresponding theory. Therefore, ultrasound in combination with this dualistic character suggests that encapsulated gas bubbles can be construed as a robust vehicle for localized delivery of free-gas bubbles, the ultimate ultrasound contrast agent. © *1999 Acoustical Society of America.* [S0001-4966(99)04903-6]

PACS numbers: 43.80.Ev [FD]

INTRODUCTION

The most important purpose of ultrasound contrast agents, up till a few years ago, was to enhance the acoustical signal from blood-filled regions. This allows better characterization of perfusion and blood flow for B-mode images and for Doppler modes. Nowadays, new imaging techniques are being explored that take advantage of the nonlinear acoustic property of the bubbles, like ''harmonic imaging.'' [1,2] With these techniques, the discrimination between contrast and surrounding tissue can be improved. This becomes quite apparent for increased acoustic pressures and small bubbles.[3] However, due to the presence of a shell, the scatter efficiency and nonlinear response of encapsulated gas bubbles are much lower than for free-gas bubbles.[4–6] The shell serves as a stabilizing goal, since the life span of free-gas bubbles, the ultimate ultrasound contrast agent, is limited.

Nevertheless, encapsulated types of contrast agents (e.g., Sonovist™, Schering AG, Berlin and Germany, Quantison™, Andaris Ltd., Nottingham, UK) possess a specific acoustical signature.[7,8] When the applied acoustic pressure exceeds a specific threshold, the scattering level increases abruptly for a short time. In conventional B-mode imaging, this transiently enhanced scattering is visualized as an increased echogenicity (Fig. 1) and in color Doppler imaging as a colored mosaic map that is detectable even without flow.[9] Furthermore, the scattered signal becomes highly nonlinear and is very well suited for harmonic imaging. This particular signature has been addressed by several names: acoustically stimulated acoustic emission,[7] power enhanced scattering,[8] flash echo imaging,[10] scintillation sonography,[11] etc. The effect, however, is transient, and most effective when the ultrasound wave hits the bubbles for the first time. This has led to the development of intermittent imaging[12] as a new imaging modality, where single scans are made at regular time intervals (e.g., 1 Hz), resulting in an increased efficacy of the agent. Despite the variety of given names, it seems that the acoustic signature observed for different contrast agents is comparable and generally associated with bubble rupture and enhanced scattering. Takeuchi[11] reports similar effects observed with thermoplastic (poly-vinylidenchloride–acrylnitoryl) micro balloons as a mimicking contrast agent. Bright echoes, harmonic response, and spectral broadening as observed with normal contrast agents are described. The effects are explained by shell breakage, followed by release of the encapsulated gas, and last for 1 to 5 ms, equivalent to the dissolution time of the encapsulated gas in the surrounding liquid.

In this article, the phenomenon observed for Quantison™ is explained by a dualistic character of the encapsulated gas bubbles, which is related to the applied acoustic pressure. For low acoustic pressures, below a threshold, the

---

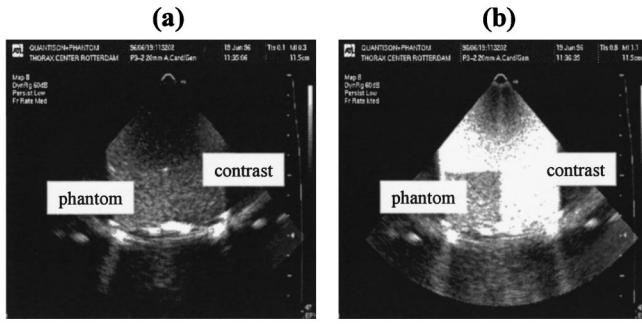[a)]Electronic mail: frinking@tch.fgg.eur.nl

(a) **(b)**

FIG. 1. Two-dimensional images of Quantison™ and a tissue-mimicking phantom made of 1% agar and 0.5% carborundum (SiC) scatterers (mean size of 10 μm), using an ATL HDI 3000, at 2.5 MHz. Left panel (a), MI=0.3; right panel (b) MI=1.1. The remaining imaging parameters are held constant.

bubbles act as encapsulated gas bubbles and are stable linear or nonlinear scatterers, depending on the applied acoustic pressure. For acoustic pressures above the threshold, the bubbles rupture and release the contained gas, subsequently acting as free-gas bubbles. The irreversible effect is transient and lasts until the released free-gas bubbles are dissolved in the surrounding liquid. This explanation is supported by three experiments and corresponding theoretical models. First, the enhancement of the scattering is measured and simulated using a free-gas bubble model. Second, the appearance of higher harmonics are measured and simulated according to the same model, since it has been shown that for free-gas bubbles the nonlinear response is superior compared to encapsulated gas bubbles.[5,6] Finally, the finite duration of the effect is measured and related to the theoretical persistence of the generated free-gas bubbles. This is demonstrated by comparing the measured disappearance time of the gas bubbles to calculated values.

I. THEORY

A. Enhanced scattering

The Rayleigh–Plesset equation is used as a free-gas bubble model. The bubble is considered to be spherically symmetric and surrounded by a liquid of infinite extent, with a constant viscosity. The bubble volume is defined by a single variable, the radius, and the motion is assumed to be spherically symmetric. The wavelength of the ultrasound field is assumed to be much larger than the bubble diameter, and only the motion of the bubble surface is of interest. It is assumed that the vapor pressure remains constant during the compression and expansion phase, and that there is no rectified diffusion during the short period of exposure to ultrasound. The gas in the bubble is assumed to be ideal and compressed and expanded according to the gas law with the polytropic exponent Γ remaining constant during vibration. The final expression is given by[6]

$$\rho R \ddot{R} + \frac{3}{2}\rho \dot{R}^2 = p_{g0}\left(\frac{R}{R_0}\right)^{3\Gamma} + p_v - p_0 - \frac{2\sigma}{R}$$
$$- \delta_{\text{tot}}\omega\rho R\dot{R} - P(t), \tag{1}$$

where

R = instantaneous bubble radius
$\dot{R}$ = first time derivative of the radius
$\ddot{R}$ = second time derivative of the radius
ρ = density of the surrounding medium
R_0 = initial bubble radius
p_{g0} = initial gas pressure in the bubble
Γ = polytropic exponent of the gas
p_v = vapor pressure
p_0 = ambient pressure
σ = surface tension coefficient
δ_{tot} = total damping coefficient
ω = angular frequency of the applied acoustic field
$p_{\text{ac}}(t)$ = applied acoustic pressure.

The initial gas pressure inside the bubble, p_{g0}, is given by

$$p_{g0} = \frac{2\sigma}{R_0} + p_0 - p_v. \tag{2}$$

The expression for the total damping coefficient is given by

$$\delta_{\text{tot}} = \delta_{\text{rad}} + \delta_{\text{vis}} + \delta_{\text{th}}, \tag{3}$$

where

δ_{rad} = damping coefficient due to reradiation
δ_{vis} = damping coefficient due to viscosity of the surrounding medium
δ_{th} = damping coefficient due to heat conduction.

Expressions for the damping coefficients and for the polytropic exponent are given by Medwin.[13] After solving Eq. (1) numerically, the scattering cross section, defined as the scattered power by the bubble divided by the incident acoustic intensity, can be calculated.[4]

For encapsulated gas bubbles like Quantison™, Frinking and de Jong[14] have given a detailed description of the scatter and attenuation properties. They adapted the Rayleigh–Plesset equation to correct for the increase of the bulk modulus and the introduction of viscous damping due to the presence of the shell.

B. Nonlinear response

In addition to the increase in scattered power at the fundamental frequency, the scattered power at higher harmonic components of the fundamental frequency increases as well for free-gas bubbles compared to encapsulated gas bubbles.[5,6] Free-gas bubbles oscillate nonlinearly when the applied acoustic pressure is increased, an effect that becomes extremely apparent for bubbles smaller than 10 μm in diameter.[3] For example, for an applied acoustic pressure of 50 kPa, a 3-μm diameter free-air bubble, insonified at 1 MHz, shows harmonic components that can exceed the scattering level at the fundamental frequency. This strong harmonic behavior is predicted by Eq. (1). For encapsulated gas bubbles, the effect is subdued as a result of the extra damping introduced by the shell. For Quantison™, is has been shown that for an acoustic pressure of 100 kPa, the second harmonic response is 60 dB below the fundamental response.[14]
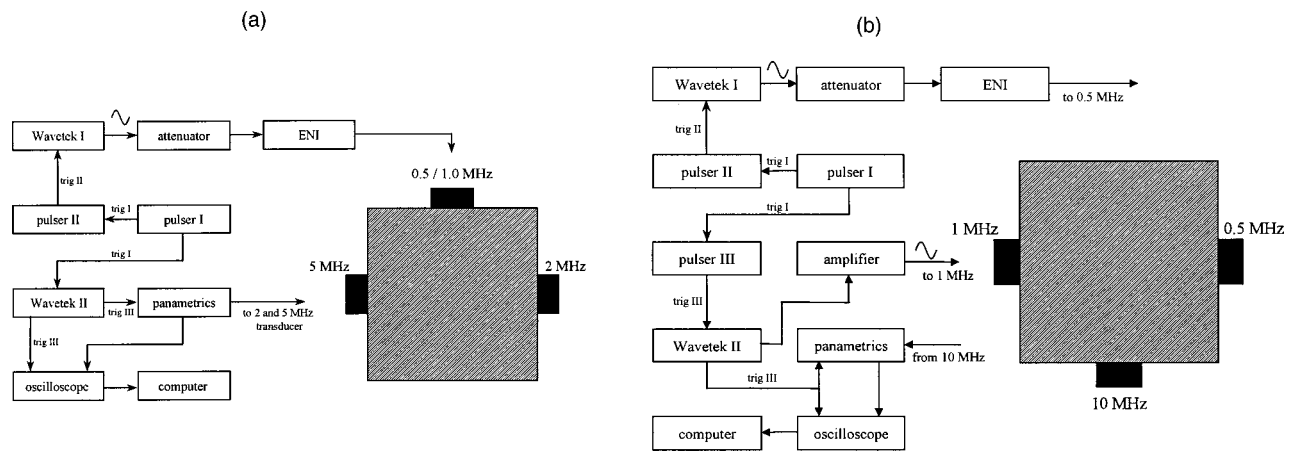
FIG. 2. Schematic setup. (a) For measuring the enhanced scattering and disappearance time; (b) for measuring the nonlinear response.

C. Disappearance time

Small free-gas bubbles tend to disappear quickly in a liquid, e.g., air bubbles of 2 μm in diameter persist for only a few milliseconds in a saturated liquid under normal conditions.[15] With the omission of translatory bubble motion, the change in equilibrium radius over time is given by[16]

$$\frac{dR}{dt} = DL \left(\frac{(C_i/C_0)-1-(2\sigma/Rp_0)}{1+(4\sigma/3Rp_0)} \right) \left(\frac{1}{R} + \frac{1}{\sqrt{\pi Dt}} \right), \quad (4)$$

where

R = bubble radius
D = diffusion coefficient
L = Ostwald coefficient
C_i/C_0 = ratio of the dissolved gas concentration to the solubility of the gas
σ = surface tension
p_0 = ambient pressure.

The surface tension is the mechanism responsible for the disappearance of the bubble. The second bracketed term in Eq. (4) resembles the penetration depth that denotes how far the gas diffuses into the liquid. The diffusion constant is a property of the gas and the surrounding liquid. The Ostwald coefficient[17] is the ratio of the amount of gas per unit volume dissolved in the surrounding liquid and in the gas phase. The diffusion coefficient and the Ostwald coefficient determine the rate of decrease of the bubble radius, which is a direct measure for the disappearance rate of the bubble. Thus, microbubbles filled with gases having smaller diffusion- and Ostwald coefficients will persist longer.

II. EXPERIMENTAL METHOD

A. Materials

We used the ultrasound contrast agent Quantison™, which consists of air-filled microspheres encapsulated by a shell of human serum albumin. The mean particle diameter is 3.2 μm, and less than 0.5% of the microspheres are larger than 6 μm [Fig. 5(a)]. The acoustical properties, in particular attenuation and scattering, are described by Frinking and De Jong.[14] Two parameters are estimated from experiments, viz., the effective bulk modulus K_{eff}, and the friction parameter

S_{fr}, with values of 17.4 MPa and 5.0 Pa·s, respectively. These two parameters describe the elasticity or stiffness of the bubble and the friction or viscosity of the shell (for free-air bubbles under atmospheric and adiabatic conditions, these parameters are 0.14 MPa and 0 Pa·s, respectively). The scatter to attenuation ratio (STAR) is around 0.1% for frequencies between 2 and 5 MHz and applied acoustical pressures up to 200 kPa. This means that the energy absorbed by the bubbles is 1000 times larger than the energy scattered by the bubbles. Also, the nonlinear response was calculated for the same acoustic pressures and shown to be minimal. However, for acoustic pressures above 200 kPa, theory and measurements start to deviate from each other: the theory underestimates the measured scattering with a difference in scattering of 20 dB for an applied acoustic pressure of 1.8 MPa.

B. Experimental setup and procedure

1. Enhanced scattering

The experimental setup is illustrated in Fig. 2(a). A 0.5- or 1.0-MHz single-element transducer (Panametrics, Waltham, MA) focused at 75 mm, with an aperture of 37 mm, is mounted in a water tank. These transducers are used to transmit a high-amplitude ultrasound burst (acoustic pressure of 1.6 MPa). The peak negative acoustic pressures are measured with a calibrated hydrophone (PVDFZ44-0400, Specialty Engineering Associates, Soquel, CA). A sine wave burst, 10 cycles, is generated by a Wavetek signal generator (Wavetek I, model 144, Wavetek, San Diego, CA) and amplified by a 60-dB linear power amplifier (A-500, ENI, NY). The amplitude can be adjusted by an attenuator from 0 to 120 dB in steps of 1 dB (355C/D, HP, Palo Alto, CA). Two broadband (100% of the central frequency at the −20-dB level) single-element transducers, with center frequencies of 2 and 5 MHz (Panametrics, Waltham, MA) are mounted perpendicularly to the first transducer. The two transducers cover a combined frequency band from 1 to 7.5 MHz. They are both focused at 75 mm and have apertures of 25 and 18 mm, respectively. Short, single-cycle, low-amplitude pulses (acoustic pressure of 100 kPa) are generated, 0.6 ms after the high-amplitude burst, and received by a pulser/receiver (5052 PR, Panametrics, Waltham, MA). The received signals
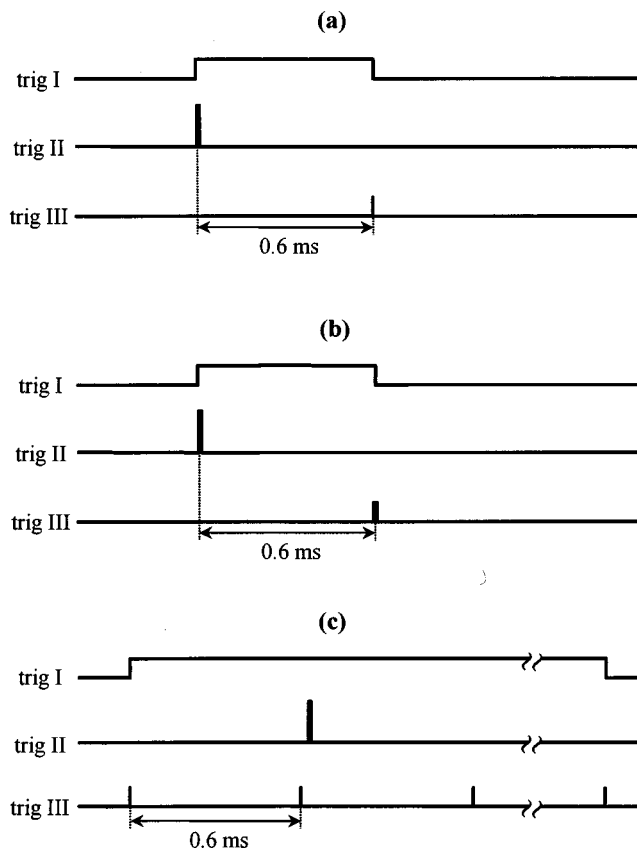
(a)

(b)

(c)

FIG. 3. Schematic representation of the triggering sequences used. (a) The enhanced scattering is measured 0.6 ms after the high acoustic amplitude burst. (b) The same as (a), only the duration of the low acoustic amplitude burst has been set to 10 μs. (c) By changing the frequency of Wavetek II to 1.6 kHz, the enhanced scattering can be measured with a PRI of 0.6 ms after the high acoustic amplitude burst, to monitor the disappearance of the bubbles. Note that the high-amplitude burst is switched on just after the second low-amplitude pulse.

can be amplified from $+40$ to -40 dB in steps of 2 dB by the pulser/receiver. The amplified signals are low-pass filtered to minimize noise and avoid aliasing, and are digitized by a Lecroy 9400A (Lecroy, Chestnut Ridge, NY) digital oscilloscope (100 MHz, 8 bits). The signals are recorded over a time window of 10 μs, are sampled at 50 MHz, and transferred to a personal computer (Compaq 386/20e) for further analysis. Two pulse generators (pulser I and II, PM 5712, Philips, Stockholm, Sweden) and a Wavetek signal generator (Wavetek II, model 144, Wavetek) are used for synchronization. The triggering sequences are shown in Fig. 3(a).

The experiments are conducted at room temperature. The water tank is filled with Isoton® II (Coulter Electronics, Lutton, UK), which was left standing overnight and therefore is air saturated. The response of a steel flat-plate reflector, placed at the focal distance of the 2 and 5 MHz transducer, is measured and used as a reference measurement. After that, the contrast agent is added and the response of the steel flat-plate reflector is measured again, to determine the additional attenuation caused by the contrast agent. The intensity of the scattered acoustic field with and without the high-amplitude burst is measured and the scattering cross section is determined, taking into account the reflection properties of

the steel flat-plate reflector, the transducer characteristics, and the attenuation of the contrast agent.[14] The scattering cross section was calculated by averaging the contribution of 62 independent scatter distributions. After fast Fourier transformation (FFT), the average power spectra are calculated and smoothed using a moving window with a width of 200 kHz to remove radio frequency (rf) noise. During the measurement, the bubble suspension was stirred by a magnetic stirrer.

2. Nonlinear response

Figure 2(b) shows the setup used for measuring the nonlinear response with and without the high-amplitude burst (acoustic pressure of 1.6 MPa). The burst is generated as described in the previous section with the 0.5-MHz transducer. A narrow-band (1 MHz, 10 cycles) sine wave is generated by a Wavetek signal generator (Wavetek II, model 144, Wavetek) and amplified (acoustic pressure of 100 kPa) by a linear power amplifier (ARS 05_40_40, Orsay, France). This signal is fed to a 1-MHz single-element, broadband transducer (100% of the central frequency at the -20-dB level), with an aperture of 37 mm, that is mounted inline with the 0.5-MHz transducer. The response of the 1-MHz signal is received by a 10-MHz single-element, broadband transducer (flat response within 3 dB between 1 and 10 MHz) that is mounted perpendicular to the 1- and 0.5-MHz transducer. The average scattered power is calculated over the FFT of 10 time traces as received with the 10-MHz transducer at a repetition rate of 1 Hz. Pulsers I, II, and III (PM 5712 and PM 5716, Philips, Stockholm, Sweden) are used for synchronization. The triggering sequences are shown in Fig. 3(b) (pulse III is set to 10 μs).

3. Disappearance time

The disappearance time is measured using the setup of Fig. 2(a). Only the 5-MHz transducer is used in pulse/echo mode. The frequency of Wavetek II is set to 1.6 kHz. In this way, a sequence of low-amplitude pulses (100 kPa acoustic pressure) is generated with a pulse-repetition interval (PRI) of 0.6 ms, so as to measure the evolution of the generated free-gas bubbles over time. The high-amplitude burst (acoustic pressure of 1.6 MPa; 0.5 MHz; 10 cycles) is switched on directly after the second low-amplitude pulse. The triggering sequences are shown in Fig. 3(c). Again, the Isoton® was air saturated.

III. RESULTS AND DISCUSSION

A. Enhanced scattering

Figure 4(a) (solid line) shows the scattered spectrum of a 1:4500 dilution of Quantison™, which corresponds to 3.3 $\times 10^5$ microspheres per ml, not using the transducer that is generating the high-amplitude burst. This is the typical scattering response of Quantison™ at low acoustic intensity, and is described in detail by Frinking and de Jong.[14] The scattering increases as a function of frequency below 4 MHz, and is independent of frequency above 4 MHz with a maximum value of -43 dB/cm. Figure 4(b) and (c) (solid lines) show the enhanced scattering, measured at the same region, 0.6 ms
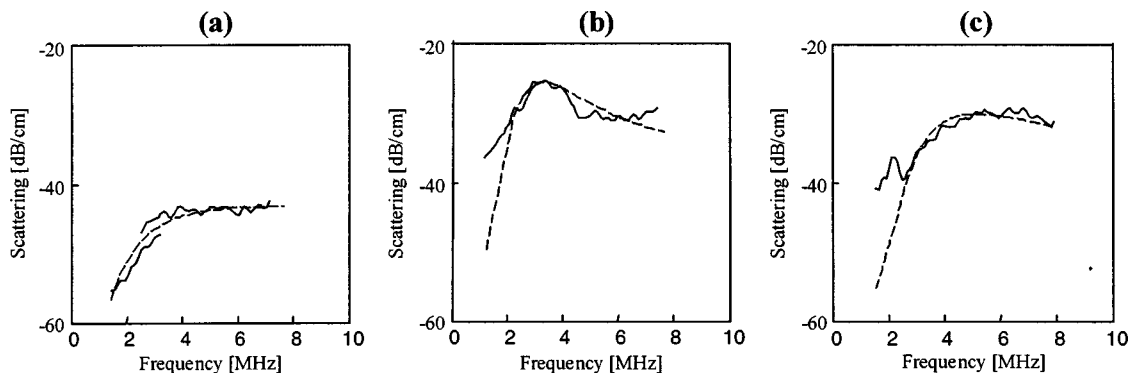
FIG. 4. (a) Scattering versus frequency of a dilution of 1:4500 of Quantison™ measured without the high-amplitude ultrasound burst. ———— = measured scattering, – – – = theoretical spectrum using the size distribution shown in Fig. 5(a). (b) ———— = measured scattering 0.6 ms after the transmission of the 0.5-MHz high-amplitude ultrasound burst at the same region. – – – = theoretical spectrum. (c) The same as in (b) but now using the 1.0-MHz transducer for generating the high amplitude burst. ———— = measurement; – – – = theoretical spectrum.

after this region has been insonified by the high-amplitude burst (at 0.5 and 1.0 MHz, respectively). An increase in scattering of 10 to 20 dB/cm can be observed, compared to Fig. 4(a). Additionally, in Fig. 4(b), a maximum at 3 MHz, the resonance frequency which is characteristic for free-gas bubbles, can clearly be appreciated. In Fig. 4(c), this maximum is shifted and broadened. A possible explanation of this effect is that the 1.0-MHz transducer generates smaller gas bubbles than the 0.5-MHz transducer. For smaller gas bubbles, the resonance frequency and the damping increase, resulting in a broadening and decrease of the resonance peak.

The dotted line in Fig. 4(a) shows the scattering of Quantison™ according to the theoretical model.[14] The size distribution of Quantison™, shown in Fig. 5(a), as measured with a Coulter Counter Multisizer II (Coulter Electronics) is used in the model. The dotted lines in Fig. 4(b) and (c) represent the theoretical spectra of the enhanced scattering induced by the 0.5- and 1.0-MHz transducers, respectively, and are calculated by means of Eq. (1). Note that in this case, the size distribution of the generated gas bubbles is not known *a priori*. We assumed a normal size distribution. The mean and standard deviation of the distributions are estimated by minimizing the absolute difference between measured and simulated spectra. This results in a mean and standard deviation of $2.00 \pm 0.48 \, \mu$m for the 0.5-MHz transducer

[Fig. 5(b)], and $1.20 \pm 0.46 \, \mu$m for the 1.0-MHz transducer [Fig. 5(c)]. It can be appreciated that with this simple approach, a reasonable agreement between measurements and theory is obtained and, from Fig. 5, that different distributions are generated for different frequencies (smaller bubbles for a higher frequency). Possible explanations are that for different frequencies, the gas bubbles originate from different parts of the Quantison™ distribution, or that different gas bubbles are generated from the Quantison™ bubbles within the same range of the size distribution. Finally, from the theoretical results, we conclude that the total number of free-gas bubbles is about 1% of the total number of the Quantison™ bubbles present in the suspension [notice the different scales of Fig. 5(a), (b), and (c)]. This means that only a very small amount of Quantison™ bubbles is actively involved in releasing free-gas bubbles.

B. Nonlinear response

Figure 6(a) shows the scattered power spectra received by the 10-MHz transducer. The measurements are corrected for the finite aperture,[4] the characteristics of the 10-MHz transducer, and the electronics. The lower line represents the spectrum of Quantison™ bubbles (dilution of 1:4500) when they are insonified by the 1-MHz burst without the high-
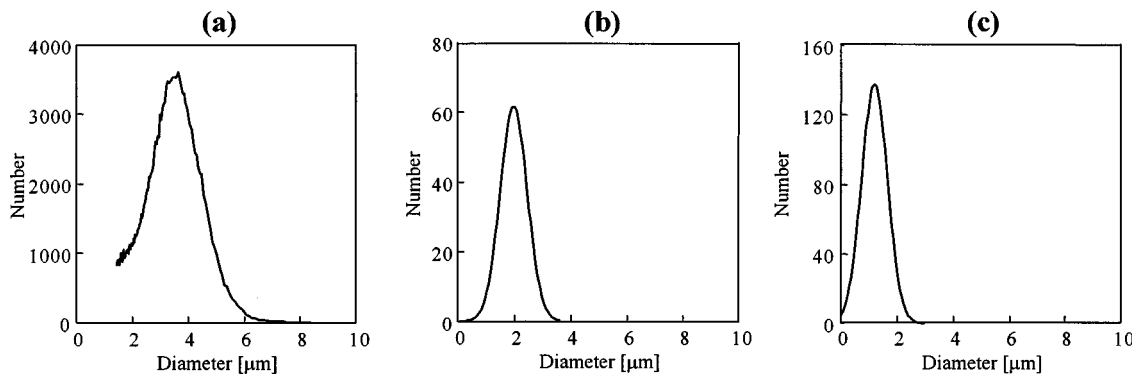

FIG. 5. (a) Size distribution of Quantison™ measured with the Coulter Counter® Multisizer II with an aperture of 70 μm employing 256 channels (diameters ranging from 1.45 to 8.33 μm). (b) Estimated distribution from the measured spectrum in Fig. 4(b). (c) Estimated distribution from the measured spectrum in Fig. 4(c).
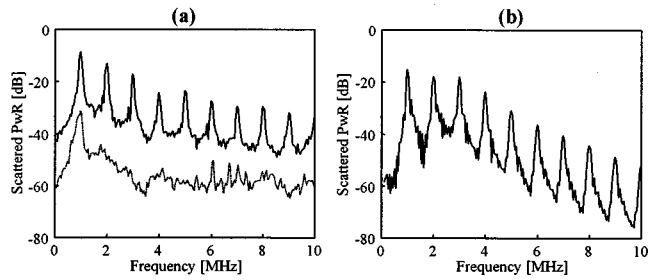
FIG. 6. (a) Received scattered power of Quantison™ by a 10-MHz single-element transducer (corrected for transducer characteristics). The signal is generated by a 1-MHz transducer (acoustic pressure of 100 kPa, 10 cycles), without the high amplitude burst (lower) and 0.6 ms after the high-amplitude burst (upper). (b) Theoretical power spectrum using Eq. (1) and the size distribution of Fig. 5(b). The acoustic pressure is 100 kPa and the actual transmitted burst is used as the input signal.

FIG. 7. The release and disappearance of air bubbles from Quantison™ shown by the enhanced scattering. (a) Sequence representation of pulse-echo response from successive survey pulses (100 kPa, 5 MHz, 0.6 ms interval). Scattering of Quantison™ up to 1.2 ms. The high-power release burst (1.6 MPa, 0.5 MHz, 10 cycles) was applied at 1.2 ms. (b) The enhanced scattering decays over time. Top panel: directly after the high power burst; middle panel: after 15 ms; bottom panel: after 30 ms, corresponding to the locations marked in (a) by B1, B2, and B3, respectively.

amplitude burst. The spectrum shows no response at higher harmonics of the fundamental frequency. The upper line represents the spectrum measured 0.6 ms after the Quantison™ bubbles are insonified by the high-amplitude burst. Two phenomenon can be observed after the agent has been insonified with this short high-amplitude burst: the spectrum shows an increase at the fundamental frequency of 20 dB and the appearance of higher harmonics of the fundamental frequency. The second harmonic is less than 6 dB below the fundamental frequency. Imaging modalities that rely on the nonlinear response of ultrasound contrast agents will therefore result in increased sensitivity.

Figure 6(b) shows the theoretical power spectrum of the generated free-gas bubbles using Eq. (1). The high-amplitude burst is the same as before; therefore, it is assumed that the generated gas bubbles have the size distribution shown in Fig. 5(b). The experimental burst was recorded (1 MHz; 100 kPa; 10 cycles) and used as an input to the model. The magnitude was adjusted to 100 kPa. Note the close agreement of the first five harmonics.

C. Disappearance time

Figure 7 shows the backscattered signal from the released air bubbles recorded at intervals of 0.6 ms. The decreasing amplitude is ascribed to the gradual shrinkage and eventual dissolution of the bubbles. The persistence of the air bubbles is measured over time and is shown in Fig. 7(a). This figure represents a sequential recording of 62 traces covering a total acquisition time of 37 ms. The high acoustic amplitude burst was switched on directly after the second low-amplitude pulse. This can be appreciated from Fig. 7(a) by the fact that the amplitude abruptly increases after two pulses. The scattering amplitude decreases as a function of time, representing the slow diffusion of the released gas into the surrounding liquid. This is depicted in detail by Fig. 7(b) at three time points, viz., 0, 15, and 30 ms after the high-amplitude burst [see corresponding locations in Fig. 7(a)]. After 30 ms, the increase in scattering amplitude has completely disappeared.

Figure 8(a) and (b) (solid lines) show the energy as function of time, within each time trace, for the gas bubbles generated by the 0.5- and 1.0-MHz transducers, respectively.

The disappearance time, t_d, is estimated from the 95%-decay point in these figures. The mean value and standard deviation of a set of ten sequence recordings is 28.8 ±2.4 ms for the 0.5-MHz transducer, and 16.3±2.3 ms for the 1.0-MHz transducer. The theoretical disappearance curves are calculated by using the size distributions of Fig. 5(b) and (c) as the starting distributions. Every 0.6 ms, the size distributions are recalculated by means of Eq. (4), and the scatter spectra are calculated at the corresponding time points using Eq. (1). The spectra include the scattering of the Quantison™ bubbles (dilution of 1:4500). Figure 8(a) and (b) (dotted lines) show the energy as a function of time as determined from the calculated spectra for the 0.5- and 1.0-MHz transducer, respectively. The energy was calculated by integrating the scattered power over a frequency band ranging from 2–8 MHz. Also, the disappearance time was measured for generated gas bubbles at different frequencies of the high acoustic amplitude burst (at a fixed amplitude of 1.6 MPa and a fixed number of cycles). The results are listed in Table I and show a decrease in disappearance time for increasing frequencies. The corresponding bubble diameters are calculated by means of Eq. (4).
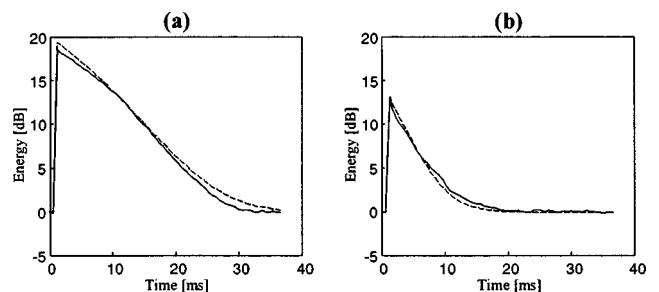
FIG. 8. The energy that is calculated from the scattering response of the generated free-gas bubbles with the 0.5-MHz transducer, (a), and with the 1.0-MHz transducer, (b). ——— = measurement; – – – = theory.

TABLE I. Disappearance time of generated free-air bubbles from Quantison™ as a function of frequency in saturated Isoton® under standard conditions (mean±STD). The second row shows the corresponding bubble diameters as calculated by means of Eq. (4).

Frequency [MHz]	0.5	1	2	5
t_d [ms]	28.8±2.4	16.3±2.0	11.6±2.2	5.1±2.1
Diameter [μm]	2.8	2.3	2.0	1.4

D. Final remarks

As was stated before, the effect is transient. In Fig. 9, the change of the acoustical properties (*viz.*, transmission and scattering) are shown. This figure shows the transmission and scattering spectra of a dilution of 1:250 of Quantison™.[14] This concentration was chosen to induce a clear minimum in transmission of −3 dB/cm at 4 MHz. The spectra are measured before and after a 15-min insonation with a commercial diagnostic echo machine at the highest power setting (MI of 1.1 at 2.5 MHz), by the solid and dotted lines, respectively. It can be appreciated from Fig. 9(a) that the minimum of the transmission spectrum at 4 MHz has completely disappeared from within this frequency range after the Quantison™ has been exposed to the high acoustic amplitude burst. A minimum in transmission as shown in Fig. 9(a) is a typical characteristic for free or encapsulated gas bubbles. For the scattering, Fig. 9(b), the difference is really apparent for frequencies below 10 MHz. An explanation is that, at these particular settings of the ultrasound machine, only the larger bubbles are destroyed.

The bubbles are not completely destroyed after sonification by the high-amplitude burst. Figure 10(a) and (b) are microscopic images of Quantison™ before and after high-power insonification, respectively. Before exposure, the microspheres appear to be darker than after exposure [see arrows in Fig. 10(b)]. This is an indication that the encapsulated air is replaced by the surrounding liquid. Therefore, the liquid-filled bubbles are less compressible and have become ineffective scatterers compared to gas-filled bubbles. The bubbles become "transparent," both optically and acoustically. Note, however, that Fig. 10(a) and (b) do not show the same particles but are just particles of a sample
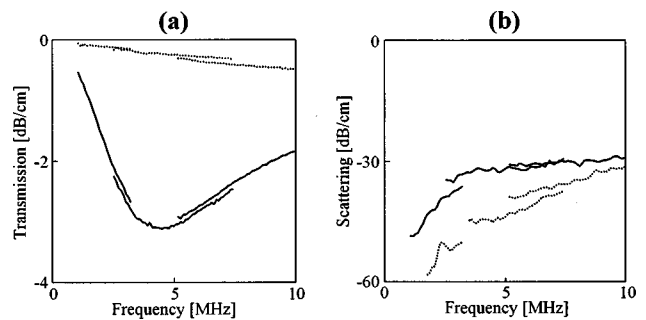
FIG. 9. Transmission (a) and scattering (b) vs frequency for Quantison™. ——— = before and, – – – = after Quantison™ has been put under an ultrasound machine and exposed to high acoustic pressure waves (MI=1.1) for 15 min. The dilution is 1:250.

before, and other particles of the same sample after, sonification.

The results in Table I show a decrease in calculated bubble size as a function of the applied frequency of the high acoustic amplitude burst. This implies that particular bubble sizes can be selectively released. Also, the simulations indicate that only about 1% of all the bubbles present are ruptured by the high acoustic amplitude burst. A possible explanation is that the shells of some of the encapsulated gas bubbles possess weak spots that are easily ruptured. This means that the release of free-gas bubbles from encapsulated gas bubbles can be optimized by machine settings and available bubble sizes, and tuned for specific purposes. For example, the presence of free-gas bubbles can be used for purposes other than imaging, such as noninvasive assessment of gas concentration, temperature, or ambient pressure. These potential applications are supported by the fact that the disappearance time of the generated gas bubbles depends on the dissolved gas concentration, temperature, and ambient pressure. Also, other gases like perfluor gases, which have lower diffusion and Ostwald coefficients, may be used. This results in longer disappearance times, so that the released gas bubbles can be used for a longer period of time.

Finally, pharmacological applications may be possible. Certain drugs can be incorporated into the shell or attached to its surface. Using ultrasound at high acoustic peak pres-
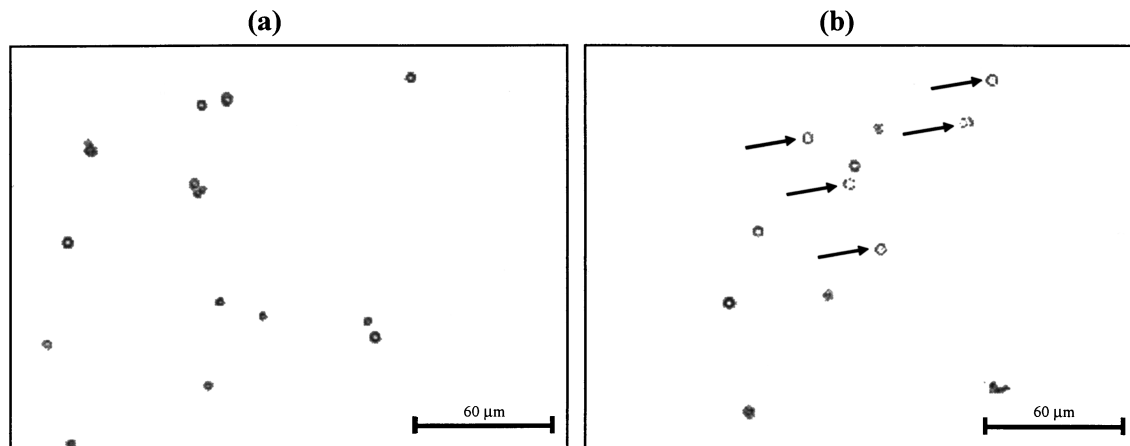
FIG. 10. Microscopic photograph of Quantison™ diluted in Isoton® at a magnification of 200X. (a) before and (b) after it has been put under an ultrasound machine and exposed to high acoustic pressure waves for 15 min. The arrows indicate fluid-filled microspheres.

sures, these drugs may be released from their microspheric carrier at specific locations within the human body. This means that drug treatment can be locally delivered, resulting in a lower systemic drug level.

IV. CONCLUSION

We provide a three-way demonstration that the enhanced transient scattering observed when encapsulated gas bubbles are exposed to ultrasound pulses of high-peak pressures exceeding a threshold is the result of the release of free-gas bubbles. Encapsulated gas bubbles are robust and last in the circulation, but their scatter efficiency and nonlinear response are suboptimal. The scatter efficiency and nonlinear response of free-gas microspheres, however, is far superior but their life span is limited to a few milliseconds. Therefore, ultrasound in combination with this dualistic character suggests that encapsulated gas bubbles can be construed as a robust vehicle for localized delivery of free-gas bubbles, the ultimate ultrasound contrast agent.

ACKNOWLEDGMENT

[1] B. Schrope, V. L. Newhouse, and V. Uhlendorf, ''Simulated capillary blood flow measurement using a nonlinear ultrasonic contrast agent,'' Ultrason. Imaging **14**, 134–158 (1992).

[2] P. N. Burns, J. E. Powers, and T. Fritzsch, ''Harmonic imaging: a new imaging and Doppler method for contrast enhanced ultrasound,'' Radiology **185**, 142 (1992).

[3] D. L. Miller, ''Ultrasonic detection of resonant cavitation bubbles in a flow tube by their second-harmonic emission,'' Ultrasonics **19**, 217–224 (1981).

[4] N. de Jong and L. Hoff, ''Ultrasound scattering of Albunex® microspheres,'' Ultrasonics **31**, 175–181 (1993).

[5] C. C. Church, ''The effect of an elastic solid surface layer on the radial pulsations of gas bubbles,'' J. Acoust. Soc. Am. **97**, 1510–1521 (1995).

[6] N. de Jong, R. Cornet, and C. T. Lancee, ''Higher harmonics of vibrating gas-filled microspheres. Part one: simulations,'' Ultrasonics **32**, 447–453 (1994).

[7] V. Uhlendorf and C. Hoffmann, ''Nonlinear acoustical response of coated microbubbles in diagnostic ultrasound,'' IEEE Ultrasonics Symp. **3**, 1559–1562 (1994).

[8] N. de Jong, P. J. A. Frinking, F. J. Ten Cate, and P. van der Wouw, ''Characteristics of contrast agents and 2D imaging,'' IEEE Ultrasonics Symp. **2**, 1449–1458 (1996).

[9] J. E. Powers, P. N. Burns, and J. Souquet, ''Imaging instrumentation for ultrasound contrast agents,'' in *Advances in Echo Imaging Using Contrast Enhancement*, edited by N. C. Nanda, R. Schlief, and B. B. Goldberg (Kluwer Academic, Dordrecht, 1997), Chap. 8, pp. 139–170.

[10] F. Moriyasu and Y. Kono, ''Flash echo imaging of liver disease,'' presented at The Leading Edge in Diagnostic Ultrasound, Atlantic City, NJ, 1998.

[11] Y. Takeuchi, ''Industrial use of thermoplastic micro-balloon to mimic the contrast agents and its in vitro behaviour including released gas dynamics,'' IEEE Ultrasonics Symp. **12**, 1579–1582 (1997).

[12] T. R. Porter and F. Xie, ''Transient myocardial contrast after initial exposure to diagnostic ultrasound pressures with minute doses of intravenously injected microbubbles. Demonstration and potential mechanisms,'' Circulation **92**, 2391–2395 (1995).

[13] M. Medwin, ''Counting bubbles acoustically: a review,'' Ultrasonics **15**, 7–13 (1977).

[14] P. J. A. Frinking and N. de Jong, ''Modeling of shell-encapsulated gas bubbles,'' Ultrasound Med. Biol. **24**, 523–533 (1998).

[15] P. S. Epstein and M. S. Plesset, ''On the stability of gas bubbles in liquid–gas solutions,'' J. Appl. Mech. **18**, 1505–1509 (1950).

[16] N. de Jong, F. J. Ten Cate, C. T. Lancée, J. R. T. C. Roelandt, and N. Bom, ''Principles and recent developments in ultrasound contrast agents,'' Ultrasonics **29**, 324–330 (1991).

[17] A. Kabalnov, D. Klein, T. Pelura, F. Schutt, and J. Weers, ''Dissolution of multicomponent microbbbles in the bloodstream: I. Theory,'' Ultrasound Med. Biol. **24**, 739–749 (1998).

Shock wave–inertial microbubble interaction: Methodology, physical characterization, and bioeffect study

Pei Zhong[a)]
Department of Mechanical Engineering and Materials Science, Duke University, Durham, North Carolina 27708

Haifan Lin
Department of Cell Biology, Duke University, Durham, North Carolina 27708

Xufeng Xi and Songlin Zhu
Department of Mechanical Engineering and Materials Science, Duke University, Durham, North Carolina 27708

Ervind S. Bhogte
Departments of Cell Biology and Biomedical Engineering, Duke University, Durham, North Carolina 27708

A method of generating *in situ* shock wave–inertial microbubble interaction by a modified electrohydraulic shock wave lithotripter is proposed and tested *in vitro*. An annular brass ellipsoidal reflector (thickness=28 mm) that can be mounted on the aperture rim of a Dornier XL-1 lithotripter was designed and fabricated. This ring reflector shares the same foci with the XL-1 reflector, but is 15 mm short in major axis. Thus, a small portion of the spherical shock wave, generated by a spark discharge at the first focus ($F1$) of the reflector, is reflected and diffracted by the ring reflector, producing a weak shock wave approximately 8.5 μs in front of the lithotripter pulse. Based on the configuration of the ring reflector (different combinations of six identical segments), the peak negative pressure of the preceding weak shock wave at the second focus ($F2$) can be adjusted from -0.96 to -1.91 MPa, at an output voltage of 25 kV. The preceding shock wave induces inertial microbubbles, most of which expand to a maximum size of 100–200 μm, with a few expanding up to 400 μm before being collapsed *in situ* by the ensuing lithotripter pulse. Physical characterizations utilizing polyvinylidene difluoride (PVDF) membrane hydrophone, high-speed shadowgraph imaging, and passive cavitation detection have shown strong secondary shock wave emission immediately following the propagating lithotripter shock front, and microjet formation along the wave propagation direction. Using the modified reflector, injury to mouse lymphoid cells is significantly increased at high exposure (up to 50% with shock number >100). With optimal pulse combination, the maximum efficiency of shock wave-induced membrane permeabilization can be enhanced substantially (up to 91%), achieved at a low exposure of 50 shocks. These results suggest that shock wave–inertial microbubble interaction may be used selectively to either enhance the efficiency of shock wave-mediated macromolecule delivery at low exposure or tissue destruction at high exposure. © *1999 Acoustical Society of America.* [S0001-4966(99)01303-X]

PACS numbers: 43.80.Ev, 43.80.Gx, 43.25.Yw [FD]

INTRODUCTION

Inspired by the success of shock wave lithotripsy (SWL) in the treatment of kidney stone disease, significant efforts have been made to explore a broad spectrum of shock wave applications in medicine.[1] Lithotripter-generated shock waves have been investigated for potential use in tumor therapy, fracture healing of bones, treatment of tendinitis, and ablation of liver tissues with various degree of success.[2–5] More importantly, it has been shown that at low dosage, lithotripter shock waves can cause a transient increase in cell membrane permeability without killing the cells.[6] This finding suggests that shock waves may facilitate the transfer of macromolecules into target cells and could potentially provide a noninvasive physical method for drug delivery and gene transfer.[7] The enhanced cytotoxicity of

several anticancer drugs *in vivo* by SWL may indeed result from shock wave-induced transient membrane permeabilization.[8–10] Most recently, lithotripter shock wave-mediated gene transfer both *in vitro* and *in vivo* have been explored.[11,12]

The biological effects of SWL are mediated by cavitation.[1,13] Cavitation in SWL is described as the oscillation of gas or vapor bubbles in a fluid under the influence of lithotripter shock waves. Although different techniques have been used for shock-wave generation and focusing, the pressure waveform produced by existing clinical lithotripters (except EDAP LT.01 and LT.02) and thus, the dynamics of SWL-induced bubble activities in general, are similar.[14,15] A typical pressure waveform at the lithotripter focus in water consists of a leading shock front (compressive wave) with a peak positive pressure up to 100 MPa, followed by a tensile wave with a peak negative pressure down to -10 MPa, and

[a)]Electronic mail: pzl@mel.egr.duke.edu

a total pulse duration of 3 to 7 μs.[14] Using the Gilmore model for bubble dynamics, Church has shown that a cavitation nucleus (1–10 μm in radius) in water impinged by a lithotripter shock wave will be initially compressed by the leading shock front, and then expanded by the ensuing tensile wave into a bubble of 1–3 mm in diameter in a few hundred microseconds.[16] Subsequently, the expanded bubble will undergo a violent inertial collapse, generating high temperature (up to 10 000 K) inside the collapsed bubble, and secondary shock wave emission into the surrounding fluid.[16] Following this primary collapse, the bubble will oscillate (rebound and then collapse again) several times with decreasing amplitude before it eventually reaches a new equilibrium size of about 40 μm due to rectified gas diffusion.[16] The basic features of such a characteristic bubble oscillation have been confirmed experimentally, using simultaneous high-speed photography and acoustic emission measurements.[17] During SWL, if bubbles generated by the earlier shock waves were stabilized by and attached to an adjacent tissue surface, the interaction of such a stable bubble with a subsequent lithotripter pulse may generate a liquid jet along the wave propagation direction, provided that the size of the bubble is within a certain range (250 μm$<R_{b0}<$750 μm, for an XL-1 lithotripter).[18] It is believed that the shear stresses, and secondary shock wave emission and jet impact associated with the rapid expansion and collapse of cavitation bubbles may contribute to the bioeffects produced by SWL.[1] When cavitation activity in the culture medium is suppressed by excessive ambient pressure, SWL-induced cell injury and membrane-permeability change can be significantly inhibited.[13] In contrast, when cavitation activity *in vivo* is enhanced by intravenous injection of ultrasound contrast agents (well-known cavitation nuclei[19]) immediately before SWL, the vascular injury produced in animal models is substantially increased,[20] even at low-pressure amplitudes ineffective for stone fragmentation.[21] These findings clearly demonstrate that cavitation is an important mechanism for SWL-induced bioeffect.

Despite this, the pressure waveform and associated cavitation activities produced by current shock wave lithotripters may not be optimal for tumor treatment and macromolecule delivery. Several studies have shown that an air–water interface near the lithotripter focus can dramatically enhance SWL-induced bioeffects on cells and small tumors.[2,22] This observation had led some investigators to suggest that a different shock waveform is needed for tumor therapy.[22] Moreover, the transfection efficiency of shock wave-mediated gene transfer is currently low compared to other established methods,[11] and air injection into the target tissue was found to be necessary to enhance the transfection efficiency *in vivo*.[12] Apparently, the ability to control the formation and subsequent oscillations of cavitation bubbles is critical for producing optimal bioeffects by SWL. However, because of the temporal profile and the low pulse-repetition rate of current lithotripter shock waves, the collapse of SWL-induced cavitation bubbles is uncontrolled and is predominantly influenced by the inertial effect of the surrounding fluid. Further, because of the limited fluid-filled space in tissue and in blood vessels, the expansion of SWL-induced cavitation

bubbles *in vivo* can be severely constrained,[17] and thus the resultant bioeffects are less dramatic as compared to *in vitro* conditions.

In this work, we studied the interaction of lithotripter shock waves with acoustically activated microbubbles and its impact on shock wave-induced bioeffects. To produce controlled and forced collapse of inertial microbubbles, we devised a simple method to modify the ellipsoidal reflectors of current electrohydraulic shock wave lithotripters so that a weak shock wave preceding a regular lithotripter pulse by a few microseconds can be produced. This preceding wave induces inertial microbubbles, which expand to a maximum size ranging from 100 to 200 μm, with a few expanding up to 400 μm before being collapsed by the ensuing incident lithotripter shock wave. This *in situ* shock wave–inertial microbubble interaction generates strong secondary shock wave emission immediately following the incident lithotripter shock front and the formation of microjets along the wave propagation direction. With an optimal pulse combination, the modified pressure waveform was found to significantly enhance the efficiency of membrane permeabilization of mouse lymphoid cells at low exposure, and to substantially increase cell damage at high exposure, compared to standard lithotripter shock waves. These results suggest that appropriate shock wave–inertial microbubble interaction may selectively improve the efficiency of shock wave-mediated macromolecule delivery and tissue ablation.

I. EXPERIMENTAL DESIGN AND METHODS

A. Modification of shock wave reflector

In electrohydraulic shock wave lithotripters, a truncated ellipsoidal reflector is used to focus the shock wave, generated by a spark discharge at the first focus ($F1$), onto the second focus ($F2$) of the reflector where the target kidney stones are located. The propagation time of the shock wave is determined by the ratio of the major axis of the ellipsoidal reflector and the shock wave propagation speed in water. Mathematically, it is valid that two ellipsoids can share the same foci ($F1$ and $F2$), but have different major and minor axes. Hence, by using a staged double-ellipsoidal reflector as shown in Fig. 1(B), a spherically divergent shock wave generated at $F1$ will be reflected partially from the first and partially from the second reflecting surfaces. While both reflected shock waves converge to $F2$, they are temporally separated by a time delay determined by the difference in the major axes of the two reflectors.

In this study, we have designed and fabricated an annular brass reflector that can be attached, via an adapter ring, to the reflector rim of a Dornier XL-1 experimental electrohydraulic shock wave lithotripter (Fig. 1). The Dornier XL-1 lithotripter uses an 80-nF discharge capacitor and a hemiellipsoidal reflector (semimajor axis $a=110.3$ mm, semiminor axis $b=78$ mm, and half-focal length $c=78$ mm). In comparison, the inner surface of the annular ring reflector fits on an ellipsoidal surface with $a=102.8$, $b=67$, and $c=78$ mm. While being confocal, the major axis of the annular ring reflector is 15 mm shorter than that of the XL-1 reflector, corresponding to a reduction of ~10 μs in acoustic

1998   J. Acoust. Soc. Am., Vol. 105, No. 3, March 1999

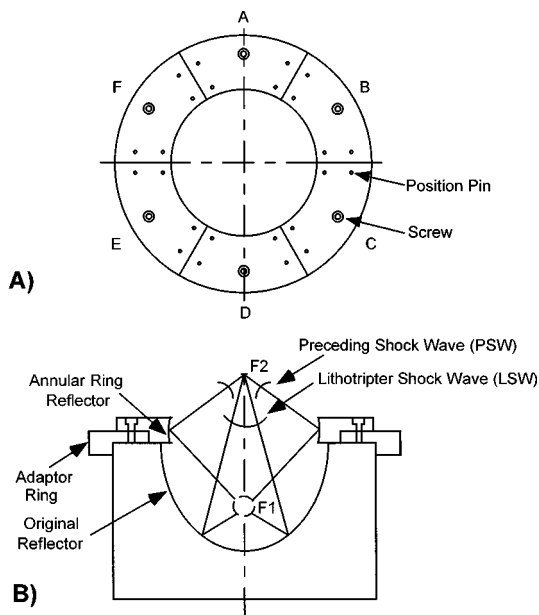Zhong *et al.*: Shock wave–inertial microbubble interaction   1998

FIG. 1. A schematic diagram of the design and layout of the annular ring reflector and the Dornier XL-1 experimental shock wave lithotripter. The annular ring reflector consists of six identical segments (thickness=28 mm), which can be connected either individually or together to the rim of the XL-1 reflector via an adapter ring.

wave-propagation time (for reflected waves) from $F1$ to $F2$. This short time delay was chosen to allow the inertial cavitation bubbles, induced by a preceding shock wave (PSW) reflected from the annular ring reflector, to grow to a size of a few hundred microns before being collapsed by the lithotripter shock wave (LSW). In order to adjust the intensity of the PSW, the annular ring reflector was fabricated into six identical segments (thickness=28 mm), with each segment able to be connected individually to the adapter ring via position pins and screws [Fig. 1(A)]. The inserted annular ring reflector shadows only a small portion (~5 deg steradian) of the original XL-1 reflector, and thus would not affect the LSW significantly. By inserting different ring segments, various intensity combinations of the preceding and lithotripter shock wave series can be produced. In this work, we have evaluated the effects of three axis-symmetric reflector combinations (see Table I for configuration) on shock wave–inertial microbubble interaction and the resulting bioeffects on mouse lymphoid cells.

B. Physical characterization

1. Pressure measurements

The acoustic field around the beam focus of the lithotripter was measured using a hydrophone system with disposable PVDF membranes (Sonic Industries).[23] The disposable

TABLE I. Annular ring reflector configurations.[a]

Configuration	Segments used
D2	A,D
D3	A,C,E
D6	A,B,C,D,E,F

[a]See Fig. 1 for the design and layout of the annular ring reflector.

PVDF membrane (25 μm thick) has a sensing element of <1 mm^2, connected to gold electrodes deposited on the surface of the membrane. During shock wave exposure in water, the electrode leads are gradually eroded by cavitation, resulting in an increase of lead resistance and a concomitant reduction of the membrane sensitivity.[23] To ensure the integrity of the hydrophone, the resistance of the lead electrodes was monitored during the course of pressure measurements. According to manufacturer's specification, when the change in lead resistance exceeded 200 Ω, the PVDF membrane was replaced.[24] Because the sensing element and the electrodes of the PVDF membrane are not electrically shielded from the water, significant electric noise from the spark discharge was picked up in water, which distorted the pressure waveform. To isolate the sensing element from the water and to protect the lead electrodes from cavitation damage,[25] we have encapsulated the original PVDF membrane in castor oil. This was done by filling up the space enclosed by the supporting frame of the PVDF membrane with castor oil and then sealing it with a 115-μm-thick polyester-membrane sheet. Care was taken to avoid trapping air bubbles inside the castor oil enclosure, which has a total thickness of about 8 mm, with the PVDF membrane located at the middle plane. The encapsulated PVDF membrane was then calibrated by comparison with the output from a calibrated PVDF needle transducer (MHA9-6, Force Institute) in the acoustic field of a 2.25-MHz focused transducer (Panametrics). For acoustic field mapping of the lithotripter, the PVDF membrane was attached to an $x-y-z$ translational stage (0.01-mm precision), and scanned both along and transverse to the shock wave axis at $F2$. Triplicate of measurements was made at each location, with the pressure waveforms registered on a LeCroy digital oscilloscope (model 9314) operated at a 100-MHz sampling rate, corresponding to a time interval of 10 ns/point.

2. High-speed photography

To visualize shock wave propagation, bubble dynamics, and shock wave–bubble interaction, a shadowgraphic imaging system was set up inside the original water tank (10 ×25×39 in., H×W×L) of the XL-1 lithotripter (Fig. 2). Two $\frac{1}{2}$-in.-thick Lucite plates were used to form a small water enclosure (10×13×25 in., H×W×L) around the shock wave generator, so that a higher image magnification could be achieved. High-speed shadowgraphs were recorded using an ICCD [intensified charge coupled device (CCD)] camera (4 Quik 05A, Stanford Computer Optics) with an exposure time of 20 ns, corresponding to a spatial resolution of, at worst, 30 μm. To provide a reliable time reference of the event, the spark discharge of the lithotripter electrode was picked up by a fast photodetector with a rise time of 35 ns (PDA50, Thorlab Inc.) and fed into the LeCroy oscilloscope. The synchronized output of the scope was then relayed to a digital delay generator (DS535, Stanford Research Systems), which was used to control the electronic shutter (i.e., the intensifier) of the ICCD camera. By adjusting the delay time with respect to the spark discharge, a series of high-speed shadowgraphs can be recorded at different stages of shock wave propagation and subsequent bubble oscillations. To
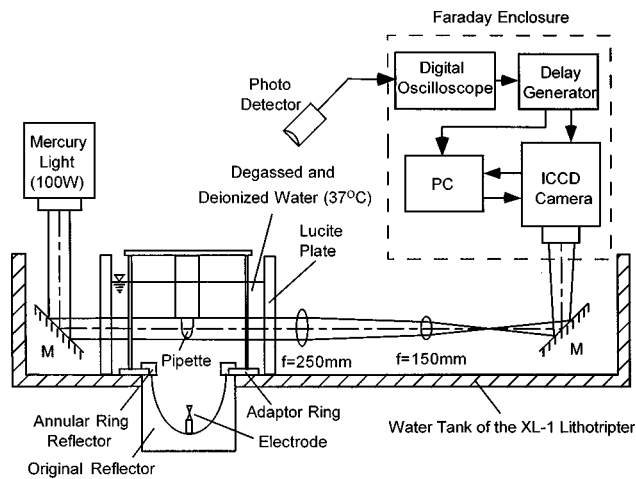
FIG. 2. A schematic diagram of the experimental setup for high-speed shadowgraph imaging of bubble dynamics and shock wave–bubble interaction produced by an XL-1 lithotripter; M: mirror.

prevent interference from the electromagnetic noise generated by the lithotripter, a Faraday enclosure was built to cover the camera, and the trigger and control instruments.

3. Acoustic emission measurements

Acoustic emission, emanating from the beam focus of the lithotripter, was measured using a passive cavitation-detection system described previously.[17] Briefly, a focused hydrophone of 1 MHz resonant frequency and 101.6 mm focal length was aligned perpendicularly to the lithotripter axis, and confocally with $F2$. The output signal of the hydrophone was fed into a high-pass filter with a 0.3-MHz cutoff frequency and a broadband amplifier (5052 PR pulser/receiver, Panametrics) before being registered on the LeCroy oscilloscope. It has been shown previously that the acoustic-emission signal associated with lithotripter shock wave-induced cavitation oscillation has a unique double-burst structure. The first burst corresponds to the initial collapse and subsequent expansion of cavitation nuclei by the incident lithotripter shock wave, and the second burst corresponds to the primary collapse of the bubble cluster.[16,17] Hence, acoustic-emission measurements were used to assess the overall dynamics of the bubble oscillation and also to correlate with the high-speed shadowgraph images.

C. Bioeffect study

Mouse T-cell hybridoma DO-11.10, a suspension cell line kindly provided by Dr. P. Marrack (National Jewish Center for Immunology and Respiratory Medicine, Denver, Colorado) were used. These cells were grown to 2–4 million cells/ml in T-75 culture flasks (Corning Costar Corp.) at 37 °C in Eagle medium containing 10% fetal bovine serum under a humidified atmosphere with 5% CO_2. Fluorescein isothiocyanate (FITC)-labeled dextran (average molecule weight: 70 kD, Sigma Chemical, Inc.), which is normally not taken up by cultured cells, was added to the suspended cell culture and adjusted to a final concentration of 1 mg/ml shortly before SWL treatment. After mixture, the cell suspensions containing FITC-dextran were loaded into 1.5-ml

polyethylene pipettes (VWR Scientific Products) with bulbs 20 mm long and 10 mm in diameter. The culture medium was filled up to the tip of the pipette, which is about 10 cm above the center of the bulb. Care was taken to avoid trapping air bubbles inside the pipette. The pipette was inverted and fitted snugly into a plastic holder and connected to a supporting platform (see Fig. 2). This arrangement was used to ensure that the center of the pipette bulb could be aligned consistently with $F2$ during the whole SWL procedure. The small enclosure surrounding the shock wave generator was filled with degassed and deionized water (O_2 concentration: <4 mg/L) close to the level of the pipette tip. The water temperature was maintained at 35–37 °C by continuous circulation. Various numbers of shock waves generated at a 25-kV output setting were delivered to the pipettes in the treatment group at a 1-Hz pulse-repetition rate. Control groups were prepared following the same procedure and placed in the water tank away from the lithotripter shock wave.

After shock wave treatment, the cells in both the treated and control groups were spun in 15-ml capped tubes and then washed with the culture medium. After repeating this process twice, the cells were resuspended in 0.5 ml of the culture medium. For all the samples, the total number of interested cells (for example, fluorescence-positive, intact surviving cells in the treated group and intact cells in the control group) was countered in a hemocytometer (which provides a fixed volume of 0.1 ml) in triplicate, using a Zeiss Axioplan microscope. Permeabilization efficiency was determined by differential interference contrast (DIC) microscopy and fluorescence microscopy. The cells in the treated group that remained morphologically intact and fluorescence positive were counted. Cell mortality, defined as the percentage of cells that are morphologically damaged (lysed and membrane rupture), was determined by measuring the number of morphologically intact cells in the treated group (the rest of the cells were damaged). Further, functional impairment of the intact surviving cells was assessed by staining with 0.1% trypan blue, a vital dye that is only taken up by cells undergoing necrosis. By combining the results of these two tests, cell injury (defined as cells that are either physically damaged or functionally impaired) was determined. All three of these parameters were expressed as a fraction of the total number of intact cells in the control group. For each combination of exposure level and reflector configuration, three independent experiments were carried out, from which the average value and standard deviation were calculated.

D. Statistical analysis

The paired student's t-test was used to determine statistically significant differences ($p < 0.05$) between the results produced by the standard and modified lithotripter shock waves.

II. RESULTS
A. Physical characterization
1. Pressure waveforms and distribution

Examples of pressure waveforms generated at $F2$ using different reflector configurations are shown in Fig. 3. With

2000   J. Acoust. Soc. Am., Vol. 105, No. 3, March 1999

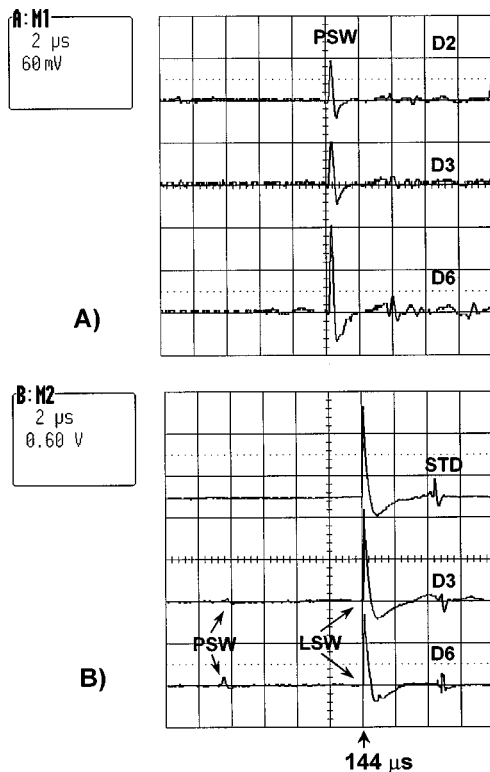Zhong *et al.*: Shock wave–inertial microbubble interaction   2000

FIG. 3. Representative pressure waveforms produced by the standard (STD) and different modified reflectors (D2, D3, and D6) at 25 kV: (A) preceding shock waves (PSW), and (B) PSW and lithotripter shock waves (LSW). Note that the vertical scale in (B) is 10 times that of (A).

the standard reflector, a single LSW was recorded about 144 μs after the spark discharge. In comparison, using the staged double-ellipsoidal reflectors, an LSW and a weak shock wave preceding the lithotripter pulse by approximately 8.5 μs were recorded [Fig. 3(A) and (B)]. Due to a higher propagation speed of the shock wave, the arrival time of the LSW at $F2$ and the time delay between the PSW and the LSW were slightly reduced from the corresponding values (147 and 10 μs, respectively) calculated based on acoustic wave propagation. Compared to the lithotripter pulse, the PSW has a similar temporal profile, but much smaller pressure amplitudes. In addition, as the surface area of the annular ring reflector increases (from D2 to D3, to D6), the PSW becomes stronger [Fig. 3(A)] while the ensuing lithotripter pulse (reflected from the remaining surface area) becomes weaker [Fig. 3(B)].

The pressure distribution of the strongest PSW, generated by reflector configuration D6, is shown in Fig. 4. The maximum pressure was measured slightly ($\sim$0.5 mm) beyond $F2$, along the major axis of the reflector. At $F2$, a peak positive pressure (P^+) of 5.53 MPa and a peak negative pressure (P^-) of -1.91 MPa were recorded. Using the positive-pressure curve, the -6-dB beam size of the preceding pulse was determined to be 5×1.2 mm along and transverse to the major axis of the reflector, respectively. In contrast, the maximum positive pressure of the LSW was measured about 10 mm beyond $F2$, for both the standard (100 MPa) and D3 (89.6 MPa) reflector configurations (Fig. 5). This significant shift of the maximum positive pressure beyond $F2$ is caused by the nonlinear propagation of the
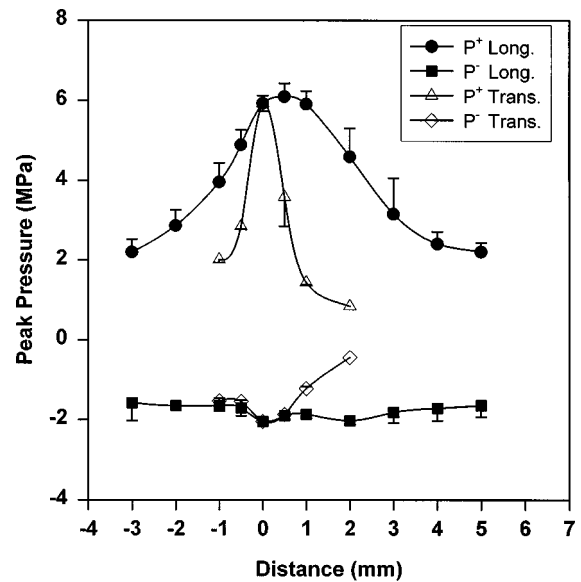
FIG. 4. Distribution of the peak pressure of the preceding shock wave generated by the D6 annular ring reflector configuration at 25 kV. Long.: longitudinal or along the shock wave axis, and Trans.: transverse to the shock wave axis at $F2$.

lithotripter shock wave.[26] At $F2$, the values of P^+ and P^- were measured to be 67.6 and -17.6 MPa using the standard reflector, and 61.7 and -15.2 MPa using the D3 reflector, respectively. These peak positive-pressure values are similar to the ones reported previously for the XL-1 lithotripter.[27] The peak negative value, however, is consistently higher than the typical values measured by a fiberoptic hydrophone either in water (-10.4 and -9.3 MPa at 14 and 18 kV, respectively[1]), or in a 5-ml polyethylene pipette 40 mm long and 12 mm in diameter filled with freshly drawn heparinized human blood washed to a hemoglobin content of 10 g/L (-7.7 MPa at 30 kV[28]). This difference is presumably due to the higher tensile strength of the castor oil that encloses the
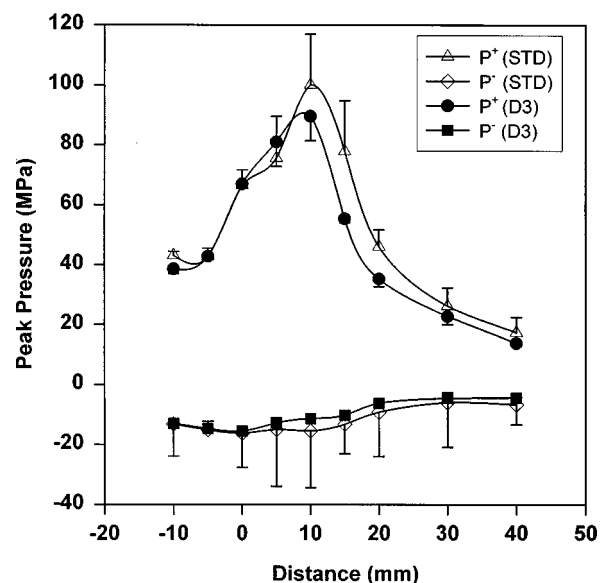

FIG. 5. Distribution of the peak pressure of the lithotripter shock wave generated by the standard and D3 reflector configuration along the major axis of the ellipsoidal reflector at 25 kV.

2001   J. Acoust. Soc. Am., Vol. 105, No. 3, March 1999

Zhong *et al.*: Shock wave–inertial microbubble interaction   2001

TABLE II. Peak pressure at lithotripter focus and beam size at 25 kV.[a]

Reflector configuration	Preceding shock wave			Lithotripter shock wave		
	P^+ (MPa)	P^- (MPa)	Beam size (mm)	P^+ (MPa)	P^- (MPa)	Beam size (mm)
Standard				67.6±4.49	−17.6±2.21	6×22
D2	2.88±0.48	−1.10±0.38		61.7±5.03	−19.4±3.36	
D3	3.01±0.32	−0.96±0.32		61.7±2.63	−15.2±2.71	4×23
D6	5.53±0.50	−1.91±0.23	1.2×5	56.9±2.87	−9.3±3.08	7×28

[a]Beam size was determined by −6-dB range of the peak positive pressure.

PVDF membrane. In addition, the maximum negative pressure of the LSW was measured at $F2$, instead of shifting closer to the shock wave source as reported from other lithotripters.[14,29] The reason for this discrepancy is unknown. The −6-dB beam size of the LSW produced by standard reflector is 22×5 mm along and transverse to the lithotripter axis, respectively. Similar beam sizes, 23×4 and 28×7 mm, were measured using the D3 and D6 reflector configurations, respectively. Table II summarizes the peak positive and peak negative pressure, and beam sizes of the preceding and lithotripter shock waves, produced by different reflector configurations.

The temporal parameters of the preceding and lithotripter shock waves produced at 25 kV are shown in Table III. The rise time (t_r) of the shock front was measured by the time duration from 10% to 90% of P^+. The positive (t^+) and negative (t^-) pulse durations of the shock waves were measured by the zero-crossing duration of the positive and negative cycles, respectively. In general, the PSW has a longer rise time, but shorter pulse duration, compared to the LSW. In addition, for the modified reflectors, the values of t_r, t^+, and t^- for both the preceding and lithotripter shock waves all become larger as the surface area of the annular ring reflector increases (from D2 to D3, to D6). Of particular interest was that the rise time of lithotripter shock fronts generated by the modified reflectors was found to be longer than that produced by the standard reflector. This increased rise time seems to correlate with the reduced peak pressure of the LSW, which may be caused partially by the slightly reduced reflector surface area and partially by the scattering of lithotripter shock waves from the inertial microbubbles.

In a separate experiment, we have acoustically masked the portion of the LSW in the shadow of the annular ring reflector by acoustic barrier materials. The acoustic masks were made essentially into the shape of the individual ring segments, except that the inner surface of the masks forms a cone enclosing the shock wave reflected from the XL-1 reflector. Therefore, even when different reflector combinations were used, the LSW was reflected effectively from the same surface area. Pressure measurements at 20 kV show that as the surface area of the annular ring reflector increases (from D2 to D3, to D6), P^+ of the LSW decreases significantly while t_r increases substantially from the values corresponding to the standard reflector [Fig. 6(B)]. Since P^- of the PSW also increases significantly from D2 to D6 [Fig. 6(A)], the size and density of inertial microbubbles generated in front of the LSW should increase accordingly, resulting in a stronger shock wave–inertial microbubble interaction (see also Fig. 8). Hence, these results indicate that the amplitude of the LSW is influenced by the scattering of the LSW from the microbubbles generated by the preceding pulse. Similar amplitude reduction and shock front thickening effects were also observed when lithotripter shock waves were scattered by stable glass beads suspended in castor oil.[25]

2. High-speed photography

Figure 7 shows a selection of high-speed shadowgraphs taken at different time instants after the spark discharge at 25 kV, using the standard ellipsoidal reflector. Several important features can be observed. The incident shock wave, moving upward, consists of a concave central part corresponding to the focused shock front, and a convex part originating from the wave diffraction at the aperture of the reflector.[30] The diffracted waves propagated laterally along the focused shock front and crossed on the central axis of the reflector. Due to nonlinear wave propagation, the diffracted and focused shock waves merged together to form a flattened shock front beyond the geometric focus of the reflector (see the third frame of Fig. 7). The position corresponding to the

TABLE III. Temporal parameters of the shock waves at 25 kV.

Reflector configuration	Preceding shock wave			Lithotripter shock wave		
	t_r[a] (ns)	t^{+}[b] (μs)	t^{-}[c] (μs)	t_r[a] (ns)	t^{+}[b] (μs)	t^{-}[c] (μs)
Standard				20±4.4	0.82±0.27	3.83±0.69
D2	126±31	0.37±0.05	0.85±0.26	24±7.4	0.51±0.05	1.77±0.06
D3	135±22	0.38±0.03	0.93±0.16	27±5.9	0.76±0.29	2.76±0.94
D6	142±39	0.48±0.13	1.62±0.57	38±9.5	0.79±0.24	3.01±0.35

[a]t_r: Rise time of the shock front, measured from 10% to 90% of the peak positive pressure.
[b]t^+: Positive pulse duration, measured by the zero-crossing duration of the positive cycle of the shock wave.
[c]t^-: Negative pulse duration, measured by the zero-crossing duration of the negative cycle of the shock wave.
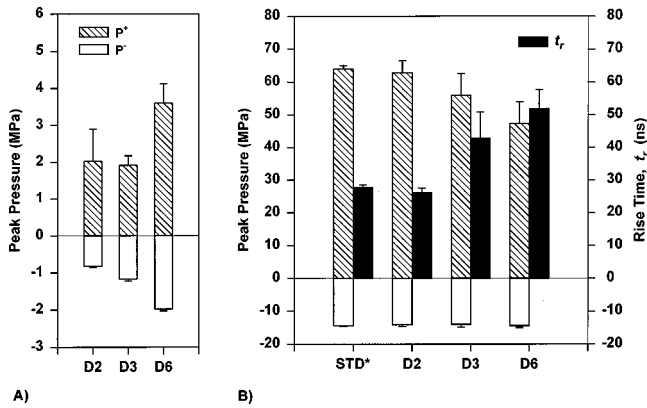
FIG. 6. Peak pressure and rise time of the shock waves produced by different reflector configurations at 20 kV: (A) the preceding shock wave, and (B) the lithotripter shock wave.

strongest wave focus on this propagating, flattened shock front is called Mach stem.[30] This observation is consistent with the shift of the peak positive pressure of the lithotripter shock waves, measured by the PVDF hydrophone.

Because of the temporal profile of the shock wave, cavitation bubbles were induced in the wake of the shock front where the tensile pressure is high. Most of these bubbles were observed to expand initially to a maximum size of 3–4 mm and then collapse violently, producing secondary shock wave emission which could be visualized as spherically divergent circular rings surrounding the collapsed bubbles (see the frame $t = 740\ \mu$s in Fig. 7). During the initial expansion, individual bubbles were nearly spherical and separated from each other. However, in the later stage of the expansion, significant bubble aggregation was observed in regions near

the shock wave axis, leading to the formation of large bubbles of 5–7 mm in diameter (see, also, the frame $t = 740\ \mu$s in Fig. 7) with various shapes. This aggregation process appears to extend the duration of bubble expansion significantly from the corresponding values for the isolated single bubbles. When the large, aggregated bubbles collapsed, much stronger secondary shock wave emission was produced (frame $t = 900\ \mu$s in Fig. 7).

When a staged double-ellipsoidal reflector was used, three major differences in the high-speed shadowgraphs could be noticed [Fig. 8(A)]. First, a PSW produced by the reflection and diffraction of the incident shock wave from the inserted reflector was observed ahead of the LSW. This PSW consists largely of diffracted waves from both the upper and lower rims of the annular ring reflector, with both waves crossing on the central axis of the reflector. In addition, another weak shock wave was also observed in between the preceding pulse and the LSW. This additional wave is speculated to correspond to the portion of the LSW that is in the shadow of the inserted reflector, which is accelerated while passing diagonally through the brass reflector. Second, small inertial bubbles were induced by the PSW, and expanded to a size of 100–200 μm, with a few grown to a size up to 400 μm (measured directly from enlarged images) before being collapsed *in situ* by the incident LSW. Consequently, strong secondary shock wave emission was generated immediately following the propagating lithotripter shock front, visualized as numerous circular rings. Third, the collapse of some inertial microbubbles by the lithotripter shock front appeared to be asymmetric, resulting in the formation of microjets [label "J" in Fig. 8(A)] along the wave-propagation direction. In general, as the PSW becomes stronger, increased numbers of

FIG. 7. Representative high-speed shadowgraphs of the incident lithotripter shock wave and subsequent dynamics of cavitation bubbles, produced by the XL-1 lithotripter at 25 kV with the standard reflector (Frame size=19×25 mm, W×H). The incident shock wave propagates from the bottom to the top of the frame. The number on top of each image frame indicates the time delay from the spark discharge in microseconds. The cross symbol indicates the geometric focus ($F2$) of the lithotripter. LSW: lithotripter shock wave, and DW: diffracted wave.
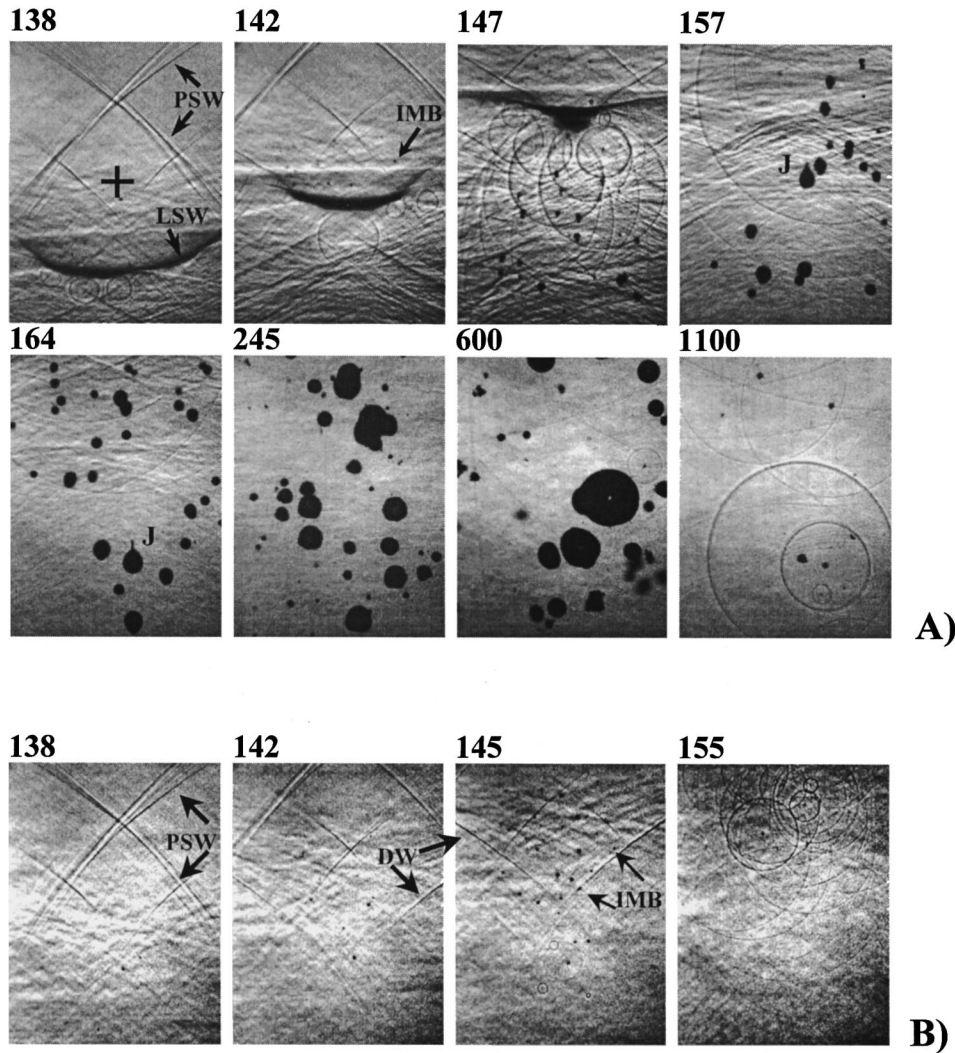
FIG. 8. Representative high-speed shadowgraphs of the incident shock waves and subsequent dynamics of cavitation bubbles produced by the XL-1 lithotripter at 25 kV, with (A) the D6 modified reflector, and (B) D6 reflector, but the focused portion of the LSW was blocked by acoustic barrier materials (Frame size is 19×25 mm, W×H). The incident shock wave propagates from the bottom to the top of the frame. The number on top of each image frame indicates the time delay from the spark discharge in microseconds. The cross symbol indicates the geometric focus ($F2$) of the lithotripter. LSW: lithotripter shock wave, PSW: preceding shock wave, IMB: inertial microbubble, DW: diffracted wave, and J: jet.

microjets will be formed following the lithotripter shock front. After the initial collapse, most microbubbles re-bounded and re-expanded again under the influence of the tensile stress of the LSW. These bubbles again reached a maximum size in several hundred microseconds and then collapsed rapidly, generating strong secondary shock wave emission.

To better visualize the dynamics of the inertial microbubbles induced by the PSW, we have acoustically masked the focused LSW by acoustic barrier materials. Figure 8(B) shows that the inertial microbubbles were induced following the PSW and expanded to a maximum size at ~t = 145 μs, before they collapsed around $t = 155 \mu$s. Similarly, the maximum size of most bubbles was measured to be in the range of 100–200 μm, with a few up to 400 μm. It should be noted that a diffracted wave associated with the LSW (only the focused shock front was blocked) was also produced, which may influence the collapse of the inertial microbubbles.

Similar characteristics of shock wave propagation and *in*

situ microbubble–shock wave interaction were also observed inside the pipette used for the bioeffects study (Fig. 9). In this series of experiments, the pipette was filled with saline solution, and a yellow filter was used to reduce the light intensity in the surrounding water so that a uniformly illuminated image could be recorded. Using the modified reflectors, inertial microbubbles were induced in front of the lithotripter shock wave (frames 1 and 2), and a more uniformly distributed bubble cluster was produced inside the pipette (frame 4), compared to the standard reflector. In the later stage (>200 μs), larger bubbles were formed both inside and on the exterior surface of the pipette wall, with the later ones lasting longer. Therefore, a clear and complete sequence of the bubble expansion and collapse inside the pipette could not be obtained.

3. Acoustic emission (AE)

Using both the standard and modified reflectors, AE signals with at least two distinct, temporally separated pressure
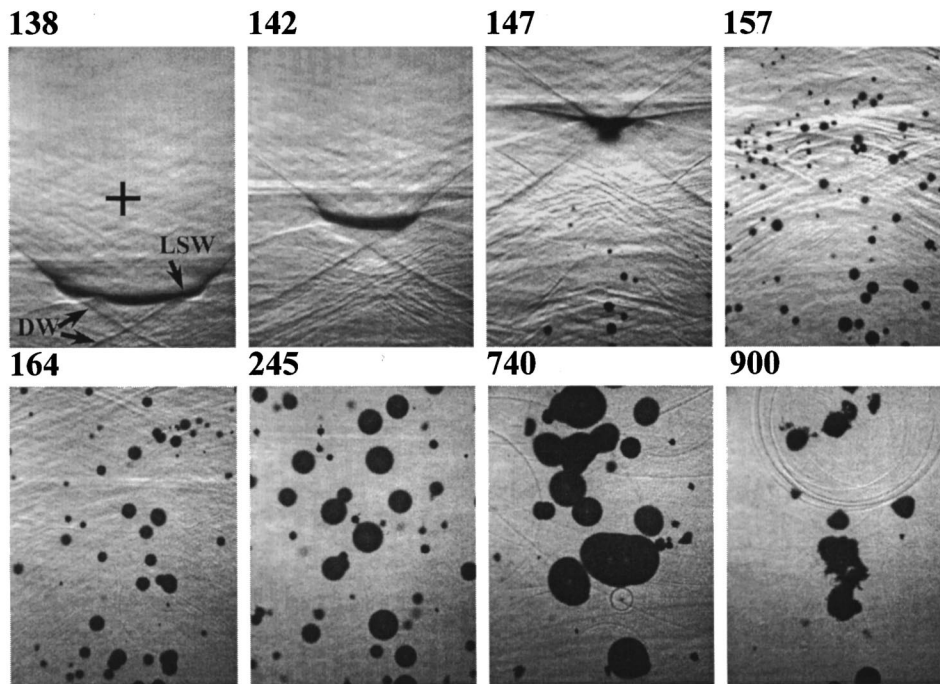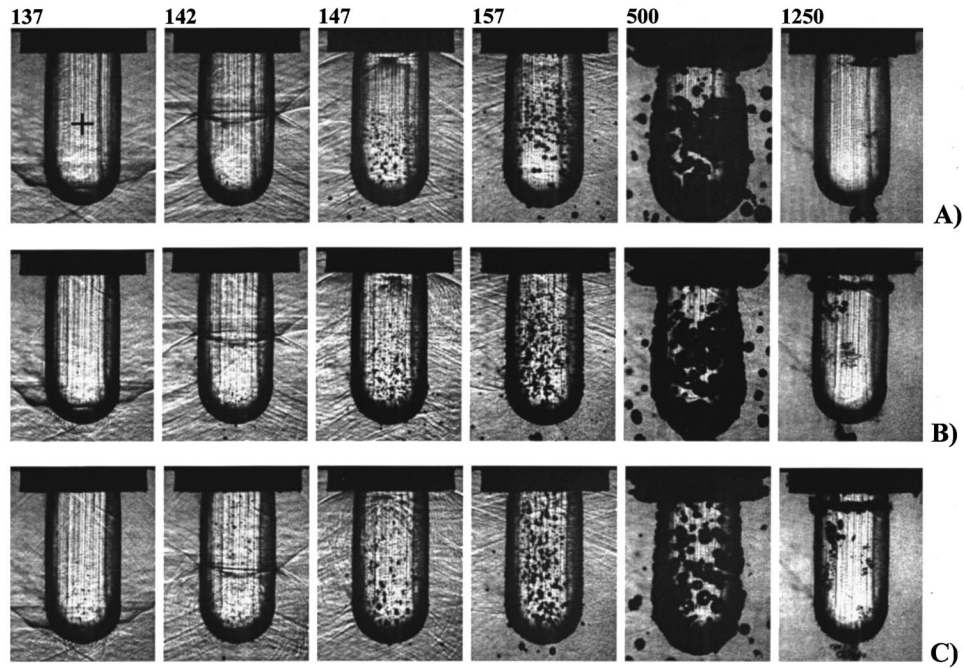
FIG. 9. Representative high-speed shadowgraphs of the incident lithotripter shock waves and subsequent dynamics of cavitation bubbles in pipettes, produced by the XL-1 lithotripter at 25 kV, with (A) the standard, the modified (B) D3, and (C) D6 reflectors (Frame size is 19×25 mm, W×H). The incident shock wave propagates from the bottom to the top of the frame.

bursts were recorded (Fig. 10). The first pressure burst (1°) corresponds to the initial compression (or collapse) and subsequent expansion of cavitation nuclei (or inertial microbubbles) by the incident LSW, and the second burst (2°) to the collapse of the large, aggregated bubbles. The collapse of small individual bubbles may contribute to the weaker pressure spikes observed before the second burst. In water, a third pressure burst (3°) was often recorded, which was found to correlate with the second collapse of the aggregated large bubbles after their first rebound. Using the modified reflector ($D6$), the peak pressure of the first AE burst was found to be much stronger than that produced by the standard reflector. This is primarily caused by the *in situ* shock

wave–inertial microbubble interaction, with resultant violent collapse of microbubbles and strong secondary shock wave emission. The scattering of the incident LSW from the microbubbles may also contribute to the increased peak pressure in the first AE burst. In addition, the collapse time of the bubble cluster (t_c), defined as the time delay between the maximum pressure peaks of the first and second AE bursts, was found to increase from standard to double reflectors in accord with the strength of the PSW [Fig. 11(A)]. A similar increase in the peak-to-peak amplitude of the first AE burst was also observed [Fig. 11(B)]. However, the peak-to-peak pressure of the second AE burst was almost independent of the reflector configuration [Fig. 11(B)], since it is determined primarily by the inertial collapse of the expanded bubbles. When acoustic-barrier materials were used to mask the focused LSW, the collapse time of the microbubbles induced by the PSW was determined to be between 9 and 17 μs. If we neglect the influence of the diffracted wave [see Fig.
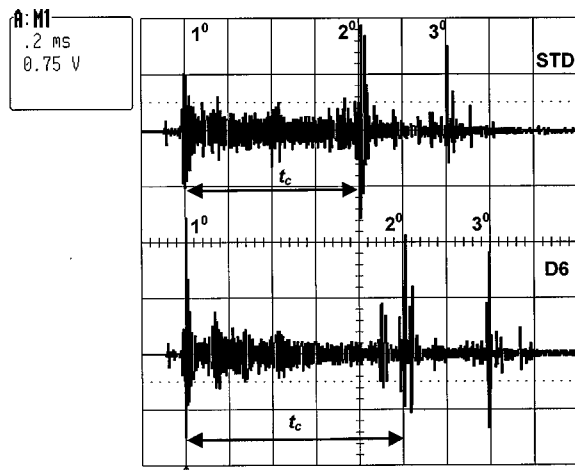
FIG. 10. Acoustic emission (AE) signals produced in water by the XL-1 lithotripter at 25 kV, using the standard (STD) and modified (D6) reflectors. The collapse time of the bubble cluster, t_c, is determined by the time delay between the peak pressure of the first (1°) and second (2°) AE bursts.
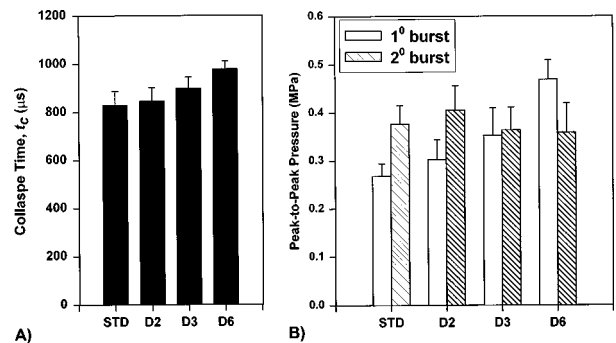
FIG. 11. (A) Collapse time (t_c) and (B) peak-to-peak pressure of the acoustic-emission signals produced by the XL-1 lithotripter at 25 kV, using the standard and modified reflectors.

8(B)] on bubble oscillation, these values would correspond to spherical bubbles with a maximum diameter between 90 and 170 μm, based on the Rayleigh collapse time for a vapor-filled cavity.[16] These estimated maximum-bubble diameters were slightly smaller than the values measured directly from high-speed images (Fig. 8), presumably because the diffracted wave may accelerate the collapse of the inertial microbubbles. Since the time delay between the PSW and LSW is 8.5 μs, this result suggests that some microbubbles may be collapsed by the LSW near their maximum size while others may be collapsed after their maximum expansion. Furthermore, a close examination of the initial portion of the first AE burst has revealed some subtle differences between bubble activity produced by the standard and modified reflectors [Fig. 12(A)]. In a 20-μs time window (from 202 to 222 μs, corresponding to the lithotripter shock front moving from 15 mm in front of $F2$ to 15 mm beyond $F2$), the averaged amplitude (rms) of the AE signal produced by the D6 reflector configuration was found to be significantly stronger than that by the standard reflector [Fig. 12(B)]. This result confirms again that *in situ* shock wave–microbubble interaction produces strong bubble collapse and secondary shock wave emission.

B. Bioeffect study

To assess the bioeffects of the modified shock waves, we tested the shock wave-mediated dextran transfer to a line of T-cell hybridoma that resembles activated T lymphocytes.[31] These hybridoma cells possess morphological and physiological features typical of most hematopoietic cells. In addition, the uniform cellular and nuclear morphology of the cell line allows easy detection of cellular damage and necrosis by DIC microscopy. Necrosis is also detected by trypan blue assay. Dextrans were chosen to characterize the efficiency of shock wave-induced membrane permeabilization because they are branched polysaccharide molecules that are noncharged, yet highly hydrophilic. These molecules, with an average molecular weight of 70 kD, mimic many globular proteins and hydrophilic macromolecules in their biophysical properties in aqueous solutions. The fluorescently conjugated dextran molecules also allow quick detection of the macromolecule transfer across the cell membrane, minimizing errors in quantification due to exocytosis.

The results of our bioeffect study clearly revealed an exposure-dependent response in cell membrane-permeabilization efficiency, and cell mortality and injury, shown in Figs. 13–15, respectively, after shock wave treatment at 25 kV. Using standard lithotripter shock waves, permeabilization efficiency was found to increase initially with the number of shock waves delivered to the target cells, and reach a maximum value of 11.2% at 100 shocks. In comparison, with double reflectors the maximum permeabilization efficiency was achieved between 50 and 100 shocks. Interestingly, at 50 shocks the permeabilization efficiency produced by the D3 reflector configuration (15%) was found to be consistently higher than that produced by the standard reflector (7.8%), while corresponding values from the D2 and D6 reflector configurations (5.8% and 7.4%, respectively) were lower (Fig. 13). This result suggests that there is

A)

B)
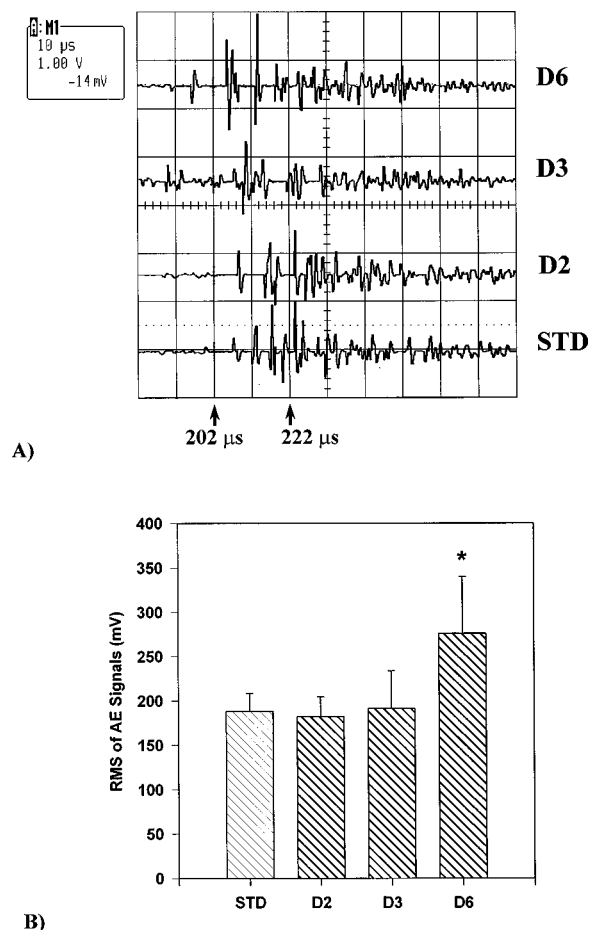
FIG. 12. (A) Expansion of the initial portion of the acoustic-emission signals produced by different reflector configurations at 25 kV. A 20-μs window (from 202 to 222 μs), indicated by arrows, corresponds to the lithotripter shock front moving from 15 mm in front of $F2$ to 15 mm beyond $F2$. (B) rms of the acoustic emission signals in the 20-μs window shown in (A). The peak-to-peak amplitude produced by the D6 reflector configuration is significantly higher ($p < 0.04$) than that from the standard reflector.

an optimal combination of the preceding and lithotripter shock waves that can produce the best permeabilization efficiency, presumably related to the optimal shock wave–microbubble interaction. For cell mortality, the double reflector produces consistently higher cell death when the number of shock waves delivered exceeds 100 shocks, compared to the standard reflector. Similar results were also observed for cell injury, which are shifted only slightly above the mortality curves. This result indicates that most cells were physically damaged, and only a small percentage of the intact surviving cells was physiologically impaired. After 250 shocks at 25 kV, the maximum injury produced by the double reflectors ranged from 70%–78%, compared to 63% by the standard reflector. These findings demonstrate clearly that shock wave–inertial microbubble interaction could be used selectively to improve the bioeffect of lithotripter shock waves.

III. DISCUSSION

The interaction of a lithotripter shock wave with an artificially produced stable air bubble has been studied previously.[18] It was shown that corresponding to the tempo-
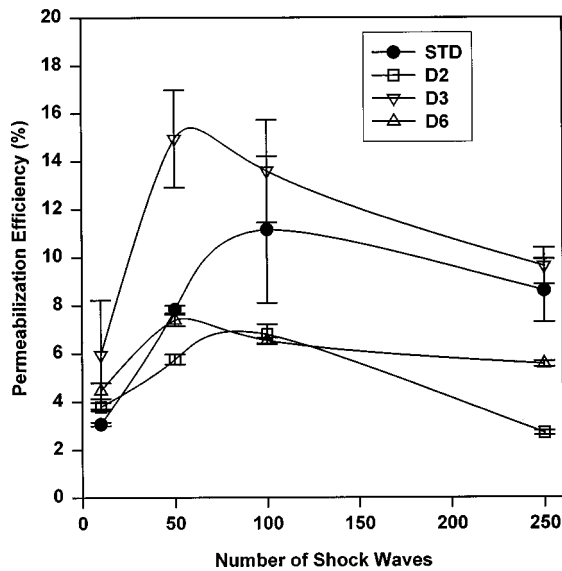
FIG. 13. Exposure-dependent permeabilization efficiency of mouse T-cell hybridoma at 25 kV. The permeabilization efficiency produced by the D3 reflector configuration at 50 shocks is significantly higher ($p < 0.03$) than that from the standard reflector.

FIG. 14. Exposure-dependent cell mortality of mouse T-cell hybridoma at 25 kV. The maximum cell mortality produced by the modified shock waves is significantly higher ($p < 0.004$) than that from the standard reflector.
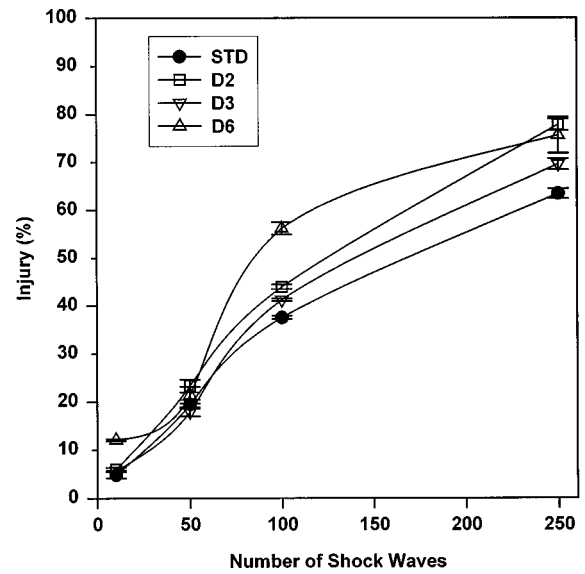
FIG. 15. Exposure-dependent cell injury of mouse T-cell hybridoma at 25 kV. The maximum cell injury produced by the modified shock waves is significantly higher ($p < 0.02$) than that from the standard reflector.

ral profile of the shock wave, bubbles within a certain size range will be collapsed asymmetrically, leading to the formation of microjets along the wave propagation direction. For a typical XL-1 lithotripter shock wave, this initial size (diameter) range is between 0.5 and 1.5 mm, with maximum jet velocity obtained at a bubble diameter of ~1.0 mm.[18] When the size of the stable bubble decreases, the momentum transfer during shock wave–bubble interaction also decreases, resulting in a lower potential for asymmetric collapse of the bubble. Using the XL-1 lithotripter, it was shown that as the bubble diameter becomes less than 500 μm, microjets would not be produced consistently.[18] Furthermore, the internal pressure of a stable bubble increases rapidly when compressed by a lithotripter shock front (as-

suming adiabatic gas compression inside the bubble), leading to a cushion effect against the violent collapse of the bubble.

In comparison, using the modified reflectors, inertial microbubbles are produced acoustically and expanded more than 4600–37 000 times (corresponding to $D_{b,\max}$ =100–200 μm and assuming initial cavitation nuclei are 6 μm in diameter) in volume before being collapsed in situ by the lithotripter shock front. Because of this large expansion, the internal pressure of the inertial microbubble when impinged by a lithotripter shock wave is much lower compared to a stable bubble of the same size. Therefore, the cushion resistance against the collapse of inertial microbubbles is very low. This explains why violent collapse of the inertial microbubbles and microjet formation were produced consistently using the modified reflectors, as revealed by high-speed shadowgraphy. Based on the results of AE measurements, it is also interesting to note that the forced collapse of inertial microbubbles is as strong as or even stronger than the inertial collapse of large bubbles. Considering that the bubble expansion produced by current lithotripter shock waves in vivo could be severely constrained by surrounding tissue and may cause capillary and small blood-vessel rupture,[32] shock wave–inertial microbubble interaction appears to be an attractive alternative for shock wave-mediated drug delivery and gene transfer in vivo. If lithotripter shock waves can be further optimized to minimize the tensile stresses, shock wave–inertial microbubble interaction could provide a better pressure waveform for macromolecule delivery in vivo, with less potential for vascular injury.

Forced collapse of inertial cavitation bubbles may also be produced by phase-inverted lithotripter shock waves. Several groups have used pressure-release reflectors to invert typical lithotripter shock waves to produce a pressure waveform with a leading tensile component followed by a compressive wave.[33–35] With such a phase-inverted lithotripter shock wave, in situ shock wave–inertial bubble interaction could also be produced.[35] However, because there is no time

delay between the leading tensile wave (which is quite strong) and the following shock front, the shock wave–bubble interaction occurs during the initial rapid-expansion phase of the bubbles. Consequently, a significant portion of the shock wave energy is consumed to terminate the rapid expansion of the bubbles, and thus less shock wave energy is used for the collapse of the bubbles. In addition, the phase-inverted lithotripter shock waves are less flexible in terms of controlling the area of shock wave–bubble interaction, as well as the pressure and energy ratio between the leading tensile wave and the following compressive wave, since both waves are generated by the same reflector surface. In comparison, using an annular ring reflector a preceding weak shock wave with a tensile stress sufficiently strong to induce inertial microbubbles can be produced. The strength and the time delay between the preceding pulse and lithotripter shock wave can be adjusted so that the inertial microbubbles are collapsed near their maximum size. Thus, most of the lithotripter shock wave energy consumed during the shock wave–inertial microbubble interaction is used for the collapse of the bubbles. Moreover, by adjusting the size and configuration of the annular ring reflector, we can also control the size and distribution of inertial microbubbles around the lithotripter focal point. This strategy may be used to control the volume of shock wave–bubble interaction to achieve optimal therapeutic effects (i.e., drug delivery and gene transfer) to the target cells with minimal damage to surrounding tissues. Our results indicate that an appropriate temporal relationship between the preceding shock wave, which induces inertial microbubbles, and the ensuing lithotripter shock wave, which collapses the microbubbles, is needed in order to achieve the best permeabilization efficiency.

IV. CONCLUSIONS

A method of producing *in situ* shock wave–inertial microbubble interaction was developed and tested *in vitro*. A series of physical measurements utilizing PVDF hydrophone, high-speed shadowgraph imaging, and passive cavitation detection revealed that the forced collapse of inertial microbubbles in a lithotripter field generates strong secondary shock wave emission and the formation of microjets along the shock wave-propagation direction. These unique features, absent from bubble dynamics induced by the standard lithotripter shock waves, contribute to the significantly enhanced cell injury at high exposure ($>$100 shocks), and the substantially augmented membrane permeabilization efficiency at low exposure (50–100 shocks) when an optimal pulse combination is used. Our results also suggest that shock wave–inertial bubble interaction may be tailored for different biomedical applications. For instance, shock wave–inertial microbubble interaction may be used to enhance SWL-mediated drug delivery and gene transfer, taking advantage of the small bubble size ($<$200 μm) that is comparable to small blood vessels. On the other hand, the interaction of lithotripter shock waves with larger cavitation bubbles ($>$1 mm) may be more suitable for tissue destruction, utilizing the strong bubble expansion and subsequent violent collapse of the bubbles.

[1] M. Delius, ''Medical applications and bioeffects of extracorporeal shock waves,'' Shock Waves **4**, 55–72 (1994).

[2] N. Weiss, M. Delius, S. Gambihler, P. Dirschell, A. Goetz, and W. Brendel, ''Influence of the shock wave application mode on the growth of *A*-Mel3 and SSK2 tumors *in vivo*,'' Ultrasound Med. Biol. **16**, 595 (1990).

[3] R. Schleberger and T. Senge, ''Non-invasive treatment of long-bone pseudarthrosis by shock waves (ESWL),'' Arch. Orthoped. Trauma Surg. **111**, 224 (1992).

[4] G. P. Dahmen, V. C. Nam, and L. Meiss, ''Extrakorporale Stosswellentherapie (ESWT) zur Behandlung von knochennahen Weichteilscheerzen: Indikatin, technik und vorlaugigo Ergenbisse,'' in *Stosswellenlithotripsie—Aspekte und Prognosen*, edited by C. Chaussy, F. Eisenberger, D. Jocham, and D. Wilbert (Attempto, Tubingen, 1993), pp. 143–148.

[5] F. Prat, J. Y. Chapelon, F. Abou El Fadil, A. Sibile, Y. Theilliere, T. Ponchon, and D. Cathignol, ''Focused liver ablation by cavitation in the rabbit: a potential new method of extracorporeal treatment,'' Gut **35**, 395–400 (1994).

[6] S. Gambihler, M. Delius, and J. W. Ellwart, ''Permeabilization of the plasma membrane of L1210 mouse leukemia cells using lithotripter shock waves,'' J. Membr. Biol. **141**, 267–275 (1994).

[7] M. Delius, P. Hofschneider, U. Lauer, and K. Messmer, ''Extracorporeal shock waves for gene therapy?,'' Lancet **354**, 1377 (1995).

[8] R. F. Randazzo, C. G. Chaussy, G. J. Fuchs, S. M. Bhuta, H. Lovrecovich, and J. B. deKernion, ''The *in vitro* and *in vivo* effects of extracorporeal shock waves on malignant cells,'' Urol. Res. **16**, 419 (1988).

[9] R. P. Holmes, L. I. Yeaman, W. J. Li, L. J. Hart, C. A. Wallen, R. D. Woodruff, and D. L. McCullough, ''The combined effects of shock waves and cisplatin therapy on rat prostate tumors,'' J. Urol. (Baltimore) **144**, 159 (1990).

[10] S. Hoshi, S. Orikasa, M. Kuwahara, K. Suzuki, S. Shirai, K. Yoshikawa, and M. Nose, ''Shock wave and THP-Adriamycin for treatment of rabbit's bladder cancer,'' Jpn. J. Cancer Res. **83**, 248 (1992).

[11] U. Lauer, E. Burgelt, Z. Squire, K. Messmer, P. H. Hofschneider, M. Gregor, and M. Delius, ''Shock wave permeabilization as a new gene transfer method,'' Gene Ther. **4**, 710–715 (1997).

[12] S. Bao, B. D. Thrall, R. A. Gies, and D. L. Miller, ''*In vivo* transfection of melanoma cells by lithotripter shock waves,'' Cancer Res. **58**, 219–221 (1998).

[13] M. Delius, ''Minimal static excess pressure minimises the effect of extracorporeal shock waves on cells and reduces it on gallstones,'' Ultrasound Med. Biol. **23**, 611–617 (1997).

[14] A. J. Coleman and J. E. Saunders, ''A survey of the acoustic output of commercial extracorporeal shock wave lithotripters,'' Ultrasound Med. Biol. **15**, 213–227 (1989).

[15] C. C. Church and L. A. Crum, ''A theoretical study of cavitation generated by four commercially available extracorporeal shock wave lithotripters,'' in *Frontiers of Nonlinear Acoustics: Proceedings of 12th ISNA*, edited by M. F. Mamilton and D. T. Blackstock (Elsevier, New York, 1990), pp. 433–438.

[16] C. C. Church, ''A theoretical study of cavitation generated by an extracorporeal shock wave lithotripter,'' J. Acoust. Soc. Am. **86**, 215–227 (1989).

[17] P. Zhong, I. Cioanta, F. H. Cocks, and G. M. Preminger, ''Inertial cavitation and associated acoustic emission produced during electrohydraulic shock wave lithotripsy,'' J. Acoust. Soc. Am. **101**, 2940–2950 (1997).

[18] A. Philipp, M. Delius, C. Scheffczyk, A. Vogel, and W. Lauterborn, ''Interaction of lithotripter-generated shock waves and air bubbles,'' J. Acoust. Soc. Am. **93**, 2496–2509 (1993).

[19] D. L. Miller and R. M. Thomas, ''Ultrasound contrast agents nucleate inertial cavitation *in vitro*,'' Ultrasound Med. Biol. **21**, 1059–1065 (1995).

[20] F. Prat, T. Ponchon, F. Berger, J. Y. Chapelon, P. Gagnon, and D. Cathignol, ''Hepatic lesions in the rabbit induced by acoustic cavitation,'' Gastroenterology **100**, 1345–1350 (1991).

[21] D. Dalecki, C. H. Raeman, S. Z. Child, D. P. Penney, R. Mayer, and E. L. Carstensen, ''The influence of contrast agents on hemorrhage produced by lithotripter fields,'' Ultrasound Med. Biol. **23**, 1435–1439 (1997).

[22] M. Delius, N. Weiss, S. Gambihler, A. Goetz, and W. Brendel, ''Tumor therapy with shock waves requires modified lithotripter shock waves,'' Naturwissenschaften **76**, 573 (1989).

[23] M. Schafer, ''Cost-effective shock wave hydrophones,'' J. Stone Disease **5**, 73–76 (1993).

[24] Sonic Industries™, ''Reference shockwave hydrophone system™— User's Manual,'' Version 1.2, Hatboro, PA, 1997.

[25] D. Howard and B. Sturtevant, ''*In vitro* study of the mechanical effects of shock-wave lithotripsy,'' Ultrasound Med. Biol. **23**, 1107–1122 (1997).

[26] T. Christopher, ''Modeling the Dornier HM3 lithotripter,'' J. Acoust. Soc. Am. **96**, 3088–3095 (1994).

[27] M. Mueller, ''Dornier-Lithotripter im Vergleich. Vermessung der Stoßellenfelder und Fragmentationswirkungen. (Comparison of Dornier lithotripters. Measurements of shock wave fields and fragmentation effectiveness),'' Biomed. Technik **35**, 250–262 (1990).

[28] M. Delius, F. Ueberle, and W. Eisenmenger, ''Extracorporeal shock waves act by shock wave–gas bubble interaction,'' Ultrasound Med. Biol. **24**, 1055–1059 (1998).

[29] A. J. Coleman, M. Whitlock, T. Leighton, and J. E. Saunders, ''The spatial distribution of cavitation induced acoustic emission, sonoluminescence and cell lysis in the field of a shock wave lithotripter,'' Phys. Med. Biol. **38**, 1545–1560 (1993).

[30] B. Sturtevant and V. A. Kulkarny, ''The focusing of weak shock waves,'' J. Fluid Mech. **73**, 651–671 (1976).

[31] J. K. Lee, J. D. Black, E. A. Repasky, R. T. Kubo, and R. B. Banbert, ''Activation induces a rapid reorganization of spectrin in lymphocytes,'' Cell **55**, 807–816 (1988).

[32] P. Zhong, I. Cioanta, S. L. Zhu, F. H. Cocks, and G. M. Preminger, ''Effects of tissue constraint on shock wave-induced bubble expansion *in vivo*,'' J. Acoust. Soc. Am. **104**, 3126–3129 (1998).

[33] M. Mueller, ''Experimental investigations on focusing of weak spherical shock waves in water by shallow ellipsoidal reflectors,'' Acustica **64**, 85–93 (1987).

[34] M. R. Bailey, ''Control of acoustic cavitation with application to lithotripsy,'' Ph.D. dissertation, Univ. of Texas at Austin, May 1997.

[35] M. T. Carnell, S. J. Barrington, and D. C. Emmony, ''A phase-inverting parabolic concentrator for the generation of negative waves in water,'' J. Acoust. Soc. Am. **102**, 2556–2560 (1997).

2009   J. Acoust. Soc. Am., Vol. 105, No. 3, March 1999

Zhong *et al.*: Shock wave–inertial microbubble interaction   2009

Effects of deafening on the calls and warble song of adult budgerigars (*Melopsittacus undulatus*)

James T. Heaton, Robert J. Dooling,[a] and Susan M. Farabaugh
Department of Psychology, University of Maryland, College Park, Maryland 20742-4411

Budgerigars are small Australian parrots that learn new vocalizations throughout adulthood. Earlier work has shown that an external acoustic model and auditory feedback are necessary for the development of normal contact calls in this species. Here, the role of auditory feedback in the maintenance of species-typical contact calls and warble song in adult budgerigars is documented. Deafened adult birds (five male, one female) vocalized less frequently and showed both suprasegmental and segmental changes in their contact calls and warble song. Contact calls of all adult-deafened budgerigars showed abnormalities in acoustic structure within days to a few weeks following surgery. Within 6 months of surgery, nearly all contact calls produced by deafened birds were strikingly abnormal, showing highly variable patterns of frequency modulation and duration. The warble song of deafened male budgerigars also differed significantly from that of normal budgerigars on several acoustic measures. These results show that auditory feedback is necessary for the maintenance of a normal, species-typical vocal repertoire in budgerigars. © *1999 Acoustical Society of America.* [S0001-4966(99)03702-9]

INTRODUCTION

It is well known that auditory feedback is critical for normal vocal development and vocal learning in young song-birds. Much less is known about the role of auditory feedback in the maintenance of normal vocal repertoires in adulthood. For the songbird species that have been investigated to date, deafening has a profound effect on the development of learned vocalizations (e.g., Brenowitz and Kroodsma, 1996; Konishi, 1965a, 1965b; Marler, 1991; Nottebohm, 1968), while deafening later in life often yields more complicated and sometimes more subtle effects. Some oscine songbirds such as white-crowned sparrows (*Zonotrichia leucophrys*) and chaffinches (*Fringilla coelebs*) can maintain their vocal repertoire for years if deafened in adulthood after song crystallization (Konishi, 1965a; Konishi and Nottebohm, 1969). The stability of song syntax and phonology in the absence of auditory feedback for these species may be related to the fact that they are closed-ended learners and normally do not change their song-syllable repertoires as adults. Consistent with this notion is the observation that canaries (*Serinus canaria*), who add and delete song notes seasonally throughout adulthood (open-ended learners), show signs of song disruption within a week of deafening, and profound deterioration within a month (Nottebohm *et al.*, 1976; Nottebohm, personal communication, 1997).

More recent experiments with Australian zebra finches (*Taeniopygia guttata*) and Bengalese finches (*Lonchura striata* var. *domestica*) have challenged the simple dichotomy that open-ended learners require auditory feedback for song maintenance and closed-ended learners do not. While both finches are closed-ended learners, zebra finches show signs of song disruption within 1–2 months of deafening, and profound deterioration in song over a period of sev-

eral months (Nordeen and Nordeen, 1992). Bengalese finches, on the other hand, show marked changes in song structure even within a few days of deafening, followed by deterioration of song phonology similar to that of zebra finches over a matter of months (Okanoya and Yamaguchi, 1997; Watanabe and Aoki, 1996; Wooley and Rubel, 1996). The difference in time course and pattern of vocal degradation between these two species may be related to differences in the flexibility of adulthood song structure (Okanoya and Yamaguchi, 1997). Although neither species normally changes its adult syllable repertoire, zebra finches produce song syllables in a highly stereotyped order, whereas Bengalese finches demonstrate plasticity in syllable ordering or syntax. This suggests that the dependence on auditory feedback for song maintenance in adulthood may be related not only to plasticity of segmental vocal features (e.g., the pitch, amplitude, and duration of syllables), but also to flexibility in suprasegmental features (e.g., the syntax and rate of syllables).

While the requirement for auditory feedback in the development and maintenance of vocal behavior is most conspicuous in humans and songbirds, deafening does affect vocal behavior to a lesser degree in a wide variety of animals. For instance, kittens deafened early in life produce louder calls than normal-hearing kittens even in adulthood (Romand and Ehret, 1984; Shipley *et al.*, 1988). Moreover, the calls of deafened kittens are abnormal in other ways including an elevation of fundamental frequency, an increase in low-frequency harmonics, and a delay in the acquisition of rapid frequency and amplitude modulations (Romand and Ehret, 1984; Shipley *et al.*, 1988). Deafening also has a small but demonstrable effect on both suprasegmental and segmental aspects of many species-typical vocal signals of nonpasserine birds that do not learn their vocalizations (Konishi, 1963; Nottebohm and Nottebohm, 1971).

There is remarkably little information on the effects of

[a]Author to whom correspondence should be addressed. Electronic mail: dooling@bss3.umd.edu

deafening on vocal output in adult animals that have acquired their species-specific adult repertoire. Studies in humans show that hearing-impaired children use high-pitched vocalizations and show abnormal variations in fundamental frequency and abnormal stress patterns (Martony, 1968; Monsen, 1978a, 1978b, 1979; Smith, 1975). It is also well established that the characteristics of vocal output disintegrate following profound hearing loss in postlingually deafened children (Binnie et al., 1982) and adults (Waldstein, 1990). Recent experiments show that the speech of cochlear-implant patients immediately undergoes specific changes when the implant is turned off (Tobey, 1993).

The present study investigated the effects of deafening on the maintenance of normal calls and songs in a small Australian parrot, the budgerigar (Melopsittacus undulatus). Budgerigars are well known for their vocal plasticity and for their ability to learn and imitate a wide variety of complex sounds throughout adulthood (see, for example, Dooling, 1986; Farabaugh et al., 1992; Farabaugh et al., 1994). Since vocal learning is believed to have evolved independently in psittacines and passerines (Nottebohm, 1972), it is of interest to know whether the effects of adult deafening in psittacines are similar to that observed in passerines. As far as we know, there have been no studies of the effects of adult deafening in parrots in spite of the fact that vocal learning appears to be widespread among psittacines (Farabaugh and Dooling, 1996).

Previous studies have shown that budgerigars deafened early in life, or reared in acoustic isolation, fail to develop normal contact calls (Dooling et al., 1987; Dooling et al. 1990). The present experiments extend the effect of deafening on the maintenance of learned contact calls and warble song to adult budgerigars. Given that adult parrots show exceptional plasticity in both segmental and suprasegmental vocal features, we expected that budgerigars would demonstrate a high degree of dependence on auditory feedback for the maintenance of normal calls and song.

I. METHODS

A. Subjects

The subjects deafened in these experiments were five adult male and one adult female budgerigars. Four additional adult budgerigars (two male, two female) were used in the behavioral observation experiments. In addition, warble song was analyzed for one adult male budgerigar which was deafened at three weeks of age (Dooling et al., 1987), one adult male budgerigar which was deafened at 9 days of age (Heaton and Brauth, 1996), and two adult male budgerigars which were isolated as nestlings (Farabaugh et al., 1992). These latter birds had been individually isolated from approximately 3 weeks to 8 months of age, but had been living in a large aviary with 50–100 other budgerigars for several months prior to vocal recording. All adult budgerigars had been in our possession for at least one year prior to experimentation; however, since many were purchased from commercial vendors, their exact ages were unknown. The birds were housed and fed in aviaries at the University of Maryland and kept on a normal photoperiod correlated with the

season. All procedures were conducted under the auspices of protocols approved by the campus Animal Care and Use Committee.

B. Deafening

The birds were deafened by bilateral extirpation of the cochlea using the procedures described by Konishi (1963) for deafening domestic fowl. Briefly, the deafening procedure involved first anesthetizing each subject with a mixture of ketamine hydrochloride (40 mg/kg, IM) and xylazine hydrochloride (10 mg/kg, IM). Next the tympanic membrane was excised, and the columella and columellar footplate were pulled from the vestibular window with a pair of curved forceps. Finally, using a fine-hooked tungsten wire, the entire basilar papilla and lagena were pulled from the bony labyrinth. The subject's ears were then filled with an antibacterial ointment (Neosporin), and it was given an intramuscular injection of the xylazine-reversing agent yohimbine hydrochloride (0.275 mg/kg; Heaton and Brauth, 1992; Kilander and Williams, 1992). The recovering bird was placed in a humidity- and temperature-controlled incubation chamber until it perched. It was then returned to the vivarium and periodically monitored for signs of discomfort and for complications arising from surgery. Subjects were killed 1–2 years after deafening for postmortem examination of each middle ear to confirm complete extirpation of the cochlea.

C. Recording

Samples of each bird's vocal repertoire were recorded both before and after surgery in a sound-attenuated chamber lined with acoustic foam wedges. The front and top of the chambers were made of clear acrylic (Plexiglas) so that we could elicit vocalizations from subjects by providing visual contact with their cagemates. Calls and song were recorded through an Electro-Voice (model PL50N/D) microphone connected to a Digitech digital-delay system (model RDS4000). Real-time output from the delay board was fed to a Uher Akustomat F411 sound-activated relay switch that turned on a Marantz PMD 221 cassette recorder. This apparatus allowed time-delayed output (1-s delay) of the bird's vocalization to reach the recorder after the tape was at full speed. Approximately 200 contact calls were collected during presurgical recording sessions for each bird. By contrast, birds typically vocalized less frequently after deafening, so some recording sessions lasted for days in order to acquire multiple contact calls. Warble song was particularly rare after deafening and was obtained from only two of the six deafened adult subjects. Warble song was recorded with either a Marantz PMD 221 cassette recorder or a Sony D7 digital-audiotape recorder.

D. Call analysis

Recorded contact calls were digitized with a Kay DSP 5500 sona-graph and stored as computer files (20 480 samples/s). Calls were then analyzed and compared using a commercial digital-signal-processing software package (SIGNAL, Engineering Design, Belmont, MA). A sample of 50 consecutive pre-surgical contact calls was digitized for each

subject. Each of the 50 calls recorded before deafening was compared to every other call in the sample (50 calls generated 1225 unique pairwise comparisons) with a spectrogram cross-correlation routine, generating a half matrix of correlation coefficients (similarity scores) ranging from 0 to 1 (Clark, Marler, and Beeman, 1987). Each half matrix of similarity scores for pre-surgical calls was then analyzed with multidimensional scaling (MDS) and average-linkage cluster analysis. Contact-call types (clusters) were identified by examination of both MDS plots and cluster results. The average pair-wise intercorrelations of calls in the call-type groupings that emerged from the cluster analysis were in all cases above 0.70. We then calculated the average similarity (i.e., mean intercorrelation) of each call to the other calls of the same type and ranked them based on these similarity scores. The five calls with the highest intercorrelation were taken as representative exemplars for that contact call type to compare with post-surgical calls, since, by definition, they had the highest average intercorrelation with all other calls of the same type (see Heaton *et al.*, 1995).

Calls recorded after deafening for each subject were compared to each other and to the five exemplar calls of each subject's pre-deafening call type(s) by spectrogram cross correlation. A post-deafening call was considered to be of a particular call type if the average similarity of that call to the five exemplars of any of the pre-surgical dominant types was greater than or equal to a criterion level of 0.65. This criterion level for assignment was intentionally chosen to be lower (by 0.05) than the average similarity of pre-deafening calls of each type to the five best exemplars. This more conservative criterion ensured that we would err on the side of including rather than excluding post-deafening calls that closely resembled a pre-deafening call type. The correlation matrices were then analyzed by MDS to produce a spatial map of the acoustic similarity among pre-surgical and post-surgical contact calls, and spectrograms of these digitized calls were produced with a Kay DSP 5500 sona-graph and a Raytheon TDU-850 gray-scale printer.

To objectively define the number of contact-call types and the average within-type call-similarity scores of normal adult budgerigars, 40 contact calls were digitized for each of five male and five female budgerigars and compared using spectrogram cross correlation. Calls examined for each subject were produced consecutively during either one or two recording sessions occurring no greater than 3 days apart, and recording sessions were conducted at various dates over a 2-year period. Call-similarity scores were analyzed for each subject with both MDS and cluster analysis in order to identify call-type groupings as described previously.

E. Warble song analysis

Budgerigar warble song consists of long sequences of both broadband and tonal syllables that are diverse in structure, ranging from simple clicks to multinote, frequency-modulated tonal syllables (Farabaugh *et al.*, 1992). These syllables are delivered at a variable tempo and variable loudness depending on a variety of social factors, presumably having to do with the animal's level of arousal and reproductive state. Males at some times deliver soft warble in a non-directed fashion while sitting alone on a perch, and at other times deliver much louder warble directed at female birds with great fervor during courtship bouts (Brockway, 1964, 1969; Farabaugh *et al.*, 1992; Nespor *et al.*, 1996). Because of the acoustic complexity of warble, the fact that many of the syllables are not stereotyped, and the high level of variation in temporal delivery, we analyzed the warble syllables reported here on four rather basic characteristics: peak frequency, bandwidth, duration, and the duration of interelement interval. We used these relatively straightforward measures to characterize the warble of six normal adult male budgerigars, and compare these results to the warble of adult birds isolated as juveniles ($n = 2$), deafened as nestlings ($n = 2$), or deafened as adults ($n = 2$) (see Sec. I A).

Recorded streams of warble song were digitized with a Kay DSP 5500 sona-graph and stored as computer files (20 480 samples/s). Measurements from 500 warble elements were made for each subject using a Kay Elemetrics DSP sonograph (model 5500). The dependent variables included peak frequency, 20-dB down bandwidth, interelement interval, and element duration. Settings for the sona-graph in the spectropgraphic analysis mode, were frequency range: 8 kHz, time axis: 1 s/screen, and analysis filter: 300 Hz. Two adjacent sounds greater than 10-ms duration were treated as part of the same syllable if the interval between them was less than 10 ms. For each of the four dependent variables, an average frequency-of-occurrence histogram was obtained for the six intact adult males. Histograms for each of the experimental birds were compared to average histograms of the normal adults using Kolmogorov–Smirnov (KS) tests.

F. Behavioral observations

Nine budgerigars (six males and three females) were housed together in a large cage (60 × 36 × 24 in.) and observed for the occurrence of behaviors which fell into five broad categories: inactive (e.g., sleeping, sitting quietly), maintenance (e.g., eating, preening), vocalizing, aggressive, and affiliative (e.g., nonaggressive interactions). Of these nine birds, four males had been deafened one year earlier. One male and one female budgerigar were observed both before and 1–3 weeks after deafening. Using a procedure of focal animal sampling, the experimenter observed the birds in daily 1/2-h sessions and recorded the total time a bird spent in each of several pre-defined behavioral categories. A total of two and one-half h of behavioral observations was conducted on each bird. Behavior was coded such that a subject was in one of the five categories at all times. Total time spent in each behavioral category was combined for the hearing males ($n = 2$), hearing females ($n = 2$), and deaf males ($n = 5$), and differences in group means were tested with t-tests. Mean times spent in each category measured before and after deafening for one male and one female subject were likewise compared with t-tests.
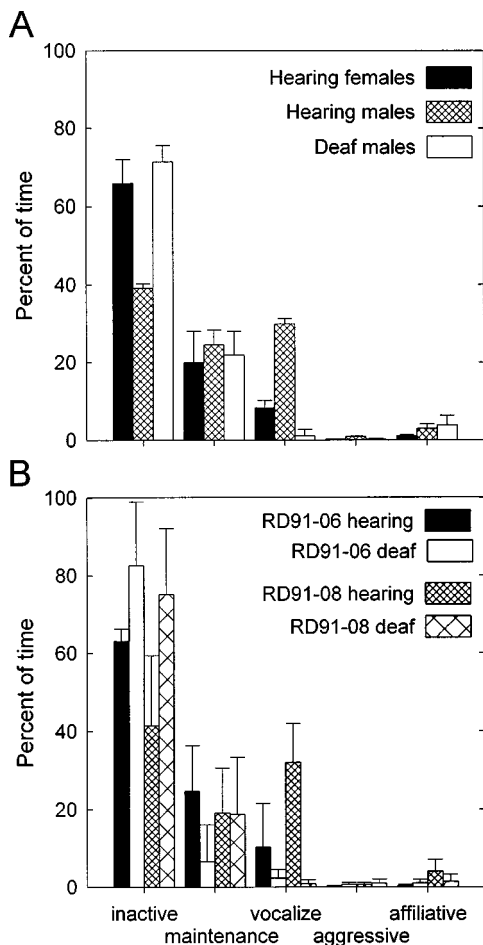
FIG. 1. Histograms (a) showing the percent of time spent in five behavioral categories for hearing females ($n=2$), hearing males ($n=5$), and deaf males ($n=5$), and (b) for a pair-bonded female (RD91-06) and male (RD91-08) budgerigar before and 1–3 weeks after deafening.

II. RESULTS

A. Behavioral observations

The percentage of time that hearing females ($n=2$), hearing males ($n=2$), and deaf males ($n=5$) spent in each of the five behavioral categories is shown in Fig. 1(a). Deafened males were less active than hearing males ($p<0.01$) and vocalized less frequently than hearing birds ($p<0.01$). Hearing females were less active than hearing males ($p<0.01$) but not significantly different from deaf males on this measure. Hearing females also vocalized less than hearing males ($p<0.01$) but vocalized more frequently than deaf males ($p<0.01$). The two birds observed both before and after deafening [Fig. 1(b)] showed similar, significant changes in their behavior in that they both became less active and less vocal after deafening ($p<0.01$).

B. Contact calls

Post-surgical audio-recording sessions were initiated for all six deafened adult budgerigars within 24 h after recovery from anesthesia. Birds were either temporarily housed in the recording chambers or placed there 4–10 h a day for the first 5–7 days after surgery. Recording sessions, each lasting 4–48 h were then conducted 1–2 times per week for 2

months, and then 1–2 times per month for a year. In spite of this fairly intensive recording schedule, two of the six budgerigars failed to produce a sufficient amount of warble song or contact calls to analyze, and thus they were dropped from further consideration. A somewhat intermediate response was observed in subject Red Three, who did not vocalize in the recording chambers for the first 8 weeks after surgery but did produce a sufficient number of calls thereafter. By contrast, numerous contact calls were obtained from the other three budgerigars during the first 1–2 weeks after deafening. Thus, in terms of the frequency of vocalizing, there was considerable variation in response to cochlear removal, from a near-total lack of calling to only a slight reduction in calling rate. The reduction in calling rate following deafening was both significant and unusual, since pre-surgical recording sessions for these and other birds typically yielded hundreds of calls within a matter of hours. These results were entirely consistent with the overall reduction of vocal behavior of deafened birds noted in our behavioral observation experiments.

Contact calls recorded during the first 2 months after surgery for subjects Red Four, Orange Nine, and RD91-08 showed a dramatic change in call stereotypy compared with pre-surgical calls. These changes were evident both by inspection of spectrograms and by quantitative analyses by MDS. MDS plots of spectrogram similarity scores for calls produced by two of these birds before deafening are shown in Fig. 2(a). Figure 2(b) shows spectrograms of five call exemplars from each call category (cluster) shown in Fig. 2(a). Of the three deafened birds that vocalized most frequently, subject Orange Nine showed relatively less initial vocal disruption, whereas contact calls from the other two birds, as well as the first calls recorded from subject Red Three at 2–6 months after deafening, showed little resemblance to their pre-surgical call patterns. To illustrate this difference in pre- versus post-surgical contact-call production between birds, MDS plots of spectrogram-similarity scores are compared in Fig. 3 for a bird from each pattern of disruption: Orange Nine (less initial, more gradual disruption) and Red Four (more rapid call disruption). Since each MDS plot is calculated independently from the others, the salient point across time periods is that calls produced after deafening are scattered and no (Red Four) or only a few (Orange Nine) post-deafening calls fall near the tight clusters of pre-deafening calls. Spectrograms of these aberrant calls for each bird are shown in Fig. 4.

Due to the variability in timing of successful post-surgical recording sessions, contact calls were grouped for analysis into three broad post-surgical time frames: 0–7 weeks, 2–9 months, and greater than 1 year. Although calls recorded in the first time frame were obtained over several recording sessions, sometimes separated by several weeks, there was no clear relationship (either between or within subjects) between time from surgery and degree of vocal disruption. This was based on both spectrogram cross-correlation analysis with pre-surgical exemplars (see Sec. I) and visual inspection of spectrograms. Across the three time periods after deafening, however, phonological changes were evident in the spectrograms of each subject's contact calls (shown in
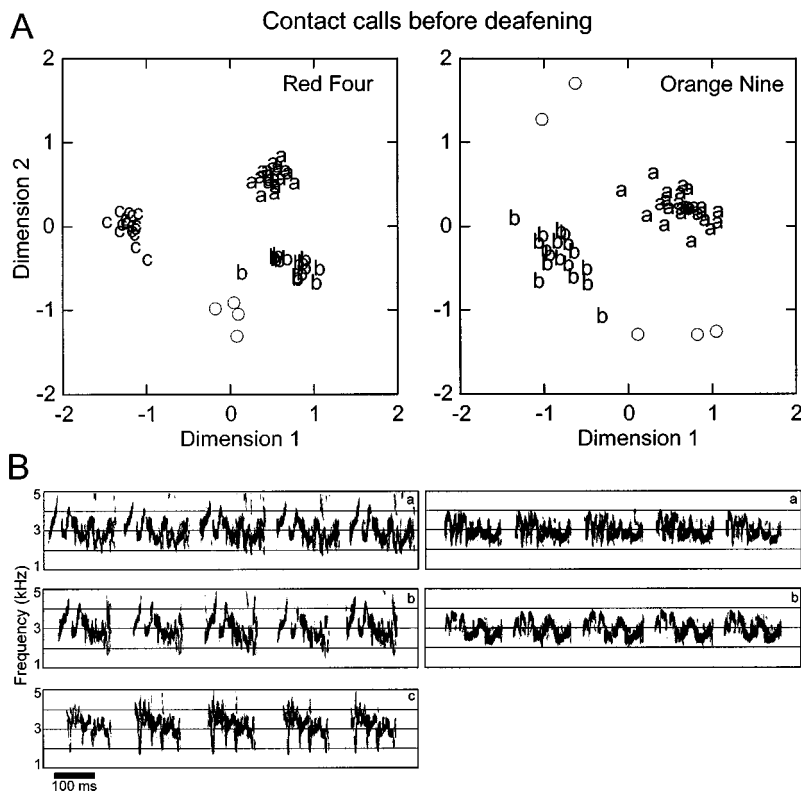
FIG. 2. Contact calls before deafening for subjects Red Four and Orange Nine. (a) MDS solutions depicting call similarity for 50 pre-deafening contact calls each from subjects Red Four and Orange Nine. Subject Red Four had three distinct call types (a), (b), and (c), with average similarities of 0.78 (± 0.02), 0.78 (± 0.04), and 0.82 (± 0.04), respectively. Subject Orange Nine had two call types (a) and (b), with average similarities of 0.77 (± 0.04) and 0.73 (± 0.06), respectively. Each bird had 4–5 calls which did not fall into a particular call type (open circles). (b) Spectrograms depict the five exemplar calls of each dominant call type. These calls had the highest average intercorrelation with all other calls of the same type.

Figs. 3 and 4). Along with a continued lack of stereotypy, contact calls from all four subjects showed a drop in frequency across the length of each call. Thus, spectrograms of these calls showed an overall downward-sweeping pattern even 1 year after deafening. This was evident not only in randomly selected post-surgical contact calls from subjects Orange Nine and Red Four, but also in the post-surgical calls from Orange Nine which were the most similar to his pre-surgical call patterns (Fig. 5).

Previous work has shown that both male and female adult budgerigars typically have one to several dominant contact-call types in their repertoires (Farabaugh *et al.*, 1994). The subjects in this experiment had four (Red Three), three (Red Four), two (Orange Nine), and one (RD91-08) dominant call types prior to deafening as determined by spectrogram cross-correlation values (see Sec. I). Only 2%–16% of the pre-deafening contact calls for these birds failed to fall into a particular call type (see, for example, open circles in Fig. 2). Within a year of deafening the reverse was true, with only 0%–6% of post-deafening contact calls for each bird meeting the criterion for inclusion into a pre-deafening call type. The few calls of deafened birds that did match a pre-surgical call type always matched the bird's most frequently produced call type prior to deafening.

The calls of these four subjects 1 year or longer after deafening were extremely variable, phonetically degraded, and typically bore little resemblance to the contact calls of intact birds. Although the calls of deafened birds showed the characteristic overall downward-sweeping pattern in frequency, they also continued to show variable patterns of frequency modulation. Consequently, new call types or clusters were not clearly identifiable either visually (by inspection of spectrograms) or quantitatively from post-surgical recording

sessions (see Fig. 3)—something which is unusual since budgerigars typically maintain highly stereotyped contact-call patterns even when learning new calls as adults (cf. Farabaugh *et al.*, 1994; Trillmich, 1976a, 1976b). For example, the contact-call repertoires of ten normal adult budgerigars contained an average of 2.4 call types (s.d.=1.07), and calls within each type had an average similarity of 0.74 (s.d. =0.076). Most notably, of the 40 calls examined for each normal subject, only 0%–17.5% ($x=7.75\%$, s.d.=5.71%) failed to fall within a call type, whereas 94%–100% of the deafened birds' calls failed to fall into call types 1–2 years after deafening. Figure 6 shows the percent of sampled calls that fell into call types both before and after deafening for all four subjects.

Calls produced by Orange Nine were initially less affected by deafening than were the calls of the other birds. Post-mortem examination of the bony labyrinths from all of the deafened subjects, with special attention paid to those of Orange Nine, showed that the basilar papillae of these birds had been completely extirpated during surgery.

C. Warble song

The warble song of adult subjects either deafened or isolated as juveniles, or deafened as adults, sounded abnormal to the human ear. The warble song of deafened subjects, in particular, sounded extremely monotonous, with relatively little variation in frequency and temporal patterning. Figure 7 shows brief streams of warble from two normal adult males, two birds deafened as adults, and one bird deafened at 3 weeks of age. As can be seen, the warble of deafened birds lacks the temporal and spectral complexity evident in the song of intact birds.
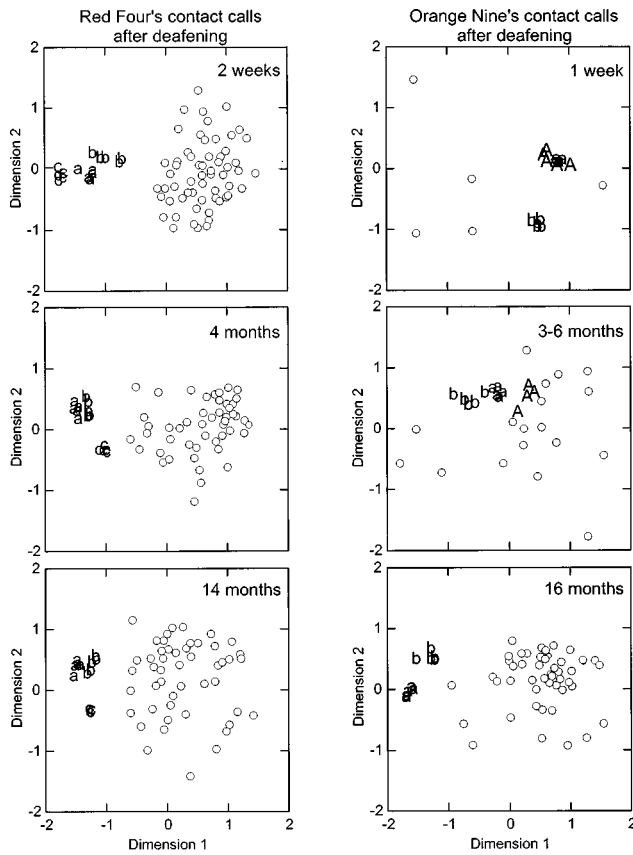
FIG. 3. MDS solutions for spectrogram cross-correlation scores of call similarity for post-deafening contact calls at three time points after deafening with the five exemplars from each pre-deafening call type for birds Red Four and Orange Nine (shown in Fig. 2). Lower-case letters indicate the exemplar calls themselves, upper-case letters indicate calls that met criterion for similarity to the exemplars, and open circles indicate calls that did not reach criterion for similarity to any of the pre-deafening call types. (Left) Red Four did not produce any calls which met the criterion for similarity to a pre-surgical call type. (Right) Five contact calls (top panel) recorded from Orange Nine during the first week after deafening met the criterion for similarity to call type (a) and five calls were not similar to the pre-deafening calls or to each other. Seven calls out of 22 recorded 3–6 months after deafening met the criterion for similarity to call type (a) and at 16 months no calls met criterion out of 49 calls measured from one recording session.

FIG. 5. Spectrograms of the five best type (a) contact calls from before deafening, and the five calls that were most similar to these calls during each of three time periods after deafening for subject Orange Nine, who showed the most gradual deterioration. At 2 days after deafening the calls still looked very similar to pre-deafening (a) calls. Four months after deafening, this bird's calls were beginning to show change from the pre-deafening. By 16 months after deafening the calls retained little of the original spectral characters of the pre-deafening type (a) calls and also began to show an overall drop in frequency of the call.

Warble-song elements were analyzed along four basic characteristics: peak frequency, bandwidth, duration, and duration of interelement interval. The average frequency distributions of warble-element values were compared for experimental-versus-control subject groups using multiple KS tests (see Table I). Comparisons with the frequency distributions from control birds were made individually for the two subjects deafened as adults, since warble-element parameters were differentially affected for these two birds (see Sec. III). Values for the pairs of subjects in the other experimental conditions were grouped for comparisons with control birds, since deafening or isolation affected these birds similarly. Warble-element parameters which differed signifi-
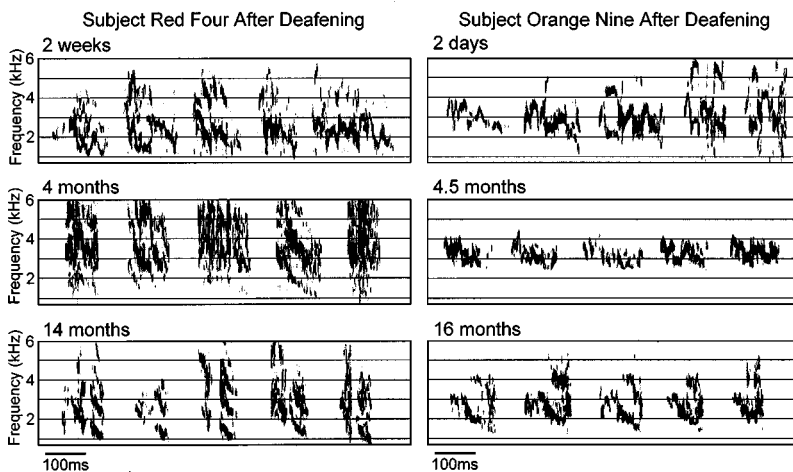
FIG. 4. Spectrograms of randomly selected calls from birds Red Four (left) and Orange Nine (right) at the three post-deafening time periods described in Fig. 3.
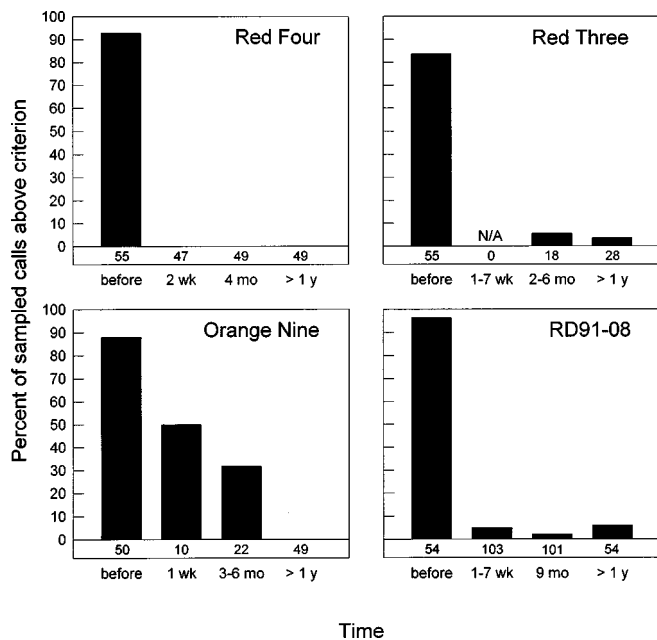
FIG. 6. Histograms of the percentage of sampled contact calls which met criterion for inclusion in a predeafening call type for four subjects. The number of calls analyzed for each time period is given below the histogram bar.

cantly from controls ($p<0.05$) are presented in bold text in Table I.

As an example, the average frequency distributions for two adult subjects deafened as juveniles are compared with the values from six normal control subjects in Fig. 8. In this example, warble element-value distributions for the deafened birds appeared notably different from those of normal subjects on three of the four element characteristics, which was consistent with the statistical findings of the KS tests. The two subjects deafened as juveniles showed the greatest disruption of warble-song features compared to birds deafened as adults or isolated as juveniles.

III. DISCUSSION

Budgerigars can learn new contact calls throughout adulthood. At any given time a bird may produce one to several dominant call types, and birds caged together in the laboratory typically come to share call patterns within a matter of weeks (Dooling, 1986; Farabaugh *et al.*, 1994). Despite this proclivity for vocal learning in adulthood, dominant call types remain highly stereotyped over time and are produced with considerable precision even as new call types are learned (Farabaugh *et al.*, 1994; Trillmich, 1976a, 1976b). In this study, we show that the maintenance of normal contact-call and warble-song repertoires in budgerigars is dependent on auditory feedback.

Adult budgerigars deafened by cochlear removal exhibited dramatic instability in contact-call frequency-modulated patterns. In some birds, these changes were evident in the calls recorded even a few days after deafening and were noticeable in all birds a few months after deafening. The calls of deafened budgerigars were abnormal by spectro-
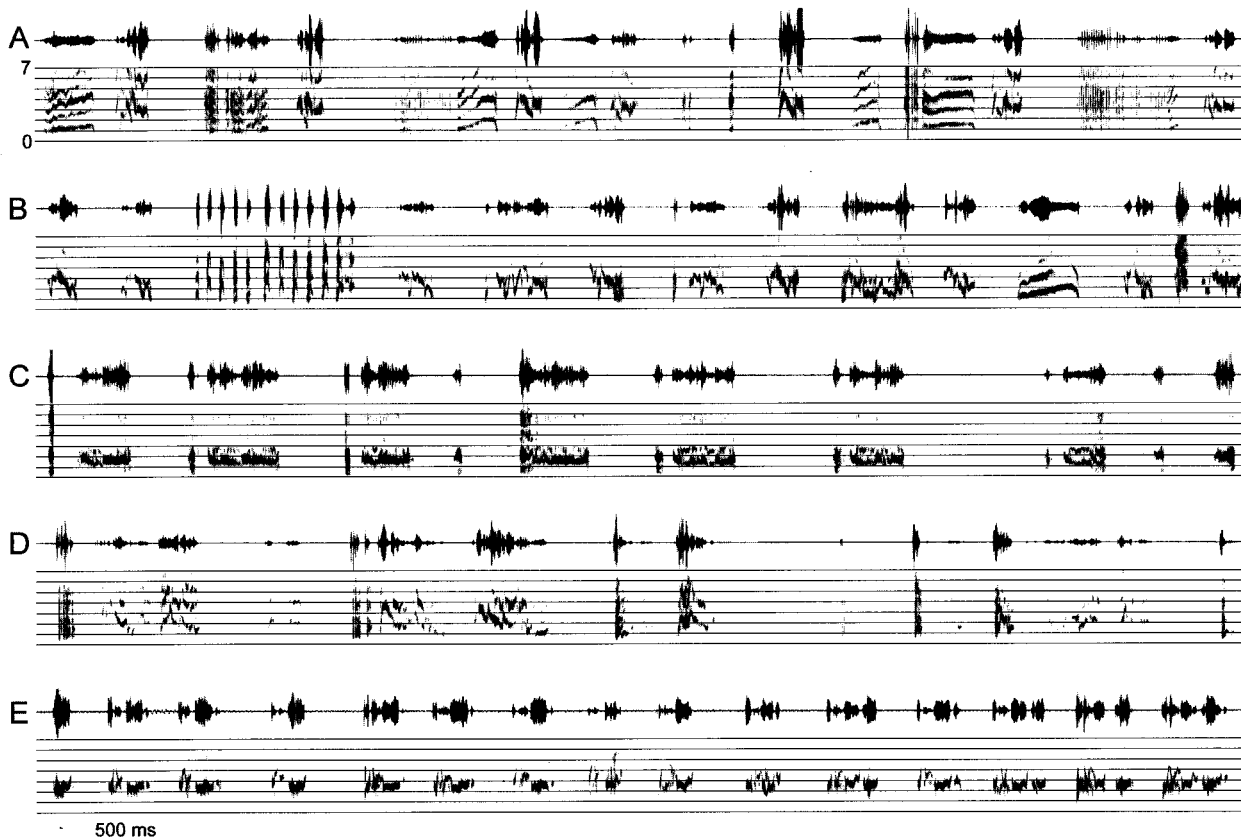
FIG. 7. Streams of warble from two normal adult males (A and B), two birds deafened as adults (C and D), and one bird deafened at 3 weeks of age (E).

TABLE I. Kolmogorov–Smirnov nonparametric two-sided probability tests of warble-element distributions. Probability values indicating statistical significance are shown in bold.

Subjects and condition	Disrupted element parameters	Bandwidth	Peak frequency	Element duration	Interval duration
Deafened as nestlings					
95-48 and Q-DJ	3/4	**0.001**	**0.001**	**0.034**	0.130
Deafened in adulthood					
Orange	2/4	**0.001**	**0.001**	0.228	0.564
RD91-08	1/4	0.604	0.260	**0.016**	0.373
Isolated as nestlings					
ISO-1 and ISO-2	2/4	**0.001**	**0.044**	0.373	0.937

graphic inspection and by objective, quantitative methods. Calls of deafened budgerigars did not resemble pre-surgical call exemplars and showed high variability from rendition to rendition. Long-term changes in the patterns of frequency modulation included a decrease in tonal quality and an increase in bandwidth, even in calls for subject Orange Nine who showed less initial disruption in contact-call repertoire. This pattern of results resembles the long-term effects of deafening on song production in adult Bengalese finches, zebra finches, and canaries (Okanoya and Yamaguchi, 1997; Nordeen and Nordeen, 1992; Nottebohm *et al.*, 1976, respectively). Moreover, two of the three budgerigars recorded within 2 months of deafening showed a dramatic increase in call variety (e.g., loss of identifiable call types), which is similar to the effects on contact-call production demonstrated by budgerigars sustaining a profound but temporary auditory-threshold shift from acoustic overexposure or ototoxic drugs (Dooling, Manabe, and Ryals, 1996; Dooling, Ryals, and Manabe, 1997).

A. Species differences in the role of auditory feedback in adulthood

As far as we know, the effects of deafening on call structure in adult budgerigars have not been described in songbirds, where the focus has been more on song. While comparing the effect of deafening on *call* production in budgerigars with *song* production in songbirds is tenuous, the present results suggest that the effects of deafening on call production in budgerigars differ from the effect of deafening on song production in songbirds both in its time course and in the immediate increase in variety of frequency-modulated patterns.

Closed-ended song learners with stable song syntax in adulthood such as white-crowned sparrows (Konishi, 1965a), chaffinches (Konishi and Nottebohm, 1969), and zebra finches (Nordeen and Nordeen, 1992; Price, 1979) seem to suffer few initial effects of deafening, and sometimes few long-term effects. Open-ended or seasonal vocal learners such as canaries, in addition to traditional closed-ended learners that have variable song syntax as adults such as Bengalese finches (Okanoya and Yamaguchi, 1997), demonstrate marked changes in suprasegmental song features (e.g., syntax) within days of deafening, and phonetic deterioration over weeks and months. Canaries seem particularly vulnerable to vocal disruption from deafening, not only demonstrating changes in song structure within 1 week, but also suffering prominent spectral changes of syllables within a month. Within a year of deafening, an adult canary will *eventually* come to sing like deafened juveniles that never had access to their own auditory feedback (Marler *et al.*,

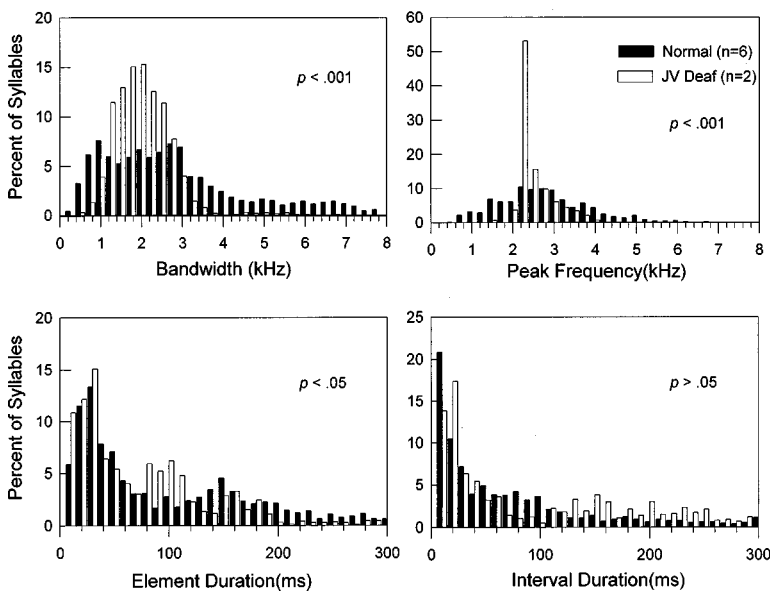FIG. 8. The average frequency distributions for warble-element bandwidth, peak frequency, duration, and the duration of interelement interval for six normal-hearing budgerigars are compared with those of two adult budgerigars deafened within the first 3 weeks of life. The warble song of these deaf subjects significantly differed from normal control subjects on three of the four warble-element characteristics (see the ''p'' values).

1973; Nottebohm *et al.*, 1976). Thus, the relative importance of auditory feedback in maintaining learned vocalizations may be tied to the nature and degree of plasticity in vocal production throughout life. Adult flexibility and versatility in either song structure or song-syllable phonology may carry with it a necessary dependence on auditory feedback. Moreover, maintaining flexibility in both may require the most auditory supervision of vocal output. The results reported here are consistent with this hypothesis, since adult budgerigars have exceptional plasticity in both segmental and suprasegmental vocal features, and show dependence on auditory feedback of both of these aspects of normal species-typical calls and song.

B. Parallels with human speech and deafness

It is common knowledge that postlingually deaf humans exhibit distortions in all classes of speech sounds, with the degree of impairment in speech somewhat dependent upon the age at onset of deafness (Waldstein, 1990). In general, the same appears to hold true for birds that learn their vocalizations, including our budgerigars. The effects of deafening and isolation on warble song in budgerigars include both segmental and suprasegmental effects, with the degree of impairment related to the age of deafening. Budgerigars isolated from conspecifics beginning several weeks after hatching show abnormal vocal repertoires as adults (Dooling *et al.*, 1990). Here and elsewhere (Brittan Powell *et al.*, 1997; Dooling *et al.*, 1987), we show that budgerigars deafened early in vocal development generally produce more abnormal calls and warble than those deafened as adults, as is sometimes the case for normal adult song in songbirds. Chaffinches, for instance, deafened earlier in song development produce more abnormal vocalizations than those deafened later in development (Nottebohm, 1968).

In humans, the exact role of auditory feedback after the acquisition of adult speech and language is surprisingly unclear. Certain experimental conditions such as delayed auditory feedback (Fairbanks, 1955) and the introduction of loud background noise cause immediate and significant changes in speech output such as stuttering and the Lombard effect (for a review, see Lane and Tranel, 1971). This suggests that auditory feedback plays an important role in the moment-to-moment guidance of the motor gestures resulting in speech. However, because it can be demonstrated that much of auditory feedback is processed after the speech gestures it is supposed to correct, others argue that auditory feedback serves more as a calibrator for other sensory feedback such as proprioception (Borden, 1979; Cowie and Douglas-Cowie, 1983). Most likely, auditory feedback is used for both ongoing speech production and for comparing phonetic output with phonemic intention for parametric control of future speech movements (Lane and Webster, 1991; Perkell *et al.*, 1992).

One compelling argument for auditory feedback serving as a calibrator for other feedback mechanisms is the common observation that the speech of postlingually deafened adults systematically deteriorates but is not completely eliminated. It is interesting in this regard that while all four adult-deafened budgerigars in our sample showed extensive deterioration of their contact calls with time, two of the birds

showed an immediate and dramatic increase in the number of different contact-call patterns they produced—an effect not usually reported in the literature on human hearing loss. We also know from recent work that budgerigars show a strong Lombard effect (Manabe, Sadr, and Dooling, 1998). These results taken together are most consistent with the idea that auditory feedback plays an active, primary role in guiding contact-call production in budgerigars and that when these birds vocalize, they are matching (through auditory feedback) a stored auditory memory (template) of their contact call.

Finally, to extend the parallels between the effects of deafening in budgerigars with what is known in humans, we examined behavioral measures of social interaction in budgerigars before and after deafening. It is well known that acquired deafness in humans often is accompanied by a host of psychological problems including social withdrawal, depression, and interpersonal anxiety (Darbyshire, 1984; Stein and Bienenfield, 1992; Weinstein and Ventry, 1982). Behavioral observations in budgerigars following deafening also point to broad effects, including an increase in the amount of time spent alone and a decrease in the amount of time spent vocalizing. This significant reduction in vocal production was evident in the infrequent post-surgical recordings of calls and song, particularly in the two birds which had to be excluded from further acoustic analysis of vocalizations. The decrease in social interaction of deafened birds is a complex issue, likely relating to multiple factors. It is unlikely to be due solely to the deaf bird's abnormal vocal repertoire. We know from other work that budgerigars sustaining profound disruption in call structure after syringeal denervation show little effect on their social interactions with intact birds (Shea *et al.*, 1997) and are able to attract and maintain breeding mates and raise young (personal observation).

IV. CONCLUSIONS

The notion of possible parallels between speech and language in humans and vocal behavior in birds is not new (Marler, 1970). Taken together, the present results extend some of these parallels to a psittacine species. The present results also reveal some differences between the role of auditory feedback in the maintenance of human speech and language, and the maintenance of learned avian vocalizations in a highly plastic avian species, the budgerigar. Future investigations of vocal production in budgerigars might use delayed auditory feedback, high levels of background noise, or temporary threshold shift to further extend the parallels between auditory feedback and call production in these birds and the production of speech in humans.

Binnie, C. A., Daniloff, R. G., and Buckingham, H. W. (**1982**). ''Phonetic disintegration in a five year old following sudden hearing loss,'' J. Speech Hear. Disorders **47**, 181–189.

Borden, G. (**1979**). ''An interpretation of research on feedback interruption during speech,'' Brain Lang. **7**, 301–319.

Brenowitz, E. A., and Kroodsma, D. E. (**1996**). ''The neuroethology of birdsong,'' in *Ecology and Evolution of Acoustic Communication in Birds*, edited by D. E. Kroodsma and E. H. Miller (Cornell U.P., Ithaca), pp. 285–304.

Brittan-Powell, E. F., Dooling, R. J., and Farabaugh, S. M. (**1997**). ''Vocal development in budgerigars (*Melopsittacus undulatus*): Contact calls,'' J. Comp. Psych. **111**, 226–241.

Brockway, B. F. (**1964**). ''Ethological studies of the budgerigar (*Melopsittacus undulatus*): Reproductive behavior,'' Behaviour **23**, 294–324.

Brockway, B. F. (**1969**). ''Roles of budgerigar vocalization in the integration of breeding behavior,'' in *Bird Vocalizations*, edited by R. A. Hinde (Cambridge U.P., London), pp. 131–158.

Clark, C. W., Marler, P., and Beeman, K. (**1987**). ''Quantitative analysis of animal vocal phonology: An application to swamp sparrow song,'' Ethology **76**, 101–115.

Cowie, R., and Douglas-Cowie, E. (**1983**). ''Speech production in profound postlingual deafness,'' in *Hearing Science and Hearing Disorders*, edited by M. Lutman and M. Haggard (Academic, New York), pp. 183–231.

Darbyshire, J. O. (**1984**). ''The hearing loss epidemic: A challenge to gerontology,'' Res. Aging **6**, 384–394.

Dooling, R. J. (**1986**). ''Perception of vocal signals by budgerigars (*Melopsittacus undulatus*),'' Exp. Biol. **45**, 195–218.

Dooling, R. J., Gephart, B. F., Price, P. H., McHale, C., and Brauth, S. E. (**1987**). ''Effects of deafening on the contact call of the budgerigar (*Melopsittacus undulatus*),'' Anim. Behav. **35**, 1264–1266.

Dooling, R. J., Manabe, K., and Ryals, B. M. (**1996**). ''Effect of masking and hearing loss on vocal production and vocal learning in budgerigars,'' Assoc. Res. Otolaryngol. Abst. **19**, 581.

Dooling, R. J., Park, T. J., Brown, S. D., and Okanoya, K. (**1990**). ''Perception of species-specific vocalizations by isolate-reared budgerigars (*Melopsittacus undulatus*), '' Int. J. Comp. Psych. **4**, 57–78.

Dooling, R. J., Ryals, B. M., and Manabe, K. (**1997**). ''Recovery of hearing and vocal behavior after hair cell regeneration,'' Proc. Natl. Acad. Sci. USA **94**, 14206–14210.

Fairbanks, G. (**1955**). ''Selected vocal effects of delayed auditory feedback on the pitch of vocal productions,'' J. Speech Hear. Res. **20**, 333–345.

Farabaugh, S. M., Brown, E. D., and Dooling, R. J. (**1992**). ''Analysis of warble song of the budgerigar *Melopsittacus undulatus*,'' Bioacoustics **4**, 111–130.

Farabaugh, S. M., and Dooling, R. J. (**1996**). ''Acoustic communication in parrots: Laboratory and field studies of budgerigars, *Melopsittacus undulatus*,'' *Ecology and Evolution of Acoustic Communication in Birds*, edited by D. E. Kroodsma and E. H. Miller (Cornell U.P., Ithaca, NY), pp. 97–117.

Farabaugh, S. M., Linzenbold, A., and Dooling, R. J. (**1994**). ''Vocal plasticity in budgerigars (*Melopsittacus undulatus*): Evidence for social factors in the learning of contact calls,'' J. Comp. Psych. **108**, 81–92.

Heaton, J. T., and Brauth, S. E. (**1992**). ''The effects of yohimbine as a reversing agent for ketamine–xylazine anesthesia in the budgerigar,'' Lab. Anim. Sci. **42**, 54–56.

Heaton, J. T., and Brauth, S. E. (**1996**). ''Effects of vocal archistriatal lesions and early deafening on vocal development in the budgerigar,'' Soc. Neurosci. Abst. **22**, 694.

Heaton, J. T., Farabaugh, S. M., and Brauth, S. E. (**1995**). ''Effect of syringeal denervation in the budgerigar (*Melopsittacus undulatus*): The role of the syrinx in call production,'' Neurobio. Learn. Mem. **64**, 68–82.

Kilander, K., and Williams, H. (**1992**). ''Yohimbine reduces neuropathology induced by ketamine/xylazine anesthesia,'' Physiol. Behav. **51**, 657–659.

Konishi, M. (**1963**). ''The role of auditory feedback in the vocal behavior of the domestic fowl,'' Z. Tierpsychol. **20**, 349–367.

Konishi, M. (**1965a**). ''The role of auditory feedback in the control of vocalization in the white-crowned sparrow,'' Z. Tierpsychol. **22**, 770–783.

Konishi, M. (**1965b**). ''Effects of deafening on song development in American robins and blackheaded grosbeaks,'' Z. Tierpsychol. **22**, 584–599.

Konishi, M., and Nottebohm, F. (**1969**). ''Experimental studies in the ontogeny of avian vocalizations,'' edited by R. A. Hinde *Bird Vocalizations*, (Cambridge U.P., Cambridge), pp 29–60.

Lane, H., and Tranel, B. (**1971**). ''The Lombard Sign and the role of hearing in speech,'' J. Speech Hear. Res. **14**, 677–709.

Lane, H., and Webster, J. W. (**1991**). ''Speech deterioration in postlingually deafened adults,'' J. Acoust. Soc. Am. **89**, 859–866.

Manabe, K., Sadr, E. I., and Dooling, R. J. (**1998**). ''Control of vocal intensity in budgerigars (*Melopsittacus undulatus*): Differential reinforcement of vocal intensity and the Lombard Effect,'' J. Acoust. Soc. Am. **103**, 1190–1198.

Marler, P. (**1970**). ''Birdsong and human speech: Could there be parallels,'' Am. Sci. **58**, 669–674.

Marler, P. (**1991**). ''Song-learning behavior: The interface with neuroethology,'' Trends Neurosci. **14**, 199–206.

Marler, P., Konishi, M., Lutjen, A., and Waser, M. S. (**1973**). ''Effects of continuous noise on avian hearing and vocal development,'' Proc. Natl. Acad. Sci. USA **70**, 1393–1396.

Martony, J. (**1968**). ''On the correction of the voice pitch level for the severely hard of hearing subjects,'' Am. Ann. Deaf. **113**, 195–202.

Monsen, R. B. (**1978a**). ''Toward measuring how well hearing-impaired children speak,'' J. Speech Hear. Res. **21**, 197–219.

Monsen, R. B. (**1978b**). ''Acoustic qualities of phonation in young hearing-impaired children,'' J. Speech Hear. Res. **22**, 270–288.

Monsen, R. B. (**1979**). ''The production of labial occlusives in young hearing-impaired children,'' Lang. Speech **22**, 311–317.

Nespor, A. A., Lukazewicz, M. J., Dooling, R. J., and Ball, G. F. (**1996**). ''Testosterone induction of male-like vocalizations in female budgerigars (*Melopsittacus undulatus*),'' Hormones and Behavior **30**, 162–169.

Nordeen, K. W., and Nordeen, E. J. (**1992**). ''Auditory feedback is necessary for the maintenance of stereotyped song in adult zebra finches,'' Behav. Neur. Bio. **57**, 58–66.

Nottebohm, F. (**1968**). ''Auditory experience and song development in the chaffinch (*Fringilla coelebs*),'' Science **110**, 549–568.

Nottebohm, F. (**1972**). ''The origins of vocal learning,'' Anim. Behav. **106**, 116–140.

Nottebohm, F. (**1997**). Personal communication.

Nottebohm, F., and Nottebohm, M. E. (**1971**). ''Vocalizations and breeding behaviour of surgically deafened ring doves (*Streptopelia risoria*),'' Anim. Behav. **19**, 313–327.

Nottebohm, F., Stokes, T. M., and Leonard, C. M. (**1976**). ''Central control of song in the canary (*Serinus canaria*),'' J. Comp. Neurol. **165**, 457–486.

Okanoya, K., and Yamaguchi, A. (**1977**). ''Adult Bengalese finches (*Lonchura striata var. domestica*) require real-time auditory feedback to produce normal song syntax,'' J. Neurobiol. **33**, 343–356.

Perkell, J., Lane, H., Svirsky, M., and Webster, J. (**1992**). ''Speech of cochlear implant patients: A longitudinal study of vowel production,'' J. Acoust. Soc. Am. **91**, 2961–2978.

Price, P. H. (**1979**). ''Development determinants of song structure in zebra finch song,'' J. Comp. Physiol. Psychol. **93**, 260–277.

Romand, R., and Ehret, G. (**1984**). ''Development of sound production in normal, isolated and deafened kittens during the first postnatal months,'' Dev. Psychobio. **17**, 629–649.

Shea, S. D., Heaton, K. J., Heaton, J. T., Hall, W. S., and Brauth, S. E. (**1997**). ''The role of contact calls in social behavior of the budgerigar,'' Ann. (N.Y.) Acad. Sci. **807**, 571–573.

Shipley, C., Buchwald, J. S., and Carterette, E. C. (**1988**). ''The role of auditory feedback in the vocalizations of cats,'' Exp. Brain Res. **69**, 431–438.

Smith, C. R. (**1975**). ''Residual hearing and speech production in deaf children,'' J. Speech Hear. Res. **18**, 795–811.

Stein, L. M., and Bienenfeld, D. (**1992**). ''Hearing impairment and its impact on elderly patients with cognitive, behavioral, or psychiatric disorders: A literature review,'' J. Ger. Psych. **25**, 145–156.

Tobey, E. A. (**1993**). ''Speech Production,'' in *Cochlear Implants: Audiology Foundations*, edited by R. S. Tyler (Singular, San Diego), pp. 257–316.

Trillmich, F. (**1976a**). ''Spatial proximity and mate-specific behavior in a flock of budgerigars (*Melopsittacus undulatus*; Aves, Psittacidae),'' Z. Tierpsychol. **41**, 307–331.

Trillmich, F. (**1976b**). ''Learning experiments on individual recognition in budgerigars (*Melopsittacus undulatus*),'' Z. Tierpsychol. **41**, 372–395.

Waldstein, R. S. (**1990**). ''Effects of postlingual deafness on speech production: Implications for the role of auditory feedback,'' J. Acoust. Soc. Am. **88**, 2099–2114.

Watanabe, A., and Aoki, K. (**1996**). ''The role of auditory feedback on song behavior in adult male Bengalese finches,'' Zool. Sci. **13**, S59.

Weinstein, B. E., and Ventry, I. M. (**1982**). ''Hearing impairment and social isolation in the elderly,'' J. Speech Hear. Res. **25**, 593–599.

Wooley, S. M. N., and Rubel, E. W. (**1996**). ''Bengalese finches depend upon auditory feedback for maintenance of stable adult song,'' Soc. Neurosci. Abst. **22**, 693.

Modeling the role of nonhuman vocal membranes in phonation

Patrick Mergell[a)]
*Department of Phoniatrics and Pedaudiology, University Erlangen-Nuremberg, Bohlenplatz 21,
D-91054 Erlangen, Germany*

W. Tecumseh Fitch[b)]
*Harvard/MIT Speech and Hearing Sciences, Room 1036 William James Hall, 33 Kirkland Street,
Cambridge, Massachusetts 02138*

Hanspeter Herzel[c)]
Institute for Theoretical Biology, Humboldt University Berlin, Invalidenstr. 43, D-10115, Berlin, Germany

Although the mammalian larynx exhibits little structural variation compared to sound-producing organs in other taxa (birds or insects), there are some morphological features which could lead to significant differences in acoustic functioning, such as air sacs and vocal membranes. The vocal membrane (or ''vocal lip'') is a thin upward extension of the vocal fold that is present in many bat and primate species. The vocal membrane was modeled as an additional geometrical element in a two-mass model of the larynx. It was found that vocal membranes of an optimal angle and length can substantially lower the subglottal pressure at which phonation is supported, thus increasing vocal efficiency, and that this effect is most pronounced at high frequencies. The implications of this finding are discussed for animals such as bats and primates which are able to produce loud, high-pitched calls. Modeling efforts such as this provide guidance for future empirical investigations of vocal membrane structure and function, can provide insight into the mechanisms of animal communication, and could potentially lead to better understanding of human clinical disorders such as sulcus vocalis. © *1999 Acoustical Society of America.* [S0001-4966(99)03602-4]

PACS numbers: 43.80.Ka, 43.70.Aj, 43.64.Bt [FD]

INTRODUCTION

In contrast to the sound-producing organs in other taxa (e.g., insects or birds), the mammalian larynx has a conservative evolutionary history, and shows little qualitative variation from species to species (Negus, 1949; Harrison, 1995; Schön-Ybarra, 1995; Fitch and Hauser, 1995). The gross anatomy (cartilages, muscles, nerve supply) and physiological function of the mammalian larynx appear to be highly constrained by the necessities of airway protection and respiratory function. Despite this, there are a number of interesting differences among mammals in laryngeal anatomy, and the precise effects of such differences on the acoustic output of the larynx remain unknown. For example, the histological fine structure of the vocal folds, particularly the number and distribution of tissue layers, varies from species to species in ways that may have an effect on the vibratory behavior of the fold (Kurita *et al.*, 1983; Hirano, 1991). In nonhuman mammals, two gross morphological features are particularly prominent: air sacs and vocal membranes. A variety of air sacs is seen in a diverse array of mammals; they can be paired or unpaired, large or small, and sub- or supra-glottal (Negus, 1949, gives a review). The precise acoustic function of air sacs is currently unknown (reviewed in Schön-Ybarra, 1995; Gautier, 1971; Fitch and Hauser, 1995).

In this study we focus on the vocal membranes, which are thin upward extensions of the membranous portion of the vocal folds (see Fig. 1). They are variously referred to as ''vocal membranes'' in bats (Griffin, 1958; Griffiths, 1978; Suthers, 1988; Suthers and Fattu, 1973), ''sharp-edged vocal folds'' (Hill, 1957; Hill and Booth, 1957; Hast, 1989), or ''vocal lips'' in primates (Schön-Ybarra, 1995; Brown and Cannito, 1995; Fitch and Hauser, 1995). Here we adopt the term vocal membrane because it is most descriptive, and because vocal lip has an unrelated anatomical meaning in human laryngeal anatomy (Thomas, 1989). They are formed of connective tissue and lack muscle fibers, and can be as thin as a few microns across in bats (Suthers and Fattu, 1973; Suthers, 1988). They are found in many microchiropteran bats and a variety of primate species, including most New World (platyrrhine) monkeys, some Old World (catarrhine) monkeys, including some common laboratory species, and in our closest primate relatives, the apes (Griffin, 1958; Schön-Ybarra, 1995; Starck and Schneider, 1960). We are not aware of a taxonomic review of vocal membranes for all mammals, but they are found in members of the genus *Felis* (the smaller members of the cat family; Hast, 1989), and we have observed them in both llamas and young pigs (W. T. Fitch, personal observation).

Both bat and primate-vocal membranes have been postulated to serve as independent low-mass oscillators (e.g., Griffin, 1958; Griffiths, 1978; Schön-Ybarra, 1995; Fitch and Hauser, 1995), and thus to support the extremely high-

---
[a)]Electronic mail: mergell@phoni.med.uni-erlangen.de
[b)]Electronic mail: tec@wjh.harvard.edu
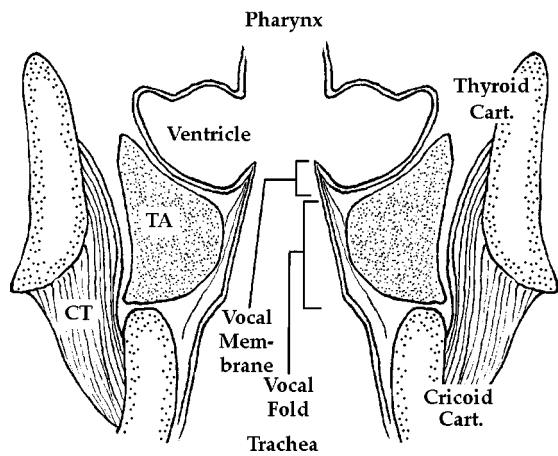[c)]Electronic mail: h.herzel@biologie.hu-berlin.de

FIG. 1. Schematic coronal section through middle of larynx showing anatomy of the vocal membrane. The membrane projects upward (rostrally) from main body of vocal fold. CT: Cricothyroid muscle. TA: Thyroarytenoid (''vocalis'') muscle.

frequency (sometimes ultrasonic) calls found in many primate species and most echolocating bats. In primates, the vocal lips have been suggested to underlie vibration at multiple frequencies, or biphonation (Kelemen, 1949, 1969; Schön-Ybarra, 1995; Brown and Cannito, 1995). It has been suggested that the nonhuman primate larynx has a broader range but less control of fundamental frequency than the human larynx (Lieberman, 1968; Pressman and Kelemen, 1969), and that this constraint has led to a different pattern of evolution in primate communication (Schön-Ybarra, 1995). However, detailed investigations of the properties and functions of the vocal membranes are lacking, and at present these suggestions remain speculative.

In addition to providing information relevant to animal communication, investigations of the vocal membrane have potential clinical significance. The addition of masses (tumors, polyps, nodules) and/or additional surfaces or flaps (sulcus vocalis, Reinke's edema) to the vocal folds represent common disorders in the voice clinic. A better understanding of the acoustic manifestations of such features could pave the way for enhanced voice diagnostics based on the acoustic signal. Detailed theoretical and experimental investigations of the vocal membranes could prove extremely useful for such an endeavor (especially since the range of possible experimental manipulations is much greater in animals than in human subjects).

I. POSSIBLE FUNCTIONS OF THE VOCAL MEMBRANES

A number of hypotheses have been advanced as to the function of the vocal membranes. Many researchers have suggested that the stiff, lightweight membranes could vibrate relatively independently from the rest of the vocal fold, and thus result in the production of extremely high-frequency calls, thus giving a wider pitch range (Griffin, 1958; Starck and Schneider, 1960; Schön-Ybarra, 1995; Fitch and Hauser, 1995). We will refer to this as the ''increased pitch range'' hypothesis.

Another suggestion is that the vocal membranes could result in greater vocal efficiency: the ''increased efficiency''

hypothesis. For example, Schön-Ybarra (1995) suggested that the decreased damping that presumably accompanies vocal membranes could result in a decrease in phonation-threshold pressure. Phonation threshold pressure P_s^{th} is an extremely useful parameter for measuring phonatory efficiency. It is defined as the minimum pressure required for self-sustained vocal-fold oscillations. Model calculations by Titze (1988) and Lucero (1993, 1995, 1996) revealed an inverse proportionality between subglottal-threshold pressure and the vertical depth of the vocal folds. Thus, one can expect that vertical extensions of the vocal folds lower the phonation threshold, which is equivalent to an increased phonatory efficiency.

Within the framework of nonlinear dynamics, the phonation threshold can be considered as a supercritical Hopf bifurcation: a sudden change of vocal-fold dynamics from a fixed point (damped oscillation) to a limit-cycle attractor (sustained oscillation) at a critical subglottal pressure. Once the threshold-pressure value is surpassed, the oscillation amplitude increases monotonically with pressure. Hence, lower phonation-threshold pressures typically result in higher oscillation amplitudes for a given lung pressure (Mergell et al., 1998).

A final possible effect of the vocal membranes would be the production of subharmonic or chaotic vibration. Recent research suggests that many broadband, complex acoustic signals produced by animals result from chaotic dynamics in the vocal production mechanism (Wilden et al., 1998). Such dynamics could result from coupling between various oscillatory components within the source, e.g., interactions between the right and left vocal folds, between upper and lower portions of the same fold, or between the air column in the vocal tract and the tissue of the vocal fold, and from turbulence generated at constrictions in the vocal tract. The ''chaos hypothesis'' holds that one function of the vocal membranes is to support the production of broadband chaotic signals via increased oscillatory coupling. The production of ''noisy'' signals is held to be intimidating and could be useful in agonistic contexts (Morton, 1977). Alternatively, broadband sounds can provide an accurate outline of the vocal-tract transfer function of the caller, which in turn could carry information about body size, oral configuration, or other features (Fitch, 1997).

II. MODEL

The model explored here is a modification of the original two-mass model by Ishizaka and Flanagan (1972). In this model, the vocal folds are represented by damped mass-spring pairs forming a rectangular-shaped glottal valve. Steinecke and Herzel (1995) simplified this model in order to focus on the basic dynamical features of the larynx: vocal-tract resonances, viscous losses, and nonlinear restoring forces are neglected in this first approximation. For the calculation of the driving aerodynamical force, laminar flow exists below the narrowest constriction in the glottis and a jet separates above that point, giving a pressure drop to atmospheric pressure (gauged to zero pressure). Although more complex models which simulate the precise physiology of

the vocal folds have been created (Titze and Talkin, 1979; Alipour-Haghighi and Titze, 1985), they are computationally expensive, and recent analyses (e.g., Berry *et al.*, 1994) suggest that normal vocal-fold vibration is dominated by the first two low-vibrational modes anyway. These two basic vibration modes are the in-phase and out-of-phase oscillation in the vertical (caudal–cranial) direction; their superposition corresponds to 98% of the variance of all excited vibrational modes found in a highly complex and realistic three-dimensional continuum model (Berry *et al.*, 1994). This suggests that simple low-dimensional models are appropriate for exploratory investigations like ours.

Guided by the anatomical model proposed by Hirano (1974), which subdivides the vocal-fold tissue into a muscle and ligament ''body'' and a mucosal ''cover,'' a variety of representations of the vocal membrane could be chosen. The membrane could move independently of the upper mass, or vary its angle of attachment dynamically. Obviously, modeling the vocal membrane as a third low-mass, high-tension oscillator would allow the production of arbitrarily high frequencies; calculations to this effect are given in Griffin (1958). Unfortunately, the critical data on which to base these calculations (the tension on the membranes and the stress–strain relationships within the vocal membrane) are currently unavailable. In the present study, our goal was to build the simplest model which would have some physiological validity, be compatible with anatomical knowledge and still be likely to give appreciable effects, without speculating beyond the available (basically geometric) data. Thus, to the basic two-mass model we added the simplest geometric representation of a vocal membrane: an upward extension of the upper mass, attached to that mass at a fixed angle.

Specifically, we modified the two-mass model of Steinecke and Herzel (1995) by adding a massless rigid reed connected to the upper mass with an angle θ. The vertical depth of the vocal membranes is given by d_3. Figure 2(a) shows a 3D representation of this model, and Fig. 2(b) gives the corresponding frontal section. The horizontal (dorsal–ventral) length and the vertical depth of the masses are given by l, d_1, and d_2, respectively. During vocalization, the areas at the level of the lower-mass pair a_1, upper-mass pair a_2, and at the glottal outlet a_{vl} limited by the upper edges of the vocal membranes vary, and interact with aerodynamical forces. The glottal rest areas $a_{0i}=2lx_{0i}$, where the x_{0i} define the distances of the masses to the glottal symmetry plane prior to oscillation onset [the index (i) distinguishes the lower $(i=1)$ and upper $(i=2)$ mass pairs]. Besides the parameters introduced above, the set of parameters comprises masses m_i, stiffness coefficients k_i and c_i, damping coefficients r_i, a coupling stiffness k_c, the air density ρ at body temperature, and the subglottal pressure P_s generated by the respiratory system. Since the current model is intended as a general model of the vocal membranes in any species, we did not attempt to scale the model dimensions or parameters to those of (for example) a bat or chimpanzee. Instead, we simply used the ''standard parameter set'' listed in Table I. (All units are expressed in cm, g, ms, and respective combinations). These parameters were originally developed for the human larynx and have been extensively tested. Although it

(a)

(b)
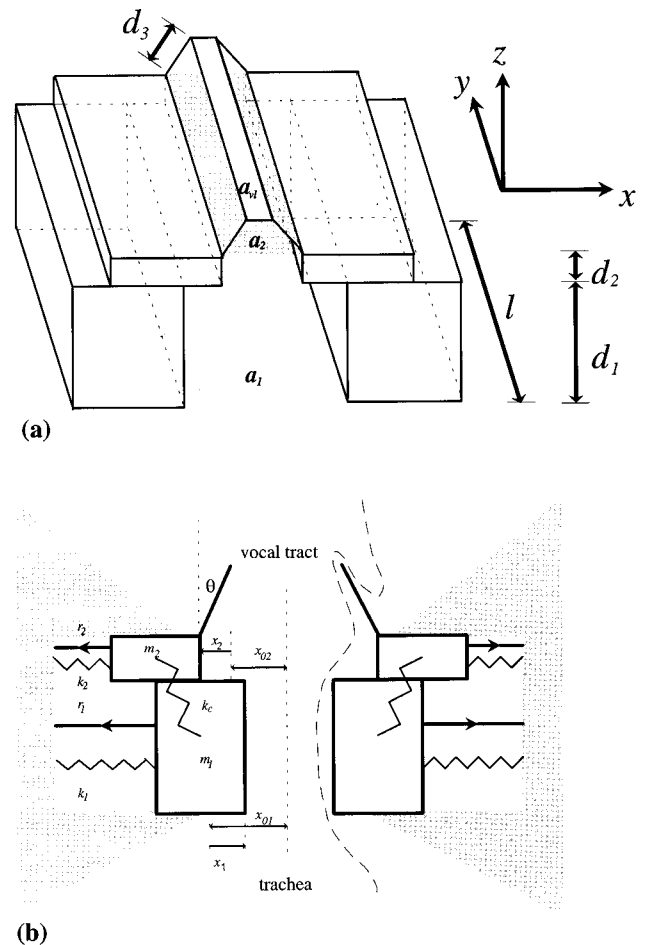
FIG. 2. (a) 3D representation of the two-mass model with vocal membranes. (b) Frontal section of the model. For further explanantions, see the text.

would clearly be more appropriate to use values for an organism which has vocal membranes, few if any of the required parameters are available for such species. Thus, it seems safer at present to use parameter values whose effects on phonation are well understood, and whose validity has been subjected to extensive empirical tests. One practical effect of this decision is that the oscillation frequencies observed in this study will not go into the ultrasonic range (as would be the case if we specifically modeled the much smaller vocal folds of bats or small rodents).

TABLE I. Standard parameters of the employed model.

m_1	m_2	k_1	k_2	k_c	r_1	r_2	c_1
0.125	0.025	0.08	0.008	0.025	0.02	0.02	$3k_1$
c_2	a_{01}	a_{02}	d_1	d_2	l	ρ	P_s
$3k_2$	0.05	0.05	0.25	0.05	1.4	0.001 13	0.008

Using matrix notation, the motion of the masses can be written as follows:

$$\frac{d}{dt}\begin{pmatrix} x_1 \\ v_1 \\ x_2 \\ v_2 \end{pmatrix} = \begin{vmatrix} 0 & 1 & 0 & 0 \\ -\dfrac{k_1+k_c}{m_1} & -\dfrac{r_1}{m_1} & \dfrac{k_c}{m_1} & 0 \\ 0 & 0 & 0 & 1 \\ \dfrac{k_c}{m_2} & 0 & -\dfrac{k_2+k_c}{m_2} & -\dfrac{r_2}{m_2} \end{vmatrix}$$

$$\times \begin{pmatrix} x_1 \\ v_1 \\ x_2 \\ v_2 \end{pmatrix} + \begin{pmatrix} 0 \\ I_1(x_1)+F_1(x_1,x_2) \\ 0 \\ I_2(x_2)+F_2(x_1,x_2) \end{pmatrix}. \quad (1)$$

This is a system of four coupled ordinary differential equations. The coordinates x_i are the oscillation amplitudes of the masses and v_i are the corresponding velocities. The rightmost term of Eq. (1) contains the nonlinearities, i.e., the driving forces and the vocal-fold contact terms given by

$$I_i(x_i) = -\Theta(-a_i)\frac{c_i}{m_i}\frac{a_i}{2l}, \quad (2)$$

where $\Theta(x)=1$ for $x>0$ and $\Theta(x)=0$ for $x\le 0$. At vocal-fold collision ($a_i\le 0$), an additional restoring force controlled by the stiffness coefficients c_i becomes active via the Θ-step function.

We must consider nine different glottal configurations (see Fig. 3) to deduce the aerodynamic forces. We assume jet separation at the minimum glottal cross section, and laminar airflow obeying the Bernoulli law below that point (Story and Titze, 1995; Steinecke and Herzel, 1995). According to Bernoulli's law, total pressure, which is equal to static pressure plus the kinetic energy density, is invariant along a streamline for steady, inviscid flow. Above the jet-separation point, the static pressure drops to zero (atmospheric pressure) and the hydrodynamic energy is carried completely by the airflow. Thus, above the separation point, we write

$$P_s = P(z) + \frac{\rho}{2}\left(\frac{U}{a(z)}\right)^2 = \frac{\rho}{2}\left(\frac{U}{a_{\min}}\right)^2, \quad (3)$$
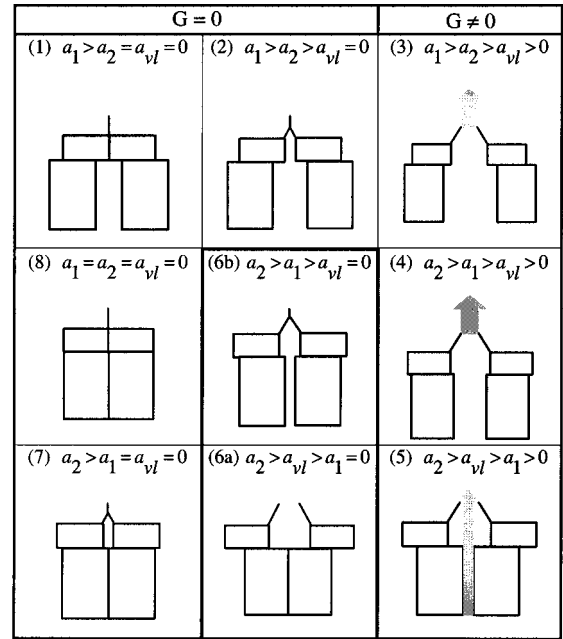
FIG. 3. Glottal configurations during one oscillation cycle. A typical cycle corresponds to clock-wise succession in this diagram: (1) $a_1>0\ge a_2\ge a_{vl}$ → (2) $a_1>a_2>0\ge a_{vl}$ → (3) $a_1>a_2>a_{vl}>0$ → (4) $a_2>a_1>a_{vl}>0$ → (5) $a_2>a_{vl}>a_1>0$ → (6a) $a_2>a_{vl}>0\ge a_1$ or (6b) $a_2>a_1>0\ge a_{vl}$ → (7) $a_2>0\ge a_1\ge a_{vl}$ → (8) $0\ge a_1\ge a_2\ge a_{vl}$. The first two columns show configurations with closed glottis and zero air flow ($U=0$). The jet is indicated by a gray arrow ($U>0$).

where $P(z)$ is the static pressure, U is the airflow, $a(z)$ corresponds to the z-dependent glottal area, and $a_{\min}=\min(a_1,a_2,a_{vl})$. The driving force is a direct consequence of the static pressure

$$dF(z) = P(z)l\,dz, \quad (4)$$

where ldz is an infinitesimally small segment of the inner vocal-fold surface. Integration over the inner-surface portions yields the acrodynamic-force terms considering the corresponding glottal configurations,

$$F_1(x_1,x_2) = \begin{cases} \dfrac{ld_1 P_s}{m_1}, & [1,2,6b]. \\[4mm] \dfrac{ld_1 P_s}{m_1}\left[1-\left(\dfrac{a_{vl}}{a_1}\right)^2\right], & [3,4]. \\[4mm] 0, & [5,6a,7,8]. \end{cases}$$

$$\quad (5)$$

$$F_2(x_1,x_2) = \begin{cases} \dfrac{P_s}{m_2}\left(ld_2+\dfrac{1}{2}a_2\cot\theta\right), & [2,6b]. \\[4mm] \dfrac{ld_2 P_s}{m_2}\left[1+\dfrac{d_3}{d_2}\cos\theta-\left(\dfrac{a_{vm}}{a_2}\right)^2\left(1+\dfrac{a_2}{2\tan\theta ld_2}\left\{\dfrac{1}{1-\dfrac{2ld_3\sin\theta}{a_2}}-1\right\}\right)\right], & [3,4,5]. \\[4mm] 0, & [1,6a,7,8], \end{cases}$$

Mergell *et al.*: Role of nonhuman vocal membranes in phonation

FIG. 4. Hopf bifurcation diagram showing the dependence of the subglottal-threshold pressure P_s^{th} on the vocal membrame overhang $d_3 \sin \theta$. Around $d_3 \sin \theta = 0.0019$ cm, the phonation-threshold pressure exhibits a minimum indicating an optimal membrane geometry ($d_3 \cos \theta = 0.1$ cm, $P_s = 8$ cm H_2O).

FIG. 5. Frequency-dependent Hopf bifurcation of the two-mass model with (filled squares) and without (circles) vocal membranes. The curves separate the graph plane into phonation and aphonia region. Considering a constant lung pressure P_s, the frequency range of the extended model is clearly increased relative to the range of the unmodified model ($d_3 = 0.1$ cm, $\theta \approx 1.8°$).

taking into account that at collision, the respective aerodynamic driving force drops to zero (Fig. 3, cases [1,6a,7,8]). In the limit $d_3 \rightarrow 0$ (not a straightforward limit case), Eq. (5) reduces to
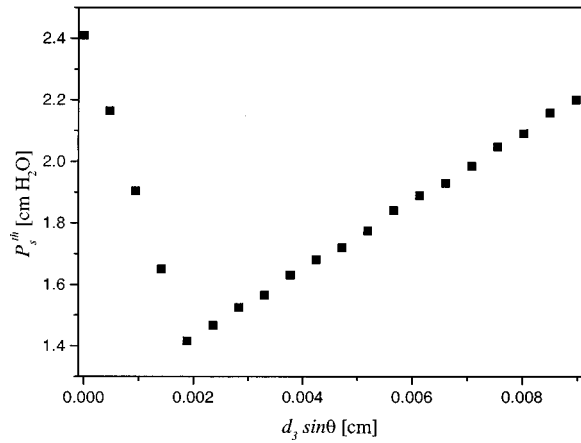
$$F_1 = l d_1 P_s \left[1 - \left(\frac{U}{a_{min}} \right)^2 \Theta(a_{min}) \right] \Theta(a_1),$$
$$F_2 = 0, \quad a_{vl} = a_2, \tag{6}$$

which corresponds to the force equations in the two-mass model without vocal membranes (Steinecke and Herzel, 1995). Thus, the vocal membranes couple the aerodynamic force directly to the upper-mass pair, whereas in the two-mass model without vocal membranes, the upper masses are driven only indirectly via mechanical coupling to the lower masses.

We explored the dynamic behavior of this model using discrete-time numerical integration of the differential equations described above (using Runge–Kutta). To present the results, we make use of the phonation-threshold concept described above, so we observe the changes in phonation threshold that depend upon variation in some other variable, such as frequency or the angle of the vocal membranes. In nonlinear dynamical terms, these threshold plots are formally identical to bifurcation diagrams. To vary frequency, we used a parameter q to scale the natural frequencies of the model masses $f_i^{nat} = q f_i^{nat}$, where $f_i^{nat} = \sqrt{k_i/m_i}$ are the natural frequencies for standard parameters given in Table I (see Mergell and Herzel, 1997).

III. RESULTS

First, we address the increased efficiency hypothesis. Varying the parameters d_3 and θ, we found that the overhang $d_3 \sin \theta$ is the crucial measure controlling the phonatory effect of the vocal membrane. At fixed vertical projection of the vocal membranes, i.e., $d_3 \cos \theta = 0.1$ cm, we analyzed the behavior of the threshold pressure when changing the overhang (Fig. 4). The resulting dependence of the threshold

pressure on the overhang indicates that there is an optimal membrane geometry: at $d_3 \sin \theta \approx 0.0019$ cm, the threshold curve exhibits a minimum ($d_3 \approx 0.1$ cm, $\theta \approx 1.8°$). These results indicate that for any set of parameters, there will be an optimum angle of attachment for the membranes. In general, this angle will be very small so the optimum orientation of the membranes will be nearly vertical. Hence, the increased vertical dimension does not solely explain the increased phonatory efficiency. It must be adjusted to the inclination angle of the vertical extensions or vice versa. The precise optimum value of θ will depend on a number of other parameters (e.g., actual fold dimensions, natural frequencies of the masses, etc.) which show considerable biological variation. Lacking data to precisely specify these parameters for a given nonhuman species, we will focus on qualitative results, fixing the length and angle of theta to values which seem anatomically reasonable based upon cross-sections of primate larynges (see Fig. 1).

Figure 5 plots phonation-threshold pressure vs natural frequency with and without vocal membranes. These curves separate the $q - P_s^{th}$-plane into phonation and nonphonating regions for the respective model configurations. The upper boundary of the phonation region is determined by the maximum pressure which can be produced by the respiratory muscles. Assuming a frequency-independent maximum pressure, the maximum achievable frequency is determined by the intersection of the threshold curve with this constant upper boundary. This plot thus defines a total frequency range. In clinical practice, similar voice-range profile diagrams are very useful diagnostics of vocal functioning (Wendler et al., 1996).

At low fundamental frequencies, the effect of the vocal membranes on the threshold pressure is moderate, while at high frequencies, the increase in the phonation region is pronounced. Figure 5 shows that the vocal membrane effects an overall decreased threshold pressure in the investigated frequency range. Assuming constant lung pressure P_s, we find that the intersection point with the threshold curve of the

FIG. 6. Energy-balance diagram of the two-mass model with (dotted line) and without (solid line) vocal membranes for $q=3$, $P_s=8$ cm H_2O, $d_3=0.1$ cm, and $\theta=1.8°$. The area enclosed by the F_1-x_1 curve which corresponds to the energy pumped into the lower mass duri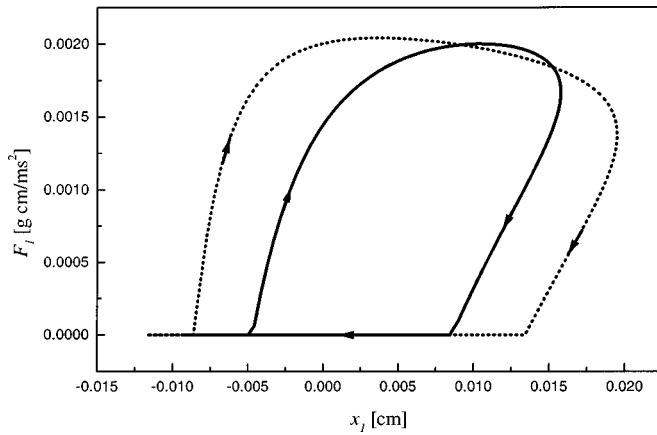ng one glottal cycle is increased with addition of vocal membranes. Due to a higher glottal efficiency, the oscillation amplitudes are increased.

model with vocal membrane occurs at a much higher frequency than is the case for the model without the extension. Consequently, the phonation region, and the pitch range, are increased by the vocal membranes. Thus, the related increased pitch range and the increased efficiency hypotheses are both supported by the results of these simulations.

To better illustrate the effects of the vocal membranes on phonation efficiency, Fig. 6 shows how much energy E_1^{in} is pumped from the airflow into one of the lower masses during one glottal cycle. It corresponds to the area which is enclosed by the force-amplitude curve (solid line: model without vocal membranes; dotted line: model with vocal membranes).

$$E_i^{in} = \oint F_i \, dx_i = \int_0^T F_i v_i \, dt, \tag{7}$$

where T is the duration of the oscillation period and the index i again distinguishes the lower ($i=1$) and upper ($i=2$) mass pairs. Equation (7) helps to understand the condition which has to be fulfilled for sustained phonation (see also Titze, 1988). Assuming a time-invariant force, it is clear that $E_i^{in}=0$ because the velocity v_i oscillates in time and thus contributes to the integration with a positive sign in the same amount as with a negative sign. Consequently, oscillation cannot be supported by a static driving force. A dynamic driving force with an opposite sign compared to the velocity v_1 results in a negative integral: the oscillator is damped by the external force. Clearly, the condition for sustained phonation is a positive integral which can only be obtained with a time-varying driving force which agrees in sign with the oscillator velocity. The optimal situation for phonation is given when the driving force is large during glottal opening (pushing the masses apart) and small (or negative) during closing (not resisting inward movement) (Stevens, 1977).

Since the oscillation amplitude reaches a saturation value after phonation onset, an energy equilibrium is obtained, i.e., all energy pumped into the masses is dissipated. The dissipated energy reads

$$E_i^{out} = r_i \oint v_i \, dx_i = r_i \int_0^T v_i^2 \, dt, \tag{8}$$

where the energy-equilibrium relation can be written as

$$\sum_i E_i^{in} + E_i^{out} = 0, \tag{9}$$

The lung is considered to be the energy source providing

$$E_s = P_s \int_0^T U \, dt = P_s V, \tag{10}$$

where V is the air volume leaving the lung during one glottal cycle. We can now define the glottal efficiency η

$$\eta = 2 \frac{E_1^{in} + E_2^{in}}{E_s}, \tag{11}$$

which is the ratio between the energy pumped into the system and the compression work which is done by the respiration muscles (the factor 2 takes into account that energy is transferred into mass pairs). For the parameters $q=3.0$, $\theta=1.8°$, $d_3=0.1$ cm, and $P_s=8$ cm H_2O, we find in the model with vocal membranes an efficiency $\eta_{vm}=2.82\%$, which is double that of the unmodified model $\eta=1.36\%$. Since the area surrounded by the dotted curve in Fig. 6 is enlarged due to higher peak amplitudes, we can conclude that higher efficiency and an amplitude increase are closely related.

Finally, in order to test the chaos hypothesis, we explored the effects of asymmetries of geometrical and tissue properties on the model, with and without vocal membranes. In our model, the tissue properties of the membranes are simulated with the upper-model masses, whereas the geometrical aspects have been realized by adding the extensions of vertical dimension d_3. Thus, for the upper-left (l) and the upper-right (r) model mass, we used the relations

$$m_{2l}=m_2/q_2, \quad m_{2r}=m_2, \quad k_{2l}=q_2k_2, \quad k_{2r}=k_2, \tag{12}$$

where $q_2=0.2$ is an asymmetry factor changing mass and stiffness coefficients of the left-upper mass. The upper graph of Fig. 7 shows a spectrogram of the glottal flow created by running the model with the pressure curve shown in the lower graph of Fig. 7. At $P_s=13$ cm H_2O, period doubling appears, followed by a cascade of subharmonic-oscillation patterns with increasing subglottal pressure. In contrast, the model version without vocal membranes but with identical asymmetry coefficient q_2 shows regular oscillation in the investigated pressure range (see the middle graph of Fig. 7).

IV. DISCUSSION

The most significant finding of these simulations is that a very simple change in the geometry of the vocal fold can produce major differences in the dynamics of phonation. Several conclusions can be drawn regarding the implications of our model for phonation dynamics in animals which possess vocal membranes. We will focus here on echolocating bats, but similar arguments apply for nonhuman primates and other mammals. In a night of foraging, insectivorous bats spend a considerable amount of energy producing the ultra-
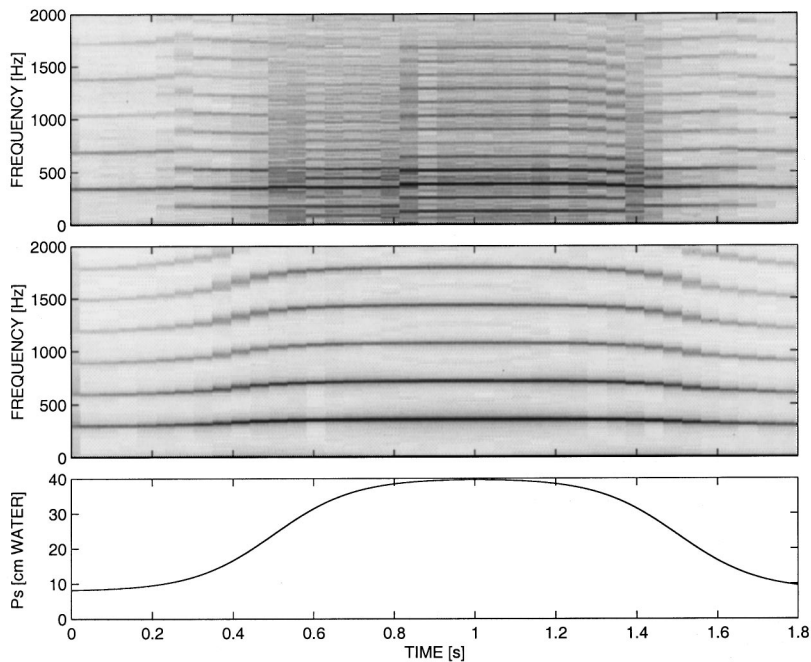
FIG. 7. In the spectrogram of an airflow simulation with asymmetric properties of the upper-mass pair including vocal membranes (upper graph), a cascade of bifurcations sets in at 0.2 s. Increasing subglottal pressure leads to various subharmonic-phonation patterns ($q_2=0.2$, $d_3=0.1$ cm, and $\theta=1.8°$). In contrast, the same conditions in the model without vocal membranes do not produce irregularities, as can be seen in the middle graph. The lower graph shows the pressure variation during the simulations.

sonic pulses which subserve echolocation (Suthers and Fattu, 1973; Hartley and Suthers, 1988). The frequency of the echolocation pulses determines the spatial discrimination of the biosonar system, while pulse intensity controls the range within which the animal can detect its insect prey or other targets (Griffin, 1958; Suthers and Fattu, 1973; Suthers, 1988). Thus, there is a powerful selective pressure for the bat to produce very loud, very high-pitched sounds. For example, *Pteronotus parnellii* produces pulses with a 30-kHz fundamental and most energy at 60 kHz with loudness of 100 dB SPL, and appears to have a vocal efficiency two orders of magnitude greater than humans (Suthers and Fattu, 1973; Suthers, 1988). Unfortunately for the bat, the subglottal pressures necessary to produce these pulses are great enough (20–50 cm H_2O) to potentially counteract pulmonary blood flow and thus impede respiration, and this is "arguably the most important factor ultimately limiting pulse intensity" (Suthers and Fattu, 1973; Suthers, 1988).

Our simulations suggest that the vocal membranes may permit the vocal folds to oscillate at lower subglottal-threshold pressures, and indicate that this effect increases with increasing frequency. Thus, a simple geometrical modification of glottal morphology could enable an organism which habitually makes loud, high-pitched sounds to do so using less energy, or alternatively to increase the loudness and pitch range of sounds produced using a certain subglottal pressure. In other words, the addition of vocal membranes to the standard mammalian vocal folds may not only allow an organism to produce higher-pitched phonation (as previously suggested by many researchers, e.g., Griffin, 1958; Griffiths, 1978; Schön-Ybarra, 1995; Brown and Cannito, 1995; Fitch and Hauser, 1995), but also to produce a given sound louder and more efficiently. While the significance of this effect for echolocating bats is obvious and could be substantial, more subtle benefits could be accrued to any animal producing loud vocalizations for long-distance communication.

To our knowledge, this hypothesis has not been sug-

gested previously, and it indicates that a proper understanding of the role of the vocal membranes requires detailed information on the anatomy and geometry of these structures. Because the importance of geometry has not been recognized previously, most anatomical descriptions of vocal membranes have been based on serial sections of the larynx, which distort the angle of attachment of the membranes to the rest of the vocal folds. Our simulations suggest that there is an angle of attachment for any given membrane length which is optimal for lowering threshold pressure; this prediction could easily be tested by careful measurements of this angle in intact larynges.

Our final finding was that the addition of the vocal membranes made our model more susceptible to the effects of vocal-fold asymmetry, and thus more likely to enter regimes of subharmonic or chaotic vibration. Many examples of similar vocal instabilities have been found in humans, e.g., in newborn cries (Sirviö and Michelsson, 1976; Mende *et al.*, 1990), noncry vocalizations of infants (Robb and Saxman, 1988), Russian lament (Mazo *et al.*, 1995), and also in conversational speech (Dolansky and Tjerlund, 1968; Kohler, 1996). Pathological voices in particular exhibit a wide variety of vocal instabilities (Herzel and Wendler, 1991; Herzel, 1993). The concepts of nonlinear dynamics provide a framework suitable for understanding complex vocal-fold oscillations and for classifying this menagerie of irregularities. Left–right asymmetries of the larynx, manifested in glottal geometry, tissue properties, or in nervous function, induce subharmonic, toroidal, and chaotic oscillations of the vocal folds. Sub- and supraglottal resonances and turbulent airflow can also lead to nonlinear effects (Herzel, 1996). These findings can be generalized to phonation in nonhuman mammals as well (see Wilden *et al.*, 1998). The current results suggest that vocal membranes can heighten the sensitivity of the vocal folds to asymmetries, thus increasing instability, and thus add support for the notion that the larynges of nonhuman primates may be prone to instabilities (Lieberman, 1968;

Pressman and Kelemen, 1963). Moreover, the experimentation with simple models with geometric modifications like the one explored here may provide potential and clinical valuable insights into the functioning of diseased or damaged vocal folds. In particular, the phenomenon of sulcus vocalis offers an interesting parallel to the geometric addition of the vocal membrane considered here. The term sulcus vocalis is applied to a vast array of organic changes ranging from minor vocal-fold indentations to severe scarred lesions. Like the vocal membranes, sulcus vocalis is often bilateral and extends down the whole length of the vocal fold (Hirano *et al.*, 1990). Thus, while the flaps of membrane seen in a sulcus vocalis patient differ in several ways from vocal membranes (they may be thicker, may be located on the inside of the fold instead of the top edge, and may point up or down), they may have qualitative effects on phonation dynamics similar to those described here, and could be investigated using similar modeling strategies.

V. FUTURE DIRECTIONS

The model of the vocal membranes described here only scratches the surface of the problem. Two obvious extensions of the current model are addition of a vocal tract (exploring possible effects of source-tract coupling on phonation) and allowing θ to vary dynamically (thus adding a third independent oscillator). Source-tract coupling is based on the possibility of a novel mode of phonation resulting from interaction between vibrations of the laryngeal source and vocal-tract resonances. In wind instruments, strong coupling between the source (e.g., the reed of a clarinet, or the lips of a trumpet player) and column of air in the instrument body leads to a situation in which the length of the air column effectively dictates the possible vibration frequencies of the source; there is a strong source-tract interaction (Fletcher and Rossing, 1991; Sundberg, 1991). In contrast, source and tract in human speech appear in general to be almost completely independent: a singer can produce any arbitrary pitch with any configuration of the vocal tract (Fant, 1960; Lieberman and Blumstein, 1988; Sundberg, 1987; Fletcher, 1992). Although most data gathered to date have supported the idea that source and filter are also independent in animal vocalization (as in the human voice), there are some conflicting reports, it would probably be premature to conclude that no animal vocalizations involve any source-tract coupling (for a review of the data for nonhuman primates, see Fitch and Hauser, 1995; for birds, see Nowicki and Marler, 1988).

The coupling of a resonator tube to a simplified two-mass model was studied by Mergell and Herzel (1997), who showed that the combination of small asymmetries, moderate subglottal pressures, and a strong vocal-tract coupling can induce various complex vocal-fold oscillations. For the simulation of Fig. 7 we used a relatively large asymmetry, but the results of Mergell and Herzel (1997) indicate that resonance of the fundamental frequency with sub- or supra-glottal formants and a strong source-tract coupling based on a narrow epilarynx and incomplete glottal closure can lead to instabilities at smaller laryngeal asymmetries. Because the vocal membranes provide a larger surface area upon which formant-generated pressure variations could act on the vocal folds, the vocal membranes could lead to an increase in this destabilization. Alternatively, an increase in coupling could allow the animal to stabilize call fundamental frequency via vocal-tract resonances, as is the case in wind instruments. Studies of a model including both a vocal tract and vocal membranes are currently in progress.

Finally, although no video endoscopy or excised larynx observations of phonating animals with vocal membranes are available to support this conjecture, it seems reasonable to assume that the membranes can vary their angle of attachment to the rest of the vocal fold during phonation, acting as an independent oscillator, and thus adding another degree of freedom to the current model. Unfortunately, the data necessary to model such behavior are not currently available, particularly data on stress–strain relationships within the membrane and tensions applied across the membrane. Even details of the geometry and mass of the membrane are lacking for most species. We are currently gathering data of this sort from nonhuman primates, and hope to implement more complex models in the future. For now, the present study demonstrates that even a very simple change in vocal-fold morphology can have nontrivial effects on phonation dynamics, and demonstrates the usefulness of low-order models in exploratory analyses of nonhuman phonation.

Alipour-Haghighi, F., and Titze, I. R. (**1985**). ''Simulation of particle trajectories of vocal fold tissue during phonation,'' in *Vocal Fold Physiology: Biomechanics, Acoustics, and Phonatory Control*, edited by I. R. Titze and R. C. Scherer (Denver Center for the Performing Arts, Denver, CO).

Berry, D. A., Herzel, H., Titze, I. R., and Krischer, K. (**1994**). ''Interpretation of biomechanical simulations of normal and chaotic vocal fold oscillations with empirical eigenfunctions,'' J. Acoust. Soc. Am. **95**, 3595–3604.

Brown, C. H., and Cannito, M. P. (**1995**). ''Modes of vocal variation in Syke's monkey (*Cercopithecus albogularis*) squeals,'' J. Comp. Psych. **109**, 398–415.

Dolansky, L., and Tjernlund, P. (**1968**). ''On certain irregularities of voiced-speech wave-forms,'' IEEE Trans. Audio Electroacoust. **AU-16**, 51–56.

Fant, G. (**1960**). *Acoustic Theory of Speech Production* (Mouton, The Hague).

Fitch, W. T. (**1997**). ''Vocal tract length and formant frequency dispersion correlate with body size in rhesus macaques,'' J. Acoust. Soc. Am. **102**, 1213–1222.

Fitch, W. T., and Hauser, M. D. (**1995**). ''Vocal production in nonhuman primates: Acoustics, physiology, and functional constraints on 'honest' advertisement,'' Am. J. Prima. **37**, 191–219.

Fletcher, N. H. (**1992**). *Acoustic Systems in Biology* (Oxford U.P., Oxford, UK).

Fletcher, N. H., and Rossing, T. D. (**1991**). *The Physics of Musical Instruments* (Springer-Verlag, New York).

Gautier, J. P. (**1971**). ''Etude morphologique et fonctionnelle des annexes extra-larynges des cercopithecinae; liaison avec les cris d'espacement,'' Biol. Gabonica **7**, 230–267.

Griffin, D. R. (**1958**). *Listening in the Dark* (Yale U.P., New Haven, CT).

Griffiths, T. A. (**1978**). ''Modification of *M. cricothyroideus* and the larynx in the *Mormoopidae*, with reference to amplification of high-frequency pulses,'' J. Mammal. **59**(4), 724–730.

Harrison, D. F. N. (**1995**). *The Anatomy and Physiology of the Mammalian Larynx* (Cambridge U.P., New York).

Hartley, D. J., and Suthers, R. A. (**1988**). ''The acoustics of the vocal tract in the horseshoe bat, *Rhinolophus hildebrandti*,'' J. Acoust. Soc. Am. **84**, 1201–1213.

Hast, M. (**1989**). ''The larynx of roaring and non-roaring cats,'' J. Anat. **163**, 117–21.

Herzel, H., and Wendler, J. (**1991**). ''Evidence of chaos in phonatory samples,'' in Proceedings of ROSPEECH, Genova, 1991 (ESCA), pp. 263–266.

Herzel, H. (**1993**). ''Bifurcations and chaos in voice signals,'' Appl. Mech. Rev. **46**, 399–413.

Herzel, H. (**1996**). ''Possible mechanisms of vocal instabilities,'' in *Vocal Fold Physiology: Controlling Complexity & Chaos*, edited by P. J. Davis and N. H. Fletcher (Singular, San Diego), pp. 63–75.

Hill, W. C. O. (**1957**). *Primates: Comparative Anatomy and Taxonomy; 3 Pithecoidea, Platyrrhini* (Interscience, New York).

Hill, W. C. O., and Booth, A. H. (**1957**). ''Voice and larynx in African and Asiatic Colobidae,'' J. Bombay Nat. Hist. Soc. **54**, 309–321.

Hirano, M. (**1974**). ''Morphological structure of the vocal cord as a vibrator and its variations,'' Folia Phoniatr. **26**, 89–94.

Hirano, M., Yoshida, T., Tanaka, S., and Hibi, S. (**1990**). ''Sulcus vocalis: functional aspects,'' Ann. Otol. Rhinol. Laryngol. **99**, 679–683.

Hirano, M. (**1991**). ''Phonosurgical analomy of the larynx,'' in *Phonosurgery: Assessment and Surgical Management of Voice Disorders*, edited by C. N. Ford and D. M. Bless (Raven, New York).

Ishizaka, K., and Flanagan, J. L. (**1972**). ''Synthesis of voiced sounds from a two-mass model of the vocal cords,'' Bell Syst. Tech. J. **51**, 1233–1268.

Kelemen, G. (**1949**). ''Structure and performance in animal language,'' Arch. Otolaryngol. **50**, 74–744.

Kelemen, G. (**1969**). ''Anatomy of the larynx and the anatomical basis of vocal performance,'' in *The Chimpanzee, Vol. 1*, edited by G. Bourne (Karger, Basel, Germany), pp. 165–187.

Kohler, K. J. (**1996**). ''Articulatory reduction in German spontaneous speech,'' in *Proceeding of the 4th Speech Prod. Seminar, Autrans*, edited by P. Perrier (European Speech Communcation Assocation, Grenoble), pp. 1–4.

Kurita, S., Nagata, K., and Hirano, M. (**1983**). ''A comparative study of the layer structure of the vocal fold,'' in *Vocal Fold Physiology: Contemporary Research and Clinical Issues*, edited by D. M. Bless and J. H. Abbs (College-Hill, San Diego).

Lieberman, P. (**1968**). ''Primate vocalization and human linguistic ability,'' J. Acoust. Soc. Am. **44**, 1574–1584.

Lieberman, P., and Blumstein, S. E. (**1988**). *Speech Physiology, Speech Perception, and Acoustic Phonetics* (Cambridge U.P., Cambridge, UK).

Lucero, J. C. (**1993**). ''Dynamics of the two-mass model of the vocal folds: Equilibria, bifurcations, and oscillation region,'' J. Acoust. Soc. Am. **94**, 3104–3111.

Lucero, J. C. (**1995**). ''The minimum lung pressure to sustain vocal fold oscillation,'' J. Acoust. Soc. Am. **98**, 779–784.

Lucero, J. C. (**1996**). ''Nonlinear dynamics of the vocal fold oscillation,'' First ESCA Totorial and Research Workshop on Speech Production Modeling—4th Speech Production Seminar, pp. 185–188.

Mazo, M., Erickson, D., and Harvey, T. (**1995**). ''Emotion and expression: temporal data on voice quality in Russian lament,'' in *Vocal Fold Physiology*, edited by O. Fujimura and M. Hirano (Singular, San Diego), pp. 173–178.

Mende, W., Herzel, H., and Wermke, K. (**1990**). ''Bifurcations and chaos in newborn cries,'' Phys. Lett. A **145**, 418–424.

Mergell, P., and Herzel, H. (**1997**). ''Modelling biphonation—The role of the vocal tract,'' Speech Commun. **22**, 141–154.

Mergell, P., Herzel, H., Wittenberg, Th., Tigges, M., and Eysholdt, U. (**1998**). ''Phonation onset: Modeling and high speed clottography,'' J. Acoust. Soc. Am. **104**, 467–470.

Morton, E. S. (**1977**). ''On the occurrence and significance of motivation-structural rules in some birds and mammal sounds,'' Am. Nat. **111**, 855–869.

Negus, V. E. (**1940**). *The Comparative Anatomy and Physiology of the Larynx* (Hafner, New York).

Nowicki, S., and Marler, P. (**1988**). ''How do birds sing?,'' Mus. Percep. **5**, 391–426.

Pressman, J., and Kelemen, G. (**1963**). ''Physiology of the larynx,'' Physiol. Rev. **35**, 506–554.

Robb, J. B., and Saxman, J. (**1988**). ''Acoustic observations in young children's vocalizations,'' J. Acoust. Soc. Am. **83**, 1876–1882.

Sirviö, P., and Michelsson, K. (**1976**). ''Sound-spectrographic cry analysis of normal and abnormal newborn infants,'' Folia Phoniatr. **28**, 161–173.

Schön-Ybarra, M. (**1995**). ''A comparative approach to the nonhuman primate vocal tract: Implications for sound production,'' in *Frontiers in Primate Vocal Communication*, edited by E. Zimmerman and J. D. Newman (Plenum, New York).

Starck, D., and Schneider, R. (**1960**). ''Respirationsorgane,'' in *Primatologia III/2*, edited by H. Hofer, A. H. Schultz, and D. Starck (Karger, Basel).

Steinecke, I., and Herzel, H. (**1995**). ''Bifurcations in an asymmetric vocal-fold model,'' J. Acoust. Soc. Am. **97**, 1874–1884.

Stevens, K. N. (**1977**). ''Physics of laryngeal behavior and larynx modes,'' Phonetica **34**, 264–279.

Story, B. H., and Titze, I. R. (**1995**). ''Voice simulation with a body-cover model of the vocal folds,'' J. Acoust. Soc. Am. **97**, 1249–1260.

Sundberg, J. (**1987**). *The Science of the Singing Voice* (Northern Illinois U.P., DeKalb, IL).

Sundberg, J. (**1991**). *The Science of Musical Sounds* (Academic, New York).

Suthers, R. A., and Fattu, J. M. (**1973**). ''Mechanisms of sound production in echolocating bats,'' Am. Zool. **13**, 1215–1226.

Suthers, R. A. (**1988**). ''The production of echolocation signals by bats and birds,'' in *Animal Sonar: Processes and Performance*, edited by P. E. Nachtigall and P. W. B. Moore (Plenum, New York), pp. 23–45.

Thomas, C. L. (**1989**). *Taber's Cyclopedic Medical Dictionary* (Davis, Philadelphia.).

Titze, I. R., and Talkin, D. T. (**1979**). ''A theoretical study of the effects of various laryngeal configurations on the acoustics of phonation,'' J. Acoust. Soc. Am. **66**, 60–74.

Titze, I. R. (**1988**). ''The physics of small-amplitude oscillation of the vocal folds,'' J. Acoust. Soc. Am. **83**, 1536–1522.

Wendler, J., Seidner, W., Kittel, G., and Eysholdt, U. (**1996**). *Lehrbuch der Phoniatric und Pädaudiologie* (Georg Thieme, Stuttgart, New York).

Wilden, I., Herzel, H., Peters, G., and Tembrock, G. (**1998**). ''Subharmonics, biphonation, and deterministic chaos in mammal vocalization,'' Bioacoustics **9**, 171–196.

Detection of modulation in spectral envelopes and linear-rippled noises by budgerigars (*Melopsittacus undulatus*)

Satoshi Amagai and Robert J. Dooling
Department of Psychology, University of Maryland at College Park, College Park, Maryland 20742

Shihab Shamma
Department of Engineering, University of Maryland at College Park, College Park, Maryland 20742

Tracy L. Kidd and Bernard Lohr
Department of Psychology, University of Maryland at College Park, College Park, Maryland 20742

Budgerigars were trained to discriminate complex sounds with two different types of spectral profiles from flat-spectrum, wideband noise. In one case, complex sounds with a sinusoidal ripple in (log) amplitude across (log) frequency bandwidth were generated by combining 201 logarithmically spaced tones covering the frequency region from 500 Hz to 10 kHz. A second type of rippled stimulus was generated by delaying broadband noise and adding it to the original noise in an iterative fashion. In each case, thresholds for modulation depth (i.e., peak-to-valley in dB) were measured at several different ripple frequencies (i.e., cycles/octave for logarithmic profiles) or different repetition pitches (i.e., delay for ripple noises). Budgerigars were similar to humans in detecting ripple at low spatial frequencies, but were considerably more sensitive than humans in detecting ripples in log ripple spectra at high spatial frequencies. Budgerigars were also similar to humans in detecting linear ripple in broadband noise over a wide range of repetition pitches. Taken together, these data show that the avian auditory system is at least as good, if not better, than the human auditory system at detecting spectral ripples in noise despite gross anatomical differences in both the peripheral and central auditory nervous systems. © *1999 Acoustical Society of America.* [S0001-4966(99)03802-3]

PACS numbers: 43.80.Lb, 43.66.Gf [FD]

INTRODUCTION

A primary goal of hearing research is to understand how complex, naturally occurring sounds such as species-specific vocalizations and speech sounds are processed by the nervous system. Comparative investigations with such sounds can provide an important window on the evolution and adaptation of auditory systems, especially when these sounds can be systematically manipulated. While complex communication signals have become popular stimuli for exploring auditory function in different species, their very complexity renders them a difficult class of sounds to describe and manipulate when used in a systematic exploration of auditory function.

Historically, the alternatives to complex, natural sounds in both physiological and psychophysical experiments have been pure tones and noises. Approaches using these sounds tend to reduce the auditory system to equivalent acoustic engineering systems. This succeeds in addressing the problem of description and logical manipulation of sounds, but such an approach is intrinsically limited by its simplicity, restricting our understanding to an arbitrary and probably unrealistic view of the auditory system. The use of spectrally complex, broadband sounds offers some compromise between simple sounds such as pure tones and noises and more complex, natural sounds such as vocalizations. In particular, spectrally complex sounds with rippled spectral envelopes share some of the characteristics of natural sounds, but may be generated mathematically allowing for precise, quantifiable, and systematic manipulation.

One type of sound having rippled spectral profiles has become useful because of its noted parallel with sine-wave gratings used in studies of vision. These sounds, called log-rippled noises in this paper, are generated by imposing a sinusoidal spectral envelope onto broadband noise in the frequency domain, or by algebraically adding frequency components with amplitudes determined by a sinusoidal envelope. The spectral envelope is sinusoidal when frequency is represented on a logarithmic scale and sinusoidal envelopes are expressed in units of cycles/octave. In vision, this class of stimuli purports to allow for a linear systems analysis of visual function as long as the underlying principle of linearity of summation is not violated (De Valois and De Valois, 1988). Whether a linear systems analysis approach will prove useful for understanding complex signal processing in the auditory system remains to be seen. This approach could provide a powerful tool for comparative explorations of auditory system function at different levels and in different species (Shamma and Versnel, 1995; Shreiner and Calhoun, 1995). In humans, there are strong arguments for studying rippled spectra based on their parallels with the vowel sounds of human speech (Hillier, 1991; Summers and Leek, 1994).

A second class of rippled stimuli may be created by delaying a portion of wideband noise and adding it back to the undelayed original. The resulting stimulus has been

called rippled noise, repetition noise, or cosine noise (Fay *et al.*, 1983; Bilsen *et al.*, 1975; Yost and Hill, 1978). It has spectral peaks at integer multiples of $1/T$, where T is the time of delay. If the delay and add process is combined in a feedback loop, the result is comb-filtered noise (Bilsen and Wieman, 1980; Pick, 1980). These linear-rippled noises produce the perception of pitch corresponding to $1/T$ Hz in human subjects (Bilsen, 1970; Yost *et al.*, 1978). Yost *et al.* (1996) have recently described a variant of these noises created by iterating the delay and add process. Two different digital networks have been outlined for producing iterated rippled noises. In one network, delayed and attenuated noise is added back to the original noise in an iterative process. In the second network, the output of the previous add is delayed and attenuated before the next add. These two networks produce rippled noises with slightly different spectra (Yost, 1996).

The experiments reported herein followed the former procedure for generating iterated rippled noise, and used a large (999) number of iterations to approximate the infinitely iterated comb-filtered noise of Bilsen and Wieman (1980). These stimuli are referred to here as linear-rippled noise, in contrast to the log-rippled noise discussed earlier. The amount of spectral modulation in linear-rippled stimuli is controlled by varying the attenuation of the delayed sound before it is added back to the undelayed original. A series of sounds ranging from spectrally flat to deeply rippled were created by decreasing the amount of attenuation from about 25 to 0 dB. As the attenuation is reduced, the depth of modulation increases, as does the saliency of the repetition pitch. Human subjects are most sensitive to repetition pitches between 100 and 1000 Hz; the sensitivity is independent of overall level above about 20-dB sensation level (Bilsen and Ritsma, 1970; Yost and Hill, 1978).

The details of linear-rippled noise processing are important for theories of vertebrate hearing because models and theories of pitch must be able to account for the pitches and pitch strengths of rippled noises. A variety of sounds can produce the perception of the same pitch in human subjects (Fastl and Stoll, 1979), and it is possible that the neural mechanisms underlying pitch perception share some common properties for these various stimuli. From an ecological standpoint, a case has also been made that complex sounds occurring from multiple reflections in the environment, creating rippled spectra, might be discriminated on the basis of their pitch strength and coloration (Yost *et al.*, 1996).

There is less work on the processing of rippled noises in animals than in humans. As far as we know, log-rippled noises have been used only in studies of ferrets (Shamma *et al.*, 1995; Shamma and Versnel, 1995; Versnel *et al.*, 1995) and cats (Shreiner and Calhoun, 1995) in electrophysiological recordings in the cortex. On the other hand, linear-rippled noises have been used in a number of physiological and psychophysical studies of hearing in a variety of species including cats (Pickles, 1979), guinea pigs (Evans *et al.*, 1992), and chinchillas (Niemiec *et al.*, 1992; Shofner and Yost, 1995; Shofner, 1991). The psychophysical data on repetition-noise perception by goldfish are perhaps the most comprehensive so far published for any nonhuman. As with

humans and other animals, these data show that as $1/T$ increases, discrimination of delay differences requires greater spectral modulation depth (Fay *et al.*, 1983). Otherwise said, "pitch strength" probably declines for the goldfish at higher values of $1/T$ (Fay, 1988; Fay *et al.*, 1983).

Birds are excellent subjects, in general, for the comparative study of complex sound processing. Furthermore, in spite of many psychophysical and physiological studies over the years using both simple tones and noises as well as natural vocalizations, our understanding is still far from complete. The purpose of the present experiments is to provide baseline data on the perception of these two types of complex sounds with rippled spectra as a foundation for future investigations involving other types of manipulations in rippled spectra, such as phase, shape, pitch strength, or coloration, etc. To this end, thresholds for detecting spectral modulation in log-rippled and linear-rippled sounds were measured in three budgerigars. Budgerigars are small Australian parrots known for their tractability for auditory testing (Okanoya and Dooling, 1987) and superiority in discriminating complex harmonic sounds (Lohr and Dooling, 1998), as well as for their complex learned vocal repertoire and adult vocal plasticity (Farabaugh *et al.*, 1994).

I. METHODS

A. Subjects

The subjects in these experiments were three budgerigars (*Melopsittacus undulatus*, two females and one male). All birds were either bought at a local pet store or hatched at the University of Maryland and housed in individual cages in a vivarium at the University of Maryland. The birds were kept on a normal day/night cycle correlated with the season at approximately 90% of their free-feeding weights. Although the primary focus of the present study was to obtain psychophysical data from budgerigars, four human subjects (students and research assistants) were also tested on the same stimulus conditions. This provided a check on the validity of the test procedures and apparatus, a comparison with existing human data, and a procedural control.

B. Testing apparatus

The birds were tested in a wire cage ($25 \times 25 \times 25$ cm) placed in a small animal IAC chamber lined with acoustic foam. A response panel consisting of two sensitive microswitches with light-emitting diodes (LEDs) was mounted on the wall of the test cage just above the food hopper. The microswitch was tripped by the bird pecking the LED. The left microswitch was the observation key, and the right microswitch was the report key. Stimuli were delivered from a JBL loudspeaker (model 2105H) mounted 20 cm above the test cage. All experimental events were controlled by an IBM 486 microcomputer operating Tucker-Davis signal-processing modules. Stimulus calibration was performed using a General Radio (model 1982) sound-level meter with octave band filters. Stimulus intensities were measured by placing the microphone in front of the keys of the response panel in the approximate position normally occupied by the bird's head during testing. The intensities of the stimuli were

measured several times during the conduct of these experiments to ensure that the entire system remained calibrated. During testing, the behavior of the bird was monitored by a video camera system.

C. Training and testing procedures

The training and testing procedures have been described in detail previously by Okanoya and Dooling (1987, 1990). The bird was trained by a standard operant auto-shaping program to peck at the left microswitch key (observation key) during a repeating background until a new stimulus was presented alternately with the background sound. If the bird pecked the right microswitch and LED (report key) within 2 s of this alternating pattern, the food hopper was activated for 2 s. The dependent variables in these experiments were percent correct and response latency on trials involving an alternating sound pattern. A failure to peck the report key within 2 s of sound alternation was recorded as a miss, a response latency of 2000 ms recorded, and a new trial sequence initiated. Thirty percent of all trials were "sham" trials in which the "target" sound was the same as the repeating "background" sound. A peck to the report key during a sham trial was recorded as a false alarm and the lights in the test chamber were extinguished while the repeating background continued. The length of this time-out period was normally 5 s, but varied according to the bird's behavior, with longer time-out periods applied with higher false-alarm rates. Sessions with a total false-alarm rate of 16% or higher were discarded. No more than 20% of the sessions for any bird were discarded for this reason.

D. Stimuli

1. Log-rippled spectra

These complex broadband sounds were created using the procedures described by Shamma and his colleagues (Shamma *et al.*, 1995). Briefly, the stimuli were generated by algebraically summing 201 sinusoidal components sampled at 40 kHz that were equally spaced along the logarithmic frequency axis, spanning the frequency range from 0.5 to 10 kHz. The phases of the individual sinusoids were randomized to avoid large-amplitude onset effects. This range was chosen to completely encompass the range of hearing in budgerigars (Dooling and Saunders, 1975). The duration of each stimulus was 100 ms with 10 ms rise/fall times. The spectral envelope of this stimulus complex was then modulated sinusoidally on a logarithmic scale to create a "ripple" whose frequency, measured in cycles/octave, was varied from 0.5 to 10 cycles/octave. The phase of the ripple was uniformly set to zero at the low-frequency edge of the complex. A range of sounds with different ripple amplitudes was created for each ripple frequency. The amplitude of the ripple was taken as the ratio of the amplitude of the peak to the trough of the spectral envelope in dB. The resulting waveform was normalized to ±15 bits for playback through the digital-to-analog converter. The overall level of the complex stimulus was measured in the test box and adjusted to 60 dB(A). For each ripple frequency, the repeating background was the sound with 0-dB ripple amplitude. The test stimuli the ani-

mal was asked to detect consisted of rippled noises with the same ripple frequency but with varying amount of ripple amplitudes. In each trial, seven test stimuli were used consisting of ripple amplitudes that ranged from either 1–7 or 2–14 dB, depending on the performance of the birds. During testing, the overall level was varied randomly (roved) from stimulus presentation to presentation by ±5 dB to minimize amplitude cues.

2. Linear-rippled stimuli

The second type of rippled stimuli tested were those with a linear-rippled spectra. Figure 1 shows the spectrum of a log-rippled noise and a linear-rippled noise used in these experiments. These sounds were generated by starting with a wideband noise, delaying it, attenuating it, and repeatedly adding this delayed noise to the undelayed noise. In practice, frozen segments of rippled noise with 999 iterations were created with a Tucker-Davis Technologies array processor (AP2) at a sampling rate of 40 kHz. This network used to create these noises has been referred to as iterated rippled noise in an add-original network (Yost, 1996). The overall level of these complex sounds was adjusted so that the wideband noise and rippled noise had equal root-mean-squared (rms) voltages. All sounds were then randomized in amplitude by ±5 dB during stimulus presentation. Thus, the birds could not use a loudness cue during the presentation of rippled noise. The six delays (T) used to generate rippled noises ranged from 8 down to 0.25 ms to create repetition pitches (as perceived by humans) ranging from 125 to 4000 Hz in octave steps.
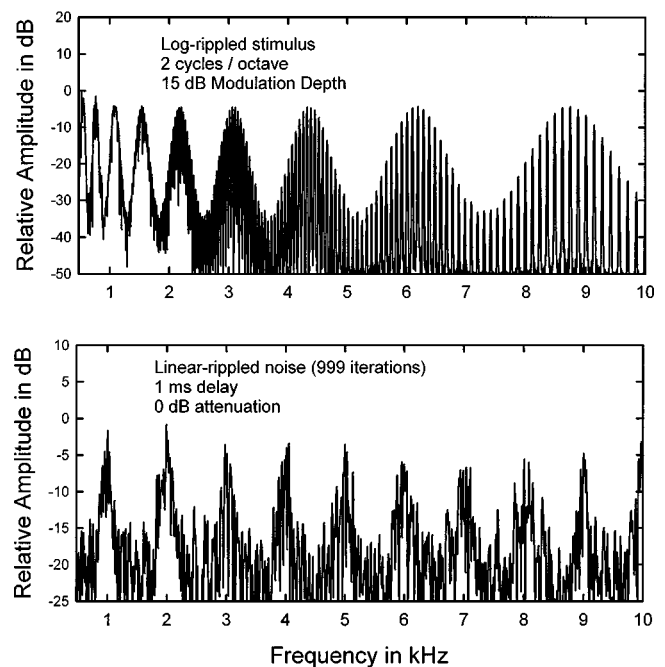

FIG. 1. (Top) Power spectrum of a log-rippled stimulus used in these experiments. This stimulus has a ripple frequency of 2 cycles/octave and a peak-to-valley modulation depth of 15 dB. (Bottom) Power spectrum of a linear-rippled stimulus used in these experiments. This stimulus was constructed using 999 iterations, a delay of 1 ms, and no attenuation (i.e., gain or "*g*" is equal to 1).
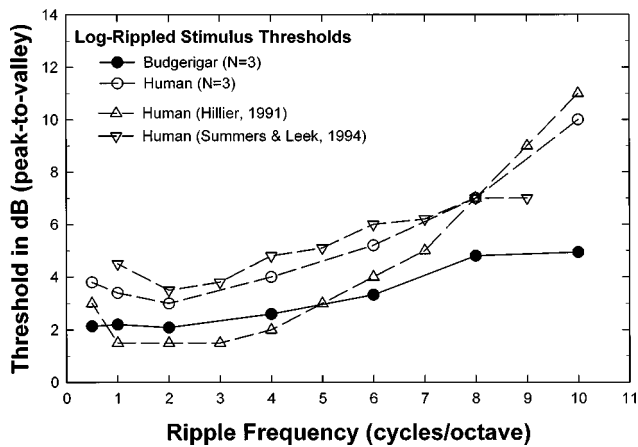
FIG. 2. Detection thresholds for log-rippled noise. The ripple amplitude threshold for detection defined as 50% chance of detection is plotted in peak-to-valley ripple amplitude in dB as a function of the ripple envelope frequency (cycles/octave). Solid circles are data from budgerigars ($n=3$) and open circles are data from human subjects ($n=3$) tested with the same stimuli and procedures. Other open symbols are previously published data from Hillier (1991) and Summers and Leek (1994).
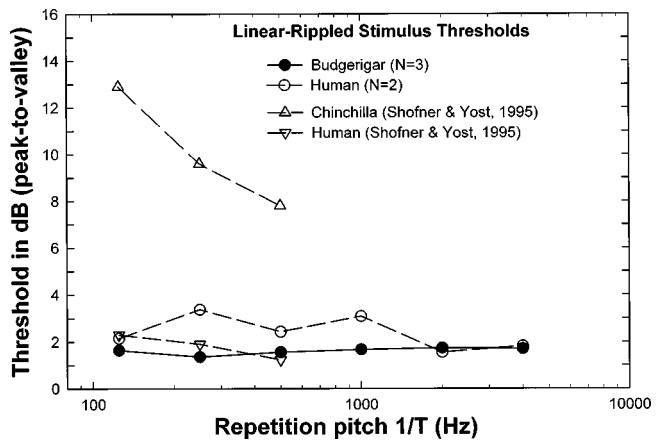

FIG. 3. Detection thresholds for linear-rippled noise. Threshold for ripple detection (50% chance of detection) is plotted as a function of the repetition pitch $1/T$, where T is the delay of the added waveform. The amplitude of the ripple is expressed as a peak-to-valley of the resulting waveform as calculated from the attenuation of the added waveform. Solid circles are data from budgerigars ($n=3$), and open circles are data from humans subjects ($n=2$) tested with the same stimuli and procedures. Other open symbols are from previously published human and chinchilla data (Shofner and Yost, 1995).

In this experiment, the repeating background was always a frozen noise sample with zero iterations of delayed addition. Target rippled noises had varying amounts of attenuation ranging from 25 to 0 dB. Spectral modulation depth (P/V in dB) was calculated as described by Shofner and Yost (1995) as:

$$\frac{P}{V}(\text{dB}) = 10\log\left(\frac{(1+g)^2}{(1-g)^2}\right),$$

where "g," the gain or attenuation of the delayed noise, is greater than 0. The level of these stimuli presented during testing was monitored by placing a condenser microphone from a General Radio sound-level meter (model 1982) in the free-field in the approximate position of an animal's head and measuring the A-weighted sound pressure level.

To permit comparison, both log- and linear-rippled noises are plotted on the same linear abscissa in Fig. 1. Note that these spectra differ not only in their envelope frequency but also in their shape. The spectral envelope for the log-rippled stimulus is sinusoidal (on a log axis), while the spectrum resulting from 999 iterations of iterated rippled noise is nearly a line spectrum. Spectral modulation depth for the log-rippled stimuli is specified directly in the creation of these stimuli (peak-to-valley in dB). For linear-rippled stimuli, spectral modulation depth is also calculated as a peak-to-valley ratio in dB as described by the formula above.

II. RESULTS

The average modulation-depth thresholds for log-rippled sounds are shown in Fig. 2 for three budgerigars, along with similar data from several human studies. Budgerigars showed thresholds of modulation detection that were in the range of 2–3 dB at low ripple frequencies rising to about 4 dB as ripple-envelope frequency increased above about 4 cycles/octave. For comparison, data from our human subjects and from two previous investigations on human subjects (Hillier, 1991; Summers and Leek, 1994) are plotted on the

same axes. The human thresholds ranged from a 3–4 dB peak-to-valley modulation depth at low ripple envelope frequencies to about 10 dB peak-to-valley depth as the ripple frequency exceeded 10 cycles per octave. The results for our humans, tested with the same procedures used for testing our birds, are very similar to previous human data in both the amplitude of the threshold values and the shape of the threshold curves as a function of envelope frequency. In the direct comparison of our bird and human data, budgerigars consistently outperformed our human subjects throughout the range of ripple frequencies, especially at high ripple frequencies. The point of testing humans on the same stimuli using the same procedures used for testing the birds is to ensure the validity of the present procedures and provide a hedge against the existence of any stimulus artifacts that might contaminate the bird thresholds.

The average results for three budgerigars tested on linear-ripple noise are shown in Fig. 3. Both budgerigars and humans show a reasonably flat pattern of thresholds of between 2 to 4 dB peak-to-valley modulation depth over a range of repetition pitch from 125 to 4000 Hz. For comparison, human and chinchilla data from a previous study (Shofner and Yost, 1995) are also plotted. The present values for humans are very similar to those reported by Shofner and Yost (1995) over the same range. The results for birds, however, while agreeing well with the human data, stand in marked contrast to data from the chinchilla, which shows much higher thresholds in the range of 8 to 12 dB.

III. DISCUSSION AND CONCLUSIONS

These experiments show that despite having remarkably different peripheral and central auditory systems (Manley, 1990; Manley et al., 1993), budgerigars are roughly similar to humans in the ability to detect amplitude modulation in both log- and linear-spaced spectral rippled stimuli. These

results raise a number of questions, including a set of methodological issues involved in the conduct of comparative studies with complex sounds. On the methodological issues, studying the detection, discrimination, or perception of complex sounds in animals always carries the concern that procedural differences between animal and human tests weaken the comparison of sensory capabilities. To this end, the agreement of our human data (obtained with the same repeating-background procedure used to test the birds) with data from humans tested on both log- and linear-ripples in other laboratories can be taken as evidence that no stimulus or procedural artifacts affect thresholds in our tests. In addition, the amplitude of the stimulus was randomly varied over a range of 10 dB on a stimulus presentation-by-presentation basis, so that any slight overall amplitude changes that might have occurred through spectral manipulations could not be used by the birds to detect the presence of rippled spectral envelopes in these sounds.

Potentially more problematic is the use of frozen noise samples in the test using linear-rippled noises. The use of frozen stimulus samples raises the possibility that a particular sample might have some unique features that aid detection. The evidence against this possibility is that it would likely lead to spuriously low thresholds or psychometric functions with an unusual shape, neither of which occurred in these experiments. As an additional check against this kind of problem influencing our results, once our birds and humans reached threshold levels of performance on a set of stimuli at a particular ripple frequency or delay, they were transferred to several entirely new sets of rippled stimuli and their thresholds were measured again. In all cases, birds and humans gave similar threshold values on the new stimulus sets. As a final control, an additional budgerigar was tested using multiple background and target exemplars presented at random during testing. Thus, the bird was tested with random presentations of 10 different frozen background stimuli and 5 different frozen targets at each ripple depth. The thresholds for this bird were very similar to those for the three budgerigars in the main experiment.

Another interesting issue raised by the present results concerns the mechanisms underlying modulation detection for the two different kinds of ripple stimuli. The theoretical basis for studying the detection and perception of noise spectra with log-spaced ripple patterns is, first and foremost, the logarithmic representation of frequency along the cochlear partition that underlies a number of related phenomena including critical bands, critical ratios, frequency difference limens, etc. (Hillier, 1991; Moore, 1997). The construction of log-spaced rippled noises parallels the increasing filter widths in the auditory system at higher frequencies. At low ripple envelope frequencies, the width of the ripple peaks and troughs span more than a single critical-band filter, allowing for comparisons across critical-band filters (channels). As the ripple envelope frequencies increase, however, the differences in stimulation in any two adjacent auditory system filters or channels diminish and eventually disappear as the ripple frequency exceeds the critical bandwidth. This is the likely reason that thresholds for detection of sounds with log-rippled spectra become worse at higher ripple frequencies in humans. The fact that budgerigars are better than humans at detecting modulation at high-ripple frequencies is consistent with other psychophysical data showing exceptionally narrow filter bandwidths for the budgerigar around 3 kHz as measured by critical ratios, critical bands, and psychophysical tuning curves (Dooling and Saunders, 1975; Saunders *et al.*, 1979; Okanoya and Dooling, 1987).

Log-rippled spectra lend themselves particularly well to explorations of spectral or place-code models of auditory processing. Linear-rippled noises, by contrast, lend themselves more to an analysis of time domain processing by the auditory system. Linear-rippled stimuli have been studied more frequently than log-rippled stimuli, and the prevailing interpretation of the processing of linear-rippled noises is that the auditory system is performing a time-domain waveform analysis something like an autocorrelation (Fay *et al.*, 1983; Shofner, 1991; Shofner and Yost, 1994, 1995; Yost *et al.*, 1996). The similarity between budgerigars and humans in the detection of modulation in linear-rippled noises is consistent with a wealth of other comparative data on birds (including budgerigars and zebra finches) that show they are at least as good as humans on a variety of temporal detection and discrimination tasks including duration discrimination, gap detection, temporal integration, and modulation transfer functions (Dooling, 1979; Dooling and Searcy, 1979, 1981; Dooling, Zoloth, and Baylis, 1978; Fay, 1988; Klump and Maier, 1989; Okanoya and Dooling, 1990). It is interesting in this regard that the chinchilla, the only other mammal besides humans tested on linear ripples, is so poor at detecting linear-rippled spectra (Shofner and Yost, 1995).

The promise of using linear-spaced and log-spaced ripples as probes of auditory system function and complex sound perception is that they may offer a solution to the dilemma of whether to use simple, artificial signals or complex, natural sounds to understand the function, adaptation, and evolution of the vertebrate auditory system. Comparative studies have shown there are numerous species, spanning different vertebrate classes, including fish, frogs, birds, and mammals, that preferentially use complex, multiple-harmonic, periodic sounds as communication signals. In these species, there is strong evidence at the behavioral and physiological levels that the auditory system extracts periodicity cues from these harmonic patterns and transmits the information by arrays of phase-locked activity to the central auditory system (Langner, 1992; Simmons and Buxbaum, 1996).

In the spectral domain, there are also countless examples from a variety of vertebrates including humans in which spectral features or the change in spectral features are the important components of species-specific communication signals. One particularly relevant example is the discrimination and categorization of vowel sounds. Studies have shown adult humans, prelinguistic humans, and other mammals whose auditory systems are structurally and functionally similar to those of humans, are generally quite sensitive to the acoustic features that define vowel phonetic categories and can form phonetically appropriate acoustic categories (see, for example, Burdick and Miller, 1975; Kuhl, 1986, 1991; Sinnott, 1989). It is somewhat surprising that several

species of birds, whose peripheral and central auditory systems are structurally very different from mammalian auditory systems, can also discriminate among vowels (Hienz *et al.*, 1981) and perceive vowel categories in a phonetically appropriate way without extensive training, even in the face of talker variation (see, for example, Dooling and Brown, 1990).

Parallels in the perception of complex sounds, including speech sounds, by birds and humans present somewhat of a conundrum. On the one hand, such parallels are consistent with general similarities in psychoacoustic thresholds between birds and mammals in their respective ranges of best hearing (Fay, 1988). This fits with the wealth of evidence that some birds can mimic human speech sounds, which argues that they must hear the sounds of speech as humans do. On the other hand, there are consistent differences in the hearing of birds and mammals. In the lower frequency range critical for human speech, pure-tone thresholds, masked thresholds, and frequency- and intensity-difference limens in humans are generally much superior to birds (Fay, 1988). From these psychoacoustic data, then, one might not predict strong similarities between birds and humans in the perception of speech sounds. It is interesting, then, that the present results show considerable similarity between humans and budgerigars in the detection of modulation in log-rippled noises.

In considering the perception of vowel sounds particularly, the preservation of spectral contrast in the internal representation of spectral shapes is undoubtedly important for locating formant peaks underlying vowel identity. For humans, previous work has shown that the perceived similarities among vowels is mainly determined by the amount of spectral similarity and contrast present at ripple frequencies up to about 2–3 cycles/octave (van Veen and Houtgast, 1985). These results are consistent with an analysis of English vowels spoken by male, female, and child talkers (Peterson and Barney, 1952) that suggests that frequency resolution at ripple frequencies above 4 cycles/octave is probably unnecessary for accurate vowel identification (Summers and Leek, 1994). Budgerigars, like humans, show best detection performance at ripple frequencies below 4 cycles/octave—a capability that may underlie the similarities between budgerigars and humans in vowel speech-sound categories (Dooling and Brown, 1990; Dooling, 1992). Future probes of avian hearing using log-rippled stimuli might explore sensitivity to other aspects of these complex sounds that are known to be represented at the single-unit level in the mammalian primary auditory cortex, such as ripple frequency, ripple phase, and ripple shape (Shamma *et al.*, 1995; Shamma and Versnel, 1995; Versnel *et al.*, 1995).

Finally, there has long been the suggestion that the avian auditory system may be specialized for processing certain kinds of complex sounds. The two classes of complex sounds used in the present experiments may shed new light on this issue. In the case of log-rippled stimuli, it would be interesting to know whether the superior performance of budgerigars at higher ripple frequencies is related to the rapid frequency-modulation characteristic of the vocalizations of budgerigars and many other birds. In the case of linear-spaced ripples, these sounds offer a way of probing the limits of a kind of temporal processing, and birds may turn out to be exceptional in detecting or discriminating certain aspects of these sounds as well. For example, thresholds for detecting the mistuned harmonic in budgerigars and zebra finches are up to an order of magnitude smaller than human thresholds (Lohr and Dooling, 1998). This task almost certainly involves sensitivity to the temporal fine structure of harmonic waveforms. A recent study on single-unit responses in the zebra finch auditory forebrain to complex harmonic stimuli shows greater sensitivity to temporal rather than to spectral cues (Theunissen and Doupe, 1998). Further, this study provides evidence that this extremely precise preservation of temporal cues in the auditory forebrain is necessary for a full response to complex, learned, species-specific vocalizations.

ACKNOWLEDGMENTS

Bilsen, F. A. (**1970**). ''Repetition pitch; its implication for hearing theory and room acoustics,'' in *Frequency Analysis and Periodicity Detection in Hearing*, edited by R. Plomp and G. F. Smoorenburg (A. W. Sijthoff, Leiden), pp. 291–302.

Bilsen, F. A., and Ritsma, R. J. (**1970**). ''Some parameters influencing the perceptibility of pitch,'' J. Acoust. Soc. Am. **47**, 469–475.

Bilsen, F. A., ten Kate, J. H., Buunen, T. J. F., and Raatgever, J. (**1975**). ''Responses of single units in the cochlear nucleus of the cat to cosine noise,'' J. Acoust. Soc. Am. **58**, 858–866.

Bilsen, F. A., and Wieman, J. G. (**1980**). ''Atonal periodicity sensation for comb filtered noise signals,'' in *Psychophysical, Psychological and Behavioral Studies in Hearing*, edited by G. van Den Brink and F. A. Bilsen (Delft U.P., London).

Burdick, C. K., and Miller, J. D. (**1975**). ''Speech perception by the chinchilla: Discrimination of sustained /a/ and /i/,'' J. Acoust. Soc. Am. **58**, 415–427.

De Valois, R. L., and De Valois, K. K. (**1988**). *Spatial Vision* (Oxford U.P., New York).

Dooling, R. J., and Saunders, J. C. (**1975**). ''Hearing in the parakeet (*Melopsittacus undulatus*): Absolute thresholds, critical ratios, frequency difference limens, and vocalizations,'' J. Comp. Physiol. Psychol. **88**, 1–20.

Dooling, R. J. (**1979**). ''Temporal summation of pure tones in birds,'' J. Acoust. Soc. Am. **65**, 1058–1060.

Dooling, R. J., and Brown, S. D. (**1990**). ''Speech perception by budgerigars (*Melopsittacus undulatus*): Spoken vowels,'' Percept. Psychophys. **47**, 568–574.

Dooling, R. J. (**1992**). ''Perception of speech sounds by birds,'' in *Y. Cazals*, edited by L. Demany and K. Horner, *The 9th International Symposium on Hearing: Auditory Physiology and Perception, Carcans, France* (Pergamon, Oxford), pp. 407–413.

Dooling, R. J., and Searcy, M. H. (**1981**). ''Amplitude modulation thresholds for the parakeet (*Melopsittacus undulatus*),'' J. Comp. Physiol. **143**, 383–388.

Dooling, R. J., and Searcy, M. H. (**1979**). ''The relation among critical ratios, critical bands, and intensity difference limens in the parakeet (*Melopsittacus undulatus*),'' Bull. Psychon. Soc. **13**, 300–302.

Dooling, R. J., Zoloth, S. R., and Baylis, J. R. (**1978**). ''Auditory sensitivity, equal loudness, temporal resolving power, and vocalizations in the house finch (*Carpodacus mexicanus*),'' J. Comp. Physiol. Psychol. **92**, 867–876.

Evans, E. F., Pratt, S. R., Spenner, H., and Cooper, N. P. (**1992**). ''Comparisons of physiological and behavioral properties of auditory frequency selectivity,'' in *Y. Cazals*, edited by K. Horner and L. Dermany, *The 9th International Symposium on Hearing: Auditory Physiology and Perception* (Pergamon, Oxford), pp. 159–169.

Farabaugh, S. M., Linzenbold, A., and Dooling, R. J. (**1994**). ''Vocal plasticity in budgerigars (*Melopsittacus undulatus*): Evidence for social factors in the learning of contact calls,'' J. Comp. Psych. **108**, 81–92.

Fastl, H., and Stoll, G. (**1979**). ''Scaling of pitch strength,'' Hearing Res. **1**, 293–301.

Fay, R. R. (**1988**). *Hearing in Vertebrates: A Psychophysics Databook* (Hill-Fay, Winnetka, IL).

Fay, R. R., Yost, W. A., and Coombs, S. (**1983**). ''Psychophysics and neurophysiology of repetition noise processing in a vertebrate auditory system,'' Hearing Res. **12**, 31–55.

Hienz, R. D., Sachs, M. B., and Sinnott, J. M. (**1981**). ''Discrimination of steady-state vowels by blackbirds and pigeons,'' J. Acoust. Soc. Am. **70**, 699–706.

Hillier, D. A. (**1991**). ''Auditory processing of sinusoidal spectral envelopes,'' Ph.D. dissertation. Washington University, Saint Louis, Missouri.

Klump, G. M., and Maier, E. H. (**1989**). ''Gap detection in the starling (*Sturnus vulgaris*): I Psychophysical thresholds,'' J. Comp. Physiol. **164**, 531–539.

Kuhl, P. K. (**1986**). ''The special-mechanisms debate in speech: Contributions of tests on animals and the relation of these tests to studies using non-speech signals,'' Exp. Biol.: Sens. Percept. Process. **45**, 233–265.

Kuhl, P. K. (**1991**). ''Human adults and human infants show a 'perceptual magnet effect' for the prototypes of speech categories, monkeys do not,'' Percept. Psychophys. **50**, 93–107.

Langner, G. (**1992**). ''Periodicity coding in the auditory system,'' Hearing Res. **60**, 115–142.

Lohr, B., and Dooling, R. J. (**1998**). ''Detection of changes in timbre and harmonicity in complex harmonic stimuli by zebra finches (*Taeniopygia guttata*) and budgerigars (*Melopsittacus undulatus*),'' J. Comp. Psych. **112**, 36–47.

Manley, G. A. (**1990**). *Peripheral Hearing Mechanisms in Reptiles and Birds* (Springer-Verlag, Heidelberg).

Manley, G. A., Schwabedissen, G., and Gleich, O. (**1993**). ''Morphology of the basilar papilla of the budgerigar *Melopsittacus undulatus*,'' J. Morphol. **218**, 153–165.

Moore, B. C. J. (**1997**). *Psychology of Hearing* (Academic, Cambridge, England).

Niemiec, A. J., Yost, W. A., and Shofner, W. P. (**1992**). ''Behavioral measures of frequency selectivity in the chinchilla,'' J. Acoust. Soc. Am. **92**, 2636–2649.

Okanoya, K., and Dooling, R. J. (**1987**). ''Hearing in passerine and psittacine birds: A comparative study of masked and absolute auditory thresholds,'' J. Comp. Psych. **101**, 7–15.

Okanoya, K., and Dooling, R. J. (**1990**). ''Detection of gaps in noise by budgerigars (*Melopsittacus undulatus*) and zebra finches (*Poephila guttata*),'' Hearing Res. **50**, 175–184.

Peterson, G. E., and Barney, H. L. (**1952**). ''Control methods in the study of vowels,'' J. Acoust. Soc. Am. **24**, 175–184.

Pick, G. F. (**1980**). ''Level dependence of psychophysical frequency resolution and auditory filter shape,'' J. Acoust. Soc. Am. **69**, 1085–1095.

Pickles, J. O. (**1979**). ''Psychophysical frequency resolution in the cat as determined by simultaneous masking and its relation to auditory-nerve resolution,'' J. Acoust. Soc. Am. **66**, 1725–1732.

Saunders, J. C., Rintelmann, W. F., and Bock, G. R. (**1979**). ''Frequency selectivity in bird and man: A comparison among critical ratios, critical bands, and psychophysical tuning curves,'' Hearing Res. **1**, 303–323.

Shamma, S. A., and Versnel, H. (**1995**). ''Ripple analysis in ferret primary auditory cortex II. Prediction of unit responses to arbitrary spectral profiles,'' Aud. Neurosci. **1**, 255–270.

Shamma, S. A., Versnel, H., and Kowalski, N. (**1995**). ''Ripple analysis in ferret primary auditory cortex I. Response characteristics of single units to sinusoidally rippled spectra,'' Aud. Neurosci. **1**, 233–254.

Shofner, W. P. (**1991**). ''Temporal representation of rippled noise in the anteroventral cochlear nucleus of the chinchilla,'' J. Acoust. Soc. Am. **90**, 2450–2466.

Shofner, W. P., and Yost, W. A. (**1994**). ''Repetition pitch: auditory processing of rippled noise in the chinchilla,'' 10th International Symposium on Hearing, Irsec, Bavaria, Germany, 26 June–1 July.

Shofner, W. P., and Yost, W. A. (**1995**). ''Discrimination of rippled-spectrum noise from flat-spectrum wideband noise by chinchillas,'' Aud. Neurosci. **1**, 127–138.

Shreiner, C. E., and Calhoun, B. M. (**1995**). ''Spectral envelope coding in cat primary auditory cortex,'' Aud. Neurosci. **1**, 39–61.

Simmons, A. M., and Buxbaum, R. C. (**1996**). ''Neural codes for 'pitch' processing in a unique vertebrate auditory system,'' in *Neuroethological Studies of Cognitive and Perceptual Processes*, edited by C. F. Moss and S. J. Shettleworth (Westview, Boulder, CO), pp. 185–228.

Sinnott, J. M. (**1989**). ''Detection and discrimination of synthetic English vowels by Old World monkeys (*Cercopithecus, Macaca*) and humans,'' J. Acoust. Soc. Am. **86**, 557–565.

Summers, V., and Leek, M. R. (**1994**). ''The internal representation of spectral contrast in hearing-impaired listeners,'' J. Acoust. Soc. Am. **95**, 3518–3528.

Theunissen, F. E., and Doupe, A. J. (**1998**). ''Temporal and spectral sensitivity of complex auditory neurons in the nucleus Hvc of male zebra finches,'' J. Neurosci. **18**, 3786–3802.

van Veen, T. M., and Houtgast, T. (**1985**). ''Spectral sharpness and vowel dissimilarity,'' J. Acoust. Soc. Am. **77**, 628–634.

Versnel, H., Kowalski, N., and Shamma, S. A. (**1995**). ''Ripple analysis in ferret primary auditory cortex. III. Topographic distribution of ripple response parameters,'' Aud. Neurosci. **1**, 271–285.

Yost, W. A., and Hill, R. (**1978**). ''Strength of pitches associated with ripple noise,'' J. Acoust. Soc. Am. **64**, 485–492.

Yost, W. A., Hill, R., and Perez-Falcon, T. (**1978**). ''Pitch and pitch discrimination of broadband signals with rippled power spectra,'' J. Acoust. Soc. Am. **63**, 1166–1173.

Yost, W. A., Patterson, R., and Sheft, S. (**1996**). ''A time domain description for the pitch strength of iterated rippled noise,'' J. Acoust. Soc. Am. **99**, 1066–1078.

Yost, W. A. (**1996**). ''Pitch of iterated rippled noise,'' J. Acoust. Soc. Am. **100**, 511–518.

LETTERS TO THE EDITOR

This Letters section is for publishing (a) brief acoustical research or applied acoustical reports, (b) comments on articles or letters previously published in this Journal, and (c) a reply by the article author to criticism by the Letter author in (b). Extensive reports should be submitted as articles, not in a letter series. Letters are peer-reviewed on the same basis as articles, but usually require less review time before acceptance. Letters cannot exceed four printed pages (approximately 3000–4000 words) including figures, tables, references, and a required abstract of about 100 words.

On the lowest radial frequencies of a rigid-walled narrow toroidal duct

H. P. W. Gottlieb[a]

Faculty of Science, Griffith University, Nathan, Queensland 4111, Australia

For a rigid-walled toroidal duct of rectangular cross section, narrow in the radial direction, the lowest radial characteristic frequency approximation appears to form a sequence proportional to the angular wave number integer [C. C. Lawrenson, L. D. Lafleur, and F. D. Shields, ''The solution for the propagation of sound in a toroidal waveguide with driven walls (the acoustitron),'' J. Acoust. Soc. Am. **103**, 1253–1260 (1998)]. By use of properties of Bessel functions, a more accurate higher-order formula for these frequencies is presented which, moreover, shows that there is, in fact, some deviation from the strict harmonicity. © *1999 Acoustical Society of America.* [S0001-4966(99)04203-4]

INTRODUCTION

Before dealing with the acoustics of a rectangular cross-sectioned toroidal waveguide with driven walls, Lawrenson *et al.*[1] first considered the modal frequencies with the rigid wall condition, and dealt explicitly with the case of a narrow toroidal duct with width much less than the radius. Although their results are correct to first order in the relative radial difference, their formulas could be expressed more naturally. Furthermore, it turns out that the apparent direct proportionality to angular wave number found in Ref. 1 is not maintained at higher orders. In this paper, we elaborate upon these features in terms of the properties of the exceptional zeros of cross products of derivatives of Bessel functions which arise from the characteristic equation for the radial frequencies with Neumann boundary conditions, and present higher-order corrections for the frequencies.

I. BACKGROUND

The toroidal duct occupies the region specified in terms of cylindrical polar coordinates r, θ, z by $0 < a \leq r \leq b$, $0 \leq \theta \leq 2\pi$, and $0 \leq z \leq h$. Following Ref. 1, the characteristic radian frequency for rigid walls, resulting from the solution of the wave equation for the velocity potential with sound speed c, is given by

$$\omega_{mnp} = c \sqrt{\left(\frac{\beta_{mp}}{a}\right)^2 + \left(\frac{n\pi}{h}\right)^2}, \tag{1}$$

where $n = 0, \pm 1, \pm 2, \ldots$ is the axial wave number (referring to the z direction), $m = 0, 1, 2, \ldots$ is the angular or azimuthal wave number (referring to the θ direction), and p is a radial number (integer, referring to the r direction) which labels the successive roots of the characteristic equation

$$J'_m(\beta) Y'_m((1+\varepsilon)\beta) - J'_m((1+\varepsilon)\beta) Y'_m(\beta) = 0 \tag{2}$$

whose roots are β_{mp}. Here, J_m and Y_m are the Bessel functions of the first and second kind, and $\varepsilon = (b-a)/a > 0$ is the relative radius difference.

For a *narrow* (in the radial direction) toroid, i.e., $\varepsilon \ll 1$, Lawrenson *et al.*[1] then expanded the Bessel functions in Eq. (2), ignoring terms of order ε^2, to obtain the approximated formulas

$$\beta \approx m \sqrt{\frac{2-3\varepsilon}{2-\varepsilon}}; \tag{3}$$

$$\omega_{mn} \approx c \sqrt{\left(\frac{m}{a}\right)^2 \left(\frac{2-3\varepsilon}{2-\varepsilon}\right) + \left(\frac{n\pi}{h}\right)^2}; \tag{4}$$

and hence, for $n = 0$ (i.e., no z dependence), to first order in ε,

$$\omega_m \approx \frac{mc}{a}\left(1 - \frac{1}{2}\varepsilon\right). \tag{5}$$

We now derive more accurate formulas for Eqs. (3)–(5) and discuss them.

[a]Electronic mail: h.gottlieb@sct.gu.edu.au

II. IMPROVED FORMULAS

It should first of all be noted that Eq. (5), to first order in ε, only gives (for $m \neq 0$) the lowest, in fact "exponential," root of Eq. (2). There are other, higher, roots not obtained by this method: they are given by an asymptotic formula of a type due to McMahon[2] (see references cited in Ref. 3) and they tend to infinity as ε tends to zero. Thus it is convenient to label the exceptional root, which tends to m as ε tends to zero, by an index $p = 0'$ (where the prime indicates that the corresponding radial function is not constant). Then the standard McMahon-type roots correspond to $p = 1, 2, \ldots$; they are not under discussion here.

For the exceptional roots, which are of central interest here as being the lowest root for each $m \neq 0$, we use a procedure similar to that of Ref. 3, which dealt with the case of spherical Bessel functions. Here, the ordinary Bessel functions J_m and Y_m satisfy Bessel's differential equation

$$J_m''(X) = -\frac{1}{X}J_m'(X) + \left[\frac{m^2}{X^2} - 1\right]J_m(X) \tag{6}$$

and have Wronskian value given by[4]

$$W(X) \equiv J_m(X)Y_m'(X) - J_m'(X)Y_m(X) = \frac{2}{\pi X}. \tag{7}$$

We may now make a Taylor series expansion of the whole entity on the left-hand side of Eq. (2), for small ε, and use Eqs. (6) and (7) and their differentiations, and eventually obtain, for $m \neq 0$,

$$\frac{\beta^2 - m^2}{m^2} = -\varepsilon + \frac{5}{6}\varepsilon^2 - \frac{2}{3}\varepsilon^3 + \frac{16 - m^2}{30}\varepsilon^4 + O(\varepsilon^5). \tag{8}$$

Then from a Taylor expansion of the square root expression obtained from Eq. (8), β is found to be

$$\beta = m\left[1 - \frac{1}{2}\varepsilon + \frac{7}{24}\varepsilon^2 - \frac{3}{16}\varepsilon^3 + \frac{751 - 96m^2}{5760}\varepsilon^4\right] + O(\varepsilon^5). \tag{9}$$

(This result, in fact, holds for any real $m \neq 0$, not just integer values. The first three terms only, up to second order in ε, have been reported in Ref. 5.) This series (9) agrees, up to the order given, with an expression eventually obtainable by recasting a result of Buchholtz[6] whose expansion is, however, for β^{-1} and which involves not ε but even powers of $(\gamma^{1/2} - \gamma^{-1/2})$, where $\gamma = 1 + \varepsilon = b/a$ in the above context. Equation (9) is much more useful for purposes such as that considered here.

In view of Eq. (8), Eq. (3) above [which is Eq. (12) appearing in Ref. 1] might more simply and naturally be written as

$$\beta_{m0'} \approx m\sqrt{1 - \varepsilon}, \tag{10}$$

and Eq. (4) above [which is Eq. (13) in Ref. 1] as

$$\omega_{mn0'} \approx c\sqrt{\left(\frac{m}{a}\right)^2(1 - \varepsilon) + \left(\frac{n\pi}{h}\right)^2}. \tag{11}$$

TABLE I. Values of lowest solution β to Eq. (2) with $m = 1$: approximations from Eq. (9) for various orders in ε, and exact values.

	ε			
	0.01	0.05	0.1	0.5
1st	0.995	0.975	0.95	0.75
2nd	0.995 029	0.975 729	0.952 917	0.822 917
3rd	0.995 029	0.975 706	0.952 729	0.799 479
4th	0.995 029	0.975 706	0.952 741	0.806 586
Exact	0.995 029	0.975 706	0.952 740	0.805 092

To first order in ε, Eq. (5) above [i.e., Eq. (14) of Ref. 1] remains the same, although perhaps following more transparently from Eq. (11) with $n = 0$:

$$\omega_{m00'} \approx \frac{mc}{a}\left(1 - \frac{1}{2}\varepsilon\right). \tag{12}$$

By Eq. (8), a more accurate expression for the frequencies given approximately by Eq. (11) is

$$\omega_{mn0'}$$
$$\approx c\sqrt{\left(\frac{m}{a}\right)^2\left[1 - \varepsilon + \frac{5}{6}\varepsilon^2 - \frac{2}{3}\varepsilon^3 + \frac{16 - m^2}{30}\varepsilon^4\right] + \left(\frac{n\pi}{h}\right)^2}. \tag{13}$$

By Eq. (9), a more accurate expression for the lowest radial frequencies ($n = 0$, $p = 0'$), extending Eq. (12), is

$$\omega_{m00'} \approx \frac{mc}{a}\left(1 - \frac{1}{2}\varepsilon + \frac{7}{24}\varepsilon^2 - \frac{3}{16}\varepsilon^3 + \frac{751 - 96m^2}{5760}\varepsilon^4\right). \tag{14}$$

This is, of course, not obtainable from Eq. (10) or Eq. (3).

III. NUMERICAL EXAMPLES

Table I shows the effects on the lowest solution of the characteristic equation (2) of including increasing orders of ε in the approximation (9), i.e., on the fundamental frequency via Eq. (14), for several values of ε. Also tabulated are the corresponding exact values obtained using Maple V®. It can be seen that for very small ε the first-order approximation is actually quite good, but higher-order approximations improve matters. (In fact, for $\varepsilon = 0.01$ the fourth-order approximation agrees with the exact solution up to 11 significant figures.) As ε increases above about 0.1, the higher approximations are needed for good agreement.

Table II contains ratios of exact lowest solution to Bessel function order (angular number), i.e., β/m, arising

TABLE II. Variation with respect to order m of ratio of exact lowest solution to Bessel function order, β/m, for Eq. (2).

m	ε			
	0.01	0.05	0.1	0.5
1	0.995 029	0.975 706	0.952 740	0.805 092
5	0.995 029	0.975 704	0.952 709	0.796 860
10	0.995 029	0.975 697	0.952 610	0.775 972

from Eq. (2), for increasing m values. This table shows that, while proportionality to m is quite good for small ε, there is a loss of this harmonicity as ε increases.

IV. DISCUSSION

Equation (14) gives higher-order corrections, in powers of $\varepsilon = (b/a) - 1$, to Eq. (5), i.e., to Eq. (14) of Ref. 1, obtained in solving Eq. (2) for the z-independent modes. As pointed out in Ref. 1, when the toroidal walls are driven, there will be pressure response peaks corresponding to the characteristic frequencies of the toroid with rigid walls, as determined above, so our Eqs. (13) and (14) may become important.

Arguments were presented at several points in Ref. 1 concerning an integral number m of wavelengths along the "center" or average circumference of the toroid, equal to $\pi(a+b)$, for large wavelengths, i.e., small width ε. Because the coefficient of the second-order term in Eq. (14) is positive, the first-order approximation (5) systematically underestimates $\omega_{m00'}$ for small ε, i.e., the actual frequency is higher. Physically, this could be interpreted as the duct having an effective circumference which is somewhat less than that of the equivalent straight duct.

Finally, our Eq. (14) shows that there is not, in fact, strict proportionality to angular wave number m of the n =0 frequencies, there being corrections to Eq. (12) consisting not merely of higher terms in ε with constant coefficients but also eventually depending on m itself, although, intriguingly, this does not become apparent until the coefficient of the fourth-order term in ε. It should be noted that coefficients of higher-order terms depending on m may lead to non-negligible contributions to the expansion for moderate or large m values, but in any case the exact solutions in Table II show that this inharmonicity increases as ε increases. It would be interesting to know whether this effect could be discerned in experiments.

[1] C. C. Lawrenson, L. D. Lafleur, and F. D. Shields, "The solution for the propagation of sound in a toroidal waveguide with driven walls (the acoustitron)," J. Acoust. Soc. Am. **103**, 1253–1260 (1998).

[2] J. McMahon, "On the roots of the Bessel and certain related functions," Ann. Math. **9**, 23–40 (1894-95).

[3] H. P. W. Gottlieb, "On the exceptional zeros of cross-products of derivatives of spherical Bessel functions," ZAMP **36**, 491–494 (1985).

[4] G. Arfken, *Mathematical Methods for Physicists* (Academic, Orlando, 1985), 3rd ed., Chap. 11.

[5] H. P. W. Gottlieb, "Eigenvalues of the Laplacian with Neumann boundary conditions," J. Aust. Math. Soc. B, Appl. Math. **26**, 293–309 (1985).

[6] H. Buchholz, "Besondere Reihenentwicklungen für eine häufig vorkommende zweireihige Determinante mit Zylinderfunktionen und ihre Nullstellen," Z. Angew. Math. Mech. **29**, 356–367 (1949).

Deduction of ground impedance from measurements of excess attenuation spectra

Shahram Taherzadeh and Keith Attenborough[a)]

Engineering Mechanics Discipline, Faculty of Technology, The Open University, Milton Keynes MK7 6AA, England

An efficient numerical method of deducing ground-surface impedance from measurements of short-range propagation from a point source is proposed. The method involves finding the root of a complex equation and uses the fact that the classical approximation for the spherical wave-reflection coefficient near grazing incidence is an analytic function of the impedance. Examples of fitting measured excess-attenuation spectra are given. Methods for ensuring the uniqueness of the resulting impedance fits are discussed. Subsequent deductions of parameters in a two-parameter impedance model are also considered and exemplified. © *1999 Acoustical Society of America.* [S0001-4966(99)01603-3]

PACS numbers: 43.28.En [LCS]

INTRODUCTION

Knowledge of ground-surface impedance is important for accurate prediction of sound propagation outdoors. Sampling soils for subsequent application of standard acoustical laboratory techniques[1] is time consuming and difficult. The acts of sampling and transport to the laboratory can alter the characteristics of the sampled ground. Although the impedance tube has been used outdoors *in situ*, it is intrusive and relatively laborious. Less intrusive *in situ* methods have been devised. These include (a) indirect deduction of impedance from (plane-wave) reflection coefficient,[2] and (b) deduction of physical parameters such as flow resistivity by fitting impedance models either to short-range measurements of excess attenuation or to the level difference between vertically separated microphones.[3–8] The deduction of parameters is of particular interest to acoustical monitoring of soils. The fitting of excess-attenuation or level-difference spectra, obtained near grazing incidence, is achieved by means of the classical theory for propagation from a point source over an impedance plane. As well as not requiring the assumption of plane waves, which is valid only at sufficient source height and near normal incidence, the short-range propagation method also includes effects of small-scale surface roughness which may be considered to produce an effective impedance.[9]

An ANSI working group has proposed a standard method based on fitting measurements to templates of theoretical excess-attenuation or level-difference spectra.[10] These templates are based on the likely range of ground-surface parameters and the resulting variation in excess-attenuation or level-difference spectra predicted according to various impedance models. It is noted in the draft standard that, in the context of predicting outdoor sound, it would be preferable to deduce impedance directly, since the result would be independent of the adequacy of any particular impedance model. A method of direct-impedance deduction has been proposed based on two-dimensional minimization of the difference between data and theory at each frequency.[11] This requires considerable computation and is rather inefficient. After reviewing the two-dimensional minimization technique, we propose an alternative numerical method based on root finding. The proposed technique takes advantage of the fact that the classical approximation to the spherical wave-reflection coefficient is an analytic function of the impedance. The resulting savings in computation time can be up to 100-fold without any loss in accuracy. In addition, we revise problems of nonuniqueness in the context of the new technique. Some examples of excess-attenuation fitting are given. Finally, least-squares algorithms for subsequent fitting of impedance models are explored.

I. DIRECT DEDUCTION OF IMPEDANCE

A. Minimization method

The first step in direct-impedance deduction is to calculate the spherical reflection coefficient (Q) from measuring excess-attenuation spectra of sound at short ranges. The next step is to search for a theoretical value of the impedance that best fits the measured Q at each frequency point. This search can be accomplished, as in Ref. 11, by minimizing the following complex function (or some power of it) with variables being the real and imaginary parts of the impedance:

$$\Gamma(\beta, f) = Q(\beta, f) - Q_{\text{measured}}, \tag{1}$$

where β is the admittance (inverse of the impedance) and f is the frequency, with

$$Q = R_p + (1 - R_p) F(w), \tag{2}$$

$$R_p = \frac{\cos\theta - \beta}{\cos\theta + \beta}, \tag{3}$$

$$F(w) = 1 + i\pi^{1/2} w e^{-w^2} \text{erfc}(-iw), \tag{4}$$

$$w = \sqrt{\tfrac{1}{2} i k R_2}(\cos\theta + \beta). \tag{5}$$

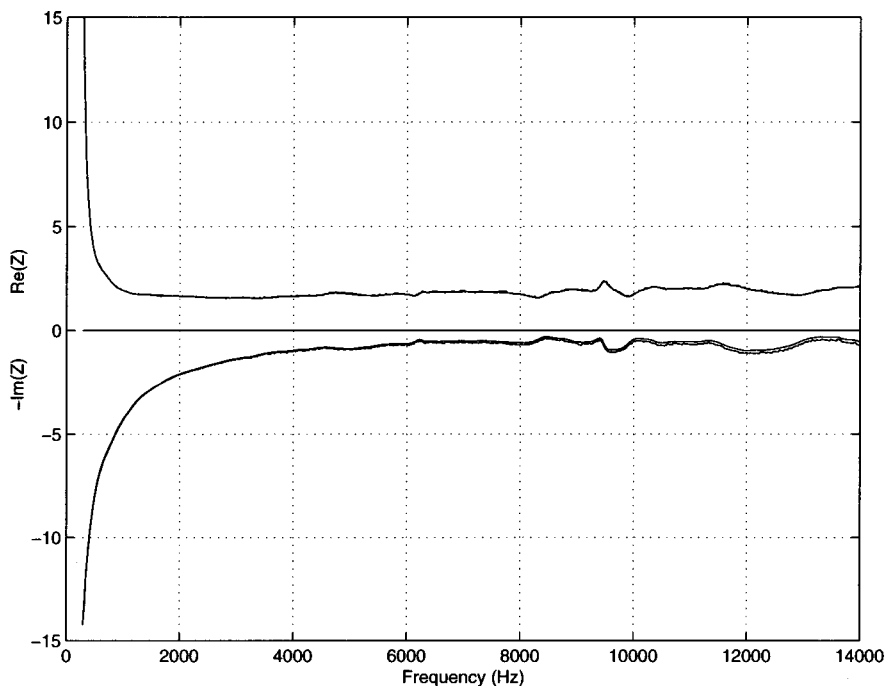[a)]Author to whom all correspondence should be addressed.

FIG. 1. Deduced normalized impedance of sand. The impedance was deduced from the measurement of the excess-attenuation spectra using a minimization method and the proposed root-finding method. The two impedance spectra are identical except at high frequencies, where a small deviation in the imaginary parts can be observed.

The terms Q, R_p, $F(w)$, and w are called the spherical-reflection coefficient, the plane-wave reflection coefficient, the boundary-loss factor, and the numerical distance, respectively. This requires a time-consuming multidimensional minimization procedure such as the simplex method.

B. Root-finding method

An alternative approach is to consider the equation

$$\Gamma(\beta) = 0. \tag{6}$$

Since Q is an analytical function of w (itself a function of β) and therefore has a continuous derivative, a simple and efficient solution technique such as the Newton–Raphson method can be used. In the Newton–Raphson method, a ''better'' approximation, say x_1, to the solution of $\Gamma(x)$ can be obtained from

$$x_1 - x_0 = \delta x = -\frac{\Gamma(x_0)}{\Gamma'(x_0)}, \tag{7}$$

where x_0 is an initial approximation and the prime denotes differentiation with respect to the argument. A final solution is obtained by iterating Eq. (7) until a desired accuracy is achieved. Hence, in our case

$$\delta\beta = -\frac{\Gamma(\beta)}{d\Gamma/d\beta}, \tag{8}$$

where reference to f has been dropped for brevity. Q may be rewritten as

$$Q = 1 + 2(w - \tau\cos\theta)[i\sqrt{\pi}W(w)], \tag{9}$$

with

$$W(w) = e^{-w^2}\,\mathrm{erfc}(-iw), \tag{10}$$

and

$$\tau = \sqrt{\tfrac{1}{2}ikR_2}. \tag{11}$$

The function $W(z)$ and its derivative have been defined in equations 7.1.3 and 7.1.20 of Ref. 12. The derivative term required in (8) may be obtained for each frequency from

$$\frac{d\Gamma}{d\beta} = \frac{dQ}{dw}\cdot\frac{dw}{d\beta}$$
$$= 2\tau[i\sqrt{\pi}W(w) - 2(w - \tau\cos\theta)(1 + i\sqrt{\pi}wW(w))]. \tag{12}$$

Less than ten iterations are needed to find the required answer in most cases of interest. This method is far more efficient than the two-dimensional minimization technique suggested in Ref. 11 and can be performed in ''real time'' on desktop computers. The best starting estimate for admittance is zero at low frequencies (<500 Hz). This suggests that the search should begin at the low end of the frequency spectrum and with a starting value of zero. For subsequent frequency points, the best ''guess'' is the best-fit admittance at the previous frequency point.

Figure 1 shows impedances as a function of frequency derived from excess attenuation data (Ref. 11, Fig. 4) using both a 2-D minimization and the Newton–Raphson method. In this particular example, the minimization method is that denoted as method I in Ref. 11. As can be seen, the impedance determined by the two methods is almost identical except for a small deviation in the imaginary parts at higher frequencies. The computation time, on a PC, is about 2 h for the minimization method, and less than 1 min for the technique proposed here.

A second example of the proposed impedance-deduction technique is based on a set of three short-range excess-attenuation spectra measured above a sand surface. The grazing angles for the measurements are 11.3°, 21.8°, and 31.0°. Figure 2(a) and (b) show the measured excess-attenuation spectra and the fitted specific-surface impedance, respectively, from all three geometries. If one then applies the de-
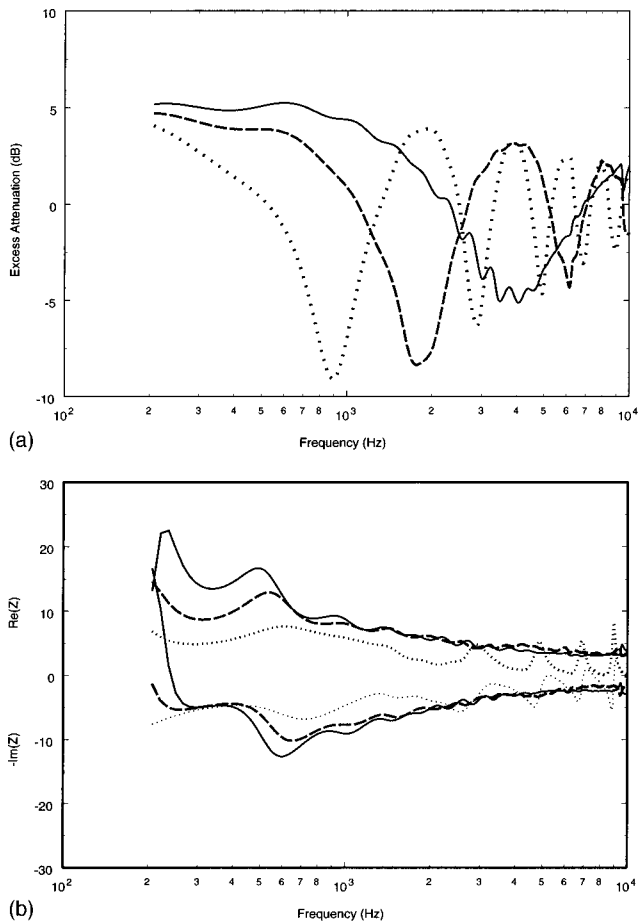
(a)

(b)

FIG. 2. Measured excess-attenuation spectra (a) and the corresponding deduced normalized impedance (b) of a sand surface. Solid line: source and receiver heights 0.1 m (grazing angle 11.3 deg); dashed line: 0.2 m (21.8 deg) and the dotted line: 0.3 m (31.0 deg). The horizontal separation in all three cases was 1.0 m. At frequencies below 300 Hz, the source output was below the background noise; hence, the deviation from the expected values.

rived impedance values in the theoretical expressions for the excess attenuation, one arrives at exactly the same excess-attenuation curve (to the width of the line). It is seen that the deduced impedance from the measurements at the lowest grazing angles of 11.3° and 21.8° are consistent, while the third measurement (at the largest grazing angle) results in a different set of values. This can be attributed to the fact that at grazing angles greater than about 25°–30° the spectrum is less sensitive to the ground impedance and is determined mainly by the geometrical path difference between the direct and the reflected ray paths.[13]

C. Uniqueness of the solution

Under certain circumstances, more than one value of admittance can give the same value for the spherical wave-reflection coefficient. This gives rise to the problem of choosing the right solution. An example is shown in Fig. 3, where a 2-D surface of $|\Gamma(\beta)|$ is drawn with x and y axes being the real and imaginary parts of the admittance. The frequency is 500 Hz, the source and receiver heights are at 0.03 m, and their horizontal separation is 1.0 m. Apart from the "true" solution near the origin at $(0.1-0.25i)$, there is a "rogue" solution (or minimum) near $(0.05-4.5i)$. Any nu-
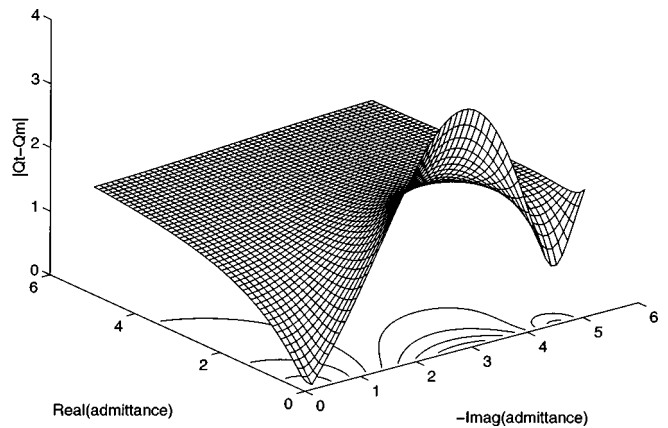

FIG. 3. The magnitude of the difference between the measured and theoretical spherical-reflection coefficient plotted against the real and imaginary parts of the normalized admittance at 500 Hz. The true minimum is the one near the origin.

merical impedance-fitting routine would home in on the rogue solution from a wrong starting point. Moreover, it should be noted that neither solution could be discounted on physical grounds.

However, the position of the rogue minimum is dependent on the geometry of the system (i.e., source and/or receiver heights) while the true solution is not [see, for example, Fig. 2(b)]. Therefore, it is important to have at least two measurements of excess-attenuation spectra with differing source and/or receiver positions to verify a true value of the admittance.

II. PARAMETER DEDUCTION

In this section, having obtained the specific surface impedance as a function of frequency, the possibility of fitting an impedance model to the impedance data is investigated. Once again, the emphasis is on speed and efficiency. The impedance model chosen here for fitting purpose is a two-parameter model.[14,15] This model has been shown to give good agreement with data taken both indoors and outdoors. It is given by

$$Z=\frac{1+i}{\sqrt{\pi\gamma\rho}}\sqrt{\frac{\sigma_e}{f}}+\frac{ic_0\alpha_e}{8\pi\gamma f}, \qquad (13)$$

where $\sigma_e=s_p^2\sigma/\Omega$ and $\alpha_e=(n'+2)\alpha/\Omega$; σ, Ω, α, s_p, and n' are the flow resistivity and porosity at the surface, the rate of change of porosity with depth, the pore shape factor, and the grain shape factor, respectively. The two adjustable parameters are σ_e and α_e. This model has the added advantage that the real and imaginary parts of the impedance have a simple power dependence on frequency so that a least-squares fitting can be used

$$\mathrm{Re}(Z)=Af^{-1/2}, \qquad (14a)$$

$$\mathrm{Im}(Z)-\mathrm{Re}(Z)=Bf^{-1}, \qquad (14b)$$

where A depends on σ_e and B on α_e [see Eq. (13)]. A simple Gaussian least-squares fitting of the two parts of impedance should yield estimates for σ_e and α_e. The resultant values will depend strongly on the range of frequencies used in the

TABLE I. List of best-fit parameters using the two-parameter impedance model. The frequency range indicates the range at which the least-squares fitting was implemented.

Data	Grazing angle (deg)	Frequency range (Hz)	σ_e (Nsm^{-4})	α_e (m^{-1})
1	11.3	1 k–10 k	265 000	175
2	21.8	800–1 k	280 000	141
Average			**272 500**	**158**

fitting. Since the ground-effect minimum is most sensitive to the changes in the parameters, the best choice would be the frequency range that encompasses the first ground-effect minimum and excludes very low and high frequencies.

As an example, the values of the impedance of a sandy ground deduced in Sec. I. B and given in Fig. 2, are used. Making use of Eqs. (14a) and (14b) and the impedance model given in Eq. (13), one arrives at the best-fit values given in Table I. It is seen that the deduced parameter values from the two nearest grazing measurements are very close. Figure 4 shows the measured and best-fit excess-attenuation spectra with parameter values given in Table I. Although the fit is acceptable, there is room for improvement at the higher frequencies. The frequency range for the fitting process was chosen so that it would include the first minimum only.
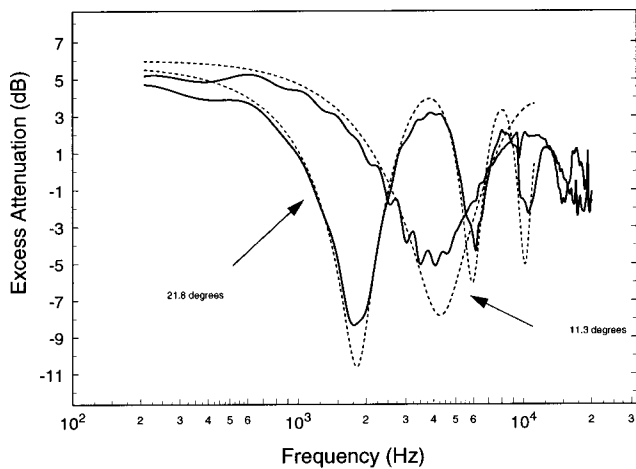

FIG. 4. Measured and predicted excess-attenuation spectra for the two source and receiver heights specified for Fig. 2(a). The prediction was obtained by least-squares best fit of the two-parameter impedance model to the deduced normalized impedance in Fig. 2(b). The solid lines represent the measured data with grazing angles of 11.3 and 21.8 deg and the broken lines are the predicted spectra. The values for the parameters are given in Table I.

III. CONCLUSION

An efficient procedure to deduce the specific surface impedance of ground directly from the measured excess-attenuation spectra has been proposed that allows real time determination of the impedance. It is shown that the proposed method is as accurate as the minimization methods suggested earlier, yet it is more efficient. Simple Gaussian least-squares fitting routines have been suggested to obtain ground parameters from the deduced-impedance spectra based on a two-parameter model.

[1] F. J. Fahy, ''Rapid method for the measurement of sample acoustic impedance in a standing wave tube,'' J. Sound Vib. **97(1)**, 168–170 (1984).

[2] A. J. Cramond and C. G. Don, ''Reflection of impulses as a method of determining acoustic impedance,'' J. Acoust. Soc. Am. **75**, 382–389 (1984).

[3] J. M. Sabatier, H. M. Hess, W. P. Arnott, K. Attenborough, M. J. M. Roemkens, and E. H. Grissinger, ''*In situ* measurements of soil physical properties by acoustical techniques,'' Soil Sci. Soc. Am. J. **54**, 658–672 (1990).

[4] H. M. Hess, K. Attenborough, and N. W. Heap, ''Ground characterisation by short-range propagation measurements,'' J. Acoust. Soc. Am. **87**, 1975–1986 (1990).

[5] C. Hutchinson-Howorth, K. Attenborough, and N. W. Heap, ''Indirect *in situ* and free-field measurement of impedance model parameters or surface impedance of porous layers,'' Appl. Acoust. **39**, 77–117 (1993).

[6] J. M. Sabatier, R. Raspet, and C. K. Frederickson, ''An improved procedure for the determination of ground parameters using level difference measurements,'' J. Acoust. Soc. Am. **94**, 396–399 (1993).

[7] R. Raspet and J. M. Sabatier, ''The surface impedance of grounds with exponential porosity profiles,'' J. Acoust. Soc. Am. **99**, 147–152 (1996).

[8] D. G. Albert, ''Acoustic waveform inversion with application to seasonal snow covers,'' J. Acoust. Soc. Am. (submitted for publication).

[9] K. Attenborough and S. Taherzadeh, ''Propagation from a point source over a rough finite impedance boundary,'' J. Acoust. Soc. Am. **98**, 1717–1722 (1995).

[10] ANSI Working Group S1/WG20 on Outdoor Impedance Measurement. (working draft) unpublished (1997).

[11] C. Nocke, T. Waters-Fuller, K. Attenborough, V. Mellert, and K. M. Li, ''Impedance deduction from broad-band, point-source measurements at grazing angles,'' Acust. Acta Acust. **83**, 1085–1090 (1997).

[12] M. Abramowitz and I. A. Stegun, *Handbook of Mathematical Functions* (Dover, New York, 1972).

[13] K. Attenborough, ''A note on short-range ground characterization,'' J. Acoust. Soc. Am. **95**, 3103–3108 (1994).

[14] K. Attenborough, ''Models for the acoustical properties of the air-saturated granular media,'' Acta Acust. **1**, 213–226 (1993).

[15] K. Attenborough, ''Ground parameter information for propagation modeling,'' J. Acoust. Soc. Am. **92**, 418–427 (1992).

Predicting the detectability of tones with unexpected durations

Huanping Dai

Boys Town National Research Hospital, 555 North 30th Street, Omaha, Nebraska 68131

Beverly A. Wright

Audiology and Hearing Sciences Program, 2299 North Campus Drive, Northwestern University, Evanston, Illinois 60208-3550

This letter supplies the predictions of the energy-detector model and two versions of the multiple-look model for detecting tones with unexpected durations. © *1999 Acoustical Society of America.* [S0001-4966(99)03603-6]

PACS numbers: 43.66.Ba, 43.66.Dc, 43.66.Mk [JWH]

INTRODUCTION

An auditory signal is detected better when its duration is expected than unexpected (Wright and Dai, 1994; Dai and Wright, 1995). This suggests that listeners detect signals through a temporal-integration window matched to the duration of the expected signal. Here, we report the predictions of the energy-detector and multiple-look models of signal detection (Green and Swets, 1966) for the detectability of *tonal* signals with unexpected durations, and compare those predictions to data we already reported (Dai and Wright, 1995). According to the energy-detector model, the listener makes one observation through a temporal window whose duration is matched to the expected signal duration and decides about the presence of the signal based on the energy within that single window (Green, 1960). The multiple-look model instead holds that the listener takes multiple short looks totaling the expected signal duration during each presentation interval, and statistically combines the information from those looks to decide about the signal's presence (Viemeister and Wakefield, 1991).

We previously derived the predictions of both models for noise signals under the assumption of a matched temporal window (Dai and Wright, 1995). Due to the stochastic nature of the noise signals, the predictions of the two models are nearly identical, both giving a reasonably good description of the time-intensity trade—threshold as a function of signal duration—and detectability of signals with unexpected durations. We did not include predictions for *tonal* signals, because it was not clear then how to incorporate a matched temporal window into models of the time-intensity trade for tones. At the time, we knew that listeners use wider effective-listening bandwidths for short than for long tonal signals (van den Brink and Houtgast, 1990; Wright and Dai, 1994), but did not know the effective-listening bandwidth for every window duration. Thus, we believed we did not have all of the information necessary for applying the energy-detector model. Only subsequently did we realize that the time-intensity trade for tonal signals could be accounted for using an energy-detector model with a matched temporal window (Dai and Wright, 1996) given the following. First, listeners detect the signal based on the signal energy within a single fixed-width frequency channel, even though they may be monitoring multiple channels when the expected signal is short. Second, spectral splatter reduces the effective signal energy. That solution now allows us to derive the predictions of the energy-detector model for the detection of tones of unexpected duration.

Accounting for the time-intensity trade of tonal signals using the multiple-look model with a matched integration window remains problematic. This is because increasing d', and thus heavier weighting, for later looks is required to predict the time-intensity trade of tonal (Viemeister and Wakefield, 1991), but not noise (Dai and Wright, 1995), signals. Here, we also report the predictions of the multiple-look model for the detection of tones of unexpected duration using both weighting schemes.

The assumptions and steps involved in the calculations are described in Appendix A for the energy-detector model and Appendix B for the multiple-look model.

I. RESULTS AND DISCUSSION

Figure 1 shows the measured (circles; replotted from Fig. 1 in Dai and Wright, 1995) and predicted (lines) signal levels corresponding to pc=85% as a function of signal duration for three signal frequencies (panels). As observed by other investigators (e.g., Garner and Miller, 1947; Watson and Gengel, 1969; Gengel and Watson, 1971; Gengel, 1972; Gerken *et al.*, 1990; Dai and Wright, 1996), the slope of the measured time-intensity-trade function becomes shallower with increasing signal frequency, from about 11 dB per decade at 250 Hz to about 9 dB per decade at 4000 Hz. The predictions of the energy-detector model (solid lines) capture this trend, although the change in slope with frequency is somewhat overpredicted. Overall, the energy-detector predictions fit the data reasonably well; the root-mean-square (rms) error of 1.7 dB is close to the size of the measurement error. In contrast, the multiple-look model, assuming equal d' for all looks (dashed lines), underpredicts the slope of the time-intensity trade, more so at low than at high frequencies. The rms error of 3.7 dB is about twice that for the energy-detector model. For comparison, the equal-d' multiple-look model predicts the time-intensity trade for noise signals adequately (rms error of 0.77 dB; Dai and Wright, 1995). No
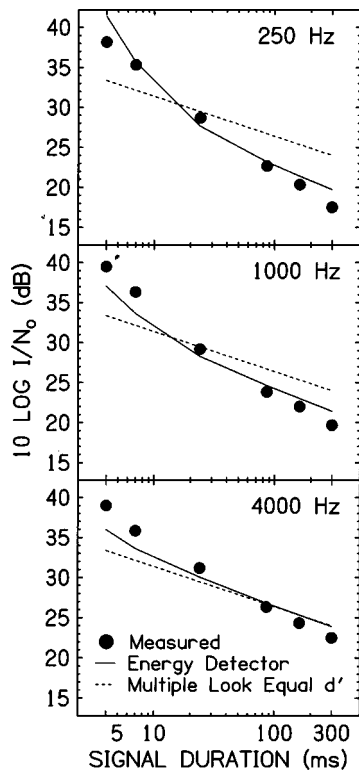
FIG. 1. Time-intensity trades. Measured (circles, from Dai and Wright, 1995) and predicted (solid lines for energy-detector model and dashed lines for equal-d' multiple-look model) signal levels corresponding to pc=85% as a function of signal duration at 250 Hz (top panel), 1000 Hz (middle panel), and 4000 Hz (bottom panel) when each duration is known and expected.
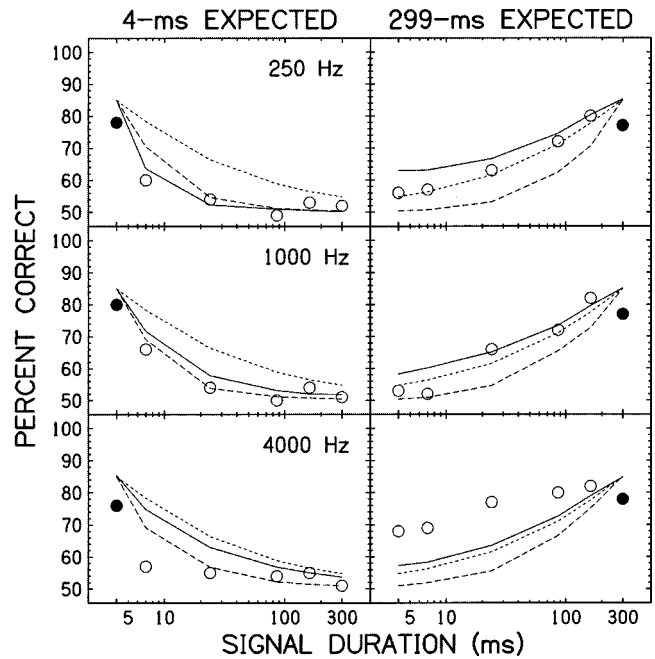

FIG. 2. Measured (filled circles for expected, and open circles for unexpected signal durations, from Dai and Wright, 1995) and predicted (solid lines for energy-detector model, short-dashed lines for equal-d', and long-dashed lines for unequal-d' multiple-look models) percent correct as a function of signal duration at three frequencies (rows) when the expected duration was 4 ms (left column) or 299 ms (right column).

predictions are shown for the multiple-look model using unequal weights because the d' weights are determined directly from the data for the time-intensity trade.

Plotted in Fig. 2 are the measured (circles; replotted from the mean panels of Fig. 2 in Dai and Wright, 1995) and predicted (lines) percent-correct values for expected (filled circles) and unexpected (open circles) signal durations at three signal frequencies (rows). With a few exceptions, signals with unexpected durations are less detectable than those with expected durations. Overall, signals with unexpected durations are less detectable when the expected duration is short (left column) than when it is long (right column). The greatest contrast occurs at 4000 Hz, where the mean percent correct calculated across all unexpected signals (open circles) was 54% when the expected duration was 4 ms, and 75% when the expected duration was 299 ms.

Unlike the data, which show frequency dependence only for the long expected duration, the energy-detector predictions (solid lines) depend on the signal frequency for both short and long expected durations. For the expected duration of 4 ms, the predicted percent correct decreases faster at lower than at higher frequencies as the signal duration departs from the expected duration. For the expected duration of 299 ms, the effect is greater at higher than at lower frequencies, which is opposite to the data. The mean rms errors between the data and the energy-detector predictions are 6% and 7% for the short and long expected durations, respectively.

The predictions of the equal-d' multiple-look model are independent of signal frequency (short-dashed lines). For the short expected duration, all the predicted percent-correct values are higher than the data. For the long expected duration, the predictions give adequate descriptions of the data at 250 and 1000 Hz, but fall below the data at 4000 Hz. The mean rms errors for percent correct between the data and the equal-d' multiple-look predictions are 10% for the short and 7% for the long expected durations.

When the d' of later looks is assumed to increase based on the data for the time-intensity trade (long-dashed lines), the predictions of the multiple-look model clearly improve for the data obtained with the short expected duration, but worsen for those obtained with the long expected duration. The mean rms errors are 6% for the short and 11% for the long expected durations.

In sum, both the energy-detector and multiple-look models explain, at least qualitatively, the reduced detectability of tones with unexpected durations. This is useful information because, unlike for noise signals (Dai and Wright, 1995), the predictions differ across each model version. Thus, these predictions for tonal signals had the potential to, but do not, provide a critical test of the models. It is worth noting that, with a coherent set of assumptions, the energy-detector model provides a reasonable prediction of the time-intensity trade for both tonal (here and Dai and Wright, 1996) and noise (Green, 1960; Dai and Wright, 1995) signals. The multiple-look model, however, requires different assumptions to explain the time-intensity trades for both tonal and noise signals. Consistency tips the scale in favor of the energy-detector model.

APPENDIX A: ENERGY-DETECTOR PREDICTIONS

We derive the energy-detector predictions of the time-intensity trade for tones (solid lines in Fig. 1) using the same basic procedure described by Dai and Wright (1996). The only notable difference is that the predicted signal levels correspond to 85%-correct responses here compared to 79%-correct responses in the earlier paper.

Now, we derive the energy-detector predictions for the detectability of tones with expected and unexpected durations (solid lines in Fig. 2). Let T be an ideal rectangular time window that matches the expected signal duration, let W be an ideal rectangular frequency window with the same equivalent-rectangular bandwidth (ERB) as the auditory filter $[W = 24.7((4.37f_c/1000)+1)$, Glasberg and Moore, 1990], and $E_{in}(t)$ be the actual energy of a signal of duration t. The effective signal energy, $E_{out}(t)$, is that part of $E_{in}(t)$ that falls within the time-frequency window defined by T and W. Two factors influence the relationship between $E_{in}(t)$ and $E_{out}(t)$ for signals of unexpected duration. First, short signals suffer an energy reduction due to spectral splatter. We correct this effect here, as in our previous paper on expected signal durations (Dai and Wright, 1996), by multiplying the signal spectrum with the Roex-filter-weighting function (Patterson and Moore, 1986). Second, signals with durations (t) longer than the expected duration (T) have their energy reduced by a factor of T/t. We obtain the percent correct for expected and unexpected signal durations by substituting $E_{out}(t)$ into the psychometric function for the expected signal duration.

APPENDIX B: MULTIPLE-LOOK PREDICTIONS

We follow the procedures described by Dai and Wright (1995) to derive the multiple-look predictions of the time-intensity trade for tones (dashed lines in Fig. 1) and the detectability of tonal signals of expected and unexpected duration (short-dashed lines in Fig. 2) under the assumption that all looks have equal d', and thus receive equal weight.

Now, we derive the multiple-look predictions for the detectability of signals with expected and unexpected durations, under the assumption that individual looks have different d', and thus receive different weights (long-dashed lines in Fig. 2). We adopt the same two assumptions used by Viemeister and Wakefield (1991). First, we assume that for each look $d_i' = k_i I$, where I is the signal intensity, and the value of k_i varies for different looks. Second, we assume that each look at the unexpected signal is weighted by the d' value associated with the same look in the expected signal. To avoid confusion, we denote D' for expected signals and d' for unexpected signals. Let t be the signal duration, T the expected duration, and τ the duration of a single look (4 ms).

Then, $n_T = T/\tau$ is the expected number of looks on each stimulus presentation. Following the second assumption, the decision statistic can be expressed as

$$z = \sum_{i=1}^{n_T} D_i' x_i, \qquad (B1)$$

where x_i represents the listener's estimate of the stimulus on the ith look.

When the signal is presented at the expected duration ($t = T$), the detectability is

$$D'(T) = \sqrt{\sum_{i=1}^{n_T} D_i'^2(T)} = I(T)\sqrt{\sum_{i=1}^{n_T} k_i^2}. \qquad (B2)$$

For our cases, $D'(T) = 1.47$ for each of the six signal durations, as confirmed for each signal duration when it was the only one presented (Dai and Wright, 1995).

When the expected duration was $T = 4$ ms, the detectability for an unexpected signal of duration t is simply $d_1'(t) = k_1 I(t)$. Since $k_1 = D'(T)/I(T)$, we have

$$d'(t) = D'(T)\frac{I(t)}{I(T)} \quad \text{for } t > T, \qquad (B3)$$

where $D'(T) = 1.47$, and $I(T)$ and $I(t)$ are the signal intensities from the time-intensity trade (Fig. 1) at the signal durations of $T = 4$ ms and t, respectively.

When the expected duration was $T = 299$ ms, the detectability for the unexpected signal of duration t is

$$d'(t) = \frac{\sum_{i=1}^{n_t} D_i'(T)d_i'(t)}{\sqrt{\sum_{i=1}^{n_t} D_i'(T)^2}} = D'(t)\frac{I(T)}{I(t)} \quad \text{for } t < T \quad (B4)$$

where $D'(t) = 1.47$ and $I(T)$ and $I(t)$ are the signal intensities from the time-intensity trade (Fig. 1) at the signal durations of $T = 299$ ms and t, respectively.

We apply Eqs. (B3) and (B4) at all six durations and three frequencies to obtain the d' values, which we then convert to percent-correct values and plot in Fig. 2.

Dai, H., and Wright, B. A. (**1995**). ''Detecting signals of unexpected or uncertain durations,'' J. Acoust. Soc. Am. **98**, 798–806.

Dai, H., and Wright, B. A. (**1996**). ''The lack of frequency dependence of threshold for short tones in continuous broadband noise,'' J. Acoust. Soc. Am. **100**, 467–472.

Garner, W. R., and Miller, G. A. (**1947**). ''The masked threshold of pure tones as a function of duration,'' J. Exp. Psychol. **37**, 293–303.

Gengel, R. W. (**1972**). ''Auditory temporal integration at relatively high masked-threshold levels,'' J. Acoust. Soc. Am. **51**, 1849–1851.

Gengel, R. W., and Watson, C. S. (**1971**). ''Temporal integration: I. Clinical implications of a laboratory study. II. Additional data from hearing impaired subjects,'' J. Speech Hear. Res. **36**, 213–224.

Gerken, G. M., Bhat, V. K. H., and Hutchison-Clutter, M. (**1990**). ''Auditory temporal integration and the power function model,'' J. Acoust. Soc. Am. **88**, 767–778.

Glasberg, B. R., and Moore, B. C. J. (**1990**). ''Derivation of auditory filter shapes from notched-noise data,'' Hearing Res. **47**, 103–138.

Green, D. M. (**1960**). ''Auditory detection of a noise signal,'' J. Acoust. Soc. Am. **32**, 121–131.

2045   J. Acoust. Soc. Am., Vol. 105, No. 3, March 1999

H. Dai and B. A. Wright: Letters to the Editor   2045

Green, D. M., and Swets, J. A. (**1966**). *Signal Detection Theory and Psychophysics* (Wiley, New York).

Patterson, R. D., and Moore, B. C. J. (**1986**). ''Auditory filters and excitation patterns as representations of frequency resolution,'' in *Frequency Selectivity in Hearing*, edited by B. C. J. Moore (Academic, New York), pp. 123–177.

van den Brink, W. A. C., and Houtgast, T. (**1990**). ''Spectro-temporal integration in signal detection,'' J. Acoust. Soc. Am. **88**, 1703–1711.

Viemeister, N. F., and Wakefield, G. H. (**1991**). ''Temporal integration and multiple looks,'' J. Acoust. Soc. Am. **90**, 858–865.

Watson, C. S., and Gengel, R. W. (**1969**). ''Signal duration and signal frequency in relation to auditory sensitivity,'' J. Acoust. Soc. Am. **46**, 989–997.

Wright, B. A., and Dai, H. (**1994**). ''Detection of unexpected tones with short and long durations,'' J. Acoust. Soc. Am. **95**, 931–938.

Comments on "Broadband spectra of seismic survey air-gun emissions, with reference to dolphin auditory thresholds" [J. Acoust. Soc. Am. 103, 2177–2184 (1998)]

S. H. Ridgway and D. A. Carder
SPAWARSYSCEN D3503 PLBS, San Diego, California 92152-6266

T. Kamolnick and C. E. Schlundt
SAIC Maritime Services, 3990 Old Town Avenue, San Diego, California 92110

W. Elsberry
Marine Acoustics Laboratory, Texas A&M University, Galveston, Texas 77551

M. Hastings
Department of Mechanical Engineering, Ohio State University, Columbus, Ohio 43210

Responses of marine mammals to human-generated sound are of interest due to concern for protection of animals with sensitive hearing from acoustic harassment or injury. Goold and Fish [J. Acoust. Soc. Am. **103**, 2177–2184 (1998)] compare their limited observations of wild common dolphins (*Delphinus delphis*) near operating seismic vessels off Wales, with studies of trained bottlenose dolphins (*Tursiops truncatus*) in San Diego Bay [Ridgway *et al.*, Tech. Rpt. 1751, NCCOSC RDTE (1997)]. Because of the considerable difference between numerous seismic pulses and the single 1-s tones employed by Ridgway *et al.*, the comparison is not valid. Further, Goold and Fish do not accurately represent the bottlenose dolphin responses. © *1999 Acoustical Society of America.* [S0001-4966(99)03903-X]

PACS numbers: 43.80.Lb, 43.80.Nd [WWLA]

INTRODUCTION

In their paper on broadband spectra of seismic survey air-gun emissions, with reference to dolphin auditory thresholds, Goold and Fish (1998) cite a preliminary laboratory technical report (Ridgway *et al.*, 1997). Concerning trained dolphins employed in the study, Goold and Fish say "captive dolphins cannot swim away and may be more tolerant through necessity!" This statement misleads the reader about the work of Ridgway *et al.* (1997) on dolphin responses to human-made sound. Further emphasis by an exclamation point for such a statement is extraordinary, and, in our experience, unprecedented in the Journal of the Acoustical Society of America. The use of the exclamation mark should be associated with authoritative certainty, whereas the mark mentioned above is an instance of ungrounded speculation.

A more complete report of the work reported by Ridgway *et al.* (1997) is being prepared for submission for a peer-reviewed publication; however, the technical report makes it clear that the trained dolphins could respond to sound by swimming away. Swimming away was one of the criteria for behavioral response to the sound. All of the audiograms cited in Goold and Fish (1998) were done with captive animals. There is no basis for the claim that the wild dolphins observed in the Goold and Fish report were more sensitive to sound.

The claim of increased sensitivity compared with animals in the Ridgway *et al.* (1997) report is not justified, in the first instance, because it is based on inadequate shipboard-observer data. The report gives no basis by which to evaluate how many dolphins approached nearer than 1 km to the seismic source. Goold and Fish do not quantify observer data in such a way as to produce accurate counts of animals in a given area (see Barlow, 1995; Schweder and Hagen, 1995, for methods required for accurate surveys).

To further confound their analysis, Goold and Fish use acoustic-field data from a March 1996 survey to correlate with some dolphin observations taken during an October 1994 survey. If the surveys were identical, why were the 1994 data not used? Without seeing the actual data, the reader must question the authors' assumption that the acoustic fields were identical, even if the surveys were operationally identical, because of the change in seasons. Different seasons can result in vast difference in sound propagation (see Rogers and Cox, 1988), especially within 10 m of the surface where the hydrophone array was located for this study.

I. INVALID SENSITIVITY COMPARISON—PULSE TO TONE BURST

In addition, the comparison with Ridgway *et al.* (1997) is not justified based on the considerable difference in the tone burst test sounds compared to seismic sources. Ridgway *et al.* tested the response of dolphins to tones of 1-s duration at frequencies of 3, 20, and 75 kHz, whereas the seismic sounds were broadband with peak frequencies below 1 kHz. In addition, Ridgway *et al.* tested only one loud sound each test day, while the seismic sources were repetitive.

Goold and Fish (1998) naively assume that human psychophysical measures, determined by testing human subjects in air, apply equally well to dolphins in water. Their entire

analysis is at least speculative. Anyone knowledgeable in psychophysics would not likely pick out a ''loudness level'' at a single frequency (i.e., 20 kHz) in a broadband sound and draw conclusions by comparing it to a pure-tone auditory threshold. Goold and Fish (1998) proceed to estimate loudness level in ''phons'' for dolphins. (In humans, perceived loudness in sones would be calculated based on critical bandwidth measures). Dolphin estimates plotted in their Fig. 5 indicate that all frequencies above about 400 Hz would be contributing roughly the same perceived loudness. As the authors acknowledge, very little is known about critical bandwidths in dolphins (Goold and Fish, 1998, second paragraph, p. 2183), and therefore they really cannot estimate perceived loudness, so how can they say anything about the thresholds presented by Ridgway et al., 1997? It is even possible that the dolphin's perceived loudness for an airgun array at 1 km under certain conditions might be greater than the 181-dB tone burst at 20 kHz that caused a behavioral response by dolphins studied by Ridgway et al. (1997).

Despite the marked difference in the types of sound studied, Goold and Fish infer that dolphins are disturbed by and avoid seismic sounds of 133 dB and claim that their observation ''suggests a far greater sensitivity to environmental noise than that presented in the Ridgway report.'' The controlled observations of Ridgway et al. (1997), on the other hand, showed that at 3 and 20 kHz, a 1-s tone had to be greater than 186 and 181 dB, respectively, at the dolphin before the tone burst produced a behavioral response indicative of avoidance in trained bottlenose dolphins.

Bottlenose dolphins tested by Ridgway et al. (1997) and common dolphins observed by Goold and Fish are from the same biological family, *Delphinidae*. The common dolphins that are the subjects of speculation by Goold and Fish (1998) are often seen at sea in large herds. Almost-constant whistling can usually be recorded from such herds (Moore and Ridgway, 1995; Evans, 1995). These whistles may have source levels as great as 170 dB at 1m, although the 155 dB cited by Goold and Fish (1998) as a private communication from J. D. Hall is a more usual upper-level whistle. The dolphin whistles are tonal and more similar to the sounds tested by Ridgway et al. (1997) than to the seismic sounds. For a tonal sound, the 133-dB level that Goold and Fish (1998) suggest is ''distressing'' for a dolphin could perhaps best be described in human terms as a ''conversational level.''

Barlow, J. (**1995**). ''The abundance of cetaceans in California waters Part I: Ship Surveys in Summer and fall of 1991,'' Fish. Bull. **93**, 1–14.

Evans, W. E. (**1994**). ''Common Dolphin, White-bellied Porpoise, *Delphinus delphis*,'' in *Handbook of Marine Mammals Volume 5, The First Book of Dolphins*, edited by S. H. Ridgway and R. J. Harrison (Academic, London), pp. 191–224.

Goold, J. C., and Fish, P. J. (**1998**). ''Broadband spectra of seismic survey air-gun emissions, with reference to dolphin auditory thresholds,'' J. Acoust. Soc. Am. **103**, 2177–2184.

Moore, S. E., and Ridgway, S. H. (**1995**). ''Whistles produced by common dolphins from the Southern California Bight,'' Aqua. Mamm. **21**, 55–63.

Ridgway, S. H., Carder, D., Smith, R., Kamolnick, T., Schlundt, C. E., and Elsberry, W. (**1997**). ''Behavioral Responses and Temporary Shift in Masked Hearing Threshold of Bottlenose Dolphins, *Tursiops truncatus*, to 1-Second Tones of 141 to 201 dB *re*: 1 μPa,'' Technical Report 1751, NCCOSC RDTE, San Diego, CA, p. 16.

Rogers, P. H., and Cox, M. (**1988**). ''Underwater Sound as a Biological Stimulus,'' in *Sensory Biology of Aquatic Animals*, edited by J. Atema, R. R. Fay, A. N. Popper, and W. N. Tavolga (Springer, New York), pp. 131–149.

Schweder, T., and Hagen, G. (**1995**). ''Effective search width in shipboard surveys of minke whales in the northeastern Atlantic: Concepts and methods,'' in *Whales, Seals, Fish, and Man*, edited by A. S. Blix, L. Walloe, and O. Ulltang (Elsevier, Amsterdam), pp. 13–25.

Response to "Comments on 'Broadband spectra of seismic survey air-gun emissions with reference to dolphin auditory thresholds'" [J. Acoust. Soc. Am. 105, 2047–2048 (1999)]

John C. Goold
*University of Wales Bangor, School of Ocean Sciences, Menai Bridge, Anglesey LL59 5EY,
United Kingdom*

Peter J. Fish
*University of Wales Bangor, School of Electronic Engineering and Computer Systems, Dean Street, Bangor,
Gwynedd LL57 1UT, United Kingdom*

In a prior paper, "Broadband spectra of seismic survey air-gun emissions with reference to dolphin auditory thresholds" [Goold and Fish, J. Acoust. Soc. Am. **103**, 2177–2184 (1998)] a comparison was drawn between the estimation of sound levels at a distance which unconstrained dolphins would appear to maintain from a seismic air-gun source and the sound threshold at which captive dolphins displayed behavioral changes as reported by Ridgway *et al.* [Tech. Rpt. 1751, NCCOSC RDTE (1997)]. This prompted comments in the letter above on the validity of the conclusions of the prior paper. In this rebuttal, it is pointed out that uncertainties in the sound levels estimated in the prior paper arising from uncertainties in distance estimation, sound-propagation model, frequency weighting, and allowance for pulse duration are most unlikely to account for the very large difference of 48 dB between Goold and Fish's results and Ridgway's. The differences in criteria for deciding the threshold—behavior suggesting distress in captive dolphins (Ridgway *et al.*) and the assumption that dolphins swim to a distance at which the sound is tolerated (Goold and Fish), is the most likely explanation for the difference in the published figures. © *1999 Acoustical Society of America.* [S0001-4966(99)04003-5]

PACS numbers: 43.80.Lb, 43.80.Nd [WWLA]

I. REBUTTAL

In our response to the letter of Ridgway *et al.*, it is worth noting that we were initially unaware of the technical report "Behavioral responses and temporary shift in masked hearing threshold of bottlenose dolphins, *Tursiops truncatus*, to 1-second tones of 141 to 201 dB *re* 1 μPa," by Ridgway *et al.* (1997), and were prompted to draw a comparison between our conclusions and those of this report by one of the referees for our paper, and were pleased to do so.

The concern behind our paper, "Broadband spectra of seismic survey air-gun emissions, with reference to dolphin auditory thresholds" (Goold and Fish, 1998), and central to Ridgway's report is that of limiting marine acoustic noise to acceptable levels; both have added to the store of knowledge on this subject and therefore should lead to a more informed debate by interested parties.

Bearing in mind the driving concern behind this type of work—that of determining suitable "do-not-exceed" levels for acoustic-emission devices in order to avoid harm to proximal marine mammal species—it is right that such a large difference (181 dB for behavioral changes and 193–196 dB for TTS reported by Ridgway and 133 dB reported in our paper) should be debated.

First, it is worth dealing with a few specific points raised in the letter above.

(1) "There is no basis for the claim that the wild dolphins observed in the Goold and Fish report were more sensitive to sound."

We did not make this *claim*—we *suggested* that captive dolphins having a different threshold to wild dolphins is "one possible explanation." This hypothesis is certainly worth testing.

(2) We relied on "inadequate shipboard-observer data."

Again, we acknowledged in our paper the uncertainty in estimating an avoidance distance. This uncertainty is simply not sufficient, whichever spreading model is used, to account for a difference in behavioral threshold of 48 dB.

(3) "To further confound their analysis, Goold and Fish use acoustic-field data from a March 1996 survey to correlate with some dolphin observations taken during an October 1994 survey. If the surveys were identical, why were the 1994 data not used?"

It was explained in our paper that seismic pulses were recorded only as a by-product of the dolphin survey during 1994, and gain levels were set at a level which clipped seismic signals recorded on tape until the source–receiver range typically reached 2.5 km. In addition, a 6-kHz high-pass filter stage had been used on both recording channels. We felt that the combination of these factors precluded a sensible analysis of 1994 seismic pulses, and this case was made in the discussion section of our paper. It was only during the 1996 seismic surveys that an informed attempt was made to record seismic pulses for analysis, during which there was negligible dolphin contact due to the seasonal nature of their occurrence in the southern Irish Sea.

(4) Our use of data and observations from different years lead to the possibility of differences in acoustic fields due to differences in sound propagation.

Once again, this is covered in the discussion section of our original paper. We make the point that the sea area under investigation does not undergo thermal stratification due to strong tidal mixing, and even if it were to stratify during the summer months, both our surveys were conducted in the autumn, when stratification would have broken down. Confirmation of a homogenous temperature/salinity profile was provided by a CTD cast, again referred to in our original paper.

(5) The use of measurement techniques used in human measurements and the comparison with measurements made at a single frequency.

One of the major points of our paper was to demonstrate that emissions from the air-gun source, which is normally considered a source of low-frequency acoustic emissions with negligible high-frequency components, could have a significant impact on dolphins at power levels at which the predominately low-frequency components would be expected to have little impact. This results from a rising sensitivity with frequency, which appears to compensate for the fall in source power with frequency. For such a perceived wideband signal, the use of frequency weighting similar to that used in humans (but making use of the best available data on the variation of hearing sensitivity with frequency for dolphins) is entirely appropriate. Again, the uncertainties in perceived sound level are most unlikely to account for the large difference in reported thresholds between ourselves and Ridgway *et al.* Contrary to the statement in Ridgway's letter, we do not ''pick out a 'loudness level' at a single frequency in a broadband sound'' but rather use the frequency weighting to calculate the power having an equivalent effect at a single frequency. In human environmental noise measurements, the reference frequency is 1 kHz when using the A-weighting curve— approximately 1/3 of the frequency of maximum sensitivity; we have taken a reference frequency of 20 kHz as being at about an equivalent position in the dolphin-sensitivity spectrum. The choice of reference frequency, however, is fairly arbitrary in both human and dolphin cases—choosing another frequency would lead to a different equivalent power level but a compensating shift in the reference-sensitivity level.

Our paper was concerned with exploring the possible use of frequency-weighted noise measurements similar to those used for assessing the impact of environmental noise on humans. It is acknowledged in the paper that there are greater uncertainties in the frequency variation of hearing sensitivity in dolphins than in the human case. Again, it is unlikely that this can explain such a large difference in behavioral threshold.

Just as in the human case, the use of frequency- (and duration) weighting has the potential advantage of allowing comparison between the effects of different ''noise'' sources. The uncertainties in some of the parameters required should not lead us to turn away from this methodology, but rather to research further to reduce these uncertainties and refine the method.

It is clear that by far the most likely explanation for the difference in results is the difference in testing conditions, and we should probably have discussed this in more detail in our paper, for which omission we apologize. In terms of setting allowable levels for acoustic-emission devices, choosing appropriate measures of environmental damage is important as well as ensuring accuracy of those measures.

The tests carried out by Ridgway and colleagues are concerned with measurement of behavioral changes and TTS. Typical behavioral changes observed in order to determine a behavioral-change threshold were:

''Attacked biteplate''
''Porpoised away from louder S1, swam in circles, broke station 5X''
''Reluctant station on S1, very skittish''
''Turned in direction opposite S2''
''Very reluctant to go or return to S1''
''Stopped responding''

(The biteplate, S1, S2, and 5X refer to structures in the testing enclosure.)

It should be stressed that these observations were at levels >10 dB below those measured for TTS. Ridgway and colleagues take issue with our original statement that ''captive dolphins cannot swim away and may be more tolerant through necessity!,'' taking particular issue with the use of the exclamation point and saying that the statement misleads the reader, further stating themselves that ''swimming away was one of the criteria for behavioral response to the sound.'' Although this criticism by Ridgway and colleagues may be true in the literal interpretation, we point to their own behavioral observations stating that ''On several occasions, animals attacked the S1 biteplate upon hearing the louder S1 signal. This included backing away from the biteplate initially, then rushing towards it, biting it, thrashing around, and shaking the entire underwater platform before going to the S2 station.'' These observations would seem to us to be an overt sign of distress and, if the animal were not held in an enclosure, we question if the animal would not ''swim away'' in the sense that we had intended this comment.

The ''behavioral change'' observed in our work was a presumed reluctance to come closer to the source than approximately 1 km—the dolphins simply removed themselves from the source to a distance at which they were no longer distressed.

The choice of an appropriate behavior-change metric when deciding allowable levels for marine noise sources is, of course, open to debate.

Goold, J. C., and Fish, P. J. (**1998**). ''Broadband spectra of seismic survey air-gun emissions with reference to dolphin auditory thresholds,'' J. Acoust. Soc. Am. **103**, 2177–2184.

Ridgway S. H., Carder D. A., Smith, R. R., Kamolnick, T., Schlundt, C. E., and Elsberry, W. R. (**1997**). ''Behavioral responses and temporary shift in masked hearing threshold of bottlenose dolphins *Tursiops truncatus*, to 1-second tones of 141 to 201 dB *re* 1 μPa,'' Technical Report 1751. NRAD, RDT&RE Div., Naval Command, Control & Ocean Surveillance Center, San Diego, CA.

Comments on "Elephant hearing" [J. Acoust. Soc. Am. 104, 1122–1123 (1998)]

Caitlin O'Connell
Ecology Graduate Group, Department of Population Health and Reproduction, School of Veterinary Medicine, University of California, Davis, California 95616

Lynette A. Hart
Department of Population Health and Reproduction, School of Veterinary Medicine, University of California, Davis, California 95616

Byron T. Arnason
Tezar, Inc., P.O. Box 26235, Austin, Texas 78755-0235

Reuter, Nummela, and Hemila's recent letter hypothesized that elephants may sense ground vibrations by bone conduction and use of the massive ossicles of their middle ears. Their inner ears also are specialized for low frequencies, having reverted to a reptilian-like cochlear structure that may facilitate detection of seismic signals. Although bone conduction could be used for detection of seismic signals, mechanoreceptors with neural transmission are also a possibility. For localization of 20-Hz signals, the pinnae are limited given the large wavelengths involved, unless higher harmonics are reliably present. © *1999 Acoustical Society of America.* [S0001-4966(99)06503-0]

We would like to expand upon the comments put forward by Reuter, Nummela, and Hemila in their letter to the editor entitled "Elephant hearing,"[1] written in response to our abstract where we presented data on the existence of seismic properties of elephant low-frequency vocalizations.[2] They propose that elephants might detect these seismic signals through bone conduction, producing a differential vibration of the middle-ear ossicles in relation to the skull, thus explaining the massive ossicles of the Indian and African elephants. We would like to further discuss this possibility, along with several others. First of all, the modern elephant inner ear appears to have lost characteristics that were present in their ancestors.[3] Modern elephant ears have a primitive anatomical condition that facilitates a greater sensitivity to lower frequencies and which might also play a role in vibrational sensitivity.

The cochlear anatomy of the oldest-known proboscidean indicates that it was tuned to include responding to relatively high frequencies in contrast with the low-frequency specialization of the inner ear of modern proboscideans.[3] In addition, the lack of development of the perilymphatic foramen into the round window and cochlear canaliculus in elephants is a primitive condition, more typical of reptilian ears, and is not known in any therian mammals.[4] These reptilian features, previously found only in the embryonic stages of metatherian and eutherian mammals, persist in the adult stages of elephants and their nearest relatives the sirenians, indicating the development and subsequent loss of these features over evolutionary time.[4] In other modern mammals, the perilymphatic foramen subdivides into the round window and the cochlear canaliculus, the perilymphatic duct leaving the inner ear via the cochlear canaliculus. In elephants and sirenians, the duct leaves through the perilymphatic foramen, a derived state of the modern mammalian round window and cochlear canaliculus.[4]

This unique, primitive, reptilian feature of elephant ears also suggests that they might be suited to detect vibrational signals, as some reptiles are known to have a keen sensitivity to vibrations.[5] One other mammal that exhibits characteristics suited to the detection of low-frequency sounds is the golden mole, which has a hypertrophied malleus and also demonstrates the ability to detect seismic signals.[6] The blind mole rat has a unique ossicle and lower-jaw morphology thought to facilitate the detection of seismic signals via bone conduction,[7] although it has also been suggested that detection of seismic signals over long distances in blind mole rats might better be facilitated by somatoreceptors.[8] Some amphibians have special adaptations which may contribute to their keen sensitivity to seismic activity.[9] It is conceivable that the primitive ear of the elephant, a derived adaptation, might also facilitate the detection of seismic signals. Massive ossicles may play a role in facilitating bone conduction, as the authors suggest, but the primitive perilymphatic foramen may also play a role, as this characteristic is correlated to the huge tympanic membrane, strongly developed ossicles, and the large oval window.

We are open to the idea that bone conduction might be the mechanism used to detect seismic signals, but caution that it may not be the most parsimonious way for an elephant to receive seismic signals, especially over long distances. Although the cartilaginous pads in the foot may facilitate coupling with the ground, they may also serve to dampen vibrations. There would also be a loss due to attenuation through each joint between the foot and the ear. Mechanoreceptors in the toes or feet that are responsive to vibrations might serve as superior sensors for this modality. The elephant's trunk has mechanoreceptors highly sensitive to

vibrations,[10] raising the possibility that such receptors may also occur in the feet or toes. Elephants have two sets of nerve endings beneath their toe nails, the superior peroneal nerve and the deep peroneal nerve,[11] which may provide a more direct and possibly more efficient mode for detection of seismic signals than bone conduction.

We would also like to point out that classic work showing the use of the elephant's pinna in sound localization was tested in a frequency range of 125 Hz to 8 kHz,[12] but lower frequencies were not tested. The wavelength of a 125-Hz sound is approximately 2.75 m (given the average speed of sound in air is 344 m/s), making localization seem feasible. Localizing a 20-Hz sound with pinna, however, may not be possible given a wavelength of 17.2 m, unless higher harmonics are present. Localization of low-frequency sounds therefore might be facilitated by seismic reception of signals, the distance between the front and back legs of an elephant being much greater than the distance between the ears.

[1] T. Reuter, S. Nummela, and S. Hemila, ''Elephant hearing,'' J. Acoust. Soc. Am. **104**, 1122–1123 (1998).

[2] C. E. O'Connell, B. T. Arnason, and L. A. Hart, ''Seismic transmission of elephant vocalizations and movement,'' J. Acoust. Soc. Am. **102**(5 Pt. 2), 3124 (1997).

[3] N. Court, ''Cochlea anatomy of *Numidotherium koholense*: Auditory acuity in the oldest known proboscidean,'' Lethaia **25**(2), 211–215 (1992).

[4] M. S. Fischer, ''The unique ear of elephants and manatees (*Mammalia*): a phylogenetic paradox,'' C. R. Acad. Sci., Ser. III: Sciences de la vie **311**(4), 157–162 (1990).

[5] P. H. Hartline, ''Mid-brain responses of the auditory and somatic vibration system in snakes,'' J. Exp. Biol. **54**, 349–371 (1971).

[6] P. M. Narins, E. R. Lewis, J. U. M. Jarvis, and J. O'Riain, ''The use of seismic signals by fossorial Southern African mammals: A neuroethological gold mine,'' Brain Res. Bull. **44**, 641–646 (1997).

[7] R. Rado, M. Himelfarb, B. Arensburg, J. Terkel, and Z. Wollberg, ''Are seismic communications signals transmitted by bone conduction in the blind mole rat?'' Hearing Res. **41**(1), 23–30 (1989).

[8] E. Nevo, G. Heth, and H. Pratt, ''Seismic communication in a blind subterranean mammal: A major somatosensory mechanism in adaptive evolution underground,'' Proc. Natl. Acad. Sci. USA **88**, 1256–1260 (1991).

[9] P. M. Narins, E. R. Lewis, P. Bishop, L. Minter, and D. P. Lawson, ''Unusual middle ear adaptations in an Old World frog,'' Abstract of the 34th Animal Behav. Society Meeting 55 (1997).

[10] L. E. L. Rasmussen and B. Munger, ''The sensorineural specializations of the trunk tip (Finger) of the Asian elephant, *Elephus maximus*,'' Anatom. Record **246**, 127–134 (1996).

[11] D. Mariappa, *Anatomy and Histology of the Indian Elephant* (Indira, Oak Park, MI, 1986).

[12] R. Heffner, H. Heffner, and N. Stichman, ''The role of elephant pinna in sound localization,'' Anim. Behav. **30**, 628–629 (1982).

Erratum: "Plane-wave reflection and transmission coefficients for a three-layered elastic medium" [J. Acoust. Soc. Am. 97, 954–961 (1995)]

Michael A. Ainslie

BAeSEMA Ltd., Apex Tower, 7 High Street, New Malden, Surrey KT3 4LH, England

Equation (29) of this article is incorrect and should include additional factors of (ρ_j/ρ_i) in front of the transmission coefficient terms t_{ij}^{pp}, because the coefficients are ratios of displacements and not pressures. The corrected equation reads

$$r_{12}^{pp} \approx -r_{21}^{pp} \approx (\rho_2/\rho_1)t_{12}^{pp} - 1$$
$$\approx 1 - (\rho_1/\rho_2)t_{21}^{pp} \approx r_{12}^{(0)}.$$

The derivation of Eq. (C12) is unaffected because the density ratios cancel in the product $t_{12}^{pp}t_{21}^{pp}$.

The author also wishes to acknowledge some related work by Deschamps and Cao[1] that came to his attention after the subject article had gone to press.

[1] M. Deschamps and C. Cao, "Reflection/refraction of a solid layer by Debye's series expansion," Ultrasonics **29**, 288–293 (1991).